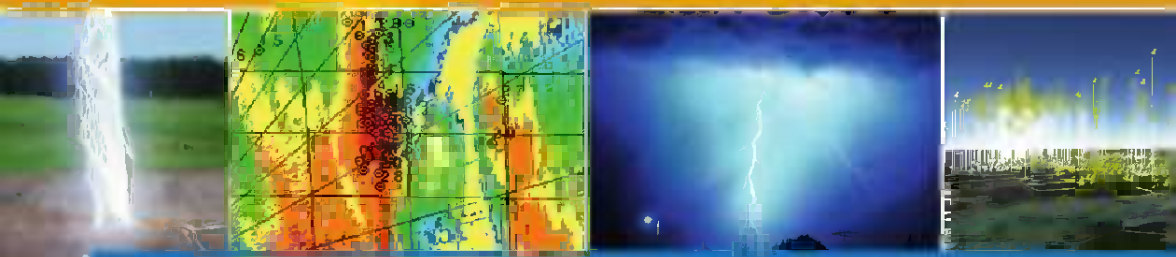


H.D. Betz · U. Schumann
P. Laroche (Eds.)



Lightning: Principles, Instruments and Applications

Review of Modern Lightning
Research

Lightning: Principles, Instruments and Applications

Hans Dieter Betz · Ulrich Schumann ·
Pierre Laroche
Editors

Lightning: Principles, Instruments and Applications

Review of Modern Lightning Research



Editors

Prof. Dr. Hans Dieter Betz
Physics Department
University of Munich
Am Coulombwall 1
85748 Garching
Germany
hans-dieter.betz@abs.de

Prof. Dr. Ulrich Schumann
Deutsches Zentrum für
Luft- und Raumfahrt
Institut für Physik der Atmosphäre
82230 Oberpfaffenhofen
Germany
ulrich.schumann@dlr.de

Prof. Dr. Pierre Laroche
Physics, Instrumentation and Sensing
Department ONERA
29 avenue de la Division
Leclerc, BP 72
92322 Chatillon
France
pierre.laroche@onera.fr

ISBN: 978-1-4020-9078-3

e-ISBN: 978-1-4020-9079-0

Library of Congress Control Number: 2008937155

© Springer Science+Business Media B.V. 2009

No part of this work may be reproduced, stored in a retrieval system, or transmitted in any form or by any means, electronic, mechanical, photocopying, microfilming, recording or otherwise, without written permission from the Publisher, with the exception of any material supplied specifically for the purpose of being entered and executed on a computer system, for exclusive use by the purchaser of the work.

Cover images (from left to right): Photograph of lightning flash triggered at camp Blanding, Florida (courtesy of University of Florida Lightning Research Group). Radar (second left) and Antenna (background) - courtesy of nowcast GmbH, Munich. Lightning @ 2008 JupiterImages Corporation. Three-dimensional view of a thunderstorm, enabled by the total-lightning capability of LINET (courtesy of nowcast GmbH, Munich).

Printed on acid-free paper

9 8 7 6 5 4 3 2 1

springer.com

Preface

Lightning is a natural phenomenon that has always produced much impact on humans and their societies, mainly because of its impressive appearance and the threats imposed on life and structures. As one consequence, modern lightning research continues to develop effective tools and procedures suited to recognize severe thunderstorms and to generate reliable alert. During the long time of past lightning investigation, much understanding of the discharge processes has been gathered and efficient detection techniques have been implemented. Today, numerous institutions all over the world deal with unraveling the numerous questions about lightning that have remained open, with much success, but as is typical for research in subjects of natural science, the complexity of the phenomena defies fast and comprehensive clarification. Meanwhile, the many competent research efforts and their impressive results render it impossible to present the gathered knowledge in a single book. Thus, the present monograph is designed to describe in 27 chapters merely some of the highlights of current research. Moreover, the topics have been selected to elucidate the lightning phenomena that are readily understandable by a general, educated readership, rather than addressing only specialists in the field. Accordingly, a more deeply interested reader is referred to the ample reports in literature.

At first, the basic phenomenon – the lightning return stroke – is introduced and in the first four chapters, some fundamental charging and discharge mechanisms are illustrated by Baba and Rakov, Rakov, Stolzenburg and Marshall, and Tessendorf. The following five chapters describe lightning detection networks in Europe (Betz et al.), Italy (Biron), Spain (Pineda and Montanya), Australia (Kuleshov et al.), and Brazil (Pinto et al.). Systems that allow mapping of lightning channels are described in two chapters (Defer and Laroche, and Lojou et al.), followed by three chapters that deal with lightning observations from space (Finke, Adamo et al., and Hamlin et al.). Dwyer explains the close coincidence between lightning and high-energy radiation. In the next three chapters the connection between lightning and higher atmosphere effects is depicted, including Schumann resonances that travel around the globe (Satori et al.), and sprites that show up high above thunderclouds (Lyons et al., Farges). The subsequent five chapters describe the relation between lightning and micro-physical parameters (Katsanos et al.), precipitation (Soula), and strong storms (Dombai, Dotzek and Price, Tuomi and Mäkelä). Three chapters are devoted

to climate (Price), and chemistry and climate (Grewe, Pickering et al.). Finally, Loboda summarizes important aspects about lightning protection.

Although current topics of importance are addressed so that the reader receives a quite comprehensive view about the status of modern lightning research, many worthwhile techniques, procedures, and associated aspects are not covered. Nevertheless, the presented material informs about our understanding of the lightning discharge, and works out the many open questions that are often fascinating and deserve future attention.

Hans D. Betz
U. Schumann
P. Laroche

Contents

1 Present Understanding of the Lightning Return Stroke	1
Yoshihiro Baba and Vladimir A. Rakov	
2 Triggered Lightning	23
Vladimir A. Rakov	
3 Electric Field and Charge Structure in Lightning-Producing Clouds .	57
Maribeth Stolzenburg and Thomas C. Marshall	
4 Characteristics of Lightning in Supercells	83
Sarah A. Tessendorf	
5 LINET – An International VLF/LF Lightning Detection Network in Europe	115
Hans D. Betz, Kersten Schmidt and Wolf P. Oettinger	
6 LAMPINET – Lightning Detection in Italy	141
Daniele Biron	
7 Lightning Detection in Spain: The Particular Case of Catalonia	161
Nicolau Pineda and Joan Montanyà	
8 Spatial Distribution and Frequency of Thunderstorms and Lightning in Australia	187
Yuriy Kuleshov, David Mackerras and Mat Darveniza	
9 Cloud-to-Ground Lightning Observations in Brazil	209
Osmar Pinto Jr., Iara R.C.A. Pinto, Marcelo M.F. Saba and Kleber P. Naccarato	

10 Observation and Interpretation of Lightning Flashes with Electromagnetic Lightning Mapper	231
Eric Defer and Pierre Laroche	
11 Nowcasting of Thunderstorms Using VHF Measurements	253
Jean-Yves Lojou, Martin J. Murphy, Ronald L. Holle and Nicholas W.S. Demetriades	
12 Optical Detection of Lightning from Space	271
Ullrich Finke	
13 Space- and Ground-Based Studies of Lightning Signatures	287
Timothy Hamlin, Kyle C. Wiens, Abram R. Jacobson, Tracy E.L. Light and Kenneth B. Eack	
14 Lightning Measurements from Satellites and Significance for Storms in the Mediterranean	309
Claudia Adamo, Steve Goodman, Alberto Mugnai and James A. Weinman	
15 Energetic Radiation and Lightning	331
Joseph R. Dwyer	
16 Schumann Resonance Signatures of Global Lightning Activity	347
Gabriella Sátori, Vadim Mushtak and Earle Williams	
17 The Meteorological and Electrical Structure of TLE-Producing Convective Storms	387
Walter A. Lyons, CCM, Mark A. Stanley, Jonathan D. Meyer, Thomas E. Nelson, Steven A. Rutledge, Timothy L. Lang and Steven A. Cummer	
18 Infrasound from Lightning and Sprites	417
Thomas Farges	
19 Lightning in the Mediterranean in Relation with Cloud Microphysical Parameters	433
Dimitrios Katsanos, Vassiliki Kotroni and Kostas Lagouvardos	
20 Lightning and Precipitation	447
Serge Soula	

21 Comparative Analysis of Flash and Radar Characteristics of Thunderstorm Cells	465
Ferenc Dombai	
22 Lightning Characteristics of Extreme Weather Events	487
Nikolai Dotzek and Colin Price	
23 Flash Cells in Thunderstorms	509
Tapio J. Tuomi and Antti Mäkelä	
24 Thunderstorms, Lightning and Climate Change	521
Colin Price	
25 Impact of Lightning on Air Chemistry and Climate	537
Volker Grewe	
26 Lightning and NO_x Production in Global Models	551
Kenneth Pickering, Heidi Huntrieser and Ulrich Schumann	
27 Lightning Protection of Structures	573
Marek Łoboda	
Color Plate Section	593
Index	633

Contributors

Claudia Adamo Institute of Atmospheric Sciences and Climate, Italian National Research Council, Roma, Italy, c.adamo@isac.cnr.it

Yoshihiro Baba Department of Electrical Engineering, Doshisha University, 1-3 Miyakodani, Tatara, Kyotanabe, Kyoto 610-0321, Japan, ybaba@mail.doshisha.ac.jp

Daniele Biron Centro Nazionale di Meteorologia e Climatologia Aeronautica, Aeroporto Militare “De Bernardis” – Via Pratica di Mare, 45, 00040 Pomezia (RM), Italy, biron@meteoam.it

Steven A. Cummer Duke University, Durham, NC 27708, USA, cummer@ee.duke.edu

Mat Darveniza School of Information Technology and Electrical Engineering, University of Queensland, and Lightning and Transient Protection Pty Ltd, Brisbane, Australia

Eric Defer LERMA-Observatoire de Paris, France, eric.defer@obspm.fr

Nicholas W. S. Demetriades Vaisala Inc, Tucson Operations, 2705 East Medina Road, Tucson, AZ 85706, USA, Nicholas.Demetriades@vaisala.com

Ferenc Dombai Hungarian Meteorological Service, Gilice tér 1. 1156, 1181 Budapest, Hungary, dombai.f@met.hu

Nikolai Dotzek Deutsches Zentrum für Luft- und Raumfahrt (DLR), Institut für Physik der Atmosphäre, Oberpfaffenhofen, 82234 Wessling, Germany, nikolai.dotzek@dlr.de; European Severe Storms Laboratory, Münchner Str. 20, 82234 Wessling, Germany, nikolai.dotzek@essl.org

Joseph R. Dwyer Department of Physics and Space Sciences, Florida Institute of Technology, Melbourne, Florida, USA, jdwyer@fit.edu

Kenneth B. Eack Langmuir Laboratory, New Mexico Institute of Mining and Technology, Socorro, New Mexico, USA

Thomas Farges Commissariat à l'Energie Atomique, Centre DAM-Ile de France, DASE, 91297 Arpajon Cedex, France, thomas.farges@cea.fr

Ullrich Finke University of Applied Sciences and Arts, Ricklinger Stadtweg 120, Hannover, Germany, ullrich.finke@fh-hannover.de

Steve Goodman Center for Satellite Application and Research, NOAA Satellite and Information Service, National Oceanic and Atmospheric Administration, Camp Springs, Maryland, USA

Volker Grewe Deutsches Zentrum für Luft- und Raumfahrt, Institut für Physik der Atmosphäre, Oberpfaffenhofen, 82234 Wessling, Germany, volker.grewe@dlr.de

Timothy Hamlin Space and Remote Sensing Group, ISR-2, Los Alamos National Laboratory, Los Alamos, New Mexico, USA, thamlin@lanl.gov

Ronald L. Holle Vaisala Inc, Tucson Operations, 2705 East Medina Road, Tucson, AZ 85706, USA, Ronald.Holle@vaisala.com

Heidi Huntrieser Deutsches Zentrum für Luft- und Raumfahrt (DLR), Institut für Physik der Atmosphäre, Oberpfaffenhofen, 82234 Wessling, Germany, heidi.huntrieser@dlr.de

Abram R. Jacobson Earth and Space Sciences, University of Washington, Seattle, Washington, USA

Dimitrios Katsanos Institute for Environmental Research and Sustainable Development, National Observatory of Athens, Greece, katsanos@meteo.noa.gr

Vassiliki Kotroni Institute for Environmental Research and Sustainable Development, National Observatory of Athens, Greece, kotroni@meteo.noa.gr

Yuriy Kuleshov National Climate Centre, Australian Bureau of Meteorology, GPO Box 1289K, Melbourne, Vic., 3001, Australia, Y.Kuleshov@bom.gov.au

Kostas Lagouvardos Institute for Environmental Research and Sustainable Development, National Observatory of Athens, Greece, lagouvar@meteo.noa.gr

Timothy L. Lang Colorado State University, Fort Collins, CO 80523, USA,
tlang@atmos.colostate.edu

Tracy E. L. Light Space and Remote Sensing Group, ISR-2, Los Alamos National Laboratory, Los Alamos, New Mexico, USA

Marek Loboda Department of High Voltage Engineering and Electrical Apparatus, Warsaw University of Technology, ul. Koszykowa 75, 00-665 Warsaw, Poland, marek.loboda@ien.pw.edu.pl

Jean-Yves Lojou Vaisala Inc, Tucson Operations, 2705 East Medina Road, Tucson, AZ 85706, USA, jean-yves.lojou@vaisala.com

Walter A. Lyons FMA Research, Inc, Fort Collins, CO 80524, USA,
walyons@frii.com

David Mackerras School of Information Technology and Electrical Engineering, University of Queensland, and Lightning and Transient Protection Pty Ltd, Brisbane, Australia

Antti Mäkelä Finnish Meteorological Institute, P.O. Box 503, 00101 Helsinki, Finland, antti.makela@fmi.fi

Thomas C. Marshall Department of Physics and Astronomy, University of Mississippi, MS 38677-1848, USA, marshall@olemiss.edu

Jonathan D. Meyer FMA Research, Inc, Fort Collins, CO 80524, USA

Joan Montanya Department of Electrical Engineering, Technological University of Catalonia, Colon 1, 08222 Terrassa, Spain, montanya@ee.upc.edu

Alberto Mugnai Institute of Atmospheric Sciences and Climate, Italian National Research Council, Roma, Italy, a.mugnai@isac.cnr.it

Martin J. Murphy Vaisala Inc, Tucson Operations, 2705 East Medina Road, Tucson, AZ 85706, USA, martin.murphy@vaisala.com

Vadim Mushtak Massachusetts Institute of Technology, Parsons Laboratory, Cambridge, Massachusetts, USA, vadimcm@gmail.com

Kleber P. Naccarato Atmospheric Electricity Group – ELAT, Brazilian Institute of Space Research (INPE), S.J. Campos, Brasil, kleberp@dge.inpe.br

Thomas E. Nelson FMA Research, Inc, Fort Collins, CO 80524, USA

Wolf P. Oettinger nowcast GmbH, 81377 Munich, Germany

Kenneth Pickering NASA Goddard Space Flight Center, Laboratory for Atmospheres, Greenbelt, MD, USA, Kenneth.E.Pickering@nasa.gov

Nicolau Pineda Servei Meteorològic de Catalunya (Meteorological Service of Catalonia) C/Berlin 38–46, 08029 Barcelona, Spain, npineda@meteocat.com

Iara R.C.A. Pinto Atmospheric Electricity Group – ELAT, Brazilian Institute of Space Research (INPE), S.J. Campos, Brasil, iara@dge.inpe.br

Osmar Pinto Jr. Atmospheric Electricity Group – ELAT, Brazilian Institute of Space Research (INPE), S.J. Campos, Brasil, osmar@dge.inpe.br

Colin Price Tel Aviv University, Department of Geophysics and Planetary Science, Ramat Aviv, 69978, Israel, cprice@flash.tau.ac.il

Vladimir A. Rakov Department of Electrical and Computer Engineering, University of Florida, 553 Engineering Building #33, Gainesville, FL 32611-6130, USA, rakov@ece.ufl.edu

Steven A. Rutledge Colorado State University, Fort Collins, CO 80523, USA, Steven.Rutledge@colostate.edu

Marcelo M.F. Saba Atmospheric Electricity Group – ELAT, Brazilian Institute of Space Research (INPE), S.J. Campos, Brasil, msaba@dge.inpe.br

Gabriella Sátori Geodetic and Geophysical Research Institute, HAS, Csatkai u. 6–8, 9400 Sopron, Hungary, satori@ggki.hu

Kersten Schmidt Faculty of Physics, University of Munich, 85748 Garching, Germany

Serge Soula Université de Toulouse; UPS; LA (Laboratoire d’Aérologie); 14 avenue Edouard Berlin; F-31400 Toulouse CNRS; LA (Laboratoire d’Aérologie); F-31400 Toulouse

Mark A. Stanley FMA Research, Inc, Fort Collins, CO 80524, USA

Maribeth Stolzenburg Department of Physics and Astronomy, University of Mississippi, MS 38677-1848, USA, mstolzen@olemiss.edu

Sarah A. Tessendorf Research Applications Laboratory, National Center for Atmospheric Research, P.O. Box 3000, Boulder, CO 80307, USA, saraht@ucar.edu

Tapio J. Tuomi Finnish Meteorological Institute, P.O. Box 503, 00101 Helsinki, Finland, tapio.tuomi@fmi.fi

James A. Weinman Department of Atmospheric Sciences, University of Washington, Seattle, Washington, USA

Kyle C. Wiens Department of Geosciences, Texas Tech University, Lubbock, Texas, USA

Earle Williams Parsons Laboratory, Massachusetts Institute of Technology, Cambridge, Massachusetts, USA, earlew@ll.mit.edu

Chapter 1

Present Understanding of the Lightning Return Stroke

Yoshihiro Baba and Vladimir A. Rakov

Abstract In this chapter, a general picture of downward negative lightning discharges that take place between cloud and ground are described. Then, first and subsequent return strokes, which are the optically brightest processes and produce the most intense wideband electromagnetic signatures in the overall cloud-to-ground lightning discharge, referred to as the lightning flash, are presented. The first return stroke follows the path of initial downward-progressing stepped leader emerging from the cloud, and subsequent return strokes are usually initiated by dart leaders propagating downward along channels traversed by the preceding stroke(s). Representative models of lightning return strokes are also described.

Keywords Lightning flash · Return stroke · First stroke · Subsequent stroke · Stepped leader · Dart leader · Lightning return-stroke model

1.1 Introduction

Lightning discharges that take place between cloud and ground, referred to as cloud-to-ground lightning discharges, are classified, based on the polarity of the charge effectively transferred to ground and the direction of the initial leader, into four types. These are downward negative lightning, upward negative lightning, downward positive lightning, and upward positive lightning. The leader is a process that precedes the return stroke. It creates a conducting path between the cloud charge source and ground, and deposits charge along this path. It is believed that downward negative lightning discharges account for about 90% of all cloud-to-ground lightning, and that about 10% of cloud-to-ground lightning are downward positive lightning discharges. It is thought that upward lightning discharges occur only from tall objects (higher than 100 m or so) or from objects of moderate height located

Y. Baba (✉)

Department of Electrical Engineering, Doshisha University, 1-3 Miyakodani, Tatara,
Kyotanabe, Kyoto 610-0321, Japan
e-mail: ybaba@mail.doshisha.ac.jp

on mountain tops. Note that terms, “lightning”, “the lightning discharge”, and “the lightning flash” are used interchangeably to refer to the overall lightning discharge process.

In this chapter, only downward negative lightning discharges are considered. This chapter is organized as follows. In Section 1.2, a general picture of downward negative lightning discharges to ground is presented. In Section 1.3, first return strokes that follow the path of initial downward-progressing stepped leader emerging from the cloud, and subsequent return strokes that are usually initiated by dart leaders propagating downward along channels conditioned by the preceding strokes are discussed. In Section 1.4, representative models of lightning return strokes are described.

1.2 General Picture of Downward Negative Lightning Discharges to Ground

In this section, a general picture of downward negative lightning flashes to ground is presented. Figure 1.1a and b schematically show still and time-resolved images of a downward negative lightning flash containing three strokes, respectively. Figure 1.1c shows the corresponding current at the channel base. In Figure 1.1b and c, time advances from left to right. Each of the three strokes is composed of a downward-moving process termed a leader and an upward-moving process termed a return stroke. The leader creates a conducting path between the cloud charge source and ground, and deposits negative charge along the path. The return stroke traverses the leader path upward from ground to the cloud charge source and neutralizes the negative leader charge. Thus, both leader and return-stroke processes contribute to transporting negative charge from the cloud to ground. The leader initiating the

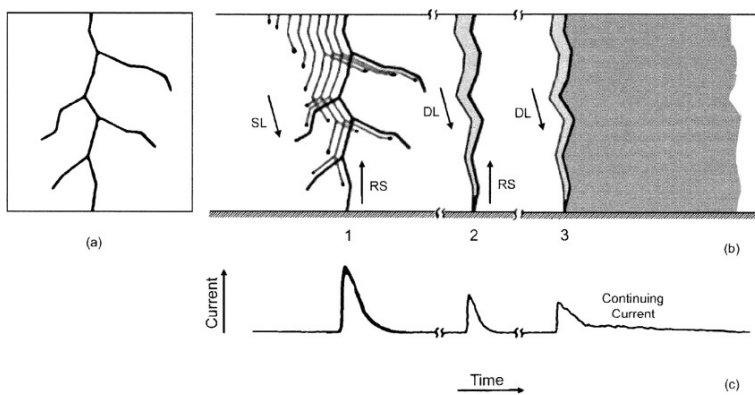


Fig. 1.1 Diagram showing the luminosity of a downward negative lightning flash to ground containing three strokes and the corresponding current at the channel base: (a) still image, (b) time-resolved image, and (c) channel-base current. Adapted from Rakov and Uman (2003)

first return stroke develops in virgin air, and appears to be an optically intermittent process. Therefore, it is termed “stepped leader”. The stepped-leader branches are directed downward, which indicates that the stepped leader (and the flash) is initiated in the cloud and develops downward. The leaders initiating the two subsequent return strokes in Fig. 1.1 move continuously, as a downward-moving dart, along the pre-conditioned path of the preceding return stroke or strokes. Hence, these leaders are termed “dart leaders”. Note that each downward negative lightning flash typically contains three to five strokes.

In the following, a sequence of the processes involved in a typical downward negative lightning flash is presented in more detail. The source of lightning is usually a thundercloud. The generally accepted features of the charge structure in the thundercloud include a net positive charge near the top, a net negative charge below it, and an additional positive charge at the bottom. The stepped leader is preceded by an in-cloud process called the initial breakdown or preliminary breakdown. There is no consensus on the mechanism of the initial breakdown. It can be viewed as a discharge process between the negative and lower positive charge regions, but it can also involve a sequence of channels extending in random directions from the cloud charge source. One of these events (in the case of multiple channels) evolves into the stepped leader which is a negatively charged plasma channel that bridges the cloud charge source and the ground. The stepped leader extends toward ground at an average speed of 2×10^5 m/s in a series of discrete steps, with each step being typically 1 μ s in duration and tens of meters in length, with the interval between steps being 20–50 μ s (e.g., Rakov and Uman 2003). The peak value of the current pulse associated with an individual step is inferred to be 1 kA or greater. Several coulombs of negative charge are distributed along the stepped-leader channel. The stepped-leader duration is typically some tens of milliseconds, and the average leader current is some hundreds of amperes. The stepped-leader channel is likely to consist of a thin core that carries the longitudinal channel current, surrounded by a corona sheath whose diameter is typically several meters.

As the stepped leader approaches ground, the electric field at the ground surface or objects increases until it exceeds the critical value for the initiation of upward connecting leaders. The initiation of an upward connecting leader from ground in response to the descending stepped leader marks the beginning of the attachment process. The process by which the extending plasma channels of the upward and downward leaders make contact, after forming common streamer zone, is called the break-through phase or final jump. The break-through phase can be viewed as a switch-closing operation that serves to launch two return-stroke waves from the point of junction between the two plasma channels. The length of an upward connecting leader involved in a first stroke is some tens of meters if that leader is launched from the ground, and it can be several hundred meters long if it is initiated from a tall object.

The return stroke serves to neutralize the leader charge, although it may not neutralize all the leader charge or may deposit some excess positive charge onto the leader channel and into the cloud charge source region. The speed of the return stroke, averaged over the visible channel, is typically between one-third and one-half

the speed of light (e.g., Rakov 2007). The speed decreases with increasing height, dropping abruptly after passing each major branch. The first return-stroke current measured at ground rises to an initial peak of about 30 kA in some microseconds and decays to half-peak value in some tens of microseconds while exhibiting a number of subsidiary peaks, probably associated with the branches (e.g., Rakov and Uman 2003). This impulsive component of current may be followed by a current of some hundreds of amperes lasting for some milliseconds. The return stroke effectively lowers to ground the several coulombs of charge originally deposited on the stepped-leader channel, including that on all the branches. The high-current return-stroke wave rapidly heats the channel to a peak temperature near or above 30,000 K and creates a channel pressure of 10 atm or more (e.g., Rakov and Uman 2003), which results in channel expansion, intense optical radiation, and an outward propagating shock wave that eventually becomes the thunder.

When the first return stroke ceases, the flash may end. In this case, the lightning is called a single-stroke flash. However, more often the residual first-stroke channel is traversed downwards by a leader that appears to move continuously, a dart leader. During the time interval between the end of the first return stroke and the initiation of a dart leader, J and K-processes occur in the cloud. The J-process is often viewed as a relatively slow positive leader extending from the flash origin into the negative charge region, the K-process then being a relatively fast “recoil streamer” that begins at the tip of the positive leader and propagates toward the flash origin. Both the J-processes and the K-processes in cloud-to-ground discharges serve to transport additional negative charge into and along the existing channel, although not all the way to ground. In this respect, K-processes may be viewed as attempted dart leaders. The processes that occur after the only stroke in single-stroke flashes and after the last stroke in multiple-stroke flashes are sometimes termed final (F) processes. These are similar, if not identical, to J-processes.

The dart leader progresses downward at a typical speed of 10^7 m/s, typically ignores the first stroke branches, and deposits along the channel a total charge of the order of 1 coulomb (e.g., Rakov and Uman 2003). The dart-leader current peak is about 1 kA. Some leaders exhibit stepping near ground while propagating along the path traversed by the preceding return stroke, these leaders being termed dart-stepped leaders. Additionally, some dart or dart-stepped leaders deflect from the previous return-stroke path, become stepped leaders, and form a new termination on the ground.

When a dart leader or dart-stepped leader approaches the ground, an attachment process similar to that described for the first stroke takes place, although it probably occurs over a shorter distance and consequently takes less time, the upward connecting-leader length being of the order of some meters. Once the bottom of the dart leader or dart-stepped leader channel is connected to the ground, the second (or any subsequent) return-stroke wave is launched upward and serves to neutralize the leader charge. The subsequent return-stroke current at ground typically rises to a peak value of 10–15 kA in less than a microsecond and decays to half-peak value in a few tens of microseconds. The upward propagation speed of such a subsequent return stroke is similar to or slightly higher than that of the first stroke (e.g.,

Rakov 2007). Note that due to the absence of branches the speed variation along the channel for subsequent return strokes does not exhibit abrupt drops. The radius of return-stroke channels is about 3 cm, the conductivity is about 10^4 S/m, and the resistance per unit length is about $0.035 \Omega/\text{m} [= 1/(10^4 \times \pi \times 0.03^2)]$ (Rakov 1998).

The impulsive component of the current in a subsequent return stroke is often followed by a continuing current that has a magnitude of tens to hundreds of amperes and a duration up to hundreds of milliseconds. Continuing currents with a duration in excess of 40 ms are traditionally termed long continuing currents. Between 30 and 50 percent of all negative cloud-to-ground flashes contain long continuing currents. The source for continuing current is the cloud charge, as opposed to the charge distributed along the leader channel, the latter charge contributing to at least the initial few hundred microseconds of the return-stroke current observed at ground. Continuing current typically exhibits a number of superimposed surges that rise to a peak in some tens to hundreds of microseconds, the peak being generally in the hundreds of amperes range but occasionally in the kiloamperes range. These current surges are associated with enhancements in the relatively faint luminosity of the continuing-current channel and are called M-components.

The time interval between successive return strokes in a flash is usually several tens of milliseconds, although it can be as large as many hundreds of milliseconds if a long continuing current is involved and as small as one millisecond or less. The total duration of a flash is typically some hundreds of milliseconds, and the total charge lowered to ground is some tens of coulombs. The overwhelming majority of negative cloud-to-ground flashes contain more than one stroke. Although the first stroke is usually a factor 2 to 3 larger than a subsequent stroke, about one-third of multiple stroke flashes have at least one subsequent stroke that is larger than the first stroke in the flash (e.g., Rakov et al. 1994).

1.3 First and Subsequent Lightning Return Strokes

In this section, parameters of lightning return-stroke currents, return-stroke wave-front propagation speeds, and generated electromagnetic fields are presented.

1.3.1 *Lightning Return-Stroke Current*

The most complete characterization of the lightning return stroke in the downward negative flash has been given by Berger et al. (1975). This characterization is based on oscillograms of current measured using resistive shunts installed at the tops of two 70-m high towers on the summit of a 915-m high mountain (above sea level). Since the mountain contributed to the electric field enhancement near the tower tops, the effective heights of the towers are considered to be several times greater than the actual tower heights. Therefore, the majority of lightning strikes to the towers was of the upward type. Here, only return strokes in downward negative flashes are

considered. It is important to note that Berger et al.'s direct current measurements for downward flashes are unique in that they were obtained over a period of more than 20 years, were continuous (that is, covering all processes in the flash), and were often accompanied by time-resolved optical records.

Figure 1.2 shows, on two time scales, A and B, the average impulsive current waveshapes for negative first and subsequent strokes. The rising portion of the first-stroke waveform has a characteristic concave shape. Figure 1.3 shows the cumulative statistical distributions (the solid curves) of return-stroke peak currents for (1) negative first strokes, (2) negative subsequent strokes, and (3) positive strokes (each of which was the only stroke in a flash), the latter not being further discussed here. These empirical results are approximated by log-normal distributions (the

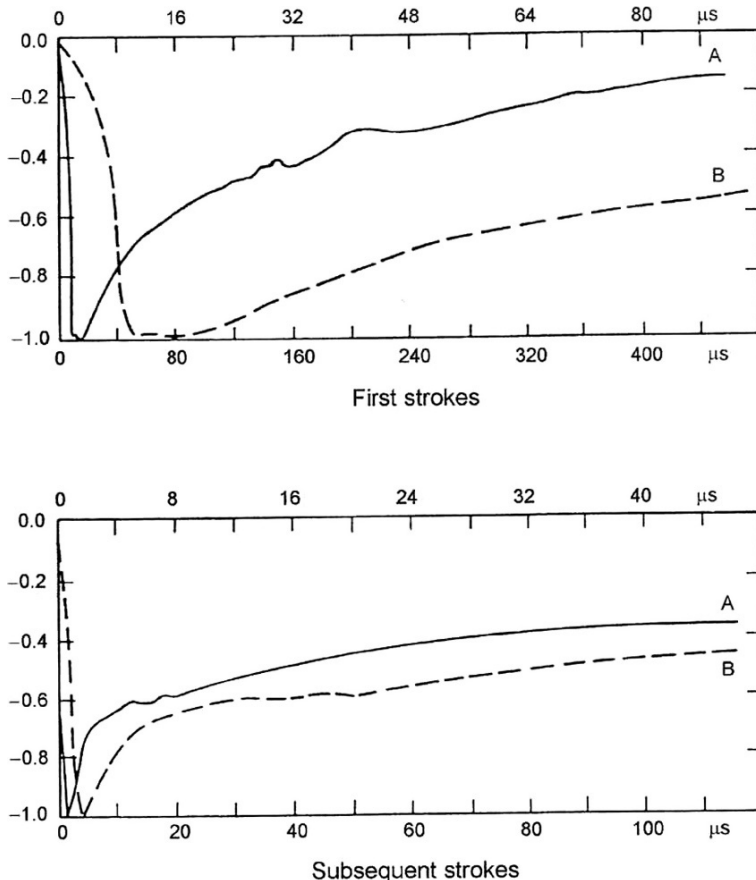


Fig. 1.2 Average negative first- and subsequent-stroke current each shown on two time scales, A and B. The lower time scales (**a**) correspond to the solid-line curves, while the upper time scales (**b**) correspond to the broken-line curves. The vertical scale is in relative units, the peak values being equal to negative unity. Adapted from Berger et al. (1975)

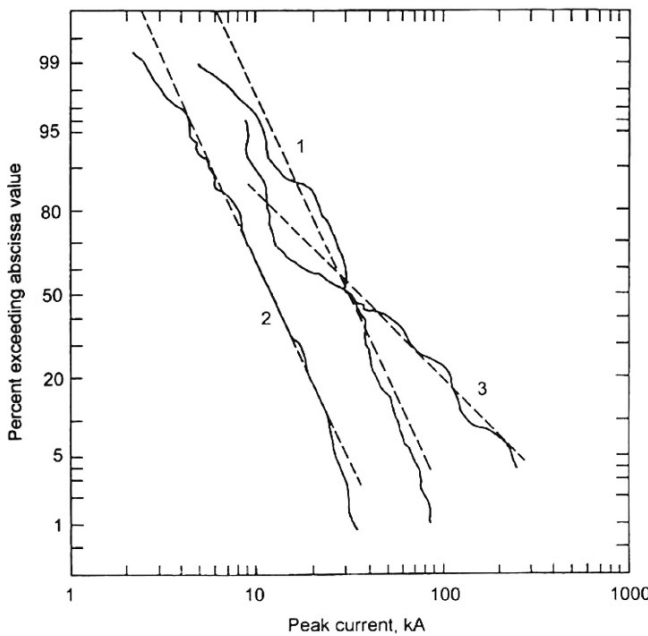


Fig. 1.3 Cumulative statistical distributions of return-stroke peak current from directr measurements at tower top (solid-line curves) and their log-normal approximations (broken lines) for (1) negative first strokes, (2) negative subsequent strokes, and (3) positive first (and only) strokes, as reported by Berger et al. (1975)

broken lines) and are given as they appear on cumulative-probability-distribution graph, on which a Gaussian cumulative distribution appears as a slanted straight line, the horizontal scale being logarithmic to base 10. The ordinate gives the percentage of peak currents exceeding the corresponding value on the horizontal axis. The lightning peak current distributions for negative first and subsequent strokes shown in Fig. 1.3 are characterized by 95, 50, and 5 percent values based on the log-normal approximations given in Table 1.1, which contains a number of other parameters derived from the current oscillograms. Note from Fig. 1.3 and Table 1.1 that the median return-stroke current peak for first strokes is two to three times higher than that for subsequent strokes. Also, negative first strokes transfer about a factor of four larger total charge than do negative subsequent strokes. On the other hand, subsequent return strokes are characterized by three to four times higher current maximum rate of rise. Note that the smallest measurable time in Berger et al.'s oscillograms was 0.5 μ s versus the 95 percent value of 0.22 μ s for the front duration for subsequent strokes in Table 1.1, which is a prediction of the log-normal approximation. Only a few percent of negative first strokes are expected to exceed 100 kA. The action integral in Table 1.1 represents the energy that would be dissipated in a 1- Ω resistor if the lightning current were to flow through it.

Table 1.1 Parameters of downward negative lightning derived from channel-base current measurements

Parameters	Units	Sample size	Percentage exceeding tabulated value		
			95%	50%	5%
Peak current (minimum 2 kA)	kA				
First stroke		101	14	30	80
Subsequent stroke		135	4.6	12	30
Charge (total charge)	C				
First stroke		93	1.1	5.2	24
Subsequent strokes		122	0.2	1.4	11
Complete flash		94	1.3	7.5	40
Impulse charge (excluding continuing current)	C				
First strokes		90	1.1	4.5	20
Subsequent strokes		117	0.22	0.95	4
Front duration (2 kA to peak)	μs				
First strokes		89	1.8	5.5	18
Subsequent strokes		118	0.22	1.1	4.5
Maximum dI/dt	kA μs ⁻¹				
First strokes		92	5.5	12	32
Subsequent strokes		122	12	40	120
Stroke duration (2 kA to half peak value on the tail)	μs				
First strokes		90	30	75	200
Subsequent strokes		115	6.5	32	140
Action integral	A ² s				
First strokes		91	6.0 × 10 ³	5.5 × 10 ⁴	5.5 × 10 ⁵
Subsequent strokes		88	5.5 × 10 ²	6.0 × 10 ³	5.2 × 10 ⁴
Time interval between strokes	ms	133	7	33	150
Flash duration	ms				
All flashes		94	0.15	13	1100
Excluding single-stroke Flashes		39	31	180	900

Source: Adapted from Berger et al. (1975).

1.3.2 Lightning Return-Stroke Luminosity Profile and Propagation Speed

Since the variation in current along the channel is impossible to measure directly, the luminosity profile along the channel is generally viewed as representative of the current variation.

When a first return stroke wavefront reaches a branch, there is usually a brightening of the channel below the point, this brightening being termed a branch component. Branch components are thought to be responsible for the secondary maxima

usually observed in the channel base current waveforms. Because of the lack of branches, the light profile along a subsequent return-stroke channel is relatively simple, usually showing a gradual intensity decay with height. Jordan et al. (1997) found that in two out of three events the return-stroke luminosity peak at 480 and 1400 m had decayed to, respectively, 70–75 percent and 25–30 percent of its value at the bottom of the channel and in the third event to, respectively, 90–95 percent and about 70 percent of the channel-bottom value.

Besides a decrease in peak value, the return-stroke light pulses also exhibit an appreciable increase in risetime with increasing height. Jordan et al. (1997) reported that the 20–80 percent risetime increased from 1.5 to 4.0 μs (mean values) as the return stroke propagated from ground to the cloud base at about 1400 m. Note that Wang et al. (2005) found from their comparative analysis for the channel-base current and light waveforms of rocket-triggered lightning strokes that the current and light signals had a remarkable linear relationship in their rising portions although the linearity disappeared after the peaks.

The average propagation speed of negative first or subsequent return stroke below the lower cloud boundary is typically between one-third and one-half of the speed of light (Rakov 2007). The speed usually decreases with height for both first and subsequent return strokes. There exists experimental evidence that the negative return-stroke speed may vary non-monotonically along the channel, initially increasing and then decreasing with increasing height. Note that the often assumed relationship between the return-stroke speed and peak current is generally not supported by experimental data.

1.3.3 Electric and Magnetic Fields Produced by Lightning Return Strokes

Typical vertical electric and horizontal magnetic field waveforms at distances ranging from 1 to 200 km for both first and subsequent strokes were published by Lin et al. (1979). These waveforms are drawings based on many measurements acquired in Florida and reproduced in Fig. 1.4. Four features have been identified by Nucci et al (1990) in these waveforms, which include (1) a sharp initial peak that varies approximately as the inverse distance beyond a kilometer or so in both electric and magnetic fields; (2) a slow ramp following the initial peak and lasting in excess of 100 μs for electric fields measured within a few tens of kilometers; (3) a hump following the initial peak in magnetic fields within a few tens of kilometers, the maximum of which occurs between 10 and 40 μs ; and (4) a zero crossing within tens of microseconds of the initial peak in both electric and magnetic fields at 50–200 km.

The higher-frequency components of the return-stroke fields are preferentially attenuated in propagating over a finitely conducting earth (e.g., Lin et al. 1979; Cooray and Lundquist 1983). Lin et al. (1979) reported from two-station measurements that normalized field peaks were typically attenuated by 10 percent in propagating

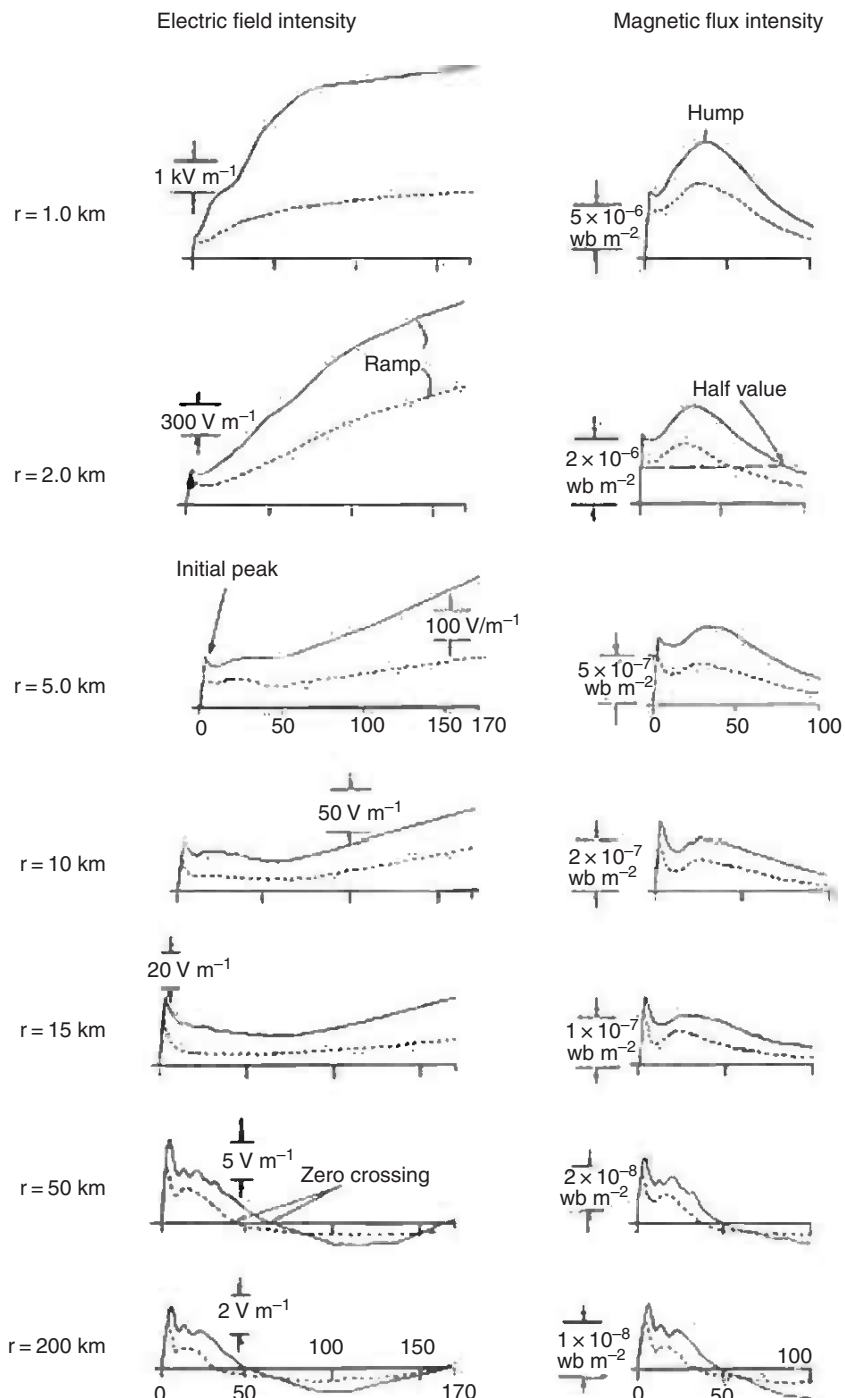


Fig. 1.4 Typical vertical electric field intensity (left column) and azimuthal magnetic flux density (right column) waveforms for first (solid line) and subsequent (broken line) return strokes at distances of 1, 2, 5, 10, 15, 50, and 200 km. The scales in the third row of diagrams from the top and in the bottom row of diagrams are in μs . Adapted from Lin et al. (1979)

over 50 km of Florida soil and 20 percent in propagating over 200 km. As to field risetimes, they are increased by an amount of order 1 μs in propagating 200 km across Florida soil for typical strokes (Uman et al. 1976).

1.4 Modeling of Lightning Return Strokes

In this section, classification of lightning return-stroke models is given and so-called engineering models are discussed. General equations for computing the vertical electric field and azimuthal magnetic field due to a lightning return-stroke current wave are presented.

1.4.1 Classification of Lightning Return-Stroke Models

Lightning return-stroke models are needed in studying lightning effects on various objects and systems and in characterizing the lightning electromagnetic environment. Rakov and Uman (1998), based on governing equations, have categorized return-stroke models into four classes: gas dynamic models, electromagnetic models, distributed-circuit models, and “engineering” models.

Gas dynamic models are primarily concerned with the radial evolution of a short segment of the lightning channel and its associated shock wave. These models typically involve the solution of three gas dynamic equations representing the conservation of mass, momentum, and energy, coupled to two equations of state with the input being an assumed channel current versus time (e.g., Plooster 1971). Principal model outputs include temperature, pressure, and mass density as a function of radial coordinate and time.

Electromagnetic models are based on a lossy, thin-wire antenna approximation to the lightning return-stroke channel. In this class of models, Maxwell’s equations are solved to yield the distribution of current along the lightning channel using numerical techniques. These models allow a self-consistent full-wave solution for both current distribution along the lightning channel and associated electromagnetic fields. They have attracted considerable attention during the last ten years or so (e.g., Baba and Rakov 2007).

Distributed-circuit models of the lightning return stroke usually consider the lightning channel as an $R-L-C$ transmission line (e.g., Gorin 1985; Rakov and Uman 1998), where R , L , and C are series resistance, series inductance, and shunt capacitance, all per unit length, respectively. In an $R-L-C$ transmission line model, voltage and current are the solutions of the telegrapher’s equations.

Engineering models prescribe the longitudinal current along the lightning channel, based on the existing knowledge on evolution of return-stroke waveform as it propagates from ground toward the cloud (e.g., Nucci et al. 1990; Rakov and Uman 1998). The return-stroke waveform speed in these models can be set arbitrarily since it is one of the input parameters.

Note that the so-called hybrid electromagnetic/circuit (HEM) model (e.g., Visacro and Silveira 2004), which employs electric scalar and magnetic vector potentials for taking account of electromagnetic coupling but is formulated in terms of circuit quantities, voltages and currents, occupies an intermediate place between electromagnetic and distributed-circuit models.

1.4.2 Representative Engineering Return-Stroke Models

Out of four or five classes of lightning return-stroke models, the class of engineering models is most widely used. An engineering return-stroke model is an equation that relates the longitudinal channel current $I(z',t)$ at any height z' and any time t to the current $I(0,t)$ at the channel origin ($z' = 0$). A number of simple engineering models can be expressed by the following equation:

$$I(z', t) = u(t - z'/v_f) P(z', t) I(0, t - z'/v) \quad (1.1)$$

where u is the Heaviside function equal to unity for $t \geq z'/v_f$ and zero otherwise, $P(z',t)$ is the height- and time-dependent current attenuation factor, v_f is the upward-propagating front speed, and v is the current-wave propagation speed. Table 1.2 summarizes $P(z',t)$ and v for five engineering models, the transmission-line model (TL) (Uman and McLain 1969); the modified transmission-line model with linear current decay with height (MTLL) (Rakov and Dulzon 1987); the modified transmission-line model with exponential current decay with height (MTLE) (Nucci et al. 1988); the modified transmission-line model with linear current decay and dispersion with height (MTLD) (Baba and Ishii 2002); and the traveling current source model (TCS) (Heidler 1985). The Diendorfer and Uman model (DU) (Diendorfer

Table 1.2 Height- and time-dependent current attenuation factor $P(z',t)$ and the current-wave propagation speed v in Eq. (1.1), $I(z', t) = u(t-z'/v_f)P(z', t)I(0, t-z'/v)$, for five simple engineering return-stroke models. Note that $I(z',t)$ is the longitudinal channel current at any height z' and any time, $I(0,t)$ is the longitudinal current at the channel origin ($z' = 0$), v_f is the upward-propagating front speed, and u is the Heaviside function equal to unity for $t \geq z'/v_f$ and zero otherwise

Model	$P(z',t)$	v
TL (Uman and McLain 1969)	1	v_f
MTLL (Rakov and Dulzon 1987)	$1 - z'/H$	v_f
MTLE (Nucci et al. 1988)	$\exp(-z/\lambda)$	v_f
MTLD (Baba and Ishii 2002)	$\left[1 - \exp\left(-\frac{t - z'/v_f}{\tau} \frac{\lambda_p}{z'}\right) \right] \left(1 - \frac{z'}{H}\right)$	v_f
TCS (Heidler 1985)	1	$-c$

H is the total channel height for the MTLL model, λ is the current decay constant for the MTLE model (it is assumed to be $\lambda = 2000$ m in Nucci et al. (1998)), and c is the speed of light. For the MTLD model, $\tau(z'/\lambda_p)$ controls the risetime of the channel current (the risetime increases with increasing the height z'), and $(1-z'/H)$ controls the attenuation of the channel current. Baba and Ishii (2002) assumed that $\tau = 0.3$ μ s, $\lambda_p = 1000$ m.

and Uman 1990) can be expressed by the following extension of Eq. (1.1) for the TCS model ($P(z',t) = 1$, $v = -c$):

$$I(z', t) = u \left(t - \frac{z'}{v_f} \right) \left[I \left(0, t + \frac{z'}{c} \right) - I \left(0, \frac{z'}{v_f} + \frac{z'}{c} \right) \exp \left(-\frac{t - z'/v_f}{\tau_D} \right) \right] \quad (1.2)$$

where τ_D is the discharge time constant. It is usually assumed that $\tau_D = 0.6 \mu\text{s}$ or so. Note that Diendorfer and Uman (1990) used a current waveform given as the sum of two currents, each of which is given by Eq. (1.2) but has a different discharge constant, in order to match model-predicted fields with measured fields. One of the two time constants is for breakdown current and its value is assumed to be $0.6 \mu\text{s}$, and the other is for corona current and its value is assumed to be $5 \mu\text{s}$ (Diendorfer and Uman 1990).

The TL, MTLL, MTLE, and MTLD models are the TL-type models, and the TCS and DU models are the TCS-type models. The TL-type models can be viewed as incorporating a current source at the channel base. This is why they are also referred to as lumped-source (LS) models. The source injects a specified current wave into the channel, that wave propagating upward without either dispersion or attenuation in the TL model, without dispersion but with specified attenuation in the MTLL and MTLE models, or with both specified dispersion and attenuation in the MTLD model. The conceptual illustration for the TL model and waveforms of current at different heights along the vertical lightning channel calculated for the TL model are shown in Figs. 1.5a and 1.6, respectively.

The TCS-type models can be viewed as incorporating a current source at the wavefront, which moves upward with speed v_f and injects a current wave into the

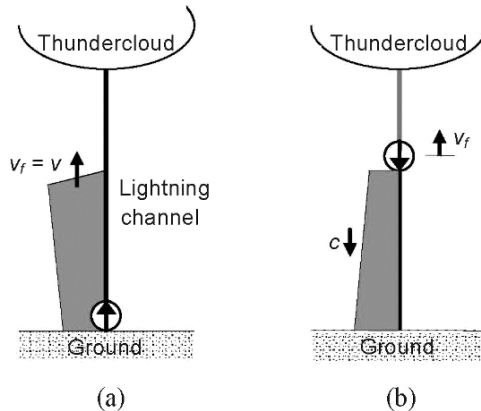


Fig. 1.5 Conceptual illustrations of (a) the TL model and (b) the TCS model. In the TL model, a current source incorporated at the channel base injects a specified current wave into the channel, and the current wave propagates upward with speed $v = v_f$ without either dispersion or attenuation. In the TCS model, a current source at the wavefront moves upward with speed v_f , and injects a current wave into the channel that propagates downward at speed c

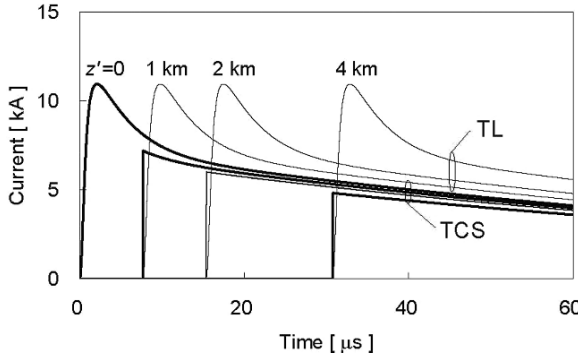


Fig. 1.6 Waveforms of current at different heights along the vertical lightning return-stroke channel calculated for the TL and TCS models. The channel-base current waveform, $I(0, t)$, is characterized by a magnitude of 11 kA and a 10-to-90% risetime of 1 μ s. The return-stroke front speed is set to $v_f = 130\text{m}/\mu\text{s}$. Current in the TCS model exhibits a discontinuity at the upward-moving wavefront

channel that propagates downward at speed c (see Fig. 1.5b). In the TCS model, current at a given channel section turns on instantaneously as this section is passed by the front, and therefore this model exhibits an inherent discontinuity at the upward-moving wavefront. In the DU model (see Eq. (1.2)), the first term is the same as the downward-propagating current in the TCS model, and the second term is an opposite polarity current which rises instantaneously to the value equal in magnitude to the current at the wavefront and then decays exponentially with a time constant τ_D . The second current component in the DU model eliminates any current discontinuity at the wavefront. The conceptual illustration for the TCS model and waveforms of current at different heights along the vertical lightning channel calculated for the TCS model are shown in Figs. 1.5b and 1.6, respectively. TCS-type models can be also represented by current sources distributed along the lightning channel and progressively activated by upward-moving return-stroke front. Therefore, they can be viewed as distributed-source (DS) models, as suggested by Maslowski and Rakov (2007).

Cooray (2003) showed that any LS model can be formulated in terms of sources distributed along the lightning channel. This has been previously demonstrated for one model (MTLE) by Rachidi and Nucci (1990). The approach suggested by Cooray (2003) was used by Rachidi et al. (2002) to generalize five engineering models in order to take into account a tall strike object. It has been recently shown by Maslowski and Rakov (2007) that any engineering return-stroke model can be expressed using an appropriate continuity equation in terms of either lumped or distributed current sources with the resultant longitudinal current distribution (and total charge density distribution) along the channel being the same. This property can be viewed as the duality of engineering models. Lumped-source (LS)-type and distributed-source (DS)-type models are illustrated in Fig. 1.7a and b, respectively. Both longitudinal (upward or downward propagating wave) and radial corona (sinks or sources) currents are shown in this Figure. The conversion alters the actual corona

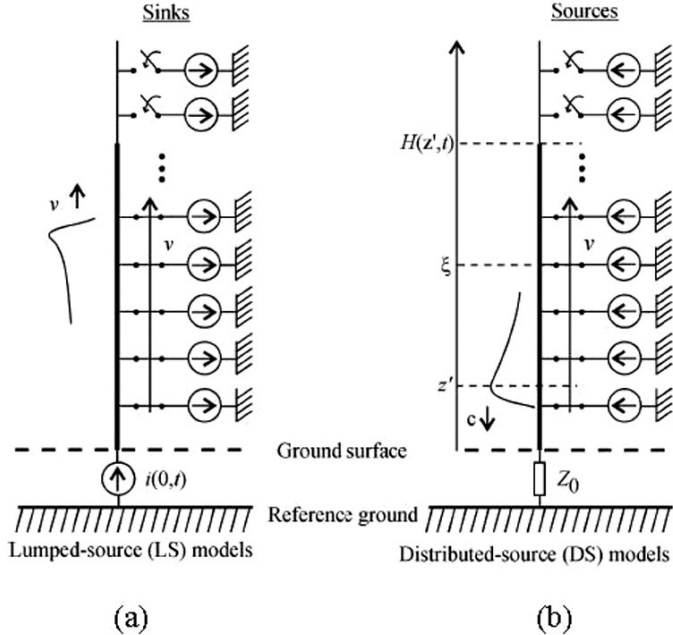


Fig. 1.7 Schematic illustration of engineering return-stroke models that employ (a) a lumped current source at the lightning channel base (LS-type models) and (b) distributed current sources along the channel (DS-type models). v is the upward return-stroke front speed, c is the speed of light, and Z_0 is the characteristic impedance of the lightning channel (matched conditions at ground are implied in DS-type models). LS-type models with longitudinal-current decay with height imply current sinks distributed along the channel, as shown in (a). Adapted from Maslowski and Rakov (2007)

current (if any) of the model. For LS-type models, the actual corona current is unipolar and directed radially out of the channel core, while for DS-type models it is unipolar and directed into the channel core. For LS-type models converted to DS-type models, the corona current is the sum of the negated actual corona current and a fictitious corona current, the latter being bipolar. For the TL model (no longitudinal-current attenuation with height) expressed in terms of distributed sources, there is only a fictitious bipolar corona current component. Conversion of the TCS model to its equivalent LS-type model involves replacement of the actual, unipolar corona current with a fictitious one, the latter current being bipolar near the channel base and unipolar at higher altitudes.

Baba et al. (2004) proposed a modification to the DU model, which could reproduce all the four features identified in measured waveforms and listed in Section 1.3.3 and one additional feature, a characteristic flattening within 15 μs or so of vertical electric fields observed at tens to hundreds of meters from triggered lightning strokes (Rakov and Uman 1998). This model (modified DU model with additional decay, referred to as the MDUD model here) is expressed by

$$I_{MDUD}(z', t) = I_{DU}(z', t) [1 - \exp(-(\lambda_d/z')^n)] \quad (1.3)$$

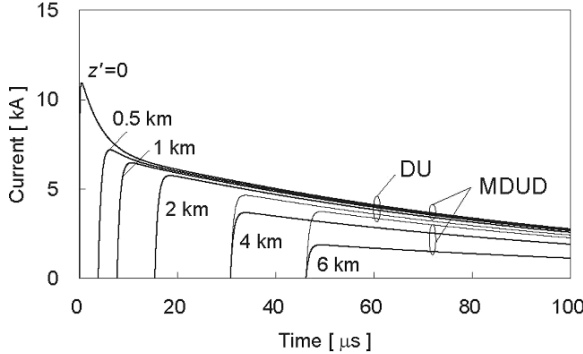


Fig. 1.8 Waveforms of current at different heights along the vertical lightning channel calculated for the DU and MDUD models. The channel-base current waveform, $I(0, t)$, is characterized by a magnitude of 11 kA and a 10-to-90% risetime of 0.15 μs . The return-stroke front speed is set to $v_f = 130 \text{ m}/\mu\text{s}$. In the DU model, Eq. (1.2), the discharge time constant is set to $\tau_D = 0.6 \mu\text{s}$. In the MDUD model, Eq. (1.3), λ_d and n are set to 5000 m and 2, respectively. When these values of input parameters are used, the magnitude of the MDUD model current is reduced, relative to that in the DU model, to about 80 and 50% at heights $z' = 4$ and 6 km, respectively, while it is essentially the same as that for the DU model at heights below $z' = 2 \text{ km}$

where $I_{DU}(z', t)$ is the channel current given by Eq. (1.2). The recommended constant values are $\lambda_d = 5000 \text{ m}$ and $n = 2$. When these constant values are used, the magnitude of the MDUD model current is reduced, relative to that in the DU model, to about 80 and 50% at heights $z' = 4$ and 6 km, respectively, while it is essentially the same as the DU model current at heights below $z' = 2 \text{ km}$. Figure 1.8 shows waveforms of current at different heights along the vertical lightning channel calculated for the DU and MDUD models. The channel-base current waveform, $I(0, t)$, is characterized by a magnitude of 11 kA and a 10-to-90% risetime of 0.15 μs .

1.4.3 Equations for Computing Electric and Magnetic Fields

The most general equations for computing the vertical electric field E_z and azimuthal magnetic field B_ϕ due to an upward-moving return stroke for the case of an observation point P on perfectly conducting ground (see Fig. 1.9) are given by Thottappillil et al. (1997) and reproduced below.

$$\begin{aligned}
 E_z(r, t) = & \frac{1}{2\pi\epsilon_0} \int_0^{H(t)} \frac{2z'^2 - r^2}{R^5(z')} \int_{v_f + \frac{R(z')}{c}}^t I(z', \tau - R(z')/c) d\tau dz' \\
 & + \frac{1}{2\pi\epsilon_0} \int_0^{H(t)} \frac{2z'^2 - r^2}{cR^4(z')} I(z', \tau - R(z')/c) dz' \\
 & - \frac{1}{2\pi\epsilon_0} \int_0^{H(t)} \frac{r^2}{c^2 R^3(z')} \frac{\partial I(z', t - R(z')/c)}{\partial t} dz' \\
 & - \frac{1}{2\pi\epsilon_0} \frac{r^2}{c^2 R^3(H(t))} I(H(t), v_f) \frac{dH(t)}{dt} \quad (1.4)
 \end{aligned}$$

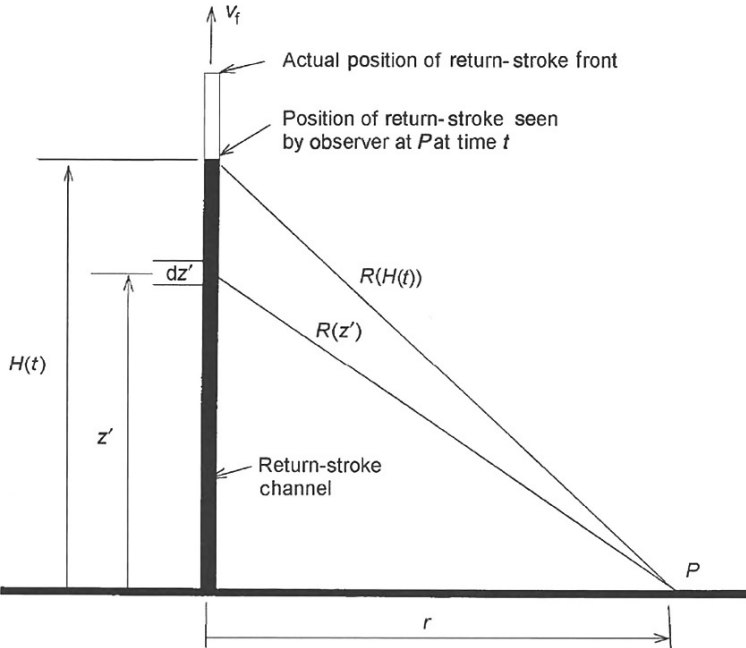


Fig. 1.9 Geometry used in deriving equations for the electric and magnetic fields at a point P on perfectly conducting ground at a horizontal distance r from the vertical lightning return-stroke channel extending upward with speed v_f . Adapted from Thottappillil et al. (1997)

$$B_\varphi(r, t) = \frac{\mu_0}{2\pi} \int_0^{H(t)} \left[\frac{r}{R^3(z')} I(z', t - R(z')/c) + \frac{r}{cR^2(z')} \frac{\partial I(z', t - R(z')/c)}{\partial t} \right] dz' + \frac{\mu_0}{2\pi cR^2(H(t))} I(H(t), H(t)/v_f) \frac{dH(t)}{dt} \quad (1.5)$$

where $I(z', t)$ is the current along the vertical lightning channel at height z' and time t , and $H(t)$ is the height of the front as seen by the observer at time t . This height can be found from the equation, $t = H(t)/v_f + R(H(t))/c$. $I(z', t)$ can be specified by electromagnetic, distributed-circuit, or engineering lightning return-stroke model.

The first three terms in Eq. (1.4), traditionally referred to as the electrostatic, induction, and electric radiation field components, respectively, and the first two terms in Eq. (1.5), referred to as the magnetostatic (or induction) and magnetic radiation field components, respectively, describe the field due to sources below the upward-moving front. The last term in each of these two equations accounts for a possible current discontinuity at the moving front. The front discontinuity produces only a radiation field component, no electrostatic or induction field components.

Figure 1.10a, b, and c show waveforms of vertical electric field on the surface of perfectly conducting ground at horizontal distances $r = 50$ m, 5 km, and 100 km from the vertical lightning channel, calculated using Eq. (1.4) for the MDUD

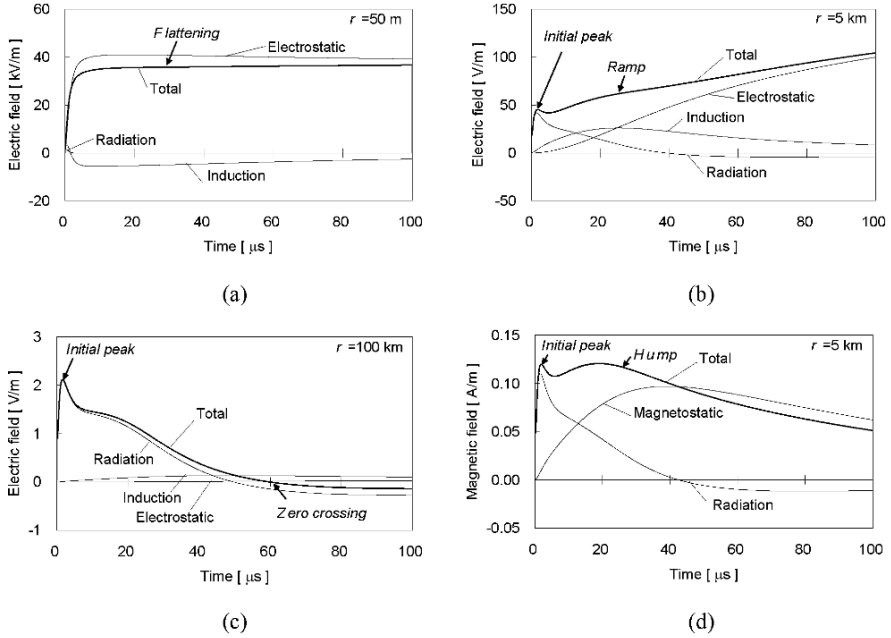


Fig. 1.10 Waveforms of vertical electric field on the surface of perfectly conducting ground at horizontal distances (a) $r = 50\text{ m}$, (b) 5 km , and (c) 100 km from the vertical lightning channel, calculated using Eq. (1.4) for the MDUD model (see Eq. (1.3)), and (d) the waveform of azimuthal magnetic field at $r = 5\text{ km}$ calculated using Eq. (1.5) for the same model. The corresponding distribution of current along the lightning channel is shown in Fig. 1.8 ($v_f = 130\text{ m/ms}$, $\tau_D = 0.6\text{ ms}$, $\lambda_p = 5000\text{ m}$, $n = 2$)

model (see Eq. (1.3)). Figure 1.10d shows the waveform of azimuthal magnetic field at $r = 5\text{ km}$ calculated using Eq. (1.5) for the same model. Note that the corresponding distribution of current along the lightning channel is shown in Fig. 1.8 ($v_f = 130\text{ m/ms}$, $\tau_D = 0.6\text{ ms}$, $\lambda_p = 5000\text{ m}$, $n = 2$). In Fig. 10a-d, fields contributed by each term of Eq. (1.4) or (1.5) are shown as well as the total field. It follows from Fig. 1.10 that at $r = 50\text{ m}$ the contribution of the so-called electrostatic field component to the total field is dominant, at $r = 5\text{ km}$ each of the three field components contributes significantly to the total field, and at $r = 100\text{ km}$ the contribution of the radiation field component is dominant, as predicted by Eq. (1.4). As to the magnetic field, at $r = 50\text{ m}$ (the corresponding figure is not shown in this paper) the contribution from the magnetostatic field component is dominant, at $r = 5\text{ km}$, both the magnetostatic and radiation components contribute significantly, and at $r = 100\text{ km}$ (not shown in this paper) the contribution of the radiation field component is dominant, as predicted by Eq. (1.5). Note that the electrostatic, induction, and electric radiation field components, referred to above, are not unique (Thottappillil and Rakov 2001). For example, they are different for the so-called dipole (as in Eqs. (1.4) and (1.5)) and monopole field formulations, with the difference being largest at closer distances.

Table 1.3 Ability of engineering models to reproduce five features in electric and magnetic field waveforms observed at different distances from the lightning channel

Model	Close E-field flattening	H-field hump	E-field ramp	E- & H-fields initial peak	Far E- & H-fields zero crossing
TL	No	Yes	No	Yes	No
MTLL	Yes	No	Yes	Yes	Yes
MTLE	No	No	Yes	Yes	Yes
MTLD	Yes	No	Yes	Yes	Yes
TCS	Yes	Yes	Yes	Yes	No
DU	Yes	Yes	Yes	Yes	No
MDUD	Yes	Yes	Yes	Yes	Yes

Testing of model validity is discussed by Nucci et al. (1990), Thottappillil and Uman (1993), Thottappillil et al. (1997), Rakov and Uman (1998), and Schoene et al. (2003). Table 1.3 summarizes the ability of different engineering models to reproduce the five characteristic features in electric and magnetic field waveforms. Note that Thottappillil et al. (1991) have shown that the TCS and DU models with a somewhat different channel-base current waveform whose time to half peak value is 20 μ s reproduce all of the five features. On the other hand, the TCS model (and probably DU) model cannot reproduce measured fields at 15 and 30 m during the first microsecond or so (Schoene et al. 2003) due to unrealistic boundary conditions at the channel base (see Fig. 1.7b).

1.5 Summary

In this chapter, a general picture of downward negative lightning discharges that take place between cloud and ground has been described. Then, first and subsequent return strokes, which are the optically brightest processes and produce the most intense wideband electromagnetic signatures in the lightning flash, have been characterized. The first return stroke follows the path of initial downward-progressing stepped leader emerging from the cloud, and subsequent return strokes are usually initiated by dart leaders propagating downward along channels traversed by the preceding stroke(s). Representative models of lightning return strokes have been described, and their ability to reproduce the characteristic features of measured field waveforms at different distances from the lightning channel have been evaluated.

References

- Baba, Y. and Ishii, M. (2002). Lightning return stroke model incorporating current distortion. *IEEE Trans. Electromagn. Compat.*, 44:476–478.
- Baba, Y., Miyazaki, S., and Ishii, M. (2004). Reproduction of lightning electromagnetic field waveforms by engineering model of return stroke. *IEEE Trans. Electromagn. Compat.*, 46:130–133.

- Baba, Y. and Rakov, V. A. (2007). Electromagnetic models of the lightning return stroke. *J. Geophys. Res.*, 112, doi:10.1029/2006JD007222.
- Berger, K., Anderson, R. B., and Kroninger, H. (1975). Parameters of lightning flashes. *Electra*, 80:223–237.
- Cooray, V. (2003). On the concepts used in return stroke models applied in engineering practice. *IEEE Trans. Electromagn. Compat.*, 45:101–108.
- Cooray, V. and Lundquist, S. (1983). Effects of propagation on the rise times and the initial peaks of radiation fields from return strokes. *Radio Sci.* 18: 409–415.
- Diendorfer, G. and Uman, M. A. (1990). An improved return stroke model with specified channel-base current. *J. Geophys. Res.*, 95:13621–13644.
- GORIN, B. N. (1985). Mathematical modeling of the lightning return stroke. *Elektrichestvo*, 4:10–16 (in Russian).
- Heidler, F. (1985). Traveling current source model for LEMP calculation. Proc. 6th Int. Zurich Symp. Electromagn. Compat., Zurich, Switzerland, 157–162.
- Jordan, D. M., Rakov, V. A., Beasley, W. H., and Uman, M. A. (1997). Luminosity characteristics of dart leaders and return strokes in natural lightning. *J. Geophys. Res.*, 102:22025–22032.
- Lin, Y. T., Uman, M. A., Tiller, J. A., Brantley, R. D., Beasley, W. H., Krider, E. P., and Weidman, C. D. (1979). Characterization of lightning return stroke electric and magnetic fields from simultaneous two-station measurements. *J. Geophys. Res.*, 84:6307–6314.
- Maslowski, G. and Rakov, V. A. (2007). Equivalency of lightning return-stroke models employing lumped and distributed current sources. *IEEE Trans. Electromagn. Compat.*, 49:123–132.
- Nucci, C. A., Mazzetti, C., Rachidi, F., and Ianoz, M. (1988). On lightning return stroke models for LEMP calculations. Proc. 19th Int. Conf. Lightning Protection, Graz, Austria.
- Nucci, C. A., Diendorfer, G., Uman, M. A., Rachidi, F., Ianoz, M., and Mazzetti, C. (1990). Lightning return stroke current models with specified channel-base current: a review and comparison. *J. Geophys. Res.*, 95:20395–20408.
- Plooster, M. N. (1971). Numerical model of the return stroke of the lightning discharge. *Phys. Fluids*. 14:2124–2133.
- Rachidi, F. and Nucci, C. A. (1990). On the Master, Uman, Lin, Standler and the modified transmission line return stroke current models *J. Geophys. Res.*, 95:20389–20393.
- Rachidi, F., Rakov, V. A., Nucci, C. A., and Bermudez, J. L. (2002). Effect of vertically extended strike object on the distribution of current along the lightning channel. *J. Geophys. Res.*, 107:ACL 16-1-ACL 16-6.
- Rakov, V. A. (1998). Some inferences on the propagation mechanisms of dart leaders and return strokes. *J. Geophys. Res.*, 103:1879–1887.
- Rakov, V. A. (2007). Lightning return stroke speed. *J. Lightning Res.*, 1:80–89.
- Rakov, V. A. and Dulzon, A. A. (1987). Calculated electromagnetic fields of lightning return stroke. *Tekh. Elektrodinam.*, 1:87–89.
- Rakov, V. A. and Uman, M. A. (1998). Review and evaluation of lightning return stroke models including some aspects of their application. *IEEE Trans. Electromagn. Compat.*, 40:403–426.
- Rakov, V. A., Uman, M. A., and Thottappillil, R. (1994). Review of lightning properties from electric field and TV observations. *J. Geophys. Res.*, 99:10,745–10,750.
- Rakov, V. A. and Uman, M. A. (2003). *Lightning: Physics and Effects*. Cambridge University Press.
- Schoene, J., M. A. Uman, V. A. Rakov, K. J. Rambo, J. Jerauld, and G. H. Schnetzer (2003). Test of the transmission line model and the traveling current source model with triggered lightning return strokes at very close range. *J. Geophys. Res.*, 108, doi:10.1029/2003JD003683.
- Thottappillil, R., M. A. Uman, and G. Diendorfer (1991). Influence of channel base current and varying return stroke speed on the calculated fields of three important return stroke models. Paper presented at Int. Conf. Lightning and Static Electricity, Cocoa Beach, FL.
- Thottappillil, R. and Uman, M. A. (1993). Comparison of lightning return-stroke models. *J. Geophys. Res.*, 98:22903–22914.

- Thottappillil, R., Rakov, V. A., and Uman, M. A. (1997). Distribution of charge along the lightning channel: relation to remote electric and magnetic fields and to return-stroke models. *J. Geophys. Res.*, 102:6987–7006.
- Thottappillil, R. and Rakov, V. A. (2001). On different approaches to calculating lightning electric fields. *J. Geophys. Res.*, 106:14191–14205, 2001.
- Uman, M. A. and McLain, D. K. (1969). Magnetic field of the lightning return stroke. *J. Geophys. Res.*, 74:6899–6910.
- Uman, M. A., Swanberg, C. E., Tiller, J. A., Lin, Y. T., and Krider, E. P. (1976). Effects of 200 km propagation in Florida lightning return stroke electric fields. *Radio Sci.* 11: 985–990.
- Visacro, S. and Silveira, F. H. (2004). Evaluation of current distribution along the lightning discharge channel by a hybrid electromagnetic model. *J. Electrostatics*, 60: 110–120.
- Wang, D., Takagi, N., Watanabe, T., Rakov, V. A., Uman, M. A., Rambo, K. J., and Stapleton, M. V. (2005). A comparison of channel-base currents and optical signals for rocket-triggered lightning strokes. *Atmos. Res.*, 76:412–422.

Chapter 2

Triggered Lightning

Vladimir A. Rakov

Abstract Classical and altitude rocket-and-wire techniques for triggering lightning are described. Various characteristics of triggered lightning derived from measurements of current at the lightning channel base and from close electric and magnetic field records are reviewed. New insights into lightning processes gained from triggered-lightning experiments are discussed.

Keywords Lightning triggering techniques · Triggered-lightning parameters · Lightning current · Grounding conditions · Ground surface arcing · Fulgurites · Current time-derivative · Close lightning electromagnetic environment

2.1 Introduction

Many aspects of lightning are not yet well understood and are in need of research that often requires the termination of lightning channel at a specific object or in its immediate vicinity. The probability for a natural lightning to strike a given point on the earth's surface or an object or structure of interest is very low, even in areas of relatively high lightning activity. Simulation of the lightning channel in a high-voltage laboratory has very limited application, since it does not allow the reproduction of many lightning features and it does not allow the testing of large distributed systems. One promising tool for studying both the direct and the induced effects of lightning is an artificially initiated (or triggered) lightning discharge from a thunderstorm cloud to a designated point on ground. In most respects the triggered lightning is a controllable analog of natural lightning. The most effective technique for artificial lightning initiation is the so-called rocket-and-wire technique. This technique involves the launching of a small rocket extending a thin wire (either grounded or ungrounded) into the gap between the ground and a charged cloud overhead.

V.A. Rakov (✉)

Department of Electrical and Computer Engineering, University of Florida, 553 Engineering Building #33, Gainesville, FL 32611-6130, USA
e-mail: rakov@ece.ufl.edu

The use of term “triggered lightning” is limited here to those discharges intentionally stimulated to occur by ground-based activity, the energy source being a naturally electrified cloud. Upward lightning discharges between a stationary, ground-based object (usually of large height) and an electrified cloud, as well as discharges initiated by airborne vehicles are outside the scope of this review.

The possibility of artificially initiating lightning by ground-based activity was apparently first discussed by Newman (1958) and by Brook et al. (1961). Brook et al. (1961) showed that, in the laboratory, a spark discharge could be triggered by the rapid introduction of a thin wire into an electric field, while the steady presence of the wire did not result in a spark. They suggested that the corona discharge from a stationary conductor acts to shield this conductor so that the high fields necessary to initiate electrical breakdown are not obtained, whereas the field enhancement due to the rapid introduction of a conductor is not significantly reduced by corona, since there is insufficient time for its development.

The first triggered lightning discharges were produced in 1960 by launching small rockets trailing thin grounded wires from a research vessel off the west coast of Florida (Newman 1965; Newman et al. 1967; Newman and Robb 1977). The first triggering over land was accomplished in 1973, at Saint-Privat d’Allier in France (Fieux et al. 1975, 1978). In the following decades, a number of triggered-lightning programs have been developed in different countries, as summarized in Table 2.1. Rocket-triggered lightning experiments in France have been reviewed by Fieux et al. (1978), in Japan by Horii (1982), Kito et al. (1985), Nakamura et al. (1991, 1992) and Horii et al. (2006), in New Mexico by Hubert et al. (1984), at the Kennedy Space Center, Florida, by Willett (1992), at Camp Blanding, Florida, by Uman et al. (1997) and Rakov et al. (1998, 2000, 2005), in China by Liu et al. (1994) and Liu and Zhang (1998), and in Brazil by Pinto et al. (2005). Triggered-lightning experiments conducted in different countries have been reviewed by Uman (1987), Horii and Nakano (1995), Rakov (1999b), and Rakov and Uman (2003).

In all published experiments, the triggering wires were made of either steel or copper with a diameter of typically about 0.2 mm, wound on a spool located either on the ground or on the rocket. Various rockets made of plastic and of steel have been used, with the rocket length being typically about 1 m. Most of the experiments in Japan were conducted in the winter, the several attempts made to trigger in the summer months being unsuccessful. At Camp Blanding, Florida, lightning has been triggered in both summer and winter storms. All other triggering sites have apparently been operated only during the summer. The results from these programs have made possible a number of new insights into the various lightning processes and effects.

Descriptions of the classical and altitude rocket-and wire triggering techniques are given in Sections 2.2.1 and 2.2.2, respectively. Probably close to a thousand lightning discharges have been triggered using these techniques to date. An overview of lightning-triggering facilities is found in Table 2.1, with a description of Camp Blanding facility being given in Section 2.2.3. Over 300 lightning flashes were triggered to date at the Camp Blanding site. Properties of rocket-triggered lightning (including its close electromagnetic environment) are reviewed in Sections 2.3– 2.6.

Table 2.1 An overview of major triggered-lightning programs

Experimental site	Height above sea level, m	Years of operation*	Wire material	Location of wire spool	Selected references
Saint Privat d'Allier, France	1100	1973–1996	Steel or copper	Ground or rocket	Fieux et al. (1978), SPARG (1982)
Kahokugata, Hokuriku coast, Japan	0	1977–1985	Steel	Ground	Horii (1982), Kito et al. (1985)
Langmuir Laboratory, New Mexico	3230	1979–present	Steel	Ground	Hubert et al. (1984), Idone et al. (1984)
KSC, Florida (south of Melbourne, Florida in 1983)	0	1983–1991	Copper	Rocket	Eybert-Berad et al. (1986, 1988), Willett (1992)
Okushishiku, Japan	930	1986–1998	Steel	Ground or rocket	Nakamura et al. (1991, 1992)
Different sites in China	Various	1989–present	Steel or copper	Ground or rocket	Liu et al. (1994), Qie et al. (2007)
Fort McClellan, Alabama	190	1991–1995	Copper	Rocket	Fisher et al. (1993), Morris et al. (1994)
Camp Blanding, Florida	20–25	1993–present	Copper	Rocket	Uman et al. (1997), Rakov et al. (1998, 2005)
Cachoeira Paulista, Brazil	570	1999–2007	Copper	Rocket	Pinto et al. (2005), Saba et al. (2000)

* As of this writing and not necessarily continuous. Additionally, triggered-lightning experiments have been conducted in Germany (Hierl 1981), in Indonesia (Horii et al. 1990), and in Russia (Beituganov and Zashakuev 1992).

2.2 Triggering Techniques

Two techniques for triggering lightning with a small rocket that extends a thin wire in the gap between a thundercloud and the ground are discussed here. “Classical” triggering is described in Section 2.2.1 and “altitude” triggering in Section 2.2.2. These descriptions primarily apply to triggering negative lightning.

2.2.1 Classical Triggering

This triggering method involves the launching of a small rocket trailing a thin grounded wire toward a charged cloud overhead, as illustrated in Fig. 2.1. Still photographs of classical triggered lightning flashes are shown in Fig. 2.2. To decide when to launch a triggering rocket, the cloud charge is indirectly sensed by

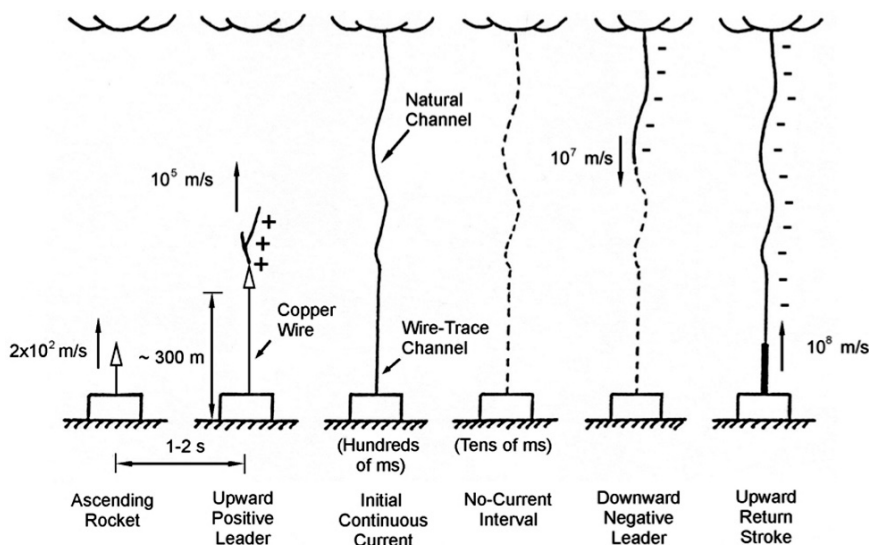


Fig. 2.1 Sequence of events (except for the attachment process; Wang et al. 1999a) in classical triggered lightning. The upward positive leader (UPL) and initial continuous current (ICC) constitute the initial stage (IS). Adapted from Rakov et al. (1998)

measuring the electric field at ground, with absolute values of 4 to 10 kVm⁻¹ generally being good indicators of favorable conditions for negative lightning initiation in Florida, as seen in Fig. 2.3. However, other factors, such as the general trend of the electric field and the frequency of occurrence of natural lightning discharges, are usually taken into account in making the decision to launch a rocket. The triggering success rate is generally relatively low during very active periods of thunderstorms, one reason being that during such periods the electric field is more likely to be reduced by a natural lightning discharge before the rocket rises to a height sufficient for triggering.

When the rocket, ascending at about 200 m s⁻¹, is about 200–300 m high, the field enhancement near the rocket tip launches a positively charged leader that propagates upward toward the cloud. This upward positive leader (UPL) vaporizes the trailing wire, bridges the gap between the cloud charge source and ground, and establishes an initial continuous current (ICC) with a duration of some hundreds of milliseconds that transports negative charge from cloud charge source to the triggering facility. The ICC can be viewed as a continuation of the UPL when the latter has reached the main negative charge region in the cloud. At that time the upper extremity of the UPL is likely to become heavily branched. The UPL and ICC constitute the initial stage (IS) of a classical triggered lightning discharge. After the cessation of the initial continuous current, one or more downward dart leader/upward return stroke sequences may traverse the same path to the triggering facility. The dart leaders and the following return strokes in triggered lightning are similar to dart leader/return stroke sequences in natural lightning, although the initial processes in natural downward and classical triggered lightning are distinctly different.

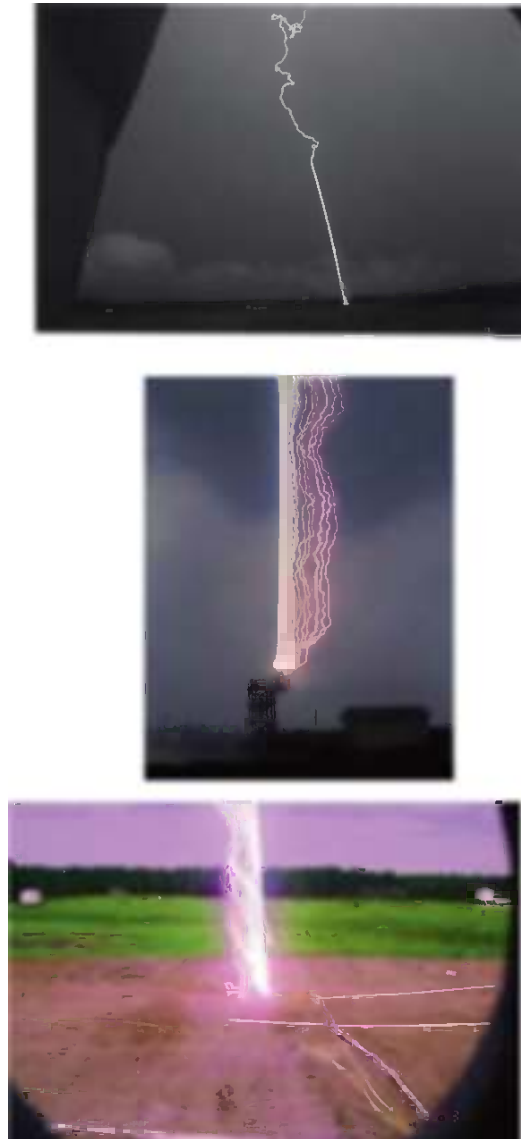


Fig. 2.2 Photographs of lightning flashes triggered at Camp Blanding, Florida. Top – a distant view of a strike to the test runway; middle, a strike to the test power system initiated from the tower launcher; bottom – a strike initiated from the underground launcher at the center of a $70 \times 70 \text{ m}^2$ buried metallic grid (See also Plate 1 in the Color Plate Section on page 593)

In summer, the triggering success rate for positive lightning is apparently lower than for negative lightning (e.g., Fieux et al. 1978), one known exception being the triggered lightning experiment in northern China (Liu et al. 1994; Liu and

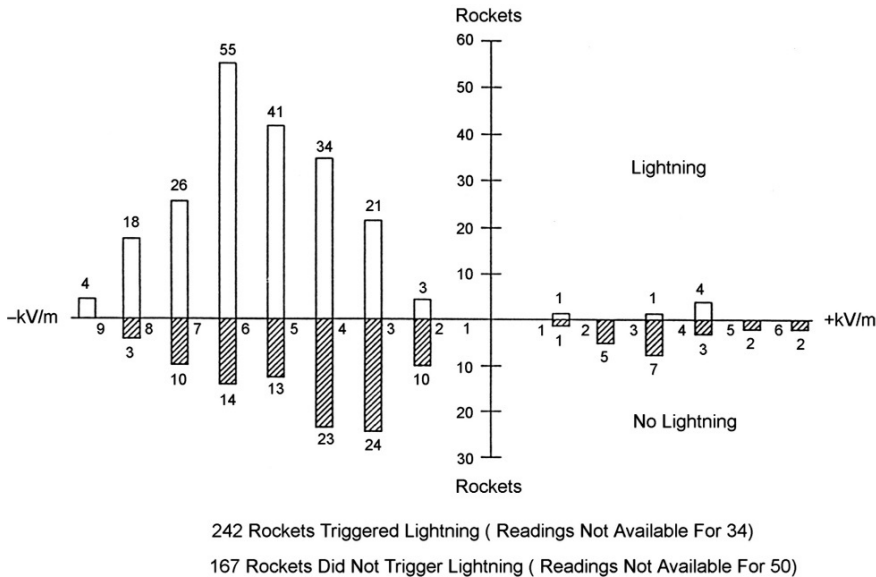


Fig. 2.3 Histograms of successful (above the horizontal axis) and unsuccessful (below the horizontal axis) classical triggering attempts in 1983 to 1991 at the NASA Kennedy Space Center. Individual histogram bins correspond to different positive and negative values of surface electric field at the time of rocket launch. Upward-directed field is considered negative (atmospheric electricity sign convention). Adapted from Jafferis (1995)

Zhang 1998), although all discharges triggered there were composed of an initial stage only, that is, no leader/return stroke sequences occurred.

There is contradictory information regarding whether the height H of the rocket at the time of lightning triggering depends on the electric field intensity E at ground at the time of launching the rocket. Hubert et al. (1984) found a strong correlation (correlation coefficient = -0.82) between H and E for triggered lightning in New Mexico. They gave the following equation between H (in meters) and E (in kV m^{-1})

$$H = 3900 E^{-1.33} \quad (2.1)$$

In Hubert et al.'s (1984) study, E varied from about 5 to 13 kV m^{-1} and H from about 100 to 600 m, with a mean value of 216 m. On the other hand, in winter triggered-lightning studies at the Kahokugata site in Japan (Table 2.1), no clear relation was observed between H and E for either sign of E (Horii and Nakano 1995; Fig. 6.2.3).

Willett et al. (1999b), who used electric field sounding rockets in Florida, studied ambient-field conditions that are sufficient to initiate and sustain the propagation of upward positive leaders in triggered lightning. It was found that lightning can be initiated with grounded triggering wires approximately 400 m long when the ambient fields aloft are as small as 13 kV m^{-1} . When lightning occurred, ambient potentials

with respect to earth at the triggering-rocket altitude were 3.6 MV (negative with respect to earth). These potentials were referred to as triggering potentials by Willett et al. (1999b).

2.2.2 Altitude Triggering

A stepped leader followed by a first return stroke in natural downward lightning can be reproduced to some degree by triggering lightning via a metallic wire that is not attached to the ground. This ungrounded-wire technique is usually called altitude triggering and is illustrated in Fig. 2.4 which shows that a bidirectional (positive charge up and negative charge down) leader process is involved in the initiation of the first return stroke from ground. Note that the “gap” (in this case, the length of the insulating kevlar cable) between the bottom end of the upper (triggering) wire and the top end of the grounded (intercepting) wire is some hundreds of meters. Altitude triggering can also be accomplished without using an intercepting wire

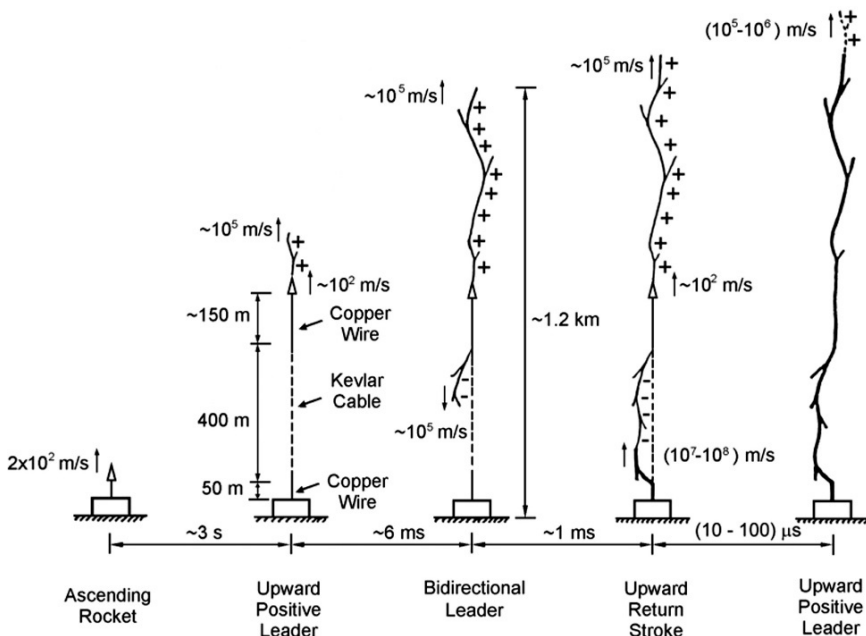


Fig. 2.4 Sequence of events in altitude triggered lightning leading to the establishment of a relatively low-resistance connection between the upward-moving positive leader tip and the ground (except for the attachment process; Lalande et al. 1998), based on the event described by Laroche et al. (1991). The processes that follow the sequence of events shown, the initial continuous current and downward leader/upward return-stroke sequences, are similar to their counterparts in classical triggered lightning (see Fig. 2.1). Adapted from Rakov et al. (1998)

whose only function is to increase the probability of lightning attachment to the instrumented rocket-launching facility. In some triggered-lightning experiments, the bottom end of the triggering wire has been attached to an air gap of up to 10 m in length (e.g., Nakamura et al. 1992). Such triggering is not considered as being of the altitude type, since it was not intended to simulate the downward stepped leader (discussed below) from the bottom of the triggering wire. On the other hand, altitude triggering may also occur as a result of the accidental breakage of the wire during classical triggering, so that the wire connection to ground is unintentionally lost. Additionally, altitude triggering has been accomplished using a two-stage rocket system in which the two rockets separated in the air with the triggering wire extending between them (e.g., Nakamura et al. 1992). The properties of altitude triggered lightning are discussed by Laroche et al. (1991), Lalande et al. (1996, 1998), Uman et al. (1996a), Rakov et al. (1996, 1998), Wang et al. (1999d), Chen et al. (2003), and Saba et al. (2005).

In the following, we briefly discuss the sequence of processes involved in altitude triggered lightning, as illustrated in Fig. 2.4. A downward negative leader is usually launched from the lower end of the elevated triggering wire some milliseconds after the initiation of the upward positive leader from the upper end of the wire (Lalande et al. 1998; Fig. 6). The downward negative leader shown in Fig. 6 of Lalande et al. (1998) was apparently initiated after two unsuccessful attempts. As the negative downward leader approaches the triggering facility, an upward connecting leader (not shown in Fig. 2.4) is initiated from the grounded intercepting wire. Once the attachment between the two leaders is made, the return stroke is initiated. Since (1) the length of the channel available for the propagation of the first return stroke in altitude triggered lightning is relatively small (of the order of 1 km) and (2) the return-stroke speed is two to three orders of magnitude higher than that of the leader, the return stroke catches up with the tip of the upward leader within 10 μ s or so. As a result, the upward leader becomes strongly intensified. The processes that follow, the initial continuous current and downward leader/upward return-stroke sequences, are probably similar to those in classical triggered lightning (see Fig. 2.1). Thus the downward-moving negative leader of the bidirectional leader system and the resulting return stroke in altitude triggered lightning serve to provide a relatively low-resistance connection between the upward-moving positive leader tip and the ground. The initial stage of altitude triggered lightning can be viewed as composed of an initial upward leader, a bidirectional leader (part of which is a continuation of the initial upward leader), an attachment process, an initial-stage return stroke, an intensified upward leader, and an initial continuous current.

Wang et al. (1999d) reported on a positive flash that was initiated using the altitude triggering technique from a summer thunderstorm in China. This is the first documented triggering of a positive lightning using the altitude triggering technique. For this flash, the length of grounded intercepting wire was 35 m and the length of insulating cable was 86 m. The flash was apparently initiated when the rocket was at an altitude of 550 m, so that the length of the ungrounded triggering wire was 429 m.

2.2.3 Triggering Facility at Camp Blanding, Florida

The lightning-triggering facility at Camp Blanding, Florida was established in 1993 by the Electric Power Research Institute (EPRI) and Power Technologies, Inc. (PTI). Since September 1994, the facility has been operated by the University of Florida (UF). Over 40 researchers (excluding UF faculty, students, and staff) from 15 countries representing 4 continents have performed experiments at Camp Blanding concerned with various aspects of atmospheric electricity, lightning, and lightning protection. Since 1995, the Camp Blanding facility has been often referred to as the International Center for Lightning Research and Testing (ICLRT) at Camp Blanding, Florida. A summary of the lightning triggering operations conducted for various experiments from 1993 to 2007 is presented in Table 2.2. Over the 14-year period (there was no triggering in 2006), the total number of triggered flashes was 317, that is, on average about 23 per year, with 16 (about 70 percent) of them containing return strokes. Out of the total of 317 flashes in Table 2.2, 314 transported negative charge and 3 either positive charge or both negative and positive charges to ground.

The principal results obtained from 1993 to 2007 at the ICLRT include

- characterization of the close lightning electromagnetic environment (Rakov et al. 1998, 2001; Uman et al. 2000, 2002; Crawford et al. 2001; Schoene et al. 2003a);
- first lightning return-stroke speed profiles within 400 m of ground (Wang et al. 1999c; Olsen et al. 2004).
- new insights into the mechanism of the dart-stepped (and by inference stepped) leader (Rakov et al. 1998; Wang et al. 1999c);

Table 2.2 1993–2007 Triggered-lightning experiments at the ICLRT at Camp Blanding, Florida

Year(s)	Rocket Launchers Used	Total Flashes Triggered	Flashes with Return Strokes	Positive or Bipolar Flashes	Time Period
1993	1	32	22	–	June 7 – Sept. 21
1994	2	15	11	–	August 4 – Sept.
1995	2	14	13	–	June 25 – August 19
1996	2	30	25	–	June 20 – Sept. 11
1997	4	48	28	1	May 24 – Sept. 26
1998	3	34	27	–	May 15, July 24 – Sept. 30
1999	2	30	22	1	Jan. 23, June 26 – Sept. 27
2000	2	30	27	–	June 12 – Sept. 6
2001	2	23	11	–	July 13 – Sept. 5
2002	2	19	14	–	July 9 – Sept. 13
2003	2	24	12	1	June 30 – Aug. 15
2004	1	5	3	–	June 23 – July 24
2005	2	11	8	–	July 2 – August 5
2007	1	2	1	–	July 13 – July 31
1993–2007	(14* years)	317	224	3	

*There was no lightning triggering in 2006.

- identification of the M-component mode of charge transfer to ground (Rakov et al. 1995, 1998, 2001);
- first optical image of upward connecting leader in lightning strokes developing in previously conditioned channels (Wang et al. 1999a);
- electric fields in the immediate vicinity of the lightning channel core, inside the radial corona sheath (Miki et al. 2002);
- inferences on the interaction of lightning with ground and with grounding electrodes (Rakov et al. 1998, 2002, 2003a; Bejleri et al. 2004);
- discovery of X-rays produced by triggered-lightning strokes (Dwyer et al. 2002, 2003; Al-Dayeh et al. 2002; Dwyer et al. 2004a, 2004b);
- new insights into the mechanism of cutoff and reestablishment of current in the lightning channel (Rakov et al. 2003b; Olsen et al. 2006);
- first direct measurements of NO_x production by lightning (Rahman et al. 2006);
- direct estimates of lightning input energy (Jayakumar et al. 2006);
- ground-truth evaluation of the performance characteristics of the U.S. National Lightning Detection Network (Jerauld et al. 2005; Nag et al. 2008);
- new insights into the lightning attachment process (Jerauld et al. 2007);
- characterization of currents induced by lightning in a buried loop conductor and in a grounded vertical conductor (Schoene et al. 2008).

2.3 Overall Current Waveforms

In this section, we discuss currents measured at the rocket launcher. For both classical and altitude triggered lightning, the emphasis will be placed on the initial stage, with the characterization of current waveforms due to return strokes (primarily from classical triggered lightning) being presented in Section 2.4. Initial-stage return strokes in altitude triggered lightning are discussed in Section 2.3.2. For classical triggered lightning, initial-stage current initially flows through the triggering wire until the wire is destroyed and replaced by a plasma channel, as described by Rakov et al. (2003b) and Olsen et al. (2006). For altitude triggered lightning, current exceeding some amperes is first measured when an upward connecting leader (not shown in Fig. 2.4) emanates from the launcher (or from a grounded intercepting wire) in response to the approaching downward-extending, negative part of the bidirectional leader system.

2.3.1 *Classical Triggering*

The overall current record for a typical negative classical triggered lightning flash is presented in Fig. 2.5, and portions of this record are shown on expanded time scales in Figs. 2.6 and 2.7. The record is intentionally clipped at the 2-kA level in order to accentuate the current components in the hundreds of amperes range. Other researchers (e.g., Eybert-Berad et al. 1986, 1988) used recorders with a logarithmic

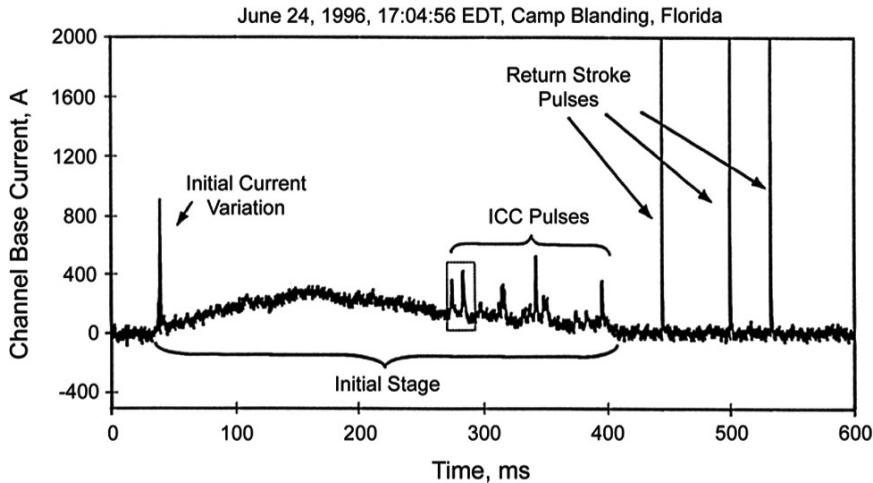


Fig. 2.5 Example of the overall current record of a triggered lightning at Camp Blanding, Florida, containing an initial stage (IS) and three return strokes. The initial tens of milliseconds of IS are due to the upward positive leader (UPL), while the rest of IS is due to the initial continuous current (ICC). The record is intentionally clipped at about 2 kA. Adapted from Wang et al. (1999b)

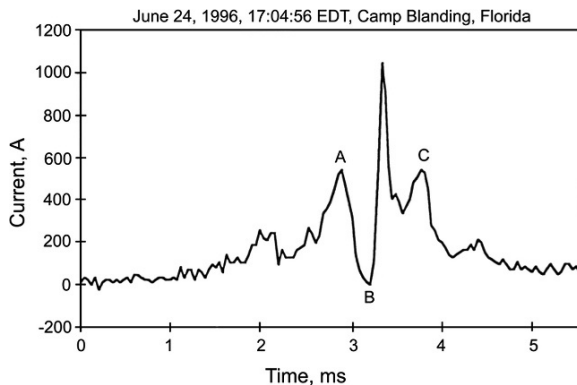


Fig. 2.6 Initial current variation (ICV) shown in Fig. 2.5 but on an expanded time scale. Adapted from Wang et al. (1999b)

scale in order to be able to view both small currents and large currents on the same record. Median values of the overall flash duration from triggered lightning experiments in France and New Mexico are 350 and 470 ms (Hubert 1984), respectively. The median flash charges from the same studies are 50 and 35 C, respectively. Both the flash duration and charge transferred are comparable, within a factor of 2 to 4, to their counterparts in object-initiated lightning and in natural downward lightning.

We first consider the overall characteristics, that is, the duration, the charge transfer, and the average current, of the initial stage (IS), and then discuss (1) the current

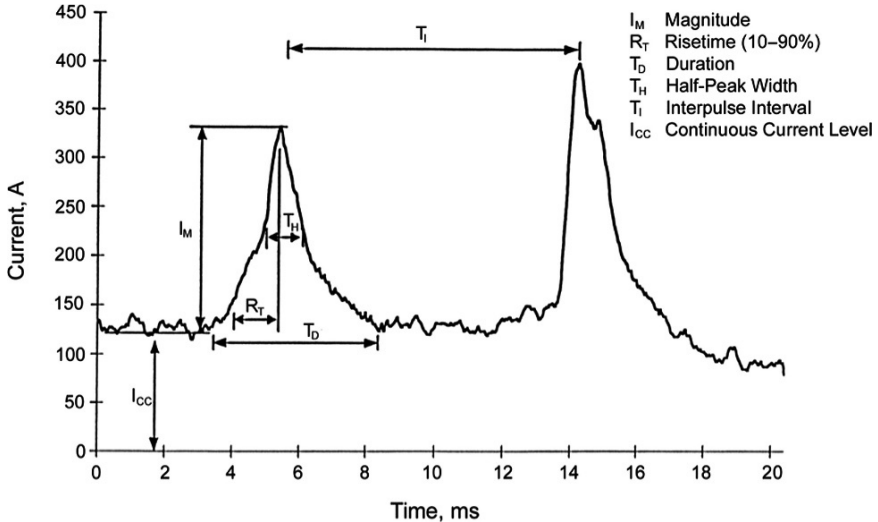


Fig. 2.7 First two initial continuous current (ICC) pulses of Fig. 2.5 on an expanded time scale. This Figure illustrates the definitions of the ICC pulse magnitude I_M , 10–90 percent risetime R_T , duration T_D , half-peak width T_H , interpulse interval T_I , and preceding continuous current level I_{cc} . All these parameters have been found to be similar to the corresponding parameters of M component current pulses analyzed by Thottapillil et al. (1995). Adapted from Wang et al. (1999b)

variation at the beginning of the IS, termed the initial current variation (ICV), and (2) the current pulses superimposed on the later part of the IS current, referred to as initial continuous current (ICC) pulses. Parameters of the return-stroke current pulses (three pulses are shown in Fig. 2.5) that often follow the initial stage current are discussed in Section 2.4.

Miki et al. (2005), based on data from Camp Blanding, Florida (see Table 2.1), reported that the initial stage had a geometric mean (GM) duration of 305 ms and lowered to ground a GM charge of 30 C. The average initial stage current in an individual lightning discharge had a GM value of 100 A.

In many cases the initial current variation includes a current drop, as illustrated in Fig. 2.6 where it is labeled ABC. This current drop is associated with the disintegration of the copper triggering wire (abrupt current decrease from A to B in Fig. 2.6) and the following current re-establishment (abrupt current increase from B to C in Fig. 2.6). The processes of current cutoff and re-establishment were studied in detail by Rakov et al. (2003b) and Olsen et al. (2006). Sometimes upward positive leaders exhibit pronounced stepping in current records.

The initial continuous current usually includes impulsive processes, illustrated in Fig. 2.7, that resemble the M processes observed during the continuing currents that often follow return strokes in both natural and triggered lightning (Rakov et al. 1995, 2001). Wang et al. (1999b), from a comparison of various characteristics of the initial continuous current pulses with the characteristics of the M-component current pulses analyzed by Thottapillil et al. (1995), concluded that these two types

of pulses are similar and hence likely due to similar lightning processes. Like M component pulses, the initial continuous current pulses sometimes have amplitudes in the kiloamperes range.

2.3.2 Altitude Triggering

As noted in Section 2.2.2, the initial stage of altitude triggered lightning includes an initial upward leader, a bidirectional leader (which includes a continuation of the initial upward leader), an attachment process, an initial-stage return stroke, an intensified upward leader, and an initial continuous current. Since the triggering wire is ungrounded, no current can be directly measured at ground during the initial upward leader and bidirectional leader stages. Shown in Fig. 2.8 is the current associated with an upward positive connecting leader initiated in response to the approaching downward negative leader of the bidirectional leader system (Fig. 2.4), with the corresponding electric field measured 50 m from the lightning attachment point being shown in Fig. 2.8a. This current record, reported by Lalande et al. (1998), suggests that the upward positive connecting leader is stepped, with the interstep interval being 20 s or so. When contact is established between the downward leader and the upward connecting leader, the initial-stage return stroke begins. The current waveform of this return stroke differs appreciably from a typical return-stroke current waveform in that the former appears to be chopped soon after reaching its peak value (see, for example, Fig. 7c of Hubert (1984)). As a result, the width of the current waveform produced by the initial-stage return stroke is appreciably smaller than that of the following return strokes in the same flash. As discussed in Section 2.2.2, the initial-stage return stroke front catches up with the upward-moving leader tip

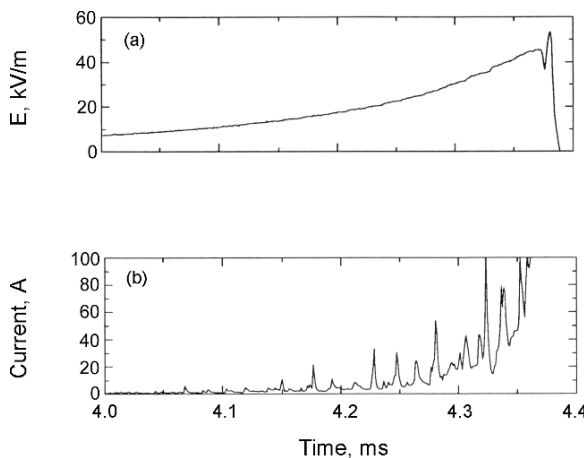


Fig. 2.8 (a) Electric field measured 50 m from the lightning attachment point and (b) current produced by the upward connecting positive leader from the grounded 50 m wire in altitude triggered lightning 9516 at Camp Blanding, Florida. Adapted from Lalande et al. (1998)

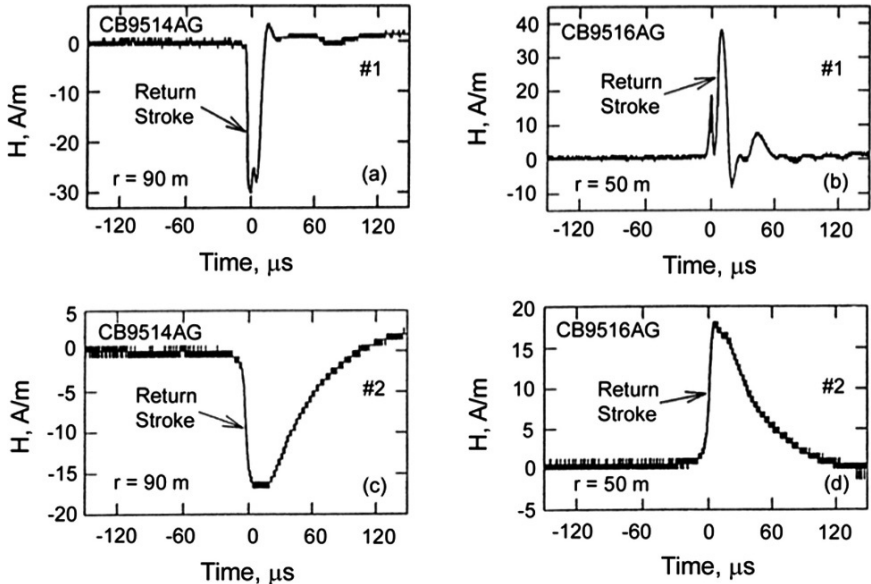


Fig. 2.9 The magnetic fields produced by the first two strokes of the Camp Blanding altitude triggered lightning flashes 9514 (a, first stroke; c, second stroke; four strokes total) and 9516 (b, first stroke; d, second stroke; four strokes total). In each case, the waveshapes of all the higher-order strokes are similar to the second-stroke waveshape. The measuring system's decay time constant was about 120 μ s. The difference in polarity of the waveforms is due to different positions of the lightning channel with respect to the magnetic field antenna, all strokes lowering negative charge to ground. Note that the first-stroke magnetic field pulses in (a) and (b) are appreciably shorter than the corresponding second-stroke magnetic field pulses in (c) and (d), respectively. Adapted from Rakov et al. (1998)

after 10 μ s or so. This is likely to produce an opposite polarity downward-moving reflected current wave that is presumably responsible for the chopped shape of both the channel-base current and the close magnetic field waveforms. Examples of the latter are shown, along with waveforms produced by “normal” return strokes, in Fig. 2.9. The initial stage characteristics of altitude triggered lightning, after the return stroke has established a relatively low-resistance connection between the upward-moving positive leader tip and ground (see Fig. 2.4), are apparently similar to their counterparts in classical triggered lightning (Rakov et al. 1996). Further, the downward leader/upward return-stroke sequences that follow the initial stage in altitude triggered lightning are thought to be similar to those in classical triggered lightning (see Fig. 2.1).

2.4 Parameters of Return-Stroke Current Waveforms

In this section, we discuss return-stroke current peak and current waveform parameters such as risetime, rate of rise (steepness), and half-peak width. We will

additionally consider interstroke intervals and characteristics that may involve both the return-stroke current component and the following continuing current component, such as the total stroke duration, the total stroke charge, $\int I(t) dt$, and the total stroke action integral, $\int I^2(t) dt$. The action integral is measured in A s², which is the same as J Ω⁻¹, and represents the Joule or Ohmic heating energy dissipated per unit resistance at the lightning attachment point. The action integral is also called the specific energy. We will additionally discuss correlations among the various parameters listed above. The characterization of the return-stroke current waveforms presented in this section is based primarily on data for classical triggered lightning. It is possible that some of the samples on which the statistics presented here are based contain a small number of initial-stage return strokes from altitude triggered lightning, but their exclusion would have essentially no effect on the statistics.

Some researchers (e.g., Hubert et al. 1984; Horii and Ikeda 1985), in presenting statistics on triggered lightning currents, do not distinguish between current pulses associated with return strokes and those produced by other lightning processes such as M components and processes giving rise to the initial current variation and initial continuous current pulses described in Section 2.3.1. In this section, we consider only return-stroke current pulses. These can usually be distinguished from other types of pulses by the absence of a steady current immediately prior to a pulse (Fisher et al. 1993). Further, we do not consider here three unusual New Mexico triggered lightning flashes, each of which contained 24 return strokes (Idone et al. 1984). For these three flashes, the geometric means of the return-stroke current peak and interstroke interval are 5.6 kA and 8.5 ms, respectively, each considerably smaller than its counterpart in either natural lightning or other triggered lightning discussed below.

We first review measurements of the peak values of current and current derivative. Summaries of the statistical characteristics of measured return-stroke currents, I, and derivatives of current with respect to time, dI/dt, taken from Schoene et al. (2003a), are given in Tables 2.3 and 2.4, respectively. As seen in Table 2.3, the geometric mean values of current peak range from about 12 to 15 kA. These values are similar to the median value of 12 kA reported by Anderson and Eriksson (1980) for subsequent strokes in natural lightning. The geometric mean values of dI/dt peak based on data from two studies presented in Table 2.4 are 73 and 97 kA μs⁻¹.

Scatter plots of dI/dt peak vs. I peak from the triggered lightning experiments in Florida (1985, 1987, and 1988) and in France (1986) are shown in Fig. 2.10. Correlation coefficients are 0.87, 0.80, and 0.70 for the 1985, 1987, and 1988 Florida data, respectively, and 0.78 for the 1986 data from France. The largest measured value of dI/dt is 411 kA s⁻¹, as reported from Florida (KSC) studies by Leteinturier et al. (1991). The corresponding measured peak current is greater than 60 kA, the largest value of this parameter reported for summer triggered lightning to date. Also shown in Fig. 2.10 are the linear regression line and the regression equation for each of the four subsets of the data. Note that the correlation coefficients between the logarithms of dI/dt and I for the same data were found to be lower: 0.79, 0.56, and 0.60 for the 1985, 1987, and 1988 Florida data, respectively, and 0.71 for the 1986 data from France (Depasse 1994; Table 10).

Table 2.3 Current waveform parameters for negative rocket-triggered lightning

Location/Year	n	Min.	Max.	Arithmetic Mean	σ	Geometric Mean	σ_{\log}	Reference ^b
<i>Current Peak, kA</i>								
Kennedy Space Center, Florida; 1985–1991	305	2.5	60.0	14.3	9.0	—	—	1
Saint-Privat d'Allier, France; 1986, 1990–1991	54	4.5	49.9	11.0	5.6	—	—	1
Kennedy Space Center, Florida and Fort McClellan, Alabama; 1990, 1991	45	—	—	—	—	12	0.28	2
Camp Blanding, Florida; 1993	37	5.3	44.4	15.1	—	13.3	0.23	3
Camp Blanding, Florida; 1997	11	5.3	226	12.8	5.6	11.7	0.20	4
Camp Blanding, Florida; 1998	25	5.9	33.2	14.8	7.0	13.5	0.19	5
present study	64	5	36.8	16.2	7.6	14.5	0.21	
<i>Current 10–90% Risetime, ns</i>								
Kennedy Space Center, Florida and Fort McClellan, Alabama; 1990, 1991	43	—	—	—	—	370	0.29	2
Saint-Privat d'Allier, France; 1990–1991	37	250	4900	1140	1100	—	—	1
Camp Blanding, Florida; 1997	11	300	4000	900	1200	600	0.39	4

Table 2.3 (continued)

Location/Year	n	Min.	Max.	Arithmetical Mean	σ	Geometric Mean	σ_{\log}	Reference ^b
<i>Current 30–90% Risetime, ns</i>								
Kennedy Space Center, Florida and Fort McClellan, Alabama; 1990, 1991	43	—	—	—	190	280	0.28	2
present study	65	54	1751	260	316	191	0.29	
<i>Current Half-Peak Width, μs</i>								
Saint-Privat d'Allier, France; 1990–1991	24	14.7	103.2	49.8	22.4	—	—	1
Kennedy Space Center, Florida and Fort McClellan, Alabama; 1990, 1991	41	—	—	—	—	18	0.30	2
Camp Blanding, Florida; 1997	11	6.5	100	35.7	24.6	29.4	0.29	4
present study	64	2.4	37.2	13.2	8.5	10.5	0.32	

^a The polarity of the peak values is ignored.^b References: 1, Depasse [1994a]; 2, Fisher et al. [1993]; 3, Rakov et al. [1998]; 4, Crawford [1998]; 5, Uman et al. [2000].

Table 2.4 Current derivative waveform parameters for negative rocket-triggered lightning

Location/Year	n	Min.	Max.	Arithmetic Mean	σ	Geometric Mean	σ_{\log}
<i>dI/dt Peak, kA/μs</i>							
Kennedy Space Center, Florida; 1985–1991 ^b	134	5	411	118	97	—	—
Saint-Privat d'Allier, France; 1986, 1990–1991 ^b	47	13	139	43	25	—	—
Camp Blanding, Florida; 1998 ^c	15	45	152	80	35	73	0.17
present study ^d	64	8	292	117	65	97	0.31
<i>dI/dt 30–90% Risetime, ns</i>							
present study	29	17	69	32	13	30	0.16
<i>dI/dt 10–10% Width, ns</i>							
Saint-Privat d'Allier, France; 1990–1991 ^b	17	70	2010	400	210	—	—
present study	29	49	149	92	25	89	0.12

Adapted from Schoene et al. (2003a)

^a The polarity of the peak values is ignored.

^b Depasse (1994a)

^c Uman et al. (2000).

^d Fifteen dI/dt peaks obtained from differentiating I.

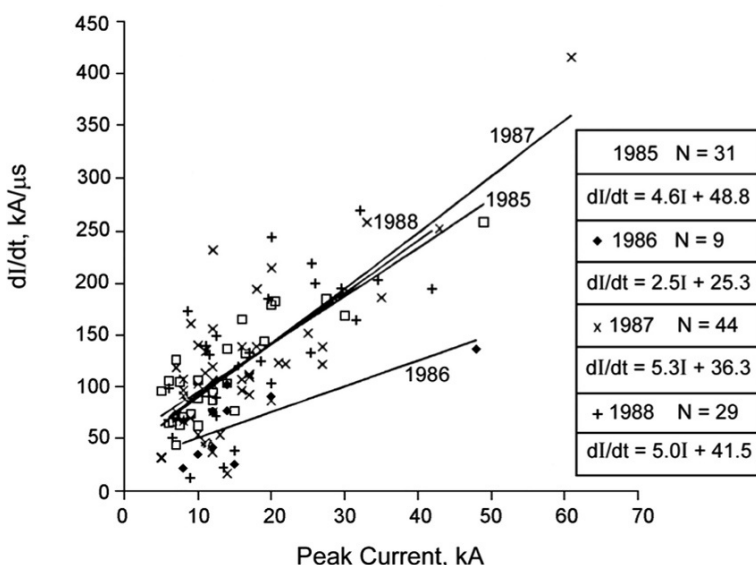


Fig. 2.10 Relation between peak current rate of rise, dI/dt , and peak current I , from triggered-lightning experiments conducted at the NASA Kennedy Space Center, Florida, in 1985, 1987, and 1988 and in France in 1986. The regression line for each year is shown, and the sample size and the regression equation are given. Adapted from Leteinturier et al. (1991)

Fisher et al. (1993) compared a number of return-stroke current parameters for classical triggered-lightning strokes from Florida and Alabama with the corresponding parameters for natural lightning in Switzerland reported by Berger et al. (1975) and Anderson and Eriksson (1980). Since triggered-lightning strokes are similar to subsequent strokes in natural lightning, the comparison applies only to subsequent strokes that are usually initiated by leaders that follow the path of the previous stroke. Distributions of peak currents are very similar, with median values being 13 and 12 kA for triggered and natural lightning, respectively. On the other hand, there appear to be appreciable differences between the triggered-lightning data of Fisher et al. (1993) and the natural-lightning data of Berger et al. (1975) and Anderson and Eriksson (1980) in terms of current waveform parameters, half-peak

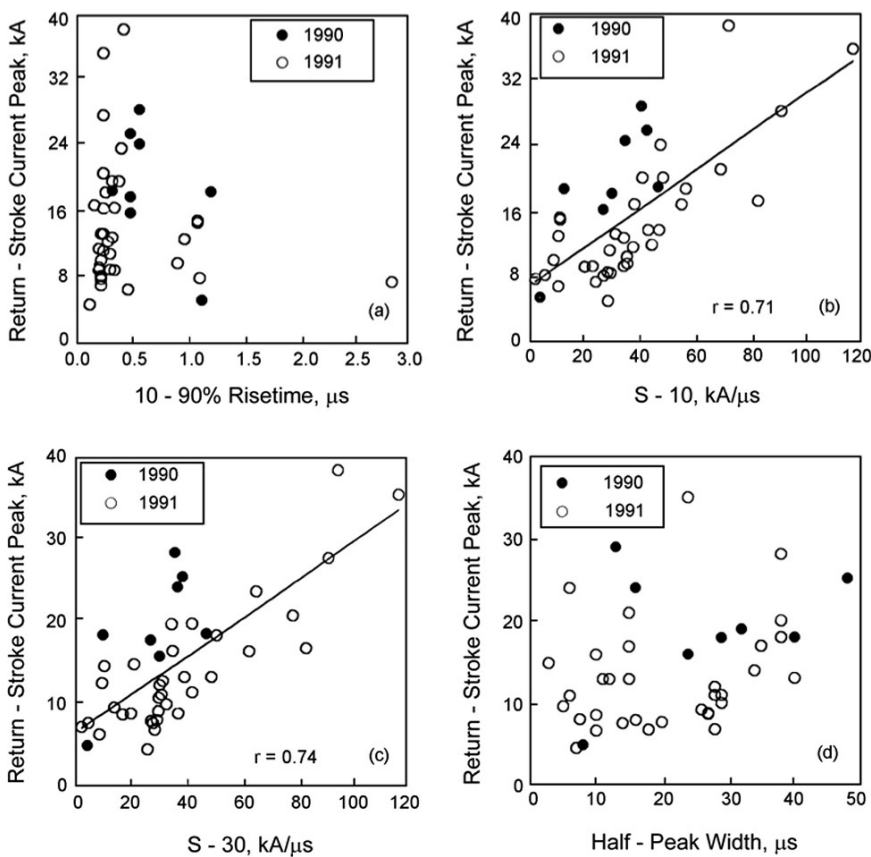


Fig. 2.11 Scatterplots relating various return stroke parameters. Solid circles represent 1990 data from KSC, Florida, and open circles represent 1991 data from Fort McClellan, Alabama. **(a)** Current peak versus 10–90 percent risetime; **(b)** current peak versus $S-10$; **(c)** current peak versus $S-30$; **(d)** current peak versus half-peak width. Regression lines and correlation coefficients (r) are given in **(b)** and **(c)**. Adapted from Fisher et al. (1993)

width, and stroke charge. The shorter risetime and higher average slope (steepness) in the triggered-lightning data may be explained by the better time resolution of the measuring systems used in the triggered-lightning studies. The Swiss data were recorded as oscilloscopic traces with the smallest measurable time being 0.5 μ s (Berger and Garabagnati 1984).

Fisher et al. (1993) also studied relations among some return-stroke parameters, the results being shown in Fig. 2.11. They found a relatively strong positive correlation between the 10–90 percent average steepness (S-10) and current peak (correlation coefficient = 0.71) and between the 30–90 percent average steepness (S-30) and current peak (correlation coefficient = 0.74). As seen in Fig. 2.11a, there is essentially no linear correlation between current peak and 10–90 percent risetime.

2.5 Return-Stroke Current Peak Versus Grounding Conditions

In examining the lightning current flowing from the bottom of the channel into the ground, it is convenient to approximate lightning by a Norton equivalent circuit (Carlson 1996), i.e., by a current source equal to the lightning current that would be injected into the ground if that ground were perfectly conducting (a short-circuit current) in parallel with a lightning-channel equivalent impedance Z_{ch} assumed to be constant. The lightning grounding impedance Z_{gr} is a load connected in parallel with the lightning Norton equivalent. Thus the “short-circuit” lightning current I effectively splits between Z_{gr} and Z_{ch} so that the current measured at the lightning-channel base is found as $I_{meas} = I Z_{ch}/(Z_{ch} + Z_{gr})$. Both source characteristics, I and Z_{ch} , vary from stroke to stroke, and Z_{ch} is a function of channel current, the latter nonlinearity being in violation of the linearity requirement necessary for obtaining the Norton equivalent circuit. Nevertheless, if we are concerned only with the peak value of current and assume that for a large number of strokes the average peak value of I and the average value of Z_{ch} at current peak are each more or less constant, the Norton equivalent becomes a useful tool for studying the relation between lightning current peak and the corresponding values of Z_{ch} and Z_{gr} . For instance, if the measured channel-base current peak statistics are similar under a variety of grounding conditions, then Z_{ch} must always be much larger than Z_{gr} at the time of the current peak. In the following, we will compare the geometric mean current peaks from triggered lightning experiments in which similar rocket launchers having a relatively small height of 4–5 m were used, but grounding conditions differed considerably. All the information needed for this comparison is given in Table 2.5.

As seen in Table 2.5, Camp Blanding measurements of lightning currents that entered sandy soil with a relatively poor conductivity of 2.5×10^{-4} S m $^{-1}$ without any grounding electrode resulted in a value of the geometric mean return-stroke current peak, 13 kA, that is similar to the geometric mean value, 14 kA, estimated from measurements at KSC made in 1987 using a launcher of the same geometry which was

Table 2.5 Geometric mean peak current versus grounding conditions from different triggered-lightning experiments

Experiment	Reference	Trigger Threshold, kA	Sample Size	GM Peak Current, kA	Soil	Artificial Grounding	Grounding Resistance, Ω
KSC, Florida, 1987	Eybert-Berard et al. (1988), Leteinturier et al. (1991), as reported by Fisher et al. (1993)	5	36	14	0.5-m deep salt water ($3\text{--}6 \text{ S m}^{-1}$)	$1.2 \times 1.2 \text{ m}^2$ metal plane connected through three 0.5 m long wires at the four corners to salt water	0.1
Fort McClellan, Alabama 1991	Fisher et al. (1993)	2 (two strokes below 2 kA from continuous tape record included)	37	11	clay ($3 \times 10^{-3} \text{ S m}^{-1}$)	rebar framework of the munitions storage bunker interconnected with lightning protection system including air terminals, down conductors and buried counterpoise	presumably low
Camp Blanding, Florida, 1993	Uman et al. (1999a, 1997)	3.3 and 4.2	37	13	sand ($2.5 \times 10^{-4} \text{ S m}^{-1}$)	none; launcher was based on two parallel 15-m long, 2 m apart concrete slabs above three unenergized power cables buried 1 m deep and 5 m apart	64×10^3 (assuming that the contact surface between the channel and ground was a hemisphere with 1-cm radius)
Fort McClellan, Alabama 1993	Fisher et al. (1994)	~4	31	10	heavy red clay ($1.8 \times 10^{-3} \text{ S m}^{-1}$)	single 0.3-m or 1.3-m long vertical ground rod	260

KSC = Kennedy Space Center. The values of grounding resistance are determined by the geometry of the grounding electrode (or the geometry of the contact surface between the channel and the ground in the absence of grounding electrode) and soil conductivity. They are measured under low-frequency, low-current conditions and should be understood as the initial values of resistance encountered by lightning before the onset of any breakdown processes in the soil or along the ground surface.

Adapted from Rakov et al. (1998).

much better grounded into salt water with a conductivity of $3\text{--}6 \text{ S m}^{-1}$ via underwater braided metallic cables. Additionally, fairly similar geometric mean values were found from the Fort McClellan, Alabama, measurements using a poorly grounded launcher (10 kA) and the same launcher well grounded (11 kA) in 1993 and 1991, respectively. Also, Ben Ben Rhouma et al. (1995) give arithmetic mean values of return stroke current peaks in the range from 15 to 16 kA for the Florida triggered-lightning experiments at Camp Blanding in 1993 and at KSC in 1987, 1989, and 1991.

The values of grounding resistance (probably the dominant component of Z_{gr}) given in Table 2.5 should be understood as the initial values encountered by a lightning downward leader before the onset of any breakdown processes in the soil or along the ground surface associated with the return stroke. Note from Table 2.5 that the grounding resistance varies from 0.1Ω to $64 \text{ k}\Omega$, while Z_{ch} , assumed to be a real number, was estimated from the analysis of the current waves traveling along the 540-m high tower to be in the range from hundreds of ohms to some kilohms (Gorin et al. 1977; Gorin and Shkilev 1984). The observation that the average return stroke current is not much influenced by the level of man-made grounding, ranging from excellent to none, implies that lightning is capable of lowering the grounding impedance it initially encounters (Table 2.5) to a value that is always much lower than the equivalent impedance of the main channel. On the basis of (1) the evidence of the formation of plasma channels (fulgurites) in the sandy soil at Camp Blanding (Uman et al. 1994b, 1997; Rakov et al. 1999a; Jones et al. 2005) and (2) optical records showing arcing along the ground surface at both Camp Blanding and Fort McClellan (Fisher et al. 1994; Rakov et al. 1998), Rakov et al. inferred that surface and underground plasma channels are important means of lowering the lightning grounding impedance, at least for the types of soil at the lightning triggering sites in Florida and Alabama (sand and clay, respectively). Further, Bazelyan and Raizer (2000a) found from their laboratory experiments and modeling that surface arcs developing at a speed of $10^6\text{--}10^7 \text{ m s}^{-1}$ is the most likely mechanism of grounding impedance reduction by lightning current. They stated that a voltage as low as 135 kV was required to bridge a 5 m long gap by such an arc. Since the arcs develop at a speed of 1 to $10 \text{ m } \mu\text{s}^{-1}$ (see above), some reduction of grounding impedance should occur before the current peak, particularly when the risetime is greater than 1 μs .

A photograph of ground surface arcing during a triggered-lightning flash from Fort McClellan, Alabama, is shown in Fig. 2.12, and evidence of surface arcing in natural lightning is presented in Fig. 2.13. Injection of laboratory currents up to 20 kA into loamy sand in the presence of water sprays simulating rain resulted in surface arcing that significantly reduced the grounding resistance at the current peak (M. Darveniza, personal communication 1995; Wang et al. 2005). The fulgurites (glassy tubes produced by lightning in sand; Figs. 2.14 and 2.15) found at Camp Blanding usually show that the in-soil plasma channels tend to develop toward the better conducting layers of soil or toward buried metallic objects that, when contacted, serve to further lower the grounding resistance. The percentages of return strokes producing optically detectable surface arcs developing from ver-



Fig. 2.12 Photograph of ground surface arcing associated with the second stroke (current peak of 30 kA) of flash 9312 triggered at Fort McClellan, Alabama. Lightning channel is outside of field of view. One of the surface arcs approached the right edge of the photograph, a distance of 10 m from the rocket launcher. Adapted from Fisher et al. (1994) (See also Plate 2 in the Color Plate Section on page 594)



Fig. 2.13 Evidence of ground surface arcing on a golf course green in Arizona. Courtesy of E.P. Krider

tical ground rods versus return stroke peak current, from the 1993 and 1995 Fort McClellan experiments, are shown in Fig. 2.16. Such arcs were produced by essentially all strokes with peak currents exceeding 15 kA. The surface arcing appears to be random in direction and often leaves little if any evidence on the ground. Even within the same flash, individual strokes can produce arcs developing in different directions. In one case, it was possible to estimate the current carried by one arc branch which contacted the instrumentation. That current was approximately 1 kA, or 5 percent of the total current peak in that stroke. The observed horizontal extent

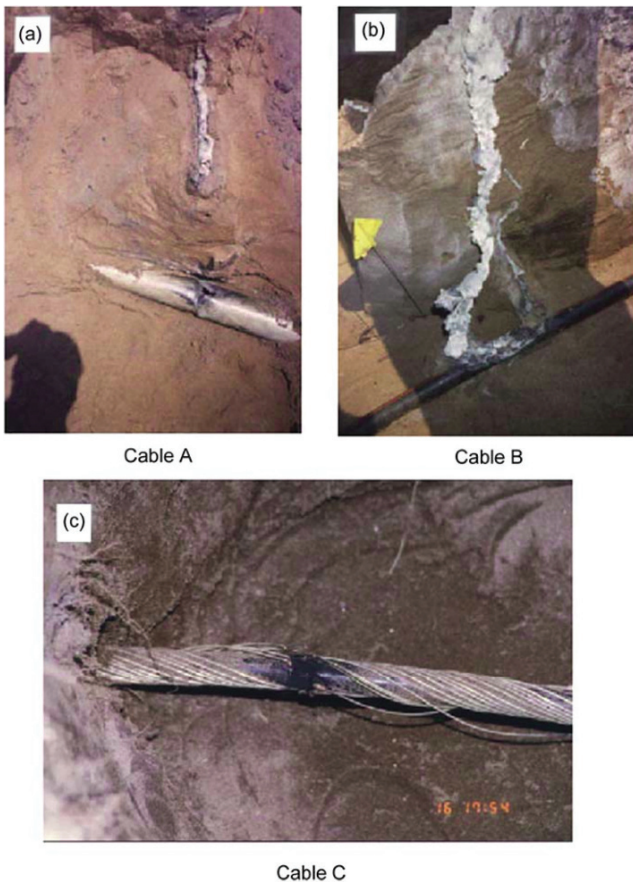


Fig. 2.14 Lightning damage to underground power cables. (a) coaxial cable in an insulating jacket inside a PVC conduit; note the section of vertical fulgurite in the upper part of the picture (the lower portion of this fulgurite was destroyed during excavation) and the hole melted through the PVC conduit, (b) coaxial cable in an insulating jacket, directly buried; note the fulgurite attached to the cable, (c) coaxial cable whose neutral (shield) was in contact with earth; note that many strands of the neutral are melted through. The cables were tested at Camp Blanding, Florida in 1993. Photos in (a) and (b) were taken by V.A. Rakov and in (c) by P.P. Barker

of surface arcs was up to 20 m, which was the limit of the photographic coverage during the 1993 Fort McClellan experiment. No fulgurites were found in the soil (red clay) at Fort McClellan, only concentrated current exit points at several spots along the 0.3- or 1.3-m steel ground rod (Table 2.5). It is likely that the uniform ionization of soil, usually postulated in studies of the behavior of grounding electrodes subjected to lightning surges, is not an adequate assumption, at least not in the southeastern United States, where distinct plasma channels in the soil and on the ground surface appear to contribute considerably to lowering the grounding resistance.



Fig. 2.15 A Florida fulgurite of about 5 m length excavated by the University of Florida lightning research group

2.6 Characterization of the Close Lightning Electromagnetic Environment

A knowledge of close lightning electric and magnetic fields is needed for the evaluation of lightning-induced effects in various electric circuits and systems (e.g., Nucci and Rachidi 1995) and for the testing of the validity of lightning models (e.g., Rakov and Uman 1998; Schoene et al. 2003b). The close (within tens to hundreds of meters) lightning electromagnetic environment is most easily studied using rocket-triggered lightning for which the termination point on ground is known (Leteinturier et al. 1990; Depasse 1994; Rubinstein et al. 1995; Rakov et al. 1995, 1998, 2001; Uman et al. 2000, 2002; Crawford et al. 2001; Schoene et al. 2003a).

Rubinstein et al. (1992, 1995) measured and analyzed electric field waveforms at 500 m for 31 leader/return stroke sequences and at 30 m for two leader/return stroke sequences in lightning flashes triggered at the Kennedy Space Center, Florida, in 1986 and 1991, respectively. They found that, at tens to hundreds of meters from the lightning channel, leader/return-stroke vertical electric field waveforms appear as asymmetrical V-shaped pulses, the negative slope of the leading edge being lower than the positive slope of the trailing edge. The bottom of the V is associated with

the transition from the leader (the leading edge of the pulse) to the return stroke (the trailing edge of the pulse). The first multiple-station electric field measurements within a few hundred meters of the triggered-lightning channel were performed in 1993 at Camp Blanding, Florida (Uman et al. 1999a) and at Fort McClellan, Alabama (Fisher et al. 1994). Detailed analyses of these data have been presented by Rakov et al. (1998). From the 1993 Florida experiment, the geometric mean width of the V at half of peak value is 3.2 μs at 30 m, 7.3 μs at 50 m, and 13 μs at 110 m, a distance dependence close to linear.

In 1997, the multiple-station field measuring experiment at Camp Blanding, Florida, was extended to include seven stations at distances of 5, 10, 20, 30, 50, 110, and 500 m from the triggered-lightning channel (Crawford et al. 1999). Most of the data obtained at 5 m appeared to be corrupted, possibly due to ground surface arcs (see Section 2.5) and are not considered here. Leader/return-stroke electric field waveforms in one flash (S9721) simultaneously measured at 10, 20, 30, 50, 110, and 500 m are shown in Fig. 2.17. The evolution of the leader/return-stroke electric field waveform as distance increases is consistent with previous measurements (Rubinstein et al. 1995; Rakov et al. 1998) and reflects an increasing contribution to the field from progressively higher channel sections.

Crawford et al. (2001) analyzed net electric field changes due to dart leaders in triggered lightning from experiments conducted in 1993, 1997, 1998, and 1999 at Camp Blanding, Florida, and in 1993 at Fort McClellan, Alabama. In 1997–

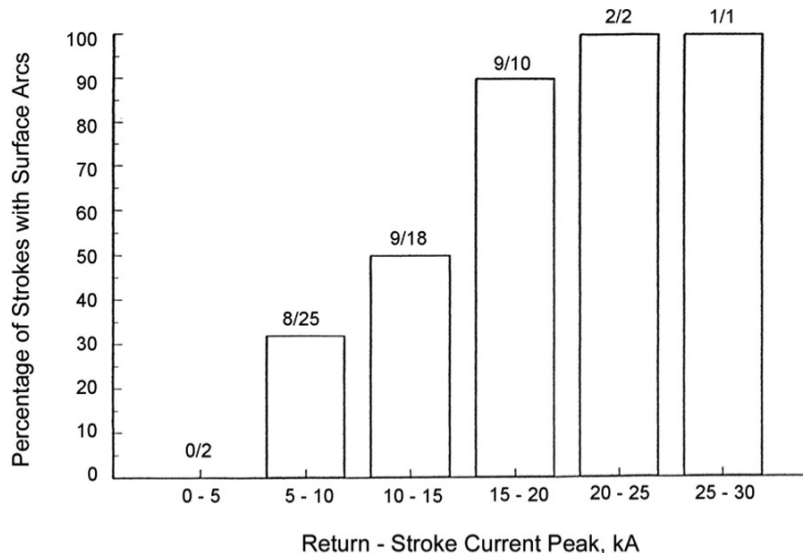


Fig. 2.16 Percentages of return strokes producing optically detectable ground surface arcing as a function of return-stroke current peak (Fort McClellan, Alabama, 1993 and 1995). Numbers above each histogram column indicate the number of strokes producing optically detectable arcing (numerator) and the total number of strokes in that current peak range (denominator). Adapted from Rakov et al. (1998)

1999, the fields were measured at 2–10 stations with distances from the lightning channel ranging from 10 to 621 m, while in 1993 the fields were measured at 3 distances, 30, 50, and 110 m, in Florida, and at two distances, about 10 and 20 m, in Alabama. The data on the leader electric field change as a function of distance for Florida are presented in Table 2.6. With a few exceptions, the 1997–1999 data indicate that the distance dependence of the leader electric field change is close to an inverse proportionality (r^{-1}), in contrast with the 1993 data (from both Florida, shown in Table 2.6, and Alabama, not shown) in which a somewhat weaker distance dependence was observed. The typically observed r^{-1} dependence is consistent with a uniform distribution of leader charge along the bottom kilometer or so of the channel. This observation simply indicates that for such a relatively short channel section a non-uniform charge density distribution will appear approximately uniform. Cooray et al. (2004) compared Crawford et al.’s (2001) experimental results with theoretical predictions for a vertical conductor in an external electric field and found a fairly good agreement. A variation of ΔE_L with distance slower than r^{-1} implies a decrease of leader charge density with decreasing height.

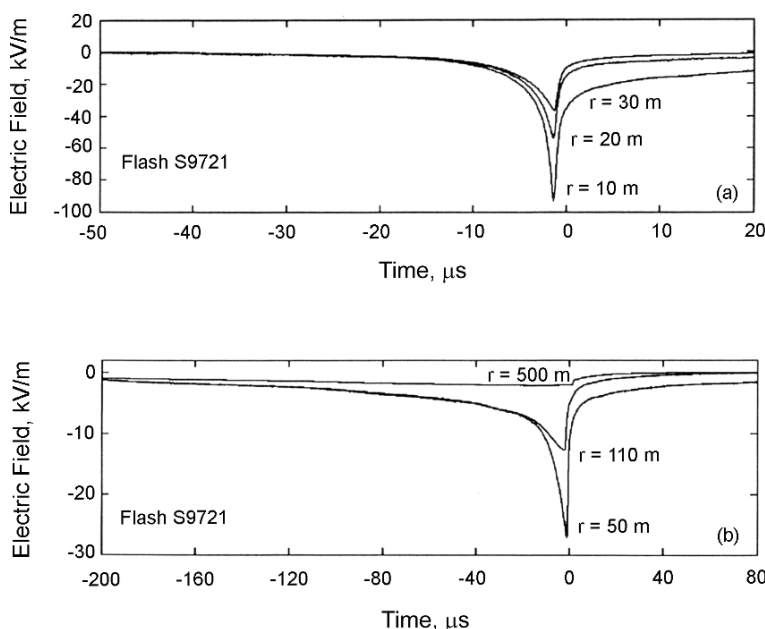


Fig. 2.17 Electric field waveforms of the first leader/return-stroke sequence of flash S9721 as recorded in 1997 at distances (a) 10, 20, and 30 m and (b) 50, 110, and 500 m at Camp Blanding, Florida. The initial downward-going portion of the waveform is due to the dart leader, and the upward-going portion is due to the return stroke. Adapted from Crawford et al. (1999)

Table 2.6 Dart-leader electric field change as a function of distance from the lightning channel for events recorded at the ICLRT in 1993–1999

Year	Flash	Stroke	Number of stations	I_p (kA)	$\Delta E_L = f(r)$ (kV/m)	Distances (m)
1993	9313	2	3	9.7	$61r^{-0.28}$	30/50/110
		3	3	11	$69r^{-0.30}$	30/50/110
		4	3	13	$76r^{-0.30}$	30/50/110
		5	3	11	$56r^{-0.25}$	30/50/110
		9320	1	9.6	$1.7 \times 10^2 r^{-0.51}$	30/50/110
		2	3	8.4	$1.0 \times 10^2 r^{-0.42}$	30/50/110
	S9711	1	3	6.5	$1.6 \times 10^3 r^{-1.1}$	50/110/500
		S9712	1	5.3	$1.4 \times 10^2 r^{-0.59}$	10/20/30
		S9718	1	12	$2.1 \times 10^3 r^{-1.1}$	20 – 500
			3		$1.4 \times 10^3 r^{-1.0}$	30/50/110
		S9720	1	21	$2.6 \times 10^3 r^{-1.1}$	30 – 500
			3		$1.7 \times 10^3 r^{-0.99}$	30/50/110
1997	S9721	1	6	11	$1.3 \times 10^3 r^{-1.0}$	10 – 500
			3		$9.9 \times 10^2 r^{-0.93}$	30/50/110
			3		$7.1 \times 10^2 r^{-0.84}$	10/20/30
		U9801	1	10	8.7	$2.8 \times 10^3 r^{-1.2}$
		U9822	1	10	11	$2.6 \times 10^3 r^{-1.1}$
		U9824	1	10	17	$5.1 \times 10^3 r^{-1.2}$
		U9825	1	10	NR	$5.8 \times 10^3 r^{-1.2}$
		U9827	1	9	41	$7.1 \times 10^3 r^{-1.2}$
		S9806	1	10	9.1	$1.5 \times 10^3 r^{-0.96}$
		U9901	1	10	8.2	$3.3 \times 10^3 r^{-1.2}$
1999	U9902	1	10	12	$2.1 \times 10^3 r^{-1.1}$	91 – 380
		S9915	1	9	11	$1.0 \times 10^3 r^{-0.98}$
		S9918	1	9	26	$5.3 \times 10^3 r^{-1.2}$
		S9930	1	3	39	$4.0 \times 10^3 r^{-1.0}$
		S9932	1	4	19	$3.6 \times 10^3 r^{-1.1}$
		S9934	1	4	30	$3.0 \times 10^3 r^{-1.0}$
		S9935	1	3	21	$2.1 \times 10^3 r^{-1.0}$
						15 – 507
						15 – 507
						15 – 507

NR = not recorded. I_p = return-stroke peak current.

Adapted from Crawford et al. (2001).

2.7 Concluding Remarks

The rocket-and-wire technique has been routinely used since the 1970s to artificially initiate (trigger) lightning from natural thunderclouds for purposes of research and testing. To date, approximately 1,000 lightning flashes were triggered using the rocket-and-wire technique, with over 300 of them at Camp Blanding, Florida. Leader/return stroke sequences in triggered lightning are similar in most (if not all) respects to subsequent leader/return stroke sequences in natural downward lightning and to all such sequences in object-initiated lightning. The initial processes in triggered lightning are similar to those in object-initiated (upward) lightning and are distinctly different from the first leader/return stroke sequence in natural downward lightning. The results of triggered-lightning experiments have provided considerable insight into natural lightning processes that would not have

been possible from studies of natural lightning due to its random occurrence in space and time. Among such findings are the observation of an upward connecting leader in a dart leader/return stroke sequence, identification of the M-component mode of charge transfer to ground, the observation of a lack of dependence of return stroke current peak on grounding conditions, discovery of X-rays produced by lightning dart leaders, new insights into the mechanism of cutoff and reestablishment of current in the lightning channel, direct measurements of NO_x production by an isolated lightning channel section, and the characterization of the electromagnetic environment within tens to hundreds of meters of the lightning channel. Triggered-lightning experiments have contributed significantly to testing the validity of various lightning models and to providing ground-truth data for the U.S. National Lightning Detection Network (NLDN). Triggered lightning is a very useful tool to study the interaction of lightning with various objects and systems.

References

- Al-Dayeh, M., Dwyer, J.R., Rassoul, H.K., Uman, M.A., Rakov, V.A., Jerauld, J., Jordan, D.M., Rambo, K.J., Caraway, L., Corbin, V., and Wright, B. 2002. A New Instrument for Measuring Energetic Radiation from Triggered Lightning. 2002 Fall AGU Meeting, San Francisco, California.
- Anderson, R.B., and Eriksson, A.J. 1980. Lightning parameters for engineering application. *Electra* 69: 65–102.
- Bazelyan, E.M., and Raizer, Yu. P. 2000a. *Lightning Physics and Lightning Protection*, 325 p., Bristol: IOP Publishing.
- Bejleri, M., Rakov, V.A., Uman, M.A., Rambo, K.J., Mata, C.T., and Fernandez, M.I. 2004. Triggered Lightning Testing of an Airport Runway Lightning System. *IEEE Trans. EMC*, Vol. 46, No. 1, pp. 96–101.
- Ben Rhouma, A., Auriol, A.P., Eybert-Berard, A., Berlandis, J.-P., and Bador, B. 1995. Nearby lightning electromagnetic fields. In Proc 11th Int. Zurich Symp. on Electromagn. Compat., Zurich, Switzerland, pp. 423–428.
- Berger, K., Anderson, R.B., and Knoninger, H. 1975. Parameters of lightning flashes. *Electra* 41: 23–37.
- Berger, K., and Garabagnati, E. 1984. Lightning current parameters. Results obtained in Switzerland and in Italy. URSI Conf., Florence, Italy, 13 p.
- Brook, M., Armstrong, G., Winder, R.P.H., Vonnegut, B., and Moore, C.B. 1961. Artificial initiation of lightning discharges. *J. Geophys. Res.* 66: 3967–9.
- Carlson, A.B. 1996. *Circuits*. 838 pp., New York: John Wiley & Sons.
- Chen, M., T. Watanabe, N. Takagi, Y. Du, D. Wang, and X. Liu. 2003. Simultaneous observations of optical and electrical signals in altitude-triggered negative lightning flashes, *J. Geophys. Res.*, Vol. 108, No. D8, 4240, doi:10.1029/2002JD002676.
- Cooray, V., Montano, R., and Rakov, V. 2004. A model to represent negative and positive lightning first return strokes with connecting leaders, *J. Electrostatics*, 60, 97–109.
- Crawford, D.E. 1998. Multiple-station measurements of triggered lightning electric and magnetic fields. M.S. Thesis, Univ. of Florida, Gainesville, 282 p.
- Crawford, D.E., Rakov, V.A., Uman, M.A., Schnetzer, G.H., Rambo, K.J., and Stapleton, M.V. 1999. Multiple-station measurements of triggered-lightning electric and magnetic fields. In Proc. 11th Int. Conf. on Atmospheric Electricity, Guntersville, Alabama, pp. 154–157.

- Crawford, D.E., Rakov, V.A., Uman, M.A., Schnetzer, G.H., Rambo, K.J., Stapleton, M.V., and Fisher, R.J. 2001. The close lightning electromagnetic environment: Dart-leader electric field change versus distance. *J. Geophys. Res.* 106: 14,909–917.
- Depasse, P. 1994. Statistics on artificially triggered lightning. *J. Geophys. Res.* 99: 18,515–522.
- Dwyer, J.R., Al-Dayeh, M., Rassoul, H.K., Uman, M.A., Rakov, V.A., Jerauld, J., Jordan, D.M., Rambo, K.J., Caraway, L., Corbin, V., and Wright, B. 2002. Observations of Energetic Radiation from Triggered Lightning, 2002 Fall AGU Meeting, San Francisco, California.
- Dwyer, J.R., Rassoul, H.K., Al-Dayeh, M., Caraway, L., Wright, B., Chrest, A., Uman, M.A., Rakov, V.A., Rambo, K.J., Jordan, D.M., Jerauld, J., and Smyth, C. 2004a. Measurements of x-ray emission from rocket-triggered lightning. *Geophys. Res. Lett.*, 31, L05118, doi: 10.1029/2003GL018770, 4 p.
- Dwyer, J.R., Rassoul, H.K., Al-Dayeh, M., Caraway, L., Wright, B., Chrest, A., Uman, M.A., Rakov, V.A., Rambo, K.J., Jordan, D.M., Jerauld, J., and Smyth, C. 2004b. A ground level gamma-ray burst observed in association with rocket-triggered lightning. *Geophys. Res. Lett.*, 31, L05119, doi: 10.1029/2003GL018771, 4 p.
- Dwyer, J.R., Uman, M.A., Rassoul, H.K., Al-Dayeh, M., Caraway, L., Jerauld, J., Rakov, V.A., Jordan, D.M., Rambo, K.J., Corbin, V., and Wright, B. 2003. Energetic Radiation Produced by Rocket-Triggered Lightning. *Science*, 299, 694–697.
- Eybert-Berard, A., Barret, L., and Berlandis, J.P. 1986. Campagne foudre aux ETATS-UNIS Kennedy Space Center (Florida), Programme RTLP 85* (in French). STT/ASP 86–01, Cent. D'Etud. Nucl. de Grenoble, Grenoble, France.
- Eybert-Berard, A., Barret, L., and Berlandis, J.P. 1988. Campagne d'expérimentations foudre RTLP 87, NASA Kennedy Space Center, Florida, USA (in French). STT/LASP 88–21/AEB/JPB-pD, Cent. D'Etud. Nucl. de Grenoble, Grenoble, France.
- Fieux, R., Gary, C., and Hubert, P. 1975. Artificially triggered lightning above land. *Nature* 257: 212–4.
- Fieux, R.P., Gary, C.H., Hutzler, B.P., Eybert-Berard, A.R., Hubert, P.L., Meesters, A.C., Perroud, P.H., Hamelin, J.H., and Person, J.M. 1978. Research on artificially triggered lightning in France. *IEEE Trans. Pow. Appar. Syst.* PAS-97: 725–33.
- Fisher, R.J., Schnetzer, G.H., and Morris, M.E. 1994. Measured fields and earth potentials at 10 and 20 meters from the base of triggered-lightning channels. In Proc. 22nd Int. Conf. on Lightning Protection, Budapest, Hungary, Paper R 1c–10, 6 p.
- Fisher, R.J., Schnetzer, G.H., Thottappillil, R., Rakov, V.A., Uman, M.A., and Goldberg, J.D. 1993. Parameters of triggered-lightning flashes in Florida and Alabama. *J. Geophys. Res.* 98: 22,887–902.
- Gorin, B.N., Levitov, V.I., and Shkilev, A.V. 1977. Lightning strikes to the Ostankino tower. *Elektrichestvo* 8: 19–23.
- Gorin, B.N., and Shkilev, A.V. 1984. Measurements of lightning currents at the Ostankino tower. *Elektrichestvo* 8: 64–5.
- Hierl, A. 1981. Strommessungen der Blitztriggerstation Steingaden. In Proc. 16th Int. Conf. on Lightning Protection, Szeged, Hungary, paper R-1.04, 10 p.
- Horii, K. 1982. Experiment of artificial lightning triggered with rocket. *Memoirs of the Faculty of Engineering, Nagoya Univ. Japan* 34: 77–112.
- Horii, K., and Ikeda, G. 1985. A consideration on success conditions of triggered lightning. In Proc. 18th Int. Conf. on Lightning Protection, Munich, Germany, paper 1–3, 6 p.
- Horii, K., Nakamura, K., and Sumi, S.I. 2006. Review of the experiment of triggered lightning by rocket in Japan. In Proc. 28th Int. Conf. on Lightning Protection, Kanazawa, Japan.
- Horii, K., and Nakano, M. 1995. Artificially triggered lightning. In *Handbook of Atmospheric Electrodynamics*, vol. 1. ed. H. Volland, pp. 151–166. Boca Raton, Florida: CRC Press.
- Horii, K., Wada, A., Nakamura, K., Yoda, M., Kawasaki, A., Sirait, K.T., Soekarto, J., Sunoto, A.M. 1990. Experiment of rocket-triggered lightning in Indonesia. *Trans. IEE Japan* 110-B: 1068–9.
- Hubert, P. 1984. Triggered lightning in France and New Mexico. *Endeavour* 8: 85–9.

- Hubert, P., Laroche, P., Eybert-Berard, A., and Barret, L. 1984. Triggered lightning in New Mexico. *J. Geophys. Res.* 89: 2511–21.
- Idone, V.P., Orville, R.E. Hubert, P. Barret, L., and Eybert-Berard, A. 1984. Correlated observations of three triggered lightning flashes. *J. Geophys. Res.* 89: 1385–94.
- Jafferis, W. 1995. Rocket triggered lightning – Kennedy Space Center and beyond. In Proc. 1995 Int. Conf. on Lightning and Static Electricity, Williamsburg, Virginia, pp. 57/1-57/20.
- Jayakumar, V., Rakov, V.A., Miki, M., Uman, M.A., Schnetzer, G.H., and Rambo, K.J. Estimation of input energy in rocket-triggered lightning, *Geophys. Res. Lett.*, 33, L05702, 2006, doi:10.1029/2005GL025141.
- Jerauld, J., Rakov, V.A., Uman, M.A., Rambo, K.J., Jordan, D.M., Cummins, K.L., and Cramer, J.A. 2005. An evaluation of the performance characteristics of the U.S. National Lightning Detection Network in Florida using rocket-triggered lightning, *J. Geophys. Res.*, Vol. 110, D19106, doi:10.1029/2005JD005924.
- Jerauld, J., Uman, M.A., Rakov, V.A., Rambo, K.J. and Schnetzer, G.H. 2007. Insights into the ground attachment process of natural lightning gained from an unusual triggered-lightning stroke. *J. Geophys. Res.*, 112, D13113, doi:10.1029/2006JD007682.
- Jones, B.E., K.S. Jones, K.J. Rambo, V.A. Rakov, J. Jerauld, and M.A. Uman. 2005. Oxide reduction during triggered-lightning fulgurite formation, *Journal of Atmospheric and Solar-Terrestrial Physics*, Vol. 67, 427–428.
- Kito, Y., Horii, K., Higashiyama, Y., and Nakamura, K. 1985. Optical aspects of winter lightning discharges triggered by the rocket-wire technique in Hokuriku district of Japan. *J. Geophys. Res.* 90: 6147–6157.
- Lalande, P., Bondiou-Clergerie, A., Laroche, P., Eybert-Berard, A., Berlandis, J.P., Bador, B., Bonamy, A., Uman, M.A., and Rakov, V.A. 1996. Connection to ground of an artificially triggered negative downward stepped leader. In Proc. 10th Int. Conf. on Atmospheric Electricity, 1996, Osaka, Japan, pp. 668–671.
- Lalande, P., Bondiou-Clergerie, A., Laroche, P., Eybert-Berard, A., Berlandis, J.-P., Bador, B., Bonamy, A., Uman, M.A., and Rakov, V.A. 1998. Leader properties determined with triggered lightning techniques. *J. Geophys. Res.* 103: 14,109–115.
- Laroche, P., Idone, V., Eybert-Berard, A., and Barret, L. 1991. Observations of bi-directional leader development in a triggered lightning flash. In Proc. 1991 Int. Conf. on Lightning and Static Electricity, Cocoa Beach, Florida, pp. 57/1–57/10.
- Leteinturier, C., Hamelin, J.H., and Eybert-Berard, A. 1991. Submicrosecond characteristics of lightning return-stroke currents. *IEEE Trans. Electromagn. Compat.* 33: 351–357.
- Leteinturier, C., Weidman, C., Hamelin, J. 1990. Current and electric field derivatives in triggered lightning return strokes. *J. Geophys. Res.* 95: 811–828.
- Liu, X.-S., Wang, C., Zhang, Y., Xiao, Q., Wang, D., Zhou, Z., and Guo, C. 1994. Experiment of artificially triggering lightning in China. *J. Geophys. Res.* 99: 10,727–731.
- Liu, X., and Zhang, Y. 1998. Review of artificially triggered lightning study in China. *Trans. IEE Japan* 118-B (2): 170–175.
- Miki, M., V.A. Rakov, T. Shindo, G. Diendorfer, M. Mair, F. Heidler, W. Zischank. M.A. Uman, R. Thottappillil, and D. Wang. 2005. Initial stage in lightning initiated from tall objects and in rocket-triggered lightning, *Journal of Geophysical Research*, Vol. 110, D02109, doi:10.1029/2003JD004474.
- Miki, M., Rakov, V.A., Rambo, K.J., Schnetzer, G.H., and Uman, M.A. 2002. Electric fields near triggered lightning channels measured with Pockels sensors. *J. Geophys. Res.*, 107(D16), 4277, doi: 10.1029/2001JD001087.
- Morris, M.E., Fisher, R.J., Schnetzer, G.H., Merewether, K.O., and Jorgenson, R.E. 1994. Rocket-triggered lightning studies for the protection of critical assets. *IEEE Trans. Ind. Appl.* 30:791–804.
- Nag, A., Jerauld, J. Rakov, V.A., Uman, M.A., Rambo, K.J., Jordan, D.M., DeCarlo, B.A., Howard, J., Cummins, K.L., and Cramer, J.A. 2008. NLDN responses to rocket-triggered lightning at Camp Blanding, Florida, in 2004, 2005, and 2007. *Proc. of 29th Int. Conf. on Lightning Protection, Uppsala, Sweden, June 23–26, 2008.*

- Nakamura, K., Horii, K., Kito, Y., Wada, A., Ikeda, G., Sumi, S., Yoda, M., Aiba, S., Sakurano, H., and Wakamatsu, K. 1991. Artificially triggered lightning experiments to an EHV transmission line. *IEEE Trans. Pow. Del.* 6: 1311–1318.
- Nakamura, K., Horii, K., Nakano, M., and Sumi, S. 1992. Experiments on rocket triggered lightning. *Res. Lett. Atmos. Electr.* 12: 29–35.
- Newman, M.M. 1958. Lightning discharge channel characteristics and related atmospherics. In *Recent Advances in Atmospheric Electricity*, ed. L.G. Smith, pp. 475–484, New York: Pergamon Press.
- Newman, M.M. 1965. Use of triggered lightning to study the discharge channel. In *Problems of Atmospheric and Space Electricity*, pp. 482–490, New York: Elsevier.
- Newman, M.M., and Robb, J.D. 1977. Protection of aircraft. In *Lightning, vol. 2: Lightning Protection*, ed. R. H. Golde, pp. 659–696, London: Academic Press.
- Newman, M.M., Stahmann, J.R., Robb, J.D., Lewis, E.A., Martin, S.G., and Zinn, S.V. 1967. Triggered lightning strokes at very close range. *J. Geophys. Res.* 72: 4761–4764.
- Nucci, C.A., and Rachidi, F. 1995. On the contribution of the electromagnetic field components in field-to-transmission line interaction. *IEEE Trans. Electromagn. Compat.* 37: 505–8.
- Olsen, R.C., Jordan, D.M., Rakov, V.A., Uman, M.A., and Grimes, N. 2004. Observed one-dimensional return stroke propagation speeds in the bottom 170 m of a rocket-triggered lightning channel. *Geophys. Res. Lett.*, 31, L16107, doi: 10.1029/2004GL020187.
- Olsen, R.C., Rakov, V.A., Jordan, D.M., Jerauld, J., Uman, M.A., and Rambo, K.J. 2006. Leader/return-stroke-like processes in the initial stage of rocket-triggered lightning. *J. Geophys. Res.*, 111, D13202, doi: 10.1029/2005JD006790, 11 p.
- Pinto, O., Jr., I.R.C.A. Pinto, M.M.F. Saba, N.N. Solorzano, D. Guedes. 2005. Return stroke peak current observations of negative natural and triggered lightning in Brazil, *Atmospheric Research* 76, 493–502.
- Qie, X., Zhang, Q., Zhou, Y., Feng, G., Zhang, T., Yang, J., Kong, X., Xiao, Q., and Wu, S. 2007. Artificially triggered lightning and its characteristic discharge parameters in two severe thunderstorms. *Science in China Series D: Earth Sciences*, vol. 50, No. 8, 1241–1250.
- Rahman, M., Cooray, V., Rakov, V.A., Uman, M.A., Liyanage, P., DeCarlo, B.A., Jerauld, J., and Olsen III, R.C. 2006. Measurements of NO_x produced by rocket-triggered lightning. *Geophys. Res. Lett.*, 34, L03816, doi:10.1029/2006GL027956.
- Rakov, V.A., and Uman, M.A. 1998. Review and evaluation of lightning return stroke models including some aspects of their application. *IEEE Trans. Electromagn. Compat.* 40: 403–26.
- Rakov, V.A. 1999b. Lightning makes glass. *Journal of the Glass Art Society*, pp. 45–50.
- Rakov, V.A. 1999c. Lightning discharges triggered using rocket-and-wire techniques. In *Recent Res. Devel. Geophysics*, vol. 2, Research Signpost, India, pp. 141–171.
- Rakov, V.A., Crawford, D.E., Kodali, V., Idone, V.P., Uman, M.A., Schnetzer, G.H., and Rambo, K.J. 2003b. Cutoff and re-establishment of current in rocket-triggered lightning. *J. Geophys. Res.*, Vol. 108, No. D23, 4747, doi:10.1029/2003JD003694.
- Rakov, V.A., Crawford, D.E., Rambo, K.J., Schnetzer, G.H., Uman, M.A., and Thottappillil, R. 2001. M-Component Mode of Charge Transfer to Ground in Lightning Discharges. *J. Geophys. Res.*, 106, 22,817–22,831.
- Rakov, V.A., V. Kodali, D.E. Crawford, J. Schoene, M. A. Uman, K.J. Rambo, and G.H. Schnetzer. 2005a. Close electric field signatures of dart leader/return stroke sequences in rocket-triggered lightning showing residual fields, *Journal of Geophysical Research*, Vol. 110, D07205, doi:10.1029/2004JD0054.
- Rakov, V.A., Mata, C.T., Uman, M.A., Rambo, K.J., and Mata, A.G. 2003a. Review of Triggered-Lightning Experiments at the ICLRT at Camp Blanding, Florida. In Proc. of 5th IEEE Power Tech Conference, Bologna, Italy, Paper 381, 8 p.
- Rakov, V.A., Thottappillil, R., Uman, M.A., and Barker, P.P. 1995a. Mechanism of the lightning M component. *J. Geophys. Res.* 100: 25,701–710.
- Rakov, V.A., and Uman, M.A.. 2003. Lightning: Physics and Effects, Cambridge University Press, 687 p., ISBN 0521583276.

- Rakov, V. A., Uman, M.A., Fernandez, M.I., Mata, C.T., Rambo, K.T., Stapleton, M.V., and Sutil, R.R. 2002. Direct Lightning Strikes to the Lightning Protective System of a Residential Building: Triggered-Lightning Experiments, IEEE Transactions on Power Delivery, Vol. 17, No. 2, April 2002, 575–586.
- Rakov, V.A., Uman, M.A., Fernandez, M.I., Thottappillil, R., Eybert-Berard, A., Berlandis, J.P., Rachidi, F., Rubinstein, M., Guerrieri, S., and Nucci, C.A. 1996b. Observed electromagnetic environment close to the lightning channel. In Proc. 23rd Int. Conf. on Lightning Protection, Florence, Italy, pp. 30–35.
- Rakov, V.A., Uman, M.A., Rambo, K.J. 2005b. A review of ten years of triggered-lightning experiments at Camp Blanding, Florida. *Atmos. Res.*, vol. 76, issue 1–4, pp. 504–518.
- Rakov, V.A., Uman, M.A., Rambo, K.J., Fernandez, M.I., Fisher, R.J., Schnetzer, G.H., Thottappillil, R., Eybert-Berard, A., Berlandis, J.P., Lalande, P., Bonamy, A., Laroche, P., and Bondiou-Clergerie, A. 1998. New insights into lightning processes gained from triggered-lightning experiments in Florida and Alabama. *J. Geophys. Res.* 103: 14,117–130.
- Rakov, V.A., Uman, M.A., Wang, D., Rambo, K.J., Crawford, D.E., and Schnetzer, G.H. 2000a. Lightning properties from triggered-lightning experiments at Camp Blanding, Florida (1997–1999). In Proc. of the 25th Int. Conf. on Lightning Protection, Rhodes, Greece, pp. 54–59.
- Rubinstein, M., Rachidi, F., Uman, M.A., Thottappillil, R., Rakov, V.A., and Nucci, C.A. 1995. Characterization of vertical electric fields 500 m and 30 m from triggered lightning. *J. Geophys. Res.* 100: 8863–72.
- Rubinstein, M., Uman, M.A., Thomson, E.M., Medelius, P., and Rachidi, F. 1992. Measurements and characterization of ground level vertical electric fields 500 m and 30 m from triggered-lightning. In Proc. 9th Int. Conf. on Atmospheric Electricity, St. Petersburg, Russia, pp. 276–278.
- Saba, M.M.F., Pinto, O., Pinto, I.R.C.A., Pissolato, F.J., Eybert-Berard, A., Lefort, A., Potvin, C., Heine, L.F., and Chauzy, S. 2000. An international center for triggered and natural lightning research in Brazil. In Proc. 2000 Int. Lightning Detection Conf., GAI, 2705 East Medina Road, Tucson, Arizona 85706–7155, paper 40, 7 p.
- Saba, M.M.F., O. Pinto Jr., N.N. Solorzano, and A. Eybert-Berard. 2005. Lightning current observation of an altitude-triggered flash, *Atmospheric Research* 76, 402–411.
- Schoene, J., Uman, M.A., Rakov, V.A., Hanley, B.D., Rambo, K.J., Howard, J., and DeCarlo, B. 2008. Lightning-induced currents in a buried loop conductor and a grounded vertical conductor. *IEEE Trans. on EMC*, Vol. 50, No. 1, February 2008, pp. 110–117.
- Schoene, J., Uman, M.A., Rakov, V.A., Kodali, V., Rambo, K.J., and Schnetzer, G.H. 2003a. Statistical characteristics of the electric and magnetic fields and their time derivatives 15 m and 30 m from triggered lightning. *J. Geophys. Res.*, Vol. 108, No. D6, 4192, doi:10.1029/2002JD002698.
- Schoene, J., Uman, M.A., Rakov, V.A., Rambo, K.J., Jerauld, J., and Schnetzer, G.H. 2003b. Test of the transmission line model and the traveling current source model with triggered lightning return strokes at very close range. *J. Geophys. Res.*, Vol. 108, No. D23, 4737, doi:10.1029/2003JD003683.
- Thottappillil, R., Goldberg, J.D., Rakov, V.A., and Uman, M.A. 1995. Properties of M components from currents measured at triggered lightning channel base, *J. Geophys. Res.*, 100, 25,711–25,720.
- Uman, M.A. 1987. *The Lightning Discharge*. 377 p., San Diego, California: Academic Press.
- Uman, M.A., Cordier, D.J., Chandler, R.M., Rakov, V.A., Bernstein, R., and Barker, P.P. 1994b. Fulgurites produced by triggered lightning. *Eos Trans. AGU* 75 (44), Fall Meet. Suppl., 99.
- Uman, M.A., Rakov, V.A., Rambo, K.J., Vaught, T.W., Fernandez, M.I., Bach, J.A., Su, Y., Eybert-Berard, A., Berlandis, J.-P., Bador, B., Lalande, P., Bonamy, A., Audran, F., Morillon, F., Laroche, P., Bondiou-Clergerie, A., Chauzy, S., Soula, S., Weidman, C.D., Rachidi, F., Rubinstein, M., Nucci, C.A., Guerrieri, S., Hoidalen, H.K., and Cooray, V. 1995a. 1995 triggered lightning experiment in Florida. In Proc. 10th Int. Conf. on Atmospheric Electricity, Osaka, Japan, pp. 644–647.

- Uman, M.A., Rakov, V.A., Rambo, K.J., Vaught, T.W., Fernandez, M.I., Cordier, D.J., Chandler, R.M., Bernstein, R., and Golden, C. 1997. Triggered-lightning experiments at Camp Blanding, Florida (1993–1995). *Trans. IEE Japan* 117-B: 446–452.
- Uman, M.A., Rakov, V.A., Schnetzer, G.H., Rambo, K.J., Crawford, D.E., and Fisher, R.J. 2000. Time derivative of the electric field 10, 14, and 30 m from triggered lightning strokes. *J. Geophys. Res.* 105: 15,577–595.
- Uman, M.A., Rakov, V.A., Versaggi, J.A., Thottappillil, R., Eybert-Berard, A., Barret, L., Berlandis, J.-P., Bador, B., Barker, P.P., Hnat, S.P., Oravsky, J.P., Short, T.A., Warren, C.A., and Bernstein, R. 1994a. Electric fields close to triggered lightning. In Proc. Int. Symp. on Electromagn. Compat. (EMC'94 ROMA), Rome, Italy, pp. 33–37.
- Uman, M.A., Schoene, J., Rakov, V.A., Rambo, K.J., and Schnetzer, G.H. 2002. Correlated Time Derivatives of Current, Electric Field Intensity, and Magnetic Flux Density for Triggered Lightning at 15 m. *J. Geophys. Res.*, 107(D13), 10.1029/2000JD000249, 11 p.
- Wang, C., Yan, M., Liu, X., Zhang, Y., Dong, W., and Zhang, C. 1999d. Bidirectional propagation of lightning leader. *Chinese Sci. Bull.* 44(2): 163–166.
- Wang, D., Rakov, V.A., Uman, M.A., Fernandez, M.I., Rambo, K.J., Schnetzer, G.H., and Fisher, R.J. 1999b. Characterization of the initial stage of negative rocket-triggered lightning. *J. Geophys. Res.* 104: 4213–4222.
- Wang, D., Rakov, V.A., Uman, M.A., Takagi, N., Watanabe, T., Crawford, D.E., Rambo, K.J., Schnetzer, G.H., Fisher, R.J., and Kawasaki, Z.-I. 1999a. Attachment process in rocket-triggered lightning strokes. *J. Geophys. Res.* 104: 2141–2150.
- Wang, D., Takagi, N., Watanabe, T., Rakov, V.A., and Uman, M.A. 1999c. Observed leader and return-stroke propagation characteristics in the bottom 400 m of the rocket triggered lightning channel. *J. Geophys. Res.* 104: 14,369–376.
- Wang, D., N. Takagi, T. Watanabe, V.A. Rakov, M.A. Uman, K.J. Rambo, M.V. Stapleton. 2005. A comparison of channel-base currents and optical signals for rocket-triggered lightning strokes, Atmospheric Research 76, 412–422.
- Wang, J., Liew, A.C., and Darveniza, M. 2005. Extension of dynamic model of impulse behavior of concentrated grounds at high current, IEEE Trans. Power Delivery, 20(3), 2160–2165.
- Willett, J.C. 1992. Rocket-triggered-lightning experiments in Florida. *Res. Lett. Atmos. Electr.* 12: 37–45.
- Willett, J.C., Davis, D.A., and Laroche, P. 1999b. An experimental study of positive leaders initiating rocket-triggered lightning. *Atmos. Res.* 51: 189–219.

Chapter 3

Electric Field and Charge Structure in Lightning-Producing Clouds

Maribeth Stolzenburg and Thomas C. Marshall

Abstract This chapter gives an overview of typical charge structures observed with balloons inside mesoscale convective systems, supercells, and New Mexico mountain storms. Typical maximum electric field magnitudes, along with several extreme field values observed near lightning initiations, are presented in comparison to the theoretical values that are thought to be required for lightning initiation at various altitudes within active storms. The chapter emphasizes the physical effects that the electrical structure has on lightning initiation, lightning propagation, and lightning type, including a detailed discussion of the controlling effect that the electric potential has on the altitude of horizontal lightning channels and the existence or absence of preliminary breakdown. Some indications of the countereffects of lightning on electrical structures, particularly through deposition of charge and increased complexity of the charge structure are also described.

Keywords Balloon measurements · Charge distribution · MCS stratiform region · Outside convective updraft · Within convective updraft · Charge density · Charge deposition by lightning · Channel propagation · Electric potential · Lightning energy estimate · Lightning initiation · Cloud-to-ground flash · Intracloud flash · Observed maximum E magnitude · Lightning mapping array · Mesoscale convective system · Convective region · Stratiform precipitation region · Mountain thunderstorm · Potential wells · Preliminary breakdown · Supercell thunderstorm

3.1 Introduction and Perspective

While it is the occurrence of a lightning flash that makes an ordinary cloud into a thunderstorm, it is the electric charge within that cloud which determines when and where lightning initiates. The charge distribution also dictates how, or even if, the flash subsequently propagates through the cloud and possibly to the ground. Charge and the resulting electric field and potential distributions are thus the most

M. Stolzenburg (✉)

Department of Physics and Astronomy, University of Mississippi, Mississippi, USA

e-mail: mstolzen@olemiss.edu

basic of parameters needed to describe both thunderstorms and lightning. Mechanisms responsible for the development and separation of charge inside clouds—on the microphysical scale between individual particles and on the macrophysical scale of the entire cloud—are beyond the scope of this chapter. Instead, we review the resulting electrical structures observed within typical thunderstorms. The bulk of the chapter focuses on observations of the physical effects that the electrical structure has on lightning initiation, flash type, and channel propagation. Because lightning also moves charge within and beyond the cloud, we include some recent results on the direct consequences of lightning flashes on the electrical structures.

The best way to describe the electricity inside active thunderstorms would be to measure the entire charge distribution, and then calculate the electric field (E) and electrostatic potential (V). Unfortunately, the measurement of charge on all the hydrometeors inside clouds is extremely difficult due to the wide range of particle sizes and small individual charges involved in this electrically noisy and hazardous environment. Sampling of a small portion of the charge distribution on relatively large particles inside a few clouds has been accomplished with aircraft and balloons (e.g., Weinheimer et al., 1991; Takahashi and Keenan, 2004). Most in situ observations of the electrical structure of storms have instead measured E . From such measurements, inferences about the charge distribution are possible.

Because balloon-borne electrical measurements are relatively inexpensive to acquire, balloon E soundings are the most prevalent in situ data available across different types of thunderclouds. Balloons have the desirable capability of sampling the entire cloud depth in a reasonably short time (10–30 min), which yields valuable information about the vertical distribution of electrical quantities and their variation with respect to other storm parameters such as pressure, temperature, and hydrometeor type. For these reasons, we will focus primarily on E data acquired with balloons to describe the basic electrical structure inside thunderstorms. In situ E data are also valuable for validating remote and modeling techniques that are used to infer parts of the thunderstorm charge structure; results of these techniques are increasingly important sources of information but details of these methods are beyond the space limitations of this review.

Although the E magnitude and polarity inside a cloud are of fundamental interest, the altitude, polarity, and density of net charge also can be inferred from a vertical profile of E . This analysis is usually done using a one-dimensional approximation to Gauss's Law (e.g., Stolzenburg et al., 1998a), in part because the largest component and largest divergence of E measured in a sounding are usually in the vertical. In addition, V as a function of altitude can be estimated from an E sounding by integrating upward from the ground (e.g., Marshall and Stolzenburg, 2001). Distributions of electric field, charge, and potential are essentially different ways of describing the same electrical structure of a storm. The main goal of this chapter is to show how these three parameters can be used to better understand the physical conditions governing the initiation, type, and propagation characteristics of typical cloud-to-ground (CG) and intracloud (IC) lightning flashes.

3.2 Overview of Typical Charge Structures

This section is based partly on a review by Stolzenburg and Marshall (2008a). In describing the electric field, the sign convention used throughout this chapter is that a positive vertical E is exerts an upward force on a positive charge.

3.2.1 Mature Convection

The earliest models of thunderstorm charge distribution were vertical dipoles (e.g., Simpson, 1909; Wilson, 1916). To better fit all contemporaneous observations, Simpson and colleagues proposed a tripole, with a positive charge center near cloud base and negative and positive charge centers successively higher in the cloud (e.g., Simpson and Scrase, 1937). This tripolar model for thunderclouds remains essentially valid as a first order description, although there is ample evidence it is overly simplified in many situations (e.g., Rust and Marshall, 1996).

Our current understanding of the typical vertical charge distribution within different types of mature convection is depicted in Fig. 3.1. This conceptual model shows common features from analysis of 49 E soundings through three types of convection frequently studied with modern balloon instruments: isolated supercells and multi-cellular squall lines of mesoscale convective systems (MCSs) over the U.S. Great Plains, and small single- and multi-cell storms over the mountains of central New Mexico. (Supercell storms are reviewed separately by Tessendorf (this volume).)

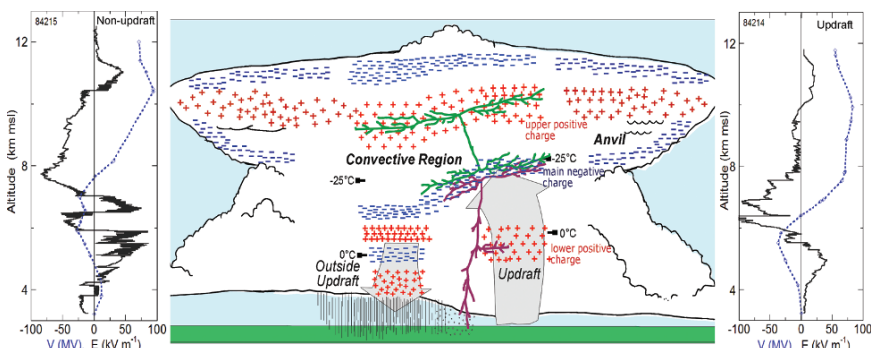


Fig. 3.1 Conceptual model of the electrical structure in mature, mid-latitude convection. Four main charge regions (with red + for positive charge, blue - for negative charge) are typically found in soundings through updrafts, while soundings outside updrafts have at least six charge regions in common. Representative electric field (E) and electrostatic potential (V) profiles in the non-updraft (*left*) and updraft (*right*) of the convective region are also shown; the altitudes in these soundings do not correspond exactly to the conceptual model. Charge structure depicted in the upshear and downshear anvil clouds is based on Marshall et al. (1989). Schematic representations of an intracloud flash (in green) and a cloud-to-ground flash (in purple) are shown as they might appear in lightning mapping data. (Adapted from Stolzenburg et al., 1998c, and Stolzenburg and Marshall, 2001)

To describe the vertical electrical structure across convective regions in general, Stolzenburg et al. (1998a, 1998b, 1998c) classified available soundings according to the balloon location relative to the storm updraft. Thus, soundings in which the average vertical air velocity exceeded 1 m s^{-1} are ‘updraft’ soundings, while those in weaker or downward vertical motion (or in very heavy precipitation) within the convective region are ‘non-updraft’ soundings.

For convective updrafts the basic structure derived by Stolzenburg et al. (1998c) and shown in Fig. 3.1 is comprised of four charge regions. Relatively weak positive charge is lowermost; above this are the main negative and upper positive charge regions historically described as the “main dipole” of the cloud. The fourth and uppermost region has negative charge and is usually shallow. This basic four-charge structure modifies the earlier tripolar charge structure by adding a negative charge layer near the upper cloud boundary. Outside the updrafts, but still within a storm’s convective region, there are typically at least six charge regions, alternating in polarity from lowest to highest, and the uppermost region has negative charge. While they are generally more complex than updraft soundings, non-updraft soundings also tend to exhibit more variability from one storm to another, or, as recently shown by Weiss et al. (2008) even from one sounding to the next within a storm. One key feature of the thunderstorm electrical structure is that the charge regions tend to be horizontally stratified: the vertical thickness of each charge region is less (often much less) than its horizontal dimension.

Among the three types of convection studied by Stolzenburg et al. (1998c), the heights and temperatures of the basic four charge regions differed. For example, the center height of the main negative charge averaged 9.1 km (-22°C) in supercell updrafts, 6.9 km (-16°C) in MCS convective region updrafts, and 6.0 km (-7°C) in New Mexico mountain storm updrafts. These differences generally scaled with the maximum updraft speeds in each storm type, although storm depth and surface altitude (for the mountain storms) are also important. Overall, the altitude of the main negative charge region was well correlated with the average updraft speed. Outside updrafts the center of the main negative charge region was at lower altitude and warmer temperature (5.5 km, -6.2°C) than within updrafts. In addition, the inferred charge regions outside updrafts tended to be shallower and had larger charge densities (Stolzenburg et al., 1998c), consistent with the larger maximum E magnitudes typically observed in non-updraft soundings (Section 2.3).

It should be noted that the above-described dependence of the observed thundercloud convective charge structure on updraft speed does not contradict any basic dependencies (in temperature, liquid water content, E, etc.) of the underlying charging mechanism or mechanisms. Because the convective region is highly dynamic, the charged particles do not stay at the place in the cloud where they become charged. Thus, as hypothesized by MacGorman et al. (1989), for the case of larger updraft speeds, even the larger particles (e.g., negatively charged graupel in the simplest forms of the non-inductive ice-ice collisional mechanism) will ascend. The in situ observations would find this negative charge at a higher altitude (e.g., Marshall et al., 1995). In weaker updrafts or downdrafts, these large particles would be observed near or below the altitude where they underwent charge-transferring

interactions. The complex history of the charged particles within the cloud is not revealed through the “snapshot” of the *in situ* E soundings, and a detailed understanding of this history is best suited to computational modeling techniques.

Figure 3.1 depicts the distribution of net charge based on E soundings, but whether the charge is carried primarily on cloud or precipitation particles cannot be determined from E measurements alone. The few E soundings that have included measurements of charge carried on individual precipitation particles indicate that most charge in the lower positive and main negative charge regions is carried on precipitation-sized particles (e.g., Marshall and Marsh, 1993; Bateman et al., 1999). Outside the updraft, one sounding with precipitation charge data (Stolzenburg and Marshall, 1998) indicated that the charge in the two additional charge regions is also carried mainly on precipitation-sized particles. Estimations have suggested that the charge on cloud-sized particles dominates the net charge from just above the main negative charge region to cloud top (e.g., Marshall and Stolzenburg, 1998), although reliable measurements of cloud charge are scarce.

The updraft and non-updraft electrical structures in the conceptual model (Fig. 3.1) have been found simultaneously within mature convection (Stolzenburg et al., 2002; MacGorman et al., 2005). In some cases, the simpler structure may evolve into a more complex structure as a storm develops and its updraft weakens; we describe an example of this in Section 3.4. Lightning discharges throughout the cloud also add complexity to the charge structure as the storm ages, as discussed in Section 3.6.

Two representative E profiles observed in mature convection are shown along with the charge structures in Fig. 3.1. In the simpler (updraft) soundings (as in the profile on the right side in Fig. 3.1), there is generally a region of low magnitude E up to cloud base, larger positive E values up to a positive peak 1–2 km above cloud base, then decreasing E upward through a few km to a negative E peak. About 1–4 km above the negative E peak, the profiles have a transition to positive E and a positive peak, and finally a sharp decrease in E (to ~ 0) near the cloud top. In the more complicated soundings, at least two additional E peaks of opposite polarity are typically found below the negative E peak (e.g., Marshall et al., 1995b). Within both these structures, particularly near and above the negative E peak, many large lightning-related E changes are commonly detected. The V profiles inferred from the two E soundings are also shown in Fig. 3.1. In general, both types of soundings have a deep minimum in V at mid-levels and a V maximum at upper levels (e.g., Marshall and Stolzenburg, 2001). The more complicated (non-updraft) E soundings (as in the profile on the left side in Fig. 3.1) have additional relative maxima in V at low altitude and also within the overall minimum.

While later sections of this chapter provide details, a few general statements about lightning initiation, type, and propagation are useful here regarding Fig. 3.1. Normal IC flashes begin with a bidirectional leader in which the negatively charged end propagates upward, and normal negative CG flashes begin with a bidirectional leader in which the negatively charged end travels downward (e.g., Shao and Krebsbach, 1996). Hence, normal IC flashes initiate in regions where the vertical component of E is negative, and normal negative CG flashes initiate where the vertical component of E is positive (e.g. Maggio et al., 2005; Coleman et al., 2003). In terms

of Fig. 3.1, normal IC flashes initiate between the upper positive and main negative thundercloud charge regions, where the negative E tends to be largest. Likewise, normal negative CG flashes would initiate between the main negative and lower positive thundercloud charge regions, where the positive E tends to be largest. Note also that for normal negative CG flashes to occur, there must be a region of large positive E relatively low in the storm; hence the main negative and lower positive charges must be present. Regarding propagation, it is generally accepted that after initiation of a normal IC flash, the bi-directional leader travels first vertically, then spreads horizontally through the upper positive and main negative charge (e.g., Shao and Krehbiel, 1996; Coleman et al., 2003) which correspond to altitudes of a maximum and minimum, respectively, in V (Coleman et al., 2003). Similarly, the bi-directional leader of a normal negative CG flash propagates horizontally through the main negative charge and vertically to the ground, perhaps with a horizontal branch through the lower positive charge en route to ground. Features of the two most common types of lightning are shown in Fig. 3.1 and have been observed with lightning mapping arrays (e. g., Proctor, 1981; Rison et al., 1999).

We note that the conceptual model for mature convection shown in Fig. 3.1 does not represent some supercells in which balloon and lightning data have indicated an ‘inverted polarity’ charge structure (e.g., Rust et al., 2005); see Tessendorf (this volume) for a review of this important class of severe storms. In addition, it is vital to bear in mind that the conceptual model is based on convective region soundings in mature storms that occurred over a limited portion of the lower midlatitudes. The extent to which this model fits mature convection in other midlatitude regions or in the tropics and high latitudes is not known, since in situ data are still too scarce to derive complete charge structures for storms in most other regions. An exception to this is the east Asian monsoon cloud systems sampled extensively and recently reviewed by Takahashi (2007).

3.2.2 Stratiform Precipitation Regions of Mesoscale Convective Systems

In the midlatitudes MCSs are characterized by deep convection, often forming a line or arc, followed by a broad region of stratiform precipitation. The MCS trailing stratiform cloud typically has a weak mesoscale updraft, a radar bright band associated with melting, light to moderate rain, and sometimes contains embedded elements of dying convective cells (e.g., Houze, 1993). An MCS is organized on the mesoscale, lasting for 2–12 h and covering 2000–20000 km². All these features make the electrical structure of midlatitude MCS stratiform regions complex. (Observations by Chauzy et al. (1985), have confirmed this complexity for tropical MCSs, as well.) The MCS stratiform charge structure has been of particular interest since early studies (e.g., Rutledge and MacGorman, 1988), showed that CG flashes in this region are often predominantly positive. In situ data (e.g. Marshall and Rust, 1993) have indicated large amounts of positive charge (up to ~20 000 C,

over an estimated area of 16 000 km² and depth of 250 m) can be present near the melting level. As reviewed by Lyons (this volume), perhaps the greatest interest in MCS electricity stems from observations of sprites and other transient luminous events above extensive stratiform clouds and often associated with positive CG flashes.

Marshall and Rust (1993) described two different modes of electrical structure in MCS stratiform cloud regions. The ‘Type A’ is more complex, with at least five significant charge regions, vertically stacked and sequentially of opposite polarity. The ‘Type B’ is relatively simple, having four main charge regions. Although the data are limited, evidence suggests that the charge regions in both types can be horizontally extensive over 100 km or more. Both types tend to have a dense charge region near the level of the 0°C isotherm. From a study of all their available balloon E soundings through MCS stratiform regions, Stolzenburg et al. (2007b) found strong positive charge at 0°C in 14 cases, and strong negative charge in 16 cases. Another 11 soundings had essentially no net charge at 0°C because there was a relative maximum or minimum in E precisely at that altitude, although these cases did show dense charge regions immediately above and below 0°C. The variability of the charge polarity at the melting level, in different MCSs or at different locations, may indicate that the charging mechanism at work there is also variable or possibly even dependent on the E polarity.

Stolzenburg et al. (2007b) also identified a third stratiform region electrical structure as ‘Anvil Type’ for soundings in which cloud base is above the melting level and there is no charge region near 0°C. The ‘Anvil Type’ charge structure resembles that of typical non-precipitating anvil clouds (e.g., Marshall et al., 1989) in that there is a deep, internal positive charge region and a lower negative screening layer. However, the upper negative charge region is not always located at the upper cloud boundary, perhaps because it descends into the cloud or becomes masked at the top by subsequent positively charged screening (e.g., Byrne et al., 1989; Stolzenburg et al., 1994). Stolzenburg et al. (2007b) speculated that this structure is the simplest for MCS stratiform clouds due to the lack of significant numbers of aggregates melting, and possibly becoming charged, near the 0°C isotherm. For the overall charge structure, most of the 28 complete MCS stratiform E soundings analyzed by Stolzenburg et al. (2007b) showed three to six major charge regions inside the cloud. The average center altitude of the uppermost charge region, not including the upper screening layer, was about 8 km (or –20°C).

The positive charge regions in MCS stratiform clouds, whether at or above the melting level, are important due to their association with positive CG flashes and sprites. Positive CG lightning flashes with large peak currents and large charge transfers have been observed during one Type A sounding in which the two positive charge regions were above the altitude of 0°C (Marshall et al., 2001). Although large E values are often present in MCS stratiform cloud soundings (maximum E of 100 kV m⁻¹ is common) recent results by Lang et al. (2004) and Carey et al. (2005) show that much of the lightning which travels through (and to ground beneath) the stratiform region initiates within the MCS convective region.

3.3 Electrical Structure and Lightning Initiation

The exact electric field magnitude and the specific mechanism for lightning initiation remain unknown. Until the 1990s, it was assumed that lightning initiation inside clouds occurs via conventional dielectric breakdown, in which low-energy electrons are driven by the local electric field to create an electron avalanche. This avalanche, in turn, creates a conducting medium via the expanding ionization. The E necessary for conventional breakdown at standard atmospheric pressure (1 atm) is about 3000 kV m^{-1} . However, conventional breakdown might initiate lightning in a smaller ambient E when hydrometeors cause local field enhancements. Laboratory measurements with raindrops (Crabb and Latham, 1974) have indicated that E as small as 350 kV m^{-1} (at 1 atm) could lead to conventional breakdown.

Another theory for lightning initiation, in which a runaway electron avalanche causes dielectric breakdown, was proposed by Gurevich et al. (1992). In the runaway breakdown mechanism, electrons with relatively high initial energies (0.3–1.0 MeV) gain enough energy from the ambient E to produce additional electrons with similarly high energies. This electron production quickly yields an avalanche of energetic electrons and production of thermal electrons (Gurevich and Zybin, 2001), and leads to ionization of the medium. The threshold E for runaway breakdown is about 280 kV m^{-1} at 1 atm (Symbalisty et al., 1998; Dwyer, 2003).

3.3.1 Typical Electric Fields Observed Inside Active Storms

In contrast to the lightning initiation theories, many observations inside active storms show E magnitudes are typically less than 150 kV m^{-1} (e. g., Marshall and Rust, 1991) with a few extreme values up to 400 kV m^{-1} (e.g., Winn et al., 1974). Maximum E magnitudes among the 49 soundings examined by Stolzenburg et al. (1998a, 1998b) were $\sim 80 \text{ kV m}^{-1}$ or less in convective updraft soundings, while most soundings outside updrafts in convection had maximum E magnitudes of 100–120 kV m^{-1} . In general, E maxima of both polarities tend to be at higher altitudes within the updrafts, consistent with the charge being elevated in the updraft.

Some of the differences between observed E values inside thunderstorms and the theoretical E value needed for lightning are due to inherent sampling biases: there are observations at relatively few places compared to the vast scale of thunderstorms, instruments are statistically (or intentionally) unlikely to be very near a localized region of initiation, and the instruments are unlikely to successfully acquire useful data when exposed to such extreme conditions. In other words, clouds are large and observations are rare, the volume of large E values may be small, and instruments are fragile with limited dynamic range. However, because the energy needed for the breakdown process to occur is a function of the density of the air, the E value needed for both the conventional and runaway mechanisms to occur decreases with decreasing air pressure. Thus, for appropriate comparison, the

observations should be adjusted to standard atmospheric pressure, or the theoretical values should be scaled with altitude (Marshall et al., 1995a; 2005).

The importance of the altitude of the observed maximum E magnitude within the storm is evident from Fig. 3.2, which shows the theoretical threshold E curves as a function of altitude for runaway breakdown and conventional breakdown in the presence of raindrops. For example, at 8 km the E magnitude needed for lightning initiation by these processes may be as small as 108 or 135 kV m⁻¹, respectively, much closer to the typical maxima observed in soundings. The E value at each peak in all the convective region soundings tabulated by Stolzenburg et al. (1998a, 1998b), along with those in some recent studies (Coleman et al., 2003; Maggio et al., 2005), are also shown in Fig. 3.2 at the appropriate altitude. (Eleven “extreme” values are included in Fig. 3.2; these are discussed in Section 3.3.2.) Comparison of these

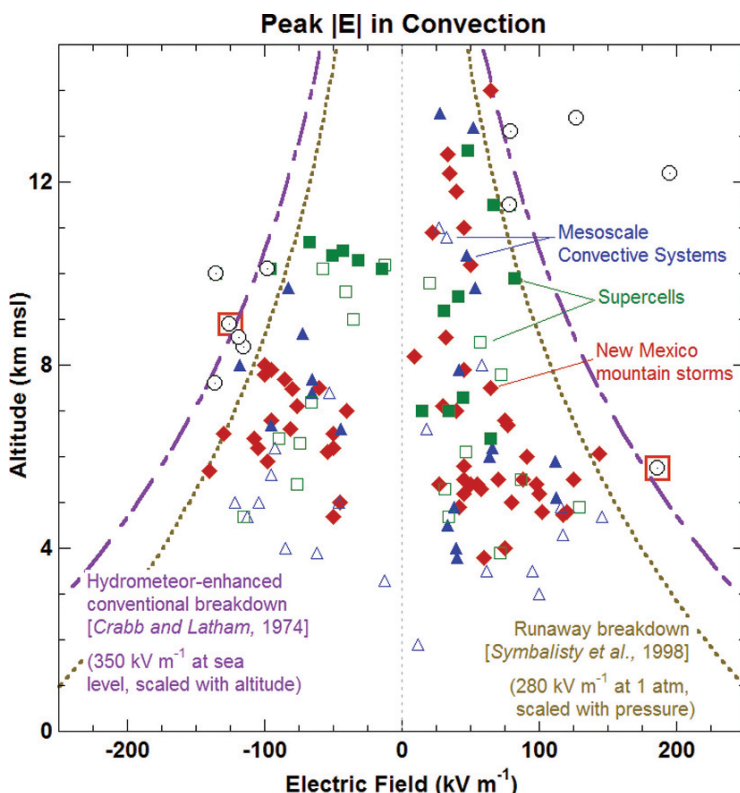


Fig. 3.2 Observed electric field at altitudes of relative maxima and minima in more than 50 balloon soundings through convection, compared to theoretical initiation thresholds as a function of altitude. Typical values within updrafts (*filled marks*) and outside updrafts (*open marks*) of three storm types are shown (Stolzenburg et al., 1998a; 1998b; Coleman et al., 2003; Maggio et al., 2005). Circled values are “extremes” associated with close lightning; two values enclosed by red boxes are at known distances of 1100–2100 m from a subsequent lightning initiation location based on lightning mapping data (Marshall et al., 2005; Stolzenburg et al., 2007a)

typical peak E values observed at various altitudes to both of the theoretical curves indicates that the thresholds are rarely exceeded in the balloon data. Among the peak values in all the typical soundings, there are only four instances where E exceeded the runaway breakdown threshold, and in no case did E exceed the hydrometeor-enhanced conventional breakdown threshold.

From Fig. 3.2, we can also get an indication of typical altitudes for lightning initiation. Where the observed positive values are closest to the threshold curves, between about 4 and 6 km, normal negative CG flashes would likely initiate. This altitude range is consistent with negative CG flashes typically initiating between the lower positive and main negative charge regions in the storm. (Evidence for this statement is presented in Section 3.4.) Similarly, between about 6 and 11 km, normal IC flashes would initiate where the observed peak negative E values tend to be near the threshold curves. This result is consistent with the notion that normal IC flashes begin above the main negative charge, where lightning-related E changes are typically largest and most numerous (e.g., Marshall and Rust, 1991; Stolzenburg et al., 1998c; 2002). The altitude of this initiation region varies greatly with the sounding location and storm type. It is interesting to note that above about 10 km, there are numerous observations of positive E peaks approaching the threshold curves; lightning initiating in these conditions (i.e., above the upper positive charge) would likely be high-altitude inverted IC flashes or upward discharges of the type described by Krehbiel et al. (2008).

3.3.2 Extreme Electric Fields Observed near Lightning Initiations

Acquiring useable data with balloons near lightning initiations is a non-trivial task. Stolzenburg et al. (2007a) examined more than 250 soundings of E and found only nine with useable data in which lightning had catastrophically affected the balloon or instruments. (In that study “catastrophically affected” cases were those in which the balloon ascent sounding data ended at the time of a lightning flash, and the balloon or one of the instruments was destroyed by the flash.) Those nine soundings were presumed to end very close to lightning initiation locations. Peak E values observed just prior to the lightning flash are included in Fig. 3.2, and these are clearly some of the largest values ever recorded with balloons inside storms. When adjusted to standard pressure, the largest observed E was 626 kV m^{-1} (127 kV m^{-1} at 13.4 km) and the largest estimated E was 929 kV m^{-1} ($\sim 200 \text{ kV m}^{-1}$ at an estimated altitude of 12.2 km). The runaway breakdown threshold was exceeded in all these soundings, by factors of 1.1–3.3, before each flash. Four of the E values also exceeded the hydrometeor-enhanced conventional breakdown threshold, although these were all above 10 km altitude (about -25°C) where liquid particles would be uncommon. (Hydrometeor-enhanced conventional breakdown can also occur with ice particles, but the threshold E for this is larger, $400\text{--}500 \text{ kV m}^{-1}$ at sea level (Latham and Stromberg, 1977).) In the sounding for which the peak E value of -115 kV m^{-1} was measured at 8.4 km, independent lightning mapping data indicated that a flash initiated at the same altitude and within 100 m horizontally of the balloon.

Two examples of E soundings that ended catastrophically, presumably near the initiation of a lightning flash, are shown in the top panels of Fig. 3.3. In both these soundings from MCS convective regions, the data from the radiosonde flown on the balloons ended at the time of a large E change that is indicative of a nearby flash. The E just before the flash in one sounding was 127 kV m^{-1} at 13.4 km, or 224% of the runaway breakdown threshold. For the other sounding, E before the flash was -119 kV m^{-1} at 8.6 km, or 118% of the runaway threshold. In these soundings and in five of the others described by Stolzenburg et al. (2007a), there is a rapid increase in the E magnitude (at rates of $11\text{--}100 \text{ kV m}^{-1} \text{ s}^{-1}$) in the few seconds prior to the flash. Very large lightning-related E changes immediately after the flashes are also evident in both these soundings.

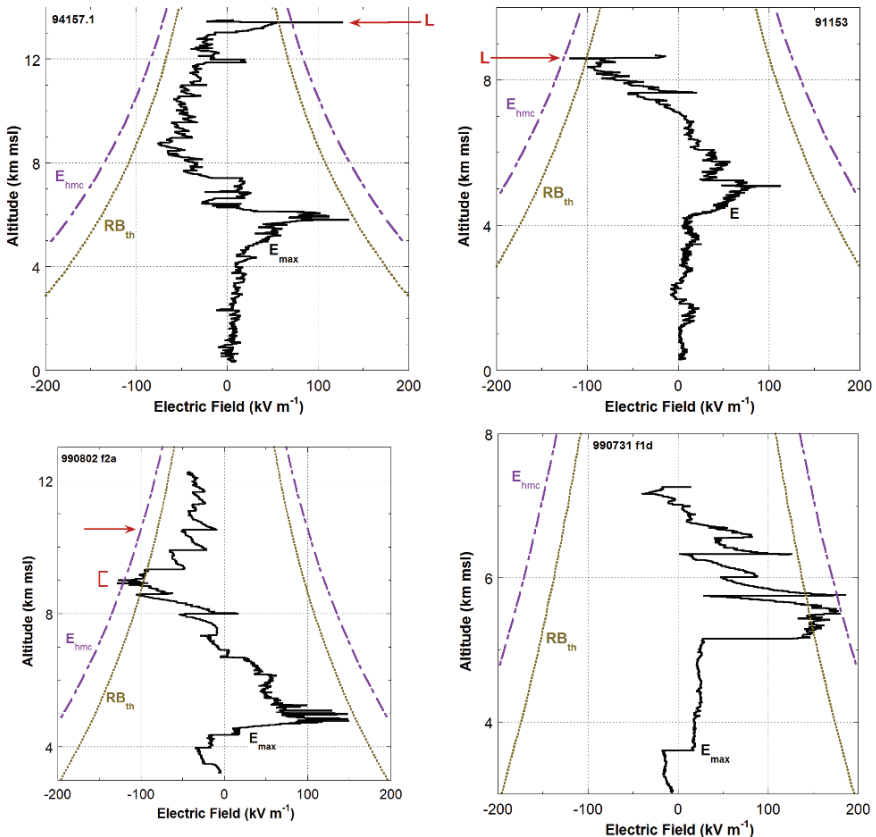


Fig. 3.3 Examples of balloon soundings showing extreme E values, compared to theoretical initiation threshold vs. altitude for runaway breakdown (brown) and liquid hydrometeor-enhanced conventional breakdown (purple). Upper panels are cases where lightning is presumed to have initiated very close by, based on the catastrophic end of data acquisition. The lightning-related E changes are marked with L. Lower panels show cases where lightning did not initiate very close to the balloon (based on instrument survival and on lightning mapping data), despite E values observed in excess of the theoretical thresholds. (Adapted from Stolzenburg et al., 2007a and Marshall et al., 2005.)

As Fig. 3.2 shows, except for the nine cases with very close lightning, there are relatively few E measurements in excess of the theoretical threshold E values. Two recent studies have included measurements of very large E along with lightning mapping data to shed information on the relative location of initiation. Maggio et al. (2005) describe one sounding where negative E values exceeded the runaway breakdown threshold for 38 s and exceeded the liquid hydrometeor-enhanced threshold for 2 s near 9 km, but no flashes started nearby. In that case, the period of large E values ended when an IC flash initiated 2.1 km away at the altitude of the negative E peak in the sounding. Marshall et al. (2005) describe a case in which the peak E was $+186 \text{ kV m}^{-1}$ at 5.8 km, before a CG lightning flash initiated at the altitude of the positive peak but 1.1 km away from the balloon location. The E then recovered and exceeded the runaway breakdown threshold for 30 s before another CG flash initiated 1.0 km away. These two soundings without very close lightning are shown in the bottom panels of Fig. 3.3, and their peak E values are included in Fig. 3.2 for comparison. It is important to note that the flash initiation locations, from the remotely acquired lightning mapping data, verify the idea that CG flashes initiate at the altitude of the low-level peak positive E and IC flashes initiate at the altitude of the mid-level peak negative E in the soundings.

Taken together, the results reviewed in this section suggest that it is necessary for E to exceed at least one of the theoretical breakdown values for lightning to initiate: in all cases of nearby lightning, E exceeded the runaway breakdown threshold at that altitude. However, meeting this condition at the location of the sounding balloon is apparently not always sufficient for nearby initiation. It appears that additional conditions (such as a threshold volume or time with large E) must be met, or a larger threshold E value must be exceeded, or perhaps the rate at which E increases to initiation values must meet some criterion (Dwyer, 2005). We also note that measurements of such extreme E values are still rather rare amid the increasing number of observations, despite the fact that lightning is clearly initiating in many places within storms. We might thus infer that the temporal and/or spatial scale of extreme E values inside storms is small, at least relative to the in situ data. Remote measurements, such as lightning mapping data, are useful in showing the spatial extent of initiation locations and hence the extent of large E values (Maggio et al., 2005). Unfortunately, the precise E value cannot be determined from the remote measurements.

3.4 Electrical Structure and Lightning Type

The type of lightning flash that occurs first in a storm may be either IC or CG, but many thunderstorms begin with a series of normal IC flashes (e.g., Krehbiel, 1986; Defer et al., 2001). As stated above, normal IC flashes initiate in a large negative E at mid-levels, and normal negative CG flashes initiate in large positive E at relatively low levels in the storm. Thus, it is the early evolution of the charge structure that dictates the type of lightning that occurs during a storm's initial growth stage. The underlying reasons that charging mechanisms inside developing thunderstorms often lead first to IC flashes is not fully understood, due in part to the lack of adequate

observations during the early electrification phase. Modeling studies (e.g., Ziegler et al., 1991) of storm electrification indicate that the non-inductive ice–ice collisional charging mechanism (e.g., Saunders, 2008) between graupel and ice crystals can lead to the correct conditions for early IC flashes. In this section, we present in situ evidence for the relationship between lightning type and electrical structure as it can be studied during the early evolution of a storm, when it evolves from producing IC flashes only to making both IC and CG flashes.

One study using sequential balloon soundings and three-dimensional lightning mapping data has provided unique information about the early, “IC-only” vertical charge structure of New Mexico mountain storms (Stolzenburg et al., 2003). For one storm, the first balloon ascended into a new convective cell that did not produce lightning until 14 min after balloon launch. Lightning activity in the storm began when the first balloon was at 9.1 km altitude, and the storm’s first 24 flashes were IC. Initiation altitudes of flashes that occurred during the first 10 min of lightning activity (37 IC and 7 CG flashes) are shown in Fig. 3.4, along with the altitudes of the two balloons. Note that the IC flashes initiate at 7.5–9.2 km altitude, while the CG flashes start 5 min later and initiate at altitudes of 4.7–6.2 km.

Figure 3.5 shows the sounding data from the first balloon (Stolzenburg et al., 2003) documenting the pre-lightning electrical structure through most of the cloud depth. The sounding differs from typical thunderstorm soundings, as described in Section 3.2.1 (and shown in Fig. 3.1) in several ways. First, E magnitudes are generally smaller, with the maximum of only 35 kV m^{-1} compared to at least 80 kV m^{-1} in typical E soundings. Second, there are only two regions of substantial net charge: a negative region centered near 7.4 km altitude ($T = -12^\circ\text{C}$) and a positive region centered near 8.7 km altitude (-20°C). Third, there are no substantial net charge regions below about 7 km altitude, while most soundings, particularly in

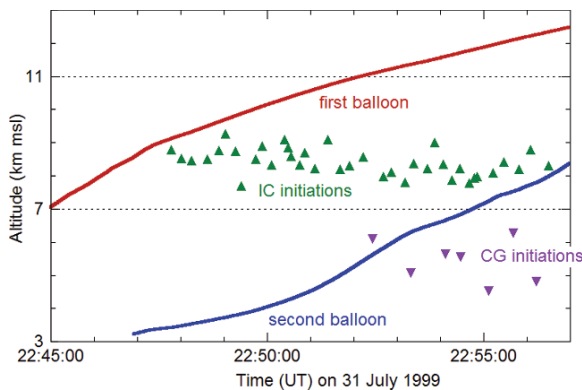


Fig. 3.4 Time series of initiation altitudes for the first 37 intracloud flashes (green) and first 7 cloud-to-ground flashes (purple) in a storm on July 31, 1999, based on Lightning Mapping Array data. Only the earliest 10 min of lightning activity is included here. Also shown are altitude curves for two instrumented balloons flown through the storm (soundings are in Fig. 3.5). (Adapted from Stolzenburg et al., 2003)

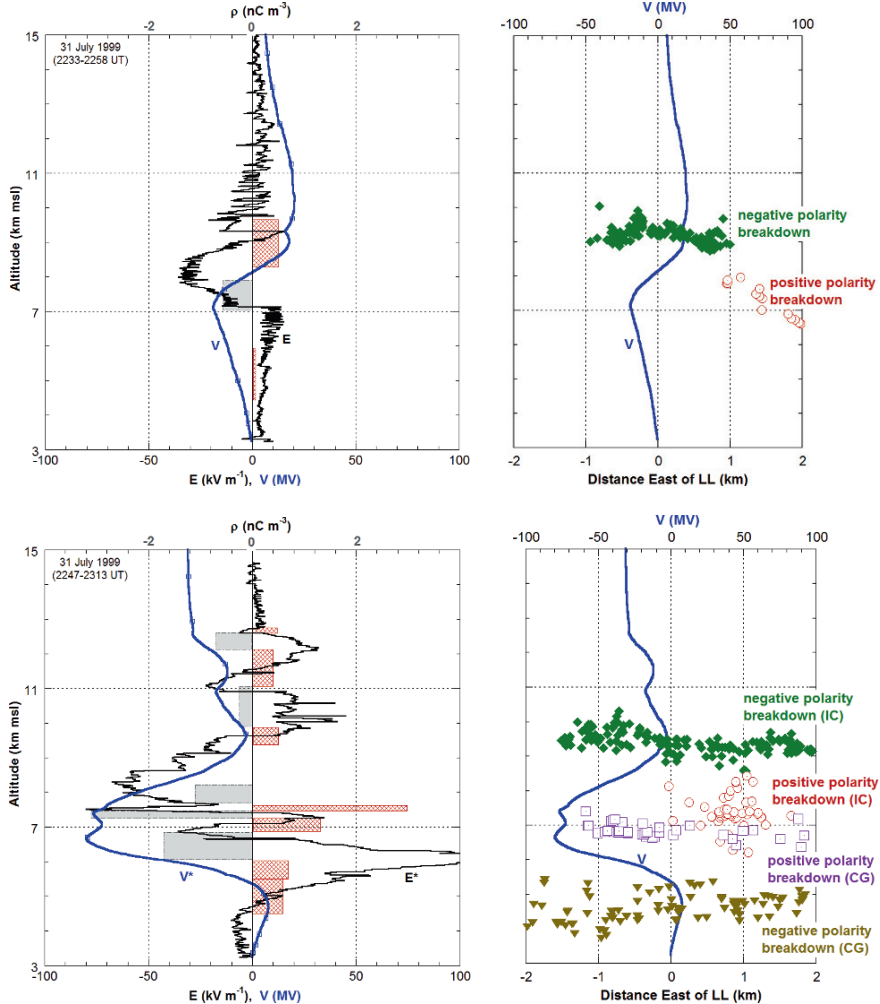


Fig. 3.5 Two soundings of electric field (E), potential (V), and charge density (ρ), along with radiation source altitudes (as a function of distance from Langmuir Laboratory) of three lightning flashes that occurred during the soundings. Blue curves are V relative to the surface as integrated from the vertical component of E. Pink (grey) areas indicate positive (negative) charge regions determined from the vertical component of E using a one-dimensional approximation to Gauss's law. *Upper panels* show data from the first balloon early in the storm, which was at 9.1 km altitude when the first lightning (IC flash shown *upper right*) occurred. The first IC flash initiated at 8.8 km altitude; the positive (negative) end of the bi-directional leader propagated near the altitude of the minimum (maximum) in V and main negative (*upper positive*) charge region. *Lower panels* show data from the second balloon, which was in the storm 10 min later during the mature stage. The first CG flash (shown *lower right*, nearby radiation sources are in purple and brown) initiated at 6.1 km altitude, where the balloon observed peak positive E of 150 kV m^{-1} . The positive (negative) end of the bi-directional leader propagated near the altitude of the minimum (maximum) in V and main negative (*lower positive*) charge region. The IC flash shown in the *lower right* behaved similarly to the first IC flash. (*Left panels* adapted from Stolzenburg and Marshall, 2008b. Lightning data adapted from Stolzenburg et al., 2003)

mountain thunderstorms, have one or more substantial charge regions as low as 5 km altitude. Stolzenburg et al. (2003) ascribed these differences to the fact that the first balloon's data were acquired very early in the electrical development of the storm. Radiation sources, as detected with the Lightning Mapping Array (LMA, e.g., Rison et al., (1999)), for the storm's first flash are included Fig. 3.5; consistent with the early electrical structure, the IC flash initiated at 8.8 km did not extend below 6.5 km. (The LMA data show where the flash's bi-directional leader traveled; further details are given in Section 3.5.1.)

The second balloon in the study by Stolzenburg et al. (2003) was launched just before the first lightning flash and ascended through the storm about 10 min after the first balloon. Unlike the first sounding, these data (lower left panel, Fig. 3.5) are similar to typical mountain thunderstorm soundings (Stolzenburg et al., 1998b). There are large peak E magnitudes (with a maximum of almost 150 kV m^{-1} at 6.1 km), and numerous regions of inferred net charge of both polarities, extending down to 4.5 km altitude. In the 10 min between the two soundings, the storm had evolved from an early, "IC-only" stage, with nearly all the net charge above 7 km, to an electrically mature stage. The key differences regarding lightning type between these two soundings are the presence of a lower positive charge region (4.5–6.1 km altitude), and the very large positive E at low levels (6.1 km) in the storm. Remotely detected radiation sources for an IC flash and the first CG flash are also shown in Fig. 3.5 (lower right panel). While the IC flash was localized in the same, upper part of the cloud as the earlier IC flashes, the CG flash initiated near the peak positive E at 6.1 km altitude and traveled below 7.5 km.

The data in Fig. 3.5 suggest that in thunderstorms which initially produce IC flashes only, the early electrification and net charge development occurs entirely at upper altitudes. As described by Stolzenburg et al. (2003), this early stage provides the large negative E necessary to initiate IC flashes, but not the large positive E at low levels needed to initiate CG flashes. The CG flashes begin occurring once a lower positive charge region and a substantial positive E develop at low levels. These findings are consistent with modeling results of the early electrification phase. In addition, as in the previous section, we see from this example that the remotely acquired lightning data provide useful information about internal the electrical structure of the storm.

3.5 Electrical Structure and Lightning Propagation

The controlling physical mechanisms for the path taken by a lightning flash are only partially understood. Details of why the leader is "stepped" and why it bifurcates are beyond the scope of this chapter (see e.g., Rakov and Uman (2003)). In this section we focus on how the charge structure in a storm influences the lightning's ionized conducting path, which is only a few centimeters in diameter and can be many kilometers long.

The lightning path immediately after initiation is controlled by the ambient thunderstorm E, which accelerates the positive and negative charges liberated by the initial breakdown. Since the storm E is mainly vertical, the bidirectional leader propagation is mostly vertical at first (Kasemir, 1960). The net-neutral leader has opposite polarity charges concentrated at its ends and some charge distributed along its length. As the leader extends, E due to the induced charge at its tips quickly becomes large enough to cause additional breakdown independent of the cloud E magnitude, although the direction of leader propagation can still be partially influenced by the cloud E (Bazelyan and Raizer, 2000). Since lightning causes dielectric breakdown along its path, and dielectric breakdown requires energy (specifically, kinetic energy), the lightning path at large scales (km) must be ultimately controlled by the cloud electrical structure. The flash gets the energy required to propagate from the electrical energy of the separated charges within the cloud. In this way the storm's electrical energy decreases with each flash; if lightning activity is to continue, the storm's energy must then be replenished by the thunderstorm charging mechanisms.

3.5.1 Electric Potential and Horizontal Propagation

One way of seeing how a flash can acquire energy to propagate from the storm's electrostatic energy and of estimating that energy is with the electrical potential profile (e.g., Fig. 3.1). Coleman et al. (2003) hypothesized that a lightning flash gets energy by moving charges into the appropriate potential 'wells,' i.e., moving negative charge into a relative potential maximum (which is a low energy location for negative charge), and moving positive charge into a relative potential minimum (a low energy location for positive charge). This hypothesis applies basic principles of electromagnetism to help understand how a lightning flash can use a storm's electrostatic energy to drive the flash's propagation, and it has been used as a framework for recent fine-scale modeling of individual lightning discharges (e.g., Tan et al., 2006). A potential maximum (or minimum) is associated with a substantial region of positive (or negative) charge. For example, the balloon sounding in Fig. 3.6 shows vertical profiles of E, V, and charge density (Coleman et al. 2003). Also shown are radiation sources from an IC flash located with the LMA; only sources within 2.5 km of the balloon's vertical path are shown. The IC flash initiated 3 km east of the balloon at 5.9 km altitude, which is consistent with the large negative E measured by the balloon at the same altitude. Consistent with the hypothesis about gaining energy, Fig. 3.6 shows that the flash moved negative charge above the initiation into a V maximum at 6.4–7.1 km and positive charge below the initiation into a V minimum at 5.2–5.7 km (Coleman et al., 2003). Thus, the characteristic bilevel structure of typical IC flashes is dictated by the presence of potential wells in the storm's electrical structure (e.g., Tan et al., 2006).

To get an idea of the energy used by a lightning flash (and thereby depleted from the storm), we can assume that the IC flash in Fig. 3.6 moves a modest 10 C of

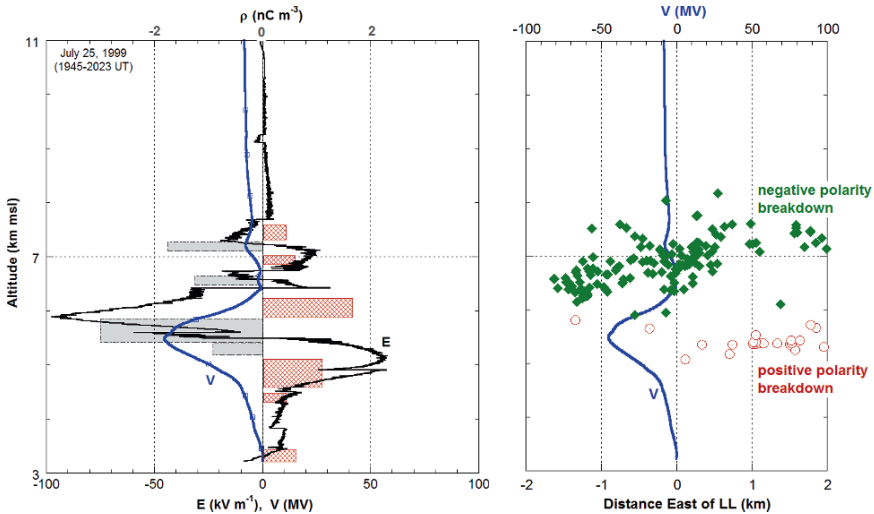


Fig. 3.6 Similar to Fig. 3.5, showing vertical profiles of electric field, potential, and charge density (ρ), along with radiation source altitudes (as a function of distance from Langmuir Laboratory) of an IC flash that occurred when this balloon was at 6.4 km altitude. (Left panel adapted from Stolzenburg and Marshall, 2008b. Lightning data adapted from Coleman et al., 2003)

charge. With ΔV of about 45 MV between wells, this flash would get about 450 MJ of energy from the storm.

Additional examples of IC and CG flashes moving charge into potential wells are in Fig. 3.5 (right panels); for three flashes depicted, negative lightning charge propagates in a V maximum and positive lightning charge propagates in a V minimum. The CG flash shows a horizontal, bilevel structure (opposite in polarity from the IC flashes) because there was a substantial lower positive charge region and associated potential well (for negative lightning charge) in addition to the well (for positive lightning charge) associated with the main negative charge region. To date all comparisons of LMA data and vertical V profiles have indicated that lightning moves charges into the potential wells (e.g., Coleman et al., 2003; Maggio, 2007; Coleman et al., 2008). These findings are consistent with lightning obtaining energy from the storm via the movement of charge. The charge motions determine the lightning's propagation path and are evident in lightning mapping data as approximately horizontal branches with vertical connecting channels in between.

In addition to affecting individual flashes, the storm's electrical structure has a longer term influence on the overall lightning propagation. An example of this can be seen in Fig. 3.7, which shows LMA radiation sources for 36 flashes that occurred during a six-minute period of a New Mexico thunderstorm (Coleman et al., 2003). Also included in the figure are the vertical charge and potential profiles in the storm based on a simultaneous sounding. Each flash type shows two levels of breakdown activity corresponding to the two ends of the bi-directional leader. The negative breakdown of the two types of flashes are located in different potential maxima, one

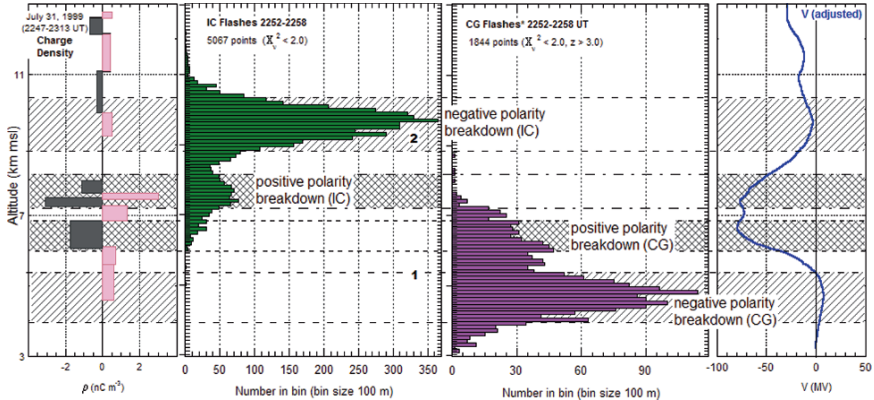


Fig. 3.7 Balloon sounding data and lightning mapping data from a New Mexico thunderstorm. (Left panel) Vertical profile of charge density (ρ). (Middle left panel) Altitude histogram of lightning radiation sources for 27 IC flashes that occurred during a six-minute period. (Middle right panel) Altitude histogram of lightning radiation sources for 8 CG flashes and a low-level, inverted IC flash that occurred in the same six-minute period. (Right panel) Vertical profile of electric potential. Diagonal hatching indicates altitudes of potential wells with relative V maximum; cross hatching indicates potential wells with relative V minimum. (Adapted from Coleman et al., 2003)

at upper levels for the IC flashes and another at low altitude for the CG flashes. The positive breakdown of both flash types is located within the same deep potential minimum between 6 and 8 km altitude. Coleman et al. (2003) noted a surprising segregation of these positive leaders in the same potential well: the positive breakdown of the IC flashes tended to be located in the upper part of the well (above 7 km), while the positive breakdown of CG flashes tended to be in the lower part of the well (below 7 km). Coleman et al. (2003) further suggested that the 10 MV bump (or slight relative maximum) at 7 km altitude within the potential minimum caused this segregation of flash propagation altitudes by type. They concluded that the potential bump was due to the accumulated positive charge deposited by lightning in the well. Such altering of the electrical structure by the lightning activity is discussed further in Section 3.6.

3.5.2 Horizontal Propagation in CG Flashes Before the First Return Stroke

The influence of potential wells on the path of a lightning flash is evident in the application to ‘preliminary breakdown,’ which is the electromagnetic radiation, lasting tens or hundreds of ms, emitted by some CG flashes before the first return stroke. Since not all CG flashes have preliminary breakdown, its cause has long been a puzzle (e.g., Clarence and Malan, 1957; Beasley et al., 1982). Coleman et al. (2008) found that for 14 flashes when a low-level potential well was present, the preliminary breakdown averaged 117 ms; when no low-level well was present, the time

between initiation and first return stroke in 15 flashes averaged 15 ms (a typical time for the vertically propagating leader to reach ground). Using balloon and surface E data with LMA lightning paths, Coleman et al. (2008) further showed that for CG flashes with preliminary breakdown, the downward descending negative leader makes a horizontal branch in a low-altitude potential well before continuing its vertical descent to the ground; they speculated that the leader “must deposit enough negative charge, as it moves horizontally at the altitude of the potential well, to ‘fill’ the well” before the leader can continue downward to ground. Thus, preliminary breakdown is the delay period caused by the horizontal motion of the descending leader in the potential well. If the low-level well is deep enough, then the leader may

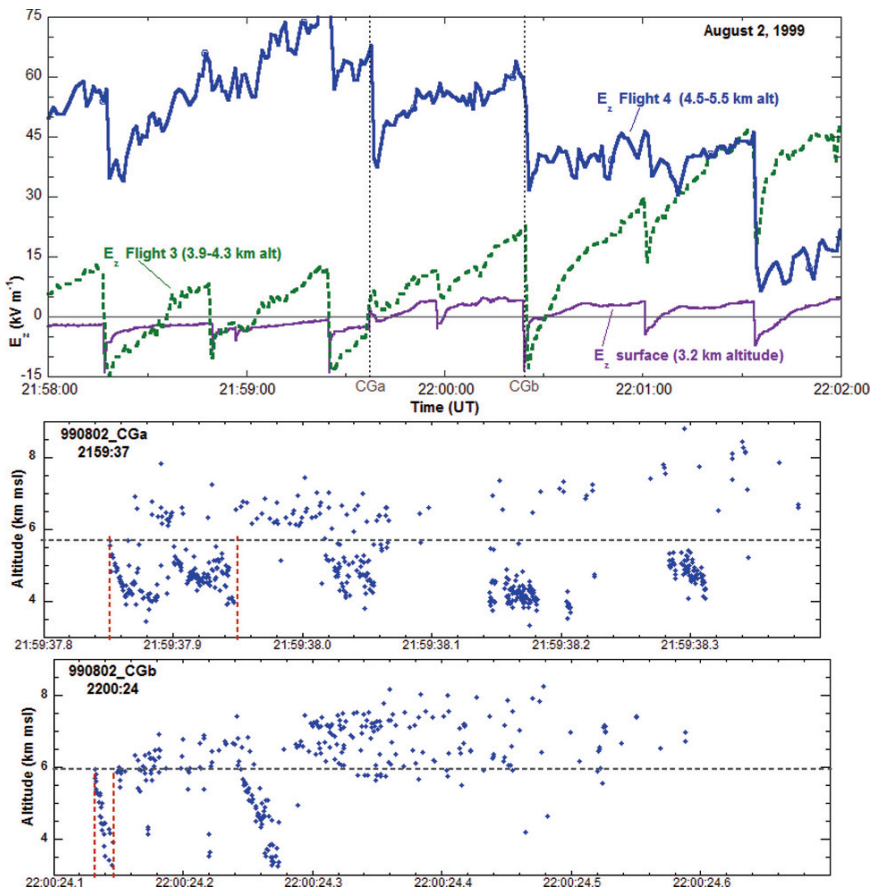


Fig. 3.8 (Upper panel) Four min of E data from a mountain storm collected at the mountaintop and at two balloons. Times of two CG flashes CGa and CGb are marked. (Middle panel) Time-altitude of lightning radiation sources for flash CGa; radiation sources span about 550 ms. (Lower panel) Time-altitude plot of radiation sources for flash CGb; radiation sources span about 500 ms. Vertical red lines in the lower panels mark the times of initiation and first return stroke. (From Coleman et al., 2008; ©American Geophysical Union)

not be able to continue downward, and the result is an inverted polarity, low-level IC flash (Coleman et al., 2008; Qie et al., 2005).

An example of a horizontal lightning channel traveling during a period of preliminary breakdown within a potential well is illustrated in Fig. 3.8. The E data from two balloons plus lightning data for two CG flashes are shown (Coleman et al., 2008). Before the flash labeled CGa, E was negative at the lower balloon (-7 kV m^{-1} at 4.0 km) and positive at the upper balloon ($+68 \text{ kV m}^{-1}$ at 4.8 km), indicating the presence of a low-level potential well in between. After initiation, flash CGa had a low-level horizontal branch and period of preliminary breakdown which lasted 98 ms before the first return stroke. Flash CGb occurred 47 s later, by which time E had become positive at both balloons and at the surface. The E data thus indicate that the low-level potential well was no longer present, probably because flash CGa deposited enough negative charge in it to neutralize it locally. Without a low-level well, flash CGb exhibited no low-level horizontal branch prior to the return stroke and no preliminary breakdown: there was only 15 ms between initiation and the first return stroke. This example gives clear evidence of the effect of the electrical structure on the horizontal propagation of lightning.

3.6 Effects of Lightning on Electrical Structure

It has long been known that lightning moves charge inside clouds, and many studies have estimated the magnitudes of the charges moved and their approximate location (e.g., Reynolds and Neill, 1955; Koshak and Krider, 1989). These studies assumed the lightning charges were one or two point charges or point dipoles; they found charge transfer magnitudes were 1 to 60 C and distributed vertically in a tripolar structure of opposite polarity to the cloud's charge structure, (e.g., see Section 3.2.1). As we noted previously, the *in situ* balloon measurements of storm charge structures indicate that the simple tripole is an important component in a more complex structure, with four to six (or more) charge regions.

The development of lightning mapping arrays has provided two important details for improving estimates of lightning charge deposition: (1) a map of a flash's path through the storm and (2) an indication of which parts (branches) of a flash deposit positive charge and which deposit negative charge (e.g., Rison et al., 1999). Coleman et al. (2008) verified the LMA charge polarity indication using several periods of simultaneous E data from two balloons. An example is seen in Fig. 3.8, discussed earlier. Flash CGa had an LMA-inferred negative branch pass between the balloons; E increased at the lower balloon and decreased at the upper balloon, as expected if negative charge was deposited between the balloons, thus verifying the negative charge of the lightning branch. This study thus verified that normal negative CG flashes often deposit a substantial amount of negative charge in the cloud, despite having the net effect of lowering negative charge to ground.

Recent studies have combined information about the path of a flash through a cloud with *in situ* electrical measurements, especially the field change due to the

flash, to obtain a more complete understanding of how the lightning charge is distributed in the cloud (e.g., Sonnenfeld et al., 2006; Maggio, 2007). At present, new algorithms are being developed to determine where lightning deposits charge, so a detailed review of the results is premature. One notable finding is that early in the life of a storm, point charge algorithms (with the location given by the mean location of LMA radiation sources) give results as good as those based on distributing charge along the LMA path, while later in the storm's life the distributed charge solutions are significantly better (Maggio, 2007). This finding of greater lateral extent in the electrical structure is consistent with radar and photographic studies showing growth of the horizontal extent of precipitation and cloud structures.

The data in Fig. 3.8 also give one indication of how lightning charge deposition can alter the storm's charge structure. Before flash CGa, the potential and charge structures included a low-level potential well associated with a lower positive charge region. Flash CGa deposited negative charge in the well to neutralize it, at least locally, so that the negative leader could continue down to the ground (and cause the first return stroke). Thus, charge deposited by flash CGa changed the local charge and potential structures, neutralizing the lower positive charge region and the low-level potential well, and this change influenced the development 47 s later of flash CGb (i.e., no preliminary breakdown needed).

Coleman et al. (2003) discussed another example of lightning charge deposition and its effect on the charge structure depicted in Fig. 3.6. The IC flash shown occurred when the balloon was at 6.4 km altitude and changed E from about -30 to $+20 \text{ kV m}^{-1}$. A branch of negative polarity breakdown passed just above the balloon (Coleman et al., 2003). At the time of the flash, the balloon was rising through the upper positive charge region that extended from about 5.9–7.1 km. The balloon data collected after the flash show that the negative branch of the flash deposited enough negative charge to reverse the net charge polarity just above the balloon between 6.4 and 6.6 km and essentially neutralized the region between 6.6 and 6.8 km. Thus, the branch effectively split the upper positive charge region into two parts and inserted negative charge in its midst.

The preceding discussion helps explain the differences between in situ measurements of the storm charge structure, with four to six charge regions or more, and lightning-inferred indications of the structure, with only two or three charge regions. In comparing balloon and lightning indications of charge structure, Coleman et al. (2003) discussed two ways in which potential profiles and the idea that lightning moves charge into potential wells "bridge the gap" between these seemingly disparate observations. First, Coleman et al. (2003) noted that multiple lightning flashes depositing the same polarity of charge into a potential well associated with cloud charge of the opposite polarity will tend to split the well and thereby lead to the more complicated electrical structures often seen with balloons. In a detailed analysis of LMA and balloon data (Fig. 3.7), they showed that the positive charge region analyzed near 7 km altitude was probably caused by multiple lightning flashes depositing positive charge near the bottom of the deep negative potential well at the same altitude. The second 'bridge' stems from the fact that the V profile is essentially an integral of the E profile, while the charge profile is essentially a derivative

of the E profile. Because of this, smaller charge regions (in either density or depth) have little effect on the V profile. Thus, the V profile tends to have only two or three main wells, and it is the V profile that guides where the lightning charges are deposited. Lightning measurements of storm charges typically reveal the main charge regions that are participating in the flashes, while in situ measurements can reveal these and the smaller charge regions, too. Overall, the potential profile due to the storm charge structure guides where the lightning charges are deposited, and these deposited charges tend to make the cloud charge structure more complex.

3.7 Summary

This chapter has focused on the basic electrical structure of thunderstorms and the ways in which the electric field, potential, and charge influence lightning flashes that initiate within and travel through the storm. In a wide variety of electrified clouds, the charge regions tend to be horizontally stratified such that the principal variations in the quasi-static E and V structures are seen in the vertical. Convective updrafts typically have four vertically stacked charge regions, non-updraft portions of convection show at least six charge regions, and MCS stratiform clouds are characterized by three to five main charge regions.

The in situ measurements reviewed herein indicate that the large-scale E typically observed in storms is at least an order of magnitude less than the conventional breakdown E. Data acquired closest to lightning initiation locations give values exceeding the runaway breakdown threshold by as much as $\sim 300\%$ and apparently also exceeding the hydrometeor-enhanced conventional breakdown threshold. The rapid increase in E observed just before some nearby flashes may also be an important clue about initiation physics. Vertical E and charge profiles show that the largest E magnitudes are found between charge regions of opposite polarity, and lightning data indicate that flashes initiate at these altitudes. This observation also explains why CG flashes are delayed in some storms until a substantial lower positive charge has developed. After initiation the two ends of a flash's bi-directional leader propagate along and opposite to the local E (i.e., down the potential gradient). Potential wells in the vertical V profile determine the altitude at which a lightning flash will have an extensive horizontal branch or branches; this branching is explained by energy considerations. The combination of the initiation altitude along with the number, altitude, and depth of each of the potential wells controls both the flash type (IC or CG) and the detailed development of the flash (e.g., horizontal propagation within a well interrupting a leader's propagation to the ground). Lightning also influences the electrical environment: lightning charge deposition alters the charge, E, and V structures in a cloud, making these structures more complex by interjecting charge of opposite polarity into existing charge regions.

Our improved understanding of the relations between lightning and the electrical structure in a storm increases the possibility of using remote lightning measurements to obtain information about a storm's electrical structure. Lightning mapping data

(e.g., Rison et al., 1999) are especially useful for this type of inversion, as evidenced by recent studies that have compared and verified the LMA interpretations about the electrical structure with in situ measurements. For example, Maggio et al. (2005) showed that LMA data can be used to determine both a lightning flash's initiation location, and thereby the region of large E values, as well as the direction of the cloud E vector at that location. The approximately horizontal lightning branches seen in the LMA data of nearly all flashes give an indication of the three-dimensional structure of the potential wells (Coleman et al., 2003) that cannot easily be determined from balloon soundings; horizontal gradients in the potential have been reasonably represented in two-dimensional computer simulations of lightning propagation (e.g., Tan et al., 2006). The polarities of lightning charges inferred from LMA data also have been used to help identify atypical storm electrical structures (e.g., Rust et al., 2005; Weiss et al., 2008). Thus, lightning mapping measurements could provide much needed information about both the lightning and the thunderstorms that have not been studied extensively or at all with in situ measurements, including high-latitude storms, tropical storms, winter storms, and hurricanes.

Acknowledgments Much of the research reviewed herein was supported by the U.S. National Science Foundation (recent Grant Nos. ATM-9626542, ATM-0220842, ATM-0605026).

References

- Bateman, M.G., T.C. Marshall, M. Stolzenburg, W.D. Rust, Precipitation charge and size measurements inside a New Mexico thunderstorm, *J. Geophys. Res.*, **104**, 9643–9653, 1999.
- Bazelyan, E.M., Y.P. Raizer, *Lightning Physics and Lightning Protection*, 325 pp., Inst. of Phys. Publ., Bristol, Berkshire, 2000.
- Beasley, W.H., M.A. Uman, P.L. Rustan, Electric fields preceding cloud-to-ground lightning flashes, *J. Geophys. Res.*, **87**, 4883–902, 1982.
- Byrne, G.J., A.A. Few, M.F. Stewart, Electric field measurements with a severe thunderstorm anvil, *J. Geophys. Res.*, **94**, 6297–6307, 1989.
- Carey, L.D., M.J. Murphy, T.L. McCormick, N.W.S. Demetriades, Lightning location relative to storm structure in a leading-line, trailing-stratiform mesoscale convective system, *J. Geophys. Res.*, **110**, D03105, doi: 10.1029/2003JD004371, 2005.
- Chauzy, S., M. Chong, A. Dellano, S. Despiau, The June 22 tropical squall line observed during COPT 81 experiment, *J. Geophys. Res.*, **90**, 6091, 1985.
- Clarance, N.D., D.J. Malan, Preliminary discharge processes in lightning flashes to ground, *Q. J. R. Meteorol. Soc.*, **83**, 161–172, 1957.
- Coleman, L.M., T.C. Marshall, M. Stolzenburg, et al., Effects of charge and electrostatic potential on lightning propagation, *J. Geophys. Res.*, **108**, 4298, doi:10.1029/2002JD002718, 2003.
- Coleman, L.M., M. Stolzenburg, T.C. Marshall, M. Stanley, Horizontal lightning propagation, preliminary breakdown, and electric potential in New Mexico thunderstorms, *J. Geophys. Res.*, **113**, D09208, doi:10.1029/2007JD009459, 2008.
- Crabb, J.A., J. Latham, Corona from colliding drops as a possible mechanism for the triggering of lightning. *Quart. J. Roy. Meteor. Soc.*, **100**, 191, 1974.
- Defer, E., P. Blanchet, C. Thery, P. Laroche, J. Dye, M. Venticinque, K. Cummins, Lightning activity for the July 10, 1996, storm during the STERAO-A experiment, *J. Geophys. Res.*, **106**, 10 151, 2001.

- Dwyer, J.R., A fundamental limit on electric fields in air, *Geophys. Res. Lett.*, 30, 2055, doi:10.1029/2003GL017781, 2003.
- Dwyer, J.R., The initiation of lightning by runaway air breakdown, *Geophys. Res. Lett.*, 32, L20808, doi:10.1029/2005GL023975, 2005.
- Gurevich, A.V., K.P. Zybin, Runaway breakdown and electric discharges in thunderstorms, *Phys. Usp.*, 44, 1119, 2001.
- Gurevich, A.V., G.M. Milikh, R. Roussel-Dupre', Runaway electron mechanism of air breakdown and preconditioning during a thunderstorm, *Phys. Lett. A*, 165, 463, 1992.
- Houze, R.A., Jr., *Cloud Dynamics*, 573 pp., Academic, San Diego, 1993.
- Kasemir, H. W., A contribution to the electrostatic theory of a lightning discharge, *J. Geophys. Res.*, 65, 1873–1878, 1960.
- Koshak, W.J., E.P. Krider, Analysis of lightning field changes during active Florida thunderstorms, *J. Geophys. Res.*, 94, 1165–1186, 1989.
- Krehbiel, P.R., The electrical structure of thunderstorms, in *The Earth's Electrical Environment*, E.P. Krider, R.G. Roble (eds.), pp. 90–113, Natl. Acad. Press, Wash., 1986.
- Krehbiel, P.R., J.R. Riouset, V.P. Pasko, R.J. Thomas, W. Rison, M.A. Stanley, H.E. Edens, Upward electrical discharges from thunderstorms, *Nature Geoscience*, 1, 233–237, 2008
- Lang, T.J., S.A. Rutledge, K.C. Wiens, Origins of positive cloud-to-ground lightning flashes in the stratiform region of a mesoscale convective system, *Geophys. Res. Lett.*, 31, L10105, doi: 10.1029/2004GL019823, 2004.
- Latham, J., I.M. Stromberg, Point-discharge. in *Lightning*, R.H. Golde, ed., Academic Press, 99–117, 1977.
- Lyons, W.A., The Meteorological and Electrical structures of TLE-producing convective storms, this volume, 2008.
- MacGorman, D.R., D.W. Burgess, V. Mazur, W.D. Rust, W.L. Taylor, B.C. Johnson, Lightning rates relative to tornadic storm evolution on 22 May 1981, *J. Atmos Sci.*, 46, 221–250, 1989.
- MacGorman, D.R., W.D. Rust, P.R. Krehbiel, et al., The electrical structure of two supercell storms during STEPS, *Mon. Weather Rev.*, 133, 2583, 2005.
- Maggio, C.R., Estimations and applications of lightning charge transfers in New Mexico thunderstorms, *Ph.D. diss.*, Univ. of Miss., University, 209 pp., 2007.
- Maggio, C.R., L.M. Coleman, T.C. Marshall, et al., Lightning initiation locations as a remote sensing tool of large thunderstorm electric field, *J. Oceanic Atmos. Technol.*, 22, 1059, 2005.
- Marshall, T.C., S.J. Marsh, Negatively charged precipitation in a New Mexico thunderstorm, *J. Geophys. Res.*, 98, 14 909–14 916, 1993.
- Marshall, T. C., W.D. Rust, Electric field soundings through thunderstorms, *J. Geophys. Res.*, 96, 22297, 1991.
- Marshall, T.C., W.D. Rust, Two types of vertical electrical structures in stratiform precipitation regions of mesoscale convective systems, *Bull. Amer. Meteorol. Soc.*, 74, 2159, 1993.
- Marshall, T.C., M. Stolzenburg, Estimates of cloud charge densities in thunderstorms, *J. Geophys. Res.*, 103, 19 769–19 775, 1998.
- Marshall, T.C., M. Stolzenburg, Voltages inside and just above thunderstorms, *J. Geophys. Res.*, D106, 4757, 2001.
- Marshall, T.C., W.D. Rust, W.P. Winn, K.E. Gilbert, Electrical structure in two thunderstorm anvil clouds, *J. Geophys. Res.*, 94, 2171, 1989.
- Marshall, T.C., M.P. McCarthy, W.D. Rust, Electric field magnitudes and lightning initiation in thunderstorms, *J. Geophys. Res.*, 100, 7097, 1995a.
- Marshall, T.C., W.D. Rust, M. Stolzenburg, Electrical structure and updraft speeds in thunderstorms over the southern Great Plains, *J. Geophys. Res.*, 100, 1001, 1995b.
- Marshall, T.C., M. Stolzenburg, W.D. Rust, E.R. Williams, R. Boldi, Positive charge in the stratiform cloud of a mesoscale convective system, *J. Geophys. Res.*, 106, 1157–1163, 2001.
- Marshall T.C., M. Stolzenburg, C.R. Maggio, et al., Observed electric fields associated with lightning initiation, *Geophys. Res. Lett.*, 32, 10.1029/2004GL021802, 2005.
- Proctor, D.E., VHF radio pictures of cloud flashes, *J. Geophys. Res.*, 86, 4041–4071, 1981.

- Qie, X., T. Zhang, C. Chen, et al., The lower positive charge center and its effect on lightning discharges on the Tibetan Plateau, *Geophys. Res. Lett.*, 32, L05814, doi:10.1029/2004GL022162, 2005.
- Reynolds, S.E., and H.W. Neill, The distribution and discharge of thunderstorm charge-centers, *J. Meteorol.*, 12, 1–12, 1955.
- Rison, W., R.J. Thomas, P.R. Krehbiel, T. Hamlin, J. Harlin, A GPS-based three-dimensional lightning mapping system: Initial observations in central New Mexico, *Geophys. Res. Lett.*, 26, 3573–3576, 1999.
- Rust, W.D., T.C. Marshall, On abandoning the thunderstorm tripole-charge paradigm, *J. Geophys. Res.*, 101, 23499, 1996.
- Rust, W.D., D.R. MacGorman, E.C. Bruning, et al., Inverted-polarity electrical structures in thunderstorms in the Severe Thunderstorm Electrification and Precipitation Study, *Atmos. Res.*, 76, 247, 10.1016/j.atmosres.2004.11.029, 2005.
- Rutledge, S.A., D.R. MacGorman, Cloud-to-ground lightning activity in the 10–11 June 1985 mesoscale convective system observed during OK PRE-STORM, *Mon. Weather Rev.*, 116, 1393–1408, 1988.
- Saunders, C.P.R., Charge separation mechanisms in clouds, *Space Sci. Rev.*, in press, 2008.
- Shao, X.M., P.R. Krehbiel, The spatial and temporal development of intracloud lightning, *J. Geophys. Res.*, 101, 26641, 1996.
- Simpson, G.C., On the electricity of rain and its origin in thunderstorms, *Philos. Trans. R. Soc. London*, A209, 379, 1909.
- Simpson, G., F.J. Scrase, The distribution of electricity in thunderclouds, *Proc. R. Soc. London*, A161, 309, 1937.
- Sonnenfeld, R.G., J. Battles, G. Lu, W.P. Winn, Comparing E-field changes aloft to lightning mapping data, *J. Geophys. Res.*, 111, doi:10:1029/2006JD007242, 2006.
- Stolzenburg, M., T.C. Marshall, Charged precipitation and electric field in two thunderstorms, *J. Geophys. Res.*, 103, 19 777–19 790, 1998.
- Stolzenburg, M., T.C. Marshall, Charge structure and dynamics in thunderstorms, *Space Sci. Rev.*, 137, 355–372, doi: 10.1007/s11214-009-9338, 2008a.
- Stolzenburg, M., T.C. Marshall, Serial profiles of electrostatic potential in five New Mexico thunderstorms, *J. Geophys. Res.*, 113, D13207, doi:10.1029/2007JD009495, 2008b.
- Stolzenburg, M., T.C. Marshall, E.D. Rust, B.F. Smull, Horizontal distribution of electrical and meteorological conditions across the stratiform region of a mesoscale convective system, *Mon. Weather Rev.*, 122, 1777–1797, 1994.
- Stolzenburg, M., W.D. Rust, B.F. Smull, T.C. Marshall, Electrical structure in thunderstorm convective regions 1. Mesoscale convective systems, *J. Geophys. Res.*, 103, 14059, 1998a.
- Stolzenburg, M., W.D. Rust, T.C. Marshall, Electrical structure in thunderstorm convective regions 2. Isolated storms, *J. Geophys. Res.*, 103, 14079, 1998b.
- Stolzenburg, M., W.D. Rust, T.C. Marshall, Electrical structure in thunderstorm convective regions 3. Synthesis, *J. Geophys. Res.*, 103, 14097, 1998c.
- Stolzenburg M., T.C. Marshall, W.D. Rust, D.L. Bartels, Two simultaneous charge structures in thunderstorm convection, *J. Geophys. Res.*, 107, 4352, 2002.
- Stolzenburg, M., T.C. Marshall, L.M. Coleman, et al., Evolution of charge and lightning type in developing thunderstorms, *Proc. 12th Intl. Conf. on Atmos. Elec.*, Versailles, France, 2003.
- Stolzenburg M., T.C. Marshall, W.D. Rust, et al., Electric field values observed near lightning flash initiations, *Geophys. Res. Lett.*, 34, L04804, 10.1029/2006GL028777, 2007a.
- Stolzenburg, M., T.C. Marshall, W.D. Rust, et al., The stratiform precipitation region of mesoscale convective systems, *Proc. 13th Intl. Conf. on Atmos. Elec.*, Beijing, China, 2007b.
- Symbolisty, E.M.D., R. Roussel-Dupre, V. Yukhimuk, Finite volume solutions of the relativistic Boltzmann equation for electron avalanche studies, *IEEE Trans. Plasma Sci.*, 26, 1575, 1998.
- Takahashi, T., *Proc. 13th Intl. Conf. on Atmos. Elec.*, Beijing, China, 2007.
- Takahashi, T., T.D. Keenan, *J. Geophys. Res.*, 109, D16208, 10.1029/2004JD004667, 2004.

- Tan, Y., S. Tao, B. Zhu, Fine-resolution simulation of the channel strictures and propagation features of intracloud lightning, *Geophys. Res. Lett.*, 33, L09809, doi:10.1029/2005GL025523, 2006.
- Tessendorf, S., Characteristics of Lightning in Supercells, (this volume), 2008.
- Weinheimer, A.J., J.E. Dye, D.W. Breed, et al., Simultaneous measurements of the charge, size, and shape of hydrometeors in an electrified cloud, *J. Geophys. Res.*, 96, 20809, 1991.
- Weiss, S.A., W.D. Rust, D.R. MacGorman, E.C. Bruning, P.R. Krehbiel, Evolving electrical structure of the STEPS 25 June 2000 multicell storm, *Mon. Weather Rev.*, 2008.
- Wilson, C.T.R., On some determinations of the sign and magnitude of electric discharges in lightning flashes, *Proc. R. Soc. London*, A92, 555, 1916.
- Winn, W.P., G.W. Schwede, C.B. Moore, Measurements of electric fields in thunderclouds, *J. Geophys. Res.*, 79, 1761, 1974.
- Ziegler, C.L., D.R. MacGorman, J.E. Dye, and P.S. Ray, A model evaluation of non-inductive graupel-ice charging in the early electrification of a mountain thunderstorm, *J. Geophys. Res.*, 96, 12 833–12 855, 1991.

Chapter 4

Characteristics of Lightning in Supercells

Sarah A. Tessendorf

Abstract This chapter focuses on the lightning and charge structure observed in supercells; a particular class of severe thunderstorms that are typically responsible for producing the most violent hailstorms and tornadoes. The chapter reviews common supercell features, the classification of supercells based on structural and visual characteristics, as well as the microphysics of supercells related to hail growth and electrification. A summary of observed flash rates, lightning polarity, and charge structure within supercells is also presented, along with descriptions of a few case studies as examples. Specific attention has been given to recent observations of anomalous positive cloud-to-ground lightning and inverted charge structures. Though this behavior is not exclusive to supercells, it has typically been observed in strong and/or severe storms that often meet supercell criteria.

Keywords Supercells · Lightning flash rate · Lightning polarity · Severe storms · Charge structure · Inverted charge structure · Positive cloud-to-ground (CG) lightning

4.1 Introduction

There are several characteristics of supercells that distinguish them from ordinary thunderstorms, most notably their ability to persist for several hours, while the lifetime of an ordinary thunderstorm is on the order of tens of minutes to one hour. Supercells, however, tend to occur less frequently than ordinary single- and multi-cell convection, therefore it has been challenging to build up a database of detailed observations of lightning in supercells. With the advent of cloud-to-ground lightning detection networks, mobile electric field balloon facilities, and three-dimensional lightning mapping systems, more information on lightning properties of thunderstorms has been collected, occasionally within supercell storms. This

S.A. Tessendorf (✉)

Research Applications Laboratory, National Center for Atmospheric Research,

P.O. Box 3000, Boulder, CO 80307, USA

e-mail: saraht@ucar.edu

chapter presents some background on supercell features, especially those that pertain to electrification, and summarizes observations of lightning and charge structure within supercells that have been documented to date.

4.2 A Review of Supercell Storms

Supercells have been the focus of much research due to their association with severe weather. They have commonly been defined as strong convective storms that are long-lived (order of a few hours) and contain a temporally and spatially persistent mesocyclone, or a region of vertical vorticity that is present over much of the storm depth in or near the updraft region (Browning 1964, Browning 1977, Lemon and Doswell 1979, Brandes 1984, Weisman and Klemp 1984, Doswell and Burgess 1993, Moller et al. 1994). Specific characteristics about the structure and airflow within supercells have been revealed by numerous detailed field studies. Due to the inherent variability of the weather, however, these characteristics may apply to many, but not all, supercells. Regardless, it is still important to understand the generalized structure of supercells to put the remainder of this discussion in context.

4.2.1 Supercell Structure

Characteristics that are typically recognized as supercellular have been the development of a bounded weak echo region (BWER), forward- and rear-flank downdrafts, and a low-level reflectivity hook echo. The BWER, or vault-like structure, is a radar feature that has been associated with a strong and persistent updraft that does not allow hydrometeors enough time to grow from vapor condensation on cloud condensation nuclei (CCN) just above cloud base to significant drop sizes, hence the low reflectivity values in this region (Browning and Donaldson 1963; Browning 1964, 1965, Lemon 1980). The existence of a BWER feature indicates the precipitation efficiency, or the efficiency of a storm to convert cloud water to precipitation, is reduced. This has implications for hail growth, which will be discussed in more detail in the following section. The forward-flank downdraft is normally located in the forward and right flanks of the storm and produces a weak surface discontinuity (Lemon and Doswell 1979). A rear-flank downdraft (RFD) is located on the upwind side of the storm and is typically drier, more dense and cooler than the forward-flank downdraft (Lemon and Doswell 1979). Convergence between the low-level environmental airflow and the strong outflow from the RFD lifts low-level moist air to help sustain the updraft. The hook echo, which partially surrounds the BWER and is usually detected at low levels by radar, has been used to indicate the likely presence of a mesocyclone, and is often associated with tornadoes (Browning 1964). Supercells have also been documented to travel in a direction to the right of the mean winds. An early conceptual model of this behavior was presented by Browning (1964; see his Fig. 4.5), and still remains an accepted model

of supercell airflow and motion. Though most supercells have been documented to move to the right of the mean winds, “left-moving” supercells have also been observed (Hammond 1967, Nielsen-Gammon and Read 1995, Grasso and Hilgendorf 2001, Dostalek et al. 2004, Lindsey and Bunkers 2005).

The previous discussion describes the common features of a “classic” supercell, but deviations from this classic structure have been documented and as such supercells are often classified into three categories (Doswell and Burgess 1993): low-precipitation (LP), classic, and high-precipitation (HP). Bluestein and Parks (1983) defined LP supercells as storms with a clear mesocyclone, but very little rainfall. Due to the lack of rainfall, there is typically no strong precipitation core and the mesocyclone is found in weaker reflectivity, making LP supercells difficult to detect with radar even though they often contain large hail. Visual observations help aid in the determination of LP storms as they often exhibit spiraling striations around the updraft and a clear wall cloud, indicative of the mesocyclone (Bluestein and Woodall 1990, Moller et al. 1994). LP supercells are common in the high plains east of the Rocky Mountains and western Great Plains along the surface dryline, and can produce large hail and tornadoes. In contrast to LP supercells, HP storms are distinguished by heavy precipitation in the region of the mesocyclone for much of its lifetime (Moller et al. 1990, Doswell and Burgess 1993, Moller et al. 1994). Given the heavier rainfall, the mesocyclone is more easily detected by radar, but visually the mesocyclone is more obscured. HP storms have not been linked to as many strong and violent tornadoes as classic supercells, but they can produce large hail, tornadoes, and often flash floods and damaging winds (Moller et al. 1994). It is worthy to note that a given supercell may not exhibit the characteristics of one supercell type for its entire lifetime, as it is common for supercells to evolve from one type to another, as well as from (to) an ordinary thunderstorm or mesoscale convective system before (after) exhibiting supercellular characteristics.

4.2.2 Microphysics of Supercells

Though supercells represent only a small portion of all hailstorms—multicellular and hybrid supercell-multicell (Nelson and Knight 1987, Nelson 1987) storms comprise the majority—supercells tend to be responsible for much of the damage from hailstorms given the large size and quantity of hail they can produce (Browning and Foote 1976, Browning 1977). Nelson (1983) concluded it is the persistence and width of the updraft that influences hailstone size. A weak echo region (WER), whether it is bounded (BWER) or unbounded, is indicative of a strong updraft and is a common feature of hailstorms (Marwitz 1972a, 1972b, Chisholm 1973, Nelson and Knight 1987, Tessendorf et al. 2005, Schlatter et al. 2008). Figure 4.1 illustrates an observed BWER and coincident strong updraft from a large hail-producing supercell that occurred on 29 June 2000 in northwest Kansas (Tessendorf et al. 2005). In supercells, the WER tends to be bounded (e.g. a BWER, or vault), is quite persistent, and indicates reduced precipitation efficiency, yielding high quantities

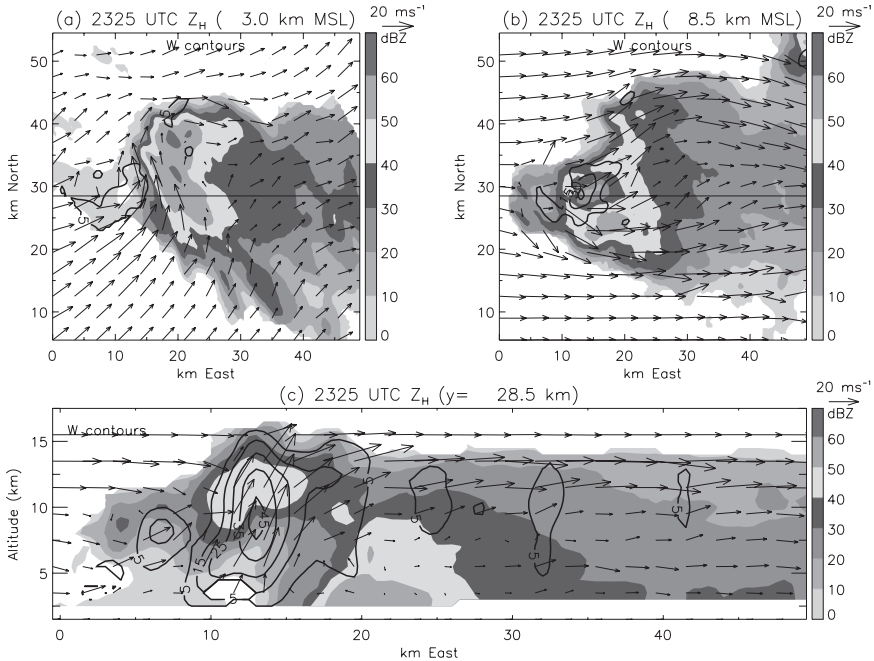


Fig. 4.1 Winds and storm structure illustrating the beginning of the tornadic period in the 29 June 2000 supercell at 2325 UTC: (a) horizontal cross section of grayscale reflectivity at $z = 3$ km and bold black updraft contours beginning at 5 m s^{-1} with a contour interval of 10 m s^{-1} , (b) horizontal cross section of grayscale reflectivity at $z = 8.5$ km with bold black updraft contours beginning at 15 m s^{-1} with a contour interval of 15 m s^{-1} , and (c) vertical cross section of grayscale reflectivity at $y = 28.5$ km with bold black updraft contours beginning at 5 m s^{-1} with a contour interval of 10 m s^{-1} . All panels have storm-relative wind vectors overlaid. (Reprinted with permission from Tessendorf et al. 2005)

of supercooled liquid water in the mixed phase region of the storm. Browning and Foote (1976) suggested that, “it is this very inefficiency that encourages the growth of large hail, provided that at least some embryos are able to re-enter the main updraught.” They outlined a three-stage process for hail growth, where drops grow to millimeter sizes on their first ascent through the updraught, then they descend along the “embryo curtain”, or forward flank downdraft, and are finally re-circulated by the mesocyclonic flow back into the main updraught for further growth into hail. The mesocyclonic flow found in supercells was shown to be fundamental for hail embryos to be recirculated back into the updraught for further growth into large hail (Tessendorf et al. 2005).

A strong updraft and enhanced liquid water content (LWC) in the mixed phase region, often found in supercells and important to hail growth, are also key ingredients for an active electrification process via the subsequent production of large quantities of graupel. It is suspected that hail itself has a small role in electrification due to its small integrated surface area compared to graupel (Williams 2001), and given its tendency to undergo wet-growth in high LWC regimes, which reduces its

ability to separate charge (Saunders and Brooks 1992). In order for charge to be separated via collisional charging processes, smaller particles (e.g. ice crystals or water drops) must collide with larger particles (rimed ice particles, e.g. graupel), which transfers charge between the two such that each obtains net charge of opposite polarity (Reynolds et al. 1957, Takahashi 1978, Jayaratne et al. 1983, Illingworth 1985, Saunders et al. 1991). After a collision, the particles are size sorted within the updraft (i.e. smaller particles are carried to the cloud top, while the larger particles remain in the midlevels of the cloud) to create distinct regions of opposite sign of charge, or a cloud-scale dipole moment (Williams 1989).

Collisional charging processes have generally been categorized into two groups: those that depend on a pre-existing electric field to determine the sign of charge transfer (inductive) versus those that do not (non-inductive). Several laboratory experiments have investigated the conditions under which particles obtain charge during non-inductive collisions, and concluded that the sign of charge transferred to the rimer (e.g. graupel) is dependent on the temperature and cloud LWC of the environment in which the collision occurs (Takahashi 1978, Jayaratne et al. 1983, Saunders et al. 1991, Saunders 1994), though differences in the results of these experiments exist.¹ As one example, Takahashi (1978) showed that for cloud LWC near $1\text{--}2 \text{ g m}^{-3}$, a charge reversal level of -10°C was found such that for warmer (colder) temperatures the rimer received positive (negative) charge. For especially large values of cloud LWC, and thus high riming rates, the larger riming particles were found to obtain a positive charge under all cloud temperatures used in the experiment (0 to -30° C). In a supercell, the strong updraft carries much of the precipitation-sized hydrometeors to higher altitudes (i.e. the top of the vault), and thus to colder temperatures, which would favor negative charging of graupel. Nonetheless, in some strong and broad supercellular updrafts, the cloud LWC at these altitudes is enhanced due to the inefficient precipitation process discussed earlier, as well as due to limited entrainment of the updraft core, which may lead to positive charging of graupel.

These structural, kinematic, and microphysical features of supercells have an effect on the resulting electrification in these unique storms. Observations of the lightning and charge structures that result in supercells will be presented in the following sections.

4.3 Lightning in Supercells

4.3.1 Flash Rates

In addition to having unique kinematic and microphysical features, supercells also tend to produce large amounts of lightning. As shown in Williams (2001; his Fig. 13.28), based on a synthesis of work by Holle and Maier (1982), Knapp (1994), and Perez et al. (1995), cloud-to-ground (CG) flash rates tended to be much higher

¹ The details of these differences are beyond the scope of this chapter, but interested readers should also refer to Saunders et al. (2006) since they presented results that possibly rectify the differences.

in severe storms than ordinary (non-severe) thunderstorms. Severe storms had observed CG flash rates as high as ten per minute, whereas non-severe storms rarely produced CG flash rates higher than one per minute. While most supercells are severe, not all severe storms can be classified as supercells, thus Table 4.1 summarizes lightning characteristics from several recent studies of supercell storms that utilize the National Lightning Detection Network (NLDN; Cummins et al. 1998), or a similar CG detection network.² It is clear that CG flash rates in supercells vary greatly from having no CG lightning (such as in the 3 June 2000 STEPS supercell in northwestern Kansas; Tessendorf et al. 2007a) to having flash rates as high as 30 per minute (such as in the Plainfield, IL, supercell on 28 August 1990; Seimon 1993, MacGorman and Burgess 1994). This variability in CG flash rate among severe storms and supercells makes it difficult to use CG flash data as a tool for predicting severe weather. In their study of CG lightning in 42 tornadic supercells, Perez et al. (1997) concluded that the occurrence of peak CG flash rate alone offered “little predictive value for tornadogenesis”, but suggested that if combined with other observations (i.e. Doppler radar), CG flash data may have the potential to help distinguish changes in storm intensity.

Maximum total flash rates (intracloud and cloud-to-ground flashes combined) for severe storms also vary greatly, but have been observed on the order of 10^2 flashes per minute, whereas a non-severe storm typically averages 1–3 flashes per minute (Williams 2001). Williams et al. (1999) reported for Florida thunderstorms that total flash rates in excess of 60 per minute (or 1 per second) were an indicator of a severe thunderstorm. Based on recent case studies of supercells that had access to total lightning flash data (see Table 4.1), the variability of total flash rates in supercells is obvious, nonetheless all of these studied supercells had a maximum total flash rate on the order of ten per minute or greater. However, the measured flash rate is also dependent on the instrument used to infer the total flash rate. For example, flash rates may be underestimated in cases where the storm was viewed by the network over a short portion of its lifetime (e.g. the Optical Transient Detector, OTD, satellite-borne sensor overpass may have been toward the end of the storm lifetime as in Knupp et al. 2003). Furthermore, flash rates may be overestimated by Very High Frequency (VHF)-based sensor calculation methods,³ such as those from the New Mexico Tech Lightning Mapping Array (LMA; Rison et al. 1999) or Vaisala’s Lightning Detection and Ranging (LDAR; Demetriades et al. 2001) systems, if “singletons” (Williams et al. 1999) are included in the flash counts. The quantitative flash rate is also sensitive to the VHF source threshold used in the calculation, so it is best to

² The other CG detection networks used by studies in Table 4.1 are the National Severe Storms Laboratory (NSSL)/State University of New York Albany (SUNYA) magnetic direction finder (MDF; Mach et al. 1986), the French Meteorage MDF network (Tourte et al. 1988), and the Blitz Informationsdienst von Siemens (BLIDS) system operated by the Siemens AG in Germany and Switzerland.

³ A VHF-based instrument referred to in Table 4.1 but not discussed in the text is the Office National d’Etudes et de Recherches Aérospatiales (ONERA) interferometric lightning mapper (ITF; Laroche et al. 1994, Mazur et al. 1997).

Table 4.1 Summary of flash rates in recent supercell lightning studies and associated characteristics. Storm types are classic supercell (CL), low-precipitation supercell (LP), high-precipitation supercell (HP), hybrid supercell-multicell (H; as defined by Nelson and Knight 1987), and mesoscale convective system (MCS). Maximum total flash rate (TFR) and CG flash rate (CG FR), as well as dominant CG polarity (P = positive, N=negative) are also included. Values indicated in parentheses those when supercell type or dominant polarity changed later in the storm evolution. Values with asterisk indicate they were calculated within 10 km of the mesocyclone region only. Nil values in the table are from when a study didn't report that particular characteristic

Investigators	Date	Location	Type	Max TFR (min ⁻¹)	Max CG FR (min ⁻¹)	CG Polarity	Instruments
MacGorman et al. 1989	22-May-81	Binger, OK	CL	14	4*	N	L-band radar and NSSL MDF
Keighton et al. 1991	23-May-81	Southern OK	H (MCS)	—	3	N	NSSL MDF
MacGorman and Nielson 1991	8-May-86	Edmond, OK	CL	—	10*	N	NSSL MDF
Curran and Rust 1992	26-Apr-84	Western OK	LP (CL)	—	1(3)	P (N)	NSSL MDF
MacGorman and Burgess 1994	28-Aug-90	Planfield, IL	(CL HP)	—	12 (30)	P (N)	NSSL/SUNYA MDF
"	21-Mar-91	Tishomingo, OK	CL (HP)	—	12 (30)	P (N)	"
"	26-Mar-91	Hutchinson, KS	LP (CL)	—	3	P	"
"	26-Apr-91	Andover, KS	CL	—	4 (1)	P (N)	"
Lopez and Aubagnac 1997	19-Jun-91	Northern OK	CI	—	5	N	NLDN
Bluestein and MacGorman 1998	31-May-90	Spearmen, TX 1	CL	—	2	N	"
"	31-May-90	Spearmen, TX 2	LP	—	5	N	"
"	31-May-90	Spearmen, TX 3	CL	—	1 (2)	P (N)	"
"	31-May-90	Spearmen, TX 4	CL	—	7 (3)	P (N)	"

Table 4.1 (continued)

Investigators	Date	Location	Type	Max TFR (min ⁻¹)	Max CG FR (min ⁻¹)	CG Polarity	Instruments
Carey and Rutledge 1998	7-Jun-95	Colorado	—	17	<1 (1)	N (to P)	flat plate antenna and NLNDN
Soula et al. 1998	7-Aug-96	Spain	—	—	12	N	French Meteorage
Williams et al. 1999	31-Oct-97	Florida	—	500	15	—	LDAR and NLNDN
"	23-Feb-97	Florida	—	>500	~17	—	LDAR and NLNDN
Bouchler et al. 2000	17-Apr-95	Oklahoma	—	78	3 & 2	N & P	OTD and NLNDN
Shafer et al. 2000	26-May-85	Oklahoma	LP (MCS)	—	20	N	NSSL MDF
Defer et al. 2001	10-Jul-96	Kimball, NE.	—	58	3	N	ONERA/NLNDN
McCaul et al. 2002	3-Jun-99	Alamena, KS	LP (CL)	100	≤ 1	N	audio detector and NLNDN
Carey et al. 2003b	30-May-98	Spencer, SD	—	—	18	P	NLNDN
Knupp et al. 2003	18-May-95	TN valley A	CL (HP)	21	11 & 16	N & P	OTD and NLNDN
"	"	TN valley B	CL	63	10 & 15	N & P	OTD and NLNDN
"	"	TN valley C	CL (HP)	—	14	N	NLNDN
Fehr et al. 2005	21-Jul-98	Germany	—	45	3 (1)	N (P)	ONERA/TIFF and BLIDS
Goodman et al. 2005	11-Nov-02	Tennessee	—	70	—	—	LMA and NLNDN
"	"	Tennessee	—	100	10	N	LMA and NLNDN
Wiens et al. 2005	26-Jan-00	Bird City, KS	CL	300	4	P	LMA and NLNDN
Steiger et al. 2007	13-Oct-01	Dallas, TX	—	40	12*	N	LDARI and NLNDN
Tessendorf et al. 2007a	3-Jun-00	Northwest KS	LP	30	0	n/a	LMA and NLNDN

focus on the general order of magnitude and trends of the flash rates inferred by the VHF systems, rather than on a specific rate at any given time (Wiens et al. 2005). Nevertheless, it is clear that total flash rates in supercells often are on the order of 10^2 per minute, as reported in Williams (2001), though they can also be an order of magnitude lower (Table 4.1).

Regardless of the method for calculating total flash rate, flash rate *trends* tend to be consistent between methods (Wiens et al. 2005). In total flash rate trends of severe thunderstorms and/or supercells, lightning ‘jumps’ have been observed, which represent a marked increase in total flash rate that precedes the maximum observed flash rate (Williams et al. 1999, Goodman and Coauthors 2005, Wiens et al. 2005). Williams et al. (1999) noted that this jump tended to occur tens of minutes before severe weather (e.g. hail, downbursts) reached the ground in Florida thunderstorms, and Goodman and Coauthors (2005) presented similar results for Alabama storms. Wiens et al. (2005) also showed a total lightning flash rate jump coincident with the production of an F1 tornado and prior to a surge in hail production in the 29 June 2000 Kansas supercell (Fig. 4.2). Steiger et al. (2007) also showed such relationships for Texas supercells, but in their study they also found that increased height of the lightning sources was highly correlated with severe weather occurrence. These relationships between increased total lightning flash rate and lightning source height with severe weather onset in the central and southern U.S. suggest that *total* lightning data may provide more useful severe weather warning information than that from radar, given the higher temporal and spatial resolution of lightning mapping data. Nonetheless, future research must examine these relationships further for a variety of regions and storm types to verify this relationship and ensure a high probability of detection and a low false alarm rate, and at present total lightning data is not available in all regions. Moreover, such future studies need to analyze the lightning data on shorter temporal scales than that of radar volume scan times to get the most out of the higher temporal resolution in the total lightning data (Steiger et al. 2007).

In some cases, high total flash rates have been observed in severe storms, while CG flash rates remain low (<1 per minute), thus the relationship between intracloud (IC) and CG flashes (also known as the IC:CG ratio) becomes very high, if not infinite (MacGorman et al. 1989, Carey and Rutledge 1998, Lang et al. 2000, Lang and Rutledge 2002, McCaul et al. 2002, Tessendorf et al. 2007a). Lang et al. (2000) and Tessendorf et al. (2007a) both observed severe convective storms that produced high IC flash rates (>30 per minute), while the CG flash rates in Lang et al. (2000) were particularly low (<1 per minute), and there was no CG lightning in Tessendorf et al. (2007a). McCaul et al. (2002) also documented a similar phenomenon in the Alamena, KS, supercell (see Table 4.1), where the IC flash rate was on the order of 10^2 per minute, and yet fewer than one CG flash per minute was observed (average of 0.06 per minute). Observations suggest that the IC:CG ratio tends to increase with increased storm severity and electrical activity, and perhaps could also be used as an indicator of enhanced severe weather potential (Rutledge et al. 1992, Cheze and Sauvageot 1997, MacGorman et al. 1989, Carey and Rutledge 1998, Lang and

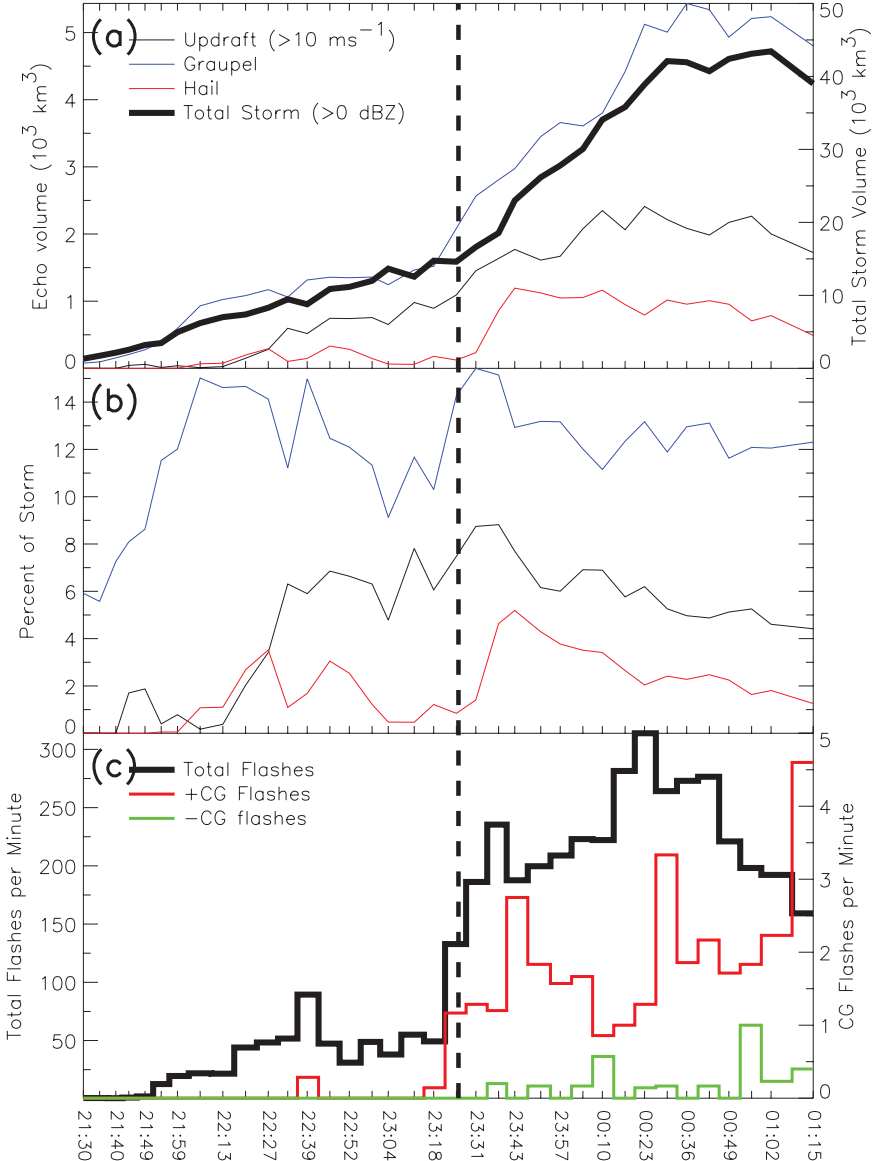


Fig. 4.2 Time series summary of the 29 June 2000 supercell. **(a)** Radar-inferred echo volumes of storm updraft ($w > 10 \text{ m s}^{-1}$), graupel, and hail. Thick black line shows total storm volume (defined as volume of storm with radar reflectivity exceeding 0 dBZ). **(b)** As in **(a)**, but with echo volumes plotted as percent of total storm volume. **(c)** Total flash rate and CG flash rate averaged over each radar volume scan time interval. Vertical dashed line indicates the time (2325 UTC) when the storm made a right turn and produced an F1 tornado. (Reprinted with permission from Wiens et al. 2005)

Rutledge 2002, Kamra and Pawar 2007). Further details on the hypotheses for this behavior will be discussed in Section 4.4.1.

4.3.2 *Lightning Polarity*

Based on CG lightning climatologies in the United States as well as other regions with CG lightning detection networks, negative polarity CG lightning is by far the most common polarity of CG lightning (Orville and Huffines 2001, Chen et al. 2002, Schulz et al. 2005, Soriano et al. 2005, Pinto et al. 2006, Sonnadara et al. 2006). Furthermore, even in severe storms that produce large hail and/or violent tornadoes, typically supercells, it has been shown that negative polarity CG lightning is also customary (Perez et al. 1997, Carey et al. 2003a). In fact, out of the 42 violent tornadic supercell cases studied in Perez et al. (1997), 32 cases had greater than 75% of their total CG lightning come to ground as negative polarity flashes.

Steiger et al. (2007) presented observations of a supercell dominated by negative CG lightning that occurred on 13 October 2001 near Dallas, TX. This supercell produced large hail and two F2 tornadoes, and exhibited intense flash rates before producing its first tornado. Total flash rates observed by the LDARII (Demetriades et al. 2001) VHF lightning mapping system were as high as 26 per minute and negative CG flash rates peaked at 12 per minute nearly 10 minutes prior to the touchdown of the first tornado (Fig. 4.3). Both total and CG flash rates decreased during tornadogenesis, reaching a minimum during the second tornado, but the total flash rate peaked again, as high as 40 per minute, near the end of the second tornado. Other documented tornadic supercells dominated by negative CG lightning have shown peaks in negative CG flash rate coincident with tornadogenesis (e.g., Bluestein and MacGorman 1998), during the tornadic period (e.g., MacGorman and Nielson 1991, Bluestein and MacGorman 1998), or even after all tornadic activity had ended (e.g., MacGorman et al. 1989). Thus, as reported in MacGorman (1993) and Perez et al. (1997), CG flash rates relative to tornadogenesis are quite variable. Most of the lightning activity in the 13 October 2001 supercell was downwind (east) of the mesocyclone (Steiger et al. 2007; their Fig. 4.4), consistent with findings by Ray et al. (1987) regarding the location of lightning in supercells. The IC:CG ratio in this storm began around 10 and then slowly declined until the tornadic period when it reached a minimum (Fig. 4.3). Then during the second tornado, it hit a maximum of 20 before settling roughly back to 10. The percent positive CG lightning was never greater than 20%, and was also at a minimum during the second tornado (Fig. 4.3).

Supercells have been documented to occasionally produce unusually large amounts of positive CG lightning during portions of their lifetimes and many recent studies have focused on these anomalous storms (Reap and MacGorman 1989, Branick and Doswell 1992, Curran and Rust 1992, Seimon 1993, MacGorman and Burgess 1994, Stolzenburg 1994, Carey and Rutledge 1998, Carey et al. 2003b, MacGorman et al. 2005, Wiens et al. 2005). Orville and Huffines (2001) showed that enhanced positive CG activity tends to occur more frequently in the High Plains

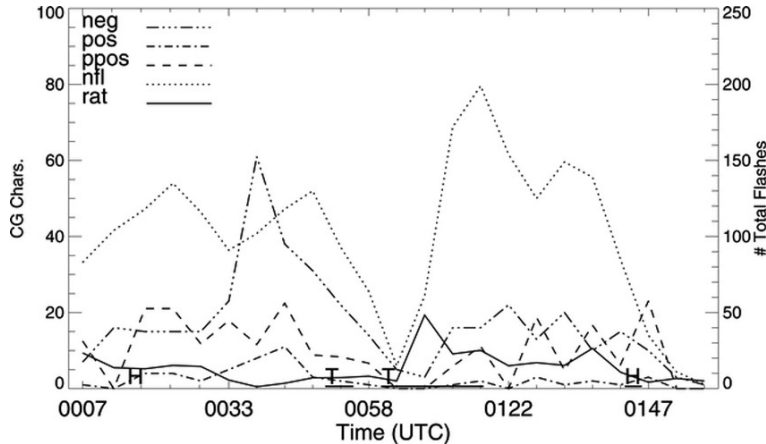


Fig. 4.3 Time history of lightning characteristics calculated within 10 km of the 13 October 2001 mesocyclone for each radar volume scan interval (~ 5 min). The characteristics shown are: \pm CG flash rate per 5 minute interval (pos, neg), percent positive CG flashes (ppos), total flash rate per 5 minute interval (nfl; right y axis), and IC:CG ratio (rat). Severe hail (H) and tornado (T) reports are also plotted. (Reprinted with permission from Steiger et al. 2007)

region of the United States. Besides situations where positive polarity CG lightning dominates a storm's CG activity, positive CG lightning has also been observed at the demise of a storm (Pierce 1955, Fuquay 1982, Orville et al. 1983, Nielsen et al. 1994), from the storm anvil or trailing stratiform region of a mesoscale convective system (Rust et al. 1981, Rutledge and MacGorman 1988, Engholm et al. 1990, Rutledge et al. 1990, Nielsen et al. 1994, Shafer et al. 2000, Lang et al. 2004a), and also from within the convective line of mesoscale convective systems (Shafer et al. 2000, Lang et al. 2004a). Positive CG lightning has also been shown to dominate CG activity in winter storms in Japan, especially those that formed in high wind shear (Takeuti et al. 1978, Takeuti et al. 1985, Brook et al. 1982).

Some transient luminous events (TLEs) have also been associated with supercells, mostly blue jets, gigantic jets, and cloud top events termed “gnomes”, and “pixies” (Lyons et al. 2003, 2008a). Limited evidence is beginning to suggest these types of TLEs are most often observed above the overshooting convective domes of intense thunderstorms and supercells. The most common form of TLEs—sprites—are often associated with positive CG lightning, particularly those strokes with charge moment changes $>500\text{--}600 \text{ C km}$ in the trailing stratiform region of mesoscale convective systems. Sprites, however, are rarely observed over supercells, even those which produce predominantly positive CG lightning (Lyons et al. 2008a). In the few occasions where sprites have been observed over supercells they have typically occurred during the decaying portion of the supercell’s lifecycle, though in one recent case a few also occurred during the mature stage of the supercell (Lyons et al. 2008a). For more information on sprites, see Lyons et al. (2008b).

Perez et al. (1997) noted that tornadic storms occasionally exhibited polarity reversals, usually from predominantly positive to negative CG polarity. A well-known

example of this behavior is the Plainfield, IL tornadic supercell that occurred on 28 August 1990 (Seimon 1993, MacGorman and Burgess 1994). This supercell began producing predominantly positive CG lightning (recorded at >75% positive by Seimon 1993) as it developed, and even maintained positive CG lightning percents greater than 90% with CG flash rates greater than five per minute up through what the author called a downburst phase. In this phase, the supercell produced a long-lived downburst and the mesocyclone underwent rapid intensification. Tornadogenesis occurred at the end of this phase leading to the production of an F5 tornado.⁴ The CG polarity also reversed at this time from predominantly positive to greater than 95% negative, and the storm remained predominantly negative until its demise. Curran and Rust (1992) and Bluestein and MacGorman (1998) also noted polarity reversals from positive to negative in tornadic supercells, where a tornado occurred after the polarity reversal, and MacGorman and Burgess (1994) documented that polarity reversals (from positive to negative) also occurred when supercells transitioned from having LP to classic or from classic to HP characteristics. Polarity reversals have also been noted in the opposite manner (from negative to positive) also often accompanying a notable shift in the storm's behavior (Carey and Rutledge 1998), and some storms have even been observed to remain dominated by positive CG lightning throughout their lifetime (MacGorman and Burgess 1994, Carey et al. 2003b, MacGorman et al. 2005, Wiens et al. 2005).

A recent example of a supercell entirely dominated by positive CG lightning that was well documented by radar and lightning observations occurred on 29 June 2000 during the Severe Thunderstorm Electrification and Precipitation Study (STEPS; Lang et al. 2004b, MacGorman et al. 2005, Tessendorf et al. 2005, Wiens et al. 2005). This supercell only produced two (both positive) CG flashes during the first two hours of its evolution, and then, coincident with a dramatic storm intensification (increased updraft volume and hail production) and the production of an F1 tornado, it began producing frequent positive CG lightning, with positive CG flash rates up to four per minute (Fig. 4.2; Wiens et al. 2005). Nearly 90% of the CG flashes in this storm were positive. The total flash rate in this storm was as high as 300 per minute, and IC flashes accounted for greater than 95% of the total lightning (Wiens et al. 2005). As in Ray et al. (1987) and Steiger et al. (2007), the majority of this supercell's lightning activity was above and downwind (east) of the updraft and mesocyclone (see Fig. 4.7). The charge structure in this storm was documented by the New Mexico Tech three-dimensional Lightning Mapping Array (LMA; Rison et al. 1999), and will be discussed in Section 4.4.2.

4.3.2.1 Hypotheses on Positive CG lightning

The mechanisms behind why some storms produce predominantly positive CG (PPCG) lightning, as opposed to the more commonly observed supercells that

⁴ An F5 is the strongest tornado rating on the Fujita scale (Fujita 1971), which is a scale based on damage that occurred from the tornado passage, and not necessarily on the actual winds achieved by tornado.

produce predominantly negative CG lightning, are not well understood. Some hypothesize that the difference lies in the kinematic structure and microphysical properties of the storm or storm intensity (Rust et al. 1985, Branick and Doswell 1992, MacGorman and Burgess 1994, Gilmore and Wicker 2002, Lang and Rutledge 2002, Wiens et al. 2005). In particular, Stolzenburg (1994) suggested that large amounts of positive CG lightning may be due to rapid increases in radar echo top height and were coincident with the production of large hail. Reap and MacGorman (1989) and MacGorman and Burgess (1994) also showed that large hail was common to storms dominated by positive CG lightning. Carey and Rutledge (1998) found that large hail and positive CG lightning appeared to be anticorrelated, with broad peaks in the positive CGs lagging behind the peaks in large hail falling out of the storm. However, Carey and Rutledge (1998) did state that there was a direct correlation between the initial increase in the IC:CG ratio, the first positive CG, and the early production of hail aloft. Whether hail really influences charging processes and the polarity of CG lightning is unknown. Given the arguments outlined in Section 4.2.2, though, it seems less likely that hail directly affects storm electrification.

Several studies have recognized that PPCG storms tend to occur in a similar and distinct region from negative CG dominated storms, implying that the environment in which a storm exists could influence the dominant CG polarity (Branick and Doswell 1992, MacGorman and Burgess 1994, Bluestein and MacGorman 1998, Smith et al. 2000, Gilmore and Wicker 2002, Carey et al. 2003a, Williams et al. 2005, Carey and Buffalo 2007). Following on this premise, Smith et al. (2000) revealed an intriguing relationship between surface equivalent potential temperature (θ_e) and the polarity of CG lightning for a sample of severe storms. Their study indicated that severe storms dominated by negative CG flashes formed in regions of weak θ_e gradients and downstream of a θ_e ridge axis. On the other hand, severe storms that formed in regions with a strong θ_e gradient or upstream of a θ_e maximum were usually dominated by positive CG lightning. They also noted that when storms crossed the θ_e ridge axis the polarity switched from positive to negative, while those that remained upstream from the θ_e maximum continued to produce positive CG lightning throughout their lifetimes. Carey et al. (2003a) also showed a general relationship between CG lightning polarity in severe storms and the climatological monthly location of the θ_e ridge, such that PPCG lightning was west and northwest of the ridge, while predominantly negative CG lightning was southeast of the PPCG area closer to ridge axis.

Williams et al. (2005) also noted that the climatological maximum in PPCG lightning was located coincident with local maximum instability along with higher cloud base heights. They speculated that higher cloud base heights (and thus shallower warm cloud depth) and strong and large updrafts reduce the warm rain efficiency allowing more liquid water to reach the mixed phase region. This enhancement of liquid water content in the mixed phase region may lead to positive charging of graupel via non-inductive charging processes (see Section 4.2.2). They also suggested that enhanced aerosol concentration could have a similar result on storm micro-physics (i.e. reduce warm rain efficiency), and could possibly explain occurrences of positive CG lightning in storms that ingested smoke (Lyons et al. 1998, Murray

et al. 2000). Carey and Buffalo (2007) showed that the greatest statistical thermodynamic difference between PPCG⁵ storms and storms dominated by negative CG lightning in the southern Great Plains was in warm cloud depth, with PPCG storms having less warm cloud depth and higher cloud base heights. These observations are consistent with the ideas put forth by Williams et al. (2005). These results, if proved consistent for a larger sample of storms, including non-severe storms, are promising for understanding the lightning polarity of storms and for predicting severe weather based on CG polarity. However, to fully understand the physical mechanisms that relate the polarity of lightning in supercells to their environment, further research is needed. Nonetheless, these observations are the foundation for the hypothesized charge structures conducive to positive CG lightning that are discussed in Section 4.4.1.

4.4 Charge Structure in Supercells

The most commonly observed charge structure in ordinary, and to some extent supercell, thunderstorms is typically referred to as a “normal” charge structure (see also Stolzenburg and Marshall (2008)). The most basic form of the normal charge structure consists of two charge layers: an upper level positive charge and a main midlevel region of negative charge. It is generally understood that a thunderstorm has this dipole moment due to the charge separation from collisions between graupel and ice particles. Via the non-inductive charging process, these collisions tend to transfer negative charge to the larger (graupel) particles, which, due to gravity, fall faster than the positively charged ice particles. This results in a negative charge region in the lower part of the storm and a positive charge region aloft. Often, a small region of positive charge is also detected below the main negative charge region (Fig. 4.4). One explanation for this lower positive charge is that it results from non-inductive collisions between graupel and ice below the charge reversal level, such that the graupel attains positive charge at the warmer temperatures and falls to the lowest part of the cloud, while the negatively charged ice is carried higher and into the main negative region (Williams 1989, Stolzenburg et al. 1998c). Though most studies show that non-inductive processes are primarily responsible for this tripole charge structure, it has also been suggested that inductive charging processes do play a secondary role in thunderstorm charging and could contribute to the lower positive charge layer, and that screening layer processes create additional charge layers along the cloud edge (Ziegler et al. 1991, Brooks and Saunders 1994, Stolzenburg et al. 1998c, Mansell et al. 2005).

Altogether, these three charge layers make up the normal tripole structure that has been discussed in the literature for decades (Simpson and Scrase 1937, Marshall and

⁵ Note that Carey and Buffalo (2007) defined PPCG storms as those having greater than 25% positive CG lightning, whereas other studies have used 50% or even 75% positive CG fractions to define a PPCG storm.

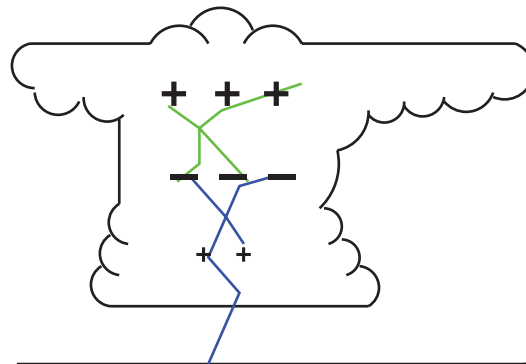


Fig. 4.4 Schematic illustration of a normal tripole charge structure, with intracloud flashes initiating between the upper positive and main negative regions, and negative CG flashes initiating between the main negative and lower positive charge regions

Winn 1982, Krehbiel 1986, Williams 1989, Marshall and Rust 1991, Stolzenburg et al. 1998a–c). This charge structure (illustrated in Fig. 4.4) has been shown to be conducive to, if not optimal for, negative CG lightning via the lower positive charge layer (Clarence and Malan 1957, Jacobson and Krider 1976, Williams 1989, Williams et al. 1989). This hypothesis suggests that the presence of the lower positive charge locally enhances the electric field below the main negative charge region, and thus provides a bias for the negative charge transfer to go to ground, whereas it is less energetically favorable to transfer negative charge to ground otherwise (Williams et al. 1989). The behavior of modeled lightning discharges (Williams et al. 1985, Solomon and Baker 1998, Mansell et al. 2002) also supports this idea.

Observations in supercells, however, indicate that a more complex charge structure than the basic normal tripole is common (Marshall and Rust 1991, Marshall et al. 1995, Stolzenburg et al. 1998a–c, MacGorman et al. 2005, Wiens et al. 2005). In particular, Marshall et al. (1995) and Stolzenburg et al. (1998b) used data from several electric field balloon soundings of supercells to show that strong updrafts have a simpler charge structure than regions of downdraft or weak updraft (Fig. 4.5). Soundings in updrafts greater than 10 m s^{-1} showed only three charge regions, similar to the normal tripole, though the main negative charge region was, on average, higher in supercells than for other storm types (Stolzenburg et al. 1998a–c). They pointed out, however, that none of the balloon soundings in their study ascended entirely through the top of the supercells, and thus additional charge layers may have existed above the balloon path. In particular they speculated a fourth region, most likely of negative charge, existed above the normal tripole given the strong electric fields at the top of the truncated supercell updraft soundings. Furthermore, Ziegler and MacGorman (1994) modeled the charge structure of the Binger supercell (MacGorman et al. 1989) and found a similar four-layer charge structure in the updraft region, and Stolzenburg et al. (1998c) observed similar four-layer structures in the other storm types they studied.

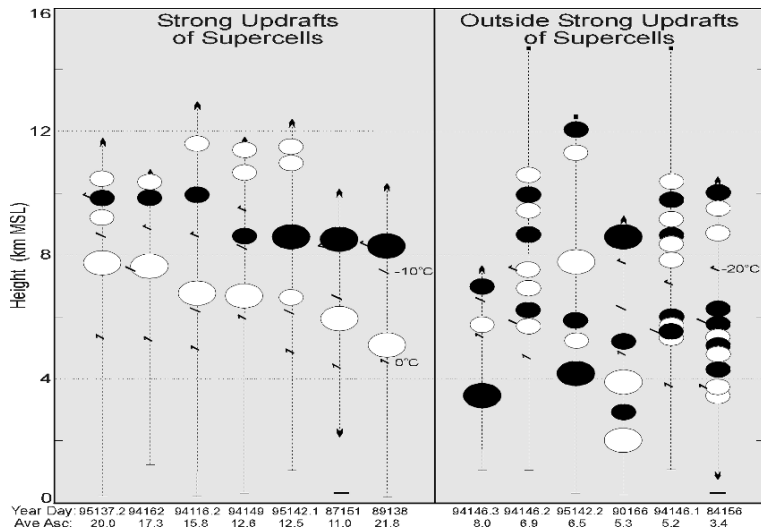


Fig. 4.5 Charge distributions inside and outside strong updrafts of supercell thunderstorms. Each vertical dashed line represents an electric field sounding (labeled with year and day along the horizontal axis). Number below sounding identifier is average balloon ascent rate between the surface and 12 km msl (or top of the sounding, if below 12 km). Still-air rise rates of the balloons are about $5\text{--}6 \text{ m s}^{-1}$. Negative (positive) charge layers are represented by solid (open) ellipses, with larger ellipses for layers deeper than 1 km. Charge ellipses are centered at the center height of each layer as analyzed with the one-dimensional approximation to Gauss's law. Surface height at the sounding launch position is indicated by a horizontal bar; upper limit of E data is shown by an upward pointing arrowhead (if below cloud top) or small square (if above cloud top). Lower limit of E data, if not at the surface, is shown by a downward pointing arrowhead. Short slanted lines indicate the heights of the 0° , -10° , and -20°C temperature in each sounding. (Reprinted with permission from Stolzenburg et al. 1998b)

Weak updraft soundings in supercells showed at least six charge layers, typically alternating in polarity (Fig. 4.5; Marshall et al. 1995, Stolzenburg et al. 1998b). The heights and polarities of each layer outside strong updraft varied from storm to storm quite a bit, though, such that there was not a typical pattern to the charge structure of supercells in these regions. MacGorman et al. (2005) presented soundings of the rainy downdraft region of two supercells and also showed that the charge structure outside of the strong updraft was more complex, as well as charge tended to extend to lower heights in the storm than that of the lowest charge in the strong updraft. Three-dimensional lightning mapping studies have also shown that charge structures in supercells outside the updraft are more complex (Wiens et al. 2005), which also agrees with results of supercell electrification model simulations (Kuhlman et al. 2006). MacGorman et al. (2005) concluded that the additional lower charge regions were too low to correspond to any of those in the strong updraft, and thus perhaps a different charging process was responsible for their production. They argued that non-inductive processes would not be as effective at these low heights and lower liquid water contents outside the updraft, but that inductive mechanisms might be able to account for the charge regions generated there. Stolzenburg et al. (1998c)

came to a similar conclusion that inductive processes might be responsible for some of the additional charge layers observed in their soundings outside of strong updrafts.

Another possible reason for increased charge structure complexity in supercells, especially outside the updraft, is due to lightning (see also Stolzenburg and Marshall 2008). Model simulations by Helsdon et al. (1992), Ziegler and MacGorman (1994), Mansell et al. (2002), and Kuhlman et al. (2006) showed that lightning could deposit charge on uncharged particles, which could lead to the formation of new charge regions. Observations by Coleman et al. (2003), MacGorman et al. (2005), and Rust et al. (2005) also support the idea that charge deposition by lightning can change the charge polarity in the vicinity of the lightning channel, and increase the complexity of the charge structure. Tessendorf et al. (2007b) also noted that in a large multicellular storm system, the flash initiation heights broadened when the total flash rate underwent a two-fold increase. Since flashes are thought to originate between regions of opposite charge polarity, where the electric field is enhanced, the broadening of the initiation heights indicated more charge layers were present than a common tripole. However, they could not determine whether the increased flash rate added to the complexity of the charge structure or if the complicated charge structure yielded higher flash rates in that particular storm. Nonetheless, in supercells, where lightning flash rates have been observed to often exceed one flash per second (see Table 4.1), lightning could easily contribute to more complex charge structures.

As discussed in Section 4.3.1, during a storm's intense phase the IC:CG ratio becomes very high, or even infinite. After studying similar behavior in the Binger supercell, MacGorman et al. (1989) suggested that during intense periods the charge layers may be elevated to higher altitudes, increasing the separation distance of the negative charge from the ground. Observational studies by Marshall et al. (1995), Stolzenburg et al. 1998b-c), Lang and Rutledge (2002), and MacGorman et al. (2005), to name a few, support this notion as well. In particular, Stolzenburg et al. (1998c) showed that the altitude of the main negative charge layer increases with increasing updraft speed with a high level of correlation (0.94), and that the temperature of the main negative charge region decreases with increasing updraft speed, though the correlation is less profound (0.64). They also showed the main negative region was higher in supercell updrafts compared updrafts in mesoscale convective systems and ordinary New Mexico thunderstorms (Fig. 4.6). Ziegler and MacGorman (1994) also showed that the main negative and upper positive charge regions were elevated much higher in their simulation of the Binger supercell than in most non-severe storms. MacGorman et al. (2005) presented new observations that the lowest charge region in supercell updrafts was higher than had been documented in other storms, and they related the height of the lowest charge in the updraft to the height of 40 dBZ reflectivity above the weak-echo vault. They concluded that the height of the weak-echo vault may be more related to elevated charge than updraft speed itself, but they also conceded that updraft size and strength are key factors for producing WERs.

Occasionally, in really intense storms, a "lightning hole" feature in three-dimensional total lightning data has been observed (Krehbiel et al. 2000a, Goodman and

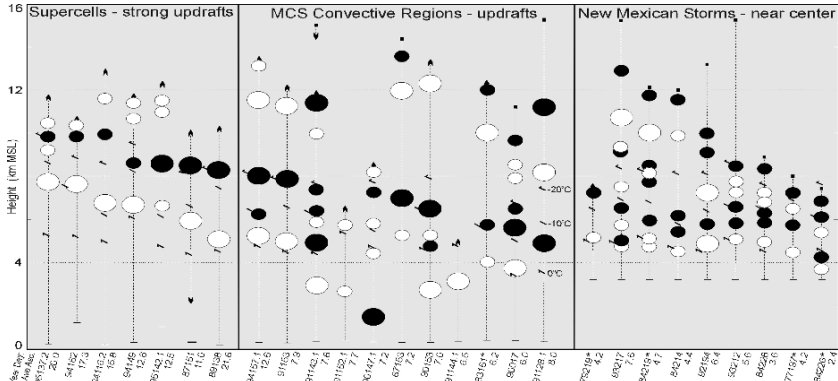


Fig. 4.6 Same as Fig. 4.5, except from convective updraft E soundings through three types of thunderstorms. With a few exceptions, still-air rise rates of the balloons are $5\text{--}6 \text{ m s}^{-1}$ after 1985 and $3\text{--}4 \text{ m s}^{-1}$ before 1985. Soundings identified with asterisks are from the published work of others (see Stolzenburg et al. 1998a and Stolzenburg et al. 1998b for references). (Reprinted with permission from Stolzenburg et al. 1998c)

Coauthors 2005, Wiens et al. 2005, Steiger et al. 2007, MacGorman et al. 2008). This feature is thought to result from an excessively strong updraft, similar to a BWER in radar reflectivity, which prevents non-inductive charging collisions and thus lightning. Wiens et al. (2005) observed lightning hole features coincident with BWERs in midlevel radar reflectivity in the 29 June 2000 STEPS supercell (Fig. 4.7), and Tessendorf et al. (2005) showed those BWERs were coincident with intense updrafts (Fig. 4.1). Wiens et al. (2005) also showed that lightning activity atop the lightning hole, coincident with the high reflectivity capping the BWER aloft, was very active. Nonetheless, observations by Steiger et al. (2007) (first shown by Murphy and Demetriades (2005) for the same storm) have shown that lightning holes are related to BWERs, but not necessarily always collocated with them. Rather, the lightning hole they observed was collocated with high radar reflectivity a few kilometers above the BWER, which if the high reflectivity is made up of graupel and hail undergoing wet growth, or even a small concentration of large hail, conditions unfavorable to non-inductive charging result (see section 4.2.2). Steiger et al. (2007) also showed that lightning holes were not evident in all supercells they studied, and thus are not a consistent feature of supercell storms. Nevertheless, it is becoming clear that lightning holes, like BWERs, are indicators of strong and broad updrafts. Clearly as more three-dimensional total lightning data becomes available, additional case studies on the conditions in which lightning holes form and their potential use as severe weather indicators are warranted.

4.4.1 Hypothesized Charge Structures for Positive CG Lightning

In Section 4.3.2, the tendency for supercells to produce anomalous positive cloud-to-ground lightning was introduced. Many recent studies have emerged addressing

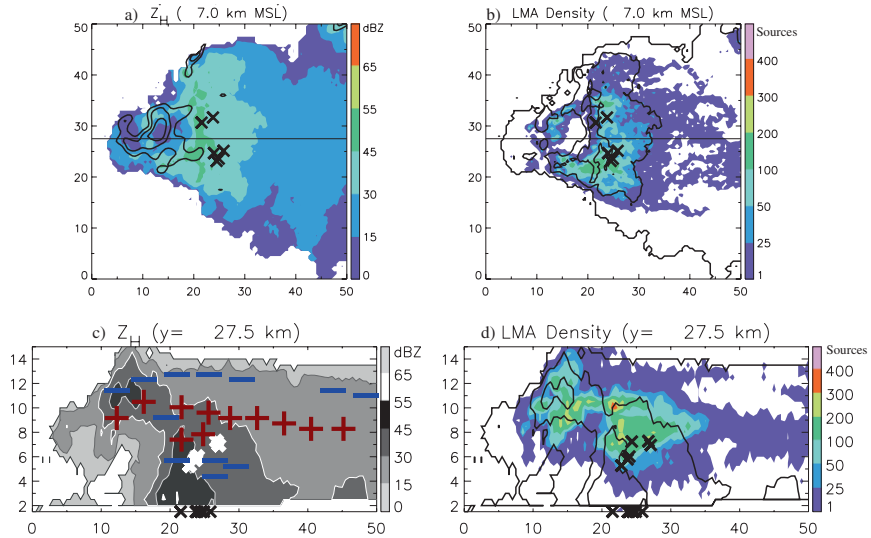


Fig. 4.7 Representative cross sections of the 29 June 2000 supercell at 2325 UTC. Horizontal cross sections of (a) radar reflectivity (Z_H) and (b) LMA source density at 7 km altitude. East–west vertical cross sections of the same quantities along the lines indicated in (a) and (b). LMA source density plots show the number of sources within 2.5 (5.0) km of each horizontal (vertical) cross section. Updraft contours every 10 m s^{-1} are overlaid as thin black lines in (a). Z_H contours are overlaid for reference in (b) and (d), with intervals of 0, 30, and 45 dBZ. The \times symbols overlaid on (a) and (b) and along the bottom of (c) and (d) indicate the NLDN strike locations of positive CG flashes. The \times symbols at higher altitudes on (c; white) and (d; black) indicate the LMA-inferred origin locations of positive CG flashes. Only those CG flashes that struck within 5 km of the cross-section plane are shown on the vertical cross sections in (c) and (d). LMA-inferred charge structure is overlaid in (c) as a composite schematic with red plus (blue minus) symbols for positive (negative) charge. (Adapted from Wiens et al. 2005) (See also Plate 3 in the Color Plate Section on page 594)

this issue and four primary hypotheses outlining the charge structure that could contribute to the positive CG flashes were summarized in Williams (2001).

The first hypothesis is typically referred to as the *tilted dipole* hypothesis (Brook et al. 1982) (Fig. 4.8a). In this situation, the upper positive charge region has been displaced laterally from the midlevel negative of the normal dipole structure by a tilted updraft and strong upper level winds. Positive CG strokes would then result from the transfer of positive charge over the distance from the upper positive charge layer to the ground. Support for this hypothesis comes from studies revealing strong wind shear in PPCG storms (Takeuti et al. 1978, Brook et al. 1982, Rust et al. 1985, Takeuti et al. 1985, Curran and Rust 1992, Levin et al. 1996). However, a study by Reap and MacGorman (1989) found no correlation between strong wind shear and storms with positive CG lightning, but instead found that positive CG lightning was common in storms with large hail. This hypothesis does not explain the lack of

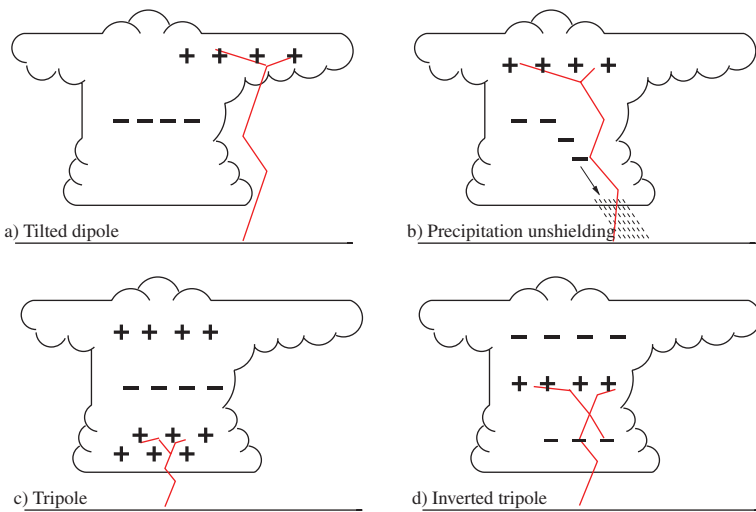


Fig. 4.8 Hypothesized charge structures that result in positive CG lightning, and illustrations of positive CG flashes originating in each structure. The (a) tilted dipole hypothesis, (b) precipitation unshielding mechanism, (c) tripole hypothesis, and (d) inverted tripole hypothesis

negative CG flashes observed at the time of PPCG activity, however, since the lower negative charge layer has not been altered from the traditional thunderstorm model.

A second hypothesis attempts to account for the reduction of negative CG flashes in predominantly positive CG storms. It has been referred to as the *precipitation unshielding* hypothesis (Fig. 4.8b). This hypothesis suggests that precipitation carries the negative charge out of the storm as it falls and “unshields” the upper positive charge layer (Carey and Rutledge 1998). The upper positive charge layer would then be more capable of producing a ground stroke. Support in favor of this hypothesis comes from observations of precipitation mass fluxes increasing prior to the onset of positive ground flashes (Carey and Rutledge 1998). This hypothesis, as well as the tilted dipole hypothesis, both presume that positive CG lightning emanates from the upper positive charge region of an otherwise normal charge structure.

The third hypothesis, generally called the *tripole* hypothesis, assumes that the lower positive charge found in an normal thunderstorm tripole is enhanced and can then dominate the midlevel negative charge region in the production of ground flashes (Fig. 4.8c). Both this hypothesis and the “unshielding” hypothesis seem to allow intracloud lightning to occur simultaneously with the positive ground flashes. More so, the intracloud lightning may “short-circuit” the negative ground flashes since the negative charge layer would be shared for both types of lightning (Williams 2001). This would further explain the reason for the lack of negative ground flashes observed in PPCG storms. This model does not recognize the involvement of the tripole’s lower positive charge layer in the production of negative CG flashes, however. Thus, if one accepts the tripole as the optimal charge structure for negative CG production, then this hypothesis is harder to accept as one for

positive CG flash production. Furthermore, a recent study presented observations of a thunderstorm exhibiting a normal charge structure and during the mature phase when the lower positive charge layer appeared deeper and more extensive, negative CG flashes diminished and IC flashes between the lower positive and midlevel negative layers were active, but no positive CG flashes resulted either (Tessendorf et al. 2007b). Thus, perhaps an enhanced lower charge region in the tripole could potentially reduce CG flash production. The conditions that lead to CG flash production, of either polarity, is certainly an area that warrants future study motivated by both a scientific and public lightning safety perspective.

The *inverted dipole* hypothesis proposes that the polarity of the normal thunderstorm dipole (depicted in Fig. 4.4) is reversed (illustrated in Fig. 4.8d as an inverted tripole) yielding a midlevel positive charge layer and upper level negative layer. In this hypothesis, the positive charge is now closer to the ground to initiate positive CG strokes (Seimon 1993). Williams (2001) stated that the weakness of this hypothesis was that field changes in the intracloud lightning would have the opposite polarity than that of the normal charge layer model, and this had not been observed. However, recent observations have shown that so-called inverted intracloud lightning does occur (Rust et al. 2005, Wiens et al. 2005, Tessendorf et al. 2007a, 2007b, Bruning et al. 2007, Weiss et al. 2008). Examples of inverted intracloud flashes are illustrated in Fig. 4.9 (flashes 1, 2, and 4). Furthermore, several studies have now also shown evidence of inverted charge structures and their relationship to positive CG lightning (Marshall et al. 1995, Krehbiel et al. 2000b, Rust and MacGorman 2002, MacGorman et al. 2005, Rust et al. 2005, Wiens et al. 2005, Weiss et al. 2008). These observations will be discussed in greater detail in the following section.

4.4.2 Observed Charge Structure in Positive CG Storms

An electric field balloon sounding through a severe thunderstorm near Dalhart, TX was one of the first observations to suggest that inverted charge structures might exist (Marshall et al. 1995). Further evidence in support of inverted charge structures in relation to positive CG lightning has recently come from measurements taken during the STEPS field campaign (Krehbiel et al. 2000b, Rust and MacGorman 2002, MacGorman et al. 2005, Rust et al. 2005, Wiens et al. 2005, Tessendorf et al. 2007a, 2007b, Weiss et al. 2008).

A well-studied example of a PPCG supercell was introduced in Section 4.2.2 (the STEPS 29 June 2000 supercell). The charge structure of this storm had a mid-level negative and lower positive charge region, much like the lowest two layers of the normal tripole, early in its evolution with IC flashes between these two (Wiens et al. 2005). No lightning occurred aloft to indicate the presence of an upper level positive charge region during its early evolution. After the storm's first surge in intensity, upper level charge regions were also observed, such that there were five charge layers that alternated in polarity with positive nearest the ground (Fig. 4.9). Near the time of the first two positive ground flashes, the charge structure became

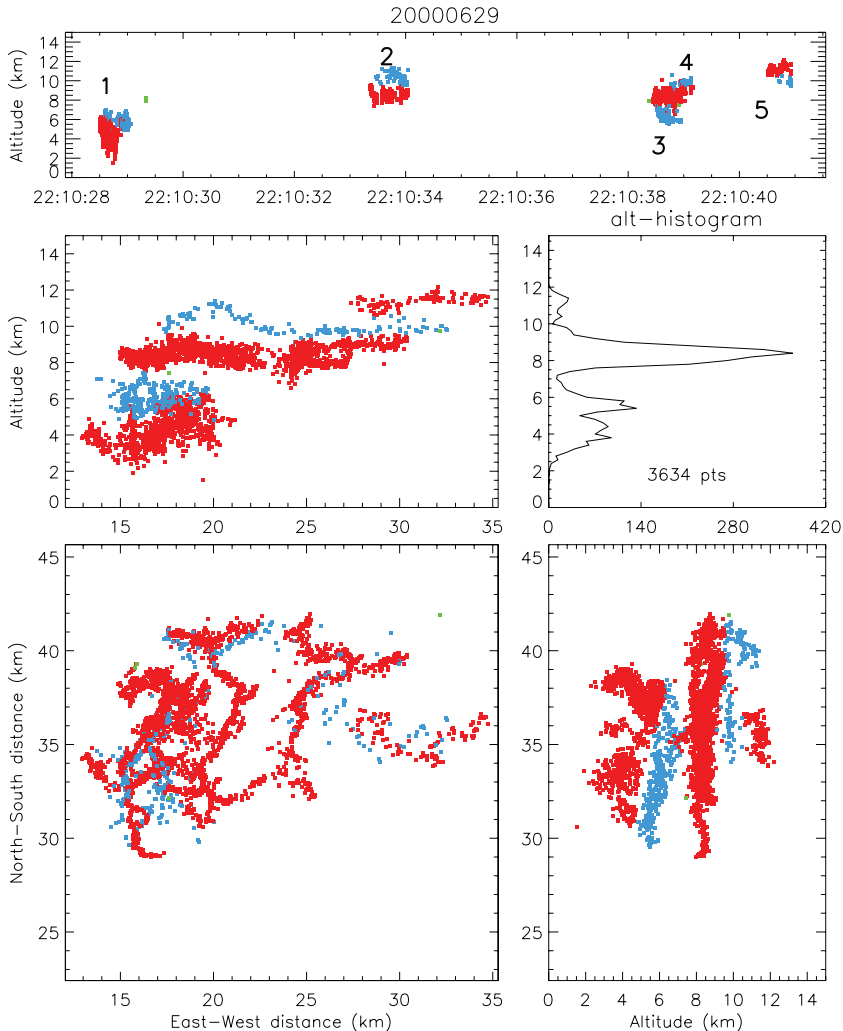


Fig. 4.9 Lightning mapping of five flashes showing five-layer charge structure at 2210 UTC 29 June 2000 from the New Mexico Tech Lightning Mapping Array (Rison et al. 1999). (*top*) Altitude versus time with a label for each flash. (*lower*) Three different spatial projections along with an altitude histogram of the number of sources. LMA sources are color-coded by inferred ambient charge region, with red for positive and blue for negative. Flashes 1, 2, and 4 are inverted flashes (negative over positive charge). Flashes 3 and 5 are normal flashes (positive over negative). (Reprinted with permission from Wiens et al. 2005)

more complex, but generally exhibited a mid-level positive region with negative charge regions above and below, thus an inverted tripole (Wiens et al. 2005). At the time of the dramatic storm intensification and onset of frequent PPCG lightning, the charge structure was even more complex, due to the frequent total lightning activity (flash rates exceeding 300 per minute), but the general inverted charge structure was

still evident with an inverted dipole in the updraft region, and a general inverted tripole sloping downward downwind of the updraft (MacGorman et al. 2005, Wiens et al. 2005). Wiens et al. (2005) also noted that the positive CG flashes all originated from between 5 and 9 km MSL altitude, which corresponded with the midlevel positive charge, and were typically clustered downwind of the main precipitation core below the mid-level positive and lower negative charge regions of the inverted tripole (Fig. 4.7). These results cast doubt that the tilted dipole and precipitation unshielding hypotheses are responsible for the PPCG lightning production since they suggested positive CG lightning emanates from the upper positive charge of a normal charge structure.

Results from both electrification models and observations also show that lower negative charge may be required for positive CGs (Mansell et al. 2002, Mansell et al. 2005, Tessendorf et al. 2007a, Weiss et al. 2008), much like the lower positive charge is for negative CGs (see Section 4.4.2). The 3rd June 2000 STEPS supercell presented in Tessendorf et al. (2007a) illustrated an inverted dipole charge structure and moderate IC flash activity, but no lower negative charge layer was ever detected as well as no CG lightning of either polarity. The authors speculated that the lack of the lower charge layer, which would have completed the inverted tripole (see Fig. 4.8d), may have prevented this supercell from producing (positive) CG lightning. On a related note, supercells that produce CG lightning in their anvils have been shown to have at least two opposite charge layers in the anvil. Kuhlman et al. (2008) showed negative CG lightning in the anvil of an inverted supercell and Tessendorf et al. (2007b) showed this for an inverted multicell storm. Both studies illustrated the negative CG flashes initiated in the anvil below upper level negative charge and above what may have been a horizontal extension of the midlevel positive charge region of the inverted charge structure, thus further emphasizing a lower layer of opposite polarity was involved in the CG flash. These observations of negative CG lightning from anvils contrast previous observations that anvil CGs usually were of positive polarity, as shown in Rust et al. (1981), although Bluestein and MacGorman (1998) presented observations of some negative CG anvil flashes in their study of tornadic Texas supercells. In conclusion, it is becoming more accepted that CG lightning, of either polarity and independent of strike location relative to the storm, requires a charge region of opposite polarity immediately below it for flash initiation.

These results from STEPS have provided considerable evidence that storms can have inverted charge structures, and that frequent positive CG lightning typically originates from the midlevel positive charge (above low level negative charge) of the inverted tripole structure (Fig. 4.8d). Supercells, such as the STEPS 29 June 2000 storm, also highlight how a storm may not clearly be inverted initially, but may evolve into a more inverted structure, perhaps as it intensifies. However, the 3 June 2000 LP supercell, also observed during STEPS (Tessendorf et al. 2007a), showed a clear inverted charge structure, but produced no CG lightning of either polarity and exhibited only moderate kinematic and electrical intensity. Thus, the conditions that cause a storm to become inverted are still unknown, but may be related to the processes outlined in Williams et al. (2005) and discussed in Sec-

tion 4.2.2 for PPCG storms. However, since not all inverted storms produce PPCG lightning (e.g. Tessendorf et al. 2007a) and observations of inverted supercells are still quite rare, more measurements of inverted storms are needed to fully understand the generation of this unique charge structure.

4.5 Summary

Supercells are clearly a complex class of thunderstorms, both from structural and microphysical perspectives. Though they exhibit great variability in their electrical behavior, they tend to be the extraordinary outlier on a spectrum of electrification intensity via several metrics (total flash rate, CG flash polarity, etc.). Our understanding of supercells has grown over recent decades with the availability of Doppler radar and the NLDN, nonetheless our understanding of lightning within this unique class of storms is still incomplete given that technology to measure total lightning in a three-dimensional manner has only recently become available, and only in limited areas. As three-dimensional lightning mapping ground-based networks become more widespread and satellites with the capability to measure total lightning flash rates are brought online, more information on lightning in supercells can be collected and analyzed. Studies to better understand the relationship of lightning behavior to severe weather will help enhance the warning decision-making process, and such studies are crucial to gaining the most benefit from the advancing lightning technologies. Features that have been documented to date, such as lightning holes and total flash rate jumps, require examination over a broader scale of storm types and locations to verify how they relate to severe weather and supercell evolution. Moreover, future studies need to analyze lightning data on shorter temporal scales than that of current radar volume scan times to get the most out of the higher temporal resolution in the total lightning data (Steiger et al. 2007).

The physical mechanisms that lead to CG flash production, of either polarity and regardless of storm type, are also still uncertain. Observational and numerical modeling results present evidence suggesting that the presence of a lower opposite charge region (lower positive charge for negative CGs and vice versa for positive CGs) may be required to initiate CG flashes, but we still do not fully understand why some storms produce many CGs while others produce so few. Additional studies utilizing three-dimensional charge structure data will help shed light on this area of uncertainty. Furthermore, we have now documented the existence of inverted charge structures and the tendency for them to be associated with positive CG lightning, but more measurements of inverted storms are still needed to better understand the environmental conditions and physical processes that lead to this atypical charge structure and its relation to CG flash polarity.

Acknowledgments Many thanks to Eric Bruning, Kristin Kuhlman, Nicole Lund, Walt Lyons, Don MacGorman, Scott Steiger, Maribeth Stolzenburg, and Kyle Wiens for sharing their expertise and for providing resources that greatly aided the preparation of this chapter.

References

- Bluestein, H.B., and C.R. Parks, 1983: A synoptic and photographic climatology of low-precipitation severe thunderstorms in the Southern Plains. *Mon. Wea. Rev.*, **111**, 2034–2046.
- Bluestein, H.B., and G.R. Woodall, 1990: Doppler-radar analysis of a low-precipitation severe storm. *Mon. Wea. Rev.*, **118**, 1640–1664.
- Bluestein, H.B., and D.R. MacGorman, 1998: Evolution of cloud-to-ground lightning characteristics and storm structure in the Spearman, Texas, tornadic supercells of 31 May 1990. *Mon. Wea. Rev.*, **126**, 1451–1467.
- Brundt, E. A., 1984: Vertical vorticity generation and mesocyclone sustenance in tornadic thunderstorms: The observational evidence. *Mon. Wea. Rev.*, **112**, 2253–2269.
- Branick, M.L., and C.A. Doswell, III, 1992: An observation of the relationship between supercell structure and lightning ground-strike polarity. *Wea. Forecasting*, **7**, 143–149.
- Brook, M., M. Nakano, P. Krehbiel, and T. Takeuti, 1982: The electrical structure of the Hokuriku winter thunderstorms. *J. Geophys. Res.*, **87**, 1207–1215.
- Brooks, I.M., and C.P.R. Saunders, 1994: An experimental investigation of the inductive mechanism of thunderstorm electrification. *J. Geophys. Res.*, **99**, 10,627–10,632.
- Browning, K.A., 1964: Airflow and precipitation trajectories within severe local storms which travel to the right of the winds. *J. Atmos. Sci.*, **21**, 634–639.
- Browning, K.A., 1965: Some inferences about the updraft within a severe local storm. *J. Atmos. Sci.*, **22**, 669–677.
- Browning K.A., 1977: The structure and mechanisms of hailstorms. *Hail: A Review of Hail Science and Hail Suppression*, G.B. Foote and C.A. Knight, Eds., *Meteor. Monogr.*, No. 38, Amer. Meteor. Soc., 1–43.
- Browning, K.A., and R.J. Donaldson, 1963: Airflow and structure of a tornadic storm. *J. Atmos. Sci.*, **20**, 533–545.
- Browning, K.A., and G.B. Foote, 1976: Airflow and hail growth in supercell storms and some implications for hail suppression. *Quart. J. Roy. Meteor. Soc.*, **102**, 499–533.
- Bruning, E.C., W.D. Rust, T.J. Shuur, D.R. MacGorman, P.R. Krehbiel, and W. Rison, 2007: Electrical and polarimetric radar observations of a multicell storm in TELEX. *Mon. Wea. Rev.*, **135**, 2525–2544.
- Buechler, D.E., K.T. Driscoll, S.J. Goodman, and H.J. Christian, 2000: Lightning activity within a tornadic thunderstorm observed by the Optical Transient Detector (OTD). *Geophys. Res. Lett.*, **27**, 2253–2256.
- Carey, L.D. and S.A. Rutledge, 1998: Electrical and multiparameter radar observations of a severe hailstorm. *J. Geophys. Res.*, **103**, 13,979–14,000.
- Carey, L.D., S.A. Rutledge, and W.A. Peterson, 2003a: The relationship between severe storm reports and cloud-to-ground lightning polarity in the contiguous United States from 1989–98. *Mon. Wea. Rev.*, **131**, 1211–1228.
- Carey, L.D., W.A. Petersen, and S.A. Rutledge, 2003b: Evolution of cloud-to-ground lightning and storm structure in the Spencer, South Dakota, tornadic supercell of 30 May 1998. *Mon. Wea. Rev.*, **131**, 1811–1831.
- Carey, L.D., and K.M. Buffalo, 2007: Environmental control of cloud-to-ground lightning polarity in severe storms. *Mon. Wea. Rev.*, **135**, 1327–1353.
- Chen, S.M., Y. Du, L.M. Fan, H.M. He, and D.Z. Zhong, 2002: A lightning location system in China: Its performance and applications. *IEEE Trans. Electromagn. Compat.*, **44**, 555–560.
- Cheze, J.-L., H. Sauvageot, 1997: Area-average rainfall and lightning activity. *J. Geophys. Res.*, **102**, 1707–1715.
- Chisholm, A.J., 1973: Alberta hailstorms, Part I: Radar case studies and airflow models, *Met. Mon.*, **14**, 1–36.
- Clarence, N.D., and D.J. Malan, 1957: Preliminary discharge processes in lightning discharges to ground. *Quart. J. Roy. Meteor. Soc.*, **83**, 161–172.

- Coleman, L.M., T.C. Marhsall, M. Stolzenburg, T. Hamlin, P.R. Krehbiel, W. Rison, and R.J. Thomas, 2003: Effects of charge and electrostatic potential on lightning propagation. *J. Geophys. Res.*, **108**, doi: 10.1029/2002JD002718.
- Cummins, K. L., M. J. Murphy, E. A. Bardo, W. L. Hiscox, R. B. Pyle, and A. E. Pifer, 1998: A combined TOA/MDF technology upgrade of the U.S. National Lightning Detection Network. *J. Geophys. Res.*, **103** (D8), 9035–9044.
- Curran, E.B., and W.D. Rust, 1992: Positive ground flashes produced by low-precipitation thunderstorms in Oklahoma on 26 April 1984. *Mon. Wea. Rev.*, **120**, 544–553.
- Defer, E., P. Blanchet, C. Thery, P. Laroche, J.E. Dye, M. Venticinque, and K. Cummins, 2001: Lightning activity for the July 10, 1996, storm during the Stratosphere-Troposphere Experiment: Radiation, Aerosol, and Ozone-A (STERAO-A) experiment. *J. Geophys. Res.*, **106**, 10,151–10,172.
- Demetriades N., M. J. Murphy, and K. L. Cummins, 2001: Cloud and cloud-to-ground lightning detection at LF and VHF: Early results from Global Atmospherics Dallas-Fort Worth LDAR II and IMPACT/ESP research networks. *Eos, Trans. Amer. Geophys. Union*, **82**, AE21A-07, (Fall Meeting Suppl.), Abstract.
- Dostalek J. F, J. F Weaver, and G. L Phillips, 2004: Aspects of a tornadic left-moving thunderstorm of 25 May 1999. *Wea. Forecasting*, **19**, 614–626.
- Doswell, C.A. III and D.W. Burgess, 1993: Tornadoes and tornadic storms: A review of conceptual models. *The Tornado: Its Structure, Dynamics, Prediction, and Hazards*. Church et al., Eds, *Geophys. Monogr.* No. 79, Amer. Geophys. Union, 161–172.
- Engholm, C.D., E.R. Williams, and R.M. Dole, 1990: Meteorological and electrical conditions associated with positive cloud-to-ground lightning. *Mon. Wea. Rev.*, **118**, 470–487.
- Fehr, T., N. Dotzek, and H. Holler, 2005: Comparison of lightning activity and radar-retrieved microphysical properties in EULINOX storms. *Atmos. Res.*, **76**, 167–189.
- Fujita, T.T., 1971: Proposed characterization of tornadoes and hurricanes by area and intensity. SMRP Res. Pap. 91, University of Chicago, 42 pp.
- Fuquay, D.M., 1982: Positive cloud-to-ground lightning in summer thunderstorms. *J. Geophys. Res.*, **87**, 7131–7140.
- Gilmore, M.S., and L.J. Wicker, 2002: Influences of the local environment on supercell cloud-to-ground lightning, radar characteristics, and severe weather on 2 June 1995. *Mon. Wea. Rev.*, **130**, 2349–2372.
- Goodman, S.J., and Coauthors, 2005: The North Alabama lightning mapping array: Recent severe storm observations and future prospects. *Atmos. Res.*, **76**, 423–437.
- Grasso L. D., and E. R. Hilgendorf, 2001: Observations of a severe left-moving thunderstorm. *Wea. Forecasting*, **16**, 500–511.
- Hammond G. R., 1967: Study of a left moving thunderstorm of 23 April 1964. ESSA Tech. Memo. IERTM-NSSL-31, Norman, OK, 75 pp.
- Helsdon, et al. 1992: An intracloud lightning parameterization scheme for a storm electrification model. *J. Geophys. Res.*, **97**, 5865–5884.
- Holle, R.L., and M.W. Maier, 1982: Radar echo height related to cloud-ground lightning in South Florida. Preprints, *12th Conf. on Severe Local Storms*, San Antonio, TX, Amer. Meteor. Soc., 330–333.
- Illingworth, A.J., 1985: Charge separation in thunderstorms: Small-scale processes. *J. Geophys. Res.*, **90**, 6026–6032.
- Jacobson, E.A., and E.P. Krider, 1976: Electrostatic field changes produced by Florida lightning. *J. Atmos. Sci.*, **33**, 103–117.
- Jayaratne, E.R., C.P.R. Saunders, and J. Hallett, 1983: Laboratory studies of the charging of soft hail during ice crystal interactions. *Quart. J. Roy. Meteor. Soc.*, **109**, 609–630.
- Kamra, A.K., and S.D. Pawar, 2007: Evolution of lightning in an isolated hailstorm of moderate size in the tropics. *J. Geophys. Res.*, **112**, doi:10.1029/2006JD007820.
- Keighton, S.J., H.B. Bluestein, and D.R. MacGorman, 1991: The evolution of a severe mesoscale convective system: cloud-to-ground lightning location and storm structure. *Mon. Wea. Rev.*, **119**, 1533–1556.

- Knapp, D.I., 1994: Using cloud-to-ground lightning data to identify tornadic thunderstorm signatures and nowcast severe weather. *Natl. Wea. Dig.*, **19**, 35–42.
- Knupp, K.R., S. Paech, and S. Goodman, 2003: Variations in cloud-to-ground lightning characteristics among three adjacent tornadic supercell storms over the Tennessee Valley region. *Mon. Wea. Rev.*, **131**, 172–188.
- Krehbiel, P.R., 1986: The electrical structure of thunderstorms. *The Earth's Electrical Environment*, National Academy Press, Washington, D.C., 90–113.
- Krehbiel, P.R., R.J. Thomas, W. Rison, T. Hamlin, J. Harlin, and M. Davis, 2000a: GPS-based mapping system reveals lightning inside storms. *Eos, Trans. Amer. Geophys. Union*, **81**, 21–25.
- Krehbiel, P.R., R.J. Thomas, W. Rison, T. Hamlin, J. Harlin, M. Stanley, J. Lombardo, and D. Shown, 2000b: Inverted polarity lightning in STEPS. *Eos, Trans. Amer. Geophys. Union*, **81** (Suppl.), Abstract A62D-06.
- Kuhlman K. M., C. L. Ziegler, E. R. Mansell, D. R. MacGorman, and J. M. Straka, 2006: Numerical simulations of the 29 June 2000 STEPS supercell: Microphysics, electrification, and lightning. *Mon. Wea. Rev.*, **134**, 2734–2757.
- Kuhlman, K.M., D.R. MacGorman, M.I. Biggerstaff, and P.R. Krehbiel, 2008: Lightning initiation in the anvil of supercell storms. *Geophys. Res. Lett.*, in press.
- Lang, T.J., and S.A. Rutledge, 2002: Relationships between convective storm kinematics, precipitation, and lightning. *Mon. Wea. Rev.*, **130**, 2492–2506.
- Lang, T.J., S.A. Rutledge, J.E. Dye, M. Venticinque, P. Laroche, and E. Defer, 2000: Anomalously Low Negative Cloud-to-Ground Lightning Flash Rates in Intense Convective Storms Observed during STERAO-A. *Mon. Wea. Rev.*, **128**, 160–173.
- Lang, T.J., S.A. Rutledge, and K.C. Wiens, 2004a: Origins of positive cloud-to-ground lightning flashes in the stratiform region of a mesoscale convective system. *Geophys. Res. Lett.*, **31**, doi: 10.1029/2004GL109823.
- Lang, T.J., and Coauthors, 2004b: The Severe Thunderstorm Electrification and Precipitation Study. *Bull. Amer. Meteor. Soc.*, **85**, 1107–1125.
- Laroche, P., A. Bondiou, P. Blanchet, J. Pigere, M. Weber, and B. Boldi, 1994: 3D mapping of lightning discharge within storms. ONERA Publ. 1994–186, 11 pp.
- Lemon, L.R., 1980: Severe thunderstorm radar identification techniques and warning criteria: A preliminary report. NOAA Tech. Memo. NWS NSSFC-1, 60 pp. [NTIS PB273049]
- Lemon, L.R., and C.A. Doswell III, 1979: Severe thunderstorm evolution and mesocyclone structure as related to tornadogenesis. *Mon. Wea. Rev.*, **107**, 1184–1197.
- Levin, Z., Y. Yair, and B. Ziv, 1996: Positive cloud-to-ground flashes and wind shear in Tel-Aviv thunderstorms. *Geophys. Res. Lett.*, **23**, 2231–2234.
- Lindsey, D.T., and M.J. Bunkers, 2005: Observations of a severe, left-moving supercell on 4 May 2003. *Wea. Forecasting*, **20**, 15–22.
- Lopez, R., and J.-P. Aubagnac, 1997: The lightning activity of a hailstorm as a function of changes in its microphysical characteristics inferred from polarimetric radar observations. *J. Geophys. Res.*, **102**, 16,799–16,813.
- Lyons, W.A., T.E. Nelson, E.R. Williams, J. Cramer, and T. Turner, 1998: Enhanced positive cloud-to-ground lightning in thunderstorms ingesting smoke. *Science*, **282**, 77–81.
- Lyons, W.A., T.E. Nelson, R.A. Armstrong, V.P. Pasko, and M. Stanley, 2003: Upward electrical discharges from the tops of thunderstorms. *Bull. Amer. Meteor. Soc.*, **84**, 445–454.
- Lyons, W.A., S.A. Cummer, M.A. Stanley, G.R. Huffines, K.C. Wiens, and T.E. Nelson, 2008a: Supercells and sprites. *Bull. Amer. Meteor. Soc.*, in press.
- Lyons, W.A., M.A. Stanley, J.D. Meyer, T.E. Nelson, S.A. Rutledge, T.L. Lang, and S.A. Cummer, 2008b: The meteorological and electrical structure of TLE-producing convective systems. (this volume).
- MacGorman, D.R., 1993: Lightning in tornadic storms: A review. *The Tornado: Its Structure, Dynamics, Prediction, and Hazards*. Church et al., Eds, *Geophys. Monogr.* No. 79, Amer. Geophys. Union, 173–182.
- MacGorman, D.R., and K.E. Nielson, 1991: Cloud-to-ground lightning in a tornadic storm on 8 May 1986. *Mon. Wea. Rev.*, **119**, 1557–1574.

- MacGorman, D.R., and D.W. Burgess, 1994: Positive cloud-to-ground lightning in tornadic storms and hailstorms. *Mon. Wea. Rev.*, **122**, 1671–1697.
- MacGorman, D.R., D.W. Burgess, V. Mazur, W.D. Rust, W.L. Taylor, and B.C. Johnson, 1989: Lightning rates relative to tornadic storm evolution on 22 May 1981. *J. Atmos. Sci.*, **46**, 221–250.
- MacGorman, D.R., W.D. Rust, P. Krehbiel, W. Rison, E. Bruning, and K. Wiens, 2005: The electrical structure of two supercell storms during STEPS. *Mon. Wea. Rev.*, **133**, 2583–2607.
- MacGorman, and Coauthors, 2008: TELEX The Thunderstorm Electrification and Lightning Experiment. *Bull. Amer. Meteor. Soc.*, **89**, 997–1013.
- Mach, D.M., D.R. MacGorman, L.W.D. Rust, and R.T. Arnold, 1986: Site errors and detection efficiency in a magnetic direction-finder network for locating lightning strikes to ground. *J. Atmos. And Oceanic Tech.*, **3**, 67–74.
- Mansell, E.R., D.R. MacGorman, C.L. Ziegler, and J.M. Straka, 2002: Simulated three-dimensional branched lightning in a numerical thunderstorm model. *J. Geophys. Res.*, **107**, doi: 10.1029/2000JD000244.
- Mansell, E.R., D.R. MacGorman, C.L. Ziegler, and J.M. Straka, 2005: Charge structure and lightning sensitivity in a simulated multicell thunderstorm. *J. Geophys. Res.*, **110**, doi: 10.1029/2004JD005287.
- Marshall, T.C., and W.P. Winn, 1982: Measurements of charged precipitation in a New Mexico thunderstorm: Lower positive charge centers. *J. Geophys. Res.*, **87**, 7141–7157.
- Marshall, T.C., and W.D. Rust, 1991: Electric field soundings through thunderstorms. *J. Geophys. Res.*, **96**, 22,297–22,306.
- Marshall, T.C., W.D. Rust, and M. Stolzenburg, 1995: Electrical structure and updraft speeds in thunderstorms over the southern Great Plains. *J. Geophys. Res.*, **100**, 1001–1015.
- Marwitz, J.D., 1972a: The structure and motion of severe hailstorms. Part I: Supercell storms. *J. Appl. Meteor.*, **11**, 166–179.
- Marwitz, J.D., 1972b: The structure and motion of severe hailstorms. Part II: Multicell storms. *Ibid.*, **11**, 180–188.
- Mazur, V., E. Williams, R. Boldi, L. Maier, and D. E. Proctor, 1997: Initial comparison of lightning mapping with operational Time-Of-Arrival and Interferometric systems, *J. Geophys. Res.*, **102**, 11,071–11,085.
- McCaul, E.W., Jr., D.E. Buechler, S. Hodanish, and S.J. Goodman, 2002: The Alamena, Kansas, tornadic storm of 3 June 1999: A long-lived supercell with very little cloud-to-ground lightning. *Mon. Wea. Rev.*, **130**, 407–415.
- Moller, A.R., C.A. Doswell III, and R. Przybylinski, 1990: High-precipitation supercells: A conceptual model and documentation. Preprints, *16th Conf. on Severe Local Storms*, Kananaskis Park, Alberta, Canada, Amer. Meteor. Soc., 52–57.
- Moller, A.R., C.A. Doswell III, M.P. Foster, and G.R. Woodall, 1994: The operational recognition of supercell thunderstorm environments and storm structures. *Wea. Forecasting*, **9**, 327–347.
- Murphy, M.J., and N.W.S. Demetriadis, 2005: An analysis of lightning holes in a DFW supercell storm using total lightning and radar information. *Extended Abstracts, Conf. on Meteorological Applications of Lightning Data, San Diego*, CA, Amer. Meteor. Soc., CD-ROM, 2.3.
- Murray, N., R. Orville, and G. Huffines, 2000: Effect of pollution from Central American fires on cloud-to-ground lightning in May 1998. *Geophys. Res. Lett.*, **28**, 2597–2600.
- Nelson, S.P., 1983: The influence of storm flow structure on hail growth. *J. Atmos. Sci.*, **40**, 1965–1983.
- Nelson, S.P., 1987: The hybrid multicellular-supercellular storm—an efficient hail producer. Part II: General characteristics and implications for hail growth. *J. Atmos. Sci.*, **44**, 2060–2073.
- Nelson, S.P. and N. C. Knight, 1987: The hybrid multicellular-supercellular storm—an efficient hail producer. Part I: An archetypal example. *J. Atmos. Sci.*, **44**, 1942–1959.
- Nielsen, K., R. Maddox, and S. Vasiloff, 1994: The evolution of cloud-to-ground lightning within a portion of the 10–11 June 1985 squall line. *Mon. Wea. Rev.*, **122**, 1809–1817.

- Nielsen-Gammon J. W., and W. L. Read, 1995: Detection and interpretation of left-moving severe thunderstorms using the WSR-88D: A case study. *Wea. Forecasting*, **10**, 127–140.
- Orville, R.E., and G.R. Huffines, 2001: Cloud-to-ground lightning in the United States: NLDN results in the first decade, 1989–98. *Mon. Wea. Rev.*, **129**, 1179–1193.
- Orville, R.E., R.W. Henderson, and L.F. Bosart, 1983: An east coast lightning detection network. *Bull. Amer. Meteor. Soc.*, **64**, 1029–1059.
- Perez, A.H., R.E. Orville, and L.J. Wicker, 1995: Characteristics of cloud-to-ground lightning associated with violent-tornado producing supercells. Preprints, *14th Conf. on Weather and Forecasting*, Dallas, TX, Amer. Meteor. Soc., 409–413.
- Perez, A.H., L.J. Wicker, and R.E. Orville, 1997: Characteristics of cloud-to-ground lightning associated with violent tornadoes. *Wea. Forecasting*, **12**, 428–437.
- Pierce, E.T., 1955: The development of lightning discharges. *Quart. J. Roy. Meteor. Soc.*, **81**, 229–240.
- Pinto, O., Jr., K.P. Naccarato, I.R.C.A. Pinto, W.A. Fernandes, and O.Pinto Neto, 2006: Monthly distribution of cloud-to-ground lightning flashes as observed by lightning location systems. *Geophys. Res. Lett.*, **33**, doi:10.1029/2006GL026081.
- Ray P. S., D. R. MacGorman, W. D. Rust, W. L. Taylor, and L. W. Rasmussen, 1987: Lightning location relative to storm structure in a supercell storm and a multicell storm. *J. Geophys. Res.*, **92**, 5713–5724.
- Reap, R. M., and D. R. MacGorman, 1989: Cloud-to-ground lightning: Climatological characteristics and relationships to model fields, radar observations, and severe local storms. *Mon. Wea. Rev.*, **117**, 518–535.
- Reynolds, S.E., M. Brook, and M.F. Gourley, 1957: Thunderstorm charge separation. *J. Meteor.*, **14**, 426–436.
- Rison, W., R. J. Thomas, P. R. Krehbiel, T. Hamlin, and J. Harlin, 1999: A GPS-based three-dimensional lightning mapping system: Initial observations in Central New Mexico. *Geophys. Res. Lett.*, **26**, 3573–3576.
- Rust, W.D., and D.R. MacGorman, 2002: Possibly inverted-polarity electrical structures in thunderstorms during STEPS. *Geophys. Res. Lett.*, **29**, doi: 10.1029/2001GL014303.
- Rust, W.D., D.R. MacGorman, and R.T. Arnold, 1981: Positive cloud-to-ground lightning flashes in severe storms. *Geophys. Res. Lett.*, **8**, 791–794.
- Rust, W.D., D.R. MacGorman, and S.J. Goodman, 1985: Unusual positive cloud-to-ground lightning in Oklahoma storms on 13 May 1983. Preprints, *14th Conf. Severe Local Storms*, Indianapolis, Amer. Meteor. Soc., 372–375.
- Rust, W.D. et al., 2005: Inverted-polarity electrical structures in thunderstorms in the Severe Thunderstorm Electrification and Precipitation Study. *Atmos. Res.*, **76**, 247–271.
- Rutledge, S.A., and D.R. MacGorman, 1988: Cloud-to-ground lightning activity in the 10–11 June 1985 mesoscale convective system observed during the Oklahoma-Kansas PRE-STORM project. *Mon. Wea. Rev.*, **116**, 1393–1408.
- Rutledge, S.A. C. Lu, and D.R. MacGorman, 1990: Positive cloud-to-ground lightning in mesoscale convective systems. *J. Atmos. Sci.*, **47**, 2085–2100.
- Rutledge, S.A., E.R. Williams, and T.D. Keenan, 1992: The Down Under Doppler and Electricity Experiment (DUNDEE): Overview and preliminary results. *Bull. Amer. Meteor. Soc.*, **73**, 3–16.
- Saunders, C.P.R., 1994: Thunderstorm electrification laboratory experiments and charging mechanisms. *J. Geophys. Res.*, **99**, 10,773–10,779.
- Saunders, C.P.R., and I.M. Brooks, 1992: The effects of high liquid water content on thunderstorm charging. *J. Geophys. Res.*, **97**, 14671–14676.
- Saunders, C.P.R., W.D. Keith, and R.P. Mitzeva, 1991: The effect of liquid water on thunderstorm charging. *J. Geophys. Res.*, **96**, 11,007–11,017.
- Saunders, C.P.R., H. Bax-norman, C. Emersic, E.E. Avila, and N.E. Castellano, 2006: Laboratory studies of the effect of cloud conditions on graupel/crystal charge transfer in thunderstorm electrification. *Quart. J. Roy. Meteor. Soc.*, **132**, 2653–2673.

- Schlatter P.T., Schlatter T.W., and Knight C.A., 2008: An unusual hailstorm on 24 June 2006, Boulder, Colorado. Part I: Mesoscale setting and radar features. *Mon. Wea. Rev.*, in press.
- Schulz, W., K. Cummins, G. Diendorfer, and M. Dorninger, 2005: Cloud-to-ground lightning in Austria: A 10-year study using data from a lightning location system. *J. Geophys. Res.*, **110**, doi:10.1029/2004JD005332.
- Seimon, A., 1993: Anomalous cloud-to-ground lightning in an F5-tornado-producing supercell thunderstorm on 28 August 1990. *Bull. Amer. Meteor. Soc.*, **74**, 189–203.
- Shafer, M.A., D.R. MacGorman, and F.H. Carr, 2000: Cloud-to-ground lightning throughout the lifetime of a severe storm system in Oklahoma. *Mon. Wea. Rev.*, **128**, 1798–1816.
- Simpson, G.C., and F.J. Scrase: 1937: The distribution of electricity in thunderclouds. *Proc. Roy. Soc. London, Ser. A*, **161**, 309–352.
- Solomon, R., and M. B. Baker, 1998: Lightning flash rate and type in convective storms. *J. Geophys. Res.*, **103**, 14,041–14,057.
- Sonnadara, U., V. Cooray, and T. Gotschl, 2006: Characteristics of cloud-to-ground lightning flashes over Sweden. *Phys. Scr.*, **74**, 541–548.
- Soula, S., H. Sauvageot, G. Molinié, F. Mesnard, and S. Chauzy, 1998: The CG lightning activity of a storm causing a flash-flood. *Geophys. Res. Lett.*, **25**, 1181–1184.
- Soriano, L.R., F. de Pablo, and C. Tomas, 2005: Ten-year study of cloud-to-ground lightning activity in the Iberian Peninsula. *J. Atmos. Terr. Phys.*, **67**, 1632–1639.
- Steiger, S.M., R.E. Orville, and L.D. Carey, 2007: Total lightning signatures of thunderstorm intensity over North Texas. Part I: Supercells. *Mon. Wea. Rev.*, **135**, 3281–3302.
- Smith, S. B., J. G. LaDue, and D. R. MacGorman, 2000: The relationship between cloud-to-ground lightning polarity and surface equivalent potential temperature during three tornadic outbreaks. *Mon. Wea. Rev.*, **128**, 3320–3328.
- Stolzenburg, M., 1994: Observations of high ground flash densities of positive lightning in summertime thunderstorms. *Mon. Wea. Rev.*, **122**, 1740–1750.
- Stolzenburg M., W. D. Rust, B. F. Smull, and T. C. Marshall, 1998a: Electrical structure in thunderstorm convective regions, 1. Mesoscale convective systems. *J. Geophys. Res.*, **103**, 14059–14078.
- Stolzenburg, M., W.D. Rust, and T.C. Marshall, 1998b: Electrical structure in thunderstorm convective regions 2. Isolated storms, *J. Geophys. Res.*, **103**, 14,079–14,096.
- Stolzenburg, M., W.D. Rust, and T.C. Marshall, 1998c: Electrical structure in thunderstorm convective regions 3. Synthesis. *J. Geophys. Res.*, **103**, 14,097–14,108.
- Stolzenburg, M., and T.C. Marshall, 2008: Electric field and charge structure in lightning-producing clouds. (this volume).
- Takahashi, T., 1978: Riming electrification as a charge generation mechanism in thunderstorms. *J. Atmos. Sci.*, **35**, 1536–1548.
- Takeuti, T., M. Nakano, M. Brook, D.J. Raymond, and P. Krehbiel, 1978: The anomalous winter thunderstorms of the Hokuriku coast. *J. Geophys. Res.*, **83**, 2385–2394.
- Takeuti, T., A.-I. Kawasaki, K. Funaki, N. Kitagawa, and J. Huse, 1985: On the thundercloud producing the positive ground flashes. *J. Meteor. Soc. Japan*, **63**, 354–357.
- Tessendorf, S.A., L.J. Miller, K.C. Wiens, and S.A. Rutledge, 2005: The 29 June 2000 supercell observed during STEPS. Part I: Kinematics and microphysics. *J. Atmos. Sci.*, **62**, 4127–4150.
- Tessendorf, S.A., K.C. Wiens, and S.A. Rutledge, 2007a: Radar and lightning observations of the 3 June 2000 electrically inverted storm from STEPS. *Mon. Wea. Rev.*, **135**, 3665–3681.
- Tessendorf, S.A., S.A. Rutledge, and K.C. Wiens, 2007b: Radar and lightning observations of normal and inverted polarity multicellular storms from STEPS. *Mon. Wea. Rev.*, **135**, 3682–3706.
- Tourte, J.L., F. Hellocq, M. Le Boulch, and J. Hamelin, 1988: First results obtained with the Meteorage thunderstorm monitoring system. *Proc. 8th Conf. on Atmos. Elec.*, 697–702.
- Weisman, M.L., and J.B. Klemp, 1984: The structure and classification of numerically simulated convective storms in directionally-varying wind shears. *Mon. Wea. Rev.*, **112**, 2479–2498.

- Weiss, S.A., W.D. Rust, D.R. MacGorman, E.C. Bruning, and P.R. Krehbiel, 2008: Evolving complex electrical structures of the STEPS 25 June 2000 multicell storm. *Mon. Wea. Rev.*, **136**, 741–756.
- Wiens, K.C., S.A. Rutledge, and S.A. Tessendorf, 2005: The 29 June 2000 supercell observed during STEPS. Part II: Lightning and charge structure. *J. Atmos. Sci.*, **62**, 4151–4177.
- Williams, E.R., 1989: The tripole structure of thunderstorms. *J. Geophys. Res.*, **94**, 13,151–13,167.
- Williams, E.R., 2001: The electrification of severe storms. *Severe Convective Storms*, C.A. Doswell, III, Ed., *Meteor. Monogr.*, No. 50, Amer. Meteor. Soc., 527–561.
- Williams, E.R., C.M. Cooke, and K.A. Wright, 1985: Electrical discharge propagation in and around space charge clouds. *J. Geophys. Res.*, **90**, 6059–6070.
- Williams, E.R., M.E. Weber, and R.E. Orville, 1989: The relationship between lightning type and convective state of thunderclouds. *J. Geophys. Res.*, **94**, 13,213–13,220.
- Williams, E.R., et al., 1999: The behavior of total lightning activity in severe Florida thunderstorms. *Atmos. Res.*, **51**, 245–265.
- Williams, E.R., V. Mushtak, D. Rosenfeld, S. Goodman, and D. Boccippio, 2005: Thermodynamic conditions favorable to superlative thunderstorm updraft, mixed phase microphysics, and lightning flash rate. *Atmos. Res.*, **76**, 288–306.
- Ziegler, C. L., D. R. MacGorman, J. E. Dye, and P. S. Ray, 1991: A model evaluation of non-inductive graupel-ice charging in the early electrification of a mountain thunderstorm. *J. Geophys. Res.*, **96**, 12833–12855.
- Ziegler, C.L., and D.R. MacGorman, 1994: Observed lightning morphology relative to modeled space charge and electric field distributions in a tornadic storm. *J. Atmos. Sci.*, **51**, 833–851.

Chapter 5

LINET – An International VLF/LF Lightning Detection Network in Europe

Hans D. Betz, Kersten Schmidt and Wolf P. Oettinger

Abstract During the past years a lightning detection network (LINET) was developed at the University of Munich, which utilizes the low-frequency range (VLF/LF). It is steadily expanded and presently comprises about 90 sensors in 17 countries, covering an area from longitude 10° W–35° E to latitude 30° N–65° N. The network is serviced and continuously operated by nowcast GmbH, the official provider of lightning data for the German Weather Service, and offers real-time and historic data for many national and international scientific projects. LINET presents numerous options for users of lightning data, because it detects small signal amplitudes and, thus, is sensitive not only to weak cloud-to-ground strokes (CG) but also to cloud lightning (IC). The number of located IC discharges is large enough to attribute ‘total-lightning’-quality to the network, otherwise accessible only by additional implementation of VHF technologies. Discrimination of CG from IC is achieved by means of a new 3D time-of-arrival (TOA) method, applicable within the sufficiently dense parts of the network. IC emission heights are extracted for each cloud event, which are thought to reflect the central region of the involved lightning channel. Position accuracy of strokes reaches an average value as small as \sim 150 m, provided that corrections for site-errors and propagation effects have been carried out. Important for many applications is the narrow distribution of errors around the mean, i.e. false locations (‘outliers’) rarely occur, enhancing the efficiency of cell-tracking and other nowcasting applications of lightning data. During international co-operations in scientific campaigns directed by DLR (Deutsches Zentrum für Luft- und Raumfahrt), a smaller version of LINET has been deployed and tested in four continents, Europe, South America, Australia, and Central Africa. In order to examine the achieved features in some detail lightning data have been compared between LINET and many national and global networks.

Keywords Lightning detection · Lightning location · VLF/LF measurements · Total-lightning · Cloud lightning · Cell-tracking · Severe weather

H.D. Betz (✉)

University of Munich, Faculty of Physics, 85748 Garching, Germany
e-mail: hans-dieter.betz@physik.uni-muenchen.de

5.1 Introduction

Lightning detection with automated networks has reached a high standard and is applied in numerous countries around the world. Prominent examples in the U.S. are regional VLF/LF arrays for CG detection (Shao et al., 2006; see also Hamlin et al., this volume) and VHF systems for IC mapping (Thomas et al., 2004; see also Lojou et al., this volume). The largest network is the commercially operated NLDN (National Lightning Detection Network, Orville et al., 2002) with a VLF/LF sensor technology that is in use for CG reporting in many other national networks. Extensive lightning research has been performed for several decades, yet many important questions remain open that concern both theoretical understanding and practical applications. Examples are the lightning initiation process, cloud charge distributions, mechanisms for cloud discharges, real total number of IC discharges and CG strokes (i.e. the identification of events in its entirety that represent the 100%-level), damage potential of very weak CG strokes, and effective nowcasting of severe thunderstorms. Data from LINET is sufficiently comprehensive and detailed to allow elucidation of some of the unresolved issues.

At the University of Munich the sferics research group began development of VLF/LF-sensors for lightning detection in 1994 and operated a number of successively improved networks in steadily larger areas. A major goal was to achieve high detection efficiency especially for low-amplitude strokes in order to provide meteorologically useful data for early recognition of thunderstorms. As a surprise, the chosen design allowed detection and location of so many cloud strokes that it is justified to attribute a new type of ‘total-lightning’ feature to the VLF/LF network (Betz et al., 2004), different from the previously used method for IC detection. It was not the mere occurrence of IC events in VLF/LF records – well known in the literature (Shao and Krehbiel, 1996) – but its frequent appearance that allows a novel and relatively simple yet highly effective method for ‘total-lightning’ detection, based solely on VLF/LF measurements. This finding raises the question why so many distinct cloud events have escaped attention in the past, and calls for a better understanding of cloud lightning, an undertaking still in progress (Loboda et al., 2008) and producing new insight into lightning initiation and cloud discharge processes (Section 5.6). Concurrent recording of IC and CG requires discrimination of the two types of lightning; since traditional wave-form criteria turned out not to be as reliable as initially expected (Cummins et al., 1998; Orville et al., 2002; Krider et al., 2006; Nag and Rakov, 2008), an independent alternative has been worked out that relies on a three dimensional time-of-arrival (TOA) analysis (Betz et al., 2004). With these new features and its enduring availability – the entire network is continuously operated and maintained by nowcast GmbH, the official provider of lightning data to the German Weather Service –, LINET represents an additional meteorological data source that can be useful for a variety of research goals in atmospheric electricity. In the present contribution, the most prominent features of LINET are described and critically examined; wherever possible, comparisons with other data sources are utilized to better assess the characteristics of the lightning data. Particular emphasis will be given to the detection of low-amplitude signals and cloud

lightning, locating accuracy, and recognition of storm cells for nowcasting purposes. Since lightning discharges produce inherently both CG and IC pulses that are often quite similar, VLF/LF cloud records will be termed “IC-strokes”, not to be confused with CG return strokes. A more detailed argumentation for this notation is given in Section 5.5.

5.2 Network Design

LINET was designed to achieve high performance standards by means of an easy-to-handle and economic 4-part modular design, employing up-to-date technology in all components. Module 1 consists of two crossed loops that serve as passive sensor for magnetic field components without making use of any active electronics; therefore, no power supply or preamplifier is needed. Two sensor loops oriented orthogonal to each other measure the components $B_x(t)$ and $B_y(t)$ of the magnetic flux directly as a function of time in the frequency range of interest (~ 1 to 200 kHz), without the need for subsequent integration. This feature is helpful for the treatment of small signals close to the noise level and is achieved – in full compliance with the basic induction law – by measuring the induced current rather than the induced voltage, whereby the antenna circuit parameters have to be appropriately dimensioned. Signal timing is achieved by means of a GPS clock with an accuracy of better than 100 ns (module 2). Special and partly sophisticated measures are taken to transport this level of basic accuracy as far as possible to the actual event timing. Signal amplification, filtering, AD-conversion and data processing are performed with a single plug-in device (module 3) in a separately positioned processing unit (module 4).

The sampling rate was set to 1 MHz and incoming signals are recorded with 14 -bit resolution in a continuous mode. Triggered events are transferred to and processed in a parallel circuit so that no data loss occurs and no allowance for rearm time must be provided (zero dead-time). A pre-trigger time of $100\ \mu s$ is chosen and, somewhat arbitrarily, a window of standard length $512\ \mu s$ is inspected for occurrence of a lightning pulse, i.e. no more than 1 event is searched within this time period. Overlap of different signals within this time span is rare and will be disentangled by future software-developments. More frequently, certain IC pulses last longer than $512\ \mu s$ and justify assignment of a single IC-stroke. In order to discriminate signals of technical origin a fast Fourier analysis is performed and pulses with spectra far from the range of acceptable patterns are eliminated. Depending on the sensor site several types of technical noise may show up which display a signature similar to the one of true lightning pulses and cannot be sorted out at once; these false signals are eliminated by time coincidence considerations in the central processing software. As regards signal rates, each time window containing pulses above threshold can be handled, possibly utilizing a FIFO buffer in case of overload, but usually a rate of about $100\ s^{-1}$ suffices, even during storms observed with LINET in central Africa.

All signals are treated irrespective of their waveform; notably, IC-CG discrimination is performed not by means of finding shape differences between IC and

CG signals, but by a specially adopted 3D-algorithm in the central processing unit. For research purposes, the complete data sets including the waveforms are stored locally and transmitted on demand for later inspection, if desired. Each sensor collects data and transmits packets of condensed information to the central station at Munich. Depending on the type of chosen line-connection, typically via Internet, this transmission can take place immediately after completion of an individual signal analysis, or within a pre-selected time span for a group of signals accumulated within this interval. Due to transmission line bandwidth the transfer is sometimes limited to some 100 signals/s; though this capacity is usually sufficient, a buffer is provided for handling delayed transmission in case of temporary overload. At the operational centre all software modules and functional parameters for the stations can be controlled and set remotely, including programming of an FPGA in module 3. These options are vital for control of the operational network status and the quality of both raw data and the final output. Incoming data is duplicated for further handling, immediate locating is performed, and results are transferred to servers for distribution, storage and availability for secondary off-line jobs.

While smaller versions of LINET have produced real-time data for more than 10 years, especially in southern Germany, the international European network started operation on 01 May 2006 and presently comprises some 90 sensors (Fig. 5.1); in southern Germany the sensor density is relatively large because of continued research with respect to extremely weak lightning signals and other open issues. Otherwise, the concept aims at a baseline of 200–250 km in order to enable 3D discrimination between CG and IC, reasonably well fulfilled within Germany and several other countries, but some areas await completion and expansion of the network geometry. Figure 5.2 shows lightning locations retrieved during a storm that extended from northern Great Britain to southern Greece. In areas near and beyond

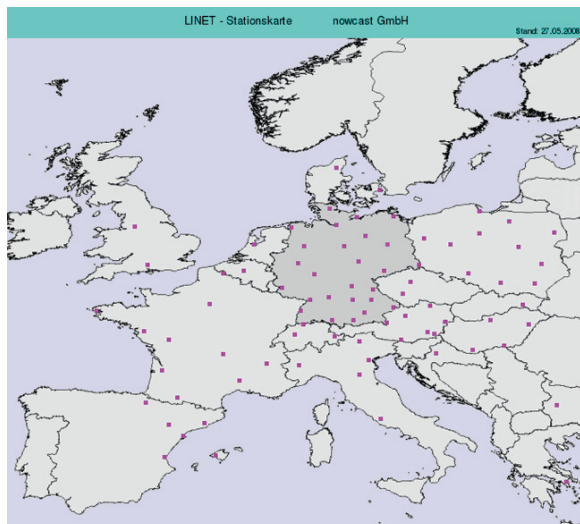


Fig. 5.1 LINET sensor map as of May, 2008

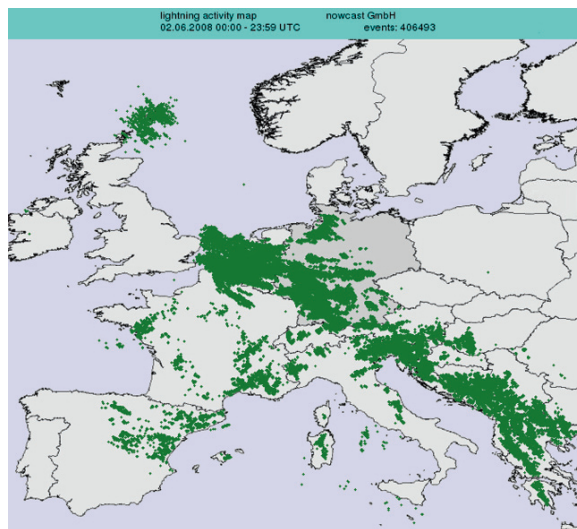


Fig. 5.2 Lightning map for 2 June 2008, from 0:00 – 24:00 UTC. In total, more than 400.000 strokes have been recorded and located. Here, IC and CG are not identified separately. All shown locations have been obtained from at least 5 sensor reports. For this reason, the location accuracy is quite good and allows reproducing relatively sharp contours of storm cells even when the sensor density is not as high as for an ideal configuration

the network borders, and also over the Sea, the detection efficiency decreases so that only stronger strokes will be located; still, storms can be identified far away and traced over long paths.

5.3 Location Accuracy

Particular efforts have been made to attain high location accuracy everywhere in the network area. Exploiting all optimization possibilities a statistical average accuracy of approximately 150 m was achieved. This could be verified by means of strikes into towers: when numerous lightning locations concentrate closely around a tower while no strokes are found further away from the tower, it may be assumed that the tower is either struck by upward-initiated lightning or induces a lightning event solely in the cloud right above the tower (a particularly intriguing case that will be communicated elsewhere); then, deviations between the known object position and the corresponding network locations reflect the precision of the system. Of course, the use of instrumented towers is the best of available options, because recorded event times and signal amplitudes provide useful additional information. Figure 5.3 presents an example where the average location error is less than 100 m as deduced from 58 independent strikes from five flashes, which occurred during a particular storm situation in wintertime. This low error was achieved after careful network fine-tuning, partly due to propagation effects, thereby remedying a systematic data

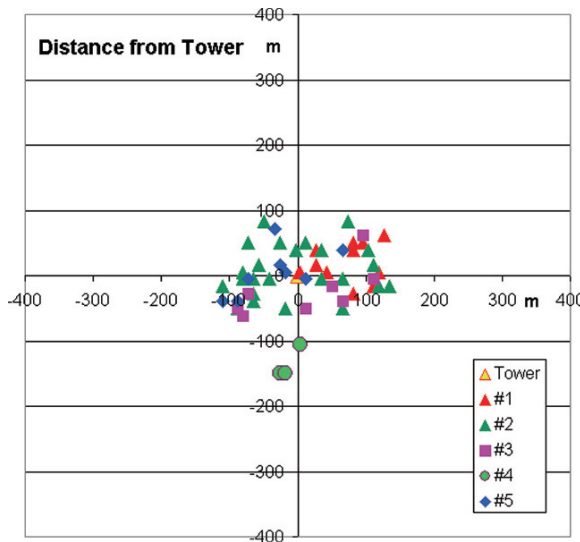


Fig. 5.3 Location accuracy of LINET: during a winter storm in Slovenia on 1 January 2007 five flashes with 58 strokes have been induced by an instrumented tower and located with an average error of less than ~ 100 m

shift due to which the point cloud of LINET locations exhibited initially a slight dispersion and a displacement of ~ 200 m to the East.

Pinpointing of strokes depends on many influential hardware parameters and software procedures related to data handling. Clearly, the reported high precision touches the limits of VLF/LF techniques, but we consider it as being important to demonstrate that this unusual level of accuracy can be attained. Incidentally, the discrimination between IC and CG strokes within the network configuration requires an average 2D-error of less than ~ 300 m, which is further detailed in Section 5.5. A high level of locating accuracy is attained only when TOA techniques are applied, excluding the direct use of or combination with direction finding (DF) procedures. Since bearing angles exhibit intrinsic inaccuracies that cannot be corrected to the extent required here, LINET uses DF only as plausibility check for a TOA solution. Figure 5.4a shows a typical example for the initial site error of a station. It is well known that site errors depend on the direction of incidence and can be described in first order by a sinusoidal function; Fig. 5.4b gives the correspondingly corrected error distribution. Nevertheless, the residual error remains relatively large (Fig. 5.4c), especially when compared to TOA techniques. As a consequence, when weak strokes are reported by only few sensors, DF can lead to substantial location errors up to several 10 km or even more; in any case, the distribution around a well acceptable mean error, achieved by TOA, broadens substantially with the inclusion of DF. Insofar, rather than providing an advantage it is definitely an inferior procedure to combine TOA and DF for the calculation of precise numerical strike points.

Avoidance of DF must be compensated by use of more sensor reports. While DF is principally feasible with only 2 sensors, TOA solutions require at least 3 sensors or, when DF is not at all available, 4 sensors in order to avoid possible ambiguities.

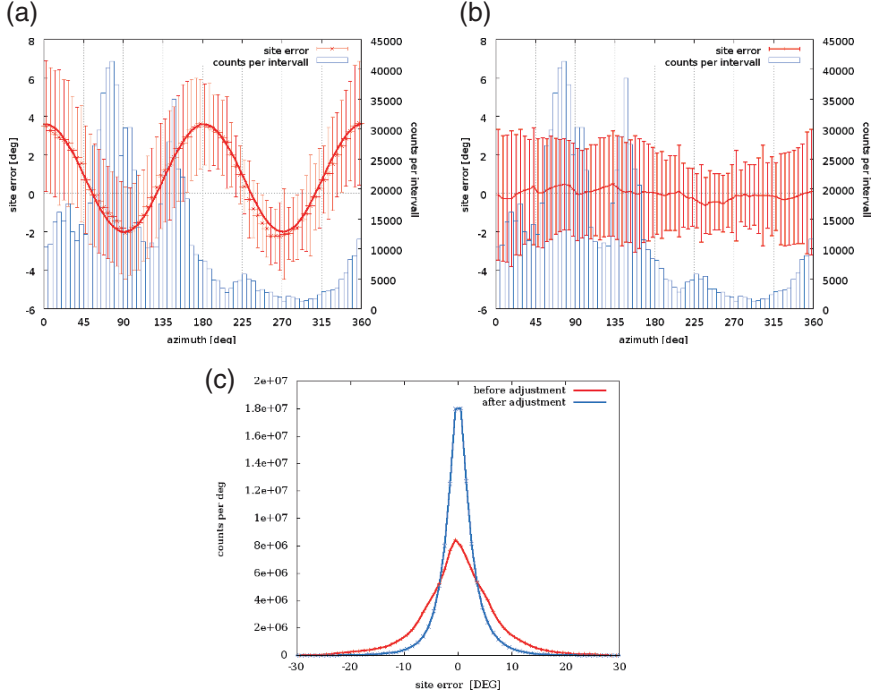


Fig. 5.4 (a) Typical site error of a LINET station, as a function of direction of incidence. (b) Residual site error of the station from Fig. 5.4a after correction. (c) Example for LINET site error before and after correction

As regards LINET, the determination of an emission height for IC-strokes introduces an additional parameter so that always a minimum of 4 sensor reports is needed. In order to have some redundant information, locations are determined from at least 5 sensors in those parts of the network where the baseline amounts to 200–250 km, whereas in other areas, mostly border regions, a minimum of 4 sensors can be used. In all cases, site-error corrected bearing angles are also available, which help to confirm a TOA solution produced with the minimum number of sensor reports. Clearly, TOA suffices when plenty of sensors participate, but otherwise bearing angels can help to reduce erroneous locations that result from either time-errors or unfortunate geometry of lightning and sensor positions.

Typically, TOA-values at the sensor level derived from the peak of the lightning pulse exhibit an accuracy of $\sim 0.2 \mu\text{s}$, corresponding to a signal travel time of 60 m; in some cases, inconsistencies may arise during the treatment of the entire associated signal group that lead to large residual errors of a solution and, consequently, to either erroneous reports or final rejection of a solution. One reason for this is a complex waveform with more than one prominent peak; then, matching of peak times from the different sensors can become difficult, especially when the maximum amplitude is found at the first peak for some sensors, but at the second peak for other sensors. To remedy this problem several peak positions are eval-

uated; in most instances this option works successfully. Well-known alternatives such as cross-correlations between waveforms (Lee, 1989) or time-of-group-arrival (Dowden et al., 2002) are not employed because of either too much data transfer to the central processing unit or problematic performance in case of noisy small signals. Global networks do successfully apply the quoted alternatives in a narrow frequency band with sensitivity to only a particular wave shape (see Katsanos et al., this volume); at the expense of reduction of detection efficiency, pulse recording is achieved at long ranges, but specific lightning parameters such as amplitude, CG or IC signature and polarity become lost and the location accuracy suffers. An example for residual error distributions of LINET locations from a least squares analysis is shown in Fig. 5.5 for both the χ^2 - and the related δt -values. Here, δt signifies the difference between the arrival times of the lightning signal measured at a site, and expected on the basis of the obtained stroke solution. It becomes obvious that the χ^2 -distribution centres near the theoretically expected value of 1, while the associated δt -distribution peaks near 0.2 μs and falls off rapidly towards higher residual time errors, implying that very few solutions must be rejected. It is important to add that the error distribution must not reveal all bad solutions; in case of low degree of freedom a χ^2 -value may be exceedingly small, yet the actual location error may be large. In these cases, the combination of TOA and DF helps to recognize a false location. It is customary to assess the accuracy of a location by means of an error-ellipse, which represents the 2-dimensional statistical error; it must be pointed out, though, that there are also systematic errors, rarely discussed in the literature. They are not contained in the statistical analysis and do not become dominant until the statistical errors decrease to very small values. The latter situation happens in LINET: purely statistical errors reach values as low as ~ 100 m, but the real deviations usually lie at higher values; fortunately, these systematic errors can be compensated as is proven by the location results shown in Fig. 5.3.

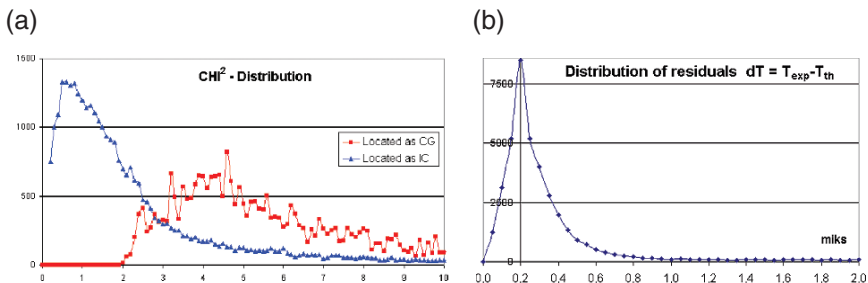


Fig. 5.5 (a) Characteristic χ^2 -distribution from locating IC-strokes with a 3D fit, giving a centre at $\chi^2 \sim 1$. Attempts to fit IC-strokes with a 2D (CG) model yield unsatisfactory χ^2 -values (cut off above 10) and do not qualify for acceptable solutions. (b) Distribution of residual time errors from a least-squares analysis, which centres around 0.2 μs (bin size 0.05 μs). The small time error is indicative of high location accuracy (see Fig. 5.3)

5.4 Detection Efficiency and Current Distributions

VLF/LF waves from lightning propagate primarily as a ground wave with signal intensity $\sim 1/R^p$ in a range of several 100 km, while for longer distances frequency-dependent attenuation must be taken into account. Figure 5.6 displays the power exponent derived from an analysis of copious data: evidently, $p=1$ represents an excellent approximation. Based on this simple finding, sensor signals can be range normalized in order to arrive at current distributions. Fortunately, a connection with the absolute peak current in the lightning channel for CG strokes, I , is closely obtained by exploiting the adapted Biot-Savart relation, yielding

$$I = 2\pi R B c / (c_{RS} \mu_0),$$

where R is the distance between lightning and sensor, B is the magnetic induction measured at the sensor, c the speed of light, c_{RS} the relevant return stroke speed, and μ_0 the magnetic permittivity. The far field relation $E = B \times c$ can be used to derive currents from measured electrical fields E . Calibration is achieved, for example, by correlating the signals with currents measured at instrumented towers (see Rakov, this volume). Of course, the influential values of c_{RS} give rise to some uncertainty

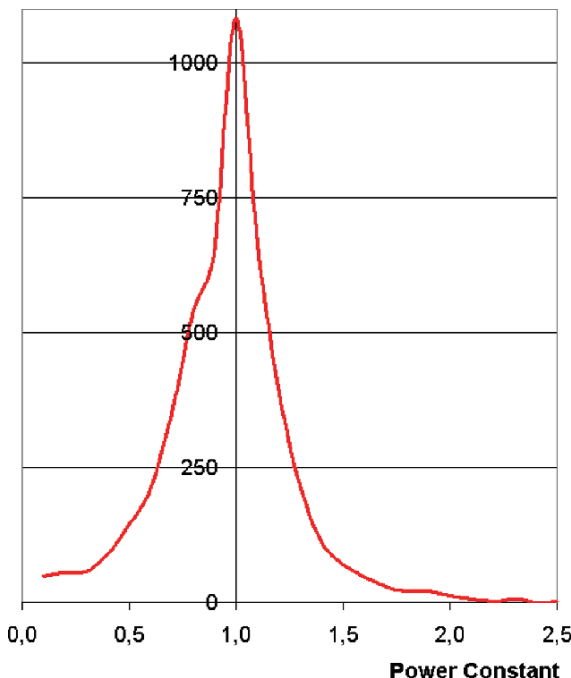


Fig. 5.6 Distribution of best power constants, p , from least-squares fitting of experimental signal amplitudes according to the propagation law $\sim 1/R^p$, suggesting $p=1$

because different observations lead to a range of varying results, but an accuracy of some 20% seems to be realistic in the far field, sufficient for all practical applications of the data.

An important feature of a lightning detection network is its detection efficiency (DE), quantifying the percentage of located events, N_{ex} , in relation to all events that exist, N_0 , and could have been located by a hypothetical perfect system. More specifically, the notation ‘event’ may signify flashes, strokes, radio sources or other signal types that characterize lightning. Assignment of DE to a given network would be easy if N_0 was known; however, since there is neither a perfect system nor a reliable theory for quantitative production of lightning effects, various approximations, estimates and educated guesses are in use, with widely varying reliability. The problem with DE becomes immediately obvious when one compares amplitude distributions (range-normalized currents) published for different networks with allegedly similar DE’s: indeed, the high current tails agree well in quantity and shape and, thus, suggest excellent efficiency, but the low current parts of the distributions may differ dramatically, becoming evident in variations of peak values from below 10 kA to above 30 kA. Apparently, quotation of a lower threshold along with DE seems to be necessary, but is often omitted from network descriptions in the literature.

As an illustration of efficiency considerations in different amplitude ranges the international TROCCINOX campaign in 2005 may be mentioned that was organized by the atmospheric physics division of DLR (Oberpfaffenhofen, Germany). Supported by local teams, DLR has set up a 6-sensor version of LINET that operated for several months in the area of Bauru, Brazil (Schmidt et al., 2005; Schumann and Huntrieser, 2007; Huntrieser et al., 2008). Though the principal goal was related to lightning-induced NO_x-measurements, LINET data could be compared with the local network RINDAT (Pinto, 2003). Figure 5.7 displays an example of scatter plots for the lightning activity recorded by LINET (CG: Fig. 5.7a, IC: Fig. 5.7b) and RINDAT (Fig. 5.7c); obviously, LINET locates far more lightning than RINDAT. Moreover, when LINET locations with fewer sensor reports are accepted, even more strokes show up, which are thought to reflect mainly IC activity (not shown in Fig. 5.7b). The situation becomes transparent when one inspects the current distributions depicted in Fig. 5.8. Clearly, the additional strokes located by LINET are characterized by weak amplitudes and represent mainly though not exclusively IC-strokes, while no significant difference of DE is found for strokes above ~ 15 kA. Nevertheless, based on LINET results and other observations (Krider et al., 2006), there are substantiated reasons to expect that a significant, maybe dominant fraction of CG strokes does occur for currents around 10 kA. For further understanding, it should be added that the baseline of RINDAT amounts to ~ 300 km (similar to NLDN), while LINET sensor separations were ~ 100 km, facilitating more quantitative location of small amplitudes and, thus, also of cloud lightning. This reasoning becomes supported from a comparison with LIS observations (for LIS see the chapters by Adamo et al., and Finke, this volume): as an example, a satellite overpass on 4 February 2005 is presented, which lasted 90 s and yielded marked activity in the area of interest. The reported optical signals are grouped in Fig. 5.9a, and a search for corresponding VLF/LF-activity reveals that LINET reproduces the

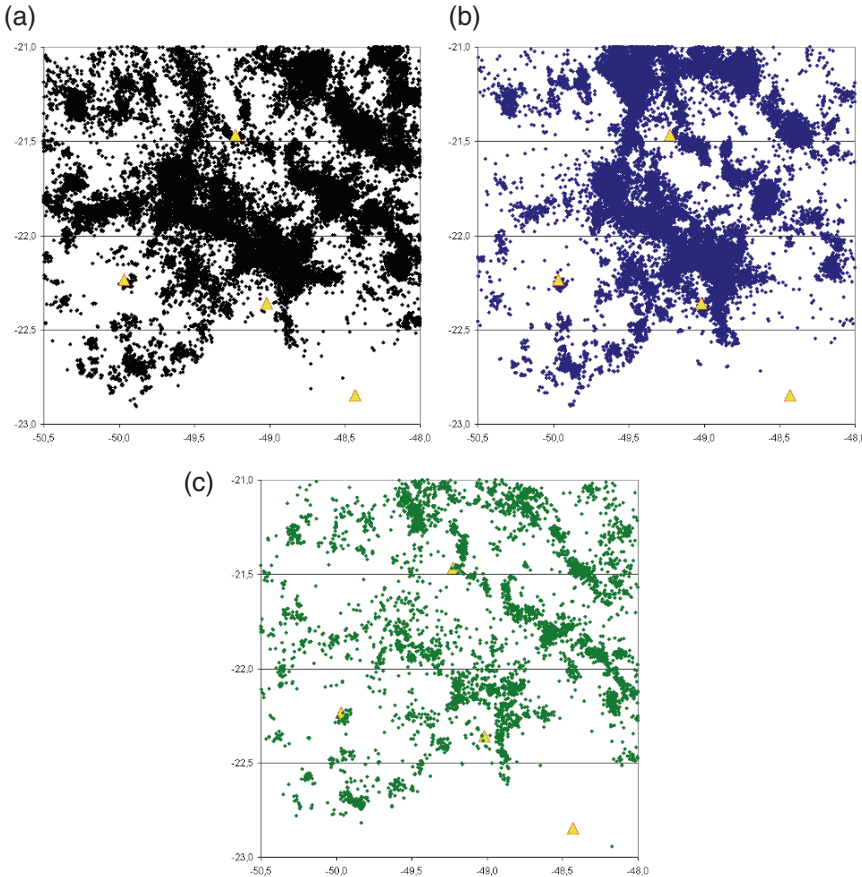


Fig. 5.7 (a) Scatter plot of 49783 CG strokes measured on 4 February 2005 with LINET during the EU-BRAZIL TROCCINOX / TroCCiBras Campaign in 2005 (Schmidt et al., 2005). Triangles: sensor positions (four sensors have been used). (b) Scatter plot of 42606 IC-strokes corresponding to the case (a). (c) Scatter plot of 6583 strokes located with the Brazilian Lightning Detection Network RINDAT in the same area and during the same time as shown in (a) and (b) (Schmidt et al., 2005)

LIS-groups very well (Fig. 5.9b). Most but not all of the coincident LINET signals were of the IC-type and exhibited small amplitudes; this is why the LIS pattern could be reproduced quite well by LINET but not by RINDAT.

Although baselines influence the DE in a decisive manner, a number of other factors also determine how many strokes can be located. The five most important parameters that influence the DE of a network are:

- sensor baseline and network geometry;
- sensor sensitivity, noise handling, thresholds, and dead-time;
- signal treatment and discrimination;

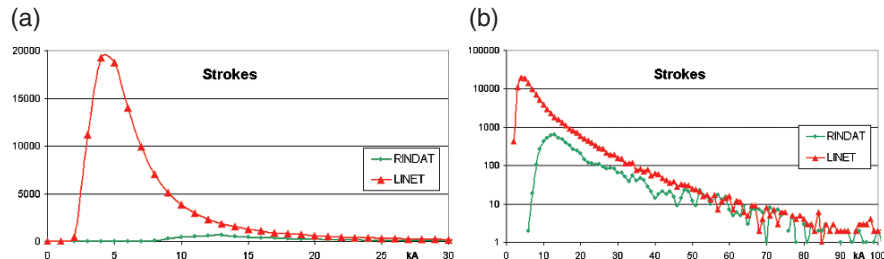


Fig. 5.8 (a) Amplitude distribution of LINET and RINDAT strokes (CG and IC), as a function of normalized channel current in kA, in a linear scale with bin size 1 kA (Schmidt et al., 2005). (b) Amplitude distribution as in (a), in a semi-logarithmic scale

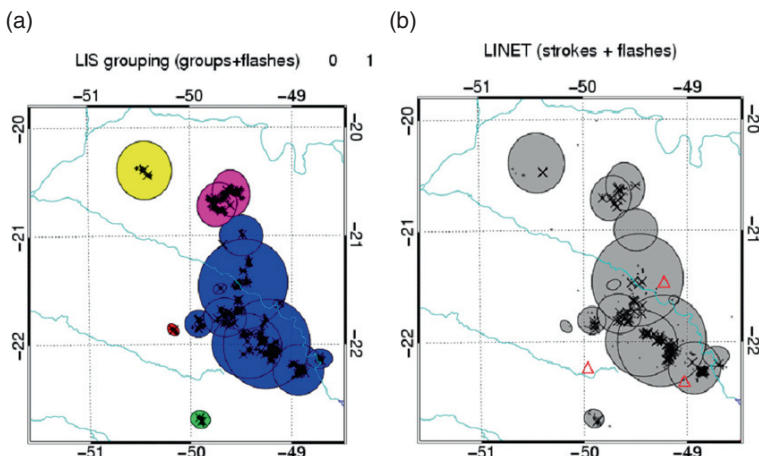


Fig. 5.9 Satellite-based LIS observations during one overpass on 4 February 2005 (*left*) and corresponding LINET strokes (*right*), from Schmidt et al., 2005

- d) procedures for correlation of signals belonging to one and the same stroke;
- e) numerical locating software.

Influence of the baseline (a) is easily recognized because the signal from a discharge must reach a certain number of sensors before the distance becomes too large to keep the attenuating amplitude above the detection threshold. High antenna sensitivity (b) is not problematic, but the site must have low noise in the relevant frequency range. LINET processes any signal because no specific waveform is expected (c); in particular, CG-IC discrimination does not occur at the sensor level so that no CG stroke is omitted when its pulse shape resembles some types of IC or vice versa. In a large network with many unavoidable noise-signals present, identification of a signal group originating from a specific lightning event may be a tedious task (d), especially when pulse shapes become altered due to travel paths of different length and alternating soil conductivity. Finally, the software used for

optimised event location (e) must take care of many circumstances in order to extract a maximum number of real strokes, while avoiding the report of too erroneous or totally false locations. In the above, it has been assumed that all network sensors are operational, though in practice technical failures or line transmission interruptions may cause additional problems; these can be avoided but their occurrence must be monitored and considered in connection with quality checks.

For the reasons quoted above, a stroke signal may be detected at a sensor but not be located by the network, resulting in reduced stroke DE. Since a flash often contains more than one stroke the chance is substantial that higher signal amplitudes occur, giving the chance to locate at least one of the strokes and, thus, yielding a flash DE markedly above the stroke DE. In most networks, the flash DE is claimed to range from approximately 60–90%, though the numbers often come from manufacturer and independent proof is rare (Pinto et al., 2007). While high flash DE is certainly attained for stronger strokes that trigger many sensors, the low-amplitude range is less clarified and the true “100%” level for strokes continues to raise questions. For example, current distributions reported for the U.S. NLDN exhibit a peak near 15 kA (Jerauld et al., 2004; Cramer et al., 2004) with relatively few reports around 5 kA, but specific video observations in a limited areas revealed a substantial number of strokes in the 5 kA range (Krider et al., 2006). From many observations it must be reckoned with quite different current distributions for different types of storms in different areas, so that no unique and general current curve can be postulated. Nevertheless, LINET campaigns in four continents (Europe, South America, Australia, Africa; Hoeller et al., 2008) with the same technical set up and small baselines revealed that the lightning measurements always had the maximum number of CG strokes at currents well below 10 kA. It may be concluded that distributions, which peak at substantially higher values, reflect small partial DE for lower currents. Incidentally, inspection of 1st and subsequent return strokes from LINET data for many regions did not reveal any noteworthy difference in normalized currents; in fact, as a first order approximation the chance for producing a specific current value is independent of the stroke order (Schmidt et al., 2005). Apparently, the charge reservoir in strongly convective clouds is much larger than what becomes neutralized by a single flash. Measurements of field jumps by local networks contribute to a quantitative clarification of charge separation and neutralization by specific strokes (e.g. Loboda et al., 2008).

5.5 Cloud Lightning

In the VHF radio range advanced techniques have been developed for the detection of IC sources, with applications for both research and operational purposes. Notably, ONERA presented the interferometric system SAFIR (Richard et al., 1986; Richard, 1991; Lojou, this volume), and the New Mexico group designed LMA, a time-of-arrival Lightning Mapping Array (Shao and Krehbiel, 1996; Thomas et al., 2004). Likewise, the VHF system LDAR (Lightning Detection and Ranging,

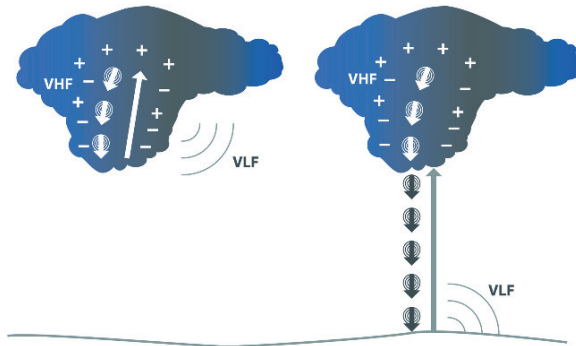
operated at the Kennedy Space center, Florida) provides extensive data on cloud lightning. Systems of this kind succeed to map flashes in fine details; especially when based on high-precision time-of-arrival (TOA) techniques, IC radio sources become detectable with a spatial resolution which may reach down to below 100 m. Due to a tremendous number of located source points, many branches of cloud flashes can be traced as well as leader channels that prepare CG strokes. However, due to short sensor baselines, the need to select sensor locations with small RF noise levels (still producing up to 1,000 triggers per second in the absence of lightning, see Thomas et al., 2004), limitations of wave propagation (line of sight) and very large data rates, it remains a challenging task to monitor continuously complete storms occurring over large geographical areas and to deliver results in real time.

According to present understanding, VHF techniques detect those portions of cloud lightning that are associated with discharge steps fast in time and short in length. The relevant processes are believed to occur during initial breakdown and propagation of stepped leaders. On the one hand, any lightning flash will produce sources that can be located with VHF arrays. On the other hand, actual lightning *strokes*, i.e. the neutralization of strong charges within long channels, preferentially emit VLF/LF radiation and, thus, are not the primary target of VHF systems. For example, the discharge activities within clouds and along a downward leader preceding a CG can be located quite well, but the subsequent return stroke itself is not seen. Similar arguments are likely to apply to distinct IC-strokes as will be evident from the discussion in Section 5.6.

An alternative to record electromagnetic cloud activity consists in appropriate design and application of VLF/LF networks. Early EM-field records of lightning discharges revealed that in the VLF/LF regime not only CG strokes can be recognized by means of field steps ('slow records') or prominent pulses ('fast records'), but also distinct IC events show up (Shao and Krehbiel, 1996; Rakov and Uman, 2003, Chapter 9). In fact, all VLF/LF networks aimed at CG reporting reckon with a certain fraction of IC signals and contain some measures for discrimination of this initially unwanted contribution. LINET is the first network that exploits systematically and quantitatively the circumstance that lightning discharges lead to both CG and IC signals in the VLF/LF regime. With this, a hitherto un-accessed inherent total-lightning feature becomes available from VLF/LF records (see Section 5.6), even without application of CG-IC discrimination. Of course, separation of the two types of lightning is desirable and can be performed by exploiting the fortunate fact that IC emission occurs from a substantial height above ground, while CG radiation originates dominantly from a point near attachment very close to ground (Fig. 5.10). Accordingly, TOA differences as illustrated in Fig. 5.11 can be used to disentangle IC from CG strokes (Betz et al., 2004, 2007). This technique renders a usual VLF/LF network capable of locating and identifying both IC and CG strokes. Attempts along these lines have also been undertaken by Shao et al. (2006) who determine IC-strokes by means of a VLF/LF array.

Traditionally, the term 'stroke' has been reserved to CG return strokes. Still, it seems adequate to term distinct VLF/LF cloud records as "IC-strokes" because the signals exhibit features that are typical for what is generally understood by a

Fig. 5.10 Scheme for VHF and VLF emission associated with CG and IC events



lightning *stroke*, namely occurrence of a relatively strong current within a short time and along an extended discharge channel, first described as ‘recoil strokes’ by Ogawa and Brook (1964), and taken up as ‘K strokes’ by Volland (1982, ‘Low Frequency radio Noise’, p. 197). As has been noted in the Introduction, waveforms and amplitudes of CG and IC pulses are often similar enough to cause misclassification. The technical term ‘IC-stroke’ allows a reasonable distinction from IC radio sources that are typical signatures of cloud lightning, observable with VHF equipment, and reflect a physically different process during certain phases of a lightning discharge. It is of utmost importance to stress two points very explicitly: first, there is a fundamental difference between well understood CG return strokes and the IC-strokes presented here, mainly because CG strokes involve a reference electrode (ground potential) and proceed over relatively long channels (ignoring cases of elevated areas close to or inside clouds). Second, use of the term IC-stroke does not imply any prejudice concerning the actual nature of the underlying production mechanism, which, as a matter of fact, remains largely unexplained; further comments in section 5.6 reveal that classical descriptions of IC activity in the VLF/LF regime have been incomplete if not erroneous, especially with respect to initiation.

It becomes obvious from Fig. 5.11 that reliable identification of a TOA difference requires an adequate 2D locating accuracy. Let us consider the limiting situation: for an average emission height of 8 km and a sensor distance of 100 km from the

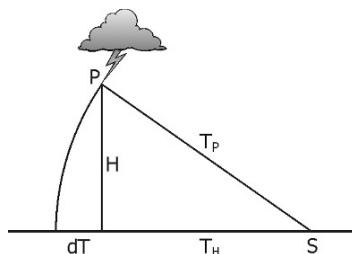


Fig. 5.11 Principle of IC recognition in the VLF/LF regime: IC and CG signals from the same 2D-location arrive with a time difference $dT = T_P - T_H$ (P = center of VLF emission; S = sensor site; H = emission source height), from Betz et al., 2004

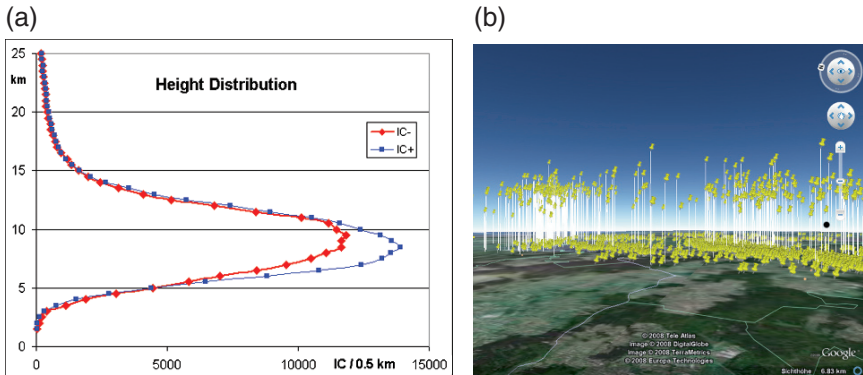


Fig. 5.12 (a) Emission height distribution of IC-strokes (from Betz et al., 2007). (b) Three-dimensional view of a thunderstorm, enabled by the total-lightning capability of LINET: CG-strokes are placed at ground and IC-strokes are shown at their individual VLF/LF emission heights (see Fig. 5.12a); the vertical lines serve to guide the eye to their 2D-locations (See also Plate 4 in the Color Plate Section on page 595)

lightning, the direct path of an IC signal relative to the CG ground wave originating from the same 2D location differs by ~ 320 m. Consequently, the 2D precision must fall into this range; as has been shown in section 3, LINET provides the required small errors and allows IC discrimination for sensor baselines of up to 200–250 km. Figure 5.12a gives an example for a distribution of emission heights measured during a storm in southern Germany. Interestingly, the resulting heights dominate around ~ 8 km and agree very well with high reflectivity zones visible in radar scans (Betz et al., 2007; Hoeller et al., 2008). The nominal statistical accuracy of the extracted heights amounts usually to less than about 30%, otherwise the specification as IC-stroke should not be considered as reliable. With this, a comfortable 3D-visualization of thunderclouds becomes possible in real time, showing the return strokes at ground and the IC-strokes in variable heights (Fig. 5.12b), undoubtedly an attractive feature not available in any other large network. For example, advent of severe weather conditions becomes directly visible as a dominant fraction of IC-strokes shows up (Section 5.7). It must be conceded that the systematic errors have not yet been examined thoroughly; for example, a great number of large heights result, partly above the upper cloud level, which are not confirmed by radar. It remains to be clarified whether, and what kind of systematic errors or, perhaps, charged layers above the convective clouds are partly responsible for the effect.

From the description above it becomes evident that IC signal amplitudes are comparable with the ones known for CG strokes, though there is a clear trend towards smaller values. Figure 5.13 displays an example for a series of IC pulses from a cloud flash. Among the signals, 16 were large enough to allow detection at the chosen minimum number of five sensor sites, allowing redundant 3D-locating. When the signals are range-normalized and converted to currents in the way it is done for CG (CG-equivalent current), the minimum current of locatable IC-strokes amounts to 1.5 kA. It must be conceded that there is no certified model for this

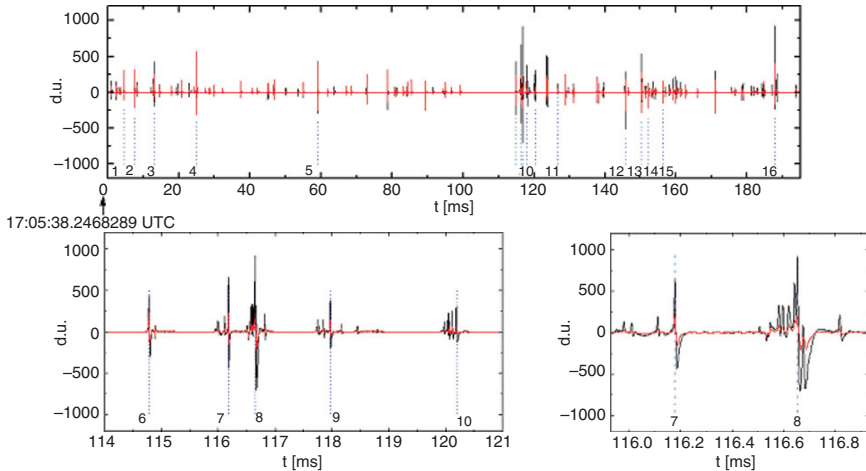


Fig. 5.13 Signal train with a series of small and large IC pulses in a single cloud flash (from Betz et al., 2007)

normalization procedure, but it is generally assumed that the derived currents are not too far from being realistic. When an entire storm is analysed, current distributions result as depicted in Fig. 5.14. In line with general expectations, IC-stroke amplitudes tend to be smaller than the ones for CG strokes, but significant overlap is verified. In contrast to the situation found for CG strokes, the distribution of IC amplitudes, especially of IC+ in Fig. 5.14, does not seem to show its real maximum, because the decrease towards small values results from deteriorating detection efficiency. Thus, as is directly evident from the many small pulses in Fig. 5.13, still weaker signals must be expected and a determination of all IC-strokes (100%) is not

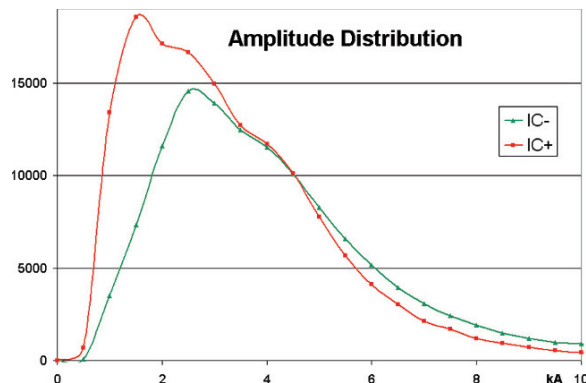


Fig. 5.14 Amplitude distribution of IC events measured with LINET in Germany, using a network configuration with small baseline (CG-equivalent currents, taken from Betz et al., 2007). While the IC- events peak near 3 kA, the IC+ events continue to become more abundant at lower currents and the drop below 2 kA reflects the limitations of the network efficiency (bin size 0.5 kA)

feasible. It must be added that a positive or negative polarity can be attributed to an IC-stroke only when its channel orientation is substantially vertical; there is ample evidence for both horizontal and vertical IC-stroke orientations, but complete statistics about the corresponding distributions of are not available so that IC polarities must be interpreted with caution.

5.6 Total-Lightning

A network that reports both CG strokes and cloud lightning is said to have ‘total-lightning’ capability. Traditionally, the cloud part is comprehensively detected by means of VHF radio signals, while VLF/LF arrays have previously been considered to allow a sufficiently representative picture only of CG strokes but not of cloud lightning. Thus, total-lightning networks utilize both VHF and VLF/LF techniques (see Lojou et al., this volume). Total-lightning information is of interest not only for basic research, but also for monitoring severe weather conditions and for the development of lightning-based nowcasting applications (see Fig. 5.12b and Section 5.7). When high-resolution mapping of discharge channels is desired, use of VHF methods is imperative, but for less demanding purposes other characteristic signatures of the complex discharge process in convective clouds can be exploited. It has been demonstrated in the preceding section that LINET measures a prominent and abundant type of cloud lightning so that the question arises whether the described procedure of locating IC-strokes suffices to attribute ‘total-lightning’ capability to the VLF/LF system. In order to shed light on this issue in a quantitative manner, LINET data has been compared with output from a particular operational version of networks with principally undisputed total-lightning capability, namely the above-mentioned SAFIR-type systems that are in use in several European countries. Although their performance is lower than the one from small, but highly developed research versions of VHF arrays (Thomas et al., 2004), it is proven that large amounts of radio source signals are located. Comparisons have been carried out with data for Belgium, The Netherlands, Germany, Spain, Hungary and Poland. Because of space limitations and other constraints the data comparison will be presented only for the Polish system PERUN, but the results are representative for the other systems as well.

PERUN operates with 9 sensor sites in Poland; details have been described by Maciazek and Bartosik (2004), and Loboda et al. (2006). An interferometric VHF technique provides DF of radio source signals that radiate sufficiently strong within a $100\ \mu\text{s}$ time window (integration of signal bursts). It is generally assumed that the sources mainly reflect the development of leader channels. Up to $\sim 100\text{s}^{-1}$ source points can be located, but mostly only one or a very few points per channel are processed. Thus, the system is not ideal for precise channel mapping and can hardly compete in efficiency with the TOA systems for research quoted above, yet it offers detection of cloud activity adequate for standard use by weather services. The VHF array works in the 2D mode, and at each site an additional LF sensor is added for

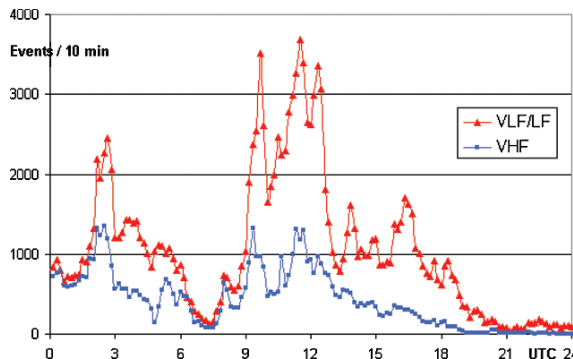


Fig. 5.15 Example for the time evolution of total-lightning, recorded with LINET in the VLF/LF (strokes) and PERUN in the VHF (leader channels) regime, as discussed in Loboda et al. (2006) and Betz et al. (2008a), for time windows of 10 min. LINET effectively detects all time variations of cloud activity

locating strong CG strokes (peak current above ~ 20 kA). For the present purpose, an entire storm is considered and the number of located leader channels is counted, as given by time- and space-connected source points, complemented by the reported CG counts. Figure 5.15 displays a typical example for the resulting total-lightning count rate as a function of time within 10 min intervals.

For the same storm and the same area, LINET CG and IC counts are displayed likewise in Fig. 5.15. It becomes obvious that the storm produces both VHF and VLF/LF signals in a comparable time structure, even in many details. While it is well known that VHF arrays are sensitive to cloud lightning, the shown comparison surprises as it shows that VLF/LF networks also reflect total-lightning activity in a quantitative way, though measuring physically different processes of a discharge as compared with VHF observation. Comparison of data from many storms revealed that even the onset of lightning is recognized as early by VLF/LF as by VHF, at least within a time window of less than a few minutes. As regards practical applications of total-lightning with no need for precise mapping of complex channel structures in the clouds, it may be worthwhile to point to the circumstances that VLF/LF networks can be set up and operated much more economically than VHF systems, particularly in large areas. When scientific issues are targeted, the total-lightning feature of LINET can serve many purposes, among others in atmospheric chemistry targeting the investigation of lightning-induced NO_x production (Schumann and Huntrieser, 2007; Huntrieser et al., 2008), where it is vital to account for all major discharge effects that may produce strong currents and hot channels.

It is worthwhile to enlighten more closely that VHF and VLF/LF systems do not detect the same signals of a discharge. This fact is well known for the evolution of a CG stroke: initial breakdown occurs in the clouds and stepped leader activities first prepare a channel, detectable with VHF systems, and then enable the return stroke, locatable with VLF/LF arrays. In this scenario, VHF radiation clearly precedes VLF/LF emission, with typical time differences in the order of

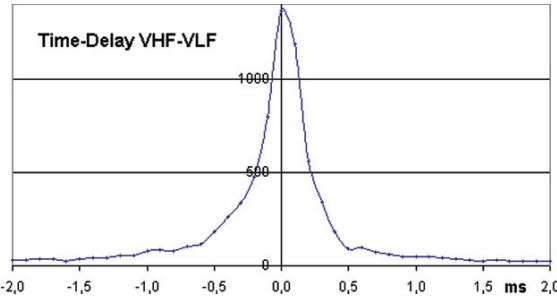


Fig. 5.16 Example for the distribution of delay between initial VHF event times and correlated VLF/LF stroke times: number of cases for bin resolution 100 μ s, as a function of time in ms. Positive delay signifies that VHF sources are detected later than VLF/LF strokes

\sim 10 to \sim 50 ms. Likewise, an IC-stroke (often termed streamer or K-process) may be produced after appearance of VHF sources, but this effect has been studied less intensively because IC-strokes have not been routinely identified and located. As a surprise, inspection of event times for first VHF sources and first VLF/LF strokes of a flash revealed that there is a large group of pulse pairs that exhibit virtually no time difference, at least not within the time resolution of 100 μ s as given by PERUN. Figure 5.16 displays an example for the distribution of observed time differences. Clearly, almost simultaneous production of a first VHF source and a strong VLF/LF discharge pulse is observed and signifies that another type of initial breakdown mechanism is at work, different to conventional models discussed in the past. A most likely process is the advent of runaway electrons, recently described in connection with a particular type of relatively strong VLF/LF pulses, so-called NBE's (Smith et al., 1999; see also Hamlin et al., this volume). More detailed evaluations of this challenging finding on the initial discharge phase and the nature of IC-strokes is given by Betz et al. (2008c). Another task to be performed concerns more accurate lightning data comparisons devoted to alleged time advantages obtained by using either VHF or VLF/LF, and either IC or CG signals with respect to early recognition of upcoming storms. One of the issues has already become clarified: contrary to an often-promoted opinion all data acquired with LINET and compared with SAFIR systems show that storms produce VHF signals not noticeably earlier than VLF/LF strokes. All together, for a large variety of applications, extended studies of lightning data from VLF/LF and VHF networks reveal far-reaching equivalence of the two types of systems.

5.7 Cell Tracking and Detection of Severe Weather

It is well known that IC activity and especially large increases of the IC flash rate within a short time often correlate with the advent of severe weather (Williams et al., 1999). Heavy thunderstorms have been investigated thoroughly by Lang et al. (2004), who give also an overview of the well-known STEPS field campaign;

further details can be found in MacGorman et al. (2005), Wiens et al. (2005), and Rust et al. (2005). In a significant number of storms particularly strong convection rapidly develops and, in rare cases, leads to supercells (Tessendorf, this volume). For many practical applications it is advantageous to both recognize a severe cell at an early stage and predict cell development in time and space. Accordingly, cell-tracking algorithm have been frequently developed that allow investigation of specific storm cells. The Munich group generated a version customized to LINET data in order to identify cells containing a minimum number of strokes, to track the cell, and to extrapolate the path for now casting purposes (Betz et al., 2008b). Figure 5.17 demonstrates an example for a storm in Southern Germany: numerous cells are automatically identified and tracked, partly over many hours. In general, many cell paths are relatively straight and allow a warning time of about one hour. Depending on the desired accuracy of the warning, different alert times and areas can be defined. Figure 5.17 shows the actual path of the cell centres (blue trace), the centre positions predicted one hour in advance (arrow), and the positions of the cell centres predicted one hour ahead (purple trace); the deviations are often small enough to justify the extrapolation as a warning tool. Inclusion of other influential parameters such as the cell size, stroke frequency and life cycle, as well as radar

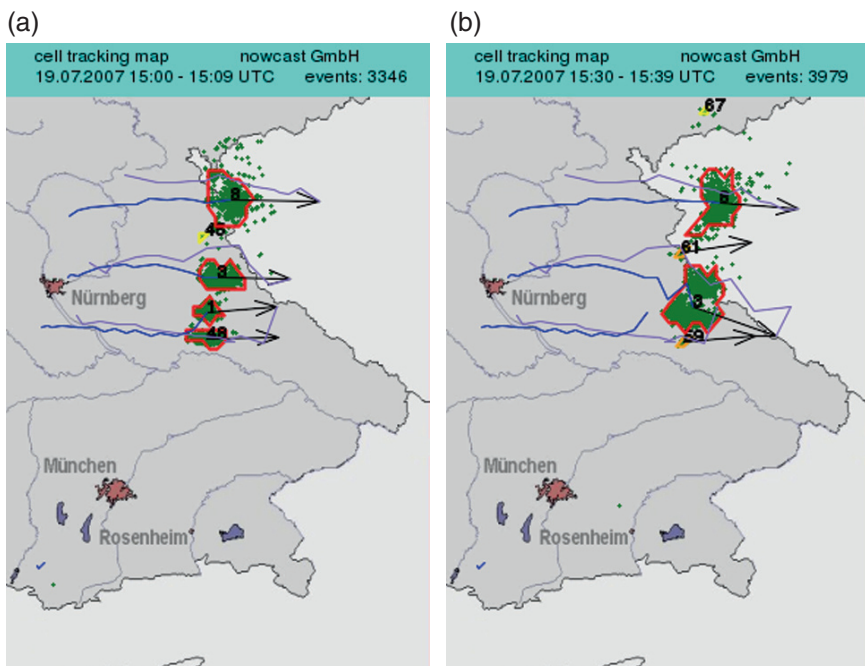


Fig. 5.17 Cell-tracking of a storm on 19 July 2007 in Southern Germany: identified cells and propagation of the actual cell center (blue trace), and the center positions predicted one hour in advance (purple trace), for the time intervals 15:00-15:10 (left) and 15:30-15:40 (right) (See also Plate 5 in the Color Plate Section on page 595)

reflectivity are expected to improve the quality of alert in space and time; efforts along these lines are pursued in the RegioExAKT program presently under way in Germany, specifically designed for utilization by airports and air traffic. Part of this study is the detailed correlation between lightning and radar reflectivity, namely the question to what extent the two types of data are either redundant or allow an advantage with respect to the storm evolution. Upon completion, a tool of this kind is expected to be suited for any demand in connection with recognition and nowcasting of severe weather.

Extending the above, it is obvious that once storm cells have been identified and tracked, it becomes feasible to inspect the cells and to extract lightning parameters that are characteristic for the considered cell (Dombai, this volume; Tuomi and Mäkelä, this volume). A typical example of strong convection is depicted in Fig. 5.18 for a storm in southern Germany on 19 July 2007: the flash rate of the lightning from cell #29 increases steeply at 18:00 UTC and the number of IC-strokes becomes much larger than the one for CG strokes (Fig. 5.18a). For this area in the quoted time interval, the German Weather Service reported strong winds and micro-bursts, heavy rain and hailstones on the ground with sizes up to 2 cm. By comparison, cell #51 does not exhibit a marked change of rate or IC/CG ratio. In addition, other parameters such as cell area, lightning density, amount of positive and negative strokes, strength of strokes, and distribution of IC emission heights can be utilized. As example, we reproduce the variation of cell speed in Fig. 5.18b: over a lifetime of three hours the speed of cell #8 increased continuously to a maximum of 80 km/h, followed by the decay of the cell. No damage report became known in this case. These examples demonstrate that real-time observation of lightning parameters from identified and tracked cells may be useful for estimates about life cycle and severity of the convective cells. More storms must be studied in order to attain a better assessment of this kind of nowcasting application and its usefulness for practical applications.

Severe weather conditions can also be visualized by means of a 3D display of the CG and IC strokes. Figure 5.19 presents an example for a storm cell that approached

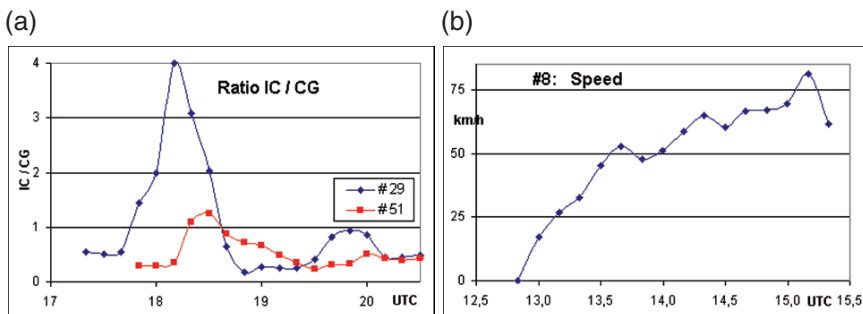


Fig. 5.18 (a) Example for the IC/CG ratio of storm cells tracked on 19 July 2007. (b) Example for lightning parameter: the speed of cell #8 during the storm on 19 July 2007 (uppermost cell in Fig. 5.17)

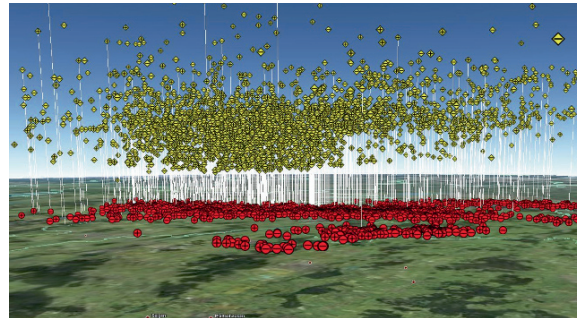


Fig. 5.19 Storm on 07 July 2007 approaching Munich from south-west, displayed with the LINET 3D-visualization from 17-18 UTC; the number of IC's has sharply increased and surpasses the CG stroke-number by a factor of 4, indicating severe weather conditions. CG: red, near ground; IC: yellow, located in the determined emission height (the vertical lines serve to estimate the 2D positions) (See also Plate 6 in the Color Plate Section on page 596)

Munich from a south-west direction on 07 July 2007. The cell could be tracked for almost two hours and exhibited a sharp increase of IC strokes at 17:00 UTC, easily visible in the 3D graph. Since this visual information is available almost in the entire network area in real time – most effective in areas with adequate sensor baselines and, depending on the chosen time slots, with a delay in the order of minutes, – it can be utilized for recognition of severe weather and storm alert.

5.8 Conclusion

A spatially extended and continuously operating international lightning detection network such as LINET in Europe allows recognition and detailed analysis of thunderstorms with the inclusion of large-scale storms even when they move across many countries. Numerous specific network features, namely detection efficiency, location accuracy, and in particular the total-lightning capability render LINET data suited for both scientific research and practical applications. Better understanding of lightning discharges is attained from quantitative detection of relatively strong VLF/LF signals due to cloud processes, and their often-observed occurrence right at the beginning of a discharge, elucidating poorly understood initiation mechanisms. An optimized network configuration allows discrimination of IC and CG strokes even in the range of low amplitudes, and small locating errors enable investigation of contact points during multiple CG strokes and identification of strokes induced by tall objects. Cell-tracking becomes more effectual because of both the large number of strokes located within short time intervals and the virtual absence of large locating errors, rendering the cell borders relatively sharp. The latter point is helpful for better risk assessment in areas outside of direct storm centers. Finally, the combination of lightning with other meteorological data sources, mainly radar and satellite-based observations such as microwave temperatures, implies a significant

potential for improved nowcasting. Taking the many discussed arguments together, lightning detection networks of all kinds are expected to represent an important data source at present and in the future.

Acknowledgments This work was partially supported by Deutsche Forschungsgemeinschaft (DFG) and German Ministry for Education and Research (BMBF) in the project RegioExAKT (*Regionales Risiko konvektiver Extremwetterereignisse: Anwenderorientierte Konzepte zur Trendbewertung und -anpassung*, Regional Risk of Convective Extreme Weather Events: User-oriented Concepts for Trend Assessment and Adaptation). The authors are indebted to DLR (Oberpfaffenhofen, Germany) for successful operation of LINET in many countries and express special thanks to Ulrich Schumann and Hartmut Hoeller for fruitful suggestions and discussions.

References

- Betz, H.-D., K. Schmidt, W. P. Oettinger, and M. Wirz, "Lightning Detection with 3D-Discrimination of Intracloud and Cloud-to-Ground Discharges", *J. Geophys. Res. Lett.*, Vol. 31, L11108, doi: 10.1029/2004GL019821, 2004.
- Betz, H.-D., K. Schmidt, B. Fuchs, W. P. Oettinger, and H. Höller, "Cloud Lightning: Detection and Utilization for Total-lightning measured in the VLF/LF Regime", *J. of Lightning Research*, Vol. 2, 1–17, 2007.
- Betz, H.-D., K. Schmidt, P. Laroche, P. Blanchet, W. P. Oettinger, E. Defer, Z. Dzwiet, and J. Konarski, "LINET – An International Lightning Detection Network in Europe", *Atmos. Res.*, in print, 2008a.
- Betz, H.-D., K. Schmidt, W. P. Oettinger, and B. Montag, "Cell-tracking with lightning data from LINET", *Ann. Geophys.* 26, 1–7, 2008b.
- Betz, H.-D., T. C. Marshall, M. Stolzenburg, K. Schmidt, W. P. Oettinger, E. Defer, J. Konarski, P. Laroche, and F. Dombai, "Detection of In-Cloud Lightning with VLF/LF and VHF Networks for Studies of the Initial Discharge Phase", *Geophys. Res. Lett.*, 2008GL035820, 2008c.
- Cramer, J. A., K. L. Cummins, A. Morris, R. Smith, T. R. Turner, "Recent Upgrades to the U.S. National Lightning Detection Network", 18th Int. Lightning Detection Conference, 7–9 June, Helsinki, Finland, #48, 2004.
- Cummins, K. L., M. J. Murphy, E. A. Bardo, W. L. Hiscox, R. B. Pyle, and A. E Pifer, "A combined TOA/MDF technology upgrade of the U.S. National Lightning Detection Network. *J. Geophys. Res.* 103, 9035–9044, 1998.
- Dowden, R. L., J. B. Brundell, and C. J. Rodger, "VLF lightning location by time of group arrival (TOGA) at multiple sites", *J. Atmos. and Solar-Terr. Phys.* 64, #7, 817–830, 2002.
- Hoeller, H., H.-D. Betz, K. Schmidt, R. V. Calheiros, P. May, E. Houngninou, and G. Scialom, "Lightning characteristics observed by a VLF lightning detection network (LINET): An overview of world-wide field measurements", submitted to *Atmos. Chem. and Phys.*, 2008.
- Huntrieser, H., U. Schumann, H. Schlager, H. Höller, A. Giez, H.-D. Betz, D. Brunner, C. Forster, O. Pinto, and R. Calheiros, "Lightning activity in Brazilian thunderstorms during TROCCI-NOX: Implications for NOx production", *Atmos. Chem. Phys.*, 8, 921–953, 2008.
- Jerauld, J., V. A. Rakov, M. A. Uman, K. J. Rambo, and D. M. Jordan, "An Evaluation of the Performance Characteristics of the NLDN Using Triggered Lightning", 18th Int. Lightning Detection Conf., Helsinki, 2004.
- Krider, E. P., Ch. J. Biagi, K. L. Cummins, and K. E. Kehoe, "NLDN Performance in Southern Arizona, Texas and Oklahoma in 2003–2004", *Int. Conf. on Grounding and Earthing, GROUND 2006*, 471–486, Maceió, Brazil, 2006.

- Lang, T. J., L. J. Miller, M. Weisman, S. A. Rutledge, L. J. Barker, V. N. Bringi, V. Chandraseka, A. DetWiler, N. Doesken, J. Helsdon, Ch. Knight, P. Krehbiel, W. A. Lyons, D. MacGorman, E. Rasmussen, W. Rison, W. D. Rust, and R. J. Thomas, "The Severe Thunderstorm Electrification and Precipitation Study", Bull. Am. Met. Soc., pp. 1107–1125, August 2004.
- Loboda, M., G. Maslowski, Z. Dziewit, H.-D. Betz, B. Fuchs, P. Oettinger, K. Schmidt, M. Wirz, and J. Dibbern, "A new Lightning Detection Network in Poland", Int. Conf. on Grounding and Earthing, Maceió, Brazil. 2006.
- Loboda, M., H.-D. Betz, K. Schmidt, P. Baranski, J. Wiszniowsky, and Z. Dziewit, "New Lightning Detection Networks in Poland – LINET and LLNDN", 29th Int. Conf. on Lightning Protection, June 23–26, Uppsala, #2.2, 10 pp, 2008.
- Lee, A.C., "Ground truth confirmation and theoretical limits of an experimental VLF arrival time difference lightning flash locating system", Quart. J. of the Royal Met. Soc., 115, No. 489, 1989.
- MacGorman, D. R., W. D. Rust, P. Krehbiel, W. Rison, E. Bruning, and K. Wiens, "The Electrical Structure of two Supercell Storms during STEPS", Monthly Weather Review, Vol. 133, 2583–2607, 2005.
- Maciazeck, A., and B. Bartosik, "Availability of Lightning data in Poland from the Lightning Detection System SAFIR 3000 – IMGW", 18th Int. Lightning Detection Conf. (ILDC), No. 41, Helsinki. 2004.
- Nag, A., and V. A. Rakov, "Pulse trains that are characteristic of preliminary breakdown in cloud-to-ground lightning but not followed by return stroke pulses", J. Geophys. Res. 113, D01102, doi:10.1029/2007 JD008489, 2008.
- Ogawa, T., and M. Brook, "The Mechanism of the Intracloud Lightning Discharge", J. Geophys. Res. 69, No. 24, 5141–5150 (1964).
- Orville, R. E., G. R. Huffines, W. R. Burrows, R. L. Holle, and K. L. Cummins, "The North American Lightning Detection Network (NALDN) – First Results: 1998–2000", Monthly Weather Review, Vol. 133, 2098–2109, 2002.
- Pinto, O., "The Brazilian lightning detection network: a historical background and future perspectives", SIPDA Proc., Curitiba, 2003.
- Pinto, O., I. R. pinto, and K. P. Naccarato, "Maximum cloud-to-ground lightning flash densities observed by lightning location systems in the tropical region: a review", Atmos. Res. 84, 189–200, 2007.
- Rakov, V. A., and M. A. Uman, "Lightning: Physics and Effects", 850 pp., Cambridge Univ. Press, New York, 2003.
- Richard, P., A. Delannoy, G. Labaune, and P. Laroche, "Results of spatial and temporal characterization of the VHF-UHF radiation of lightning", J. Geophys. Res., Vol. 91 (D1), 1248–1260, 1986.
- Richard, P., "Operational Applications of the SAFIR System. International Aerospace and Ground Conference on Lightning and Static Electricity", KSC Florida, April 16–19, 1991.
- Rust, W. D., D. R. MacGorman, E. C. Bruning, S. A. Weiss, P. R. Krehbiel, R. J. Thomas, W. Rison, T. Hamlin, and J. Harlin, "Inverted-polarity electrical structures in thunderstorms in the Severe Thunderstorm Electrification and Precipitation Study (STEPS)", Atmospheric Research, Vol. 76, 247–271, 2005.
- Schmidt K., H.-D. Betz, W. P. Oettinger, M. Wirz, O. Pinto, K. P. Naccarato, H. Höller, Th. Fehr, and G. Held, "A Comparative Analysis of Lightning Data during the EU TROCCINOX / TroCCiBras Campaign", VIIIth International Symposium on Lightning Protection, Sao Paulo, Brazil, 2005.
- Schumann, U., and H. Huntrieser, The global lightning-induced nitrogen oxides source, *Atmos. Chem. Phys.*, 7, 3823–3907, SRef-ID: 1680-7324/acp/2007-7-3823, 2007.
- Shao, X. M., and P. R. Krehbiel, "The spatial and temporal development of intracloud lightning", J. Geophys. Res., Vol. 101, No. D21, pp. 26641–26668, 1996.
- Shao, X. M., M. Stanley, A. Regan, J. Harlin, M. Pongratz, and M. Stock, "Total-lightning Observations with new and Improved Los Alamos Sferic Array (LASA)", J. Atmosph. and Oceanic Techn. 23, 10, 1273–1288, 2006.

- Smith, D. A., X. M. Shao, D. N. Holden, and C. T. Rhodes, "A distinct class of isolated intracloud lightning discharges", *J. Geophys. Res.* 104, 4189–4212, 1999.
- Thomas R. J., P. R. Krehbiel, W. Rison, S. J. Hunyady, W. P. Winn, T. Hamlin, and J. Harlin, "Accuracy of the Lightning Mapping Array", *J. Geophys. Res.*, Vol. 109, D14207, 2004.
- Volland, H., in *Handbook of Atmosphericics*, Vol. I, ed. H. Volland, CRC, Boca Raton, Fl., USA (1982).
- Wiens, K. C., S. A. Rutledge, and S. A. Tessendorf, "The 29 June 2000 supercell observed during STEPS. Part II: Lightning and charge structure", *J. Atmospheric Sciences*, Vol. 62, No. 12, 4151–4177, 2005.
- Williams E., B. Boldi, A. Matlin, M. Weber, S. Hodanish, D. Sharp, S. Goodman, R. Raghavan, and D. Buechler, "The behaviour of total-lightning activity in severe Florida thunderstorms", *Atmospheric Research* 51, 245–265, 1999.

Chapter 6

LAMPINET – Lightning Detection in Italy

Daniele Biron

Abstract In 2004 the Italian Air Force Meteorological Service has set up a modern lightning detection network, LAMPINET, in order to monitor comprehensively atmospheric discharges. The requirements arose from the fact that lightning still represents a severe threat for both military and commercial aircraft; despite continuous improvement of aircraft materials, assembling techniques, navigation technology and computer controlled procedures during flights, a rendezvous between aircraft and lightning, even though a very rare event, could be potentially fatal. Topics of this contribution are lightning-aircraft interaction in order to illustrate why the Meteorological Service of Italian Air Force has taken actions, the description of the Italian lightning detection network LAMPINET, and lightning statistics over Italy based on data from the first three years of LAMPINET operation.

Keywords Lightning detection · Lightning locating · Lightning-aircraft interaction · Lightning detection network · Convective rain · Network comparison · Lightning statistics

6.1 Introduction

For several reasons, electromagnetic interaction of lightning with aircraft has received increasing interest in recent years. In the 1980s it has been demonstrated that the major part of lightning strikes to an aircraft is initiated by the plane itself, rather than being a casual interception of a discharge with an aircraft (Uman and Rakov 2003). In the past, lightning menace stimulated the Italian Air Force (IAF), because several cases of lightning hits into aircraft caused a wide spectrum of damage, from removal of segments of the body paint to burning or destruction of plane fragments, in rare cases accompanied by communication black out or total loss. Becoming aware of the potential risks of lightning, the Air Force urged the Italian

D. Biron (✉)

Centro Nazionale di Meteorologia e Climatologia Aeronautica
Aeroporto Militare “De Bernardis”, Via Pratica di Mare, 45, 00040 Pomezia (RM), Italy
e-mail: biron@meteoam.it

Air Force Meteorological Service to study the phenomena more closely and to set up an adequate system to monitor lightning. This task was intended to serve the needs of both the Air Force and a number of governmental and commercial institutions, where direct and real time lightning information was thought to be advantageous.

In the first part of the chapter, lightning-aircraft interaction is introduced, a phenomenon that, despite all modern technology, continues to represent a potential risk. In the second part the endeavours of the IAF Meteorological Service in lightning research and operation are described, devoted to efficient detection and useful application of the retrieved information, and an illustration is given about the Italian lightning detection network LAMPINET, with its headquarters located in Centro Nazionale di Meteorologia e Climatologia, Pratica di Mare, situated south of Rome. Finally, in the third part, lightning statistics over Italy are shown along with a discussion based on data from the first three years of operations of LAMPINET.

6.2 Aircraft and Lightning Interaction

On 11 February 2008 an Italian Air Force F-16A/B ADV fighter aircraft from the 37° Wing, 18° Interceptors' Group, based at Trapani Birgi in Sicily, south Italy, was hit at 18:38:55 UTC by a lightning.¹ As member of a group of three other fighters, the aircraft was flying in low altitude around 800 m, and approached Trapani airport from the sea with a speed of ~ 370 km/h. Figure 6.1 shows its position between MARETTIMO and Levanzo islands, 25 km west of Trapani. During this time, the area showed low cumulus with short and weak showers of rain, and rare lightning activity was reported 80 km from the fighters position; over the rest of South Italy the weather was substantially stable (Fig. 6.2). Cloud tops in the area were around 4.1 km (Fig. 6.3), indicating neither severe or deep convection, nor threatening phenomena that could suggest a rerouting of the fighters path.

Analysis of the meteorological conditions revealed that the air around the path of the aircraft was clear, but saturated with water vapors below the cloud base. At 18:38:55 UTC, in complete darkness, a bright flash occurred at the first aircraft in line, blinding the eyes of the pilots in the entire group for at least a second. The pilot in the struck aircraft remained conscious, but the aircraft suffered a complete black out, and after 13 s of no recovery of the systems the pilot ejected, just 5 s before the F-16 crashed into the sea. The pilot was rescued around one hour later and survived without injuries.

Since the Air Force was aware of the potential risk of lightning to aircraft, especially because having experienced several other cases like the one described above, it decided to assign to the Italian Air Force Meteorological Service the task of monitoring lightning phenomena, to perform research on detection techniques, to develop user requirements for protection of infrastructure and personnel, and to acquire and maintain a lightning detection network representing the present state of the art.

¹ <http://www.aeronautica.difesa.it/SitoAM/Default.asp?idnot=20355&idsez=2&idarg=&idente=1398>

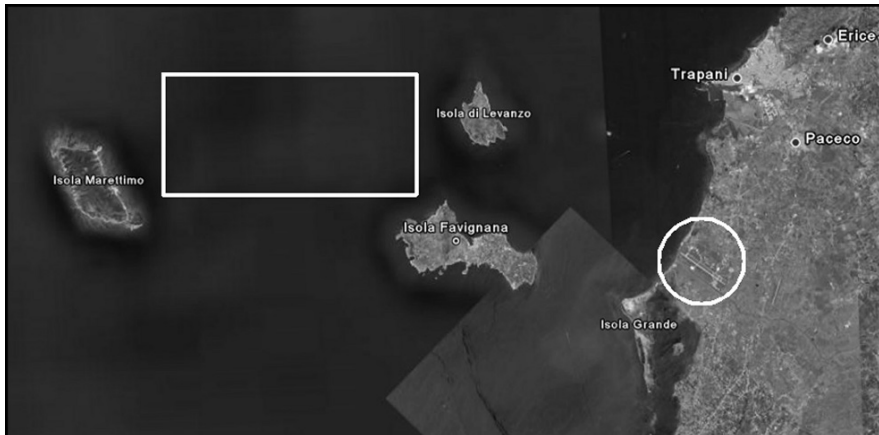
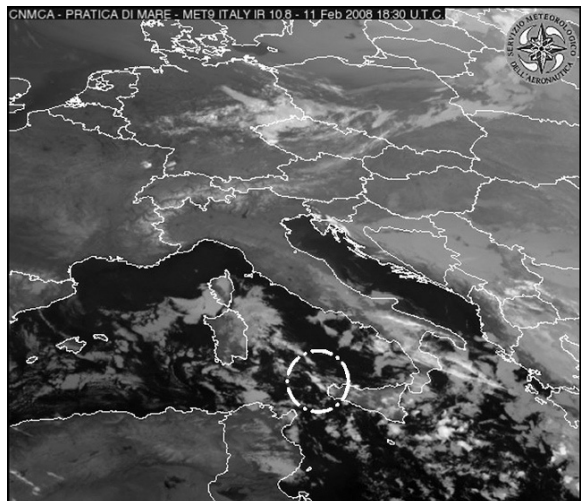


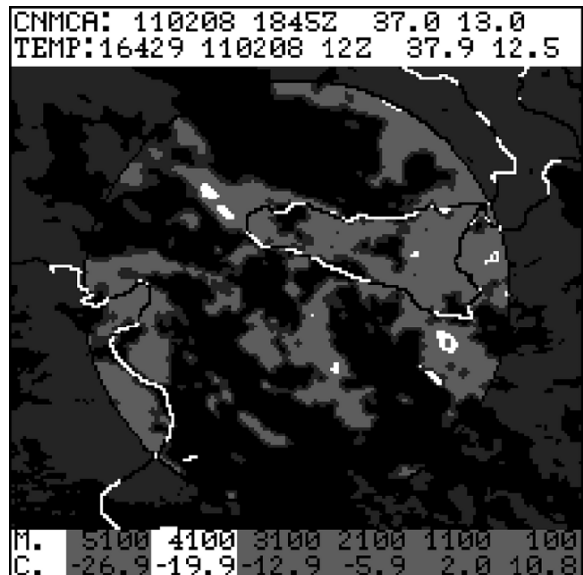
Fig. 6.1 Accident area on 11 February 2008 (rectangle) west of Trapani Birgi airport (circle)

Fig. 6.2 Accident area on 11 February 2008 (dashed circle)



For several reasons, air companies, aircraft owners and air traffic operators are interested in having access to continuous monitoring of lightning activity in the atmosphere. The first reason concerns aspects of aircraft technology. Present and future aircraft are partly made out of certain composite materials (Harris et al. 2001), providing advantageous strength-to-weight ratios when compared to metal bodies. Maintaining the same level of robustness as with metal structures, the level of humidity inside can be kept low and the apertures in the body of the carrier can be made wider (windows). A commercial composite-material aircraft may burn less fuel, fly higher in the atmosphere where less turbulences are encountered, have a longer range, and permit more comfortable humidity insides. The composite material does not offer as much electromagnetic shielding as do metals, but the outer

Fig. 6.3 Cloud top in the accident area on 11 February 2008 (white spot west of Sicily)



skin is covered with a layer of conductive fiber designed to carry lightning currents, keeping the flow of charges on the exterior surface of the aircraft along the body and then away from the plane, typically via static discharge wicks.

A second reason is the abundance of low-level semiconductor circuitry, which is of critical importance for fly-by-wire systems.² The navigation of modern aircraft is no longer based on hydraulic actuators enacted by pilot commands, but relies on computer-controlled electronic commands, that interpret directives from the pilot by interfaces in order to activate the movement of mechanical parts. Redundancy of central processing units, cables, motors, etc. may not completely eliminate the remote risk of a complete failure of aircraft systems caused by a lightning hit. It is interesting to note that lightning strikes to jet airliners occur about once every 1000 flying hours, most of the time without severe consequences so that passengers and crew remain safely transported to their destinations. By contrast, military aircrafts are more affected, because they frequently fly at low altitude (few thousand feet) and at high speed (around 0.9 mach). Due to the technical complexity, it is more difficult to manage a blackout of a processing unit, or errors in transmission of navigation information for longer than a few seconds. If vital systems fail, the only alternative is to save the pilot by launching the jet seat, but losing the plane. Another military aspect concerns air refuelling by means of a flexible (basket) or rigid (boom) devices, frequently losing traces of fuel; again, a potential threat is given because the plane itself may trigger a lightning hit.

A third reason arises from the completely automatic air navigation system, which USA and Europe have developed in recent years (Kostiuk et al. 1998). The goal

² http://en.wikipedia.org/wiki/Aircraft_flight_control_systems

is that aircraft of the next generation can receive, without any intervention of the pilot, external data in real time from other planes, ground infrastructures, observational networks, meteorological and positioning satellites, and networks belonging to central processing units. This allows re-routing in order to avoid flight corridors with thunderstorms and lightning, arrival on time at the destination airport with the minimum quantity of fuel and without air traffic jam. One of the components that will provide an important input, essential to a completely automatic air navigation system, is information from ground-based lightning location networks.

For these reasons, it is necessary to understand the electromagnetic interaction between lightning and aircraft, to estimate the potential risk in routing an aircraft close to a lightning-active area, and to work out rules to assess situations and potential threats.

In the early 1980s, NASA obtained a comprehensive amount of data from an eight-year research effort on lightning-aircraft interaction, the Storm Hazards Research Program (Rudolph and Perala 1982, Rudolph et al. 1987, Rudolph et al. 1989). A two-seat F106B fighter jet was specifically instrumented and penetrated more than 1400 thunderstorms with the intent of being struck by lightning, usually at a relatively high altitude (~ 5 km) so that cloud-to-cloud discharges were encountered, rather than cloud-to-ground strokes. During the experiments the F106B was hit more than 700 times, but the really dangerous aspect of the experiment was the severe turbulence connected with thunderstorms, generating instantaneous up and downdrafts of three or four thousand feet.

During the experiment NASA discovered that the great majority of in-flight lightning strikes to aircraft, especially around 5 km altitude near or inside cumulonimbus, were triggered by the aircraft's presence, rather than originating from a random interception of the airplane route and a naturally occurring lightning channel.

Continuous monitoring of the atmosphere is the only way to recognise lightning risk situations, and to obtain clear indications about safe aircraft routes. This was the principal requirement that stimulated the Italian Air Force Meteorological Service at the end of 1990 with respect to planning acquisition of a modern lightning detection network. The name LAMPINET of the new project was the acronym of the Italian word LAMPI, signifying 'flash', and NET for network.

6.3 LAMPINET: the Italian Air Force Lightning Detection Network

LAMPINET is the Italian lightning detection network, ordered in early 2000 and built up in 2003 by the Meteorological Service of the Italian Air Force, which represents de facto the Italian Meteorological Service. LAMPINET consists of 15

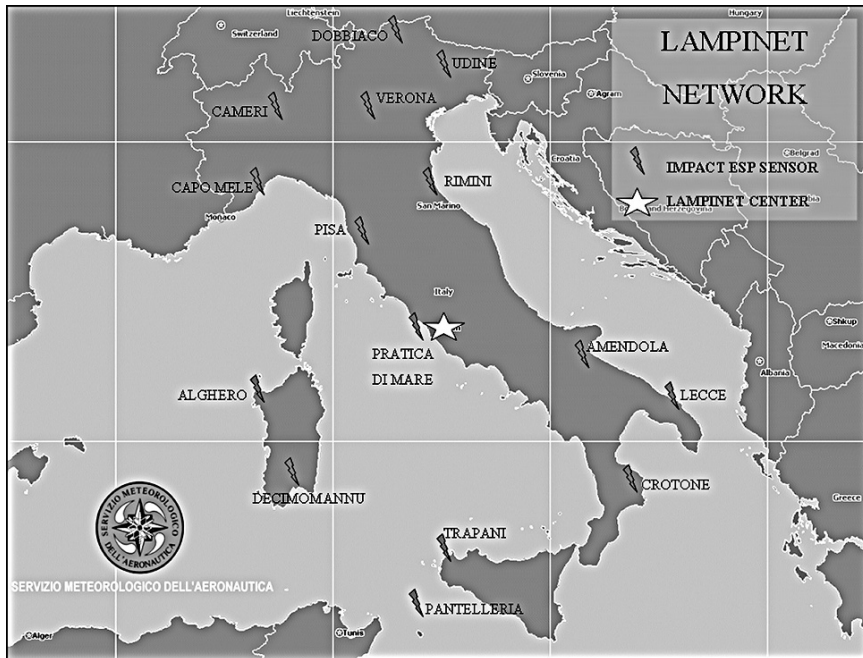


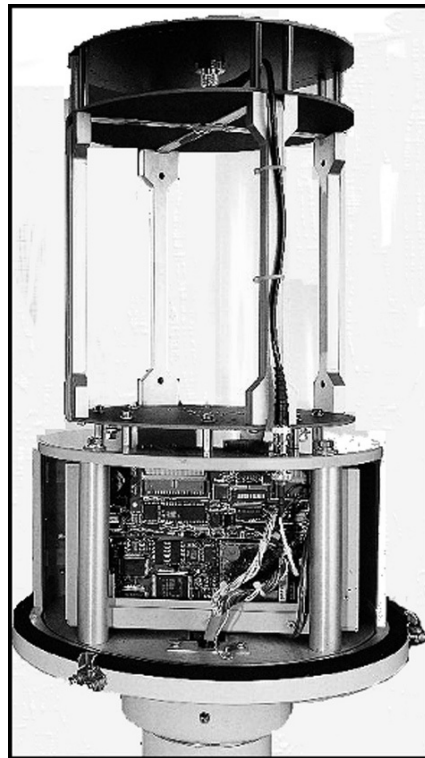
Fig. 6.4 Sensor positions in LAMPINET

IMPACT ESP³ sensors uniformly distributed over the national territory (Fig. 6.4), and started operation during 2004 (Biron and De Leonibus 2005). It is utilizing both MDF (Magnetic Direction Finding) and TOA (Time Of Arrival) techniques. As communicated by the manufacturer, LAMPINET can reach a detection efficiency of 90% for normalized currents $I > 50$ kA, and a location accuracy of 500 m in the central areas of Italian; larger errors are expected in the border areas and beyond the network. Basic requirements were high reliability, redundancy, scalability, and implementation into existing systems.

The network was adopted primarily for nowcasting of strong electrical activity connected with atmospheric instability, to prevent risks both in air operations and ground activities, such as aircraft refuelling and protection of power plants, but also of human life outdoors. LAMPINET data are used by the Italian Air Force, Army, Navy, Civil Protection Agency and other governmental institutions, like National Research Council (ISAC-CNR). Some users pay for the dataset in real time or offline, for instance insurance companies, film studios, media groups and others. It has to be noted that a purely commercial lightning detection network is already operating in Italy, managed by the national electric power supply company (Sistema Italiano Rilevamento Fulmini, SIRF).

³ <http://www.vaisala.com>

Fig. 6.5 IMPACT ESP sensor installed at Pratica di Mare



LAMPINET sensors (Fig. 6.5) detect lightning E-B field signatures and waveforms of CG (Cloud-to-Ground) and to some extent CC (Cloud–Cloud) discharges. Discrimination between CG and CC is performed by application of wave-form criteria. The bandwidth is 1–350 kHz, and measured parameters are bearing angles, time of signal arrival, peak signal strength, rise-time and pulse width of the signal. The E (electrical) field is recorded by means of a parallel plate capacitor, and the B (magnetic) field by means of crossed loops; from the latter the angle of incidence is derived (direction finding). Further components are a GPS (Global Positioning System) clock, a signal analyzer, and electronics for power supply and telecommunications that link each sensor to the central processing unit.

All 15 LAMPINET sensors are connected to the Centro Nazionale di Meteorologia e Climatologia (C.N.M.C.A.), the national weather center of the Italian Air Force Meteorological Service, placed in Pratica di Mare, via 64 kb LAN (Local Area Network) links that connect Italian peripheral airport meteorological offices. The same LAN links are utilized for transmission of meteorological information, such as bulletins, satellite images, NWP (numerical weather prediction) charts, radar scans, etc., but the bandwidth needed for LAMPINET data traffic is far lower than 64 kb and is automatically reserved depending the amount of information to be transferred; usually, rates remain well below 1 kb.

After availability of lightning data in 2004, the interest for LAMPINET grew up gradually, with first use at C.N.M.C.A. by forecasters in connection with preparation of bulletins for severe weather warning, including national warnings. Additional interest arose for control of satellite post-processing products, recognition of convective areas with at least a minimum lightning activity not clearly identified by visible and infrared images, and for the control of NWP in order to verify forecasted areas and intensities with heavy convective precipitation. Finally, lightning data were studied to reconstruct meteorological parameters that cannot be measured in other ways. One of these studies concerns the determination of convective rainfall rates, where poor or no synoptic observation is present (De Leonibus et al. 2008).

The radar network in Italy still suffers from sub-optimal operational coverage (Fig. 6.6), principally due to orographic complexity, high cost of maintenance, and lack of diffuse radar-raingauge calibration. Moreover, different government institutions, regional or national, have taken steps to manage weather radar, but frequently without any possibility of integration with the existing radar network of the Air Force. A tool developed at C.N.M.C.A. connects lightning observation and estimates for convective rain, using a relation to retrieve an estimate of convective rainfall rate according to literature (Tapia and Smith 1997), implying

- the relation between rain-rate and lightning-rate (RLR);
- spatial distribution of rain with respect to lightning location;
- temporal distribution of rain with respect lightning events.

Tapia and Smith presented a relation from the analysis of 22 thunderstorms over Florida during August 1992 and 1993, utilizing lightning locations obtained from the National Lightning Detection Network (NLDN) and rain rates from the Melbourne radar. The resulting estimate for convective rain is given by:

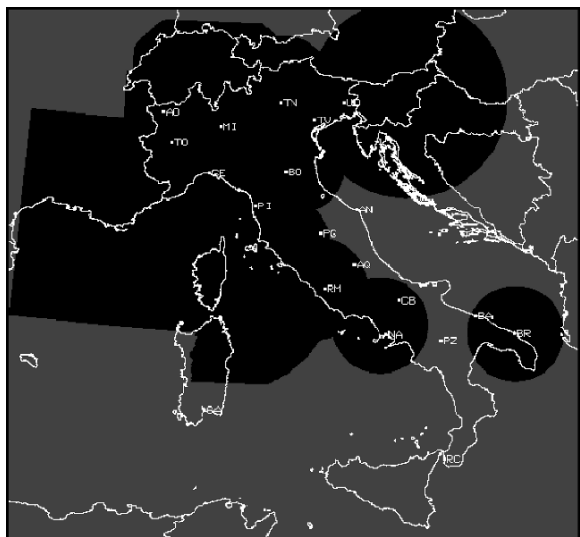


Fig. 6.6 Radar coverage over Italy in 2008, in black

$$R(t, x) = C \sum_{i=1}^{N_t} \Phi f(t, T_i) g(x, X_i)$$

where the sum is performed over N_t flashes observed in the time frame $t \pm \Delta t/2$, and the parameters are:

$R(t, x)$ - rain rate (mm/h) in the x location at time t ;

T_i - time of observation of each individual lightning;

X_i - spatial location of each individual lightning;

Φ - RLR factor (kg/flash);

C - a conversion factor;

$g(x, X_i)$ - precipitation flux in x linked to a lightning occurred in X_i ;

$f(t, T_i)$ - temporal distribution at time t induced by a lightning at time T_i .

Tapia and Smith suggest an RLR factor of 43×10^6 kg/flash. This factor is strongly correlated with the area of observation and the particular climatology of the region of interest. The temporal precipitation distribution is considered uniform over a period of duration Δt , centred at the timestamp of the lightning event:

$$f(t, T_i) = 1 \quad \text{for } |t - T_i| < \Delta t/2$$

$$f(t, T_i) = 0 \quad \text{for } |t - T_i| \geq \Delta t/2$$

In our case Δt amounts to 5 min, while precipitation is assumed uniform in the area of lightning activity:

$$g(x, X_i) = 1 \quad \text{for } |x - X_i| < 5 \text{ km}$$

$$g(x, X_i) = 0 \quad \text{for } |x - X_i| \geq 5 \text{ km}$$

Tapia and Smith report that each individual lightning produces a precipitation of 0.55 mm at ground, uniform in a circle of 10 km of diameter, and centred on the lightning location.

A calibration was necessary for optimising the coefficients of the quoted formula, in order to get the best correlation for spatial and temporal rainfall distributions in relation to lightning locations. In 2006 a thesis was carried out at C.N.M.C.A. (Ciolfi 2006) to investigate a link between lightning and convective rainfall rates; a result is present in Fig. 6.7, using real radar scans from Aleria in France, and the reconstructed rainfall rate pattern for the same time span by means of lightning data. The results for POD = 0.75 (Probability Of Detection) and FAR = 0.32 (False Alarm Rate) are encouraging. A useful RLR value was estimated 15×10^6 kg/flash, while other parameters were chosen similar to the ones by Tapia and Smith.

C.N.M.C.A. personnel try to maintain high detection efficiency and location accuracy of LAMPINET, and periodically perform data comparisons with other systems in Europe that can cover the operational area of LAMPINET. One comparison was with LINET (Biron et al. 2007); Betz et al., this volume. LINET is a European lightning detection network developed by a co-operation between the

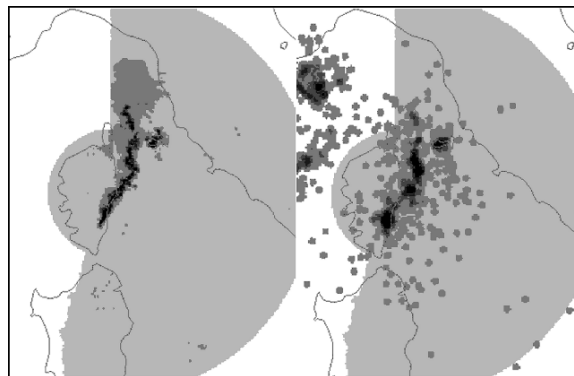


Fig. 6.7 Rain rate from radar scan, Aleria (France), *left*, and reconstructed rain rate from lightning detection, *right*; white areas signify no radar coverage, *light gray* areas are covered, *darker gray* corresponds to rain rates between 25 and 50 mm/h, while *black* corresponds to rain rates greater than 50 mm/h

University of Munich and nowcast GmbH, Munich. Some differences were found among the reported data sets, probably due to the different locating procedures.

LAMPINET requires at each sensor that the signal displays a certain wave-shape, otherwise it is discarded. LINET treats all signals at the sensor level and decides in the central processing unit whether a lightning stroke can be located. Despite the fact that the overall picture of lightning is correctly displayed by both networks, differences are found. An example is depicted in Fig. 6.8: the major part of location reports from LINET are well concentrated within cells, while the ones from LAMPINET are more diffuse, with reports of numerous isolated strokes in areas where LINET measured fewer or no events. When time-coincident signals are examined, it is found that isolated LAMPINET events are often positioned by LINET inside cells. Further tests will be carried out in order to clear up whether different location accuracy is causing the effect. It must be added that at the time of comparison LINET had only five sensors placed in northern Italy so that the finally

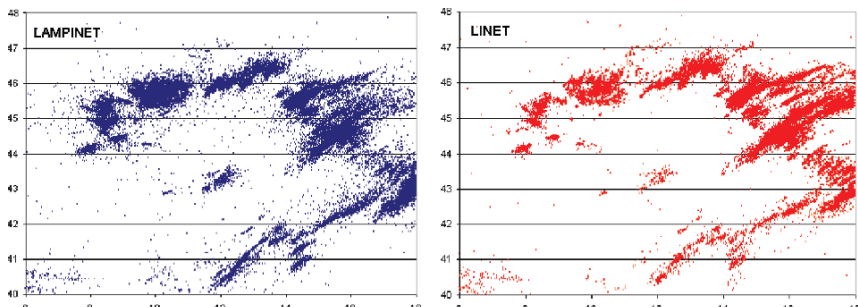


Fig. 6.8 Storm on 04 October 2006: stroke locations from LAMPINET (*left*, with 39200 strokes) and LINET (*right*, with 39700 strokes)

envisioned network density and, thus, efficiency, was not yet attained. It is concluded that the LAMPINET detection efficiency has to be monitored continuously to allow a reliable data assessment. It is necessary to maintain the sensors in operation, to keep stable functioning at all time, and to minimize periodic maintenance with dismounting and remounting of sensor parts. Furthermore, changes in the surrounding environment of sensors must be monitored. All together, one must conclude that inter-comparisons between lightning networks can be helpful in order to control data quality.

6.4 Lightning Statistics in Italy

Italy is positioned in the central Mediterranean area and every year the maximum in lightning activity occurs during summer, when the diurnal cycle maximises afternoon and evening convection, frequently accompanied by heavy rain, hail, and wind gusts. The month with most strokes is July, usually with nearly 2 million reported locations, while the less active period is the one from January to March, usually with a mean of 50000 reports each month. Figure 6.9 shows the monthly total of stroke reports for the period October 2005 – June 2007, whereby the light and dark grey colours signify the negative and positive polarity fraction, respectively.

Regarding the relation between the positive and negative fraction of the stroke database, it is seen from Fig. 6.10 that it varies between 9% (autumn) and 23% (summer). This wide range is plausible, when one considers the particular climatol-

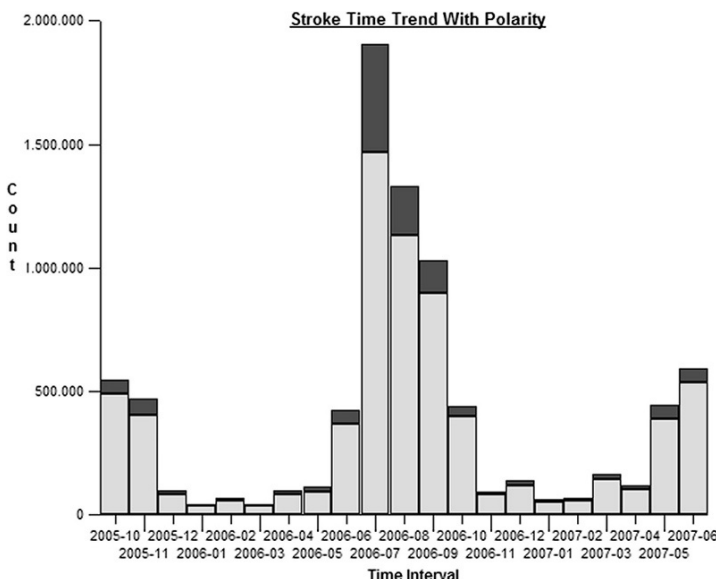


Fig. 6.9 Monthly number of LAMPINET strokes for Oct. 2005 – June 2007

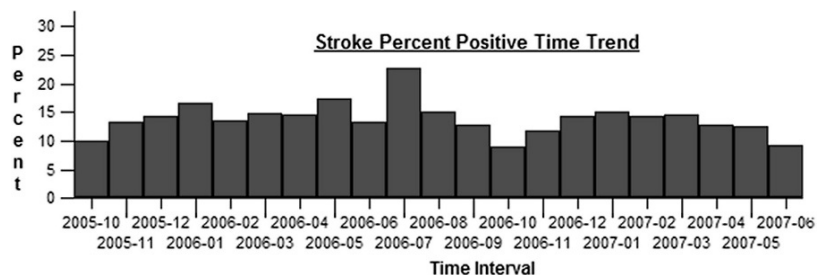


Fig. 6.10 LAMPINET strokes with positive polarity for Oct. 2005 – June 2007

ogy of the Italian peninsula. During summer, severe thunderstorms are generated on a daily basis, with formation of high towering cumulus and cumulonimbus. During autumn lightning activity is more correlated with the synoptic movement of atlantic depressions approaching from the east, producing instability, heavy rainfalls, and lightning activity concentrated in substantially lower-lying layers.

The different seasonal locations of discharges reflect the typical climate of a central Mediterranean country. Seasonal lightning density and peak current frequency with polarity are represented in Figs. 6.11–6.22. It becomes obvious, for example, that lightning density reaches 16 strokes/km² during summer for a large portion of Italian territory, while for wintertime a mean value of 0.5–1 strokes/km² is reported. The shown statistical results are based on data from the three-year period 2005–2007.

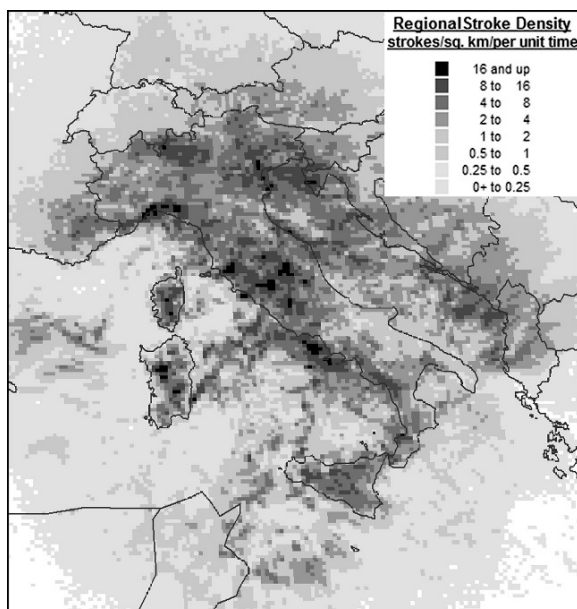


Fig. 6.11 LAMPINET stroke density over Italy in summer (strokes/km²)

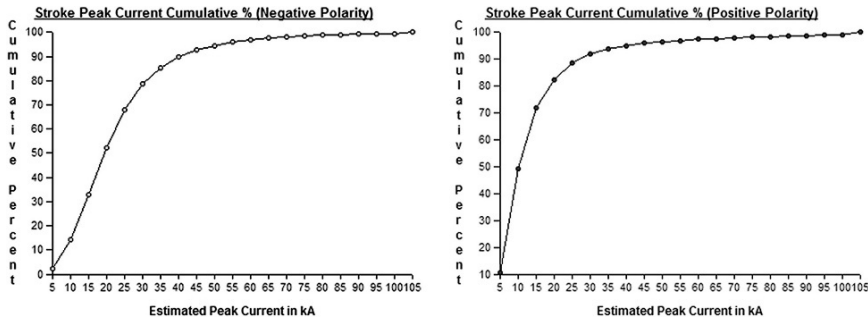


Fig. 6.12 LAMPINET stroke peak-current for Italy in summer, accumulated in percent, for negative (left) and positive currents (right)

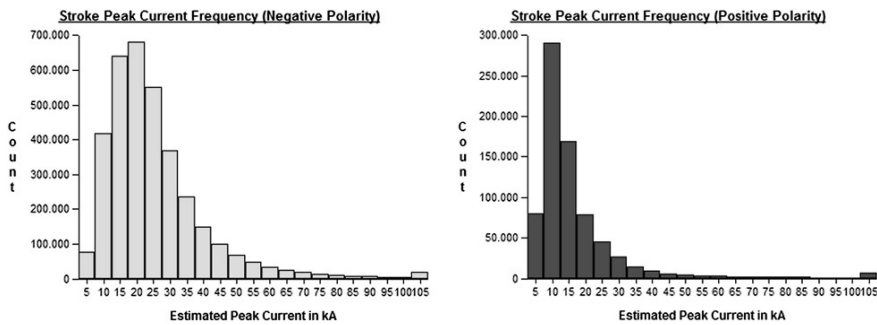


Fig. 6.13 LAMPINET distribution of range-normalized stroke currents over Italy in summer, for negative (left) and positive (right) polarity. The last column accumulates currents above 100 kA

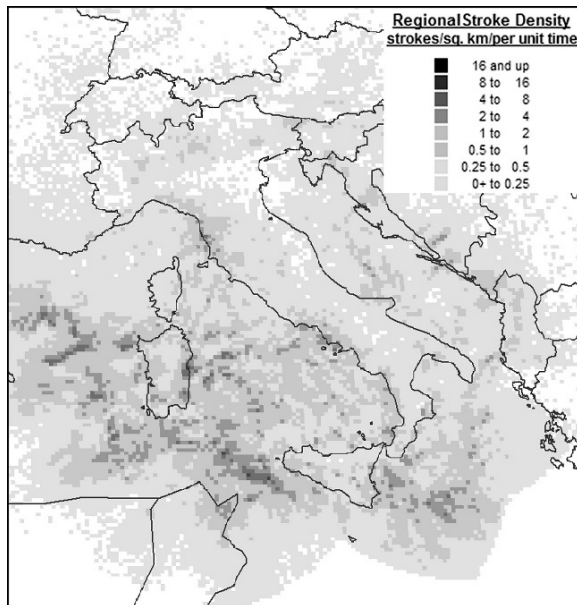
6.4.1 Lightning Statistics in Italy: Summer

During the summer (Fig. 6.11), lightning occurs principally over land, both along coastal or mountainous regions, where the moist air resides at low level and is lifted by heat due to hot soil or by orographic barriers, forming high towering cumulus and cumulonimbus that give rise to strong convection. The most active areas are Lake Como, Gulf of Trieste, Liguria and central Apennine, Gulf of Naples, and inland Sardinia. The more modest stroke density in summer over the sea in the Adriatic sector is due to very slow circulation of air mass. Accumulation of humidity then causes, frequently in summer afternoons, thunderstorms with some lightning activity.

Figure 6.12 report the stroke peak-current for summer, cumulative in percent. Among positive-polarity discharges, 70% (90%, 95%) have currents lower than 15 kA (27, 40 kA), respectively. For negative-polarity discharges, 70% (90%, 95%) have currents lower than 26 kA (40, 52 kA), respectively.

Figure 6.13 display the distribution of range-normalized stroke currents for the summer season (negative and positive polarity). In summer, LAMPINET may sometimes record nearly half million locations within a single day.

Fig. 6.14 LAMPINET stroke density over Italy in autumn (strokes/km²)



6.4.2 Lightning Statistics in Italy: Autumn

During autumn (Fig. 6.14) lightning activity is concentrated over the sea in the central and southern parts of Italy. The reason is that the hot summer warms up the sea, thereby releasing significant amounts of humidity into the cool autumn air; the condensation produces instability, convective clouds, and lightning activity over the southern part of the peninsula. Over northern Italy there is frequently a perturbation approaching from the Atlantic region, producing heavy rainfalls with only moderate lightning, localized especially along reliefs. Thunderstorm activity is also frequent along the coasts of Liguria and Tuscany, in the Gulf of Naples, the Sardinian sea,

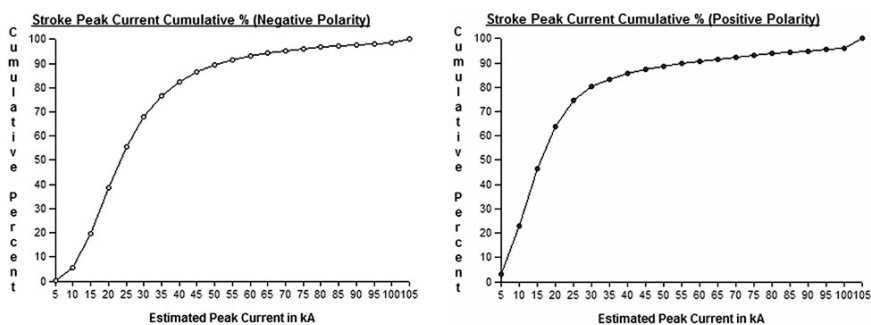


Fig. 6.15 LAMPINET stroke peak-current for Italy in autumn, accumulated in percent, for negative (left) and positive-polarity (right)

the central and southern Tyrrhenian sea, the strait of Sicily, and the southern Ionian sea (2–8 strokes/km²).

Figure 6.15 report the stroke peak-current for autumn, accumulated in percent.

Among positive-polarity discharges, 70% (90, 95%) have currents lower than 23 kA (55, 95 kA), respectively. For negative-polarity discharges, 70% (90, 95%) have currents lower than 31 kA (51, 70 kA), respectively. Figure 6.16 display the distribution of range-normalized stroke currents for the autumn season (negative and positive polarity).

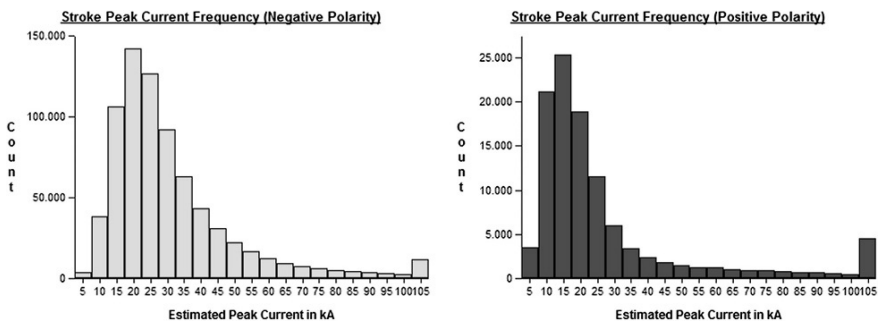


Fig. 6.16 LAMPINET distribution of range-normalized stroke currents over Italy in autumn, for negative (left) and positive (right) polarity. The last column accumulates currents above 100 kA

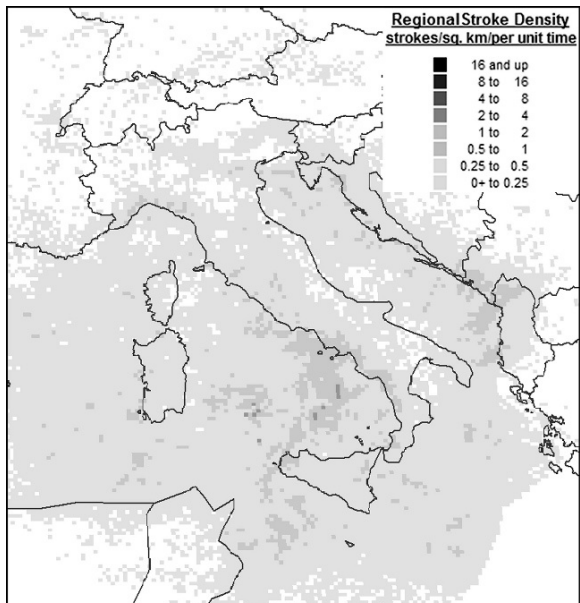


Fig. 6.17 LAMPINET stroke density over Italy in winter (strokes/km²)

6.4.3 Lightning Statistics in Italy: Winter

In winter lightning activity is low (Fig. 6.17), with maxima along the Tyrrhenian coasts, the strait of Sicily and the southern Adriatic sea ($0.5\text{--}1$ strokes/km 2).

Figure 6.18 report the stroke peak-current for autumn, accumulated in percent.

Among positive-polarity discharges, 70% (90, 95%) have currents lower than 50 kA (120, 170 kA), respectively. For negative-polarity discharges, 70% (90, 95%) have currents lower than 33 kA (63, 85 kA), respectively. Figure 6.19 display the distribution of range-normalized stroke currents for the winter season (negative and positive polarity).

6.4.4 Lightning Statistics in Italy: Spring

During spring lightning occurs more concentrated over the peninsula, the Adriatic area and the south-west Tyrrhenian sea, caused by the presence of cold air masses that face warm and humid fronts arriving continuously from the warmer Tyrrhenian

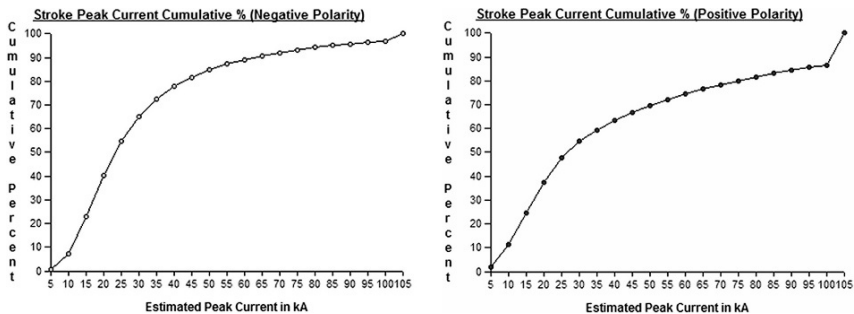


Fig. 6.18 LAMPINET stroke peak-current for Italy in winter, accumulated in percent, for negative (left) and positive-polarity (right)

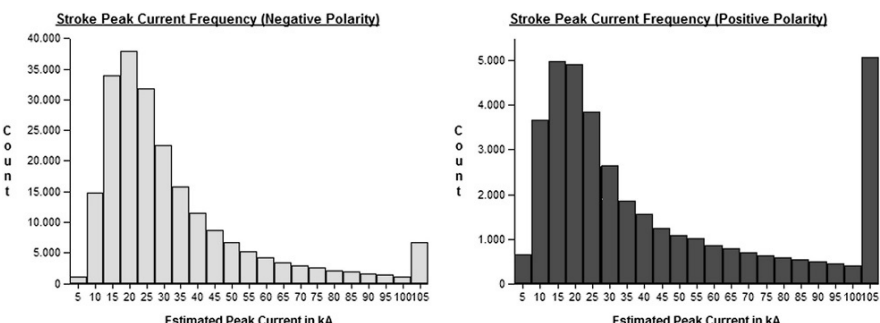


Fig. 6.19 LAMPINET distribution of range-normalized stroke currents over Italy in winter, for negative (left) and positive (right) polarity. The last column accumulates currents above 100 kA

Fig. 6.20 LAMPINET stroke density over Italy in spring (strokes/km²)

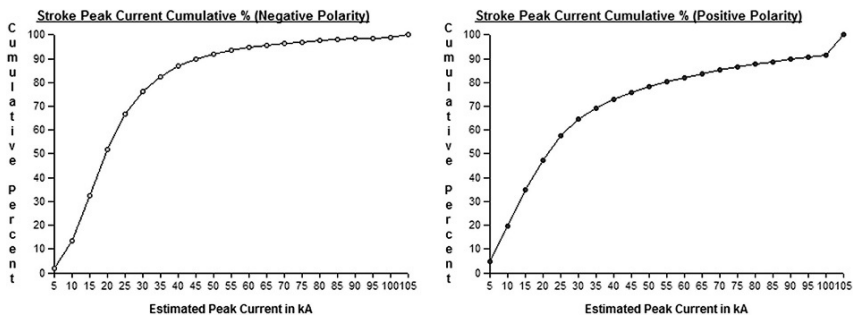
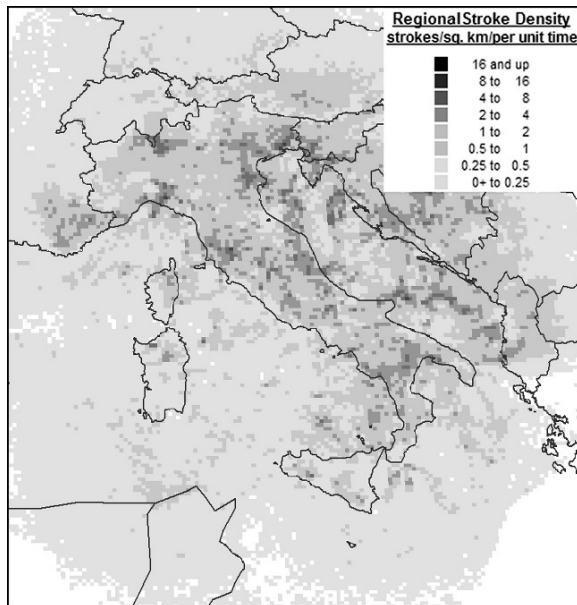


Fig. 6.21 LAMPINET stroke peak-current for Italy in spring, accumulated in percent, for negative (left) and positive-polarity (right)

area in the west. Low-level convective clouds are formed, often accompanied by discharges (Fig. 6.20). For the areas named, a mean value between 2 and 8 strokes per km² is observed, while for other basins and the two major islands, Sicily and Sardinia, the mean rate is near 0.5 strokes/km².

Figure 6.21 report the stroke peak-current for spring, accumulated in percent.

Among positive-polarity discharges, 70% (90, 95%) have currents lower than 36 kA (90, 120 kA), respectively. For negative-polarity discharges, 70% (90, 95%) have currents lower than 27 kA (45, 65 kA), respectively. Figure 6.22 display the distribution of range-normalized stroke currents for the winter season (negative and positive polarity).

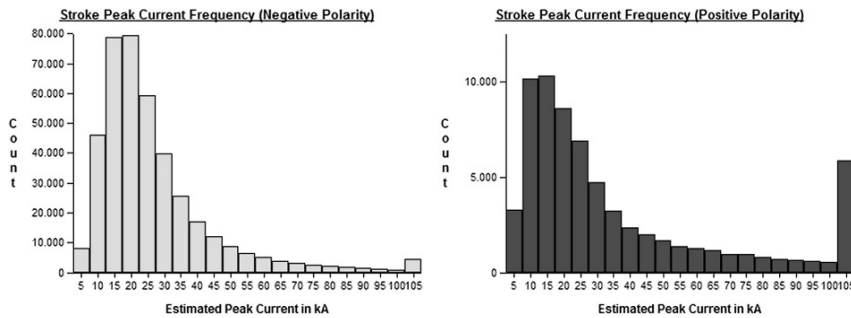


Fig. 6.22 LAMPINET distribution of range-normalized stroke currents over Italy in winter, for negative (*left*) and positive (*right*) polarity. The last column accumulates currents above 100 kA

6.5 Conclusions

For several reasons, the electromagnetic interaction of lightning with aircraft has received increasing interest in recent years. It has been described how lightning menace stimulated the Italian Air Force to arrange that the Italian Air Force Meteorological Service studies the phenomena and sets up adequate systems for monitoring the environment. The lightning detection network LAMPINET serves the needs of the Air Force and of a number of governmental institutions and commercial operators that benefit from direct and real-time lightning information. It has been shown that lightning-aircraft interaction is still a wide research field and that the IAF Meteorological Service continues lightning research and related operations. Finally, seasonal lightning statistics for Italy are discussed, based on data from the first three years of LAMPINET operation.

References

- Biron D., De Leonibus, The lightning network LAMPINET of the Italian Air Force Meteorological Service, proceedings of EGU 2005, European Geosciences Union, Geophysical Research Abstracts, Vol.7, 04340, 2005.
- Biron D., De Leonibus, Betz H.-D., Giorgi C., A lightning data comparison campaign, with locations produced by two different detection network in central Europe: LAMPINET and LINET, proceedings of ICOLSE 2007, EUROCAE, Paris 27–31 August 2007.
- De Leonibus L., Biron D., Laquale P., Zauli F., Melfi D., Rainfall field reconstruction over Italy through LAMPINET lightning data, proceedings of ILDC/ILMC 2008, Vaisala, Tucson 21–25 April 2008.
- Harris C.E., Starnes J.H., Shuart M., An assessment of the state-of-the-art in the design and manufacturing of large composite structures for aerospace vehicles, NASA TM-2001-210844 (2001). http://amelia.db.erau.edu/nasacds/200307Disc1/research/20030059016_2003065136.pdf
- Kostiuk P., Shapiro G., Hanson D., Kolitz S., Leong F., Rosch G., Bonesteel C., A method for evaluating the safety impacts of air traffic automation, NASA CR-1998-207673 (1998). http://ntrs.nasa.gov/archive/nasa/casi.ntrs.nasa.gov/19980137409_1998163307.pdf
- Rudolph T., Perala R.A., Interpretation methodology and analysis of in-flight lightning data, NASA CR 3590 (1982). 19830003391_1983003391.pdf, <http://ntrs.nasa.gov/search.jsp>

- Rudolph T., Easterbrook C.C., Ng P.N., Haupt W., Perala R.A., Experimental and analytic studies of the triggered lightning environment of the F106B, NASA CR 4104 (1987). 19880003515_1988003515.pdf, <http://ntrs.nasa.gov/search.jsp>
- Rudolph T., Horembala J., Eriksen F.J., Weigel H.S., Elliott J.R., Parker S.L., Perala R.A., Interpretation of F106B and CV580 in-flight lightning data and form factor determination, NASA CR 4250 (1989), 19890018744_1989018744.pdf, <http://ntrs.nasa.gov/search.jsp>
- Tapia A, Smith J.A., Estimation of convective rainfall from lightning observations, *J. Appl. Meteor.*, 37, 1497–1509 (1997).
- Uman M.A., Rakov V.A., The interaction of lightning with airborne vehicles, *Progress in Aerospace Sciences* 39 (2003) 61–81. <http://www.lightning.ece.ufl.edu/PDF/ProgressinAerospaceSciencespaper.pdf>
- Ciolli P., Utilizzo dei dati radar meteo e di fulminazione per il nowcasting dell'attività temporalesca, Thesis, 36° specialization course in atmospheric physics, (2006), Italian Air Force internal publication (in Italian).

Chapter 7

Lightning Detection in Spain: The Particular Case of Catalonia

Nicolau Pineda and Joan Montanyà

Abstract This chapter reviews the lightning detection in Spain. It focuses on the region of Catalonia (NE Spain), which has the particularity of being covered by two different lightning detection systems. Since 1992, the Spanish Lightning Detection Network provides the location and characteristics of the cloud-to-ground lightning activity for the whole country. In 2003, an interferometric detection system was installed in Catalonia, providing total lightning data for this region. The performance of this system was evaluated using experimental field measurements. Afterwards, the chapter summarizes some aspects of the lightning climatology in Spain and Catalonia. Finally, in the particular case of Catalonia, other aspects are reviewed, like the convective precipitation and the lightning relationship, and the total lightning activity in hail episodes.

Keywords Lightning detection · Interferometry · Lightning climatology · Convective precipitation · Total lightning · Hail

7.1 Introduction

Lightning detection technology has been used in Spain more than 100 years ago. The first lightning detection system in Spain dated from about 1904 where a kerauno-graph was installed at the Observatori de l'Ebre. More than 80 years had passed before a modern generation lightning detection system was installed. The Spanish Lightning Detection Network (SLDN) started in 1992 with fourteen magnetic-direction finding and time-of-arrival combined detection techniques in the low-frequency (LF) radio spectrum. Up to now the SLDN has been expanded several times and nowadays uses more than thirty sensors. The second lightning location network was the Catalan Lightning Detection Network (XDDE) initially composed by three very-high-frequency (VHF) interferometers able to detect intra-cloud

N. Pineda (✉)
Servei Meteorològic de Catalunya (Meteorological Service of Catalonia)
C/ Berlín 38–46, 08029 Barcelona, Spain
e-mail: npineda@meteo.cat

sources. With data of this network a number of interesting studies have been carried out, ranging from severe weather studies to the lightning activity related to transient luminous events (TLE). The importance of obtaining reliable information from the XDDE network motivated to conduct field campaigns in order to evaluate the detection efficiency, stroke discrimination and location accuracy (Montanyà et al., 2006). This evaluation was carried out by means of electrostatic, electric field and magnetic field measurements as well digital video recordings.

The SLDN allowed to study the lightning climatology in the country. One of the most comprehensive works is the analysis of a ten-year period of SLDN data by Rivas Soriano et al. (2005). The study shows how the cloud-to-ground (CG) lightning flash-density is primarily related to the orography and other factors like the general atmospheric circulation over the country, or sea temperature. The maximum lightning activity is found at the Pyrenees and the Iberian Range. Regarding coastal areas, the highest lightning activity tends to be located along the Mediterranean Sea, especially along the coasts of Catalonia. Special attention is given to Catalonia, the northeastern region of Spain, situated between the Pyrenees in the north and the Mediterranean Sea in the east. The lightning climatology in Catalonia was studied by means of the XDDE with its five years of operation and the annual thunderstorm days (T_D) registered since 1910. The results show that the annual average of T_D analyzed in the Catalan region ranges from 9 to 46 thunderstorm days. Monthly thunderstorm activity is discussed, including characteristic regional and daily variations.

As thunderstorms produce rainfall and lightning, the relation between them arouses interest of many researchers. For the Iberian Peninsula, Rivas Soriano et al. (2001b) analyzed the rain yield for a period of three years, finding a typical value around $\sim 1 \cdot 10^8$ kg per CG flash. In a first detailed study in Catalonia, Pineda et al. (2007) studied nine convective events where rain rates were obtained from the analysis of meteorological radar. The mean value of the rainfall-lightning ratio resulting for these events was $38.9 \cdot 10^3 \text{ m}^3 \text{CG}^{-1}$, which is very close the ratios calculated in other areas (Buechler and Goodman, 1990; Tapia et al., 1998; Soula and Chauzy, 2001; Seity et al., 2001; Kempf and Krider, 2003). This chapter includes an extended analysis of 35 thunderstorms during the period from June to October. It will be seen that the ratio increases in the middle of September. This change is due to the origin of the storms. While during late spring and early summer thunderstorms mainly originate inland, in late summer and autumn thunderstorms originate over the sea. The warm and humid conditions over the Mediterranean promote the formation of highly efficient rainfall structures, which are characterized by lower cloud developments and a lower lightning activity. This change in the rainfall regime is reflected in a higher rainfall volume per CG flash.

At the end of this chapter the highlights of the total lightning activity in hail-bearing thunderstorms observed in Catalonia are presented. Several cases of severe thunderstorms that occurred in Catalonia have been reported in different works (Montanyà et al., 2006, 2007a, b). In these cases, the severe storms were characterized by large hailstones (up to 40 mm) and produced a remarkable increase in IC activity before severe weather was reported on ground. These storms had low CG

flash rates (typically much lower than 2 min^{-1}) and practically no CG activity when the presence of hail was suspected from high radar reflectivity and ground in-situ observations. An interesting feature in all of the observations was that during the periods when +CG flashes occurred, -CG flashes presented low peak currents and their multiplicity was strictly one. The case analyzed by Montanyà et al. (2007b) displayed a large amount of -CG flashes with very low peak currents and low multiplicity values. In that case, by considering all -CG detections of the SLDN, the median value of the peak current was close to -5 kA and the average multiplicity was practically 1. But the analysis of the evolution of different lightning flash categories showed how the rate of the -CG flashes with low peak currents ($< 10 \text{ kA}$ in absolute value) evolved very similarly to that of the IC flashes and differently to those with higher peak currents ($> 10 \text{ kA}$ in absolute value). That could indicate a misclassification of IC flashes by SLDN. To support this hypothesis it may be necessary to assume the storm had an inverted-polarity charge structure. Among the IC flashes detected by the XDDE, a large amount (higher than 31%) were 1-VHF source events, which indicate short propagation lightning events.

7.2 Early Measurements

The first references of lightning measurements in Spain date from 1904, just after the foundation of the Observatori de l'Ebre (near the Ebro river delta). This observatory was founded with the aim of improving knowledge on the interaction between

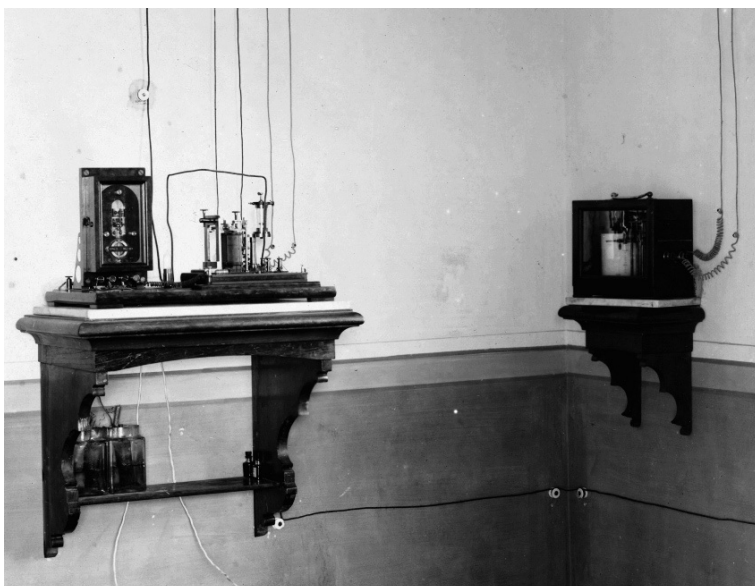


Fig. 7.1 Keraunograph of the Observatori de l'Ebre in 1908. Photograph provided by J.M. Torta

sun-earth electrical and magnetical influences. For several years the Observatory's electrical department measured atmospheric electrical potential gradient and air ionization. In all probability, the first remote lightning detector device in Spain was a keraunograph based on a cohesor (Fig. 7.1), which was used at the Observatory for recording distant lightning activity (García Mollá, 1910).

7.3 The First Modern Lightning Detection Network

In January 1992, more than 80 years after the first remote lightning detection measurements, the National Institute of Meteorology (INM) started to operate the Spanish Lightning Detection Network (SLDN) (Fig. 7.2). This network was started with fourteen sensors, distributed over the Iberian Peninsula and Balearic Islands. Their low-frequency combined with magnetic-direction finding and time-of-arrival sensors are similar to those employed by the NLDN in the United States. In 1996 the coverage and performance were improved by sharing sensors with the French network. In 2003 the network capabilities were expanded by sharing four sensors with the Portuguese network. The last expansion of the SLDN was in 2005, when the coverage was extended to cover the Canary Islands through the REDRIM project (Pérez Puebla, 2005).

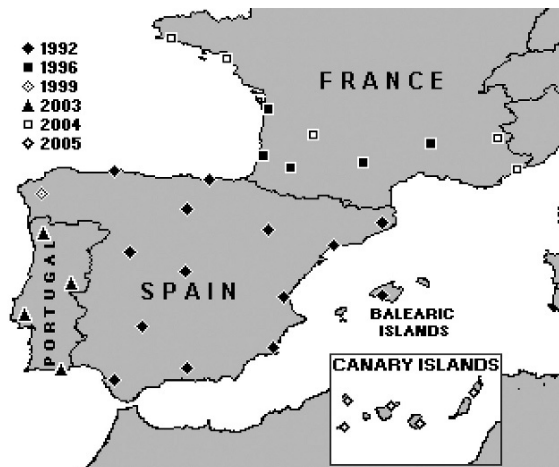


Fig. 7.2 Evolution of the number of sensors used by the SLDN since the network was setup in 1992

7.4 Detection of Total Lightning: The SMC Network

The Catalonia Meteorological Service (SMC) operates a total lightning SAFIR system (hereafter XDDE) which covers the area of Catalonia in the NE of Spain (Fig. 7.3). The system is composed of three detection stations that provide 2-D

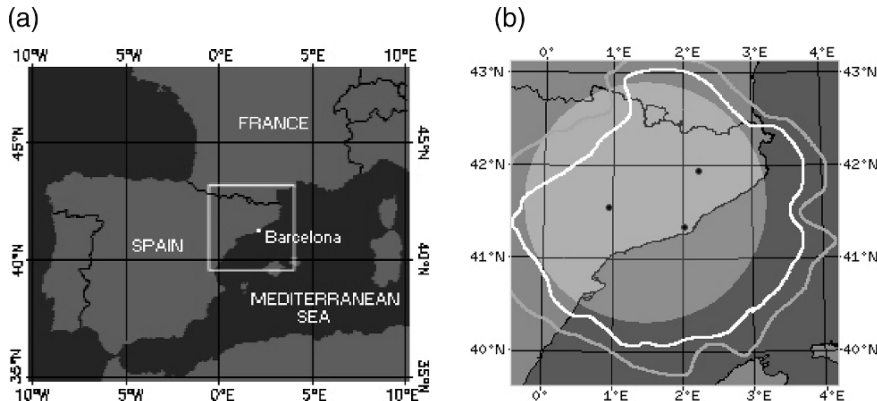


Fig. 7.3 (a) Region of the XDDE coverage in NE Spain. (b) XDDE detection stations (*black dots*) and the 99% limits (*white line*) and 90% (*grey line*) in theoretical detection efficiency areas

location of VHF sources produced by any lightning flashes (intra-cloud and cloud-to-ground).

The SAFIR system (Richard and Lojou, 1996) uses an interferometric technique in the VHF range (108–116 MHz). The VHF sources detected are attributed to the same flash when they are separated by less than 7 km and less than 100 ms. The detection of cloud-to-ground (CG) return strokes is performed in the LF range. Strokes are grouped into CG flashes considering a multiplicity delay of 0.5 s in a radius of 7 km. The SAFIR system then discriminates intracloud (IC) and CG flashes by comparing VHF and LF records.

7.4.1 Experimental Network Evaluation Methods

A common concern for lightning detection system operators is the evaluation of its performance. Detection efficiency, stroke discrimination and location accuracy are the major issues to be evaluated. In addition to theoretical methods which involves reprocessing historical data, experimental in-situ electric field measurements and video recordings mean a further step in the verification of lightning detection network performance.

The XDDE has been experimentally evaluated with two field measurement campaigns, performed in the summers of 2004 and 2005 (Montanyà et al., 2006). The CG flash detection efficiency of the XDDE was found to be between 86 and 92%, in agreement with the SAFIR manufacturer specifications. The methodology undertaken was based on: (i) electrostatic field measurements in order to validate the short range lightning flash detection efficiency; (ii) slow-electric field recordings, used with the aim to discriminate the CG flash strokes; and (iii) video recordings, which allow for the evaluation of stroke efficiency and location accuracy.

7.4.1.1 Lightning Flash Efficiency

It is well known that lightning flashes cause abrupt step changes in the electrostatic field in the vicinity of a thunderstorm. The measurement of these changes is used to infer the charges related to a flash and its location. Moreover, these electric field changes are also used to evaluate flash detection efficiency. Figure 7.4 shows an example of the electrostatic field evolution and some of the aforementioned electric field changes.

The experimental detection efficiency analysis in 12 episodes resulted in efficiencies ranging from 82% to almost 98%. Those are consistent with the theoretically inferred efficiency for the XDDE. However, this analysis does not take into account detected flashes that were not appropriately geo-located. A method to include these cases is outlined in Figure 7.5 where three different situations are considered: i) a flash located within a range that produced a consistent electric field change; ii) a flash located within a range of 10 km that produced an abnormally low electric field change; and iii) a flash located within a range that did not produce an appreciable electric field change. Consistent electric field changes are checked by a single charge point model. The experimental short range analysis of the XDDE produced a reduction of around 10% in the detection efficiency percentages, ranging from 70 to 93%.

7.4.1.2 Stroke Discrimination

Experimental stroke discrimination can be conducted in different ways. Electric field changes, derivative magnetic fields and video recordings were analyzed and compared with the multiplicity and polarity assigned by the network. Video record-

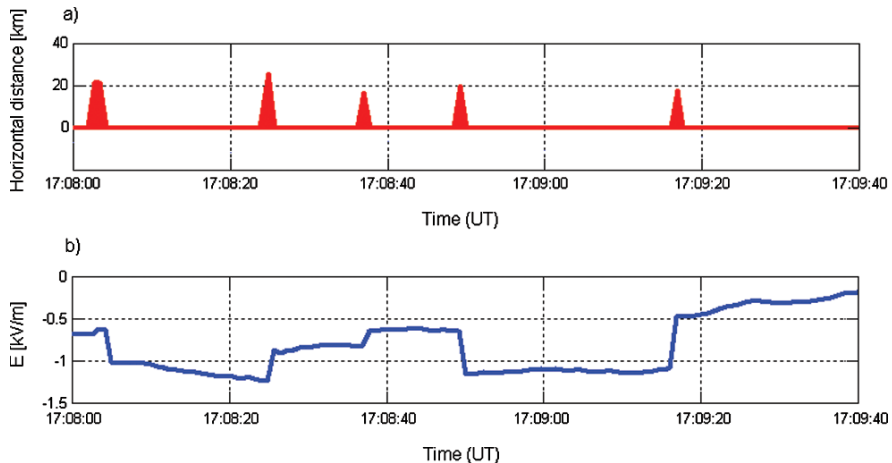


Fig. 7.4 (a) Distances between XDDE detections and the measurement site; and (b) Electrostatic field evolution during a storm

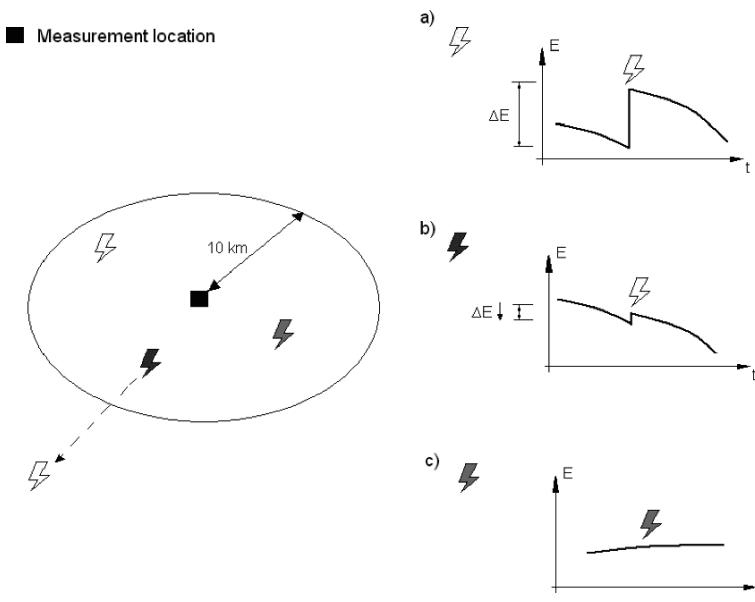


Fig. 7.5 Ten kilometer range location analysis: (a) flashes located within 10 km that produced a predicted electric field change ΔE ; (b) flashes located within 10 km that produced a very low electric field change ΔE ; and (c) flashes located within 10 km that did not produce an appreciable electric field change ΔE

ings are valuable in order to group strokes in a CG flash. Figure 7.6 displays the electric and magnetic field records corresponding to a cloud-to-ground flash (CG).

An example of the strokes obtained by image recordings is displayed in Fig. 7.7. This shows a sequence of five strokes with two strike points. Normal video cameras have 25 or 30 frames per second meaning that the duration of the frames is of 20 ms and 16.7 ms respectively, if video is deinterlaced. Since the median time between strokes is 33 ms, ranging from 7 to 150 ms, the aforementioned frame rates are not appropriate for fine stroke discrimination. Nowadays faster digital cameras are available as well as time stamp systems which insert GPS time to the images.

7.4.1.3 Permanent Quality Control

Permanent data quality control is performed for the XDDE data. The aim of permanent quality control is to give a level of reliability to the data obtained. The typical problems experienced in processing data are mostly due to: continuous repetition of strokes at the exact same location during storms; high frequency of bipolar flashes; high presence of positive flashes; high presence of low peak current negative strokes; and wrongly located strokes. Most of these problems are due to measured waveform characterization and sensor problems such as the malfunction of one of the detection stations. Some typical problems related to polarity are due to misclassification of ground flashes that were in fact cloud flashes (IC). Those misclassified IC appeared

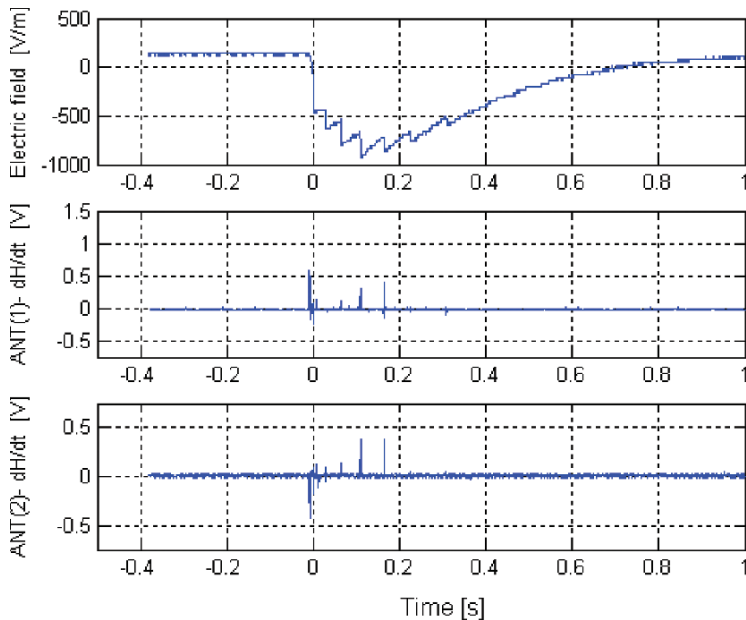


Fig. 7.6 Electric field changes and derivative magnetic field pulses related to individual strokes in a flash. Derivative magnetic field units are in [V] corresponding to the antenna amplifier output

as CG strokes with low peak currents of both polarities (typically less than 10 kA in absolute value). Other problems related to locations are due to those strokes near the boundaries of ‘shadow’ regions. Shadow regions are those regions which, due to the detection technique and the network geometry, the network is not able to appropriately locate the strokes. In the XDDE post-processing quality control a code number is assigned to each detection indicating a certain level of uncertainty due to such described occurrences.

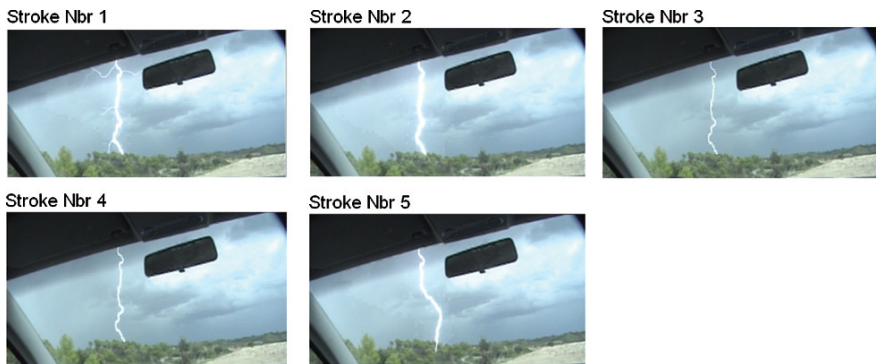


Fig. 7.7 Sequence of five strokes for a same lightning flash with two strike locations recorded during 2004 campaign

7.5 Lightning Climatology in Spain

Different approaches to lightning climatology in Spain can be found in literature. Some works focused on the analysis of cloud-to-ground lightning characteristics of the SLDN data (Rivas Soriano et al., 2001a, 2005; Pérez and Zancajo, 2008). Others introduce the relationship between lightning and convective precipitation (Rivas Soriano et al., 2001b) or with circulation weather types (Tomás et al., 2004). Figure 7.8a shows the keraunic level for the Iberian Peninsula for the period of 2000–2007 (Pérez Puebla, 2005) and Fig. 7.8b shows the annual average of CG flash density for the period 1992–2001 (Rivas Soriano et al., 2005).

Lightning in the western Mediterranean Sea (the part covered by the SLDN) has also been studied through general analysis (De Pablo and Rivas Soriano, 2002) or through analysis of significant convective events (Tudurí and Ramis, 1997; Correoso et al., 2006).

According to Rivas Soriano et al. (2005) who analyzed a ten-year period of SLDN data (1992–2001), while lightning activity exhibits a strong year-to-year variability, some climatic patterns can be drawn from their analysis. The yearly cycle shows a clear difference between winter and summer months, being related to the annual cycle of surface air temperature. The lightning season starts in May and lasts until September. More than 80% of annual CG flashes take place during these five months. Lightning activity increases from April to June, reaching its peak in the summer months and sharply decreases after September. The average daily cycle shows an increment after mid-day, with a peak in the afternoon, indicating a clear response of convection to the diurnal cycle of solar radiation.

Looking at the average CG flash density distribution over ten years found by Rivas Soriano et al. (2005) (Fig. 7.8b), it is interesting to note that the pattern is primarily related to orography. Besides this, other factors like the general atmospheric circulation over the Iberian Peninsula (hereafter IP), or sea temperature, modulate

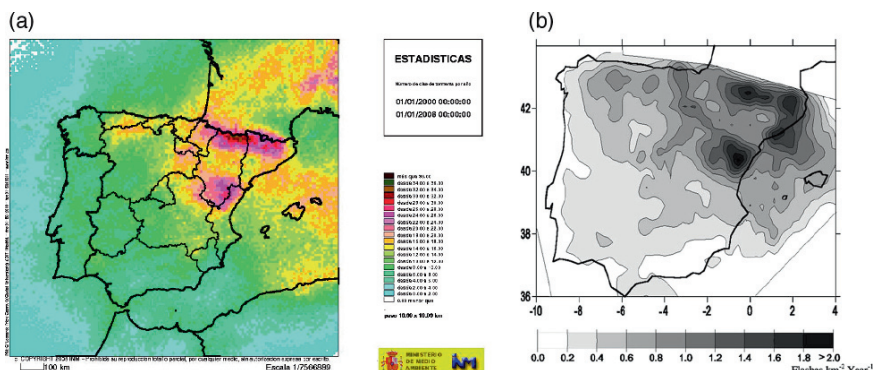


Fig. 7.8 (a) Annual average of the number of thunderstorms days per year in the Iberian Peninsula (2000–2007), from (Pérez and Zancajo, 2008) with permission from AEMET; and (b) Annual average of the CG flash density (1992–2001), from Rivas Soriano et al. (2005) with permission from Elsevier (See also Plate 7 in the Color Plate Section on page 596)

this pattern. Lightning activity tends to concentrate over the Northeastern IP. Maximum lightning activity is found in the Pyrenees and the Iberian Range. Finally, other mountainous areas contribute to the overall spatial distribution, but in those areas densities are somewhat lower.

Looking at IP coastal areas, the highest lightning activity tends to be located in the Mediterranean coastal area, specially the Catalan coast, with densities of some magnitude along the Atlantic coast or the southern Mediterranean coastal areas. The Mediterranean sea supplies warm and humid air through onshore breezes, especially during autumn. After the summer air masses over the Mediterranean remain warm and humid and the thermodynamic atmospheric background becomes very appropriate for convection (Romero et al., 2001).

Tomás et al. (2004) analyzed the relationship between circulation weather types and the CG flash density distribution in the IP over a nine-year period. They found that the highest percentages of CG flashes are related to cyclonic situations, although they are not the most frequent. These cyclonic situations are due to the entry of low pressure that affects the north of the IP, also producing flows from the E and the SE over the Mediterranean coast, especially in autumn. Situations with an easterly component (NE, E, SE) also generate an important percentage of annual lightning. Easterly situations are the dominant flow in the summer months, and the flows of warm and humid air associated to these situations cause the highest flash frequency in mountainous zones of the Peninsula.

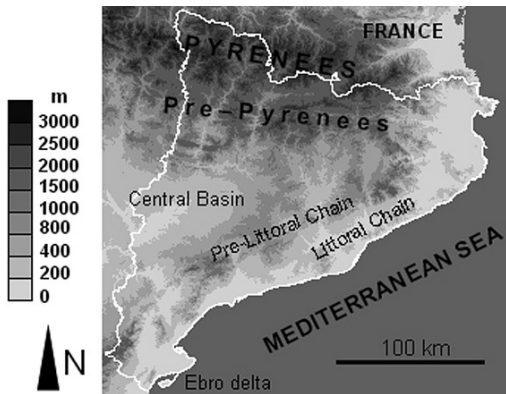
7.6 Lightning Climatology in Catalonia

Catalonia has a surface area of approximately 32 000 km² and is located in the Northeast of the Iberian Peninsula. Although it is a relatively small area, it has high climatic variability with strong contrasts, due to its relief, its proximity to the Mediterranean Sea, its geographical situation and because it also receives Atlantic influences. To the East it borders with the Mediterranean Sea, to the North with the Pyrenees, and to the West with the Ebro river valley. The Pyrenees and Pre-Pyrenees mountain ranges boast the highest altitudes in the country. The rest of the area is made up of the Central Basin (inland areas of the country), and the coastal and Pre-coastal mountain chains (parallel to the Mediterranean coast). Figure 7.9 shows these main orographic features.

7.6.1 Temporal Lightning Distribution

In the five year period between 2003 and 2007 the XDDE recorded around 85.000 CG flashes per year over Catalonia. In spite of the fact that thunderstorms occur somewhere in Catalonia on an average of 127 days per year, 80% of the CG flashes were recorded on an average of only 26 days. Every month registered thunderstorms, but thunderstorm activity was higher from April to October. 99% of CG flashes are

Fig. 7.9 Main orographic features of Catalonia



concentrated in these seven months. Activity increases continually from April to August, a month that registers 30% of CG flashes for the whole year with more than 25.000 CG flashes as its five year average (Fig. 7.10).

The annual thunderstorm season starts inland in late April or early May, affecting mainly the Pyrenean region. During these months there is little thunderstorm activity above the sea area covered by the XDDE, with only 5% of CG flashes. In July and August thunderstorms become more intense and affect the entire region not only the mountainous areas. In August an average of almost 1400 CG flashes were recorded every thunderstorm day over Catalonia in the analyzed five year period. During September thunderstorms are still intense (more than 1000 CG per thunderstorm day) but the spatial pattern begins to change and thunderstorms tend to be located near the Mediterranean coast and offshore. In October and November thunderstorms occur mainly offshore, concentrating near the coast. CG flashes over the sea covered by the XDDE in September and October represented 59% of the average annual number of CG flashes over the sea. Rivas Soriano and De Pablo (2002)

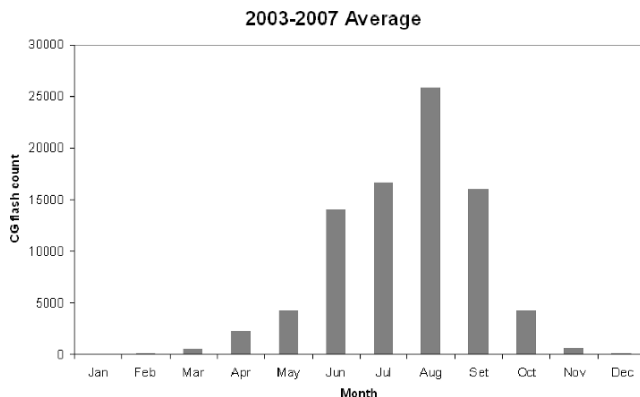


Fig. 7.10 Monthly average of the number of cloud-to-ground flashes in Catalonia for the 2003–2007 period

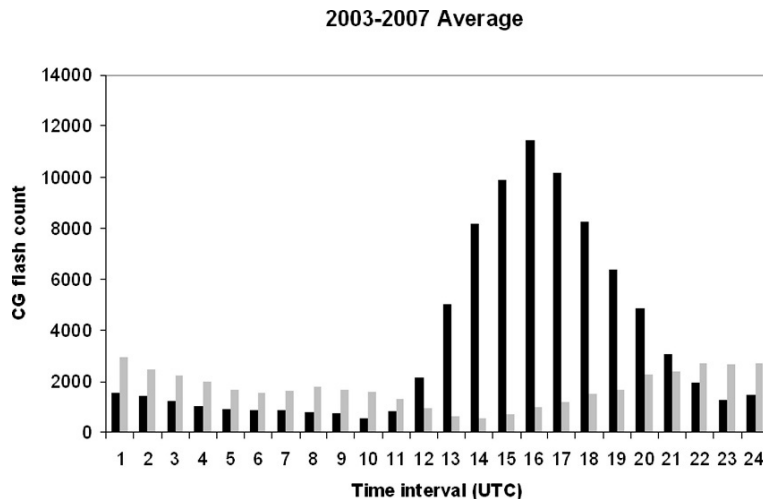


Fig. 7.11 Annual average of the daily time trend of the CG flash count in Catalonia (black) and in its contiguous sea (grey) for the 2003–2007 period. Local Solar Time is UTC+2 in summer and UTC+1 in winter

studied approximately the same sea region (period 1992–1994), with SLDN data and obtained a similar CG flash proportion for September and October over the sea (60%). They related the annual CG flash distribution to the annual Mediterranean Sea surface temperature distribution, which reaches its maximum in September.

Concerning daily variation of lightning activity, Fig. 7.11 shows the daily time trend over Catalonia and over its contiguous sea. It can be seen that land and sea areas show a quite different pattern. Over land, lightning distribution is associated with the solar radiation daily cycle. Ordinary convective cells develop almost every afternoon during summer over Pyrenees and Pre-Pyrenees region. These storms are normally the result of intense solar heating which destabilizes the boundary layer, activating upslope and valley wind systems and the inflow of maritime air through sea-breeze circulations (Alonso et al., 1994). The daily time trend for Catalonia found for the years 2003–2007 was similar to the one reported in Rivas Soriano et al. (2005) for the whole Iberian Peninsula.

Over the sea lightning activity is rather regularly distributed throughout the day, while there is more activity at night. September and October are the months that have the highest night maximums. Such results agree with the previous analysis done in the same area by Rivas Soriano and De Pablo (2002).

7.6.2 Spatial Lightning Distribution

The annual number of thunderstorm days (T_D), also known as keraunic level, is one of the parameters that can be calculated to analyze the spatial distribution of

thunderstorm activity. Thunderstorm-days data is recorded at weather stations by human observers on a local basis. However this parameter can be also calculated nowadays using remote lightning sensing detection systems. In order to be able to compare estimations of T_D from observers with the T_D estimated from lightning detection networks, the T_D should be calculated in a similar resolution. As the range of audibility of thunder is between 15 and 25 km, it seems reasonable to calculate T_D from lightning detection in a grid of 20×20 km. Using this mesh, T_D was calculated for the region of Catalonia and its contiguous Mediterranean Sea area (Fig. 7.12) for the period 2003–2007. The annual average of T_D ranges from 9 to 46 thunderstorm days, with a mean of 27 for the whole region. However T_D in the upper right cells of the analyzed region is very low, as a result of the low efficiency of the XDDE in this area (see Fig. 7.3b). The spatial distribution of T_D is mainly related to geography, with higher values for the Pyrenean and Pre-Pyrenean areas. The higher values in the lower left side correspond to thunderstorms that originated in the Iberian Range and often move to this area.

Although T_D records from manual stations are a spatially discontinuous series of data, they constitute the only parameter related to lightning available worldwide and which extends over many decades. The spatial distribution of T_D that can be currently obtained from lightning detection networks can be helpful in inferring a better spatial lightning distribution in past decades from manual T_D records.

The SMC is currently working on the digitalization and validation of a lengthy series of data from weather stations in Catalonia, including T_D series (Herrero et al., 2007; Rius et al., 2008). As an example, T_D records from the weather station at the Observatori de l'Ebre are presented in Fig. 7.13. This T_D series starts in 1910,

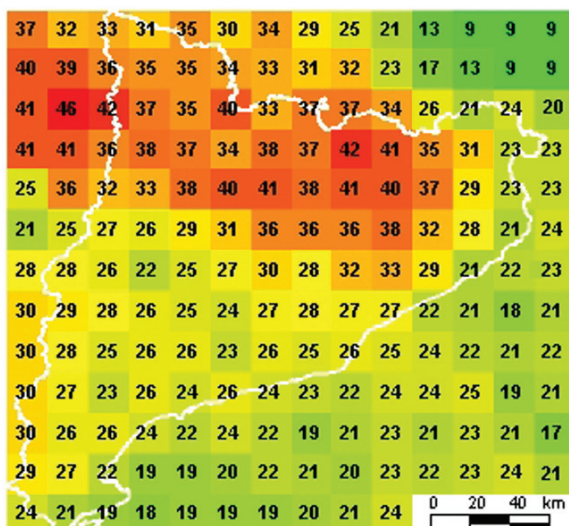


Fig. 7.12 Annual average (2003–2007) of the number of thunderstorm days in Catalonia, calculated in a 20×20 km mesh basis (See also Plate 8 in the Color Plate Section on page 597)

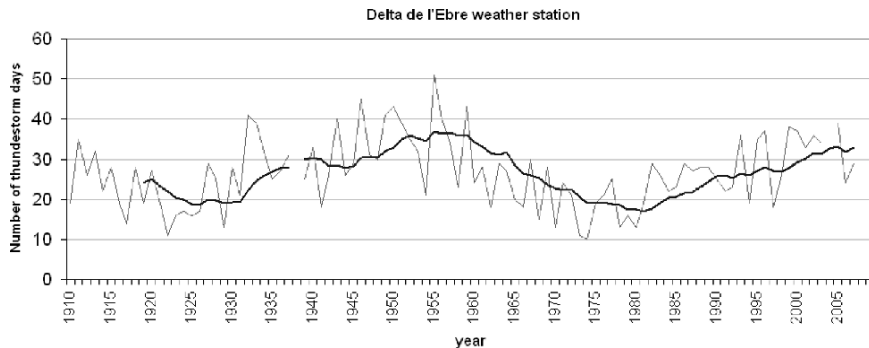


Fig. 7.13 Thunderstorm days recorded at the Observatori de l'Ebre weather station from 1910 to 2007. The bold line is the ten-year running average

with only a few short interruptions until the present day. The 98-year T_D series has an average of 26 thunderstorm days per year, although it shows a strong year-to-year variability. The ten-year running average moves in a range window between 17 and 37 T_D , exhibiting important differences between decades in the number of thunderstorm days per year.

From the XDDE, an average of 27 thunderstorm days was obtained in the area of 20×20 km, where the Observatori de l'Ebre is placed. From manual observations a mean of 31 T_D was obtained for the same period (2003–2007). Further analysis should be done in order to find the appropriate mesh to be used in the XDDE T_D calculations and so as to be able to compare the results with the T_D weather station records.

Finally, the inter-annual cloud-to-ground flash density (Ng) for Catalonia presents a pattern similar to T_D , with higher values in the Pyrenees and the Pre-Pyrenees region, and lower values in the Central basin and in coastal areas. The average for Catalonia for the period 2003–2007 is of $3.0 \text{ CG flash } \text{km}^{-2} \text{ yr}^{-1}$.

7.6.3 Temporal and Spatial Lightning Patterns

The lightning daily time trend and the T_D spatial distribution in Catalonia were analyzed through a clustering technique in order to identify areas with similar convective triggering mechanisms.

A hierarchical agglomerative clustering (Fraley and Raftery, 2003) was used to classify the 20×20 km cells in which the region of interest was divided (Fig. 7.12). This method allows for analyzing the main patterns in the thunderstorm daily variation, as well as the behavior of thunderstorms on a more detailed scale. Two outputs of the clustering are represented in Fig. 7.14. Labels A and B correspond to a two-category classification, while the sub-indexes added to this two main categories correspond to a classification into seven categories. Table 7.1 presents the average T_D for the seven categories classification.

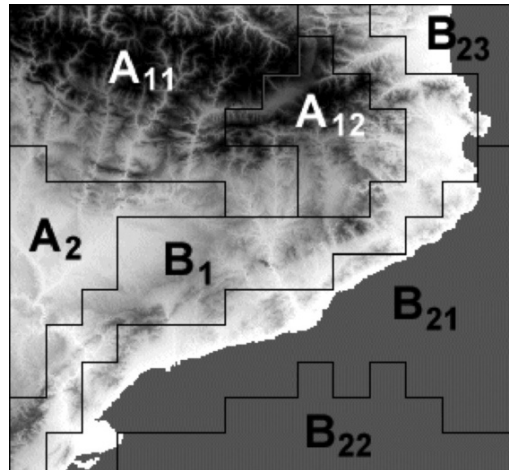


Fig. 7.14 Categories of two hierarchical clustering classifications. The two-category classification is labeled A and B. The seven-category classification is labeled with A,B and sub-indexes

Table 7.1 Average Thunderstorm Days (T_D) per category

Cluster	A ₁₁	A ₁₂	A ₂	B ₁	B ₂₁	B ₂₂	B ₂₃
T_D 03–07	34	36	29	27	22	20	23

The two main categories arising from the clustering classification (A and B) are related to the two major factors that determine the spatial distribution of the thunderstorms in the region, the complex orography of Catalonia, and its proximity to the Mediterranean Sea. The mountain and inland region (category A) is linked to orography, where thunderstorm activity is at its highest, with a sharp daily solar heating pattern. Category B is related to the Mediterranean Sea influence, showing a rather uniform pattern throughout the day. As more categories are considered in the hierarchical clustering, it can be seen that the two main categories are sub-divided in more local categories. On one hand category B splits into B₁ and B₂. B₁ is located inland and combines the inland pattern of thunderstorms with the influence of the adjacent sea. B₂ corresponds to the pattern of thunderstorms over the sea. Figure 7.15 shows the annual average of 3-hour period thunderstorm days for categories A, B₁ and B₂.

On the other hand, category A splits first into A₁ and A₂, and afterwards A₁ splits into A₁₁ and A₁₂. A₂ corresponds to the Central basin region, while A₁₁ and A₁₂ separate the Pyrenees into two different behaviors. The difference between these two categories is shown in Fig. 7.16, where it can be seen that thunderstorm activity starts earlier in the afternoon in the eastern part of the Pyrenees (A₁₁). Such behavior is related to the sea breeze, which has a major influence in this Mediterranean closeness area of the Pyrenees.

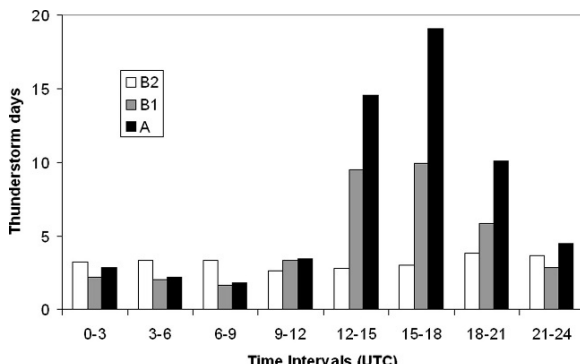


Fig. 7.15 Average thunderstorm days for the 3-hour periods for categories A, B₁ and B₂

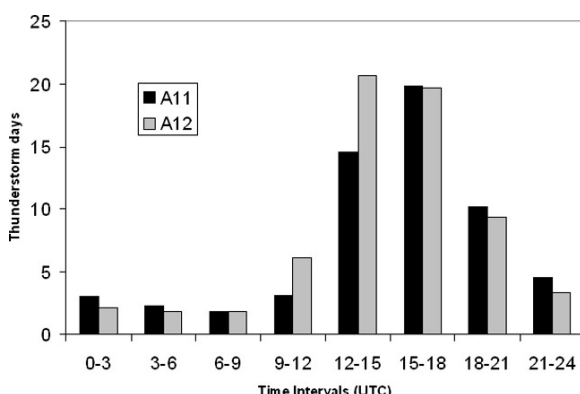


Fig. 7.16 Average thunderstorm days in 3-hour periods for categories A₁₁ (Eastern Pyrenees) and A₁₂ (Western Pyrenees)

7.7 Convective Precipitation and Lightning Relationship

The relations between convective precipitation and lightning have been discussed in many papers (see compilation by Rakov and Uman, 2003). As thunderstorms typically produce both rainfall and lightning, the relation seems obvious. Though qualitatively undeniable, qualitative relations are being studied and are still not well understood.

Considering the bibliography about the relationship between convective precipitation and lightning, two types of approach can be distinguished. On one hand, rain yields (ratio of rain mass to cloud-to-ground flash over a common area) has been calculated for long temporal and spatial domains and using rain-gauge records to estimate the amounts of precipitation (e.g. Petersen and Rutledge, 1998; Sheridan et al., 1997). On the other hand, a case-by-case approach has been used in many studies to analyze the relationship between convective precipitation and lightning in

individual storms, using weather radar data to estimate rainfall volumes (eg. Tapia et al., 1998; Soula and Chauzy, 2001).

Rivas Soriano et al. (2001b) analyzed rain yield for the Iberian Peninsula, using 3 years of data from the SLDN and precipitation data from 68 meteorological observatories distributed around the IP. Rain yield values obtained for the warm season (Jun–Aug) are centered around $\sim 10^8$ kg per CG flash, which are similar to those obtained by Petersen and Rutledge (1998) for the continental United States. They have also found different values for the two main climate regimes in which they divided the IP.

Considering a local thunderstorm case study approach, the relation between rainfall and lightning is usually quantified as the Rainfall-Lightning ratio (RLR). This ratio estimates the convective rainfall volume per cloud-to-ground lightning flash (Tapia et al., 1998). According to a summary provided by Kempf and Krider (2003) about studies where precipitation was estimated using radar, RLR ranged from 38 to $72 \text{ } 10^3 \text{m}^3$ per CG flash for isolated thunderstorms (Southeastern and Central United States, Florida, France and Spain). Other studies found values for isolated thunderstorms ranging from 14 to $35 \text{ } 10^3 \text{m}^3 \text{CG}^{-1}$ in China (Zhou et al., 2002) and from 3 to $33 \text{ } 10^3 \text{m}^3 \text{CG}^{-1}$ in the Pyrenees (Molinie et al., 1999).

Intense storms tend to produce lower RLR values than moderate storms, but the range of RLR found in diverse studies is quite wide (Rakov and Uman, 2003). This relationship apparently depends on thunderstorm type, local climatology and other meteorological factors such as the convective regime (Williams et al., 1989; Tapia et al., 1998; Seity et al., 2001; Lang and Rutledge, 2002).

7.7.1 Rainfall-Lightning Ratio in Catalonia

Pineda et al. (2007) analyzed the Rainfall Lightning ratio in nine convective events that occurred during the summer season of 2004 in Catalonia and its coastal area. Rain rate fields were obtained from the SMC C-band radar located 25 km west of the city of Barcelona. The RLR obtained for these events had a mean value of $38.9 \text{ } 10^3 \text{m}^3 \text{CG}^{-1}$, with a wide range of variation between episodes (10.8 to $87.2 \text{ } 10^3 \text{m}^3 \text{CG}^{-1}$). These results agree in magnitude with other case studies (see summary in Kempf and Krider, 2003). The mean RLR value for the studied episodes is closer to the ones found over Florida with a RLR of $43 \text{ } 10^3 \text{m}^3 \text{CG}^{-1}$ (Tapia et al., 1998) or the Southeastern United States $38 \text{ } 10^3 \text{m}^3 \text{CG}^{-1}$ (Buechler and Goodman, 1990) than in France $72 \text{ } 10^3 \text{m}^3 \text{CG}^{-1}$ (Soula and Chauzy, 2001) and $68 \text{ } 10^3 \text{m}^3 \text{CG}^{-1}$ (Seity et al., 2001). Pineda et al. (2007) have obtained a positive correlation ($R^2 = 0.56$) between the rainfall volume and the total number of CG flashes.

Following the same procedure as the one described in Pineda et al. (2007), a comparison of the daily CG flash number with the daily rain field for 35 thunderstorm days from June to October 2006 was undertaken. The daily average RLR is of $28.4 \text{ } 10^3 \text{m}^3$ per CG flash, with a range of variation from 11.9 to $69.3 \text{ } 10^3 \text{m}^3 \text{CG}^{-1}$.

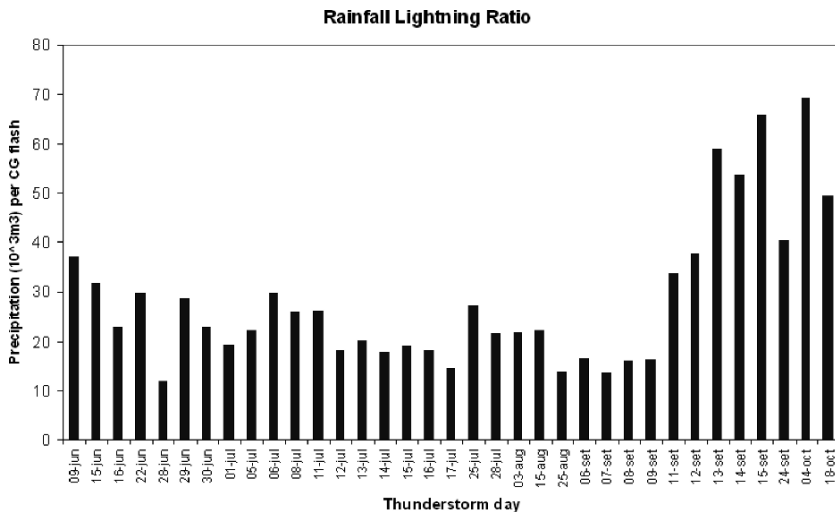


Fig. 7.17 Rainfall Lightning Ratio for 35 thunderstorm days from June to October 2006 in the area of Catalonia

Figure 7.17 shows the RLR for the 35 thunderstorm days analyzed. It can be seen that the ratio increases in middle of September. This change is due to the origin of the storms. While during late spring and early summer thunderstorms mainly originate inland, in late summer and autumn thunderstorms originate over the sea. The warm and humid conditions over the Mediterranean promote the formation of high-efficient rainfall structures, which are characterized by lower cloud developments and a lower lightning activity (Caracena et al., 1979; Martín León et al., 2007). This change in the rainfall regime is reflected in a higher rainfall volume per CG flash.

Comparing the rainfall volume and the total number of CG flashes in the analyzed thunderstorm days (Fig. 7.18), the correlation is linear with $R^2 = 0.68$. When

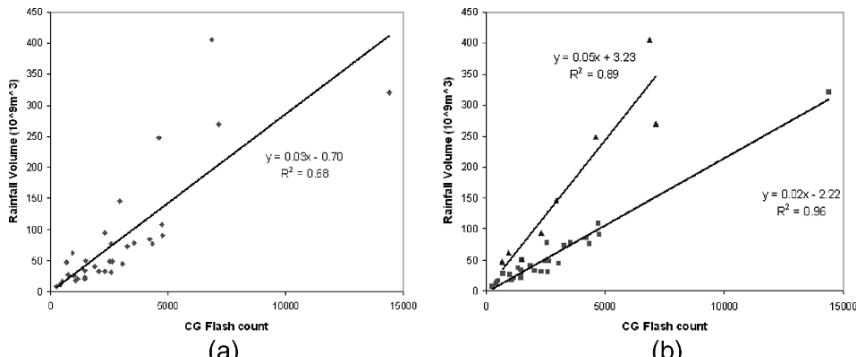


Fig. 7.18 Distribution of the Rainfall volume per CG flash for (a) the 35 analyzed thunderstorm days from summer 2006 and (b) separating days before (square symbol) and after (triangle symbol) September 10th

considering separately the days before and after September 10th, the linear fittings for the two groups present a better correlation coefficient. For the 27 late-spring and early summer days, R^2 is 0.96 and for the late-summer and fall days it is 0.89.

It is interesting to note here that among all severe convective weather situations, fall season heavy rainfall represents the most threatening phenomenon in the western Mediterranean region. Devastating flash floods occur every year somewhere in eastern Spain, southern France, Italy, or North Africa, and are responsible for a great proportion of the fatalities, property loss and destruction of infrastructure caused by natural hazards. These events tend to be most frequent and intense during the fall because of warm Mediterranean Sea moisture supply. Weather surveillance staff have to be aware of this change in the rainfall regime, because as such thunderstorms approach the coast but are still far from radar coverage, the summer RLR can not be accurately applied to infer the precipitation volume expected, possibly resulting in underestimation.

7.8 Total Lightning Activity in Hail-Bearing Thunderstorms

Even though hail consequences can not be compared to those of flash floods, hail-bearing thunderstorms occur quite often in Catalonia and every year they cause important losses, especially in the agricultural sector. These events are of special interest and are being analyzed in the region in order to better understand the relationships between lightning activity and the particular microphysics of such thunderstorms.

7.8.1 Overview

Some severe storms present dominant positive CG (+CG) flashes during their mature phase and for periods of several tens of minutes (Reap and Mac Gorman, 1989; Branick and Doswell, 1992; Stolzenburg, 1994; Carey and Rutledge, 1998; Soula et al., 2004; Wiens et al., 2005). This +CG activity is remarkable insofar that its density is comparable to the negative CG (-CG) density generally observed below non severe storms. On the other hand, severe weather often occurs in the absence of clustered +CG flash activity (Williams, 2001).

A negative correlation between hail production and -CG flashes was observed in several studies (Lang et al., 2000; Knupp et al., 2003; Soula et al., 2004). In the case of a severe hailstorm with dominant +CG flashes (over 74%), Carey and Rutledge (1998) also found a negative correlation between temporal and spatial behavior of large hail and +CG flashes. Lang and Rutledge (2002) noted larger updrafts volumes in the cases of thunderstorms with dominant +CG flashes. Several hypotheses have been reviewed by Williams (2001) to explain this dominant +CG activity.

Recent studies show a tendency for total lightning activity to lead severe weather on the ground (Williams et al., 1999) but high flash rates ($>30 \text{ min}^{-1}$) are no guarantee of severe weather (Williams, 2001). A study of 32 severe storm cases by Williams et al. (1999) showed that an abrupt increase in the total flash rate systematically preceded the severe weather at the ground by 5–20 min. Carey and Rutledge (1998) had reported a very high IC/CG ratio in a hailstorm after it became severe and produced large hail and weak tornadoes. The initial production of hail in a high position corresponded very well with a rapid increase of the IC/CG ratio. In the study by Lang et al. (2000), devoted to two long-lived storms of STERAO-A, low –CG flash rates ($<1 \text{ min}^{-1}$) and relatively high IC flash rates ($>30 \text{ min}^{-1}$) were observed, and even long periods without any CG flashes (from 10 to 30 min) also occurred. According to the authors of this study, the observations were consistent with the elevated charge hypothesis. This hypothesis, proposed by MacGorman et al. (1989), supposes that the strong updrafts present in severe storms could lift the negative charge to higher altitudes in the thundercloud, which could favor IC flashes to the detriment of CG flashes. Furthermore, according to the authors, in strong updrafts the particle could not spend enough time at a given level to acquire and separate charge, and therefore the charge density would be weaker. However, some observations were not clearly explained by this hypothesis, especially the low CG lightning flash rates during the thundercell collapse. In order to interpret the –CG and +CG flash activities throughout the whole lifetime of both storms, other mechanisms were suggested. For example, the wet growth for ice particles could limit the charging process of non inductive theory, but apparently, observations could not validate this. The rainfall charge transport was also noted as a possible explanation, but once again, observations did not allow for the confirmation of this. During STEPS, the charge and cloud structures of several cases of severe storms were documented in a US area very favorable for dominant +CG storms (Lang et al., 2004). On one hand, results from this experiment infer a low CG rate, with the lack of a lower charge center below the main charge at middle level of the cloud (Wiens et al., 2005). On the other hand, the production of dominant +CG flashes was explained by an inverted dipole structure (Rust et al., 2005; Wiens et al., 2005). Recent modeling studies (Mansell et al., 2005) confirm the role of the lower charge center for the production of strong electric fields required for initiating CG flashes. These results also confirm the possible presence of an inverted dipole with some non-inductive charging schemes dependent on the graupel rime accretion rate. Observations of total lightning by means of the Lightning Mapping Array (LMA) (Wiens et al., 2005) revealed that inverted-dipole storms produce a lot of inverted polarity IC discharges between the mid-level positive and upper negative charges instead of normal IC lightning flashes. In this process, the storms often develop a double inverted dipole structure (+, −, +, −) in which inverted polarity ICs occur independently in the upper and lower levels of the storm. Thus, these storms can be extremely active electrically, producing essentially continuous lightning in different parts of the storm. Indeed, these anomalous storms often develop lightning that is chaotic and random, exhibiting little structure (Weiss et al., 2007).

7.8.2 Analyzed Hail Events in Catalonia

Several cases of severe thunderstorms that occurred in Catalonia have been reported in different works [Montanyà et al., 2006, 2007a,b)]. In these cases, the severe storms were characterized by large hailstones (up to 40 mm) and presented a remarkable increase in IC activity before the severe weather at ground level. These storms had low CG flash rates (typically much lower than 2 min^{-1}) and practically no CG activity when the presence of hail was suspected from high radar reflectivity and ground in-situ observations. The studied cases presented maximum IC flash rates between 60 and 92 min^{-1} and the peak of IC(CG) flash ratio reached values higher than 60. An interesting feature in all of the observations was that during the periods where +CG flashes occurred, -CG flashes presented low peak currents and their multiplicity was strictly one. Among the IC flashes detected by the XDDE, a large amount (higher than 31%) were 1-VHF source events which indicate short propagation lightning events. Figure 7.19 displays the time series of different lightning activities and radar ($A_f(57)$) of one of the studied cells in Montanyà et al. (2007a). $A_f(57)$ represents the fractional area of certain reflectivity levels (Steiner et al., 1995; Parker and Johnson, 2000; Montanyà et al., 2007a). The fractional area $A_f(57)$, is the relation of cumulative areas where the maximum reflectivity exceeds 57 dBZ and 40 dBZ, respectively. Areas with reflectivity higher than 57 dBZ correspond to an indicator of hail probability while areas with reflectivity higher than 40 dBZ are chosen to represent the convective region.

Although the cases analyzed in the region presented similar characteristics, the case analyzed by Montanyà et al. (2007b) displayed a large amount of –CG flashes with very low peak currents and low multiplicity values. In that case, by considering

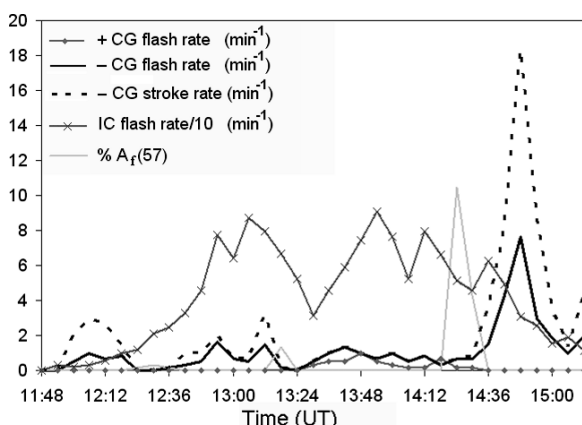


Fig. 7.19 Time series of different lightning activities and fractional area $A_f(57)$ for one of the cells in the case of the 17th of August, 2004 (Montanyà et al., 2007a). Reproduced by permission of American Geophysical Union.

all –CG detections of the SLDN, the median value of the peak current was close to -5 kA and the average multiplicity was practically 1. But the analysis of the evolution of different lightning flash categories showed how the rate of the –CG flashes with a low peak currents ($<10\text{ kA}$ in absolute value) evolved very similarly to that of the IC flashes and differently to those with higher peak currents ($>10\text{ kA}$ in absolute value). That could indicate a misclassification of IC flashes by SLDN. To support this hypothesis it may be necessary to assume the storm had an inverted-polarity charge structure. Other observations that can lead to this assumption are: the +CG proportion was high ($> 50\%$) during the mature phase, the rate and the multiplicity of the –CG flashes markedly increased at the end of the storm lifetime. By considering these observations, the –CG flashes were filtered by using a criterion of minimum peak current fixed at -10 kA and thus the –CG flash characteristics recovered its typical values for thunderstorms in the region. In conclusion, the features of the hailstorm analyzed by Montanyà et al. (2007b) highlighted in the analysis, may correspond to those revealed in several studies of severe storms from the STEPS experiment in the Great Plains area of the US.

7.9 Conclusions

This chapter highlighted the studies that emerged from lightning detection in Spain. In the first part, both networks, the SLDN and the XDDE have been described. But the future becomes more exciting since two new networks are being installed: the Spanish expansion of LINET (see Betz et al., this volume) and the Basque Country network that is similar to the XDDE.

In the case of XDDE the methodology employed for network data evaluation has been described. The results show the good detection efficiency of the XDDE, enabling adjustments of the network as well as data quality control.

The availability of lightning detection networks, the long time records of annual thunderstorm days over the country and the radar networks helped to assemble a lightning climatology of Spain and in the particular region of Catalonia. In addition, the chapter presented the results of the rainfall-lightning ratios calculated by different methods. The resulting ratios are comparable with those determined in other regions in the world.

Finally, the ability to detect and locate IC sources by means of the XDDE allows displaying the total lightning evolution during severe thunderstorms characterized by hail. The results showed a remarkable increase in IC activity and low CG activity before severe weather at ground. Also, +CG flashes are observed during severe storms and, during periods in which those flashes occurred, –CG flashes exhibited low peak currents with a multiplicity of strictly one. Finally, in one case, a large number of very low peak currents of –CG flashes suggested misclassifications of intra-cloud lightning by the lightning location networks that may be due to the inverted-polarity charge structure of the storm.

References

- Alonso, S., A. Portela, and C. Ramis (1994). First considerations on the structure and development of the Iberian thermal low. *Ann. Geophys.*, 12: 457–468.
- Buechler, D.E., and S.J. Goodman (1990). Echo size and asymmetry: Impact on NEXRAD storm identification. *J. Appl. Met.*, 29: 962–969.
- Branick, M.L., and C.A. Doswell III (1992). An observation of the relationship between supercell structure and lightning ground strike polarity. *Wea. Forecast.*, 7: 143–149.
- Carey, L.D., and S.A. Rutledge (1998). Electrical and multiparameter radar observations of a severe hailstorm. *J. Geophys. Res.*, 103(D12): 13979–14000.
- Caracena, F., R.A. Maddox, L.R. Hoxit, and C.F. Chappell (1979). Mesoanalysis of the Big Thompson Storm. *Mon. Wea. Rev.*, 107: 1–17.
- Correoso J.F., E. Hernández, R. García-Herrera, D. Barriopedro, and D. Paredes (2006). A 3-year study of cloud-to-ground lightning flash characteristics of Mesoscale convective systems over the Western Mediterranean Sea. *Atmos. Res.*, 79(2): 89–107.
- De Pablo F., and L. Rivas Soriano (2002). Relationship between cloud-to-ground lightning flashes over the Iberian Peninsula and sea surface temperature. *Q. J. R. Meteorol. Soc.*, 128: 173–183.
- Fraley, C., and A.E. Raftery (2003). Enhanced model-based clustering, density estimation, and discriminant analysis software: MCLUST. *J. Classif.*, 20(2): 263.
- García Mollá, P.J. (1910). La section électrique, Mémoires de l'Observatoire de l'Èbre, Ed. Gustavo Gili, Barcelona.
- Herrero, M., M.J. Prohom, and A. Rius (2007). Identificació, catalogació i digitalització dels registres climàtics de Catalunya (ss. XVIII a XXI). XIII Jornades de Meteorologia Eduard Fontserè, pp. 121–129. Barcelona.
- Kempf, N.M., and E.P. Krider (2003). Cloud-to-ground lightning and surface rainfall during the great flood of 1993. *Mon. Wea. Rev.*, 131: 1140–1149.
- Knupp, K.R., S. Paech, and S. Goodman (2003). Variations in cloud-to-ground lightning characteristics among three adjacent tornadic supercell storms over the Tennessee valley region. *Mon. Wea. Rev.*, 131: 172–188.
- Lang, T.J., S.A. Rutledge, J.E. Dye, M. Venticinque, P. Laroche, and E. Defer (2000). Anomalously low negative cloud-to-ground lightning flash rates in intense convective storms observed during STERAO-A. *Mon. Wea. Rev.*, 128: 160–173.
- Lang, T.J., and S.A. Rutledge (2002). Relationships between convective storm kinematics, precipitation, and lightning. *Mon. Wea. Rev.*, 130: 2492–2506.
- Lang, T.J. et al. (2004). The severe thunderstorm electrification and precipitation study (STEPS). *Bull. Am. Meteorol. Soc.*, 85: 1107–1125.
- MacGorman, D.R., D.W. Burgess, V. Mazur, W.D. Rust, W.L. Taylor, and B.C. Johnson (1989). Lightning rates relative to tornadic storm evolution on 22 May 1981. *J. Atmos. Sci.*, 46: 221–250.
- Mansell, E.R., D.R. MacGorman, C.L. Ziegler, and J.M. Straka (2005). Charge structure and lightning sensitivity in a simulated multicell thunderstorm. *J. Geophys. Res.*, 110(D12): D12101, doi:10.1029/2004JD005287.
- Martín León, F., F. Elizaga, O. Carretero, and I. San Ambrosio (2007). Diagnóstico y predicción de la convección profunda. Nota Técnica STAP 35, Instituto Nacional de Meteorología, pp.174.
- Molinie G., S. Soula, and S. Chauzy (1999). Cloud-to-ground lightning activity and radar observations of storms in the pyrénées range area. *Q. J. R. Meteorol. Soc.*, 125(560): 3103–3122.
- Montanyà, J., N. Pineda, V. March, A. Illa, D. Romero, and G. Solà (2006). Experimental evaluation of the Catalan Lightning Detection Network. 19th International Lightning Detection Conference, Tucson.
- Montanyà J., S. Soula, and N. Pineda (2007a). A study of the total lightning activity in two hailstorms, *J. Geophys. Res.*, 112: D13118, doi:10.1029/2006JD007203.

- Montanyaà J., S. Soula, N. Pineda, O. van der Velde, P. Clapers, G. Solà, J. Bech, and D. Romero (2007b). Study of the total lightning activity in a hailstorm. 13th International Conference on Atmospheric Electricity, Beijing, China.
- Parker, M.D., and R.H. Johnson (2000). Organizational modes of midlatitude mesoscale convective systems. *Mon. Wea. Rev.*, 128: 3413–3436.
- Pérez Puebla, F. and C. Zancajo Rodríguez (AEMET) (2008). La frecuencia de las tormentas eléctricas en España. Boletín de la quinta etapa de la Asociación Meteorológica Española, Vol. 21, pp. 37–44.
- Petersen, W.A., and S.A. Rutledge (1998). On the relationship between cloud-to-ground lightning and convective rainfall. *J. Geophys. Res.*, 103: 14025–14040.
- Pineda, N., T. Rigo, J. Bech, and X. Soler (2007). Lightning and precipitation relationship in summer thunderstorms: Case studies in the North Western Mediterranean region. *Atmos. Res.*, 85(2): 159–170.
- Rakov, V.A., and M.A. Uman (2003). *Lightning: Physics and effects*. Cambridge University Press, Cambridge, pp.687.
- Rius, A., M.J. Prohom, and M. Herrero (2008). Identification and digitization of instrumental climate data from Catalan documentary sources (19th and 20th centuries). International Workshop on Rescue and Digitization of Climate Records in the Mediterranean Basin. Proceedings of the MEDARE Workshop – WMO (WCDMP n° 67 – WMO-TD n° 1432), June 2008, pp. 109–112. Tarragona.
- Reap, R.M., and D.R. MacGorman (1989). Cloud-to-ground lightning: Climatological characteristics and relationships to model fields, radar observations, and severe local storms. *Mon. Wea. Rev.*, 117: 518–535.
- Richard, P., and J.Y. Lojou (1996). Assessment of application of storm cell electrical activity monitoring to intense precipitation forecast. In 10th International Conference on Atmospheric Electricity, Osaka, Japan, pp. 284–287.
- Rivas Soriano, L., F. De Pablo, and E. García Díez (2001a). Cloud-to-ground lightning activity in the Iberian Peninsula: 1992–1994. *J. Geophys. Res.*, 106(D11): 11891–11901.
- Rivas Soriano, L., F. De Pablo, and E. García Díez (2001b). Relationship between convective precipitation and cloud-to-ground lightning in the Iberian Peninsula. *Mon. Wea. Rev.*, 129(12): 2998–3003.
- Rivas Soriano, L., and F. De Pablo (2002). Maritime cloud-to-ground lightning: The Western Mediterranean Sea. *J. Geophys. Res.*, 107(D21): 4597–4608.
- Rivas Soriano, L., F. De Pablo, and C. Tomas (2005). Ten-year study of cloud-to-ground lightning activity in the Iberian Peninsula. *J. Atmos. Terr. Phys.*, 67(16): 1632–1639.
- Romero, R., C.A. Doswell III, and R. Riosaldo (2001). Observations and fine-grid simulations of a convective outbreak in northeastern Spain: Importance of diurnal forcing and convective cold pools. *Mon. Wea. Rev.*, 129: 2157–2182.
- Rust, W.D. et al. (2005). Inverted-polarity electrical structures in thunderstorms in the severe thunderstorm electrification and precipitation study (STEPS). *Atmos. Res.*, 76(1–4): 247–271.
- Seity, Y., S. Soula, and H. Sauvageot (2001). Lightning and precipitation activities in coastal thunderstorms. *J. Geophys. Res.*, 106(D19): 22801–22816.
- Sheridan, S.C., J.F. Griffiths, and R.E. Orville (1997). Warm season cloud-to-ground lightning–precipitation relationships in the south-central United States. *Wea. Forecast.*, 12(3): 449–458.
- Soula, S., and S. Chauzy (2001). Some aspects of the correlation between lightning and rain activities in thunderstorms. *Atmos. Res.*, 56: 355–373.
- Soula, S., Y. Seity, L. Feral, and H. Sauvageot (2004). Cloud-to-ground lightning activity in hail-bearing storms. *J. Geophys. Res.*, 109(D2): D02101, doi:10.1029/2003JD003669.
- Steiner, M., R.A. Houze Jr., and S.E. Yuter (1995). Climatological characterization of three-dimensional storm structure from operational radar and rain gauge data. *J. Appl. Meteorol.*, 34, 1978–2007.

- Stolzenburg, M. (1994). Observations of high ground flash densities of positive lightning in summertime thunderstorms. *Mon. Wea. Rev.*, 122: 1740–1750.
- Tapia, A., J.A. Smith, and M. Dixon (1998). Estimation of convective rainfall from lightning observations. *J. Appl. Meteorol.*, 37: 1497–1509.
- Tomás C., F. Fernando de Pablo, and L. Rivas Soriano (2004). Circulation weather types and cloud-to-ground flash density over the Iberian Peninsula. *Int. J. Climatol.*, 24(1): 109–123.
- Tudurí E., and C. Ramis (1997). On the environments of significant convective events in the Western Mediterranean. *Wea. Forecast.*, 12: 294–306.
- Weiss, S.A., W.D. Rust, D.R. MacGorman, E.C. Bruning, and P.R. Krehbiel (2007). Evolving complex electrical structure of the STEPS 25 June 2000 multicell storm. *Mon. Wea. Rev.*, 136(2): 741–756.
- Wiens, K.C., S.A. Rutledge, and S.A. Tessendorf (2005). The 29 June 2000 supercell observed during STEPS. Part II: Lightning and charge structure. *J. Atmos. Sci.*, 62: 4151–4177.
- Williams, E.R., M.E. Weber, and R.E. Orville (1989). The relationship between lightning type and convective state of thunderclouds. *J. Geophys. Res.*, 94(D11): 13213–13220.
- Williams, E., B. Boldi, A. Matlin, M. Weber, S. Hodanish, D. Sharp, S. Goodman, R. Raghavan, and D. Buechler (1999). The behavior of total lightning activity in severe Florida thunderstorms. *Atmos. Res.*, 51: 245–265.
- Williams, E.R. (2001). The electrification of severe storms. *Meteorol. Monogr.*, 28(50): 527–561.
- Zhou, Y., X. Qie, and S. Soula (2002). A study of the relationship between cloud-to-ground lightning and precipitation in the convective weather system in China. *Ann. Geophys.*, (20): 107–113.

Chapter 8

Spatial Distribution and Frequency of Thunderstorms and Lightning in Australia

Yuriy Kuleshov, David Mackerras and Mat Darveniza

Abstract A review of thunderstorm and lightning observations in Australia, with emphasis on studies of their spatial distribution and frequency over the Australian continent, is presented. Long-term thunderday records, lightning data obtained by ground-based lightning detection instruments CIGRE-500 and CGR3 and by NASA satellite-based instruments OTD and LIS have been analyzed to develop maps of total lightning flash density, N_t , (i.e. cloud-to-ground and intracloud) and of ground flash density, N_g . The peak lightning occurrence is in the north-western part of the Australian continent with N_t values up to about $35 \text{ km}^{-2}\text{yr}^{-1}$. Ground flash density (N_g) values vary from over $6 \text{ km}^{-2}\text{yr}^{-1}$ in the northern parts of Australia to about $1 \text{ km}^{-2} \text{ yr}^{-1}$ and below in the southern parts. There are significant seasonal and yearly variations in the frequency of thunderdays. Some aspects of the hazards from thunderstorms and lightning appear to be special to Australia, including lightning initiated wildfires, lightning injuries to telephone users and faults on power lines caused by high wind gust speeds.

Keywords Thunderstorms · Lightning · Lightning flash density · Australia · Lightning flash counters

8.1 Introduction

Thunderstorms are spectacular but hazardous weather phenomena and the associated lightning and wind gusts can be very hazardous to people, buildings, and industry and utility assets. The thunderstorm hazards in Australia are in most respects similar to those in other countries, but some are worthy of special comment. Given the potential hazards associated with lightning, knowledge about spatial and temporal distributions of thunderstorm and lightning activity is of great importance for developing comprehensive protective measures.

Y. Kuleshov (✉)

National Climate Centre, Australian Bureau of Meteorology, GPO Box 1289K,
Melbourne, Vic., 3001, Australia
e-mail: Y.Kuleshov@bom.gov.au

Traditionally, thunderstorm activity is recorded at meteorological sites as a number of thunderdays per year. Thunderday records are commonly used as proxy information for describing lightning activity. To obtain instrumental records of lightning incidence, many lightning flash counters (LFC) have been installed at meteorological and other sites worldwide. Lightning location systems (LLS) are also used in most developed countries, beginning in America in the 1980s and then worldwide, including two commercial systems in Australia [GPATS and Kattron websites]. Recently, remotely-sensed lightning data gathered by the National Aeronautics and Space Administration (NASA) satellite-based instruments became available.

In this chapter, a review of studies on spatial and temporal distribution of thunderstorms and lightning in Australia is presented. Geographical distribution of thunderstorm and lightning activity for the Australian continent has been analysed in detail based on long-term records from LFCs and thunderday records, as well as recently acquired NASA satellite-based lightning data. Several aspects of thunderstorm hazards special to Australia are also described.

8.2 Spatial Distribution and Frequency of Thunderstorms

Thunderstorm occurrence at a particular location is traditionally expressed in terms of thunderdays. A thunderday, is defined as ‘an observational day (any 24-hour period selected as the basis for climatological or hydrological observations) during which thunder is heard at the station. Precipitation need not occur’ [Huschke, 1959]. The 24-hour period selected at the Australian Bureau of Meteorology for the phenomenon registration is midnight to midnight (local standard time). The requirement that thunder should actually be heard limits the area covered by each observing point, under favourable listening conditions, to a circular area with a radius of some 20 km [WMO, 1953].

Using the Australian thunderday records, the thunderstorm distribution across the country was analyzed in detail and an updated average annual thunderday map of Australia (Fig. 8.1) was prepared at the National Climate Centre, the Australian Bureau of Meteorology [Kuleshov et al., 2002]. Clearly thunderstorms are most frequent over the northern half of the country, and generally decrease southward, with lowest frequencies in southeast Tasmania. A secondary maximum is also apparent in southeast Queensland and over central and eastern New South Wales, extending into the northeastern Victorian high country.

To understand this distribution, it is important to note that thunderstorm development generally requires three factors:

- 1) An unstable convective atmosphere, with generally high surface temperatures and a strong vertical lapse rate (i.e., temperature falls rapidly with height), which provides a favourable environment for the strong vertical atmospheric motions that produce thunderstorms.
- 2) A trigger for this vertical motion, such as low level convergence of airstreams, a frontal system, local differences in heating or orography.
- 3) High atmospheric moisture levels.

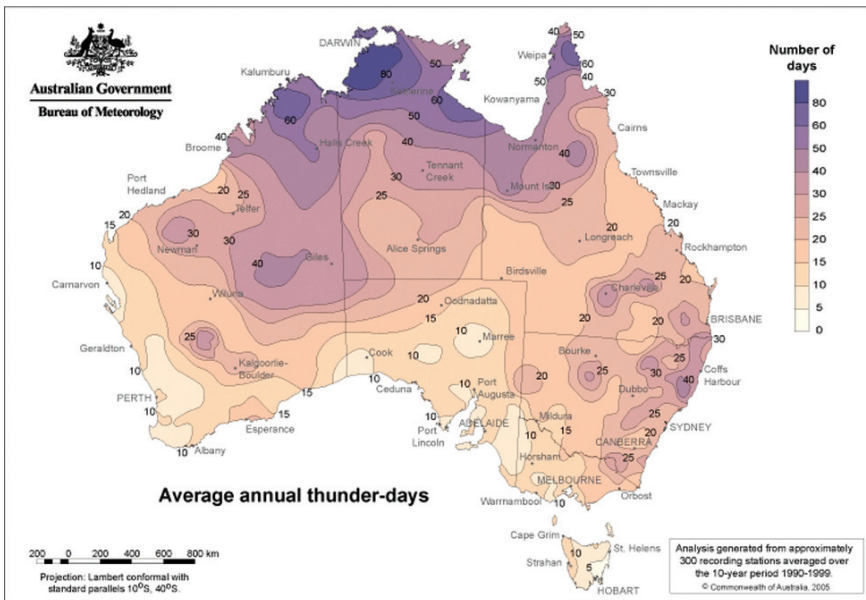


Fig. 8.1 Map of average annual thunderdays for Australia (1990–1999) (*Kuleshov et al.*, 2002)

High moisture levels, especially near the coast, affect the tropical north of Australia in the summer half of the year. Lower pressure lies across northern and central Australia, and gives rise to the vertical motion and low level convergence that favour thunderstorm development. The northern half of Australia is thus very favourable for thunderstorms in the warmer months October through March, and especially in the far north, thunderstorms are frequent and often associated with heavy rainfall and intense lightning. In the remainder of the year dry, stable outflow from the subtropical high pressure belt, which normally lies over the continent, inhibits convective showers and storms.

Thunderstorm frequencies generally decrease in the southern parts of the tropics and the adjacent desert areas of central Australia. This is because the air, though often very hot, is generally drier. The exception appears to be over inland western Australia where a wide area experiences over 30 thunderdays a year. However, many of these would be so-called “dry” thunderstorms, with little or no rain, because low-level relative humidity tends to be low and acts to evaporate any falling precipitation.

8.3 Estimating Lightning Flash Density from Thunderday Records

The lightning flash density, defined as the number of flashes of a specific type occurring on or over unit area in unit time, is commonly used to describe lightning activity.

The lightning flash densities are denoted as N_g , N_c and N_t for cloud-to-ground (CG, or simply ground), intra-cloud (IC, or simply cloud) and total (CG + IC) flashes, respectively, and expressed as a number of flashes per square kilometre per year ($\text{km}^{-2} \text{ yr}^{-1}$).

In the absence of better information, the lightning ground flash density, N_g , may be estimated from average annual number of thunderdays, T_d , using an equation of the form $N_g = aT_d^b$, in which **a** and **b** are empirically derived constants that depend on the meteorological conditions at a given location. The earliest estimates of the equation for Australia were by *Mackerras* [1978], who derived values of **a** = 0.01 and **b** = 1.4. This study was based on results from 26 sites for the period 1965–1977 and the Australian Bureau of Meteorology thunderday map based on data from 1954 to 1963. *Anderson and Eriksson* [1980], based on 120 observations over two years in South Africa, derived values of **a** = 0.023 and **b** = 1.3. The corresponding equation has since become known as ‘Eriksson’s Formula’. A subsequent study using 62 stations over a longer period of five years from 1976 to 1980 yielded the values **a** = 0.04 and **b** = 1.25 [Anderson et al., 1984]. The equation using these two values of the constants is generally known as the ‘CIGRE Formula’. Both the CIGRE and Eriksson’s equations are used in the literature, although they were both derived at the same location. But there are very few systematic studies enabling one to compare their results with those from other parts of the world. Recently, using long-term (up to 22 years) LFC registrations and thunderday observations for 17 Australian localities, *Kuleshov and Jayaratne* [2004] updated Mackerras’ empirical formula and compared the results with Eriksson’s and CIGRE formulas. It was concluded that the empirical formula, $N_g = 0.012 T_d^{1.4}$, gives the best estimate of N_g in Australia.

However, lightning flash densities derived from such empirical relationships to thunderday records are less accurate than those derived from direct measurements of N_g .

8.4 Instruments of Lightning Registration

Based on earlier work in the UK by *Pierce* [1956], two types of LFC were developed that have been used extensively around the world. These are the 500 Hz and 10 kHz CIGRE (Comité Internationale des Grands Réseaux Electriques), (that is, International Committee on Large Electric Systems) LFCs developed at the University of Queensland, Australia, and in Pretoria, South Africa [Anderson et al., 1979]. The 500 Hz LFC initially referred to as the RBQ 500 Hz LFC [Barham, 1965; Barham and Mackerras, 1972] was developed and tested in SE Queensland, Australia. The CIGRE 10 kHz counter was developed and tested in South Africa by Anderson and his colleagues in Pretoria. It used a 10 kHz filter instead of the 500 Hz filter and was initially referred to as RSA 10 kHz [Anderson et al., 1979]. CIGRE counters were intended primarily to register ground flashes, but also respond to some cloud flashes. With the 10 kHz counter, less than 10% of the total registrations are caused by cloud flashes. Such counters have a dead time of 1 s after each registration, so that lightning flashes are counted rather than strokes.

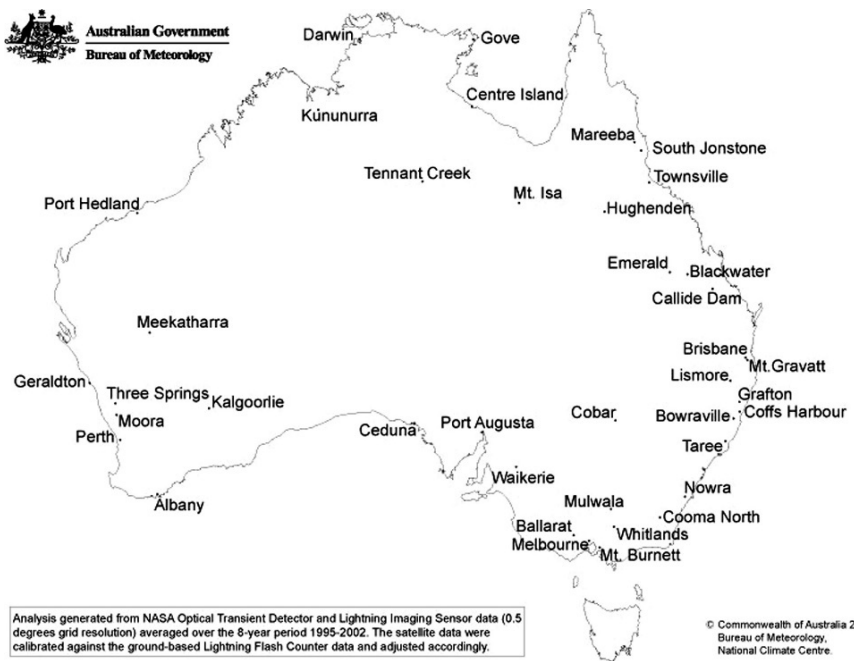


Fig. 8.2 Geographical distribution of the CIGRE-500 counters over the Australian continent (*Kuleshov et al., 2006*)

The CIGRE-500 counter is the instrument used by the Australian Bureau of Meteorology for its network of LFCs (the LFC site locations are shown in Fig. 8.2). It was designed primarily to register ground flashes, [Barham, 1965; Prentice, 1972a]. However, the electric field changes caused by cloud flashes and positive ground flashes often exhibit positive steps (K changes) and truncated negative ramps that may cause the instrument to register such an event [Bunn, 1968]. Therefore, the determination of N_t and N_g values from annual counter registrations require estimates of the effective ranges of the instrument for ground and cloud flashes and estimates of cloud flash-to-ground flash ratio, $Z = N_c / N_g$. Effective ranges of the counter are estimated as $L_g = 30$ km for ground flashes [Prentice and Mackerras, 1969] and $L_c = 18$ km for cloud flashes [Kuleshov et al., 2006]. Long-term measurements in Australia (1995–2004) using CGR3 instruments gave an average annual value of $Z = 2 \pm 30\%$ [Kuleshov et al., 2006].

Another type of counter, primarily developed for research purposes, is the CGR3 (Cloud-to-Ground Ratio #3) instrument [Mackerras, 1985]. The CGR3 counter is a modification of the original forms of the instrument (CGR1 and CGR2) developed at the University of Queensland (Brisbane, Australia). The CGR3 instrument was used for lightning research for a number of years and it is described in detail by Mackerras and Darveniza [1992; 1994] and by Baral and Mackerras [1992; 1993]. The CGR3 counter has separate registers for negative ground flashes (NGF), positive ground flashes (PGF), and cloud flashes (CF). The effective ranges are estimated as

12 km for CF, 14 km for NGF, and 16 km for PGF. CGR3 counters were installed in 11 countries and were used for the derivation of total, intra-cloud and ground flash density estimates around the world [Mackerras and Darveniza, 1994; Mackerras et al., 1998]. In Australia, these counters have been installed in Brisbane (27.5° S, 153.0° E) and Darwin (12.3° S, 131.0° E), and were used for estimating ground, cloud, and total flash densities, and Z at those localities. A later generation CGR4 counter is described in 8.6. It should be noted that the role of such LFC differs from that of a lightning location system (LLS). The LFC records the occurrence of local lightning ground flashes with effective ranges between about 10 and 30 km, whereas the LLS records lightning locations and stroke data with ranges between about 50 and 300 km between its multiple detectors. The LFC registrations are more accurate than the LLS data for ranges below 30 km. In respect of relative costs, the LFC is an inexpensive instrument.

LFCs have proved to be useful and reliable sources of lightning data. However, their sparse spatial distribution makes it difficult to prepare a map of lightning distribution without supplementary information. Data from two NASA satellite-based instruments, the MicroLab-1 Optical Transient Detector (OTD) [Christian et al., 1996] and the Tropical Rainfall Measuring Mission (TRMM) Lightning Imaging Sensor (LIS) [Christian et al., 1999], became recently available for estimating global lightning activity. These lightning detectors were designed by the Global Hydrology Resource Centre Lightning Team and were manufactured at the Marshall Space Flight Centre in Alabama, USA (see Finke, this volume).

Satellite observations provide better spatial coverage of lightning which is, by its nature, widely distributed geographically. The remotely-sensed data are a valuable source of information for the areas with little or no local observation data (i.e. LFC or thunderday observations). Using five years of the satellite data, a world map of average annual distribution of total lightning activity was constructed [Christian et al., 2003] and it was demonstrated that the spatial distribution of flash density is in broad general agreement with the world thunderday map [WMO, 1953].

8.5 Variation of Lightning Distribution

Geographical distribution and seasonal variability of lightning activity for the Australian continent have been analysed in detail based on long-term records from LFCs and NASA satellite-based lightning data [Kuleshov et al., 2006]. For the first time, a total lightning flash density map (Fig. 8.3) and a lightning ground flash density map (Fig. 8.4) for Australia have been prepared. The maps are contoured in units of flash density ($\text{km}^{-2} \text{ yr}^{-1}$). The N_g map is now the standard reference on lightning ground flash density in Australia [Lightning Protection, 2007].

8.5.1 Geographic Distribution

The spatial distribution of average annual total flash density, N_t , (Fig. 8.3) is in general qualitative agreement with the thunderstorm climatology (Fig. 8.1) as

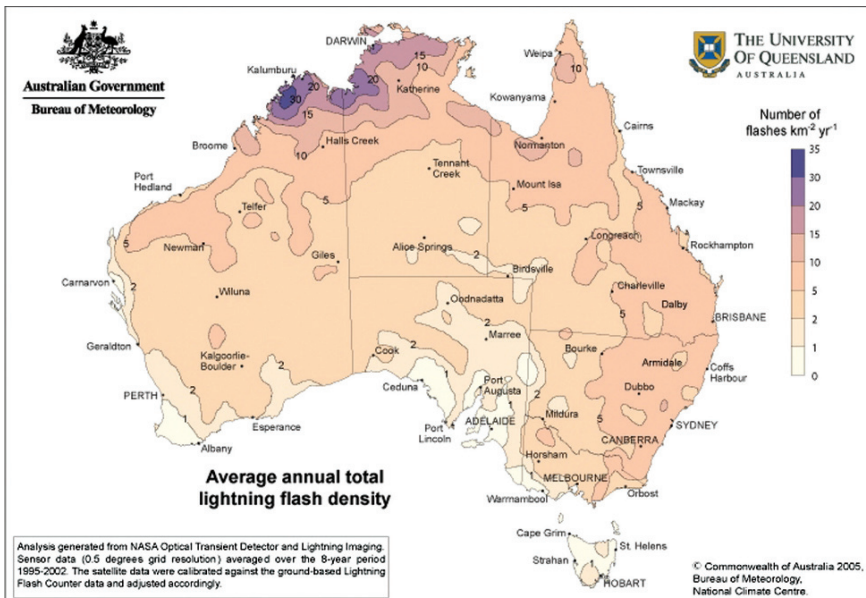


Fig. 8.3 Map of average annual total lightning flash density for Australia (*Kuleshov et al.*, 2006)

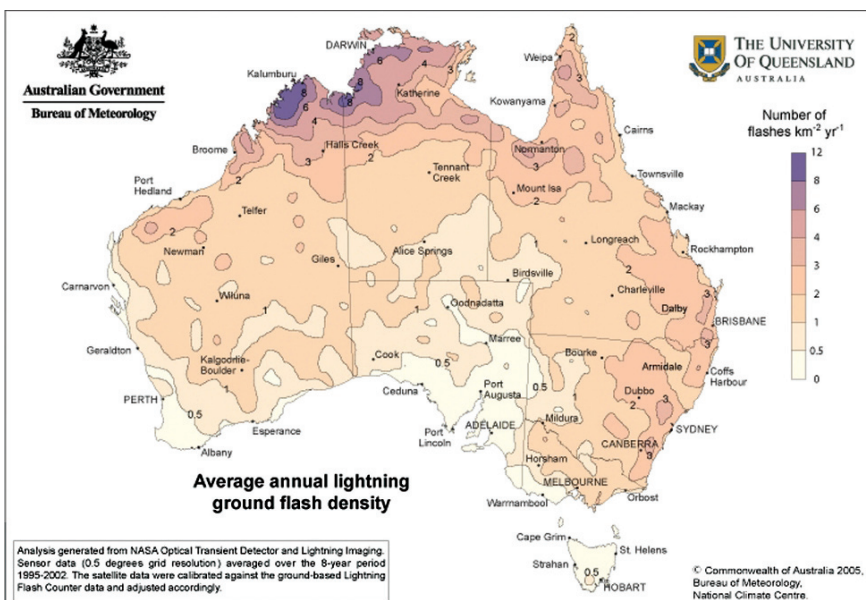


Fig. 8.4 Map of average annual lightning ground flash density for Australia (*Kuleshov et al.*, 2006)

represented by the average annual thunderday map of Australia [Kuleshov *et al.*, 2002]. Both maps demonstrate high annual thunderstorm ($T_d > 40 \text{ day yr}^{-1}$) and lightning activity ($N_t > 10 \text{ km}^{-2} \text{ yr}^{-1}$) in the northern parts of Australia, and decreases in annual thunderdays and total flash density southwards.

The peak lightning occurrence is in the north-western part of the Australian continent with N_t values above $15 \text{ km}^{-2} \text{ yr}^{-1}$ and it is in the region of the peak in thunderstorm occurrence ($T_d > 50 \text{ day yr}^{-1}$) as it appears in the thunderday map. The two peaks do not exactly coincide, however this finding is not unexpected. Discussing the world distribution of lightning as observed by the OTD, Christian *et al.* [2003] reported values of total flash density of about $23 \text{ km}^{-2} \text{ yr}^{-1}$ at Entebbe ($T_d = 206$) and Kampala ($T_d = 242$), Uganda, while the planet's "lightning hot spot", Kamembe, Rwanda, had $83 \text{ km}^{-2} \text{ yr}^{-1}$ and 221 thunderdays recorded.

The maximum value of $T_d > 80$ is in the vicinity of Darwin, where storms triggered over the Arnhem Land ranges and over Bathurst Island are very common (Fig. 8.1). High frequency of thunderstorms (40–60 thunderdays per year) is observed at the King Leopold and Durack Ranges in the north of Western Australia. This approximately corresponds to the area of the maximum average annual total lightning flash density with $N_t > 30 \text{ km}^{-2} \text{ yr}^{-1}$ centred around $16^\circ \text{ S } 126^\circ \text{ E}$ (Fig. 8.3). The highest value of N_t as derived from the satellite data is about $35 \text{ km}^{-2} \text{ yr}^{-1}$.

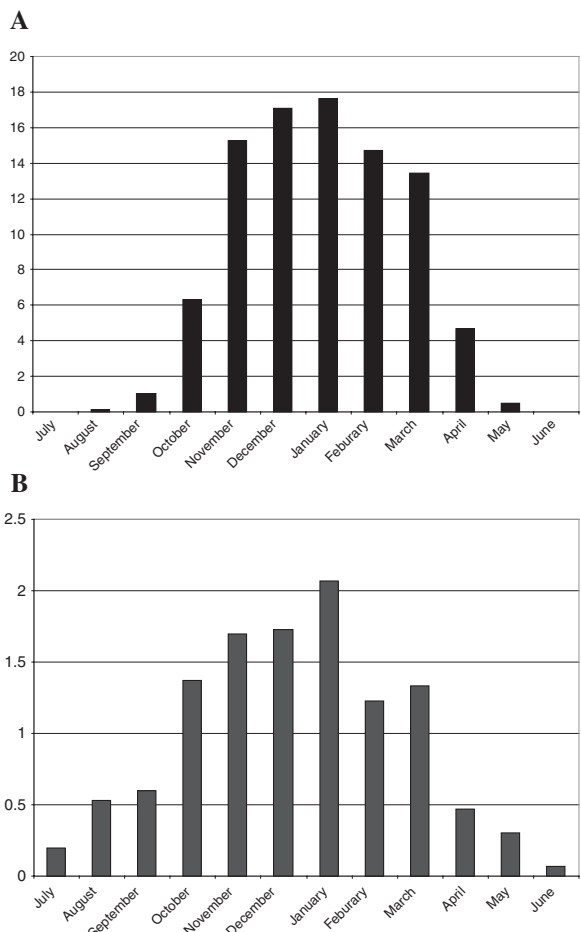
The secondary maximum of thunderstorm and lightning occurrence is over the north-eastern part of the Northern Territory and northern part of Queensland, with values of T_d between 40 and 60 days per year, and with N_t values between 5 and $15 \text{ km}^{-2} \text{ yr}^{-1}$. Another secondary maximum is evident over eastern part of Australia, with local maxima over the Great Dividing Range. Average annual number of thunder days is between 20 and 40 in this area, and lightning activity is also high with N_t values up to $10 \text{ km}^{-2} \text{ yr}^{-1}$. Lightning occurrence generally decreases southward, and number of total lightning flashes is small in Victoria, South Australia, the southern parts of Western Australia and New South Wales, and Tasmania, with the values of $N_t < 5 \text{ km}^{-2} \text{ yr}^{-1}$.

8.5.2 Seasonal Variations

Analysis of annual distributions of thunderstorms and lightning occurrences, as registered by number of thunderdays and lightning days, demonstrates dominance of these phenomena in Australia in summer months (typical distributions are presented in Figs. 8.5A and 8.5B for Darwin and Melbourne, respectively).

Data obtained by the CIGRE 500 LFCs demonstrate that on average, 90% of annual lightning registrations have been recorded between October and April, with 55% recorded in three months December to February. Comparison of seasonal distributions of standardized monthly mean lightning registrations for Kununurra (10 years of data for 1987–1992 and 1999–2002), Brisbane (15 years of data for 1980–1994) and Perth (21 years of data from 1982 to 2002) in Fig. 8.6

Fig. 8.5 Seasonal distributions of monthly mean thunderdays in Darwin (A) and Melbourne (B) (*Kuleshov et al. 2002*)



demonstrates this summer peak occurrence of lightning. Atmospheric conditions (high boundary-layer moisture levels and lower surface pressure) are favorable for thunderstorm and lightning development in this part of the continent in wet season months. The seasonal distributions for the sites located in the northern half of Australia show clear seasonality of the phenomenon: 99.8% of annual lightning registrations in Kununurra and 97.5% in Brisbane were recorded in warmer months October to April. Seasonal distribution of lightning activity in higher latitudes is more uniform. The distribution for Perth (Fig. 8.6) demonstrates that in higher latitudes, lightning is still more frequent in warmer months (65% of annual lightning registrations in Perth), but it also occurs in cooler months (May – September) in association with active frontal systems.

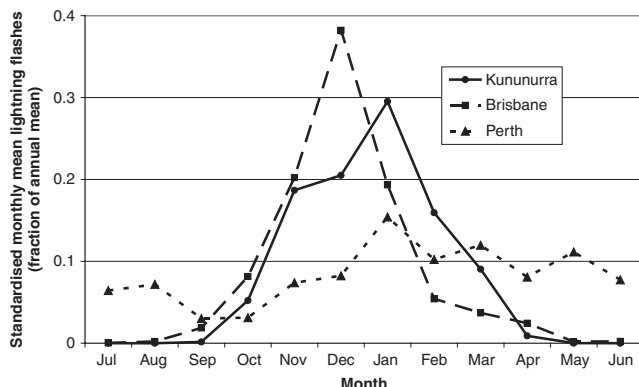


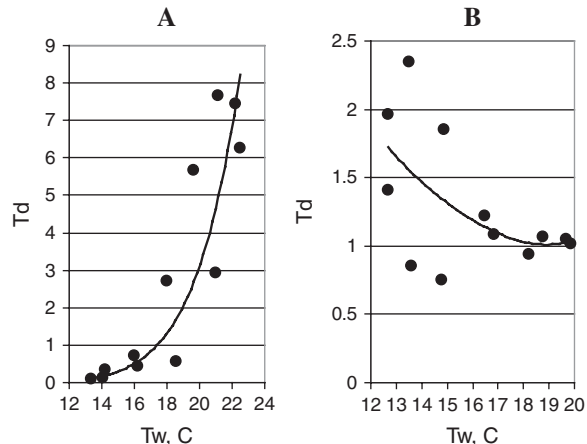
Fig. 8.6 Seasonal distributions of monthly mean lightning ground flashes in Kununurra, Brisbane and Perth, expressed as a fraction of the annual mean (Kuleshov et al., 2006)

8.5.3 Variation of Total Flash Density with Latitude

Latitudinal dependence of lightning characteristics is a subject of long-term investigations. *Orville and Spencer* [1979] reported satellite-based optical observations of total lightning flash density at local dusk and midnight over a latitude range 60° N to 60° S and demonstrated a reduction in flash frequency by a factor of 10 for a 40° increase in latitude in the southern hemisphere. Results of another satellite-based observations using radio-frequency detection of lightning indicated a similar rate of change of total flash density – a reduction in lightning flash rate by a factor of about 10 for a change in latitude from 20° S to 60° S [Kotaki et al., 1981]. *Macker-
ras and Darveniza* [1994] analyzed latitudinal variation in lightning activity using data from ground-based lightning flash counters recorded at 14 sites in 11 countries covering latitudes from 60° N to 27° S, and concluded that total flash density falls by a factor of 10 for every 30° increase in latitude. Using the data gathered by the satellite detectors over the landmass of Australia, [Kuleshov et al., 2006] described the variation of N_t for the range of latitudes from 10° S to 40° S by the empirical relationship $N_t = \exp(3.85 - 0.088\lambda)$ $\text{km}^{-2} \text{ yr}^{-1}$, where λ is the magnitude of the latitude in degrees. Once again, a reduction in lightning total flash density, N_t , by a factor of about 10 for a change in latitude from 10° S to 40° S was found, which was in agreement with the earlier studies.

One of the explanations of variation in lightning rate is traditionally sought in convective available potential energy (CAPE) which is a driving force for a thunderstorm development [Williams, 1995]. CAPE determines the updraft velocity in deep convective systems and therefore determines electrical charge separation rates and rate of lightning occurrence. Based on results of the Down-Under Doppler and Electricity Experiment (DUNDEE) conducted during the periods of November 1988–February 1989 and November 1989–February 1990 near Darwin, *Rutledge et al.* [1992] and *Williams et al.* [1992] demonstrated a strong increase in lightning activity with CAPE as well as nearly linear relationship between CAPE and wet

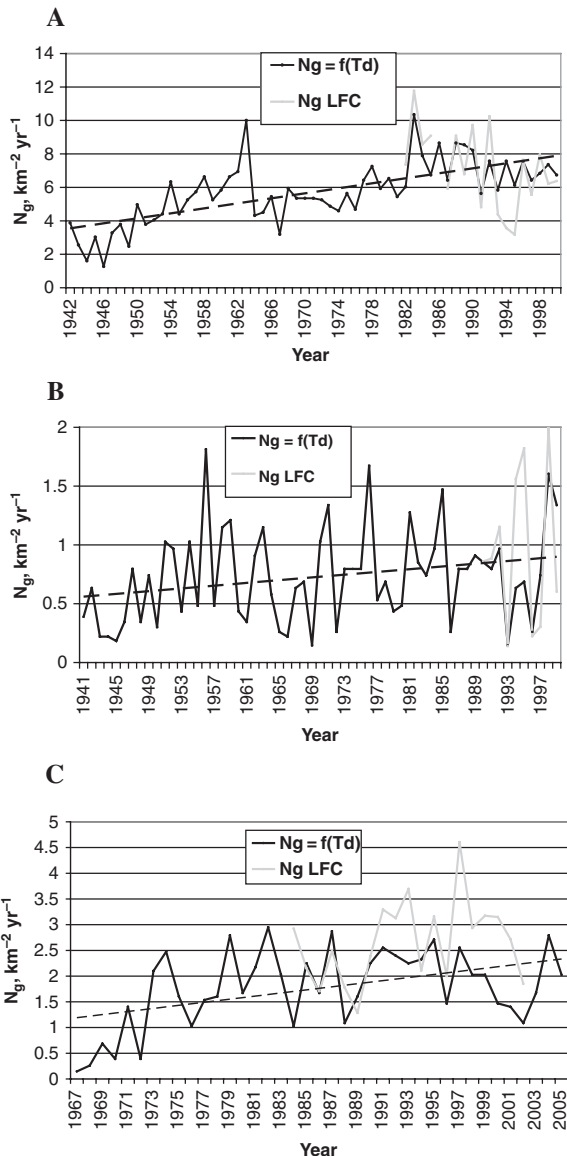
Fig. 8.7 Monthly mean number of thunderdays, T_d , plotted against monthly mean daily maximum wet bulb temperature, T_w , for Mt Isa (A) and Perth (B)



wet bulb potential temperature. In view of the observations by Rutledge *et al.* [1992], Williams [1992], and Williams *et al.* [1992], Mackerras and Darveniza [1994] suggested that the physical basis for the annual variation in monthly total lightning flash density in Darwin is to be sought mainly in the annual variation in wet bulb temperature, T_w , and CAPE. Investigating further the relationship between lightning activity and surface wet bulb temperature and its variation with latitude in Australia, Jayaratne and Kuleshov [2006] examined data from ten LFCs gathered over a sufficiently long period (ranging from 15 to 21 years of records) and widely distributed across continental Australia. It was demonstrated that at each of the stations the monthly total of lightning ground flashes increased with the monthly mean daily maximum wet bulb temperature. The dependence was most pronounced in the tropics (in Darwin, a modest 3–4°C increase in wet bulb temperature increased the lightning activity by over two orders of magnitude) and decreased in temperate latitudes (in Melbourne, an increase of about half an order of magnitude in the monthly total of ground flashes within a 10°C range of wet bulb temperature was observed). Further examining relationship between thunderstorm occurrences and T_w , we found strong increase in monthly mean number of thunderdays, T_d , with increase in monthly mean daily maximum wet bulb temperature, T_w , for tropical localities in Australia (example for Mt Isa is given in Fig. 8.7.A). However, only weak increase or even decrease was observed for non-tropical localities (e.g. Perth, Fig. 8.7.B). These results are in line with earlier findings of Mackerras and Darveniza [1994] and Jayaratne and Kuleshov [2006] about variation in lightning rate in Australia.

It appears that the main explanation for the annual variation in monthly flash density in tropical parts of the Australian continent is found in the variation in wet bulb temperature and CAPE. However, other factors such as variation in freezing level [Mushtak *et al.*, 2005; Williams *et al.*, 2005], in aerosol loading [Williams and Stanfill, 2002], as well as variation in topography [Boccippio *et al.*, 2001], may also influence the geographical and seasonal variations of lightning parameters in other parts of the continent.

Fig. 8.8 Time series of lightning ground flash density N_g (as derived from T_d records and measured by the LFCs) for Darwin (A), Townsville (B) and Mt Isa (C)



8.5.4 Yearly Variations in Thunderdays

Climatic hazards such as thunderstorms and lightning can accompany destructive weather, particularly in the tropical regions. It is important to examine how the frequencies of thunderstorms have changed over the periods for which thunderday records are available in Australia and, perhaps more importantly, how they are likely to change in the future.

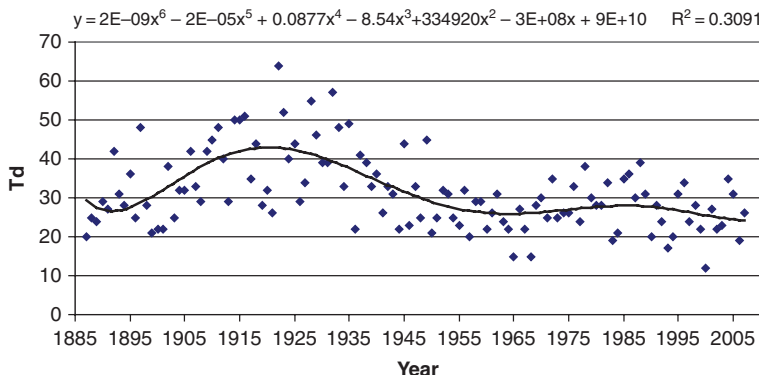


Fig. 8.9 Time series of yearly thunderdays for Brisbane 1887–2007 with sixth-order polynomial trendline

Based on the results of earlier studies which demonstrated that sensitivity of thunderstorm and lightning activity to environmental changes is high in the tropics (section 8.5.3), we examined time series of T_d for several Australian tropical and subtropical observational sites in the following Figures – 50 year records for Darwin Fig. 8.8A, Townsville Fig. 8.8B, Mt Isa Fig. 8.8C, and the 118 year record for Brisbane Fig. 8.9. While the correlation coefficients (R^2) are rather low for all the data sets (less than 0.1), it is possible to perceive small trends in the long-term T_d data. For about the 50 year period 1940–1990, it would appear that there has been a general upward trend in T_d for all sites, possibly followed by a subsequent downward trend. However, the longer-term T_d data for Brisbane appear to indicate an upward trend to about 1930, then a downward trend to about 1950, an upward trend to about 1995, followed by a downward trend, with an overall yearly mean of 32.8 and standard deviation of 10.2 thunderdays.

It would be of interest to attempt to relate these T_d data to *Climate Change 2007*, the Fourth Assessment Report of the United Nations Intergovernmental Panel on Climate Change (IPCC). It states that “Warming of the climate system is unequivocal” and “Most of the observed increase in globally averaged temperatures since the mid-20th century is very likely due to the observed increase in anthropogenic greenhouse gas concentrations” [IPCC, 2007]. Clearly, the effects of climate change on thunderstorms in Australia need to be studied in much greater detail, because thunderstorms and lightning are temperature-sensitive weather phenomena.

8.6 CGR4 Lightning Flash Counter

Recently, a new generation of ground-based LFCs has been developed [Farnsworth *et al.*, 2004]. The new CGR4 LFC (Cloud to Ground Ratio #4) is able to record ground flashes, cloud flashes, and total flashes. From this information one can



Fig. 8.10 The CGR4 LFCs installed at the Meteorological Station at the Brisbane Airport. The waterproof cabinet contains the CGR4 and three data loggers on a shelf above the CGR4

obtain, for example, diurnal and annual variation in lightning occurrence, and the cloud flash to ground flash ratio.

One of the CGR4 LFCs has been installed at the Meteorological Station at the Brisbane Airport (Fig. 8.10). The waterproof cabinet contains the CGR4 and three data loggers on a shelf above the CGR4. The instrument is connected to the vertical aerial.

The Australian Bureau of Meteorology is at present testing the six CGR4s in various parts of Australia to assess their suitability for proposed use in conjunction with Automatic Weather Stations (AWSs). The CGR4 effective range of detection is about 12 km for cloud flashes and about 14 km for ground flashes. These ranges are close to the range at which thunder can be heard, so a day on which the CGR4 detects lightning will usually be a thunder day. Connection of the CGR4 LFCs to AWSs will provide a possibility to establish a widespread network of about 500 sites across Australia.

8.7 Some Aspects of Thunderstorm Hazards

The normal hazards associated with thunderstorms are common in Australia. In some instances, the effects of severe thunderstorm winds and of lightning-initiated bushfires are so extreme that they are classified as natural disasters [*Natural Disasters in Australia*, 1985]. Insurance-related claims arising from thunderstorms (wind,

hail and flash flood damage) from 1967 to 1999 amount to about 5 billion Australian dollars [*Insurance Council of Australia*, 2000]. Direct and nearby cloud-to-ground lightning strikes can be hazardous to persons, structures and industrial and utility installations. Three aspects of thunderstorm hazards with characteristics that seem special to Australia include lightning-initiated wildfires (bushfires and grass fires), lightning mediated injuries to telephone users, and wind gust damage to power lines.

8.7.1 Lightning-Initiated Wildfires

Lightning can start wildfires, which cause damage to the natural environment, property and loss of life. The source of the ignition is the lightning current in ground flashes, and firing is known to be associated with low moisture contents of (potential) fuels such as duff in trees and dense grass, and the occurrence of multiple stroke currents and continuing current between strokes [Zhou and Darveniza, 1994]. The last is known as the “hot” component of lightning current, and typically is a current of about 150 A that flows for times of over 50 ms, and the associated arc is of sufficient duration to volatilise the moisture and to pyrolise cellulosic materials. Lightning initiated grass fires are a major problem in inland areas where winter rainfall has produced a good cover of grass that then dries out. In critical areas with a high fire risk rating, almost every lightning strike leads to immediate firing of the grass and then widespread wildfires. There is usually a different time process for bushfires caused by lightning strikes to trees. Often, the firing starts as a small localised fire in or near the crown of the tree, and it may take a few hours for the fire to spread to other trees and to become a wildfire. It is well known that electric field changes from multiple stroke ground flashes can display a detectable presence of continuing current provided the aerial and measurement system have a bandwidth from 1 Hz to 10 kHz. So there is an opportunity to combine such a detection capability with the real-time LLS recording of ground flashes in areas of high fire rating. If the ground flash has a continuing current component, then the risk of initiating a fire is high, and this information might be used to extinguish the fire while it is still localized and before it becomes a wildfire.

8.7.2 Lightning Mediated Injuries to Telephone Users

In Australia, lightning poses a greater threat to individuals than almost any other natural hazard, accounting for five to ten lives and well over 100 injuries annually [*Prentice*, 1972b]. There have been 650 registered fatalities in Australia in the period 1803–1992 caused by lightning strikes [*Coates*, 1996]. Most fatalities and serious injuries are to people outdoors during thunderstorms. That is why AS/NZS 1768:2007 included the so-called 30:30 rule in its chapter on personal (lightning) safety precautions with advice on when to seek shelter. The threat is greatest if the person is outdoors when the thunderstorm is local, i.e. for an approaching thunder-

storm, when the time between the flash and the thunder is less than 30 s, and for a receding local thunderstorm, until more than 30 min have elapsed after the last thunder is heard. However, injuries also occur to people indoors, particularly if using a land-line telephone during a local thunderstorm. In Australia about 20–30 years ago, between 50 and 70 people were injured annually by telephone mediated lightning events [Andrews *et al.*, 1992]. The injury results from the large voltage difference that can occur between the telephone and the local earth, caused either by a surge entering the building via the telephone wires, or (and much more frequently) by a local earth potential rise caused by a lightning surge imposed on nearby power lines or by a nearby lightning flash to ground. The likelihood of such an injury is greatly reduced if a surge protective device (SPD) is fitted between the telephone wires and a telecom earth and this is equi-potential bonded to the electricity earth. In recent years, the frequency of such injuries has reduced greatly, because of a combination of widely publicised warnings not to use telephones during local thunderstorms, the selective fitting of SPDs in lightning prone areas, and the trend to the widespread use of cordless and mobile (cell) phones.

8.7.3 Wind Gust Damage to Power Lines

It is common electrical power system practice to record lightning as the cause of overhead line faults, outages and customer interruptions during thunderstorms. However, lightning flashes during thunderstorms are invariably accompanied by strong winds. There are about 25–35 thunderstorm-days per year in south-east Queensland; during typical thunderstorms, the numbers of ground flashes range between about 500 and 5000, and wind gust speeds can reach 100 km/hr. Also, there about 5–10 windstorms (with very little or no lightning) each year, and the wind gust speeds can reach up to 80 km/hr. Obviously, the wind alone causes the faults on overhead lines during windstorms, these being due to clashing conductors and wind-driven movement of trees and branches onto line conductors. But during thunderstorms, both lightning ground flashes to and near the line and wind gust effects can cause faults – it is of interest to determine the relative contributions that lightning and wind make to the frequency of the faults. This has been done by analyzing the weather and system data for the ENERGEX system in south-east Queensland for the years 2004/05, 2005/06 and 2006/07 using statistical correlations between the relevant weather variables (lightning ground flashes and wind gust speeds) and system events (line outages and customer interruptions) [Davreniza *et al.*, 2008]. Data are available for 68 storms during the three years; these were grouped into thunderstorms (47) and windstorms (21), and comparisons were made of the effects of lightning ground flashes and wind gusts on system outages and interruptions. The analyses show that the strongest correlation is between wind gust speeds and system events, with R^2 usually in the range 0.5–0.75: Fig. 8.11 is an example for 2006/07. In contrast, the correlation with lightning ground flashes (during thunderstorms) is smaller, with R^2 usually in the range 0.25–45. The relative

Fig. 8.11 2006/2007 feeder outages (lockouts) versus mean wind gust speeds

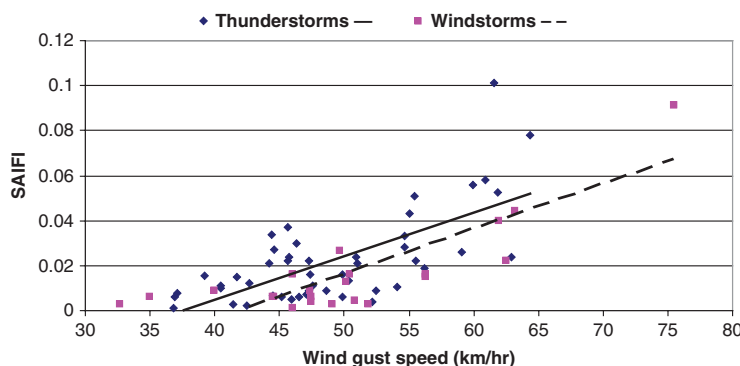
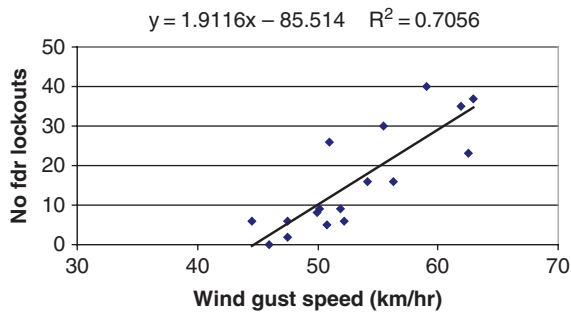


Fig. 8.12 3 years of thunderstorms and wind storms, SAIFI versus wind gust speeds

contributions of lightning and wind during thunderstorms can be deduced from the following linear correlation equations (for windstorms and thunderstorms) between wind gust speeds (WGS in km/hr) and the system average interruption frequency index (SAIFI, which characterizes customer interruption frequencies per storm, and is usually about 1–2 interruptions per year). The relative contributions are also illustrated by the correlation plots in Fig. 8.12.

$$\text{Windstorms: } \text{SAIFI} = 0.0017 \text{ WGS} - 0.0693 \quad (8.1)$$

giving $\text{SAIFI} = 0.016, 0.033, 0.05, 0.067$ for $\text{WGS} = 50, 60, 70, 80 \text{ km/hr}$

$$\text{Thunderstorms: } \text{SAIFI} = 0.0019 \text{ WGS} - 0.0702 \quad (8.2)$$

giving $\text{SAIFI} = 0.025, 0.044, 0.063, 0.082$ for $\text{WGS} = 50, 60, 70, 80 \text{ km/hr}$

It can be seen that the thunderstorm SAIFI are larger than the windstorm SAIFI. The latter vary between 63 and 81% of the thunderstorm SAIFI, and as might be expected, the influence of wind relative to lightning increases with wind gust speed. This is an important finding in respect of the relative sensitivity of the EN-ERGEX distribution network to wind and lightning, and demonstrates that during

thunderstorms, high wind gust speeds are the dominant cause of faults rather than lightning ground flashes.

8.8 Summary and Conclusions

Long-term lightning data obtained by lightning flash counters (CIGRE-500 and CGR3) over a period of up to 23 years at 39 localities around Australia, as well as lightning data gathered by the NASA satellite-based instruments (OTD and LIS), have been used in order to analyze spatial distribution and frequency of lightning activity in Australia. The lightning data were used to produce lightning flash density maps, the first for Australia. Long-term records of thunderdays registered at the Australian stations were also used to produce an updated thunderday map.

In general, the geographical distribution of lightning incidence expressed as total lightning flash density, N_t , (i.e. cloud-to-ground and intracloud flashes) demonstrates high level of lightning activity ($N_t > 10 \text{ km}^{-2} \text{ yr}^{-1}$) in the northern parts of Australia and a decrease in total flashes southwards ($N_t < 5 \text{ km}^{-2} \text{ yr}^{-1}$ in Victoria, the southern parts of Western and Southern Australia, and Tasmania). The peak lightning occurrence is in the north-western part of the Australian continent with N_t values above $30 \text{ km}^{-2} \text{ yr}^{-1}$ centred around $16^\circ \text{ S } 126^\circ \text{ E}$. Secondary maxima are evident over the north-eastern part of the Northern Territory and northern part of Queensland, and over the eastern parts of Queensland and New South Wales, with N_t values up to $10 \text{ km}^{-2} \text{ yr}^{-1}$. Spatial distribution of lightning occurrence is in general agreement with the spatial distribution of thunderstorms as it is presented in the map of average annual thunderdays for Australia.

Seasonal distributions of lightning occurrence at the selected localities demonstrate predominance of lightning in Australia in warmer months, with peak occurrence of lightning in January. In the northern half of the country, development of thunderstorms and lightning is enhanced by high boundary-layer moisture levels and lower surface pressure in the wet season months (October – April). Seasonal distribution of lightning activity in higher latitudes is more uniform; lightning is still more frequent in warmer months, but it also occurs in cooler months (May – September) in association with active frontal systems.

A reduction in lightning total flash density, N_t , by a factor of about 10 for a change in latitude from 10° S to 40° S was found, and this is in agreement with the earlier studies. The variation of N_t for the range of latitudes over the Australian continent is approximately expressed by the empirical relationship $N_t = \exp(3.85 - 0.088\lambda) \text{ km}^{-2} \text{ yr}^{-1}$, where λ is the magnitude of the latitude in degrees. It appears that the main explanation for the annual variation in monthly flash density and latitudinal variation in annual flash density across the Australian continent is found in the variation in wet bulb temperature and convective available potential energy CAPE.

Time series of T_d for several Australian tropical and subtropical observational sites have been examined. For about the 50 year period 1940–1990, it would appear that there has been a small upward trend in T_d for all sites, possibly followed by a subsequent downward trend. However, the longer-term T_d data (118 years) for

Brisbane appear to indicate both upward and downward trends. The effects of climate change on thunderstorms in Australia need to be studied in much greater detail, because thunderstorms and lightning are temperature-sensitive weather phenomena.

A new generation of ground-based LFCs has been developed. The new CGR4 LFC (Cloud to Ground Ratio #4) is able to record ground flashes, cloud flashes, and total flashes. Connection of the CGR4 LFCs to Automatic Weather Stations will provide a possibility to establish a widespread network of about 500 sites across Australia.

In addition to the normal hazards associated with thunderstorms, there are three hazards that are special to Australia, including lightning-initiated wildfires, lightning current injuries to telephone users, and wind gust damage to power lines.

The wildfires started by lightning are known locally in Australia as bushfires and grass fires, and these can cause extensive damage and loss of life. The ignition is caused by the lightning current in ground flashes, and firing is associated with low moisture contents of (potential) fine fuels such as duff in trees and dense grass, and the occurrence of multiple stroke currents and continuing current. During dry periods, lightning initiated grass fires are a major problem in inland areas, as are lightning initiated bushfires in remote forest areas. Once ignited, grass fires spread quickly, whereas in bushfires, ignition often starts as a small localised fire in or near the crown of the tree, and it may take a few hours for the fire to spread to other trees and to become an uncontrollable wildfire.

The lightning threat to people in Australia is greater than almost any other natural hazard, and causes five to ten fatalities and well over 100 injuries annually. Most of the fatalities and more numerous injuries are from lightning strikes to people who are outdoors during thunderstorms. However, injuries also occur to people indoors, particularly if using a land-line telephone during a local thunderstorm. In Australia about 20–30 years ago, many people were injured annually by telephone mediated lightning events. The rate of such injuries has been reduced markedly by fitting a surge protective device between the telephone wires and a telecom earth and bonding this to the electricity earth.

Electrical power system staff often attribute the cause of overhead line faults, outages and customer interruptions during thunderstorms to lightning. However, strong winds also occur during thunderstorms. Analyses of weather and system data demonstrate that during thunderstorms, high wind gust speeds are the dominant cause of overhead line faults rather than lightning ground flashes. Wind gusts cause between 63 and 81% of the interruptions during thunderstorms, and as might be expected, the influence of wind relative to lightning increases with wind gust speed.

References

- Anderson, R. B., and A. J. Eriksson (1980), Lightning parameters for engineering application, *Electra*, 69, 65–102.
Andrews, C. J., M. A. Cooper, M. Darveniza, and D. Mackerras (1992), Lightning injuries: electrical, medical and legal aspects, CRC Press, Boca Raton, Florida, Appendix 1: Special aspects of telephone mediated lightning injury: an Australian perspective, pp. 163–176.

- Anderson, R. B., A. J. Eriksson, H. Kroninger, D. V. Meal, and M. A. Smith (1984), Lightning and thunderstorm parameters, paper presented at IEEE Int. Conf. Lightning and Power Systems, London, UK.
- Anderson, R. B., H. R. van Niekerk, S. A. Prentice, and D. Mackerras (1979), Improved lightning flash counter, *Electra*, 66, 85–98.
- Baral, K. N., and D. Mackerras (1992), The cloud flash-to-ground flash ratio and other lightning occurrence characteristics in Kathmandu thunderstorms, *J. Geophys. Res.*, 97, 931–938.
- Baral, K. N., and D. Mackerras (1993), Positive cloud-to-ground lightning discharges in Kathmandu thunderstorms, *J. Geophys. Res.*, 98, 10331–10340.
- Barham, R. A. (1965), Transistorised lightning flash counter, *Electron. Lett.*, 1, 173.
- Barham, R. A., and D. Mackerras (1972), Vertical-aerial CIGRE-type lightning flash counter, *Electron. Lett.*, 8, 480–482.
- Boccippio, D. J., K. L. Cummins, H. J. Christian, and S. J. Goodman (2001), Combined satellite-and surface-based estimation of the intracloud-cloud-to-ground lightning ratio over the continental United States, *Mon. Wea. Rev.*, 129, 108–122.
- Bunn, C. C. (1968), Application of electric field change measurements to calibration of lightning flash counters, *J. Geophys. Res.*, 73, 1907–1912.
- Christian, H. J., K. T. Driscoll, S. J. Goodman, R. J. Blakeslee, D. A. Mach, and D. E. Buechler (1996), The Optical Transient Detector (OTD), paper presented at 10th Int. Conf. on Atmospheric Electricity, Osaka, Japan, 10–14 June.
- Christian, H. J., R. J. Blakeslee, S. J. Goodman, D. A. Mach, M. F. Stewart, D. E. Buechler, W. J. Koshak, J. M. Hall, W. L. Boeck, K. T. Driscoll, and D. J. Boccippio (1999), The Lightning Imaging Sensor, paper presented at 11th Int. Conf. on Atmospheric Electricity, Guntersville, Alabama, 7–11 June.
- Christian, H. J., R. J. Blakeslee, D. J. Boccippio, W. L. Boeck, D. E. Buechler, K. T. Driscoll, S. J. Goodman, J. M. Hall, W. J. Koshak, D. M. Mach, and M. F. Stewart (2003), Global frequency and distribution of lightning as observed from space by the Optical Transient Detector, *J. Geophys. Res.*, 108(D1), 4005, doi:10.1029/2002JD002347.
- Coates, L. (1996), An overview of fatalities from some natural hazards in Australia. *Proceedings of NDR96 Conference on Natural Disaster Reduction*, Gold Coast, Australia.
- Darveniza, M., C. Dunn, and B. Holcombe (2008), A comparison of faults and outages on an electrical distribution system caused by lightning and wind gusts, 29th Int. Conf. on Lightning Protection (ICLP), Uppsala, Sweden, June, paper 6b-2, 6pp.
- Farnsworth, N., D. Mackerras, and M. Darveniza (2004), Lightning occurrence in Brisbane, Melbourne and Darwin thunderstorms recorded by CGR4 lightning flash counters, paper presented at Int. Conf. on Storms, Austral. Meteorol. and Oceanographic Soc. and Meteorol. Soc. of New Zealand, Brisbane, Australia, 5–9 July.
- GPATS website, www.gpats.com.au
- Huschke, R. E. (Ed.) (1959), *Glossary of meteorology*, 638pp., Am. Meteorol. Soc., Boston, Massachusetts.
- Insurance Council of Australia (2000), Risk Zone Accumulation Guide, Appendix F.
- Intergovernmental Panel on Climate Change (IPCC) (2007), *Climate Change 2007*, the Fourth Assessment Report, WMO and UNEP, Geneva, Switzerland.
- Jayaratne, E. R., and Y. Kuleshov (2006), The relationship between lightning activity and surface wet bulb temperature, *Meteorol. Atmos. Phys.*, 91, 17–24, doi:10.1007/s00703-004-0100-0.
- Kattron website, www.lightning.net.au
- Kotaki, M., I. Kuriki, C. Katoh, and H. Sugiuchi (1981), Global distribution of thunderstorm activity observed with ISS-b, *J. Radio Res. Lab. Japan*, 28, 48–71.
- Kuleshov, Y., G. de Hoedt, W. Wright, and A. Brewster (2002), Thunderstorm distribution and frequency in Australia, *Aust. Meteorol. Mag.*, 51, 145–154.
- Kuleshov, Y., and E. R. Jayaratne (2004), Estimates of lightning ground flash density in Australia and its relationship to thunder-days, *Aust. Meteorol. Mag.*, 53, 189–196.
- Kuleshov, Y., D. Mackerras, and M. Darveniza (2006), Spatial distribution and frequency of lightning activity and lightning flash density maps for Australia. *J. Geophys. Res.*, 111, D19105, doi:10.1029/2005JD006982.

- Lightning Protection (2007), Australian Standard/New Zealand Standard 1768–2007, 188pp., Standards Australia, Sydney, Australia and Standards Association of New Zealand, Wellington, New Zealand.
- Mackerras, D. (1978), Prediction of lightning incidence and effects in electrical systems, *Electr. Eng. Trans., Inst. Eng. Aust.*, *EE-14*, 73–77.
- Mackerras, D. (1985), Automatic short-range measurement of the cloud flash to ground flash ratio in thunderstorms, *J. Geophys. Res.*, *90*, 6195–6201.
- Mackerras, D., and M. Darveniza (1992), Design and performance of CGR3 instruments for measuring the cloud flash-to-ground flash ratio in thunderstorms, *Internal Report EE92/2*, 99pp., Univ. of Queensland, St. Lucia, Australia.
- Mackerras, D., and M. Darveniza (1994), Latitudinal variation of lightning occurrence characteristics, *J. Geophys. Res.*, *99*, 10813–10821.
- Mackerras, D., M. Darveniza, R. E. Orville, E. R. Williams, and S. J. Goodman (1998), Global lightning: total, cloud and ground flash estimates, *J. Geophys. Res.*, *103*, 19791–19809.
- Mushtak, V., E. Williams, and D. Boccippio (2005), Latitudinal variations of cloud base height and lightning parameters in the tropics, *Atmos. Res.*, *76*, 222–230.
- Natural Disasters in Australia (1985), *Proc. 9th Symp. Australian Academy of Technological Sciences*, Sydney, 16/17 October 1985, 373pp, AATSE, Melbourne, Australia.
- Orville, R.E., and W. Spencer (1979), Global lightning flash frequency, *Mon. Wea. Rev.*, *107*, 934–943.
- Pierce, E. T. (1956), The influence of individual variations in the field changes due to lightning discharges upon the design and performance of lightning flash counters, *Archiv für Meteorologie, Geophysik und Bioklimatologie, Serie A: Meteorologie Und Geophysik, Band 9*, 78–86.
- Prentice, S. A. (1972a), CIGRE Lightning flash counter. Part 1 Specification. Part 2 Guide for estimating ground flash density CIGRE lightning flash counter, *Electra*, *22*, 149–171.
- Prentice S. A. (1972b), Lightning fatalities in Australia, *Elec. Eng. Trans. Inst. Eng. Aust.*, *EE8*, September, 55–63.
- Prentice, S. A., and D. Mackerras (1969), Recording range of a lightning flash counter, *Proc. Inst. Elect. Eng. (London)*, *116*, 294–302.
- Rutledge S. A., E. R. Williams, and T. D. Keenan (1992), The Down Under Doppler and Electricity Experiment (DUNDEE): Overview and Preliminary results, *Bull. Am. Meteorol. Soc.*, *73*(1), 3–15.
- Williams, E. R. (1992), The Schumann resonance: A global tropical thermometer, *Science*, *256*, 1184–1187.
- Williams, E. R. (1995), Meteorological aspects of thunderstorms, in *Handbook of Atmospheric Electrodynamics*, edited by H. Volland, pp. 27–60, CRC Press, London, UK.
- Williams, E. R., S. A. Rutledge, S. G. Geotis, N. Renno, E. Rasmussen, and T. Rickenbach (1992), A radar and electrical study of tropical “hot towers”, *J. Atmos. Sci.*, *49*, 1386–1395.
- Williams, E., and S. Stanfill (2002), The physical origin of the land-ocean contrast in lightning activity, *C. R.-Acad. Sci. Phys.*, *3*, 1277–1292.
- Williams, E., V. Mushtak, D. Rosenfeld, S. Goodman, and D. Boccippio (2005), Thermodynamic conditions favorable to superlative thunderstorm updraft, mixed phase microphysics and lightning flash rate, *Atmos. Res.*, *76*, 288–306.
- World Meteorological Organization (WMO) (1953), World distribution of thunderstorm days. Part 1: Tables. *WMO Publ. 21, TP 6*, WMO, Geneva, Switzerland.
- Zhou, Y., and M. Darveniza (1994), Lightning initiated fires – the energy absorbed by fibrous materials from impulse current arcs, *J. Geophys. Res. Atmos.*, *99*, 10663–10670.

Chapter 9

Cloud-to-Ground Lightning Observations in Brazil

**Osmar Pinto Jr., Iara R.C.A. Pinto, Marcelo M.F. Saba and
Kleber P. Naccarato**

Abstract A comprehensive review of cloud-to-ground (CG) lightning observations in Brazil is presented. Brazil is the largest country in the tropical region and it is believed to have the largest cloud-to-ground (CG) lightning activity in the world, estimated from thunderstorm days and satellite data in about 50 millions CG lightning flashes every year. Emphasis is given to recent observations made by lightning location systems and high-speed cameras in the Southeast region of the country. At the present time, they correspond to the largest CG lightning data set available for the tropics. Some specific parameters emerging from these observations are quantified. The observations are compared with similar ones made in other tropical and temperate countries, as well as with past observations obtained by other techniques in Brazil.

Keywords Tropical lightning · Brazil · Lightning location systems · High-speed cameras

9.1 Introduction

The first systematic observations of cloud to ground (CG) lightning in Brazil were done in the decade of 1960 based on the number of thunderstorm days (or thunderdays for short) at different sites. Later, they were complemented by observations through a network of flash counters, an instrumented tower and a triggered site, most of them in the Southeast region of the country. More recently, a large dataset of observations by a large lightning location network and by high-speed cameras were obtained.

Brazil is the largest country in the tropical region of the world and, probably, has the largest lightning activity in the world. Based on the thunderdays information

O. Pinto (✉)

Atmospheric Electricity Group – ELAT, Brazilian Institute of Space Research (INPE),
São José dos Campos, São Paulo, SP, Brazil
e-mail: osmar@dge.inpe.br

it is estimated that about 50 million CG lightning flashes occur every year. This estimation is in reasonable agreement the value calculated based on simultaneous total lightning observations by satellites and CG lightning observations by Lightning Location Systems (LLS) in the tropical region (Pinto et al., 2003a, 2007; Pinto 2003; Chisholm and Cummins 2006), which also suggest that tropical CG lightning has a geographical distribution similar to total lightning. Such a perspective suggests that the study of the CG lightning in Brazil may be very important to improve both the understanding of many aspects of the phenomenon, as well as the response of tropical CG lightning to different phenomena at many time scales, contributing also to our understanding of climate changes (Pinto et al. 2007; Pinto and Pinto 2008).

In this chapter we review the present knowledge about the CG lightning in Brazil, with emphasis on observations provided by LLS and high-speed cameras. These observations form the largest data set of CG lightning data in the tropics available in the present time. They are then compared with similar observations made in other countries in the tropical region and with past CG lightning observations obtained by other techniques in Brazil.

9.2 Observations of Cloud-to-Ground Lightning by Lightning Location Systems

9.2.1 Brief History

LLS can operate at different frequency ranges from VLF to VHF to detect and locate CG lightning. At VLF/LF range, they consist basically of several sensors, which determine the direction and/or the time to the lightning stroke at the sensor location, and a processing unit, which calculates stroke characteristics such as the strike point location and time, peak current, and others. For a comprehensive description of lightning locating techniques, see for example Cummins et al. (1988a,b) and Rakov and Uman (2003). VLF/LF LLS have collected a large number of CG lightning data, which have been used in many applications by power utilities, weather services, aviation, geophysical research and others.

The first LLS in Brazil was installed in 1988. It was a small regional network in Southeast region of the country consisting of four LPATS (Lightning Positioning and Tracking System) sensors using the time-of-arrival technology. In 1996 it was upgraded to include IMPACT (Improved Accuracy from Combined Technology) sensors, which combines magnetic direction finder and time-of-arrival technologies. In 1999 the network was named Brazilian Integrated Lightning Detection Network (RINDAT). The number of sensors increased gradually up to 24 sensors at the end of 2005. The RINDAT has been reported extensively on the literature (Pinto 2003, 2005; Pinto 2003; Pinto et al. 1996, 1999a, 1999b, 2003a, 2003b, 2006a) and so will not be discussed further here.

In 1999 another LLS was installed in the North region of Brazil with the goal to provide ground truth data for the Lightning Imaging Sensor (LIS). It operated up to 2005 (Pinto 2003; Pinto et al. 2003a; Blakeslee et al. 2003; Fernandes 2005).

In 2006 two other regional networks began to operate in the South and North regions of Brazil. The network in the South consists of ten IMPACT sensors, while the network in the North consists of 13 LPATS sensors.

At the present time, only one network exists in Brazil, named Brazilian Lightning Detection Network (BrasilDAT), which has 47 sensors installed of both (LPATS and IMPACT) types. It is a result of the integration of all regional networks. More details about the BrasilDat can be found in Pinto et al. (2006b, 2007) and Pinto and Pinto (2008). Figure 9.1 shows the location of the BrasilDAT sensors.

9.2.2 Detection Efficiency Models

Like any other measurement system, LLS has its own limitations. Perhaps the most significant one is its flash (stroke) detection efficiency (DE) or the ratio between the number of detected flashes (strokes) by the number of flashes (strokes) that actually

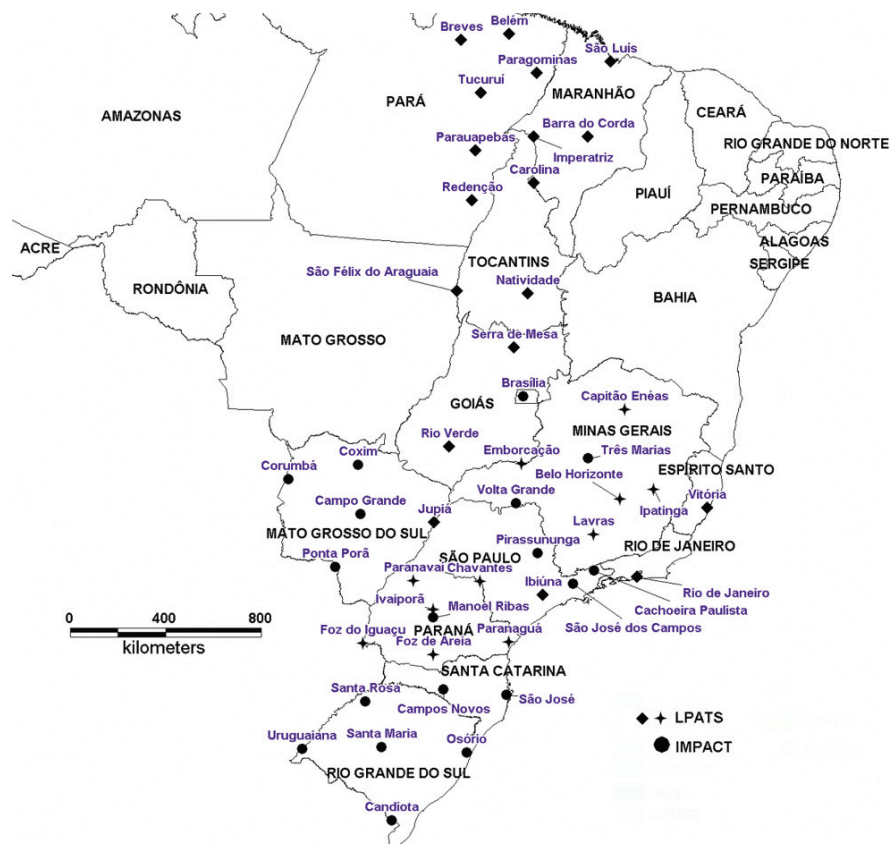


Fig. 9.1 The location of the BrasilDAT sensors at the present time

occur. One of the primary motivations for evaluating LLS performance (particularly its DE) is its effect over the actual climatological variations in CG lightning parameters provided by the network (Cummins and Bardo 2004). In Brazil, this is particularly important because the network has changed its configuration many times during the last two decades.

Several approaches for developing a flash detection efficiency model (DEM) were already proposed: Schulz and Diendorfer (1996), Murphy et al. (2002) and Rompala et al. (2003). All of them use a set of CG flash data reported by the network to compute the flash DE and for this reason they are called relative detection efficiency models (RDEM). When the RDEM use a CG lightning dataset collected over areas associated with higher values of DE (estimated by independent data) as a reference, the relative detection efficiency (RDE) can be approximated to the absolute detection efficiency with a reasonable confidence.

The first Brazilian RDEM was in fact a very simple computational tool (Naccarato et al. 2004), combining the Murphy et al. (2002) and Rompala et al. (2003) methods. The model was able to assess the RDE of the LLS with relative high accuracy. However, the higher the number of events, the longer the computational time, because it is based on the number of CG lightning flashes detected within adjacent cells. Also, in order to compute the RDE for different sensor configurations, the model requires reprocessing all the data. The second Brazilian RDEM (Naccarato et al. 2006a,b) was based on Schulz (1997) and Schulz and Diendorfer (1996). It computes the RDE for each sensor, which depends on the peak current and the distance from the event to the sensor. Thereby, using these individual sensor RDE distributions, the network DE is computed based on the combined probability of each sensor to detect or not an event, considering the distance among the sensors. This reduces drastically the calculations and leads to a very short computational time.

The two previous RDEM were capable to reproduce several features of the LLS. However, the results still show a “border effect” due to the reduced number of CG flashes detected near to the network boundaries. Thus, a new approach was considered (Naccarato and Pinto 2008) that not only takes into account the peak current values and the distance of the CG lightning to the sensors, but also neglects the solutions that have no redundancy. Such solutions, mainly for the outmost areas (near the network boundaries), cause a fake effect of increasing in the DE. This third model is able to recover the actual CG flash rates at these areas. Furthermore, this model neglects the periods that each sensor is offline (due to communications problems or even hardware faults) with a daily resolution, instead of the monthly resolution adopted in the second RDEM.

Figures 9.2 and 9.3 show the BrasilDAT network DE computed by the second RDEM (RDEM2) and the third RDEM (RDEM3) using the same average sensor RDE curves. The values shown in magenta represent DE values lower than 30% (minimum values). Similarly, values in white represent DE values greater than 90% (maximum values). It can be observed that the overall network DE for the RDEM3 is relatively low compared to the results from RDEM2, revealing that the RDEM2 overestimates the network DE, particularly closer to the network boundaries.

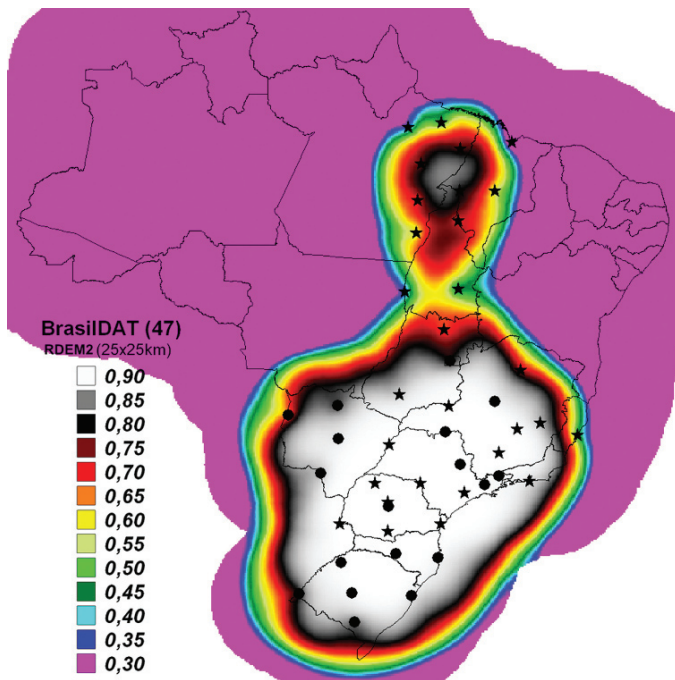


Fig. 9.2 The BrasILDAT network detection efficiency computed by the RDEM2 model, for a spatial resolution of 25×25 km (See also Plate 9 in the Color Plate Section on page 597)

The DE values computed by the RDEM3 were validated in the Southeast region of Brazil by triggering lightning (Solorzano 2003) and high-speed camera observations (Ballarotti et al. 2006).

9.2.3 Flash Parameters from Lightning Location Systems

Figure 9.4 shows a map of the annual average CG lightning flash density for a spatial resolution of 10×10 km observed in the Southeast region of Brazil from 1999 to 2004 based on approximately 20 million lightning flashes (Naccarato 2005). Data in this figure are not corrected for the LLS DE, following the format that it is usually presented in the literature. The regions in white in Fig. 9.4 correspond to densities larger than $7.5 \text{ flashes } \text{km}^{-2} \text{ year}^{-1}$. The region of maximum CG lightning flash density in this figure occur around 23° S and 47° W (showed by a large white spot) and it is coincident with the urban area of the city of São Paulo, suggesting an urban effect on lightning activity (Pinto et al. 2004a; Naccarato et al. 2003). For the spatial resolution in Fig. 9.4, the maximum CG lightning flash density in this region is $9\text{--}10 \text{ flashes } \text{km}^{-2} \text{ year}^{-1}$, while for a 1×1 km spatial resolution (the lowest possible value adopted for the resolution, considering the location accuracy of the network) this maximum is $17 \text{ flashes } \text{km}^{-2} \text{ year}^{-1}$.

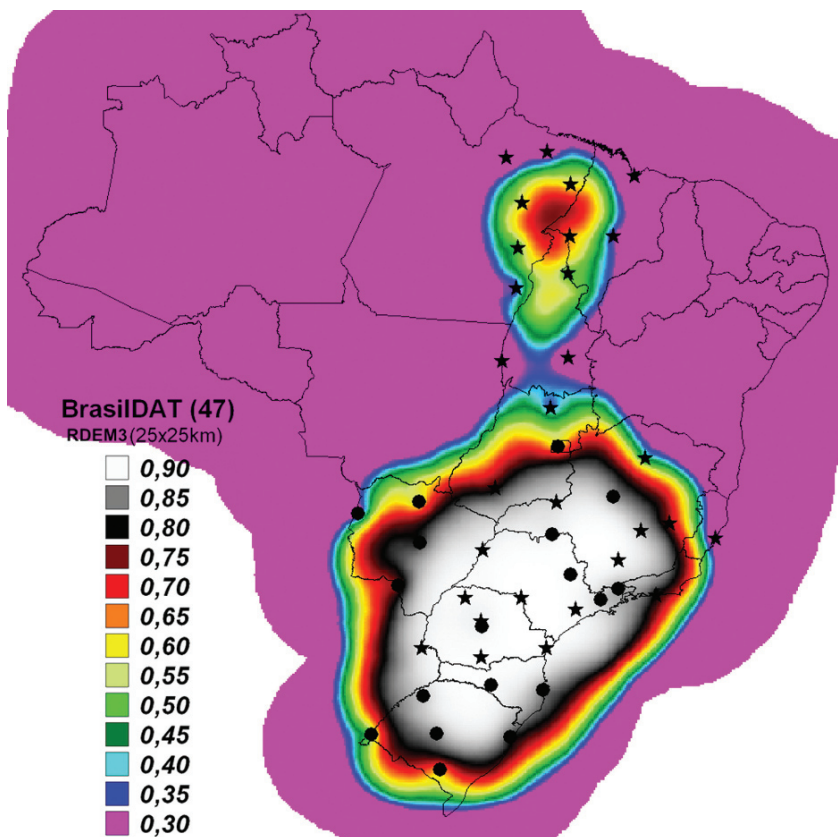


Fig. 9.3 The BrasilDAT network detection efficiency computed by the RDEM3 model, for a spatial resolution of 25×25 km (See also Plate 10 in the Color Plate Section on page 598)

Table 9.1 shows the lightning characteristics obtained in the Southeast region of Brazil by the LLS from 1999 to 2005.

The flash density is expressed in terms of maximum values, instead of average values, in order to minimize the influence of the DE of the LLS in the borders of the network. The value of $21 \text{ flashes } \text{km}^{-2} \text{ year}^{-1}$ corresponds to a $1 \times 1 \text{ km}$ spatial resolution and is corrected by the local DE of the network. The effect of the location accuracy on the maximum flash density has been discussed by Campos and Pinto (2007).

The average percentage of positive flashes was calculated considering only positive flashes above 10 kA to avoid intracloud contamination and shows large variations from a few percents to almost 30%. This peak current threshold was assumed considering the BrasilDAT network configuration (Cummins et al. 1988a, 1998b). The largest values of the percentage of positive flashes are apparently found in regions with a larger occurrence of frontal systems.

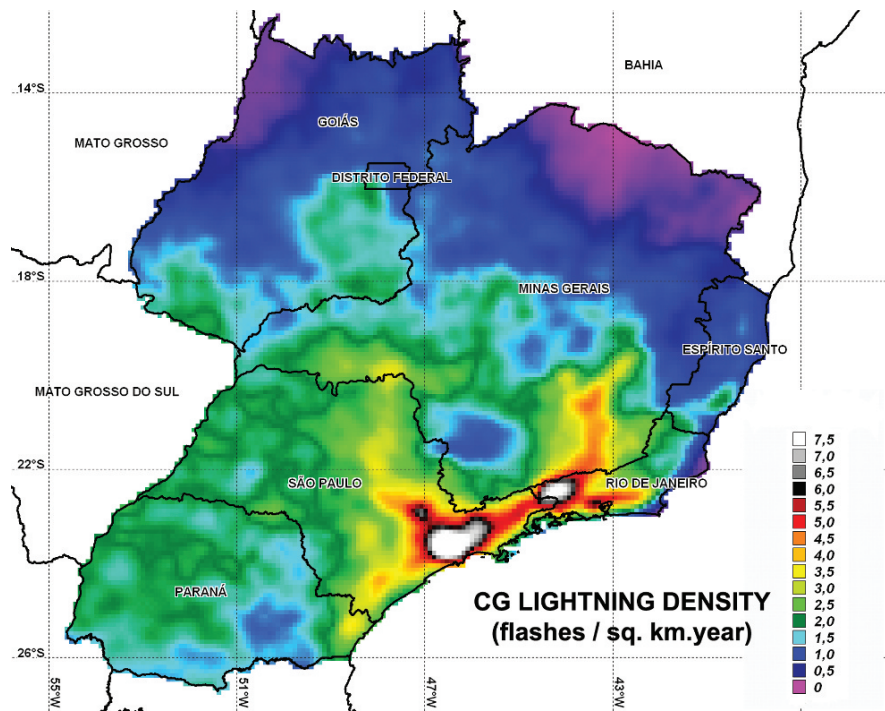


Fig. 9.4 Annual average CG lightning flash density in the Southeast region of Brazil from 1999 to 2004 for a spatial resolution of 10×10 km. Regions in white correspond to densities larger than $7.5 \text{ flashes km}^{-2} \text{ year}^{-1}$. No correction for the DE was applied (See also Plate 11 in the Color Plate Section on page 599)

Table 9.1 Lightning characteristics obtained by LLS in Brazil from 1999 to 2005

Parameter	Mean value
Annual maximum flash density ¹ (flashes $\text{km}^{-2} \text{ year}^{-1}$)	21
Percentage of positive flashes ² (%)	12
Negative peak current ³ (kA)	23
Positive peak current ^{2,3} (kA)	29
Negative multiplicity	1.9

¹ Value is referred to a 1×1 km spatial resolution and is corrected by the RDEM3. It occurs over the city of São Paulo where the overall DE is 80%.

² Values are referred to peak currents above 10 kA.

³ Values are referred to first strokes and are not corrected by the DE of the network.

The average values observed for negative and positive peak currents corresponds to peak current of first-strokes and are dependent of the stroke DE of the network (Naccarato et al. 2006a). Also, the exclusion of positive flashes below 10 kA causes a bias in the average value for these flashes. The same is true for the average multiplicity of negative CG flashes. The stroke DE of the network was observed to be approximately 55% (Ballarotti et al. 2006).

9.2.4 Comparison with Similar Observations in the Tropical Region

Lightning Location Systems were installed in many other countries in the tropical region: Colombia (Torres et al. 2001; Younes et al. 2003, 2004), Venezuela (Raizman et al. 2004; Tarazona et al. 2006), Java Island (Hidayat et al. 1996; Hidayat and Ishii 1998, 1999; Berger and Zoro (2004), South of China (Chen et al. 2002, 2004), Papua New Guinea (Orville et al., 1997), Australia (Sharp 1999; Kilinc and Beringer 2007) and Malaysia (Abidin and Ibrahim 2003). However, due to differences in the networks, the comparison of these observations with the observations in Brazil is restricted to values of maximum CG lightning flash densities, normalized to a same spatial resolution and corrected for the different detection efficiency and level of contamination by intracloud flashes of each LLS (Pinto et al. 2007).

Table 9.2 shows the maximum CG lightning flash densities for the other tropical networks. All values are larger than the value for Brazil indicated in Table 9.1, except that for Australia. No value is shown for Malaysia in Table 9.2, because the data are considered not reliable (Abidin and Ibrahim 2003).

No comparison was done for the other lightning parameters indicated in Table 9.1 because, for most of the LLS in the tropical region, they are considerably affected by the low detection efficiency of these LLS to low peak current subsequent strokes (Schulz and Diendorfer 1998). In general, for the majority of the LLS, mean peak current (multiplicity) values are overestimated (underestimated) considerably, not allowing knowing if regional differences in these parameters are real or due to differences in the LLS performance (Pinto et al. 2004b; Cummins and Bardo 2004).

9.2.5 Comparison with Similar Observations Outside the Tropical Region

Table 9.3 shows the maximum CG lightning flash densities observed in the temperate region in each continent: in the North America, the highest value was observed in Florida, United States (Orville et al. 2002; Murphy and Holle 2005); in Europe, the highest value was observed in the Northwest region of Italy (Schulz

Table 9.2 Maximum CG lightning densities in the tropical region

Country	Period of observation	Annual maximum flash density ¹ (flashes km ⁻² year ⁻¹)
Colombia	1997–2001	34
	1997	46
Venezuela	2000–2003	56
Java Island	1995	33
Java Island	1999	65
Australia	1998–2003	8

¹ Values are referred to a spatial resolution of 1 × 1 km and are corrected by the DE of the networks.

Table 9.3 Maximum CG lightning flash densities outside the tropics

Continent	Period of Observation	Annual Maximum Flash Density ¹ (flashes km ⁻² year ⁻¹)
North America	1996–2000	18
Europe	1992–2001	17
Asia	1997–2001	24
Africa	2001–2003	27

¹ Values were referred to for a spatial resolution of 1×1 km and corrected by the DE of the networks.

et al. 2005); in Africa, the highest value was observed in the Northwest region of South Africa (Ndlovu and Evert 2006; Evert and Schulze 2005; Bhikha et al. 2006); and, finally, in Asia the highest value was observed in the South region of China (Chen et al. 2002, 2004). The values were obtained following the same procedure for Table 9.2. The following detection efficiency values, taking from the articles cited previously, were used to correct the observed densities: 90% for the regions in United States and Italy, 85% for the region in China and 80% for the region in South Africa. The values in Table 9.3 are close to the value in Brazil (Table 9.1) and lower than the values in Table 9.2.

9.3 Observations of Cloud-to-Ground Lightning by High-Speed Cameras

9.3.1 History

Lightning observations with high-speed cameras began in Brazil in 2000. The first observations were made in Southeast region by a high-speed digital video camera model Red Lake Motion Scope 8000S with a resolution and exposure time of 1 ms. All high-speed video recordings had a 1 s pre-trigger time and a total recording time of two seconds (2,000 frames). The pre-trigger time of 1 s proved to be long enough to prevent missing of first strokes. Also, the total recording time of 2 s is long enough to capture the whole flash. All images were GPS synchronized, time stamped and without any image persistence (Saba et al. 2006a). Initially, the main goal of these observations was to validate LLS data (Saba et al. 2004). Later, the observations were extended to the South region of the country and, also, to investigate other lightning characteristics. The use of these cameras is particularly interesting in order to avoid bias introduced by finite video resolution of standard video tape recordings (Thomson et al. 1984). The advent of high-speed motion CCD video cameras (Fig. 9.5) allowed the use of temporal high-resolution observation of lightning flashes. This observation technique can be considered an accurate-stroke-count technique, that is, a reliable way to study lightning parameters (e.g. multiplicity, percentage of single-stroke flashes) that are sensitive to stroke counting (Saba et al. 2006a). With these cameras several processes (stepped leaders, return strokes, and



Fig. 9.5 Digital high-speed video camera

continuing currents) that occur during a lightning flash can be visualized with high temporal resolution and detail (Fig. 9.6).

It is advisable to use a red filter in front of the lens in order to increase the contrast between the lightning channel and the background during diurnal recordings. It is also highly recommended that the video frames of the high-speed camera shall be GPS time-stamped to an accuracy of one millisecond. This synchronization allowed the comparison of each flash recorded by the camera with the same flash detected by a LLS or other technique (e.g. electric-field measurements). Data from the LLS, for instance, are used to obtain the stroke polarity, an estimate of the peak current near the ground, and the location of the ground strike point.

9.3.2 Flash Parameters from High-Speed Video Observations

During five consecutive summers (from 2003 to 2007), more than 1500 CG lightning flashes were recorded with high-speed cameras in South and Southeast regions of Brazil (Saba et al. 2006a). The statistics of some parameters obtained from these observations for negative and positive CG flashes are summarized in Tables 9.4 and 9.5, respectively.

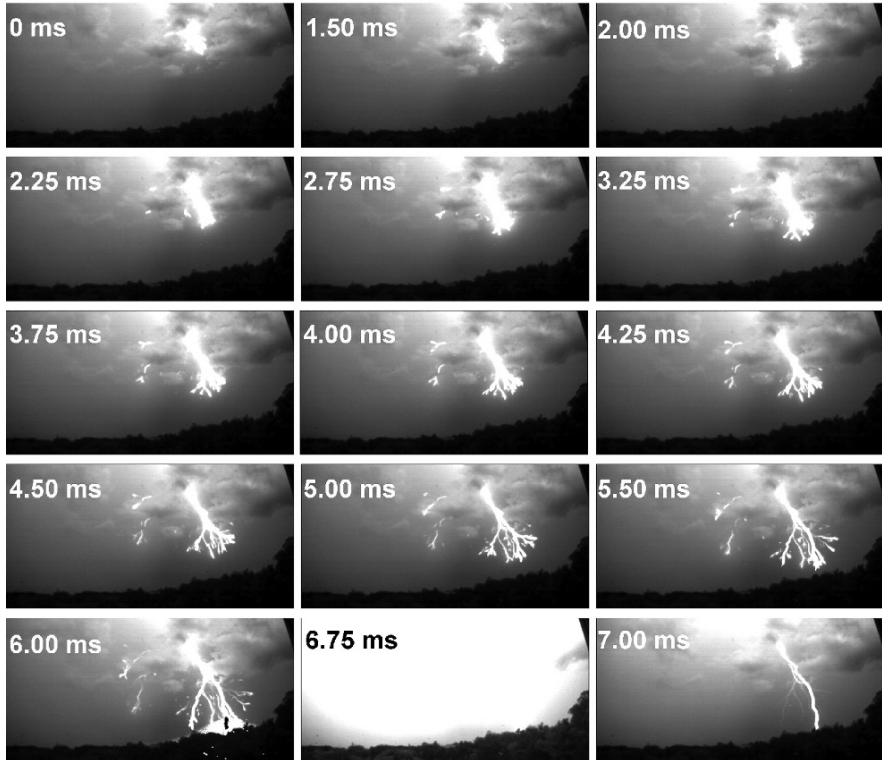


Fig. 9.6 Example of a negative cloud-to-ground leader observation at 4,000 frames per second (some frames are missing)

Table 9.4 Negative CG lightning parameters obtained by high-speed cameras

Parameter	Number of Events	Mean Value
Negative leader speed ($\times 10^5 \text{ m s}^{-1}$)	59	3.4
Percentage of single flashes (%)	233	20
Multiplicity	233	3.8
Flash duration (ms)	221	276
Number of strike points per flash	138	1.7
Interstroke intervals (ms)	608	83
Continuing current duration (ms)	250	32

The mean leader speed in Tables 9.4 and 9.5 are 2-D leader speeds based on the distances between the camera and the flashes and on the geometric characteristics of the camera and lenses used (Saba et al. 2008). The flash duration is defined as the time interval between the occurrence of the first return stroke and the end of the continuing current following the last return stroke, if present.

It is interesting to note that although most of the positive flashes are single, the median value of the duration of positive flashes (143 ms) is similar to negative ones

Table 9.5 Positive CG lightning parameters obtained by high-speed cameras

Parameter	Number of events	Mean value
Positive leader speed ($\times 10^5$ m s $^{-1}$)	9	2.7
Percentage of single flashes (%)	44	70
Multiplicity	44	1.3
Flash duration (ms)	40	177
Number of strike points per flash	37	1.2
Interstroke intervals (ms)	16	174
Continuing current duration (ms)	50	100

(188 ms). This similarity may be explained by the fact that nearly 80% of positive flashes contain at least one long continuing currents and also because interstroke intervals are longer in positive flashes.

Up to 5 different contact points were observed in a negative flash and the vast majority (90%) of the new terminations was created after there had been just one stroke in the previous channel. The average number of lightning strike points is 70% higher than the number of flashes.

Considering that the missing of strokes in high-speed videos is practically negligible, it can be inferred from the average negative multiplicity (3.8) and from the average number of strike points per flash (1.7), that each ground contact point is, in average, struck 2.2 times. For positive CG flashes the average number of strike points per flash is 1.2 and all subsequent strokes in multiple-stroke flashes created a new termination on ground.

In negative CG flashes, long time intervals between strokes are usually associated with the presence of long continuing current. Less than 1% of all interstroke intervals observed lasts more than 500 ms, while 19% of the interstroke intervals presented values less than 33 ms. For positive CG flashes the geometric mean of the time intervals is about two times greater than the respective value for negative flashes. Sometimes a subsequent stroke happens while the continuing current of the previous stroke is still occurring (never observed for negative CG flashes).

In negative CG flashes the presence of long continuing current (CC), that is, CC lasting more than 40 ms, after first strokes is very rare. Only four first strokes of multiple-stroke flashes and six single flashes were observed to be followed by long CC. In addition, we found that on average, the longer is the CC, the lower is the return stroke peak current preceding it.

It was found that negative strokes with peak current higher than 20 kA are never followed by CC durations greater than 40 ms, while negative strokes that have peak currents lower than 20 kA are followed by CC of any duration. Considering the high number of cases observed, these parameters determine an “exclusion zone” for negative strokes, which seems to indicate that high peak current negative strokes followed by long CC do not exist (Fig. 9.7). The “exclusion zone” found for negative strokes was not observed for positive strokes (Saba et al. 2006b).

The CC intensity presents variations with time. They can be either M-components (approximately symmetrical short duration current pulses superimposed to the

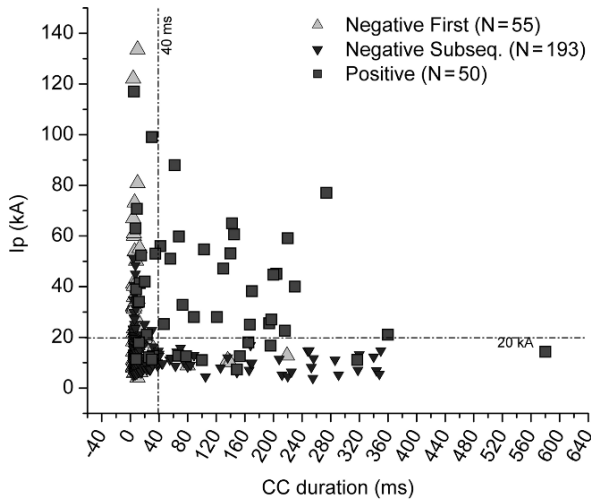


Fig. 9.7 Peak current (I_p) versus CC duration for 248 negative strokes and 48 positive strokes

current base level) or long duration variations that define the CC wave shape (Fig. 9.8). They can be grouped into six wave shape types (Campos et al. 2007, 2008). In extremely long CC it has been observed more than 30 M-components. For the first time, evidence of M-components was observed in positive CG flashes.

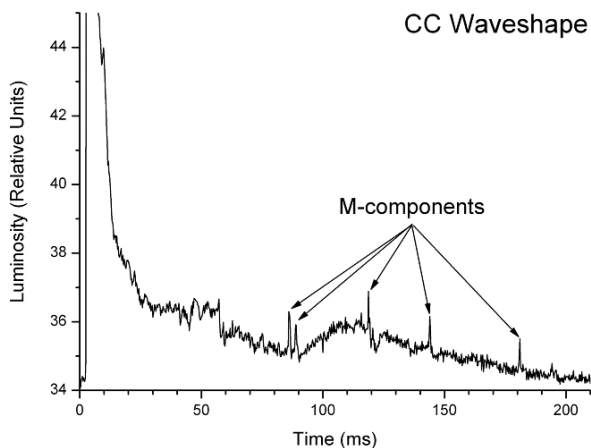


Fig. 9.8 Example of continuing current with M-components superimposed. The M-components are indicated by arrows

9.4 Comparison with Observations by Other Techniques

9.4.1 Thunderstorm Days and Flash Counters

The first systematic observations of CG flashes in Brazil were done in the decade of 1960 by assessing the number of thunderstorm days (thunderdays) at different sites. The observations were done up to 1980, when the first map of the CG activity in the country was obtained. However, due to the limited number of observation sites, only a very approximate distribution of the lightning activity was obtained (Fig. 9.9). Based on the maximum number of thunderstorm days observed in the Southeast region of the country (120), a maximum flash density of approximately 12 flashes. $\text{km}^{-2}\cdot\text{year}^{-1}$ can be estimated (Pinto and Pinto 2003).

The thunderstorm day observations were followed by observations from a network of flash counters in the Southeast region of the country. A 43-flash counter network operated from 1985 to 1995, recording pulses by a trigger circuit with a band pass filter centered at 10 kHz. (Pinto et al. 2003a). Again, the coverage was

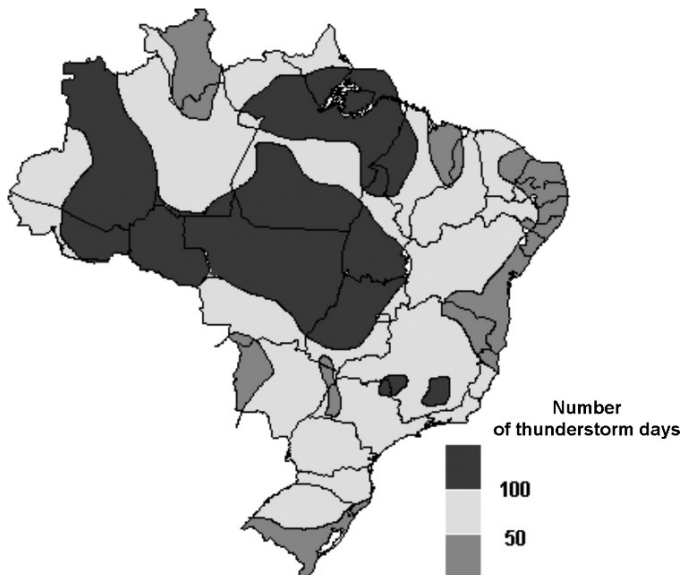


Fig. 9.9 Isoceraunic map of Brazil obtained by thunderstorm day observations from 1960 to 1980

Table 9.6 Lightning characteristics obtained by thunderdays and a network of flash counters

Parameter	Mean value
Annual maximum flash density (flashes $\text{km}^{-2}\cdot\text{year}^{-1}$) ¹	12
Annual maximum flash density (flashes $\text{km}^{-2}\cdot\text{year}^{-1}$) ²	14

¹ Value estimated from thunderdays.

² Values obtained from a network of flash counters.

limited. The observations of CG flashes by flash counters indicate a maximum flash density of approximately 14 flashes.km⁻².year⁻¹.

9.4.2 Instrumented Tower

Observations of CG flashes using instrumented towers in Brazil began in 1985, in the Morro do Cachimbo Station (MCS), in the Southeast region of the country. The station is very similar to that installed in South Africa some years earlier (Eriks-son 1979). The station records the nearby CG lightning activity, the atmospheric electric field, and the direct current measurements. In addition, it provides photograph records and video images of the flashes striking the 60-m metallic tower. The tower is located on the top of a mountain about 1430 m above the sea level and 200 m above any other mountain in the region. The current is measured by two current transducers, with a bandwidth of DC to 1 MHz. The accuracy of the current and sampling time of the data were initially limited to 760 A – 1 μ s and 116 A – 0.2 μ s for the main and the parallel transducer, respectively. The MCS uses a fiber optic link installed into an open duct with a copper plate ground system to transmit the information from the sensor to equipment room (Pinto et al. 2005). Figures 9.10 and 9.11 show the details of the base of the tower and of the current sensors, respectively. Pinto et al. (1997) presented a comparative analysis of mean peak current at MCS with similar observations in San Salvatore, Switzerland, Italy, and South Africa, and Pinto et al. (2003b) and Visacro et al. (2004) extended the comparison to other waveform parameters.

From 1985 to 2000, 29 CG flashes with a total of 88 return strokes were captured in the MCS, 29 negative and only one positive flash.

Table 9.7 summarizes the parameters obtained in the MCS for negative CG flashes. Data for positive flashes are not shown, due to the low number of events. Only parameters that can be compared with those obtained by LLS and high-speed cameras are shown



Fig. 9.10 The photo shows the detail of the base of the tower in the Morro do Cachimbo Station

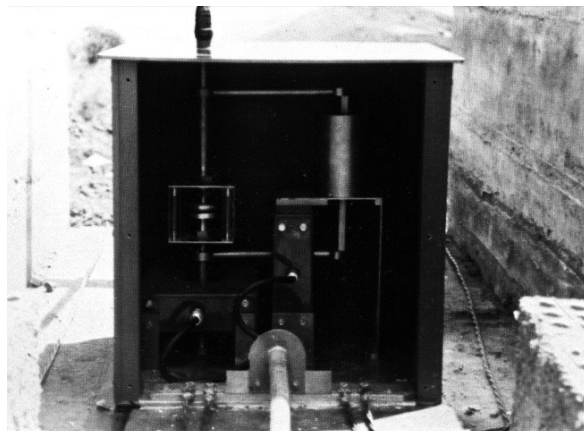


Fig. 9.11 The photo shows the detail of the current sensors in the Morro do Cachimbo Station

Table 9.7 Negative CG lightning parameters obtained in the MCS

Parameter	Mean value
Percentage of positive flashes (%)	2
Percentage of single flashes (%)	48
Multiplicity	3.1
Peak current (kA) ¹	41
Peak current (kA) ²	18

¹ Value is referred to first strokes.

² Value is referred to subsequent strokes.

9.4.3 Triggered Lightning

Triggered lightning were observed from 1999 to 2005 in the International Center for Triggered and Natural Lightning Studies, which was located in Cachoeira Paulista ($22^{\circ}41'S$ and $44^{\circ}59'W$; altitude of 625 m), a small city located halfway between São Paulo and Rio de Janeiro (Pinto et al. 2005). The triggering site was located on a flat 120×70 m area of a hilltop (Fig. 9.12). The control room was located 45 m away from the rocket launcher and has a capability of launching up to 12 rockets during the same event. A field mill connected to the control room via fiber optic link monitored the ambient electric field. The plastic rockets are 0.85 m long and carry a wire spool with them. Around the launcher several instruments were mounted: standard video cameras, a high-speed digital camera, current sensors (a magnetic coil, a resistive shunt and magnetic cards), fast E-field sensors and optical sensors. The current measurements were done by a 1-mW coaxial shunt placed inside a metallic box located under the rocket launcher (Fig. 9.13). The accuracy of the current measurements is considered to be better than 1 kA for currents below approximately 50 kA.

During the period, peak currents of 2 classical and one altitude flashes, with a total of 9 and 7 return strokes, respectively, were recorded. All strokes had peak

Fig. 9.12 The launching system surrounded by three lightning rods and the control room behind it in the triggering site



Fig. 9.13 Detail of the current sensors in the triggering site



Table 9.8 Negative triggered flash parameters obtained in the ICTNLS

Parameter	Mean Value
Peak current (kA) ¹	19
Peak current (kA) ²	34

¹ Value is referred to strokes in classical flashes.

² Value is referred to subsequent strokes of an altitude flash.

currents above 2 kA. The altitude flash was triggered using a 30-m Kevlar insulator cable under the copper wire (Saba et al. 2005). Table 4.3 summarizes the parameters for triggered negative CG flashes. None triggered positive flash was recorded.

Peak current of return strokes of classical flashes and subsequent strokes of altitude flashes are believed to be similar to subsequent strokes of CG flashes.

9.5 Concluding Remarks

The CG lightning data obtained in Brazil in the last two decades by LLS and high-speed cameras, complemented with data obtained by other techniques, give a unique opportunity to characterize the CG flashes in Brazil. Also, the data set is the largest one ever obtained in the tropical region.

The comparison of the lightning characteristics in Brazil with observations in other regions, however, is limited by the differences in the techniques used. Except for the maximum flash density, most differences in the other characteristics can be explained in terms of different limitations associated with each technique. Some of these limitations are: low stroke DE of LLS, absence of peak current information on high-speed camera data, physical basis behind the estimation of flash density from thunderstorm days, low spatial coverage of flash counters, influence of the local orography on the observations by an instrumented tower and low number of triggered flashes observed. Many other aspects should also taken into account such as: sensor calibration of LLS sensors, sensitivity of high-speed cameras to low luminosity features of the flashes, the inability to instrumented towers to record strokes striking different points on ground and the physical differences of natural and triggered lightning.

References

- Abidin HZ, Ibrahim R (2003) Thunderstorm day and ground flash density in Malaysia. Proceedings of the Nuclear Power and Energy Conference (PECon), Bangi, Malaysia
- Ballarotti MG, Saba MMF, Pinto O Jr (2006) A new performance evaluation of the Brazilian Lightning Location System (RINDAT) based on high-speed camera observations of natural negative ground flashes. Proceedings of the 19th International Lightning Detection Conference (ILDC), Tucson, AZ
- Berger G, Zoro R (2004) Lightning density in Indonesia: Is the Guinness book of records right? Proceedings of the 1st International Conference on Lightning Physics and Effects, Belo Horizonte

- Bhikha B, Ojelede ME, Annegarn HJ et al. (2006) Advancing lightning counts by using LIS efficiency factor derived from comparison with SAWS lightning detection network. Proceedings of the LIS International Workshop, Huntsville, AL
- Blakeslee RJ, Bailey JC, Pinto O Jr et al. (2003) The Rondônia lightning detection network: network description, science objectives, data processing/archival, methodology, and results. Proceedings of the XII International Conference on Atmospheric Electricity, Versailles, France
- Campos DR, Pinto O Jr (2007) Investigation about the intensity and location of the maximum cloud-to-ground lightning flash density in the city of São Paulo. Proceedings of IX International Symposium on Lightning Protection, Foz do Iguaçu, Brazil
- Campos LZS, Saba MMF, Pinto O Jr et al. (2007) Waveshapes of continuing currents and properties of M-components in natural negative cloud-to-ground lightning from high-speed video observations. *Atmos. Res.* doi:10.1016/j.atmosres.2006.09.002
- Campos LZS, Saba MMF, Pinto O Jr et al. (2008) Waveshapes of continuing currents and properties of M-components in natural positive cloud-to-ground lightning. *Atmos. Res.* doi:10.1016/j.atmosres.2008.02.020
- Chen SM, Du Y, Fan LM et al. (2002) A lightning location system in China: its performance and applications. *IEEE Trans Electromagn Compat* 44:555–560
- Chen SM, Du Y, Fan LM (2004) Lightning data observed with lightning location system in Guang-Dong province, China. *IEEE Trans Power Delivery* 19:1148–1153
- Chisholm WA, Cummins KL (2006) On the use of LIS/OTD flash density in electric utility reliability analysis. Proceedings of the LIS International Workshop, MSFC, Huntsville, AL
- Cummins KL, Bardo EA (2004) On the relationship between lightning detection network performance and measured lightning parameters. Proceedings of 1st International Conference on Lightning Physics and Effects, Belo Horizonte, Brazil
- Cummins KL, Murphy MJ, Bardo EA et al. (1998a) A combined TOA/MDF technology upgrade of the U.S. national lightning detection network. *J Geophys Res* 103:9035–9044
- Cummins KL, Krider EP, Malone MD (1998b) The U.S. national lightning detection network and applications of cloud-to-ground lightning data by electric power utilities. *IEEE Trans Electr Compatibility* 40:465–480
- Eriksson AJ (1979) The lightning ground flash – an engineering study. Ph.D. Thesis, University of Natal, Pretoria, South Africa, 400 p
- Evert R, Schulze G (2005) Impact of a new lightning detection and location system in South Africa. Proceedings of the IEEE PES Conference and Exposition in Africa, Durban, South Africa
- Fernandes WA (2005) Lightning characteristics associated with thunderstorms formed in ambient with large concentration of smoke from fires. PhD. Thesis, INPE, 161p (in Portuguese)
- Hidayat S, Ishii M (1998) Spatial and temporal distribution of lightning activity around Java. *Geophys Res* 103:14,001–14,009
- Hidayat S, Ishii M (1999) Diurnal variation of lightning characteristics around Java island. *J Geophys Res* 104:24,449–24,454
- Hidayat S, Ishii M, Hojo J et al. (1996) Observation of lightning in Indonesia by magnetic direction-finder network. Proceedings of the 10th International Conference on Atmospheric Electricity, Osaka, Japan
- Kilinc M, Beringer J (2007) The Spatial and Temporal Distribution of Lightning Strikes and Their Relationship with Vegetation Type, Elevation, and Fire Scars in the Northern Territory. *J Climate* 20: 1161–1173
- Murphy MJ., Holle RL (2005) Where is the real cloud-to-ground maximum in North America? *weather and Forecasting* 20:125–133
- Murphy M, Pifer A, Cummins K et al. (2002) The 2002 upgrade of the U.S. NLDN. Proceedings of 17th. International Lightning Detection Conference, Tucson, AZ
- Naccarato KP (2005) Analysis of the lightning characteristics in the Southeast region of Brazil, PhD. Thesis, INPE, 258p
- Naccarato, KP, Pinto O Jr (2008) The evolution of the detection efficiency model for the Brazilian lightning detection network (BrasilDAT). *Atmos. Res.*, submitted.

- Naccarato, KP, Pinto O Jr, Pinto IRCA (2003) Evidence of thermal and aerosol effects on the cloud-to-ground lightning density and polarity over large urban areas of Southeastern Brazil. *Geophys Res Lett* 30:1674–1677
- Naccarato, KP, Pinto O Jr, Pinto IRCA (2004) Application of a detection efficiency model to correct cloud-to-ground flash density maps in southeastern Brazil. Proceedings of the 18th International Lightning Detection Conference, Vaisala, Helsinki
- Naccarato, KP, Pinto O Jr, Pinto IRCA (2006a) A detection efficiency model for the Brazilian Lightning Detection Network (RINDAT). Proceedings of the 19th International Lightning Detection Conference, Vaisala, Tucson, AZ
- Naccarato KP, Pinto O Jr, Pinto IRCA (2006b) Different types of detection efficiency models to correct cloud-to-ground data obtained by Lightning Detection Networks, Proceedings of the International Conference on Grounding and Earthing & 2nd International Conference on Lightning Physics and Effects, SB-RAI, Maceió, CD-ROM
- Ndlovu N, Evert CR (2006) Statistical analysis of data from an aged LPATS network. Proceedings of the 19th International Lightning Detection Conference (ILDC), Tucson, AZ
- Orville RE, Zipser EJ, Brook M et al. (1997) Lightning in the region of TOGA Coare, *Bull. Am Meteorol Soc* 78: 1055–1067
- Orville RE, Huffines GR, Burrows WR et al. (2002) The North American lightning network (NALDN) - first results: 1998–2000. *Mon Wea Rev* 130:2098–2109
- Pinto IRCA, Pinto O Jr, Rocha RML et al. (1999a) Cloud-to-ground lightning in the southeastern Brazil in 1993, 2. Time variations and flash characteristics. *J Geophys Res* 104:31381–31388
- Pinto IRCA, Pinto O Jr (2003) Cloud-to-ground lightning distribution in Brazil. *J Atmos Solar-Terr Physics* 65:733–737
- Pinto IRCA, Pinto O Jr, Gomes MASS et al. (2004a) Urban effect on the characteristics of cloud-to-ground lightning over Belo Horizonte – Brazil. *Ann Geophysicae* 22:697–700
- Pinto O Jr (2003) The Brazilian lightning detection network: a historical background and future perspectives. Proceedings of VII International Symposium on Lightning Protection, Curitiba, Brazil
- Pinto O Jr (2005) The art of war against lightning. São Paulo, Oficina de Texto (in Portuguese)
- Pinto O Jr, Gin RBB, Pinto IRCA et al. (1996) Cloud-to-ground lightning flash characteristics in the southeastern Brazil for the 1992–1993 summer season. *J Geophys Res* 101:29,627–629,635
- Pinto O Jr, Pinto IRCA, Lacerda M et al. (1997) Are equatorial negative lightning flashes more intense than those at higher latitudes? *J Atmos Solar-Terr. Phys* 59:1881–1883
- Pinto O Jr, Pinto IRCA, Gomes MASS et al. (1999b) Cloud-to-ground lightning in the southeastern Brazil in 1993, 1. Geographical distribution. *J Geophys Res* 104:31369–31380
- Pinto O Jr, Pinto IRCA, Faria HH (2003a) A Comparative Analysis of Lightning Data from Lightning Networks and LIS Sensor in the North and Southeast of Brazil. *Geophys Res Lett* 30: 1029–1032
- Pinto O Jr, Pinto IRCA, Diniz JH et al. (2003b) A seven-year study about the negative cloud-to-ground lightning flash characteristics in the southeastern Brazil. *J Atmos Terr Phys* 65: 739–748
- Pinto O Jr, Naccarato KP, Pinto IRCA et al. (2004b) Characteristics of cloud-to-ground lightning flashes in the Vale do Paraíba region (Southeast Brazil). Proceedings of the International Conference on Lightning Physics and Effects, Belo Horizonte, MG
- Pinto O Jr, Pinto IRCA, Saba MMF et al. (2005) Return stroke peak current observations of negative natural and triggered lightning in Brazil. *Atmos Res* 76:493–502
- Pinto O Jr, Naccarato KP, Saba MMF et al. (2006a) Recent upgrade to the Brazilian integrated lightning detection network, Proceedings of the 19th International Lightning Detection Conference (ILDC), Tucson, AZ
- Pinto O Jr, Naccarato KP, Pinto IRCA et al. (2006b) Monthly distribution of cloud-to-ground lightning flashes as observed by lightning location systems. *Geophys Res Lett.* doi: 10.1029/2006GL026081
- Pinto O Jr, Pinto IRCA; Naccarato KP (2007) Maximum cloud-to-ground lightning flash densities observed by lightning location systems in the tropical region: A review. *Atmospheric Research* 84:189–200

- Pinto O Jr, Pinto IRCA (2008) About the sensitivity of cloud-to-ground lightning activity to surface air temperature changes at different time scales in the city of São Paulo, Brazil. *J Geophys Res*, submitted
- Raizman S, Mendez Y, Vivas Jet al. (2004) Caracterization of the ceraunic level in Venezuela based on a lightning detection system. Proceedings of IV Congress of Electrical Engineer, Caracas, (in Spanish)
- Rakov VA, and Uman MA (2003) Lightning: Physics and Effects. pp. 687, Cambridge Univ. Press, New York
- Rompala JT, Blakeslee RJ, Bailey JC (2003) Detection efficiency contours for regions serviced by lightning detection networks of limited scope. Proceedings of the 12th International Conference on Atmospheric Electricity, ICAE, Versailles 1:101–104
- Saba MMF, Pinto O Jr, Ballarotti MG et al. (2004) Monitoring the performance of the lightning detection network by means of a high-speed camera. Proceedings of the International Lightning Detection Conference (ILDC), Helsinki, Finland
- Saba, MMF, Pinto O Jr, Solorzano NN et al. (2005) Lightning current observation of an altitude triggered flash". *Atmos Res* 76: 402–411
- Saba MMF, Ballarotti MG, Pinto O Jr (2006a) Negative cloud-to-ground lightning properties from high-speed video observations. *J Geophys Res.* doi:10.1029/2005JD006415.
- Saba MMF, Pinto O Jr, Ballarotti MG (2006b) Relation between lightning return stroke peak current and following continuing current. *Geophys Res Lett.* doi:10.1029/2006GL027455.
- Saba MMF, Cummins KL, Warner TA, et al. (2008) Positive Leader Characteristics from High-Speed Video Observations. *Geophys Res Lett.* doi:10.1029/2007GL033000
- Schulz W (1997) Performance evaluation of lightning location systems. PhD Thesis, Technical University of Vienna, Faculty of Electrical Engineering, Austria, 136p
- Schulz W, Diendorfer G (1996) Detection efficiency and site errors of lightning location systems. Proceedings of the 14th International Lightning Detection Conference, Tucson, AZ
- Schulz W, Diendorfer G (1998) Effect of lightning location network setup on evaluated lightning characteristics. Proceedings of the 15th International Lightning Detection Conference (ILDC), Tucson, AZ
- Schulz, W, Cummins K, Diendorfer G et al. (2005) Cloud-to-ground lightning in Austria: a 10-year study using data from a lightning location system. *J Geophys Res.* doi:10.1029/2006JD007831, 2007
- Sharp AJ (1999) Operational LPATS network in Australia. Proceedings of the International Conference on Atmospheric Electricity (ICAE), pp. 234–237, Hunstville, AL
- Solorzano NN (2003) Triggered lightning study in Brazil, PhD Thesis, INPE, 178 p (in Portuguese)
- Tarazona J, Ferro C, Urdaneta AJ (2006) Cartographic representation of the Venezuelan keraunic activity. Proceedings of the CIGRE Meeting, Paris
- Thomson EM, Gali MA, Uman MA, et al. (1984) Some features of stroke occurrence in Florida lightning flashes. *J Geophys Res* 89: 4910–4916
- Torres H, Gallego L, Salgado M et al. (2001) Variation of ground stroke density with latitude. Proceedings of the International Symposium on Lightning Protection (SIPDA), Santos, Brazil.
- Visacro S, Soares A Jr, Schoroeder MAO et al. (2004) Statistical analysis of lightning current parameters: measurements at morro do Cachimbo Station. *J Geophys Res.* doi:10.1029/2003JD003662
- Younes C, Torres H, Pérez E et al. (2003) Lightning polarity variation in Colombia. Proceedings of the International Symposium on Lightning Protection (SIPDA), Curitiba, Brazil
- Younes C, Torres H, Pérez E et al. (2004) Lightning parameters evaluation in the Colombian highest atmospheric activity zone. Proceedings of the International Conference on Lightning Protection (ICLP), Avignon, France

Chapter 10

Observation and Interpretation of Lightning Flashes with Electromagnetic Lightning Mapper

Eric Defer and Pierre Laroche

Abstract We detail concurrent measurements recorded during natural lightning flashes with the ONERA-ITF VHF interferometers, the NASA-LDAR VHF time-of-arrival mapper and the space borne NASA-OTD optical sensor. The development of an intracloud (IC) flash is described based on the measurements of the VHF signal radiated during its occurrence. Optical radiation is compared to VHF radiation recorded during an IC flash and during a negative cloud-to-ground (CG) flash. The results of the analysis suggests that the new ONERA PROFEO lightning mapping sensor which combines both interferometric and time-of-arrival techniques will fit perfectly our observational needs to study the development of lightning flashes, to relate their occurrence relatively to the dynamical and microphysical properties of their parent storms, and to help modelling the multi-scale processes of a lightning flash. We also discuss the weakness of the use of lightning NO_x (LiNO_x) production per flash for global scale LiNO_x estimate. We assess the importance of global lightning detection with respect to having sufficient information about lightning flashes for more realistic estimates LiNO_x production.

Keywords Lightning phenomenology · Discharge physics · Electromagnetic radiation · Lightning detection technique · NO_x

10.1 Introduction

A natural lightning flash is not a continuous phenomenon but is in fact composed of successive events, also called flash components, with different physical properties in terms of discharge propagation, radio frequency radiation type, current properties, duration. A lightning flash then consists in a multi-scale physical process spanning from the electron avalanche to the propagation of discharges over large distances. Consequently a detailed description of a natural lightning flash and its modeling

E. Defer (✉)
LERMA-Observatoire de Paris, Paris, France

require simultaneous observations from different techniques sensitive to different properties of the lightning flash.

A lightning flash is the result of a breakdown occurring in an ambient electric field strong enough to ignite a discharge. The ambient electric field is the result of the presence of space charged regions within the cloud. Those regions of charges are created through electrification processes, predominantly dominated by ice-ice interaction, where charges are exchanged during collisions between ice particles in presence of liquid water (Takashi, 1978; Saunders et al., 1991). Laboratory studies have shown that the amount and sign of charges transferred between ice particles depends on the difference of velocity between the two ice particles, on the temperature and on the liquid water content. The lighter hydrometeors are transported upward, the heaviest being located at lower altitude in the cloud. It then leads to a stack of charged zones in the thundercloud more or less with complex vertical distributions (Stolzenburg et al, 1998; Rust et al., 2005). The lightning activity of a thundercloud is then the product of complex and simultaneous microphysical, dynamical and electrical processes.

Two types of lightning flashes exist: IntraCloud (IC) flashes occur in clouds while Cloud-to-Ground (CG) flashes connect to the ground. Negative (positive) CG flashes lower negative (positive) charges and exhibit a significant radiation when the connection to the ground occurs. Negative CG flashes are more often observed and exhibit multiple connections to the ground. Positive CG flashes are often composed of a single or very few connections to the ground and exhibit higher current than negative CG flashes. IC activity often precedes any CG activity (e.g. Defer et al., 2001). IC flashes tend to be vertical in the early beginning of the life of the storm and then exhibit significant horizontal branches when the storm reaches its maturity (e.g. Krehbiel et al., 2000).

In the present chapter we first provide a basic phenomenology of lightning flashes. We then discuss the development of IC and CG flashes based on VHF mapping, VLF and optical detection techniques. We determine several properties on the flashes and on its successive components. We finally discuss the Lightning NOx (LiNOx) production and the potential of the new ONERA PROFEO (PRO-gramme Francilien d'Etudes des Orages) lightning mapper for future observational and modeling studies.

10.2 Basic Phenomenology of Lightning Flashes

If one wants to understand the kind of information that can be measured with a radio-electric lightning mapper, it is worthwhile to keep in mind the following basic scientific knowledge about lightning flashes.

A *lightning flash* consists of the successive in-air and/or in-cloud propagation of different electrical discharges. The reason to gather those discharges within what is called a lightning flash is that they are all triggered by the preceding discharges. The lightning flash is initiated by events produced by the high-magnitude electrostatic

field induced by electrically charged regions in the cumulonimbus cloud. The lightning flash stops when its propagation can not be sustained anymore within the ambient atmospheric field. A successive flash will be created when sufficient electrostatic conditions will appear somewhere else in the cloud or at the same location. The “engine” of discharges behavior is the electric field; discharges will propagate or stop according to electric field criteria. Charged cloud particles may play a role in the initiation process of a lightning flash but it remains to be understood. Runaway electron processes are also evidenced to be involved in lightning initiation.

To obtain an electrical breakdown of the clear and cloudy air, which both are good insulators, three main stages must be reached:

- 1) *The corona or streamer* stage consists in discharges driven by electronic avalanches and for which the gas particules are cold (~ 300 K). Streamer discharge exhibits a bushy aspect.
- 2) *The thermalized channel* discharges are fed by the streamers at the root of which a filamentary discharge develops; temperature of gas particules reaches 1500 K and the electric field along the channel becomes lower than 1 kV/cm.
- 3) Electronic detachment occurs above 1500 K due to electron collision. Above 5000 K ionization drastically occurs due to thermal collision and the channel becomes highly thermalized; all gas particules become dissociated; neutral particule temperature can reach temperature as high as 30 000 K and the longitudinal electric field in the channel reach value as low as few a fraction of V/cm.

The behavior of those discharges is strongly dependent of the discharge polarity. Discharges are named positive when its propagation has the same orientation as the electric field. A positive discharge is fed by electron avalanches propagating in the opposite direction to the electric field, toward the channel in a region where the magnitude of the field is increasing. On the contrary, a negative corona discharge propagates away from the channel tip in an area where the electric field is rapidly decreasing. Then two important consequences can be stated:

- 1) The positive discharge is able to propagate continuously as commonly observed. Irregularities of the propagation is more associated with a “pulsed” behavior than a “stepped behavior”; these irregularities might be produced by effects of the water vapor or by branching.
- 2) The negative discharge cannot propagate continuously. Its propagation is “stepped”: negative streamers stop and a powerful junction discharge starting from the edge zone of the streamer propagate toward the channel tip. The mean field value in the negative streamer zone is 10 kV/cm; it is only 4.7 kV/cm in the positive streamer zone. Propagation of both processes has been described in Gallimberti et al. (2002) and is presented in Fig. 10.1.

All those properties are observed in long air gap laboratory discharges for which the streamer length is about 1 m. They have also been observed with artificially triggered lightning, and modeling and observations confirm that natural lightning flash exhibits the same behavior (Lalande et al., 2002). The length of the natural streamers reaches several meters.

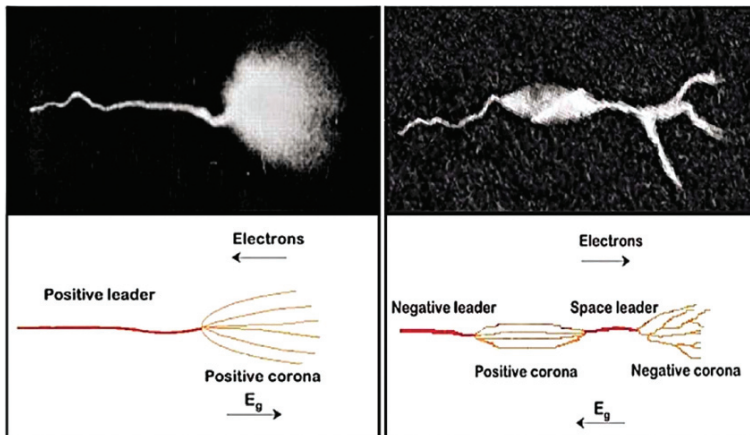


Fig. 10.1 Positive and negative discharge structures with indication of the electron drift direction from Gallimberti et al. (2002)

Those physical considerations, whose descriptions are obviously simplified to stay on the track of the objective of this paper, are fundamental for the design and interpretation of electromagnetic lightning mapper data. Lightning discharges are initiated in cloud by a bi-directional propagation process: from the area where the lightning flash is triggered positive and negative discharges propagate in opposite direction. Due to discharge properties, the current of the positive discharge is of lower magnitude and slower variation compared to the current of the negative discharge. As the electromagnetic radiation is proportional to the current I and its time derivative dI/dt , the radiation of the positive branches is much lower (-30 dB Kawasaki et al. (1991)) compared to the radiation of negative branches. This natural property makes possible the use of electromagnetic lightning mapper for the detection and location of the negative branches of the discharges whatever the detection technique of the lightning mapper. Some instruments are described in Section 10.3 but we just mention here after what different technology actually detects within a flash.

The return stroke (RS) of a CG is a high-energy discharge initiated by the connection to ground of a leader discharge propagating downward from the cloud to the ground. RS propagates rapidly upward from ground at a velocity of roughly one order of magnitude less than the light speed, within the track of the leaders. This lightning flash component is a propagating current pulse with initial characteristics such as rise time between 0.1 and 3 μ s, decay time between 10 and 30 μ s and magnitude between 10 and 100 kA. RS strongly radiate from low to high frequency range, i.e. few kHz to few tens MHz.

The negative stepped leader is a highly branched discharge propagating either toward ground or inside the cloud. The typical stepping period ranges between few hundreds μ s down to 10 μ s; each step is associated with a strong negative current pulse (up to few kA) with a typical 100 ns/ 1 μ s rise time/decay time. The negative stepped leader head propagates at an average speed of 5×10^5 m.s $^{-1}$. Stepped leader

radiate from ~ 1 MHz up to ~ 200 MHz. They can be easily detected and mapped with lightning mappers as shown in the next sections.

The *dart leader* of a CG is a discharge propagating downward on the track of a preceding return stroke. This direct and fast (few 10^7 m/s) discharge propagates a short current pulse of few-kA magnitude; when connected to the ground it initiates a subsequent RS. Dart leaders also radiate strongly in Very High Frequency (VHF) range.

The *recoil streamer* (RSE) is a strong negative discharge – the strongest discharge during IC flashes – propagating within the track of the positive branches of a bileader. Several authors consider dart leader and recoil streamer as similar discharge processes. Recoil streamer emits intense short-duration pulses (also called the K changes), radiates over the wide band VHF domain and propagates at a velocity of few 10^7 m/s.

Finally the *positive leader* of a natural or artificially triggered flash is a continuous rather slow propagating discharge (from 10^4 m/s up to few 10^5 m/s) of limited current (few tens up few hundreds amperes). It has been demonstrated that positive leader does not radiate significantly in both High Frequency (HF) and VHF ranges. This natural property prevents any efficient use of electromagnetic lightning mapper to detect and localize their occurrence. But, inversely this property offers the opportunity to detect and localize negative component of the flash which radiation would have been otherwise mixed up with simultaneous positive component radiation.

Detection and localization of any lightning flash component is, of course, of paramount importance to understand the processes involved in the lightning physics and its relationships with the dynamic and cloud particle physics. Finally because all of those thermalized discharges produce nitrogen oxides (NOx) during the freezing process, detection and localization of all lightning flash components are the first step in the evaluation of Lightning NOx (LNOx) production during thunderstorms as we discuss in the last section of our contribution.

10.3 Instruments

Different techniques can be used to detect and to locate lightning flashes (MacGorman and Rust, 1995, Chapter 6). One method consists of recording the electromagnetic radiation of the lightning flashes. A broad band spectra characterizes the electromagnetic radiation emitted by lightning flashes (Pierce, 1977). Two types of radiation are recorded in Radio Frequency (RF) domain. The first type is related to pulse processes with a rate ranging from 10^4 to 10^5 pulses per second with an averaged duration of 1 μ s (Proctor, 1981; Richard et al., 1986). It is often recorded during the first part of the flash and is associated with virgin air breakdown during the propagation of negative stepped leaders. The second type of radiation consist of radiation bursts with a duration lower than few hundreds microseconds (Richard et al., 1986; Proctor, 1998).

Two techniques can be employed to depict both intra-cloud (IC) and cloud-to-ground (CG) lightning flashes by recording their VHF radiation. The interferometric

technique provides the directions, i.e. azimuth and elevation, of VHF radiation by analyzing the phase difference of an incident wave on an array of close antennas (Richard et al., 1986; Rhodes et al., 1994). The time-of-arrival (TOA) technique analyzes waveforms of radiation detected on distant sites and retrieves the three-dimensional locations of radiating sources from hyperboloid curves deduced from time equations (Proctor, 1981; Proctor et al., 1988; Rison et al., 1999). In TOA technique the waveform of the received signal at the station is sampled during a given recording time window and the time of the peak radiation, precisely dated, is used to compute the location of the radiation source. Consequently TOA-based lightning detection systems are best skilled for pulse-like isolated emissions. An individual pulse occurring during a burst of pulses or a continuous burst of radiation cannot be distinguished with TOA technique within the recording time window. The interferometric technique locates both types of radiation as we detail in the next section.

Lightning flashes also radiate in the Very Low Frequency (VLF) domain and different instruments are locating ground connections occurring during CG flashes such as the US National Lightning Detection Network (NLDN) (Cummins et al., 1998). In Europe the LINET network monitors the total (IC+CG) lightning activity from its VLF/LF radiation (Betz et al., 2004; Betz, in this volume). Lightning flashes also emit optical radiation. Numerous studies have been performed to characterize CG flashes based on ground based optical records (e.g. Parker and Krider, 2003). The NASA Optical Transient Detector (OTD) and the NASA Lightning Imaging Sensor (LIS) on the Tropical Rain Measuring Mission (TRMM) have demonstrated the possibility to detect total lightning activity in both daytime and nighttime from space based on the detection of the optical radiation (Christian et al., 2003).

We analyze here the measurements from the ONERA ITF interferometric mapper deployed in Florida in 1992 and in Colorado in 1996. The ONERA VHF lightning mapper consists in two independent interferometers located 40-km away each other (Laroche et al., 1994; Defer et al., 2001). Each station provides azimuth direction of VHF signal radiated during the development of a lightning flash. One station, labelled ST1, is equipped with a second sensor that determines the elevation of the VHF sources. The combination of the angular observations provides the 3D locations of the VHF sources inside an area of reconstruction also called lobes (Fig. 10.2). Each interferometric station detects the VHF radiation at 114 MHz with 1-MHz bandwidth and with 23- μ s time resolution. GPS time is used to stamp precisely the samples. VHF records are stored when the magnitude of the VHF signal exceeds an adjustable threshold. Raw data recorded by each station is first processed to provide direction of VHF sources. Afterwards an algorithm combines the two separate sets of angular measurements from each station and reconstructs the three-dimensional locations of VHF sources.

Measurements from the ONERA sensors are compared with other lightning observations from the NASA-LDAR (Lightning Detection and Ranging), the NLDN and the space borne NASA-OTD. The NASA-LDAR system is based on a time-of-arrival (TOA) technique (Maier et al., 1996). LDAR system is composed of 7 remote stations, including a central station, which detects VHF radiation centred at 66 MHz at Kennedy Space Center (Florida). When the receiver of the central station

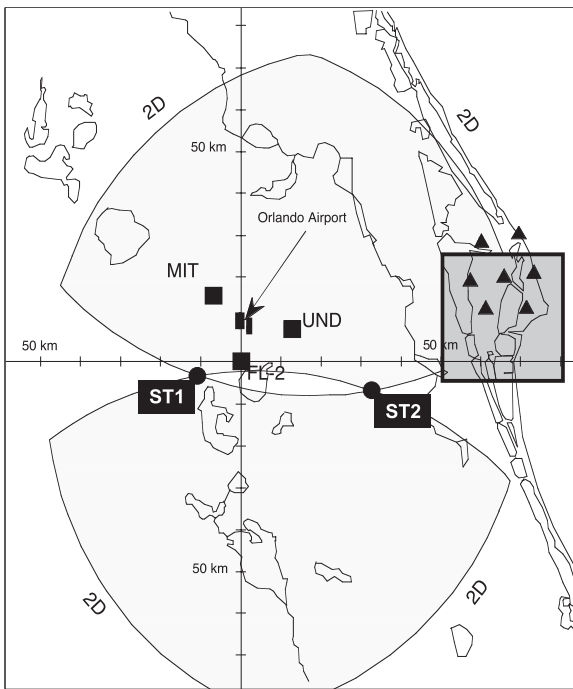


Fig. 10.2 Locations of the remote stations and the intra-cloud lightning flash in Florida. The lightning flash was located in the eastern dark grey square of 30-km side. Circles and triangles locate respectively the ONERA stations and the LDAR antennas. Light grey areas, called lobes, cover the area where the interferometric mapper retrieved the XYZ locations of the VHF sources

records a signal with a magnitude exceeding a threshold, digitalization of the continuously transmitted signal (from each station to the central station) is performed during a 81.92- μ s window period with a 10-ns sampling rate. Time and magnitude of the peak of the signal recording during the window period are stored. Three-dimensional positions of the recorded events are then retrieved using the differences in time of arrival of VHF signals at the different LDAR stations.

The space borne optical OTD sensor was orbiting Earth as payload on the micro-satellite Microlab-1. The OTD sensor was designed to record the optical pulses radiated by the lightning flashes at 777 nm (Christian et al., 2003). The OTD sensor consisted in a staring 128×128 pixel CCD camera pointing to Earth. OTD frame time was 2 ms. Its field of view spanned over 1500 km while OTD orbited at 750 km altitude. The OTD sensor was calibrated in laboratory (Koshak et al., 2000) and a study of its performances was presented in Boccippio et al. (2000).

The US NLDN senses the Medium Frequency (MW) electric and magnetic radiation due to high current of return strokes during ground connections (Cummins et al., 1998). It then monitors the (negative and positive) cloud-to-ground activity. The 1-ms NDLN dataset was used for the present study. It includes millisecond

time of each stroke, its location, the estimated peak current of each stroke, and other parameters, which determine the reliability of the location. In the experimental area the estimated median location accuracy for the NLDN is 500 m.

10.4 Concurrent Observations of Lightning Flashes

In this section we present concurrent observations recorded with different instruments measuring either different properties of the discharges recorded in the VHF domain or different physical aspects of the discharges in the optical, VLF and VHF domains.

10.4.1 Observations of the Intra-Cloud Lightning Flash with Interferometric and TOA VHF Lightning Mappers

The ONERA mapper was deployed in a West-East configuration with ST1 station, measuring azimuth and elevation of the VHF sources, located at the western site (Fig. 10.2). The studied lightning flash, originally investigated in Mazur et al. (1997), occurred in the eastern part of the ONERA lightning mapper lobes and partially outside, close to ST2 station and LDAR antennas (Fig. 10.2). The flash was recorded the 23rd of August 1993 at 1804:32 UT. It should be noted that the ONERA mapper was not deployed to perform measurement comparison with LDAR at all but to record total lightning activity in conjunction with ground-based radar over a relatively extended domain. The ITF deployment configuration at the time of the field campaign was optimal for the purpose of the field campaign.

Figure 10.3a shows the time evolution of the altitude of VHF LDAR sources recorded during the studied flash. The vertical distribution of the LDAR sources exhibits two main peaks centered at 6 km above mean sea level (amsl) and 10 km amsl (Fig. 10.3c). The altitude of the lower peak is consistent with the altitude associated with the lower negative charge region in Florida storms (Maier et al., 1986). The upper peak, which is located at the heights of the positive charge region, is more extended and retrieved LDAR sources reached 14 km amsl heights (Fig. 10.3). During two thirds of the flash duration, LDAR sources were located at the two levels (Fig. 10.3a). The last part of the flash exhibited only very few LDAR sources at high altitude and most of the LDAR sources were located at roughly 6–7 km amsl altitude. The ground projection of the LDAR sources can be contained in a square of about 25 km side (Fig. 10.3d).

Figure 10.4 shows the time series of the magnitude of the VHF signal (in arbitrary units) that the two ONERA interferometers recorded simultaneously. As expected ST2, the closest station to the lightning flash, recorded more samples. Because samples from both interferometers are combined to retrieve the XYZ locations of VHF sources, it is obvious that in the present case the three-dimensional mapping of the flash is limited due to the under-sampling of the farthest station. It then explains,

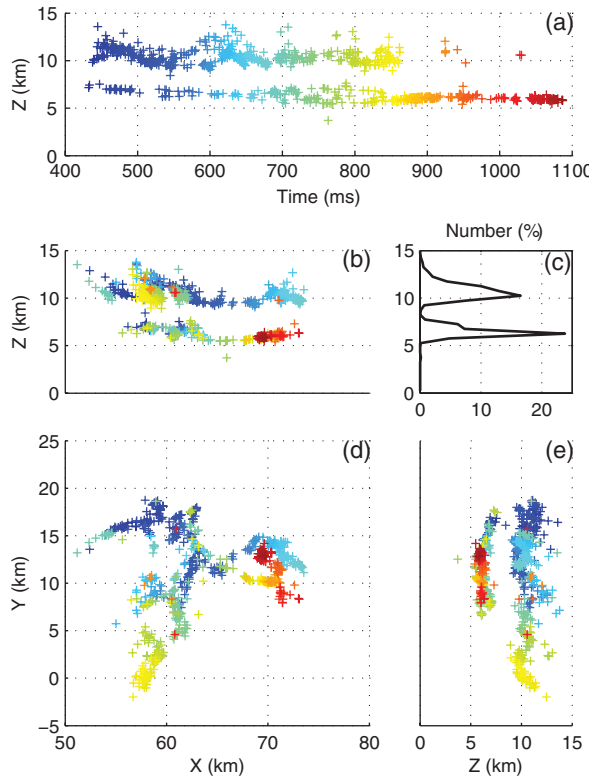


Fig. 10.3 Case of an intracloud flash (23 August 1993, 1804:32 UT) with (a) time series of LDAR source altitude; (b) XZ projection of the LDAR sources; (c) vertical distribution of the LDAR sources per 500-m vertical increment; (d) ground projection of the LDAR sources; (e) YZ projection of the LDAR sources (See also Plate 12 in the Color Plate Section on page 600)

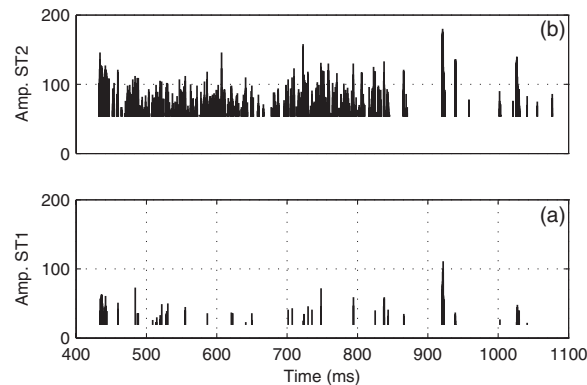


Fig. 10.4 Time evolution of VHF magnitude (in an arbitrary unit) recorded during the studied flash by the two ONERA interferometric stations

“a rather sporadic radiation mapped with the ONERA-3D” pointed out by Mazur et al. (1997). Consequently only the measurements recorded at ST2 were studied.

Azimuth of the LDAR sources was computed relatively to ST2 to be overlaid on ST2 records. Times of the LDAR sources were also changed to take into account the time required for the radiation located by LDAR to reach ST2. Figure 10.5 shows the overlay of both LDAR and ST2 sources plotted as function of time (0° azimuth is North, 90° azimuth is East). Low altitude LDAR sources, i.e. sources with altitude lower than 8 km amsl, were separated from high altitude LDAR sources. According to the radiation recorded by both lightning mappers, the studied IC flash lasted for 660 ms (Fig. 10.5).

The first regime of the flash, part A (Fig. 10.5), lasted for about 200 ms and started with a 12-ms period of continuous VHF emission partially reported by LDAR (only 5 sources) and recorded at a roughly constant azimuth (46° , Fig. 10.4). Few milliseconds later, the interferometer reported successive trains of VHF sources while LDAR located isolated high-altitude VHF pulses more or less ahead of the interferometric bursts of VHF sources (Fig. 10.6a). During that regime interferometric measurements and high-altitude LDAR sources propagated in the same direction at same azimuth (Figs. 10.5 and 10.6a). Low-altitude LDAR sources were also recorded during the first regime but at a lower rate compared to the ones recorded at high altitude.

The second regime of the flash, part B, started at about 620 ms and lasted for 200 ms (Fig. 10.5). During that regime pulse-like VHF sources at high altitude (as sensed by LDAR) at a lower rate and radiation bursts (as sensed by the interferometer) were

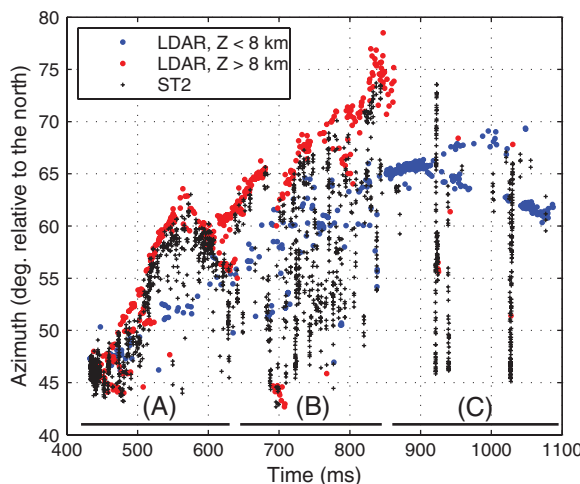


Fig. 10.5 Time evolutions of LDAR and ST2 sources plotted in azimuth ST2 axis. Red and blue dots correspond to high-altitude and low-altitude LDAR sources respectively while interferometric ST2 measurements are plotted with pluses (See also Plate 13 in the Color Plate Section on page 601)

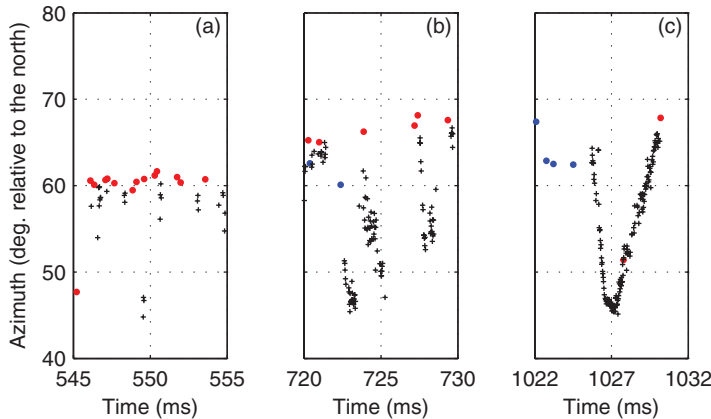


Fig. 10.6 Same as in Fig. 10.4 but for three different 10-ms periods during the studied flash (See also Plate 14 in the Color Plate Section on page 601)

recorded in a similar manner as during regime A (Figs. 10.5 and 10.6b). Interferometric data also show VHF activity in the azimuth range previously traversed during the first regime. Low-altitude VHF sources were also recorded during that regime.

The last regime of the flash, C, started at the time 850 ms. The interferometer recorded few sources during the 250-ms duration of that regime except during three events at the times 922, 939 and 1025 ms. During these three events VHF radiation was recorded over a large part of the angular range already ionized during the previous phases (Fig. 10.6c). These events lasted for 2, 1.4 and 4.4 ms respectively. During the last regime of the flash LDAR sources were almost only located at low altitude and recorded at a much higher rate than during the two first stages of the flash (Fig. 10.5).

Three stages were recorded in the present flash. During the initial stage, A, the two techniques record the IC negative stepped leader. The negative leader propagates by steps and can be easily mapped with a time-of-arrival instrument. Additionally the propagation of the negative leader reported by the interferometer as composed of successive radiation trains confirms the results of Shao et al. (1996a). The negative intra-cloud leader progressed away from the location of the flash ignition. The active phase, part B, is composed of successive VHF radiation occurring in the angular range ionized during the previous events. LDAR reported pulse-like radiation in the upper part of the cloud. It indicates that the negative leaders continued to propagate. Finally the junction stage is composed of three events exhibiting typical characteristics of recoil streamers as seen by the ONERA instrument, and a low altitude impulsive process well resolved by LDAR. The low altitude LDAR sources are located within the lower negative charge region and they progressed away from the area where the lightning flash started. Mazur (1989) suggested that a lightning flash starts with a bi-leader system, i.e. the propagation of two discharges with opposite signs in opposite directions from the same origin. During the beginning of a normal IC flash, the negative leader propagates upward while

positive leader propagates downward, and both leader branch horizontally later. In the present case the high (low) altitude LDAR sources are associated with the propagation of the negative (positive) leader because of their locations relative to the main positive (negative) charged region and because of their propagation away from the ignition area. Laboratory studies, triggered lightning investigations and also records of positive CG flashes indicate that the positive leader radiate less than the negative leader in the VHF domain. From measurements with the time-of-arrival Lightning Mapping Array (LMA) Thomas et al. (2001) reported VHF radiation associated with the propagation of the negative leaders in the 60–66 MHz band being one order of magnitude stronger than the VHF radiation emitted during the propagation of positive leaders.

A sketch of the development at the two (6 and 10 km amsl) levels is plotted in Fig. 10.7. The studied flash started at the location (S) (black dot in Fig. 10.7a and 10.7e). A first vertical negative IC leader is assumed to progress to the upper part of the cloud at a roughly constant azimuth. It is followed by a horizontal negative leader (1), which progressed in a southwest direction (Fig. 10.7a). When this first upper leader reached its final location, a new upper negative leader (2) started from the trigger zone and progressed to the north. Two others leaders (3) and (4) progressed to the east. At about time 600 ms, event (4) exhibited a branching from where (5) and (6) progressed away. The lightning flash reached its upper eastern final extension when (7) ceased to propagate. At time 750 ms, a new branching was recorded at the final extremity of (6) where (6') and (7') progressed away. Event (8)

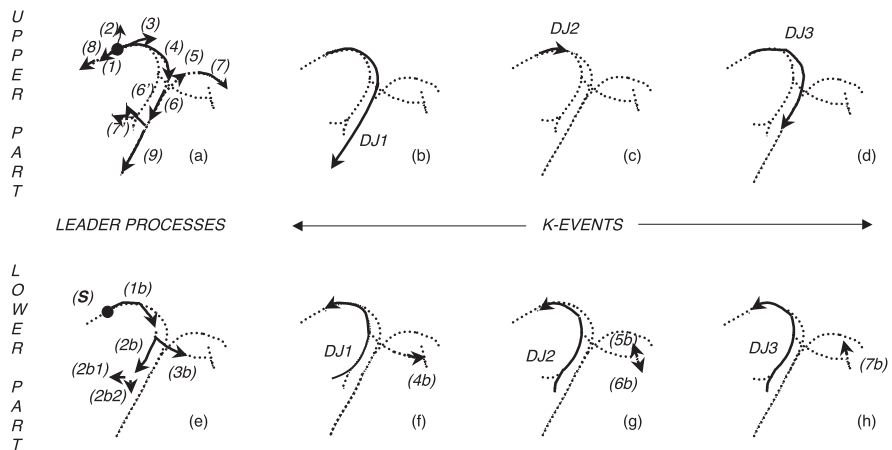


Fig. 10.7 Development of the studied intracloud flash deduced from the ONERA-ITF and NASA-LDAR measurements. Components located in the upper (*lower*) part of the cloud are plotted in panels **a, b, c** and **d** (**e, f, g** and **h**). Each component is represented by line and the arrow indicates the direction of the propagation at the considered level. Dot lines give a footprint of all flash components

was recorded moving away the trigger zone to a West direction at time 700 ms. A last event (9) propagated to a southwest direction until the upper part of the lightning flash reached its final extension. Simultaneously the positive discharge progressed in the lower part of the cloud. A first positive leader (1b) progressed away from the trigger zone and was followed by two branched leaders (2b) and (3b) (Fig. 10.7e). The positive leader (2b) propagated to a southwest direction and slipped up into two positive leaders (2b1) and (2b2). Note that the leaders for the two polarities seem to follow almost similar paths but at two different levels (Fig. 10.3d and 10.7). The first recoil streamer event (DJ1, at 922 ms) progressed from the lower negative charge zone, started at low altitude and along the channels created by the events (2b1), (2b) and (1b), (Fig. 10.7f). It kept on progressing close to the trigger zone and along the channels created by the components (4), (6) and (9), as shown in Fig. 10.7b. Before the triggering of the K-change, LDAR detected the component (4b) located at the eastern extremity of event (3b). The second recoil streamer event (DJ2, at 939 ms) started along the channel (2b2) and took channels (2b) and (1b) to reach the trigger zone (Fig. 10.7g). Interferometric measurements indicated that the DJ2 event stopped radiating along the path (4). LDAR mapper recorded here again an impulsive activity (5b) and (6b) close to the final location of event (4b). The last long discharge resolved by the ONERA interferometer (DJ3 at 1025 ms) took the way of DJ2 event but progressed more to the southeast in the upper part of the cloud. After that event LDAR mapper located impulsive activity (7b) in the lower part of the cloud close to the channel (5b). The K-events progressed from the lower part of the cloud to its upper part. This behavior is consistent with the measurements analyzed by Shao et al. (1996b).

From locations of LDAR sources we estimated global velocity for the different components. Successive long-distance recoil streamers progressed at 1.7×10^7 m.s $^{-1}$, 1.3×10^7 m.s $^{-1}$ and 0.6×10^7 m.s $^{-1}$ respectively for events (DJ1), (DJ2) and (DJ3). The negative intra-cloud leader propagated with a global velocity evolving between 5×10^4 m.s $^{-1}$ and 2×10^5 m.s $^{-1}$ while the positive leader moved with an averaged 4×10^4 m.s $^{-1}$.

In summary the studied flash consists of a vertical channel connected to horizontal branched discharges at two levels. The lightning discharges developed horizontally on one side of the vertical channel, structure already observed by Shao et al. (1996a) or Rison et al. (1999). Three regimes were recorded during the 660-ms flash with different properties: the first regime corresponds to the development of the two (negative and positive) leaders. During the second regime the two leaders kept progressing while discharges propagated in parts of the already ionized channels. The last regime is composed of long-distance recoil streamers of few milliseconds starting from a zone close to the final position of the positive leader tip, propagating through the channel ionized during the positive leader toward the ignition region of the flash, then progressing upward to finally propagate in the channel ionized during the negative leader. The estimated velocity of the negative leader is an order of magnitude higher than the one deduced for the positive leader.

10.4.2 Concurrent Observations of Lightning Flashes from the Ground-Based ONERA VHF Interferometers and Space Borne NASA OTD Optical Sensor

In the present section we present concurrent VHF and optical measurements sensed during one –CG flash and one IC flash with the ONERA lightning interferometers and the space borne NASA OTD sensor. The OTD observations presented here were recorded during the 4-min pass over the Stratosphere-Troposphere Experiment: Radiation, Ozone and Aerosol – Deep convection (STERAO-A) domain in Colorado (Dye et al., 2000) on the 9th of July 1996 between 20:44 and 20:48 UT (14:44 and 14:48 LT). During the STERAO-A experiment the two ONERA interferometers were deployed in a North-South configuration (Dye et al., 2000; Defer et al., 2001).

The locations of the OTD optical pulses were recomputed in azimuth relative to the two ONERA interferometers in order to identify flashes and derive their characteristics from optical and VHF measurements. NLDN reports were also recomputed in azimuth. For each flash reported by OTD the VHF radiation was analyzed per 3-s analysis time window centered at the time of the OTD flashes. Because of inaccurate locations determined by OTD as we detailed later, we associated the OTD optical pulses with the VHF signal considering temporal matching of successive flash components as recorded in both VHF and optical domains. For storms located in the lobes of the ONERA lightning mapper, a flash-by-flash analysis has been performed, but not discussed here, to investigate flash detection efficiencies of the different sensors. Even if the number of flashes (31) recorded by OTD during the overpass is statistically unrepresentative, the analysis shows however a very encouraging behavior in terms of OTD detection efficiency especially during daytime observations.

Figure 10.8 shows concurrent measurements during a single stroke negative CG flash as identified by NLDN with -41 kA peak current. The VHF signature of the downward stepped leader-return stroke process (Defer et al., 2001) confirms the polarity of the ground connection as well as the time of the connection (2046:27.288 UT). The flash lasted for 620 ms based on the time interval between the first and the last VHF sources. Only three OTD frames were recorded during the life of the flash. The two first frames were recorded few milliseconds after the first stroke. These two frames were preceded by a relatively continuous VHF radiation associated with the in-cloud preliminary breakdown and the propagation of the downward negative stepped leader. Before the occurrence of the last OTD frame, trains of VHF pulses were recorded by the two interferometers. The last OTD frame was preceded by a relative strong VHF signal. Figure 10.8g shows the NLDN location of the CG flash which is consistent with the locations of the VHF sources reconstructed from the measurements of the two direction finders. The location of the flash as given by OTD is about 30 km away from the locations determined by the two other instruments. The satellite carrying on OTD experienced problems in its attitude restitution that explain such difference in term of location accuracy (Boccippio et al., 2001). Finally Fig. 10.8f shows the locations of the OTD pixels illuminated for the entire flash. The brightest pixels were recorded in the center of the pixel distribution. The

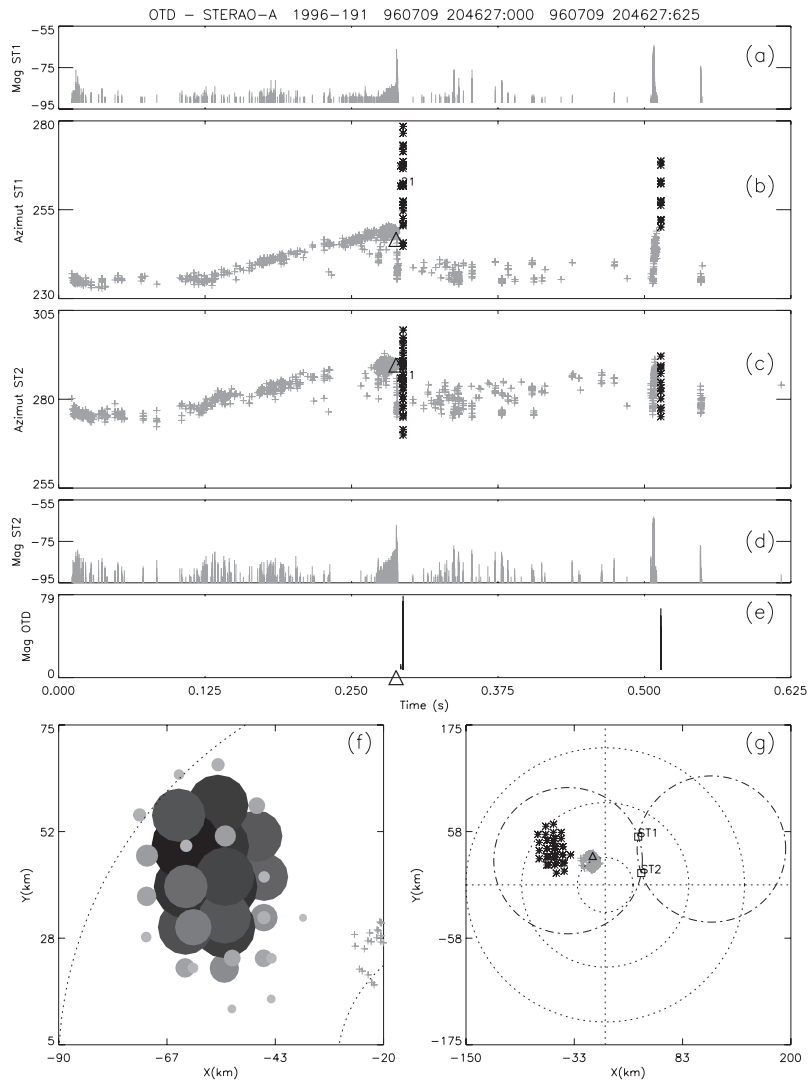


Fig. 10.8 Concurrent observations of a negative cloud-to-ground flash (07/09/1996 2046:27 UT). Panels a, d: VHF magnitude recorded at the two interferometric stations. Panels b, c: azimuth of the VHF sources (grey pluses) and locations of OTD optical pulses (asterisks) relative to ST1 and ST2. Triangles indicate azimuth of the 1-s NLDN flash locations. Panel e: magnitude of OTD pixels (in arbitrary unit). Panel f: locations of the light pulses reported by OTD. The largest and darkest disks correspond to the brightest OTD pixels. Reconstructed VHF sources are plotted with grey pluses. Panel g: locations of the same flashes from the three lightning sensors in the STERAO-A domain. The origin of the coordinates is the CSU-CHILL radar (Dye et al., 2000)

optical pulse distribution covers an area larger than the area delimited by the VHF sources suggesting a significant spatial scattering of the radiated light from the microphysical properties of the cloud. The VHF signal was less intense before the first OTD frames than during the events recorded during the last OTD frame while the magnitude of the emitted light was greater during the first frames.

The observations recorded during the present CG flash are different from what Thomas et al. (2000) reported from concurrent observations of the NASA Lightning Imaging Sensor (LIS) and the New Mexico Tech Lightning Mapping Array (LMA) for storms over Oklahoma. In their analysis mostly no optical pulses were recorded during CG flashes including ground connections until high-altitude IC components were recorded by the LMA. In the present CG case optical pulses were measured at the times of the ground connections and in the early stages of the CG flash life. In addition the measurements analyzed in the present study were done from daytime observations while Thomas et al. (2000) analyzed observations after midnight local time suggesting that OTD had very good detection efficiency in daytime for the present study. However as pointed out by Thomas et al. (2000) and Boccippio et al. (2001), the detection efficiency depends not only of the flash characteristics but also on the cloud properties along the path of the radiated light.

For the studied CG flash, OTD reported only three frames. Only flash components with strong VHF signal were recorded by OTD. As already noted by Goodman et al. (1988), no optical pulses were sensed during the preliminary breakdown and the downward negative stepped leader process, which mostly lasted for half of the flash duration. It also implies that OTD measurements are not reliable to infer the duration of the studied CG flash.

Figure 10.9 presents the concurrent measurements recorded during an IC flash recorded during the same OTD overpass (2046:55 UT). The flash lasted for 650 ms. The IC flash started with very intermittent VHF radiation during its first 20 ms (Fig. 10.9). Then a more continuous VHF radiation associated with the development of an IC negative stepped leader process was recorded during 50 ms then followed by a new regime of intermittent radiation. A second episode of continuous VHF radiation was recorded for almost 50 ms. Very short trains of VHF sources were then recorded up to the end of the flash. A short-duration and continuous radiative component as sensed in the VHF domain was recorded at the end of the flash duration propagating in the same angular sector as the one created by the leader processes, suggesting the development of a K-change event.

For the same flash, OTD recorded 28 frames (Fig. 10.9b, c and e). A first series of frames were recorded in the early stage of the flash and exhibited a low optical magnitude, just above the acquisition threshold, while weak VHF signal, but also above the acquisition VHF threshold, was also sensed. The brightest light pulses were sensed during the first negative IC stepped leader. The successive frames recorded an increase of the magnitude of the optical signal up to the time 2046:55.359 UT. The brightest pixels were roughly located at the center of the spatial distribution of the light pulses. A new set of optical pulses was recorded during the second leader process. The amplitude of the optical signal was less than the one recorded during the first leader process. The OTD pixel distribution almost covered the same area

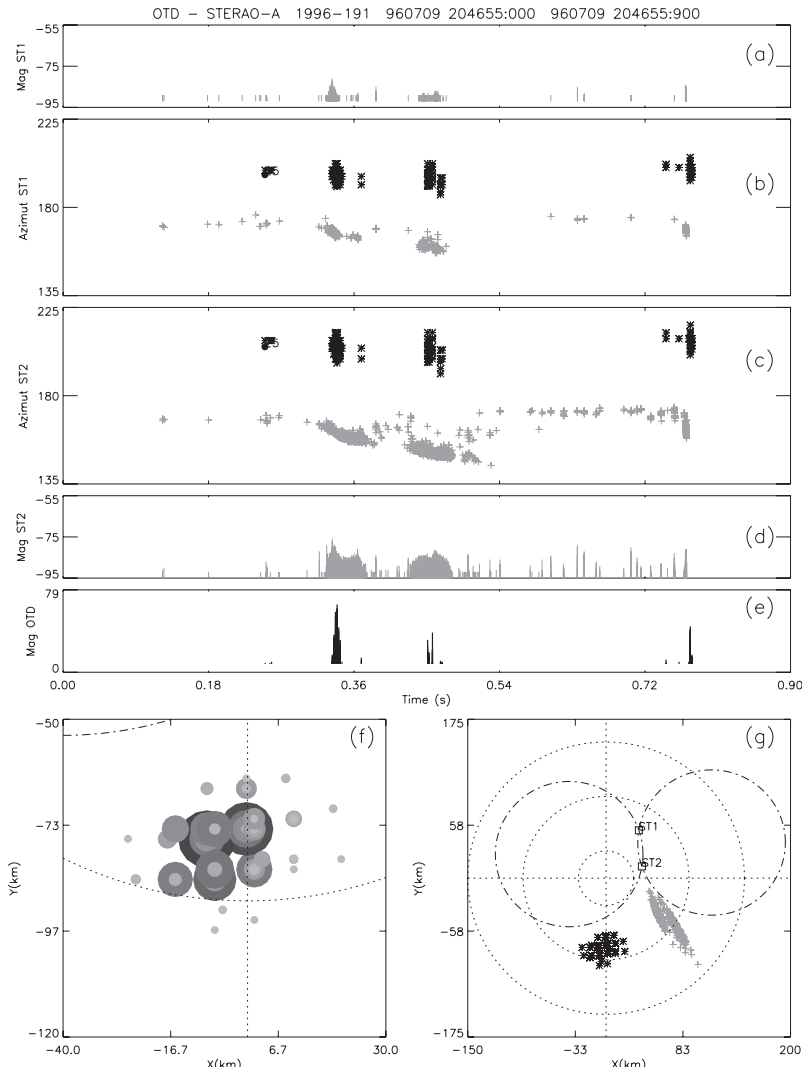


Fig. 10.9 Concurrent observations of an intracloud flash (07/09/1996 2046:55 UT). See Fig. 10.8 for description of the panels

than the one covered during the first leader process except during the last frame where the pixels were located in the eastern part of the pixel distribution. A final set of optical events was reported during the final components of the flash when the K-change process occurred.

Figure 10.9g shows that the IC flash was reconstructed at the edge of the ITF lobes. So it is impossible to determine accurately the position of the studied flash from the VHF signal. However Fig. 10.9g shows that OTD located the flash mostly

60 km away from the average locations of the VHF sources. Again the problem with the attitude restitution of OTD satellite can easily explain that large error in location.

10.5 Implication for the Lightning NO_x Production

Lightning flashes are obviously all different. Indeed they present different properties in terms of duration, structure or development. But as shown in Section 10.4 a lightning flash is not only a developing discharge. It also contains many components that propagate through the track of the channels which has been previously ionized. A time-of-arrival instrument will definitively provide the skeleton of the flash but would miss the bursts of radiation. Consequently an instrument such as PROFEO designed at ONERA (Blanchet et al., 2006) where both time-of-arrival and interferometric techniques are used simultaneously would definitively provide the best description of the flashes in the VHF domain.

In consequence it definitively appears mistaking to use a constant Lightning NO_x (LiNO_x) production per flash for the two types of lightning flashes. An initial way to alleviate the problem would be to determine a LiNO_x production per flash component. But we would face quickly the same problem as when using flash counts: component and/or flash counts would only be rough proxies of the production, because here too all flash components, even if their physical properties remain more or less the same, have different duration and spatial extension. One would then need to take into account the length of the flash component when lightning mappers such as New Mexico LMA or ONERA PROFEO are used, or the duration of the flash components from optical space borne devices such as the upcoming Lightning Mapper Sensor (LMS) on the Geostationary Operational Environmental Satellite (GOES-R). In the latter the use of the time information, i.e. the component duration, appears more pertinent than using the spatial distribution of the optical pixels because the use of LiNO_x production per pixel and per intensity of the optical signal would suffer of scattering process from the cloud particles. Finally while it is hardly conceivable the full Earth to be covered with VHF lightning mappers, lightning detection from geostationary and/or constellation satellites would definitively offer the proper coverage as well as the continuous monitoring of the lightning activity over the entire life of the storms which is not available with low orbit lightning sensors such as OTD or LIS.

In such approaches the LiNO_x production would be assumed to be constant during the flash components, assumption that needs to be really demonstrated, but the estimated LiNO_x production would be really related to what happens during the flash. One could also think using a non-constant production during the lifetime of the components but it would require very detailed in situ measurements of the flash components, discharge studies in laboratory and modelling efforts.

Defer et al. (2003) developed a method to determine the lightning length based on the VHF radiation as proxy to study the LiNO_x production in the 10 July 1996 STERAO-A storm. Skamarock et al. (2003) determined the LiNO_x production per

lightning length unit based on the new lightning metric, in situ chemistry measurements and modelling work. The technique developed in Defer et al. (2003) consists to identify from the VHF radiation recorded at one of the ONERA interferometers the type of flash components based on temporal criteria applied on the VHF signal recorded during a given flash. Arbitrary Defer et al. (2003) assumed that one step during the negative stepped leaders is 20-m long. The length of the negative stepped leaders is then deduced by multiplying the number of VHF sources recorded during the leader process by the step length. The K-change processes are assumed to propagate with a velocity of 10^7 m s⁻¹ from their beginning to their end. Defer et al. (2003) then estimate the length of fast processes by multiplying the number of VHF sources by the previous velocity and by the time resolution of the interferometer (23 μ s).

This method was applied to the measurements of the IC flash described in Section 10.4.1. By drawing the skeleton of the flash with the high (low) altitude LDAR sources projected on 10 (6) km height horizontal plane, we estimated that the flash extended over 61 (53) km in its upper (lower) part. We also applied some basic algorithms based on time (2 ms threshold) and space criteria (2 km threshold) combining LDAR XYZ sources in components, the sum of upper (lower) components extended over 47 (32) km without considering 60 (80) isolated LDAR sources. From the analysis of the interferometric data, the total VHF flash length was estimated at about 140 km. During the first 250 ms of the flash, flash length in the upper part was 38 (27; 42) km long based on the interferometric (LDAR algorithm; LDAR skeleton) data. A total length of 76 km was estimated for all K change processes recorded 500 ms after the beginning of the flash. For the three major K change processes we determined a length of 26, 10, 34 km based on the interferometric data. All those numbers might surprise the Reader but one needs to keep in mind that even if the method developed by Defer et al. (2003) is rather crude, a lightning flash is a succession of events with different duration, length and probably LiNO_x production (per length unit and per component type).

10.6 Perspectives

As mentioned in the previous sections ONERA has developed a brand new instrument PROFEO that is currently in deployment to cover Paris (France) and its suburbs. The new instrument is designed to record the development of flashes based on two techniques that are providing information on different properties of the discharges. In addition a dense network of VLF LINET stations (Betz et al., 2004; Betz, in this volume) will be deployed also in the area of Paris offering the possibility to investigate both VHF and VLF radiation simultaneously. Additional instruments such as high temporal resolution camera and ground-based change field sensors could be also deployed. With such battery of instrument one could expect a more detailed description of the lightning flashes to investigate its ignition and its development. These measurements should provide new insights for the model-

ing of the lightning discharges both at small and large scales and to explore new parameterizations for the LiNOx production. PROFEO will also provide key information to investigate the links between kinematics, microphysical and electrical processes in thunderstorms.

References

- Betz, H.-D., K. Schmidt, P. Oettinger, and M. Wirz, 2004, Lightning detection with 3-D discrimination of intracloud and cloud-to-ground discharges, *Geophys. Res. Lett.*, 31, L11108, doi:10.1029/2004GL019821.
- Blanchet, P., P. Lalande, and P. Laroche, 2006, PROFEO: Programme francilien d'études des orages, Proceeding of the 9th International Lightning Detection Conference, 24–25 April, Tucson, Arizona, USA.
- Boccippio, D. J., W. Koshak, R. Blakeslee, K. Driscoll, D. Mach, D. Buechler, W. Boeck, H. J. Christian, and S. J. Goodman, 2000, The Optical Transient Detector (OTD): Instrument Characteristics and Cross-Sensor Validation, *J. Atmos. Oceanic Technol.*, 17, 441–458.
- Boccippio, D. J., K. L. Cummins, H. J. Christian, and S. Goodman, 2001, Combined satellite and surface-based estimation of the intracloud / cloud-to-ground lightning ratio over the continental United States, *Mon. Wea. Rev.*, 129, 108–122.
- Christian, H. J.; R. J. Blakeslee, D. J. Boccippio, W. L. Boeck, D. E. Buechler, K. T. Driscoll, S. J. Goodman, J. M. Hall, W. J. Koshak, D. M. Mach, and M. F. Stewart, 2003, Global frequency and distribution of lightning as observed from space by the Optical Transient Detector, *J. Geophys. Res.*, 108.
- Cummins, K. L., M. J. Murphy, E. A. Bardo, W. L. Hiscox, R. B. Pyle, and A. E. Pifer, 1998, A Combined TOA/MDF Technology Upgrade of the U.S. National Lightning Detection Network, *J. Geophys. Res.*, 103(D8), 9035–9044.
- Defer, E., J. E. Dye, W. Skamarock, and P. Laroche, 2003, Use of total lightning lengths to estimate NO_x Production in a Colorado Storm, Proceedings of 12th International Conference on Atmospheric Electricity, Versailles, France.
- Defer, E., P. Blanchet, C. Théry, P. Laroche, J. Dye, M. Venticinque, and K. Cummins, 2001, Lightning activity for the July 10, 1996, storm during the Stratosphere-Troposphere Experiment: Radiation, Aerosol, and Ozone-A (STERAO-A) experiment, *J. Geophys. Res.*, 106, 10,151–10,172.
- Dye, J., B. A. Ridley, K. Bauman, W. Skamarock, M. Barth, M. Venticinque, E. Defer, P. Blanchet, C. Théry, P. Laroche, G. Hubler, D. D. Parnish, T. Ryerson, M. Trainer, G. Frost, J. S. Halloway, F. C. Fehsenfeld, A. Tuck, T. Matejka, D. Bartels, S. A. Rutledge, T. Lang, J. Stith, and R. Zern, 2000, An overview of STERAO/deep convection experiment with results for the July 10th storm, *J. Geophys. Res.*, 105, 10,023–10,045.
- Gallimberti, I., G. Bacchigia, A. Bondiou-Clergerie, and P. Lalande, 2002, Fundamental processes in long air gap discharges, *C. R. Physique*, 3,1335–1359.
- Goodman, S. J., H. J. Christian, and W. D. Rust, 1988, A comparison of the optical pulse characteristics of intracloud and cloud-to-ground lightning as observed above clouds, *J. Appl. Met.*, 1369–1381.
- Kawasaki, Z., T. Kanao, K. Matsuura, M. Nakano, K. Horii, and K. Nakamura, 1991, The electric field changes and UHF radiations caused by the triggered lightning in Japan, *Geophys. Res. Lett.*, 18(9), 1711–1714.
- Koshak, W. J., M. F. Stewart, H. J. Christian, J. W. Bergstrom, J. M. Hall, and R. J. Solakiewicz, 2000, Laboratory Calibration of the Optical Transient Detector and the Lightning Imaging Sensor, *J. Atmos. Oceanic Technol.*, 17, 905–915.
- Krehbiel, P. R., R. J. Thomas, W. Rison, T. Hamlin, J. Harlin, and M. Davis, 2000, GPS-based mapping system reveals lightning inside storms, *EOS*, 81, 21–25.

- Lalande, P., A. Bondiou-Clergerie, G. Bacchegia, and I. Gallimberti, 2002, Observations and modeling of lightning leaders, *C.R.Physique*, 3, 1375–1392.
- Laroche P., A. Bondiou, P. Blanchet, and J. Pigère, 1994, 3D VHF mapping of lightning discharge within a storm, Proceedings SEE “lightning and mountains”, Chamonix, France.
- MacGorman, D. R., and W. D. Rust, 1998, *The Electrical Nature of Storms*, 422 pp., Oxford Univ. Press, New York. 687 pp, Cambridge Univ. Press, New York.
- Maier L., C. Lennon, P. Krehbiel and M. Maier, 1996, Lightning as observed by a four-dimensional lightning location system at Kennedy Space Center, proceedings of 10th International Conference on Atmospheric Electricity, Osaka, Japon, 280–283.
- Maier L. M., and E. P. Krider, 1986, The charges that are deposited by cloud-to-ground lightning in Florida, *J. Geophys. Res.*, 91, 13275–13289.
- Mazur V., E. Williams, R. Boldi, L. Maier, and D. E. Proctor, 1997, Initial comparison of lightning mapping with operational time-of-arrival and interferometric systems, *J. Geophys. Res.*, 102, 11071–11085.
- Mazur V., 1989, Triggered lightning strikes to aircraft and natural intracloud discharges, *J. Geophys. Res.*, 94, 3311–3325.
- Parker, N. G. and E. P. Krider, 2003, A Portable, PC-Based System for Making Optical and Electromagnetic Measurements of Lightning, *J. Appl. Met.*, 42, 739–751.
- Pierce E. T., 1977, Atmospheric and radio noise , in “Lightning”, ch. 10, edited by R. H. Golde, Academic Press Inc., London.
- Proctor D. E., R. Uyttenbogaardt, and B. M. Meredith, 1988, VHF radio pictures of lightning flashes to ground, *J. Geophys. Res.*, 93, 12,683–12,727.
- Proctor D. E., 1981, VHF radio pictures of cloud flashes, *J. Geophys. Res.*, 86, 4041–4071.
- Rhodes C. T., X.-M. Shao, P. R. Krehbiel, R. J. Thomas, and C. O. Hayenga, 1994, Observations of lightning phenomena using radio interferometry, *J. Geophys. Res.*, 99, 13059–13082.
- Richard P., A. Delannoy, G. Labaune and P. Laroche, 1986, Results of spatial and temporal characterization of the VHF-UHF radiation of lightning, *J. Geophys. Res.*, 91, 1248–1260.
- Rison, W., R. T., P. Krehbiel, T. Hamlin, and J. Harlin, 1999, A GPS-Based Three-Dimensional Lightning Mapping System: Initial Observations in Central New Mexico, *Geophys. Res. Lett.*, 26, 3573–3576.
- Rust, W. D., D. R. MacGorman, E. C. Bruning, S. A. Weiss, P. R. Krehbiel, R. J. Thomas, W. Rison, T. Hamlin and J. Harlin, 2005, Inverted-polarity electrical structures in thunderstorms in the Severe Thunderstorm Electrification and Precipitation Study (STEPS), *Atmospheric Research*, 76, 247–271.
- Saunders, C. P. R., W. D. Keith and P. P. Mitzeva, 1991, The effect of liquid water on thunderstorm charging, *J. Geophys. Res.*, 96, 11007–11017.
- Shao X.-M., and P. Krehbiel, 1996a, The spatial and temporal development of intracloud lightning, Proceedings of 10th International Conference on Atmospheric Electricity, Osaka, Japan.
- Shao X.-M., and P. R. Krehbiel, 1996b, The spatial and temporal development of intracloud lightning, *J. Geophys. Res.*, 101, 26,641–26,668.
- Skamarock, W. C., J. E. Dye, E. Defer, M. C. Barth, J. L. Stith, B. A. Ridley, K. Baumann, 2003, Observational- and modeling-based budget of lightning-produced NO_x in a continental thunderstorm, *J. Geophys. Res.*, 108 (D10), 4305, doi:10.1029/2002JD002163.
- Stolzenburg, M., W. D. Rust, and T. C. Marshall, 1998, Electrical structure in thunderstorm convective regions. 3. Synthesis, *J. Geophys. Res.*, D103, 14,097–14,108.
- Takashi, T., 1978, Rimming electrification as a charge generation mechanism in thunderstrom, *J. Atmos. Sci.*, 35, 1536–1548.
- Thomas, R. J., P. R. Krehbiel, W. Rison, T. Hamlin, J. Harlin, and D. Shown, 2001, Observations of VHF Source Powers Radiated by Lightning, *Geophys. Res. Lett.*, 28(1), 143–146.
- Thomas, R. J., P. R. Krehbiel, W. Rison, T. Hamlin, T., D. J. Boccippio, S. J. Goodman, and H. Christian, 2000, Comparison of ground-based 3-dimensional lightning mapping observations with satellite-based LIS observations in Oklahoma, *Geophys. Res. Lett.*, Vol. 27, 1703–1706.

Chapter 11

Nowcasting of Thunderstorms Using VHF Measurements

Jean-Yves Lojou, Martin J. Murphy, Ronald L. Holle and Nicholas W.S. Demetriades

Abstract Cloud electrical activity represents a significant portion of the ability to determine thunderstorm severity. The radiation processes that are involved in cloud lightning lead to a very rich information source for those events in the VHF spectrum. Two types of events occur concomitantly: (1) very short duration impulsive events easily locatable with time-of-arrival techniques; and (2) almost continuous events well suited for interferometric location. These two mapping methods are described in some detail in this chapter, and some comparisons of the results from each method are shown at the flash and storm levels. The comparisons demonstrate a great deal of similarity, despite the fact that these two methods do not display the same individual components within the lightning flash. This chapter concludes with a sample application for nowcasting the thunderstorm threat by showing the great improvement resulting from the use of such VHF location information in thunderstorms warnings.

Keywords Total Lightning · Cloud Discharge · VHF · Nowcasting · Warning · Mapping · Interferometry · Time-of-Arrival · Storm Cell

11.1 Introduction

The lightning phenomena most commonly observed and analyzed using lightning detection systems over the last few decades are related to cloud-to-ground (CG) lightning, and in particular, the return strokes in CG flashes. However, those events represent only a small fraction of the total lightning activity, which includes the in-cloud components of CG flashes (Mazur et al. 1995) as well as cloud lightning flashes (Shao and Krehbiel 1996). Observing cloud lightning is important for a number of reasons. Cloud flashes typically outnumber CG flashes by a factor of two to ten in most ordinary convection (e.g. Boccippio et al. 2001). Severe storms,

J.-Y. Lojou (✉)

Vaisala Inc, Tucson Operations, 2705 East Medina Road, Tucson AZ 85706 US
e-mail: jean-yves.lojou@vaisala.com

however, have much higher rates of cloud lightning activity than CG flashes, with some storms producing no CG flashes at all (MacGorman et al. 1989; Williams et al. 1999; Wiens et al. 2005). Cloud flash rates, therefore, can be an important indicator of both the growth and strength of thunderstorms, leading to important applications in nowcasting (Richard 2002; Patrick and Demetriades 2005). In most thunderstorms, cloud flashes also precede the first CG flash as the storm first develops and becomes electrified. Typical times between the first cloud flash and first CG flash range from a few minutes to a few tens of minutes (MacGorman et al. 2006; Weber et al. 1998). This lead time makes it advantageous to use cloud lightning observations for warnings of the threat of CG lightning when storms develop overhead. Finally, cloud lightning activity in larger storm systems such as mesoscale convective systems (MCS) often has a large, horizontal extent (Mazur et al. 1998). Embedded within this lightning activity are intermittent CG strokes. Detection of the cloud lightning activity associated with these systems allows for better monitoring of the CG lightning threat.

Many lightning detection systems operate in the low-frequency (LF) part of the spectrum. These systems are optimized for detecting the return strokes in CG flashes, for a variety of reasons. Cloud flashes, and the in-cloud components of CG flashes, are more easily and thoroughly detected using emissions in the very high frequency (VHF) portion of the spectrum. In this chapter, we first give an overview of the radio-frequency (RF) emissions from lightning discharges, comparing LF and VHF emission characteristics. Then, we describe the two major methods of detecting and locating VHF emissions, time-of-arrival (TOA) and interferometry (Lojou and Cummins 2005, 2006). We then show the similarities between the information obtained using these two techniques, although they detect different components of the lightning discharge. Finally, we briefly discuss one of the major applications of the information obtained from a VHF lightning mapping system.

11.2 Radiation from Lightning in VHF and LF

Both cloud and CG flashes are detectable in either VHF or LF, but the differences in the nature of the signal, as well as in detection techniques lead to differences in the results and the possible applications. Figure 11.1, based on Malan (1963), presents a summary of radio-frequency emissions from cloud and CG lightning flashes in a variety of frequency bands, as well as the evolution of the electrostatic field.

It is now well established that the return strokes in CG flashes mainly radiate in the low frequency (LF) and very low frequency (VLF) portions of the spectrum. This is due to the relatively large amount of current carried over a relatively long distance of several kilometers (the lightning channel). Indeed, the typical wavelength of emissions is related to the length of the radiating element. In a cloud flash, certain phenomena such as the recoil streamer also produce moderate currents of around 1 kA or so over relatively long distances and therefore they radiate in the LF as well (Brook and Ogawa 1977). However, the LF emissions from cloud flashes

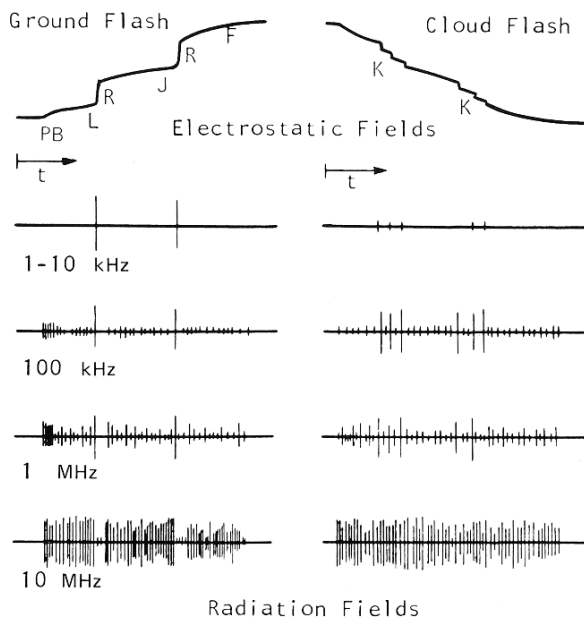


Fig. 11.1 Electrostatic field and time series of the radiation in several bands from a typical CG flash and a typical cloud flash normalized at 20 km. Amplitudes are scaled differently for the different frequency bands. The length of the “t” arrow corresponds to about 30 ms. Adapted by Uman (1987) from Malan (1963): PB = Preliminary Breakdown, L = Leader, R = Return Stroke, J / K = J / K processes, F = Final Field Change

are typically an order of magnitude weaker than those due to CG return strokes (Weidman et al. 1981), except in the case of a unique in-cloud phenomenon known by its LF signature as a Narrow Bipolar Event (LeVine 1980).

The detection and location of LF emissions provide only one location close to the point where the current derivative (di/dt) is the highest. For the return strokes in CG flashes, this corresponds to a point just above the ground impact. LF emission sources in cloud flashes are more difficult to locate accurately. The difficulty with recoil streamers stems from the fact that they are often partly or mostly horizontal because of the extensive horizontal channel structure found in the main charge regions of the storm (Shao and Krehbiel 1996). Because of the conductivity of the ground, however, LF and VLF signals are predominantly vertical, and LF lightning detection systems are designed to be sensitive to vertically-polarized signals. Emission sources with a substantial horizontal component are difficult to detect, and they are subject to greater measurement errors that lead to poorer resolution of their positions.

By far, the high-current, long-channel phenomena that lead to LF emissions are outnumbered by the much smaller processes associated with breakdown processes in the cloud, as well as the stepped leaders to ground in a CG flash. These processes have typical dimensions on the order of tens to hundreds of meters (Proctor 1981)

rather than km, and they do not carry high currents. The RF emissions due to these processes are predominantly in the VHF portion of the spectrum. Because the physical sizes of the radiating elements are relatively small, a large number of them are generated by both CG and cloud lightning flashes during many phases of the discharge process (Mazur et al. 1995; Shao and Krehbiel 1996). By locating these numerous emission sources, it is possible to map the spatial extent of a lightning flash as a function of time during the evolution of the flash.

Different processes within a flash produce different kinds of emissions (Krehbiel et al. 2002; 2003). Proctor (1981), Rhodes et al. (1994), and others have described two basic types of VHF emissions from lightning. One type is quasi-continuous over a couple of milliseconds and does not exhibit distinct peaks during that time. The other type consists of well-defined microsecond-scale impulses. Fast-moving negative streamers (recoil streamers) and dart leaders tend to emit more continuous radiation bursts, while preliminary breakdown tends to correspond to impulsive radiation events. Stepped leaders in negative CG flashes also produce impulsive emissions, but as the leader approaches ground and the branched structure becomes more complex, the emissions begin to look more continuous. Figure 11.2 shows the r.m.s. amplitude of a waveform captured in Texas using a dipole filtered at 114 MHz and integrated over 4 μ s. The signal is drawn in arbitrary units for a duration of 3 ms. Figure 11.2 clearly shows several very narrow pulses occurring together with a more continuous process whose duration is about 300 μ s. This difference of behavior will

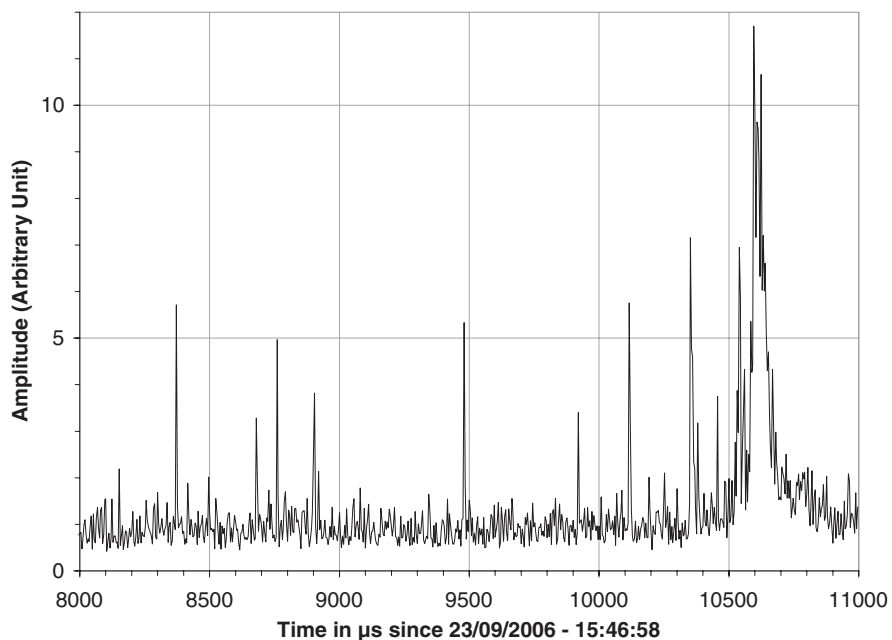


Fig. 11.2 Typical VHF waveform showing impulsive radiation events and one continuous burst of radiation lasting for about 300 μ s

allow different methods of detection and mapping: The short duration events will be well suited to time-of-arrival mapping techniques while the continuous ones will be perfectly adapted to interferometry.

11.3 Mapping the Flashes Detected in VHF

11.3.1 VHF Time-Of-Arrival

As the name time-of-arrival (TOA) implies, this lightning detection technique relies on measuring the arrival times of impulsive emissions at a number of antennas in different locations. As discussed previously, the emissions best handled by a TOA-based lightning detection system are the impulsive emissions, for which a precise and consistent time-of-arrival measurement is most easily made at widely separated antenna sites. These impulsive emission sources have been shown to be consistent with essentially point-source emitters with spatial dimensions on the order of a fraction of a km (Thomas et al. 2004). The RMS accuracy of the TOA measurements in VHF TOA lightning locating systems is typically 50–100 nsec (e.g., Thomas et al. 2004). The method of localizing the emission sources is based on differences in time of arrival between pairs of antennas. Because VHF signals propagate along a direct line of sight between the emitter and the receiving antenna, the VHF TOA lightning locating technique is inherently three-dimensional. Figure 11.3 shows a two-dimensional representation of the TOA-difference localization technique, but the picture in Fig. 11.3 is extensible to three dimensions.

The major difficulty in VHF TOA technique resides in the consistent identification and correlation of the numerous impulsive events between the various sensors of the detection system. This is because the emissions are often separated by a period that can easily be shorter than the distance between sensors (also called the baseline distance) converted to time using the speed of light. Therefore the sequence of pulses may not arrive at each sensor in the same order, making this identification process quite complex. The standard remedy is then to use relatively short baselines to minimize this effect, and to require a significant amount of redundant information for the determination of each emission source location (e.g. 6 or more TOA measurements to determine 3 spatial coordinates and time). In practical terms, typical baselines are about 30 km long and provide for unambiguous resolution of emissions separated by at least 100 μ s.

11.3.2 VHF Interferometry

VHF interferometry also consists of a measure of time differences between pairs of antennas, but with a distance between the antennas on the order of magnitude of a wavelength, that is in VHF about one to five meters. In that case, the time difference can be determined as a phase difference, and the system then takes advantage of

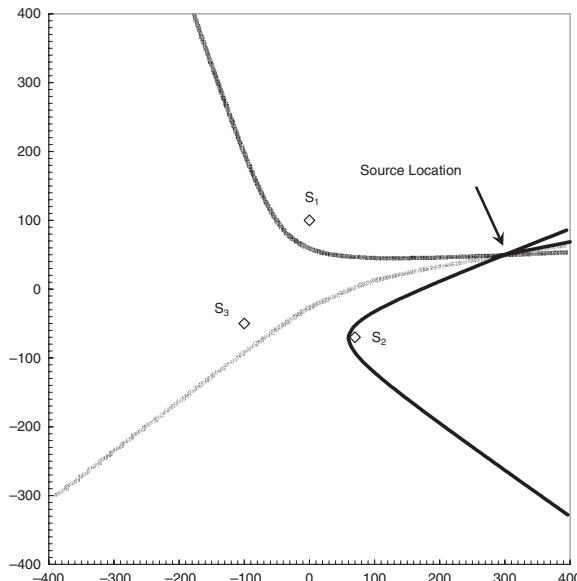


Fig. 11.3 Time-of-arrival location technique. The difference of time of arrival for each pair of sensors is confined on a hyperbola (area of constant distance difference to the foci). The intersection of the hyperbolas gives the source location. This illustration is limited to a two-dimensional (2D) location system for readability; the principle is identical in three dimensions (3D)

the temporal repetitiveness of the signal in order to integrate on a large number of periods to make the measurements very accurate. The only assumption therefore is that the source does not change apparent direction over the integration time.

Figure 11.4 shows almost the same situation as in Fig. 11.3, but reducing the spacing between dipoles to very small values. In that case all hyperbolas will have one of their branches parallel to each other, thus giving only access to the direction of the source of the radiation.

Now the maximum time difference for such a system whose typical size is on the magnitude of one meter will be shorter than about 3 nanoseconds. Achieving an angular accuracy of one degree would mean that to determine a precise time difference the accuracy needs to be as small as about 10 picoseconds. This is obviously not achievable easily in a straightforward way, and this is where interferometry shows a great advantage.

Assuming that the source will not move significantly in azimuth for a given duration, interferometry will take advantage of the numerous periods of the signal to determine an average time difference over the whole integration period by means of a phase difference. To illustrate this, let's assume a 100 MHz interferometric system, for which we integrate the signal over 100 microseconds, the integration factor, equal to the ratio between the integration time and the period will be equal to 10 000, thus leading to a huge improvement in the time (i.e. phase) determination.

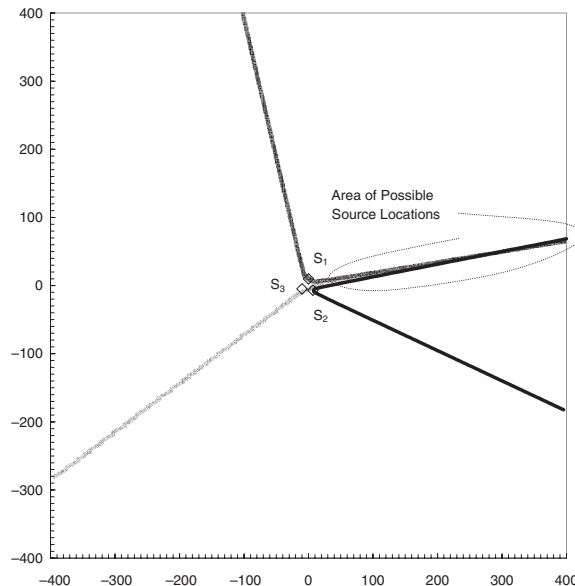


Fig. 11.4 Interferometry seen as an extension of time-of-arrival location technique. When the distance between antennas becomes very small, the intersection between the hyperbolas tends to a straight line corresponding to the direction of the source

11.3.2.1 Principle of Interferometry

Interferometry, in the way we use it, consists of determining the direction of the source of radiation from a combination of phase measurements in a relatively small bandwidth. The antenna is made up of an array, more or less complex, of VHF dipoles and is connected to an interferometric receiver that is able to determine phase differences over quite a large dynamic range. The phase difference is usually obtained by mixing the signals from several antennas either together, or to a common local oscillator and then by integrating over the desired time resolution (where the accuracy on the phase measurements is achieved). The final step consists of processing those phase differences in order to obtain an azimuth from a two-dimensional (2D) network, or a pair (azimuth, elevation) from a three-dimensional (3D) network of the source that produced the radiation. The central processor will then receive that information from several sensors and will locate each individual event by triangulation.

Note that in our case it is difficult to speak about an interferometer as such, since only one radiation source is involved. By definition, interferometry consists of the observation of interferences created by several coherent sources. But the way the radiation source observed from several locations is combined to produce angular information is very similar to what is done in many other fields such as astronomy. Nevertheless, it is customary to call this detection method “interferometry”.

11.3.2.2 Interferometry Foundations

When two spaced ideal dipoles are illuminated by a monochromatic wave front, assumed plane,¹ the phase of the signal is proportional to the spacing between the dipoles and the incident angle.

Using the coordinate system described in Fig. 11.5, the phase difference between a signal whose wavelength is λ caught by two dipoles situated at the same altitude and separated by a distance D will be equal to:

$$\delta\phi = 2\pi \frac{D}{\lambda} \sin \theta \cos \varphi \quad (11.1)$$

The only difficulty now resides in finding a way to separate the inter-dependence of this phase measurement with both azimuth and elevation. The very basic solution consists of simply installing a second such interferometric pair orthogonal to the previous one. The azimuth θ will then be rotated by 90° , resulting in a transformation of the sine to a cosine. The equation system of such an array is then given by:

$$\begin{cases} \delta\phi_1 = 2\pi \frac{D}{\lambda} \cos \varphi \sin \theta \\ \delta\phi_2 = 2\pi \frac{D}{\lambda} \cos \varphi \cos \theta \end{cases} \quad (11.2)$$

Thus, as illustrated in Fig. 11.6, in the Cartesian plan ($\delta\phi_1, \delta\phi_2$) the azimuth of the vector representing the pair of measurements made from this system will correspond to the azimuth of the source. The length of the vector will be proportional to the cosine of the elevation with very poor resolution close to the horizon. The angular accuracy of such a network will be strictly related only to the accuracy achievable by the phase measurement.

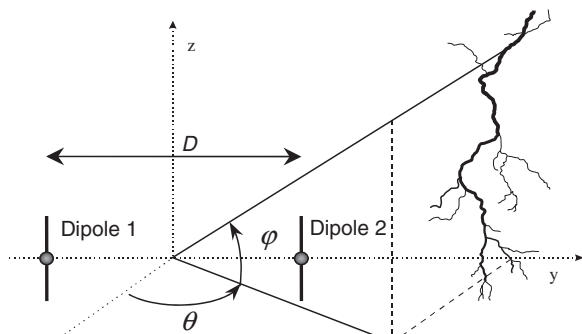


Fig. 11.5 Notations for an interferometric pair

¹ The wave can be assumed plane as long as the path variation, i.e. the height of the circle segment, is sufficiently small compared to the wavelength not to alter the phase by more than a significant amount. This is obtained once the observing distance is great compared to the square of the antenna size divided by twice the wave length. In practical terms this is true as soon as the observing distance is greater than a few hundreds of meters for an antenna array operating at 100 MHz and whose size is on the order of magnitude of the wavelength.

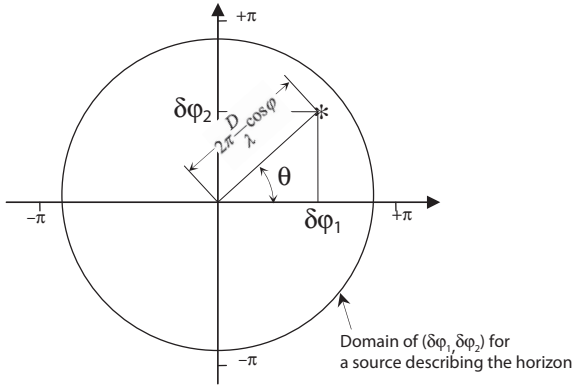


Fig. 11.6 Representation of the measurements of two orthogonal interferometric pairs in the phase domain (see text)

11.3.2.3 Noise Consideration

When determining the phase of a vector whose amplitude is A_o , the thermal noise then acts as a perturbing vector whose amplitude is A_p . Signal to Noise Ratio SNR expressed in dB is thus given by:

$$SNR = 20 \log \frac{A_o}{A_p} \quad (11.3)$$

Introducing $L = \frac{A_p}{A_o} = 10^{-\frac{SNR}{20}}$, the instantaneous phase error is obtained by:

$$d\Phi_1 = \text{ArcTan} \frac{L \cdot \sin \alpha}{1 + L \cdot \cos \alpha} \quad (11.4)$$

where α denotes the instantaneous angle between A_p and A_o .

Since the noise is completely uncorrelated with the measurement, one can deduce the r.m.s. value:

$$d\Phi_{1 rms}^2 = \frac{1}{2\pi} \int_{-\pi}^{+\pi} \left[\text{ArcTan} \frac{L \cdot \sin \alpha}{1 + L \cdot \cos \alpha} \right]^2 d\alpha \quad (11.5)$$

In the case of measuring a phase difference, each signal will be affected by incoherent noise that will be summed in a quadratic way. Therefore the resulting square of the r.m.s. value, assuming the same SNR on each vector, will be twice as high. Furthermore, if we consider that $L \ll 1$, the previous equation can be written as:

$$d\Phi_{rms}^2 \approx \frac{1}{\pi} \int_{-\pi}^{+\pi} [L \cdot \sin \alpha]^2 d\alpha = \frac{L^2}{\pi} \left[\frac{\alpha}{2} - \frac{1}{4} \sin 2\alpha \right]_{-\pi}^{+\pi} = L^2 \quad (11.6)$$

And finally:

$$d\Phi_{rms} \approx 10^{-\frac{SNR}{20}} \quad (11.7)$$

On the other hand, the time integration of the signal reduces the r.m.s. phase noise by a factor equal to $\sqrt{B\tau}$, where B is the input bandwidth and τ the integration time.

Since thermal noise is equal to kTB where k is the Boltzmann constant ($k = 1.38 \cdot 10^{-23}$ J/K) and T the temperature; if S corresponds to the received signal strength in dBm and NF to the receiver Noise Figure (i.e. the degradation of the SNR due to the electronic) in dB we obtain:

$$d\Phi_{rms} \approx \sqrt{\frac{1000kT}{\tau}} 10^{\frac{NF-S}{20}} \quad (11.8)$$

In summary, the accuracy of the phase measurement will mainly depend on the signal strength and some other fixed parameters such as the integration time, the Noise Figure of the electronics, and the temperature. Typically, the achievable phase measurement accuracy is about one degree r.m.s. for a signal strength in the -92 dBm assuming a 7 dB Noise Figure and a 100 μ s integration time (Fig. 11.7).

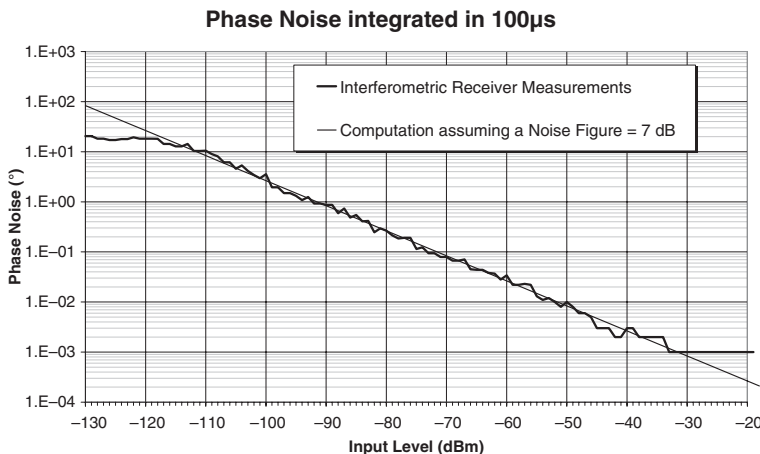


Fig. 11.7 Example of the phase noise as measured by an interferometric receiver. The operating temperature is 35°C, the integration time is 100 μ s and the noise figure of the receiver is 7 dB. The saturation above -35 dBm is due to the resolution of the measuring equipment; the saturation below -116 dBm is due to thermal noise in the 125 kHz analysis bandwidth

Therefore, to minimize the relative effect of the phase noise there could be two alternatives:

- 1) Increase the spacing between the dipoles: Since the phase noise appears to be incompressible, increasing the slope of the antenna (i.e. the number of phase degrees per degree of azimuth = $\frac{2\pi D}{\lambda}$ from Equation (11.2)) will improve the quality of the measurements. There is however a limitation induced by the

- ambiguities that will appear as soon as the spacing is larger than half the wavelength, unless a specific processing takes place;
- 2) Increase the number of dipoles in order to further integrate the measurement and use the resulting redundancy to improve the accuracy.

11.3.2.4 Coupling Corrections

Note that in the above discussion, we assumed that the dipoles were ideal, with no coupling between each other or with an eventual structure. In the real world, the coupling will result in an extra phase deviation of up to several tens of degrees, depending on the geometry and the distance between dipoles. According to how the antenna array is built and how the processing algorithm operates, this coupling effect can be dramatically reduced, but will remain an azimuthal error, usually dependent on both the azimuth and the elevation, which is in the range of one to several degrees. However, since this is a constant of the system which only depends on the geometry of the antenna, it is possible to correct the measurements by coupling correction tables that can be either computed numerically or measured on a calibration bench. As long as the antenna is installed in the recommended configuration (no close obstacles that may affect this coupling), there is no need of in-situ calibration.

11.3.2.5 Summary: The VHF Interferometric Sensor

In summary, a VHF interferometric sensor will operate in a frequency band close to about 100 MHz. This band ensures a good detection of cloud events with a sufficient Signal to Noise Ratio leading to a detection range of up to 300 km, which is mainly limited by the field of view of the sensor due to propagation in straight lines at these frequency ranges. When installing a sensor, great care must be taken concerning the surrounding terrain in order to allow a maximum detection range.

Although the dynamic range of lightning is somehow limited,² the receiver will need to have a huge dynamic range in order to coexist with strong emitters such as FM radios. The integration time should range between several microseconds up to about 100 μ s to be in good accordance with the observed phenomena, and then be able to depict them. To improve the noise performance, the sensor will require a relatively large size and several dipoles with advanced processing for achieving acceptable angle noise from a level dependent phase noise. The other critical aspect of the installation of such a sensor will reside in nearby obstacles such as antennas, pylons, metallic roofs and hangar doors which may dramatically change the apparent azimuth of a source, even though they do not affect a time-of-arrival system very much. Finally, these very sensitive electronic devices require a minimum amount of attention to check for any possible source of phase mismatch between the dipoles due to issues such as aging, corrosion, thermal elongation, and extreme weather stress.

² Statistics collected with this method have shown that the distance-normalized amplitude of lightning acquired at 114 MHz, 500 kHz bandwidth and 100 μ s integration time follows a Gaussian distribution with a standard deviation of about 5 dB.

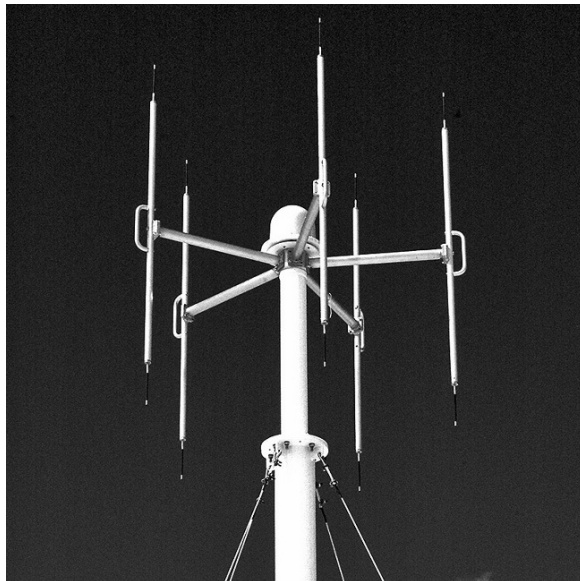


Fig. 11.8 The VHF interferometric sensor. This photograph shows Vaisala's LS8000 sensor with 5 vertical dipoles. The dome at the center of the antenna shelters the LF sensor used for detecting and locating CG flashes. The VHF receiver is usually installed at the bottom of the mast holding the antenna some 15 m below

11.3.3 Example of Flash Mapping

In order to develop a presentation of the two main location techniques in VHF, a single flash has been plotted in Fig. 11.9 as it would have been seen from above. The branches are derived by a flash grouping algorithm that uses time and space difference criteria between the located sources. It is confirmed that both technologies

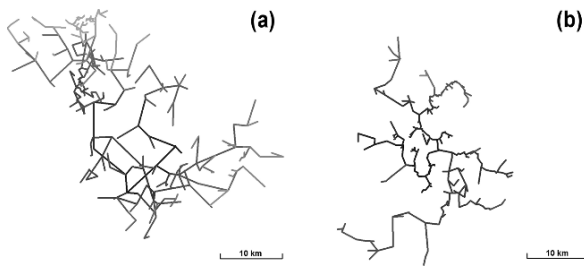


Fig. 11.9 Top view of two-dimensional cloud flash mapping of one flash detected in the Dallas-Fort Worth (DFW), Texas, USA area on 7 July 2005 as located by (a) interferometry and (b) time-of-arrival techniques. Shading corresponds to the time of occurrence, starting with dark gray at 15:03:33 UTC and ending in light gray at 15:03:35. Plots show the expansive growth of the flash using both techniques. Time resolution is 100 μ s in both cases

do not depict the exact same events, although the flash is seen at the same location with the same extent with both location techniques.

11.4 Mapping Thunderstorms

Both location methods, time-of-arrival and interferometry, provide a huge amount of data that can be somewhat difficult to handle. The point data will therefore only be used in very rare cases, and most of the time some advanced processing will be performed in order to make this dataset more manageable. The more frequently used process consists of building density maps, either of source density or flash density. In order to take into account the fact that the extent of each cloud flash or cloud component of CG flashes may occupy several density bins, usually one to several km across, the notion of flash extent density (FED) has been introduced (Lojou and Cummins 2005). With this method, each bin crossed by any branch of a flash receives a count of one. As a result, this method is far less sensitive to the detection efficiency of the network and is therefore preferred. Figure 11.10 shows a comparison of FED from a thunderstorm in the Dallas area by two VHF detection networks, one using interferometry and the other using time of arrival. This comparison shows similar results with the two techniques, and confirms that either can be used in total lightning monitoring applications.

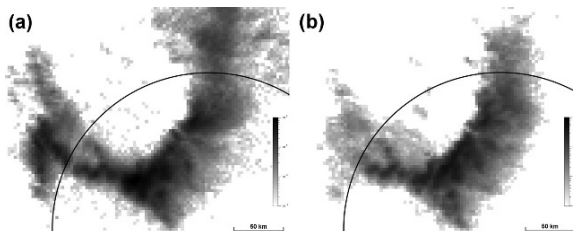


Fig. 11.10 Flash extent density (FED) of a thunderstorm system detected in the Dallas-Fort Worth (DFW), Texas, USA area on 01 July 2005 as depicted by (a) interferometry and (b) time-of-arrival networks. Shading corresponds to flash density in flash/km²: darker pixels correspond to higher densities. The results are very similar, except for a longer detection range for interferometry, and better accuracy for time-of-arrival detection. The black arc indicates the area where the detection efficiency of both networks is satisfactory (better than 90%)

11.5 Comparison between VHF Interferometry and VHF Time-of-Arrival

The major differences between VHF interferometry and VHF time-of-arrival techniques reside in the fact that time-of-arrival operates on the shape of the signal and will thus need to have well identifiable pulses, while interferometry works on the

Table 11.1 Comparison of features of interferometric and time-of-arrival networks

	Interferometry	Time-of-arrival
Coverage	<ul style="list-style-type: none"> Can cover a larger area with fewer sensors 	<ul style="list-style-type: none"> Provides a better source location accuracy thanks to a large number of closely spaced sensors
Site	<ul style="list-style-type: none"> Requires very “clean” sites 	<ul style="list-style-type: none"> Has the only constraint of line-of-sight
Number of sensors	<ul style="list-style-type: none"> Only two sensors are required to build a solution 	<ul style="list-style-type: none"> Requires quite a large number of sensors reporting
Communications	<ul style="list-style-type: none"> Is well suited to use standard communication media 	<ul style="list-style-type: none"> Needs wideband communication channel

carrier itself and therefore requires a steady signal over several to tens of microseconds, according to system performance. There are two main consequences to these facts:

- 1) Both techniques will not have the same specifications or requirements as a system. Table 11.1 gathers what is specific to each technology, concluding that VHF interferometry is more devoted to commercial networks, while VHF time-of-arrival appears to be better suited for research applications.
- 2) Both techniques will not locate exactly the same components. As seen in the example of flash mapping, each technology will locate different events occurring in the flash, thus leading to different pictures of the flashes, but with the same location and the roughly the same extent. The mapping of the storm will reproduce exactly the same feature and therefore can equally be used in warning applications.

11.6 Application: Nowcasting of Thunderstorm Threats

One of the major applications of lightning detection is the nowcasting of thunderstorm threats to allow the user to take all the necessary preventive actions to protect sites or individuals. Those actions can consist of shutting down sensitive equipment, isolating the site from the mains or communication networks, or avoiding workers being in areas highly exposed to lightning. Therefore the main criteria for such warning systems will be:

- 1) A sufficient lead time to allow taking the preventive actions; typically 5–10 min
- 2) A decent false alarm rate (FAR) to avoid long unnecessary down time of protected equipment
- 3) A low failure to warn (FTW) ratio to be sure that the site will be “protected” in the event of a direct strike

There is a type of competition between the two last parameters, because if the warning algorithm is tuned to be very sensitive in order to minimize the FTW,

the FAR will consequently increase. Therefore the parameters of the warning system should be set according to the nature of the site to protect. When the cost of downtime is very important, the warning system should try to minimize the FAR while, when human safety is to be considered, the FTW becomes the predominant parameter.

The simpler approach to building such a warning system consists in detecting, and eventually locating the CG flashes, and then trying to analyze the evolution to elaborate a warning for a given location. However this method has been proven to not be very efficient, especially during mesoscale convective systems (MCS). In an MCS, most CG flashes are located in the convective line, ahead of the displacement of the front. But a large trailing stratiform region behind this line shows evidence of charged regions, based on a large amount of cloud lightning activity, where spider lightning can develop over tens of kilometers and is often associated with quite intense CG flashes.

In such conditions, the basic warning system as described above will not work, since the convective line can easily be sufficiently far away for a long enough time to put the site of interest back into operation, when such CG flashes occur. Figure 11.11 shows an example of an MCS where most of the CG flashes are located in a very narrow convective line about 20 km wide, while the trailing stratiform region, depicted by the cloud flash activity, extends about 80 km behind the line. All scattered CG flashes in this area are potentially very dangerous. The great advantage of VHF based detection techniques resides, then, in the fact that they can provide accurate mapping of in-cloud events. These events can be either the cloud component of CG flashes or cloud flashes themselves, which are grouped into the term “Total Lightning”, which allows a clearer picture of the hazardous area.

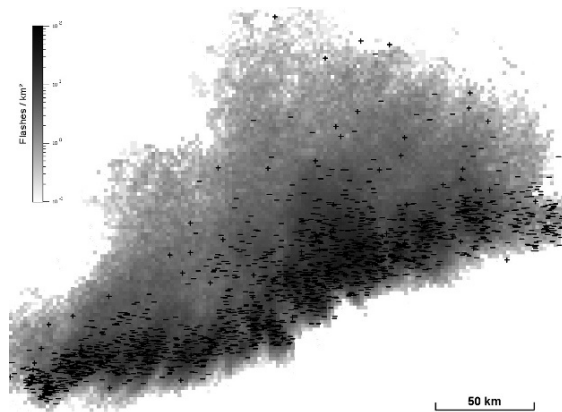


Fig. 11.11 30 minutes of lightning activity in an MCS detected in the Dallas-Fort Worth (DFW), Texas, USA area on 15 June 2001 from 02:30 to 03:00 GMT. Gray shading represents the cloud flash density. The + and – signs indicate CG flashes and their associated polarity. Most CG flashes are concentrated in the convective line but some occur in the trailing stratiform region, with a larger than usual proportion of positive events

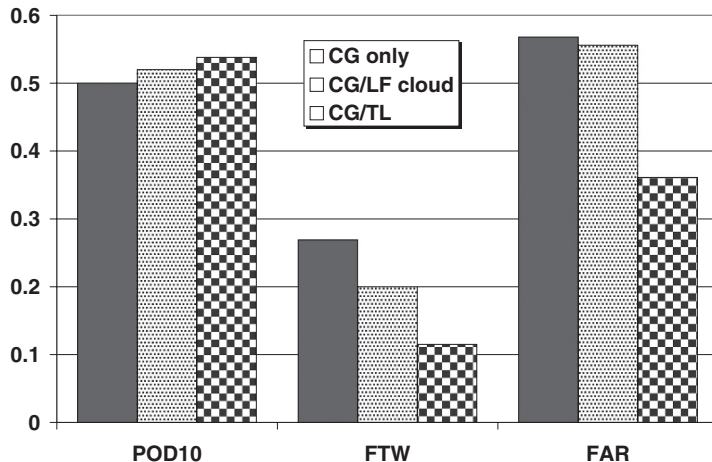


Fig. 11.12 Warning performance metrics for best possible usage of the datasets. CG flash data are always involved in the analysis as the predictand. The other datasets are 1) LF cloud discharge data in light gray stippled bars, and 2) VHF total lightning mapping in checkerboard bars

At present, some LF detection systems are tuned to also locate some of the cloud flash events radiating in this band; these returns are called “LF cloud” (such as recoil streamers as stated in the introduction). These systems help to improve the efficiency of warning algorithms, but because they are mostly sensitive to nearly vertical discharge components, LF cloud detection systems produce a more compact spatial representation of a storm (Loboda et al. 2006; Murphy et al. 2007). VHF systems are able to map the total extent of the cloud flashes, which results in more efficient warning methods. Figure 11.12 summarizes results where a comparative study of warning algorithms based on network data has been made (Murphy and Holle 2006). The use of VHF total lightning clearly shows an improvement in the probability of detection 10 minutes prior to the occurrence of the first CG flash (POD10). In addition, there is also a dramatic reduction of the failure to warn (FTW) rate, and the false alarm rate (FAR) is decreased by almost a factor of two.

Abbreviations

2D:	Two Dimensional
3D:	Three Dimensional
CG:	Cloud Flash
FAR:	False Alarm Rate
FED:	Flash Extent Density
FTW:	Failure To Warn
LF:	Low Frequency
MCS:	Mesoscale Convective Systems

- POD10: Probability Of Detection 10 minutes prior
to the occurrence of the first CG flash
- RF: Radio Frequency
- TOA: Time Of Arrival
- VHF: Very High Frequency
- VLF: Very Low Frequency

References

- Boccippio, D.J., Cummins, K.L., Christian, H.J., Goodman, S.J.: Combined satellite and surface-based estimation of the intracloud–cloud-to-ground lightning ratio over the continental United States. *Mon. Wea. Rev.* **129**, 108–122 (2001).
- Brook, M. and T. Ogawa, The cloud discharge. In *Lightning*, vol. 1, *Physics of Lightning*, R. Golde (ed.), Academic Press, London, pp. 191–230 (1977).
- Krehbiel, P., Hamlin, T., Zhang, Y., Harlin, J., Thomas, R., Rison, W.: Three-dimensional total lightning observations with the lightning mapping array. *Preprints, Intl. Lightning Detection Conf.*, Oct. 16–18, Tucson, Arizona, Vaisala, 6 pp. (2002).
- Krehbiel, P., Hamlin, T., Harlin, J., Thomas, R., Rison, W., Zhang, Y.: Thunderstorm observations with the Lightning Mapping Array. *Proceedings, 12th Intl. Conf. on Atmospheric Electricity*, June 9–13, Versailles, France, 147–150 (2003).
- LeVine, D.M.: Sources of the strongest RF radiation from lightning. *J. Geophys. Res.*, **85**, 4091–4095 (1980).
- Loboda, M., G. Maslowski, Z. Dziewit, H.D. Betz, B. Fuchs, P. Oettinger, K. Schmidt, M. Wirz, and J. Dibbern, A new lightning detection network in Poland. *International Conference on Grounding and Earthing/2nd International Conference on Lightning Physics and Effects*, November 26–29, Maceio, Brazil, 487–494 (2006).
- Lojou, J.Y., K.L. Cummins: On the representation of two- and three-dimensional total lightning information. *Conf. on Meteorological Applications of Lightning Data*, San Diego, Cal., Amer. Meteor. Soc., paper 2.4 (2005).
- Lojou, J.Y., K.L. Cummins: Recent Comparisons of VHF Lightning Mapping Using Interferometry and Time-of-Arrival Techniques, *Eos Trans. AGU*, 86(52), Fall Meet. Suppl., Abstract AE43A-02 (2005).
- Lojou, J.Y., K.L. Cummins: Total Lightning Mapping Using Both VHF Interferometry and Time of Arrival Techniques, *28th Intl. Conf. on Lightning Protection*, Sept 18–22, Kanazawa, Japan, (2006).
- MacGorman, D.R., Burgess, D.W., Mazur, V., Rust, W.D., Taylor, W.L., Johnson B.C.: Lightning rates relative to tornadic storm evolution on 22 May 1981. *J. Atmos. Sci.*, **46**, 221–250 (1989).
- MacGorman, D., Apostolakopoulos, I., Nierow, A., Murphy, M., Demetriades, N., Cramer, J., Krehbiel, P.: Improved timeliness of thunderstorm detection from mapping a larger fraction of lightning flashes. *Lightning Imaging Sensor Intl. Workshop*, 11–14 September, Huntsville, Ala., Univ. of Ala. Huntsville and National Space Science and Tech. Center. (2006).
- Malan, D.J.: *Physics of lightning*. English Univ. Press, London, 176 pp. (1963).
- Mazur, V., Krehbiel, P.R., Shao, X.M.: Correlated high-speed video and radio interferometric observations of a cloud-to-ground lightning flash. *J. Geophys. Res.*, **100**, 25731–25753 (1995).
- Mazur, V., Shao, X.M., Krehbiel, P.R.: “Spider” lightning in intracloud and positive cloud-to-ground flashes. *J. Geophys. Res.*, **103**, 19811–19822 (1998).
- Murphy, M., Holle R. : Warnings of cloud-to-ground lightning hazard based on combinations of lightning detection and radar information. *Preprints, Intl. Lightning Detection Conf.*, Apr. 24–25, Tucson, Arizona, Vaisala, 6 pp. (2006).
- Murphy, M.J., N.W.S. Demetriades, K.L. Cummins, and R.L. Holle, Cloud lightning from the U.S. National Lightning Detection Network (NLDN), *13th International Conference on Atmospheric Electricity*, August 13–17, Beijing, China, 4 pp. (2007).

- Patrick, G.R. and N.W.S. Demetriadis: Using LDAR II total lightning data in an operational setting: Experiences at WFO Fort Worth TX. Preprints, 21th Conf. on Weather Analysis and Forecasting/17th Conf. on Numerical Weather Prediction, July 31-August 5, Washington, DC, U.S., American Meteorological Society, 8 pp. (2005).
- Proctor, D.E.: VHF radio pictures of cloud flashes. *J. Geophys. Res.*, **86**, 4061–4071 (1981).
- Richard, P.: Data fusion concepts for storm nowcasting. Preprints, 17th Intl. Lightning Detection Conf., October 16–18, Tucson, Arizona, U.S., Vaisala, (2002).
- Rhodes, C.T., Shao, X.M., Krehbiel, P.R., Thomas, R.J., Hayenga, C.O.: Observations of lightning phenomena using radio interferometry. *J. Geophys. Res.*, **99**, 13059–13082 (1994).
- Shao, X.M., Krehbiel, P.R.: The spatial and temporal development of intracloud lightning. *J. Geophys. Res.*, **101**, 26641–26668 (1996).
- Thomas, R.J., Krehbiel, P.R., Rison, W., Hunyady, S.J., Winn, W.P., Hamlin, T., Harlin, J.: Accuracy of the Lightning Mapping Array. *J. Geophys. Res.*, **109**, doi:10.1029/2004JD004549 (2004).
- Uman, M.A.: The lightning discharge. Academic Press, San Diego, 377 pp. (1987).
- Weber, M.E., E.R. Williams, M.M. Wolfson, and S.J. Goodman, 1998: An assessment of the operational utility of a GOES lightning mapping sensor. Project Rept. NOAA-18, Lincoln Lab., MIT, Lexington, Mass, 108 pp.
- Weidman, C.D., Krider, E.P., Uman, M.A.: Lightning amplitude spectra in the interval from 100 kHz to 20 MHz. *Geophys. Res. Lett.*, **8**, 931–934 (1981).
- Wiens, K.C., Rutledge, S.A., Tessendorf, S.A.: The 29 June 2000 supercell observed during STEPS. Part II: Lightning and charge structure. *J. Atmos. Sci.*, **62**, 4151–4177 (2005).
- Williams, E., Boldi, B., Matlin, A., Weber, M., Hodanish, S., Sharp, D., Goodman, S., Raghavan, R., Buechler, D.: The behavior of total lightning activity in severe Florida thunderstorms. *Atmos. Res.*, **51**, 245–265 (1999).

Chapter 12

Optical Detection of Lightning from Space

Ullrich Finke

Abstract Lightning detection by optical means from satellites provides a globally uniform observation of lightning. Prototypes of optical detectors have been operated by NASA on low orbit satellites for more than 10 years. For the next generation of geostationary satellites optical lightning location sensors are planned.

This contribution gives an overview of the principles of optical detection of lightning from satellites and a description of the existing systems. The specifics of the data from space based sensors are discussed and the scientific results which were achieved so far are presented.

Keywords Lightning · Optical lightning detection · Location · Satellite-borne lightning detection · Thunderstorms · Global lightning observation

12.1 The Optical Radiation from Lightning

Optical observation of lightning has a long tradition. Various techniques and instruments have been developed and used successfully in lightning physics research. The ground based location of lightning for larger regions, however, is preferably performed in the lower frequency radio wave bands, since any optical observation is easily hindered by obstacles and the detection range is restricted to the line of sight, hence limited by the Earth's curvature. A space based observation has the advantage of an unobstructed view from above the clouds and a potentially almost hemispheric field of view which can be achieved with a single instrument.

Lightning location by optical means bases on the observation of the radiation of light, which is emitted from the hot lightning channel and propagates subsequently through the atmosphere and clouds, where it is mainly affected by scattering, until it reaches an observer above the clouds.

U. Finke (✉)

University of Applied Sciences and Arts, Ricklinger Stadtweg 120, Hannover, Germany
e-mail: ullrich.finke@fh-hannover.de

12.1.1 Lightning Source Characteristics

Sources of optical radiation are the manifold electrical discharge processes with luminous phase, mainly the lightning return stroke in cloud to ground lightning and recoil streamers in intracloud lightning (see e.g. Rakov and Uman, 2003 pp. 163–164) The radiated optical signal from all these processes can be characterised by its spectral content, pulse shape in time and spatial geometry. Observations of the optical characteristics of the lightning source were made by means of streak cameras, photodetectors from the ground and aboard aircraft.

12.1.1.1 Optical Emission and Spectral Characteristics

The strong electrical current flow in the conducting lightning channel dissipates thermal energy by Ohmic heating. This, being a positive feedback process heats the air up to 30'000 K in the channel centre. Subsequently, the overheated channel cools down by radiation, expansion and convection.

Spectrum

The optical spectrum of lightning in the visible and near infrared range is made of spectral lines of the excited and ionized gases of the air. Orville and Henderson (1984) analysed spectra in the wavelength range 375–880 nm from ground based observation of 10 return strokes at 15 km distances (see Fig. 12.1).

One of the few strong lines well above the continuous background is the atomic oxygen OI(1) triplet line found in the near infrared at 777.4 nm with total width less 0.5 nm. This line is being used for space based optical detection of lightning. It contains about 6% of the total energy of the optical spectrum of lightning (Orville and Henderson, 1984).

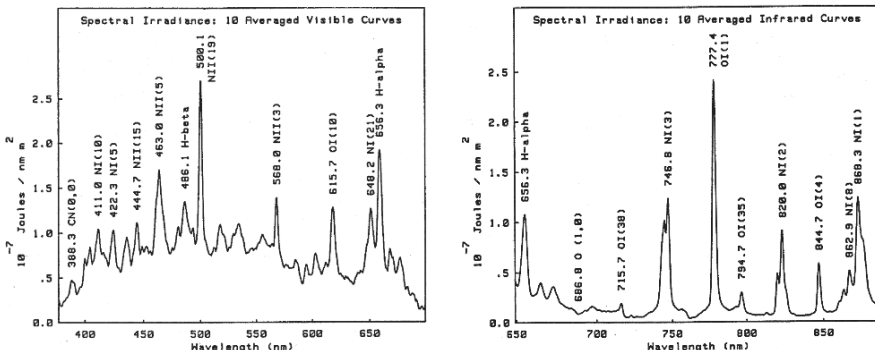


Fig. 12.1 Spectral irradiance of lightning in the visible and near infrared range (from Orville and Henderson (1984)). The curve displays the averaged spectrum of 10 strokes. Note the dominant emission lines and the low continuous background in the near infrared

Spectral measurements of the lightning signal above clouds made from board of a U-2 aircraft were reported by Christian and Goodman (1987). These spectra have no significant differences to the ground based observations, hence the authors concluded, that the spectra remain unchanged by the propagation through the clouds.

Optical Pulse Form and Power

The observed optical pulse from a return stroke is produced by the superposition of the sources along the channel. The rise time of the pulse is determined by the propagation speed of the luminous phase of the channel, i.e. the upward velocity of the return stroke, which is in the order of 10^8 m/s (Rakov and Uman, 2003 pp. 150–152). The duration of the optical pulse is determined by the cooling processes in the lightning channel. High resolution optical measurements made by Guo and Krider (1982) found a mean rise time of $15\ \mu\text{s}$ and mean width of $158\ \mu\text{s}$ for return strokes.

The optical power from lightning varies strongly between the individual flashes and for the different types of lightning. The power scales with the channel length, but also changes with the altitude. Guo and Krider (1982) derived from ground based observations in the range 400–1000 nm a time averaged power of $1.3 \times 10^6\ \text{W/m}$ for first strokes. Peak power values for the whole channel were found to be in the order of $2 \times 10^9\ \text{W}$ for first strokes. Subsequent strokes tend to have lower power values by about a half order of magnitude.

For the optical energy, defined as the integrated power over the pulse duration, a mean value of $3.7 \times 10^5\ \text{J}$ was calculated in Guo and Krider (1982) for first return strokes. This optical energy represents about 1% of the total input energy in the lightning flash (Krider and Guo, 1983).

For intracloud lightning the source function is less well known, due to the lack of unobscured observations. The aircraft based measurements reported by Christian and Goodman (1987) and more recently by Mach et al. (2005) and the satellite based observations aboard FORTE (Kirkland et al., 2001) allowed the estimation of the source power. Generally, intracloud lightning radiates lower optical power, but contains more pulses per flash and has longer duration (Goodman et al., 1988).

12.1.2 Light Scattering in Clouds

The optical source pulse is transformed along its path through the atmosphere. For observations from a satellite orbit the relevant process is the scattering of the light wave by cloud particles. Scattering of visible and near infrared light by hydrometeors shows little absorption and is nearly energy conserving. Consequently, all the optical lightning energy is finally transported through one of the cloud surfaces.

Assuming spherical particles this process is described by the Mie-theory. For optically thick clouds, the light is subject to multiple scattering. After a large number of single scattering events the initial direction information is lost and the scattering

can be treated as an isotropic diffusion process with an effective diffusion constant depending on the cloud's optical thickness.

The effects of multiple scattering on an optical pulse from lightning have been studied theoretically and numerically using Monte Carlo simulations (Thomason and Krider, 1982, Koshak et al., 1994, Light et al., 2001) with the following main results:

- The vertical position of the lightning source in the cloud determines the partitioning of the energy between the upper and the lower surface. This partition depends linearly on the distance to the surfaces.
- Light from a source below the cloud is reflected to a large part at the lower cloud surface and does not penetrate into the cloud. Hence, the radiation seen from above originates predominantly from intracloud lightning and the in-cloud parts of cloud to ground return strokes.
- The optical pulse is delayed and broadened according to the total optical path of the photons.
- The radiance distribution pattern on the upper cloud surface is enlarged in proportion to the source's distance to surface.

The driving parameters for the resulting signal at the surface are the optical thickness of the cloud and the distance of the source to the cloud surface.

12.1.3 Optical Pulse Characteristics at the Cloud Surface

While the spectrum is nearly unchanged (Christian and Goodman, 1987), the other characteristics are strongly determined by the multiple scattering.

The point source results given in the previous section can be superposed for real geometrically extended sources. A direct calculation would require the source geometry, the optical source strength and also the scattering parameters of the cloud, all largely unknown parameters. Therefore, the signal is characterised basing on observations made above clouds from the U-2 airplane at altitude 20 km (Christian and Goodman, 1987, the unmanned Altus aircraft (Mach et al., 2005) and satellite (Kirkland et al., 2001). These observations are in good consistence with the scattering simulations.

The **spatial pattern** is blurred by scattering to a size of about 5–10 km (Fig. 12.2). Goodman et al., (1988) note from their U-2 observations that the illuminated cloud area is in the average less than 50 km^2 . A nearly circular pattern with radially decreasing radiance is observed as long as the horizontal extend of the lightning source is smaller then the scatter broadening. This is also confirmed by statistical analyses of the data from the space based lightning imager (Finke, 2007).

The **time function** of the optical pulse is delayed and widened by the scattering process. The typical travel times from the source to the surface is in the order of $100 \mu\text{s}$, i.e. larger than the typical growth times of the lightning channel. Hence the time function of outcoming signal is determined by the scattering process. This is

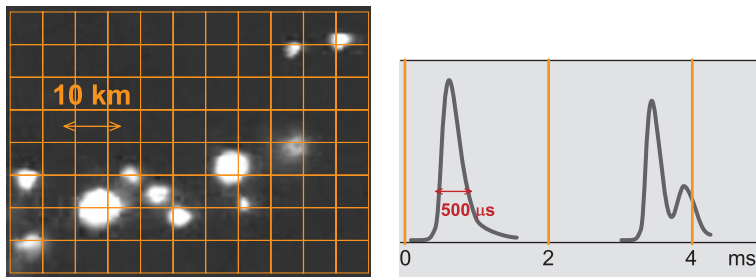


Fig. 12.2 Spatial pattern and idealised pulse form of the lightning pulse on the surface on the cloud. The overlayed mesh and time frames mark the sampling which is applied in the NASA lightning detectors (see next section)

confirmed by observations from aircraft (Christian and Goodman, 1987) and satellite (Kirkland et al., 2001). The statistics of these observations yield a mean rise time of $150\text{ }\mu\text{s}$ and a mean pulse width of about $400\text{--}500\text{ }\mu\text{s}$.

For the **radiation** energy density of the signal at the 777.4 nm line Goodman et al., (1988) observed from the U-2 measurements a median energy density of $3 \times 10^{-6}\text{ J m}^{-2}\text{ sr}^{-1}$. Christian and Goodman (1987) reported, that 90% of the flashes have optical pulses with an energy density larger than $4.7 \times 10^{-6}\text{ J m}^{-2}\text{ sr}^{-1}$ (at 868.3 nm). The median radiance was $7 \times 10^{-3}\text{ W m}^{-2}\text{ sr}^{-1}$, while the reflected solar radiation from clouds in the same wavelength interval can be as large as $380 \times 10^{-3}\text{ W m}^{-2}\text{ sr}^{-1}$ if an albedo of 1 is assumed.

The optical signal at the cloud upper surface is given by a function which describes the radiance as function of space, time and direction. This function is the input for a detection device on board of a satellite.

12.2 Optical Lightning Detectors on Satellites

Since the first Earth observing satellites many of their optical devices detected lightning – as an unintentional by-product. From the photographic data of the sun-synchronous DMSP (Defense Meteorological Satellite Program) satellites estimates for the global lightning distribution and the global flash rate were published (Orville and Spengler, 1979, Turman and Edgar, 1982, Orville and Henderson, 1986). Despite the poor spatial resolution of about 100 km and the low temporal sampling rate these observations proved the feasibility of satellite based lightning detection (Goodman and Christian, 1993). For a permanent lightning observation with high spatial resolution a lightning detector on a geostationary platform is required.

The concept of a dedicated lightning location sensor operating from satellites with the aim of geostationary detection was developed since the 1980s (Davis et al., 1983, Christian et al., 1989). As the result of these developments in 1995 the first NASA lightning detector was brought into space. Currently the installation of a lightning mapper on the next generation of geostationary weather satellites is being prepared.

12.2.1 OTD and LIS Sensors on Low Orbit Satellites

Since the mid of the 1990s two optical instruments for lightning detection have been operated by NASA on board of low orbit satellites. Both instruments with weight of about 20 kg are staring wide angle cameras detecting the optical lightning signal.

12.2.1.1 Orbit Parameters

The Optical Transient Detector (OTD) was launched into space in April 1995 on board of the MicroLab-1 satellite (later renamed to OV-1) and was in operation until March 2000. Its circular orbit had an inclination of 70° with an altitude of 735 km above ground and an orbital period of about 100 min (Christian et al., 2003). Lightning is detected with a 128×128 pixel CCD matrix. Projected onto the Earth surface this corresponds to an instantaneous field of view of 1250×1250 km.

The Lightning Imaging Sensor (LIS) is an integral part of the Tropical Rainfall Measuring Mission (TRMM) satellite, which was launched in November 1997 (Kummerow et al., 1998). According to the objectives of the TRMM the satellite's orbit limited the observation area to the latitudes $\pm 35^\circ$. The altitude of 350 km and orbital period of 92 min were changed in August 2001 during the TRMM boost to 402 km and 93 min.

The construction of the LIS instrument resembles the OTD with several improvements in sensitivity, design and electronics (Christian et al., 1999). Due to the lower altitude the instantaneous field of view for the LIS is about 670×670 km.

The orbit parameters (see Table 12.1) determine the observational area and also the spatial and temporal sampling of the observation. The LIS area of detection is limited to $\pm 35^\circ$ around the equator, i.e. to the tropics and subtropics, while the OTD sensor covers also the higher latitudes of the Earth up to 70° (see Fig. 12.3).

The orbit inclination also makes the observation times depend on latitude. It is highest near the turning latitudes and lowest over the tropics, where the median total observation time per year exceeds 12 h for OTD (Christian et al., 2003) and 10 h for LIS.

Due to the precession of the orbit around the Earth, the satellite needs 55 days for OTD (49 days for LIS) to return to a given location (at equator) at the same local

Table 12.1 Orbital parameters and detection geometry of the OTD and LIS sensors

	OTD	LIS(*)
Altitude	735 km	402 km
Inclination	70°	35°
Total FOV	1250×1250 km	670×670 km
Location view time	1–270 s	93 s
Pixel array	128×128	128×128
Pixel resolution	8–20 km	4–10 km
Single frame integration time	2 ms	2 ms
Data span	May 1995 – March 2000	Jan 1998 – present

(*) LIS post-boost orbit (after August 2001).

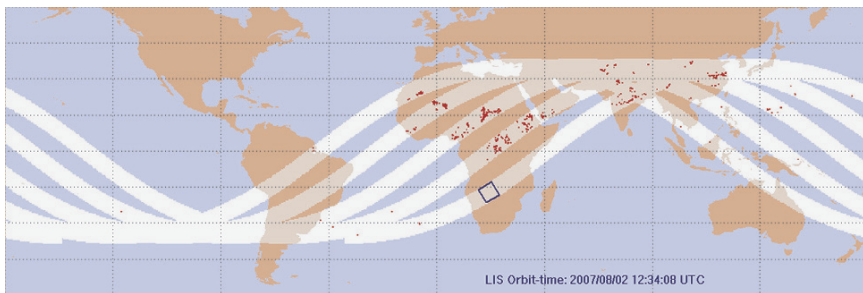


Fig. 12.3 Satellite orbits for LIS with detected lightning positions. Note the larger view time near the orbit's highest latitude and the gap between subsequent orbits. The instantaneous field of view is marked by the *square*

time. This implies the requirement for the statistical analyses to be long enough to avoid any bias in diurnal statistics. As the sensor's field of view moves over the Earth surface, the contiguous observation time for a given point is about 92 s for LIS and more variable (1–270 s) for OTD due to a less stable directional orientation of the satellite.

FORTE Satellite

The multi sensor satellite FORTE (Fast On-Orbit Recording of Transient Events) is a joint Los Alamos National Laboratory (LANL) and Sandia National Laboratories project. The satellite was launched in 1997 in a circular, 825-km-altitude orbit with 70° inclination. Besides an optical lightning location system of the same design as the OTD and LIS it carries a broad band photo diode with 15 μ s resolution and VHF receivers which allows for a combined optical and radio frequency observations of lightning (Jacobson et al., 2000, Suszcynsky et al., 2001). The FORTE platform is described in more detail in Chapter 13 of this volume.

12.2.2 *Methodology of Location and Detection*

The OTD and LIS instruments are designed to detect the short transient optical signal from lightning. Their basic components are entrance optics, the wavelength filter, detection matrix and electronics for data processing and communication.

The optical radiation of lightning is detected with a 128×128 pixel CCD matrix. As described in Section 12.1 the optical signal from lightning is a light pulse containing characteristical spectral lines with duration shorter 500 μ s and a spatial size of about 10 km.

12.2.2.1 *Lightning Detection by Filtering and Real Time Event Processing*

The optical signal from lightning has to be discriminated under conditions of a high background signal, which is produced by the reflected solar radiation at the cloud

surfaces. This background signal is strong at daytime, usually much brighter than then lightning signal.

The distinguishing feature of the lightning signal is its transient character of just 500 µs duration. To detect successfully lightning events with high detection efficiency during day and night a special filtering, a sampling strategy and on-board processing has been developed (Christian et al., 2003).

Firstly, the signal passes a 1 nm narrow wavelength filter centred around the spectral line at 777.4 nm. This enhances the signal to noise ratio, since the above line contains about 6% of the lightning energy but only about 0.09% of the reflected solar radiation.

Secondly, the spatial size of the detection pixels and the integration time are optimized in order to collect as much lightning energy as possible and to avoid a splitting of the energy between pixels and time frames. The intervals (2 ms) and pixel footprint size (6 km) were chosen according to typical sizes of the lightning pulse and pattern at the upper cloud surface (see Fig. 12.2).

At last, a real time event processing is applied in order to detect the short lightning signal pulse on the bright but slowly varying background. A moving average of the detected energy for each pixel is calculated and compared against the actual energy for each time frame. If the difference exceeds a threshold (adaptable to day and night conditions) a lightning event for the corresponding pixel is notified.

This filtering and event processing method detects successfully lightning events on the bright background. Primary data output are the events from pixels exceeding the threshold during the single time frame. These data are stored together with their orbit parameters and background radiation images.

12.2.2.2 Data Processing and Organization

After calibration and geolocation the event data are organized according to their space time distribution and non-lightning data are removed.

The data processing performs a hierarchical clustering of the pixel event data into groups, flashes and areas according to their proximity in time and space (Christian et al., 2000). A single lightning pulse will, generally, illuminate more than one pixel. Therefor, in any time frame all adjacent pixel events are assembled into a lightning ‘group’, which corresponds to a single detected optical pulse from a lightning stroke. Further, lightning strokes (groups) observed in a temporal interval of less 330 ms and closer 5.5 km are collected into a lightning flash. Finally, flashes found in the same spatial area are clustered in ‘areas’ being a proxy for electrically active storm areas. Figure 12.4 shows an example detection scene.

Non-lightning events are pixel events exceeding threshold, which are not attributed to lightning. They are caused by electronic noise or high energetic particles. While crossing the Southern Atlantic Anomaly (SAA), the sensor is exposed to enhanced radiation of high energetic cosmic particles, which generate non-lightning events in the detector. Due to its lower altitude the LIS is less affected by this type of noise. Other sources of non-lightning events are sun glint, other specular reflections and fast changes in background radiation due to the sensor motion.

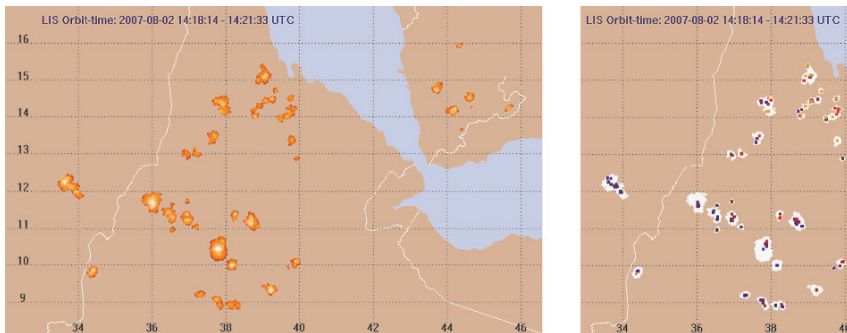


Fig. 12.4 Lightning flashes detected over Ethiopia. *Left:* Pixel events composing the flashes are coloured by their radiant energy. The total energy of the brightest flash is $9100 \mu\text{J m}^{-2} \text{ sr}^{-1}$. *Right:* Centroid positions of the identified flashes coloured according the incident time

The non-lightning events are artefacts in the data and can be recognized by their distinct spatio-temporal distribution. While real lightning is clustered in time and space and always related to clouds, the non-lightning events are scattered randomly or show other clearly artificial distribution. Several filtering procedures have been developed to sort out the non-lightning events from the data (Christian et al., 2000).

12.2.2.3 Data Availability

The data sets from both sensors along with the data analysis software library are freely available for the scientific community. Each detected event and the group-flash-area hierarchy is provided with location, time and radiation energy. Ancillary information about the orbit, observation conditions, noise, instrument status and also the background images complete the data sets.

12.2.2.4 Data Characteristics

Optical observation detects the optical radiation from both intracloud and cloud to ground lightning. This **total lightning** reflects more completely the electrical activity of the storm cloud. On the other hand, the separation of the cloud-to-ground lightning by optical means alone is difficult and may require additional data and new algorithms (Boccippio et al., 2001).

Detection efficiency (DE) denotes the fraction of detected lightning events to the total number. It is a function of the sensor's sensitivity, threshold settings and the signal to noise ratio. This makes the detection efficiency depend on the local time with lower values during the daytime. Boccippio et al. (2002) analysed the diurnal change of the DE for OTD and LIS. With respect to the threshold radiances they estimated a daily mean flash detection efficiency of 88% for LIS and 54% for OTD, both with a diurnal variation of about 20%.

LIS and OTD data were compared with ground based lightning location systems operating on radio frequencies on various scales. On the regional scale intercomparisons with the National Lightning Detection Network (NLDN) which covers the

whole US yield a high coincidence of lightning flashes detected by both systems Boccippio et al. (2002). Up to 90% of the NLDN lightning was found in the LIS data. On the other hand, optical detection often shows multiple pulses for single NLDN strokes.

The observation by optical and radio frequency (RF) means detect different features of the lightning discharge whose mutual relation is still under research. Nevertheless, instrument intercomparisons between LIS and ground based RF systems with high detection efficiency such as LINET (Betz et al., 2004) were performed for single storms during the short times of the LIS overpasses (e.g. Schmidt et al., 2005). These studies show a high partition (60–80%) of coincident events between the LIS lightning events and the lightning strokes detected with the ground based systems.

Comparison with a 3-dimensional high resolution detection system (Thomas et al., 2000) has shown, that the LIS detects presumably the discharges in the middle and upper cloud regions. Hence, also cloud to ground return strokes with in-cloud parts reaching high enough in the cloud are detected by LIS.

The **false alarm rate** (FAR) is the partition of wrongly detected non-lightning events. On the instrument level the FAR depends on the signal to noise ratio and an the detection threshold. Generally, there is a trade off between false alarm rate and detection efficiency. A lower detection threshold increases the FAR. It was found for OTD and LIS, that the external noise, particularly from high energetic cosmic particles, exceeds the internal detector noise. Applying the post processing described above, false alarms can be removed almost completely from the data and reduce the FAR to just a few events per day Boccippio et al. (2002).

The **location accuracy** of any optical lightning detection from space is limited by the pattern widening due to the light scattering in the cloud, which is of the order of 5–10 km for a point source. The spatial sampling of the existing instruments was chosen to be of the same order for an optimal detection efficiency. Given an accurate satellite pointing, the location accuracy is a simple geometric function for the whole detection area. For LIS the location accuracy was found to be within the nominal accuracy of 3–6 km.

12.2.3 Future Lightning Detection from a Geostationary Satellite

The concept of optical lightning detection from space has been successfully proven and the existing data have already found many applications. In order to make the space based lightning data operationally available it is planned to equip the next generation of geostationary weather satellites GOES and METEOSAT with lightning detectors.

Lightning detection from a geostationary position allows for a **continuous** observation of the whole visible disk with high timeliness in data availability. This enables to monitor the development of individual storms during their whole life cycle. Moreover, **global** observation is possible, if all geostationary weather satellites are equipped with lightning detectors.

The optical observation from space has the advantage of a uniform detection efficiency over land and water. This homogeneity makes the geostationary detection a valuable complementary system to the regionally operating ground based networks. Due to the signal to noise conditions the detection efficiency will still show a day-night difference.

The transition to lightning detection from a geostationary orbit is challenging due to the much larger distance to the Earth. The entrance optics has to realize a 100-fold higher angular resolution in order to achieve the same spatial resolution as with the low orbit instruments. Moreover, the **location accuracy** will depend on the location on Earth, due to the geometric increase of the pixel footprint with the satellite zenith angle and parallax effects.

A permanent global detection of the total lightning from a geostationary orbit will complement the established ground based networks. Due to its homogeneous detection efficiency it can serve as a background reference system and fill the gaps between the ground based networks, over the oceans and remote areas. Space based lightning location on the other hand has lower location accuracy than the high developed ground based systems and does not discriminate between intra-cloud and cloud to ground flashes.

The detection method and the data processing concepts and methods which were successful introduced with the low LIS and OTD sensors will be developed further. The additional value and the synergetics from the co-observation of clouds from the same platform will be utilized.

12.3 Scientific Results and Applications

The OTD and LIS data sets have been broadly used by the scientific community in atmospheric sciences and lightning research. Main applications were in climatology and intercomparisons between instruments and case studies on storm cloud scale. Intensive tests and validations on these sensors data have been performed with the aim to develop algorithms and methods for future sensors in space.

12.3.1 Scientific Results

The observation with both the OTD (5 years) and LIS instrument (10 years) have gathered a large unique data set. It represents the first global lightning data set with high detection efficiency and high spatial resolution. The analysis of this data set produced many scientific results and have advanced the knowledge in atmospheric and climate research.

12.3.1.1 Global Lightning Climatology

A comprehensive description of the global lightning distribution from an analysis of the 5 year OTD data set was given by Christian et al. (2003).

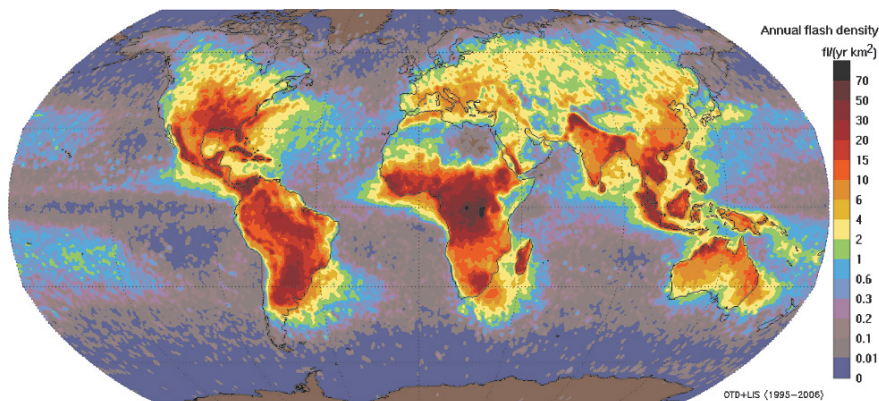


Fig. 12.5 Global distribution of annual lightning flash density (in $\text{fl}/(\text{km}^2 \text{ yr})$) from 11 years of combined OTD and LIS observation (1995–2005). Note the maximum in Central Africa and the land-ocean difference. (From the NASA LIS/OTD gridded data) (See also Plate 15 in the Color Plate Section on page 602)

The **geographical distribution** of lightning was derived from the combined OTD and LIS data from 1995 to 2005 (Fig. 12.5). As expected, highest lightning densities are found in the tropics and subtropics. 78% of lightning was detected between $\pm 30^\circ$. Maximum annual flash densities with values over $50 \text{ fl m}^{-2} \text{ yr}^{-1}$ are observed in Central Africa. Remarkable is the large difference in the distribution between land and ocean: 88% of the lightning occurs over land and coastal areas, giving a mean ratio of 10:1 between the land and oceanic flash rates (Christian et al., 2003).

The mean global lightning flash rate was established to 44 s^{-1} with an uncertainty of $\pm 5 \text{ s}^{-1}$ and an annual variation of about 23%.

The **diurnal cycle** of lightning follows locally the solar insulation and exhibits maxima at the local afternoon hours. The global flash rate peaks around 17–20 UTC and is dominated by the large continental landmasses (Fig. 12.6).

Seasonal changes in lightning activity were also analysed by Christian et al. (2003). At the most geographical locations the lightning activity is highest in the local summer months. As written above, the global lightning flash rate is dominated by the tropics. However, the annual variation (23%) of the global flash rate is attributed to the contribution from the extratropical continental landmasses. The global annual cycle peaks in July–August, i.e. the Northern summer due to the lightning over the North American and Northern Asian landmasses, which have no counterpart in the Southern hemisphere. Oceanic lightning shows only little annual change.

Despite the high interannual variability, **regional features** in the seasonal changes of lightning distribution can be seen, e.g. for the region of the Mediterranean Sea in Europe (Fig. 12.7). During summer the storm activity is predominantly found over land. In the winter months storms occur over the warmer sea waters and along the coasts.

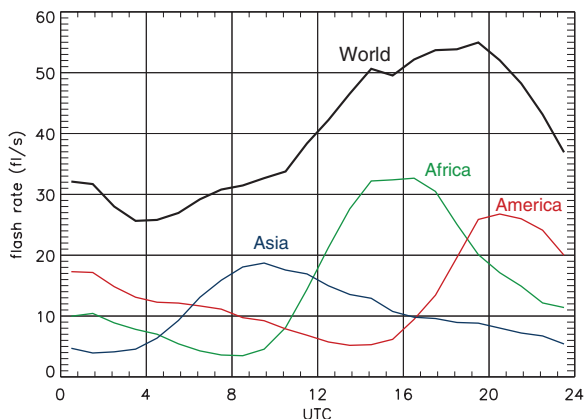


Fig. 12.6 Diurnal variation of the global lightning flash rate in Universal Time (UTC) for the world and the large continents derived from LIS data. The largest contribution is coming from Africa

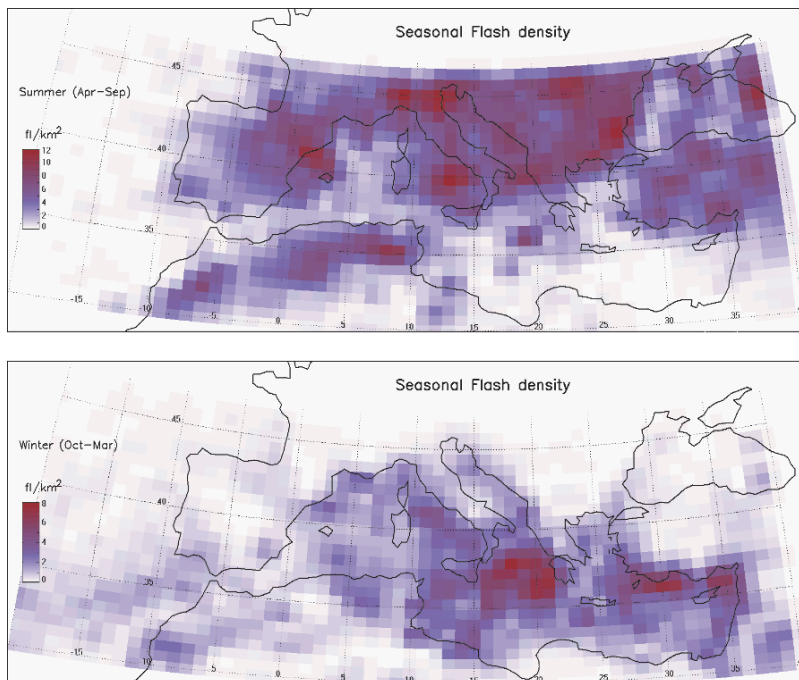


Fig. 12.7 Seasonal lightning flash density in the Mediterranean region derived from 5 year OTD data for the summer (top) and winter months (bottom). Due to the sparse sampling the interannual variance is high, single storms dominate the picture. Note the different color scaling (See also Plate 16 in the Color Plate Section on page 602)

12.3.1.2 Convective Storms and Precipitation

Analysing the LIS data in combination with the TRMM radar data Petersen et al. (2005) have studied the global relation between precipitation ice water and lightning. This and other case studies (Blyth et al., 2001; Deierling et al., 2008) revealed the high correlation between ice mass flux in high and the total lightning flash rate. Boccippio et al. (2005) presented a classification of tropical storms structure.

Huntrieser et al. (2008) combined LIS data with ground based lightning data, aircraft and radar measurements to estimate the production and transport of the nitrogen oxides from lightning. The LIS data were used to scale up the results from the field experiment TROCCINOX to the global scale.

12.3.2 Application of Space Based Lightning Data

Optical detection from space provide lightning data with high time resolution and timeliness, with potentially global uniform coverage. The detection efficiency is high under day and night conditions for both the intracloud and ground lightning. Especially with the perspective of lightning detectors on geostationary satellites a multitude of operational and scientific applications are obvious.

For nowcasting of severe storms the lightning data help to track the storm motion and to forecast its development. Changes in the lightning flash rate is a precursor for storm intensification, also for tornado formation. Thereby, early and dedicated warning of hazardous weather phenomena can be given more precisely.

In weather forecast lightning data can be used to improve Numerical Weather Prediction models, especially for rapidly developing convection. Since the lightning rate is strongly correlated with the precipitation amount, it can serve as proxy for precipitation in remote areas.

Uniform and global data of total lightning can support the management of operations depending critically on weather conditions such as air-traffic routing.

Obviously, monitoring the lightning activity allows for early and selective warning of ground and air strike risk, thus enhancing safety and protection and supporting quick emergency measures, e.g. in case of wild fires, which are mainly caused by lightning.

In climate research lightning can serve as sensitive and easy to measure indicator for changes in global and regional climate. Moreover, the global lightning data is important input for atmospheric chemistry, since lightning is a significant natural source of nitrogen oxides, an important constituent in the troposphere and stratosphere.

Acknowledgments The provision of the OTD and LIS data and software package from NASA MSFC is gratefully acknowledged. The v2.2 gridded satellite lightning data used in Figure 12.5 were produced by the NASA LIS/OTD Science Team (Principal Investigator, Dr. Hugh J. Christian, NASA/Marshall Space Flight Center) and are available from the Global Hydrology Resource Center (<http://ghrc.msfc.nasa.gov>). Part of the work was supported by EUMETSAT contract studies EUM/CO/05/1469/KJG and EUM/CO/07/4600000406/KJG.

References

- Betz HD, Schmidt K, Oettinger WP, Wirz M (2004) Lightning detection with 3D-Discrimination of intracloud and cloud-to-ground discharges. *Geophys Res Lett* 31:11108, doi:10.1029/2004GL019,821
- Blyth A, Jr HC, Driscoll K, Gadian A, Latham J (2001) Determination of ice precipitation rates and thunderstorm anvil ice contents from satellite observations of lightning. *Atmos Res* 59–60:217–229
- Boccippio DJ, Cummins KL, Christian HJ, Goodman SJ (2001) Combined satellite- and surface-based estimation of the intracloud-cloud-to-ground lightning ratio over the continental United States. *Mon Weather Rev* 129:108–122
- Boccippio DJ, Koshak WJ, Blakeslee RJ (2002) Performance assessment of the optical transient detector and lightning imaging sensor. Part I: Predicted diurnal variability. *J Atmos Oceanic Technol* 19:1318–1332
- Boccippio DJ, Petersen WA, Cecil DJ (2005) The tropical convective spectrum. Part I: Archetypal vertical structures. *J Climate* 18:2744–2769, doi: 10.1175/JCLI3335.1
- Christian HJ, Goodman SJ (1987) Optical observations of lightning from a high-altitude airplane. *J Atmos Oceanic Technol* 4:701–711
- Christian HJ, Blakeslee RJ, Goodman SJ (1989) The detection of lightning from geostationary orbit. *J Geophys Res* 94:13329–13337
- Christian HJ, Blakeslee RJ, Goodman SJ, Mach DA, Stewart MF, Buechler DE, Koshak WJ, Hall JM, Boeck WL, Driscoll KT, Boccippio DJ (1999) The Lightning Imaging Sensor. In: 11th International Conference on Atmospheric Electricity, June 7–11, Guntersville, Alabama, pp 746–749
- Christian HJ, Blakeslee RJ, Goodman SJ, Mach DM (2000) Algorithm theoretical basis document (ATBD) for the lightning imaging sensor (LIS). Tech. rep., NASA/Marshall Space Flight Center, 53 pp
- Christian HJ, Blakeslee RJ, Boccippio DJ, Boeck WL, Buechler DE, Driscoll KT, Goodman SJ, Hall JM, Koshak WJ, Mach DM, Stewart MF (2003) Global frequency and distribution of lightning as observed from space by the optical transient detector. *J Geophys Res* 108:4005, doi:10.1029/2002JD002,347
- Davis MH, Brook M, Christian H, Heikes BG, Park CG, Roble RG, Vonnegut B, Orville R (1983) Some scientific objectives of a satellite-borne lightning mapper. *Bull Amer Meteor Soc* 64:114–119
- Deierling W, Petersen WA, Latham J, Ellis S, Christian HJ (2008) The relationship between lightning activity and ice fluxes in thunderstorms. *J Geophys Res* 113:D15210, doi:10.1029/2007JD009700
- Finke U (2007) Statistics of the optical lightning radiation source derived from satellite observations. In: AGU – Fall Meeting 2007, Dec, 10–14, 2007, San-Francisco, CA, eos. Trans. AGU, 88(52), Fall Meet. Suppl., Abstract AE41A-01
- Goodman SJ, Christian HC, Rust VWD (1988) Optical pulse characteristics of intracloud and cloud-to-ground lightning observed from above clouds. *J Appl Meteor* 27:1369–1381
- Goodman SJ, Christian HJ (1993) Global observations of lightning. In: Gurney RJ, Foster JL, Parkinson CL (eds) *Atlas of satellite observations related to global change*, Cambridge University Press, pp 191–219
- Guo C, Krider EP (1982) The optical and radiation field signatures produced by lightning return strokes. *J Geophys Res* 87:8913–8922
- Huntrieser H, Schumann U, Schlager H, Hoeller H, Giez A, Betz HD, Brunner D, Forster C, Pinto O Jr, Calheiros R (2008) Lightning activity in Brazilian thunderstorms during TROCCI-NOx: implications for NOx production. *Atmos Chem Phys* 8:921–953
- Jacobson AR, Cummins KL, Carter M, Klingner P, Roussel-Dupre D, Knox SO (2000) FORTE radio-frequency observations of lightning strokes detected by the National Lightning Detection Network. *J Geophys Res* 105:15653–15662

- Kirkland MW, Suszcynsky DM, Guillen JLL, Green JL (2001) Optical observations of terrestrial lightning by the FORTE photodiode detector. *J Geophys Res* 106:33499–33509
- Koshak WJ, Solakiewicz RJ, Phanord DD, Blakeslee RJ (1994) Diffusion model for lightning radiative transfer. *J Geophys Res* 99:14361–14371
- Krider EP, Guo C (1983) The peak electromagnetic power radiated by lightning return strokes. *J Geophys Res* 88:38471–38474
- Kummerow C, Barnes W, Kozu T, Shiue J, Simpson J (1998) The Tropical Rainfall Measuring Mission (TRMM) sensor package. *J Atmos Oceanic Technol* 15:809–817
- Light TE, Suszcynsky DM, Kirkland MW, Jacobson AR (2001) Simulations of lightning optical waveforms as seen through clouds by satellites. *J Geophys Res* 106:17103–17114
- Mach DM, Blakeslee RJ, Bailey JC, Farrell WM, Goldberg RA, Desch MD, Houser JG (2005) Lightning optical pulse statistics from storm overflights during the Altus Cumulus Electrification Study. *Atmos Res* 76:386–401
- Orville RE, Spengler DW (1979) Global lightning flash frequency. *Mon Weather Rev* 107:934–943
- Orville RE, Henderson RW (1984) Absolute spectral irradiance measurements of lightning from 375 to 880 nm. *J Atmos Sci* 41:3180–3187
- Orville RE, Henderson RW (1986) Global distribution of midnight lightning: September 1977 to August 1978. *Mon Weather Rev* 114:2640–2653
- Petersen W, Christian HJ, Rutledge S (2005) TRMM observations of the global relationship between ice water content and lightning. *Geophys Res Lett* 32:L14819, doi:10.1029/2005GL023236
- Rakov VA, Uman MA (2003) Lightning – Physics and Effects. Cambridge University Press, 687 pp
- Schmidt K, Betz HD, Oettinger WP, Wirz M, Pinto O Jr, Naccarato KP, Hoeller H, Fehr T, Held G (2005) A comparative analysis of lightning data during the EU-Brazil TROCCINOX / TroCCi-Bras campaign. In: VIII International Symposium on Lightning Protection (SIPDA), November 2005, Sao Paulo, Brazil
- Suszczynsky DM, Light TE, Davis S, Green JL, Guillen JLL, Myre W (2001) Coordinated observations of optical lightning from space using the FORTE photodiode detector and CCD imager. *J Geophys Res* 106:17897–17906
- Thomason LW, Krider EP (1982) The effects of clouds on the light produced by lightning. *J Atmos Sci* 39:2051–2065
- Thomas RJ, Krehbiel PR, Rison W, Hamlin T (2000) Comparison of ground-based 3-dimensional lightning mapping observations with satellite-based LIS observations in Oklahoma. *Geophys Res Lett* 27:1703–1706
- Turman BN, Edgar BC (1982) Global lightning distributions at dawn and dusk. *J Geophys Res* 87:1191–1206

Chapter 13

Space- and Ground-Based Studies of Lightning Signatures

Timothy Hamlin, Kyle C. Wiens, Abram R. Jacobson, Tracy E.L. Light
and Kenneth B. Eack

Abstract This article provides a brief survey of the space- and ground-based studies of lightning performed by investigators at Los Alamos National Laboratory (LANL). The primary goal of these studies was to further understand unique lightning signatures known as Narrow Bipolar Events (NBEs). First, an overview is presented of the Fast On-orbit Recording of Transient Events (FORTE) satellite and of the ground-based Los Alamos Sferic Array (LASA). This is followed by a summary of the phenomenology, physics, and meteorological context of NBEs and NBE-related discharges. This article also discusses additional radio frequency and optical observations of lightning made by the FORTE satellite and concludes with an outlook on LANL's growing interest in the use of lightning observations in the study of severe weather and hurricane intensification.

Keywords Narrow Bipolar Event (NBE) · FORTE satellite · Los Alamos Sferic Array (LASA) · Transitionospheric Pulse Pair (TIPP) · Blackbeard experiment · ALEXIS satellite

13.1 Introduction

Los Alamos National Laboratory's (LANL) interest in lightning science began in 1993 when the Blackbeard experiment aboard the ALEXIS satellite began observing unique radio burst signatures of unknown origin. At this time, not much was known about these radio bursts other than that they came in pairs and were far more powerful and of considerably shorter temporal scales than what was usually observed from ordinary lightning. The term transitionospheric pulse pair (TIPP) was coined to describe these intense satellite-observed phenomena. Over the last ten years the source of these burst signatures has been identified as a form of intra-cloud

T. Hamlin (✉)

Space and Remote Sensing Group, ISR-2, Los Alamos National Laboratory, Los Alamos, New Mexico, USA
e-mail: thamlin@lanl.gov

lightning. They are often associated with what appears to be a unique class of lightning termed “narrow bipolar events” or NBEs.

This article provides a brief survey of the space- and ground-based studies performed by investigators at LANL in order to further understand the origin of the unique lightning signatures. Section 13.2 describes the Fast On-orbit Recording of Transient Events (FORTE) satellite as well as the ground-based Los Alamos Sferic Array (LASA). Section 13.3 summarizes recent efforts to further understand the phenomenology, physics, and meteorological context of NBEs and NBE-related discharges. Section 13.4 discusses additional radio frequency and optical observations from the FORTE satellite. Section 13.5 presents an outlook for LANL’s future role in the study of severe weather.

13.2 Instrumentation

This section briefly discusses two key platforms LANL has used over the last decade in order to further investigate lightning phenomena. The first is the FORTE satellite. The second is the ground-based array of very low frequency/low frequency (VLF/LF) lightning sensors called LASA.

13.2.1 FORTE

The FORTE satellite was launched in August of 1997 and was the second in a series of U.S. Department of Energy research satellites that provided for the study of radio-frequency (RF) and optical emissions from lightning. FORTE is in an 800-km altitude, 70° inclination, circular orbit, and is pointed at nadir. As with its predecessor, the Blackbeard payload aboard the ALEXIS satellite (Holden et al., 1995; Massey and Holden, 1995; Massey et al., 1998a), the FORTE RF payload functioned like a “flying digital oscilloscope”. Jacobson et al. (1999) provide a detailed description of FORTE’s capabilities, which are summarized in the next subsections.

13.2.1.1 FORTE Antennas

FORTE’s large RF antenna structure was supported by a 10-m long nadir-pointing antenna boom. The antenna was deployed two months after launch from its folded storage in the satellite. Along the boom were mounted two passive orthogonal log-periodic antenna arrays designed to point the 25–50 MHz beam-lobe maximum at nadir with the first null of the electric-field-plane lobe at the limb of the Earth (Shao and Jacobson, 2001, 2002). The separation of the antenna’s electrical center from the spacecraft, and its intrinsic passive gain, made the FORTE RF signal-to-noise ratio (SNR) much improved over Blackbeard’s. The FORTE RF payload achieved background-limited SNR; the background noise in the signal recordings

was dominated by anthropogenic and geophysical sources, and was not limited by spacecraft-generated interference.

13.2.1.2 FORTE's TATR Receiver

FORTE's primary RF receiver was named "TATR" (Twenty megahertz And Twelve bit Receiver) and had two channels with 22-MHz of analog bandwidth each. The base frequency for each channel was selectable from a grid covering the entire high frequency (HF) to very high frequency (VHF) spectrum. The base frequencies of the two TATR channels could be independently selected. When set on the same band, the two channels typically derived their signals from alternate orthogonal antennas. This enabled polarimetry of the incoming signal as described in Shao and Jacobson (2001, 2002) as well as crude direction finding based on antenna-lobe structure (Jacobson and Shao, 2002b). When TATR was set to use different bands on the two channels the combined information was used to examine spectral slope. In either operation mode, the trigger was derived from one channel with the other "slaved" to that trigger. Each channel was digitized synchronously with the other channel with 12-bits of resolution at a rate of 50 megasamples per second. This maintained inter-channel coherence in the recording and enabled coherent polarimetry.

TATR relied upon an eight-channel coincidence trigger. The eight channels were spaced 2.5 MHz apart, and each was 1-MHz wide. The power in each trigger channel was continuously monitored, and the coincident rise of a selectable number of channels above a selectable trigger level caused a trigger signal to be issued. This multichannel trigger design revolutionized the satellite-borne study of lightning RF emissions (Jacobson et al., 1999) because it enabled triggering upon faint pulsed signals which otherwise would be lost in the background (e.g., Lehtinen et al., 2004). The design also prevented undesired triggering by anthropogenic communications signals (Jacobson et al., 1999). In addition to the signal-derived trigger, TATR could be programmed to trigger at a selected time, such as the recording of scheduled illumination by engineered RF pulsers (Massey et al., 1998b).

The powers from TATR's eight multichannel-triggers were continually digitized and stored, even when the TATR systems were not recording events. Burr et al. (2004) used this to produce a global atlas of frequency-resolved VHF noise in the space environment which was unmatched by any other system reported at that time.

During almost six years of operations, FORTE's RF payload recorded over three-million lightning VHF bandpass-filtered waveforms. The vast majority of information was gleaned from the 26 to 48 MHz passband (the so-called "low-band") with an accompanying simultaneous recording either at 118–140 MHz ("high-band") or at low-band but on the alternately-polarized antenna. The signal trigger almost always derived from a low-band channel.

Satellite-borne RF observations suffer from many constraints and complications to which ground-based systems are immune:

1. The propagation path from the lightning emitter to the satellite transits the ionosphere, leading to spectral dispersion of the VHF signal (Fig. 13.2) (Massey,

1990; Massey et al., 1998b; Roussel-Dupré et al., 2001). This is especially severe below 30 MHz, and 20 MHz is the practical limit below which signals from terrestrial lightning cannot be reliably studied by satellite.

2. The satellite views a huge source region for emitters of background noise, against which the lightning signal must compete. As a result, only lightning VHF signals of moderate to high power can be studied.
3. Single-satellite VHF observations cannot straightforwardly locate lightning (Jacobson and Shao, 2001, 2002b; Shao and Jacobson, 2001, 2002). For interpretation of the physical context of the VHF observation, source location is extremely useful. FORTE observing programs were weighted whenever possible toward either joint FORTE VHF/ground-based array observations (Section 13.4.2) or FORTE joint VHF/optical observations (Section 13.4.4).

However, satellite-borne VHF observations have some unique advantages over ground-based systems:

1. Within the limitations of the orbit, satellites offer global coverage.
2. When an intracloud discharge is located by some other means, the recorded RF signal contains information on the emission altitude (Jacobson et al., 2000).
3. Since the satellite is moving and lightning source locations vary, the satellite obtains data from a variety of elevation angles. This diversity of elevation angles facilitates inference of the VHF emission lobe (the lightning “antenna beam pattern”) for different lightning processes (Shao et al., 2004, 2005b).

13.2.1.3 FORTE Optical

In addition to its RF instruments, FORTE also had an Optical Lightning Sensor (OLS) on board (Suszczynsky et al., 2001). This included a broadband (0.4–1.1 μm) silicon photodiode detector (PDD) and a charge-coupled device imager, called the Lightning Location System (LLS). OLS data were Global Positioning System (GPS) time-stamped to a precision of 1 μs . The FORTE/OLS field-of-view was 80°, providing a 1200-km diameter footprint on the Earth below.

The PDD allowed for excellent temporal resolution of optical lightning emissions at 15 μs per sample, but could only geolocate events to within its footprint. The PDD could be operated such that it triggered autonomously when a signal was detected that rose above a noise-riding threshold level, or it could be triggered in a “slaved” mode where it recorded data whenever the LLS triggered. Record lengths were either 1.92 ms (autonomous) or 6.75 ms (slaved). The LLS offered complementary information, in that it geolocated events to within 10 km and provided two-dimensional imagery, but only sampled the light at 2.5 ms intervals. The LLS front-end operated autonomously and included a narrow band 777.4 nm spectral filter.

Note, there are two additional articles in this text which discuss space-based optical lightning measurements; see also: Adamo et al. (this volume) and Finke (2009).

13.2.2 The Los Alamos Sferic Array

Since its construction in 1998, the Los Alamos Sferic Array (LASA) has been in continuous operation. LASA is a network of electric field change meters that was originally built to provide support and ground-truth for the FORTE mission. Over time LASA has been used as a collaborative tool not only for FORTE, but also for providing ground-truth support to VHF observations by orbital receivers aboard the GPS satellites (Suszcynsky et al., 2005). In addition to the joint studies, LASA has demonstrated great utility as a stand-alone resource for performing lightning investigations.

By recording arrival times of lightning electric field change sferics at multiple geographically-distributed sensors and taking the difference between unique combinations of pairs of these arrival times, the location of the lightning discharge can be calculated via time difference of arrival techniques. Note that we use the term “sferic” as a colloquialism of the word *atmospheric*: the remotely-observed transient electric field change produced by lightning. The magnitude and sign of the measured electric field change are used to deduce physical properties of the discharge, such as peak current, polarity, and type of lightning. Smith et al. (2002) characterized the location accuracy of the LASA by comparison with the National Lightning Detection Network (NLDN: Cummins et al., 1998), and found it to be approximately 1 km for sources inside the array of stations.

The initial configuration of LASA consisted of five flat-plate “fast” electric field change sensors distributed across the U.S. state of New Mexico. The LASA expanded to 11 stations by 1999 (four in New Mexico, one in Texas, one in Nebraska, and five in Florida). See Smith et al. (2002) for a more complete description. As described by Shao et al. (2006), the LASA sensor hardware and trigger design were recently improved. A set of these improved sensors was deployed in Florida in 2004, and a second set of improved sensors was deployed in the U.S. Great Plains in 2005. Wiens et al. (2008) provides a detailed analysis of the performance of the improved Great Plains LASA. At present, LASA sensors use a 1 ms time constant and digitize the 0.2–500-kHz filtered output voltage change waveforms from the fast antenna circuit/flat plate antenna at 1 MHz with approximately 15 bits of resolution. The LASA sensors utilize a software-controllable floating bipolar event trigger. The record length for each triggered event varies but is usually between 1.5 and 3 ms. Time stamping is achieved via a GPS receiver and is accurate to roughly one microsecond.

13.3 The Characteristics of Narrow Bipolar Events

NBEs are a distinct class of intra-cloud (IC) lightning discharges first detected and reported by Le Vine (1980) and Willett et al. (1989), and described in more detail by Smith et al. (1999). The term “NBE” is derived from the phenomenological description of the sferic based on its VLF/LF waveform. NBE is perhaps not the best descriptive term for these discharges because any discharge involving a current that

turns on then off will produce a bipolar waveform in the radiation zone. However, NBE sferics are distinguished uniquely from ordinary cloud-to-ground (CG) and IC lightning sferics by their narrow ($\sim 10\text{-}\mu\text{s}$) bipolar pulse widths, high SNR values, and their temporal isolation from other lightning-related field changes. For example, Fig. 13.1 shows two 500- μs -long recorded NBE sferic waveforms detected by a LASA sensor from a range of approximately 500 km. The upper panel shows a typical positive NBE (+NBE), and the lower panel shows a typical negative-polarity NBE (−NBE).

There is strong phenomenological evidence that NBEs are co-located and occur simultaneously with sources of strong VHF emissions, such as the so-called TIPPs. Ground-based observations (Le Vine, 1980; Willett et al., 1989; Smith et al., 1999; Thomas et al., 2001) and space-based observations with FORTE (e.g., Jacobson et al., 2000; Jacobson and Light, 2003), and observations from an experimental receiver aboard a GPS satellite (Suszczynsky et al., 2005) have shown that NBE-related

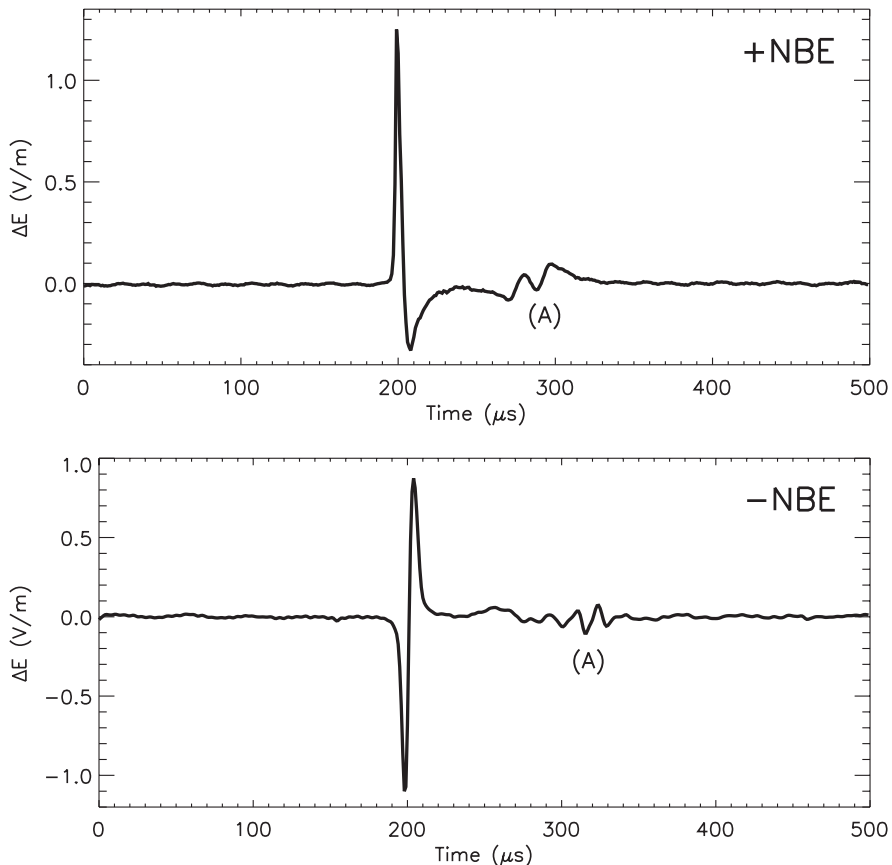


Fig. 13.1 Example sferics from a +NBE (top) and −NBE (bottom). Labels “(A)” show the ionospheric and ground-ionospheric reflections like those used by Smith et al. (2004) to determine the intracloud discharge source height as well as the virtual ionospheric reflection height

processes emit the most powerful pulses of VHF radiation produced by lightning. They constitute the majority of VHF lightning emissions detected from space at GPS orbit. Hence, Suszcynsky and Heavner (2003) have identified NBEs and NBE-related processes as the “primary target of opportunity for future satellite-based VHF global lightning monitors.”

It is important to make a distinction between the NBE sferic observed at VLF/LF and the strong VHF pulses associated with NBEs. It is not yet clear that both components always occur together (Jacobson, 2003a). However, for brevity, we will loosely apply the term “NBE” to describe the overall discharge process observed at any frequency.

13.3.1 Ground-Based Observations of NBEs

13.3.1.1 Electrical Characteristics

Smith et al. (1999) collected some of the first detailed ground-based measurements of +NBEs made by LANL. Among their results are: (1) peak +NBE electric field change amplitudes are comparable to those of return strokes, (2) the amplitudes of HF/VHF emissions from NBE-related discharges are approximately 10 times greater than those from normal lightning, (3) NBEs are compact in both time and space ($\sim 10 \mu\text{s}$ pulse widths, and less than 1 km in length).

NBE waveforms typically contain smaller amplitude pulses that lag the initial pulse (Smith et al., 2004). See, for example, the features labeled “(A)” in Fig. 13.1. These delayed pulses are due to ionosphere and ground-ionosphere reflections of the NBE skywave. Such reflection signatures are further evidence that NBEs are elevated sources (i.e., intra-cloud), and when combined with the horizontal location of the source the time delays of these pulses provide both the emission altitude of the NBE as well as the virtual reflection height of the ionosphere.

When observed by broadband field change antennas from large distances, NBEs exhibit their characteristic bipolar radiation field waveform. When observed at close range (less than ten kilometers), NBE’s electrostatic and inductive field changes can often be observed in addition to the bipolar radiation field change in their electric field change records. LASA measurements in 1998 and 1999 located NBEs of both positive- and negative-polarity, a small number of which were located within 10 km of one of the ground stations. For these events, the dipole moment change could be determined directly from the electrostatic field change in combination with the independently-measured radiation field change from a distant station. This allowed for the average propagation velocity to be determined by equating the two dipole moment change determinations; one in the static- and the other in the radiation-zone. From this, the length of the discharge was estimated using the velocity and the duration of the event. Additional details about these calculations can be found in Eack (2004), who determined that on average, a NBE transfers 0.3 C of charge over a distance of 3.2 km, and that the discharge wave-front propagates at an average speed equal to one-half the speed of light (similar to that of return-strokes). The average current was 16 kA, with a peak current as high as 29 kA measured for one NBE.

Hamlin et al. (2007) describe another technique for determining the spatial extent of NBEs. In a dataset consisting of 133 +NBE lightning discharges located by LASA, Hamlin et al. investigated a secondary positive peak that occurred in each record that followed the primary positive peak in the +NBE waveform. The secondary peak was a small positive perturbation in the negative trough of the otherwise ordinary NBE waveform. The perturbation was seen at multiple LASA stations per event and is co-located with the primary NBE discharge source. The secondary peaks are not to be confused with the signatures from ground or ionospheric reflections. In fact, the results were shown to be consistent with what would be expected for a propagating current pulse reflecting off an impedance discontinuity along a transmission line. With an assumed propagation speed, the time difference between the primary and secondary (assumed to be the reflected) peak in the field change record offered a direct technique for estimating the (presumed vertical) length of the discharge channel. The technique, analogous to measuring the length of a transmission line via time domain reflectometry techniques (except in the radiation-zone rather than along the conductor itself) was used to find the upper-limit-length for NBE discharge channels. Bounded by the speed of light, the limit on channel length for the typical positive narrow bipolar event was shown to be approximately 2 km. This value was twice the estimate by Smith et al. (1999) and about two-thirds the 3.2 km reported in Eack (2004) and can be considered a refinement of the original length estimates. The study also used the ratio of the primary-to-reflected signal amplitudes to obtain an attenuation coefficient. Using this, a temporal decay constant of approximately 4 μ s was found for +NBEs. Assuming a propagation speed of one-half the speed of light the temporal decay constant translates to a spatial decay scale length of \sim 600 m (i.e., the conductive-length of the channel decays from its initial value to “1/e” of this in about 600 m).

13.3.2 FORTE Observations of NBEs

By definition, a NBE sferic is the unique waveform signature observed at VLF/LF frequencies. However, an intense burst of noise is also often observed simultaneously at higher frequencies. The power of the higher-frequency noise is essentially constant versus frequency through FORTE’s the range of VHF frequencies. The original observations of NBEs by Le Vine (1980) included simultaneous recordings of both the sferic and the HF noise, and he noted that the HF signal appears like a noise burst added to the sferic which lasts a few microseconds. That is, the HF/VHF noise is not a coherent extension (to higher frequencies) of the basic sferic waveform. Le Vine’s data could not constrain the emission height of the sferic or the HF noise pulse.

Blackbeard’s VHF receiver lacked a multichannel coincidence trigger and required a high trigger threshold. As a result, Blackbeard could be triggered by only the most intense lightning phenomena. What Blackbeard recorded were almost always the same sort of intense pulses described in Le Vine (1980) as the noise burst accompanying the sferic. However, the Blackbeard observations systematically

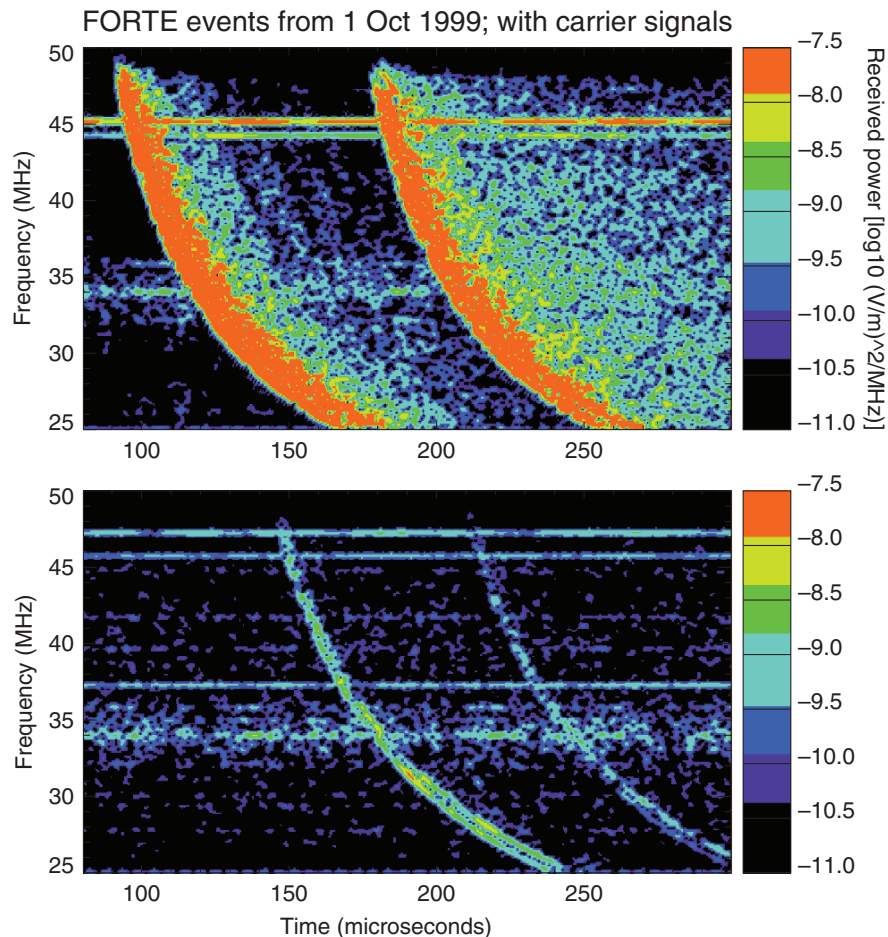


Fig. 13.2 Spectrograms of a (top) strong intracloud pulse typically associated with a VLF NBE and (bottom) a weaker polarized/coherent intracloud pulse. Note the difference in pulse width and strength between the two events, as described in Jacobson and Light (2003). The ionospherically-induced, frequency-dependent dispersion is evident in the graphics, as well as the geomagnetic splitting (most visible in the lower panel at the lower frequencies of the primary signature). In addition to the lightning signals, one can discern interference from anthropogenic radio transmissions, apparent as narrow, horizontal bands. In each spectrogram, the ground-reflection accounts for the echo which occurs approximately 50–75 μ s after the primary pulse (See also Plate 17 in the Color Plate Section on page 603)

revealed a second pulse, or the “pulse pair” in the term TIPP. Statistical study of the second-pulse delay times suggested strongly that the second pulse was a ground reflection of the first pulse rather than a physically delayed second emission process (Holden et al., 1995; Massey and Holden, 1995; Massey et al., 1998a). This is not inconsistent with Le Vine’s original single-pulse HF recording as a ground-based receiver would not see a distinct second pulse (Jacobson et al., 1999).

FORTE results on their own (Jacobson et al., 1999), as well as the joint FORTE and NLDN campaign (Jacobson et al., 2000), definitively confirmed the Blackbeard inference that the second pulse in a TIPP was merely a ground reflection of the first pulse. The inferred height of the TIPP pulses and the sferic, determined via altogether different data and methods but on simultaneous and common events, agreed to within ~ 2 km; this was consistent with the height-determination error from Smith et al. (2004). Moreover, the sferic and VHF signals were simultaneous to within the timing uncertainty (~ 1 μ s). Figure 13.2 shows two example TIpps detected by FORTE. The top panel shows a “strong” intracloud pulse typically associated with a VLF NBE. The bottom panel shows a weaker intracloud pulse. Both types of pulses occur in pairs at the FORTE satellite; the delayed second pulse of each pair is the reflection from the earth’s surface.

13.3.2.1 Weak Versus Strong RF Pulses

FORTE’s RF data led to several robust findings about the characteristics of VHF pulses originating from IC discharges. The overall picture was that IC pulses diverged broadly into two categories: weak or strong in effective radiated power (ERP). An ERP of ~ 40 kW (integrated over the FORTE low-band; 26–48 MHz) appears to be a dividing region, on either side of which FORTE IC pulses have distinctive behaviors. Those with $ERP \ll 40$ kW are categorized as weak, polarized, narrow, and coherent pulses, while those with $ERP > 40$ kW are in the broader and incoherent “strong IC pulses” category (see also, Figure 13.2).

With regard to their polarization characteristics, the weak pulses are linearly polarized while the strong pulses are less polarized; more work is required to clarify whether their polarization is random or something more organized. Waveform coherence is related to the ratio of the pulse-width to the inverse of the signal bandwidth, i.e. coherence may be quantified by the “time-bandwidth product”. The weak pulses tend to have time-bandwidth products of roughly unity, while the strong pulses have products much larger (i.e., the strong pulses are extended wave trains of noise). Thus with regard to waveform coherence, the weak pulses tend to be perfectly coherent, while the strong pulses appear to be incoherent. We summarize the two archetypes’ widely differing characteristics as follows (Jacobson, 2003a, 2003b; Jacobson and Light, 2003):

1. Emission intensity: Those categorized as strong pulses have intensities that are two (and sometimes three) orders-of-magnitude greater than the weaker polarized/coherent pulses.
2. The strong pulses are randomly polarized, whereas the weaker polarized/coherent pulses show linear polarization.
3. The strong pulses are either isolated in time, or serve as initiators of flashes whose subsequent emissions are not as strong and are frequently polarized/coherent. In contrast, the weaker polarized/coherent pulses can occur anywhere in an IC flash and are not uniquely observed as initiators of flashes.

- The weaker polarized/coherent pulses are usually accompanied closely in time by other pulses of the same type.
- 4. The strong pulses show deep frequency-dependent fading within the pulse, whereas the weaker polarized/coherent pulses have a simple, coherent monopulse structure.
 - 5. The strong pulses are very wide compared to the weaker polarized/coherent pulses ($\sim 3\text{--}5 \mu\text{s}$ versus $\sim 0.1 \mu\text{s}$).
 - 6. The strong pulses are the RF pulses seen with simultaneous NBEs recordings of the radiation-field vertical electric field sferic near the ground. By contrast, the weaker polarized/coherent pulses have no special simultaneity or preferred association with NBEs.
 - 7. In storms that produce both strong RF pulses recorded by FORTE and NBE field changes recorded by LASA, there are always more strong RF pulses than NBEs. It appears that strong RF pulses can occur without an associated NBE, but NBEs are always accompanied by strong RF pulses (Jacobson, 2003a).
 - 8. Storms containing strong RF pulses along with coincident NBE field changes have few if any flashes. That is, NBE-coincident strong pulses are more isolated from neighboring lightning activity than are strong pulses lacking coincidence with a NBE sferic.
 - 9. In storms containing lightning flashes that are initiated by strong RF pulses, and in which both FORTE and LASA could observe the same storm, there are almost never NBEs.
 - 10. In flashes that are initiated by strong RF pulses, the subsequent leader-like pulses in the flash tend to occur at higher altitude than where the flash is initiated by the strong RF pulse.
 - 11. In flashes that are initiated by strong RF pulses, optical concurrence tends to occur only for subsequent pulses (if at all) and tends not to occur for the initiator strong RF pulse.
 - 12. The strong RF pulses in a given storm appear to have a truncated ERP distribution, staying below a limiting ERP. For most storms this ERP limit is on the order of 1 MW peak, integrated over the FORTE low-band of 26–48 MHz.

13.3.2.2 Optical Signatures and NBEs

Light and Jacobson (2002) examined the joint optical and RF data from the specific class of lightning detected and classified by FORTE as “impulsive intracloud VHF events”. These impulsive events comprised 47% of the FORTE VHF data overall. However, in the sub-set of events that comprised the most powerful VHF events (those likely to have VLF/LF NBE counterparts) the “impulsive” events were over-represented and accounted for 60–70% of the data. Light and Jacobson showed that, in general, as the detected VHF peak power increased, the likelihood of optical coincidence similarly increased. A surprising finding, however, was that in the NBE-corresponding class of very-powerful, impulsive VHF events, the likelihood of optical coincidence was inversely proportional to the peak VHF power. The data showed a transition point in power where the optical coincidence rate continued

to climb for all types of events, except VHF-impulsive events which dramatically begin to lose their optical counterparts. This led to the suspicion that the strongest impulsive VHF events may be a distinct class of discharge, which produces little or no optical emission. This new finding of “dark lightning” has yet to be explained. We do not yet know whether there truly is no optical emission at all from NBEs or if it is just a detection/sensitivity issue. All we know presently is that the optical emission is below the detection threshold of current instruments. Unpublished data have shown agreement with the “dark lightning” finding, in that photodiodes fielded alongside ground-based VLF/LF sensors typically show no optical light curves detected from corresponding VLF/LF NBE detections. Therefore, the upper limit to radiated power of any NBE-optical-emission appears to be low.

13.3.3 The Meteorological Context of NBEs

Research at LANL has established the basic meteorological context of NBEs. A survey of the publications from this research reveals that some of the observed characteristics of NBEs are consistent from one study and geographical region to the next. However, there are also inconsistencies. The key points may be summarized as follows:

NBEs occur in the same general meteorological context as other lightning, that is, within or near the convective cores of thunderstorms (Smith et al., 1999; Suszcynsky et al., 2005; Jacobson and Heavner, 2005). NBEs have been observed in air mass thunderstorms and frontal storms (Smith et al., 1999; Shao et al., 2006) in severe multi-cell and supercell storms (Tessendorf et al., 2007; Wiens et al., 2008) as well as in tropical cyclones (Suszczynsky et al., 2005). Though NBEs occur in the same storms as other lightning, they tend to occur in relative temporal isolation from other lightning, i.e., not as part of ordinary lightning flashes. When they do occur as part of a flash, they usually initiate the flash, and their emission altitudes are in the same general range (10–15 km) as ordinary IC flashes (Rison et al., 1999; Jacobson, 2003a, 2003b; Jacobson and Heavner, 2005; Smith et al., 1999, 2004). Indeed, Jacobson and Heavner show that NBE emission altitudes are generally constrained to below the height of the tropopause.

NBEs constitute a small percentage of all lightning discharges (probably much less than 1%). Table 13.1 lists the percentage of NBEs relative to other lightning observed in several recent studies. These percentages should be treated as very rough estimates because the NBE percentage is difficult to quantify. Total lightning itself is not a readily measured (or measurable) quantity, especially when large spatial and temporal domains are considered. The percentages in Table 13.1 are overestimating the NBE percentage because the total lightning counts are underestimated (see, for example, Wiens et al., 2008). Furthermore, the instrumentation used to observe NBEs and other lightning varies from one study to the next, as does the geographical region.

The majority of NBEs observed are positive-polarity (Table 13.1). The percentage of +NBE relative to all NBEs observed varies from study-to-study and also

Table 13.1 Percentage of NBEs observed relative to all lightning observed and percentage of all NBEs observed that were of positive-polarity. Results are listed by study and by geographical region

Study	NBE (% of all)	+NBE (% of NBEs)
Smith et al. (2002)		
New Mexico Only	0.63	84
New Mexico and Florida	1.57	70
Suszczynsky and Heavner (2003)		
Florida	N/A	65
Jacobson and Heavner (2005)		
Florida	3.35	76.6
Wiens et al. (2008)		
Great plains	0.5	77

by geographical region (New Mexico versus Florida versus the Great Plains), but +NBEs are consistently more common. Smith et al. (2004) found that the distribution of NBE emission source heights is roughly bimodal, with a lower mode near 13 km associated with +NBEs and an upper mode near 18 km associated with -NBEs. These collective results are consistent with the idea that +NBEs are intra-cloud discharges that initiate between the main negative and upper-positive charge regions of the commonly observed tripolar charge configuration of thunderstorms. In fact, Rison et al. (1999) show a specific example of a +NBE initiating a normal intra-cloud discharge in a tripolar thunderstorm. Perhaps the less common -NBEs are discharges that initiate between the upper-positive and an additional overlying negative charge region, possibly a screening layer charge. Or perhaps the -NBEs are indicative of storms with an elevated charge structure, or even an inverted tripole charge structure. In their statistical study, Jacobson and Heavner (2005) found that Florida storms rarely produce both polarities of NBEs, while Wiens et al. (2008) found that Great Plains storms often do produce both polarities. Great Plains storms differ from storms elsewhere in the U.S. in many ways, such as severity, ground flash polarity, and charge structure (e.g., Lang et al., 2004; Rust et al., 2005; Wiens et al., 2005). Perhaps the difference in NBE production in Great Plains versus Florida storms is another manifestation of the difference in the storms themselves.

In a statistical sense, the NBE rate is correlated with the total lightning rate. We must stress that this is true only in a statistical sense, not necessarily in any given storm. This relationship between NBE rate and total lightning rate also appears to vary according to the geographic region. For example, Suszczynsky and Heavner (2003) found a significant positive correlation (with large variance) between NBE rates and CG flash rates in Florida storms when considering a large sample of storms. However, there were many storms in their sample which produced CG flashes but did not produce any NBEs. In comparison, Wiens et al. (2008) found a weaker (but still positive) statistical correlation between NBE rates and total lightning rates for storms of the Great Plains. Wiens et al. (2008) also found

that most thunderstorms do not produce NBEs. This leads to the following general observations about NBE phenomenology:

1. NBEs do not seem to occur in all thunderstorms. For those storms that do produce NBEs, the NBEs tend to cluster more closely in both space and time than does other lightning. Strong evidence of this clustering may be found in the statistical studies of both Jacobson and Heavner (2005) and Wiens et al. (2008). Individual case studies also show this NBE clustering (e.g., Smith et al., 1999; Suszcynsky et al., 2005; Tessendorf et al., 2007; Wiens et al., 2008). For example, in one of the storms they studied, Smith et al. noted that the NBEs occurred in sporadic clusters during relatively intense periods of thunderstorm activity. In comparison with the lightning in general, the NBEs were more highly confined to a small region centered on the high radar reflectivity core.
2. It may be that NBEs are indicative of specific types of storms and/or a specific phase of storm development. There is some circumstantial evidence that NBEs are indicative of stronger storms (storms with rapidly increasing or extreme convective strength), and that weaker storms do not produce any NBEs at all. Recall that Suszcynsky and Heavner (2003) found many cases in which Florida storms produced CG flashes but no NBEs. These cases were largely associated with low CG flash rates, suggesting that only the stronger storms produced NBEs. To investigate whether NBEs were indicative of stronger storms in the Great Plains, Wiens et al. (2008) binned their observations into 20-km by 20-km by 10-min space-time cells and then separated these binned observations into two statistical sub-samples: space-time cells with lightning of any kind, and space-time cells with at least one NBE. The cells containing at least one NBE were much more convectively intense than those without any NBEs. In the statistical median, the maximum radar reflectivity was 11–13 dBZ larger, the maximum 30-dBZ altitude was 4–5 km higher, and the total lightning flash rate was an order of magnitude greater. Furthermore, Wiens et al. found that the probability that a cell contained a NBE increased within the increase of every measure of convective strength they considered. They cautioned, however, that even the strongest convection did not always produce NBEs.

13.4 Other FORTE Lightning Observations

13.4.1 Emission Height for Intracloud VHF Emitters

A VHF pulse propagates from an above-ground lightning emitter to the satellite along two distinct paths: the direct path to the satellite and the ground-reflected path, which is longer. The added length of the ground-reflected path causes that path's contribution to the received signal to be delayed relative to the direct path. If the emitter's latitude and longitude are known, e.g., from a lightning-location array's simultaneous detection of the same event, then the VHF recording can be used to infer the emission height (Jacobson et al., 1999, Tierney et al., 2002). This was

done automatically for hundreds of thousands of FORTE recordings of intracloud pulses. The primary pulse usually derives either from leader-step-like discharges or from much more powerful emissions associated with NBEs. Occasionally a TIPP can be formed by an exceptionally brief ($\sim 10 \mu\text{s}$) intracloud streamer discharge, such as seen in association with positive cloud-to-ground (CG) discharges (Jacobson et al., 2000).

13.4.2 Coordinated Campaigns with Ground-Based Arrays

FORTE observations were coordinated region-by-region so as to maximize triggered recordings where there was also coverage by various lightning-location arrays. The most extensive coordination was with the National Lightning Detection Network (NLDN) circa 1998–2000, and resulted in a comprehensive understanding of the relationship of space-borne VHF and ground-based LF detection, both in terms of trigger relative biases and detailed timing differences between the VHF and LF emissions (Jacobson et al., 2000). The FORTE/NLDN coordinated campaign established the following:

1. NLDN-FORTE coincidences which rise above the accidental coincidence level are prompt to within $\sim 30 \mu\text{s}$.
2. FORTE-observed VHF emissions in the North America sector are often as strong as, or stronger than, Blackbeard-observed TIQQPs.
3. Satellite-observed VHF emissions are much more likely to be associated with intracloud discharges than with cloud-to-ground discharges.
4. Satellite-observed VHF emissions are more likely to be associated with positive- than with negative-cloud-to-ground discharges.
5. Satellite-observed VHF emissions associated with intracloud discharges tend to be narrower in pulse-width than are VHF emissions associated with either polarity of cloud-to-ground discharges.
6. TIQQPs that are associated with NLDN discharges display a region-dependent emission-height distribution, suggestive of the height-versus-latitude dependence of key isotherms, e.g. -20°C , in the troposphere. Over the Continental U.S./Canadian interior above 45° N , the half-points of the distribution are at roughly 6 and 9 kilometers, and the peak is at 7–8 km. Over the southern maritime region, the peak is at $> 13 \text{ km}$, and the distribution is broader. There is no statistically significant evidence, among the TIQQPs that are associated with NLDN discharges, for TIQQP-emission heights above 15 km.

In addition to the NLDN study, there were intensive campaigns involving joint FORTE-VHF recordings with other lightning-location systems. These included the United Kingdom Meteorological Office's array (Lee, 1986a, 1986b), LASA (Smith et al., 2002) and the World Wide Lightning Location Array (Lay et al., 2004; Rodger et al., 2004, 2005).

13.4.3 Negative Cloud-to-Ground Discharges Over Sea Water

The joint campaigns with both NLDN and LASA allowed FORTE to identify a unique VHF emission associated with the contact of the downward stepped leader with seawater (Jacobson and Shao, 2002a; Shao et al., 2004, 2005b). This species of especially narrow sferic pulse (~ 100 ns) had been seen by early ground-based observations (Willett et al., 1990, 1998; Willett and Krider, 2000). The FORTE-sferic array campaigns established some interesting characteristics of the VHF radiation for a negative CG on seawater:

1. The VHF signal from a negative CG on seawater is simply a coherent extension of the sferic waveform. Because of this, the spectral roll-off is much steeper than for the noise-like strong intracloud VHF emissions.
2. By combining data from VHF recordings when the satellite was at various elevation angles (as seen from the discharge), the antenna beam lobe of the VHF emission could be inferred statistically (Shao et al., 2005b). The lobe is oblique-upward beamed, unlike a simple horizon-directed dipole pattern. The oblique-upward beaming is consistent with the field being radiated by an upward moving current front moving at 75% of the speed of light (in the leader-prepared channel).
3. The radiated VHF field is perfectly linearly polarized, as expected from a single vertical emitter.
4. The emission lobe is inconsistent with a “bidirectional leader” model, which has been proposed in the past for the ground-connection process in a negative CG discharge (see discussion in Section 5 of Shao et al. (2005b)).
5. The 100-nanosecond-duration sferic is radiated from a vertical extent of no more than 20 m in height.

13.4.4 FORTE Optical Observations

13.4.4.1 Comparison with NLDN

Kirkland et al. (2001) compared FORTE’s photodiode detector (PDD) observations with the NLDN. They found a PDD detection efficiency of $\sim 6\%$ for individual NLDN-reported cloud-to-ground strokes and a $\sim 23\%$ detection efficiency for NLDN-reported flashes, which contain ground strokes. The flashes detected by both PDD and NLDN included only 8% of the PDD data, leading to the interpretation that the PDD was sensitive to a far greater fraction of in-cloud discharges, whereas the NLDN is known to predominantly detect (or at least record) ground strikes. The detection efficiency was only marginally higher for positive-polarity CGs compared to those of negative-polarity.

13.4.4.2 Discrimination of Lightning Type

A comparison of FORTE RF and FORTE optical data was first presented in Suszcynsky et al. (2000). In that work, the authors considered the potential for “fingerprinting” the type of lightning discharge according to its VHF time series structure. For example, initial, negative-polarity return strokes are readily identifiable because the intense emission that accompanies the attachment of the channel to ground is preceded by many milliseconds of increasingly strong VHF spikes, presumably from stepped leader activity, superimposed on a rising background, and an abrupt return to original VHF noise levels shortly after attachment. In all, six types of discharges were described in that work: (1) initial, negative return strokes with stepped leader; (2) subsequent negative return strokes, sometimes showing evidence of dart leader; (3) initial positive return strokes; (4) impulsive in-cloud discharges; (5) non-impulsive in-cloud discharges; and (6) mixed IC (with both impulsive and temporally broad emission, combined).

Light et al. (2001) used the VHF classification scheme of Suszcynsky et al. (2000) to explore the optical characteristics of VHF-detected lightning for each discharge type. It was shown that, in general, RF peak power and optical peak irradiance were broadly correlated. Both the VHF and optical emission were weaker for in-cloud discharges of any type, compared to ground strokes; ground strokes were also approximately 30% more likely to have coincident VHF-optical signals than were in-cloud events, regardless of event peak power. The correspondence between optical and VHF emissions for initial negative return strokes was much greater than for any other type of lightning (Light et al. 2001 looked only at events within a common field of view of both the optical and VHF sensors): every one detected and identified in the VHF data also had a coincident optical signal. The difference in peak VHF power between these events and other types of ground strokes was not significant, although they were the strongest optical detections by a factor of two to five. Therefore this high VHF/optical coincidence rate is not simply an effect of these discharges being generally strong, but rather is intrinsic to the nature of initial negative-polarity return strokes. The question of whether one can ascertain the lightning discharge type on the sole basis of optical emission was addressed by Davis et al. (2002). Again, optical waveform characteristics were found to be statistically slightly different among the assorted lightning types, but not such as to allow individual event discrimination. The greatest peak optical power, on average, arose from waveforms associated with positive-polarity ground strokes, which also showed greater effective pulse widths by 30–50%.

13.5 LANL and the Study of Severe Weather

Many types of extreme weather that cause loss of life or crop and structure damage (tornadoes, flash floods, hail and lightning) are generated by late-stage, severe convective storms. The transition from “regular” to “severe” weather has

been associated with a rapid increase or “jump” in the lightning activity (Williams et al., 1999). Improved early warning methods, including efficient detection and tracking of intense-convection cells through lightning activity by systems like the LASA could help to mitigate some of the effects of these storms. For example, studies of lightning as a precursor to severe weather indicate that tornado-related deaths can be reduced by 20% with the improved warning lead time gained through lightning monitoring (Weber et al., 1998).

It was previously thought that another serious weather-related threat, namely hurricanes, did not reveal itself through lightning intensification. However, during the deadly 2005 hurricane season LASA observed abundant lightning activity within hurricanes Katrina, Rita, and Wilma (Shao et al., 2005a). The vertical ascent of the lightning discharge emission sources can be used as a proxy for convective-cell development and, through this, it may be possible to use lightning to gauge the likelihood of severity increase. A demonstration of this occurred when LASA-detected lightning activity from Rita peaked as the hurricane transitioned from Category 3 to 5 (Shao et al.). These observations of the lightning in the hurricane eyewall region have motivated recent LANL efforts to discover, investigate, and monitor the convective activity in the critical eyewall region.

The great uncertainty in hurricane intensification forecasting is the prediction of the intensification triggering mechanism, thought to be small-scale violent convective events in the eyewall known as “vortical hot towers”. Current observational techniques do not allow for continuous real-time observations of vortical hot tower formation. However, systems like LASA can, in principle, provide continuous, all-weather, remote monitoring of eyewall processes with high spatial and temporal accuracy. LANL is in the process of deploying a new high-density dual-band (both VLF/LF and VHF) LASA network in the Gulf of Mexico which is hoped to provide maps of the developing lightning-source regions inside individual convective towers, as well as information about the overall charge structure and flash rate.

LANL also operates a constellation of VHF sensors which are a payload on the GPS satellites. The same VLF/LF NBEs that offer severe-storm monitoring capabilities on the ground also comprise a significant portion of the VHF lightning signals detected by these sensors in orbit (Suszczynsky et al., 2005). Thus, the GPS-based receiver constellation has the capability to eventually offer real-time convection tracking and storm assessment across the globe.

Acknowledgments This work was sponsored by the Department of Energy/National Nuclear Security Agency (DOE/NNSA). The FORTE RF payload functioned for almost six years, three times longer than the expected mission lifetime. This extraordinary longevity was the product, in part, of the robust design architecture by satellite-development leader S. Knox and his team and also due to the scrupulous on-orbit maintenance and resourceful problem-solving skills of the mission-operations leaders D. Roussel-Dupré and P. Klingner. The success of LASA’s design, deployment, and long-term operations and maintenance is due to a long list of people and institutions, to whom we owe an enormous debt of gratitude and offer our most sincere thanks. Although the many cited references are authored by members of our science team, each finding depended greatly on the skill and dedication of the development and operations teams as well as our many external collaborators and site hosts.

References

- Adamo C, Goodman S, Mugnai A, Weinman JA, Lightning Measurements from Satellites and Significance for Storms in the Mediterranean, ch. 14, this volume.
- Burr T, Jacobson A, Mielke A (2004) A global radio frequency noise survey as observed by the FORTE satellite at 800 km altitude. *Radio Sci* 39(4), DOI 10.1029/2002RS002865
- Cummins KL, Murphy MJ, Bardo EA, Hiscox WL, Pyle RB, Pifer AE (1998) A combined TOA/MDF technology upgrade of the U.S. National Lightning Detection Network. *J Geophys Res* 103(D8):9035–9044
- Davis SM, Suszynsky DM, Light TEL (2002) FORTE observations of optical emissions from lightning: Optical properties and discrimination capability. *J Geophys Res* 107(D21):4579–4579
- Eack KB (2004) Electrical characteristics of narrow bipolar events. *Geophys Res Lett* 31(20):L20, 102–104
- Finke U (2009), Optical Detection of Lightning from Space, ch. 12, this volume.
- Hamlin T, Light TE, Shao XM, Eack KB, Harlin JD (2007) Estimating lightning channel characteristics of positive narrow bipolar events using intra-channel current reflection signatures. *J Geophys Res* 112:D14108, DOI 10.1029/2007JD008471
- Holden DN, Munson CP, Devenport JC (1995) Satellite observations of transitionospheric pulse pairs. *Geophys Res Lett* 22(8):889–892
- Jacobson AR (2003a) How do the strongest radio pulses from thunderstorms relate to lightning flashes? *J Geophys Res* 108, DOI 10.1029/2003JD003936
- Jacobson AR (2003b) Relationship of intracloud lightning radio frequency power to lightning storm height, as observed by the FORTE satellite. *J Geophys Res* 108, DOI 10.1029/2002JD002956
- Jacobson AR, Heavner MJ (2005) Comparison of narrow bipolar events with ordinary lightning as proxies for severe convection. *Mon Weather Rev* 133(5):1144–1154
- Jacobson AR, Light TEL (2003) Bimodal radio frequency pulse distribution of intracloud-lightning signals recorded by the FORTE satellite. *J Geophys Res* 108(D9), DOI 10.1029/2002JD002613
- Jacobson AR, Shao XM (2001) Using geomagnetic birefringence to locate sources of impulsive, terrestrial VHF signals detected by satellites on orbit. *Radio Sci* 36(4):671–680
- Jacobson AR, Shao XM (2002a) FORTE satellite observations of very narrow radiofrequency pulses associated with the initiation of negative cloud-to-ground lightning strokes. *J Geophys Res* 107(D22), DOI 4610.1029/2001JD001542
- Jacobson AR, Shao XM (2002b) On-orbit direction-finding of lightning radiofrequency emissions recorded by the FORTE satellite. *Radio Sci* 37(4), DOI 10.1029/2001RS002510
- Jacobson AR, Knox SO, Franz R, Enemark DC (1999) FORTE observations of lightning radiofrequency signatures: Capabilities and basic results. *Radio Sci* 34(2):337–354
- Jacobson AR, Cummins KL, Carter M, Klingner P, Dupre DR and Knox SO (2000) FORTE radiofrequency observations of lightning strokes detected by the National Lightning Detection Network. *J Geophys Res* 105:15653–15662
- Kirkland MW, Suszynsky DM, Guillen JLL, Green JL (2001) Optical observations of terrestrial lightning by the FORTE satellite photodiode detector. *J Geophys Res* 106:33499–33509
- Lang TJ, Miller LJ, Weisman M, Rutledge SA, III LJB, Bringi VN, Chandrasekar V, Detwiler A, Noesken N, Helldon J, Knight C, Krehbiel P, Lyons WA, MacGorman D, Rasumssen E, Rison W, Rust WD, Thomas RJ (2004) The severe thunderstorm electrification and precipitation study. *Bull Amer Meteorol Soc* DOI 10.1175/BAMS-85-8-1107
- Lay EH, Holzworth RH, Rodger CJ, Thomas JN, Pinto O, Dowden RL (2004) WWLL global lightning detection system: Regional validation study in Brazil. *Geophys Res Lett* 31(L03102), DOI 03110.01029/02003GL018882
- Le Vine DM (1980) Source of the strongest RF radiation from lightning. *J Geophys Res* 85:4091–4095

- Lee ACL (1986a) An experimental study of the remote location of lightning flashes using a VLF arrival time difference technique. *Q J R Meteorol Soc* 112:203–229
- Lee ACL (1986b) An operational system for the remote location of lightning flashes using a VLF arrival time difference technique. *J Atmos Oceanic Technol* 3:630–642
- Lehtinen NG, Gorham PW, Jacobson AR, Roussel-Dupré RA (2004) FORTE satellite constraints on ultrahigh energy cosmic particle fluxes. *Phys Rev D* 69(1), DOI 10.1103/PhysRevD.69.013008
- Light TE, Jacobson A (2002) Characteristics of impulsive VHF lightning observed by the FORTE satellite. *J Geophys Res* 107, DOI 10.1029/2001JD001585
- Light TEL, Jacobson AR, Suszcynsky DM (2001) Coincident radio frequency and optical emissions from lightning, observed with the FORTE satellite. *J Geophys Res* 106:28223–28232
- Massey RS (1990) Ionospheric group delay and phase including ionospheric refractive effects. Tech. rep., Los Alamos National Laboratory, Los Alamos, New Mexico
- Massey RS, Holden DN (1995) Phenomenology of transitionospheric pulse pairs. *Radio Sci* 30(5):1645–1659
- Massey RS, Holden DN, Shao XM (1998a) Phenomenology of transitionospheric pulse pairs: Further observations. *Radio Sci* 33(6):1755–1761
- Massey RS, Knox SO, Franz RC, Holden DN, Rhodes CT (1998b) Measurements of transitionospheric radio propagation parameters using the FORTE satellite. *Radio Sci* 33(6):1739–1753
- Rison W, Thomas RJ, Krehbiel PR, Hamlin T, Harlin J (1999) A GPS-based three-dimensional lightning mapping system: Initial observations in central New Mexico. *Geophys Res Lett* 26(23):3573–3576
- Rodger CJ, Brundell JB, Dowden RL, Thomson NR (2004) Location accuracy of long distance VLF lightning location network. *Ann Geophys* 22:747–758, sRef-ID: 1432-0576/ag/2004-22-747
- Rodger CJ, Brundell JB, Dowden RL (2005) Location accuracy of VLF World-Wide Lightning Location (WWLL) network: Post-algorithm-upgrade. *Ann Geophys* 23:277–290, sRef-ID: 1432-0576/ag/2005-23-277
- Roussel-Dupré RA, Jacobson AR, Triplett LA (2001) Analysis of FORTE data to extract ionospheric parameters. *Radio Sci* 36(6):1615–1630
- Rust WD, MacGorman DR, Bruning EC, Weiss SA, Krehbiel PR, Thomas RJ, Rison W, Hamlin T, Harlin J (2005) Inverted-polarity electrical structures in thunderstorms in the Severe Thunderstorm Electrification and Precipitation Study STEPS. *Atmos Res* 76:247–271
- Shao XM, Jacobson AR (2001) Polarization observations of broadband VHF signals by the FORTE satellite. *Radio Sci* 36(6):1573–1589
- Shao XM, Jacobson AR (2002) Polarization observations of lightning-produced VHF emissions by the FORTE satellite. *J Geophys Res* 107(D20), DOI 10.1029/2001JD001018
- Shao XM, Jacobson AR, Fitzgerald TJ (2004) Radio frequency radiation beam pattern of lightning return strokes: A revisit to theoretical analysis. *J Geophys Res* 109, DOI 10.1029/2004JD004612
- Shao XM, Harlin J, Stock M, Stanley M, Regan A, Wiens K, Hamlin T, Pongratz M, Suszcynsky D, Light T (2005a) Katrina and Rita were lit up with lightning. *EOS Trans, AGU* 86(42):398, DOI 10.1029/2005EO420004
- Shao XM, Jacobson AR, Fitzgerald TJ (2005b) Radio frequency radiation beam pattern of lightning return strokes: Inferred from FORTE satellite observations. *J Geophys Res* 110(D24), DOI 10.1029/2005JD006010
- Shao XM, Stanley M, Regan A, Harlin J, Pongratz M, Stock M (2006) Total lightning observations with the new and improved Los Alamos Sferic Array (LASA). *J Atmos Oceanic Technol* 23:1273–1288
- Smith DA, Shao XM, Holden DN, Rhodes CT, Brook M, Krehbiel PR, Stanley M, Rison W, Thomas RJ (1999) A distinct class of isolated intracloud lightning discharges and their associated radio emissions. *J Geophys Res* 104:4189–4212

- Smith DA, Eack KB, Harlin J, Heavner MJ, Jacobson AR, Massey RS, Shao XM, Wiens KC (2002) The Los Alamos Sferic Array: A research tool for lightning investigations. *J Geophys Res* 107, DOI 10.1029/2001JD000502
- Smith DA, Heavner MJ, Jacobson AR, Shao XM, Massey RS, Sheldon RJ, Wiens KC (2004) A method for determining intracloud lightning and ionospheric heights from VLF/LF electric field records. *Radio Sci* 39, DOI 10.1029/2002RS002790
- Suszczynsky DM, Heavner MJ (2003) Narrow bipolar events as indicators of convective strength. *Geophys Res Lett* 30, DOI 10.1029/2003GL017834
- Suszczynsky DM, Kirkland MW, Jacobson AR, Franz RC, Knox SO, Guillen JLL, Green JL (2000) FORTE observations of simultaneous VHF and optical emissions from lightning: Basic phenomenology. *J Geophys Res* 105(D2):2191–2201
- Suszczynsky DM, Light TE, Davis S, Green JL, Guillen JLL, Myre W (2001) Coordinated observations of optical lightning from space using the FORTE photodiode detector and CCD imager. *J Geophys Res* 106:17897–17906
- Suszczynsky DM, Jacobson AR, Linford J, Light TE, Musfeldt A (2005) VHF lightning detection and storm tracking from GPS orbit. In: Annual Mtg., Amer. Meterol. Soc., p Abstract P2.5
- Tessendorf SA, Rutledge SA, Wiens KC (2007) Radar and lightning observations of normal and inverted polarity multicellular storms from STEPS. *Mon Wea Rev* 135:3682–3706
- Thomas RJ, Krehbiel PR, Rison W, Hamlin T, Harlin J, Shown D (2001) Observations of VHF source powers radiated by lightning. *Geophys Res Lett* 28(1):143–146, DOI 10.1029/2000GL011464
- Tierney HE, Jacobson AR, Roussel-Dupré R, Beasley WH (2002) Transionospheric pulse pairs originating in marine, continental and coastal thunderstorms: Pulse energy ratios. *Radio Sci* 27(3), DOI 10.1029/2001RS002506
- Weber ME, Williams ER, Wolfson MM, Goodman SJ (1998) An assessment of the operational utility of a GOES Lightning Mapping Sensor. Project Report NOAA-18 MIT Lincoln Laboratory, Lexington, MA 13 February 1998, 108 pp
- Wiens KC, Rutledge SA, Tessendorf SA (2005) The 29 June supercell observed during STEPS. Part II: Lightning and charge structure. *J Atmos Sci* 62:4151–4177
- Wiens KC, Hamlin T, Harlin J, Suszczynsky DM (2008) Relationships among narrow bipolar events, “total” lightning, and radar-inferred convective strength in Summer 2005 Great Plains thunderstorms. *J Geophys Res* 113(D05201), DOI 10.1029/2007JD009400
- Willett JC, Krider EP (2000) Rise times of impulsive high-current processes in cloud-to-ground lightning. *IEEE Trans Ant Prop* 48(9):1442–1451
- Willett JC, Bailey JC, Krider EP (1989) A class of unusual lightning electric field waveforms with very strong high-frequency radiation. *J Geophys Res* 94:16255–16267
- Willett JC, Bailey JC, Leteinturier C, Krider EP (1990) Lightning electromagnetic radiation field spectra in the interval from 0.2 to 20 MHz. *J Geophys Res* 95(D12):20367–20387
- Willett JC, Krider EP, Leteinturier C (1998) Submicrosecond field variations during the onset of first return strokes in cloud-to-ground lightning. *J Geophys Res* 103(D8):9027–9034
- Williams ER, Boldi B, Matlin A, Weber M, Hodanish S, Sharp D, Goodman S, Raghaven R, Buechler D (1999) The behavior of total lightning activity in severe Florida thunderstorms. *Atmos Res* 51:245–264

Chapter 14

Lightning Measurements from Satellites and Significance for Storms in the Mediterranean

Claudia Adamo, Steve Goodman, Alberto Mugnai and James A. Weinman

Abstract In this chapter we demonstrate how lightning can be measured from space, and how thunderstorm clouds can be identified and characterized by using combinations of satellite data. This is done over the Southern Mediterranean area using concurrent measurements taken by the Lightning Imaging Sensor (LIS), the Precipitation Radar (PR), and the TRMM Microwave Imager (TMI) onboard the Tropical Rainfall Measuring Mission (TRMM) space observatory. Modeling and observational studies indicate that cloud electrification and microphysics are very closely related. Using lightning data obtained from satellites, we can extract quantitative relationships between microphysical characteristics and lightning flash rates. This is of great interest for future work: for nowcasting of thunderstorms, and for introducing lightning observations into mesoscale forecast models.

Keywords Lightning · Storm Characteristics · Tropical Rainfall Measuring Mission · Southern Mediterranean

14.1 How Lightning can be Measured from Space

The Lightning Imaging Sensor (LIS) developed by NASA's Marshall Space Flight Center (MSFC) for the Earth Observing System (EOS) is the only satellite lightning sensor designed to map global lightning activity with storm scale resolution (4 km) continuously day and night. LIS was launched in 1997 aboard the NASA/JAXA Tropical Rainfall Measuring Mission (TRMM) satellite at an altitude of 350 km. In August 2001 the satellite orbit was boosted to 402 km to extend the mission's life. The LIS data are available from the Global Hydrology Resource Center (GHRC) in Huntsville, Alabama, USA and from the instrument team Web site: (<http://thunder.msfc.nasa.gov/>). To date more than 300 researchers in 30 countries have used the LIS/OTD data in their research.

C. Adamo (✉)

Institute of Atmospheric Sciences and Climate, Italian National Research Council, Roma, Italy
e-mail: c.adamo@isac.cnr.it

The predecessor of LIS, the Optical Transient Detector (OTD), was also developed by NASA MSFC. The OTD, the engineering prototype for LIS, was launched in 1995 aboard the MicroLab-1 satellite into a 70° inclination low Earth orbit at an altitude of 740 km. The instrument had a spatial resolution of 8 km at nadir and a total field of view of 1300 km × 1300 km. As with LIS, the OTD detected the frame-to-frame transient changes in an optical scene which indicated the occurrence of lightning transients, under daytime conditions as well as at night. OTD provided much higher detection efficiency and spatial resolution than has been attained by earlier lightning sensors (Goodman and Christian, 1993). If OTD represents the near past, LIS is the present state of the science; so we now describe it in some detail (see also the Chapter 12 by Finke in this Volume).

LIS is also an optical sensor that detects lightning by looking for small changes in light intensity. It is capable of recognizing the presence of lightning (both intra-cloud and cloud to ground) during daylight hours (Christian et al., 1999; Christian, 1999). The LIS retrieves lightning by recording optical pulses in the near infrared. This lightning sensor consists of a staring imager which is optimized to locate and detect lightning with storm-scale resolution (4–7 km) over a large region (600 × 600 km) of the Earth's surface. The TRMM satellite travels at a ground speed of 7 km/s as it orbits the Earth, thus allowing the LIS to observe a point on the Earth or a cloud for almost 90 seconds as it passes overhead. Despite the brief duration of an observation, it is long enough to estimate the flash rate of many storms. The instrument records the time of occurrence, measures the radiant energy, and determines the location of lightning events within its field-of-view. As mentioned, cloud-to-cloud, in-cloud and cloud-to-ground flashes are recorded, but no distinction can be made between these using the optical characteristics of lightning alone. Because LIS measures slight variations in the background light intensity, these individual variations are recorded as events. If several events occur during the same 2 ms time frame and if they are also adjacent to each other, the events are bunched together to form a group. Groups that are temporally and spatially close to each other are considered to constitute a lightning flash. So, each lightning flash can be composed of many groups and up to several hundred/thousand individual events. LIS uses a wide field-of-view expanded optics lens with a narrow-band filter in conjunction with a high speed charge-coupled device detection array. The Real Time Event Processor (RTEP), inside the electronics unit, is used to determine when a lightning flash occurs, even in the presence of bright sunlit clouds. Weak lightning signals that occur during the day are hard to detect because of the background illumination. The RTEP removes the background signal, thus enabling the system to detect weak lightning and achieve 90% detection efficiency (Christian et al., 1999).

The next frontier will be the mapping of lightning from geostationary orbit with storm scale resolution. The Geostationary Lightning Mapper (GLM) will detect, locate and measure total lightning activity with nearly uniform spatial resolution of 8–12 km over the full disk as part of a 3-axis stabilized, geostationary weather satellite system (Goodman et al., 2008). The next generation NOAA

Geostationary Operational Environmental Satellite (GOES-R) series with a planned launch in December 2014 will carry a GLM that will provide continuous day and night observations of lightning from the west coast of Africa (GOES-E) to New Zealand (GOES-W) when the constellation is fully operational.

The mission objectives for the GLM are to: (1) provide continuous, full-disk lightning measurements for storm warning and nowcasting, (2) provide early warning of tornadic activity, and (3) accumulate a long-term database to track decadal changes of lightning. The GLM owes its heritage to the Lightning Imaging Sensor (1997–Present) and to the Optical Transient Detector (1995–2000).

A lightning imager is also planned as part of the sensor complement of China's FY-4 geostationary satellite. According to the China Meteorological Administration (CMA), FY-4 will be a three-axis stabilized geostationary satellite as opposed to the spin-stabilized satellites of the FY-2 series. Like its sister craft FY-3, FY-4 will carry multiple payloads on board. EUMETSAT is also reviewing requirements and implementation options for lightning observations for the Meteosat Third Generation (MTG) satellite. A formulation study to assess the feasibility of a satellite lightning mission among others was conducted and the potential role of ground-based observations to meet requirements was being assessed.

14.2 Use of Lightning Observations from Space

Satellite lightning data are related to other physical variables or parameters used in atmospheric research and they are useful for weather forecasting, providing water content profiles and cloud microphysical properties. In the next part of the chapter we will show how lightning data from satellites can be used. For example, we use the thunderstorm occurrence in the Southern Mediterranean Region (Fig. 14.1) for reasons that we will now explain. First, European convective systems (isolated and organized convection) show new features that differ from the better known systems in the U.S. and in the tropics. The relationships between lightning occurrence and precipitation and/or upwelling microwave/infrared brightness temperatures (T_B 's) are not valid everywhere in the world. For example, relationships found by other authors (Alexander et al., 1999; Chang et al., 2001; Cecil et al., 2005) are not valid over the Mediterranean Basin, in which the convection is less intense than in the places where those prior studies were conducted. Another reason is that the Mediterranean Sea represents one of the major centres of winter electrical activity in the Northern Hemisphere as seen by Orville and Henderson (1986) and Christian et al. (1999, 2003). A further consideration is that the majority of the Mediterranean islands and the North Africa territories have no radars available. Thus, the ground based data techniques used in other parts of the world for studying thunderstorms, are unavailable over much of the Southern Mediterranean Region. Satellite data provide an opportunity to measure lightning at any point on the globe with uniform quality.

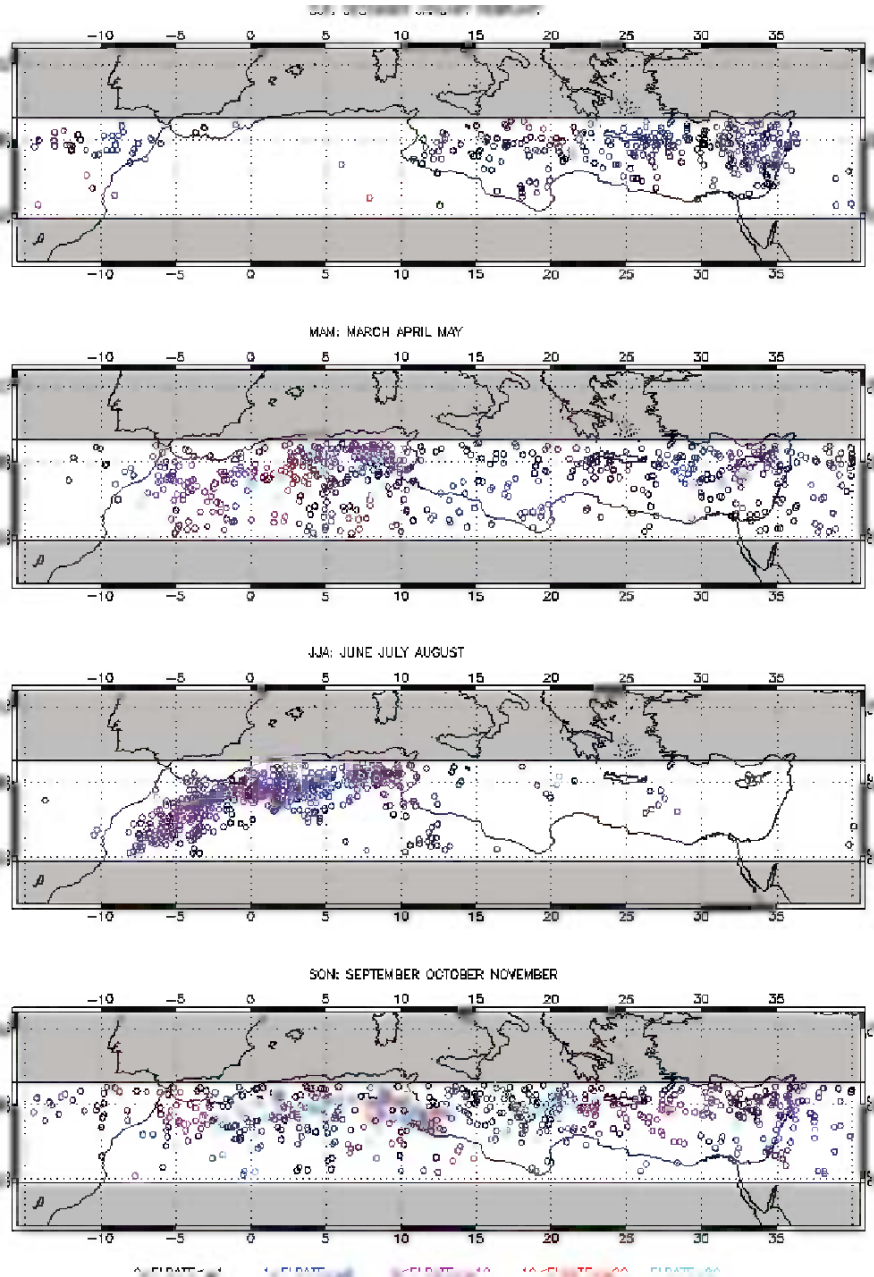


Fig. 14.1 Maps of lightning producing storms in the Mediterranean basin, during a 3-year period for the different seasons. Colours indicate the category of lightning occurrence within the precipitation features: *black* (I), *blue* (II), *fuchsia* (III), *red* (IV), *light blue* (V)

14.2.1 The Precipitation Feature Database

Lightning satellite data, measured by LIS, can be used and compared with many other types of data. One can compare such lightning data with measurements taken by other satellite sensors – such as microwave T_B 's measured by the Special Sensor Microwave/Imager (SSM/I) on board Defense Meteorological Satellite Program (DMSP) satellites, or infrared T_B 's measured by Meteosat or GOES. In these cases, the spatial and temporal concurrence between different sensors providing unique information from multiple satellites is valuable, yet infrequent. For geostationary satellites, the data are refreshed every 15 minutes and often this time is too large to be compared with highly variable lightning flash rates. On the other hand, LIS data are useful and can be compared with data from ground-based lightning observing instruments (e.g., Thomas et al., 2000). In this case, it is important to be aware that lightning data acquired from space or by ground-based sensors are measured at very different frequencies, and therefore do not sense the same component process of the lightning flash.

Thus, the best way to use LIS data is together with the other sensors on board the TRMM satellite. The LIS, the Precipitation Radar (PR) and the TRMM Microwave Imager (TMI) have been combined together to yield concurrent information about each storm observed by the satellite. These databases were developed at the University of Utah (Nesbitt and Zipser, 2003), using the Nesbitt et al. (2000) algorithm. We briefly summarize the characteristics of the other TRMM instruments and the techniques used for combining these data with LIS data.

The Precipitation Radar is the first space-borne rain radar (13.8 GHz) and the only instrument on TRMM platform directly providing vertical precipitation profiles. The measurements yield information on the intensity, distribution, and type of precipitation, storm depth, and the height at which snow melts into rain. PR has a horizontal resolution at the ground of about 4 km and a swath width of 220 km (Iguchi et al., 2000).

The TRMM Microwave Imager is a passive microwave radiometer that measures the intensity of radiation at five separate frequencies (10.7, 19.4, 21.3, 37, 85.5 GHz). Because 85 GHz and 37 GHz channels are more related to convection and high iced top cloud systems, those are of particular interest to this study. Their spatial resolutions are 7×5 km and 16×9 km, respectively (Kummerow et al., 1998, 2000).

The University of Utah precipitation feature database has been used in previous studies by Nesbitt et al. (2000) and Cecil et al. (2002a, 2002b, 2005), and more recently by Zipser et al. (2006) for analysis of hurricanes, global lightning, and extreme storm distributions. It is an on-going data source that commenced in December 1997. The precipitation features (PFs) are contiguous areas within the TRMM PR swath, larger than 4 PR pixels in size and containing either PR near-surface reflectivity greater than 20 dBZ or collocated TMI 85 GHz PCT (Polarization Corrected Temperature) of 250 K or less. The minimum size for one of these features (one with only four pixels) is 75 km^2 . The database associates each PF with: the corresponding total LIS flash rate within the PF, the corresponding PR profile

containing the maximum value of reflectivity for each single altitude level within the PF, the maximum PR reflectivity at 6 and 9 km, the volumetric rain and number of pixels in the PF, and many others parameters like size, minimum 85 GHz PCT, minimum 37 GHz PCT, maximum reflectivity at each height interval, lightning flash count, in order to assess size or convective intensity of that precipitation feature.

For this study we have used the first three years of the PF database (i.e., December 1997 through November 2000). At that time, TRMM covered only that part of the Mediterranean Basin (up to 35° N latitude). Therefore, we have analyzed a box that is limited between 30° – 35° N in latitude and between 15° W and 40° E in longitude. Noteworthy, since August 2001 the TRMM satellite has been covering a slightly larger portion of the Mediterranean Sea because of the orbit boost to 402 km. In Section 14.3 we will use the autumn database to compare thunderstorms with lightning to storms without lightning because this season is the most intense flash flood period for the target area, as we will see in the next section.

14.3 Analysis of Mediterranean Database

In the selected Mediterranean area, in the three year period there are 3400 precipitation features in summer, 13957 in spring, 12782 in autumn and 25341 in winter. Of these, only less than 5% are associated with lightning. Yet, the global percentage of lightning producing storms is lower. Cecil et al. (2005) analyzed the same database at the global scale and found that lightning producing storms are only 2% of the total number of storms. This is probably due to the fact that global analysis contains a large number of weaker storms over water that are considerably less likely to produce lightning than are comparable storms over land – according to Christian et al. (1999) who estimated that only 18% of the detected lightning occurred over oceans. We now compare global results with the characteristics of the Mediterranean database to determine how Mediterranean thunderstorms differ with respect to the strongest events that are recorded.

While the greatest observed flash rate for the global database was produced by a mesoscale convective system in Argentina having $1351 \text{ flashes min}^{-1}$ (Cecil et al., 2005), in the Mediterranean area the first and second greatest flash rates are just about $300 \text{ flashes min}^{-1}$ and $160 \text{ flashes min}^{-1}$ – i.e., average/normal values for lightning activity during summer thunderstorms in a tropical area (Christian et al., 2003) are comparable to maximum values characterizing severe events in the Mediterranean region. Correspondingly, the lowest brightness temperatures observed during 3-year period within the global database, are 42 K at 85 GHz and 69 K at 37 GHz, while in the Mediterranean basin we find minimum T_B 's of 70.3 K at 85 GHz and 115.8 K at 37 GHz, both in autumn.

From the global database, the largest precipitation features cover 335.000 km^2 and the greatest rainfall from an individual precipitation feature exceeds $2 \times 10^{12} \text{ kg}$ of water. In contrast, the largest thunderstorm complex recorded by the TRMM satellite over the Mediterranean basin, which occurred during the winter season, had an areal extent of about 95.000 km^2 . The maximum amount of precipitation

measured during these three years over the Mediterranean was 2×10^9 kg and also occurred during winter. It is clear that the nature of regional Mediterranean thunderstorm activity and the related lightning occurrence represents an undistinguished, yet interesting subset of storm characteristics with respect to other parts of the World, and should be analyzed separately in greater detail to find new and appropriate relations.

14.3.1 Seasonal Analysis

A preliminary analysis illustrates that during winter, lightning producing thunderstorms (PFs with flash rate value greater than zero) comprise only 2% of the total number of PFs, reaching a maximum of 17% in the summer and approximately 5% in autumn and spring (see first row of Table 14.1). However, an important result of this analysis is that the rainstorms with lightning produce large amounts of rain. Storms with lightning, depending on season, produce up to 70% of the total seasonal rain in summer, 56% in autumn, 46% in the spring, and 32% in winter.

Then, for each season we separated all precipitation features that are characterized by lightning activity, into five distinct categories based on the flash rates they produced, with values ranging from less than 1 flash min^{-1} km^{-2} to flash rates in excess of 20 flashes min^{-1} km^{-2} (see second to sixth rows of Table 14.1). The Mediterranean area has a lower flash rate than corresponding latitudes in the western hemisphere (Boccippio et al., 2000; Christian et al., 2003). As shown in Table 14.1, the highest flash rate category with more than 20 flashes min^{-1} km^{-2} (category V) occurs infrequently, ranging from 1% to about 11.3% depending on the season. In contrast, during 3 years of observations there are many small thunderstorms having flash rates less than 1 min^{-1} km^{-2} (category I). During winter, for instance, these represent 44% of the lightning producing storms, while only 15.6% of Mediterranean thunderstorms have more than 5 flash min^{-1} km^{-2} and the strongest thunderstorms have only 1.1% frequency of occurrence.

For the other seasons, category II is the most common. Noteworthy, the largest value for the highest category (V) is found in autumn – a season which is characterized by devastating flash floods along the Mediterranean coasts. In addition, we

Table 14.1 Percentage of precipitation features (PFs) showing lightning (first row) for different seasons [winter (DJF), spring (MAM), summer (JJA), and autumn (SON)], and seasonal percent distribution of these lightning producing storms (second to sixth rows) within five different categories of lightning flash rate (FL) (flashes min^{-1} km^{-2})

	Category	DJF	MAM	JJA	SON
% PF with lightning (FL > 0)		2.3	5.3	17	5.5
% PF with $0 < \text{FL} \leq 1$	I	44.4	34.8	37	33.8
% PF with $1 < \text{FL} \leq 5$	II	40	38.5	41.9	34.9
% PF with $5 < \text{FL} \leq 10$	III	9.2	12.6	11.8	10.8
% PF with $10 < \text{FL} \leq 20$	IV	5.3	8.1	6.2	9.2
% PF with $\text{FL} > 20$	V	1.1	6	3.1	11.3

found that in autumn the percentage (31.3%) of high flash rate storms (categories III-V) is approximately the same as that for low (category I: 33.8 %) and medium (category II: 34.9%) flash rate storms. In contrast, for the other seasons the high flash rate storms are considerably less frequent. It is remarkable that lightning occurrence is a natural proxy for intense events, since lightning producing storms occur in only 5% of autumn rainstorms, yet they produce 56% of the total rain.

14.3.2 Geographical Analysis

We now consider Fig. 14.1 that shows the spatial distribution of the analyzed thunderstorms during the different seasons. Obviously, during the winter season there are thunderstorms only over the sea, while during summer they are nearly all over land; for spring and autumn periods, they are in both. This is because summer thunderstorms are often connected to strong convection over land, while winter thunderstorms are maritime events with weaker updrafts and as a result are less electrified; for autumn and spring, the trend is not so well definite. This is consistent with the published results of Holt et al. (2001).

The other main factor is the orographic effect. During the summer the Atlas Mountains become very important for initiating convection. The hot and dry air from the desert rises in the presence of these mountains and, in concert with the sea breeze, advects moisture over land and provides prime conditions for convection initiation. The temperature difference between the desert and the coasts is at a maximum during the summer, but is also significant during spring and autumn – thus, the origin of the storms is similar. During winter the mechanism is reversed with the desert very cold and a weaker temperature gradient. As a consequence, during winter there is little lightning over land and instability is greatest over the water – i.e., storms are weak and are confined mostly to the first two categories of flash rates.

14.4 Relationships between Lightning and Cloud Parameters

14.4.1 Lightning and Radar Reflectivity Measurements

The Precipitation Radar measurements have been analyzed so as to obtain the average radar profiles that are associated with the five different categories of lightning producing storms. Results are shown in Fig. 14.2 for the four different seasons. Obviously, the various storm categories are characterized by distinct average reflectivity profiles. Specifically, in all cases the average radar reflectivity gradually decreases with altitude (or temperature), and steadily increases at all altitudes (or temperatures) when the flash rate of the thunderstorms increases – excepting only the two higher categories during winter, which show similar or even reversed profiles. In addition, there is a clear seasonal dependence. At any altitude, the differences between any two contiguous flash-rate categories or the seasonal differences

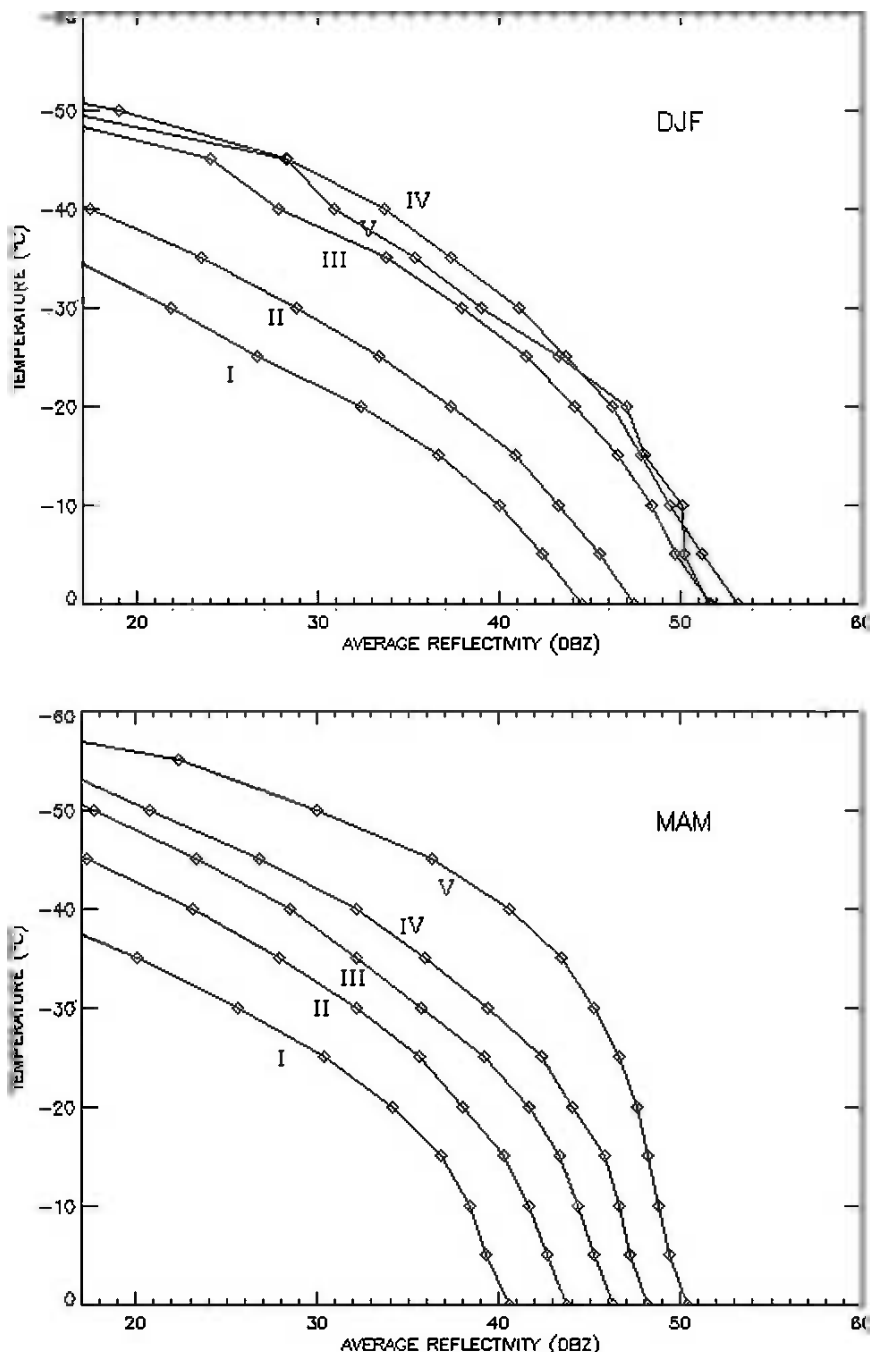


Fig. 14.2 Average PR reflectivity profiles above the freezing level for the five different categories of thunderstorms. The four panels refer to the four seasons – winter (DJF), spring (MAM), summer (JJA) and autumn (SON)

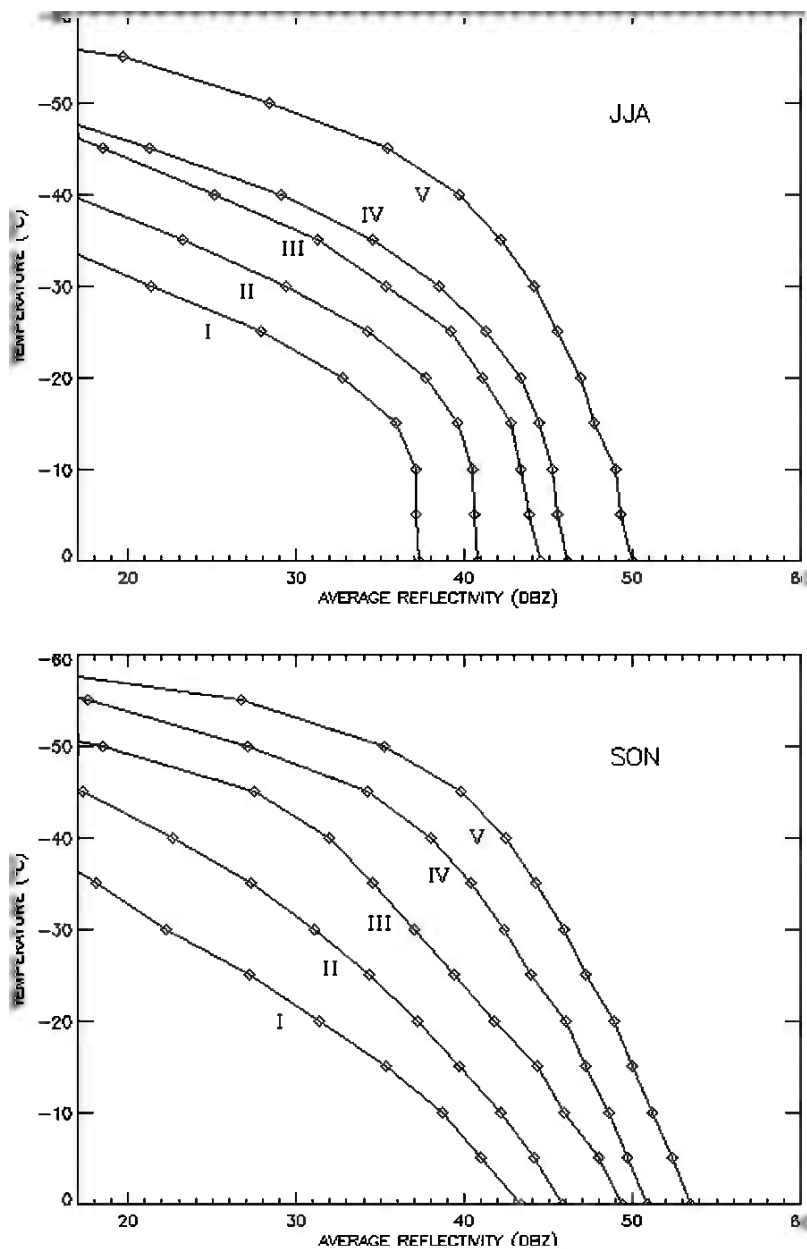


Fig. 14.2 (continued)

for any given category can vary from a few dBZ up to almost 10 dBZ. Noteworthy, in autumn the reflectivity profiles exhibit the highest values aloft for all categories. Also, note that PR sensitivity excludes reflectivity measurements lower than 17 dBZ.

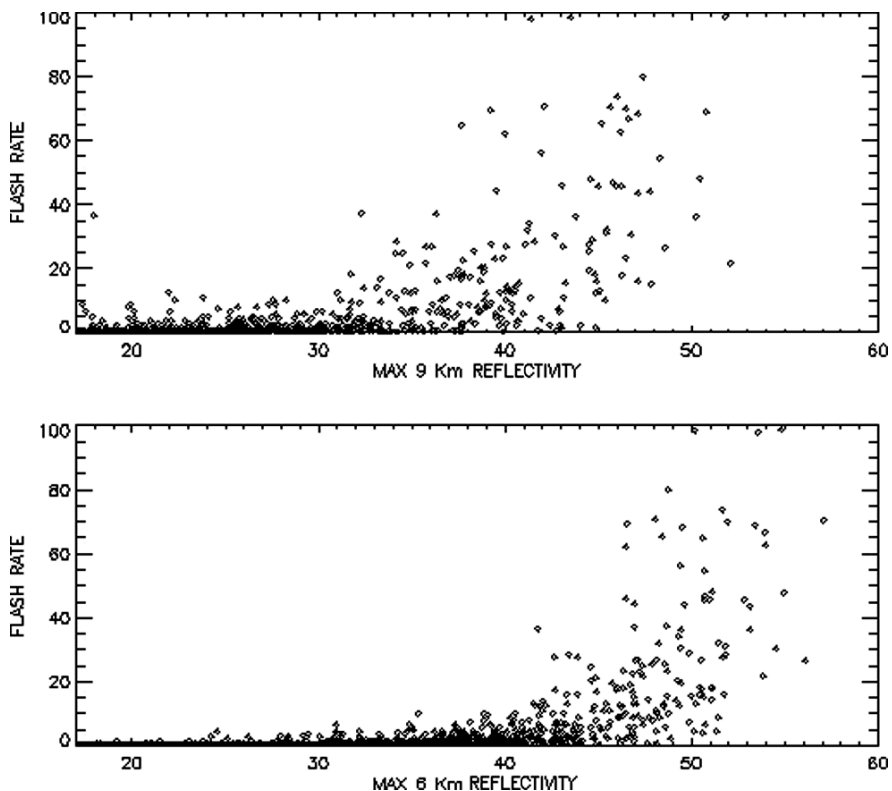


Fig. 14.3 Flash rate as a function of the maximum PR reflectivity at 9 km (*upper panel*) and at 6 km (*lower panel*) for all autumnal precipitation features

Given the importance of strong updrafts and large amounts of precipitation-sized ice particles for enhanced lightning production, we have analyzed the relationships between the radar reflectivity in the upper portions of the clouds and the occurrence of lightning. Results are shown in Fig. 14.3 for the autumn season as flash rates of all precipitation features vs. maximum PR reflectivities at 6 and 9 km. It is quite evident that at both altitudes, flash occurrence tends rapidly to increase as the reflectivity exceeds a threshold value – which is about 40 dBZ at 6 km and about 30 dBZ at 9 km. As a result, the larger reflectivity values are only observed for those thunderstorms that produce a large amount of lightning; specifically, the highest flash rates (above 40 flashes min^{-1}) are found for reflectivity values above about 35 and 45 dBZ at 9 and 6 km, respectively.

In order to derive quantitative relationships between flash rate and radar reflectivity, we show in Fig. 14.4 the maximum average reflectivity at 9 km vs. the autumn flash rates for the five categories of lightning producing storms. It turns out that the fitting curve of Fig. 14.4 can be represented by the following relationship, which may be useful to derive information on presence and amount of precipitation-sized ice particles aloft from lightning measurements in the absence of direct radar observations:

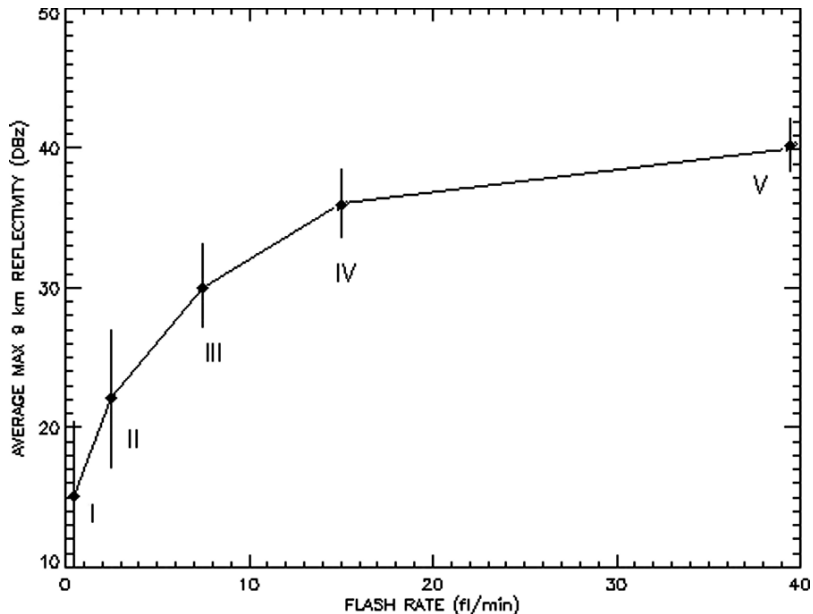


Fig. 14.4 Average values and standard deviations of the maximum PR reflectivity at 9 km as a function of flash rate for the five categories of lightning producing storms in autumn

$$\text{Reflectivity(dBZ)} = 1 + 25 \log (\text{Flash Rate})$$

We have found a similar relationship for the average PR reflectivity at 6 km; this, however, is not as well characterized as it is at 9 km because storms without any lightning may have a considerable reflectivity at 6 km, but none at 9 km.

14.4.2 Lightning and Precipitation

Precipitation is an extremely important variable in the climate system, and one that is very difficult to measure over large regions of the globe. The correlation between lightning frequency and the amount of precipitation has been analyzed by Petersen and Rutledge (2001). They found that the relationship between the measured water amount in kg and the lightning frequency varied by three orders of magnitude for a variety of events within the same region. Other studies (Sheridan et al., 1997; Tapia et al., 1998) observed the daily accumulated rain amount over very large regions and the corresponding lightning. Cheze and Sauvageot (1997) developed relationships for the accumulated rainfall as a function of lightning activity in an area of 40.000 km² during 15-minute intervals.

From analyses of individual storms, Buechler and Goodman (1990) found a good correlation between increasing flash rate and increasing rain flux. Nevertheless, Rutledge et al. (1992) in a comparison between precipitation and cloud-to-ground

lightning for continental and monsoon storms, found that while continental and monsoon storms had similar total precipitation yields, the total number of cloud-to-ground lightning flashes differed by an order of magnitude. Thus, the correlation between precipitation rate and cloud-to-ground lightning flash rate depends on the type of cloud system. Numerical model results (Solomon and Baker, 1998) show that when the flash rate increases the rain rate also increases, but there are some cases in which heavily raining clouds do not produce much if any lightning. It is thus difficult to find a “universal” relationship between instantaneous lightning flash rate and rain rate; as a consequence, the use of lightning flash rate as a surrogate for precipitation rate on a storm-by-storm basis requires care.

We now approach this problem for Mediterranean storms by relating flash rate and amount of rain, as it is measured by PR, for each single thunderstorm of the PF database. Results are shown in Fig. 14.5, where the flash rate is plotted vs. the total amount of volumetric rain ($\text{mm hr}^{-1} \text{ km}^{-2}$) for all autumnal PFs. In spite of the large scatter, there is an overall trend for which lightning occurrence tends to increase as volumetric rain increases.

Thus, we have computed the average values of the rain rate and of the total volumetric rain for the five categories of lightning producing storms during the 3-year period. Results are shown in Fig. 14.6 for the four different seasons. Both the volumetric rain and the rain rate (which is computed by dividing the total volumetric rain by the PF area) steadily increase with increasing flash rate for all seasons. In addition, the seasonal curves are usually well separated from each other – the main exception being the average rain rates for the three higher PF categories during spring and summer. However, the seasonal dependence is reversed for the two rain quantities. While the volumetric rain is usually minimum in summer and is (by far) largest for all categories in winter, the largest rain rates occur during spring and summer and the lowest ones in winter. This is because in winter, there are fewer deeply convective storms and many more precipitation events that are characterized by shallow convection and by large horizontal extents. Again, these results may be useful to infer average precipitation information from lightning measurements in the absence of direct rain measurements.

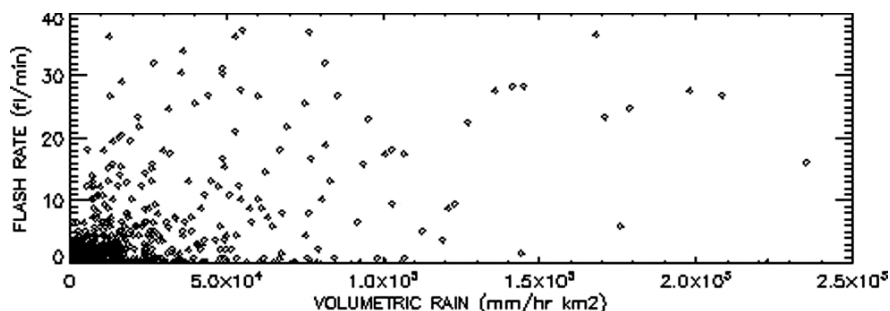


Fig. 14.5 Flash rate as a function of total volumetric rain for all autumnal precipitation features

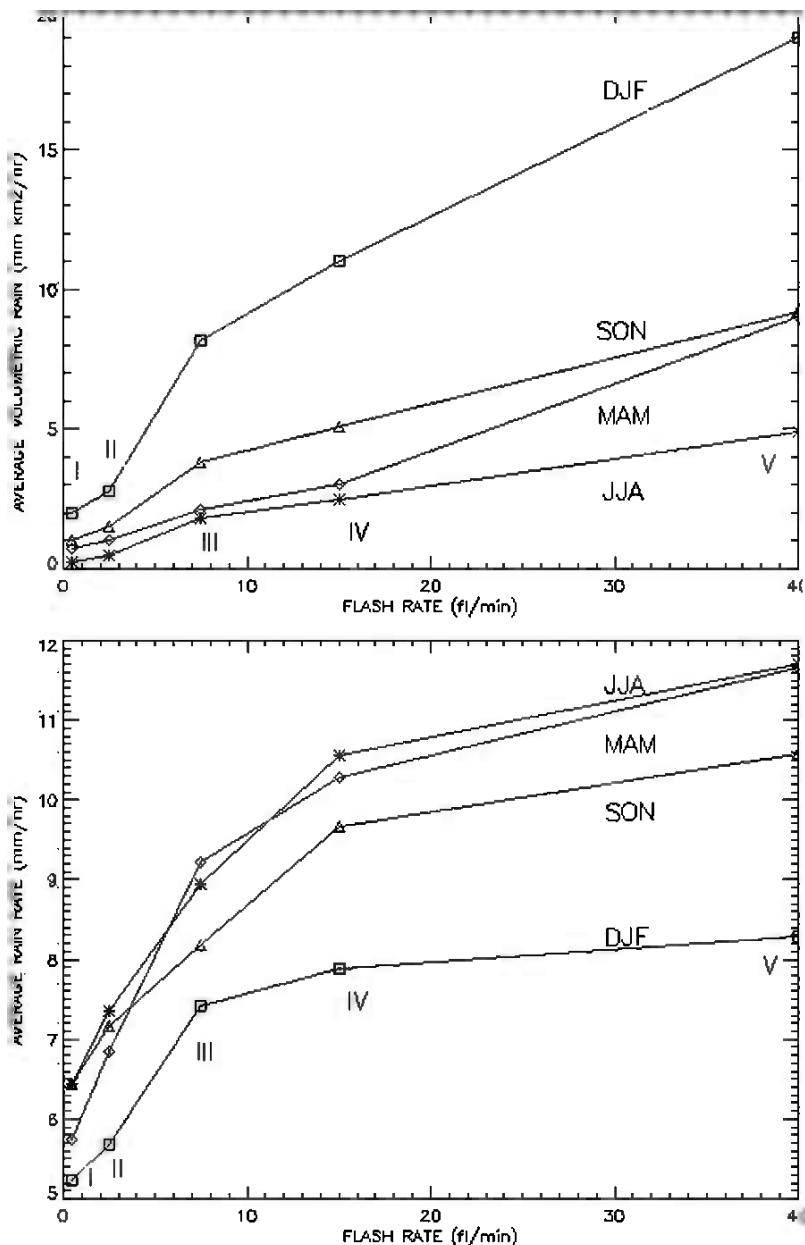


Fig. 14.6 Average values of total volumetric rain (upper panel – values $\times 10^4$) and rain rate (lower panel) as a function of flash rate for the five categories of lightning producing storms and for the four different seasons

14.4.3 Lightning and Passive Microwave Measurements

Physical reasons suggest a connection between the upwelling microwave brightness temperatures (T_B 's) at the higher frequencies (85 GHz and 37 GHz, for TMI & SSM/I) and lightning. High lightning flash rates are possible only in the presence of high concentrations of large and small ice particles and of supercooled water (Illingworth, 1985). Strong convective updrafts are also necessary to generate the requisite ice size distributions and densities for large flash rates (Keighton et al., 1991). Thus, lightning occurrence is elevated in intense convective events, where large quantities of graupel and ice particles are present in the charging zone and the strong updrafts are capable to suspend large graupel particles within the charging zone itself for extended periods of time (Takahashi, 1978; Jayaratne, 1983; Saunders, 1994; Baker et al., 1995). As shown by several model sensitivity studies (e.g. Smith et al., 1992; Mugnai et al., 1993), these hydrometeors have a primary impact on the upwelling T_B 's at 85 GHz and also at 37 GHz, that may be significantly "cooled" from scattering by large ice particles. As a matter of fact, Mohr et al. (1996) have found intense lightning in areas with SSM/I T_B 's at 85 GHz lower than 180 K.

Here, we have found it more convenient to consider the polarization corrected brightness temperatures (PCTs) (Spencer et al., 1989) rather than the brightness temperatures themselves, because the PCTs are useful to discriminate between land and sea – which is particularly important in the present study because the target zone is composed of sea, coasts and land. The relationships between lightning occurrence and the corresponding PCTs at 85 GHz and 37 GHz that have been measured by the TMI microwave radiometer during the 3-year period, have been examined using a similar methodology than that applied in Section 14.3.1 to PR measurements.

Thus, Fig. 14.7 shows the flash rates of all autumnal precipitation features vs. the minimum PCTs at 37 and 85 GHz. Obviously, precipitation events with lightning tend to have lower PCT values at both frequencies than events with no lightning. Specifically, flash occurrence tends rapidly to increase as the PCT becomes lower than a threshold value – which is about 270 K at 37 GHz and about 210 K at 85 GHz. As a result, the lower PCTs are only observed for those thunderstorms that produce a large amount of lightning; in particular, the highest flash rates (above 40 flashes min^{-1}) are found for PCT values below about 170 and 250 K at 85 and 37 GHz, respectively.

Then, we have examined the average values of the PCTs at 37 and 85 GHz for the five categories of lightning producing storms during the 3-year period. Results are shown in Fig. 14.8 for the four different seasons. In all cases, the 37 GHz PCT is significantly higher (50–100 K, depending on season and flash rate) than the corresponding PCT at 85 GHz. In addition, the PCT steadily decreases with increasing flash rate – with the 37 GHz PCT decreasing less than the 85 GHz PCT. For instance, at 85 GHz the PCT decreases as much as 40–50 K in all seasons when the flash rate increases from a few flashes min^{-1} to about 10 flashes min^{-1} ; in contrast, the corresponding 37 GHz PCT decreases only 20–30 K. Noteworthy, at both frequencies, spring and summer PCT seasonal curves are quite similar, and so are the PCT seasonal curves for autumn and winter. Also, the 85/37 GHz PCT ratio

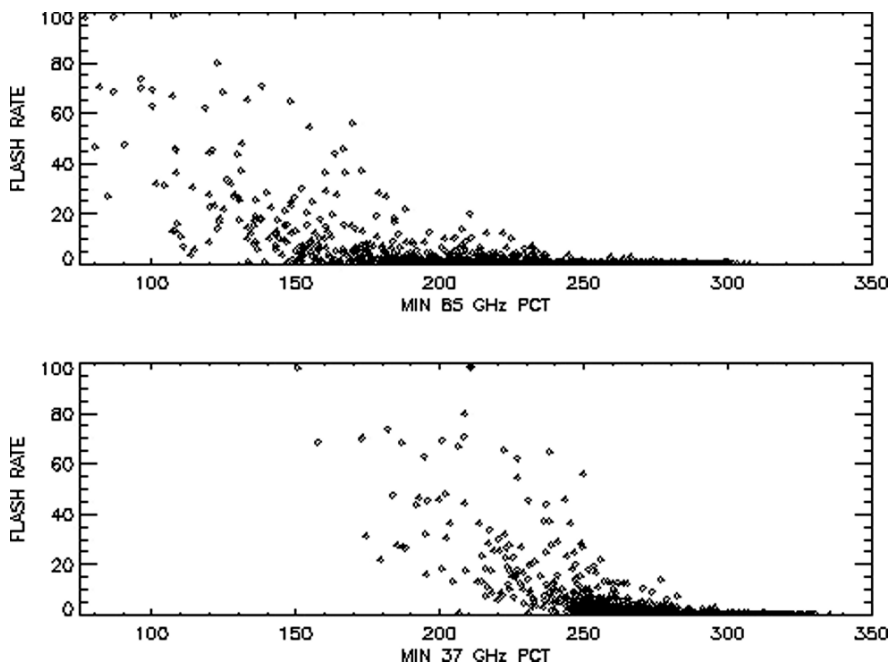


Fig. 14.7 Flash rate as a function of the of the minimum PCT at 85 GHz (*upper panel*) and at 37 GHz (*lower panel*) for all autumnal precipitation features

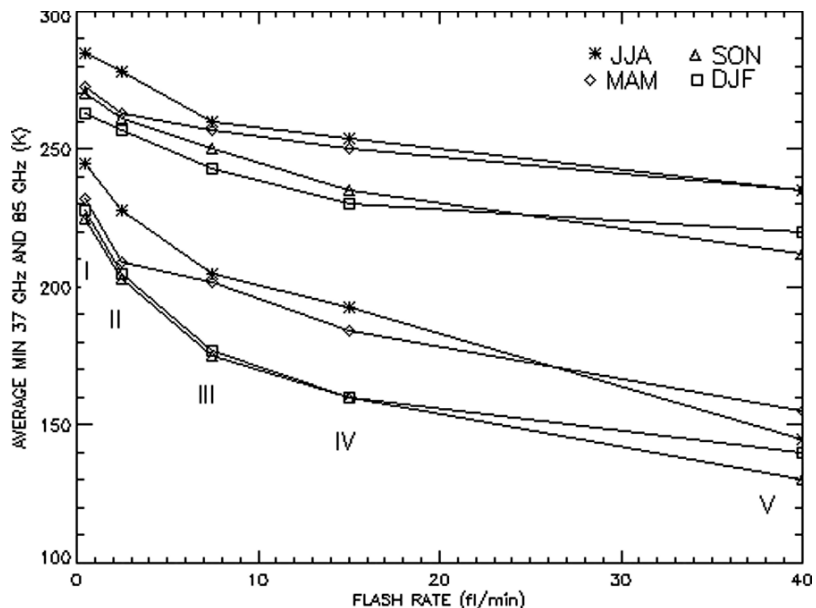


Fig. 14.8 Seasonal average values of the polarization corrected brightness temperature (PCT) at 37 GHz (*upper four lines*) and at 85 GHz (*lower four lines*) as a function of flash rate for the five categories of lightning producing storms

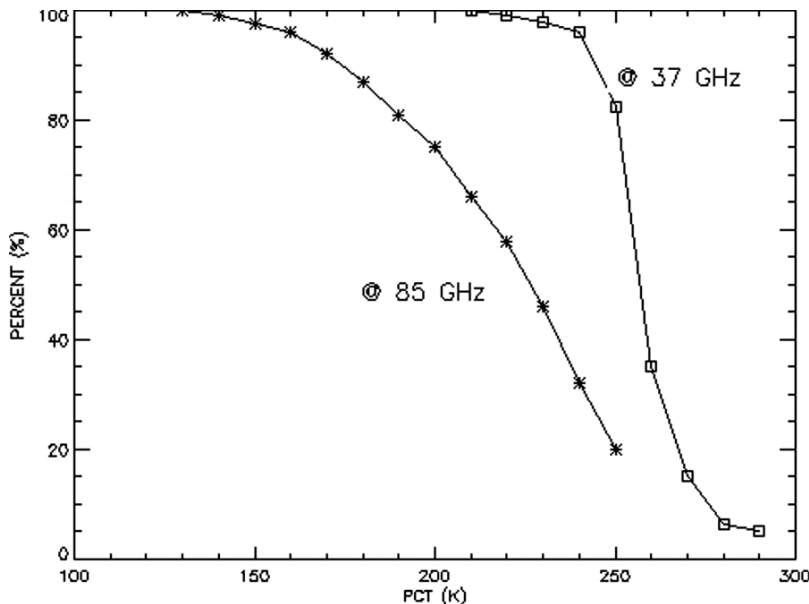


Fig. 14.9 Percent number of thunderstorms that produce lightning w.r.t the total number of precipitation features as a function of the minimum PCT values at 37 and 85 GHz

is much more dependent on flash rate rather than on season – depending on season, it decreases from 0.86–0.88 for category I to 0.62–0.66 for category V.

Finally, Fig. 14.9 shows the percent probability for a storm to produce lightning as a function of the PCTs at 85 and 37 GHz. It turns out that the 37 GHz PCT is more suitable to be used as a threshold – namely, it has to be less than about 250 K to have a high (at least, 80%) lightning probability, while lightning occurrence is rather unlikely (less than 20%) when the 37 GHz PCT is larger than about 260 K. On the other hand, the 85 GHz PCT is more suitable for inferring the lightning probability – namely, the probability of lightning gradually increases from about 20% to about 90% when the 85 GHz PCT decreases from about 250 K to about 170 K. Therefore, we can conclude that all results of Fig. 14.8 and 14.9 may help inferring lightning activity from passive microwave measurements from space.

14.5 Conclusions

By analyzing the precipitation feature database that was developed at the University of Utah using concurrent observations of the LIS, PR, and TMI instruments onboard TRMM for a 3-year period (December 1997 through November 2000), we find that for all seasons in the southern Mediterranean region, lightning producing storms (which account for between 2% to 17% of all precipitating clouds, depending on

season) are responsible for 32% of winter precipitation and as much as 70% of summer precipitation.

Clearly, lightning producing storms must be closely monitored, especially when extreme precipitation events may occur. Thus, the marked relationships between different flash rate regimes and the vertical PR profiles can be useful in determining cloud properties when lightning data are available and there are no radar and/or other remote sensing data. We also find thresholds of PCT at microwave frequencies that are associated with different lightning rate occurrences.

Specifically, this study helps us to select at least 20 reflectivity profiles to associate with a thunderstorm, based on the flash rate and on the period of the year in which the thunderstorm occurs. This information can be expanded to better understand the thunderstorm characteristics in the Southern Mediterranean region when we have no other observations. For instance, knowing the storm flash rate, we can estimate the rain rate (and the associated uncertainty) and the minimum PCT values at 85 GHz and 37 GHz. Given the occurrence of lightning we can also distinguish between a stratiform and a convective cloud, and describe how they differ. For example, in the Mediterranean area, an autumnal thunderstorm that produces more than 20 flashes min^{-1} can be associated, via this study, with the following characteristics:

- convective average reflectivity profile with values greater than 50 dBZ around the freezing level, and very well developed in altitude (see Fig. 14.2, category V);
- average value of maximum 9 km reflectivity near 40dBz ($\pm 3\text{dBZ}$) (see Fig. 14.4);
- average rain rate values near 10.5 mm/hr ($\pm 3.3 \text{ mm/hr}$) (see Fig. 14.6);
- minimum 85 GHz PCT near 130 K ($\pm 25 \text{ K}$) and 37 GHz PCT of about 215 K ($\pm 21 \text{ K}$) (see Fig. 14.8).

Also, we have shown that lightning flash rates are strongly related to the reflectivity (especially at 9 km). In addition, lightning can be used to infer precipitation when other observations are missing. For this application, the relationships between lightning and microwave is potentially very useful. When the microwave data are available every 3 hours and lightning data can be measured continuously, a transfer function can be developed to relate the two observables. This is the essence of using lightning as a proxy for a geostationary 85 GHz channel. This multi-sensor blended algorithm approach is attractive given that no weather radar in geostationary orbit is foreseeable in the near future.

Therefore, lightning provides information about strongly convective storms similar to a space-borne radar, but it can be measured continuously. It has to be emphasized that the advantage of the satellite perspective is enormous because there is the capability of registering intra-cloud flashes. In such a context, the geostationary satellite perspective has the advantage to provide more information. NOAA's Geostationary Lightning Mapper (GLM) on the next series of geostationary environmental satellites will offer such a capability after 2014.

The GLM will be capable of detecting and locating all lightning (cloud-to-ground and intra-cloud discharges) with nearly uniform (8–12 km) spatial resolution over the full disk with a detection efficiency (i.e., detect and locate all lightning with

a storm-scale resolution over large areas of the Earth's surface) in excess of 90%. Because of the relationships between lightning and other physical parameters that we show in this paper, and because of the many potential applications (severe storm detection and warning, flash floods, tornadoes, hailstorms, and downbursts; convective rainfall estimation; storm tracking; aviation hazards; improvement of long-term forecasting by quantifying lightning activity for the time of day, season, location, and storm type), the advantages of this continuous lightning coverage is evident. On the other hand, we must point out that since at present lightning coverage from space is still sporadic below 35° latitude and completely missing at higher latitudes, it is necessary to resort to existing ground-based lightning detection systems.

Acknowledgments The authors wish to thank Prof. Hans-Dieter Betz for constructive comments and suggestions. This research has been supported by the NASA MSFC Lightning Imaging Sensor science team, by the European Commission Sixth Framework Programme through the project "Observation, Analysis and Modeling of Lightning Activity in Thunderstorms, for use in Short Term Forecasting of Flash Floods" (FLASH), and by the Italian FIRS-MIUR programme "Sustainable Development and Climate Changes" through the project "Aerosol Effects on Clouds and Climate" (AEROCLOUDS). The views, opinions, and findings contained herein are those of the authors, and should not be construed as an official NASA, NOAA, or U.S. Government position, policy, or decision.

References

- Alexander, G.D., J.A. Weinman, V.M. Karyampudi, W.S. Olson and A.C.L. Lee, 1999: The effect of assimilating rain rates derived from satellite and lightning on forecasts of the 1993 Super-storm. *Mon. Wea. Rev.*, **127**, 1433–1457.
- Baker, M., H. Christian, and J. Latham, 1995: A computational study of the relationships linking lightning frequency and other thundercloud parameters. *Q. J. Roy. Met. Soc.*, **121**, 1525–1548.
- Buechler, D.E., and S.J. Goodman, 1990: Echo size and asymmetry: Impact on NEXRAD storm identification. *J. Appl. Meteor.*, **29**, 962–969.
- Boccippio, D.J., S.J. Goodman, and S. Heckman, 2000: Regional differences in tropical lightning distributions. *J. Appl. Meteorol.*, **39**, 2231–2248.
- Cecil, D.J., E.J. Zipser, and S.W. Nesbitt, 2002a: Reflectivity, ice scattering and lightning characteristics of hurricane eyewalls and rainbands. Part I: Quantitative description. *Mon. Wea. Rev.*, **130**, 769–784.
- Cecil, D.J., E.J. Zipser, and S.W. Nesbitt, 2002b: Reflectivity, ice scattering and lightning characteristics of hurricane eyewalls and rainbands. Part II: Intercomparison of observations. *Mon. Wea. Rev.*, **130**, 785–801.
- Cecil, D.J., S.J. Goodman, D.J. Boccippio, E.J. Zipser, and S.W. Nesbitt, 2005: Three years of TRMM precipitation features. Part I: Radar, radiometric, and lightning characteristics. *Mon. Wea. Rev.*, **133**, 543–566.
- Chang, D.-E., J.A. Weinman, C.A. Morales, and W.S. Olson, 2001: The effect of spaceborne microwave and ground based continuous lightning measurements on forecast of the 1998 Groundhog Day Storm. *Mon. Wea. Rev.*, **129**, 1809–1833.
- Cheze, J.L., and H. Sauvageot, 1997: Area average rainfall and lightning activity. *J. Geophys. Res.*, **102**, 1707–1715.
- Christian, H.J., R.J. Blakeslee, S.J. Goodman, D.A. Mach, M.F. Stewart, D.E. Buechler, W.J. Koshak, J.M. Hall, W.L. Boeck, K.T. Driscoll, and D.J. Boccippio, 1999: The Lightning Imag-

- ing Sensor. Proc. 11th International Conference on Atmospheric Electricity, Guntersville, Alabama, USA, 7–11 June 1999, 746–749.
- Christian, H.J., 1999: Optical detection of lightning from space. Proc. 11th International Conference on Atmospheric Electricity, Guntersville, Alabama, USA, 7–11 June 1999, 715–718.
- Christian, H.J., R.J. Blakeslee, D.J. Boccippio, W.L. Boeck, D.E. Buechler, K.T. Driscoll, S.J. Goodman, J.M. Hall, W.J. Koshak, D.M. Mach, and M.F. Stewart, 2003: Global frequency and distribution of lightning as observed from space by the Optical Transient Detector. *J. Geophys. Res.*, **108**, D1, 4005.
- Goodman, S.J., and H.J. Christian, 1993: Global observations of lightning. *Atlas of Satellite Observations related to Global Change* (R. Gurney, J. Foster, and C. Parkinson, Eds.), Cambridge University Press, New York, 191–219.
- Goodman, S.J., R.J. Blakeslee, and W. Koshak, 2008: Geostationary Lightning Mapper for GOES-R and Beyond. AMS Annual Meeting, January 2008, New Orleans, USA.
- Holt, M.A., P.J. Hardaker, and G.P. McLellan, 2001: A lightning climatology for Europe and the UK, 1990–99. *Weather*, **56**, 290–296.
- Iguchi, T., T. Kozu, R. Meneghini, J. Awaka, and K. Okamoto, 2000: Rain-profiling algorithm for the TRMM precipitation radar. *J. Appl. Meteor.*, **39**, 2038–2052.
- Illingworth, A.J., 1985: Charge separation in thunderstorms: Small scale processes. *J. Geophys. Res.*, **90**, 6028–6032.
- Jayaratne, R., 1983: Laboratory studies of the charging of soft-hail during ice crystal interactions. *Q. J. Roy. Met. Soc.*, **109**, 609–630.
- Keighton, S.J., H.B. Bluestein, and D.R. MacGorman, 1991: The evolution of a severe mesoscale convective system: Cloud-to-ground lightning location and storm structure. *Mon. Wea. Rev.*, **119**, 1533–1556.
- Kummerow, C., W. Barnes, T. Kozu, J. Shiue, and J. Simpson, 1998: The Tropical Rainfall Measuring Mission (TRMM) sensor package. *J. Atmos. Oceanic Tech.*, **15**, 809–817.
- Kummerow, C., J. Simpson, O. Thiele, W. Barnes, A. T.C. Chang, E. Stocker, R.F. Adler, A. Hou, R. Kakar, F. Wentz, P. Ashcroft, T. Kozu, Y. Hong, K. Okamoto, T. Iguchi, H. Kuroiwa, E. Im, Z. Haddad, G. Huffman, B. Ferrier, W.S. Olson, E. Zipser, E.A. Smith, T.T. Wilheit, G. North, T. Krishnamurti, and K. Nakamura, 2000: The status of the Tropical Rainfall Measuring Mission (TRMM) after two years in orbit. *J. Appl. Meteor.*, **39**, 1965–1982.
- Mohr, K.I., E.R. Toracinta, E.J. Zipser, and R.E. Orville, 1996: A comparison of WSR-88D reflectivities, SSM/I brightness temperatures, and lightning for mesoscale convective systems in Texas. Part II: SSM/I brightness temperatures and lightning. *J. Appl. Meteor.*, **35**, 919–931.
- Mugnai, A., E.A. Smith, and G.J. Tripoli, 1993: Foundations for statistical-physical precipitation retrieval from passive microwave satellite measurements. Part II: Emission source and generalized weighting function properties of a time dependent cloud-radiation model. *J. Appl. Meteor.*, **32**, 17–39.
- Nesbitt, S.W., and E.J. Zipser, 2003: The diurnal cycle of rainfall and convective intensity according to the three years of TRMM measurements. *J. Climate*, **16**, 1456–1475.
- Nesbitt, S.W., E.J. Zipser, and D.J. Cecil, 2000: A census of precipitation features in the Tropics using TRMM: Radar, ice scattering, and lightning observations. *J. Climate*, **13**, 4087–4106.
- Orville, R., and R. Henderson, 1986: Global distribution of midnight lightning: December 1977 to August 1978. *Mon. Wea. Rev.*, **114**, 2640.
- Petersen, W.A., and S.A. Rutledge, 2001: Regional variability in tropical convection: Observations from TRMM. *J. Climate*, **14**, 3566–3586.
- Rutledge, S.A., E.R. Williams, and T.D. Keenan, 1992: The Down Under Doppler and Electricity Experiment (DUNDEE): Overview and preliminary results. *Bull. Amer. Meteor. Soc.*, **73**, 3–16.
- Saunders, C.P.R., 1994: Thunderstorm electrification experiments and charging mechanisms. *J. Geophys. Res.*, **99**, 10773–10779.
- Sheridan, S., J.F. Griffith, and R.E. Orville, 1997: Warm season cloud to ground lightning precipitation relationships in the south-central United States. *Wea. Forecasting*, **12**, 449–457.
- Smith, E.A., A. Mugnai, H.J. Cooper, G.J. Tripoli, and X. Xiang, 1992: Foundations for statistical-physical precipitation retrieval from passive microwave satellite measurements. Part I: Bright-

- ness temperature properties of a time dependent cloud-radiation model. *J. Appl. Meteor.*, **31**, 506–531.
- Solomon, R., and M. Baker, 1998: Lightning flash rate and type of convective storms. *J. Geophys. Res.*, **103**, 14041–14057.
- Spencer, R.W., H.M. Goodman, and R.E. Hood, 1989: Precipitation retrieval over land and ocean with the SSM/I: Identification and characteristics of the scattering signal. *J. Atmos. Oceanic Technol.*, **6**, 254–273.
- Takahashi, T., 1978: Riming electrification as a charge generation mechanism in thunderstorms. *J. Atmos. Sci.*, **35**, 1536–1548.
- Tapia, A., J.A. Smith, and M. Dixon, 1998: Estimation of convective rainfall from lightning observations. *J. Appl. Meteor.*, **37**, 1497–1509.
- Thomas, R., P. Krehbiel, W. Rison, T. Hamlin, D. Boccippio, S. Goodman, and H. Christian, 2000: Comparison of ground-based 3-dimensional lightning mapping observations with satellite-based LIS observations in Oklahoma. *Geophys. Res. Lett.*, **27**, 1703–1706.
- Zipser, E.J., D.J. Cecil, C. Liu, S.W. Nesbitt, and D.P. Yorty, 2006: Where are the most intense thunderstorms on Earth? *Bull. Am. Meteorol. Soc.*, **87**, 1057–1071.

Chapter 15

Energetic Radiation and Lightning

Joseph R. Dwyer

Abstract Until very recently, lightning was thought to be an entirely conventional discharge, involving only low-energy (a few eV) electrons. This picture changed with the discovery of intense x-ray emission from natural cloud-to-ground lightning, rocket-triggered lightning and thunderstorms. Indeed, the intensity of the x-rays generated by thunderstorms can be so large that bright bursts of these x-rays are observed from space, 600 km above the storms, as terrestrial gamma-ray flashes (TGFs). This energetic emission cannot be produced by conventional discharges in air, and so the presence of x-rays implies that runaway electrons, accelerated in air by strong electric fields, play a role in thunderstorm and lightning processes. In this chapter, an overview will be given of the x-ray observations of thunderstorms and lightning. In addition, the physics of runaway electrons will be presented, including some recent theoretical advances.

Keywords Lightning · Thunderstorms · X-rays · Energetic radiation · Atmospheric electricity

15.1 Introduction

15.1.1 Overview

Despite many reports of x-ray emission from thunderstorms and lightning made over the years (e.g., Shaw, 1967; Parks et al., 1981; McCarthy and Parks, 1985; D’Angelo, 1987; Suszcynsky et al., 1996; Eack et al., 1996; Brunetti et al., 2000 Chubenko et al., 2000), until recently, most researchers believed that lightning was an entirely conventional, albeit large, discharge that did not involve high-energy processes that might produce energetic radiation such as x-rays. Beginning in 2001,

J.R. Dwyer (✉)

Department of Physics and Space Sciences, Florida Institute of technology, Melbourne, Florida, USA
e-mail: jdwyer@fit.edu

this view changed when Moore et al. (2001) showed that energetic radiation is produced during natural lightning and when Dwyer et al. (2003, 2004a) demonstrated that rocket-triggered lightning also produces large quantities of energetic radiation and that this radiation was predominantly made of hard x-rays. Because the only viable mechanism for explaining the x-ray emission from lightning is through the production of runaway electrons (Gurevich et al., 1992 Gurevich and Zybin, 2001), these x-ray measurements demonstrate that lightning is not just a conventional discharge. Runaway electrons are created when the electric force experienced by fast electrons is greater than the effective frictional force produced by the motion of the electrons through air, allowing the electrons to run away and gain large amounts of energy (Wilson, 1925). As the runaway electrons collide with air they copiously emit x-rays and gamma-rays via bremsstrahlung, the measurement of which can be used to infer properties of both the runaway electrons and the lightning that produced them.

15.1.2 Runaway Electron Production

The principle behind runaway electrons is illustrated in Fig. 15.1, which shows the effective frictional force and electric force experienced by an energetic electron moving through air at 1 atmosphere pressure. As can be seen, electrons with initial kinetic energies greater than K_{th} will gain more energy from the electric field than they lose from collisions with air and will run away. Such energetic seed electrons, with $K > K_{\text{th}}$, are readily supplied by the interaction of atmospheric cosmic-rays

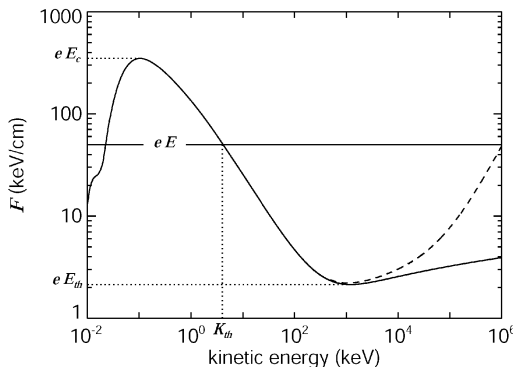


Fig. 15.1 The effective frictional force experienced by a free electron moving through air at STP as a function of kinetic energy. The *solid curve* is due to inelastic scattering of the electron with air atoms, and the *dashed curve* includes the effects of bremsstrahlung emission. The *horizontal line* shows the electric force from a 5000 kV/m electric field. Runaway electrons occur for kinetic energies greater than the threshold energy, $K > K_{\text{th}}$. E_c is the critical electric field strength, for which low-energy free-electrons will also run away, and E_{th} is the minimum field needed to produce runaway electrons. The figure is from Dwyer (2004)

with the atmospheric constituents. Once an electron runs away, it will collide with air atoms producing energetic “knock-on” electrons with $K > K_{\text{th}}$. These secondary electrons may also run away, resulting in an avalanche of relativistic electrons that grow exponentially with time and distance as long as the electric field $E > E_{\text{th}}$. This way of generating runaway electrons is called the Relativistic Runaway Electron Avalanche (RREA) mechanism, sometimes referred to as “runaway breakdown.”

For sufficiently strong electric fields, $E \geq E_c$, a large number of low-energy electrons, from the bulk free-electron population, will gain energy and run away without the need for externally supplied seed particles, *e.g.* from cosmic-rays. This mechanism is called the cold runaway electron mechanism (Gurevich, 1961; Dwyer, 2004; Moss et al., 2006). A third source of energetic seed particles comes from a positive feedback effect involving backward propagating x-rays and positrons, called the relativistic feedback mechanism (Dwyer, 2003, 2007), which is discussed in Section 15.3.4. An advantage of the relativistic feedback mechanism is that it works for relatively low electric fields ($E_{\text{th}} < E < E_c$) and allows the discharge to become self-sustaining, without the need for an external source of energetic particles.

15.1.3 Lightning Initiation

The physics of lightning initiation remain poorly understood despite many decades of research on the topic (Rakov and Uman, 2003). It is currently thought that in order to form a lightning leader, at someplace in the thundercloud, the electric field must reach a large enough value for conventional breakdown to occur. In dry air at sea-level the conventional breakdown threshold, E_b , is about 2.6×10^6 V/m (Raether, 1964). When precipitation is present, this threshold is reduced to about $1.0\text{--}1.4 \times 10^6$ V/m, depending upon the size and shape of the precipitants (Solomon, Schroeder and Baker, 2001; Cooray, 2003). However, decades of in situ electric field measurements have failed to find electric field strengths near the conventional breakdown threshold, even when the effects of precipitation are included (MacGorman and Rust, 1998). On the other hand, the thunderstorm electric fields are often observed to exceed the threshold field to create runaway electron avalanches, E_{th} (Marshall and Rust, 1991; Marshall et al., 2005), opening the possibility that runaway electrons play some role in lightning initiation. For instance, Gurevich et al. (1999) suggested that the RREA mechanism acting on extensive cosmic-ray air showers could produce enough ionization to initiate lightning. On the other hand, Dwyer (2005) suggested that runaway electron avalanches produced by the ambient cosmic-ray background, with a possible contribution from relativistic feedback, could locally enhance the electric field to the point where lightning initiates. Unfortunately, not all of the details of these models have been worked out. In particular, it is still not clear how the relatively diffuse discharge created by the runaway electrons can result in a hot lightning leader channel, measuring just centimeters across. As a result, it remains an open question whether or not runaway electrons are important for lightning initiation.

15.2 X-ray and Gamma-Ray Observations

15.2.1 Observations of x-rays from Rocket-Triggered Lightning

In 2003, Dwyer et al. reported the measurement of intense bursts of energetic radiation from rocket-triggered lightning (Dwyer et al., 2003). These results, which were later confirmed and expanded upon by Dwyer et al. (2004a), were significant because they allowed, for the first time, detailed and repeatable investigations of the x-ray emissions from lightning. An example of the x-ray observations of triggered lightning is presented in Fig. 15.2, from Dwyer et al. (2004a), which shows the response of a NaI(Tl)/photomultiplier tube (PMT) detector. The detector was housed in a heavy aluminum box, designed to keep out RF noise, moisture and light. Because the instrument was required to operate in the close vicinity of lightning, no conducting power or data cables entered or exited the box. The detector and electronics were internally powered by a 12 V battery, and switched on and off using fiber optics. Fiber optics were used to transmit the anode signal from the PMT to a shielded trailer, where the waveform was digitized and recorded. For this observation, the instrument was located 40 m from the triggered lightning channel at the University of Florida/Florida Tech International Center for Lightning Research and Testing (ICLRT) at Camp Blanding, Florida. The ICLRT is a well instrumented

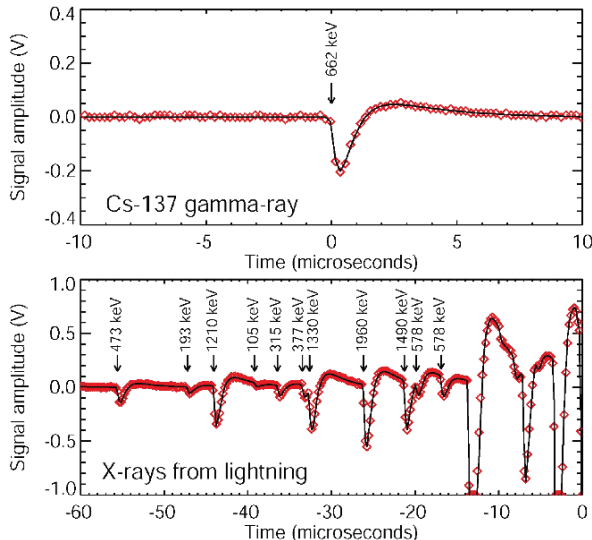


Fig. 15.2 *Top panel:* waveform from one of the NaI(Tl)/PMT detectors for a single 662 keV gamma-ray from a Cs-137 radioactive source placed temporarily on top of the instrument. The diamonds show the data as recorded by the acquisition system, and the solid line shows the detector response as calculated from the NaI decay-time and the RC-times in the front end electronics. *Bottom panel:* waveform for a time period just prior to a return stroke (at $t = 0$) of triggered lightning. The detector response (solid line) is plotted over the measured data (diamonds). The arrows indicate the times and deposited energies of the energetic radiation. The figure is from Dwyer et al. (2004a)

facility capable of measuring electric currents, electric and magnetic fields and optical emission (Jerauld et al., 2003).

To illustrate the response of the instrument to x-rays, the top panel of the figure shows the signal from one 662 keV gamma-ray from a Cs-137 radioactive source placed temporarily on top of the instrument. The solid black curve shows the fit of the response function as derived from the electronics and the 0.23 μ s NaI decay-time. The bottom panel of Fig. 15.2 shows x-rays from a stroke of rocket-triggered lightning measured during the dart leader phase. In the figure, the return stroke occurred to the right at time $t = 0$. The solid black curve is the fit of the response functions with the x-ray's deposited energies and times indicated by the arrows. The background rate during this time period was measured to be 120 counts/s for energies above 100 keV, making the odds that even one very small pulse in the 60 μ s time window shown in Fig. 15.2 was due to background at less than 1 in 100. As can be seen, some of the pulses have rather large deposited energies, more in line with the energies of gamma-ray photons. However, by operating several detectors simultaneously and placing bronze and lead attenuators of varying thicknesses over the scintillators and PMTs, it was found by Dwyer et al. (2004a) that the pulses are not usually individual gamma-rays but were instead composed of fast bursts of x-rays, mostly in the 30–250 keV range, although occasionally individual x-rays in the MeV range are observed. Using bronze collimators, the x-rays were also observed to be spatially and temporally associated with the dart leaders and possibly the beginning of the return strokes.

15.2.2 Observation of X-rays from Natural Cloud-to-Ground Lightning

During the summers of 2004 and 2005, a total of 9 natural cloud-to-ground lightning flashes, all of which lowered negative charge to the ground, struck the ICLRT or its immediate vicinity, with significant x-ray emission measured. Figure 15.3, from Dwyer et al. (2005a), shows data for a natural lightning flash on 24 August 2004, for the stepped leader phase just prior to the first return stroke. The bottom panel is the electric field changes produced by the stepped leader as it propagates to the ground. The individual steps appear as sudden drops in the electric field waveform, caused by the leader bringing negative charge closer to the ground. The top panels show the x-ray waveforms from a NaI/PMT x-ray detector, similar to that described above. As can be seen, the x-ray pulses are very closely associated with the leader steps. This is significant because the stepped leader process determines how and where lightning propagates, and, as this figure illustrates, runaway electrons are being produced during the step formation.

The x-ray emission from natural lightning stepped leaders is remarkably similar to the x-ray emission from triggered lightning dart leaders, implying that both the dart leader and stepped leader x-ray emission share a similar production mechanism. Since nearly all dart leaders emit similar x-rays, this implies that nearly all dart leaders in fact involve stepping to some degree, but that the steps are so short that

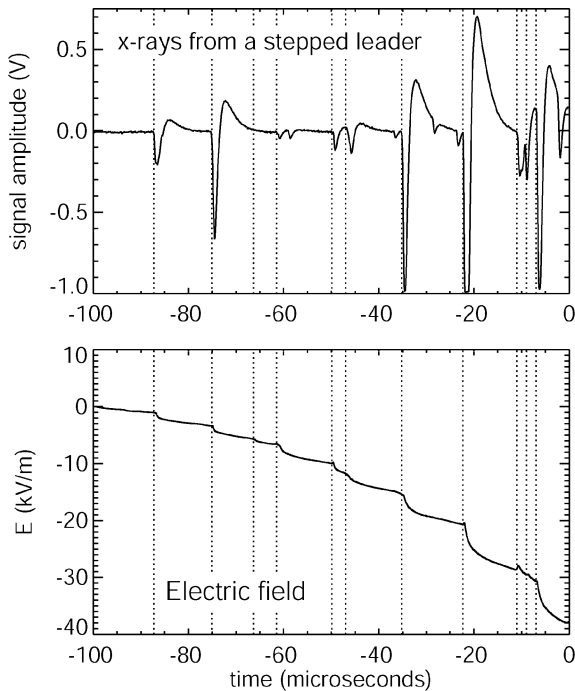


Fig. 15.3 X-rays (top panel) and electric field (integrated dE/dt) waveforms (bottom panel) for a natural cloud-to-ground lightning flash. The lightning struck within 50 m of the electric field antenna and about 260 m from the x-ray detector. Time zero in the plot corresponds to the beginning of the return stroke. The start times of the steps are denoted by vertical dotted lines. The figure illustrates that the x-ray pulses occur during the formation of the stepped-leader steps, and, therefore, the x-ray emission is related to the stepping process, which determines where lightning will go and how it branches. The Figure is taken from Dwyer et al. (2005a)

they are usually not resolved in optical records. Consequently, it may be possible to unify the different kinds of negative leaders observed in nature, which may appear optically different depending on the conditions along their propagation path (Rakov and Uman, 2003), into one basic type, with one underlying mechanism for propagation. Moreover, because x-ray emission is observed from nearly all lightning, triggered and natural, that strikes within a hundred meters or so of the detectors, x-ray emission and hence runaway electrons commonly occur in most lightning. As a result, successful models of lightning must also explain how this high-energy emission occurs.

15.2.3 Observation of Gamma-Ray Flashes from Thunderclouds

In addition to x-ray emission from lightning, Dwyer et al. (2004b) reported the observation of an intense gamma-ray flash observed on the ground at sea level,

produced in association with the initial-stage of rocket-triggered lightning at the ICLRT. The flash, which lasted about 300 μ sec, was observed simultaneously on three NaI(Tl)/PMT detectors that were located 650 m from the triggered lightning channel with gamma-ray energies extending up to more than 10 MeV. The beginning of the gamma-ray flash occurred at about the same time as the upward propagating positive leader, initiated from the top of the rocket and extended triggering wire, would have reached the overhead cloud charge at 6–8 km above the ground. It is possible that when the leader reached this charge, an intense discharge was initiated, producing runaway electrons and the accompanying gamma-rays. The gamma-ray flash, therefore, may represent a new kind of event, different from the leader emission.

If the gamma-rays were indeed produced at a height of 6–8 km above the ground, atmospheric attenuation would greatly reduce the gamma-ray intensity on the ground. Interestingly, the amount of atmosphere above 6 km is about the same as the amount below that altitude, raising the possibility that similar gamma-ray events, directed upwards, might also be observable from space, since the attenuation of the gamma-rays in the upward and downward directions would be the same. Indeed, intense gamma-ray flashes have been reported using BATSE data from the Compton Gamma Ray Observatory (CGRO) (Fishman et al., 1994). These flashes were originally inferred to be associated with high-altitude discharges such as red-sprites (Nemiroff, Bonnell, and Norris, 1997), largely because of their correlation with thunderstorms and lightning (Inan et al., 1996). It is an intriguing possibility that terrestrial gamma-ray flashes (TGFs) observed from space actually originate from the thunderclouds, deep in the lower atmosphere.

Recently, Smith et al. (2005) reported the measurement of a large number of TGFs by the RHESSI spacecraft. Dwyer and Smith (2005) used Monte Carlo simulations of the runaway electron avalanches to calculate the spectra of terrestrial gamma-ray flashes, which were then compared with RHESSI and CGRO/BATSE observations. It was found that the RHESSI spectrum is not consistent with a source altitude above 24 km but can be well fit by a source in the range of 15–21 km (also see Carlson, Lehtinen, and Inan, 2007). Because 15 km is not unusual for the tops of thunderstorms, especially at low latitudes (Williams et al., 2005), and is lower than typical minimum sprite altitudes, the RHESSI data implies that thunderstorms and not sprites may be the source of these TGFs, in agreement with the suggestion by Dwyer et al. (2004b).

Figure 15.4 shows the energy spectrum of the ground-level gamma-ray event measured at the ICLRT along with RHESSI TGF data and model results as reported by Dwyer and Smith (2005). Note that the spectrum is much harder than the spectrum measured for lightning dart and stepped leaders.

Last year, Tsuchiya et al. (2007) reported gamma-ray emission from winter thunderstorms in Japan that lasted up to 40 s and had energies up to 10 MeV. The duration of this emission is substantially longer than the millisecond long emission observed from lightning and terrestrial gamma-ray flashes. The timescale observed is more reminiscent of the in situ x-ray enhancements observed of Eack et al. (1996), which lasted about 1 min and those observed by McCarthy and Parks (1985) and

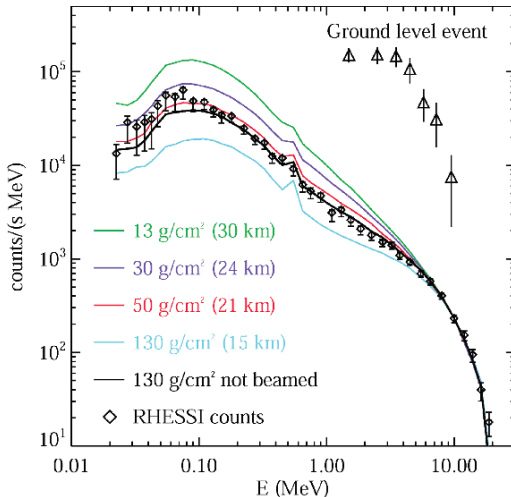


Fig. 15.4 Energy spectrum of the gamma-ray flash observed on the ground at the ICLRT as compared to the terrestrial gamma-ray flash (TGF) spectrum as measured from space by RHESSI (Dwyer and Smith, 2005). The *solid curves* are the x-ray emission spectra, corrected for the instrumental response, as calculated by the Monte Carlo simulation of runaway breakdown at four atmospheric depths. An atmospheric depth of 13 g/cm^2 corresponds to an altitude of 30 km, 30 g/cm^2 corresponds to 24 km, 50 g/cm^2 corresponds to 21 km, and 130 g/cm^2 corresponds to 15 km. For four of these spectra, the runaway breakdown is assumed to be beamed along the vertical direction. Also shown is the spectrum for a source at 15 km but for runaway breakdown that is isotropic in the upper cone with a half width of 45° (labeled non-beamed)

Parks et al. (1981), which lasted for up to 20 s. These observations may indicate that the RREA mechanism, acting on the cosmic-ray background, is taking place in the regions of the thunderstorms with large electric fields, $E > E_{\text{th}}$. At this time, it is still not clear how these results are related to TGFs or the ground level gamma-ray event discussed above.

15.2.4 X-rays from Laboratory Sparks

Until recently it was generally believed that electrical discharges in air involved only low-energy electrons having energies of at most a few tens of eV (Raether, 1964; Bazelyan and Raizer, 1998). The recent and surprising discovery that both natural and triggered lightning discharges emit x-rays, demonstrated that some kinds of discharges in air produce high-energy electrons traveling close to the speed of light and having energies of at least hundreds of keV and sometimes up to tens of MeV. Initially, the x-ray observations of lightning seemed to support the generally-accepted notion that lightning was different from laboratory sparks, the latter being assumed to involve only conventional breakdown and not runaway electrons as with lightning.

In 2005, Dwyer et al. reported the x-ray observations of long high-voltage laboratory sparks in air that demonstrate that these laboratory discharges do indeed produce x-rays similar to the x-ray emission seen from lightning (Dwyer et al., 2005b). These results imply that runaway electrons are also occurring in these relatively small high-voltage sparks and, hence, that such sparks are more than just a conventional breakdown. This finding implies that the physics used for decades to describe discharges in air may be inadequate, even for relatively small sparks.

X-ray observations were made during fourteen 1.5–2.0 m high-voltage discharges in air at 1 atmosphere pressure produced by a 1.5 MV Marx circuit at Lightning Technologies Inc. in Pittsfield, MA. All 14 discharges generated x-rays in the \sim 30–150 keV range. The x-rays, which arrived in discrete bursts, less than 0.5 microseconds in duration, occurred from both positive and negative polarity rod-to-plane discharges as well as from small, 5–10 cm series spark gaps within the Marx generator. Figure 15.5 shows examples of this x-ray emission, which is

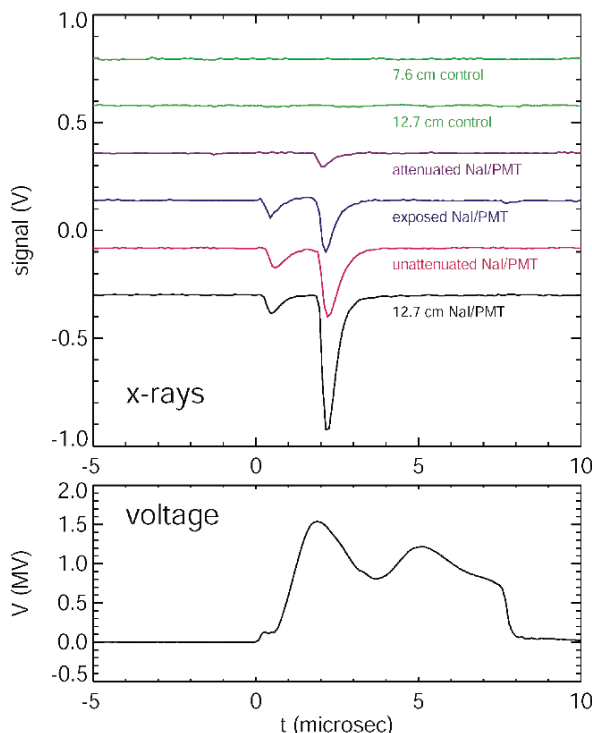


Fig. 15.5 X-ray waveforms from 4 NaI/PMT detectors and two control detectors (with no NaI) plus the gap potential for a 1.5 MV spark. A change in pulse size of -0.25 V corresponds to a deposited energy of 662 keV in all detectors. In the upper panel, from top to bottom, respectively, the signals are from the two control detectors (no NaI), an attenuated detector (0.32 cm thick bronze cap), a detector covered by a wire mesh, and two un-attenuated detectors (no bronze cap). The bottom panel shows the gap voltage, measured with a resistive divider. The figure is from Dwyer et al. (2005b)

remarkably similar to the x-ray bursts previously observed from lightning. The figures were taken from Dwyer et al. (2005b). These results have now been verified by Rahman et al. (2008), using a 1 MV Marx generator at Uppsala University, Sweden. The discovery of x-rays from laboratory sparks opens up the possibility of using laboratory sparks to study the poorly understood phenomenon of runaway electron production by lightning.

15.3 Theory and Modeling

15.3.1 Runaway Electron Simulations

Because the interactions of high-energy electrons and photons with air are well understood and simple to calculate, Monte Carlo codes, in which individual particle trajectories and interactions are simulated, are particularly useful for studying runaway electrons. One such Monte Carlo simulation, developed over the last 7 years at Florida Tech, shall be described here. This 3-D (plus time) Monte Carlo simulation has been used to investigate the theory of relativistic runaway electron avalanche (RREA) development and to model specific runaway breakdown processes, with results reported in several papers (Dwyer, 2003, 2004, 2005, 2007; Coleman and Dwyer, 2006). The simulation includes, in an accurate form, all the relevant physics for describing the interactions of photons and energetic electrons and positrons with air and is capable of modeling runaway electron avalanches for both spatially and time varying electric and magnetic fields (Dwyer, 2003). Unlike earlier work, this simulation fully models elastic scattering using a shielded-Coulomb potential, rather than relying on a diffusion approximation, and also includes bremsstrahlung production of x-rays and gamma-rays and the subsequent propagation of the photons, including photoelectric absorption in nitrogen, oxygen and argon, Rayleigh and Compton scattering and pair production. In addition, important new features include the incorporation of positron propagation and the generation of energetic seed electrons via Bhabha scattering of positrons and via Compton scattering and photoelectric absorption of energetic photons. Furthermore, bremsstrahlung production from all secondary electrons and positrons and positron annihilation gamma-rays are included.

15.3.2 Properties of Runaway Electron Avalanches

As relativistic runaway electrons propagate through air in an electric field with $E > E_{\text{th}}$, an avalanche of runaway electrons develops. The number of runaway electrons, produced by N_o energetic seed electrons, is given by

$$N_{RE} = N_o \exp \left(\int_0^L \frac{dz}{\lambda(z)} \right) \quad (15.1)$$

where L is the length of the electric field region, and λ is the characteristic length for an avalanche to develop. This avalanche length, λ , is found by the Monte Carlo simulations (Dwyer, 2003; Coleman and Dwyer, 2006) to be well fit $(300 \text{ kV/m})n \leq E \leq (3000 \text{ kV/m})n$, by the empirical formula

$$\lambda(z) = 7300 \text{ kV} [E(z) - (276 \text{ kV/m})n]^{-1}, \quad (15.2)$$

where n is the density of air relative to that at STP. The Monte Carlo simulation also shows that when elastic scattering is included, the threshold for runaway electron avalanche development is $E_{\text{th}} = (284 \text{ kV/m})n$, slightly higher than the value shown in Fig. 15.1, which only includes the effects of inelastic scattering. For $E < (300 \text{ kV/m})n$, the length-scale needed to produce substantial numbers of runaway electrons is several kilometers, too long to be applicable for thunderstorms and lightning. Simulations show that the average kinetic energy for the runaway electrons in the avalanche is about 7.3 MeV, which justifies the use of the term relativistic in the names of the mechanisms.

From Eqs. (15.1) and (15.2), an upper limit on the number of runaway electrons is given by

$$N_{RE} \leq N_o \exp(V/7.3 \text{ MV}), \quad (15.3)$$

where V is the total voltage drop in the avalanche region. The upper limit in Eq. (15.3) is very robust, and is independent of the air density and the spatial variation of the electric field.

15.3.3 Modeling Lightning Leader Emission

For negative cloud-to-ground lightning, the electric potential of the dart leader is roughly 15 MV (Rakov and Uman, 2003). Plugging 15 MV into Eq. (15.3) gives $N_{RE} \leq 8N_o$, indicating that very little avalanche multiplication is likely to occur for lightning dart leaders. This presents a big problem for the RREA model to explain the observed x-ray emission from lightning, since more than 10^{12} x-ray per m^2 per second were estimated by Dwyer et al., 2004a to be emitted by the dart leader during the last 10 microseconds or so. The number of runaway electrons that produce those x-rays is likely to be much larger. Considering that the atmospheric cosmic-ray flux is only about $200 \text{ m}^{-1} \text{ s}^{-1}$ at sea level, an avalanche multiplication factor of 8, as estimated above, is many orders of magnitude too small to account for the large fluxes of x-ray observed (Dwyer, 2004). A more dramatic problem occurs for the x-ray observation from laboratory sparks. In this case, the maximum voltage produced by the Marx generator was only 1.5 MV, resulting in almost no runaway electron avalanche multiplication as described by the RREA model.

It should be stressed that the x-ray emission from lightning cannot result from the thermal radiation of lightning, since even the maximum temperature of lightning (30,000 K during the return stroke) is many orders of magnitude too cold to account

for the hard x-ray energies (>100 keV) observed. The production of runaway electrons in air is still the only viable mechanism for explaining the x-ray emission, which then leads to the question of the origin of the seed particles that run away, the cosmic-ray and natural background fluxes being too small to account for the observations. As described above, an alternative is the so-called cold runaway electron mechanism, for which very large electric fields $E > E_c$ are required. This mechanism allows the high-energy tail of the bulk free electron population to run away, possibly with some additional energy gain from regions where the electric fields remain above E_{th} . It is possible that such large electric fields, $E > E_c$, are briefly generated at the tips of streamers or possibly by leaders. If so, then the electric field produced by streamers is at times larger than previously inferred (Bazelyan and Raizer, 1998). Once the mechanisms for producing the runaway electron are understood it may be possible to use the x-ray measurements to determine the electric field strengths produced by breakdown process, measurements that would be very difficult to carry out otherwise.

15.3.4 Positron and x-ray Feedback

In 2003, Dwyer presented a new runaway breakdown mechanism in which x-rays and positrons generate a positive feedback effect that greatly increases the flux of runaway electrons and x-rays (Dwyer, 2003). This mechanism is illustrated in Fig. 15.6, from Dwyer (2003), which shows partial results of the Monte Carlo simulation described above. In the figure, one high-energy (1 MeV) seed electron is injected at the top center of the region containing a uniform electric field. This

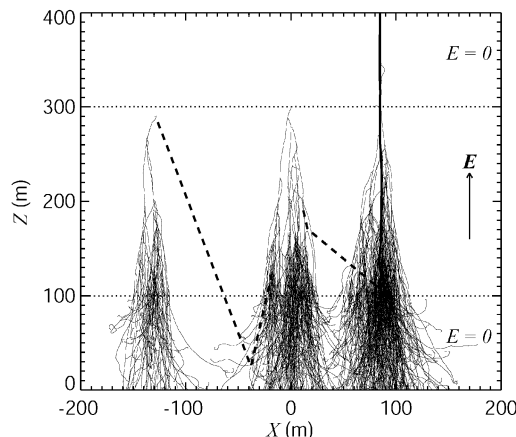


Fig. 15.6 Partial results of the Monte Carlo simulation showing the runaway breakdown of air. The light tracks are the runaway electrons, the *dashed lines* are the x-rays and the dark track is a positron. The entire avalanche is initiated by One, 1 MeV, seed electron injected at the top center of the volume. The *horizontal dotted lines* show the boundaries of the electric field volume ($E = 1000$ kV/m). For clarity, only a small fraction of the runaway electrons and x-rays (gamma-rays) produced by the avalanche are plotted

electron runs away, producing an avalanche of relativistic electrons (light tracks). Bremsstrahlung x-rays (dashed lines) are produced when the runaway electrons collide with air. The x-ray (or gamma-ray) on the right side of the figure produces a positron (dark trajectory on right) via pair production. This positron runs away, traveling to the top of the figure and producing more runaway electrons via hard elastic scattering, resulting in the secondary avalanche on the right. The x-ray on the left side of the figure Compton scatters to the top and produces another seed electron via the photoelectric effect (shown) or via Compton scattering. This seed electron then runs away producing the secondary avalanche on the left. These secondary avalanches, in turn, produce more feedback electrons via the two mechanisms described above, allowing the whole process to increase exponentially.

The avalanches on the left and right illustrate the x-ray feedback and positron feedback mechanisms, respectively. The positive feedback effect from the backward propagating positrons and the back scattered x-rays allow the discharge to become self-sustaining. As the number of runaway electrons increases exponentially with time, the large increase in conductivity will necessarily result in the collapse of the electric field. As a result, unlike the RREA mechanism (*i.e.* so called runaway breakdown), which depends upon an external source of energetic seed electrons, the relativistic feedback mechanism is a true electrical breakdown. Moreover, Dwyer (2003) showed that the relativistic feedback mechanism places a severe limit on the maximum electric field achievable in air, a limit which may be relevant to thunderstorm electrification (also see Babich et al., 2005). In addition, Dwyer (2007) showed that in some cases feedback can increase the flux of runaway electrons and the x-rays they produce by a factor of a 10^{13} over the standard RREA mechanism alone, making this mechanism a good candidate for explaining the ground-level gamma-ray flash and terrestrial gamma-ray flashes, both of which infer large intensities of runaway electrons at the source. However, it is not clear if relativistic feedback plays any role in the runaway electron production associated with lightning leaders, since like the RREA mechanism, relativistic feedback requires sizeable potential differences, more than several tens of MV.

15.4 Conclusions

15.4.1 *Open Questions Regarding the X-ray Emission from Lightning*

While great progress has been made in recent years measuring properties of the x-ray emission from lightning, a large number of questions remain. The following are just a few questions that may help direct future work:

1. What are the specific runaway electron mechanism(s) involved in the production of x-rays from lightning stepped-leaders, dart leaders and return strokes?
2. Exactly when and where are the x-rays produced?
3. How are the runaway electrons and the x-rays related to the stepping process?
Are runaway electrons important for lightning propagation?

4. Are the x-rays from dart leaders related to stepping? Since nearly all dart leaders make x-rays, does this imply that nearly all dart leaders step?
5. What are the properties of the x-rays produced by the return stroke?
6. How does x-ray emission depend upon other observable properties of lightning such as leader speed, electric field strengths, return stroke currents, etc.?
7. How does the x-ray emission change with altitude and distance from the ground?
8. Do runaway electrons play a role in lightning initiation?
9. How and where do TGFs occur and how are they related to the observed long duration x-ray emission?

15.4.2 The Next Step

Starting in 2007, a total of 24 x-ray instruments, making up the Thunderstorm Energetic Radiation Array (TERA), are now operating at the UF/Florida Tech International Center for Lightning Research and Testing (ICLRT) at Camp Blanding, FL. This array allows a more complete picture to be obtained of the x-ray emission from lightning, allowing us to study the energy spectra and the spatial and temporal properties of the emission. It is also a significant improvement for studying natural lightning, since the detectors now cover a much larger area than before. Such measurements should help us better understand the runaway electron mechanisms involved in lightning propagation and should provide new insight into the physical processes involved in the leader stepping.

15.4.3 Summary

The last few years have been an exciting time for lightning research with several new high-energy phenomena associated with thunderstorms and lightning being discovered. We are learning that many of the established ideas about how lightning and laboratory sparks work are not complete and that more work is needed. We have now firmly established that high-energy electrons and their accompanying x-ray and gamma-ray emission are routinely produced by thunderstorms and lightning in our atmosphere. We have made theoretical progress understanding this emission, but it is my expectation that most of the important work in this exciting field still remains to be done.

Acknowledgments The work was supported in part by NSF grants ATM 0420820 and ATM 0607885.

References

- Bazelyan, E. M., and Yu. P. Raizer, *Spark Discharge*, CRC Press, 1998.
Babich, L. P., E. N. Donskoy, I. M. Kutsyk and R. A. Roussel-Dupré, The feedback mechanism of runaway air breakdown, *Geophys. Res. Lett.*, 32, L09809, doi:10.1029/2004GL021744, 2005.

- Brunetti, M., S. Cecchini, M. Galli, G. Giovannini, and A. Pagliarin, Gamma-ray bursts of atmospheric origin in the MeV energy range, *Geophys. Res. Lett.*, 27, 1599–1602, 2000.
- Carlson, B. E., N. G. Lehtinen, and U. S. Inan, Constraints on terrestrial gamma ray flash production from satellite observation, *Geophys. Res. Lett.*, 34, Issue 8, CiteID L08809, 2007.
- Chubenko, A. P., V. P. Antonova, S. Yu. Kryukov, V. V. Piskal, M. O. Ptitsyn, A. L. Shepetov, L. I. Vildanova, K. P. Zybin, and A. V. Gurevich, Intense x-ray emission bursts during thunderstorms, *Phys. Lett. A*, 275, 90–100, 2000.
- Coleman, L. M., and J. R. Dwyer, The Propagation Speed of Runaway Electron Avalanches , *Geophys. Res. Lett.*, 33, L11810, doi:10.1029/2006GL025863, 2006.
- Cooray, V., *The Lightning Flash, IEE Power & Energy Series 34*, 2003.
- D'Angelo, N., On X-rays from thunderclouds, *Ann. Geophys. 5B*, 119, 1987.
- Dwyer, J. R., A fundamental limit on electric fields in air, *Geophys. Res. Lett.*, 30, 2055, 2003.
- Dwyer, J. R., Implications of x-ray emission from lightning, *Geophys. Res. Lett.*, 31, L12102, doi:10.1029/2004GL019795, 2004.
- Dwyer, J. R., The initiation of lightning by runaway air breakdown,*Geophys. Res. Lett.*, 32, L20808, doi:10.1029/2005GL023975, 2005.
- Dwyer, J. R., Relativistic breakdown in planetary atmospheres, *Physics of Plasmas*, 14, Issue 4, pp. 042901–042901–17, 2007.
- Dwyer, J. R., M. A. Uman, H. K. Rassoul, M. Al-Dayeh, E. L. Caraway, J. Jerauld, V. A. Rakov, D. M. Jordan, K. J. Rambo, V. Corbin and B. Wright, Energetic radiation produced during rocket-triggered lightning, *Science*, 299, 694, 2003.
- Dwyer J. R., M. A. Uman, H. K. Rassoul, V. A. Rakov, M. Al-Dayeh, E. L. Caraway, B. Wright, J. Jerauld, D. M. Jordan, K. J. Rambo, A. Chrest and C. Smyth, Measurements of x-ray emission from rocket-triggered lightning, *Geophys. Res. Lett.*, 31, L05118, doi:10.1029/2003GL018770, 2004a.
- Dwyer J. R., M. A. Uman, H. K. Rassoul, V. A. Rakov, M. Al-Dayeh, E. L. Caraway, B. Wright, J. Jerauld, D. M. Jordan, K. J. Rambo, A. Chrest and C. Smyth, A ground level gamma-ray burst observed in association with rocket-triggered lightning, *Geophys. Res. Lett.*, 31, L05119, doi:10.1029/2003GL018771, 2004b.
- Dwyer, J. R., M. A. Uman, H. K. Rassoul, V. A. Rakov, M. Al-Dayeh, E. L. Caraway, B. Wright, J. Jerauld, D. M. Jordan, K. J. Rambo, A. Chrest and E. Kozak, X-ray bursts associated with leader steps in cloud-to-ground lightning, *Geophys. Res. Lett.*, 32, L01803, doi:10.1029/2004GL021782, 2005a.
- Dwyer, J. R., H. K. Rassoul, Z. Saleh, M. A. Uman, J. Jerauld and J. A. Plumer, X-ray bursts produced by laboratory sparks in air, *Geophys. Res. Lett.*, 32, L20809, doi:10.1029/2005GL024027, 2005b.
- Dwyer, J. R., and D. M. Smith, A Comparison between Monte Carlo simulations of runaway breakdown and terrestrial gamma-ray flash observations, *Geophys. Res. Lett.*, 32, L22804, doi:10.1029/2005GL023848, 2005.
- Eack, K. B., W. H. Beasley, W. D. Rust, T. C. Marshall, and M. Stolzenburg, X-ray pulses observed above a mesoscale convection system,*Geophys. Res. Lett.*, 23, 2915–2918, 1996.
- Fishman, G. J., et al., Discovery of intense gamma-ray flashes of atmospheric origin, *Science*, 264, 1313, 1994.
- Gurevich, A. V., On the theory of runaway electrons, *Soviet Physics JETP*, 12(5), 904–912, 1961.
- Gurevich, A. V., G. M. Milikh, and R. A. Roussel-Dupré, Runaway electron mechanism of air breakdown and preconditioning during a thunderstorm, *Phys. Lett. A*, 165, 463, 1992.
- Gurevich, A. V., K. P. Zybin, and R. A. Roussel-Dupré, Lightning initiation by simultaneous effect of runaway breakdown and cosmic ray showers, *Phys. Lett. A*, 254, 79–87, 1999.
- Gurevich, A. V., and K. P. Zybin, Runaway breakdown and electric discharges in thunderstorms, *Physics-Uspekhi*, 44, 1119, 2001.
- Inan, S. U., S. C. Reising, G. J. Fishman, and J. M. Horack, On the association of terrestrial gamma-ray bursts with lightning and implications for sprites,*Geophys. Res. Lett.*, 23, 1017–1020, 1996.

- Jerauld, J., V. A. Rakov, M. A. Uman, D. E. Crawford, B. A. deCarlo, D. M. Jordan, K. J. Rambo, and G. E. Schnetzer, Multiple station measurements of electric and magnetic fields due to natural lightning, *Proc. Int. Conf. on Lightning and Static Electricity*, United Kingdom, 2003.
- MacGorman, D. R. and W. D. Rust, *The Electrical Nature of Storms*. Oxford University Press, New York, 1998.
- Marshall, T. C., and W. D. Rust, Electric field soundings through thunderstorms, *J. Geophys. Res.*, 96, 22,297–22,306, 1991.
- Marshall, T. C., M. Stolzenburg, C. R. Maggio, L. M. Coleman, P. R. Krehbiel, T. Hamlin, R. J. Thomas, W. Rison, Observed electric fields associated with lightning initiation, *Geophys. Res. Lett.* 32, L03813, doi:10.1029/2004GL021802, 2005.
- McCarthy, M., and G. K. Parks, Further observations of x-rays inside thunderstorms, *Geophys. Res. Lett.*, 12, 393–396, 1985.
- Moore, C. B., K. B. Eack, G. D. Aulich, and W. Rison, Energetic radiation associated with lightning stepped-leaders, *Geophys. Res. Lett.*, 28, 2141–2144, 2001.
- Moss, G. D., V. P. Pasko, N. Liu, and G. Veronis, Monte Carlo model for analysis of thermal runaway electrons in streamer tips in transient luminous events and streamer zones of lightning leaders, *J. Geophys. Res.*, 111, Issue A2, Cite ID A02307, 2006.
- Nemiroff, R. J., J. T. Bonnell, and J. P. Norris, Temporal and spectral characteristics of terrestrial gamma flashes, *J. Geophys. Res.*, 102, 9659–9665, 1997.
- Parks, G. K., B. H. Mauk, R. Spiger, and J. Chin, X-ray enhancements detected during thunderstorm and lightning activities, *Geophys. Res. Lett.*, 8, 1176–1179, 1981.
- Rakov, V. A., and M. A. Uman, *Lightning Physics and Effects*, Cambridge University Press, 2003.
- Raether, H., *Electron Avalanches and Breakdown in Gases*, Butterworth & Co. Ltd., 1964.
- Rahman, M., V. Cooray, N. A. Ahmad, J. Nyberg, V. A. Rakov, and S. Sharma, X rays from 80-cm long sparks in air, *Geophys. Res. Lett.*, 35, L06805, doi:10.1029/2007GL032678, 2008.
- Shaw, G. E., Background Cosmic Count Increases Associated with Thunderstorms, *J. Geophys. Res.*, 72, 4623–4626, 1967.
- Smith, D. M., L. I. Lopez, R. P. Lin, C. P. Barrington-Leigh, Terrestrial Gamma-Ray Flashes Observed up to 20 MeV, *Science*, 307, 1085–1088, 2005.
- Solomon, R., V. Schroeder and M. B. Baker, Lightning initiation—conventional and runaway-breakdown hypothesis, *Q. J. R. Meteorol. Soc.* 127, 2683–2704, 2001.
- Suszynsky, D. M., R. Roussel-Dupré, and G. Shaw, Ground-based search for x-rays generated by thunderstorms and lightning, *J. Geophys. Res.*, 101, 23,505–23,516, 1996.
- Tsuchiya, H., et al., Detection of high-energy gamma rays from winter thunderstorms, *Phys. Rev. Lett.*, 99, 165002, 2007.
- Williams E., et al., Lightning Flashes Conducive to the Production and Escape of Gamma Radiation to Space, *J. Geophys. Res.*, 111, Issue D16, CiteID D16209, 2006.
- Wilson, C. T. R., The acceleration of beta-particles in strong electric fields such as those of thunderclouds, *Proc. Cambridge Phil. Soc.*, 22, 534–538, 1925.

Chapter 16

Schumann Resonance Signatures of Global Lightning Activity

Gabriella Sátori, Vadim Mushtak and Earle Williams

Abstract This chapter is concerned with the Earth's Schumann resonances (SR) and their application to understanding global lightning. The natural electromagnetic waves in the SR frequency range (5 Hz to approx. 60 Hz) radiated by lightning discharges are contained by the Earth-ionosphere cavity. This cavity excitation by lightning can occur as a single energetic flash (a 'Q-burst'), or as an integration of a large number of less energetic flashes (the 'background' resonances). In principle, continuous observations of SR parameters (modal amplitudes, frequencies, and quality factors) provide invaluable information for monitoring the worldwide lightning activity from a single SR station. Relationships between the variation of SR intensity and global lightning activity are shown. Connections between the change of diurnal modal SR frequency range and the areal variation of worldwide lightning are demonstrated. The temporal variation of the diurnal SR frequency patterns characteristic of the global lightning dynamics is also presented. Distortions of ELF waves propagating between the lightning sources and the observer are theoretically discussed based on the TDTE (two-dimensional telegraph equation) technique, focusing on the role of the day-night asymmetry of the Earth-ionosphere cavity. Theoretical and observational results are compared. Both instruments for SR observations and spectral methods for deducing SR parameters are reviewed. Experimental findings by SR on global lightning variations on different time scales (diurnal, seasonal, intraseasonal, annual, semiannual, interannual, 5-day, long-term) are summarized. The growing use of SR measurements as a natural diagnostic for global climate change is emphasized.

Keywords Schumann resonance · ELF · Global lightning · Earth-ionosphere cavity · Day-night asymmetry · Q-burst · Charge moment · Tropical chimneys · Climate

G. Sátori (✉)

Geodetic and Geophysical Research Institute, HAS, 9400 Sopron, Csatkai u. 6-8, Hungary
e-mail: satori@ggki.hu

16.1 Introduction

A lightning discharge can be considered as a natural broadband transmitter radiating electromagnetic waves in a wide frequency range from ULF (Ultra Low Frequencies) up to VHF (Very High Frequencies). The mean flash rate (~ 50 flashes/second) produced by worldwide thunderstorms (Chrisian et al., 2003) assures a sustained natural electromagnetic field in the Earth's atmosphere. This field depends on the lightning source spectrum, on the source-observer distance and the propagation conditions. The electromagnetic waves in the ELF (Extremely Low Frequencies: 3 Hz to 3 kHz) range are mostly confined by the spherical cavity formed by the Earth's surface and the electrodynamically diffusive lower ionosphere. Propagation of ELF waves is characterized by low attenuation, especially in the Schumann resonance (SR) frequency range (5 Hz to approx. 60 Hz), where it does not exceed 1 dB/Mm under both day- and night-time conditions (Galejs, 1972). As a result, an effective interference between the "direct" and the "around-the-globe" waves occurs, in a phenomenon known as the Schumann resonances (SR), after the German scientist (Schumann, 1952) who predicted them theoretically, even before any attempts to explore this frequency range experimentally. The lowest, fundamental resonance mode has frequency of about 8 Hz, which corresponds to the wavelength approximately equal to the Earth's perimeter; the higher modal frequencies are observed at ~ 14 Hz, ~ 20 Hz, ~ 26 Hz, etc. In principle, continuous observations of the Schumann resonance parameters (modal amplitudes, frequencies, and quality factors) provide invaluable information for monitoring the worldwide lightning activity from a single SR station. Since the purpose of such monitoring is to determine the intrinsic spatial-temporal parameters of global lightning activity, the parameters cannot be estimated directly from observations, and an accurate ELF propagation theory is required to "correct" the "distorting" effect of the propagation process occurring between the lightning sources and observer. Therefore, the investigative SR procedure has two major components to be considered in this chapter: a receiving/processing technique and equipment as well as a theoretical apparatus for extracting intrinsic information from collected data.

In the 1980s and 1990s, four factors had intensified ELF research: (1) the application of man-made extremely low frequency signals to submarine communications; (2) the computerization of observations allowing for continuous accumulation of experimental data; (3) the interest in global change and its connection with atmospheric electricity; and (4) the discovery and intensive exploration of transient luminous events (TLEs) in the stratosphere and mesosphere. After the end of the Cold War, the international ELF collaboration has resulted in a wide exchange of ideas and in developing new methods and techniques. A series of combined – remote electromagnetic, global satellite, and local ground-based radar – experiments have provided valuable material for quantitative exploration of ELF propagation phenomena known previously only qualitatively from theoretical considerations. In particular, it was found that the extraction of information about global lightning activity

from its electromagnetic signatures could not be done in an accurate way without considering a number of propagation effects caused by the day/night asymmetry of the Earth-ionosphere, which, in its turn, requires a sufficiently accurate propagation theory.

16.2 Global Lightning Parameters Deducable from Schumann Resonance Observations

16.2.1 Schumann Resonance Intensity and Global Lightning Activity

The SR phenomenon affords two distinct methods for the measurement of global lightning activity, one from the so-called ‘background’ signals and the other from the high-amplitude transient signals. Each and every lightning flash contributes some electromagnetic energy to the background resonances, though not all flashes contribute equally. The mean time interval between flashes occurring worldwide is 10–20 ms, an interval short compared to the time required for the energy from any one flash to ‘ring-down’ (>130 ms) in its resonant interaction with the Earth-ionosphere waveguide. As a consequence, the signals from individual lightning flashes are strongly overlapping in time to form this background signal.

To maintain an electromagnetic steady state, the input energy from global lightning flashes must balance the energy dissipated in the cavity—within two characteristic layers of the lower ionosphere (Madden and Thompson, 1965; Cole, 1965; Greifinger and Greifinger, 1978). The latter dissipation rate is proportional to the field intensity and hence the mean flash rate is also proportional to field intensity. The lightning source term for field energy is a vertical charge moment squared per unit time with physical units $C^2\text{km}^2/\text{s}$. The theory for the cavity (see Section 16.3) together with calibrated measurements of the intensity of the background resonances thereby enables access to a measure of global lightning activity in absolute units, in contrast to more conventional measures in units of flashes per second, which are not absolute. Estimates of the global activity by this approach have been carried out by Clayton and Polk (1977) and by Heckman et al. (1998).

The second method for quantifying global activity involves the large-amplitude transient excitations of the cavity and is more in line with conventional methods for assessing lightning activity—a simple counting of these exceptional flashes. A small minority of superlatively energetic transient events provide more field intensity than all other lightning on the planet, for periods of a few hundred milliseconds. On this basis, they can be located by any ELF receiver worldwide (Huang et al., 1999; Hobara et al., 2006), characterized by a vertical charge moment in physical units ($C\text{-km}$), and counted as a lightning flash. Further details may be found in Section 2.1.2. Since only exceptional lightning flashes are counted (the great majority of total flashes are ‘buried’ in the signal of multiple, superimposed events of smaller ampli-

tude, which together constitute the background resonances previously discussed), the global flash rate assessed by this single-station method is less than 0.1% of the total global flash rate.

16.2.1.1 General Global Behavior of the Background Resonances

Global lightning is mainly concentrated in the land regions as shown in Fig. 16.1, primarily in the three tropical chimney regions in South America, Africa and the Maritime Continent (MC), as well as in North America in summer months.

In general, thunderstorms over land are most common in the local afternoon (Williams and Heckman, 1993; Lay et al, 2007), and the tropics dominates in lightning over higher latitudes by a two-to-one margin. As a consequence, the maximum lightning activity in the three tropical chimney regions superimposes in Universal Time (UT) to produce a characteristic diurnal variation with a relative importance of lightning activity in the three main lightning regions observed by the OTD (Optical Lightning Detector) satellite as shown in Fig. 16.2a.

The superposition of the ELF electromagnetic radiation from these lightning flashes as the background signal defines a closely related diurnal variation in SR intensities as presented for the vertical electric field, E_z , measured at the Nagycenk (NCK) station in Central Europe (Fig. 16.2b), and for the horizontal magnetic field

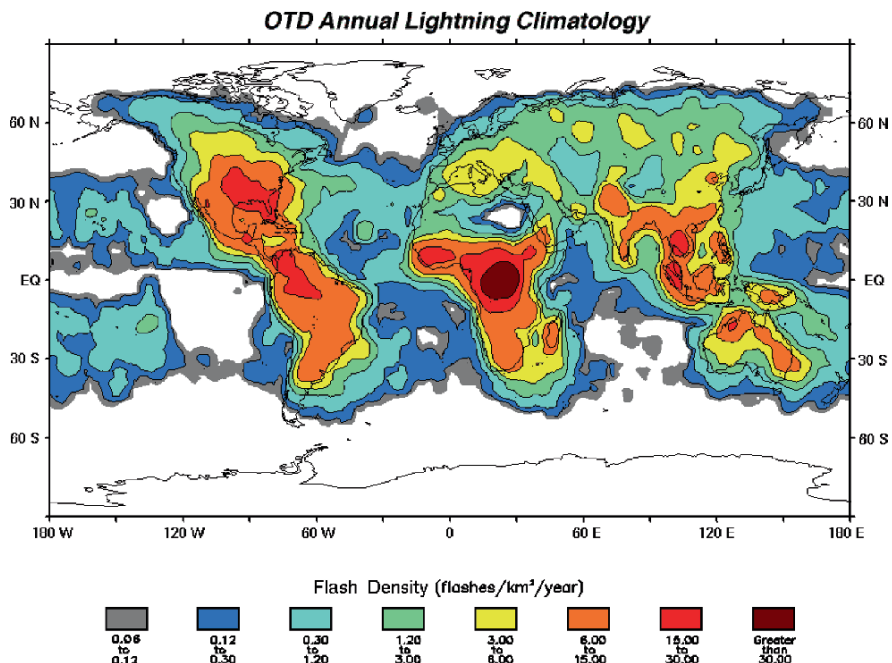


Fig. 16.1 Annual lightning climatology based on the observation of the Optical Transient Detector in space (NASA MSFC Site)

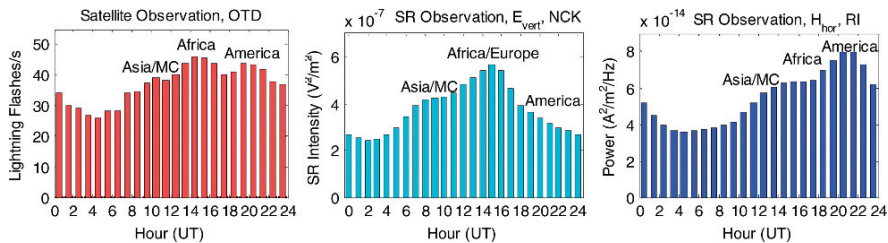


Fig. 16.2 (a) Annual mean diurnal lightning distribution (in UT) observed by OTD satellite; (b) six year mean (1994–1999) of the diurnal SR intensity variation of the vertical electric field component recorded at NCK, Hungary; (c) six year mean (1994–1999) of the diurnal SR intensity variation of the horizontal magnetic field component in RI, USA

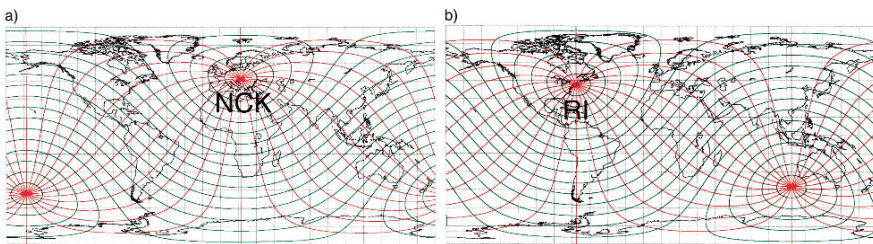


Fig. 16.3 Great circle paths (red) and iso-distance curves in intervals of 1 Mm (green) on a 15×15 grid of geographical coordinates (black) for (a) NCK, Hungary; and for (b) Rhode Island, USA, two SR stations currently operated by the authors

(H_ϕ) recorded at Rhode Island in the USA (Fig. 16.2c). In spite of the similarities between the satellite and the ELF observations, the relative importance of the lightning activity of the three tropical chimney regions indicated by SR intensities differs from the OTD observations due to the changing source-observer distances and ionospheric propagation conditions for ELF waves radiated from the “lightning antennas”.

The NCK station is roughly equidistant from both South America (SA) and the Maritime Continent (MC) (see Fig. 16.3a), but the peak lightning activity in SA is observed under local night-time condition at NCK, in contrast with the maximum MC activity recorded under local day-time condition at NCK. The American lightning sources are closest to the RI observer, while the MC is the most distant source region from RI (see Fig. 16.3b) and a local night-time condition exists at RI when MC lightning activity is maximum. Theoretical considerations are discussed in Section 3.

One important distinction between the UT time diurnal variations of global lightning as seen in SR intensity of Fig. 16.4, and the UT time variation of the surface potential gradient (also known as the ‘Carnegie curve’ of atmospheric electricity) (e.g., Markson, 2007), is the identification of individual peaks for the three major tropical source regions in the former and not in the latter. This distinction adds to the long-standing evidence that the sources for SR differ from the sources for the DC global electrical circuit (Wormell, 1930; 1953; Williams, 2008). The analyses of

OTD lightning observations by Nickolaenko and Hayakawa (2007a) overlook this distinction.

16.2.1.2 General Global Behavior of Transient Resonances

Kemp and Jones (1971) first described the global location of superlative lightning flashes from a single measurement station with SR techniques. The events themselves are called ‘Q-bursts’ following early work by Ogawa et al (1967), and many of these flashes are physically linked with ionization phenomena (sprites, haloes and elves) in the mesosphere (Boccippio et al, 1995; Huang et al, 1999; Williams, 2001; Williams et al, 2007), that are also the subject of current international research. The theory for this SR location method, involving the wave impedance for ranging, and standard crossed loops for direction-finding, is described in section 3.1.1.

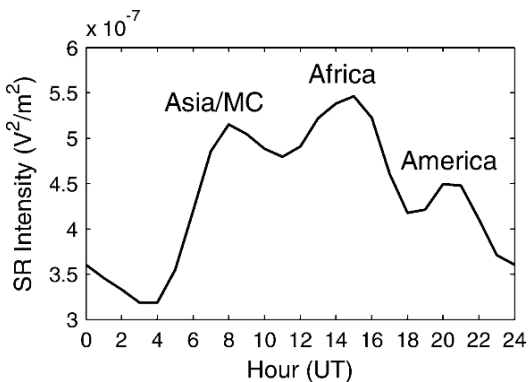


Fig. 16.4 Mean Fall-Winter SR Intensity at Nagycenk, Hungary shown SR intensity peaks at the time of maximum lightning activity in the three tropical chimney regions

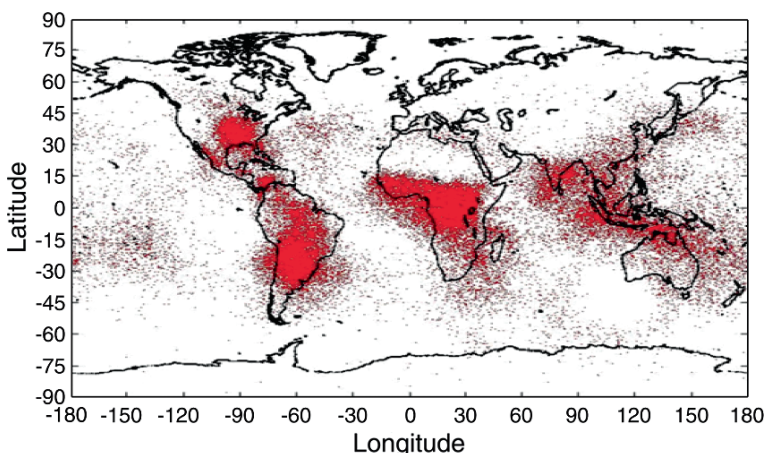


Fig. 16.5 Global map showing Q-burst locations with positive polarity and vertical charge moments greater than 500 C-km, all events located from the SR station in West Greenwich, Rhode Island

The advent of digital signal processing on personal computers (PCs), first pursued by Sentman (1987) for SR studies, has greatly expanded the use of this method, which has now been practiced on large numbers of events in England (Burke and Jones, 1995), in the USA (Cummer and Inan, 1997; Huang et al, 1999; Boccippio et al, 1998; Price et al, 2004; Williams et al, 2006; Hobara et al, 2006; Williams et al, 2007), Hungary and Israel (Greenberg et al., 2005); Japan (Hobara et al, 2000; Sato et al, 2003; Hobara et al, 2006; Ogawa and Komatsu, 2008). Event location by direction finding alone, using multiple stations, has also been carried out by Füllekrug and Constable (2000) and Füllekrug et al (2002).

A global map for these exceptional lightning flashes with positive flash polarity is shown in Fig. 16.5. As with the ‘background’ lightning in Fig. 16.1, this special subset of global lightning is also strongly land-dominated. The most prominent tropical chimney for lightning is Africa, where intense mesoscale convective systems are also predominant in other studies (Toracinta and Zipser, 2001). The meteorological origin of mesoscale lightning causal to Q-bursts is discussed in Williams (1998) and Williams and Yair (2006).

16.2.2 Schumann Resonance Frequencies and their Physical Interpretation

The electromagnetic energy in the SR frequency range exists in resonance modes whose dimensions are controlled by the size of the Earth, and which differ for the electric and magnetic field components (Wait, 1962, Sentman, 1995). The observed peak frequencies of the power spectrum shift a little relative to the eigenfrequencies of the Earth-ionosphere cavity due to the interference of adjacent modes in this highly dissipative system. The peak frequencies of the individual modes can be determined by several methods (see Section 4.2).

16.2.2.1 The Properties of the Earth-Ionosphere Resonator and Observed SR Characteristics

Theoretically, the resonance properties of any resonator are described by complex eigenfrequencies, the real parts of which present modal resonance frequencies, while their complex parts are related to the waveguide’s quality factors (Mushtak and Williams, 2002). The properties of a high-quality resonator, whose modes do not overlap, can be determined directly from observed resonance patterns, which is not the case for the Earth-ionosphere waveguide where the quality factors of detectable modes are as small as 4 to 8 (Mushtak and Williams, 2002). Due to the intra-modal overlapping effect, the observable – peak – frequencies are only related, but not equal, to the actual resonance frequencies of the waveguide; the same is also true for the modal quality factors. In the earliest SR studies (Balser and Wagner, 1962) it was found that the observed “resonance” frequencies were not

invariants and showed pronounced diurnal variations that were rightly attributed to the spatial-temporal dynamics of global lightning activity, the major source of SR excitation. Since the amplitude of each resonance mode has an individual dependence on the source-observer distance (in a uniform model of the resonator, via the corresponding Legendre polynomial; Galejs, 1972), the lightning dynamics affects the overlapping of modes, which results in variations of observable “resonance” frequencies. For instance, with the SR I amplitude decreasing and the SR II increasing, the SR I peak frequency would be “gravitating” to a higher value, and vice versa.

The exploration of the Earth-ionosphere resonator remains an important objective in SR studies, and a search continues for an effective method of extracting the actual resonance characteristics from SR observations. The shortcomings of applying the initially promising Lorentzian approach (see Section 4.2) to the background SR observations and theoretical considerations (Mushtak and Williams, 2008) indicate that efforts in this direction are to be focused rather on individual lightning-generated events (transients) than on the background signal.

16.2.2.2 Variation of Peak Frequencies with Source-Observer Distance

The peak frequencies for the different modes and field components of the SR ‘background’ can vary depending on the source-observer geometry. The diurnal frequency variations are just the manifestation of the motion of the mode structures attached to the active thunderstorm regions with changing distances from an observer fixed on the Earth. Therefore, the daily frequency patterns (DFP) are different for the different modes and field components but the same or similar for each mode and field component for the same month of consecutive years as demonstrated in Fig. 16.6. In this way, the recurrence or change of the DFP can be a reliable indicator of the global lightning position and its dynamics on longer time scales. It is important to emphasize that, with the exception of the behavior noted in the next section, the frequency variability in SR is controlled by meteorology within the SR cavity, and not by processes originating outside the cavity.

16.2.2.3 Variation of Eigenfrequencies with Modifications of the Ionosphere

The natural eigenfrequencies of the Earth-ionospheric cavity are set by the size of the cavity and the speed of light therein. This cavity speed of light is influenced by the conductivity of the diffusive lower ionosphere (Galejs, 1972). This conductivity is influenced by ionizing radiation from the Sun and other extraterrestrial sources (Hargreaves, 1992). The modulation of eigenfrequencies due to external forcing always appears with the same sign for all modes and field components as shown for the influence of the Earth-ionosphere cavity by hard solar x-ray bursts (Roldugin et al., 2003, Sátori et al., 2005) and demonstrated both for the effect of background solar x-ray flux on the 11-year solar cycle and the hard solar X-ray flux on the minutes-hours time scale (Sátori et al., 2005).

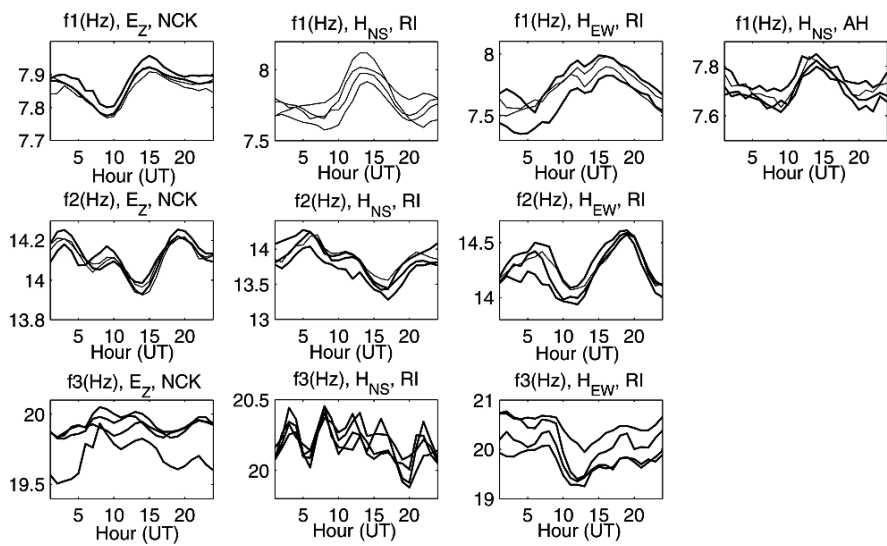


Fig. 16.6 Mean diurnal frequency patterns for the first three modes of the E_z field component recorded at NCK (left column), for the first three modes of magnetic components measured at RI (middle columns), as well as for the first mode of H_{ns} observed at the Arrival Height (AH) station in Antarctica (right hand plot) in January of four consecutive years

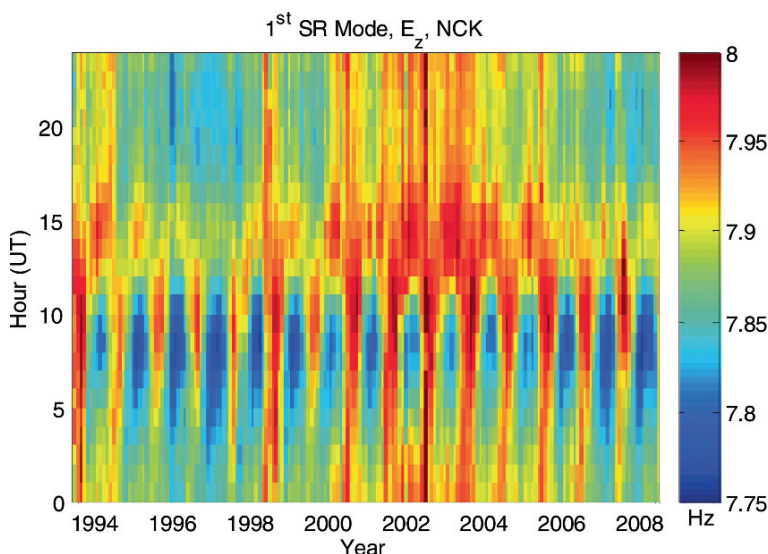


Fig. 16.7 Diurnal-annual frequency distribution of the 1st SR mode for the E_z field component recorded at NCK, Hungary (See also Plate 18 in the Color Plate Section on page 604)

16.2.2.4 Superposition of Peak Frequency and Eigenfrequency Variations

The long-term SR frequency distribution observed at Nagycenk, Hungary shown in Fig. 16.7 exhibits pronounced frequency variations on the diurnal and annual time scales as the manifestations of the diurnal zonal and annual meridional redistribution of global lightning with respect to the Nagycenk observer as well as a change of frequency level on the 11-year solar cycle (higher at solar maximum in 2002 and lower at solar minimum in 1996 and 2007). The latter signal is the manifestation of the eigenfrequency variation of the Earth-ionosphere cavity resonator which appears with the same sign at all observation sites (Sátori et al., 2005). This behavior contrasts with the source-observer distance-dependent frequency changes demonstrated on the diurnal time scale in Fig. 16.6 in Section 2.2.2.

16.2.2.5 The Frequency Range and its Connection with Global Lightning Area

The daily frequency range (DFR: $f_{\max} - f_{\min}$) is indicative of the average size of thunderstorm regions (Nickolaenko and Rabinowicz, 1995). The wider the DFR is, the smaller the lightning area is, and vice versa and it is valid for each SR mode. This relation is demonstrated in Fig. 16.8, where DFRs (vertical arrows in Fig. 16.8a, b) and satellite observations of lightning source diameters (horizontal arrows in Fig. 16.8c) are compared. The lightning areas are smaller in the Southern Hemisphere (SH) summer than in Northern Hemisphere (NH) summer due to the smaller land areas there. Consequently the DFR is wider at NCK in NH winter than in NH summer.

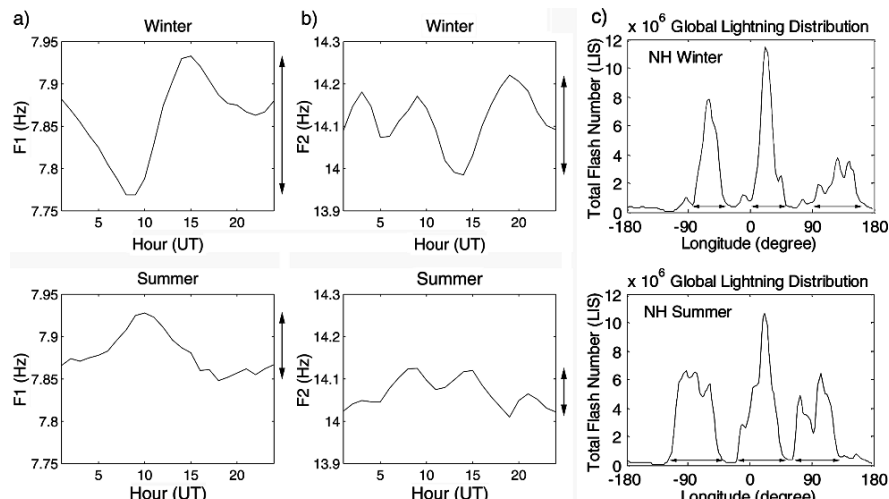


Fig. 16.8 Variation of the diurnal frequency range (DFR) for (a) the 1st and for (b) the 2nd E_z modes at NCK in NH winter and summer months marked by vertical arrows on the right hand side of each plot, and (c) lightning distributions in the three main lightning regions with zonal diameters indicated by horizontal arrows in NH winter and summer months observed by LIS satellite

16.3 Theoretical Interpretations of ELF Observations

In the 1960s, soon after the pioneering theoretical (Schumann, 1952) and experimental (Balser and Wagner, 1962) ELF publications, it had been realized that electromagnetic observations in the 5 to 40 Hz frequency range could provide, in a cost-effective way, invaluable information on worldwide thunderstorm activity considered as a global geophysical process. It had also been obvious that this process cannot be accurately monitored without an ELF theory that would adequately account for propagation phenomena “distorting” the initial information about the lightning sources. While the experimentalists had been collecting observational material, the theoreticians had been going ahead to achieve considerable progress, as presented in three brilliant monographs by Wait (1962), Galejs (1972), and Bliokh et al. [1980], as well as in hundreds of journal publications (see the detailed bibliographies in the above-listed monographs).

16.3.1 Propagation Models

16.3.1.1 Uniform Model

The most widely exploited ELF technique is based on the spherically symmetrical model of the Earth-ionosphere waveguide where the electrodynamic properties of the waveguide are assumed to be uniform over the waveguide. Omitting some non-essential numerical factors, the frequency-domain expressions for the electromagnetic field generated by a vertical lightning discharge with current moment $IdS(f)$ in a spherical system of coordinates $\{r, \theta, \varphi\}$ are given by

$$E_r(f, \theta) \sim \frac{IdS(f)}{f} \frac{\nu(f)[\nu(f) + 1]}{H_i(f)} \frac{P_\nu[\cos(\pi - \theta)]}{\sin[\nu(f)\pi]} \quad (16.1)$$

$$H_\varphi(f, \theta) \sim \frac{IdS(f)}{H_i(f)} \frac{\frac{d}{d\theta} P_\nu[\cos(\pi - \theta)]}{\sin[\nu(f)\pi]} \quad (16.2)$$

where $\nu(f)$ is the eigenvalue of the problem (Galejs, 1972), $H_i(f)$ is the effective height of the waveguide, P_ν is the Legendre function, and the source coordinates are assumed to be $\{a, 0, 0\}$, a meaning the Earth’s radius. Various sets of physical propagation parameters related to the eigenvalue $\nu(f)$ are discussed by Mushtak and Williams (2002). Models of propagation parameters practically used in ELF research are considered and compared by Williams and al. (2006).

Mathematically, the Legendre function and its derivative describe the well-known SR phenomenon – interference between the “direct” and “around-the-globe” waves, due to which the spectral forms – without the current moment factor – are uniquely dependent on the source-observer distance $D = a\theta$ and so can be used for

locating the lightning source from the fields it generates. To exclude the unknown current moment's spectra (and, as an additional bonus, the effective ionospheric height), Kemp and Jones (1971) suggested estimating the source-observer distance from the spectrum of the wave impedance:

$$Z(f; \theta) = \frac{E_r(f; \theta)}{H_\varphi(f; \theta)} \quad (16.3)$$

instead of the electric and magnetic spectra. This suggestion has proved to be extremely fruitful and, in the limits of the uniform model, provided hundreds of thousands of remote locations at the Rhode Island-based MIT ELF site (Huang et al, 1999). Several examples of theoretically computed frequency-distance variations of the wave impedance in a normalized form (related to its value in free space) are shown in Fig. 16.9. The computations have been carried out using the Ishaq and Jones (1977) model of propagation parameters formulated in terms of phase velocity $V_{ph}(f)$ [m·s⁻¹] and attenuation rate $\alpha(f)$ [dB · Mm⁻¹] vs. frequency f [Hz] as

$$\frac{c}{V_{ph}(f)} = 1.64 - 0.1759 \log f + 0.0179 \log^2 f; \alpha(f) = 0.063 f^{0.64} \quad (16.4)$$

related to the eigenvalue $v(f)$ appearing in (16.1), (16.2) via the complex sine $S_0(f)$ (Galejs, 1972):

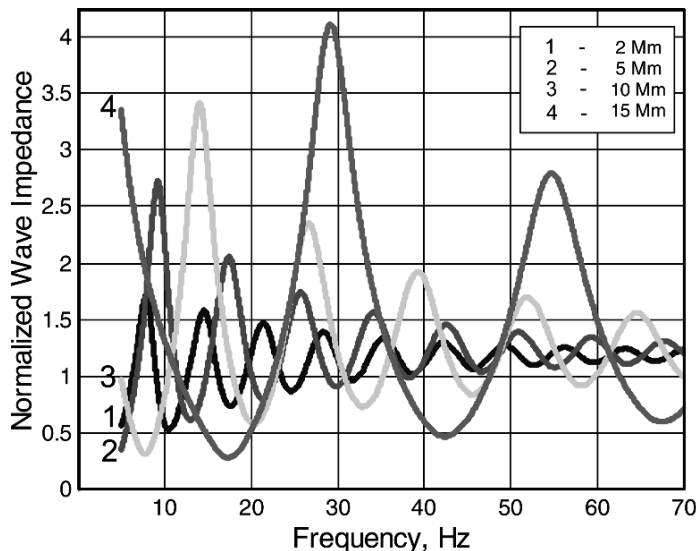


Fig. 16.9 The absolute value of the normalized wave impedance vs. frequency and source-observer distance simulated in the Ishaq and Jones (1977) model of propagation parameters

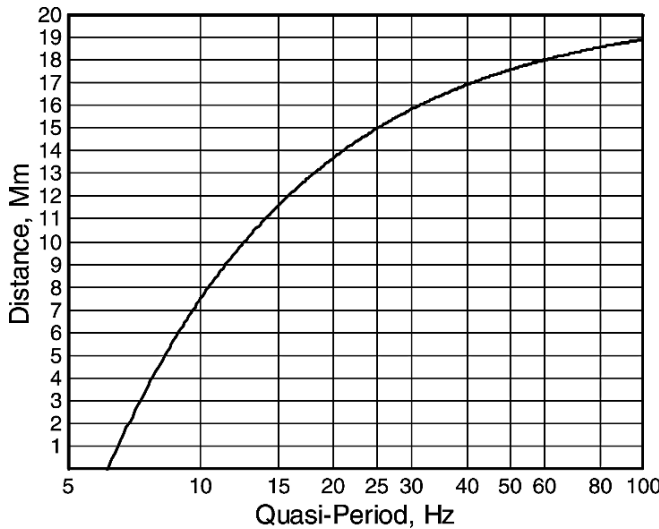


Fig. 16.10 The calibration plot for estimating the source-observer distance from the wave impedance's quasi-period (computed on the basis of the Ishaq and Jones (1977) model of propagation parameters)

$$S_0^2(f) = \frac{v(f)[v(f) + 1]}{(ka)^2} \quad (16.5)$$

$$\text{Re}S_0(f) = \frac{c}{V_{ph}(f)}, \quad |\text{Im}S_0(f)| = \frac{\alpha(f)}{0.182[\text{dB} \cdot \text{Mm}^{-1}\text{s}]f} \quad (16.6)$$

where $c[\text{m}\cdot\text{s}^{-1}]$ and $k [\text{m}^{-1}]$ are the free space speed of light and wave number, respectively. In Fig. 16.9, a dependence of the quasi-period of the wave impedance on the source-observer distance is evident. The corresponding quasi-period/distance plot, the one in use at the Rhode Island site for locating sources of transient events (Williams et al., 2007), is presented in Fig. 16.10.

16.3.1.2 Non-Uniform Model

Five decades of ELF research have provided enough evidence for propagation effects that cannot be interpreted satisfactorily in the limits of the uniform Earth-ionosphere model. Madden and Thompson (1965), who suggested considering the waveguide ELF propagation as an analogue to the propagation process in a two-dimensional transmission line, have laid the foundation of the non-uniform ELF propagation theory more than 40 years ago. The idea had been dormant for several decades, after which – with an additional stimulus from Greifinger and Greifinger's (1978) revolutionary concept of two complex characteristic altitudes – Kirillov et al. (1997) and Kirillov (2002) had developed the two-dimensional tele-

graph equation (TDTE) technique for computing ELF fields in a non-uniform waveguide. Generally, the TDTE technique can account for any non-asymmetry of the waveguide (the latitudinal dependence of propagation parameters, polar anomalies, local ionospheric disturbances, etc.), yet, since the decades of ELF research have shown that the day/night asymmetry plays a major role in ELF propagation, this asymmetry will be the one to be explored experimentally and theoretically in this subchapter.

When considering the day/night asymmetry of the Earth-ionosphere waveguide, it is natural to align the polar axis of the spherical system of coordinates $\{r, \theta, \varphi\}$ with the solar zenith (the sub-solar point on the Earth's surface), which reduces the general TDTE equation (Kirillov et al., 1997) to the form

$$\left[\frac{1}{\sin \theta} \frac{\partial}{\partial \theta} \frac{1}{H_L(f; \theta)} \sin \theta \frac{\partial}{\partial \theta} + \frac{1}{H_L(f; \theta) \sin^2 \theta} \frac{\partial^2}{\partial \varphi^2} + \frac{(ka)^2}{H_C(f; \theta)} \right] U(f; \theta, \varphi) = - \frac{(ka)^2}{H_C(f; \theta_S)} U_S, \quad U_S = i \frac{M_S(f) \delta(\theta - \theta_S) \delta(\varphi - \varphi_S)}{2\pi f \varepsilon_0 a^2 \sin \theta}; \quad (16.7)$$

where $U(f; \theta, \varphi)$ is the spectral voltage defined in a specific manner (Madden and Thompson, 1965; Kirillov, 2002) to reduce the initially three-dimensional propagation problem to a two-dimensional form, U_S is the source-intrinsic voltage related to the spectrum of the source's current moment M_S , and are the spherical coordinates of the vertical lightning source location on the Earth's surface $r = a$. (According to the spherical system's definition, it will be called below, maybe somewhat clumsily, the system of helio-geo-coordinates.) In (16.7), the actual propagation parameters are two complex characteristic altitudes, $H_C(f; \theta)$ and, that are presenting – in a condensed, integrated form – the electrodynamic properties of two vertically separated ionospheric layers responsible for ELF waveguide propagation (Kirillov et al., 1997; Mushtak and Williams, 2002). To interpret the observed and simulated propagational effects, it is convenient to present symbolically (omitting some non-essential numerical factors) the components of the ELF field via the solution of (16.7) $U(f; \theta, \varphi)$ as

$$E_r(f; S \rightarrow O) \sim \frac{M_S(f)}{f} \frac{H_L(S)}{H_C(S)} \frac{1}{H_C(O)} U(S \rightarrow O), \quad (16.8)$$

$$H_\varphi(f; S \rightarrow O) \sim M_S(f) \frac{H_L(S)}{H_C(S)} \frac{1}{H_L(O)} \frac{\partial U(S \rightarrow O)}{\partial \theta}, \quad (16.9)$$

$$H_\theta(f; S \rightarrow O) \sim M_S(f) \frac{H_L(S)}{H_C(S)} \frac{1}{H_L(O)} \frac{\partial U(S \rightarrow O)}{\partial \varphi} \quad (16.10)$$

where each component is presented as a combination of source-local (denoted by the S symbol) and observer-local (denoted by the O symbol) electrodynamic properties

of the waveguide as well as the global propagation factors (denoted by the $S - O$ symbol). In the TDTE simulations presented below, the lower characteristic altitude has been computed using a sophisticated analytical model proposed by Phyllis Greifinger (Greifinger et al., 2007) with variables determined from both aeronomical data and ELF observations (Greifinger et al., 2005). Due to the more complicated (anisotropic) conditions within the upper characteristic layer (Kirillov, 2002; Mushtak and Williams, 2002), the construction of an adequate analytical model of the upper characteristic altitude $H_L(f)$ is a more challenging problem, with various ways of resolving it presently being explored. Therefore a reasonable methodological compromise is being used in the present study: the day- and night-time values of $H_L(f)$ are determined, using the relationship

$$S_0^2(f) = \frac{H_L(f)}{H_C(f)} \quad (16.11)$$

given by Mushtak and Williams (2002) as well as Equations (16.5), (16.6), from $V_{ph}(f)$ and $\alpha(f)$ computed, in their turn, from representative day- and night-time ionospheric profiles (Galejs, 1972; Fig. 7.12).

Generally, the two-dimensional telegraph Equation (16.7) can be solved in a numerical – and so time-consuming – way for arbitrary dependences of the propagation parameters $H_C(f; \theta)$ and $H_L(f; \theta)$ on the helio-geo-latitude. Yet, since the inverse tasks of monitoring global lightning activity require repeated computations of theoretical spectra, it is preferable to make use of an analytical TDTE solution (Kirillov et al., 1997) that can be realized as a fast-running computational algorithm. Such an analytical solution is available if the waveguide's model neglects the relatively slow dependence of the propagation parameters on the helio-geo-latitude θ within the respective (day- or night-time) hemisphere and only distinguishes between their averaged values in each hemisphere: $H_C^{(D)}(f)$, $H_L^{(D)}(f)$ and $H_C^{(N)}(f)$, $H_L^{(D)}(f)$, respectively (the “partially uniform” model of the Earth-ionosphere waveguide).

16.3.2 Propagation Effects

16.3.2.1 Transient Resonances: Accuracy of Wave Impedance Distance Estimates

The results of the source-local radar observations of a sprite-producing storm in Northern Australia and the simultaneous ELF observations of the corresponding sprite-generated transients at the Rhode Island site are presented in detail by Williams et al. (2007). These results provide a unique opportunity to determine the practical accuracy of the above-discussed wave impedance procedure for estimating the global (16.6 Mm) source-observer distance, as well as to consider the propagation phenomena affecting the accuracy.

Despite the fact that the geographical position of the parent storm had been almost unchanged during the four-hour observational period, it was found that the wave impedance's quasi-period had been increasing approximately monotonically from about 26.5 to 30 Hz (Fig. 16.11, pentagram symbols), the distance estimate determined using the calibration plot (increasing from about 15.3 to 15.8 Mm, but still below the ground-true value of 16.6 Mm). The TDTE computations (Fig. 16.11, circle symbols) show an analogous variation of the quasi-period, which confirms the hypothesis that the experimental variation is to be attributed to the change in propagation conditions due to the dynamical day/night asymmetry of the Earth-ionosphere cavity.

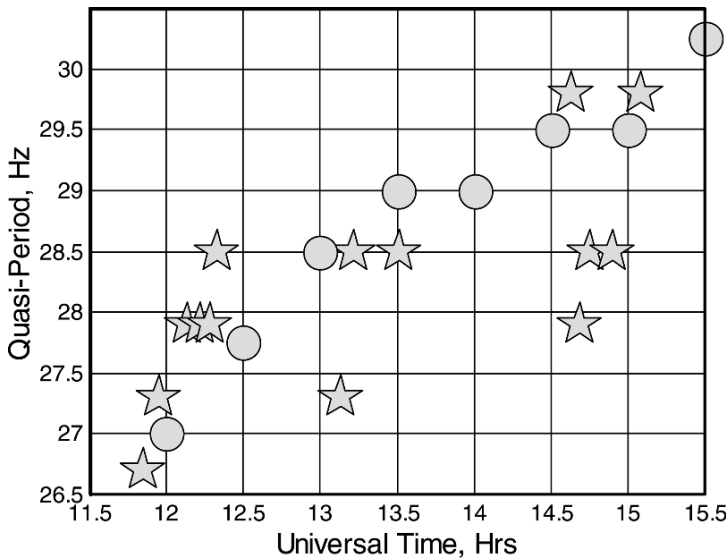
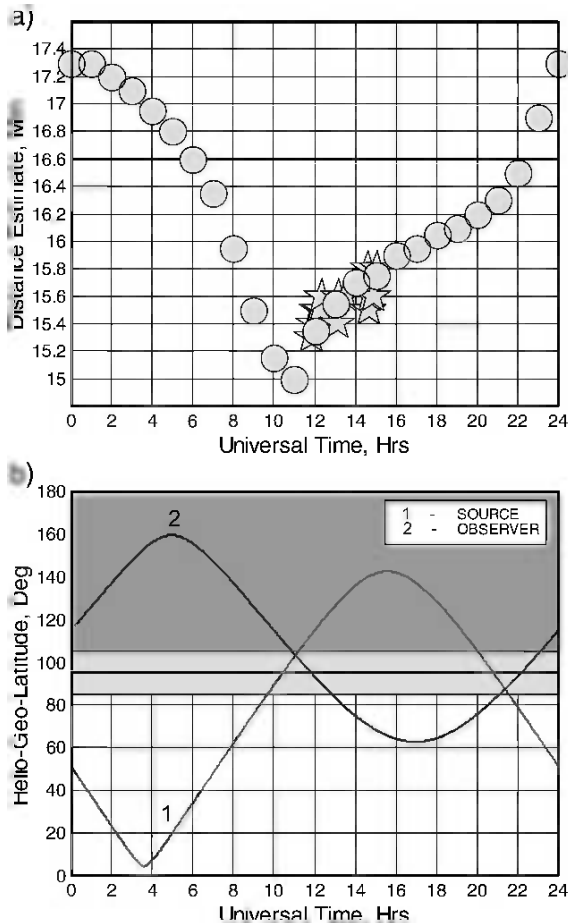


Fig. 16.11 The observed at the Rhode Island station (pentagrams) and TDTE-simulated (circles) temporal variations of the wave impedance's quasi-period for a N. Australia sprite-producing storm occurred on November 26, 1997 at a distance of 16.6 Mm from the observer

In Fig. 16.12a, the TDTE simulations of the quasi-period (recalculated into the distance estimate via the calibration plot, Fig. 16.10) are extrapolated beyond the limits of the actual four-hour observational period. To understand the dependence of the distance error on propagation conditions, Fig. 16.12b presents the helio-geo-trajectories defined as the variations, with the universal time, of the source's $\theta_S(T_U)$ and the observer's $\theta_O(T_U)$ latitudinal positions in the dynamical system of spherical coordinates. There are two periods of time when the distance error could be, presumably, minimal: 6 UT and about 22.5 UT. While the evening minimum is the result of complicated and not-so-easily interpretable phase interference between the “direct” and “around-the-globe” waves, the helio-geo-trajectories in Fig. 16.12b clearly shows the reason for the morning minimum. At 6 UT, the source and observer are positioned symmetrically (with respect to the helio-geo-latitude θ) relative to the

Fig. 16.12 (a) The source-observer distance estimated from observations (pentagrams) and TDTE simulations (circles) of the wave impedance for the Northern Australia – Rhode Island propagation path (November 26, 1997).
(b) The helio-geo-latitudinal trajectories of the North Australian sprite-producing storm (source) and the Rhode Island ELF station (observer) on November 26, 1997



day-night boundary, and the corresponding propagation conditions are being averaged in a manner providing the best electrodynamic similarity between the real asymmetrical waveguide and the model symmetrical waveguide.

16.3.2.2 Background Resonances: Amplitude Variations vs. Universal Time at a Mid-Latitude Station: Rhode Island

For about 15 years, SR background observations have been continuously collected at the MIT-operated ELF field station near West Greenwich, Rhode Island, USA. The results are being stored in a compact form – as a set of parameters (modal powers, frequencies, and quality factors) of Lorentzian fits (Mushtak and Williams, 2002) to observed spectra for the three-components (vertical electric, east-west and north-south magnetic) of background signal.

Fig. 16.13 (a) The normalized observed 12-hour variation of the background electric power at the Rhode Island ELF station on December 18, 1996. (b) The normalized simulated 12-hour variations of the background electric power for the Rhode Island ELF station in December: open circles – in a spherically symmetrical model of the Earth-ionosphere cavity; filled circles – in the cavity's model with the day/night asymmetry (the TDTE theory). The shaded area demonstrates the amplitude effect of the day/night asymmetry. (c) The helio-geo-latitudinal trajectories of the African and American “chimneys” in a December model of the global lightning activity

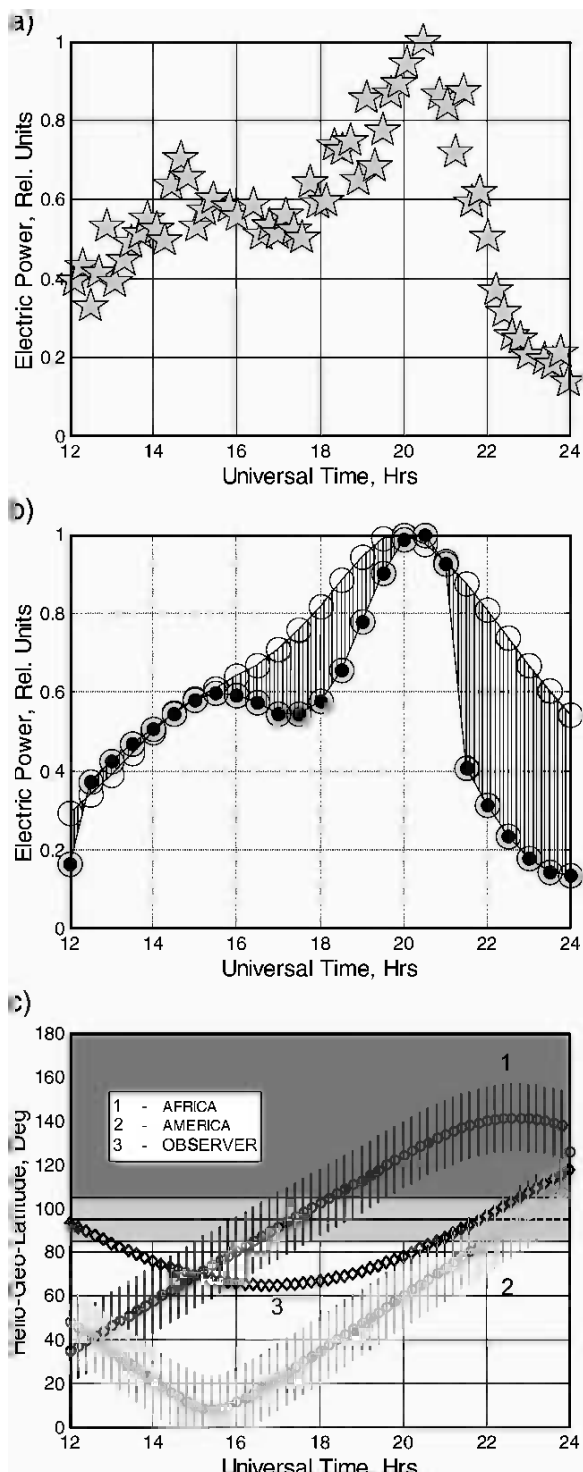
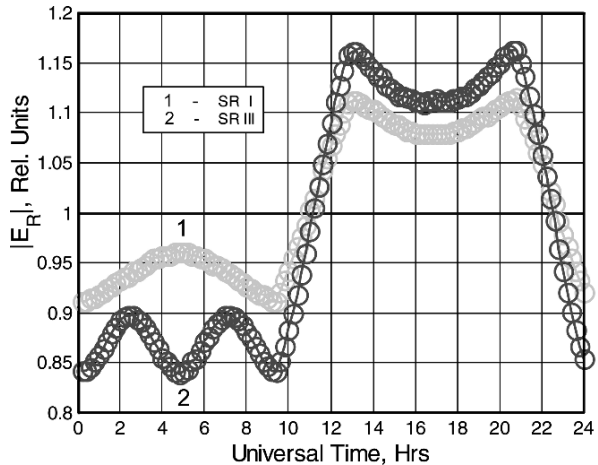


Figure 16.13a presents, as an example, a 12-hour temporal dynamics of the SR III electric power collected on a typical December day. In the figure, two maxima are evident – corresponding to the periods of maximum activity of the African and South American lightning “chimneys”, respectively. Since one of the principal goals for observing the global background signal is the single-station monitoring of the major lightning “chimneys”, it is advisable to estimate the applicability of various propagation models that are to be used to “rectify” the observed results from propagation effects. In this study, the spherically symmetrical technique described in Section 3.1.1 and the non-uniform (TDTE) method presented in Section 3.1.2 have been tested; the background signal has been modeled by means of integrating the electromagnetic contributions over the temporarily and spatially dynamical global “chimneys” (Mushtak and Williams, 2002). (Since the geographical position of the Rhode Island station is favorable for monitoring chiefly the African and American lightning activity, with the MC “chimney” playing a minor role at this receiver, the testing has been carried out for the 12-hour period of time covering the activities of the first two “chimneys”). The uniform and TDTE simulations for the December season are compared in Fig. 16.13b; to make the deviations more visual, both simulations are normalized to 1 (the absolute deviations will be discussed later). From Fig. 16.13a, it is obvious that the waveguide’s non-uniformity plays an important role in forming the American “peak” and is of lesser importance for the form of the African “peak”. There are two major differences between the uniform and non-uniform dynamics: the TDTE “peak” is much more pronounced, more “sharp”, and characterized by a steep amplitude decrease during the period of observer-local dusk (see the helio-geo-latitudinal trajectory of the receiver in Fig. 16.13c) – a pattern observed on many ELF stations for various SR modes.

The dusk amplitude effect is easily interpretable as a result of the observer-local change in the lower characteristic altitude [see Equation (16.8)]. According to aeronomical estimates (Greifinger et al., 2007) confirmed by experimental findings (Greifinger et al., 2005), this change makes, at SR I to IV, from about 20 to 25%, which means, in terms of the spectral power, a decrease of 44 to 55%. The source-local factor $H_L(S)H_C^{-1}(S)$ in Equation (16.8) causes an additional decreasing effect, but of a lesser importance. First, according to computations presented by Galejs (1972, Fig. 7.12), the day-to-night change in the phase velocity in the SR range makes about 6 to 7%, which – see Equations (16.6) and (16.11) – gives a 12 to 14% change in the source-local factor. Second, and more important: in contrast to the observer, the source – a geographically distributed lightning “chimney” – is drifting through the day/night boundary gradually, due to which the additional decreasing effect is “spread” over the period of time much longer (several hours) than that corresponding to the terminator’s crossing the observer’s location (about one hour).

Another cause of the deviations between the uniform and TDTE simulations in Fig. 16.13a is of a different, global nature defined by the global factor $U(S - O)$ in Equation (16.8). To demonstrate this reason more clearly, Fig. 16.14 presents TDTE diurnal variations of the electric field amplitude generated by an individual

Fig. 16.14 The TDTE simulated electric amplitude (related to its values in the spherically uniform model of the waveguide) generated by a single lightning source located in the center of the American “chimney” in December



lightning discharge located at the center of the American “chimney” at two SR frequencies. (In this instance, to show the dusk/dawn amplitude effects in a more realistic way, the numerical solution of the TDTE with a smooth day/night transition has been used instead of the “partially uniform” solution.) Fig. 16.14 shows: a general day-to-night amplitude variation due to the source- and observer-local factors; pre-dawn and after-dusk oscillations due to the reflection from the night-to-day terminator; and pre-dusk and after-dawn amplitude peaks due to the reflection from the day-to-night terminator. As a result, both the dusk and dawn amplitude effects are more pronounced than they would have been if only the local factors had been considered.

16.3.2.3 Background Resonances: Simultaneous Variations of H_{NS} Amplitude at a Middle-Latitude and a Sub-Polar Station

In 1998, at the Schumann Resonance Symposium and Workshop held in Sopron (Hungary), an intensive discussion had arisen concerning an apparent contradiction between SR observations and common knowledge about global lightning activity. Namely, it was reported that at the ELF station in the Negev Desert (Israel), the SR I electric background signal from the Maritime Continent (MC) “chimney” had been systematically observed to prevail over that from the American “chimney”, while it is well known from both long-time meteorological and satellite data (e.g., Chrisian et al., 2003) that the American “chimney” is systematically more active than the Maritime Continent. At the meeting, it had been agreed, principally, that a propagation factor was most likely responsible for the apparent contradiction, but no conventional theory could provide a convincing explanation. The Negev Desert station is located at approximately equal distances from both “chimneys” in question, but even if a difference of several megameters is assumed, the attenuation amounting to just about 0.2–0.3 dB/Mm for SR I (Galejs, 1972) cannot be responsible

for the observed effect. The difference in the character of propagation “paths” – prevailingly day-time to the MC during its maximum activity and night-time to the American one – is also of negligible importance due to the global nature of SR propagation. The TDTE theory with its clear distinction between the global and local propagation factors is the one that provides a feasible interpretation. Since the lightning activity in both “chimneys” is developing under approximately equal conditions relatively to its respected positions relative to the day/night boundary, the only candidate for providing a noticeable effect is the source-local factor - the lower characteristic altitude in Equation (16.8). Indeed, the maximum MC activity is being observed under the day-time ionosphere at the observer location, while the American maximum activity is being monitored under the night-time ionosphere. With the day-to-night change in the lower characteristic altitude of about 20% (Greifinger et al., 2005; Greifinger et al., 2007), the observer-local factor would “prefer” the MC “chimney”, in terms the SR I power (that is proportional to the integrated activity in flashes/sec, see Roemer (1961)), by about 40% against the American “chimney”.

Even more convincing experimental evidence has been provided courtesy of Polish colleagues by the north-south magnetic component of the first SR mode at two ELF sites – Belsk (Poland) and Hornsund (Polish Polar Station, Spitsbergen) in February, 2005 using identical induction coils (Neska and Sátori, 2006) and spectral technique (Sátori et al., 1996) for data processing.

The diurnal variations of the magnetic amplitude averaged over this month are shown in Fig. 16.15a. The Figure demonstrates a striking difference in the ratios of the observed peak signals from the MC and American “chimneys”: they are approximately equal at the Hornsund station, while the Belsk site “prefers” the MC “chimney” by about 20%. The TDTE-simulated variations computed from Equations (16.7), (16.9), and (16.10) for the “partially uniform” model are presented in Fig. 16.15b. The simulations are in a reasonable agreement with the observations, and the propagation interpretation is analogous to the above. As can be seen from Fig. 3.15c, the source-observer “paths” do not differ enough for the attenuation (global) factor to be responsible for the different patterns. The peak signal from the American “chimney” had been observed under identical (night-time) ionospheric conditions at both sites, and therefore the peak amplitudes are almost identical. In contrast, the MC activity is being observed under the day-time ionosphere at the Belsk station and under night-time ionospheric conditions at the Hornsund site (see the maps in Fig. 16.15c), which means that the 20% difference in observed peaks is to be attributed mainly to the source-observer factor. As to the larger MC effect in the simulations than in the observations ($\sim 28\%$ against $\sim 20\%$), the reason is simple: the “partially uniform” model assumes that at 9 UT the Hornsund site is located in the “full” night (see also the left panel in Fig. 16.15c), while in reality it is in the zone of transition from day to night, with a correspondingly diminished local factor. Such a scenario would be more adequately interpreted in a numerical TDTE-solution that accounted for the helio-geo-latitudinal variations of the propagation parameters.

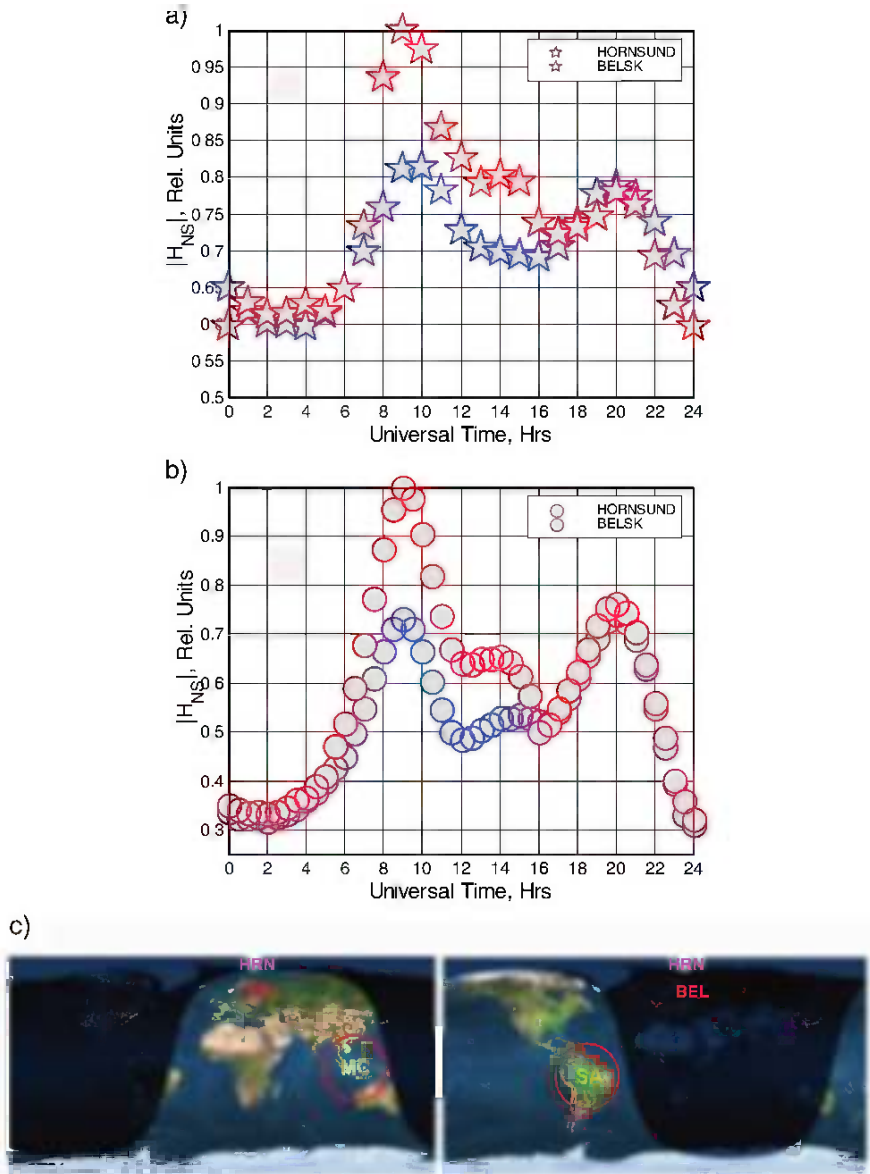
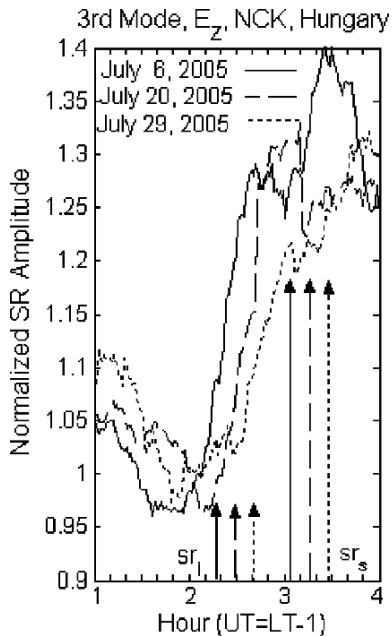


Fig. 16.15 (a) The normalized diurnal variations of the north-south magnetic background field observed at the Belsk (Poland) and Hornsund (Spitsbergen) ELF stations in February, 2005. (b) The TDTE-simulated diurnal variations of the north-south magnetic background field for the Belsk and Hornsund ELF stations in February. (c) The positions of the Belsk and Hornsund ELF stations relative to the day/night boundary during the respective periods of the maximum activities in the Asian (left) and American (right) “chimneys” (See also Plate 19 in the Color Plate Section on page 605)

Fig. 16.16 Normalized SR amplitude variations of the 3rd E_z mode at NCK in three July days, 2005 in early morning hours. Arrows at sr_i and sr_s indicate ionospheric as well as surface sunrise in the three selected days



16.3.2.4 SR amplitude variations with high-time resolution

Supporting the theoretical result in Section 3.2, jump-like amplitude variations are observed in SR records at Nagycenk with high-time resolution, Hungary, with consistent frequency dependence for the first three modes. These variations occur systematically at local ionospheric sunrise and local ionospheric sunset with some minute accuracy and with durations of about 30 minutes throughout the year (Sátori et al., 2007) and shown here for the 3rd E_z mode during three July sunrise intervals in Fig. 16.16.

Three-dimensional finite-difference-time-domain modeling of SR parameters by Yang and Pasko (2006) describes jump-like E_z field variations at the sr/ss terminator lines attributed to the changes in ionospheric height between day-time and night-time. Sentman and Fraser (1991), Heckman (1998), Melnikov et al (2004), and Ondrášková et al. (2007) also reported on SR amplitude/intensity variations related to the day/night asymmetry of the Earth-ionosphere cavity. Nickolaenko and Hayakawa (2002) concluded theoretically that the SR amplitude variations to be expected at the sr/ss terminator are practically undetectable. Pechony and Price (2005) claimed that SR intensity variations at two distant stations shown by Sentman and Fraser (1991) could be produced in a uniform cavity, too, due to changing source-receiver geometry. Pechony et al. (2007) inferred that the observed SR field variations are governed primarily by the variations in the source intensity and source-receiver geometry, and that the effect of the day-night asymmetry in the ionosphere is secondary. The review by Nickolaenko and Hayakawa (2007b) that addresses ‘controversial explanations’ for the “terminator effect”, claims that

models do not show an appreciable effect of the terminator on SR amplitudes, yet fails to acknowledge the many experimental findings (Sentman and Fraser, 1991; Heckman (1998); Melnikov et al, 2004; Mechtak et al, 2005; Sátori et al, 2007; Ondrášková et al. (2007), Williams et al, 2007) that substantiate this effect.

16.4 ELF Observational Techniques and Data Processing

16.4.1 Measurements of Electric and Magnetic Field Components in the ELF Range

The basic electromagnetic mode in the ELF range within the spherical Earth-ionosphere cavity is the TEM mode, defined for a uniform cavity by Equations (16.1) and (16.2), and consisting of a vertical electric and horizontal magnetic field. In a waveguide with perfectly conducting boundaries, one requires three component measurements to define the TEM mode (E_z , H_x and H_y). Ball antennas on mechanically-stable insulating supports have been traditionally used to measure E_z , whose magnitude is of the order of 0.1 millivolt/m, and so a million-fold less than the electrostatic fair weather field of atmospheric electricity. The original designs involved high impedance inputs, but more recent designs make use of charge amplifiers that facilitate a flat frequency response over a large dynamic range. The magnetic field components are measured with induction coils with 10–100 thousand turns of wire around a permalloy core (to enhance the sensitivity of the measurement), and aligned with geographic north-south and east-west directions. Such coils are often buried to suppress vibrations that may cause motions of the coil in the Earth's DC magnetic field (Sentman, 1995), whose strength is 7–8 orders of magnitude larger than the magnitude of the field in the SR TEM mode (~ 1 picoTesla).

The real Earth-ionosphere cavity lacks boundaries with perfect conductivity. Skin currents flow in the Earth's surface, in response to the electromagnetic field in the atmosphere, with attendant horizontal electric fields in the millivolt/km range. Some investigators have monitored the SR by measuring these horizontal electric fields with ground electrodes spaced by some hundreds of meters (Ogawa et al, 1969). Similar measurements are utilized in audio-magnetotellurics for studying the electrical resistivity structure within the solid earth (Ádám et al, 1990; Bashkuev and Khaptanov, 1999; Simpson and Taflove, 2006).

Figure 16.17 shows a standard SR recording system working since May, 1993 in the Széchenyi István Geophysical Observatory at Nagycenk, Hungary.

16.4.2 Spectral methods

Three different spectral methods have been used to extract SR parameters (amplitude, frequency, damping constant and quality factor) from SR records, both in the time domain as with the complex demodulation technique (Sátori et al., 1996) and

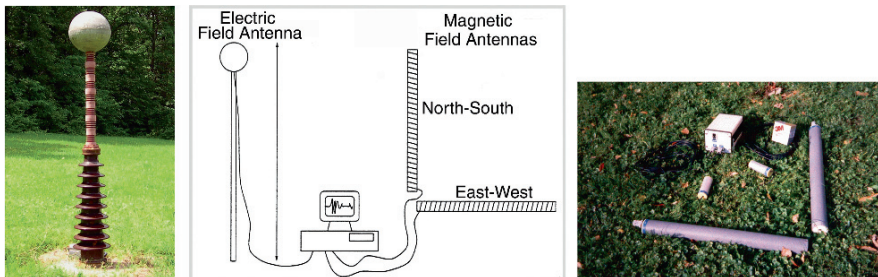


Fig. 16.17 Sketch of a standard Schumann resonance recording system (*middle*) with the ball antenna (*left*) and induction coils (*right*) working since 1993 in the Széchenyi István Geophysical Observatory at Nagycenk, Hungary

Prony method (Füllekrug 1995, Yang and Pasko 2005), and in the frequency domain as with Lorentzian fitting (Sentman 1987, Mushtak and Williams 2002; 2008). No experimental methods have been devised to obtain the complex eigenvalue (in Equations (16.1) and (16.2)) directly from observations, but these various quantities are inter-related.

The complex demodulation method, successfully has been used at Nagycenk, Hungary since 1993 (Sátori et al., 1996), is especially suitable to monitor in near-real time the temporal variation of the phase and amplitude of selected frequency components in a time series (Banks 1975, Beamish et al. 1979). SR frequency components are selected with convolution-type vectoral digital filters truncated with a Hanning-window (Verő, 1972). The magnitude of the filtered complex wave vector is proportional to the SR amplitude and its phase rotation with respect to the central period of the filter is proportional to the actual peak frequency (theoretically within one octave).

At SR field sites belonging to University of California Berkeley, USA and Arrival Height, Antarctic, the Prony algorithm was applied by Füllekrug (1994). The Earth-ionosphere cavity resonances may be described statistically by the solutions of a linear dynamic system that is excited by continuous random noise and filters out the Earth-ionosphere cavity resonances in a mean sense. The analysis of the linear dynamic system with the Prony algorithm results in a set of excitation- and internal system-parameters. While the derived amplitudes describe the excitation mechanism, the damping and eigenfrequency are related to internal properties of the Earth-ionosphere cavity as summarized in <http://people.bath.ac.uk/eesmf/eicr.html>.

At the MIT ELF station in Rhode Island, USA, a compact storage method using the Lorentzian concept has been used since 1993 and proved to be effective. Generally, the “classic” Lorentzian concept in the SR background research supposes approximating the Earth-ionosphere waveguide’s spectral response to the global lightning excitation in the form suggested initially by Balser and Wagner (1962) and later independently by Sentman (1987):

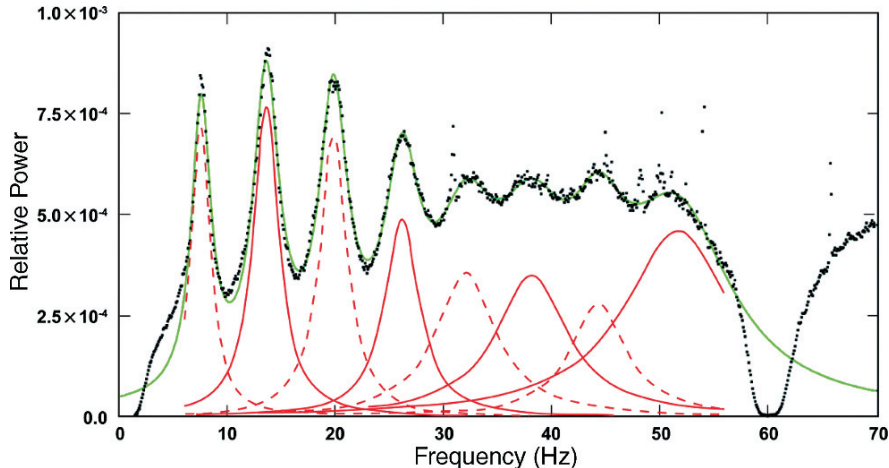


Fig. 16.18 Schumann resonance spectrum of H_{EW} mode recorded for 12-hour intervals in West Greenwich, Rhode Island, on September 6, 1997 (Courtesy of R. Boldi)

$$L^2[f; \{\lambda_n, f_n, Q_n\}_N] = \sum_{n=1}^N \frac{\lambda_n^2}{1 + \left[2Q_n \left(\frac{f}{f_n} - 1\right)\right]^2} \quad (16.12)$$

via the set

$$\{f_n, Q_n, \lambda_n\}_N \equiv f_1, Q_1, \lambda_1; f_2, Q_2, \lambda_2; \dots, f_N, Q_N, \lambda_N \quad (16.13)$$

of parameters having the physical meaning of frequencies, quality factors, and powers (electric or magnetic), respectively.

Figure 16.18 shows an example of the Lorentzian fitting procedure for SR spectra recorded in West Greenwich, Rhode Island, in September, 1997. Shown here are the individual Lorentzians for H_{EW} mode, the superposition of Lorentzians represented by equation (16.12) above, and its excellent fit over the entire frequency range with the observations.

Following the initial success of the fits shown in Fig. 16.18, it was expected that the parameters providing the best agreement between observed spectra and their Lorentzian approximations would provide reasonable estimates of the global resonance characteristics of the Earth-ionosphere waveguide, i.e., modal frequencies and quality factors. Yet detailed consideration of such estimates have revealed that they are not, as was expected, true invariants. Indeed, published extractions of these parameters from measured SR spectra (Sátori, 1996; Price and Melnikov, 2004; Sekiguchi et al, 2008) show pronounced diurnal and seasonal variations. The reason is a complicated interference between signals generated by the whole ensemble of spatially distributed lightning discharges occurring within the given observation interval (12 minutes at the MIT station), the result of which

interference is dependent on the lightning spatial-temporal dynamics and cannot be “rectified” by using the simple Lorentzian form (1). At the same time, presenting observed spectra in the Lorentzian form has two useful practical applications. First, storing the set of Lorentzian-estimated parameters (2) instead of full spectra means a major economy of data storage. Second, the comparison of observed and modeled SR background signatures – an element of the procedure for monitoring the global lightning activity – is much simpler and more effective in terms of the Lorentzian sets (2) than via full spectra (Mushtak et al. (1999)).

The pursuit of more accurate fitting of Schumann resonance spectra than is afforded by the classical Lorentzian approach, aimed at the extraction of globally invariant eigenfrequencies and quality factors from transient events, has been considered recently by Mushtak and Williams (2008).

16.5 Experimental Finding on Global Lightning Variations on Different Time Scales by Schumann Resonances

16.5.1 *Seasonal Variations of Global Lightning Activity*

Substantial seasonal changes in global lightning activity have been documented with SR methods. Like the diurnal variations, the seasonal variations are ultimately caused by variations in the energy received by the Earth from the Sun. Land and ocean surfaces have markedly different responses to incident solar radiation because the land surface is immobile and of low heat capacity, and the ocean surface is a fluid with a high heat capacity (Williams and Stanfill, 2002). This contrast in physical properties translates to a substantially larger variation in surface temperature over land than over ocean, and as a consequence, a greater propensity for deeper, lightning-favoring convection over land.

16.5.1.1 Annual Variations

A pronounced annual variation in the intensity of Schumann resonances, with maximum in boreal summer and overall variation of nearly a factor-of-two, has been documented from stations in Hungary and Rhode Island (Nickolaenko et al. 1998; 1999; Sátori et al., 1999), in Antarctica (Füllekrug and Fraser-Smith, 1997) and in Japan (Nickolaenko and Rabinowicz, 1995; Hobara et al., 2000; Nickolaenko and Hayakawa, 2002; Hayakawa et al., 2006; Sekiguchi et al., 2006). The consistent picture for receiving stations in both hemispheres supports the global nature of SR observations. A similar annual variation in total lightning is also well established from the Optical Transient Detector (OTD) and the Lightning Imaging Sensor (LIS) from satellites in Low Earth Orbit (Chrisian et al., 2003).

The cause of the annual variation is generally attributed to the asymmetrical distribution of land mass between northern and southern hemispheres, with north-

ern hemisphere dominating substantially, particularly outside the tropics (Williams, 1994). This same asymmetry also provides an explanation for the annual variation in global temperature and in integrated water vapor (Trenberth, 1981), two physical variables that are also closely linked with global lightning (Williams, 1992; Price, 2000; Williams, 2005; Williams et al., 2005).

16.5.1.2 Semiannual Variations

Superimposed on the annual variation of global lightning is a pronounced semiannual variation, as documented in SR observations by Sátori and Zieger (1996); Füllekrug and Fraser-Smith, (1997); Nickolaenko et al (1998); Nickolaenko et al (1999); Williams and Sátori, (2005); Sekiguchi et al., (2006). The validity of the SR inferences and the tropical origin of the semiannual variations are supported by a pronounced semiannual variation in global tropical thunder days (Williams, 1994) and by a detailed analysis by latitude of lightning observations from space (Chrisian et al., 2003).

The physical origin of the semiannual variation rests on the systematic but subtle changes in radiation from the Sun in the tropics as the equatorial region is traversed twice per year, at the equinoxes (Williams, 1994). Some phase lag from strict equinoctial times is evident in the global lightning activity, presumably associated with a mutual land/ocean response time to changes in shortwave radiation from the Sun. The semiannual response in temperature, rainfall and lightning is most pronounced in Africa (where the land is most ‘continental’) and least pronounced in South America and the Maritime Continent (where more maritime conditions prevail) (Williams et al, 2002; Williams and Sátori, 2004).

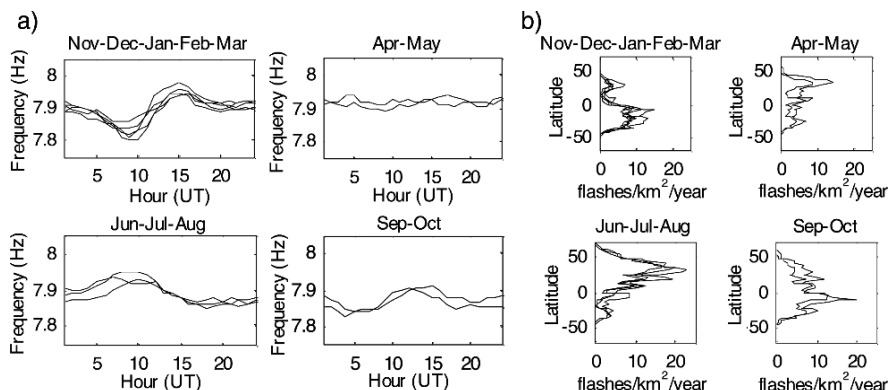


Fig. 16.19 (a) Monthly mean diurnal frequency patterns of the 1st SR mode, E_Z field component, at NCK, Hungary and (b) meridional lightning distributions observed by OTD/LIS satellites, both characteristic for the four distinct time intervals

16.5.1.3 The Global Seasonal Migration of Lightning

As noted earlier in section 2.2.2, the diurnal frequency pattern (DFP) is mainly determined by the lightning source-observer configuration. This configuration changes during the north-south seasonal migration of lightning, and as a consequence, DFP varies too (Sátori et al., 2003). Four basic DFPs have been distinguished corresponding to the four distinct time intervals during the year for each SR mode (shown here only the 1st mode) at Nagyencenk, Hungary (see Fig. 16.19a). Similar DFPs have been observed during five months (Nov-Dec-Jan-Feb-Mar) in the Southern hemisphere summer, in a pair of two-month intervals in the transition (spring and fall) seasons, and during the three months (June-July-August) of the boreal summer. The same time sequences (four seasons with different lengths) can be recognized in the meridional lightning distributions observed by the OTD (Optical Transient Detector) and LIS (Lightning Imagine Sensor) from space (see Fig. 16.19b), as shown in the seasonal distributions of DFPs in Fig. 16.19a (Sátori et al., 2003). Four seasons with different length, both in DFP and the meridional lightning distributions, suggest departures from purely sinusoidal behavior in the north-south dynamics of global lightning activity.

The global lightning maps in Figs. 16.1 and 16.5 clearly show continental dominance. Land is far more responsive to changes in insolation than the ocean, because land is immobile and has a lower heat capacity than ocean. As a consequence, surface temperature and a closely related quantity, conditional instability (Williams and Renno, 1993), follow the seasonal progression of the Sun in latitude. Since conditional instability is generally required for lightning, the latter quantity also tends to follow the Sun, with a slight lag because of the thermal inertia of the ocean, and the close communication between air over land and ocean.

The ocean influence is operative in spite of the fact that lightning is primarily a land-related phenomenon (Sátori et al., 2003). The ratio of land area to ocean area is smaller in the Southern hemisphere (SH) than in the Northern hemisphere (NH), and therefore the influence of the thermal inertia of oceans is more effective in the SH summer than in the boreal summer. This asymmetry is reflected in a longish SH summer with a long-lasting southern position of global lightning (see Fig. 16.19b upper left subplot). Figure 16.20 shows the sinusoidal annual solar march comparing it to the annual march of the centroids of the meridional lightning distributions deduced from the monthly meridional lightning distributions shown in Fig. 16.19b.

An additional behavior in the latitudinal migration of lightning activity is a distortion in the expected sinusoidal behavior manifest in the transition (spring and fall) seasons. The spring-fall asymmetry of the migration, illustrated in Fig. 16.20 is also attributable to the different thermodynamic properties of land (more rapidly cooling) and ocean. In the case of the African chimney, this behavior is also replicated in other quantities, notably rainfall (Engelstaedter and Washington, 2007), the Intertropical Front (ITF) (Lele and Lamb, 2007), the ITCZ (Ramel et al, 2006) and in the growth of vegetation (Zhang et al, 2005). The physical explanation for this asymmetry in latitudinal migration also likely lies with the thermal inertia of the oceans that surround the continents. The time scale for meteorological “commu-

nication” between the bordering oceans and the centers of continents is of order days, and is therefore a fast process in comparison with the seasonal migration. Conditional instability thrives on both temperature and moisture (i.e., water vapor), and the principle moisture supply is the ocean. But the response of the ocean surface to solar heating is substantially longer than a month. For this reason, the hurricane seasons in both hemispheres (involving vigorous lightning-producing convection over oceans rather than land (Chronis et al, 2007)) are lagged by ~ 3 months from the respective solstices.

16.5.2 Intraseasonal Variations in Global Lightning Activity

The intraseasonal variations of the tropical atmosphere lie in a range of period from 20 to 80 days, with the most prevalent signal near 45 days, known as the Madden-Julian oscillation (MJO) (Madden and Julian, 1972b; Madden and Julian 1994). This phenomenon is dominated by a zonal wavenumber-1 disturbance (one wavelength around the world) that progresses from west to east as viewed in global measurements of surface pressure, surface winds, and in satellite observations of deep convection. Anyamba et al (2000) explored the hypothesis that variations of SR published by Füllekrug and Fraser-Smith (1996), recorded at Arrival Heights, Antarctica, could be explained by intraseasonal modulations in global lightning, as an alternative explanation involving modulations in solar rotation on the solar rotation period (~ 27 days, but also variable).

Anyamba et al (2000) made use of a global convective index constructed from global IR observations of cloud top temperature. Cross-spectral analyses were performed between this index and the SR observations. Evidence was shown for a globally propagating disturbance that modulated convection and SR-representative lightning activity, with activity in Africa/South America alternating with activity in the Indian Ocean and Western Pacific Ocean on the opposite side of the Earth. This pattern was best defined during the boreal spring seasons of 1990 and 1992, but was less evident in 1993 and 1994. In contrast with previous studies finding the strongest

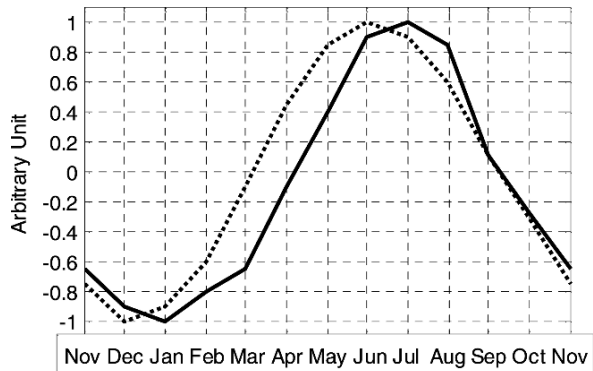


Fig. 16.20 Annual march of the Sun (dotted curve) and north-south migration of global lightning (solid curve). Sinusoidal maxima and minima (± 1 units) correspond to the two solstices as well as the southernmost/northernmost positions of global lightning

manifestation of the MJO over oceans, in this study strong signals were found over land regions as well.

Zieger and Sátori (1999) have also studied intraseasonal variations in time series of Schumann resonances. Attention is given to sorting out signals arising from modulations in the solar wind and geomagnetic activity, and signals of tropospheric origin. Important tropospheric signals are the 20 day and Madden-Julian oscillations.

16.5.3 African Lightning and Rainfall Modulations Associated with the Global 5-Day Wave

The 5-day periodicity as a climate unit was already known during the Ming Dynasty (1368–1644) according to a note referring to an assorted writing, “Ming Lang Ying Qi Xiu Lei Gao”, in the Bell Tower in Beijing. The count of 5 was assigned to the number of ceremonial ringings.

The 5-day wave is a planetary scale Rossby wave with westward propagation like the African easterly waves, but with prominent wavenumber-1 structure (Madden and Julian, 1972). This global wave is easily identified in Hovmoller diagrams of surface pressure (Madden and Julian, 1972; Patel, 2001). The wave is also manifest in modulations of African rainfall (Burpee, 1976; Castro, 2000; Patel, 2001), cloudiness (Orlanski and Polinsky, 1977), and lightning activity (Burpee, 1976; Castro, 2000; Patel, 2001). Figure 16.21 taken from the work of Castro (2000) and Patel (2001) shows simultaneous time series of daily rainfall integration over the African continent (Herman et al, 1977) and prominent Q-burst lightning flash counts, individually located over Africa using Schumann resonance observations (Huang et al, 1999) from West Greenwich, Rhode Island for a 40-day period in May/June of 1998. In-phase behavior is evident at the 5-day time scale for nearly the entire record, with increases in rainfall corresponding with increases in mesoscale lightning. (No filtering has been performed here.) The continental-scale rainfall variations are nearly a factor-of-two on the 5-day time scale.

The interpretation of this correlation follows evidence that much of the tropical atmosphere is in a state of conditional instability, but often without the necessary condition for triggering. The 5-day wave may provide that condition, by providing for low level convergence of conditionally unstable air at five-day intervals.

Another global wave with a slightly longer period (6.5 days) and also showing westward-propagating dominant wavenumber-1 structure has been considered by Talaat et al (2001). The 5-day global Rossby wave considered earlier is a free wave. The 6.5 day wave is a forced wave, and has been found to be correlated with lightning observations (Chronis et al, 2007) with different detection methods (VLF rather ELF) and over a different time interval in equatorial Africa than those described earlier.

In considering physical correlations with global waves in general, including the MJO (Section 5.2) and the 5- and 6.5- day waves, it must be emphasized that strong

correlated behavior comes and goes. Given that the sustaining mechanisms for these waves are not well understood, the reasons for this variability in correlation are likewise ill-defined.

The 5-day periodicity has also been found in the global lightning area deduced from DFR recorded at NCK, Hungary (Sátori et al., 1999), discussed earlier in a more general way in Section 2.2.4. In general, any periodicities of tropospheric origin in SR intensities (Sátori et al., 1999), indicating periodic variations of global lightning activity, are also accompanied by areal variations with similar periods inferred from time series of DFR (Sátori et.al, 2003)

16.5.4 Long-Term Variations of Global Lightning and the Global Electrical Circuit

The Earth-ionosphere cavity forms a natural framework for both the DC global electrical circuit and for the Earth's Schumann resonances, often referred to as the 'AC global circuit'. The observations showing a proportionality between lightning flash rate and Wilson cloud top conduction current for individual thunderstorms (Blakeslee et al, 1989) is evidence that the two global circuits will be correlated, and this prediction is supported by other observations (Williams, 1992; Füllekrug et al, 1999). The current interest in global change, and in particular the evidence for contemporary global warming extending over the past century (Hansen and Lebe-

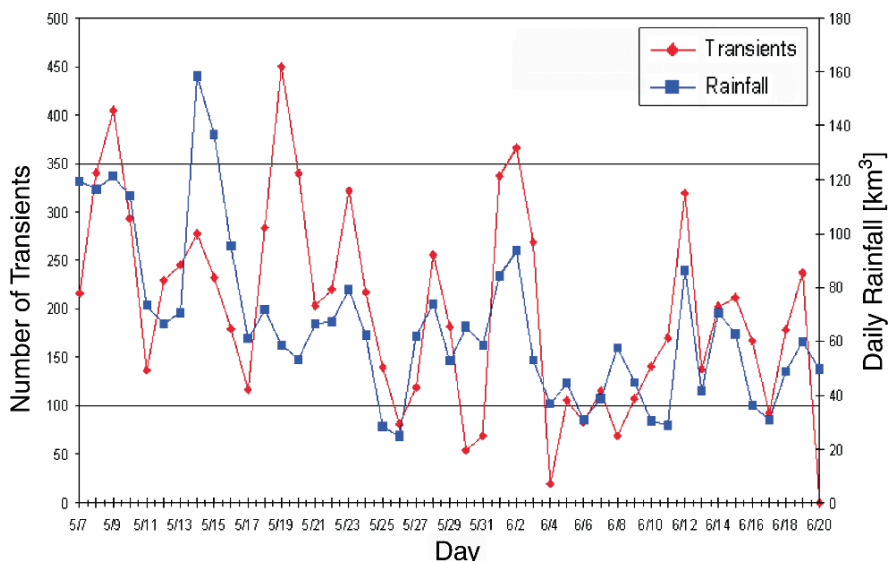


Fig. 16.21 Time series of daily-integrated African rainfall (Herman et al., 1997) and daily African transient activity (detected from Rhode Island) for the 40 day interval May 5-June 20, 1998, showing the approximate 5-day periodic cycle

deff, 1987), has raised considerable interest in possible long-term trends in global lightning activity. SR becomes a primary tool in this assessment.

Why does one expect lightning to respond positively to temperature? First and foremost, because of the nonlinear Clausius-Clapeyron relationship between water vapor and temperature, a key factor in the pronounced latitudinal dependence of lightning in the present climate. Second, because atmospheric instability and the Convective Available Potential Energy (CAPE) of the tropical atmosphere are known to increase with temperature in the present climate (Williams and Renno, 1993; Williams, 1994). Related to instability is updraft speed in thunderstorm convection, with stronger updrafts predicted in a warmer climate (Del Genio et al, 2007). The strongly nonlinear dependence of lightning flash rate on updraft speed is well recognized (Baker et al, 1995; Boccippio, 2001).

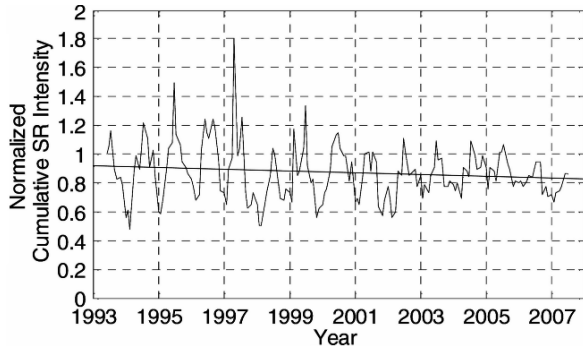
No study to date has predicted less lightning in a warmer world. Local measurements show positive correlations between lightning and temperature on many time scales (Williams, 1999; Pinto and Pinto, 2008). Studies with global climate models (Price and Rind, 1984) predict increases in lightning in warmer climates.

The available long-term observations of the global circuit are consulted raise more questions than provide definitive, self-consistent results. None of these records is longer than four decades, and the usual problems with establishing a trend with short records in the presence of considerable natural variability are commonplace. The interpretation of many of these records also remains controversial.

The most reliable measure of the DC global circuit is the ionospheric potential. This quantity shows no statistically significant trend over the last half-century, when considerations are given to the effects of nuclear weapons testing in the 1960s (Markson, 2007, and personal communication). The shortcoming of this global measure is that samples are sparse, with only a few hundred measurements over the past sixty years. The second most reliable measure of the DC global circuit, the air-earth current (which unlike ionospheric potential, can be made continuously over time), likewise shows no statistically significant trend, in either a 16-year record in Athens, Greece (Retalis, 1981) or a 28-year record from Kew Observatory near London (Harrison and Ingram, 2005). Long-term measurements of the least globally representative measure of the DC global circuit, the surface potential gradient, have shown statistically significant negative trends at Eskdalemuir, Scotland (Harrison, 2002) and Nagycenk, Hungary (Märcz and Harrison, 2003; 2005). The global representativeness of these downward trends has been questioned on the basis of local effects that may dominate the records and mask the global signal (Williams, 2003; Williams et al, 2005; Williams, 2008). More recent analysis of the electric field measurements at the NASA Kennedy Space Center over the period 1997–2005 (Harrison, 2006) shows no significant trend.

Long-term monitoring of the intensity of Schumann resonances as a measure of trends in global lightning is generally regarded as a valuable endeavor, but one that has received only recent attention by virtue of the widespread availability of digital recording methods. The longest record in the pre-digital era is that of Charles Polk in West Greenwich, Rhode Island, extending from 1969 to 1974 (Williams, 1992). Analysis of these records has shown a positive correlation with temperature over

Fig. 16.22 Normalized Cumulative SR intensity (E_z) with slight but not significant decreasing trend at the Nagycenk station in Hungary, for the period 1993–2008



one cycle of the ENSO (El Nino Southern Oscillation) with an inferred strong sensitivity of lightning to temperature. Sátori and Zieger (1999) have found evidence for southward/northward shifts in the global position of lightning activity during warm/cold ENSO episodes based the distance dependence of SR frequencies. More recent analysis of global lightning (recorded from space) on the ENSO time scale (Sátori et al., 2008) has shown substantially less sensitivity of lightning activity to the ENSO temperature variation for reasons that remain unclear. The longest well-cared-for record in the digital era is the one at Nagycenk, Hungary, shown in Fig. 16.22 for the vertical electric field component of SR, for the period 1993–2008. The trend is negative but is not statistically significant. The downward trend is noteworthy in light of ongoing analyses with the NASA LIS and OTD observations, also suggesting negative trends over the past decade (W. Petersen, presentation at the 2008 AMS Annual Meeting, New Orleans, and personal communication). We have no plausible explanation for declining trends in global lightning in a period when the global surface air temperature is increasing, and when the global tropical temperature is increasing (Hansen and Lebedeff, 1995). At the time of this writing, the issue of long-term trends of global lightning activity remains in a state of flux.

16.6 Conclusions

This chapter has attempted to summarize work involving the use of SR in the documentation of global lightning activity, their principal source. Major advances have been achieved in recent decades with both the availability of computerized digital signal processing, and with the growing interest in both global climate change and the discovery of a multitude of electrical discharges in the mesosphere. Theoretical models for interpreting SR observations have also been increasingly refined, motivating in turn improvements in measurements. The economy of these methods as a global probe is guaranteed to sustain the interest and advancement of these methods into the future.

Acknowledgments The authors thank Mariusz Neska for providing SR data from Hornsund, at the Polish Polar Station and from Belsk, Poland. G. Sátori thanks Judit Szendrői and Katalin Ábrahám for valuable assistance in processing SR data recorded both in Hungary and Poland. ERW thanks Robert Boldi for countless discussions and the development of efficient algorithms for the processing of observations and the archival of data, Tom Mitchell at the Alton Jones Campus of the University of Rhode Island for the generous use of the facility there, Michael Stewart and Darrell Word for advice, construction and maintenance of analog electronic circuits for the Rhode Island station, and a host of graduate students and research associates (Dennis Boccippio, Stan Heckman, Charles Wong, Terry Higgins, Everest Huang, Ken Morrison, Daniel Castro, Akash Patel, Tom Chang, David Lowenfels, Kunal Surana, Eric Downes and Yasu Hobara for their dedicated work with these results). G. Sátori's contribution to this study was supported by Hungarian Science Foundation (Grant No. K-72474). Earle Williams's and Vadim Mushtak's work on Schumann resonances is supported by a grant from the Physical Meteorology Section of the U.S. National Science Foundation (ATM-0337298). We thank Ron Taylor (deceased), Rod Rogers, William Cooper, Andrew Detwiler, and Brad Smull for their support.

References

- Anyamba E, Williams ER, Susskind J, Fraser-Smith A, Füllekrug M (2000) The manifestation of the Madden-Julian oscillation in global deep convection and in the Schumann resonance intensity, *J. Atmos. Sci.*, 57, 1029–1044
- Ádám A, Duma G, Horváth J (1990) A new approach to the electrical conductivity anomalies in the Drauzug-Bakony geological unit, *Physics of the Earth and Planetary Interiors*, Volume 60, Issue 1–4, 155–162
- Baker MB, Christian HJ, Latham J (1995) A computational study of the relationships linking lightning frequency and other thundercloud parameters, *Quart. J. Roy. Met. Soc.*, 121, 1525–1548
- Balser M, Wagner CA (1962) On Frequency Variations of the Earth-Ionosphere Cavity Modes, *Journal of Geophysical Research* 67, pp. 4081–4083
- Banks RJ (1975) Complex demodulation applied to Pi2 geomagnetic pulsations. *Geophys. J. R. Astr. Soc.*, 58, 471–493
- Bashkuev Y, Khaptanov V (1999) Deep radio impedance sounding of the crust using the electromagnetic field of a VLF radio installation, *Izvestiya. Physics of the Solid Earth*, 37(2), 157
- Beamish D, Hanson HW, Webb DC (1979) Complex demodulation applied to Pi2 geomagnetic pulsations. *Geophys. J. R. Astr. Soc.*, 58, 471–493
- Blakeslee RJ, Christian HJ, Vonnegut B (1989) Electrical measurements over thunderstorms, *J. Geophys. Res.*, 94, 13135–13140
- Boccippio DJ, Williams E, Heckman SJ, Lyons WA, Baker I, Boldi R (1995) Sprites, ELF transients and positive ground strokes, *Science*, 269, 1088–1091
- Boccippio DJ, Wong C, Williams ER, Boldi R, Christian HJ, Goodman SJ (1998) Global validation of single-station Schumann resonance lightning location, *J. Atmos. Sol. Terr. Phys.*, 60, 701–712
- Boccippio DJ (2001) Lightning scaling relations revisited, *J. Atmos. Sci.*, 59, 1086–1104
- Burke CP, Jones DL (1995) Global radiolocation in the lower ELF frequency band, *J. Geophys. Res.*, 100, 26263–26271
- Burpee RW (1976) Some features of global scale 4–5 day waves, *J. Atmos. Sci.*, 33, 2292–2299
- Castro DS (2000) The relationship between precipitation and electromagnetic signals in Schumann resonances, M. Eng. Thesis, Department of Electrical Engineering and Computer Sciences, Massachusetts Institute of Technology, Cambridge, MA
- Christian HJ, Blakeslee RJ, Boccippio DJ, Boeck WL, Buechler DE, Driscoll KT, Goodman SJ, Hall JM, Koshak WJ, Mach DM, Stewart MF (2003) Global frequency and distribution of lightning as observed from space by the Optical Transient Detector, *J. Geophys. Res.*, 108 (D1), 4005, doi:10.1029/2002JD002347

- Chronis TG, Williams E, Anagnostou M, Petersen W (2007) African lightning: Indicator of tropical Atlantic cyclone formation. *EOS, Transactions, American Geophysical Union*, 88 (40), 397–408
- Chronis TG, Williams E, Anagnostou EN (2007) Evidence of tropical forcing of the 6.5-day wave from lightning observations over Africa, *J. Atmos. Sci.*, 64, 3717–3721
- Clayton M, Polk C (1977) Diurnal variation and absolute intensity of world-wide lightning activity, September 1970 to May 1971, in *Electrical Processes in Atmospheres*, H. Dolezalek and R. Reiter, Eds., Steinkopff, 440–449
- Cole RK Jr (1965) The Schumann resonances. *Journal of Research of the National Bureau of Standards*, 69D, 1345–1349
- Cummer SA, Inan US (1997) Measurement of charge transfer in sprite-producing lightning using ELF radio atmospherics, *Geophys. Res. Lett.*, 24, 1731
- Del Genio AD, Mao-Sung Y, Jonas J (2007) Will moist convection be stronger in a warmer climate? *Geophys. Res. Lett.*, 34, L16703, doi:10.1029/2007GL030525
- Engelstaedter S, Washington R (2007) Atmospheric controls on the annual cycle of North African dust, *J. Geophys. Res.*, 112, D03103, doi:10.1029/2006JD007195
- Füllekrug M (1994) Schumann-resonances in magnetic field components, *J. Atmos. Terr. Phys.*, 57 (5), 479–484, 1994
- Füllekrug M, Fraser-Smith AC (1996) Further evidence for global correlation of the Earth-ionosphere cavity resonances, *Geophys. Res. Lett.*, 23, 2773–2776
- Füllekrug M, Fraser-Smith A (1997) Global lightning and climate variability inferred from ELF field variations, *Geophys. Res. Lett.*, 24, 2411–2414
- Füllekrug M, Fraser-Smith AC, Bering EA, Few AA (1999) On the hourly contribution of global cloud-to-ground lightning activity to the atmospheric electric field, *J. Atmos. Sol. Terr. Phys.*, 61, 745–750
- Füllekrug M, Constable S (2000) Global triangulation of intense lightning discharges, *Geophys. Res. Lett.*, 27, 3, 333
- Füllekrug M, Price C, Yair Y, Williams ER (2002) Oceanic lightning, *Ann. Geophys.*, 20, 133–137
- Greenberg E, Price C, Yair Y, Ganot M., Bór J, Sátori G (2007) ELF transients associated with sprites and elves in eastern Mediterranean winter thunderstorms, *J. Atmos. Solar-Terr. Physics*, 69, 1569–1586
- Greifinger C, Greifinger P (1978) Approximate method for determining ELF eigenvalues in the Earth-ionosphere waveguide. *Radio Science* 13, pp.831–837
- Greifinger P, Mushtak V, Williams E (2005) The lower characteristic ELF altitude of the Earth-ionosphere waveguide: Schumann resonance observations and aeronomical estimates. Proc. of VI International Symposium on Electromagnetic Compatibility and Electromagnetic Ecology (St.-Petersburg, Russia), pp. 250–254
- Greifinger PS, Mushtak VC, Williams ER (2007) On modeling the lower characteristic ELF altitude from aeronomical Data, *Radio Science* 42, RS2S12, doi:10.1029/2006RS003500
- Hansen JE, Lebedeff S (1987) Global trends of measured surface air temperature, *J. Geophys. Res.*, 92, 13345–13372
- Hargreaves JK (1992) *The Solar-Terrestrial Environment*. Cambridge University Press, 420
- Harrison H (2006) Atmospheric voltage gradients at the Kennedy Space Center, 1997–2005: No evidence for effects of global warming or modulation by galactic cosmic rays, *Geophys. Res. Lett.*, 33, L10814, doi:10.1029/2006GL025880
- Harrison RG, and Ingram WJ (2005) Air-earth current measurements at Kew, London, 1909–1979, *Atmos. Res.*, 76, 49–64
- Harrison RG (2002) Twentieth century secular decrease in the atmospheric potential gradient *Geophys. Res. Lett.*, 29, 10.1029/2002GL014878
- Hayakawa M, Sekiguchi M, Hobara Y, Nickolaenko AP (2006) Intensity of Schumann resonance oscillations and the ground surface temperature, *J. Atmos. Electr.*, 26, 79–93
- Heckman S (1998) The day-night asymmetry, paper presented at Schumann Resonance Symposium and Workshop, U. S.-Hung. Sci. and Technol. Joint Fund, Sopron, Hungary, 7–10 Sept

- Heckman S, Williams E, Boldi R (1998) Total global lightning inferred from Schumann resonance measurements, *J. Geophys. Res.*, 103, 31775–31779
- Herman A, Kumar V, Arkin P, Kousky J (1997) Objectively-determined 10-day African rainfall estimates created for famine early warning systems, *Int. J. Remote Sensing*, 18, 2147–2159
- Hobara Y, Iwasaki N, Hayashida T, Tsuchiya N, Williams ER, Sera M, Ikegami Y, Hayakawa M (2000) New ELF observation site in Moshiri, Hokkaido, Japan and the results of preliminary data analysis, *J. Atmos. Elec.*, 20, 99–109
- Hobara Y, Hayakawa M, Williams E, Boldi R, Downes E (2006) Location and electrical properties of sprite-producing lightning from a single ELF site, in *Sprites, Elves and Intense Lightning Discharges*. Ed. M. Füllekrug, E.A. Mareev and M.J. Rycroft, NATO Science Series, II. Mathematics, Physics and Chemistry 225, Springer, 398 pp
- Huang E, Williams E, Boldi R, Heckman S, Lyons W, Taylor M, Nelson T, Wong C (1999) Criteria for sprites and elves based on Schumann resonance observations, *J. Geophys. Res.*, 104, 16943–16964
- Ishaq M, Jones DL (1977) Method of obtaining radiowave propagation parameters for the Earth-ionosphere duct at E.L.F., *Electronics Letters* 13, pp.254–255
- Kemp DT (1971) The global location of large lightning discharges from single station observations of ELF disturbances in the Earth-ionospheric cavity, *J. Atmos. Terr. Phys.*, 33, 919–928
- Kemp DT, Jones DL (1971) A new technique for the analysis of transient ELF electromagnetic disturbances within the Earth-ionosphere cavity. *J. Atmos. Terr. Phys.*, 33, 567–572
- Kirillov VV, Kopeykin VN, Mushtak VC (1997) ELF electromagnetic waves within the Earth-ionosphere waveguide. *Geomagnetizm i Aeronomiya*, 37, 114–120 [in Russian]
- Kirillov VV (2002) Solving a two-dimensional telegraph equation with anisotropic parameters. *Radiophysics and Quantum Electronics*, 45, 929–941
- Lay EH, Jacobson AR, Holzworth RH, Rodger CJ, Dowden RL (2007) Local time variation in land/ocean lightning count rates as measured by the World Wide Lightning Location Network, *J. Geophys. Res.*, 112, D13111, doi:10.1029/2006JD007944
- Lele MI, Lamb PJ (2007) Variability of intertropicalfront and rainfall over West African Soudano-Sahelzone, African Monsoon and Multidisciplinary Analysis, 2nd International Conference, (Ed's. I. Genau, E.van den Akker and J.-L. Redelsperger,page 28,Karlsruhe, Germany, November)
- Madden T, Thompson W (1965) Low frequency electromagnetic oscillations of the Earth-ionosphere cavity. *Rev. Geophys.*, 3, 211–254
- Madden R, Julian P (1972a) Further evidence of global-scale, 5-day pressure waves, *J. Atmos. Sci.*, 29, 1464–1469
- Madden R, Julian P (1972b) Description of global scale circulation cells in the tropics with a 40–50 day period, *J. Atmos. Sci.*, 29, 1109–1123
- Madden R, Julian P (1994) Observation of the 40–50 day tropical oscillation—A review, *Mon. Wea. Rev.*, 122, 814–837
- Märucz F, Harrison RG (2003) Long-term changes in atmospheric electrical parameters observed at Nagycenk (Hungary) and the UK observatories at Eskdalemuir and Kew, *Ann. Geophys.*, 21, 2193–2200
- Markson R (2007) The global circuit intensity: Its measurement and variation over the last 50 years, *Bull. Am. Met. Soc.*, DOI:10.1175/BAMS-88-2-223, 223–241
- Mushtak V, Boldi R, Williams E (1999) Schumann resonances and the temporal-spatial dynamics of global thunderstorm activity. Proc. of XI International Conference on Atmospheric Electricity (Guntersville, Alabama), pp. 698–700
- Mushtak VC, Williams E (2002) ELF propagation parameters for uniform models of the Earth-ionosphere waveguide, *J. Atmos. Solar-Terr. Phys.*, 64, 1989–2001
- Mushtak VC, Williams ER (2008) An improved Lorentzian technique for evaluating resonance characteristics of the Earth-ionosphere cavity, *Atmospheric Research*, (in review)
- Neska M, Sátori G (2006) Schumann resonance observation at Polish Polar Station at Spitsbergen as well as in Central Geophysical Observatory in Belsk, Poland, *Przegl. Geofiz. Engl. Transl.*, 3–4, 189

- Nickolaenko AP, Rabinowicz LM (1995) Study of the annual changes of global lightning distribution and frequency variations of the first Schumann resonance mode, *J. Atmos. Terr. Phys.*, 57, 1345–1348
- Nickolaenko AP, Sátori G, Zieger B, Rabiniwicz LM, Kudintseva IG (1998) Parameters of global thunderstorm activity deduced from long-term Schumann resonance records. *J. Atmos. Sol. Terr. Phys.*, 60, 387–399
- Nickolaenko AP, Hayakawa M, Hobara Y (1999) Long-term periodic variations in the global lightning activity deduced from the Schumann resonance monitoring, *J. Geophys. Res.*, 104(D22), 27 585.27 591
- Nickolaenko AP, Hayakawa M (2002) Resonances in the Earth-ionosphere cavity, Kluwer Academic Publishers
- Nickolaenko AP, Hayakawa M (2007a) Diurnal variations in Schumann resonance intensity in local and universal times, *J. Atmos. Elec.*, 27, 83–93
- Nickolaenko AP, Hayakawa M (2007b) Recent studies of Schumann resonances and ELF transients, *J. Atmos. Elec.*, 27, 19–39
- Ogawa T, Tanaka Y, Yasuhara M (1967) Worldwide simultaneity of occurrence of a Q-type ELF burst, *J. Geomagnetism and Geoelectricity*, 377–384
- Ogawa T, Tanaka Y, Yasuhara M (1969) Schumann resonances and worldwide thunderstorm activity, in Planetary Electrodynamics, Vol. 2, Ed., S.C. Coroniti and J. Hughes, Gordon and Breach, New York
- Ogawa T, Komatsu M (2008) Q-Bursts from various distances on the Earth, Atmospheric Research, (in press)
- Ondrášková A, Kostecký P, Ševčík S, Rosenberg L (2007) Long-term observations of Schumann resonances at Modra Observatory, *Radio Sci.*, 42, RS2S09, doi:10.1029/2006RS003478
- Orlanski I, Polinsky LJ (1977) Spatial distribution of cloud cover over Africa, *J. Met. Soc. Japan*, 55, 5
- Patel AC (2001) Modulation of African lightning and rainfall by the global 5-day wave, M. Eng. Thesis, Department of Mechanical Engineering, Massachusetts Institute of Technology, Cambridge, MA
- Pinto O Jr, Pinto IRCA (2008) About the sensitivity of cloud-to-ground lightning activity to surface air temperature changes at different time scales in the city of São Paulo, Brazil, *J. Geophys. Res.*, (in press)
- Price C (2000) Evidence for a link between global lightning activity and upper tropospheric water vapor, *Nature*, 406, 290–293
- Price C, Rind D (1994) Possible implications of global climate change on global lightning distributions and frequencies, *J. Geophys. Res.*, 99, 10823–10831
- Price C, Melnikov A (2004) Diurnal, seasonal and interannual variations in Schumann resonance parameters, *J. Atmos. Sol. Terr. Phys.*, 66, 1179–1185
- Price C, Greenberg E, Yair Y, Sátori G, Bór J, Fukunishi H, Sato M, Israelevich P, Moalem M, Devir A, Levin Z, Joseph HJ, Mayo I, Ziv B, Sternlieb A (2004) Ground-based detection of TLE-producing intense lightning during the MEIDEX mission on board the space shuttle Columbia, *Geophys. Res. Lett.*, VOL. 31, L20107, doi:10.1029/2004GL020711
- Price C, Asfur M (2006) Can lightning observations be used as an indicator of upper-tropospheric water vapor availability, *Bull. Am. Met. Soc.*, 87, 291–298
- Ramel R, Gallée H, Messager C (2006) On the northward shift of the West African monsoon, Climate Dynamics, DOI 10.1007/s00382-005-0093-5
- Retalis DA (1981) Study of the air-earth current density in Athens, *Pageoph.*, 136, 217–233
- Roemer HR (1961) On Extremely Low Frequency Spectrum of the Earth-Ionosphere Cavity Response to Electrical Storms. *J. Geophys. Res.*, 66, 1580–1584
- Roldugin VC, Maltsev YV, Vasiljev AN, Schokotov AY, Belyajev GG (2004) Schumann resonance frequency increase during solar X-ray bursts. *Journal of Geophysical Research* 109, A01216
- Sato M, Fukunishi H, Kikuchi M, Yamagishi H, Lyons WA (2003) Validation of sprite-inducing cloud-to-ground lightning based on ELF observations at Showa station in Antarctica, *J. Atmos. Sol. Terr. Phys.*, 65, 607–614

- Sátori G, Szendrői J, Verő J (1996) Monitoring Schumann resonances – I. Methodology, *J. Atmos. Terr. Phys.*, 58 (13), 1475–1481
- Sátori G (1996) Monitoring Schumann resonances – II. Daily and seasonal frequency variations, *J. Atmos. Terr. Phys.*, 58 (13), 1483–1488
- Sátori G, Zieger B (1996) Spectral characteristics of Schumann resonances observed in central Europe, *J. Geophys. Res.*, 101, 29663–29669
- Sátori G, Zieger B (1999) El Niño-related meridional oscillation of global lightning activity, *Geophys. Res. Lett.*, 26, 1365–1368
- Sátori G, Williams E, Zieger B, Boldi R, Heckman S, Rothkin K (1999) Comparisons of long-term Schumann resonance records in Europe and North America, 11th International Conference on Atmospheric Electricity, NASA/CP-1999-209261, 705–708, Guntersville, Alabama, June 7–11
- Sátori G, Neska M, Williams E, Szendrői J (2007) Signatures of the non-uniform Earth-ionosphere cavity in high-time resolution Schumann resonance records, *Radio Science*, Vol.42, No.2, RS2S10 10.1029/2006RS003483
- Sátori G, Williams E, Lemperger I (2008) Variability of global lightning activity on the ENSO time scale, *Atmospheric Research*, (in print)
- Schumann WO (1952) Über die strahlunglosen Eigenschwingungen einer leitenden Kugel, die von einer Luftsicht und einer Ionosphärenhülle umgeben ist, *Z. Naturforsch. A*, 7, 6627–6628
- Sekiguchi M, Hayakawa M, Nickolaenko AP, Hobara Y (2006) Evidence for a link between the intensity of Schumann resonances and global surface temperature, *Ann. Geophys.*, 24, 1809–1817
- Sekiguchi M, Hobara Y, Hayakawa M (2008) Diurnal and seasonal variations in the Schumann resonance parameters at Moshiri, *J. Atmos. Electr.*, 28, 1–10
- Sentman DD (1987) PC monitors lightning worldwide, *Computer Science*, 1, 25
- Sentman DD (1987) Magnetic elliptical polarization of Schumann resonances, *Radio Science*, 22, 595
- Sentman DD (1995) Schumann Resonances, in *Handbook of Atmospheric Electrodynamics*, vol. 1, edited by H. Volland, p. 276, CRC Press, London
- Simpson JJ, Taflove A (2006) A novel ELF radar for major oil deposits, *IEEE Geoscience and Remote Sensing Lett.*, 3(1), 36
- Talaat ER, Yee JH, Zhu X (2001) Observations of the 6.5 day wave in the mesosphere and lower thermosphere, *J. Geophys. Res.*, 106, 20715–20724
- Toracinta ER, Zipser EJ (2001) Lightning and SSM/I-Ice-scattering mesoscale convective systems in the global tropics, *J. Appl. Met.*, 40, 983–1002
- Trenberth KE (1981) Seasonal variation in global sea level pressure and the total mass of the atmosphere, *J. Geophys. Res.*, 86, 5238–5246
- Verő J (1972) On the determination of the magneto-telluric impedance tensor. *Acta Geod. Geophys. Mont. Acad. Sci. Hung.* 7(3–4), 333–351
- Wait JR (1962) *Electromagnetic Waves in Stratified Media*, 2nd ed., Pergamon Press, New York, NY, p. 153, Section 5
- Williams ER (1992) The Schumann resonance: A global tropical thermometer, *Science*, 256, 1184–1187
- Williams ER (1994) Global circuit response to seasonal variations in global surface air temperature, *Mon. Wea. Rev.*, 122, 1917–1929
- Williams ER (1998) The positive charge reservoir for sprite-producing lightning, *J. Atmos. Sol. Terr. Phys.*, 60, 689–692
- Williams ER (1999) Global circuit response to temperature on distinct time scales: A status report, in *Atmospheric and Ionospheric Phenomena Associated with Earthquakes*, Ed., M. Hayakawa), Terra Scientific Publishing (Tokyo)
- Williams ER (2003) Comments on: “Twentieth century secular decrease in the atmospheric potential gradient” by Giles Harrison: Global changes in current or local changes in air pollution?, *Geophys. Res. Lett.*, doi:10.1029/2003GL017094
- Williams ER (2005) Lightning and climate: A review, *Atmospheric Research*, 76, 272–287

- Williams ER (2008) The global electrical circuit: A review, *Atmospheric Research*, in final review
- Williams ER, Renno NO (1993) An analysis of the conditional instability of the tropical atmosphere, *Mon. Wea. Rev.*, 121, 21–36
- Williams ER (2001) Sprites, elves and glow discharge tubes, *Physics Today*, November, 41–47
- Williams ER, Coauthors (2002) Contrasting convective regimes over the Amazon: Implications for cloud electrification, *J. Geophys. Res., LBA Special Issue*, 107, D20, 8082, doi:10.1029/2001JD000380
- Williams E, Stanfill S (2002) The physical origin of the land-ocean contrast in lightning activity, *Comptes Rendus—Physique*, 3, 1277–1292
- Williams ER, Sátori G (2004) Lightning, thermodynamic and hydrological comparison of the two tropical continental chimneys, *J. Atmos. Sol. Terr. Phys.*, 66, 1213–1231
- Williams E, Markson R, Heckman S (2005) Shielding effects of trees on the measurement of the Earth's electric field: Implications for secular variations of the global electrical circuit, *Geophys. Res. Lett.*, 32, L19810, doi:10.1029/2005GL023717
- Williams ER, Mushtak VC, Rosenfeld D, Goodman SJ, Boccippio DJ (2005) Thermodynamic conditions favorable to superlative thunderstorm updraft, mixed phase microphysics and lightning flash rate, *Atmospheric Research*, 76, 288–306
- Williams E, Boldi R, Bór J, Sátori G, Price G, Greenburg E, Takahashi Y, Yamamoto K, Chronis T, Anagnostou E, Smith D, Lopez L (2006) Lightning flashes conducive to the production and escape of gamma radiation to space, *J. Geophys. Res.*, 111, D16209, doi:10.1029/2005JD006447
- Williams ER, Mushtak VC, Nickolaenko AP (2006) Distinguishing ionospheric models using Schumann resonance spectra. *J. Geophys. Res.*, 111, D16107, doi:10.1029/2005JD006944
- Williams ER, Yair Y (2006) The microphysical and electrical properties of sprite-producing thunderstorms, in *Sprites, Elves and Intense Lightning Discharges*, Ed. M. Füllekrug, E.A. Mareev and M. J. Rycroft, NATO Science Series, II Mathematics, Physics and Chemistry- Vol. 225, Springer
- Williams E, Downes E, Boldi R, Lyons W, Heckman S (2007) Polarity asymmetry of sprite-producing lightning: A paradox?, *Radio Sci.*, 42, RS2S17, doi:10.1029/2006RS003488
- Williams ER, Mushtak VC, Boldi R, Dowden RL, Kawasaki Z-I (2007) Sprite lightning hear around the world by Schumann resonance methods, *Radio Science*. 42, RS2S20, doi:10.1029/2006RS003498
- Williams ER, Mushtak VC, Boldi R, Dowden RL, Kawasaki Z-I (2008) Reply to Comment by A. Nickolaenko and M. Hayakawa on Manuscript “Sprite Lightning Heard round the World by Schumann Resonance Methods” (accepted for publication in Radio Science)
- Wormell TW (1930) Vertical electric currents below thunderstorms and showers, *Proc. Roy. Soc., A*, 127, 567–590
- Wormell TW (1953) Atmospheric electricity: some recent trends and problems, *Quart. J. Roy. Met. Soc.*, 79, 474–489
- Yang H, Pasko VP (2005) Three dimensional finite difference time domain modeling of the Earth – ionosphere cavity resonances, *Geophys. Res. Lett.*, 32, L03114, doi:10.1029/2004GL021343
- Zhang X, Friedl MA, Schaaf CB, Strahler AH (2005) Monitoring the response of vegetation phenology to precipitation in Africa by coupling MODIS and TRMM instruments, *J. Geophys. Res.*, 110, D2103, doi:10.1029/2004JD005263
- Zieger B, Sátori G (1999) Periodic variations of solar and tropospheric origins in Schumann resonances, Proceeding of the 11th International Conference on Atmospheric Electricity, Alabama, USA, 701–704

Chapter 17

The Meteorological and Electrical Structure of TLE-Producing Convective Storms

Walter A. Lyons, CCM, Mark A. Stanley, Jonathan D. Meyer,
Thomas E. Nelson, Steven A. Rutledge, Timothy L. Lang
and Steven A. Cummer

Abstract Emerging real-time capabilities using sensitive ULF/ELF/VLF magnetic receivers can monitor the impulse charge moment changes ($i\Delta M_q$) of cloud-to-ground lightning strokes (CGs) over large regions. This provides a means to detect the parent CGs of the most common of the transient luminous events (TLEs) – sprites (often preceded by halos.) As $i\Delta M_q$ values grow larger than 100 C km, +CGs have a rapidly increasing probability of producing mesospheric sprites. If the $i\Delta M_q$ value of a +CG is >300 C km, there is a $>75\text{--}80\%$ chance this CG stroke initiates a sprite. Curiously, while negative $i\Delta M_q$ values of this size are much less common, they do occur. Yet on only a rare occasions have –CGs been documented to initiate a sprite over continental storms (the so-called polarity paradox). The total charge moment change required to initiate sprites is believed to be at least ~ 500 C km. Also, the great majority of sprite initiations are delayed after the return stroke by much more than the 2 ms time period used in the $i\Delta M_q$ estimates. This suggests that while both positive and negative CGs may have relatively large $i\Delta M_q$ values, due to the relatively low amperage continuing currents in the negative discharges, only +CGs have large enough continuing currents to routinely reach breakdown values and initiate sprites. While both CG polarities can theoretically initiate sprites, perhaps a somewhat higher breakdown threshold may exist for –CGs, and/or reduced streamer development makes them more difficult to detect optically? Preliminary climatologies of $i\Delta M_q$ for the U.S. are presented. The technique employed in the U.S. utilizes the National Lightning Detection Network for geolocation, allowing placement of $>80\text{--}90\%$ of sprite parent +CGs. Global lightning location systems such as the Worldwide Lightning Location Network (WWLLN) appear to detect approximately 25% of the CGs producing U.S. sprites, suggesting the possibility of employing such systems elsewhere.

Keywords Sprites · Halos · Elves · Lightning · Charge moment change · Convective storms · Lightning mapping arrays

W.A. Lyons (✉)
FMA Research, Inc, Fort Collins, CO 80524, USA
e-mail: walyons@frii.com

17.1 Introduction

The serendipitous discovery of red sprites in 1989 changed forever our view of the interactions between tropospheric electrical activity and middle atmospheric optical phenomena and energetics (Franz, 1990; Lyons and Armstrong, 2004). Once thought to be electrically quiescent, the stratosphere and mesosphere are increasingly found to be the home to a growing variety of lightning-related electrical discharges and intense transient electric fields (Lyons, 2006; Lyons et al., 2003a). The discovery of literal cloud-to-stratosphere electrical discharges from intense thunderstorm tops, including blue jets, giant jets and true upward lightning (Lyons et al., 2003b; van der Velde et al., 2007) continues to engender the need for intensive investigations of this region. However, the relative scarcity of cloud top discharge events make them difficult to study in a systematic manner. Red sprites and halos (Barrington-Leigh and Inan, 1999) as well as elves (Fukunishi et al., 1996), by contrast, are increasingly well understood and predictable.

During the summer of 2000, a major field program, the Severe Thunderstorm Electrification and Precipitation Study (STEPS) was conducted on the U.S. High Plains (Lang et al., 2004). While its focus was on supercell convection, the experimental design also allowed for detailed investigations of mesoscale convective systems (MCSs). Over continental regions, sprites are known to frequently occur in association with positive cloud-to-ground (+CG) strokes in MCSs (Lyons, 1994, 1996; Lyons et al., 2000), although even in the most productive storms rarely do more than 1 in 5 +CGs trigger a sprite. During STEPS, though an occasional sprite was recorded from supercellular storms (Lyons et al., 2008), the vast majority of sprites and halos were observed above large mesoscale convective systems (Lyons et al., 2003a).

Theoretical research into red sprite production has seen the proposal and disposal of a number of theories (Wilson, 1925; Rodger, 1999). At the current time, sprites are generally agreed to be the result of conventional dielectric breakdown at approximately 70–75 km height (Stanley, 2000), the result of a strong transient electrical field resulting from the removal to ground of large amounts of electrical charge in a CG flash (Wilson, 1925; Pasko et al., 1996, 1997; Williams, 2001). Though this mechanism is not strongly polarity dependent, the vast majority of sprite parent CGs are positive (SP+CGs). We note only two documented North American –CG sprite events by Barrington-Leigh et al. (1999) and several over Argentina by Bailey et al. (2007), while very occasional stand alone halos from a –CG have been observed over the years. Given that –CGs with large charge moment changes do occur in greater numbers than the observed negative TLEs above continental storms lies at the root of the so-called polarity paradox (Williams et al., 2007). While the peak current of SP+CGs is typically 50% larger than the other +CGs in the same storm (Lyons et al., 2003b; Lyons, 1996), the peak current by itself is not a good predictor of sprite formation. As initially suggested by C.T.R. Wilson (1925), the key metric is the charge moment change:

$$\Delta M_q(t) = Z_q \times Q(t) \quad (17.1)$$

defined as the product of Z_q , the mean altitude (AGL) from which the charge is lowered to ground, and the amount of charge lowered. Note that this second term is most appropriately considered as a function of time. New measurement techniques, described by Cummer and Lyons (2004, 2005) and Cummer and Inan (2000) can now routinely monitor the impulse charge moment change ($i\Delta M_q$), which is that produced by the charge lowered in roughly the first 2 ms of the CG (Berger et al., 1975). This is typically dominated by the return stroke plus the initial stages of any continuing current.

Huang et al. (1999) and Williams (2001) refined Wilson's original theory and proposed, based upon initial measurements gleaned from Schumann resonance ELF transient analyses (Boccippio et al., 1995), that for such breakdown to occur, total ΔM_q values would need to be on the order of 300–1000 C km. These values are many times larger than what have been believed to be the “typical” values for ΔM_q (<50 C km) for –CG strokes (Rakov and Uman, 2003; Cummer and Lyons, 2005). The STEPS program provided ideal circumstances to delve into the characteristics of MCS SP+CG strokes (Lyons et al., 2003a; Lyons et al., 2008). (Note: The term SP+CG is used in this paper to designate all TLE parents, recognizing the overwhelming majority of events are sprites or sprites following halos, very infrequently stand alone halos, and rarely elves). The key question that was addressed: What is different about those +CGs which trigger sprites? Where in the storms, and during what phases of their life cycle, do these unusual discharges occur? It became clear that a large charge moment change was indeed a robust sprite predictor, and a necessary if not also a sufficient condition. Though some variability in the critical threshold may occur from night to night, perhaps due to changes in the middle atmosphere (Cummer and Lyons, 2004), a total ΔM_q value of ~500 C km appears to be a reliable metric, and is usually achieved (in about 50% of sprites) after ~10 ms of the return stroke (with variability ranging from <1 ms to >100 ms.) The occurrence of long delayed sprites clearly points towards the role of continuing currents in +CGs as a major factor in the production of the majority of sprites.

The database amassed during STEPS allowed for the creation of criteria for MCS sprite production based upon the size and temperature of the cloud top canopy and the size and character of the underlying radar reflectivity pattern. TLEs occur infrequently in summer season MCSs with cloud temperatures everywhere warmer than -55°C . The MCS cloud top canopy colder than -50°C usually exceeds 25,000 km 2 . Most TLEs also require peak reflectivities somewhere within the parent MCS radar echo be >55 dBZ, though the TLEs most often occur in lower reflectivity stratiform regions that usually cover more than 20,000 km 2 . Reported upon in detail by Lyons et al. (2006a, b), these criteria have been incorporated into successful qualitative, and more recently, an automated TLE-potential forecasting system. It should be noted that these criteria apply primarily to mid-latitude, warm season, continental convective systems. If met, these criteria suggest the storm is likely producing CGs with large ΔM_q values, primarily in the trailing stratiform region. Figure 17.1 is a matrix summarizing the state-of-the-science with respect to the TLE-potential for various convective regimes. Virtually any storm producing lightning can generate a discharge with a ΔM_q value sufficient to cause mesospheric breakdown. However, it

How Does TLE-Efficiency Vary With Storm Type (Apr 08)**		
Convection Type	Sprites/Halos/Elves*	Blue Jets, etc.
Mesoscale Convective Complex	Very High	Rare (over cores?)
Mesoscale Convective Systems	High	Rare (over cores?)
Air Mass Convection	Very Rare	Rare (overshooting tops)
Storms in the Tropics	Variable	Few (overshooting tops)
Tropical Storms	Variable (Low)	Few (convective bombs)
Shallow (Winter) Convection	Medium	Unknown
Synoptic Cyclonic Storms	Low	Unknown
Squall Lines	High?	Few (overshooting tops)
Supercells	Rare (at end)	Few (overshooting tops)

* Elves, halos more common over salt water ** Lyons (2006) NATO Workshop Summary

Fig. 17.1 Current state of the science regarding likelihood of various convective systems to generate the two basic classes of TLEs (after Lyons, 2006). MCS/MCC systems are believed most prolific

appears some regimes are far more efficient than others at this task. A major research thrust continues to be the expansion of the parameter space for convective regimes generating sprite-producing lightning. Clearly the TLE prediction rules for U.S. High Plains convection will not apply to cold season, shallow convective storms such as found over the Gulf Stream, the Great Lakes and the Sea of Japan.

Radio Frequency (RF)-based remote sensing methods for the characterization of lightning charge moment changes based upon the concepts proposed by Cummer and Inan (2000) and Cummer (2006), and as exploited for STEPS data by Cummer and Lyons (2004, 2005) have detailed that ΔM_q and even $i\Delta M_q$ (if properly employed) can provide a very useful threshold to discriminate between those +CGs which produce sprites (and possibly elves and halos) and those which do not. In this paper we will investigate the characteristics of TLE-producing storms (focusing on sprites and halos + sprites) as observed using conventional NLDN data (Cummins et al., 1998), GOES satellite and NEXRAD radar reflectivity, a 3-D lightning mapping array (LMA) (Thomas et al., 2004) and impulse charge moment change data automatically extracted in real-time using ULF/ELF/VLF transient analysis. This technique forms the basis of a national Charge Moment Change Network (CMCN) that has been operating in the United States since early 2007 as part of ongoing sprite forecasting and verification activities. (Details of these techniques will be the focus of future papers.)

17.2 Impulse Charge Moment Changes

TLE research initially advanced largely due to the ability of low-light television (LLTV) systems to detect luminosity above storms during the dark of night (Franz, 1990; Lyons, 1994, 1996). However, it has clearly become desirable to have a surrogate detection method that can function throughout the diurnal cycle as well as when clouds block the view of ground-based cameras. From several studies (Huang et al., 1999; Hu et al., 2002; Lyons et al., 2003b) it appears that a relatively narrow threshold range of ΔM_q values exists to allow discriminating those CGs which do and do not produce sprites and/or halos. (Elves, while triggered by large peak current CGs do not necessarily appear to require a large charge moment change event [Barrington-Leigh and Inan, 1999]). The manual extraction of the full (10 ms or longer) ΔM_q value from ULF/ELF/VLF transient data, however, is still a rather laborious task, which has limited the conduct of both case studies and especially any potential operational utilization of this parameter. Recent advances in the extraction of the impulse ΔM_q values (Cummer and Lyons, 2004, 2005) suggested that an automated approach was feasible. The question then arose as to whether the impulse $i\Delta M_q$ contains sufficient predictive value to be a useful discriminator for sprites (high probability of detection, low false alarm rate). Unless the $i\Delta M_q$ value exceeds the nominal 500 C km breakdown threshold, there is no *a priori* reason to expect this parameter to be a predictor of sprites triggering more than 2 ms after the CG return stroke.

Initial tests conducted jointly with Duke University in conjunction with LLTV monitoring of MCSs from Colorado's Yucca Ridge Field Station (YRFS) during the summer of 2005 (Lyons et al., 2006a, 2006b) revealed that $i\Delta M_q$ values exhibit a surprisingly high predictive value for both short and long-delayed sprites. Tests demonstrated that a nominal threshold value of 100 C km (in the first 2 ms of the event) produced a >50% probability of detection (PoD) of the sprites and/or halos as confirmed by image-intensified cameras over High Plains convective storms. Moreover, false alarm rates were small. During the summer of 2005, a major field campaign entrained investigators from other institutions, resulting in a large database for further testing the relationships between CG lightning RF signatures, their parent storms' distinguishing features, and TLEs. A more sensitive receiver than used in STEPS, spanning ULF/ELF/VLF frequencies, yielded even higher TLE detection efficiencies for individual TLE parent CGs (>60% in a large mesoscale convective system), virtually assuring that most TLE-producing storms can be identified. By enhancing the Duke algorithms to employ the ULF signal component and automating the extraction processes, the technique held promise to develop a real-time system to distinguish those CGs which produce truly extraordinary stratospheric electric fields triggering mesospheric breakdown. Given an anticipated useful range of 1500 km or better, only two receivers were required to create a prototype quasi-national Charge Moment Change Network (CMCN) for real-time TLE monitoring. Often the same events were detected by both receivers. Preference was given to the retrieval from the Duke sensor given the lower background noise at that location.

The investigation of the utility of using real-time $i\Delta M_q$ data as a surrogate for TLE detection was the focus of the SPRITES 2007 program.

17.3 SPRITES 2007

The SPRITES 2007 campaign was headquartered at YRFS during May through August. Monitoring by LLTV cameras, as in past years, detected numerous TLEs at ranges to 500 km and beyond. Additional experiments were conducted with Stanford University's STAR Lab in which the ability to predict the time and location of TLE-producing storm was essential. The 2007 campaign marked the inauguration of the CMCN. The first sensor came on line at Duke University (Durham, NC) in early February 2007, and was joined by a second sensor at YRFS in early June. The highly sensitive orthogonal magnetic coils were deployed beneath wind proof enclosures in radio quiet environments. A variable threshold trigger was adjusted until such time as the local noise would not overwhelm the local PC processing capability. Candidate waveform signature metrics are sent from both sensors to a central processing facility at Duke. The automated extraction routine produce a continuous stream of GPS-time tagged $i\Delta M_q$ estimates. Once the magnitude is retrieved, there remains the matter of geolocating the event. While single and multi-station techniques do exist to approximately locate the origin of these energetic events, it was deemed more practical to use the operational NLDN CG data stream to locate the events by time matching events down to the microsecond level (with appropriate account taken for propagation delays, etc.) This approach, however, is dependent upon the NLDN's capability to detect the sprite parent CG. Experience has shown that the detection efficiency for these events may be somewhat lower than for +CGs as a whole, perhaps due to the complicated waveform patterns involved or signal strengths so large as to saturate many receivers.

A real time display of $i\Delta M_q$ estimates is shown in Fig. 17.2. The CMCN detects the $i\Delta M_q$ value from many "normal" CGs, with $\sim 90\%$ of the retrievals found between 50 and 5 C km, the estimated minimum detection level over most of the CMCN. For purposes of TLE monitoring, however, the displays were designed just to show larger events, starting with an arbitrary threshold of 75 C km, plus those events of 100–300 C km, and the largest events, >300 C km. Both positive (red) and negative (blue) $i\Delta M_q$ estimates are plotted on a 3-hour summary chart, updated every 5 minutes. Typically large (>100 C km) positive events greatly outnumber the negative events, especially above 300 C km. But a surprisingly large number of negative $i\Delta M_q$ readings >100 C km have been noted. Moreover, initial experience has shown substantial patterning in $i\Delta M_q$ reports by polarity, with many storms exhibiting structures reminiscent of the "bipolar" patterns first noted when NLDN became widely available (Orville et al., 1988; Engholm et al., 1990). It quickly became apparent from experience that when displays indicated $+i\Delta M_q > 300$ C km there was a very high probability of sprites being produced by the parent storm.

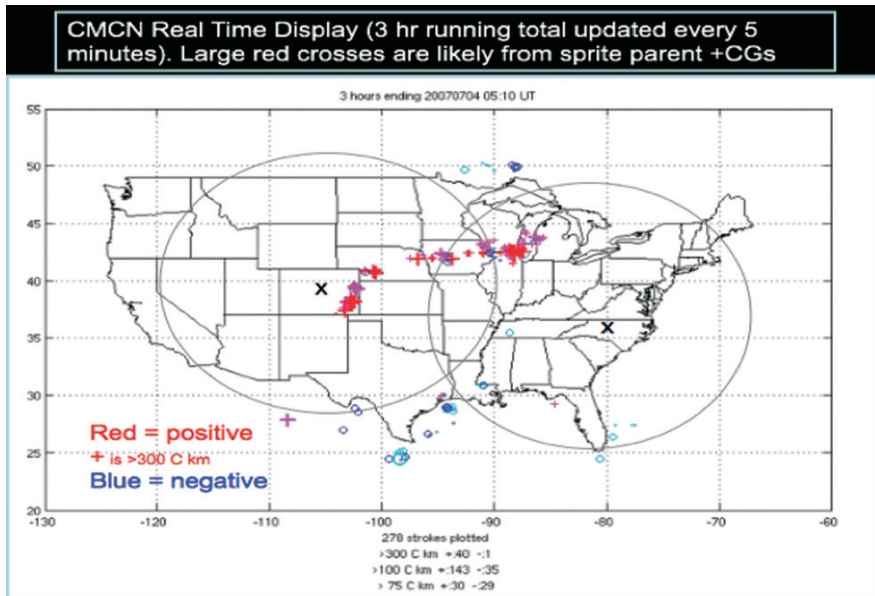


Fig. 17.2 The nominal coverage range of each CMCN sensor (~ 1500 km) and typical results from the online display. The convection in the central U.S. is dominated by large $+i\Delta M_q$ values (red), whereas negative events (blue) tend to be located over water. Smaller circles and + symbols represent $i\Delta M_q$ from 75 to 300 C km. Most detected $i\Delta M_q$ values are <50 C km

Figure 17.3 shows the TLEs (almost all sprites and/or halos; with $\sim 3\%$ being possible elves but more likely halos) that were optically confirmed by LLTVs during 2007 and geolocated by pairing them with the SP+CGs in the NLDN database. (Two events in Missouri are actually gigantic jets detected by automated cameras and reported by van der Velde et al. (2007)). No -CG TLEs were confirmed in 2007. One may note that the 2007 map reports TLEs far beyond the maximum 1000 km range of the LLTV at YRFS. A second major activity for SPRITES 2007 was establishing a Sprite Net of volunteers supplied with LLTV cameras and provided with daily forecasts and email updates as to potential targets. The CMCN displays proved to be exceptionally useful at identifying target TLE-producing storms for LLTV monitoring. The first sprites along the east coast and the upper Great Lakes have been reported. Also the CMCN alerted YRFS operators to point cameras to the northwest (for the first time ever) in order to record the first sprites over the western mountainous region of Wyoming. In January, 2008, the CMCN similarly alerted the Duke camera operators to capture the first sprites over the Gulf Stream, confirming the predictions by Price et al. (2002).

These new capabilities are allowing us to explore TLE production in a widening variety of storm types. As confidence is gained in the CMCN-derived $i\Delta M_q$ estimates to serve as surrogates for sprites, investigations into the climatology and meteorology of sprites will begin to make rapid advances. This will initially take

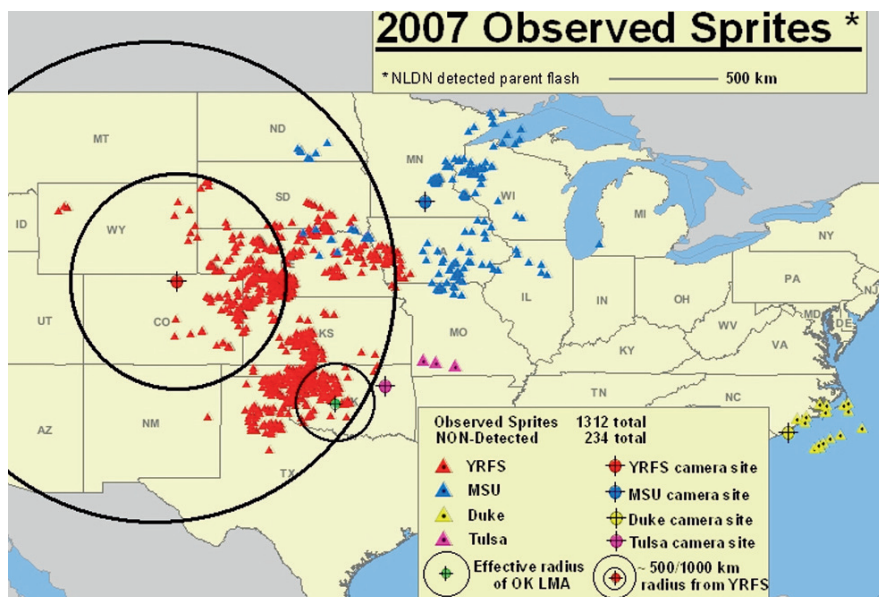


Fig. 17.3 The optically confirmed TLEs (almost all sprites) during 2007 having NLDN-detected parent CGs (See also Plate 20 in the Color Plate Section on page 606)

place with a series of detailed case studies. We herein provide one such analysis, but we will begin with the “classic” TLE-producing system, the largest of the MCSs, a mesoscale convective complex (MCC), characterized by an intense leading convective core and a large trailing stratiform region with a distinct bright band signature that evolved over many hours of time.

17.4 20 June 2007: A Prototypical TLE-Producing MCS

The synoptic pattern at 0000 UTC on 20 June 2007 revealed a flow of extremely moist, unstable air into Texas and Oklahoma which began interacting with a weak low pressure area and stationary front. Late the previous afternoon, a supercell formed in Kansas and moved south into an area of extremely high convective available potential energy (CAPE) between 3000 and 5000 J kg⁻¹ over Oklahoma and Texas. Another system grew into an MCS and moved eastward out of the Texas Panhandle. These systems merged, rapidly evolved upscale, and became a large mesoscale convective system, which by 0600 UTC covered a vast area (652,000 km² at -50°C). The NLDN was reporting around 44,000 CG flashes/hr. The CMCN real-time display, however, showed far fewer events which were clearly concentrated in large area of big +iΔM_q events in western and northern Oklahoma, with some negative iΔM_q events as well present in the eastern part of the MCC (Fig. 17.4). We

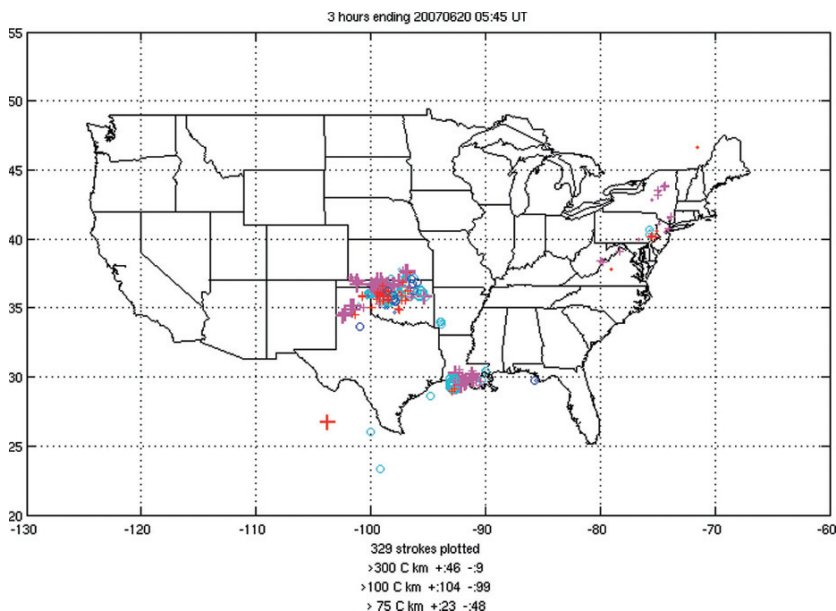


Fig. 17.4 The national Charge Moment Change Network 3-hour summary chart at 0545 UTC 20 June 2007 reveals a large concentration of very large positive $i\Delta M_q$ values in northern Oklahoma. However, as is typical, many storms fail to produce values even $>75 \text{ C km}$, and very few ($<<1\%$) CGs yield $i\Delta M_q$ values $>300 \text{ C km}$, a value for which TLE production probabilities, at least for +CGs, are very high

note that not every storm necessarily produces many, or even any, $i\Delta M_q$ events $>75 \text{ C km}$, even over extended periods of time.

Light winds aloft were typical of conditions favoring the nocturnal MCCs that frequent this region. The MCC continued surging southward and expanding through the night with an extremely large area of high, cold cloud tops. There was a classic bright band/secondary precipitation maximum in the trailing stratiform (TS) region located over the Oklahoma LMA as depicted on the 0605 UTC NEXRAD radar mosaic (Fig. 17.5). The Oklahoma LMA was ideally situated to provide detailed investigations of both the macroscale lightning patterns and for individual discharges. This MCC was perhaps the largest MCS of the season in the central U.S., as suggested by the cloud canopy display in Fig. 17.6. The NLDN-detected CGs displayed a typical pattern of high lightning densities of primarily negative CGs in the leading line convective cores, with widespread but lower density strokes in the trailing stratiform of mostly positive polarity. This basic bipolar pattern remained quasi-steady state for 4–6 hours, although with positive CGs tending to concentrate more rearwards in the trailing stratiform as the night wore on. A typical 5 minutes sample of NLDN data at 0600 UTC found that large peak current ($>75 \text{ kA}$) negative CGs were concentrating within the leading line convective cores (not shown), whereas the large peak current positives had migrated largely into the trailing stratiform

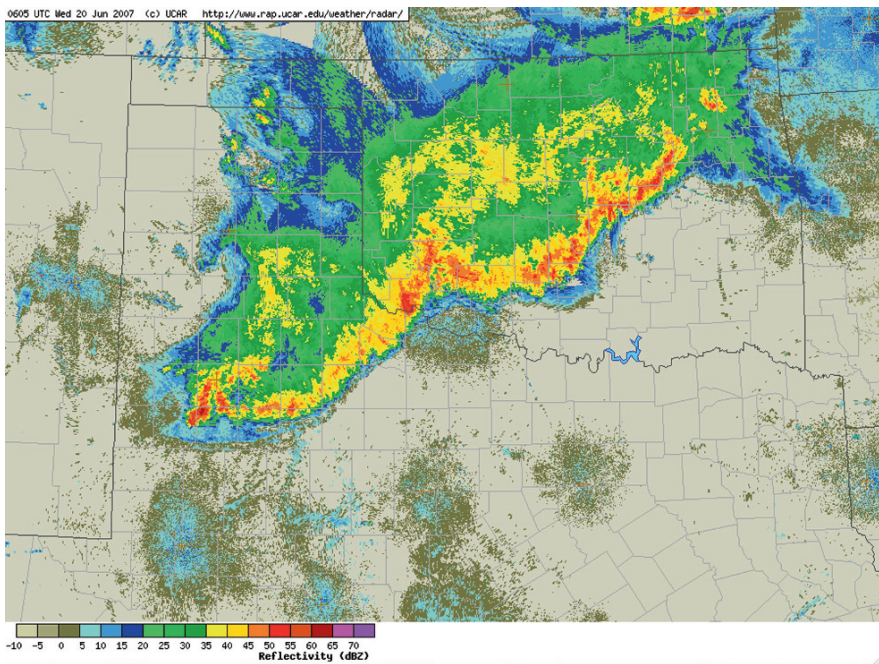


Fig. 17.5 NEXRAD reflectivity mosaic at 0605 UTC 20 June 2007 showing the classic leading edge/trailing stratiform structure of the MCC (See also Plate 21 in the Color Plate Section on page 606)

(Figs. 17.6 and 17.7). A summary of all 15,350 positive and 252,765 negative CG strokes (>10 kA) between 0000 and 0800 UTC are shown in Fig. 17.8. This storm was strongly negative CG dominated (94%) throughout its life cycle. However, as will become clear, the charge moment change characteristics of some +CGs in the trailing stratiform account for the vast number of sprites observed. As shown in Fig. 17.9, even over an eight hour period, there is also a clear spatial sorting of large peak current CGs (>75 kA) of both polarities, with positives in the trailing stratiform and negatives towards the leading (eastern and southern) edge.

Figure 17.10 shows the positions of the 230 optically confirmed TLEs (almost all sprites or spites plus halos, with 10 events being either stand alone halos or possible elves) with SP+CGs detected by the NLDN. (Sprites are typically centered within 50 km or less of the SP+CG location.) A total of 282 TLEs (>96% sprites and/or halos) were imaged by the LLTV camera. In this case, about 20% of the SP+CGs went undetected by the NLDN (assuming all sprites indeed have parent +CGs). We also note that 111 of the NLDN detected SP+CGs were within 200 km of the centroid of the Oklahoma LMA. Very little cloud blockage hindered the YRFS camera, a Watec 902H U, though some haze and/or smoke may have limited seeing somewhat given elevation angles of only several degrees above the horizon. Along the LLTV camera line of sight, light pollution from nearby Windsor, CO may also have made some dim events harder to see. Generally the sprites were flat and

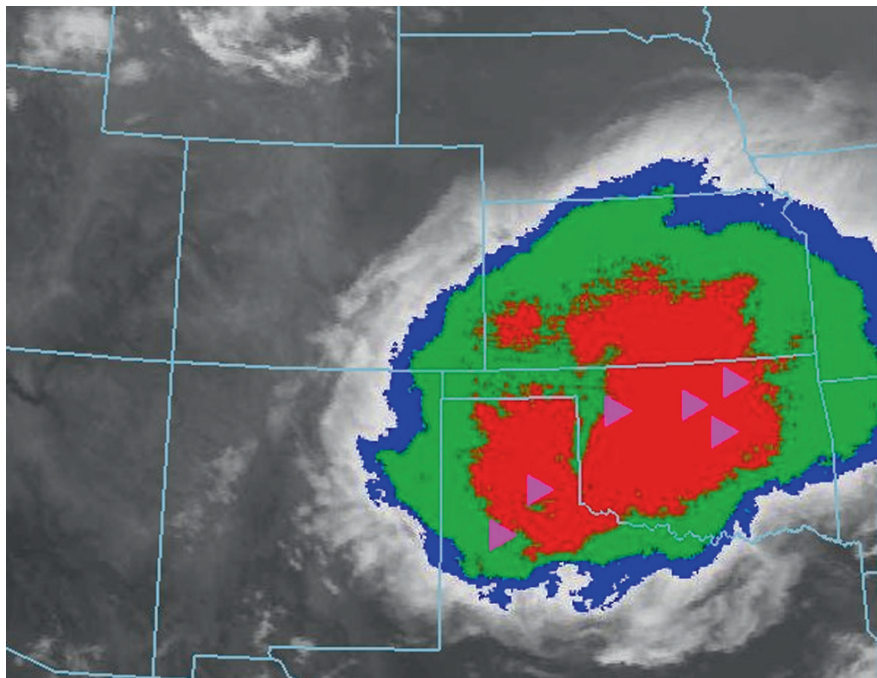


Fig. 17.6 Display at 0600 UTC 20 June 2007 showing an enhanced GOES IR image, with the -50°C canopy area (blue) of $652,000\text{ km}^2$ (with green $<-60^{\circ}\text{C}$ and red $<-70^{\circ}\text{C}$), along with those +CGs with peak currents $>75\text{ kA}$ during the prior 5 minutes (pink triangles)

wide (smudges or comb type), and most were not that bright (inherently dim or attenuation by smoke?) Distinguishing between halos and elves at these ranges was problematic. Even with these impediments, many TLEs were detected beyond 700 km. YRFS viewing began at dusk (0300 UTC) and terminated at 0700 UTC as the MCS began to move out of camera range.

Figure 17.11a shows the NLDN-detected CGs and those with $+i\Delta M_q$ values $>100\text{ C km}$ (colored pink if associated with an optically confirmed sprite or one of the 5 stand alone halos or possible elves) for the hour beginning 0400 UTC. The large $+i\Delta M_q$ values are concentrated in the TS region well to the rear of the convective line, a pattern which became even more pronounced in the following three hours. Of the 29 $+i\Delta M_q$ values $>300\text{ C km}$ 23 were associated with TLEs. About 90% of the SP+CGs had $+i\Delta M_q$ values above 100 C km , while 42% of the $+i\Delta M_q$ values $>100\text{ C km}$ had detectable sprites. While a few sprites appeared associated with $+i\Delta M_q$ values $<100\text{ C km}$, we suspect this may be due to assigning parent status to a secondary and lower peak current +CG associated with the horizontally extensive spider lightning discharge which often drops multiple +CGs separated by tens of kilometers. Thus, the CMICN has a detection efficiency for sprites on the same order as the flash detection efficiency of the pre-1994 NLDN ($\sim 60\text{--}80\%$) and, as with that system, a TLE-producing thunderstorm is unlikely to go undetected.

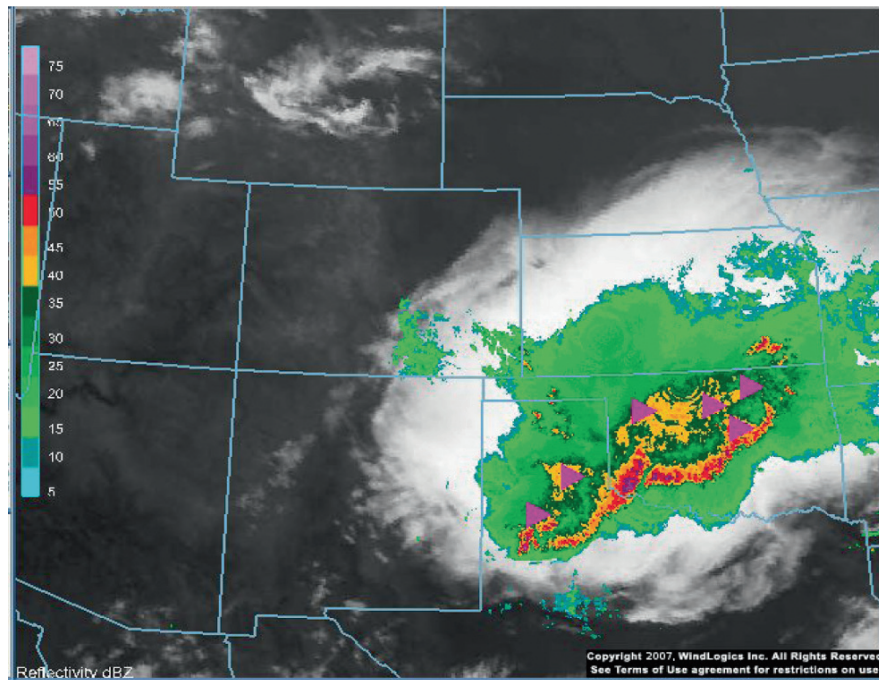


Fig. 17.7 Display at 0600 UTC 20 June 2007 showing large peak current +CGs >75 kA for the preceding 5 minutes superimposed over the NEXRAD mosaic of composite reflectivity (See also Plate 22 in the Color Plate Section on page 607)

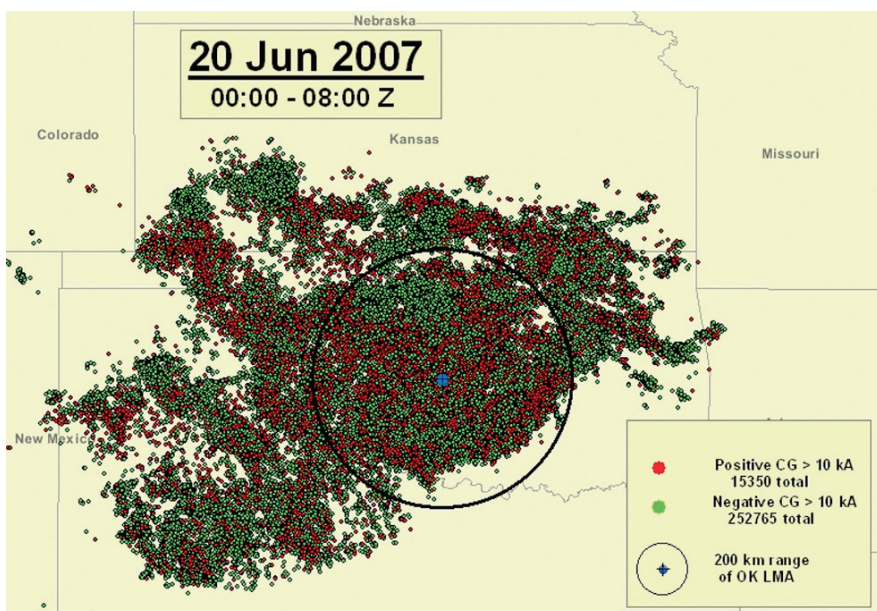


Fig. 17.8 Summary of the 252,765 negative CGs and 15,350 positive CGs between 0000 and 0800 UTC on 20 June 2007 (peak currents >10 kA). There were 282 optically confirmed TLEs (>96% sprites or halos + sprites)

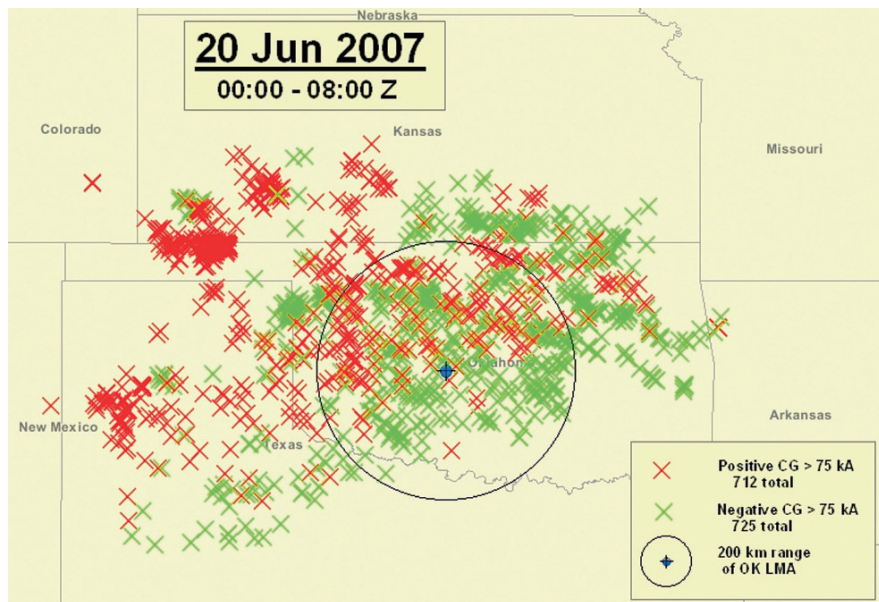


Fig. 17.9 NLDN CGs with >75 kA peak currents showing spatial segregation by polarity. Sprite parent +CGs tend to cluster in regions of large peak current +CGs

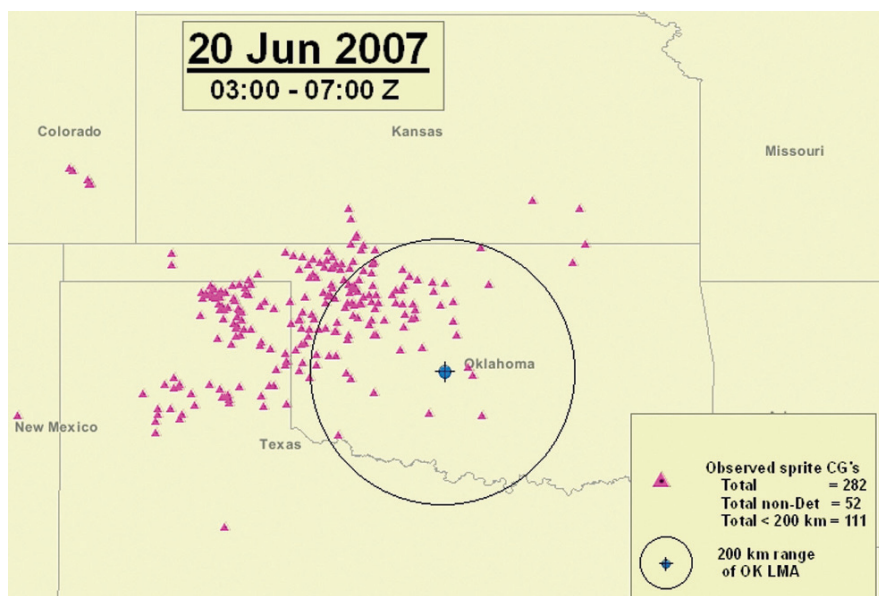


Fig. 17.10 Optically confirmed TLEs (almost all sprites) for which a parent +CG was detected by the NLDN, allowing for approximate geolocation. The actual sprite center can be offset from the +CG by up to 50 km. The coverage area of the Oklahoma LMA is indicated by the circle

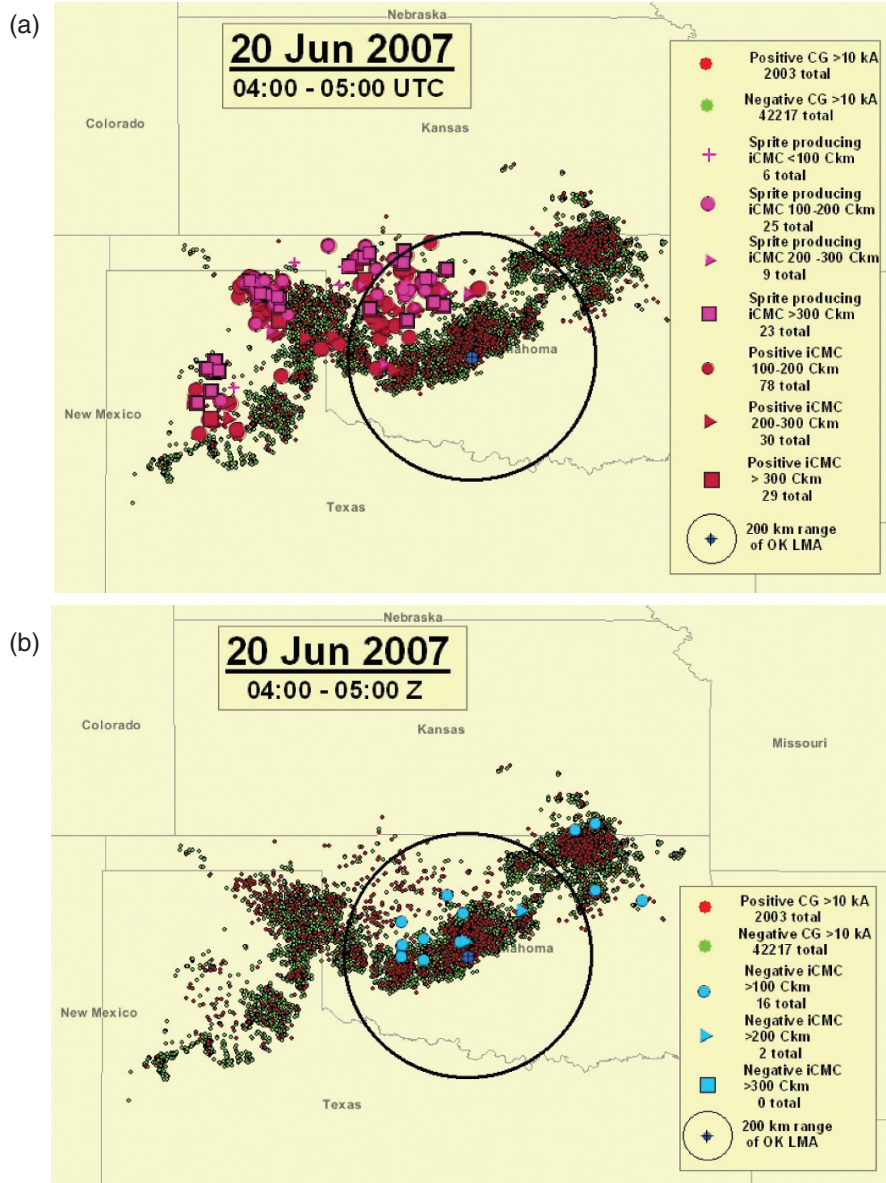


Fig. 17.11 (a) (top) One hour of NLDN CG reports, $i\Delta M_q$ values >100 C km, with optically confirmed TLEs CGs colored pink, 0400-0500 UTC 20 June 2007 and (b) (bottom) the same as above except plots of negative $i\Delta M_q$ values >100 C km are largely concentrated in the leading convective line. No TLEs were observed with these negative discharges

Also evident is that the $+i\Delta M_q$ events creating sprites were strongly concentrated deep into the trailing stratiform region of the MCC. The occasional sprite near or in the convective core tended to be dim with smaller $i\Delta M_q$ values.

Figure 17.11b (0400–0500 UTC) is typical of the distributions of negative $i\Delta M_q$ values $>100 \text{ C km}$ which were less numerous and concentrated in the leading convective line. No TLE was able to be definitively associated with a negative $i\Delta M_q$ event. However, there were a number of negative events $>100 \text{ C km}$, and three surpassed 300 C km during the LLTV observations with nothing apparent on the video record. This pattern was consistent throughout the analysis period.

The distribution of retrieved $+i\Delta M_q$ events for optically confirmed TLEs (almost all sprites) is shown in Fig. 17.12. While, as mentioned, a few sprites (21) were reported at $<100 \text{ C km}$, the remainder were substantially larger, with one attaining

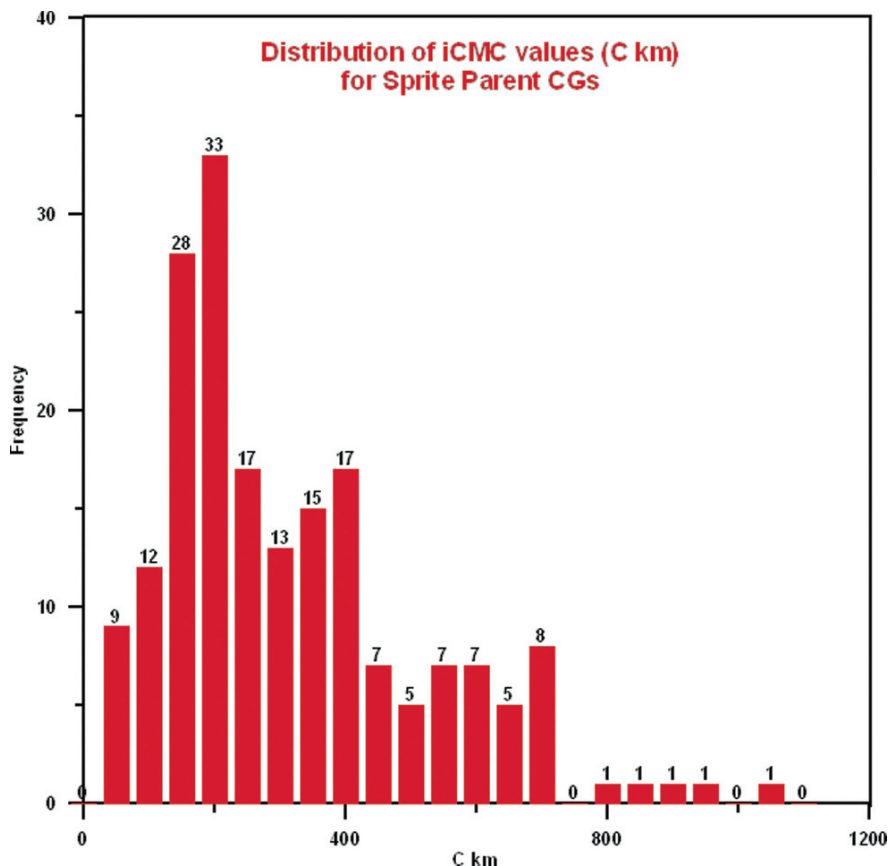


Fig. 17.12 The magnitude of the $+i\Delta M_q$ values associated with the sprites and sprites + halos on 20 June 2007 clearly are substantially larger than those for the thousands of “normal” CGs in this storm, typically $<50 \text{ C km}$. The largest impulse value was over 1000 C km , with almost all sprites associated with $+i\Delta M_q$ values $>100 \text{ C km}$. Events $>300 \text{ C km}$ have a $>75\text{--}80\%$ chance of producing an optically detectable TLE

1024 C km. Of the 40 largest $+i\Delta M_q$ values (430–1024 C km) during the four hour period of LLTV observations, fully 75% had an optically confirmed TLE. It is likely some of the “misses” were, in fact, due to a failure of the optical system to detect the dimmer TLEs as a result of the sub-optimal viewing due to the extreme ranges being worked this night. Thus, initial estimates suggest that $+i\Delta M_q$ values provided a Probability of Detection for TLEs that is very encouraging and indeed quite useful.

Initial analyses of the total lightning discharges using the Oklahoma LMA have produced some interesting results. As shown in Fig. 17.13, for most of the storm’s life cycle, there existed a bi-level structure consistent with a normal dipole (Carey et al., 2005), with some suggestion of a third layer of positive charge at 4–5 km near the melting layer. We have begun examination of the individual discharges involved in TLE production and will report these in detail in a later paper. However, unlike in earlier STEPS studies (Lyons et al., 2003a), in which the in-cloud component of the SP+CG remained largely in the melting layer (around 4 km AGL), a number of events were discovered in which the lightning initiated in the stratiform region near the melting layer, but then migrated upwards to 8–10 km AGL. If this were a consistent pattern, then many +CGs occurred with vertical channel lengths more than twice that postulated by Williams (1998) and seemingly confirmed by Lyons

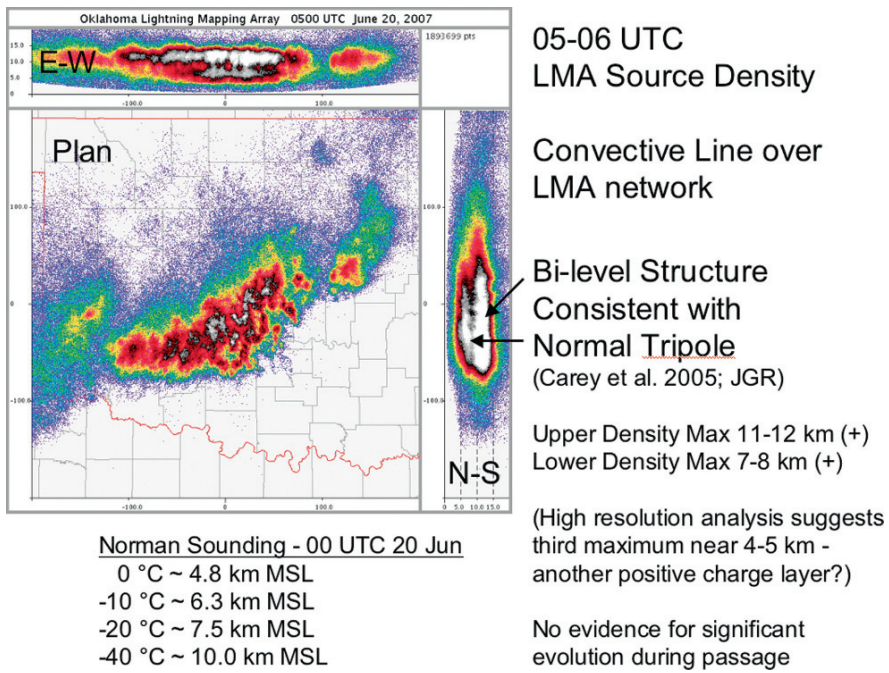


Fig. 17.13 An hour’s worth of VHF sources plotted as a density from the LMA (0500–0600 UTC 20 June 2007) reveals a structure fairly typical of a tripole charge distribution, with positive charged layers mapped out around 7–8 km and 11–12 km AGL. A possible positive charge layer was also detected around the melting layer (4–5 km)

et al. (2003a). This has one immediate implication. This storm produced sprites at a very fast rate, even considering its size and intensity. We have from time to time in the past noted MCSs that produced many more sprites than their peers. Perhaps the advantage of longer vertical channels for CGs is sufficient to push a large number of marginal +CGs over the $i\Delta M_q$ threshold and thus allow for TLEs. This aspect clearly requires further investigation.

Again, while the LMA analyses are still very preliminary, we have also found that the parent discharges of sprites can begin both in the stratiform area and near or in the convective line, and then migrate rearwards into the trailing stratiform before launching a +CG. Such discharge behavior has been noted in previous studies (Lang et al., 2004). Of interest is whether the initiating point of these discharges affects TLE production or continuing current characteristics in any systematic manner.

One discharge which produced two successive SP+CGs has proven to be truly extraordinary (Figs. 17.14 and 17.15). After initiating around 8 km AGL above the rear flank of the convective core, it then migrated rearward and downward into the stratiform region. That in itself is fairly common, but the in-cloud discharge meandered for ~ 290 km over a ~ 5.6 second duration, spawning two +CGs and sprites near the end of the discharge. The sprites were located to the rear of the trailing stratiform precipitation, well removed from the initiation point. This example was chosen at random, and brief inspection of other SP+CGs using the Oklahoma LMA has revealed numerous other discharges >100 km in length.

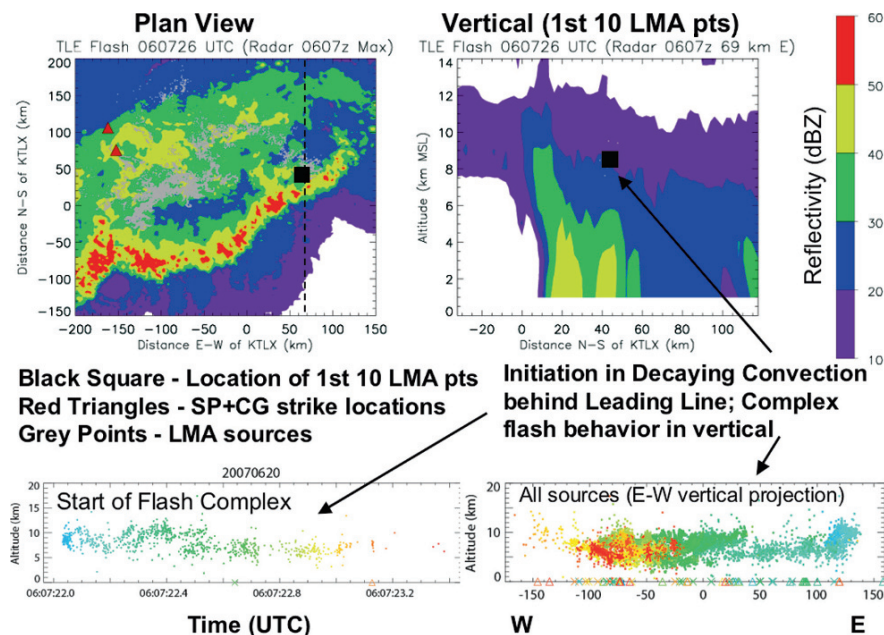


Fig. 17.14 The gray dots plot the path of a discharge approaching 300 km in total length. It initiated around 8 km AGL (white dot) above a convective element behind the leading edge and then propagated rearward and downward. The red triangles show the two +CG sprite parents (See also Plate 23 in the Color Plate Section on page 608)

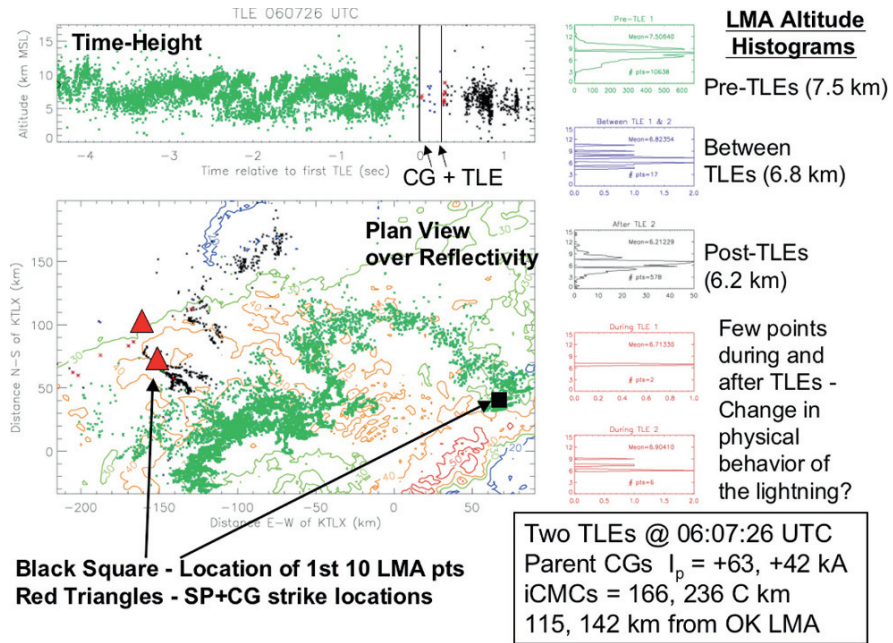


Fig. 17.15 A close up view of the 290 km long, 5.6 seconds discharge that produced two sprites from the +CGs (red triangles) at 0607 UTC 20 June 2007 (See also Plate 24 in the Color Plate Section on page 609)

17.5 Sprite Characteristics

For the over 1300 TLEs (almost all sprites or sprites preceded by halos) for which optical confirmations were obtained during SPRITES 2007, a detailed database was prepared which summarized their many characteristics. The Sprite Net cameras record video in 16.7 ms duration field increments. While the most common duration for a TLE is one video field (Fig. 17.16), about 75% last considerably longer with some continuing beyond 10 fields (167 ms). In some cases these are multiple sprite elements firing in response to horizontally extensive discharges laying down multiple +CGs to ground. But the majority brighten rapidly and achieve maximum luminosity during the first field, gradually diminishing in intensity thereafter. This has been ascribed to the role of continuing current associated with the SP+CG in maintaining the intense mesospheric electric field after the initial dielectric breakdown. High time resolution photometric observations of sprites have noted that the delay between the CG return stroke and the TLE luminosity initiation is highly variable. While an occasional sprite may fire within 1 ms, the majority are delayed more than 10 ms after the return stroke. Though the 16.7 ms video field integration period makes time resolved return stroke-TLE delay times (“delta Ts”) less precise than with photometry, the distribution of “delta Ts” obtained during 2007 is characteristic of previous studies in which more values than not are >10 ms. This is interpreted

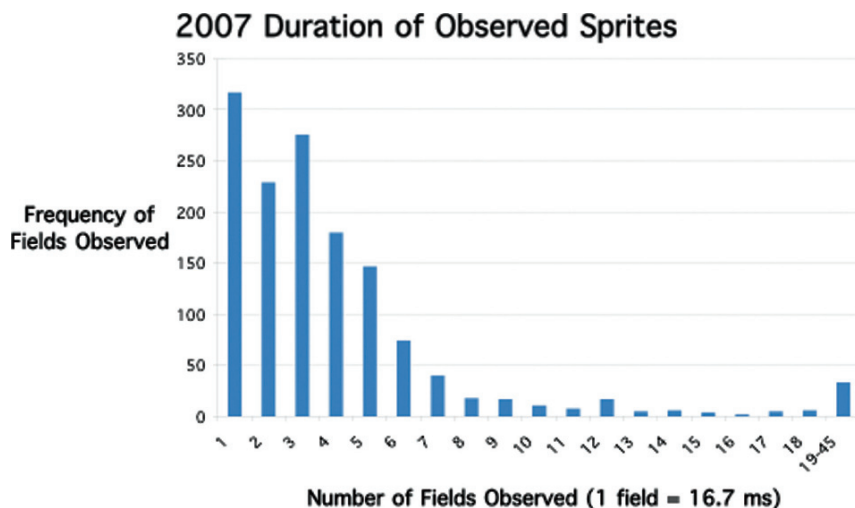


Fig. 17.16 A histogram of the duration of TLEs observed by the Sprite Net cameras in 2007, expressed in multiples of 16.7 ms video fields

as an indication of the contribution of continuing currents to lowering the additional charge beyond the initial $i\Delta M_q$ values required to reach the sprite threshold. While a few sprites can be triggered by the charge lowered during the first 2 ms, these are in the distinct minority. A plot of the NLDN-determined CG peak current versus the “delta T” times for optically confirmed sprites (Fig. 17.17) tends to support this suggestion. Very large peak current events tend to have shorter “delta Ts” yet even above 200 kA, few are shorter than 2 ms.

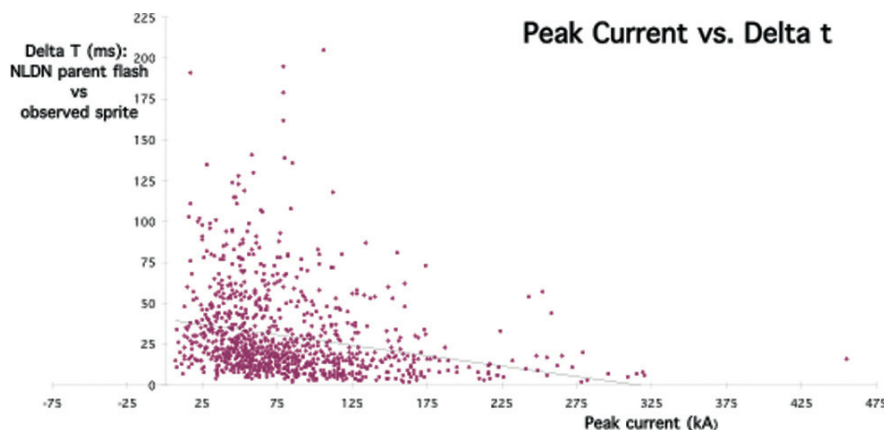


Fig. 17.17 Plot of the TLE parent CG peak current versus “delta T”(the interval between the return stroke and the onset of sprite luminosity) suggesting continuing current plays a key role in sprite initiation, especially for those CGs initially lowering lesser amounts of charge to ground

Over the U.S. High Plains, in the storms investigated to date, negative CGs have not yet been associated with sprites (though a few negative halos were noted in past years). The “polarity paradox” discussed by Williams et al. (2007) finds that far less than 1% of TLEs observed from land-based cameras occur with negative CGs, while 10× that number of threshold-exceeding negative ΔM_q events are indicated by regional and global ELF analyses. In the central U.S., some storms simply do not produce large enough negative ΔM_q values to induce TLEs (Cummer and Lyons, 2005) but that does not preclude other storms which may. The mystery may in part be resolved by noting the large number of high peak current (and large EMP) –CGs over salt water (Lyons et al., 1998). Recent analyses of ISUAL satellite measurements have found very large percentages of halos and elves, also with relatively large charge moment changes, from negative CGs over oceans (Frey et al., 2007). However, as the 20 June 2007 MCC revealed, negative CGs do on occasion approach and sometimes exceed $\sim 300\text{--}500$ C km even in the mid-continent U.S.

The results of this study introduce another variant of the polarity paradox. The $i\Delta M_q$ values reported herein show fewer, but still significant, numbers of negative $i\Delta M_q$ values > 100 C km, yet none associated with confirmed TLEs. By contrast, the probability of TLEs being reported from positive CGs rises rapidly once the $i\Delta M_q$ value exceeds 100 C km. Some (24) of the TLEs appear to be triggered by $+i\Delta M_q$ values > 500 C km. In these specific cases, the impulse values recorded within 2 ms are sufficient to trigger mesospheric breakdown. The remaining events must apparently rely upon substantial continuing currents to attain the ΔM_q threshold of ~ 500 C km during a period of time often extending beyond 10 ms after the return stroke. As illustrated in Fig. 17.18, it appears that while many CGs of both polarities can have $i\Delta M_q$ values in the 100–300 C km range in U.S. High Plains storms, the continuing currents in –CGs (which are fairly common and can extend beyond 100 ms based upon informal analysis of high speed video) are infrequently of sufficient intensity to allow further significant accumulation of charge moment change. We do note at least one optically confirmed negative sprite has been recently reported above an Argentine MCS triggered by a CG with an $-i\Delta M_q$ value of 503 C km (Bailey et al., 2007). We suggest that this event may be from a rare land –CG in which the impulse charge moment change was sufficient to initiate mesospheric breakdown, perhaps with minimal assistance from some continuing current.

The first summer of CMCN operation produced data from which a very preliminary $i\Delta M_q$ climatology can begin to be compiled. The number of reported $+i\Delta M_q$ values > 300 C km in the June–September 2007 period are displayed in Fig. 17.19a. The pattern shows some resemblance to those for large peak current +CGs (Lyons et al., 1998), with concentrations in the northern High Plains and with the intense MCCs found in northwestern Mexico. The impact of a severe drought in the east central coastal areas of the U.S. is noted by a dearth of reports in that region. A plot of $-i\Delta M_q$ values > 300 C km for the same period (Fig. 17.19b) shows, as expected, far fewer events. The rather random geographic scattering does not appear to indicate any enhanced effect over the salt water of the Gulf of Mexico or the Atlantic in the Gulf Stream region as found in negative large peak current CGs (Lyons et al., 1998).

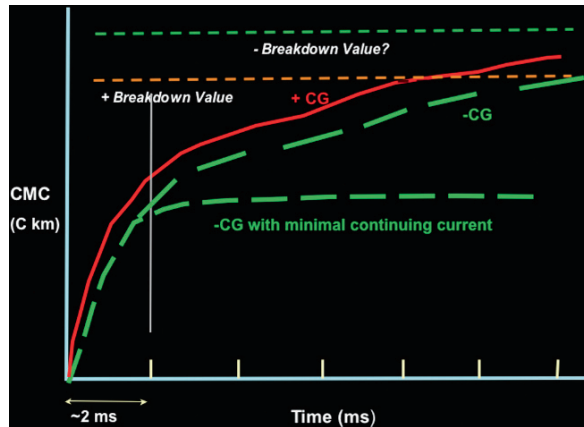
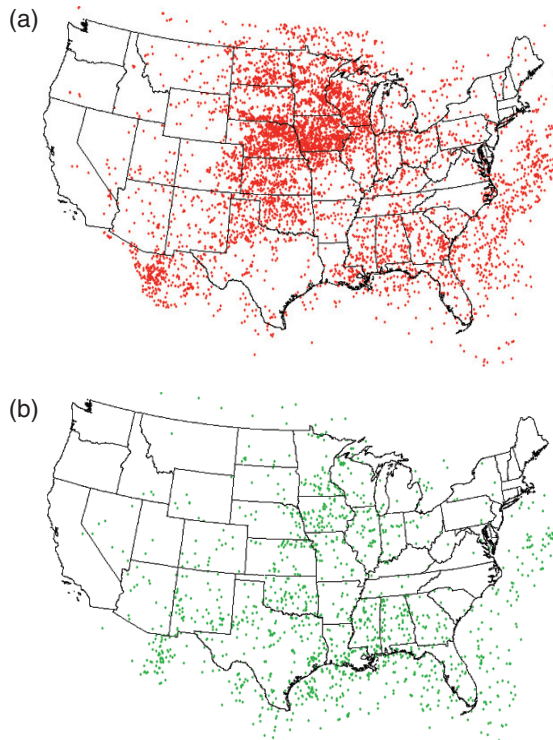


Fig. 17.18 Both positive and negative CGs produce impulse charge moment changes with values >100 C km, often approaching or even exceeding 300 C km, in the first 2 ms. Yet, for the interior of the U.S. at least, no negative CG has been linked with an optically confirmed sprite. We suggest many CGs of both polarities can have large $i\Delta M_q$ values and also can be followed by long continuing currents. Typically the continuing currents for +CGs are of sufficient magnitude to lower the additional charge needed to induce mesospheric dielectric breakdown to eventually trigger a sprite. The nominal breakdown value of ~ 500 C km is often reached after 10 ms (though some trigger within 2 ms, while others can be delayed >100 ms). Continuing current in most -CGs is much smaller, usually preventing breakdown levels to be attained. Yet some -CGs do achieve values of ~ 500 C km or higher without an observed TLE. Might it be possible that the breakdown value may be somewhat higher -CGs than for positives? Alternately, perhaps the resulting sprites and/or halos are dimmer and more difficult to detect with ground based LLTVs? (Note: A scale is not included for the y-axis in order not to imply that the breakdown values are either invariant or known with complete exactitude at this time.)

The current CMCN configuration does not compute $i\Delta M_q$ values for all CGs, but tends to trigger on those with larger peak currents. Even given this, many CGs are processed. The vast majority of ΔM_q values reported are relatively small, most being in the 5–50 C km range. Like the parent population of CGs, they are overwhelmingly negative. Figure 17.20a shows the diurnal distribution of all $i\Delta M_q$ values reported stratified by polarity. The negative events show a late afternoon/early evening peak (1800–0300 UTC), whereas the positive events tend to increase in late afternoon and persist through the nighttime hours. This is reminiscent of +CG behavior in nocturnal MCSs which dominate the central U.S. during summertime. But when $i\Delta M_q$ values >500 C km are plotted (Fig. 17.20b), the $+i\Delta M_q$ values dominate, are most pronounced during the nighttime hours, and greatly outnumber the negative events (88% of $i\Delta M_q$ values >500 C km are positive). But the residual of $-i\Delta M_q$ values >500 C km would suggest that negative sprites should occasionally have been detected after more than a decade of optical monitoring. One possible explanation is that the $i\Delta M_q$ breakdown threshold is somewhat higher for -CGs and/or that streamer growth is suppressed (Pasko, 2006), thus reducing sprite brightness and detection probabilities by LLTVs. The occasional LLTV of a negative halo (though

Fig. 17.19 (a) (top) Plot of $6415 i\Delta M_q$ values $>300 \text{ C km}$ for positive CGs during the June–September 2007 period as measured by the CMCN and (b) (bottom) the same except for 1483 negative CGs $>300 \text{ C km}$



not on 20 June 2007) suggest perhaps these events are characteristically dimmer than their positive counterparts. Clearly this area requires further investigation.

Sprites and other TLEs are known to be ubiquitous globally, capable of occurring wherever deep convection (and sometimes shallow wintertime convection) occurs. The intense convection of central Africa has long been known as a prolific generator of ELF Q-bursts, believed to be a reliable indicator of sprite-class lightning (Boccippio et al., 1995; Hobara et al., 2006, 2007; Williams and Yair, 2006). During the late summer of 2006, a Sprite Net camera system deployed by a NASA research team in Niamey, Niger (operated by Earle Williams, MIT Parson's Laboratory) achieved the first optical detection of sprites above Africa from a ground-based camera (Williams et al., 2008). However, unlike in the U.S., routine geolocation was not possible given the lack of a regional lightning detection network serving central Africa. However, the cooperative Worldwide Lightning Location Network (WWLLN) operated by the University of Washington (Jacobson et al., 2006), does detect the stronger CG events globally, with an estimated locational accuracy of $\sim 10 \text{ km}$ and a detection efficiency on the order of $\sim 10\%$ (Rodger et al., 2006). Indeed, the WWLLN did detect a sprite parent CG in northern Nigeria that was imaged by the Sprite Net camera at Niamey some 385 km to the west.

This result raises the question as to whether the CMCN sensors could be deployed elsewhere around the world not served by a conventional lightning detection

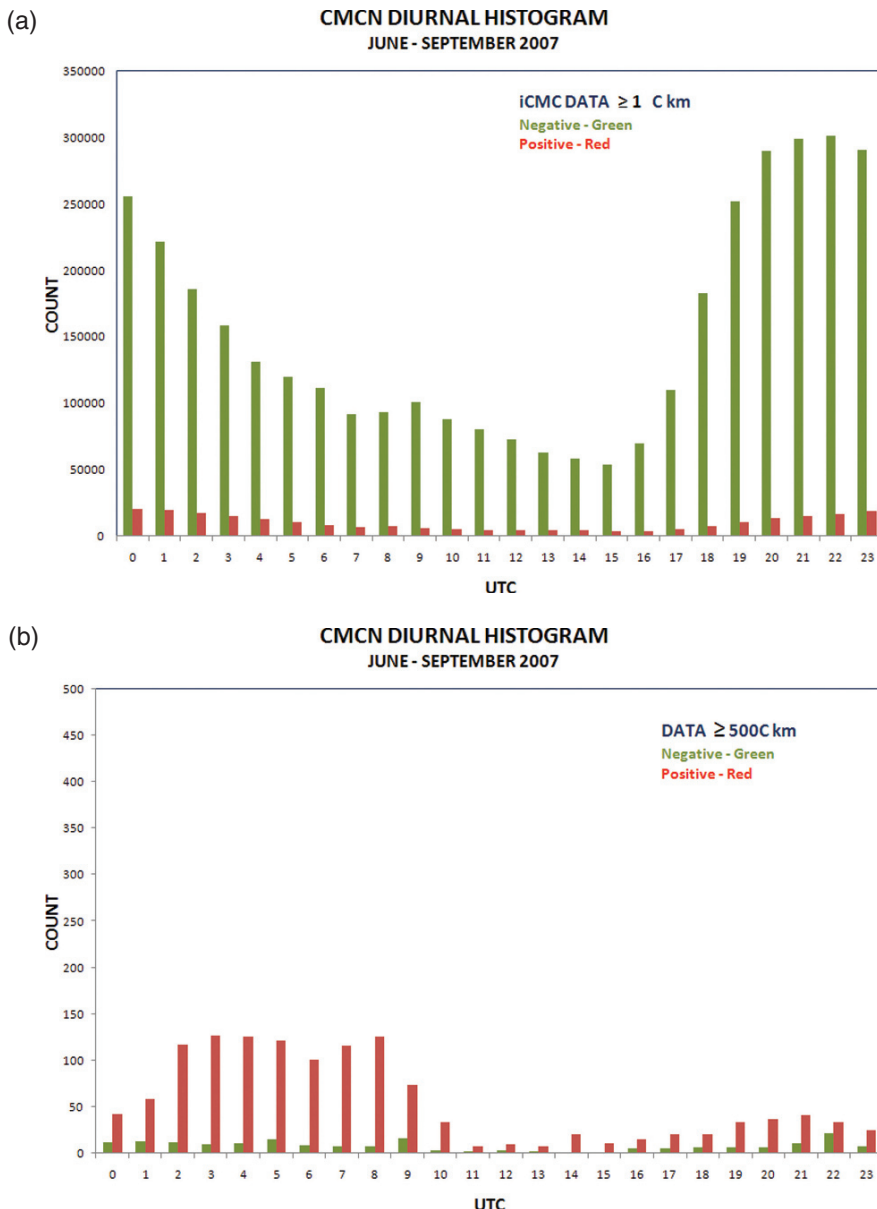


Fig. 17.20 (a) (top) Hourly histogram for all the CMCN $i\Delta M_q$ retrievals for both negative (green) CGs and positive CGs (red) during the June–September 2007 period in the U.S. and (b) (bottom) the same except for $i\Delta M_q$ values > 500 C km (12% of which are from negative CGs), the nominal sprite initiation threshold for +CGs. (Local time in the U.S. High Plains is UTC – 6 hours)

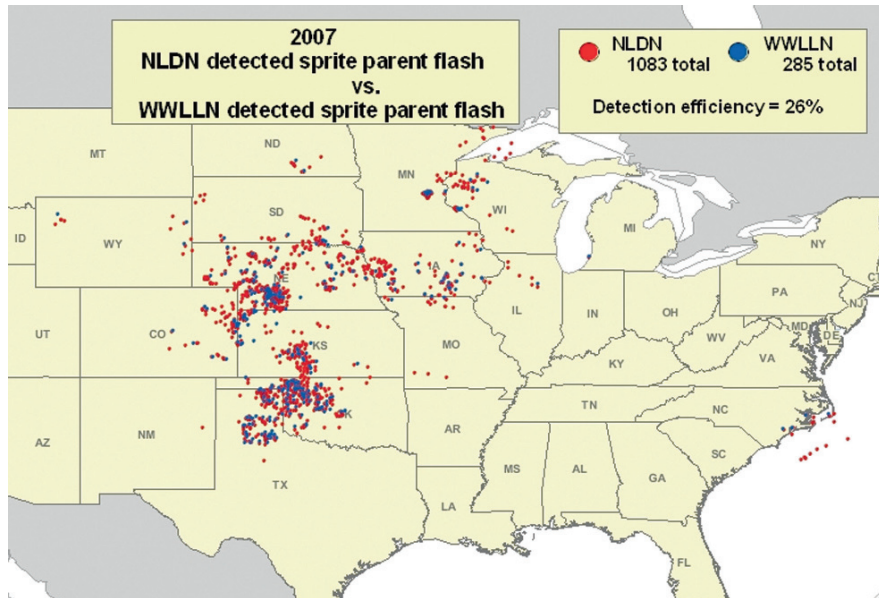


Fig. 17.21 Of 1083 optically confirmed sprites from the 2007 database with an NLDN detected parent +CG, 285 were also detected by the WWLLN (blue dots)

network but still use the WWLLN to geolocate some large $i\Delta M_q$ events. Employing the SPRITES 2007 database, we determined the approximate detection efficiency of the WWLLN for verified SP+CGs. For the sample Examined, 285 of 1083 confirmed TLE-producing CGs (26%) were detected by both the WWLLN and the NLDN (Fig. 17.21). On 20 June 2007, 68 out of 230 (30%) of confirmed NLDN SP+CGs were also reported by the WWLLN. We conclude that it is feasible to detect and track most TLE-generating storms using the CMCN approach by detecting large $i\Delta M_q$ values and geolocating them using the WWLLN. An exception would be for those systems producing only very few and infrequent large $i\Delta M_q$ values.

17.6 Discussion and Conclusions

In High Plains MCSs during spring through autumn, +CGs producing sufficiently large $i\Delta M_q$ values which induce TLEs typically occur (1) in the trailing stratiform region, (2) associated with radar reflectivities of 20–45 dBZ, (3) in radar echo (>10 dBZ) regions covering $>20,000 \text{ km}^2$, (4) in storms which a peak core reflectivity $>55 \text{ dBZ}$, (5) beneath the colder though not usually the coldest cloud tops, and (6) generally in systems with a maximum cloud top temperature of -55°C or less and -50°C canopy area of $>25,000 \text{ km}^2$.

The observation that sprites rarely occur during the active phase of High Plains supercells, even though they produce copious numbers of high peak current +CGs, has been documented (Lyons and Cummer 2005). The occasional “end-of-storm” sprites occur when the supercell is developing quasi-MCS stratiform region characteristics (Lyons et al., 2008) and +CGs likely develop longer and/or more intense continuing currents.

The new capabilities provided by the Sprite Net cameras to routinely monitor different convective regimes in various geographical regions will begin to expand our detailed understanding of TLE production for many of the storm categories listed in Fig. 17.1.

The extraction of $i\Delta M_q$ values in real-time from ULF/ELF/VLF transient analysis provides additional metrics by which the electrical activity of convective storms can be characterized (Cummer and Lyons, 2004, 2005). At a practical level, detection of $i\Delta M_q > 300 \text{ C km}$ virtually assures detection of sprites by LLTVs out to ranges approaching 700–1000 km (assuming the intervening line of sight is clear). The CMCN output allows the detection and tracking of sprite-producing storms throughout the U.S. on a 24×7 basis with geolocation of parent CGs provided by the NLDN. The technique could be applied, though with lower detection efficiencies in other regions, using CG geolocation from the WWLLN.

A classic MCC storm in Oklahoma was examined in detail. The SP+CGs with large $i\Delta M_q$ values were largely confined to the trailing stratiform precipitation region, though LMA analyses suggest some discharges (often 100–300 km in linear dimension) initiated in or near the upper reaches of the leading line convective core. The –CGs with $i\Delta M_q$ values $> 100 \text{ C km}$ were concentrated in the convective core and produced no detected TLEs.

While large positive $i\Delta M_q$ values dominate the statistics, and some storms have indeed been documented to produce no large negative $i\Delta M_q$ values (Cummer and Lyons, 2005), the emerging climatology suggests that on the order of 10% of $i\Delta M_q$ values $> 500 \text{ C km}$ occur with –CGs. The continuing drought of negative sprite, and only rare negative halo, LLTV observations remains puzzling. Possible interpretations could include that the breakdown threshold for –CGs is higher than for +CGs, and/or that the sprites and halos produced by negative strokes are dimmer and less likely to be detected by LLTV systems currently in use.

Intriguing is the likelihood that the available CMCN ULF/ELF/VLF magnetic sensors can provide information from which it is possible to extract the complete time-dependent current moment and charge moment change and the magnitude and duration of continuing currents. If the parameter Z_q is known or estimated, the charge lowered to ground may also be retrieved. This will be an area of active future research due to significant potential uses in electric utility fault finding, lightning protection design studies, forest fire detection, forensic and insurance investigations and atmospheric research.

The emergence of high-speed video imaging of lightning and sprites (Samaras and Lyons, 2008; Cummer et al., 2006) may provide useful tools to further explore polarity paradox issues. Such imagers have been producing new data on the details of the lightning discharge suitable for quantitative analysis, including the speed of

stepped and dart leaders and the newly recognized recoil streamers in +CGs. Digital high-speed video also provides an excellent means to study both qualitatively and quantitatively the continuing currents in return strokes of both polarities. In addition, earlier 1000 fps video of +CGs suggested numerous pulsations in channel luminosity (perhaps as new pockets of cloud charge are tapped by outspredding spider lightning in-cloud discharges) similar to M-components in -CGs. In +CGs, they are sometimes longer in duration and longer delayed after the return stroke. Yashunin et al. (2007) have suggested such +CG M-component-like pulsations may be causative of some long delayed sprites.

Acknowledgments This work has been supported by the National Science Foundation, Physical Meteorology and Aeronomy Programs (ATM-0221512 and ATM-0649034). Partial support of the Duke University effort was from NASA grant NAG5-10270 and from NSF. Nicolas Jaugey's contributions to the CMCN operation are enthusiastically acknowledged. The Oklahoma LMA data and assistance in its interpretation were graciously provided by Don MacGorman, with assistance from Paul Krehbiel, and Bill Rison. Robert Holzworth (University of Washington) graciously provided the WWLLN data. In addition to many useful exchanges of ideas, Earle Williams (MIT) labored mightily to operate the camera in Niamey to document the first sprites from a ground-based imager in Africa. These were confirmed via ELF in Hungary with the aid of Jo'zsef Bó. We gratefully acknowledge many valuable exchanges with Kenneth Cummins and Nick Demetriades (Vaisala, Inc.). Special thanks to the institutions which hosted Sprite Net camera systems: Minnesota State University, Mankato (Cecil Keen, Josh Jans), Duke University (Nicolas Jaugey), Florida Institute of Technology (Joe Dwyer, Ziad Saleh), Texas A&M (Joe Jurecka, Richard Orville) and the University of Oklahoma (William Beasley). Thanks to Tim Samaras and Tom Warner for their pioneering efforts to obtain high-speed imagery of +CGs.

References

- Bailey, M., M.J. Taylor, P.D. Pautet, S.A. Cummer, N. Jaugey, J.N. Thomas and R.W. Holzworth, 2007: Sprite halos and associated lightning characteristics over South America. AGU Fall Meeting, AE23A-0896, Abstract only.
- Barrington-Leigh, C.P. and U.S. Inan, 1999: Elves triggered by positive and negative lightning discharges. *Geophys. Res. Lett.*, **26**, 683–686.
- Barrington-Leigh, C.P., U.S. Inan, M. Stanley and S.A. Cummer, 1999: Sprites directly triggered by negative lightning discharges. *Geophys. Res. Lett.*, **26**, 3605–3608.
- Berger, K., R.B. Anderson and H. Kroninger, 1975: Parameters of lightning flashes. *Electra*, **80**, 223–237.
- Boccippio, D.J., E.R. Williams, W.A. Lyons, I. Baker and R. Boldi, 1995: Sprites, ELF transients and positive ground strokes. *Science*, **269**, 1088–1091.
- Carey, L.D., M.J. Murphy, T.L. McCormick and N.W.S. Demetriades, 2005: Lightning location relative to storm structure in a leading-line, trailing-stratiform mesoscale convective system. *J. Geophys. Res.*, **110**, D03105m doi: 10.1029/2003JD004371.
- Cummer, S.A., 2006: Measurements of lightning parameters from remote electromagnetic fields. *NATO Advanced Study Institute on Sprites, Elves and Intense Lightning Discharges*, M. Fullekrug et al. (eds.), Springer, 191–210.
- Cummer, S.A., N. Jaugey, J. Li, W.A. Lyons, T.E. Nelson and E.A. Gerken, 2006: Submillisecond imaging of sprite development and structure. *Geophys. Res. Lett.*, **33**, L04104, doi: 10.1029/2005GL024969.
- Cummer, S.A. and W.A. Lyons, 2005: Implications of lightning charge moment changes for sprite initiation. *J. Geophys. Res.*, **110**, A04304, doi:10.1029/004JA010812.

- Cummer, S.A. and W.A. Lyons, 2004: Lightning charge moment changes in U.S. High Plains thunderstorms. *Geophys. Res. Lett.*, **31**, L05114, doi10.1029/003GL019043, 2004.
- Cummer, S.A. and U.S. Inan, 2000: Modeling ELF radio atmospheric propagation and extracting lightning currents from ELF observations. *Radio Sci.*, **35**, 385–394.
- Cummins, K.L., M.J. Murphy, E.A. Bardo, W.L. Hiscox, R.B. Pyle and A.E. Pifer, 1998: A combined TOA/MDF technology upgrade of the U.S. National Lightning Detection Network. *J. Geophys. Res.*, **103(D8)**, 9035–9044.
- Engholm, C., R. Dole and E.R. Williams, 1990: Meteorological and electrical conditions associated with positive cloud-to-ground lightning. *Mon. Wea. Rev.*, **118**, 470–487.
- Franz, R.C., R.J. Nemzek and J.R. Winckler, 1990: Television image of a large upward electrical discharge above a thunderstorm system. *Science*, **249**, 48–51.
- Frey, H.U., S.B. Mende, S.A. Cummer, J. Li, T. Adachi, H. Fukunishi, Y. Takahashi, A.B. Chen, R.-R. Hsu, H.-T. Su and Y.-S. Chang, 2007: Halos generated by negative cloud-to-ground lightning. *Geophys. Res. Lett.*, **34**, L18801, doi: 10.1029/2007GL030908.
- Fukunishi, H., Y. Takahashi, M. Kubota, K. Sakanoi, U.S. Inan and W.A. Lyons, 1996: Elves, Lightning-induced transient luminous events in the lower ionosphere. *Geophys. Res. Lett.* **23**, 2157–2160.
- Hobara, Y., E. Williams, V. Mushtak, R. Boldi, M. Hayakawa, K. Yamashita, W. Lyons, B. Russell, G. Sátori, J. Bóré, C. Price, E. Greenberg and R. Holzworth, 2007: ELF Q-bursts from African squall lines. AGU, **88(52)**, Fall Meet. Suppl.
- Hobara, Y., M. Hayakawa, E. Williams, R. Boldi and E. Downes, 2006: Location and electrical properties of sprite-producing lightning from a single ELF site. *NATO Advanced Study Institute on Sprites, Elves and Intense Lightning Discharges*, M. Fullekrug et al. (eds.), Springer 211–235.
- Hu, W., S. Cummer, W.A. Lyons and T.E. Nelson, 2002: Lightning charge moment changes for the initiation of sprites. *Geophys. Res. Lett.*, **29**, 10.1029/2001GL014593.
- Huang, E., E. Williams, R. Boldi, S. Heckman, W. Lyons, M. Taylor, T. Nelson and C. Wong, 1999: Criteria for sprites and elves based on Schumann resonance observations. *J. Geophys. Res.*, **104**, 16943–16964.
- Jacobson, A.R., R. Holzworth, J. Harlin, R. Dowden and E. Lay 2006: Performance assessment of the World Wide Lightning Location Network (WWLLN), using the Los Alamos Sferic Array (LASA) as ground truth. *J. Atmos. Ocean. Tech.*, **23**, 1082–1092.
- Lang, T., L.J. Miller, M. Weisman, S.A. Rutledge, L.J. Barker, III, V.N. Bringi, V. Chandrasekar, A. Detwiler, N. Doesken, J. Helsdon, C. Knight, P. Krehbiel, W.A. Lyons, D. MacGorman, E. Rasmussen, W. Rison, W.D. Rust and R.J. Thomas 2004: The Severe Thunderstorm Electrification and Precipitation Study (STEPS), *Bull. Amer. Meteor. Soc.*, **85**, 1107–1125.
- Lang, T.J., S.A. Rutledge and K.C. Wiens, 2004: Origins of positive cloud-to-ground lightning flashes in the stratiform region of a mesoscale convective system. *Geophys. Res. Lett.*, **31**, L10105, doi:10.1029/2004GL019823.
- Lyons, W.A., S.A. Cummer, M.A. Stanley, K. Wiens and T.E. Nelson, 2008: Supercells and sprites. *Bull. Amer. Meteor. Soc.*, 1165–1174, doi: 10.1175/BAMS2439.1.
- Lyons, W.A., 2006: The meteorology of transient luminous events – An introduction and overview. *NATO Advanced Study Institute on Sprites, Elves and Intense Lightning Discharges*, M. Fullekrug et al. (eds.), Springer 19–56.
- Lyons, W.A., L.M. Andersen, T.E. Nelson and G.R. Huffines, 2006a: Characteristics of sprite-producing electrical storms in the STEPS 2000 domain. On line summary and CD, *2nd Conference on Meteorological Applications of Lightning Data*, AMS, Atlanta, 19 pp.
- Lyons, W.A., S.A. Cummer and G.R. Huffines, 2006b: Characterizing intense convection using conventional and advanced lightning metrics, including charge moment change. *Proceedings of First International Lightning Meteorology Conference*, Tucson, AZ. (conference CD31 pp).
- Lyons, W.A. and S.A. Cummer 2005: Lightning characteristics of the Aurora, NE record hail stone producing supercell of 22–23 June 2003 during BAMEX. *1st Conference on Meteorological Applications of Lightning Data*, AMS, San Diego (available on conference preprint CD).

- Lyons, W.A. and R.A. Armstrong 2004: A review of electrical and turbulence effects of convective storms on the overlying stratosphere and mesosphere. *AMS Symposium on Space Weather*, AMS Annual Meeting, Seattle 6 pp, CD.
- Lyons, W.A., T.E. Nelson, E.R. Williams, S.A. Cummer and M.A. Stanley 2003a: Characteristics of sprite-producing positive cloud-to-ground lightning during the 19 July STEPS mesoscale convective systems. *Mon. Wea. Rev.*, **131**, 2417–2427.
- Lyons, W.A., T.E. Nelson, R.A. Armstrong, V.P. Pasko and M. Stanley 2003b: Upward electrical discharges from the tops of thunderstorms. *Bull. Amer. Meteor. Soc.*, **84**, 445–454.
- Lyons, W.A., R.A. Armstrong, E.R. Williams, and E.A. Bering, 2000: The hundred year hunt for the red sprite. *EOS, Trans. Amer. Geophys. Union*, **81**, 373–377.
- Lyons, W.A., M. Uliasz and T.E. Nelson, 1998: Climatology of large peak current cloud-to-ground lightning flashes in the contiguous United States. *Mon. Wea. Rev.*, **126**, 2217–2233.
- Lyons, W.A., 1996: Sprite observations above the U.S. High Plains in relation to their parent thunderstorm systems. *J. Geophys. Res.*, **101**, 29641–29652.
- Lyons, W.A., 1994: Low-light video observations of frequent luminous structures in the stratosphere above thunderstorms. *Mon. Wea. Rev.*, **122**, 1940–1946.
- Orville, R.E., R.W. Henderson and L.F. Bosart, 1988: Bipole patterns revealed by lightning locations in mesoscale storms. *Geophys. Res. Lett.*, **15**, 129–132.
- Pasko, V.A., 2006: Theoretical modeling of sprites and jets. *NATO Advanced Study Institute on Sprites, Elves and Intense Lightning Discharges*, M. Fullekrug et al. (eds.), Springer, 253–311.
- Pasko, V.A., U.S. Inan, T.F. Bell and Y.N. Tarangenko, 1997: Sprites produced by quasi-electrostatic heating and ionization in the lower ionosphere. *J. Geophys. Res.*, **102(A3)**, 4529–4561.
- Pasko, V.P., U.S. Inan and T.F. Bell, 1996: Sprites as luminous columns of ionization produced by quasi-electrostatic thundercloud fields. *Geophys. Res. Lett.*, **23**, 649–652.
- Price, C., W. Burrows and P. King 2002: The likelihood of winter sprites over the Gulf Stream. *Geophys. Res. Lett.*, **29**, doi:10.1029/2002GL015571.
- Rakov, V.A. and M.A. Uman, 2003: *Lightning: Physics and Effects*. Cambridge University Press 687 pp.
- Rodger, C.J., S. Werner, J.B. Brundell, E.H. Lay, N.R. Thomson, R.H. Holzworth and R.L. Dowden, 2006: Detection efficiency of the VLF World-Wide Lightning Location Network (WWLLN): Initial case study. *Ann. Geophys.*, **24**, 3197–3214.
- Rodger, C.J., 1999: Red sprites, upward lightning and VLF perturbations. *Reviews of Geophysics*, **37**, 317–336.
- Samaras, T. and W.A. Lyons 2008: Visualization of naturally produced lightning using high-speed imaging. Preprints, *3rd Conference on Meteorological Applications of Lightning Data*, AMS, New Orleans.
- Stanley, M.A., 2000: *Sprites and their parent discharges*. Ph.D. Dissertation, New Mexico Institute of Mining Technology, Socorro, NM 163 pp..
- Thomas, R.J., P.R. Krehbiel, W. Rison, S.J. Hunyady, W.P. Winn, T. Hamlin and J. Harlin, 2004: Accuracy of the lightning mapping array. *J. Geophys. Res.*, **109**, D14207, doi: 10.1029/2004JD004549.
- van der Velde, O.A., W.A. Lyons, T.E. Nelson, S.A. Cummer, J. Li and J. Bunnell, 2007: Analysis of the first gigantic jet recorded over continental North America. *J. Geophys. Res.*, **112**, D20104, doi:10.1029/2007JD008575.
- Williams, E.R., Y. Hobara, R. Boldi, W. Lyons, T. Nelson, B. Russell, V. Mushtak, G. Sátori, J. Bór, S. Cummer, C. Price, E. Greenberg, Y. Takahashi and R. Holzworth, 2008: Meteorological origin of Q-bursts and sprites over West Africa. *Preprints 3rd Conference on Meteorological Applications of Lightning Data*, AMS, New Orleans. 4 pp.
- Williams, E.R., E. Downes, R. Boldi, W.A. Lyons and S. Heckman, 2007: The polarity asymmetry of sprite-producing lightning: A paradox? *Radio Sci.*, **42**, Special Issue on Schumann Resonances, RS2S17, doi: 10.1029/2006RS003488.
- Williams, E.R. and Y. Yair 2006: The microphysical and electrical properties of sprite-producing thunderstorms. *NATO Advanced Study Institute on Sprites, Elves and Intense Lightning Discharges*, M. Fullekrug et al. (eds.), Springer 237–247.

- Williams, E.R., 2001: Sprites, elves and glow discharge tubes. *Phys. Today*, November, **41**.
- Williams, E.R., 1998: The positive charge reservoir for sprite-producing lightning. *J. Atmos. Sol. Terr. Phys.*, **60**, 689–692.
- Wilson, C.T.R., 1925: The electric field of a thunderstorm and some of its effects. *Proc. Phys. Soc. Lond.*, **37**, 32D–37D.
- Yashunin, S.A., E.A. Mareev and V.A Rakov 2007: Are lightning M components capable of initiating sprites and sprite halos? *J. Geophys. Res.*, **112**, D10109, doi: 10.1029/2006JD007631.

Chapter 18

Infrasound from Lightning and Sprites

Thomas Farges

Abstract Thunder properties and mechanisms have been mostly studied between 20 and 40 years ago. Infrasonic signal (frequency lower than 20 Hz), also called infrasound, has been measured in parallel to acoustic signal when lightning occur. Recent technical developments and new interest to infrasound revive research about thunder. A European measurement campaign, dedicated to sprite research, has been organised in 2005. This paper shows new results about descriptions of infrasound from lightning: maximum distance from which this kind of infrasound can be detected, infrasound frequency spectrum from 0.1 to 10 Hz completing previous ones acquired above 1 Hz. More recently, it has been shown that also sprites produce infrasound. Three-dimensional locations of infrasound sources associated to infrasound from sprites are calculated using only infrasound characteristic when sprites are close to an infrasound station.

Keywords Infrasound · Thunder · Lightning · Sprites

18.1 Introduction

When you are thinking of lightning, hearing and sight are usual senses implied by your unconscious: we keep in mind a loud sound and a blinding light. Most of studies about thunder have been realised from 1960 to 1985. They have shown the presence of infrasonic waves associated to acoustic waves. Infrasound is defined as an acoustic wave whose frequency is smaller than 20 Hz that is approximately the heard limit. The infrasound frequency band ranges from the acoustic cut-off frequency (3.5 mHz at ground level) to 20 Hz. Nevertheless, not everything is known about infrasound from lightning; the source mechanism is still in debate. For about ten years, infrasound measurements have been chosen as one of the four techniques to verify the compliance of the Comprehensive Nuclear-Test-Ban Treaty

T. Farges (✉)

Commissariat à l'Energie Atomique, Centre DAM-Ile de France,

DASE, 91297 Arpajon Cedex, France

e-mail: thomas.farges@cea.fr

(Vivas Veloso et al., 2002). This revives research based on infrasound measurements and particularly allows the development of new sensors and new data processing methods. Small networks of sensors are now usually used to measure the characteristics of waves propagating over the network, as apparent speed (called also horizontal trace velocity) and arrival azimuth.

A temporary infrasound measurement network has been set up in 2005 during the Eurosprite campaign in South-West of France where lightning are numerous. Our goal was to characterize infrasound from lightning and sprites. We will present in the first section the 2005 Eurosprite campaign and more particularly our experiment. In the second section, new results are developed about the detectability of infrasonic thunder, the variation of infrasound amplitude vs. source distance and the infrasonic frequency spectrum. In the third and last section, we recall the characteristics of infrasound from sprites, describe the current assumptions on source mechanisms and lastly locate in 3D, using only infrasound characteristics, the sources for infrasound from sprites.

18.2 Eurosprite 2005 Campaign: Description and Objectives

To study Transient Luminous Events, of which sprites are an example, and their relation to thunderstorm, European sprite (Eurosprite) observation campaigns have been organised since 2000. The Eurosprite 2003 (Neubert et al., 2005) and 2005 campaigns were part of the activities of the European research training network CAL (Coupling of Atmospheric Layers). In 2005, camera observations (from two sites – at Pic du Midi de Bigorre in the French Pyrenees and at Puy de Dôme in the Massif Central), meteorological observations (weather radars, Météorage lightning detection system, SAFIR data), ELF (3–30 Hz), VLF (in broadband and in several narrow bands) and infrasound measurements were performed together.

In 2003, we use the data of a permanent infrasound station located at Flers ($48^{\circ}48'N$; $0^{\circ}30'W$) in the North-West of France (Fig. 18.1). This station is composed of four microbarometers arranged in a roughly equilateral triangle of 3 km side with a sensor at its barycentre (Le Pichon et al., 2002). Each sensor measures the local relative pressure with a sensitivity of 10^{-3} Pa, a band pass of 0.01–27 Hz, and a sampling frequency of 20 Hz. Thunderstorms pass through more frequently in the South of France than in the North. To study infrasound effects of nearby lightning we set up in 2005 a temporary station in South-West of France at St Just ($45^{\circ}20'N$; $0^{\circ}30'E$). Four identical microbarometers were there organized in a 1 km side triangle with one at its barycentre. Data are available for this station from August 12th to October 31st. In addition to measure the characteristics of infrasound from nearby lightning (frequency spectrum, amplitude decrease with distance ...), the objectives of these measurements were: to determine the distance beneath which infrasound from lightning can be detected and its variability, and to determine the 3D geometry of source of infrasound from sprite when sprite occurs close to the sensors.

We focus our analysis on two large thunderstorms on August 31st and September 9th. Both thunderstorms passed straight over infrasound St Just (JST) station while

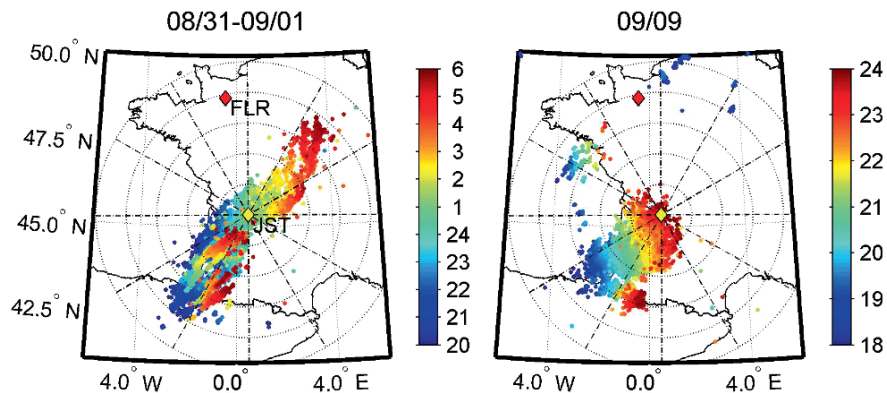


Fig. 18.1 (Left): Lightning activity recorded by Météorage in August 31st 2005 at 20 UTC to September 1st at 6 UTC; colour of the flash location is time related. Diamonds indicate location of infrasound stations: St Just (JST) in yellow and Flers (FLR) in red. Concentric circles indicate distance from JST station with a 100-km distance between each. (Right): same as left but for September 9th from 18 to 24 UTC (See also Plate 25 in the Color Plate Section on page 609)

none or weak lightning activity have been recorded around Flers station at less than 200 km (Fig. 18.1). On September 9th, two sprites were observed, by the camera at the Pic du Midi, in the vicinity of JST station.

18.3 Characteristics of Infrasound Recorded During Nearby Thunderstorms

18.3.1 Brief State of Art

This is not a review paper about thunder; such reviews can be found in books by Uman (1987) or Rakov and Uman (2003). Main results about thunder are summed up to highlight the novelty of the work presented here.

18.3.1.1 Characteristics

Most of experiments about thunder have been done from 1960 to 1985. They concern acoustical waves, audible or infrasonic, induced by thunder, but they are more numerous in its audible part. The main thunder characteristics are summed up here. Audible thunder can be heard from lightning flashes distant at less than 25 km. Lightning induce maximum pressure variations of 0.2 to 2.4 Pa at a range of some kilometres. The pressure wave is composed of several pulses; each pulse lasting from 0.2 to 2 s. Two to four pulses are usually recorded per thunder. A gap of 1 to 3 s between two pulses is observed. One thunder event lasts then about ten seconds. This duration is not only due to the distance between the closest and the farthest point of

the return stroke channel; acoustic waves produced by cloud discharges preceding the return stroke have also to be considered. This property was used to image the lightning channels by time-of-arrival technique using a microphone network (e.g. MacGorman et al., 1981).

Holmes et al. (1971) show very important results about thunder frequency spectrum. It peaks at frequencies from less than 4 Hz to 125 Hz. The intra-cloud discharges produce thunder with a frequency spectrum peaking around 28 Hz when the cloud to ground (CG) discharge thunder have a peaked frequency around 50 Hz. Nevertheless, in a single flash, two peaks can be found: below 20 Hz and between 40 and 60 Hz and a temporal variation of the spectral content is observed.

18.3.1.2 Source Mechanisms

The main difference between audible and infrasonic thunder is probably their physical process. Audible thunder is due to acoustic radiation from heated channels while infrasonic thunder could be due to conversion of the thundercloud electrostatic field to sound. Few's model (1986) explains well how heated air inside the channel produces a shock wave which, several meters away from the channel, changes in an acoustic N-shape pressure pulse. This theory can explain how the thunder frequency spectrum peaks around 50 Hz, but it cannot explain the infrasonic peak. Few's model (1985) about infrasonic thunder, which is an evolution of the Dessler's one (1973), explains how electrostatic field produces a reduction of atmospheric pressure inside the charged region of the cloud which is cancelled when a lightning discharge occurs. Dessler showed that the radiation is strongly oriented in the vertical direction, its amplitude (0.05–5 Pa) is linked to the thundercloud charge which is neutralized by the discharge and its frequency (0.2–2 Hz) is determined by the main dimension of the charge slab. Infrasound has then to be measured when the thundercloud is just over the sensors. Few (1985) modified the Dessler's model, adding a preliminary heating, to explain why overpressure is measured first.

18.3.2 Distance Beneath which Infrasonic Thunder can be Detected

During August 31st thunderstorm (Fig. 18.1), which passed just over JST, more than thousand CG discharges have been localised by Météorage 50 km around the station from 23:30 to 02:00 UTC (Fig. 18.2a). Météorage, the French Lightning Detection Network, uses the same technology that NLDN in USA to detect and locate cloud-to-ground flashes. For each return stroke, we have the location with accuracy of 1 km, the time with accuracy of less than 1 μ s and the peak current. The crest-to-crests infrasound amplitude, in the 0.1–9 Hz band, reaches 6.3 Pa when lightning was less than few kilometres from station (Fig. 18.2b). Infrasound from lightning appears in spectrogram as vertical lines from 23:30 to 02:00 UTC (Fig. 18.2c).

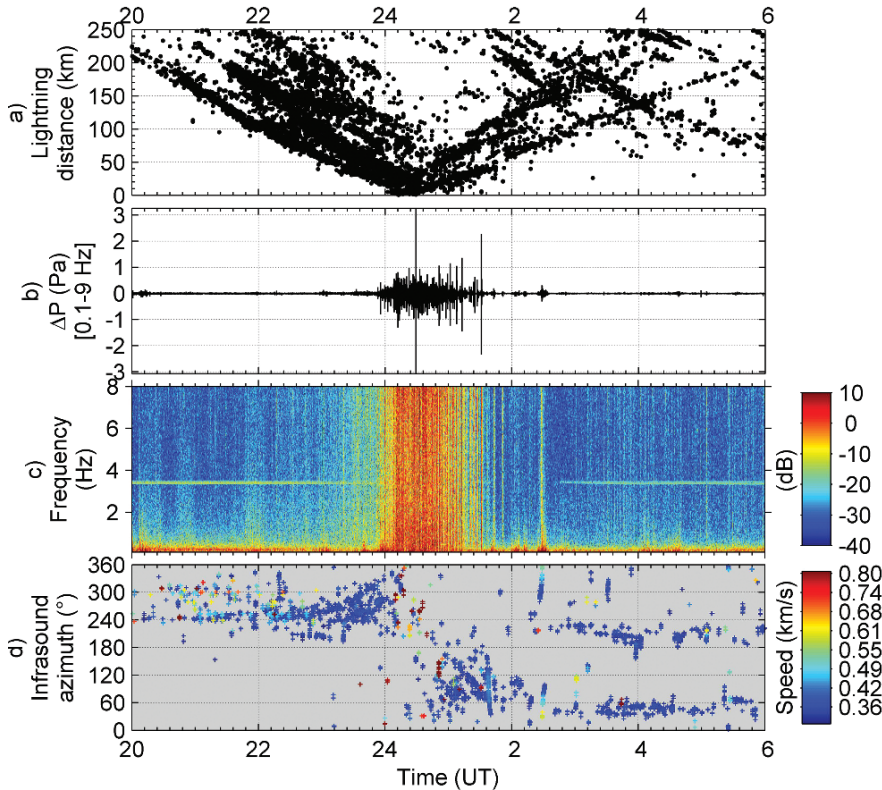


Fig. 18.2 Data recorded from August 31st at 20 UTC to September 1st at 6 UTC. (a): Lightning distance vs. time taking account propagation time of acoustic wave. (b): Pressure recorded by the central sensor in JST station and filtered from 0.1 to 9 Hz. (c): Spectrogram of the pressure signal. (d): Infrasound azimuth of arrival where colour indicates the apparent speed (See also Plate 26 in the Color Plate Section on page 610)

The Progressive Multi-Channel Correlation (PMCC) method (Cansi, 1995; Le Pichon et al., 2002) is applied on data of four sensors to calculate the apparent speed and the arrival azimuth of waves which propagate over network. Infrasound networks detect usually waves produced by oceanic swell, called microbarom (Pichon et al., 2006). The microbarom main frequencies is from 0.1 to 0.5 Hz. Infrasound azimuths of arrival, results of PMCC calculations, are shown on Fig. 18.2d. Detectors are plotted for wave having frequency higher than 1 Hz to eliminate most of those due to microbarom. At 20:00 UTC infrasound events were detected at 240° azimuth. From 22:00 UTC, the number of infrasound events grows. This increase of number of detected infrasound events is mainly due to the better detection when the thunderstorm is coming close to the station. However, the lightning activity rises also from 50 flashes per 5 minutes at 20 UTC to more than 300 flashes per 5 minutes at 23:30 UTC. Azimuths change northward until thunderstorm was just over the station at 00:00 UTC; when the storm is over the station, infrasound can come from

all directions. After 02:00 UTC two main infrasonic activities were recorded along the 200° and 45° azimuths associated with the north-eastward motion of storm and with the development of new cells located South-West of JST (see orange and red dots in Fig. 18.1).

Infrasound azimuths of arrival (black, grey and purple dots), calculated with PMCC, are compared with lightning azimuths (coloured circles) for both weather situations analysed in this paper (Fig. 18.3). Lightning azimuth are calculated using

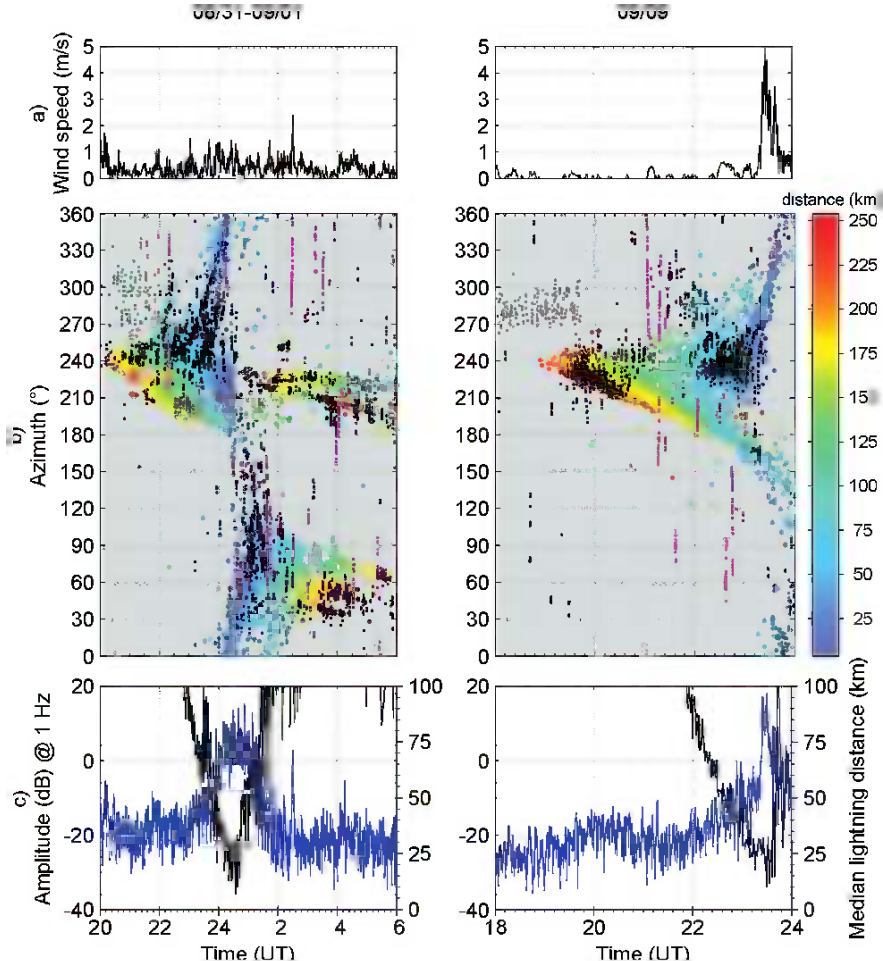


Fig. 18.3 (a) Wind speed from August 31st at 20:00 UTC to September 1st at 6:00 UTC (left) and on September 9th from 18:00 UTC to 24:00 UTC (right). Wind measurements have been realised at ground level at the central station location. (b) Comparison of lightning azimuths (coloured circles – colour indicating lightning distance as shown on legend at right) and infrasound azimuths (coloured dots; black for lightning, purple for long lasting events, and grey for microbarom). (c) Comparison of the signal amplitude (in dB) at 1.00 ± 0.02 Hz (blue) and the median distance of lightning (black) (See also Plate 27 in the Color Plate Section on page 611)

Météorage location data in comparison to JST location. Propagation time of acoustic wave from lightning position to JST station is taken into account; it is the ratio of lightning distance and speed of sound (~ 0.34 km/s). Infrasound detections are sorted in three classes taking into account the duration and the spectral content of each detection: (i) lightning (black dots), which last few seconds, (ii) microbarom (grey dots), for which several detections appear however simultaneously in 0.1–1 Hz and 1–10 Hz bands, and (iii) long lasting (~ 1 minute) and large azimuth range (more than 30°) events are plotted with purple dots. This last class of events will be discussed in the next section dedicated to infrasound from sprite.

Black dots and mainly blue circles are in good agreement. This means that detected infrasounds come from thunderstorm location, particularly at less than 100 km from JST. We can suppose then that the source of these infrasounds is located inside the thunderstorm. There is also a good correlation between black dots and red/orange circles that are lightning which are 200–250 km away; this is particularly obvious from 19:00 to 21:00 UTC on September 9th when wind speed is very weak (Fig. 18.3a). When the wind speed is high, the noise level grows up and it is more difficult to correlate signals from several stations. For instance, from 23:30 to 24:00 on September 9th, the wind reaches 5 m/s and no detection has been found while the thunderstorm was just over JST station. At last, there is a very weak correlation when lightning are from 100 to 200 km away from JST. An explanation to this lack of correlation is the propagation mode. Beneath 100 km, propagation from thundercloud to station could be direct. Acoustic wave propagation in the Earth-atmosphere waveguide becomes possible beyond 200 km. From 100 to 200 km, the station is located in shadow area where acoustic wave hardly propagates.

Filtered signal at 1 Hz (± 0.02 Hz) and median lightning distance (calculated per 1 minute interval) are compared (Fig. 18.3c). A narrowband around 1 Hz is chosen to avoid microbarom contribution. The amplitude of the noise at 1 Hz is about -20 dB. When the thunderstorm is close enough to the station, that is distance less than 60 km, the infrasound signal increases and reaches ~ 15 dB when the thunderstorm is over JST station. Its temporal variation follows very well the shape of the median distance of lightning. When the thunderstorm is far away, more than 60 km, infrasound can be detected with azimuth in good agreement with lightning azimuth. It is thanks to very weak local noise and correlation methods allowing detection of coherent wave having weak amplitude. Nevertheless, one-to-one association is not possible for distant lightning.

18.3.3 Variation of Infrasound Amplitude vs. Distance

Significant acoustic signal is measured when thunderstorm is close to station and one-to-one correlation becomes possible. Some infrasound events have been associated to CG discharges listed in the Météorage database. One-to-one correlation is obtained by comparison of time and azimuth of arrival. As an example, Fig. 18.4 shows signals recorded simultaneously on four sensors at around 00:08:35 UTC

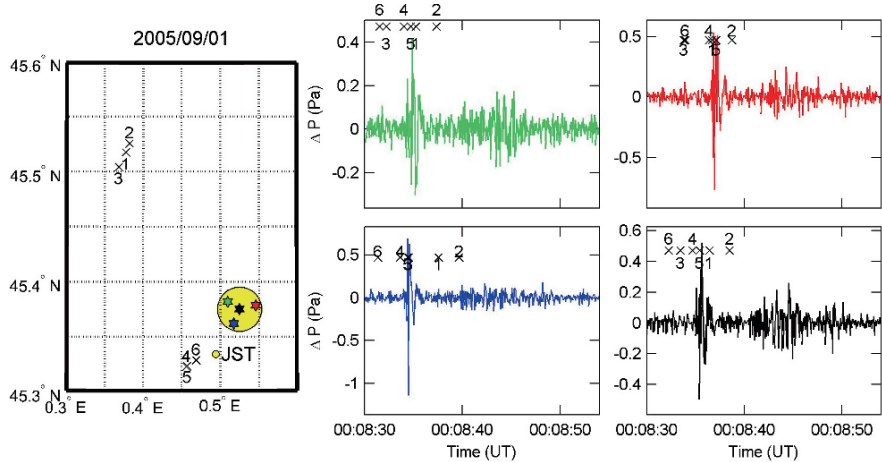


Fig. 18.4 (Left): Location of 6 lightning strokes which can produce infrasound recorded from 00:08:30 to 00:09:00 UTC on September 1st. The small yellow circle indicates JST station location while the relative location of four sensors (coloured stars) is detailed in the large yellow circle (directions are kept but distances have been magnified). (Right): Infrasound signals recorded by these sensors using the same colour code used for relative sensor location. Calculated time of arrival of the infrasound from each of these lightning is marked with a cross and numbered with the same reference as on the map

with an azimuth of arrival of $\sim 250^\circ$, and the location of six return strokes, which can contribute to these signals; they are numbered from 1 to 6. Their peak currents are respectively: -29.2 , -15.5 , -13.1 , -30.1 , -29.7 and -6 kA. Three discharges are close to the sensors (at less than 3 km and 247°) and three others are at ~ 22 km north-westward ($\sim 335^\circ$). Calculated time of arrival of waves coming from the location of lightning labelled 1, 4 and 5 is in coincidence with infrasound peaks (except lightning 1 on blue sensor data) while this is not the case for lightning labelled 2, 3 and 6. Lightning 4 and 5 have the good azimuth. They are then clearly identified as the sources of infrasound pulses recorded at that time.

Eighty eight infrasound pulses have been one-to-one associated to CG discharges from 22 UTC on August 31st to 2 UTC on September 1st when the thunderstorm is at less than 100 km from the JST station. Infrasound crest-to-crest amplitudes are plotted as a function of their respective CG distance (Fig. 18.5). Data linear regression is performed using a mean square method; the best fit is obtained with: $a = c/d$, where a is the infrasound amplitude, d the CG distance and c a coefficient equal to 6.2.

The Dessler's theory (conversion of the thundercloud electrostatic field to sound) shows that the emission pattern of infrasonic wave due to lightning is strongly oriented in vertical direction and its amplitude is proportional to the charge neutralized by the discharge. The propagation of the wave should be limited to the near field by the emission pattern. However, infrasounds from lightning are detected up to 100 km from the thundercloud. Events are sorted out in three peak current ranges (Fig. 18.5).

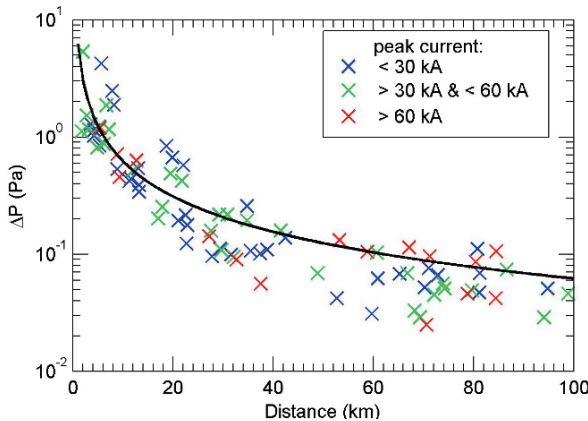


Fig. 18.5 Amplitude of infrasound from lightning vs. lightning distance (*coloured crosses*) in semi-log plot. The *black line* is the result of linear regression

We can infer that there is no clear link between peak current and infrasound amplitude, especially for discharges close to station (distance lower than 10 km). This is also in disagreement with the Dessler's theory. In these cases, infrasounds from lightning are more probably the infrasonic part of the audible thunder, as measured by Holmes et al. (1971).

Nevertheless, some infrasound detections from 00 UTC to 01 UTC (Fig. 18.2) have very high horizontal apparent speed. From the horizontal apparent speed, we can deduce the elevation angle because acoustic wave propagates at the speed of sound. When the apparent speed is much bigger than speed of sound, this means that the elevation angle is high, or in other words the source is in altitude. These infrasounds may be then explained by the Dessler's theory. Thorough analysis is more difficult (poor correlation between infrasound time and Météorage database) because Météorage does not include intracloud lightning, which seem important in this case.

18.3.4 Frequency Spectrum

Spectra, obtained in infrasonic domain (e.g. Holmes et al. [1971]), are limited to 1 Hz (lower limit). We describe here the spectral response of infrasound from lightning from 0.01 to 10 Hz. Mean spectra are calculated, in ten minutes intervals, from several consecutive spectra calculated with one minute of data. These spectra, calculated with the August 31st storm data, are plotted in Fig. 18.6. When thunderstorms approach the station, background level is raising (Fig. 18.3c) and is mainly composed of signal due to lightning. The highest level is found around midnight when the storm was just above the station. Infrasonic background level from close lightning flashes masks the acoustic signal produced by simultaneous distant lightning flashes and makes them hardly detectable.

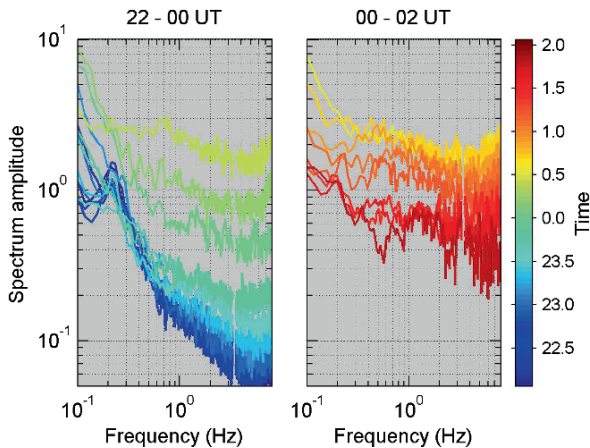


Fig. 18.6 Mean infrasound spectra, per 10-minutes interval, for data recorded from August 31st at 22:00 UTC to September 1st at 02:00 UTC. From 22:00 to 23:00 UTC, the peak at 0.2–0.3 Hz reveals microbarom (See also Plate 28 in the Color Plate Section on page 612)

To measure the infrasound spectrum of a single lightning, not “polluted” by the interference of infrasound due to other lightning, we select one infrasound pulse from a lightning occurring at 01:31 UTC. The CG discharge (+19.8 kA) was located near the station (~ 6 km) while the thunderstorm was moving away: median lightning distance was 60 km and the nearest lightning after this one occurred 10 minutes after at about 25 km from the station. The infrasound signal from this lightning, its spectrum and its spectrogram are shown on Fig. 18.7. The weak pulse from 01:31:05 to 01:31:07 is due to a small CG flash (-5.5 kA) located 1 km closer to the station and occurring 0.7 s after the +CG.

As we can see on the spectrogram, almost all the infrasound energy is concentrated in ~ 6 seconds around the infrasound pulse. The infrasound spectrum (in black) is more or less flat with a relative maximum around 1–2 Hz. We compare this spectrum to two mean spectra extracted from those calculated previously (Fig. 18.6). The red one was calculated for a 10-minute time interval including the event time and shows the background level when the studied lightning was recorded. The blue one was calculated at 22:00 UTC when the thunderstorm was far away; it is the reference noise level. In conclusion, in the 0.1–10 Hz band, the infrasound spectrum from a nearby lightning flash can be two orders of magnitude higher than the reference level.

To conclude this section, these new measurements of infrasound from near lightning show that this kind of source produces very important signals when lightning are less than 60 km from the station. Most of infrasounds from lightning are probably produced by the same mechanism than audible thunder. The emission pattern of Dessler’s theory is strongly vertical and then prevents infrasound to propagate horizontally. Numerous infrasound events have been related to lightning flashes distant up to 100 km from the sensor. Nevertheless, at short distance, some infrasound

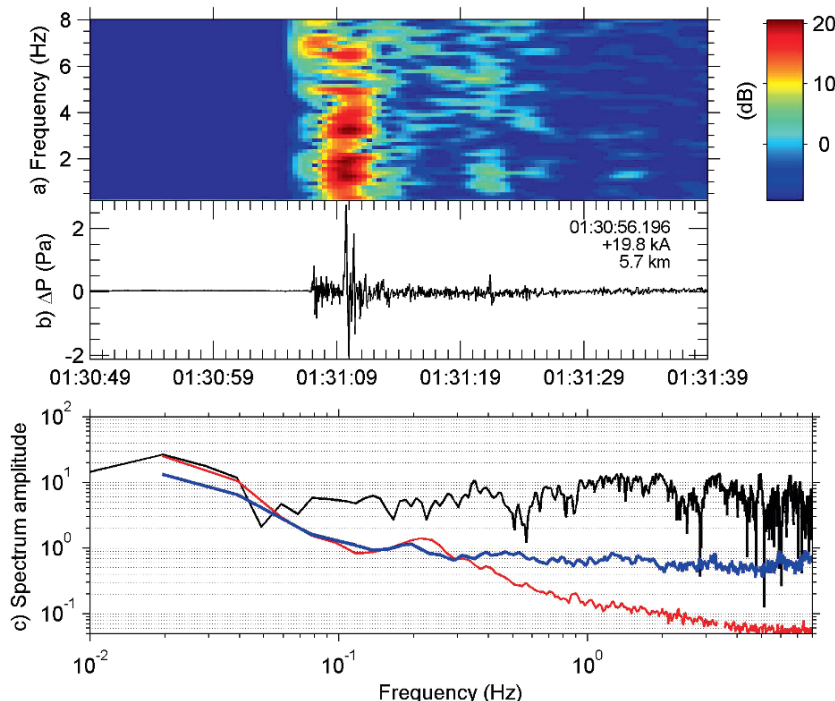


Fig. 18.7 (a) Spectrogram of the infrasound signal recorded on September 1st at 01:31:08 UTC plotted on panel. (b) Characteristics of the related CG are written in the right upper corner of panel (b). (c) Spectrum of the signal (black) compared to mean spectra calculated around this time (blue) and at 22:00 UTC on August 31st (red) (See also Plate 29 in the Color Plate Section on page 612)

events have been recorded with high elevation angle. They could be explained by the Dessler's theory. Infrasound spectrum from single lightning is relatively flat with a maximum around 1–2 Hz.

18.4 Infrasound from Sprites

TLE (Transient Luminous Event) is the generic name for phenomena occurring over thunderclouds from the troposphere to the lower thermosphere (20 to 100 km altitude). They are called sprites, elves, blue jets, gigantic jets ... A comprehensive description of TLE is proposed by Lyons et al. (ch. 17, this volume).

Bedard et al. (1999) first suggested that sprites could produce infrasound, as lightning flashes do, but they did not find any distinct signature. Liszka (2004) assumed that infrasound have a specific signature in their spectrogram (chirp) when sprite occurs. A chirp is the frequency change of the signal versus time. During the Eurosprite 2003 campaign, Farges et al. (2005) correlated such kind of infrasound with camera-based sprite observation. Using an acoustic wave propagation

model, the observed propagation delays, frequency dispersion, and duration of the infrasound bursts are found to be consistent with source altitudes at 60–80 km.

18.4.1 Characteristics

Some characteristics of infrasound from sprite are described hereafter. Infrasound from sprite are characterized by the arrival of low frequencies before high frequencies (chirp), and by pressure amplitudes on the order of 0.01–0.1 Pa at distances \sim 400 km. They are also characterized by durations of several tens of seconds (30–150 s), which are well correlated with the physical horizontal dimensions of sprites observed optically. Such infrasound has also been detected for sprites observed up to \sim 1000 km away from an infrasound station (Neubert et al., 2005). However, observation of near sprite has not succeeded up to now. Some chirp-shaped infrasounds have been also detected at dawn, when cameras could not operate because they were overexposed (Farges et al., 2005). Optical and infrasound measurements are complementary in sprite observation; sprites can still be detected by their infrasound when the camera is blind due to cloud masking or overexposure.

18.4.2 Source Mechanisms: Current Assumptions

Chirp-shape of infrasound from sprite is probably explained by the propagation of infrasonic waves and by the size of the source (Farges et al., 2005). The dispersion in frequency, with low frequencies arriving before high frequencies, may be due to different propagation paths followed. The thermosphere acts as a low-pass filter, where a wave is damped as it reflects at the upper waveguide boundary Sutherland and Bass (2004). The cut-off frequency decreases when the altitude increases. The chirp-shape can be explained by the horizontal size of the sprite because the wave coming from the nearest side of the sprite (relative to the sensor) reflects at a higher altitude than the wave generated from the farthest side.

A heating of the mesosphere air of \sim 1%, at 80-km height in a vertically extending cylindrical volume with radial dimension of about several tens of meters (in agreement with known morphology of streamer channels in sprites), is consistent with previous analyses (e.g. Pasko et al., 1998). Pasko and Snively (2007) recently showed that such heating is sufficient to explain the amplitude of infrasound from sprite. Their modelling results support the ideas advanced in (Farges et al., 2005) to explain the chirp-shape of infrasound from sprite.

18.4.3 Sprite Source Location from Infrasound Characteristics

As noticed in Section 18.3.1, up to now no occurrence of sprite close to an infrasound station has been reported. During the summer 2005, at least 2 sprites have

been observed on September 9th at less than 200 km from JST with a camera set up on the Pic du Midi (42.94°N , 0.14°E). Both sprites were small; chirp-shaped signature is then hard to find. However, numerous events lasting several tens of seconds (purple dots on Fig. 18.3b) are detected from 21:00 to 23:00 UTC when a lack of infrasound detection from lightning is simultaneously observed. A direct propagation from high-altitude sources to the ground-based sensor may explain why long duration events were measured while infrasound signal coming from ground or close-to-ground sources such as lightning flashes, did not reach JST because of their occurrence in the shadow zone. Besides their long duration, azimuth of arrival of these events also changes continuously on a very large range (from 30° to 150°). These characteristics are very different from those of infrasound from lightning (short duration and same azimuth during the entire event).

Figure 18.8 shows an example of long duration events. A clear chirp-shape is observed in the spectrogram (Fig. 18.8c). This is also the case for other long duration events detected during that night. They could then be due to sprites. The chirp-shape is slightly different from observation by Farges et al. (2005): high frequencies appear before low frequencies. Propagation being the main reason of this signature, the chirp shape modification could be explained by slightly different geometry of propagation path. Direct propagation from sprite to sensor, that is without refraction on the thermosphere, is supposed in this paper while Farges et al. (2005) assumed refractions in the Earth-atmosphere waveguide and then absorption of the acoustic wave.

Infrasound azimuths of arrival deduced from the PMCC method were compared to lightning azimuths (Fig. 18.8a). Infrasound apparent speed was investigation in function of time and wave frequency (PMCC calculates those parameters in several narrow spectral bands; Fig. 18.8b). We can deduce the elevation angle α of acoustic waves arriving on the network using the following relation: $\cos \alpha = \frac{C_s}{S_{app}}$, where C_s is the speed of sound and S_{app} is the apparent speed measured with the network of sensors. Elevation angles calculated for this event vary from 10° to 60° .

With these wave parameters, we want to calculate the 3D location of these infrasound sources. Azimuth and elevation angle are not sufficient to locate these sources; thus, we must have a reference point to determine distance. We know that sprites occur after a +CG discharge. If we know the time of parent lightning, we also know the time of sprites because they appeared a few to several tens of milliseconds after their parent lightning. As Farges et al. (2005), we assume that +CG discharges occurring in 2-minutes intervals before or after the chirp-shaped signal, can be parent lightning. This time delay is reasonable because sprite does not appear just above +CG locations but are usually shifted of several tens of kilometers. We find two candidates which occur at 21:10:40 UTC at 140 km and 230° from JST, and at 144 km and 239° . Their respective peak currents are 29.7 and 14.6 kA. With direct propagation, their infrasound signal has to arrive at JST station respectively at 21:17:44 and 21:17:58 UTC (orange squares on Fig. 18.8a). We chose the first one, having the highest peak current, as the reference point. We can then calculate the sprite distance d_s .

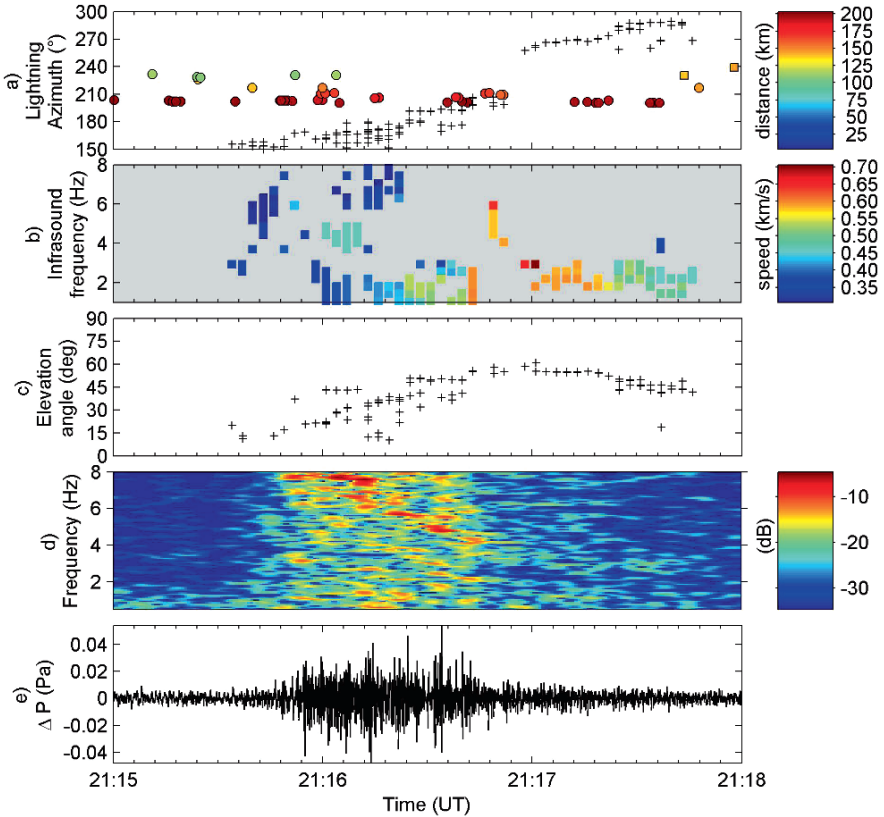


Fig. 18.8 Long duration infrasound recorded on September 9th 2005 from 21:15 to 21:18 UTC. (a) Comparison of lightning azimuth (colored circles and squares – color indicates lightning distance, circle for -CG discharge and square for +CG) and infrasound azimuth (+). (b) Infrasound apparent speed vs. time and infrasound frequency. (c) Elevation angle deduced from infrasound apparent speed. (d) Spectrogram of infrasound signal. (e) Pressure amplitude in the 0.5–9 Hz band (See also Plate 30 in the Color Plate Section on page 613)

We simplify the calculation of this distance considering that propagation is along a straight line at a mean sound speed C_s of 0.3 km/s (taking into account the variation of the speed of sound with altitude): $d_s = \Delta t \times C_s$, where Δt is the time of propagation of the infrasound to the station. Using these assumptions, 3D source location is performed on Fig. 18.9. Two groups of sprite can be identified (before and after 21:17 UTC). Both are located between +CG and JST station. The source altitude range is from 20 to 100 km but mainly between 40 and 85 km, which is the usual vertical extension of sprites. The sprites are 80–120 km far away from the parent CG (horizontal distance). This is the upper limit of observed distance between sprite and CG.

If these kinds of infrasound are due to sprites, one question has to be dealt with: why did the camera not catch them? During the considered night, both sprites (at 20:35:42 and 21:18:39 UTC) have been observed on the verge of the camera field of view (Fig. 18.9) and the thunderstorm area was not completely seen by the camera

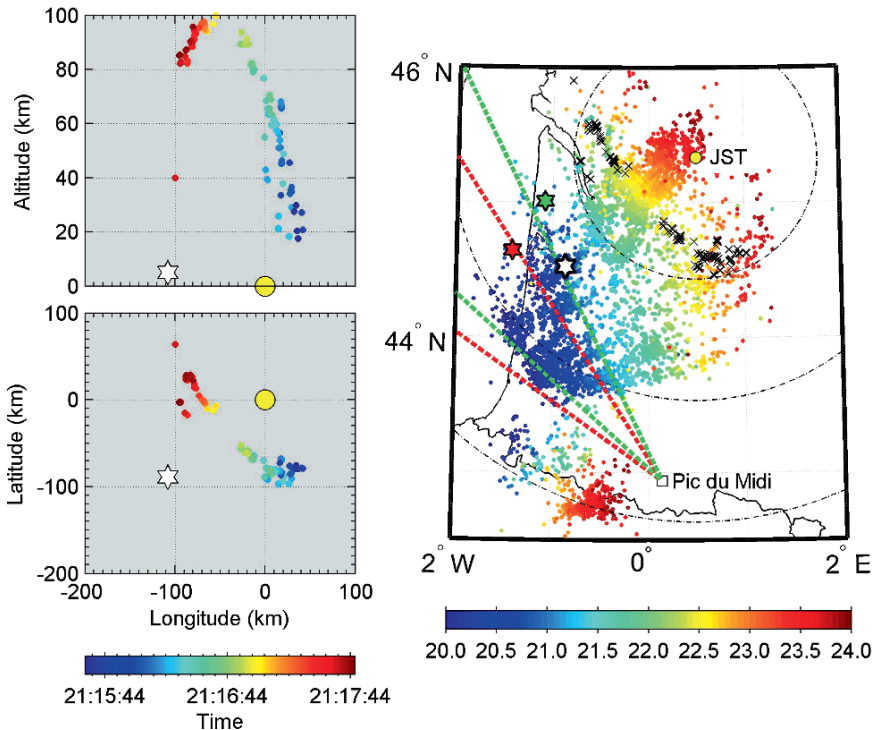


Fig. 18.9 (Left): Infrasound source locations in horizontal (bottom) and vertical (top) plane deduced from long duration event (Fig. 18.8) wave parameters and plotted with colored dots (colors indicating time). Location of parent lightning is shown with black and white star and JST station with yellow circle. (Right): Lightning activity on September 9th 2005 from 20 to 24 UTC (colored dots). Field of view of Pic du midi camera is delimited with red dashed lines at the time when first sprite is observed during that night (20:35:42; +CG location with red star). It turns clockwise, to follow thunderstorm motion, and is plotted in green dashed lines when the second sprite was observed at 21:18:39 UTC (+CG location with green star just outside the field of view). Meanwhile, infrasound from sprite is measured following +CG lightning occurring at 21:10:40 UTC (black and white star). Infrasound source locations are plotted with black crosses in horizontal plane (reported from bottom left panel) (See also Plate 31 in the Color Plate Section on page 614)

because it is close to it. Other sprites may have occurred in the same interval of time and may be missed because they appeared outside the camera field of view. The parent lightning of the sprite, which has been described just before using only infrasound measurements, occurred just after the first optically detected sprite and before the second one. The comparison of the calculated sprite location and the camera field of view show that the sprite was outside the camera field of view.

To conclude, questions are still raising in sprite physics, as the spatial distribution of sprites in comparison with the parent lightning location. Up to now, triangulation of sprites has been possible in a few cases using camera observations. We have shown, in this paper, the possibility to describe the three dimensional geometry of sources of infrasound from sprite when they occur close to the infrasound station. This new technique can help us to answer to this question.

Acknowledgments This work was in part undertaken in the framework of the EU Research Training Network “Coupling of Atmospheric Layers”, contract No.: HPRN-CT-2002-00216. The author thanks P. Herry, for PMCC application on this set of data, D. Ponceau and V. Flavin for setting up JST station, E. Blanc for her encouraging remarks, T. Neubert (CAL network leader) for camera observation and Météorage Company for real time access to lightning data over southern Europe.

References

- Bedard, A. J., Jr., W. A. Lyons, R. A. Armstrong, T. E. Nelson, B. Hill, and S. Gallagher, A search for low-frequency atmospheric acoustic waves associated with sprites, blue jets, elves and storm electrical activity, *Eos Trans. AGU*, 80(46), Fall Meet. Suppl., F227 (1999).
- Cansi, Y., An automatic seismic event processing for detection and location: the PMCC method, *Geophys. Res. Lett.*, 22, 1021–1024 (1995).
- Dessler, A. J., Infrasonic thunder, *J. Geophys. Res.*, 78, 1889–1896 (1973).
- Farges, T., E. Blanc, A. Le Pichon, T. Neubert, T. Allin, Identification of infrasound produced by sprites during the Sprite2003 campaign, *Geophys. Res. Lett.* 32, L01813, doi: 10.1029/2004GL021212 (2005).
- Few, A. A., The production of lightning-associated infrasonic acoustic sources in thunderclouds, *J. Geophys. Res.*, 90, 6175–6180 (1985).
- Few, A. A., Acoustic radiations from lightning, in *The Earth’s Electrical Environment*, 46–60 pp., Washington, DC: National Academy Press (1986).
- Holmes, C. R., M. Brook, P. Krehbiel, and R. McCrory, On the power spectrum and mechanism of thunder, *J. Geophys. Res.*, Vol. 76, 2106–2115, 1971.
- Le Pichon, A., M. A. Garcés, E. Blanc, M. Barthelemy, and D. P. Drob, Acoustic propagation and atmosphere characteristics derived from infrasonic waves generated by the Concorde, *J. Acoust. Soc. Am.*, 111, 629–641 (2002).
- Le Pichon, A., L. Ceranna, M. Garcés, D. Drob, and C. Millet, On using infrasound from interacting ocean swells for global continuous measurements of winds and temperature in the stratosphere, *J. Geophys. Res.*, 111, D11106, doi: 10.1029/2005JD006690 (2006).
- Liszka, L. J., The possible infrasound generation by sprites, *J. Low Freq. Noise Vibr. Active Control*, 23, 85–93 (2004).
- MacGorman, D. R., A. A. Few, and T. L. Teer, Layered lightning activity, *J. Geophys. Res.*, 86, 9900–9910 (1981).
- Neubert, T., T. H. Allin, E. Blanc, T. Farges, C. Haldoupis, A. Mika, S. Soula, L. Knutsson, O. van der Velde, R. A. Marshall, U. Inan, G. Satori, J. Bor, A. Hughes, A. Collier, S. Laursen, and I. L. Rasmussen, Co-ordinated observations of transient luminous events during the EuroSprite2003 campaign, *J. Atmos. Sol. Terr. Phys.*, 67, 807–820 (2005).
- Pasko, V. P., U. S. Inan, and T. F. Bell, Spatial structure of sprites, *Geophys. Res. Lett.*, 25, 2123–2126 (1998).
- Pasko, V. P., and J. B. Snively, Mechanism of infrasound radiation from sprites, *Eos Trans. AGU*, 88(52), Fall Meet. Suppl., Abstract AE23A-0899, San Francisco, CA (2007).
- Rakov, V. A., and M. A. Uman, *Lightning, Physics and Effects*, Cambridge: Cambridge University Press (2003).
- Sutherland, L. C., and H. E. Bass, Atmospheric absorption at high altitudes, *J. Acoust. Soc. Am.*, 115(3), 1012–1032 (2004).
- Uman, M. A., *The Lightning Discharge*, 377 pp., London: Academic Press (1987).
- Vivas Veloso, J. A., D. R. Christie, P. Campus, M. Bell, T. L. Hoffmann, A. Langlois, P. Martysevich, E. Demirovik, J. Carvalho, and A. Kramer, Status report on the establishment of the Comprehensive Nuclear-Test-Ban Treaty (CTBT) International Monitoring System (IMS) infrasound network, *J. Acoust. Soc. Am.*, 112, 2352–2352 (2002).

Chapter 19

Lightning in the Mediterranean in Relation with Cloud Microphysical Parameters

Dimitrios Katsanos, Vassiliki Kotroni and Kostas Lagouvardos

Abstract This chapter discusses the potential of using passive microwave satellite observations, radar, and numerical weather prediction model outputs for the investigation of the relation between lightning activity and the microphysical properties of clouds. The study concentrates in the Mediterranean area and for the winter period. Depressions of brightness temperatures at 85 GHz, measured by low orbiting satellites, are found to coincide with the areas where cloud to ground lightning occur, and thus this parameter is a useful tool which can be used as an indicator for the occurrence of lightning. The analysis of numerical weather prediction model outputs and lightning observations has been proved promising and showed that the time evolution of the profiles of solid hydrometeors relate positively with that of the lightning activity with an expected time lag, with the maximum lightning activity occurring soon after the maximization of the solid hydrometeor mixing ratio.

Keywords CG lightning · Microphysical properties of clouds · Convection · Brightness · Temperature · Spaceborne radar · Radar reflectivity · Mesoscale modeling

19.1 Introduction

The Mediterranean Sea is a relatively small and rather warm body of water which is surrounded by three major continents. According to studies performed by Orville (1981), Christian et al. (1999) and Holt et al. (2001), the Mediterranean is one of the major centers of electrical activity during the cold period of the year for the Northern Hemisphere. Altaratz et al. (2003) found that the annual distribution of lightning in the Eastern Mediterranean presents a clear maximum in January and that during midwinter the highest lightning density is observed over the sea. Price and Federmessner (2006) analyzed lightning and rainfall data from TRMM satellite for

D.K. Katsanos (✉)

Institute for Environmental Research and Sustainable Development,

National Observatory of Athens, Greece

e-mail: katsanos@meteo.noa.gr

a six-year period (1998–2003) over the central and eastern Mediterranean Sea and they found that more than 75% of rain and lightning events occur during the period from October to March while more than 90% of the thunderstorms occurs over the sea. Furthermore, lightning activity has its maximum during November while the maximum of precipitation occurs during December. They also found a connection to the ENSO cycle since the 1999–2000 lowest number of rain and lightning events coincided with the La Niña winter and the maximum number of the same events for 2002–2003 coincided with the El Niño winter of that year. The north-south shift of the winter jet stream due to El Niño, according to the authors, was the reason for such an increase of the number of events over the Mediterranean. Their study on individual storms resulted to a high correlation between lightning and convective rainfall.

Katsanos et al. (2007a) in a recent study have shown that during the wet period of the year (e.g. autumn and winter for the area of the Mediterranean) the lightning activity occurs over the maritime area and near the coasts almost delineating the Mediterranean coastline, as it can be seen in Fig. 19.1 for the Central and Eastern Mediterranean.

The significant lightning activity over the Mediterranean Sea motivated many researchers to investigate among other issues, the relationship between lightning and parameters such as rainfall, radar reflectivity or microphysical characteristics of clouds. In this paper a brief overview of such recent studies is given as well as a presentation of some new results.

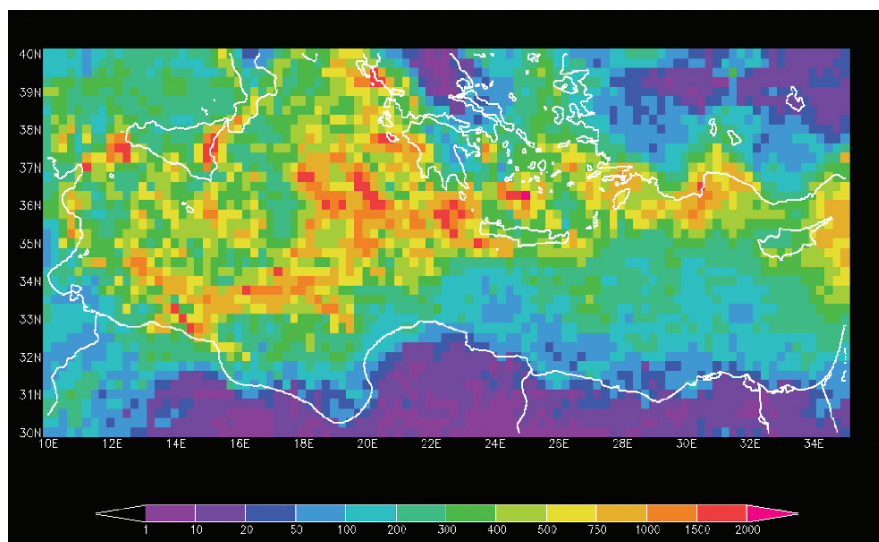


Fig. 19.1 Cloud to ground lightning in 0.25×0.25 degrees grid boxes recorded by ATD system in the region of the Central and Eastern Mediterranean during the period October 2003—March 2004 (See also Plate 32 in the Color Plate Section on page 615)

19.2 Relationship Between Lightning and Microphysical Properties of Clouds

In this section a review of the recent literature devoted to the study of the relationship of lightning activity with microphysical properties of mesoscale systems is given. Since direct measurements of the microphysical properties are sparse, many researchers suggest the use of satellite passive microwave and/or radar measurements, where microphysical properties of clouds are indirectly manifested.

More precisely, the relationship of lightning activity with brightness temperature at 85 GHz has been addressed in a number of recent studies. Brightness temperature is defined as the temperature that a blackbody would need to have in order to emit radiation of the observed intensity at a given wavelength (Ulaby et al., 1981). Obviously, passive microwave receivers sense radiation emitted by a surface that is converted into brightness temperature, which at the portion of the microwave spectrum is proportional to real temperature and has units of real temperature (e.g. K). In addition to brightness temperature, the polarization corrected temperature (PCT) at 85 GHz has been also used in some studies. The PCT is calculated using the formula suggested by Spencer et al. (1989):

$$\text{PCT}_{85} = 1.82\text{Tb}_{85(V)} - 0.82\text{Tb}_{85(H)} \quad (19.1)$$

where $\text{Tb}_{85(V)}$ and $\text{Tb}_{85(H)}$ are the brightness temperatures sensed by the two channels, for Vertical and Horizontal polarized radiation. Brightness temperature at this frequency is sensitive to the presence of ice particles that, according to lightning theory, is a necessary component for the electrification processes within clouds. A detailed presentation on the charging and electrification processes and conditions within clouds can be found in Pruppacher and Klett (2000) and Rakov and Uman (2003).

Indeed, Mohr et al. (1996), found that the flash density was inversely correlated to PCT at 85 GHz and that the amount and distribution of lightning within mesoscale convective systems (MCS) is related to the presence of large ice particles in the mixed phase region of these systems. Toracinta and Zipser (2001) used brightness temperature at 85-GHz from the SSM/I satellite and lightning data from the Optical Transient Detector. Their results showed that a land MCS is more likely to produce lightning than an oceanic MCS, implying differences in the ice microphysical processes between land and ocean convective storms. In another study by Defer et al. (2005) of a winter case over eastern Mediterranean, based on Tropical Rainfall Measurement Mission (TRMM) Lightning Imaging Sensor (LIS) data, the authors showed that the presence of lightning was associated with brightness temperature depressions as low as 110 K. More recently, Sherwood et al. (2006) based on LIS and OTD lightning data as well as on Tb measurements at 3.7 and 11 μm , showed that graupel concentrations are clearly correlated with lightning and that, lightning counts appear related to the amount of small ice ($< 30\mu\text{m}$) at cloud top. They also showed that updraft speed within clouds must exceed 6–7 m/s near the freezing level

for strong electrification and that, continental updrafts are significantly stronger than maritime ones.

Regarding the investigation of the relationship between lightning activity and radar reflectivity, a number of recent studies are found in the literature that mainly focus on summer time thunderstorms. Tapia et al. (1998) in their study used WSR-88D radar and lightning data from 22 summer thunderstorms with the aim to develop a technique for the estimation of convective rainfall based on lightning data. The authors found that the highest lightning rate periods follow the time when the cloud reaches its maximum vertical development. Also, lightning initiation was preceded by reflectivities >35 dBZ at -10°C (6.5km). However, no relation between storm duration and the peak of lightning frequency was found. They concluded that shallow storm systems are associated with low lightning frequencies and high amounts of rain per flash and that the lightning core is not always collocated with the reflectivity core. Carey and Rutledge (2000), in the framework of the Maritime Continent Thunderstorm Experiment, studied convective cells within a tropical convective complex based on C-band radar and surface lightning network observations. They found that both cloud-to-ground and total lightning were highly correlated to the radar inferred mixed-phase ice mass, both in time and space. Lang and Rutledge (2002) used radar and sounding data as well as lightning observation in order to investigate the relationships between convective storm kinematics, precipitation and lightning. In this study, based also on previous suggestions that convection typically lasts approximately one hour and becomes electrically active after the ice phase develops, the authors proposed among others that storms of greater volume with strong updrafts should have more charging. Large storms should have greater charge production overall and consequently greater number of CG lightning. Toracinta et al. (2002) used Tropical Rainfall Measurement Mission (TRMM) Precipitation Radar (PR), Microwave Imager (TMI) and Lightning Imaging Sensor (LIS) data and concluded that lightning is much more likely in tropical continental convective systems than tropical oceanic ones with similar brightness temperatures or similar reflectivity profiles. Moreover they found that features with lightning have greater magnitudes of reflectivity and smaller decreases of reflectivity with height above the freezing level than systems without detected lightning. Adamo et al. (2003) using one-year TRMM data for the region of the Mediterranean Sea, correlated average PR reflectivity profiles with various values of flash rates for both convective and stratiform regions of storms and concluded that higher flash rates are correlated with higher reflectivity values, during all seasons. They also concluded that lightning producing storms are associated with a significant percentage of precipitation during all seasons, but mostly during summer.

In a recent study by Katsanos et al. (2007b), the relationship of lightning activity with microphysical properties was investigated. They used lightning data provided mainly by the Arrival Time Difference (ATD) system, which is operated by the UK Meteorological Office but also by the TRMM LIS. Moreover they used brightness temperature measured by TRMM-TMI as well as reflectivity profiles provided by TRMM-PR. The area of study was the Central and Eastern Mediterranean Sea and for the analysis they selected the days with the largest observed lightning activity

in the period October 2003–March 2004. During the selected days, the most common synoptic situation was characterized by low pressure systems associated with frontal activity. The aim was to explore the possibility of defining indicators for the occurrence of lightning activity, by correlating lightning activity with PCT at 85 GHz. This was based on the fact that an inspection of individual case-studies had already shown a strong relationship between the regions of lower values of PCT and significant lightning activity.

A case, similar to the ones analyzed in Katsanos et al. (2007b), is presented in Fig. 19.2. Indeed on 24 December 2003 a shallow low-pressure center, located southwest of continental Greece, was associated with a cold front moving slowly eastwards over the Aegean Sea. The PCT measured by TMI at 85 GHz, at ~ 1500 UTC, 24 December 2003 is given in Fig. 19.2a. The position of the cold front over the Aegean Sea is characterized by PCT values lower than 210 K. A zoom - in on the PCT field over the area north of Crete is given in Fig. 19.2b while the lightning activity recorded by ATD during a time interval ± 10 min around the time of the TRMM overpass is given in Fig. 19.2c. It is evident that the area of low PCT values that characterizes the cold front discontinuity correlates well with the narrow line of lightning flashes and that the higher concentration of flashes is correlated with the lowest PCT values. In order to quantify this feature, the area shown in Fig. 19.2b was divided into 0.25×0.25 degrees grid boxes and in each grid box the minimum value of PCT and the number of lightning flashes, recorded by ATD in a ± 10 min time window around the time of the TRMM overpass, were calculated. The resulting scatter plot of the number of lightning flashes against PCT is provided in Fig. 19.2d, where it is clearly evident that the pixels with “colder” PCTs are those where the largest amount of lightning flashes have been observed. Finally, the cumulative frequency distribution of PCT values for the grid boxes with and without lightning is shown in Fig. 19.2e. It can be seen that the percentage of the grid boxes with lightning activity is clearly higher than the corresponding percentage for grid boxes without lightning for the lower PCT values, especially below 200 K. For instance 60% of the grid boxes with observed lightning correspond to PCT values lower than 215 K, while the respective percentage for the grid boxes without lightning is only 2%.

In addition to the presence of ice that is a necessary component for cloud electrification, another important component is the vertical development of the convective cloud. Price and Rind (1992) have shown that the lightning activity is proportional to the 5th power of the volume of a cloud. It would be interesting thus to investigate that in addition to the depression of ice content the area of important lightning activity is supported by deep convective clouds. According to Ushio et al. (2001) the cloud top height can be estimated by using the maximum height of the minimum detectable power (~ 20 dBZ) by the TRMM Precipitation Radar. Figure 19.3a shows from the TRMM/PR overpass at 1500 UTC 24 December 2003 at 2 km height that the highest reflectivity values are observed within the band of important convective activity evidenced with the coincident high concentration of lightning (Fig. 19.2c). A vertical cross section across this area shows that the cloud tops reach the height of 8–9 km (Fig. 19.3b,c), and thus the convective clouds are quite deep for maritime clouds during this period of the year.

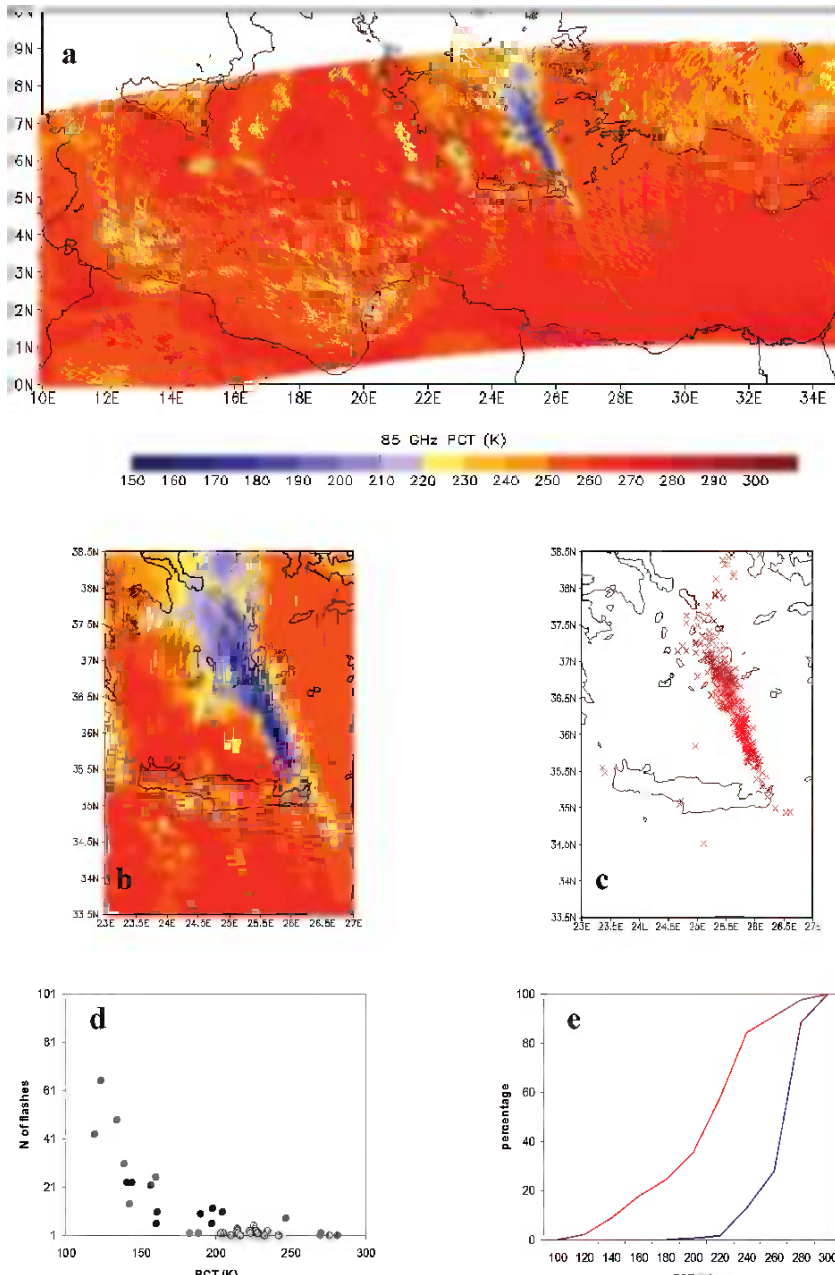


Fig. 19.2 TRMM overpass at 1500 UTC 24 December 2003: (a) PCT at 85 GHz in K, (b) zoom in (a), (c) cloud to ground lightning sensed by ATD ± 10 min around the overpass, (d) distribution of PCT values versus the number of lightning flashes, (e) cumulative frequency of number of pixels with (red line) and without (blue line) recorded lightning (See also Plate 33 in the Color Plate Section on page 616)

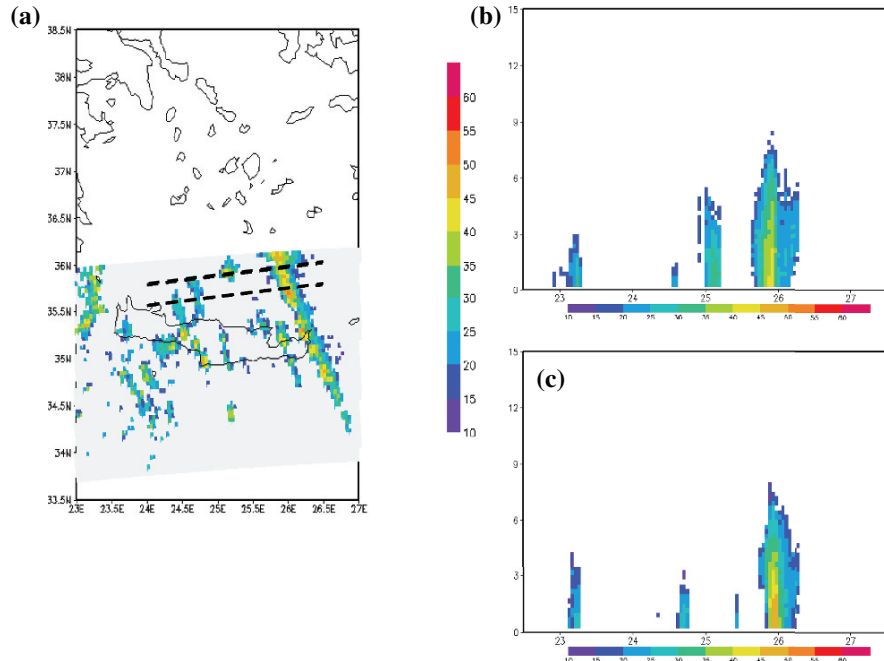


Fig. 19.3 TRMM/PR overpass at 1500 UTC 24 December 2003: (a) PR at 2 km height (b), (c) cross sections of reflectivity along the 2 dashed lines shown in (a) (See also Plate 34 in the Color Plate Section on page 617)

The above results are in line with the findings by Katsanos et al. (2007b) who analyzed 41 days of significant lightning activity during the period October 2003–March 2004. Indeed in the aforementioned study the authors showed that 50% of the grid boxes with recorded flashes, have PCTs lower than 225 K, while only 3% of the grid boxes without any lightning have PCTs below this value. They also found that PCT values can be used in order to set a threshold for the occurrence of at least one lightning flash and that this threshold decreases as the amount of expected lightning flashes increases, which means that for “colder” PCTs the possibility to expect lightning is higher. Further they correlated lightning activity with the radar reflectivity, measured by TRMM/PR. The authors found that in presence of lightning the average reflectivity profile has higher values than in absence of lightning, and that higher values of reflectivity in levels below 5 km increase the probability for lightning occurrence.

The conclusions of the 2003–2004 wet period study over the Central and Eastern Mediterranean provided the motivation to extend research concerning lightning activity and microphysical parameters of clouds. Since satellites can only provide data during their overpass above a specific area, it is difficult to both cover adequately all cases that occur and to study their temporal evolution. The comparison of satellite data with lightning confirms the relation of lightning activity with the presence of ice particles in clouds, and thus it is a tempting issue to investigate the possible relation

between lightning and ice content. As direct measurements of ice content are sparse this analysis could be based on simulated fields provided by mesoscale atmospheric numerical models, as discussed in the following section. Such an approach has been followed recently by Lagouvardos and Kotroni (2007). Furthermore, since the presence of ice crystals in a cloud is a key element but not the only prerequisite for the occurrence of lightning, it is important to investigate the relationship between lightning activity and the vertical dimension of clouds.

19.3 Relationship Between Lightning Activity and Microphysical Parameters Derived by MM5 Model

In this section a case that occurred in the Eastern Mediterranean on 13 December 2005 will be analyzed. The analysis will be based on lightning data provided by ZEUS network (operated by the National Observatory of Athens) and simulations performed with the non-hydrostatic model MM5.

19.3.1 ZEUS Lightning Detection Network

ZEUS long-range lightning detection system, operated by the National Observatory of Athens, is based on detection of sferics – the impulsive radio noise emitted by a lightning strike – in the Very Low Frequency (VLF) spectrum between 7 and 15 kHz. The ZEUS system consists of a network of six VLF receivers located around the periphery of Europe (Birmingham in UK, Roskilde in Denmark, Iasi in Romania, Larnaka in Cyprus, Athens in Greece and Lisbon in Portugal). Each receiver reports the vertical electric field as a function of time which represents the sferic's waveform, and includes a time stamp synchronized to global positioning system time. At each receiver site an identification algorithm is executed that detects a probable sferics candidate, excludes weak signal and noise and is capable of capturing up to 70 sferics per second. Then the lightning location is retrieved (at the central station of the network) using the arrival time difference triangulation technique. As it concerns the location accuracy of ZEUS system a work is underway that compares its measurements with those from LINET lightning detection network (Betz et al., 2004) over Europe. Preliminary results have shown that the location accuracy of ZEUS is of the order of 4–5 km over the study area (Betz, personal communication). Further details on ZEUS network are given in Kotroni and Lagouvardos (2008).

19.3.2 MM5 Model Configuration

The MM5 model is a non-hydrostatic, primitive equation model (Dudhia, 1993). Several physical parameterization schemes are available in the model for the

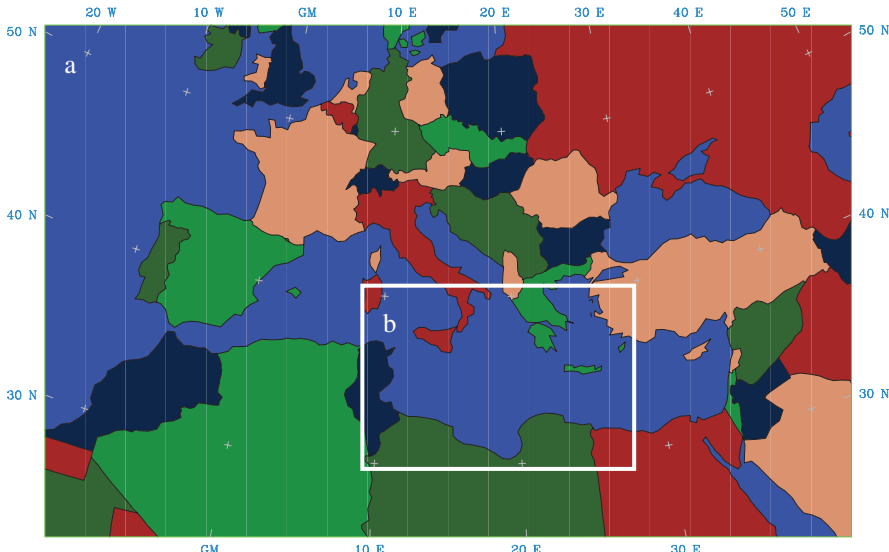


Fig. 19.4 Coarse (a) and Inner (b) domains used for the MMS simulations

boundary layer, the radiative transfer, the microphysics and the cumulus convection. For this study from the multitude of available schemes the following have been selected: the scheme by Hong and Pan (1996) for the boundary layer, the Kain and Fritsch (1993) for cumulus convection and the Schultz (1995) for explicit micro-physics. The last two schemes have been proved to provide the most skillful precipitation forecasts in the Eastern Mediterranean (Kotroni and Lagouvardos, 2001).

Two domains are used for the model simulations (Fig. 19.4). The coarse domain covers most of Europe, up to 60°N, North Africa and the Middle East with a horizontal resolution of 24 km and 220×140 grid points. The inner domain covers a part of the Central and Eastern Mediterranean with a horizontal resolution of 8 km and 220×148 grid points. In the vertical 31 sigma levels are defined from the surface up to 100 hPa. ECMWF analyses at 0.5 degrees resolution have been used to initialize the model and to nudge the boundaries of the coarse domain during the simulation period. The present simulation was initialized at 0000 UTC 13 December 2005.

19.3.3 Case Study

On 13 December 2005 at 0600 UTC, a low pressure center of 1005 hPa was located northwest of the Gulf of Sidra. The pressure low deepened to 997 hPa at 1200 UTC, and reached the lowest central pressure of 992 hPa by the end of the day, just offshore the Tunisian coast. The pressure low was accompanied by a cold front moving slowly northeastwards.

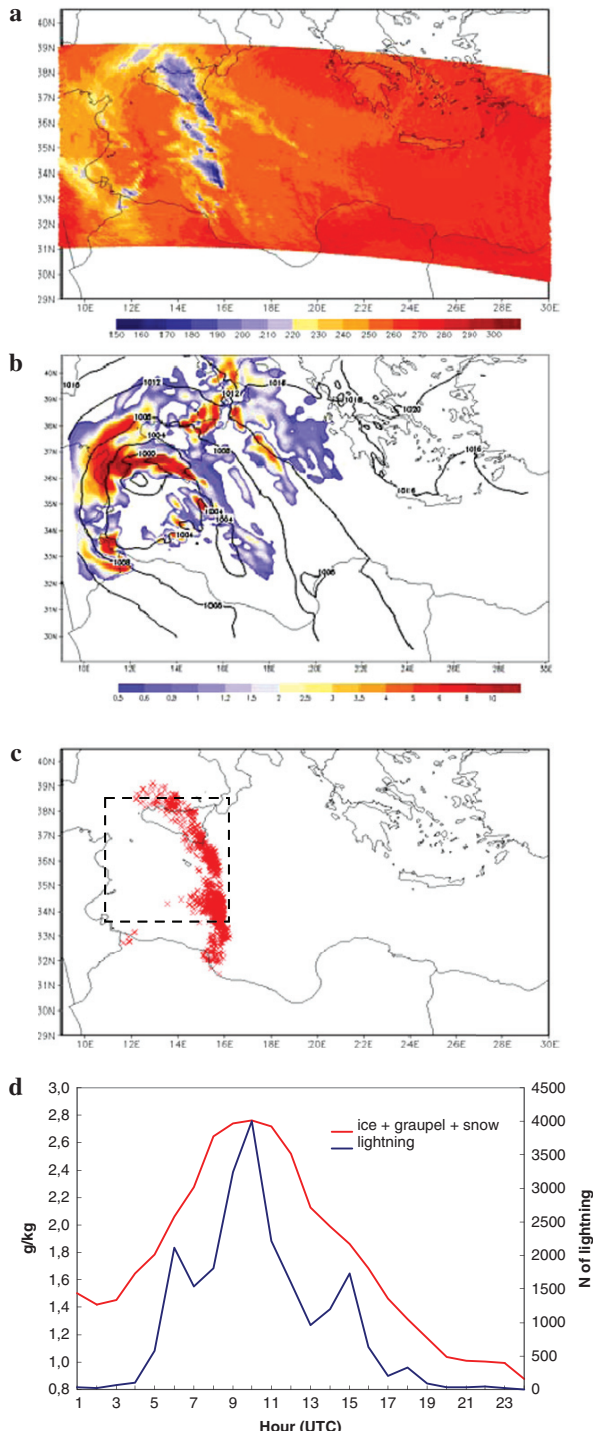


Fig. 19.5 (continued)

The most adequate TRMM overpass during that date was at 1130 UTC (Fig. 19.5a). A band of low PCT values expand from Sicily southwards to the Sidra Gulf denoting the cold front position. Figure 19.5b shows the column integrated mixing ratio of *ice+snow+graupel* as simulated by the MM5 model inner grid (8-km resolution), at 1200 UTC while Fig. 19.5c shows the lightning flashes recorded by ZEUS system for one hour time interval (from 1130 to 1230 UTC). The simulated low pressure centre of 996 hPa is located southwest of Sicily. The model has positioned the low centre almost 1° to the west of its actual position. The column integrated mixing ratio of *ice+snow+graupel* reproduces a curved band of high values that denote the simulated frontal discontinuity, which is also displaced west of the low PCT values detected by TRMM (Fig. 19.5a). Consequently the simulated high concentrations of ice (Fig. 19.5b), are also found “shifted” to the west of the lightning activity reported by ZEUS (Fig. 19.5c).

At this point it would instructive to relate the time evolution of the lightning activity with that of the microphysical parameters. For that reason a box has been selected that includes the area from 11E to 16E and from 33.5N to 38.5N (denoted with a dotted box in Fig. 19.5c) in order to account also for the “shift” of the simulated fields. Within this box the number of lightning was calculated along with the average profile of the integrated mixing ratio of *ice+snow+graupel*, derived from the MM5 simulations. The results are shown in Fig. 19.5d. The mixing ratio presents almost a “bell” shaped distribution with the maximum values from 0700 to 1200 UTC, which coincides with the time interval of the fast low pressure deepening. As expected, the building up of the lightning activity time lags the increase in the mixing ratio of *ice+snow+graupel* by about one to two hours, but the two curves coincide at their maximum which occurs at 1000 UTC. Then, within the period of decrease of the mixing ratio the lightning activity also decreases with a faster rate. Therefore, the profiles of the mixing ratio of *ice+snow+graupel* could be used as a qualitative indicator of the presence of lightning activity.

19.4 Summary

In this chapter a review of previous work that relates lightning activity with the microphysical properties of clouds was given. Based on the reviewed literature, it is evident that the distribution and number of lightning is related with the presence of ice, the strength of the updraft within the convective clouds as well as their vertical development. As a matter of fact, storms of greater volume with strong updrafts present more efficient charging and hence increased number of cloud-to-ground lightning.

Fig. 19.5 (a) PCT at 85 GHz in K derived by TRMM overpass at 1130 UTC 13 December 2005, (b) MMS column integrated mixing ratio of *ice+snow+graupel* in g/kg and sea level pressure in hPa (*black line*) valid at 12 UTC, (c) 1 h lightning activity recorded by ZEUS from 1130 to 1230 UTC, (d) time evolution of lightning (*blue line*) and average of column integrated mixing ratio of *ice+snow+graupel* within the area denoted with the *dotted rectangle* in (c) (See also Plate 35 in the Color Plate Section on page 618)

The scarcity of direct measurements of microphysical parameters such as ice content of lightning producing clouds supports the need for the use of spaceborne passive microwave observations for such type of studies. The parameter mostly used is the brightness temperature sensed at 85 GHz, the depression of which indicates the presence of ice crystals, which in their turn according to the lightning theory, are essential for the processes that lead to a lightning flash. Indeed, the results show that the areas with lower values of brightness temperatures at 85 GHz coincide with the areas where cloud to ground lightning is recorded, making this parameter a useful tool which can be used as an indicator for the occurrence of lightning. Moreover, reflectivity measurements provided by TRMM PR are very helpful in identifying the vertical extent of convective clouds mainly over the sea, where ground-based measurements are absent. From the published literature it is also evident that the higher flash rates are correlated with higher reflectivity values, but also that lightning is much more likely in continental convective systems than in maritime ones with similar brightness temperatures or similar reflectivity profiles.

As spaceborne microwave observations, available from low orbiting platforms cannot provide a continuous monitoring of lightning producing systems, but they only provide snapshots of these events (1–2 per day), another possibility is to relate lightning data with the simulated microphysical parameters provided by weather forecasting models. The analysis of a case, based on MM5 model output and lightning data from ZEUS system showed a positive relation of the lightning flashes with the profiles of mixing ratio of solid hydrometeors, and a time coincidence in their maximum. In order to quantify this behavior, the authors are convinced that it is worth to extend this study to a larger number of cases.

Acknowledgments This work has been supported by the EU financed project FLASH (Contract No. 036852). All TRMM data are downloaded from NASA's corresponding data servers. PR and TMI data are taken from: <http://lake.nascom.nasa.gov/data/dataset/TRMM/>

References

- Adamo C., Solomon R., Goodman S., Cecil D., Dietrich S., and Mugnai A., 2003: Lightning and precipitation: Observational analysis of LIS and PR. *Proceedings of 5th EGU Plinius Conference, Ajaccio, Corsica, France*.
- Altaratz O., Levin Z., Yair Y., and Ziv B., 2003: Lightning activity over land and sea on the eastern coast of the Mediterranean. *Mon. Wea. Rev.*, **131**, 2060–2070.
- Betz H.-D., Schmidt K., Oettinger P., and Wirz M., 2004: Lightning detection with 3D discrimination of intracloud and cloud-to-ground discharges, *Geophys. Res. Lett.*, **31**, L11108, doi:10.1029/2004GL019821.
- Carey L.D., and Rutledge S.A., 2000: The relationship between precipitation and lightning in Tropical island convection: A C-band polarimetric radar study. *Mon. Wea. Rev.*, **128**, 2687–2710.
- Christian H. J., Blakeslee R. J., Boccippio D. J., Boeck W. L., Buechler D. E., Driscoll K. T., Goodman S. J., Hall J. M., Koshak W. J., Mach D. M., and Stewart M. F., 1999: Global frequency and distribution of lightning as observed by optical transient detector (OTD). *Proceedings of 11th International Conference on Atmospheric Electricity*, Huntsville, AL, NASA, 726–729.

- Defer E., Lagouvardos K., and Kotroni V., 2005: Lightning activity in the eastern Mediterranean region. *J. Geophys. Res.*, **110**, D24210.
- Dudhia J., 1993: A non-hydrostatic version of the Penn State/NCAR mesoscale model: Validation tests and simulation of an Atlantic cyclone and cold front. *Mon. Wea. Rev.*, **121**, 1493–1513.
- Holt M. A., Hardaker P. J., and McClelland G. P., 2001: A lightning climatology for Europe and the UK, 1990–99. *Weather*, **56**, 290–296.
- Hong S.-Y., and Pan H.-L., 1996: Nonlocal boundary layer vertical diffusion in a medium-range forecast model. *Mon. Wea. Rev.*, **124**, 2322–2339.
- Kain J.S., and Fritsch J.M., 1993: Convective parameterization for mesoscale models: The Kain-Fritsch scheme. The representation of cumulus in numerical models, Meteor. Monogr., No 46, Amer. Meteor. Soc., 165–177.
- Katsanos D., Lagouvardos K., Kotroni V., and Argiriou A. 2007a: Combined analysis of rainfall and lightning data produced by mesoscale systems in the central and eastern Mediterranean, *Atmos. Res.*, Vol. 83.
- Katsanos D., Lagouvardos K., Kotroni V., and Argiriou A. 2007b: Correlation of lightning activity with microwave brightness temperatures and spaceborne radar reflectivity profiles in the Central and Eastern Mediterranean *J. Appl. Meteor. & Climatol.*, Vol. 46.
- Kotroni, V., and Lagouvardos, K. 2001: Precipitation Forecast Skill of Different Convective Parameterization and Microphysical Schemes: Application for the Cold Season Over Greece, *Geophys. Res. Lett.*, 28(10), 1977–1980.
- Kotroni, V., and Lagouvardos, K. 2008: Lightning occurrence in relation with elevation, terrain slope and vegetation cover in the Mediterranean, *J. Geophys. Res.*, doi:10.1029/2008JD010605, (in press)
- Lagouvardos K., and Kotroni V., 2007: TRMM and lightning observations of a low-pressure system over the Eastern Mediterranean. *BAMS*, **88**, 1363–1367.
- Lang T.J., and Rutledge S.A., 2002: Relationships between convective storm kinematics, precipitation, and lightning. *Mon. Wea. Rev.*, **130**, 2492–2506.
- Mohr K.I., Toracinta E.R., Zipser E.J., and Orville R.E., 1996: A comparison of WSR-88D reflectivities, SSM/I brightness temperatures, and lightning for mesoscale convective systems in Texas. Part II: SSM/I brightness temperatures and lightning. *J. Appl. Meteor.*, **35**, 919–931.
- Orville R.E., 1981: Global distribution of midnight lightning September to November 1977. *Mon. Wea. Rev.*, **109**, 391–395.
- Price C., and Rind D., 1992: A simple lightning parameterization for calculating global lightning distributions. *J. Geophys. Res.*, **97**, 9919–9933.
- Price C., and Federmann B., 2006: Lightning–rainfall relationships in Mediterranean winter thunderstorms. *Geophys. Res. Lett.*, **33**, L07813.
- Pruppacher H.R., and Klett J.D., 2000: *Microphysics of Clouds and Precipitation*. Kluwer Academic Publishers, Dordrecht, The Netherlands, 1997.
- Rakov V.A., and Uman M.A., 2003: *Lightning. Physics and Effects*. Cambridge University Press, Cambridge.
- Schultz P., 1995: An explicit cloud physics parameterization for operational numerical weather prediction. *Mon. Wea. Rev.*, **123**, 3331–3343.
- Sherwood S.C., Phillips V.T.J., and Wettlaufer J.S., 2006: Small ice crystals and the climatology of lightning. *Geophys. Res. Lett.*, **33**, L05804.
- Spencer R., Goodman H.M., and Hood R.E., 1989: Precipitation retrieval over land and ocean with the SSM/I: Identification and characteristics of the scattering signal. *J. Atmos. Oceanic Technol.*, **6**, 254–273.
- Tapia A., Smith J.A., and Dixon M., 1998: Estimation of convective rainfall from lightning observations. *J. Appl. Meteor.*, **37**, 1497–1509.
- Toracinta E.R., and Zipser E.J., 2001: Lightning and SSM/I-ice-scattering mesoscale convective systems in the global tropics. *J. Appl. Meteor.*, **40**, 983–1002.
- Toracinta E.R., Cecil D.J., Zipser E.J., and Nesbitt S.W., 2002: Radar, passive microwave, and lightning characteristics of precipitating systems in the tropics. *Mon. Wea. Rev.*, **130**, 802–824.

- Ulaby F.T., Moore R.K., and Fung A.K., 1981: *Microwave Remote Sensing Active and Passive. Vol. 1: Fundamentals and Radiometry*. Artech House Publishers, London.
- Ushio T., Heckman S.J., Boccippio D., Christian H.J., and Kawasaki Z.I., 2001: A survey of thunderstorm flash rates compared to cloud top height using TRMM satellite data. *J. Geophys. Res.*, **106**, 24089–24095.

Chapter 20

Lightning and Precipitation

Serge Soula

Abstract Lightning flashes and surface rainfall are two manifestations of thunderstorms, both consequences of physical processes in the cloud involving hydrometeors of different sizes and types. For several decades, observations using various techniques have shown the general trend for both activities to be tightly related and to quantify the relationship. In several regions of the world, rainfall produced by convective systems has been estimated from surface detection, from ground radar scans or from space observations, and the rate of lightning flashes generated by the same systems was determined in parallel using various detection systems. Among the parameters used to quantify the relationship between rainfall and lightning, the Rain-yield Per Flash (RPF) which is the rainfall volume or mass divided by the lightning frequency, has been estimated in different regions and in several convection regimes. The values obtained from many studies can range from less than $1 \times 10^7 \text{ kg fl}^{-1}$ in continental and arid regimes to about $3000 \times 10^7 \text{ kg fl}^{-1}$ in oceanic regime. The variation of the RPF has been attributed to various causes in the literature, according to the techniques of rainfall estimation, the region of the storm activity, the type and the phase of the storms involved, and the type of flash considered. Surface-detected rainfall can provide larger RPF values than rainfall detected at altitude because of evaporation. The RPF values are obviously lower when considering total lightning activity and higher when the storm systems cover an extended stratiform zone. A large difference is observed between oceanic and continental storms. The RPF is much larger in oceanic convective clouds, especially in warm pool. The main reason for this contrast is the weakness of the updrafts over the ocean compared to over the land. In ocean storms, the width and the height of the mixed-phase cloud region, where the non-inductive charging processes occur, are too small for the development of electrification.

Keywords Thunderstorm · Lightning · Rainfall · Rain yield · Land-ocean contrast · Convection

S. Soula (✉)

Université de Toulouse; UPS; LA (Laboratoire d'Aérologie); 14 avenue Edouard Belin; F-31400 Toulouse CNRS; LA (Laboratoire d'Aérologie), G-31400 Toulouse
e-mail: serge.soula@aero.obs-mip.fr

20.1 Introduction

Thunderstorms are characterized by both convective rainfall and lightning activity, which result from physically related processes. According to Houze (1993), convective rainfall corresponds to rain falling from cumuliform clouds with a vertical motion scale of between 1 and 10 m s⁻¹ which exceeds the terminal fall speed of snow (1 ms⁻¹). In this type of cloud, the variety of dynamics and microphysics processes is wide and complex. From laboratory experiments, Takahashi (1978), Saunders et al. (1991) have demonstrated that the coexistence of ice crystals, graupels, and supercooled water is essential for electrical charging. It is now accepted that the noninductive collisions between graupels and smaller ice crystals with the presence of liquid water, represents the most reliable charging mechanism for storm electrification. In his review about the electric structure of thunderstorms, Krehbiel (1986) concluded that particle interactions and convective motions may both account for the observed storm electrification. As noted by Saunders (1993) in the conclusions of his review about the thunderstorm electrification processes, several analyses show that the charge centres are collocated with precipitation in regions of specific temperature (Krehbiel, 1986; Williams, 1989; Krehbiel et al., 1979) and that the rapid electrical development is associated with the development of precipitation in the cloud (Reynolds and Brook, 1956). In numerous radar studies of deep, lightning- and non-lightning-producing convection, the observations support the presence of significant quantities of timed precipitation-size ice in developing thunderstorms (e.g., Williams and Lhermitte, 1983; Goodman et al., 1988; Dye et al., 1988; Williams et al., 1992; Zipser and Lutz, 1994; Petersen et al., 1996; Carey and Rutledge, 1996).

Precipitating systems in the tropics account for two-thirds of global rainfall (Simpson et al., 1986) and three quarters of all lightning flashes occur in the same latitude range (Christian et al., 1999). Both activities are therefore considered in most studies devoted to precipitating systems at global and local scales. Lightning activity depends on the latitude because of the influence of temperature on convection intensity and on freezing (Mackerras and Darveniza, 1994). The lightning activity includes two types of flashes, cloud-to-ground (CG) flashes when there is a strike to the ground and intracloud (IC) flashes which include all kinds of flashes which do not strike the ground, i.e. intracloud, intercloud, and cloud-to-air flashes. Because of the availability of data, most studies have used the CG lightning activity and only few consider the total lightning activity including both types of flashes. Recently, especially thanks to lightning detection from space, some studies have been performed on a large scale and based on all flashes (Toracinta et al., 2002; Takayabu, 2006). This chapter is devoted to a review of the works concerning the relationship between surface rainfall, often designated as precipitation, and lightning activity. So, quantitative aspects from observations are developed in a first section, the variability of the relationship is analyzed in a second section and the specific contrast between land and ocean environments is largely described in a third section.

20.2 Lightning-Precipitation Relationships

Several observations have reported simultaneous increases in the amount of surface precipitation and lightning frequency from thunderclouds (Workman and Reynolds, 1949; Israël, 1973). More recently, numerous works have demonstrated good correlations between rainfall and CG lightning activity. In particular, a correlation exists between CG lightning initiation and frequency, and the descent of hydrometeors through the lower mixed phase region of convective clouds, which ultimately produces heavy rainfall at the surface (Goodman et al., 1988; Williams et al. 1989; Carey and Rutledge, 1996; Petersen et al., 1996).

The Rain-yield Per Flash (RPF) is the amount of rainfall divided by the lightning frequency over a given period and area. Table 20.1 shows a set of results concerning this parameter obtained in various regions and climatological conditions over the world. Most studies have provided values of RPF for CG flashes only, while some recent works considered the RPF for total flashes. When Battan (1965) estimated the RPF in an early study of Arizona storms over Santa Catalina Mountains, the lightning flashes were counted by human observers and the rainfall was measured by a rain gauge network. Considering 52 storms spread out over six summer seasons,

Table 20.1 Rainfall yield per flash (CG flash or total flash) for several studies around the world, with different types of convective regime, different techniques of rainfall estimation, various types of temporal and spatial integration. (Partly from MacGorman and Rust, 1998)

Authors	Location	Cases	Yield (10^7 kg per flash)	Type of flash
Battan (1965)	Southern Arizona	52	0.3–300	CG
Kinzer (1974)	Oklahoma	1	2	CG
Grosh (1978)	Illinois	1	3	CG
Maier et al. (1978)	South Florida	22	0.3–90	CG
Piepgrass et al. (1982)	Central Florida	2	1.8–2.2	CG
Piepgrass et al. (1982)	Central Florida	2	0.67–0.85	Total
Buechler et al. (1990)	Tennessee Valley	21	0.9–20	CG
Buechler and Goodman (1991)	Florida	2	6–30	CG
López et al. (1991)	Florida coast		0.5–1000	CG
Williams et al. (1992)	Darwin, Australia	43	9–100	CG
Williams et al. (1992)	Darwin, Australia	6	200–3000	CG
Holle et al. (1994)	Central US	4	30–80	CG
Richard and Lojou (1996)	Paris area	60	0.1–1	Total
Tapia et al. (1998)	Florida	22	2.4–36.5	CG
Petersen and Rutledge (1998)	Southwestern US		5–8	CG
Petersen and Rutledge (1998)	Northern US		20–30	CG
Petersen and Rutledge (1998)	Tropics		40–1000	CG
Soula et al. (1998)	Northern Spain	1	3	CG
Soula and Chauzy (2001)	France	4	5.1–9.9	CG
Soula and Chauzy (2001)	France	4	0.7–2.0	Total
Takayabu (2006)	Over land		39.4	Total
Takayabu (2006)	Over ocean		196	Total

the RPF ranged from 0.3 to 30×10^7 kg per flash (kg fl^{-1}), with an average value of 3×10^7 kg fl^{-1} . The same average value was found by Grosh (1978) for a storm in another part of US territory (Illinois). Buechler et al. (1990) considered 21 storms in a continental area of the US (Tennessee Valley) and found a smaller range for the RPF, $0.9 \times 10^7 - 20 \times 10^7$ kg fl^{-1} , and at a similar average value, 4×10^7 kg fl^{-1} . In Central Florida, Piepgrass et al. (1982) estimated the RPF at 1.8 and 2.2×10^7 kg fl^{-1} from a small storm and a large one, respectively. They analyzed the CG lightning flash frequency and the rainfall amount, from data provided by a field mill network and a rain gauge network, respectively. In South Florida, Maier et al. (1978) found values a little larger, between 0.3 and 90×10^7 kg fl^{-1} with an average at about 10×10^7 kg fl^{-1} . By considering 22 storms in a 460×460 km area around the Melbourne radar (Central Florida), Tapia et al. (1998) found this volume between 2.4 and 36.5×10^7 kg fl^{-1} . Buechler and Goodman (1991) studied 2 cases of storm in Florida and determined the RPF to range between 6 and 30×10^7 kg fl^{-1} .

From their study for estimating the RPF in different locations around the globe and over different temporal and spatial scales, Petersen and Rutledge (1998) found similar values for several areas of the US territory. They used data from the National Lightning Detection Network (NLDN) for CG flash counting, and data from radar, rain gauges, and satellite for rainfall estimating. They calculated the RPF on large temporal (around 1 month) and spatial (around 10^5 km 2) scales, in order to limit the variability. So, they found between 5 and 8×10^7 kg fl^{-1} in arid zones of southwestern US and between 20 and 30×10^7 kg fl^{-1} in the continental zone of northern US. Soula et al. (1998) analyzed an extended and stationary system that caused a dramatic flash flooding in northern Spain on August 7th, 1996. The storm produced exceptionally high cumulative rainfall with maximum values at 200 mm collocated with maximum CG flash density values higher than 2 km $^{-2}$. The average RPF was estimated at 3×10^7 kg fl^{-1} for the whole lifetime of that storm. Soula and Chauzy (2001) analyzed data from meteorological radar and the French national CG lightning flash detection network for 4 storms in France (Paris area) and found RPF values of between 5.1 and 9.9×10^7 kg fl^{-1} .

Holle et al. (1994) described the characteristics of 4 Mesoscale Convective Systems (MCS) which occurred in central US (Kansas-Oklahoma) on 3–4 June 1985 during the PRE-STORM field program. They analyzed the CG flash activity by means of several LLP direction finder (DF) sensors and the amount of precipitation was provided by several radars of the National Weather Service. For one MCS analyzed in detail, the RPF ranged from 30 to 80×10^7 kg fl^{-1} , higher values being found in the stratiform areas compared to the convective areas. López et al. (1991) associated the radar-derived rainfall volume and the CG flash count for stormy days from June to September 1983 in east-central Florida. The RPF values covered a wide range, $0.5-1000 \times 10^7$ kg fl^{-1} , that is to say up to values one order of magnitude larger than those cited above. Williams et al. (1992) analyzed the relationship between rainfall and CG lightning activity for deep tropical convection close to the north Australian coast, by distinguishing continental and monsoon regimes. The observations were made during the Down Under Doppler and Electricity Experiment (DUNDEE) in the region of Darwin. From a set of several tens of storms, the RPF was found to be very variable and much larger in the monsoon storms. It ranged

from 9 to $100 \times 10^7 \text{ kg fl}^{-1}$ and from 200 to $3000 \times 10^7 \text{ kg fl}^{-1}$ for continental and monsoon cases, respectively. Petersen and Rutledge (1998) also considered tropical areas for their study of RPF variability. They used data collected during DUNDEE in tropical continental and island regimes (northern Australia) and during the Tropical Ocean Global Atmosphere Coupled Ocean Atmosphere Response Experiment (TOGA COARE) in two kinds of regime: tropical ocean and mixed “island-ocean” (West Pacific Warm Pool). They found average RPF values of between $40 \times 10^7 \text{ kg fl}^{-1}$ for continental regime and $1000 \times 10^7 \text{ kg fl}^{-1}$ for the western Pacific Ocean.

Zipser (1994) calculated the Rain-to-Thunder days Ratio (RTR) in several locations over the world, by dividing the rainfall by the number of thunder days. The results showed both parameters thunder days and rainfall had inverse variations, especially in the tropical regions. The RTR was therefore lower for continental rainfall regimes or during tropical break periods in northern Australia. On the contrary, the RTR was high in the case of storms associated with monsoon or oceanic-like convection.

The relationship between rainfall and lightning activity was also investigated for total flashes produced by storms. For example, Piepgrass et al. (1982) found average RPF values of 0.67 and $0.85 \times 10^7 \text{ kg fl}^{-1}$ for two thunderstorms analyzed in detail, as discussed above. Richard and Lojou (1996) used VHF interferometer-derived lightning flash location and radar-derived rainfall amounts, for about 60 thundercells in France. They found good correlations between rainfall volume and total lightning flash rate. Most of the RPF values ranged between 0.1 and $1 \times 10^7 \text{ kg fl}^{-1}$. Chèze and Sauvageot (1997) reported a stronger correlation between CG lightning and rainfall than between total lightning and rainfall. Concerning the RPF values, other examples were given by Soula and Chauzy (2001) with values ranging from 0.7 to $2 \times 10^7 \text{ kg fl}^{-1}$ in 4 storm episodes in the Paris area.

The RPF values were obviously lower when all lightning flashes were considered. However, Takayabu (2006) estimated larger values from global observations thanks to the instruments onboard the satellite Tropical Rainfall Measuring Mission (TRMM). The rainfall was estimated with radar observations and the lightning flashes were detected with the optical Lightning Imaging Sensor (LIS). The average RPF was found at $39.4 \times 10^7 \text{ kg fl}^{-1}$ and at $196 \times 10^7 \text{ kg fl}^{-1}$, over land and over ocean, respectively. The average RPF over ocean is therefore one order of magnitude lower than the values estimated by Petersen and Rutledge (1998) for the tropical ocean. Two reasons can explain this difference: (i) Petersen and Rutledge estimated RPF over the warm pool region while Takayabu estimated his value from the entire tropical ocean average. (ii) Petersen and Rutledge considered only CG flash numbers while Takayabu used total flash numbers.

20.3 Analysis of the Rainfall Yield Variations

The values of the RPF found in all these studies display a very large variability, up to several orders of magnitude. The reasons behind this variability deserve to

be looked at in detail. By considering the evolution of lightning activity and that of surface rainfall detected by rain gauges, several authors have reported the occurrence of a time lag between the maxima. Piepgrass et al. (1982) determined a delay of 4 and 9 minutes for the rainfall compared to the lightning activity, in two cases of storms. These storms in Florida were stationary and therefore the time lag was not problematic for comparing the data of the two activities. The ratio between rain and lightning count calculated at given times can vary during the lifetime of a storm. However, the calculation of the average value should not be affected by the time lag. The variations of the two activities were compared for two storm systems in Soula and Chauzy (2001). The systems consisted of several cells with individual behaviour in terms of lightning and rainfall production. The latter was evaluated from meteorological radar and therefore was detected before it reached the surface. By considering the whole activity of the whole system for both cases, variations in rainfall and lightning did not exactly coincide, even if their general trends were similar. For example, in one case the lightning activity maximum was clearly delayed by 5–10 minutes while in the other case, the CG lightning activity seemed less well correlated with rainfall, compared to the total lightning activity. The lightning activity lag time noted in this work does not coincide with the result of Piepgrass et al. (1982). The different altitude of rainfall detection can explain the opposite delay in the two works. According to several works, the CG flashes tend to peak after the IC flashes, when the core of high radar reflectivity descends in the middle or lower part of the thundercloud (MacGorman et al., 1989; Williams, 1989). On the other hand, some observations showed a rapid descent of precipitation in the presence of downdrafts, before any increase in CG flashes (MacGorman et al., 1989; Nisbet et al., 1990). In some storms like squall lines, rainfall can peak 1 or 2 hours after the CG flash rate as noted by Rutledge and MacGorman (1988) or Holle et al. (1994). These lag times can be at the origin of the variability of the RPF when it is calculated by time interval.

Chèze and Sauvageot (1997) found good correlations between lightning activity and rainfall for very active convective systems, but the parameters of the relationship could change from one system to another. When they considered integrated activities at a climatological scale, the correlations were much less good, except for a homogeneous regime of very active convection. Figure 20.1 shows the distribution of the RPF values for several separate cells but with similar measurement techniques and climatological conditions for each cell. First example (a) corresponds to the study by Battan (1965) in Arizona storms. In this case, the variation range is of about 3 orders of magnitude and it seems larger for weaker activity. When the number of CG flashes increases, the dots converge towards a value between 10^7 and 10^8 kg fl^{-1} . The second example (b) corresponds to the study of Williams et al. (1992) for tropical storms in continental and monsoon regimes. The RPF values are larger than in the previous study since only one value is found lower than 10^8 kg fl^{-1} and the dispersion is weaker since the variation range is roughly one order of magnitude for both regimes. Larger values of RPF are observed for the monsoon regime. Graph (c) displays the results from López et al. (1991) for storms close to the Florida coast without any regime selection. The dispersion is large in this case, and the RPF

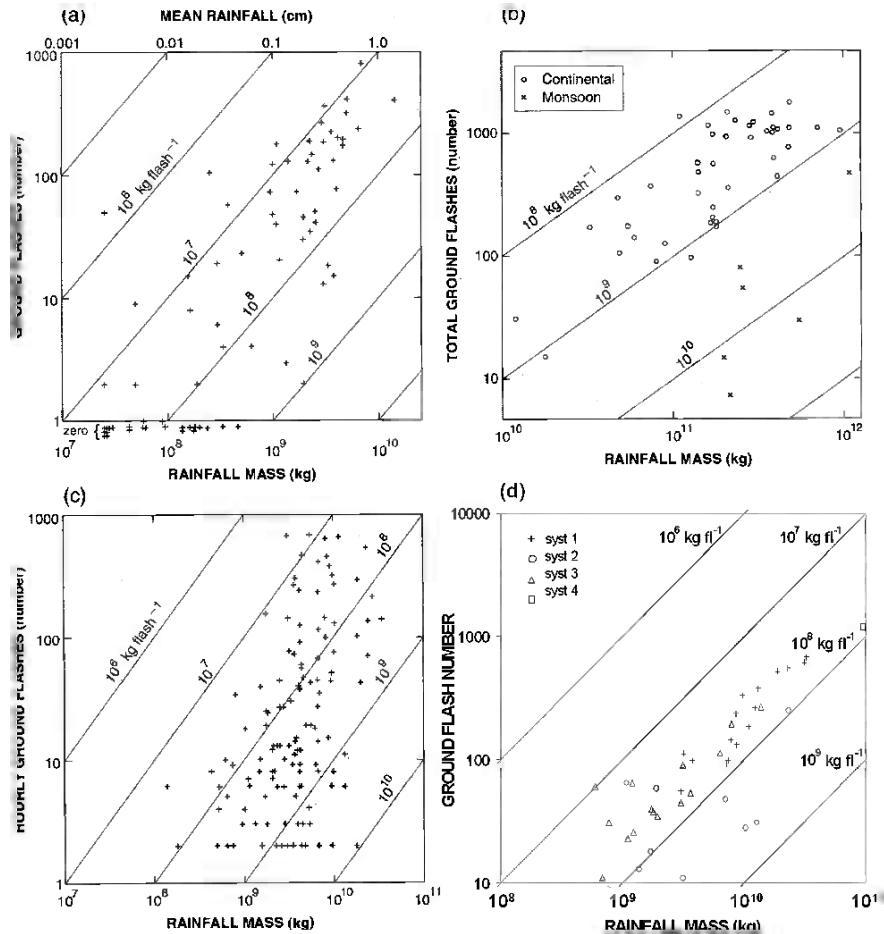


Fig. 20.1 Rainfall as a function of number of ground flashes. Diagonal lines indicate constant RPF in kg per ground flash. (a) Arizona storms. (From Battan, 1965) (b) Daily totals for storms near Darwin, Australia. (From Williams et al., 1992) (c) Hourly data from Florida storms. (From López et al., 1994) (d) Individual storms in Paris area. (Soula and Chauzy, 2001). (Partly from MacGorman and Rust, 1998)

clearly decreases, on average, when the number of CG flashes increases. The last example (d) corresponds to 4 convective systems from Soula and Chauzy (2001). The dispersion between individual cells was weaker for very active storms, i.e. for storms producing more than a few hundred flashes. In this study, 16 individual cells in system 1 gave average RPF values of between 2.86 and 7.75×10^7 kg fl $^{-1}$ for CG flashes, and between 0.71 and 2.63×10^7 kg fl $^{-1}$ for total flashes. For system 2 with 9 cells, the RPF ranged between 1.67 and 41.14×10^7 kg fl $^{-1}$ for CG flashes and between 0.62 and 1.57×10^7 kg fl $^{-1}$ for total flashes. In system 1 the dispersion was slightly larger for total lightning activity while in system 2 it was much larger

for CG lightning activity. In system 2, some thundercells exhibited a high proportion of positive CG (+CG) flashes and strong reflectivity, which could indicate a probability of severe weather. A good correlation between the RPF and the +CG proportion was found in this study. From a CG flash activity study concerning six areas in South-Central United States, Sheridan et al. (1997) deduced that the RPF was sensitive to the +CG flash percentage. So, statistically, their cases with a high RPF presented a high +CG percentage. Dominant positive CG flash production with large densities had been observed in several storms, for example in Brazil (Pinto et al., 1999, and in the United States (Rust et al., 1981; Stolzenburg, 1994). High +CG flash proportions were observed in both situations of relatively shallow thunderstorms (Engholm et al., 1990) and of severe storms (Seimon, 1993; Stolzenburg, 1994).

Petersen and Rutledge (1998) also plotted the distribution of the CG flash numbers versus the rainfall mass. Figure 20.2 represents this distribution for several cases in similar and different convection regimes and/or different locations over the world. As in Fig. 20.1, the increase of the CG flash number tends to reduce the dispersion of the dots representing activities integrated over 1 month and 10^5 km^2 .

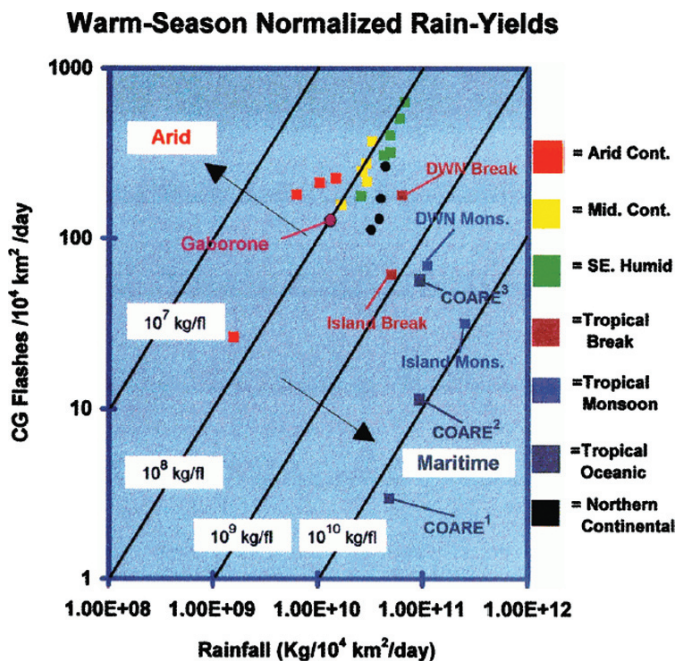


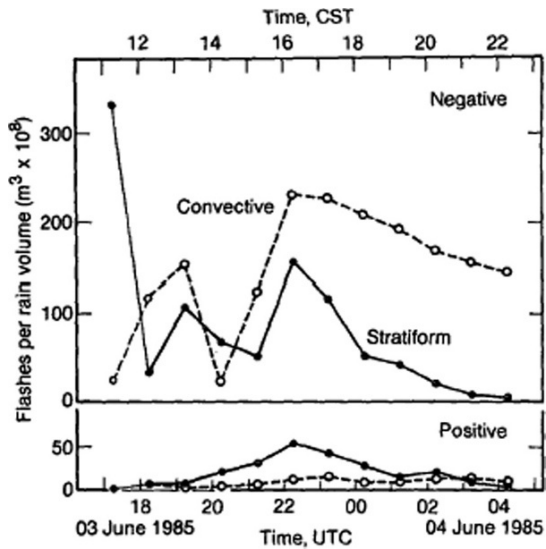
Fig. 20.2 Summer or warm-season normalized CG flash density (flashes/ $10^4 \text{ km}^2/\text{day}$, on the ordinate) versus rainfall ($\text{kg}/10^4 \text{ km}^2/\text{day}$, on the abscissa). Sloping solid *black lines* are contours of constant rain yield (kg/fl). Each data point is coloured and labelled (as indicated in the figure) according to each specific rainfall regime discussed in the text. The *large bold arrows* indicate directions for which more “arid” or “tropical oceanic” rainfall regimes are encountered. (From Petersen and Rutledge, 1998) (See also Plate 36 in the Color Plate Section on page 619)

The RPF values converge towards the 10^8 kg fl^{-1} line when the CG flash number reaches its larger values. This RPF value is close to the value reached for very active storms in the previous study by Soula and Chauzy (2001). From Fig. 20.2, it can be reasonably commented that the RPF largely depends on the convection regime. We can observe a large increase of RPF when the regime becomes tropical and oceanic. So, the largest difference for the RPF from case to case led to a ratio of about 400, between a case in arid continental regime for the lowest value and a case in tropical oceanic regime for the largest one. In fact, in the arid continental region (southwestern US) it ranged from 5 to $8 \times 10^7 \text{ kg fl}^{-1}$ and in the tropical western Pacific Ocean, it was between 1 and $2 \times 10^{10} \text{ kg fl}^{-1}$. It can be noted the values found for arid continental regions compare very well to the values calculated by Battan (1965) for storms in the same region, the average of which was about $3 \times 10^7 \text{ kg fl}^{-1}$, also determined from rain gauge data.

The values of RPF reported by Soula and Chauzy (2001) for convective systems in continental regions, between 5.1 and $9.9 \times 10^7 \text{ kg fl}^{-1}$, were slightly larger than the values given by Petersen and Rutledge (1998) for arid regions. Here, rainfall was estimated with radar. Other cases of rainfall estimation by radar can be commented for evaluating a possible influence of the measurement technique: López et al. (1991) found about 10^8 kg fl^{-1} for their lower values in Florida among the different convective regimes; Buechler et al. (1990) found up to $20 \times 10^7 \text{ kg fl}^{-1}$ for storms in Tennessee. Part of the differences observed in the RPF from one study to another can be due to the rainfall measurement technique. The evaporation of a proportion of the precipitating water can be at the origin of this difference, by making the rainfall reaching the ground lower compared to that detected by radar above the surface.

It is clear from the time series of both lightning and rainfall activities, that the RPF can vary during the lifetime of the storm. It has been noted for example, that the ground flash rate decreased more rapidly than rainfall, after peak values (Grosh, 1978; Watson et al., 1994). Especially in squall lines, the rainfall decreases very slowly and can continue for several hours after the end of the convective activity, while the lightning activity becomes very scarce (Holle et al., 1994; Rutledge and MacGorman, 1988). Figure 20.3 displays the time series of $-CG$ and $+CG$ flash numbers per rainfall volume for a Mesoscale Convective System (MCS)-like storm, by distinguishing the convective and stratiform regions, according to Holle et al. (1994). The large majority of CG flashes were negative along almost the whole lifetime of this storm. The $-CG$ flash number per rainfall volume was sometimes higher in the convective region and sometimes in the stratiform region, during the first half of the storm lifetime. In the second half, it decreased progressively in the convective region and much more rapidly in the stratiform region, which led to very different values of the $-CG$ number per rain volume at that moment in both parts of the system. For $+CG$ flashes, the number per rain volume was greater in the stratiform region throughout the lifetime. This result provides an additional explanation for the dispersion of the RPF values from one storm to another, when their storm structures are different.

Fig. 20.3 Time series of negative and positive flashes per rain volume (10^8 m^3) in convective and stratiform echoes for a MCS in Oklahoma and Kansas during PRE-STORM field program. (From Holle et al., 1994)



20.4 Land/Ocean Contrast

According to some studies, tropical continental rain dominates tropical oceanic rain by a large margin in terms of convective intensity and lightning activity, even though comparable amounts of rain are observed over tropical oceanic convergence zones (e.g. Zipser and Lutz, 1994). The occurrence of flashes differs greatly between continental and oceanic areas. This difference was shown by the study of satellite observations (Orville and Henderson, 1986; Christian and Goodman, 1992; Petersen and Rutledge, 2001; Christian et al., 2003), ground observations (Rutledge et al., 1992; Williams et al., 1992), and from the Global Atmospheric Research Program-Atlantic Tropical Experiment (GATE) data by Zipser (1994). These authors suggested that the scarcity of flashes over the oceans is due to the weakness of the convection intensity, compared to continental convection. In Fig. 20.4, the map of annual lightning density averaged over an 8-year period, illustrates this contrast between land and ocean. Total lightning detection was provided by 2 spatial instruments, the Optical Transient Detector (OTD) for the older data and the Lightning Imaging Sensor (LIS) for the more recent ones. The lightning flashes are located preferentially over land and in the inter-tropical zone. The lightning density can be larger by three orders of magnitude over land than over ocean at the same latitude. So, over the African continent the lightning density exceeds 70 fl km^{-2} , and at the same latitude over ocean, it can be lower than 0.1 fl km^{-2} .

Zipser (1994) examined variations of RTR calculated from monthly quantities during GATE. He showed that RTR values for areas over ocean were substantially higher than those for areas over land, and proposed RTR could be an index of continentality of convective rainfall. He found cases of tropical thunderstorms producing heavy rainfall and exhibiting high cloud tops which generated little if any lightning.

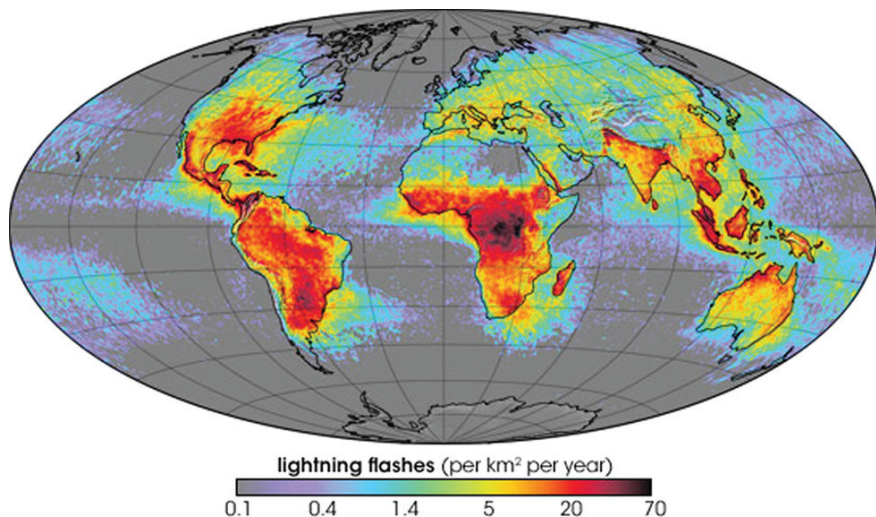


Fig. 20.4 Global distribution of averaged annual density of lightning flashes (fl km^{-2}) from the combined observations of the NASA OTD (04/1995–03/2000) and LIS (01/1998–02–2003) instruments. (From website <http://www.srh.noaa.gov>)

He reported one atoll in an equatorial area receiving 500 mm of precipitation in two months while no lightning flashes were detected. He suggested that the low lightning frequencies in oceanic storms compared to continental storms could be due to weak vertical velocities which do not reach a hypothetical threshold value necessary to allow the non-inductive charging processes to work.

Petersen and Rutledge (1998) used OTD data to calculate the RPF in various regions and seasons and obtained values of $4 \times 10^8 \text{ kg fl}^{-1}$ as typical continental values and $1\text{--}2 \times 10^{10} \text{ kg fl}^{-1}$ as typical tropical oceanic values. Results from Takayabu (2006) confirm that RPF is a reliable indicator of precipitation regimes, with a marked land-ocean contrast. The values were intermediate for monsoonal regions and continental oceans. As indicated in Section 20.2, the RPF value averaged over the entire TRMM region was about 5 times larger over ocean. If a good correlation between the RPF and the Tall Convective Rain Contribution with a threshold of -20°C (TCRC -20°C) was found over land (negative coefficient -0.55), it was much lower over ocean (-0.28). This indicates that large amounts of tall convective rain over land are fundamentally associated with intense updrafts able to sustain vigorous lightning activity. Figure 20.5 shows (a) the global distribution of 3-year mean RPF values and (b) the TCRC -20°C , for the period from March 1998 to February 2001 (Takayabu, 2006). It reveals a significant contrast in RPF over land and ocean, with smaller values over land, typically less than $1.5\text{--}2.0 \times 10^8 \text{ kg fl}^{-1}$ (orange to reddish colours). Smaller RPF values corresponded well with stronger lightning activity for the same amount of rain, while they are the opposite was true for larger RPF. Another feature in Fig. 20.5a is that relatively small RPF values (yellowish and light green colours) were recorded over oceanic areas adjacent to continents and were more pronounced to the east of continents: east of North

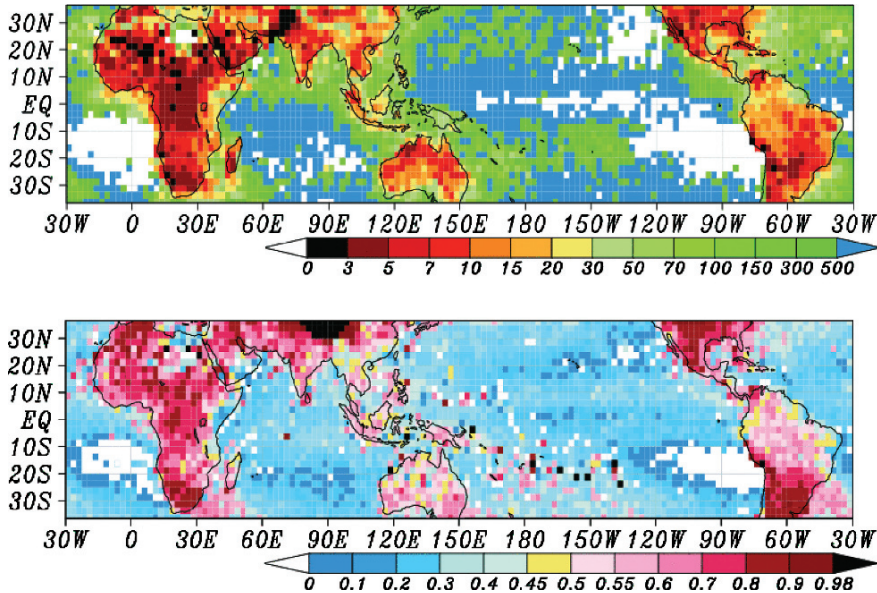


Fig. 20.5 Global distributions of 3-year (March 1998–February 2001) TRMM observations: (a) mean RPF and (b) Tall Convective Rain Contribution to surface rain with a threshold of -20°C . Units for the colour scales are 10^7 kg fl^{-1} (a) and fraction contribution (0–1) (b). RPF averages are obtained by dividing the total precipitation amount by the total flash number for the averaging period. (From Takayabu, 2006) (See also Plate 37 in the Color Plate Section on page 620)

America and south-east of South America, east of South Africa around Madagascar, and east of the Indian subcontinent. These areas of relatively small RPF (less than $5.0 \times 10^8 \text{ kg fl}^{-1}$) can extend more than 1000 km from the continents.

Toracinta et al. (2002) analyzed precipitating systems in the Tropics from TRMM data including radar, passive microwave and lightning. They noted that convective systems over the tropical continents typically have greater magnitudes of reflectivity extending to higher altitudes than tropical oceanic systems. From observation of differences in microwave scattering, they inferred greater supercooled water contents aloft in the tropical continental systems, which can be consistent with lightning activity since supercooled water plays a role in the main charging process (Takahashi, 1978; Saunders et al., 1991). Toracinta et al. (2002) noted that lightning was much more likely in continental features than oceanic features with similar brightness temperatures or similar reflectivity heights. Vertical profiles of radar reflectivity showed that convective systems with lightning had greater reflectivity values and smaller decreases of reflectivity with height above the freezing level than systems without detected lightning.

It is clear that the contrast in the RPF values for ocean and land originates from the very weak lightning activity over ocean. Two causes of this disparity in lightning intensity have been put forward, the thermodynamic influence and aerosol effects. The thermodynamic hypothesis is based on surface property differences with of course heating on land surfaces favouring the convection (Williams and

Stanfill, 2002). The aerosol hypothesis is based on the effect of the aerosol particles on the droplet size (Molinié and Pontikis, 1995). Low aerosol particle concentrations in the sub-cloud layer over sea lead to early formation of warm precipitation, thus inhibiting the cloud vertical velocities and the large droplet and ice-crystal concentrations in the mixed phase region of the thundercloud. This behaviour reduces the cloud electrification rate and hence the corresponding lightning flash frequency. Williams and Stanfill (2002) analyzed the thunderstorm activity reported in islands of various sizes. Figure 20.6 illustrates their result by displaying the distribution of the annual number of days with thunder versus the size of the island. It emphasizes an increasing thunderstorm presence versus island size, suggesting that islands behave as miniature continents of variable area. This observation tends to support the traditional thermal hypothesis against the aerosol hypothesis for lightning control. They also reported that the land-ocean contrast in updraft strength is globally supported by the observations of TRMM radar reflectivity in the mixed phase. The land-ocean updraft contrast does not correspond to the land-ocean contrast in CAPE from the standpoint of parcel theory. The authors explained how this inconsistency can be resolved by the scaling of buoyant parcel size with cloud base height, as suggested by earlier investigators. The stronger electrification of continental storms can be justified by a larger surface Bowen ratio and by larger and more strongly buoyant boundary layer parcels which more efficiently transform CAPE to kinetic energy of the updraft in the moist stage of conditional instability. Satellite-based microphysics studies by Rosenfeld and Lensky (1998) show a much shallower mixed-phase zone of precipitation in oceanic convective clouds than in continental ones. They found that glaciation of particles can occur in much colder (higher) cloud layers for continental storms and therefore, the non-inductive charging processes, which require the presence of both ice particles and super-cooled water, have a better chance of occurring.

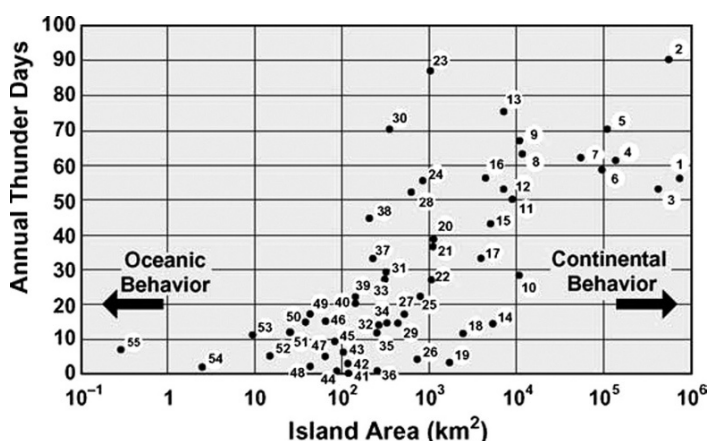


Fig. 20.6 Annual number of thunder days for islands versus island area. (From Williams and Stanfill, 2002)

20.5 Conclusion

Results from numerous studies of various observations of lightning activity and rainfall have been analysed. The data were gathered using many of the different techniques that have evolved during the last decades and which can investigate increasingly larger scales. The rainfall produced by convective systems has been estimated using surface detection, ground radar scans or space observations, and the rate of lightning flashes generated by the same systems was also determined using a variety of detection systems. The storms were of different types and occurred in different convective regimes. The rainfall was estimated at different altitudes depending on the technique used and the lightning activity records included either only CG flashes or total flashes. The regions concerned by the storm activity were continental or oceanic, and the reference duration for the analysis differed greatly from one study to another.

The main parameter used for quantifying the relationship between rainfall and lightning is the RPF which is obtained by dividing the rainfall volume or mass by the lightning frequency. It has been estimated in different regions and in several convection regimes. The values of the RPF can range from less than $1 \times 10^7 \text{ kg fl}^{-1}$ in continental and arid regimes to about $3000 \times 10^7 \text{ kg fl}^{-1}$ in oceanic regimes. The variability of the parameter was large from study to study but also from storm to storm in a given area. However, several observations showed that the variability was reduced when the number of flashes produced by the storms increased. The RPF differences were attributed to diverse causes. They were associated with the method of rainfall estimation and the type of lightning flashes taken into account, with the climatology of the region concerned by the storm activity, and with the structure and the phase of the convective systems involved. It was noted that the rainfall measured with surface rain gauges could provide larger RPF values compared to the rainfall detected at altitude with radar or from space with remote sensing devices. Evaporation as the rain crosses the sub-cloud layer can explain this. In most studies, the RPF was calculated by considering the CG lightning activity but when it was calculated with the total lightning activity, lower values were obtained. Higher RPF values were found when the storm systems had an extended stratiform zone.

Large differences were observed between oceanic and continental storms around the world. Over the ocean, lower radar reflectivity values were generally detected in the vertical structure of the convective clouds and the lightning frequency was substantially weaker. As a consequence, the RPF was much higher in oceanic convective clouds. The observed weakness of the updrafts over the ocean compared to over the continent could explain this contrast. In oceanic storms, the width and the height of the cloud region containing mixed-phase particles is thought to be too small to allow the occurrence of non-inductive charging processes which are the main causes for cloud electrification.

References

- Battan, L. J., Some factors governing precipitation and lightning from convective clouds, *J. Atmos. Sci.*, 22, 79–84, 1965.

- Buechler, D. E., P. D. Wright, and S. J. Goodman, (1990), Lightning/rainfall relationships during COHMEX. Preprints, 16th Conference on Severe Local Storm, Amer. Meteor. Soc., 710–714.
- Buechler, D. E., and S. J. Goodman, (1991), Radar characteristics of cloud-to-ground lightning producing storms in Florida. Preprints, 25th International Conference on Radar Meteorology, Amer. Meteor. Soc., 897–900.
- Carey, L. D., and S. A. Rutledge, (1996), A multiparameter radar case study of the microphysical and kinematic evolution of a lightning producing storm, *Meteor. Atmos. Phys.*, 59, 33–64.
- Chèze, J.-L., and H. Sauvageot, (1997), Area-average rainfall and lightning activity, *J. Geophys. Res.*, 102(D2), 1707–1715.
- Christian, H. J., and S. Goodman, (1992). Global observations of lightning from space, in: *Proceedings of the 9th International Conference on Atmospheric Electricity*, St. Petersburg, pp. 316–321.
- Christian, H. J., et al., (1999), The lightning imaging sensor, in: *Proceedings of the 11th International Conference on Atmospheric Electricity*, Guntersville, AL, NASA/CP-1999-209261, pp. 746–749.
- Christian, H. J., et al., (2003), Global frequency and distribution of lightning as observed from space by the Optical Transient Detector, *J. Geophys. Res.*, 108(D1), 4005, doi:10.1029/2002JD002347.
- Dye, J.E., J.J. Jones, A.J. Weinheimer, and W.P. Winn, (1988), Observations within two regions of charge during initial thunderstorm electrification, *Quart. J. R. Meteor. Soc.*, 114, 1271–1290.
- Engholm, C. D., E. R. Williams, and R. M. Dole, (1990), Meteorological and electrical conditions associated with positive cloud-to-ground lightning. *Mon. Weath. Rev.*, 118, 470–487.
- Goodman, S. J., D. E. Buechler, P. D. Wright, and W. D. Rust, (1988), Lightning and precipitation history of a microburst-producing storm, *Geophys. Res. Lett.*, 15, 1185–1188.
- Grosh, R. C., (1978), Lightning and precipitation – the life history of isolated thunderstorms, Preprints, 10th Conference on Cloud Physics and Atmospheric Electricity, Amer. Meteor. Soc., 617–624.
- Holle, R.L., A.I. Watson, R.E. López, D.R. MacGorman, R. Ortiz, and W.D. Otto, (1994), The life cycle of lightning and severe weather in a 3–4 June 1985 PRE-STORM MCS, *Mon. Wea. Rev.*, 122, 1798–1808.
- Houze, R. A. Jr., (1993), *Cloud Dynamics*. Academic, San Diego, Calif, 573 pp.
- Israël, H., (1973), *Atmospheric Electricity*, Vol. 2, *Fields, Charges, Currents, Israel Program for Scientific Translation*. Jerusalem, 478 pp.
- Kinzer, G. D., (1974), Cloud-to-Ground lightning versus radar reflectivity in Oklahoma thunderstorms. *J. Atmos. Sci.*, 31, 787–799.
- Krehbiel, P. R., (1986), The electrical structure of thunderstorms. In *The Earth's Electrical Environment*. National Academic Press, Washington, DC, pp. 90–113.
- Krehbiel, P.R., M. Brook, and R.A. McCrory, (1979), An analysis of the charge structure of lightning discharges to ground, *J. Geophys. Res.*, 84, 2432–2456.
- López, R. E., R. Ortiz, W. D. Otto, and R. E. Holle, (1991), The lightning activity and precipitation yield of convective cloud systems in central Florida. Preprints, 25th International Conference on Radar Meteorology, Amer. Meteor. Soc., 907–910.
- MacGorman, D. R., D. W. Burgess, V. Mazur, W. D. Rust, W. L. Taylor, and B. C. Johnson, (1989), Lightning rates relative to tornadic storm evolution on 22 May 1981, *J. Atmos. Sci.*, 46, 221–250.
- MacGorman, D. R., and Rust, W. D. (1998), *The Electrical Nature of Storms*. Oxford University Press, New York, USA.
- Mackerras, D., and M. Darveniza, (1994), Latitudinal variation of lightning occurrence characteristics, *J. Geophys. Res.*, 99, 10813–10821.
- Maier, M. W., A. G. Boulanger, and J. Sarlat, (1978), Cloud-to-Ground lightning frequency over south Florida. Preprints, Conference on Cloud Physics and Atmospheric Electricity, Amer. Meteor. Soc., 605–610.
- Molinié, J., and C. Pontikis, (1995), A climatological study of tropical thunderstorm clouds and lightning frequencies on the French Guyana coast, *Geophys. Res. Lett.*, 22, 1085–1088.

- Nisbet, J.S., J.R. Kasha, and G.S. Forbes, (1990), A case study of the Thunderstorm Research International Project storm of July 11, 1978. 2. Interrelations among the observable parameters controlling electrification, *J. Geophys. Res.*, 95, 5435–5445.
- Orville, R. E., and R. W. Henderson, (1986), The global distribution of midnight lightning: December 1977 to August 1978, *Mon. Wea. Rev.*, 114, 2640–2653.
- Petersen, W. A., S. A. Rutledge, and R. E. Orville, (1996), Cloud-to-ground lightning observations from TOGA COARE: Selected results and lightning location algorithms, *Mon. Weather Rev.*, 124, 602–620.
- Petersen, W. A., and S. A. Rutledge, (1998), On the relationship between cloud-to-ground lightning and convective rainfall, *J. Geophys. Res.*, 103(D12), 14,025–14,040.
- Petersen, W. A., and S. A. Rutledge, (2001), Regional variability in tropical convection: Observations from TRMM, *J. Clim.*, 14, 3566–3586.
- Piepgrass, M. V., E. P. Krider, and C. B. Moore, (1982), Lightning and surface rainfall during Florida thunderstorms, *J. Geophys. Res.*, 87, C13, 11193–11201.
- Pinto, O. Jr., I. R. C. A. Pinto, M. A. S. S. Gomes, I. Vitorello, A. L. Padilha, J. H. Diniz, A. M. Carvalho, and A. Cazetta Filho, (1999), Cloud-to-Ground lightning in southeastern Brazil in 1993: 1. Geographical distribution. *J. Geophys. Res.*, 104, D24, 31369–31379.
- Reynolds, S.E., and M. Brook, (1956), Correlation of the initial electric field and the radar echo in thunderstorms, *J. Meteor.*, 13, 376–380.
- Richard, P., and J. Y. Lojou, (1996), Assessment of application of storm cell electrical activity monitoring to intense precipitation forecast, in: *Proceedings of the 10th Conference on Atmospheric Electricity*, June 10–14, Osaka, Japan, pp. 284–287.
- Rosenfeld, D., and I. M. Lensky, (1998), Satellite based insights into precipitation formation processes in continental and maritime convective clouds, *Bull. Amer. Meteor. Soc.*, 79, 2457–2476.
- Rust, W. D., D. R. MacGorman, and R. T. Arnold, (1981), Positive Cloud-to-Ground lightning flashes in severe storms, *Geophys. Res. Lett.*, 8, 791–794.
- Rutledge, S. A., D. R. MacGorman, (1988), Cloud-to-ground lightning activity in the 10–11 June 1985 Mesoscale Convective System observed during the Oklahoma-Kansas PRE-STORM Project, *Mon. Wea. Rev.*, 116, 1393–1408.
- Rutledge, S.A., E.R. Williams, and T.D. Kennan, (1992), The down under Doppler and electricity experiment (DUNDEE): Overview and preliminary results, *Bull. Am. Meteorol. Soc.*, 73, 3–16.
- Saunders, C. P. R., W. D. Keith, and R. P. Mitzeva, (1991), The effect of liquid water on thunderstorm charging, *J. Geophys. Res.*, 96, 11007–11017.
- Saunders, C.P.R., (1993), A review of thunderstorm electrification processes, *J. Appl. Meteor.*, 32, 642–655.
- Seimon, A., (1993), Anomalous cloud-to-ground lightning in an F5-tornado-producing supercell thunderstorm on 28 August 1990, *Bull. Amer. Meteor. Soc.*, 74, 189–203.
- Sheridan, S. C., J. H. Griffiths, and R. E. Orville, (1997), Warm season cloud-to-ground lightning-precipitation relationships in the South-Central United States, *Weather Forecast.*, 12, 449–458.
- Simpson, J., R. F. Adler, and G. R. North, (1986), On the tropical rainfall measuring mission (TRMM), *Meteor. Atmos. Phys.*, 60, 19–36.
- Soula, S., H. Sauvageot, G. Molinié, F. Mesnard, and S. Chauzy, (1998), The CG lightning activity of a storm causing a flash-flood, *Geophys. Res. Lett.*, 25(8), 1181–1184.
- Soula, S., and S. Chauzy, (2001), Some aspects of the correlation between lightning and rain activities in severe storms, *Atmos. Res.*, 56/1–4, 355–373.
- Stolzenburg, M., (1994), Observations of high ground flash densities of positive lightning in summertime thunderstorms, *Mon. Wea. Rev.*, 122, 1740–1750.
- Takahashi, T., (1978), Rimming electrification as a charge generation mechanism in thunderstorms, *J. Atmos. Sci.*, 35, 1536–1548.
- Takayabu, Y. N., (2006), Rain-yield per flash calculated from TRMM PR and LIS data and its relationship to the contribution of tall convective rain, *Geophys. Res. Lett.*, 33, L18705, doi:10.1029/2006GL027531.
- Tapia, A., J. A. Smith, and M. Dixon, (1998), Estimation of convective rainfall from lightning observations, *J. Appl. Meteor.*, 37, 1497–1509.

- Toracinta, E. R., D. J. Cecil, E. J. Zipser, and S. W. Nesbitt, (2002), Radar, passive microwave, and lightning characteristics of precipitating systems in the tropics, *Mon. Wea. Rev.*, 130, 802–824.
- Watson, A.I., R.E. López, and R.L. Holle, (1994), Diurnal cloud-to-ground lightning patterns in Arizona during the Southwest Monsoon, *Mon. Wea. Rev.*, 122, 1716–1725.
- Williams, E.R., and R.M. Lhermitte, (1983), Radar tests of the precipitation hypothesis for thunderstorm electrification, *J. Geophys. Res.*, 88, 10984–10992.
- Williams, E.R., M.E. Weber, and R.E. Orville, (1989), The relationship between lightning type and convective state of thunderclouds, *J. Geophys. Res.*, 94, 13213–13220.
- Williams, E.R., (1989), The tripole structure of thunderstorms, *J. Geophys. Res.*, 94, 13151–13167.
- Williams, E. R., S. A. Rutledge, S. G. Geotis, N. Renno, E. Rasmussen, and T. Rickenbach, (1992), A radar and electrical study of tropical “hot towers”, *J. Atmos. Sci.*, 49, 1386–1395.
- Williams, E., and S. Stanfill, (2002), The physical origin of the land–ocean contrast in lightning activity, *C. R. Physique*, 3, 1277–1292.
- Workman, E.J., and S.E. Reynolds, (1949), Electrical activity as related to thunderstorm cell growth, *Bull. Amer. Meteor. Soc.*, 30, 142–144.
- Zipser, E. J., (1994), Deep cumulonimbus cloud systems in the tropics with and without lightning, *Mon. Wea. Rev.*, 122, 1837–1851.
- Zipser, E. J., and K. R. Lutz, (1994), The vertical profile of radar reflectivity of convective cells: A strong indicator of storm intensity and lightning probability? *Mon. Weather Rev.*, 122, 1751–1759.

Chapter 21

Comparative Analysis of Flash and Radar Characteristics of Thunderstorm Cells

Ferenc Dombai

Abstract In the evening of 20 August 2006 a severe thunderstorm hit Budapest causing 4 people's death and leaving seven hundred people injured who were on the streets on the occasion of the traditional Constitution Day's fireworks which attract thousands of people every year. This entailed deep and detailed analysis of the weather conditions and the development of this thunderstorm, as well as of the operation of observational now casting systems of the Hungarian Meteorological Service (HMS). The investigation of radar and flash characteristics was made by interactive and automatic cell segmentation and tracking methods developed at HMS for comparative analysis. Both methods provide the following attributes for every radar cells with different dBZ thresholds: centre and maximum dBZ values and their coordinates, area, radar rainfall intensity, water production and total water. The centre, the maximum values of flash density and their coordinates, area, flash activity and total flash count for every flash cell with different flash density thresholds are also calculated. In the course of the comparative analysis the radar and flash characteristics of the thunderstorms of the 3 August 2006 were also computed. On this day the highest flash activity was observed in Hungary since the SAFIR type lightning location network is in operation. The authors are underlying the importance of using such methods in the operational practice of HMS.

Keywords Radar · Safir · Lightning · Flash cell · Radar cell · Cell identification · Cell development · Convective rain · Flash activity

21.1 Introduction

In the evening of 20 August 2006 severe thunderstorms had developed in a squall line coming from the northwest to Hungary. The northern part of this squall line reached Budapest at 19:00 UTC with an extremely intensive thunderstorm cell with more than 30 m/s wind gusts exactly at the same time when the traditional

F. Dombai (✉)

Hungarian Meteorological Service, Gilice tér 1. 1156, H-1181 Budapest, Hungary

e-mail: dombai.f@met.hu

Constitution Day's fireworks started and more than half million people crowded on the embankments and bridges of the Danube. Broken trees, fragments from the roof of houses hit the crowd and four people were killed and hundreds were injured. The weather conditions and the process of thunderstorm development of this fatal event were analyzed profoundly and reported by Horvath et al. (2007). Among these investigations the radar and lightning location information of these thunderstorms were also completed. In the current paper we present the results of the comparative analysis of weather radar and flash cell characteristics of thunderstorms of that day. Also we present the analysis of radar and flash data of the thunderstorms on 3 August 2005, a day with the highest flash activity values in Hungary according to the archive data of the Hungarian lightning location network.

The goal of the comparative analysis of radar and flash cells is to support the more effective use of the weather radar and the lightning location network which are the most suitable meteorological remote sensing tools for tracking thunderstorm activities, and to demonstrate the usefulness of cell identification and tracking methods. Using these methods we can make the most important steps towards the improvement of an analysis based on interpretation of entire radar and flash location images. Rather we deal with the identification of the objects provided by the images and attempt an analysis of the data related to these objects, which provide information on their movement and development in time and space. The objects referred to in this paper are radar and flash cells.

In our investigations two methods were implemented for radar and flash cell calculations: an interactive and an automatic method. Both methods use different radar reflectivity and flash density thresholds for calculating the cell characteristics. Using the interactive method we have to choose a specific area for a thunderstorm cell at each time step, and after this all calculations are performed automatically for the chosen cell. Within the automatic method all processes like the segmentation and the identification of radar and flash cells with different threshold values, and the cell characteristics calculations, are produced automatically. Both methods provide the following attributes for every radar cells with different dBZ thresholds: center and maximum dBZ values and their coordinates, area, radar rainfall intensity, water production, total water. Also, we calculate the center, maximum values of flash density and their coordinates, area, flash activity and total flash count for every flash cell with different flash density thresholds. For linking together the identified radar or flash cells on the subsequent time steps into cell chains for tracking their movements and developments, the absolute cell ID, parent cell ID, predecessor cell ID, and cell chain ID attributes were calculated for each cell having 35 and 45 dBZ, and 2 and 4 flash/km²; h thresholds values. The correct definitions of the used radar and flash cell attributes are given in Appendix.

21.2 Data Sets Used for Analysis

The data sets of our investigations were the archived data of the Hungarian weather radar network and the Hungarian lightning location network, SAFIR HMS. For

incorporating the SAFIR HMS data there was a need for a preparation work providing raster type flash data, which are well aligned in space and time with the radar data. The Hungarian weather radar network consists of three stations with dual polarization Doppler weather radars at Budapest (DWSR 2500C, 2000), Napkor (DWSR 2501C, 2002), and Poganyvar (2004, DWSR 2501C). The SAFIR HMS has been operating since 1998 (Dombai, 2008) and consists of 5 stations in Hungary and 2 stations in Slovakia, connected on-line to the central processor. All stations have SAFIR 3000 type sensors operating on VHF frequency band (114–118 MHz) for detecting cloud to cloud (IC) flashes, and an LF frequency band (0–800 kHz) for detecting cloud to ground (CG) flashes. The SAFIR HMS sensors use VHF interferometric receivers for making directional measurements of both IC and CG flashes.

21.2.1 Radar Data – Hungarian Weather Radar Network

The radar data used is a composite reflectivity data (OHD type) which is an output of the Hungarian weather radar network with national coverage and built up from the 15 min the CMAX products of single radars. CMAX means that each pixel contains the maximum dBZ values from the scanned vertical volume column. It is a standard product from the EDGE software of the DWSR 2501 type EEC radars, available after completion of the volume scans. In our case the volume scan uses 9 different elevations (0, 0.5, 1.1, 1.8, 2.7, 3.8, 5.1, 6.6, 8.5) and 240 km measurement range. The OHD national coverage built up from radar's CMAX is a 400 by 250 rectangular field with approximately 2×2 km resolution in stereographic projection. The corner points of the national radar coverage are: N49.2736 / E14.0306 ; N49.1848 / E24.2548; N45.1812 / E14.2712 ; N45.1030 / E23.4642. The dBZ values range from -15 dBZ to +63 dBZ with a resolution of 0.5 dBZ.

21.2.2 Flash Data – SAFIR HMS

In this work we used so-called T\$ type lightning location data from the archived files provided by the central processing software of the SAFIR HMS, containing location and time for IC and CG flashes. According to the SAFIR documentation the T\$ files contain the following data for each localization of a flash: event time with 100 μ s resolution, x and y coordinates of the location points with 100 m resolution on the specific SAFIR HMS projection having a central point at N47:00' and E18:30' and a North-oriented y axis, event type with 6 categories (0 – separate IC flash, 1 – start, 2 – middle, 3 – ending point of IC source chain, 4 – negative CG, 5 – positive CG flash). Due to dead time limitations, SAFIR HMS can provide a maximum of 100 source points per second.

21.2.3 Alignment of RADAR and SAFIR HMS Data in Space and In Time

For a correct combined analysis it is necessary to use radar and flash data precisely aligned in time and space. There are different methods for providing raster type flash data or images. Some of them use statistical calculations providing cluster attributes of groups of flashes and visualization (Kononov and Yusupov, 2004; Tuomi, 2004). Others use a Gauss filter for providing smooth raster type flash data (Steinacker et al., 2000). These methods are typically used for the analysis of LF measurements providing relatively few CG flash data. For the VHF measurements of LDAR system the VAISALA introduced the “connect the dots” and the FED – Flash Extent Density algorithms which can be jointly used for providing raster type flash data (Demetriadis and Lojou, 2008). Although we made many efforts to enhance the location accuracy of the SAFIR HMS using recalculation of the azimuth correction files (Dombai, 2008) the typical localization accuracy is still 3–5 km, which is about two times more than the pixel resolution of our national radar composite. Taking into account this fact and having found the optimum in calculations for the comparative analysis of radar and flash data we have produced flash density images from the location data of T\$ files which have the same structures, geographical references and time steps as the OHD radar date images. For transforming x and y coordinate values of IC and CG flashes into latitude and longitude values we used formulas described in a SAFIR instrument documentation. In our case the OHD radar data time stamp is equal to the starting time of the scanning procedures although the radar takes about 5–6 min for a volume scan with 15 min repetition time. When flash density images were calculated we used a time window – in our case 10 min – placed symmetrically on the radar data time stamp. In this time window all the IC flash location data were transformed and integrated in OHD pixels. Finally the integrated flash data was normalized providing raster type flash density data with $1 \text{ km}^2/\text{h}$ measures. Before the cell identification processes all standalone pixels of flash density images were filtered out.

21.3 Interactive Method for Calculating Statistics and Tracking of Cells

This method consists of displaying the radar reflectivity and flash density images in the same projection, and time steps using different reflectivity and flash density thresholds. By alternating the consecutive time steps we are able to depict radar and flash cells. After visual selection of a cell, the software allows to use the cursor for cell identification and processing. When the cells are marked, the calculation of the different meteorological characteristics will proceed. It is possible to select one or more cells at the same time. This process represents the cell statistics calculation. In subsequent steps, one can change the time step and mark again the cells, which are assumed to be the successor cells of the ones selected previously. After the cell

statistics calculation, speed and direction of the displacements will be calculated for the same time step.

Although in this method the linking of cells to an evolving chain will remain a matter of subjective decision, the tracking of radar or flash cell movement and development with different time scales and thresholds can be realized in this simply way. In addition, subsequent analysis of radar and flash data can be executed. We demonstrate the usefulness of this interactive method by analyzing the radar and flash characteristics of the fatal Constitution Day's thunderstorm in Hungary on the 20 August 2006, which caused four casualties in Budapest.

21.3.1 Radar and Flash Characteristics of Thunderstorms on 20 August 2006 in Hungary

More specific and detailed characteristics could be derived from the behavior of thunderstorms cells, but cell identification and tracking is not a part of the original operational tools of HMS. Therefore, we have developed specific software for calculating cell parameters and radar and flash characteristics for thunderstorm cells. This software provides minimum and maximum values of dBZ, rainfall intensity and water content of radar cells for different reflectivity thresholds and specific areas around center points. The number and the maximum density of flashes, areas, and center points are also calculated with different density thresholds for flash cells. Altogether, on 20 August 2006 nine radar cells and five flash cells were identified and tracked in time slots of 15 min. The tracked radar cells and their main parameters are shown in Fig. 21.1, using 35 dBZ cell contours. The main calculated parameters and figures are shown in Table 21.1 for radar cells and in Table 21.2 for flash cells. The cell ID used in the figures and in tables mark the same thunderstorm cells. The development of the water and flash production in 15 min time slots are shown for each tracked convective cells in Figs. 21.2 and 21.3.

In Table 21.3 we show the development of thunderstorm cell #3, which hit BUDAPEST, along with the corresponding main radar and flash characteristics.

From the radar and the flash characteristics of tracked cells we can derive the following main features of cell development of thunderstorms on 20 August 2006:

- All day there was rapid eastward movement of cells. The velocity was increasing from 40 km/h (cell #1, at noon) to 97 km/h (cell #2, late evening) the direction was turning slowly to north. Most of the thunderstorms were composed of 2 or more convective cells.
- The strongest thunderstorm of that day (cell #2) developed in the southeastern region causing the maximum flash at 21:15 UTC and water at 22:15 UTC.
- The total water production was 94 million m³ and the max reflectivity 58.5 dBZ and the max area 9000 km².
- The most dangerous thunderstorm (cell #3) causing 4 casualties in Budapest was moving almost constantly eastward with 82 km/h velocity for a relatively long

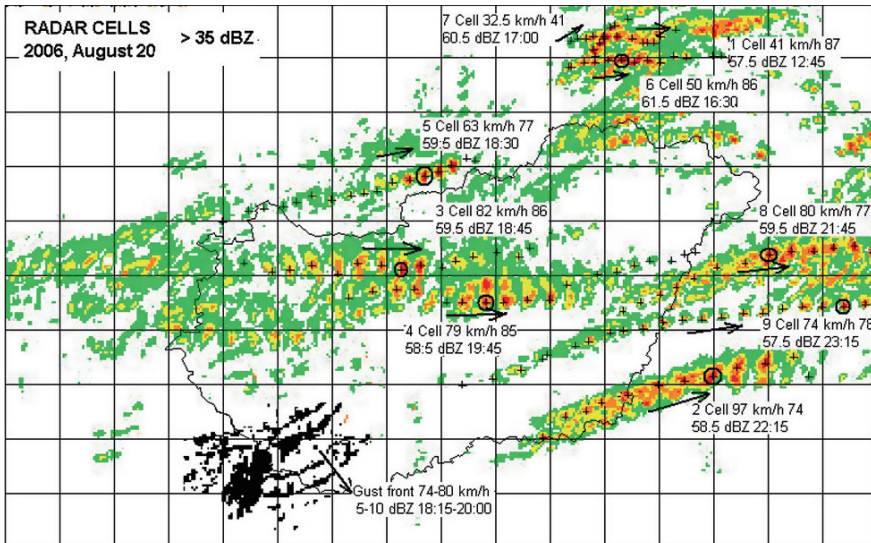


Fig. 21.1 Tracked radar cells in 15 min patterns with a 35 dBZ threshold on 20 August 2006. The main parameters are shown in boxes: cell ID, mean velocities and directions, maximum reflectivity, and time of occurrence. The radar cell with ID 3 hit Budapest. The grid size is 50 km (See also Plate 38 in the Color Plate Section on page 621)

Table 21.1 Radar characteristics of thunderstorm cells for 20 August 2006

	Max Ref.	Time of occ.	Max Area	Total Water	Mean Velocity	Mean Direction	Max Area	Max Water Production.
Thres h.			15 dBZ	15 dBZ	35 dBZ	35 dBZ	35 dBZ	35 dBZ
Cell ID	dBZ		km ²	mill. m ³	km/h	deg	Km ²	mill. m ³ /h
1	57.5	12:45	788	21.9	40.7	86.8	428	13.7
2	58.5	22:15	9062	93.4	96.7	74.3	1404	44.4
3	59.5	18:45	2596	49.0	82.2	85.5	860	24.8
4	58.5	19:45	1153	50.9	78.5	84.3	738	30.1
5	59.5	18:30	805	23.0	62.7	76.9	689	13.6
6	61.5	16:30	759	26.2	50.1	86.0	496	19.0
7	60.5	17:00	532	14.7	32.5	41.2	280	12.2
8	59.5	21:45	2346	46.5	80.3	76.7	810	26.4
9	57.5	23:15	865	27.6	73.8	77.5	349	10.1

Table 21.2 Lightning characteristics of thunderstorm cells on 20 August 2006

	Max Flash Density	Time of occ.	Max Area	Total Flash	Mean Velocity	Mean Direction	Max Area	Max Flash Activity.
Thresh.			1 /km ² h	2 /km ² h				
Cell ID								
2	28	21:15	1100	5187	96.6	92.4	668	5280
3	15	18:30	354	1313	81.7	86.7	216	1290
4	16	19:45	116	1156	91.6	106.0	64	560
5	12	18:15	176	429	62.0	71.6	76	492

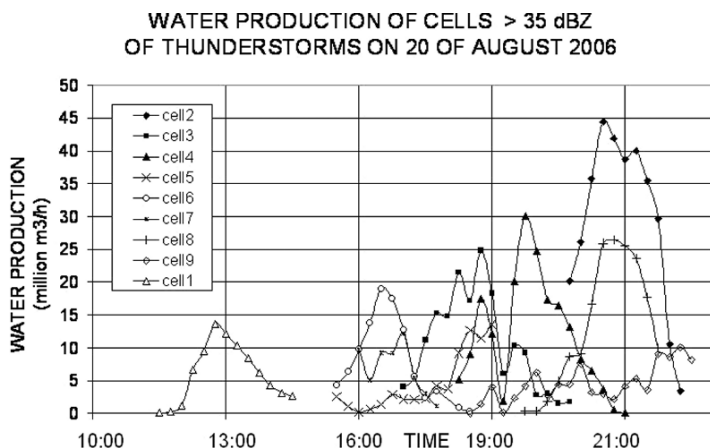


Fig. 21.2 Development of the water production in 15 min time intervals for each thunderstorm cell tracked on 20 August 2006

time. The cell reached its maximum developed phase at 18:45 with 59.5 dBZ. This cell caused a break in communication links of SAFIR HMS at 19:00 and almost total screening of the C band radar and the stop of METEOSAT image-reception at 19:15 in Budapest. This thunderstorm produced about 49 million m³ water in an area of 2500 km², composed of 2 to 3 cells when it reached its maximum intensity.

- The Budapest cells originated from strong convection development late afternoon in western Hungary. This development caused a rapidly (with about 74–80 km/h)

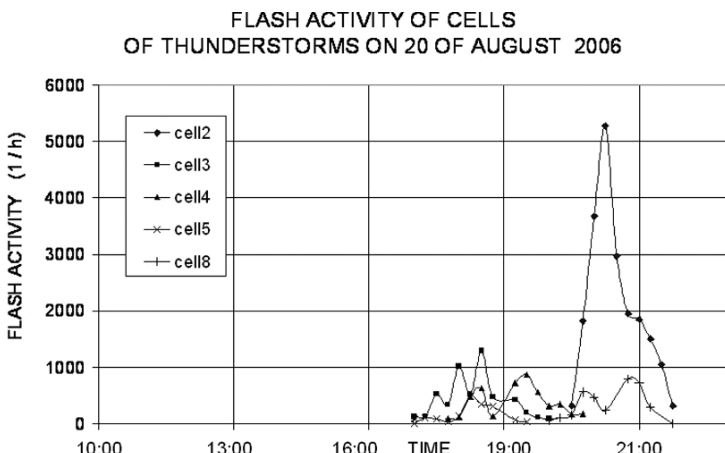


Fig. 21.3 Development of the flash activity in 15 min time intervals for each thunderstorm cells tracked on 20 August 2006

Table 21.3 Radar and flash characteristics of BUDAPEST thunderstorm cell on 20 August 2006, using 35 dBZ and 2 /km² h threshold values

Time	RADAR				FLASH			
	Max Reflectiv. dBZ	Velocity Km/h	Direction deg	Area km ²	Max Flash Density 1/km ² h	Velocity km/h	Direction deg	Area km ²
17:00	43.0	0	0	388	6	0	0	60
17:15	50.5	83	82	268	4	172	123	102
17:30	52.5	79	90	538	7	88	85	276
17:45	52.5	86	87	648	4	92	71	196
18:00	53.5	89	75	648	10	144	99	444
18:15	55.5	77	89	780	9	28	146	274
18:30	55.0	74	101	802	15	80	85	354
18:45	59.5	76	84	860	7	64	76	188
19:00	57.0	81	93	598	SAFIR HMS STOPPED			
19:15	46.5	SHADOWING		620	10	152	96	188
19:30	50.5	81	33	548	7	80	126	88
19:45	48.5	69	61	656	6	68	55	60
20:00	44.0	67	98	258	6	52	116	44
20:15	48.5	84	92	234				

moving gust front to the southeast with 5–10 dBZ reflectivity values. The gust front was observable for as long as 1.5 hour by the Poganyvar C band radar.

- There was a very interesting cell development late afternoon in the northeast region. From the eastwardly moving cell #6 a new cell was separated (marked with #7) and moved with a new direction, 45 degree to the north compared to the cell #7 direction. The velocity of cell #6 was 50 km/h, but 32 km/h for cell #7.
- Not all radar cells reaching higher radar reflectivity values than 55 dBZ were followed by observable flash activities. For all day there was no flash activity as large as on 3 August 2005, as was stated earlier.
- It was observed for all cells that the maximum flash activity preceded the maximum radar reflectivity and water production by 15–45 min.
- It was found for all cells that their displacement velocities and directions were almost constant or changed very slowly, causing straight line tracks or smoothed big curves, enabling quite precise forecasts for 2–3 hours ahead.

21.3.2 Relationship Between Water Production and Flash Activity of Thunderstorm Cells on 20 August 2006 in Hungary

As demonstrated in the previous section, the interactive method of cell identification and tracking gives a possibility for a comparative analysis of radar and flash characteristics of thunderstorm cells. Among these characteristics water production and flash activity are very important for hydrological purposes. There are many

publications dealing with the relationship between the two quantities, but the reported results are diverging. They depend on regions and seasons as well as on other influencing factors. When the fatal thunderstorm day in Hungary was analysed deeper, we searched also for a comparative analysis in order to find a relationship between the water production and the flash activity of the thunderstorm cells.

After cell segmentation and calculation of cell characteristics we collected the 15 min water production and flash activity values of all thunderstorm cells during that day and calculated the correlation between these values, using different time delays between the connected values.

At first we assumed a linear correlation between the 15 min water production as a dependent variable (y – axis values) and flash activity (x – axis values) of the thunderstorm cells and calculated the line fitting parameters ($y = M * x + B$) with the residual sum of squares of errors (H). Parameters in the calculations were 0, 15, and 30 min time shift. The results are shown in Table 21.4. For each thunderstorm cell the closest correlation has been found between the flash activity and the 15 min shifted water production values. It can also be seen from Table 21.4 that the correlation-parameters are diverging from cell to cell even on the same day.

By taking into account the total water production of thunderstorm cells which are shown in Table 21.1, further analysis reveals a relationship between the fitting parameters and the total water production values. It shows an exponential dependence between the 15-min water production values and the flash activity values of thunderstorm cells. Figure 21.4 shows all 15-min flash activity and the 0 and 15 min shifted water production values in a logarithmic scale.

From Fig. 21.4 we can see that the relationship between the logarithmic values of the flash activity and water production can be described by a linear relationship. For this case the parameters of the line fitting were calculated for different time delays and are shown in Table 21.5.

The closest relationship was found for a shift of 15 min between lightning and water production; the corresponding line fitting parameters are $M = 1.87$ and $B = -3.12$ for the thunderstorm cells on 20 August 2006.

Table 21.4 The parameters of the line fitting between the 15-min water production and flash activity of cells of thunderstorms on 20 August 2006

	Cell #2	Cell #3	Cell #4	Cell #5	Cell #8
M	0.294	10,236	1,152	19,633	29,514
B	34,032	7,903	16,032	1,711	2,633
$H (+ 00)$	8,447	6,111	7,321	2,199	7,719
$M (+ 15)$	4,955	16,694	20,645	23,377	24,059
$B (+ 15)$	22,384	4,993	7,717	2,176	6,521
$H (+ 15)$	7,765	3,767	4,358	2,142	7,414
$M (+ 30)$	7,255	10,556	20,509	19,079	20,148
$B (+ 30)$	14,646	7,381	7,553	4,302	8,884
$H (+ 30)$	10,125	6,651	4,926	3,896	6,809

**WATER PRODUCTION AND FLASH ACTIVITY OF CELLS
OF THUNDERSTORMS ON 20 OF AUGUST 2006**

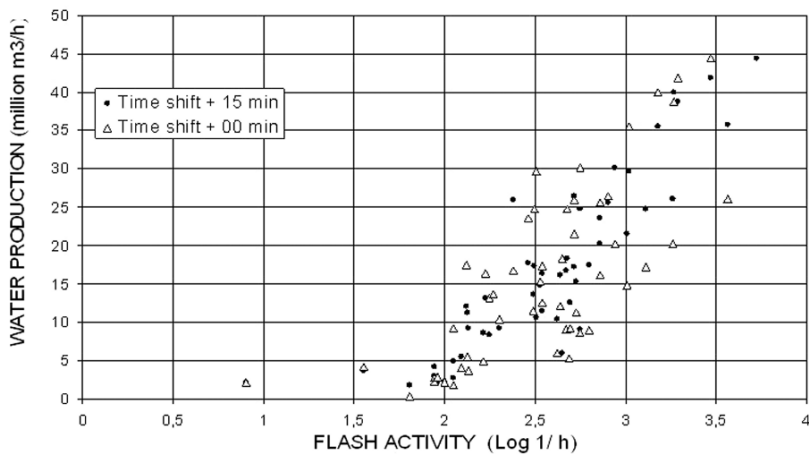


Fig. 21.4 Correlation of the 15 min values of the logarithm of flash activity and water production shifted in time of thunderstorm cells on 20 August 2006

Table 21.5 The linear fitting parameters of the relationship between the logarithm of flash activity and water production shifted in time for thunderstorm cells on 20 August 2006

	Time + 00	Time + 15	Time + 30
M	1,67	1,87	1,70
B	-2,65	-3,12	-2,69

21.4 Automatic Method for Computing Radar and Flash Characteristics of Thunderstorm Cells

The results and the experiences of the interactive identification and calculation of characteristics of thunderstorm cells applied for the detailed post analysis of the fatal thunderstorms of 20 August 2006 show the usefulness of continuously accessible cell data for forecasters, whereby the understanding of the complex meteorological situation is extremely important for arriving at the right decisions concerning alarms or warning of the public. The experiences show also that although the interactive method was useful as post analysis, it has serious drawbacks for real-time conditions. There is a need for an automatic method for real time applications. At the Hungarian Meteorological Service some efforts had been made to develop automatic procedures for cell identification and tracking in earlier periods using methods similar to TITAN (Dixon and Weiner, 1993), but none of those developments were completed. Using these experiences we have developed a robust method for automatic segmentation, calculation of cell characteristics and tracking. We applied multi level thresholds for segmentation and identification of the radar reflectivity and the flash density data fields.

The developed automatic method needs to perform the following steps:

- Building up the cell mask fields using the thresholds. This field contains the value 1 if data in the pixel is above the threshold, and the value 0 in other cases. This procedure is performed for each time step.
- Searching for continuous areas of pixels in the mask field, which will represent the cells. The area of the cells is calculated and ordered by area, and an ID number is assigned, which will be written into the cell mask field. This ID is valid locally, and is only valid for a given time step and threshold.
- Using the local ID we calculate the different radar and flash characteristics for each cells
- The procedures mentioned above are completed for each threshold and time step, and also for radar reflectivity and flash density data fields. During these calculations every cell will be marked with absolute cell ID, and using this ID the table characteristic for the cell is built up.
- When all calculations during a time step are completed, the search for the parent and predecessor cells starts. To find the predecessor cells we use the minimum distance, which can be calculated between the given cell centre and the all centres of cells of the previous time step with the same category. Of course some limitations are introduced because this method works well only if the typical distance between the cells is bigger than the displacements of the cells between the time steps.
- By using the predecessor cell ID we calculate the directions and displacements of the cells, search for chains of cells and mark the cells with the Chain ID.
- Finally we calculate aggregated characteristics for each time step, for example number of cells at each thresholds, total areas, water production, flash activity, etc.

21.4.1 Radar and Flash Characteristics of Thunderstorms on 3 August 2005 in Hungary

The results of the automatic cell identification method are demonstrated in Fig. 21.5 for the flash cells of the SAFIR HMS data, and in Fig. 21.6 for the radar cell data of the national composite of HMS weather radar network on 3 August 2005 which proved to be the most prominent 10 years-record of flash activity measured by SAFIR HMS. Figures 21.5 and 21.6 show two time steps at 20:15 UTC and 20:30 UTC. The cell characteristics, valid for radar and flash cells shown in Figs. 21.5 and 21.6, are gathered into Tables 21.6 and 21.7. Using these tables we are able to follow the cell development and movement following the absolute cell ID, which can be found in the columns with parent, predecessor, and cell chain headings. The daily course of the aggregated cell statistics is shown in Tables 21.8 and 21.9. In these tables the cell characteristics valid for the demonstrated time steps are also given.

From Tables 21.8 and 21.9 we can see that the number of flash and radar cells with lower threshold – 2 flash/km² h and 35 dBZ respectively – are close together

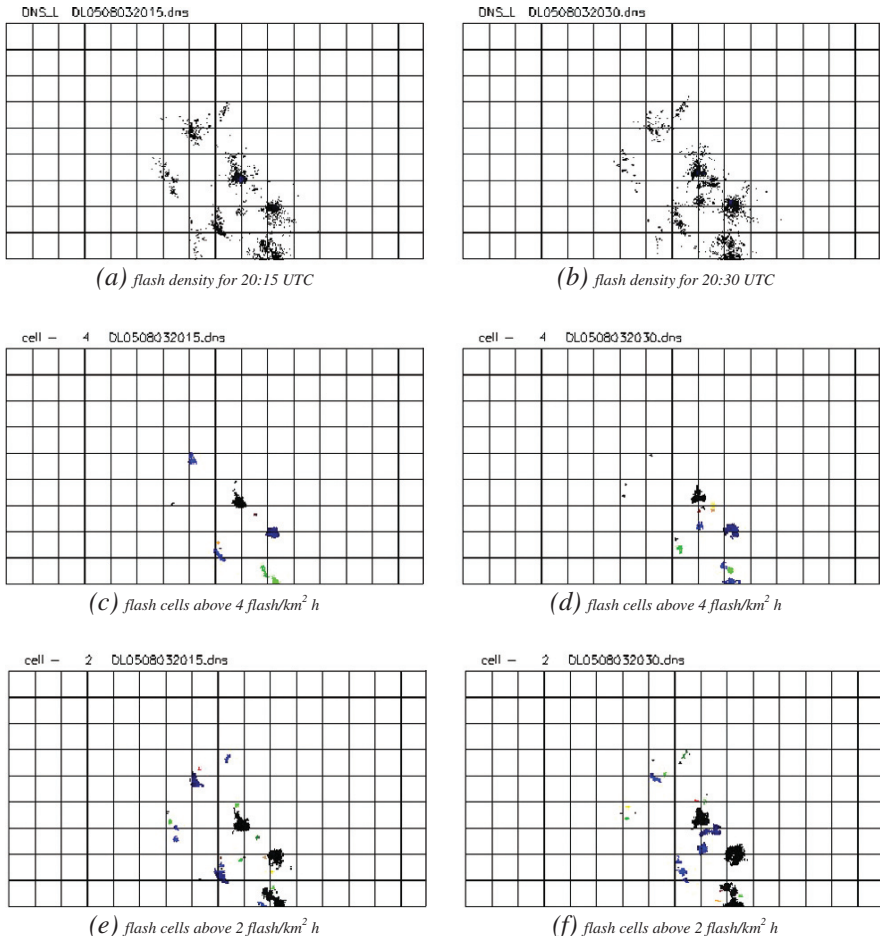


Fig. 21.5 Flash cell products of the automatic cell identification applied for SAFIR HMS data on 3 August 2005 for two subsequent time steps 20:15 UTC (left panels) and 20:30 UTC (right panels). The colours represent the relative cell ID

and the area of the radar cells are typically two times larger than the area of flash cells. It is clearly shown that at the middle thresholds – 4 flash/km² h and 45 dBZ respectively – although the number of the flash and radar cells is almost the same, the area of the flash cells are much higher than the area of the radar cells. At even higher thresholds – 8 flash/km² h and 55 dBZ, respectively – the radar cells have almost disappeared but the area of flash cells is almost the same as the area of flash cells for middle thresholds. We can state on the basis of this analysis of flash and radar cell characteristics that the flash activity record on 3 August 2005 was not a consequence of many big and strong thunderstorms, but was a consequence of the special meteorological conditions, which were very favorable for convection and corresponding charge separation.

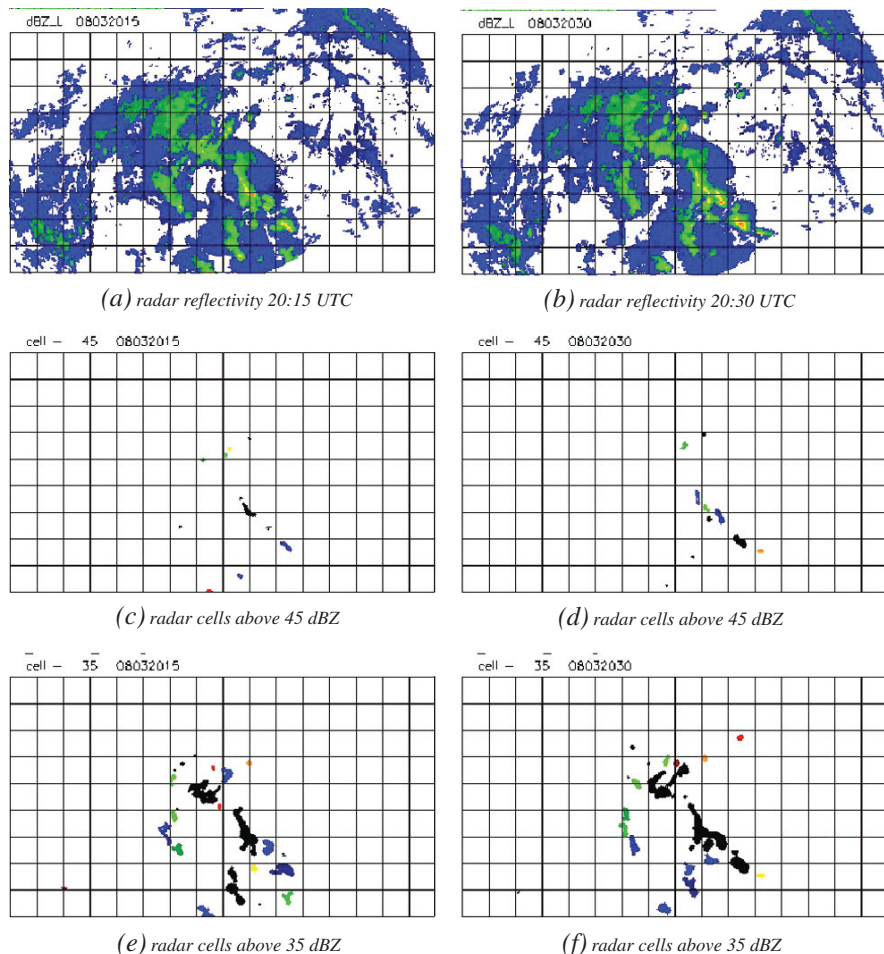


Fig. 21.6 Radar cell products of the automatic cell identification applied for SAFIR HMS data on 3 August 2005 for two subsequent time steps 20:15 UTC (left panels) and 20:30 UTC (right panels). Remark: The colors represent the cell ID valid for a given time step and thresholds only (See also Plate 39 in the Color Plate Section on page 622)

21.4.2 Comparative Analysis of Radar and Flash Characteristics of the Thunderstorms on 3 August 2005 and 20 August 2006

According to our archive of SAFIR HMS data the most active thunderstorm day was the 3 August 2005 when more than 240,000 IC flashes and more than 40,000 CG return strokes were detected. Using the automatic method we performed a comparative analysis of flash and radar activities of the thunderstorms on 3 August 2005 and 20 August 2006, which had thunderstorms resulting in casualties on the celebration day of the constitution of Hungary. The daily course of the flash activity of the cells

Table 21.6 Flash characteristics of the thunderstorm cells on 3 August 2005 at 20:15 UTC and at 20:30 UTC for flash cells with threshold of 4 flash/km² h

Abs. ID	Pred. ID	Chain ID	Rel. ID	Parent cell	Area km ²	Flash activ.	Cent.x	Cent.y	Max. Flash Dens.	Max. x	Max. y	Disp.	Azim.
TIME 20:15 UTC													
818	760	71	1	1	496	9228	223	79	90	228	77	5.8	59
819	765	75	2	2	408	3660	256	49	30	260	51	4.1	76
820	763	54	3	5	240	2172	178	120	15	183	118	6.7	26
821	761	70	4	4	216	2244	204	28	33	204	31	4.2	135
822	764	73	5	3	148	1164	247	12	27	248	15	6.0	90
823	762	72	6	3	128	828	258	4	18	260	3	8.0	90
824	761	76	7	9	44	204	203	40	6	205	41	9.2	12
825	0	80	8	11	32	372	239	67	15	240	67	0.0	0
826	771	69	9	10	16	348	160	77	24	161	78	6.3	71
827	0	10	14	16	72	220	98	9	220	98	0.0	0	0
828	760	77	11	0	12	36	218	91	12	219	92	15.0	0
829	761	78	12	4	8	0	205	35	6	206	35	5.7	45
830	771	79	13	8	0	161	64	6	161	65	13.0	147	
TIME 20:30 UTC													
869	818	71	1	0	532	6792	225	85	78	232	83	6.3	18
870	819	75	2	1	528	5676	258	52	54	257	56	3.6	33
871	823	72	3	2	212	1524	257	3	30	254	4	1.4	225
872	825	80	4	5	152	1440	227	56	24	228	57	16.3	227
873	822	73	5	2	136	1032	249	18	21	251	20	6.3	18
874	829	78	6	6	116	816	208	34	21	210	36	3.2	108
875	822	81	7	2	104	864	256	14	33	257	13	9.2	77
876	825	82	8	1	76	804	240	76	27	241	77	9.1	6
877	825	83	9	4	32	156	239	71	15	239	72	4.0	0
878	818	84	10	1	32	300	226	70	18	227	71	9.5	161
879	818	85	11	4	32	168	230	73	12	231	74	9.2	130
880	824	76	12	8	24	204	43	12	206	44	3.2	18	
881	826	69	13	11	24	456	154	85	24	154	86	10.0	-36
882	820	54	14	7	24	132	180	123	9	181	124	3.6	33
883	819	86	15	1	16	24	249	52	6	250	53	7.6	-66
884	826	87	16	15	16	228	156	96	12	157	96	19.4	-11
885	819	88	17	1	8	24	258	42	12	259	42	7.3	164

Remark: The correct understanding of headings is given in Appendix.

Table 21.7 Radar characteristics of the thunderstorm cells on 3 August 2005 at 20:15 UTC and 20:30 UTC for radar cells with threshold of 45 dBZ

Abs. ID	Pred. ID	Chain ID	Rel. ID	Parent cell	Area	Wat. Prod	Cent. x	Cent. y	Max. dBZ	Max. x	Max. y	Disp.	Azim.
TIME 20:15 UTC													
1_206	1171	17	1	1	296	8,26	224	77	51	230	75	7,3	15
1_207	1172	31	2	4	212	6,46	260	44	52,5	263	42	3,6	56
1_208	1178	30	3	3	84	1,85	216	16	46,5	218	17	11,2	100
1_209	1173	13	4	2	60	0,99	182	125	45,5	183	126	14,2	50
1_210	1175	26	5	7	56	0,97	203	130	46,5	204	131	5,1	11
1_211	1175	32	6	7	52	1,23	207	135	49,0	208	135	11,2	26
1_212	0	37	7	8	44	0,89	187	2	49,0	188	2	0,0	0
1_213	0	35	8	6	36	0,20	243	61	46,0	244	62	0,0	0
1_214	1177	33	9	14	28	0,41	225	145	45,0	226	146	4,1	14
1_215	0	0	10	9	24	0,43	160	62	46,0	161	63	0,0	0
1_216	1171	34	11	1	24	0,47	217	89	46,0	218	90	19,6	-14
1_217	1176	29	12	2	16	0,20	182	114	45,0	183	115	6,4	51
TIME 20:30 UTC													
1_244	1207	31	1	3	384	11,68	261	48	53,0	265	48	4,1	14
1_245	1213	35	2	1	292	8,14	242	72	55,5	245	69	11,0	-5
1_246	1216	34	3	1	184	2,92	221	90	48,5	222	95	4,1	76
1_247	1211	32	4	2	124	3,38	209	138	51,5	210	140	3,6	33
1_248	1206	17	5	1	112	2,57	230	79	48,5	232	79	6,3	71
1_249	0	40	6	13	88	2,09	281	39	50,0	283	40	0,0	0
1_250	1206	36	7	1	88	2,17	232	69	49,0	233	70	11,3	135
1_251	1214	33	8	14	56	1,57	227	149	51,5	228	150	4,5	26
1_252	1212	37	9	6	24	0,43	193	7	47,0	194	8	7,8	50
1_253	1208	30	10	4	24	0,46	217	34	46,5	218	34	18,0	3
1_254	1211	38	11	16	20	0,23	202	146	47,5	203	146	12,1	-24

Remark: The correct understanding of headings is given in Appendix.

Table 21.8 Evolution of the aggregated flash characteristics of the thunderstorm cells on 3 August 2005 between 18:00 and 21:45 UTC

Time	Number of cells		Max Flash Dens.		Cell cat. 2		Cell cat. 4		Cell cat. 8	
	Cat.2	Cat.4	Cat.8	1/km ² h	Area	Flash act.	Area	Flash act.	Area	Flash act.
18:00	7	3	3	45	760	5 220	356	3 840	164	2 268
18:15	5	3	2	90	556	8 628	332	7 524	260	6 960
18:30	8	2	2	90	1 064	13 452	644	11 880	484	10 896
18:45	9	4	4	69	1 244	16 812	808	14 724	592	13 368
19:00	13	6	3	117	1 964	19 452	996	16 020	704	13 452
19:15	17	11	6	69	1 924	16 044	912	12 384	552	9 756
19:30	24	9	7	93	2 116	17 292	1 000	13 728	520	10 596
19:45	27	11	5	42	2 052	12 216	744	8 064	340	5 484
20:00	28	12	14	75	3 600	29 616	1 708	22 392	1 052	17 580
20:15	32	13	8	90	3 800	27 456	1 772	20 328	1 100	15 864
20:30	30	17	13	78	4 572	29 952	2 064	20 640	1 112	14 592
20:45	27	12	6	72	5 112	45 024	2 956	37 524	1 932	29 616
21:00	34	17	13	87	5 168	39 156	2 496	30 180	1 528	23 988
21:15	35	13	17	69	7 100	50 904	3 468	38 604	2 092	29 436
21:30	32	18	10	36	5 792	39 408	2 784	29 220	1 560	21 540
21:45	25	21	18	51	8 180	58 152	4 308	44 424	2 464	32 520

Remark: The correct understanding of headings is given in Appendix.

Table 21.9 Development of the aggregated radar characteristics of the thunderstorm cells on 3 August 2005 between 18:00 and 21:45 UTC

Time	Number of cells			Max Reflect.			Cell cat35			Cell cat45			Cell cat55		
	Cat35	Cat45	Cat55	dBZ	Area	Water prod	Area	Water prod	Area	Water prod	Area	Water prod	Area	Water prod	
18:00	19	2	0	49,0	3316	28,1	264	6,3	0	0	0	0	0	0	
18:15	25	2	0	52,5	3332	31,3	368	10,3	0	0	0	0	0	0	
18:30	28	4	0	52,5	4684	46,0	508	14,8	0	0	0	0	0	0	
18:45	39	8	0	54,5	5780	65,5	964	26,0	0	0	0	0	0	0	
19:00	33	9	0	54,5	6884	74,5	832	24,3	0	0	0	0	0	0	
19:15	37	4	0	54,5	7200	78,2	1016	29,2	0	0	0	0	0	0	
19:30	42	10	0	52,5	7664	73,2	780	17,3	0	0	0	0	0	0	
19:45	32	7	0	53,0	6264	52,7	484	9,8	0	0	0	0	0	0	
20:00	29	8	0	51,0	8420	81,0	692	15,8	0	0	0	0	0	0	
20:15	27	0	52,5	8 208	78,1	932	22,4	0	0	0	0	0	0	0	
20:30	26	11	0	54,5	9 064	100,0	1 396	35,6	0	0	0	0	0	0	
20:45	34	10	1	56,5	9728	102,8	1252	33,2	40	40	2,62	0	0	0	
21:00	33	4	0	47,0	6464	45,3	176	3,5	0	0	0	0	0	0	
21:15	33	4	0	47,0	6464	45,3	176	3,5	0	0	0	0	0	0	
21:30	34	10	0	54,0	12424	147,9	2120	62,2	0	0	0	0	0	0	
21:45	18	10	0	53,0	12796	167,7	2944	76,3	0	0	0	0	0	0	

Remark: The correct understanding of headings is given in Appendix.

**INTEGRATED FLASH ACTIVITY FOR FLASH CELLS
CATEGORIES FOR 03 AUG 2005 AND 20 AUG 2006**

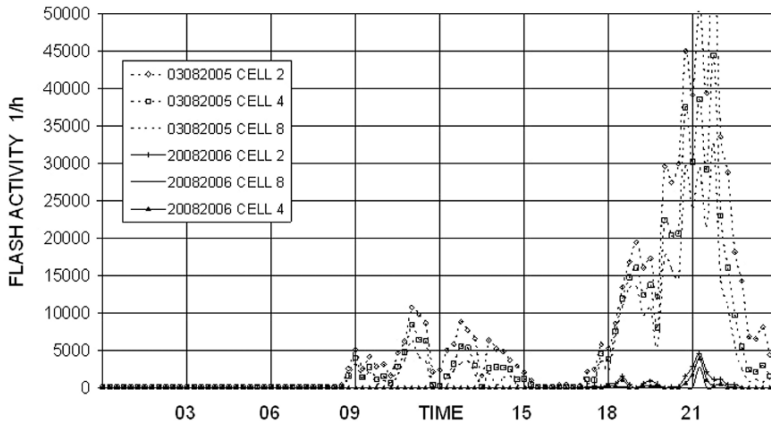


Fig. 21.7 Daily course of the aggregated flash activity based on the automatic cell identification for thunderstorms on 3 August 2005 and 20 August 2006

with different thresholds is shown in Fig. 21.7 and the daily course of the water production of the cells with different thresholds is shown in Fig. 21.8.

In view of these radar and flash characteristics the thunderstorms that had developed on 20 August 2006 did not exhibit any unique or extreme nature. There were more active thunderstorms in 2006 on 7 days in June (29, 30, 22, 27, 23, 28, 20) and on 9 days in July (29, 22, 12, 9, 13, 8, 14, 21, 23) and on 3 days in August (3,

**INTEGRATED WATER PRODUCTION OF RADAR CELL
CATEGORIES FOR 3 AUG 2005 AND 20 AUG 2006**

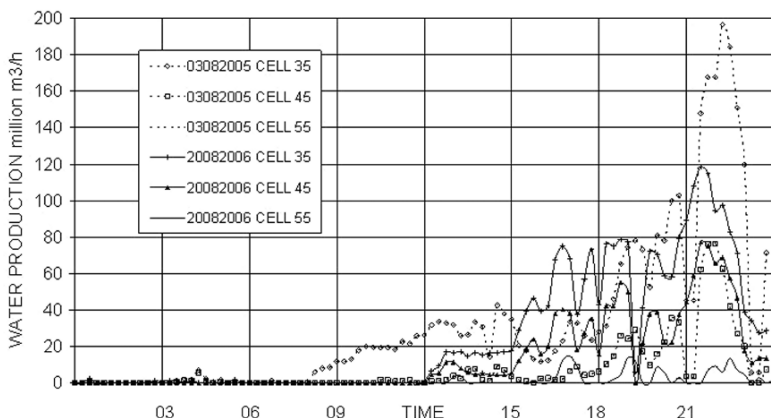


Fig. 21.8 Daily course of the aggregated water production based on the automatic cell identification for thunderstorms on 3 August 2005 and 20 August 2006

25, 1). Stronger thunderstorms were also observed in 2005 on 4 days in June and on 11 days in July, and on 7 days in August. The total amount of flashes and water produced by 20 August 2006 thunderstorms can be counted as typical in summer seasons in Hungary.

Table 21.10 shows that the electrical activity on 3 August 2005 was extremely high compared to that on 20 August 2006; the amount of IC flashes was 17 times higher and the number of CG flashes 42 times higher. The maximum flash density calculated for 15 min time slots was about 5 times higher, and the area with flashes about 9 times larger for 3 August 2005 than for 20 August 2006.

Table 21.10 General flash characteristics for 3 August 2005 and 20 August 2006

Date	Daily total			Maximum (15 min)		
	Localization	IC Flash	CG Flash	Density 1/km ² *h	Area km ²	Flashes
20050803	532375	242301	40405	34,5	17552	28808
20060820	28270	14580	964	7,5	3656	3170
Ratio	18,8	16,6	41,9	4,6	4,8	9,1

The measured radar reflectivity or the calculated water production values do not show as big differences as observed for electrical activity (see Table 21.11). The ratio of the total amount of water and the maximum area of rainfall and the water production in 15 min time slots are little more than 2 times higher on 3 August 2005 than on 20 August 2006. But the same values calculated for intense convective cells (>45 dBZ) show opposite results, telling us that the strong convective activity was the specific feature of 20 August 2006 thunderstorms. It is interesting to note that the same relation was not observable in the electrical activities.

Table 21.11 General radar characteristics for 3 August 2005 and for 20 August 2006

Date	Daily total			Maximum (15 min)			
	Water >15 dBZ million m ³	Water >45 dBZ million m ³	Mean Rainfall mm/h	Reflect. dBZ	Area >15 km ²	Water >15 dBZ million m ³	Water >45 dBZ million m ³
20050803	2040,1	44,8	1,83	57,0	98924	350,0	28,0
20060820	915,9	112,1	2,97	59,5	38940	150,0	33,0
Ratio	2,2	0,4	0,6	-2,5	2,5	2,3	0,8

21.5 Conclusions

The presented results from a comparative analysis of radar and flash characteristics of thunderstorms on 3 August 2005 and 20 August 2006 realized by interactive and automatic radar and flash cell segmentation, identification and tracking methods using multilevel thresholds, show the usefulness and the importance of radar and flash cell parameters and tracking calculations for forecasting thunderstorm developments. At the same time they underline the importance of the development

of such methods and processing tools for operational use at the Hungarian Meteorological Service. Only an analysis completed on the level of cells can provide reliable and invaluable data on thunderstorm cells useful for nowcasting and alarming purposes. These kinds of methods increase the importance and the usefulness of weather radar measurements and total lightning mapping network as well. The following conclusions can be derived from our investigations for further considerations:

- there is no strong universal connection between radar and flash characteristics of thunderstorm cells, even for the same kind of season. The variability of the flash characteristics is higher than the variability of radar characteristics.
- the temporal and spatial resolution applied in our investigations are screening many details of thunderstorm developments. To resolve these yet undisclosed details, better resolution is needed for such comparative analysis.
- existing weather radar and lightning location network are suitable to provide data for cell tracking with higher temporal and spatial resolutions and these features have to be taken into account in future developments.
- outputs of advective interpolation method developed at the HMS which provides radar reflectivity data for time periods between the volume scans should be incorporated into the operational methods. It is a promising way for enhancing the time resolution.
- the optimum parameters for time and spatial resolution of radar data and the optimum time window for providing flash density data must be found.

Appendix – Definitions of the Applied Meteorological Characteristics and Thresholds Used in the Comparative Analysis of Thunderstorm Cells

The following characteristics are calculated for each identified cell using different thresholds in case of interactive and automatic cell tracking methods.

Area of the cell: a km² value, the number of pixels of the cell multiplied with the pixel area.

Cell category: an attribute value for cells marking the threshold used for cell segmentation.

Centre of the cell: the mean X and Y coordinates of the pixels of the identified cell above a threshold.

Cell dBZMax and Cell DensMax: the maximum reflectivity or flash density of the pixels of the identified cell above a threshold.

Cell dBZ Max X, Y and Cell Dens Max X, Y: the X and Y coordinates of the pixels with the maximum reflectivity values or flash density values.

Speed and direction of the displacements of the cells: it is calculated from the differences of the centre of cells identified on radar or on flash density images of subsequent time steps.

Radar cell thresholds: The 15, 25, 35, 45, and 55 dBZ reflectivity values were used as thresholds for cell segmentation and identification of radar data.

Radar reflectivity: a dBZ value in the national radar composite data.

Rainfall intensity: a mm/h value calculated from radar reflectivity using the well known Marshall–Palmer formula.

Water production: a normalized m³/h value calculated from the rainfall intensity, a volume of water which could be fallen out in an hour above an area or cell when the rainfall intensity would be constant during that time.

Total Water / Cell water: a m³ value calculated from the water production integrated in time and for area.

Flash cell thresholds: The 1, 2 , 4, 8, 16 flash/km²h flash density values were used as thresholds for flash segmentation and identification of SAFIR HMS data.

Flash density: a flash/ km²h value, a number of flashes in an hour above a unit area if the lightning activity would be constant during that time. When we calculate the raster type flash data we sum up the flashes that occurred within the given pixel within a time window; the size of the pixels and the length of time window is used.

Flash activity: a number of flashes at a given time above an area or cells normalised for an hour.

Total Flash / Cell flashes: a number of flashes for a given area or cell and time period.

For tracking radar and flash cells over different time steps the automatic multi-level cell-tracking method provides the following attributes for each cell:

Absolute cell ID: a cell identification number, which is unique and valid during the day for each cell identified with different thresholds.

Parent cell ID: an absolute cell ID pointing to a cell in the same time step, which covers the given cell and has smaller threshold values.

Predecessor cell ID: an absolute cell ID, which is pointing to a cell on the previous time step. This cell is assumed to have occupied the former position of the given cell.

Cell chain ID: an absolute ID number marking all the cells which are detected to represent the same cell as it moves and develops during different time steps. This cell chain ID is unique and valid during the day for each chain at a given cell category.

References

- Demetriadis N, Lojou J Y (2008) The potential of high performance, regional total lightning networks and enhanced display products for public safety and broadcast meteorology applications. 2nd Conf. of Met. Appl. Lightning Data, Ref. No. 103578

- Dixon M, Weiner G (1993) TITAN: Thunderstorm identification, tracking, analysis and nowcasting. *J. Atmospheric Oceanic Technol.* **10**, No. 6, 785–797
- Dombai F (2008) Attempts to enhance the localization accuracy and to monitor the reliability of the SAFIR lightning localization system. *Időjárás* **112**, 15–31
- Horvath A, Geresdi I, Nemeth P, Dombai F (2007) The Constitution Day storm in Budapest. *Időjárás* **111**, 41–63
- Kononov I, Yusupov I (2004) Cluster analysis of thunderstorm development in relation to synoptic patterns. Helsinki, ILDC conference Ref. No. 23
- Steinacker R, Dorninger M, Wölfmaier F, Krennert T (2000) Automatic tracking of convective cells and cell complexes from lightning and radar data. *Meteorol. Atmos. Phys.* **72**, 101–110
- Tuomi T (2004) Search of flash cells and properties. Helsinki, ILDC conference Ref. No. 22.

Chapter 22

Lightning Characteristics of Extreme Weather Events

Nikolai Dotzek and Colin Price

Abstract Lightning characteristics of extreme weather events are reviewed by first introducing the variety of thunderstorm types and large scale weather systems with embedded thunderstorms which may cause extreme events. In a description of charge separation processes, we identify the non-inductive charging mechanism as the most relevant one and outline the resulting basic charge layer distribution, the normal (or inverted) polarity dipoles and tripoles. Several case studies serve to illustrate and exemplify the concepts of the introductory part and relate the lightning evolution characteristics to hail storms, tornadoes, mesoscale convective systems, derechos or tropical and extratropical cyclones. There is compelling evidence that severe weather from thundering convection is often correlated to anomalous lightning activity, for instance signified by unusual values of lightning frequency or polarity. We also identify areas in which further research is needed, like the causes of the land-ocean contrast in lightning activity or the interrelation between recently discovered cold-ring cloud top structures and the storms' total lightning evolution (cloud-to-ground and intracloud flashes). Due to recently improved total lightning discrimination capabilities of lightning detection networks, we are confident that significant progress can be achieved in clarifying these open issues in the near future.

Keywords Severe convective storms · Electrification · Lightning · Hail · Flash floods · Tornadoes · Straight-line winds · Derechos · Mesoscale convective systems · Tropical and extratropical cyclones

22.1 Introduction

Extreme weather events are increasingly being investigated over the last years due to a growing concern that they might become more frequent, more extended or more

N. Dotzek (✉)

Deutsches Zentrum für Luft- und Raumfahrt (DLR), Institut für Physik der Atmosphäre, Oberpfaffenhofen 82234 Wessling, Germany; European Severe Storms Laboratory, Münchner Str. 20, 82234 Wessling, Germany

e-mail: nikolai.dotzek@essl.org

intense in the course of natural and anthropogenic climate change (cf. Brooks and Dotzek, 2008 or Price, 2008, this volume). Among all such extreme events, those that produce lightning are normally found on the mesoscale (Fujita, 1981) and range from tropical cyclones with embedded thunderstorms in their rain-bands, mesoscale convective complexes (MCC), linear mesoscale convective systems (MCS) down to individual thunderstorms which by themselves cover a spectrum of sizes, intensity and internal organisation. This is one of the reasons why exploring the lightning characteristics of these extreme events is at the same time a difficult task and a fascinating scientific challenge.

A number of authors have taken this challenge in recent years, and comprehensive treatments of lightning in severe storms were given by MacGorman (1993), Houze (1993), MacGorman and Rust (1998), Williams (2001) and Rakov and Uman (2003). Nevertheless, they all had to acknowledge the complexity and intricacies of severe thunderstorm electrification. Not only do these arise from the range of scales covered by thunderstorms, but also from the multi-parameter phase-space created by the relevant cloud microphysical effects. First, the charge separation in developing convective clouds is influenced by the particle types and size spectra contained in the storm and by the interaction of these various hydrometeors. Second, the amount of liquid water is relevant, also in supercooled form above the freezing layer, as well as the temperature level at which the interaction of liquid and frozen hydrometeors occurs. Third, the relative motion of hydrometeors inside the cloud depends on the updraft speeds which are directly related to the vertical profile of convective available potential energy (CAPE), cf. Blanchard (1998).

It is here where the notion of “storm severity” enters the scene. So far, we had only referred to electrification processes which apply to all kinds of deep moist convection. To deal with lightning in severe storms additionally requires analysing the thermodynamic environments that may lead to severe storms in the first place, and what aspects of these environments or the internal storm dynamics can influence their electrical behaviour. One factor that is commonly tied to the development of storm severity is their longevity. Long-lived storms in a quasi-steady state will necessarily have a higher chance of developing certain dynamic and electrical characteristics which may distinguish them from shorter-lived convection which cannot evolve into a well-defined convective mode.

In that sense, severe storms can display more distinct lightning characteristics than ordinary storms, and their often destructive and disorganising effects at the ground are a result of their high degree of organisation aloft. This internal organisation is also promising for the development of improved nowcasting or early warning algorithms: Severe thunderstorms present a significant hazard, both at the ground and for aircraft (e.g., Roach and Findlater, 1983; Pike, 2000). Higher understanding of the reasons behind the evolution of lightning in severe storms may help to forecast the severe weather phenomena that result at or near the ground later on.

In this Chapter, we will explore the various extreme events which display thundering convection and identify what aspects of their structures and life-cycles bear relevance for their electrical activity. A number of illustrative case studies will serve

to point the reader to the relevant literature before we draw our conclusions and outline open research questions.

22.2 Electrification Mechanisms in Deep Moist Convection

22.2.1 Severe Convective Storms and Hurricanes

This introductory section serves as a brief overview of the various storm types relevant for our subject. Readers interested in more thorough treatments are referred to the monographs by Cotton and Anthes (1989), Houze (1993), Emanuel (1994) or Doswell (2001). These references and e.g. Doviak and Zrnić (1993) or MacGorman and Rust (1998) further contain information on the relation between lightning activity and radar characteristics, an extensive topic by itself, treated also by Dombai (2008, this volume) and many of the references cited in this Chapter.

22.2.1.1 Single-Cell Thunderstorms

The single-cell storm forms the archetype concept for any kind of deep moist convection. It is the most frequently observed thunderstorm variety and also that with the least potential of becoming severe. Its life-cycle begins with a convective cloud forming from a rising moist and warm air mass. If its vertical development is not limited by stably stratified atmospheric layers, significant precipitation formation and charge separation can take place in the cumuliform cloud.

In mid-latitudes, this requires that the cloud tops reach well above the 0°C isotherm, and that the updraft persists for at least half an hour, such that precipitation-sized hydrometeors can form in the cloud. Aside from this typical lifetime, the dimension of a single-cell storm is roughly 10 km in both the vertical and horizontal. This also puts a limit to the horizontal extent of flashes in these storms, and cloud-to-ground (CG) flashes will mainly be observed from the lower part of the cloud. The total numbers of lightning discharges as well as the CG density (per unit time and per unit area) at the ground are unlikely to attain very large values.

As the typical setting for single-cell thunderstorms is characterised by weak vertical wind shear, the storm updraft remains essentially vertical, such that any precipitation from the cloud will fall into the main updraft region and cut off the cloud from its feeding boundary layer airmass. This marks the decay of the thundercloud. Severe events from this type of storm are rare, as its short life-cycle would not support formation of sustained heavy rain, large hail or excessive lightning activity. Given the right stratification below cloud base, weak downbursts may form or occasionally a brief and weak non-mesocyclonic tornado (cf. Dotzek et al., 2005b), especially if the thunderstorm developed at a pre-existing boundary layer convergence line. Such lines are an example of thunderstorms “breeding zones” which can often trigger several nearby single-cell storms simultaneously or successively. This may eventually lead to their clustering and thus the formation of a multicell storm.

22.2.1.2 Multicell Thunderstorms

Multicell storms are larger clusters of convective entities which by themselves may follow the single-cell storm life-cycle, but which have as an important additional feature the interaction between the individual cells. Multicells can be either a more or less randomly arranged group of individual cells in various stages of their life-cycles, or they can develop as a succession of cells from the front to the rear side of a propagating storm system. The latter type requires higher vertical wind shear to develop its greater degree of internal organisation, and in turn, its likelihood to spawn severe weather phenomena is enhanced.

Typical severe weather hazards from multicells are heavy precipitation or even flash-flooding, large hail and also damaging straight-line winds. Tornadoes are not a main hazard, but possible as well. The higher likelihood of severe weather from multicell storms comes from their increased size and lifespan compared to single-cell storms. Higher amounts of precipitation and large numbers of lightning flashes can be formed from these larger storms. Due to the larger horizontal dimension of the multicell storm, intracloud (IC) lightning discharges can bridge larger distances in the cloud's upper portion. The presence and interaction of several cells at a time also leads to higher CG flash densities at the ground. The increased longevity of multicells further enables a more efficient formation and growth of hailstones, as well as the development of precipitation-cooled downdrafts which may reach the ground as damaging winds.

22.2.1.3 Supercell Thunderstorms

Supercell or mesocyclonic thunderstorms are the least frequent, but also most dangerous type of thunderstorms. Under very special environmental conditions, these storms can form and attain the highest degree of internal organisation of all convective storms. Among other things, supercell formation requires both favourable amounts of vertical wind shear and CAPE to develop their main discriminating feature: a single, deep, persistent, rotating updraft called the mesocyclone.

Note that the size of the storm is not a criterion for the presence of a supercell. Rotating, mesocyclonic storms have been observed over a wide range of scales, from barely the size of a single-cell storm (sometimes referred to as “mini-supercells”) to very large entities with cloud tops protruding into the lower stratosphere and horizontal dimensions of over 20 km. The term “persistent” in the definition of the mesocyclone refers to the timescale of an ascending airmass from the base to the top of the storm, and “deep” means that the mesocyclone should extend vertically through a significant portion of the whole cloud depth.

Due to the high wind-shear in supercell environments, the main updraft will be tilted downshear, so precipitation from the supercell will not interfere with its boundary layer inflow region. Together with the stabilising effect of the large helicity in its mesocyclone, this can lead to a quasi-steady state of the storm and to its longevity, as long as the storm environment continues to provide the necessary essential ingredients.

Supercells are capable of causing any severe weather phenomenon, from copious amounts of rain to large (and very large) hail, as well as downbursts up to F3 intensity and tornadoes up to F5 intensity on the Fujita scale (e.g., Fujita, 1981). Depending on the amount of liquid precipitation at the ground, three types of supercells are distinguished: the classic supercell, the low-precipitation (LP) and high-precipitation (HP) supercell. Despite little or no rain at the ground, LP supercells are known to be reliable producers of very large hail.

Severe thunderstorms, in particular supercells, are often marked by U- or V-shaped radar cores or cloud-top overshoots (Maddox, 1981; McCann, 1983; Adler et al., 1985; Heymsfield and Blackmer, 1988). Due to their long lifetime of several (up to 12) hours, either CG or IC lightning activity in these storms can be high (cf. Steiger et al., 2007a) and itself present a significant hazard at the ground or to aviation. On the one hand, CG numbers and densities can be very large, and CG lightning may also occur from higher regions of the cloud, for instance the anvil of the storm. On the other hand, one impetus for investigating the lightning flashes in supercells has been the observation that the evolution of their total lightning activity can display certain characteristics (cf. Williams et al., 1999) that may facilitate early detection and warning of other impending severe phenomena, like downbursts, hail or tornadoes.

22.2.1.4 Mesoscale Convective Systems

We follow the broad mesoscale convective system (MCS) definition given by MacGorman and Morgenstern (1998) which includes linear systems (like squall lines) and is not restricted to circular-shaped cumulonimbus clusters below the size of a mesoscale convective complex (MCC): “A mesoscale convective system is a group of storms which interacts with and modifies the environment and subsequent storm evolution in such a way that it produces a long-lived storm system having dimensions much larger than individual storms”.

One important type of these systems is the linear MCS, often manifesting itself by a leading line of convective cells (which may display either multicell or supercell characteristics) and a horizontally extended trailing stratiform region. Consequently, these systems have been dubbed leading-line, trailing stratiform MCS. Their lightning activity is split up between the distinct convective and stratiform regions, with a relatively small intermediate zone in between. The most notable severe events from these MCSs are flash-flooding, large hail and damaging winds. Tornadoes are less frequent in mature linear MCSs, but pose a higher threat during the early stages of MCS formation, before the initial thunderstorms have fully merged to establish the MCS.

Like with multicell or supercell storms, the lightning activity in MCSs may be high and encompass also very long IC flashes. Due to the complex internal structure of MCSs, affecting also their internal charge distribution, lightning initiation and evolution reflect this complex structure (cf. Steiger et al., 2007b; Ely et al., 2008). In addition, several studies, among them Toracinta and Zipser (2001) and Zipser et al. (2006), noted a significant difference of about one order of magnitude in

lightning activity of MCSs over land compared to those over oceans. Despite some candidate cloud-microphysical charge separation processes which may respond to the land-ocean contrast (cf. Zipser and Lutz, 1994), a generally accepted theory for the observed difference in electrical activity is not yet at hand.

22.2.1.5 Tropical Cyclones

Tropical storms and tropical cyclones are storms that have lifetimes of days to weeks as they cross the tropical oceans. Over the Atlantic, they are called hurricanes, over the Pacific typhoons, and over the Indian Ocean, they are referred to as cyclones. Unlike the storms discussed in previous sections, hurricanes spend most of their lifetime over the warm tropical oceans (sea surface temperatures greater than 27°C), and their impacts are felt mainly when they approach coastlines, islands, or enter continental regions. Hurricanes start off as atmospheric tropical waves that can develop into tropical depressions, later developing into tropical storms, and then hurricanes. Only about 10% of the waves develop all the way into hurricanes.

The damage from hurricanes is threefold: Extensive coastline flooding due to the storm surge as the hurricane crosses the coastline; extensive wind damage due to the horizontal hurricane-force winds (up to 200 km h⁻¹) that remain sustained for hours at a time, changing direction as the eye passes over; and inland flooding due to heavy sustained precipitation. Once over land, embedded thunderstorms in hurricanes often result in other types of severe weather such as tornadoes. Hurricanes passing over islands will re-intensify as they move back over the warm ocean waters.

The electrification of hurricanes has not received much attention over the years, mainly due to the fact that hurricanes spend most of their lifetime over the oceans, while lightning observations were mainly available over land. However, there is significant evidence for the existence of convective cells within eye-wall of the hurricanes, and within the outer spiral rain bands. Recent observations confirm significant lightning activity in hurricanes (Black and Hallett, 1999; Shao et al., 2005). As these lightning discharges come from embedded thunderstorms, their flash characteristics will most likely correspond to that of the individual storm types described above.

22.2.1.6 Extratropical Cyclones

Contrary to their tropical counterpart, extra-tropical cyclones pose a multitude of major severe weather threats in mid-latitudes mainly in the cool season from autumn to spring. These threats encompass the large-scale field of high winds, resulting storm surges along the affected coastlines, large amounts of precipitation and, finally, embedded thunderstorms which may occur more isolated in the cyclone's warm sector or more widespread along the cold front of the storm. In Europe, individual cases of extra-tropical cyclones have caused losses of about 10 billion Euros, and Ulbrich et al. (2001) have analysed three high-impact events of December 1999. Like for hurricanes over the North Atlantic, the question of trends in extra-tropical

cyclone activity in Europe under the influence of climate change is an area of intensive research (e.g., Ulbrich et al., 2008).

The dominant cause of damage by these cyclones is the interaction of the large-scale wind field with structures at the surface. However, on a smaller scale, the warm-sector or cold-frontal thunderstorms in these systems may be responsible for the highest observed loss densities in the cyclone damage track. The lightning activity in these storms will in principle correspond to the description given above for isolated and potentially super-cellular thunderstorms or linear MCSs, but due to the coupling of the extra-tropical cyclones to the cold season, peculiarities of winter thunderstorms as discussed by Brook et al. (1982) will also be found, like low cloud base and cloud top and a high-shear environment supportive of strongly tilted updrafts. In passing, we note that low cloud base and high low-level shear are also factors, which favour tornado genesis in the presence of strong convection. Therefore, embedded electrical activity in extra-tropical cyclones should be an especially alarming signal for operational forecasters.

22.2.2 Charge Separation and Lightning Polarity

Charge separation mechanisms and lightning physics are treated in detail by Saunders (1993), MacGorman and Rust (1998), Uman (1986, 2001) and Rakov and Uman (2003). The topic of lightning initiation and hence predictability of the lightning hazard was treated, for instance, by Zipser and Lutz (1994), Lang and Rutledge (2002) and Clements and Orville (2008). Here, we focus primarily on the charge separation process which is likely the most relevant for convective storms: the non-inductive charging mechanism.

The non-inductive charging (NIC) is based on the interaction of graupel or hail with small ice crystals in the cloud, given the side constraint that supercooled droplets are also present and riming of the graupel particles can occur. Due to differential fall speeds (cf. Berdeklis and List, 2001), these hydrometeors experience collisions by which charge is being transferred from the surface of the small particles to that of the large ones. Under the influence of differential convective updraft speeds, the charged particles of different sizes are separated vertically, with the ice crystals lifted to the upper cloud regions and the macroscopic particles remaining at mid- or low cloud levels.

The sign of the charge transfer between graupel and ice crystals is mainly determined by the ambient temperature, relative humidity and liquid water content. Takahashi (1978) and Jayaratne et al. (1983) were able to show that the graupel particles acquire negative charge if the graupel-ice collisions occur below a temperature of about -20°C , and charged positively above this reversal temperature T_R . Similarly, high liquid water contents and larger updraft size and intensity favour positive charging of graupel, while low or moderate liquid water content and less vigorous updrafts lead to negatively charged graupel (e.g., Carey and Buffalo, 2007).

As a result of the NIC mechanism, most ordinary thunderstorms are characterised by a main dipole in the cumulonimbus cell's main updraft region, with positively

charged small ice crystals in the upper part of the cloud and negatively charged larger hydrometeors at intermediate levels. If the graupel-ice collisions occur above T_R and liquid water contents are high, an inverted dipole can form, with positive charge at mid-levels and a negatively charged cloud top region. This becomes more likely for storms with a low cloud base and hence a larger cloud portion below the freezing layer.

The conceptual model of the main charge layers and cloud-to-ground (CG) or intracloud (IC) flash polarity based on the NIC mechanism is summarised in Fig. 22.1 and has gained widespread acceptance (cf. Lang and Rutledge, 2002; Hamlin et al., 2003). There are two dominant charge regions present within the storms, one between -10 and -20°C (negative in a normal polarity dipole), and another region higher up, close to the -40°C temperature level (positive in a standard dipole). Aside from this main dipole structure, there may be other, less pronounced charge layers in the thundercloud. For instance, a smaller positive charge region is often found near the freezing level, leading to a tripole setup (Williams, 1989). Figure 22.1 depicts these main layers within schematic thunderstorms and shows the possible consequences for CG and IC discharges. The left- and rightmost sketches show negative CG and IC flashes, respectively, for a normal polarity dipole storm with a main positive charge centre above the negative main charge centre.

For the positive CG flash, however, there are two different candidate processes. The first of these, favoured by Carey and Buffalo (2007), is the inverted dipole in which the charge layering inside the cloud is reversed compared to the normal polarity setup. The second alternative is the tilted dipole, a special case of a normal polarity storm. In a strongly sheared environment that favours development of supercell storms, the upper positive charge centre will be shifted downshear from the lower, negative charge region. In this way, the negative charge layer does not shield the positive charge overhead from the ground anymore, so CG+ flashes can occur

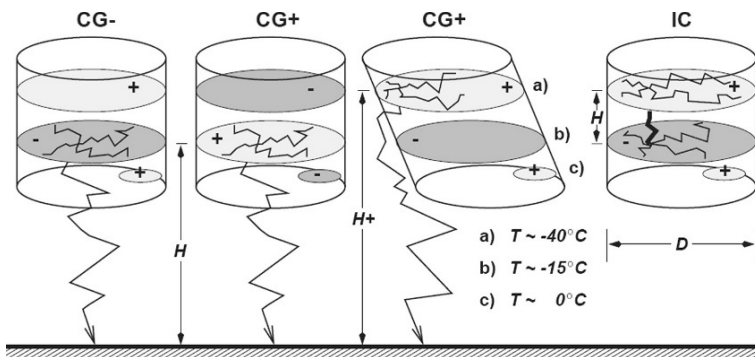


Fig. 22.1 Conceptual model of lightning types, main charge layers (*light grey* = positive, *medium grey* = negative) and their typical in-cloud temperature levels. Note two options for CG+ flashes: (i) inverted dipole, with negative charge above positive charge; (ii) normal polarity, tilted dipole in strongly sheared environments, unshielding the upper positive charge region. The tilted dipole setup could also lead to stronger CG- flashes from an inverted polarity storm

(cf. Brook et al., 1982; Reap and MacGorman, 1989; Curran and Rust, 1992). These originate from a much greater altitude and are thus likely to have higher return stroke currents (say, above ~ 100 kA) than positive discharges from an inverted polarity dipole.

CG+ flashes from a tilted dipole are often thought to provide evidence for presence of a supercell storm. However, if an inverted dipole could be verified in the course of CG+ lightning detection or electric field measurements, the non-inductive cloud electrification theory might be related to its microphysical observables (Saunders et al., 1991; Saunders, 1993) and allow making judgments on the significance of the NIC mechanism compared to other charge separation processes. For these reasons, CG+ flashes are a focal point of thunderstorm research. When using total lightning detection, it is possible to discriminate between the two possible dipole types. Aside from several studies (e.g., Hamlin et al., 2003) in the USA, Dotzek et al. (2001) showed an example of an inverted dipolar structure in a supercell hailstorm in southern Germany. In addition, Carey and Buffalo (2007) strongly questioned the relevance of the tilted dipole concept based on a review of recent evidence.

Due to a relative lack of three-dimensional lightning observations in mature MCSs, there are no similar conceptual models of in-cloud lightning structure in the trailing stratiform region of MCSs. Several balloon studies (e.g., Marshall and Rust, 1993; Stolzenburg et al., 1994) of electric fields in the stratiform region of MCSs have inferred multi-layered charge structures there, but few studies have examined in-cloud lightning behaviour. Mazur and Rust (1983) as well as Dotzek et al. (2005a) found that significantly more IC lightning occurred in the convective as compared to the stratiform region, where long (>20 km) flashes tended to occur preferentially.

22.3 Case Studies

The purpose of the case studies chosen here is to illustrate the concepts from Section 22.2 and to point the reader to persisting open questions which are active fields of research presently. Due to their potential longevity and their tendency to approach a quasi-steady state during much of their lifetime, our discussion will focus on supercell thunderstorms, mesoscale convective systems as well as tropical and extra-tropical cyclones.

22.3.1 Hail Storms

Changnon (1992) studied the spatial and temporal relationship between damaging hail and CG lightning. Lightning activity was always closely coupled to the presence of hail (Fig. 22.2), with the peak lightning activity generally associated with the start of the hail falling on the ground. In addition, the thunderstorm cells in which CG

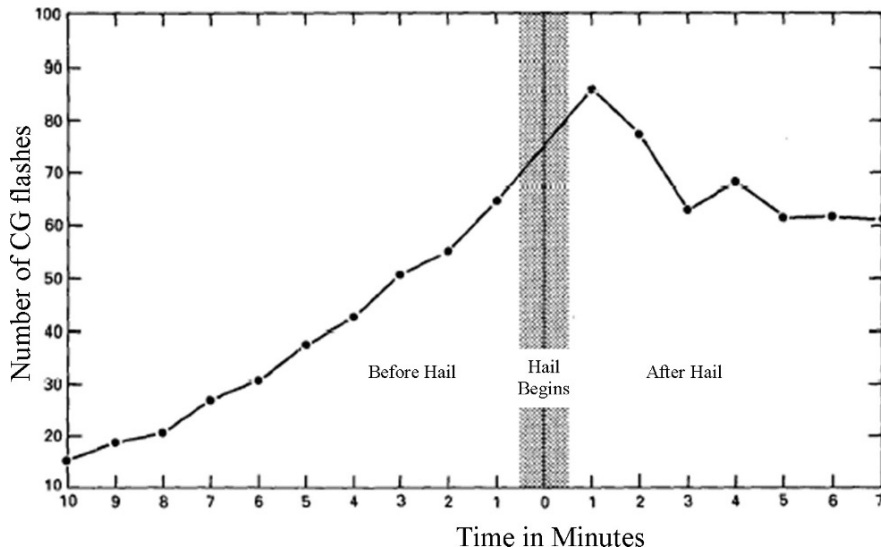


Fig. 22.2 The temporal evolution of lightning activity associate with 48 hail events in the United States (adapted from Changnon, 1992)

flashes were closely linked to hail typically developed 9 min before the hail was observed, and at a point 5 km upstorm from first hail, suggesting that CG flashes began as the hailstones were developing aloft. The hailstorm's severity was also found to be well correlated to the rate of flashing during the hailfall.

Carey and Rutledge (1998) found an extremely high IC-to-CG flash ratio (IC/C_G ~ 20–70, cf. Boccippio et al., 2001) and predominantly CG+ lightning (over 74%) when storms are producing large hail and weak tornadoes. Similar results were found during the STEPS project in the United States (Kyle et al., 2005) and observations in central and southern Europe (Dotzek et al., 2001; Soula et al., 2004).

22.3.2 Flash Floods

Many studies show a positive correlation between lightning and precipitation amounts (Piepgrass et al., 1982; Tapia et al., 1998; Petersen and Rutledge, 1998; Zhou et al., 2002, Price and Federmann, 2006; Gungle and Krider, 2006), some of which can produce flash floods with dramatic consequences to loss of life and damage to infrastructure and property. Soula et al. (1998) showed that in a flash flood that killed more than 80 persons, the CG flash density was exceptionally high, and the peak flash rate averaged over 5-min periods reached 11.6 min^{-1} within the cell area. The evolution of the CG flash rate and the radar reflectivity were closely correlated, with a very good agreement between the location of the intense rain at the ground and the high CG flash density. More importantly, the flash rate reached

high values before the arrival of the precipitation at the ground, which provides hope that lightning could possibly be used for early warnings of flash floods.

22.3.3 Tornadoes

Anomalous lightning activity associated with tornadoes has been observed in many studies. The anomalous activity is frequently observed in the polarity of the CG lightning activity, being mostly of positive polarity at the time of the tornadoes (Carey et al., 2003; Seimon, 1993). In addition, the lightning activity often peaks just before the onset of tornadic activity (Kane, 1991; Perez et al., 1997). Figure 22.3 shows the intensification of lightning activity shortly before the occurrence of a tornado, and the decrease in lightning activity commonly observed during the tornado lifetime. These results were further corroborated in an extensive study by Williams et al. (1999) using total lightning observations.

Analysis of a tornadic supercell by Dotzek et al. (2005a) showed that most ground flashes occurred in the south-eastern sector of the anvil, and most CG+ were found below the coldest cloud tops. Eight minutes before the long-lived tornado formed, the majority of CG+ lightning flashes were under a V-shaped cumulonimbus overshoot (cf. Heymsfield and Blackmer, 1988). This cold-V coincided with many NLDN (Cummins et al., 1998; Orville, 2008) CG strike locations. Just 1 min before tornado formation, there was significant CG+ activity north of the tornado, with two southern tips of concentrated CG– flashes (cf. Keighton et al., 1991). This pointed towards presence of a tilted dipole (cf. Fig. 22.1). About halfway through tornado lifetime, the CG activity attained a minimum.

Remarkable in the storms around the tornado were the high CG+ percentage prior to the tornado and few, but strong CG+ strokes near the end of tornado lifetime. Furthermore, CG– flash multiplicity was low, yet persistent and very regular 15-min oscillations of CG flash multiplicity were seen, especially for the CG+ discharges; see Dotzek et al. (2005a).

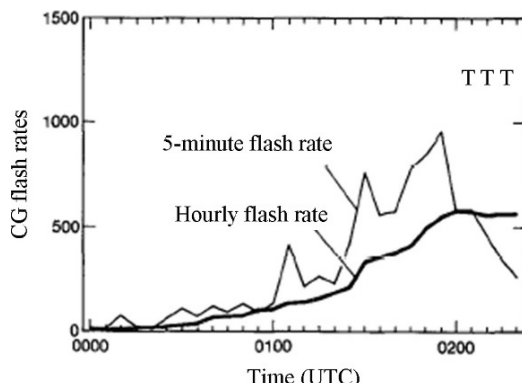


Fig. 22.3 The 5-min and hourly CG lightning flash rates prior to a tornado (T) in the USA (adapted from Kane, 1991)

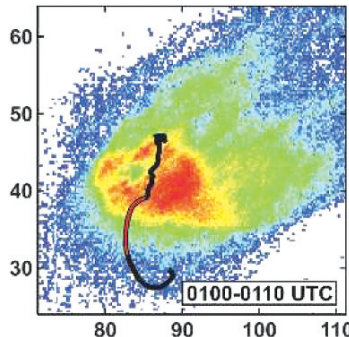


Fig. 22.4 A lightning hole is visible in the 10-min total lightning flash density of a STEPS supercell on 6 July 2000. Axis labels denote kilometres east and north of the observation network centre, while the coloured line gives the ascent track of a measuring balloon (adapted from MacGorman et al., 2005) (See also Plate 40 in the Color Plate Section on page 623)

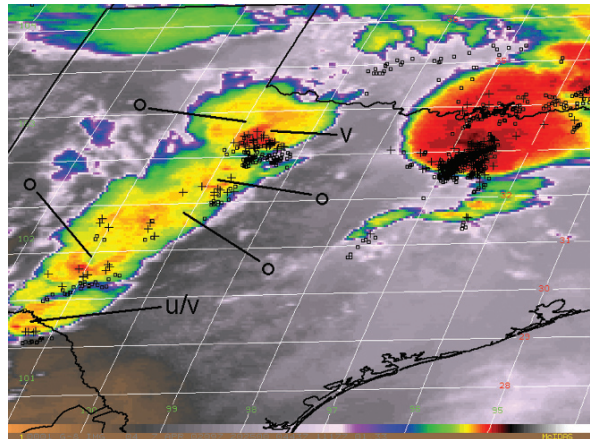
Following the initial observation by Krehbiel et al. (2000), several groups have found “lightning holes” in the total lightning (IC and CG) density of supercell storms (not exclusively tornadic). Figure 22.4 shows an example from MacGorman et al. (2005); additional examples were given by Murphy and Demetriades (2005) and Wiens et al. (2005). Comparison with simultaneous radar data has revealed that the lightning holes correspond to the bounded weak echo region (BWER) of the supercell storms. The BWER is formed by the supercell’s main updraft in which the vertical transport is too rapid to enable hydrometeor formation – and in turn charge separation by the NIC mechanism. As the BWER or the mesocyclone themselves, the lightning holes usually have diameters of 5–10 km and lifetimes of 10–20 min.

22.3.4 MCS with “Cold-Ring” Cloud Top Signatures

Dotzek et al. (2005a) studied the life cycle of a long-lived MCS. Figure 22.5 marks its transition from individual cells on a surface boundary to a line of severe thunderstorms. Near the northern tip of the linear MCS, there is the tornadic storm discussed in Section 22.3.3 with its V-shaped cloud-top signature. Figure 22.5 further shows the impressively large anvil of a separate strong storm in the Dallas–Ft. Worth region. Its CG lightning activity is mostly confined to the regions of highest cloud tops at that time.

Yet, the most striking features of Fig. 22.5 are several cold-ring cloud top structures of 50 to 100 km diameter along the forming leading-line, trailing-stratiform MCS. These are also found in the non-tornadic regions of the line and are much larger in size than the lightning holes of individual supercells discussed above, but they seem to be similarly transient phenomena: For the northern portion of the MCS, the cold-ring started to vanish from the northwest shortly before tornado formation

Fig. 22.5 GOES 8 channel 4 enhanced images of the early stage of a leading-line, trailing stratiform MCS over Texas on 7 April 2002, 2025 UTC. NLDN flash overlay (+ = CG+, □ = CG-) 10 min before to 5 min after image time (cf. Dotzek et al., 2005a). Cold-ring signatures are marked by o-symbols, and cold-U, cold-V are indicated as well (See also Plate 41 in the Color Plate Section on page 623)



and had broken up completely 15 min later. Only CG lightning data were available for the MCS at that stage, so the total lightning behaviour in the cold-ring regions had to remain unexplored.

Such cold-ring cloud top structures during MCS formation had rarely been depicted before (the exceptions being, e.g. Heymsfield et al., 1983a,b; Höller and Reinhardt, 1986). Adler and Fenn (1979a, b) showed similar but smaller structures. Bartels and Maddox (1991) discuss smaller circular, but not ring-like, clusters of storm cells and the later formation of mid-level cyclonic vortices.

Dotzek et al. (2005a) stressed the need to clarify if the cold-ring cloud tops are relatively regular phenomena which might have distinct total lightning characteristics - and in turn potential for severe weather warnings. Indeed, Setvák et al. (2007) have noted a number of cold-ring cloud top storm cases over Europe. Their total lightning activity is currently under investigation.

22.3.5 Derechos

Derechos (e.g., Fujita and Wakimoto, 1981; Johns and Hirt, 1987) are spatially extended straight-line wind storms (unlike a tornado with spiralling winds) that occur with large linear MCSs under very specific meteorological conditions. Contrary to general gust fronts often preceding lines of thunderstorms over their full length, derechos form when storm cells in a certain segment of the linear MCS persistently produce series of downbursts with much higher wind speeds than generally observed along the MCS. Thus, while the MCS progresses during its life cycle, the series of downbursts lead to a swath of maximum wind damage which is aligned roughly perpendicular to the major axis of the MCS. By convention (Johns and Hirt, 1987), such events are only classified as derechos if the length of the damage swath is at

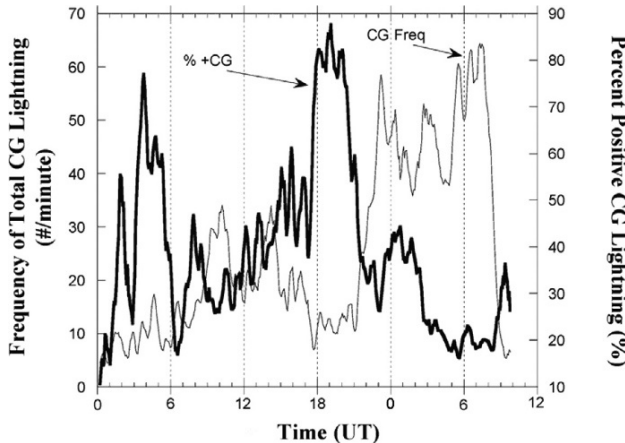


Fig. 22.6 Time series (0000 UTC, 4 July to 1000 UTC, 5 July 1999) of CG activity of the Superior derecho. Thin line gives number of CG flashes per minute, bold line shows the CG+ percentage (from Price and Murphy, 2002)

least 450 km and there are at least three F1 wind reports separated by at least 75 km and no more than 3 h apart in time.

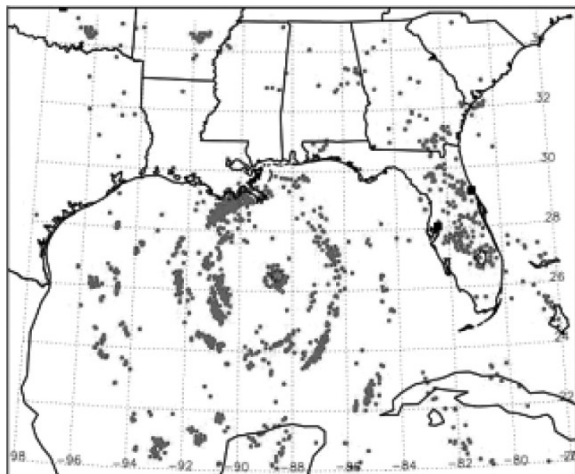
Recent derecho cases from Europe were analysed by Gatzen (2004); López (2007) and Punkka et al. (2006). Price and Murphy (2002) studied a derecho in the USA, during which 12.5 million trees were destroyed in a national park along the US-Canada border within a few hours. While normally the majority of CG lightning has negative polarity (CG-), during this derecho the positive fraction of lightning (CG+) rose to 80% for more than 2 hours (Fig. 22.6). López (2007) also reported a relatively high CG+ percentage of about 50% in their derecho case over a period of about 2 hours.

22.3.6 Tropical Cyclones

Although it was believed for many years that hurricanes were only weakly electrified, recent evidence has shown that the eye-wall and the rain-bands of hurricanes can have significant amounts of lightning (Molinari et al., 1994, 1999, Shao et al., 2005). As shown in Fig. 22.7, the lightning activity in hurricanes may therefore be a useful tool in detecting the intensification of these damaging storms.

In addition to lightning within hurricanes, it has recently been shown that the genesis of hurricanes in the Atlantic Ocean is related to lightning activity in thunderstorms over the African continent (Price et al., 2007; Chronis et al., 2007). Hence, the nature of normal MCSs over the tropical African continent (in tropical easterly

Fig. 22.7 Lightning observations (dots) of Hurricane Katrina on 28 August 2005, between 1730 and 1930 UTC (from Shao et al., 2005)



waves) may determine the likelihood of these storms developing into hurricanes as they move from the African continent into the Atlantic Ocean.

22.3.7 Extratropical Cyclones

Among the recent severe winter storms in Europe, locally highest damage levels at the ground were often coupled to the passage of the cyclone's cold front (cf. Ulbrich et al., 2001). The convection along these cold fronts can be vigorous enough to enable and sustain thunderstorm formation. In the case of winter storm "Kyrill" on 18 January 2007, frontal thunderstorms caused damaging wind gusts and hail, and also several tornadoes of up to F3-intensity. Aside from nonzero prefrontal CAPE and abundant low-level wind shear conducive to tornado formation, the large propagation speed of the cold front contributed to the high intensity of the tornadoes.

Another case of thunderstorms along the cold front of a winter cyclone in Europe is shown in Fig. 22.8: cyclone "Emma" of 1 March 2008. The one-day record of LINET total lightning discharges (Betz et al., 2004, 2007) on this day illustrates the sustained electrical activity along the NW-SE moving front. The corresponding 162 severe storm reports from the European Severe Weather Database ESWD (www.essl.org/ESWD/, cf. Dotzek et al., 2008) reveal that the extreme weather phenomena at the ground were confined to a region, which corresponds remarkably well to the swath of cold-frontal lightning activity. Aside from hail, heavy precipitation and some tornadoes, the most remarkable wind event on this day was an F3-downburst in Austria.

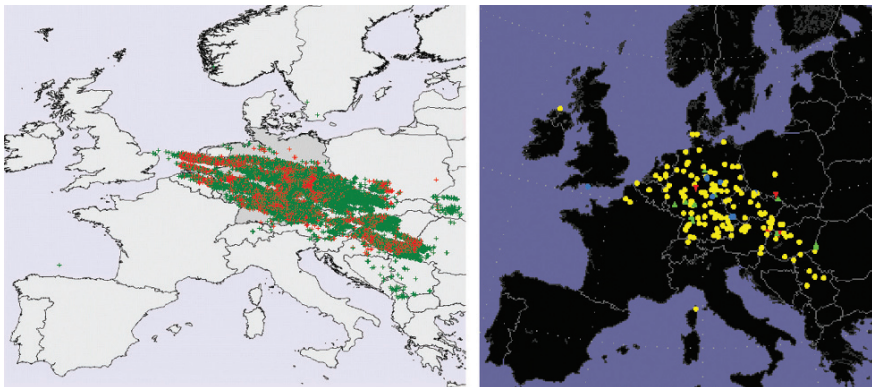


Fig. 22.8 Traces of embedded severe thunderstorms in the cold front of extra-tropical cyclone “Emma” on 1 March 2008, 000-2400 UTC. *Left:* 67811 LINET strokes (red: IC, green: CG). *Right:* 162 ESWD severe weather reports (yellow: damaging wind, red: tornado, green: large hail, blue: heavy precipitation) (See also Plate 42 in the Color Plate Section on page 624)

22.4 Conclusions

We have assessed the lightning characteristics of extreme weather events. Our main conclusions with respect to the present state of knowledge and open research questions are:

- Severe weather appears to be characterised by anomalous lightning activity, whether through lightning frequencies, lightning polarity, multiplicity, peak currents or spatial patterns;
- The increasing availability of total lightning detection networks around the globe has led to improved insights on lightning activity in severe storms over the past ten years;
- The majority of recent studies acknowledge the primary role of the non-inductive charging mechanism for (severe) thunderstorm electrification;
- The non-inductive charging process can consistently explain both negative (normal polarity) and positive (anomalous) CG flashes and thus help to quantify what environmental factors likely contributed to a dominance of either polarity;
- Lightning holes in total lightning data of supercell storms are collocated to the supercell BWER and provide further evidence for the role of the NIC mechanism for severe thunderstorm electrification;
- Severe convective storms are often characterised by a high CG+ percentage above 50% or even 75%, at least during significant parts of their lifetime. The corresponding candidate prototype thunderstorms are the inverted dipole or the tilted dipole;
- The relative role of the tilted dipole versus the inverted dipole for causing high CG+ ratios is an active area of research;

- Long-range lightning detection ability may help to improve early warning of the most hazardous regions in tropical cyclones before they make landfall;
- The contrast in lightning activity between thunderstorms and MCSs over land and over the ocean still awaits a firm explanation;
- Storm dynamics may both lead to certain lightning characteristics as well as to typical features observable by radar or satellite. For the recently discovered cold-ringing cloud top structures, a thorough analysis of their related (total) lightning activity has just started.

The most relevant application of a more thorough understanding of lightning behaviour in severe storms will be the improvement of nowcasting and warning decision procedures for protecting human lives and property.

Acknowledgments Part of this research has been funded by the European Union FP6 project FLASH (Observations, Analysis and Modeling of Lightning Activity in Thunderstorms, for use in Short Term Forecasting of Flash Floods) under contract FTS-2005-global-036852 and by the German Ministry for Education and Research BMBF under contract 01LS05125 in the project RegioExAKT (*Regionales Risiko konvektiver Extremwetterereignisse: Anwenderorientierte Konzepte zur Trendbewertung und -anpassung*, Regional Risk of Convective Extreme Weather Events: User-oriented Concepts for Trend Assessment and Adaptation).

References

- Adler, R. F., and D. D. Fenn, 1979a: Thunderstorm intensity as determined from satellite data. *J. Appl. Meteor.*, 18, 502–517.
- Adler, R. F., and D. D. Fenn, 1979b: Thunderstorm vertical velocities estimated from satellite data. *J. Atmos. Sci.*, 36, 1747–1754.
- Adler, R. F., M. J. Markus, and D. D. Fenn, 1985: Detection of severe Midwest thunderstorms using geosynchronous satellite data. *Mon. Wea. Rev.*, 113, 769–781.
- Bartels, D. L., and R. A. Maddox, 1991: Midlevel cyclonic vortices generated by mesoscale convective systems. *Mon. Wea. Rev.*, 119, 104–118.
- Betz, H.-D., K. Schmidt, P. Oettinger, and M. Wirz, 2004: Lightning detection with 3-D discrimination of intracloud and cloud-to-ground discharges. *Geophys. Res. Lett.*, **31**, L11108, doi:10.1029/2004GL019821.
- Betz, H.-D., K. Schmidt, B. Fuchs, P. Oettinger, and H. Höller, 2007: Cloud lightning: detection and utilization for total lightning measured in the VLF/LF regime. *J. Lightning Res.*, **2**, 1–17.
- Berdeklis, P., and R. List, 2001: The ice crystal-graupel collision charging mechanism of thunderstorm electrification. *J. Atmos. Sci.*, 58, 2751–2770.
- Black, T. A., and J. Hallett, 1999: Electrification of the hurricane. *J. Atmos. Sci.*, 56, 2004–2028.
- Blanchard, D. O., 1998: Assessing the vertical distribution of convective available potential energy. *Wea. Forecasting*, 13, 870–877.
- Boccippio, D. J., K. L. Cummins, H. J. Christian, and S. J. Goodman, 2001: Combined satellite- and surface-based estimation of the intracloud – cloud-to-ground lightning ratio over the continental United States. *Mon. Wea. Rev.*, 129, 108–122.
- Brook, M., N. Nakano, P. Krehbiel, and T. Takeuti, 1982: The electrical structure of the Hokuriku winter thunderstorms. *J. Geophys. Res.*, 87, 1207–1215.
- Brooks, H. E., and N. Dotzek, 2008: The spatial distribution of severe convective storms and an analysis of their secular changes. In: *Climate Extremes and Society*. H. F. Diaz and R. Murnane, Eds., Cambridge University Press, Cambridge, 340, pp. 35–53.

- Carey, L. D., and S. A. Rutledge, 1998: Electrical and multiparameter radar observations of a severe hailstorm, *J. Geophys. Res.*, 103 (D12), 13979–14000.
- Carey, L. D., and K. M. Buffalo, 2007: Environmental control of cloud-to-ground lightning polarity in severe storms. *Mon. Wea. Rev.*, 135, 1327–1353.
- Carey, L. D., W. A. Petersen, and S. A. Rutledge, 2003: Evolution of cloud-to-ground lightning and storm structure in the Spencer, South Dakota, Tornadic Supercell of 30 May 1998. *Mon. Wea. Rev.*, 131 (8), 1811–1131.
- Changnon, S. A. 1992: Temporal and Spatial Relations between Hail and Lightning, *J. Appl. Meteor.*, 31 (6), 587–604.
- Chronis, T., Williams, E., Anagnostou, M., and Petersen, W. 2007: African lightning: indicator of tropical Atlantic cyclone formation, *Eos, Trans., Amer. Geophys. Union*, 88(40), 397–408.
- Clements, N. C., and R. E. Orville, 2008: The warning time for cloud-to-ground lightning in isolated, ordinary thunderstorms over Houston, Texas. *Preprints, 3rd Conf. on Meteor. App. of Lightning Data. AMS Annual Meeting 2008*, 15 pp. [http://ams.confex.com/ams/88Annual/techprogram/paper_132309.htm]
- Cotton, W. R., and R. A. Anthes, 1989: Storm and cloud dynamics. *Int. Geophys. Ser.*, 44, Academic Press, San Diego, 883 pp.
- Cummins, K. L., M. J. Murphy, E. A. Bardo, W. L. Hiscox, and R. B. Pyle, 1998: A combined TOA/MDF technology upgrade of the U.S. National Lightning Detection Network. *J. Geophys. Res.*, 103D, 9035–9044.
- Curran, E. B., and W. D. Rust, 1992: Positive ground flashes produced by low-precipitation thunderstorms in Oklahoma on 26 April 1984. *Mon. Wea. Rev.*, 120, 544–553.
- Dombai, F., 2008: Utilization of lightning and radar data for meteorological applications. this volume.
- Doswell, C. A. (Ed.), 2001: Severe Convective Storms. *Meteor. Monogr.*, 28, Amer. Meteor. Soc., Boston, 561 pp.
- Dotzek, N., H. Höller, C. Théry, and T. Fehr, 2001: Lightning evolution related to radar-derived microphysics in the 21 July 1998 EULINOX supercell storm. *Atmos. Res.*, 56, 335–354.
- Dotzek, N., R. M. Rabin, L. D. Carey, D. R. MacGorman, T. L. McCormick, N. W. Demetriadis, M. J. Murphy, and R. L. Holle, 2005a: Lightning activity related to satellite and radar observations of a mesoscale convective system over Texas on 7–8 April 2002. *Atmos. Res.*, 76, 127–166.
- Dotzek, N., M. V. Kurgansky, J. Grieser, B. Feuerstein, and P. Névir, 2005b: Observational evidence for exponential tornado intensity distributions over specific kinetic energy. *Geophys. Res. Lett.*, 32, L24813, doi:10.1029/2005GL024583.
- Dotzek, N., P. Groenemeijer, B. Feuerstein, and A. M. Holzer, 2008: Overview of ESSL's severe convective storms research using the European Severe Weather Database ESWD. *Atmos. Res.*, in press.
- Doviak, R. J., and D. S. Zrnić, 1993: Doppler Radar and Weather Observations, 2nd ed. Academic Press, San Diego, 562 pp.
- Ely, B. L., R. E. Orville, L. D. Carey, and C. L. Hodapp, 2008: Evolution of the total lightning structure in a leading-line, trailing-stratiform mesoscale convective system over Houston, Texas, *J. Geophys. Res.*, 113, D08114, doi:10.1029/2007JD008445.
- Emanuel, K. A., 1994: Atmospheric Convection. Oxford University Press, New York, 883 pp.
- Fujita, T. T., 1981: Tornadoes and downbursts in the context of generalized planetary scales. *J. Atmos. Sci.*, 38, 1511–1534.
- Fujita, T. T., and R. M. Wakimoto, 1981: Five scales of airflow associated with a series of downbursts on 16 July 1980. *Mon. Wea. Rev.*, 109, 1438–1456.
- Gatzen, C., 2004: A derecho in Europe: Berlin, 10 July 2002. *Wea. Forecasting*, 19, 639–645.
- Gungle, B., and E. P. Krider, 2006: Cloud-to-ground lightning and surface rainfall in warm-season Florida thunderstorms, *J. Geophys. Res.*, 111, D19203, doi:10.1029/2005JD006802.
- Hamlin, T., P. R. Krehbiel, R. J. Thomas, W. Rison, and J. Harlin, 2003: Electrical structure and storm severity inferred by 3-D lightning mapping observations during STEPS. *Preprints, 12th Int. Conf. on Atmos. Elec.*, 9–13 June 2003, Versailles, 189–192.

- Heymsfield, G. M., and R. H. Blackmer, 1988: Satellite-observed characteristics of Midwest thunderstorm anvils. *Mon. Wea. Rev.*, 116, 2200–2224.
- Heymsfield, G. M., R. H. Blackmer, and S. Schotz, 1983a: Upper-level structure of Oklahoma tornadic storms on 2 May 1979. I: Radar and satellite observations. *J. Atmos. Sci.*, 40, 1740–1755.
- Heymsfield, G. M., G. Szejwach, S. Schotz, and R. H. Blackmer, 1983b: Upper-level structure of Oklahoma tornadic storms on 2 May 1979. II: Proposed explanation of “V” pattern and internal warm region in infrared observations. *J. Atmos. Sci.*, 40, 1756–1767.
- Höller, H., and M. E. Reinhardt, 1986: The Munich hailstorm of July 12, 1984: Convective development and preliminary hailstone analysis. *Contrib. Atmos. Phys.*, 59, 1–12.
- Houze, R. A., 1993: Cloud Dynamics. Int. Geophys. Ser. Vol. 53, Acad. Press, San Diego, 570 pp.
- Jayaratne, E. R., C. P. R. Saunders, and J. Hallett, 1983: Laboratory studies of the charging of soft-hail during ice-crystal interactions. *Quart. J. Roy. Meteor. Soc.*, 109, 609–630.
- Johns, R. H., and W. D. Hirt, 1987: Derechos: Widespread convectively induced windstorms. *Wea. Forecasting*, 2, 32–49.
- Kane, R. J., Correlating lightning to severe local storms in the northeastern United States. *Wea. Forecasting*, 1991, 6(1), 3–12.
- Keighton, S. J., H. B. Bluestein, and D. R. MacGorman, 1991: The evolution of a severe mesoscale convective system: Cloud-to-ground lightning location and storm structure. *Mon. Wea. Rev.*, 119, 1533–1556.
- Krehbiel, P. R., R. J. Thomas, W. Rison, T. Hamlin, J. Harlin, and M. Davis, 2000: GPS-based mapping system reveals lightning inside storms. *Eos, Trans. Amer. Geophys. Union*, 81, 21–25.
- Kyle, C. W., Rutledge, S. A., and Tessendorf, S. A. 2005: The 29 June 2000 supercell observed during STEPS. Part II: Lightning and charge structure, *J. Atmos. Res.*, 62(12), 4151–4177.
- Lang, T. J., and S. A. Rutledge, 2002: Relationships between convective storm kinematics, precipitation, and lightning. *Mon. Wea. Rev.*, 130, 2492–2506.
- López, J. M., 2007: A Mediterranean derecho: Catalonia (Spain), 17th August 2003. *Atmos. Res.*, 83, 272–283.
- MacGorman, D. R., 1993: Lightning in tornadic storms. *Geophys. Monogr.*, 79, 173–182.
- MacGorman, D. R., and W. D. Rust, 1998: The Electrical Nature of Storms. Univ. Press, Oxford, 422 pp.
- MacGorman, D. R., and C. D. Morgenstern, 1998: Some characteristics of cloud-to-ground lightning in mesoscale convective systems. *J. Geophys. Res.*, 103D12, 14 011–14 023.
- MacGorman, D., D. Rust, P. Krehbiel, B. Rison, E. Bruning, and K. Wiens, 2005: The electrical structure of two supercell storms during STEPS. *Mon. Wea. Rev.*, 133, 2583–2607.
- Maddox, R. A., 1981: Satellite depiction of the life cycle of a mesoscale convective complex. *Mon. Wea. Rev.*, 109, 1583–1586.
- McCann, D. W., 1983: The enhanced-V: A satellite observable severe storm structure. *Mon. Wea. Rev.*, 111, 887–894.
- Marshall, T. C., and W. D. Rust, 1993: Two types of vertical electrical structures in stratiform precipitation regions of mesoscale convective systems. *Bull. Amer. Meteor. Soc.*, 74, 2159–2170.
- Mazur, V., and W. D. Rust, 1983: Lightning propagation and flash density in squall lines as determined with radar. *J. Geophys. Res.*, 88D, 1495–1502.
- Molinari, J., P. K. Moore, V. P. Idone, R.W. Henderson, and A. B. Saljoughy, 1994: Cloud-to-ground lightning in Hurricane Andrew, *J. Geophys. Res.*, 99(D8), 16,665–16,676.
- Molinari, J., P. K. Moore, and V. P. Idone, 1999: Convective structure of hurricanes as revealed by lightning locations, *Mon. Wea. Rev.*, 127, 520–534.
- Murphy, M. J., and N. W. S. Demetriades, 2005: An analysis of lightning holes in a DFW supercell storm using total lightning and radar information. Preprints, Conference on Meteorological Applications of Lightning Data, January 9–13, San Diego, Amer. Meteor. Soc., 16 pp.
- Orville, R. E., 2008: Development of the national lightning detection network. *Bull. Amer. Meteor. Soc.*, 89(2), 180–190.
- Perez, A. H., L. J. Wicker, and R. E. Orville, 1997: Characteristics of cloud-to-ground lightning associated with violent tornadoes. *Mon. Wea. Rev.*, 125(3), 428–437.

- Petersen, W. A., and S. A. Rutledge, 1998: On the relationship between cloud-to-ground lightning and convective rainfall. *J. Geophys. Res.*, 103(12), 14025–14040.
- Piepgrass, M. V., E. P. Krider, C. B. Moore, 1982: Lightning and surface rainfall during Florida thunderstorms. *J. Geophys. Res.*, 87(C13), 11193–2001.
- Pike, W. S., 2000: A note on some recent lightning strikes to aircraft which were either climbing or descending through the freezing level in or near hail-producing cumulonimbus cloud. *J. Meteor.*, 25, 109–116.
- Price, C., 2008: Lightning and climate change. this volume.
- Price, C., and B. Murphy, 2002: Lightning activity during the 1999 Superior Derecho, *Geo. Phys. Res. Lett.*, 29(23), 57.1–57.4.
- Price, C. and B. Federmesser, 2006: Lightning-rainfall relationships in Mediterranean winter thunderstorms, *Geophys. Res. Lett.*, 33, L07813, doi:10.1029/2005GL024794.
- Price, C., Y. Yair, and M. Asfur, 2007: East African lightning as a precursor of Atlantic hurricane activity, *Geophys. Res. Lett.*, 34, L09805, doi:1029/2006GL028884.
- Punkka, A.-J., J. Teittinen, and R. H. Johns, 2006: Synoptic and mesoscale analysis of a high-latitude derecho-severe thunderstorm outbreak in Finland on 5 July 2002. *Wea. Forecasting*, 21, 752–763.
- Rakov, V. A., and M. A. Uman, 2003: *Lightning – Physics and Effects*. Cambridge Univ. Press, Cambridge, 687 pp.
- Reap, R. M., and D. R. MacGorman, 1989: Cloud-to-ground lightning: Climatological characteristics and relationships to model fields, radar observations, and severe local storms. *Mon. Wea. Rev.*, 117, 518–535.
- Roach, W. T., and J. Findlater, 1983: An aircraft encounter with a tornado. *Meteor. Mag.*, 112, 29–49.
- Saunders, C. P. R., 1993: A review of thunderstorm electrification processes. *J. Appl. Meteor.*, 32, 642–655.
- Saunders, C. P. R., W. D. Keith, and R. P. Mitzeva, 1991: The effect of liquid water on thunderstorm charging. *J. Geophys. Res.*, 96D, 11 007–11 017.
- Seimon, A., 1993: Anomalous cloud-to-ground lightning in an F5-tornado-producing supercell thunderstorm on 28 August 1990. *Bull. Amer. Met. Soc.*, 74(2), 189–203.
- Setvák, M., P. Novák, D. T. Lindsey, R. M. Rabin, P. K. Wang and M. Radová, 2007: Central European convective storms penetrating deep into the lower stratosphere – MSG IR and radar observations and radiative transfer modeling. Preprints, 4th European Conf. on Severe Storms, 2 pp. [Available from www.essl.org/ECSS/2007/abs/04-Satellites/setvak-1177574574.pdf]
- Shao, X.-M., J. Harlin, M. Stock, M. Stanley, A. Regan, K. Wiens, T. Hamlin, M. Pongratz, D. Suszcynsky, and T. Light, 2005: Katrina and Rita were lit up with lightning. *Eos, Trans. Amer. Geophys. Union*, 86(42), 398.
- Soula, S., H. Sauvageot, G. Molinié, F. Mesnard, and S. Chauzy, 1998: The CG lightning activity of a storm causing a flash-flood, *Geophys. Res. Lett.*, 25 (8), 1181–1184.
- Soula, S., Y. Seity, L. Feral, and H. Sauvageot, 2004: Cloud-to-ground lightning activity in hail-bearing storms. *J. Geophys. Res.*, 109 D02101, doi:10.1029/2003JD003669.
- Steiger, S. M., R. E. Orville, and L. D. Carey, 2007a: Total lightning signatures of thunderstorm intensity over North Texas. Part I: Supercells. *Mon. Wea. Rev.*, 135, 3281–3302.
- Steiger, S. M., R. E. Orville, and L. D. Carey, 2007b: Total lightning signatures of thunderstorm intensity over North Texas. Part II: Mesoscale Convective Systems. *Mon. Wea. Rev.*, 135, 3303–3324.
- Stolzenburg, M., T. C. Marshall, W. D. Rust, and B. F. Smull, 1994: Horizontal distribution of electrical and meteorological conditions across the stratiform region of a mesoscale convective system. *Mon. Wea. Rev.*, 122, 1777–1797.
- Takahashi, T. 1978: Rimming electrification as a charge generation mechanism in thunderstorms. *J. Atmos. Sci.*, 35, 1536–1548.
- Tapia A., J. Smith, and M. Dixon, 1998: Estimation of convective rainfall from lightning observations. *J. Appl. Meteorol.*, 37 (11), 1497–1509.

- Toracinta E. R., and E. J. Zipser, 2001: Lightning and SSM/I-ice-scattering mesoscale convective systems in the global tropics. *J. Appl. Meteor.*, 40, 983–1002.
- Ulbrich, U., J. G. Pinto, H. Kupfer, G. C. Leckebusch, T. Spangehl, and M. Reyers, 2001: Three extreme storms over Europe in December 1999. *Weather*, 56, 70–80.
- Ulbrich, U., A. H. Fink, M. Klawa, and J. G. Pinto, 2008: Changing northern hemisphere storm tracks in an ensemble of IPCC climate change simulations. *J. Climate*, 21, 1669–1679.
- Uman, M. A., 1986: All about Lightning. Dover Publications, New York, 167 pp.
- Uman M. A., 2001: The Lightning Discharge. Dover Publications, Mineola, 377 pp.
- Wiens, K. C., S. A. Rutledge, and S. A. Tessendorf, 2005: The 29 June 2000 supercell observed during STEPS. Part II: Lightning and charge structure. *J. Atmos. Sci.*, 62, 4151–4177.
- Williams, E. R., 1989: The tripole structure of thunderstorms. *J. Geophys. Res.* 94 D, 13 151–13 167.
- Williams, E. R., 2001: The electrification of severe storms. In: *Severe Convective Storms*, C.A. Doswell, III, Ed., Amer. Met. Soc., Meteorological Monograph Series, 28(50), 527–561.
- Williams, E. R., B. Boldi, A. Matlin, M. Weber, S. Hodanish, D. Sharp, S. Goodman, R. Raghavan, and D. Buechler, 1999: The behavior of total lightning activity in severe Florida thunderstorms. *Atmos. Res.*, 51, 245–265.
- Zhou, Y., X. Qie, and S. Soula, 2002: A study of the relationship between cloud-to-ground lightning and precipitation in the convective weather system in China. *Ann. Geophysicae*, 20(1), 107–113.
- Zipser, E. J., 1994: Deep cumulonimbus cloud systems in the tropics with and without lightning. *Mon. Wea. Rev.*, 122, 1837–1851.
- Zipser, E. J., and K. Lutz, 1994: The vertical profile of radar reflectivity of convective cells: A strong indicator of storm intensity and lightning probability? *Mon. Wea. Rev.*, 122, 1751–1759.
- Zipser, E., D. Cecil, C. Liu, S. W. Nesbitt, and S. Yorty, 2006: Where are the most intense thunderstorms on Earth? *Bull. Amer. Meteor. Soc.*, 87, 1057–1071.

Chapter 23

Flash Cells in Thunderstorms

Tapio J. Tuomi and Antti Mäkelä

Abstract When convection develops into a thundercloud stage of at least moderate intensity, its cellular appearance may be monitored not only with weather radars but also with lightning location systems. For intense thunderstorms, the ground-flash rate alone is sufficient for making apparent the underlying convection-cell structure. If flash cells can be properly identified, they show longitudinal development complementary to the usual view of advancing transverse front. A method is described to analyse the flash-cell structure of thunderstorms and is illustrated with an example from Finland. With proper choice of parameters, the largest, most interesting flash cells generally have realistic sizes, lifetimes and motion.

Keywords Convective core · Flash cell · Lightning monitoring · Thunderstorm development · Weather radar

23.1 Introduction

Convective clouds are formed when the thermal instability in the troposphere gives rise to vertical air currents with speeds of the order of 10 m/s. Due to the high vertical speed, the upward and downward currents are restricted to horizontal areas with diameters of several kilometres. As demonstrated by Byers and Braham (1949), this leads to a cellular structure of convective motion, manifested in the appearance of cumulus clouds. In favourable conditions, i.e. with enough instability, humidity and lift to intensify updraught (the convective core), the cumulus clouds may grow into shower clouds and eventually thunderclouds. These three stages of development are distinguished by the production of precipitation (shower cloud, generally also thundercloud) or lightning (thundercloud only). The two precipitating cloud stages also have the common name cumulonimbus (Cb). In a typical thundercloud, the three stages usually occur simultaneously during most of the lifetime (e.g. Stolzenburg

T.J. Tuomi (✉)

Finnish Meteorological Institute, P.O. Box 503, FIN-00101 Helsinki, Finland
e-mail: tapio.tuomi@fmi.fi

et al., 1998): the first core is already dissipating, the middle one is in its mature stage, and the third is growing from the cumulus stage. Part of the motion of the thundercloud involves the appearance of cumulus-stage cells at the leading edge and the disappearance of the dissipating-stage cores at the trailing edge. The duration of the thunder-producing mature stage is approximately half an hour. There is vagueness in the literature whether the cell concept should be associated with a single convective core, or with a system of about three cores which are spatially close and dynamically coupled, with a lifetime of an hour or more (e.g. Ushio et al., 2003); we will assume the latter but will discuss the question later on.

When a Cb has developed into a thundercloud, it usually has some prominent and observable features: the visual cloud top is located at altitudes of 10 km or more (near the tropopause), the maximum radar reflectivity is 35–40 dBZ or higher, and the cloud top temperatures are of the order of -50°C or lower. All these characteristics originate from the presence of the strong updraught, which lifts the moist air upwards towards the colder temperatures.

Cumulonimbus causes a threat of hazardous weather, i.e. flash floods, gusty winds, hail and, in the thundercloud stage, lightning strikes. While a general risk of Cb can usually be estimated, the temporal and spatial occurrence of individual cells is difficult to forecast. Because the lifetime of a cell is typically one hour, only short-term forecasting (nowcasting) is possible, and real-time monitoring of the situation is important. Weather radars are a good tool in this respect, but a better assessment of the severity can be made if also lightning monitoring is available. Indeed, ingenious commercial monitoring systems are available, but we will consider the basic problem of tracking cells of ground flashes.

It is well known that cloud lightning often provides the first and last signs of the lightning activity of a thundercloud (Williams et al., 1989; MacGorman et al., 2006), and during the lifetime it is better correlated with radar-detected precipitation than is ground lightning. Also, the intense rates of cloud lightning have been noticed to be a better precursor of severe weather than ground lightning alone (Williams et al., 1999). However, although nowadays some networks have larger coverage (e.g. Betz et al., 2007), usually cloud-lightning detection systems have more limited coverage than ground-flash location systems, or are non-existent in many countries. Also, cloud flashes tend to spread over the whole cell, or even over several adjacent cells, which might cause the calculated flash cell centre to behave sporadically. Ground flashes are more concentrated within the heavy-precipitating cell cores.

Consequently, in cases where a ground-lightning location system is available, ground flashes can be used for monitoring the development of thunderstorms, possibly superposed on weather-radar displays.

When the thunderstorm is moderate or heavy, ground flashes often tend to form front-like patterns, especially when many cells are active at the same time (for instance in mesoscale convective systems). The intensity and direction of development in the “flash front” may give valuable information to forecasters or nowcasters, but the picture may be blurred by the erratic appearance of new flashes (to one cell here, to another cell there) as well as the ubiquitous presence of stray flashes originating from the stratified clouds around the convection cores.

Useful monitoring of thunderstorm cells, when only ground-flash data are available, requires means for identifying cell cores from the data, i.e. filtering out the stray flashes, and following the development of the identified cells. Moses (1996) introduced a statistical method which groups flashes according to the logarithmic distribution of their range estimates. Steinacker et al. (2000) used both ground flash density and the weather radar based rain rate to deduce the life cycle and movement of convective cells. We describe a more direct, algorithmic method devised by Tuomi and Larjavaara (2005), illustrated by a case study. While clear clusters of flashes will naturally be grouped into cells, there is no self-evident criterion whether a nearby flash should belong to a cell or remain outside. In particular, in a real-time situation there is no advance knowledge of the status of such a flash: will it remain a stray flash or is it the first flash of a developing adjacent cell? Therefore, single-flash cells should have a similar cell status as those with many flashes. This need not pose a problem in monitoring a cell-development situation, as demonstrated below.

The estimation of the movement of a cell for real time purposes (e.g. in nowcasting) can be done by extrapolating, visually or algorithmically, the consecutive cell locations forwards in time. This is useful when determining the risk of lightning at certain critical locations a couple of hours in advance.

Before describing the method, called Cellsearch for brevity, we will mention two ways to illustrate – afterwards, not real-time – the flash-cell structure of a thunderstorm situation.

23.2 Detection and Statistical Presentation of Flash Locations

23.2.1 Flash Data

The present analysis is based on ground flashes located by a network of IMPACT-type sensors (Cummins et al., 1998) in Finland, Norway and Sweden. The mean location accuracy is about one kilometre, but some nominally accurate yet badly located flashes do occur, which are difficult to separate from scattered well-located flashes. For historical data, filtering of stray flashes might be done to enhance the cell structure, but because this is not appropriate for real-time monitoring, we have not attempted it.

A thunderstorm which occurred in Finland on July 24, 2006, shown in Fig. 23.1, is used here as an example. It was one of the most intense storms in 2006 and was caused by a cold front proceeding from north to south, remaining within the southern half of Finland during its whole lifetime of about 20 h. Flash clustering is clearly visible, but numerous stray flashes accompany the denser groups. Weather radars detected rather concentrated precipitation cores surrounded by relatively limited veils of weaker rain; a single-radar image at 0800 UTC, near the highest activity, is shown in Fig. 23.2. The cores, while divided into several separate regions, were roughly aligned to WSW-ENE, nearly perpendicular to the SE direction of propagation apparent in Fig. 23.1. The strongest cores are at the northern and central

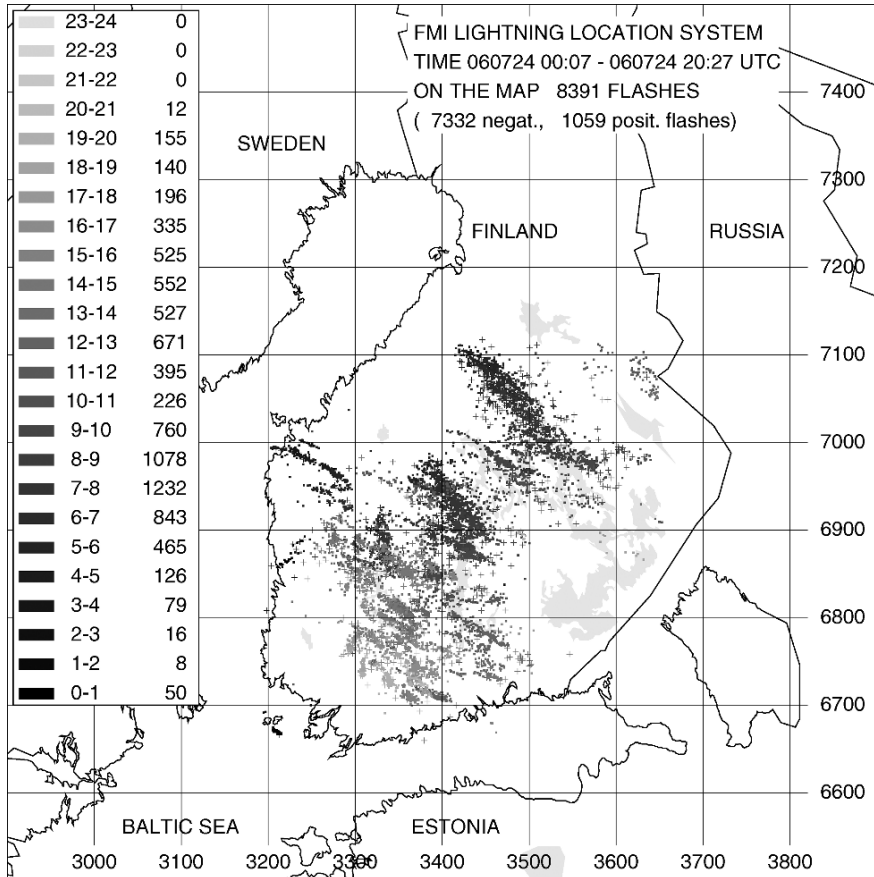


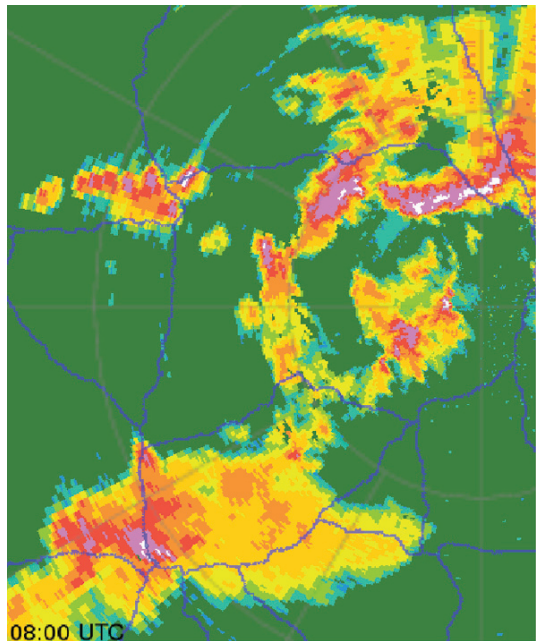
Fig. 23.1 Located flashes on 24 July 2006. Grey-shaded according to the UTC hour indicated in the inserted panel, which also shows the hourly numbers of flashes. The map grid refers to a Finnish coordinate system, expressed in kilometres east and north

parts, as might also be guessed from Fig. 23.1. We will compare the flash and radar data later on.

23.2.2 Flash Density

One way to describe thunderstorm intensity is to calculate the flash density, temporally limited to the situation in question (one day in this case). Furthermore, if the unit of area corresponds to the natural thunderstorm cell size, the flash-density distribution gives a rough estimate of the cell structure of the situation, even though cells generally move and the average density map is fixed. A good choice for the grid size is 20×20 km, for which the flash density is calculated using the data

Fig. 23.2 Weather-radar CAPPI image at 08 UTC, near the time of highest activity in Fig. 23.1. Small white areas represent radar echo exceeding 47 dBZ. The radar is near the right boundary, south of the NE peak echo, and the distance to the central peak echo, at lower left, is about 100 km (See also Plate 43 in the Color Plate Section on page 624)



shown in Fig. 23.1. The result will be presented below in a comparison with the result of the flash-cell analysis.

23.2.3 Time-Position Correlation of Flashes

Finke (1999) has presented a method to analyse the overall cell structure of a thunderstorm situation. It is not suitable for real-time monitoring and does not describe the behaviour of individual cells, but it may give some insight into the general development. As exemplified in Tuomi and Larjavaara (2005), the method illustrates the average cell motion and the coherence of development between cells. For example, if all cells follow the overall course determined by the frontal motion, the correlation is high and results in well-concentrated patterns in a correlation map. We will see that the present case is of this type. On the other hand, a randomly developing stagnant air-mass thunderstorm system would lead to a totally scattered correlation pattern.

The method is to calculate the x-separation (east) and y-separation (north) of two flashes with a given time difference (lag). In practice it is sufficient to tabulate the separations in bins of 2 km and time differences in bins of 1 min. For a short lag, say 5 min, most of the flash separations are short if there is appreciable cell formation. For a long lag, a cell once formed may still be active but may have moved to another position; then many flash pairs with this separation are found for this lag. Plotted in an x-y map, points for a given lag tend to accumulate at distances corresponding to

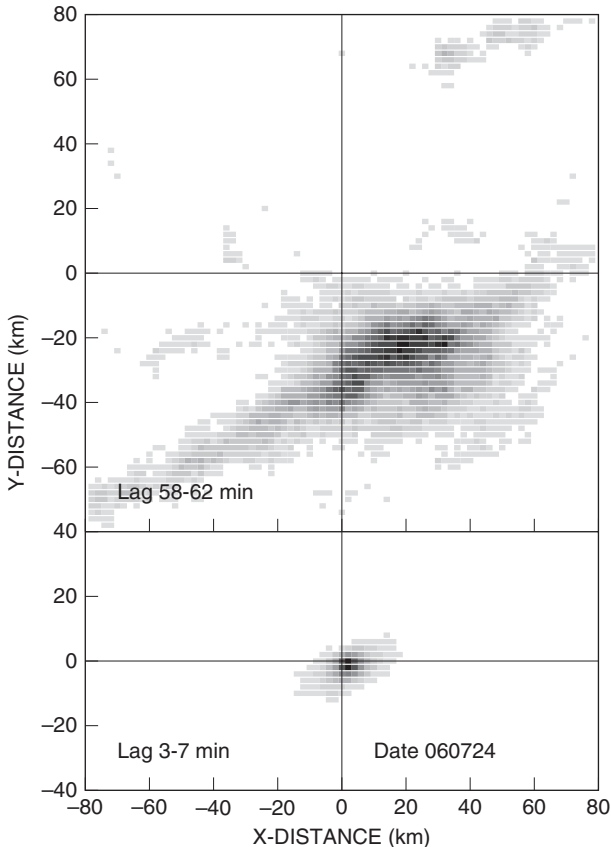


Fig. 23.3 Time-position correlation of the flashes of the example with an average lag of 5 min (lower) and 60 min (upper)

the cell motion. Figure 23.3 illustrates the result for the case of Fig. 23.1. The grey scale is proportional to the number of flash pairs in each bin, but we do not try to interpret the importance of the absolute scale. The lightest shades of grey have been set to white to better highlight the high-correlation areas.

The lower panel of Fig. 23.3, for an average lag of 5 min, represents the nearly instantaneous size of cells (size estimation would depend on how the grey-scale decrease is interpreted). It indicates a shift to SE, but the speed determination in this case would be inaccurate. The spread to WSW and ENE reflects the simultaneous existence of cells in a front-like pattern. The weakness of the spread, however, shows that the parallel progress of different cells is not easy to detect during a short time window.

An average lag of one hour, as seen in the upper panel of Fig. 23.3, reveals several facts. The longitudinal spread towards SE shows that all cells do not move exactly in tandem; the transverse spread clearly reveals the parallel, front-like motion. The position of the cluster suggests an average SE speed between 35 and 40 km/h.

23.3 Cellsearch Method

We will not present an actual algorithm – or computer code – for our method because it may be realized in different, more or less ingenious ways, and may be developed to meet different levels of requirements (e.g. commercial). We have developed it into a research tool for historical data as well as an experimental real-time version. Our main interest is the principle of the method itself, and what its results can tell us.

The following rules are quite common and by no means a unique invention. The principle is to test whether a new detected flash belongs to an existing cell or starts a new cell. Also, the motion and aging of cells are taken into account.

Rule 1: Cell definition. A cell is a collection of any number of flashes. Its critical age is determined by the time elapsed since its latest flash (see Rule 3). The current cell centre is the average of $I = 20$ latest flashes of the cell (or all flashes if the number is less than 20). The number I is a measure of “cell inertia”: it is large enough to ensure stability of the centre when new erratic flashes are added, and on the other hand, it is small enough to allow cell motion.

Rule 2: Radius of attraction R . The new flash may be accepted to a cell if its distance from the current cell centre is less than R . A value of 15 km will be used.

Rule 3: Delay time limit T . It is the time difference between the new flash and the time of the latest flash of a cell. If a cell is older, it is considered closed (no more tested for new flashes). $T = 15$ min will be used. In a real-time application, the actual time may be used to test cell ages if the waiting time for a new flash is too long.

Rule 4: Cell test. When a new flash appears, all open cells are tested. Those exceeding the delay time limit will be closed. The flash is added to the open cell whose current centre is the closest of those within R . If no open cell remains, or all open cells are beyond the radius of attraction, the flash opens a new cell.

Rule 5: Time-distance limit. If the thunderstorm behaviour is very irregular, adjacent cells may merge into one larger, deformed cell. Then the distance of the new flash from the latest flash of a cell can also be tested to prevent stray flashes causing the merging. This can be done by limiting the product of that distance with the delay time to, say, 50 km min. This rule may not be necessary in a real-time application where the finer details of cell structure are not important.

The parameter values can be varied to some degree, e.g. depending on the thunderstorm climate of the region. No set of parameter values guarantees a full set of beautifully formed cells, but most cells do show a regular behaviour (size, motion, lifetime). The above basic rules may be supplemented by finer statistical treatments to ensure more stable cell identity, but we have found that more complex rules are not necessarily free from more complications.

We want to point out two practical matters. First, the flash cell defined by Rule 1 is ideally coded as an object (e.g. Java-language class) with associated methods like `addFlash()`, `getSize()`, `getCenterX()` etc. Second, in displaying the results on the screen, the whole history of the cell centres can be drawn as “worms”, sequences of points, overlaid on a dimmer background of actual flashes, perhaps colour-coded by time; and showing open (active) and closed (dead) cells with different colours.

23.4 Cell Analysis

When the data in Fig. 23.1 is run with our Cellsearch program, the 8391 flashes are grouped into 817 cells, among which 397 contain just one flash. This may not be a beautiful feature for the “cell” concept, but we think that the abundance of stray flashes is a fact of nature and cannot be avoided; and, thunderstorm cells do exist, presumably with only one precipitation core, which produce just one ground flash, so there is no physical reason to restrict the cell size. There are further about 260 flashes in cells of 2–9 flashes. The distribution of the flashes into cells of different size classes is depicted in Fig. 23.4, which also shows the corresponding numbers of flashes in the fixed grid of 20×20 km squares (note the logarithmic vertical scale in Fig. 23.4). Because the actual size (of the electrically active part) of a cell with just one or a few flashes is probably much smaller than 20 km, it is conceivable that many such cells are counted together in the 20-km grid while Cellsearch is more faithful in preserving their cell identity. Larger cells show a fairly good agreement with the flash-density distribution.

In any case, the main features and principal development of the thunderstorm are reflected by the most active cells, as shown in Fig. 23.5. It shows all the 817 cell centres; those of the 20 most abundant cells, listed in the left panel, are plotted in black and the rest in grey. (The identity of the listed cells cannot be reasonably displayed without colour coding.) These 20 cells have a total of 3241 flashes, 39% of all flashes. The filtering effect, the resolution of cell centres with gaps between different cells, is obvious, although it is still clearer in the more intense and compact storm in Fig. 8 of Tuomi and Larjavaara (2005). The lifetimes (min) given in the left panel of Fig. 23.5 are upper-limit values because they may contain periods of low flash rate, often at the beginning or end. Estimation of a more representative lifetime would require a statistical determination of the rise and decay of the flash rate.

For 17 cells, the number of flashes exceeds 100. Their flash density, calculated by a method devised by Tuomi and Larjavaara (2005), ranges from 20 to 57 flashes per 100 km^2 , with an average of 32.5.

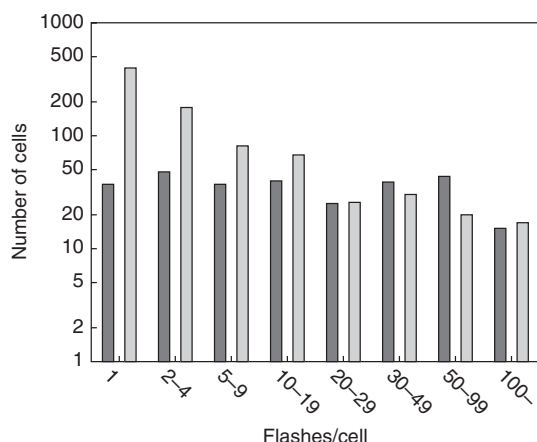


Fig. 23.4 Cell-size distribution of the thunderstorm of Fig. 23.1. Left columns (dark grey): cells represented by 20×20 km fixed squares. Right columns (light grey): cells found with Cellsearch analysis

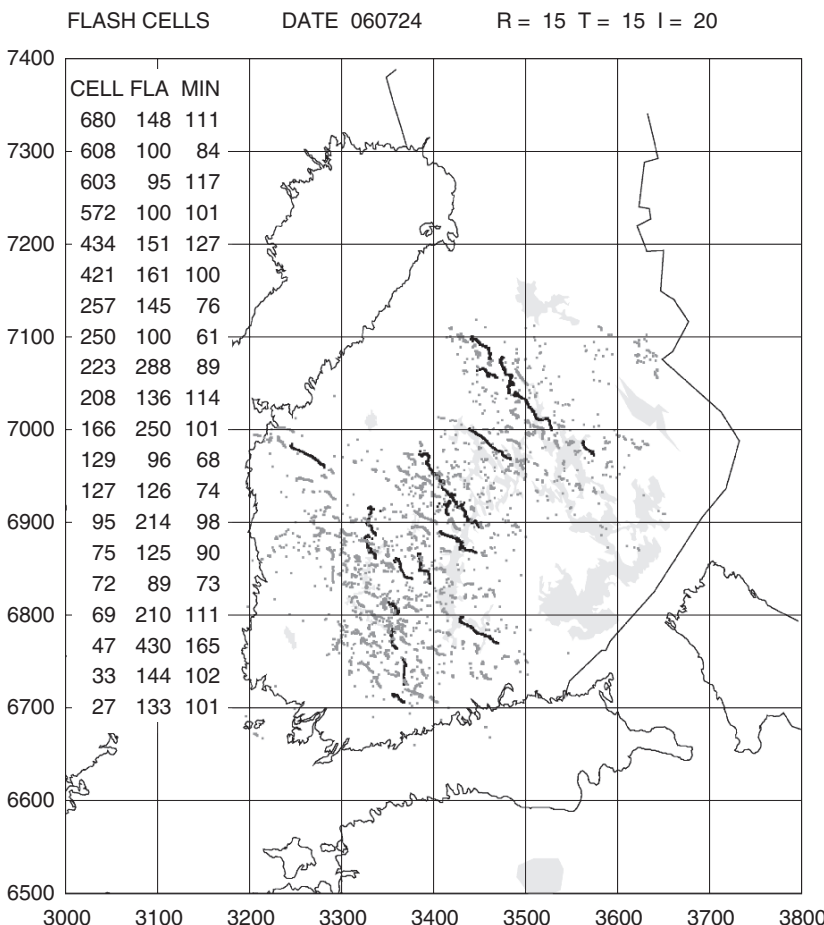


Fig. 23.5 Flash-cell display of the example. Each point is a cell centre at the time when a new flash is added to the cell. Twenty most abundant cells are plotted in full black and listed in the left panel (running cell number, number of flashes, and lifetime in minutes)

The most abundant cell, no. 47 (430 flashes), goes through the central part and is immediately followed by cell 166 (250 flashes). Note that the numbering of the cells corresponds to the temporal order of their first flash. Cell 47 is rather long, about 75 km, having a lifetime of nearly three hours. It is a relatively rare case, but a similar cell is described in Tuomi and Larjavaara (2005). The NE cluster contains several abundant cells, the longest (no. 95) having a length of 70 km. There were also several reports of large hail, exceeding 2 cm diameter, from the NE cluster.

A closer look at the long cell 47 is given in Fig. 23.6. Each dot is a flash, connected in time-order by line segments. The transverse zigzag pattern between successive flashes during the longitudinal development is typical, and results in the meandering of most of the centre-point paths seen in Fig. 23.5. There is sometimes

periodic intensification in long-living cells; in cell 47 a lower-activity phase occurs between two intense ones. But we think it remains physically as one cell, because hardly any algorithm could be able to separate this into separate cells. The weather radar image at 08:00 UTC in Fig. 23.2 confirms the intense nature of e.g. cells 47 and 95: the storm area consists of several cores with radar reflectivity >47 dBZ (white colour) especially in NW. The closeness of these high-reflectivity cores supports the view that a “cell”, when well developed, usually contains more than one core. We have studied the case of flash cells 47 and 166 more closely.

The time development of cell 47 is shown in Fig. 23.7, giving the percentage of flashes in 10-min bins. Of the 430 flashes, a typical fraction, 36, are positive. The cell lifecycle looks like a succession of two 90-min cells partly overlapping, but as noted above, they can hardly be separated algorithmically. Cell 166, spatially continuing the course of cell 47 to SE with a single maximum of flash rate, begins almost one hour before cell 47 comes too close and eventually dies. These two flash cells, or three flash-rate peaks, cover a total distance of 110 km during 3:45 h. A look at the time-resolved (5-min) radar data shows that the region of 40–47 dBZ reflectivity advances relatively smoothly along the same path as the flash cells and has a similar width; within that region, spots of reflectivity >47 dBZ appear and disappear. During the change from cell 47 to cell 166 the 40–47 dBZ region is preserved but lightning within it is temporarily more scattered, leading to the formation of the new flash cell 166, which thereafter competes with cell 47 for new flashes. This suggests

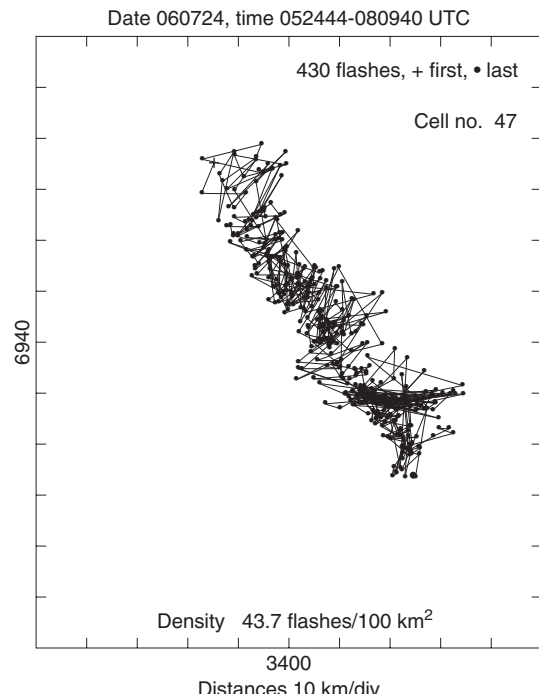
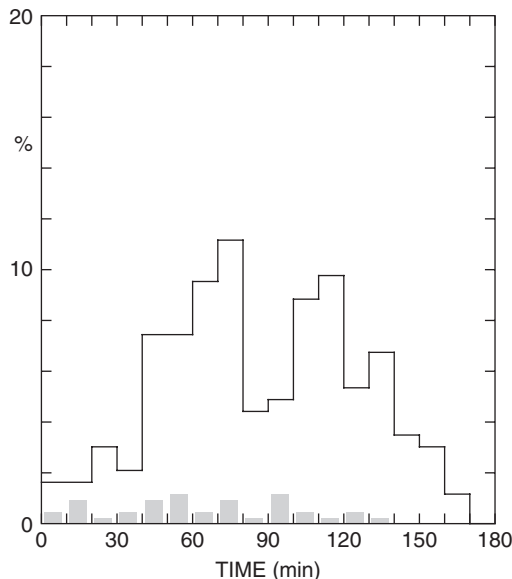


Fig. 23.6 The flashes of the long central cell no. 47, joined by line segments in time-order

Fig. 23.7 Time development of the flash rate (flashes per 10 min, percentage of the total number of 430 flashes) of cell 47



that cell 166 continues physically the existence of cell 47, so they should be the same cell. Visually, however, this makes little difference. We may conclude that for a moving thunderstorm, an intense flash cell corresponds to a persistent convection “cell”, with a lifetime from one to several hours and radar reflectivity of at least 40 dBZ, containing short-lived convection cores of reflectivity exceeding 47 dBZ. The width is about 15 km and the traversed length may be up to about 100 km.

Tuomi (2006) has studied an intense stagnant thunderstorm (July 2003) which produced “round” flash cells. For those with at least 40 flashes, the convection cells of at least 40 dBZ reflectivity had an average diameter of 6.5 km. The convection core exceeding 47 dBZ, usually only one, had an average width of 3.2 km.

23.5 Discussion

The present method is an example of how ground-flash location data can be filtered in a relatively simple way to make cell structure and development more visible. The flash-cell concept is useful when the number of flashes per cell exceeds 20–25, i.e. when the activity is at least moderate. Then the cell centre, the running mean of flash locations, can be used to visualize the cell motion.

A promising application is to compare individual radar precipitation cells with flash cells. A display is technically possible (e.g. Steinacker et al., 2000), but a detailed comparison of the properties of individual cells is more tedious. According to our preliminary studies (Mäkelä, 2006; Tuomi, 2006), onset of lightning activity requires at least 40 dBZ of radar reflectivity, and a reflectivity of 48 dBZ corresponds to the formation of flash cells of about 40 flashes (see also Motley et al., 2006).

Comparison with radar data also suggests that a flash cell, at least when appreciably developed, corresponds to a broader concept of convection cell, which is roughly the region of precipitation of at least 40 dBZ, which in turn may contain one or several (or no) heavy-precipitation cores exceeding 47 dBZ. A core lives typically half an hour while the broader cell may live several hours.

An example by Tuomi and Larjavaara (2005, Figs. 1 and 8) shows an intense multicell thunderstorm where cell centres move in different ways with respect to the general direction of motion: others follow the main course of the system while some shorter-lived cells deviate to the left. Such a divergence cannot be discerned by the time development of flashes only, without a cell analysis.

References

- Betz, H.-D., Schmidt, K., Fuchs, B., Oettinger, W.P., Höller, H.: Cloud lightning: detection and utilization for total lightning measured in the VLF/LF regime. *J. Lightning Res.* **2**, 1–17 (2007)
- Byers, H.R., Braham, R.R.: The Thunderstorm. US Government Printing Office, Washington 25, DC, USA (1949)
- Cummins, K.L., Murphy, M.J., Bardo, E.A., Hiscox, W.L., Pyle, R.B., Pifer, A.E.: A combined TOA/MDF technology upgrade of the US National Lightning Detection Network. *J. Geophys. Res.* **103**, 9035–9044 (1998)
- Finke, U.: Space-time correlation of lightning distributions. *Mon. Weather Rev.* **127**, 1850–1861 (1999)
- MacGorman, D., Apostolakopoulos, I., Nierow, A., Murphy, M.J., Demetriades, N., Cramer, J., Krehbiel, P.: Improved timeliness of thunderstorm detection from mapping larger fraction of lightning flashes. 2nd Conference on Meteorological Applications of Lightning Data 2006, Atlanta, USA (2006)
- Mäkelä, A.: Some comparisons between weather radar and lightning data in Finland in the summer of 2005. Presentation given in: First International Symposium on Lightning Physics and Effects, 3–4 April 2006, Vienna, Austria (2006)
- Moses, R.L.: Statistically based thunderstorm cell detection and mapping system. U.S. Patent No. 5528494 (1996)
- Motley, S.M., Carey, L.D., Murphy, M.J.: Total lightning characteristics and inferred charge structure of ordinary convection. 2nd Conference on Meteorological Applications of Lightning Data 2006, Atlanta, USA (2006)
- Steinacker, R., Dorninger, M., Wölfelmaier, F., Krennert, T.: Automatic tracking of convective cells and cell complexes from lightning and radar data. *Meteorol. Atmos. Phys.* **72**, 101–110 (2000)
- Stolzenburg, M., Rust, W.D., Marshall, T.C.: Electrical structure in thunderstorm convective regions 2. Isolated storms. *J. Geophys. Res.* **103**, D12, 14079–14096 (1998)
- Tuomi, T.J.: Rain and flash cells in July 2003. Presentation given in: First International Symposium on Lightning Physics and Effects, 3–4 April 2006, Vienna, Austria (2006)
- Tuomi, T.J., Larjavaara, M.: Identification and analysis of flash cells in thunderstorms. *Quart. J. R. Meteorol. Soc.* **131**, 1191–1214 (2005)
- Ushio, T., Heckman, S.J., Christian, J., Kawasaki, Z.: Vertical development of lightning activity observed by the LDAR system: Lightning bubbles. *J. Appl. Meteorol.* **42**, 165–174 (2003)
- Williams, E.R., Weber, M.E., Orville, R.E.: The relationship between lightning type and convective state of thunderclouds. *J. Geophys. Res.* **94**, 13213–13220 (1989)
- Williams, E.R., Boldi, B., Matlin, A., Weber, M., Hodanish, S., Sharp, D., Goodman, S., Raghavan, R., Buechler, D.: The behaviour of total lightning activity in severe Florida thunderstorms. *Atmos. Res.* **51**, 245–265 (1999)

Chapter 24

Thunderstorms, Lightning and Climate Change

Colin Price

Abstract The distribution of lightning around the planet is directly linked to the Earth's climate, which is driven by solar insolation. The diurnal and seasonal heating of the continental landmasses results in large fluctuations in temperature, influencing atmospheric stability, and the development of thunderstorms. Lightning activity is positively correlated with surface temperatures on short time scales, and due to projections of a warmer climate in the future, one of the key questions is related to the impact of future global warming on lightning, thunderstorms, and other severe weather. Lightning itself is also linked to variations in upper tropospheric water vapour, and tropospheric ozone, both of which are strong greenhouse gases. Climate model studies show that in a future warmer climate we may have less thunderstorms overall, but more intense thunderstorms, which may increase the amount of lightning by 10% for every one degree global warming.

Keywords Climate · Climate change · Global warming · Lightning · Thunderstorms · Global climate · General circulation · ENSO

24.1 Introduction

Lightning discharges in thunderstorms are an indication of the intensity of atmospheric convection. Atmospheric convection occurs under unstable atmospheric conditions, either due to the heating of the boundary layer by solar radiation during the day, or by the mixing of air masses of different densities. Lightning frequencies are therefore related to the regions of greatest instability in the Earth's atmosphere. These regions of instability do not occur randomly around the planet, but have an organized pattern related to the climate of the Earth which is driven by the differential heating of the Earth's surface by the sun. If we change the climate we will

C. Price (✉)

Tel Aviv University, Department of Geophysics and Planetary Science,
Ramat Aviv, 69978, Israel
e-mail: cprice@flash.tau.ac.il

change the regions of convection, their intensity, and hence will likely change the lightning patterns around the globe.

In the last decade we have learned a great deal about the spatial and temporal patterns of global lightning and thunderstorms from both satellite and ground-based observations. The two primary satellite sensors that have been used are the Optical Transient Detector (OTD) and the Lightning Imaging Sensor (LIS) (Christian et al., 2003). The satellite sensors use optical detectors to detect lightning flashes during the day and night. However, these detectors cannot differentiate between intracloud (IC) lightning and cloud-to-ground (CG) lightning. In addition, since these detectors are on polar orbiters, they observe only a small fraction of the globe at any time, while remaining above any particular thunderstorm for only 90 seconds. Nevertheless, after years of observations, a clear picture is obtained related to the global distribution of thunderstorms and lightning activity. Ground-based global observations of lightning have been based on Schumann resonance methods (Price and Melnikov, 2004; Price et al., 2007; Satori et al., 2008). These methods detect extremely low frequency (ELF) radiation emitted by global lightning flashes in the frequency range 4–45 Hz. In this frequency range, very little attenuation occurs, and hence the radiation from lightning travels around the globe a few times before decaying into the background noise. Hence, global lightning in the ELF range can be monitored by using only a few observation sites.

In Section 24.2 we will discuss global lightning activity and the circulation patterns that drive the Earth's climate. The connection between lightning and important climate parameters, such as surface temperature, atmospheric water vapor, clouds cover, NO_x, etc. will be discussed in Section 24.3. In Section 24.4 the possible changes in lightning activity due to global warming will be discussed. The discussion and summary will be presented in Section 24.5.

24.2 Global Thunderstorm Activity

While it was thought for many decades that the global lightning frequency was \sim 100 flashes/sec, recent satellite observations give the best estimate of 45 flashes/sec (Christian et al., 2003). The global observations show that 90% of the global lightning occurs in the tropics and the summer hemisphere, over land (Fig. 24.1). The remaining 10% in the winter hemisphere is primarily over the warm ocean currents such as the Gulf Stream and the Mediterranean Sea. Furthermore, 75% of the annual mean global lightning is within the tropical regions, with tropical continental lightning showing a clear diurnal peak, maximizing in the late afternoon hours (local time) (Fig. 24.2). In contrast to this, the diurnal cycle of oceanic lightning is nearly non-existent, with little variations throughout the day, in agreement with the very small variations in sea surface temperature on the daily scale. This is somewhat contradictory to the diurnal cycle of oceanic convection that shows a maximum in the early morning hours (Hendon and Woodberry, 1993).

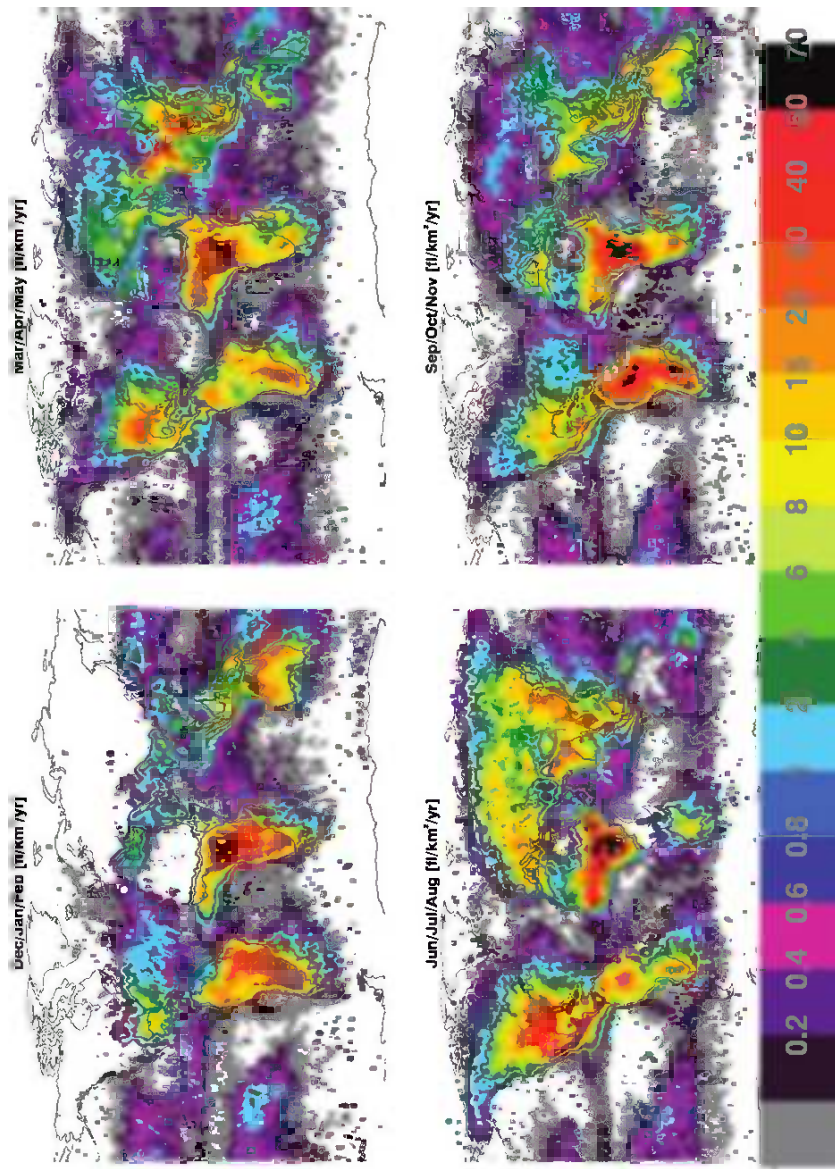


Fig. 24.1 Seasonal maps of the OTD/LIS satellite- observed lightning derived from 5 years of data collected from May 1995 to March 2000 (Christian et al., 2003) (<http://thunder.mastf.nasa.gov>) (See also Plate 44 in the Color Plate Section on page 625)

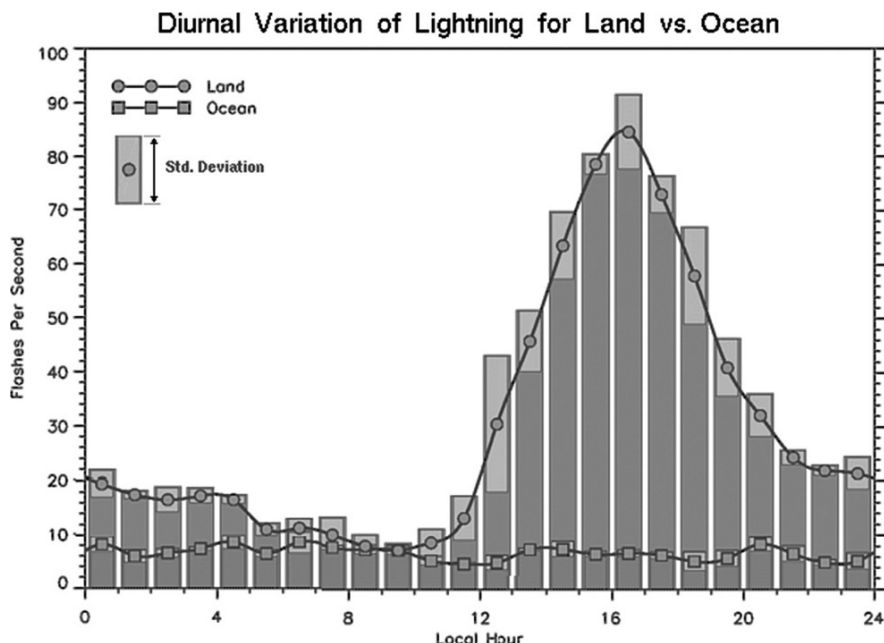


Fig. 24.2 Diurnal variations of global lightning over land and oceans (<http://thunder.msfc.nasa.gov/>)

The distribution of global thunderstorms is directly linked to the Earth's climate, and more specifically, the general circulation of the atmosphere (Wallace and Hobbs, 2006). The maximum solar heating at the surface in the tropics results in rising thermals and vertical mixing in the atmosphere. The region of rising air that occurs along the thermal equator is known as the inter-tropical convergence zone (ITCZ) due to the resulting convergence of surface winds from the northern and southern hemispheres along this boundary. The thermal equator migrates north and south of the geographic equator according to the seasons, with the thermal equator furthest north in June–August during the northern hemisphere summer, and furthest south in December–February during the southern hemisphere summer. Tropical thunderstorms are generally associated with the ITCZ and the convective clouds that form along the thermal equator.

Due to the different thermal capacity of land versus oceans, the continental regions heat up more rapidly than the oceans, resulting also in longitudinal differences in the location and width of the ITCZ. This also results in a significant difference in convective intensity observed between oceanic and continental convection in the tropics (Lemone and Zipser, 1980; Jorgenson and Lemone, 1989). Updraft velocities in oceanic thunderstorms may reach a maximum of 10 m/s, while over continental regions the updrafts may reach 50 m/s or greater (Price and Rind, 1992; Williams and Stanfill, 2002; Williams et al., 2004). Since updraft intensity plays a major role in thunderstorm electrification and lightning frequencies (Baker et al., 1995; 1999),

this dramatic difference in thunderstorm dynamics results in the lightning activity over the oceans being an order of magnitude less than over the continents. In fact the boundary between land and ocean is very clearly seen in satellite images of tropical lightning activity (Fig. 24.1). Williams et al. (2004) have readdressed this difference in land/ocean lightning, considering two opposing hypotheses. The one deals with the thermal hypothesis where the land surface heats up more rapidly during the day as compared with the oceans, and hence the instabilities, convection and lightning are more vigorous over the land areas. The other deals with the aerosol hypothesis, due to the order-of-magnitude difference in the concentration of cloud condensation nuclei (CCN) between the continents and the oceans, that can influence cloud microphysics and the intensity of deep convective storms. Using islands as miniature continents Williams et al. (2004) concluded that the thermal hypothesis still appears to be the main cause of the land-ocean contrasts in observed lightning activity.

It should be noted that not all tropical continental thunderstorms are intense lightning generators. The tropical monsoon periods are characterized by the seasonal onshore flow of moist oceanic air, resulting in heavy rainfall in continental thunderstorms, however with low lightning rates (Petersen et al., 2002; Williams et al., 2002). This generally occurs in the Indian Monsoon, the African Monsoon, the Brazilian Monsoon and the Australian Monsoon. Intense lightning activity prefers a somewhat drier environment, which may explain the difference between African and South American lightning activity (Williams and Satori, 2004; see Section 24.4).

The air that rises within the tropical convective storms along the ITCZ eventually reaches the tropopause (between 15 and 20 km altitude) and the stable stratosphere, and is then forced to flow north and south away from the equator. This poleward moving air is influenced by Coriolis's force, resulting in the deviation of the winds towards the east in both hemispheres (Price, 2006). This air continues to radiate heat to space and hence cools and sinks as it is transported northeast/southeast away from the tropics. The air eventually subsides around 30° north and south, heating adiabatically as it sinks. These regions of subsidence in the sub-tropics define the regions of our planet where deserts are found, and hence very few thunderstorms. The subsidence (resulting in high pressure at the surface) together with the heating of the air as it sinks (resulting in low relative humidity), and the stabilizing of the atmosphere, result in minimal precipitation in these regions. It should be pointed out that while the subsidence reduces the relative humidity in the mid and upper atmosphere, the capping of the boundary layer (particularly over the oceans), together with the warm temperatures, can result in very high humidities in the boundary layer in subtropical regions.

This meridional circulation pattern, with rising motion along the ITCZ and sinking motion in the subtropics, is known as the Hadley circulation, and is extremely important in the redistribution of heat, moisture and momentum around the planet. Near the surface, the Hadley circulation connects the sub-tropical regions and the ITCZ via the north-easterly (northern hemisphere) and south-easterly (southern hemisphere) trade winds that blow between ± 30 degrees latitude. It is therefore no coincidence that lightning activity is found adjacent to the ITCZ, while little lightning activity is found in the subtropics around 30 degrees north and south.

In addition to the return flow towards the equator at the surface in the Hadley circulation, part of the tropical air reaching the surface around 30° moves poleward, where it meets cold dry air arriving from the Arctic (northern hemisphere) and Antarctic (southern hemisphere). This additional region of convergence, known as the polar front, is another region of forced uplift and hence the development of clouds, thunderstorms and lightning. Frontal thunderstorms occur at the boundary (front) between different air masses, normally cold-dry polar air meeting warm-moist tropical air. The greater the density differences between the air masses (temperature and humidity) the greater the atmospheric instabilities that develop, and the greater the intensity of these storms. The manifestation of the intensity appears visibly as frequent lightning discharges. Mid-latitude storms generally rotate around a region of low pressure (anti-clockwise in the northern hemisphere (cyclonic rotation) and clockwise (anti-cyclonic) in the southern hemisphere), while simultaneously propagating eastward around the globe with the general westerly flow in the midlatitudes (30–60 degrees latitude) (Price, 2006).

As with the ITCZ, the polar front also migrates with the seasons from around 50–60 degrees latitude in the summer, to 30–40 degrees in the winter. These are the latitude bands of the midlatitude synoptic storm systems, associated with cold and warm fronts, and embedded thunderstorms. These regions are associated primarily with summer thunderstorm activity over the mid-latitude continents, although oceanic winter thunderstorm activity also occurs in these regions. As we move further poleward from the polar front we encounter another region of subsidence in the polar regions, where again few thunderstorms are observed.

Large instabilities in the atmosphere can also occur along frontal zones that divide warm-moist air from cold-dry air around high pressure cells (e.g. The Bermuda High). The flow around a High Pressure Cell is anticlockwise in the northern hemisphere, opposite to the direction of flow around a low pressure system, and can extend northward into the mid-latitude regions. The air is stable at the center of the high pressure cell resulting in clear, hot and humid weather in the summer months. As this warm humid air travels poleward around the high pressure system, mixing can occur between the cool dry air (from polar regions) and the warm moist air, triggering vigorous convection. This convection often produces a ring of thunderstorms around the high pressure center which will also rotate in a clockwise manner around the high pressure cell. This often produces the common “ring of fire” thunderstorm pattern which often develops into mesoscale convective systems (MCSs) which can produce complexes of thunderstorms called mesoscale convective complexes (MCCs). These huge thunderstorm complexes are prolific lightning producers (Lyons et al., 2003).

Global thunderstorms can therefore occur in two very different environments. First, the tropical airmass type thunderstorms resulting from the diurnal heating of the surface of the Earth. These late afternoon continental thunderstorms occur mainly in the tropics but can also occur during summer months in mid-latitudes where “static” instabilities can develop in the afternoons on hot summer days. Second, the frontal thunderstorms occur primarily in mid- to high latitudes where different types of air masses interact and result in baroclinic instabilities along cold,

warm and stationary fronts. Frontal thunderstorms can occur at any hour of the day, over continent and ocean, and during summer and winter. What is needed for these thunderstorms to develop is a strong density gradient between adjacent air masses. These density gradients can be caused either by temperature differences, humidity differences, or a combination of both.

It should be noted that in addition to the above ways of producing thunderstorms we also observe thunderstorms due to orographic forcing (uplift over topography). Mountain ranges and islands force air to flow upwards and can initiate instabilities that trigger the formation of precipitation and thunderstorms. For example, locations to the south of the Himalayas have very intense lightning activity due to the forced uplift of moist air penetrating inland from the Indian Ocean (Fig. 24.1).

24.3 Lightning and Climate

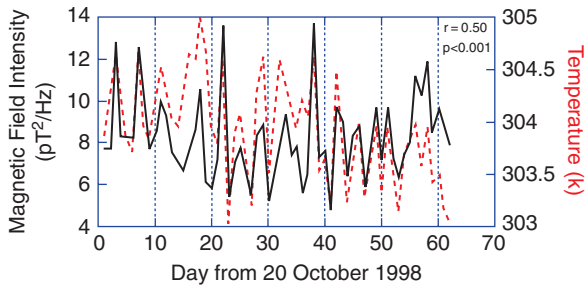
There have been numerous papers in the past few years dealing with the connection between lightning, climate and climate change. An extensive review of the topic of global climate-lightning connections was given by Williams (2005), with additional discussion by Price (2006, 2008), and the reader is directed to these papers for further information.

24.3.1 Temperature

Due to the interest in global warming, there have been numerous studies looking at the relationship and sensitivity of lightning activity to changes in surface temperature. Since long term global lightning observations do not exist, relationships are normally investigated on shorter time scales. Many time scales have been explored, from diurnal (Price, 1993; Markson and Price, 1999) and daily variations (Price and Asfur, 2006a), to 5-day waves (Patel, 2001), intraseasonal (Anyamba et al., 2000) semiannual variations (Williams, 1994; Satori and Ziegler, 1996; Fullekrug and Fraser-Smith, 1998; Nickolaenko et al., 1999), annual (Heckman et al., 1998; Christian et al., 2003; Toumi and Qie, 2004) and interannual scales, dominated by the El Nino (Williams, 1992; Reeve and Toumi, 1999; Satori and Ziegler, 1999). On all these timescales we observe a positive relationships between temperature and lightning, with lightning increasing anywhere from 10 to 100% for every one degree surface warming.

Recent studies continue to show the positive correlation between surface temperatures and lightning activity (Williams et al., 2005; Price and Asfur, 2006a; Sekiguchi et al., 2006). Figure 24.3 shows the daily regionally averaged surface temperatures over Africa compared with the regional lightning activity, based on Schumann resonance measurements, over a 2-month period (Price and Asfur, 2006a). It is clear that for the tropical lightning centers, surface temperature is a key driving factor of daily lightning activity. However, there does not appear to be

Fig. 24.3 Daily regional lightning activity (black) and regional mean surface temperatures (grey) over Africa for a 2-month period from 20 October to 20 December 1998 (from Price and Asfur, 2006a)

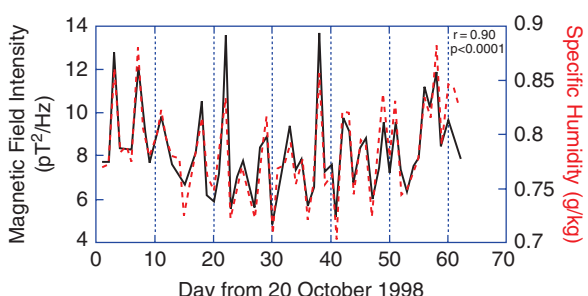


any long term trend detected in lightning activity over the last fifty years (Price and Asfur, 2006b; Markson, 2007).

24.3.2 Water Vapor

Water vapor in the atmosphere is the primary natural greenhouse gas influencing the climate of the Earth. Since water vapor absorbs infrared radiation emitted from the Earth's surface, increases in water vapor in a warmer climate would result in a positive feedback, amplifying the initial warming (Del Genio, 2002). In general, the Earth's climate is believed to be much more sensitive to changes in water vapor in the upper troposphere, where the concentrations are naturally very low. Recently it has been shown that thunderstorms deposit large amounts of water in the upper troposphere, moistening of the upper tropospheric environment (Price, 2000; Price and Asfur, 2006a), with important consequences for the Earth's climate (Rind, 1998). Figure 24.4 shows the relationship between daily lightning activity over Africa, based on Schumann resonance measurements, and the specific humidity in the upper troposphere (300 hPa). The curves have been shifted by 24 hours to show the agreement, however, the lightning peaks one day before the peak humidity fields in the upper troposphere. The lightning activity is a means of monitoring the intensity of deep convection, and hence is well correlated with the vertical transport of water vapor by thunderstorms into the upper atmosphere.

Fig. 24.4 The daily relationship between lightning activity (black) and upper troposphere specific humidity (300 hPa) (grey) over Africa during a 2-month period from 20 October to 20 December 1998. The lightning curve has been shifted forward one day to show the excellent agreement (from Price and Asfur, 2006a)



Related to water vapor, Sato and Fukunishi (2005) showed a connection between tropical lightning activity and high cloud coverage in the tropics, while strong connections between lightning and upper tropospheric ice water content (Petersen et al., 2005) and ice crystal size (Sherwood et al., 2006) have recently been demonstrated. Water vapor, cloud cover, ice water content, and ice particle size all have direct impacts on the Earth's radiation balance, and therefore lightning may supply an important tool for studying the variability and changes in these important climate parameters.

24.3.3 Tropospheric Chemistry

Lightning itself can influence the climate via the production of nitrogen oxides ($\text{NO} + \text{NO}_2 = \text{NO}_x$) followed by the production of ozone, another efficient greenhouse gas. A comprehensive review of this topic is given by Schumann and Huntrieser (2007), with references therein. Recent field experiments such as TROCCINOX (Huntrieser et al., 2007) show greatly enhanced NO_x concentrations in thunderstorm anvils, with enhanced ozone concentrations downwind. Ryu and Jenkins (2005) and Grewe (2007) have also shown the significant influence of lightning on tropospheric ozone concentrations.

The global amount of NO_x produced by lightning and thunderstorms is still highly uncertain. There are a wide variety of lightning flashes and thunderstorms, and therefore measurements in individual field experiments may not be reliable for extrapolating globally. It is also difficult to assign a certain concentration of NO_x in a specific storm to a specific lightning discharge. Even if this was possible, the important parameters of the lightning discharge (energy, length, peak current, tortuosity, altitude, number of return strokes, etc.) are needed in order to extrapolate the results to other lightning discharges around the globe. Nevertheless, lightning is believed to be the largest source of NO_x in the upper troposphere, where lifetimes of a few days result in NO_x playing an important role modulating the Earth's climate (Price et al., 1997).

24.4 Future Climate Change

There is increasing evidence that global temperatures are increasing, and the cause is very likely due to the increasing anthropogenic greenhouse gases in the atmosphere (IPCC, 2007). However, since we do not know how lightning and thunderstorms will respond to a warmer world, we need to either use climate change proxies from the present and past, or we need to run computer simulations of how global warming may impact thunderstorms in a future climate.

It needs to be emphasized that lightning-climate relationship based on data for short periods, and different regions, in the present climate cannot always be used as a proxy for future global warming. Different locations may be influenced by

factors such as topography, vegetation, atmospheric circulation patterns, ocean currents, etc., that may complicate their use as proxies for surface warming. Hence, we need to use these proxies with caution when talking about long term changes in the Earth's climate. Lindzen et al. (1995) has discussed the problems of using the annual cycle as a proxy for future climate change. Furthermore, regional climate variability such as the ENSO cycle is more related to shifts in circulation patterns in the atmosphere than changes in temperature. Hence, we need to be cautious when extrapolating present day variability to future global warming.

With that said, we now have a decade of simultaneous measurements of lightning and rainfall from space. The Tropical Rain Measuring Mission (TRMM) satellite has provided great insights into global lightning distributions (Christian et al., 2003), allowing us to examine the relationship between lightning and Earth's climate. It is well known that global lightning is divided between the three hot-spots, or chimneys, over the tropical land masses (Africa, South America and Southeast Asia), while tropical precipitation is more continuous around the tropics following the intertropical convergence zone (ITCZ) (Price, 2008).

We know that the three thunderstorm chimneys are ranked (1) Africa, (2) South America and (3) Southeast Asia, from the most active to the least active regions. However, the opposite trend is observed for precipitation, with the chimneys ranked (1) Southeast Asia, (2) South America, and (3) Africa. On a regional annual mean climate scale, less precipitation implies more lightning, which appears contradictory (Price, 2008).

Williams and Satori (2004) looked into this difference in more detail, examining the differences between tropical Africa and tropical South America. They showed that the main difference between Africa and South American lightning activity was due to Africa being hotter and drier than South America. The greater continentality of Africa is attributed to its greater elevation above sea level, and to the asymmetry of the synoptic scale delivery of moisture to the region. In addition, Williams et al. (2005) showed that as the height of thunderstorm cloud base increased, so did the lightning activity. Higher cloud base implies drier surface conditions, which would support these observations. Carey and Buffalo (2007) also recently demonstrated that thunderstorms with predominantly positive lightning (often associated with severe weather) were more likely in a drier environment.

This apparent paradox also appears evident on the ENSO timescales (Hamid et al., 2001) where during the strong El Nino of 1997–1998 severe drought conditions persisted across Indonesia, while the lightning activity increased by 57%. This could occur if we had fewer thunderstorms, with each thunderstorm more vigorous, producing more lightning, or possibly by raising the cloud base, promoting the mixed phase electrification (Williams et al., 2002) with less warm rain production (Williams et al., 2005). In support of this, Hamid et al. (2001) showed that the thunderstorms during the drier El Nino period had greater vertical development including thicker mixed-phase precipitation zones.

When looking at modeling studies of global warming scenarios, the recent IPCC report (IPCC, 2007) presents results from more than 20 different models, together with the responses of these models to rising concentrations of greenhouse gases.

As related to tropical convection and lightning, once again a paradox arises. All models show that the greatest warming due to increasing greenhouse gases will occur not at the surface, but in the equatorial upper troposphere. The reason for this is that the models predict a moistening of the upper troposphere, due to enhanced deep convection in the tropics, and this extra water vapor in the upper troposphere is a strong greenhouse gas, absorbing infrared radiation emitted from the Earth's surface. However, if the upper atmosphere is warmed relative to the surface, the atmospheric lapse rate (dT/dz) becomes more stable, tending to inhibit future convection. So we would expect that the stabilization of the atmosphere as the climate warms would reduce the amount of thunderstorms, and hence lightning.

However, numerous climate model simulations have shown that lightning activity will increase in a warmer climate (Price and Rind, 1994; Grenfell et al., 2003; Shindell et al., 2006). Although the parameterizations of lightning in global climate models are quite crude (Price and Rind, 1992; Allen and Pickering, 2002; Futyau and Del Genio, 2007), the models nevertheless manage to duplicate the present global lightning climatologies (Shindell et al., 2006). All of these modeling studies indicate an approximate 10% increase in lightning activity globally for every 1 K global warming, with most of the increase occurring in the tropics, exactly where we expect the atmosphere to become more stable. This paradox was dealt with in more depth by Del Genio et al. (2007) where they showed that in a doubled-CO₂ climate the updrafts strengthen by ~1 m/s, due to a rise in the height of the freezing level in the model. They showed that in certain regions, such as the western United States, the drying in a warmer climate reduces the frequency of thunderstorms, but the strongest storms occur 26% more often. In other words, the drier climate produces less thunderstorms overall, but those storms that do develop are more intense in a warmer climate. This agrees with recent observations (Williams et al., 2005) showing increased electrification in the drier regions of the Great Plains of the United States.

24.5 Discussion and Summary

It is clear that the spatial and temporal distributions of lightning activity on Earth are governed by the climate itself. The diurnal solar heating, the latitudinal temperature gradient, the general circulation of the atmosphere, the location of regions of convergence and divergence, static and baroclinic instabilities, etc., all influence the global distributions of thunderstorms. In addition, we know that thunderstorms track the motion of the sun during the seasons, with most lightning activity being in the summer hemisphere.

On short time scales (hourly, daily, monthly and annual) there appears to be a robust positive correlation between tropical lightning activity and surface temperature, upper tropospheric water vapor, cloud cover, and anvil ice content. Whether these relationships hold on longer time scales is still uncertain, although climate models do support the positive correlation between lightning and global temperatures.

Since lightning can be monitored easily, and continuously, from ground networks, lightning may become a useful tool for monitoring changes in important climate parameters in the future. Furthermore, lightning itself is an important source of nitrogen oxides (NO_x) in the atmosphere, with implications for ozone production, and the Earth's radiation balance. Lightning is likely the major source of NO_x in the upper troposphere.

On climatic scales, when considering the tropical continental centers of lightning activity, they rank in the opposite order when considering lightning and precipitation. While Africa has the highest lightning activity of the three chimney regions, it has the lowest rainfall, while being the hottest. When we look at the impact of the ENSO cycle on tropical lightning and rainfall, a similar negative relationship is observed, with hot drought-stricken Southeast Asia during the El Nino years having more lightning than during the wetter cooler La Nina periods. Hence, when considering lightning-climate relationships, we need to also consider the moisture availability and not only temperature.

Climate models provide some insight into this paradox that shows more lightning with less rainfall, since they too predict increasing lightning activity as the climate warms and dries. Both regionally and globally climate models predict increases in lightning activity in a warmer climate, even though the atmosphere becomes more stable and the surface tends to dry as the climate warms. However, one needs to be cautious about future climate simulations of lightning activity, both due to the crude lightning parameterizations used in these models, but also due to the problems with convective cloud parameterizations in climate models. Since the lightning parameterizations use the convective cloud parameterization for estimating the spatial and temporal distribution of lightning in the model, if there are problems with the cloud parameterizations, this will translate to problems with the lightning estimates. Furthermore, the lightning parameterizations are based on empirical relationships that may not be valid in a different climate.

All of these relationships showing less rainfall associated with more lightning may be explained if drier climates have fewer thunderstorms, with each storm being more intense. This is what model studies show happens in a warmer climate. This has also now been documented in the Mediterranean region over the past 50 years, where the total rainfall has been decreasing, while the intense rainfall events have been increasing (Alpert et al., 2002).

Previous studies have indicated that increased convective activity with associated lightning will moisten the upper troposphere (Price, 2000; Price and Asfur, 2006). Hence, a drier surface resulting in a wetter upper atmosphere appears to present a contradiction. However, the upper troposphere is naturally extremely dry, and therefore increasing the frequency and/or intensity of thunderstorms in a drier climate will indeed moisten the upper troposphere. This enhanced moistening is what drives the maximum warming in climate models in a double- CO_2 world.

One factor that has not been addressed here is the role of aerosols in thunderstorms electrification. It is possible that drier climates result in more suspended aerosols and cloud condensation nuclei, hence influencing cloud microphysics and cloud electrification (Williams et al., 2002). However, it should be pointed out that

all model simulations discussed here do not include any aerosol effects on lightning, and address only thermodynamic changes in their simulations. Whether aerosol effects would enhance these changes is a topic for future studies.

References

- Allen, D.J., and K.E. Pickering, 2002: Evaluation of lightning flash rate parameterizations for use in a global chemical transport model, *J. Geophys. Res.*, 107(D23), 4711, doi:10.1029/2002JD002066.
- Alpert, P., T. Ben-Gai, A. Baharad, Y. Benjamini, D. Yekutieli, M. Colacino, L. Diodato, C. Ramis, V. Homar, R. Romero, S. Michaelides, and A. Manes, 2002: The paradoxical increase of Mediterranean extreme daily rainfall in spite of decrease in total values, *Geophys. Res. Lett.*, 29, 11, 31-1-31-4.
- Anyamba, E., E.R. Williams, J. Susskind, A. Fraser-Smith, M. Fullekrug, 2000: The manifestation of the Madden-Julian oscillation in global deep convection and in the Schumann resonance intensity, *J. Atmos. Sci.*, 57, 1029–1044.
- Baker, M.B., H.J. Christian, and J. Latham, 1995: A computational study of the relationships linking lightning frequency and other thundercloud parameters, *Quart. J. Roy. Met. Soc.*, 121, 1525–1548.
- Baker, M.B., A.M. Blyth, H.J. Christian, J. Latham, K.L. Miller, and A.M. Gadian, 1999: Relationship between lightning activity and various thundercloud parameters: Satellite and modeling studies, *Atmos. Res.*, 51, 221–236.
- Carey, L.D, and K.M Buffalo, 2007: Environmental control of cloud-to-ground lightning polarity in severe storms, *Mon. Wea. Rev.*, 135(4), 1327–1353.
- Christian, H.J., R.J. Blakeslee, D.J. Boccippio, W.L. Boeck, et al., 2003: Global frequency and distribution of lightning as observed from space by the Optical Transient Detector, *J. Geophys. Res.*, 108, 4005, doi:10.1029/2002JD002347.
- Del Genio, A.D., 2002: The dust settles on water vapor feedback. *Science* 296, 665–666.
- Del Genio, A.D., Y. Mao-Sung, and J. Jonas, 2007: Will moist convection be stronger in a warmer climate? *Geophys. Res. Lett.*, 34, L16703, doi:10.1029/2007GL030525.
- Fullekrug, M., and A. Fraser-Smith, 1998: Global lightning and climate variability inferred from ELF field variations, *Geophys. Res. Lett.*, 24, 2411–2414.
- Futyan, J.M., and A.D. Del Genio, 2007: Relationships between lightning and properties of convective cloud clusters, *Geophys. Res. Lett.*, 34, L15705, doi:10.1029/2007GL030227.
- Grenfell, J.L., D.T. Shindell, and V. Grewe, 2003: Sensitivity studies of oxidative changes in the troposphere in 2100 using the GISS GCM, *Atmos. Chem. Phys. Discuss.*, 3, 1805–1842.
- Grewe, V., 2007: Impact of climate variability on tropospheric ozone, *Sci. Total Environ.*, 374(1), 167–181.
- Hamid, E.Y., Z. Kawasaki, and R. Mardiana, 2001: Impact of the 1997–98 El Nino on lightning activity over Indonesia, *Geophys. Res. Lett.*, 28, 147–150.
- Heckman, S., E. Williams, and B. Boldi, 1998: Total global lightning inferred from Schumann resonance measurements, *J. Geophys. Res.*, 103, 31775–31779.
- Hendon, H.H., and K. Woodberry, 1993: The diurnal cycle of tropical convection, *J. Geophys. Res.*, 98(D9), 16623–16638.
- Huntrieser, H., H. Schlager, A. Roiger, M. Lichtenstern, U. Schumann, C. Kurz, D. Brunner, C. Schwierz, A. Richter, and A. Stohl, 2007: Lightning-produced NO_x over Brazil during TROC-CINOX: Airborne measurements in tropical and subtropical thunderstorms and the importance of mesoscale convective systems, *Atmos. Chem. Phys.*, 7, 2987–3013.
- Intergovernmental Panel on Climate Change (IPCC), 2007: Climate Change 2007: The Physical Science Basis. World Meteorological Organization (WMO) and UN Environment Programme (UNEP).

- Jorgenson, D.P., and M.A. Lemone, 1989: Vertical velocity in oceanic convection off tropical Australia, *J. Atmos. Sci.*, 51, 3183–3193.
- Lemone, M.A., and E.J. Zipser, 1980: Cumulonimbus vertical velocity events in GATE. Part I: Diameter, intensity and mass flux, *J. Atmos. Sci.*, 37, 2444–2457.
- Lindzen, R.S., B. Kirtman, D. Kirk-Davidoff, and E.K. Schneider, 1995: Seasonal surrogate for climate, *J. Clim.*, 8, 1681–1684.
- Lyons, W.A., T.E. Nelson, E.R. Williams, S.A. Cummer, and M.A. Stanley, 2003: Characteristics of sprite-producing positive cloud-to-ground lightning during the 19 July 2000 STEPS mesoscale convective system, *Mon. Wea. Rev.*, 131, 2417–2427.
- Markson, R., 2007: The global circuit intensity: Its measurement and variation over the last 50 years, *Bull. Amer. Meteor. Soc.*, 88, 1–19.
- Markson, R., and C. Price, 1999: Ionospheric potential as a proxy index for global temperatures, *Atmos. Res.*, 51, 309–314.
- Nickolaenko, A.P., M. Hayakawa, and Y. Hobara, 1999: Long-term periodical variations in global lightning activity deduced from Schumann resonance monitoring, *J. Geophys. Res.*, 104, 27585–27591.
- Patel, A., 2001: Modulation of African lightning and rainfall by the global five day wave, MSc thesis, Department of Mechanical Engineering, MIT, Cambridge, MA, 176 pp.
- Petersen, W.A., S.W. Nesbitt, R.J. Blakeslee, R. Cifeli, P. Hein, and S.A. Rutledge, 2002: TRMM observations of intraseasonal variability in convective regimes over the Amazon, *J. Clim.*, 15, 1278–1294.
- Petersen, W.A., H.J. Christian, and S.A. Rutledge, 2005: TRMM observations of the global relationship between ice water content and lightning, *Geophys. Res. Lett.*, 32, L14819, doi:10.1029/2005GL023236.
- Price, C., 1993: Global surface temperatures and the atmospheric electrical circuit, *Geophys. Res. Lett.*, 20, 1363–1366.
- Price, C., 2000: Evidence for a link between global lightning activity and upper tropospheric water vapor, *Nature*, 406, 290–293.
- Price, C., 2006: Global thunderstorm activity, in *Sprites, Elves and Intense Lightning Discharges*, M. Fullekrug, et al. (eds.), Springer, Amsterdam, The Netherlands, 85–99.
- Price, C., 2008: Lightning sensors for observing, tracking and nowcasting severe weather, *Sensors*, 8, 157–170.
- Price, C., and D. Rind, 1992: A simple lightning parameterization for calculating global lightning distributions, *J. Geophys. Res.*, 97, 9919–9933.
- Price, C., and D. Rind, 1994: Possible implications of global climate change on global lightning distributions and frequencies, *J. Geophys. Res.*, 99, 10823–10831.
- Price, C., J. Penner, and M. Prather, 1997: NO_x from lightning, part I: Global distribution based on lightning physics, *J. Geophys. Res.*, 102, 5929–5941.
- Price, C., and A. Melnikov, 2004: Diurnal, seasonal and inter-annual variations in the Schumann resonance parameters, *J. Atmos. Sol. Terr. Phys.*, 66, 1179–1185.
- Price, C., and M. Asfur, 2006a: Can lightning observations be used as an indicator of upper-tropospheric water vapor variability? *Bull. Amer. Meteor. Soc.*, 87, 291–298.
- Price, C., and M. Asfur, 2006b: Long term trends in lightning activity over Africa, *Earth Planets Space*, 58, 1–5.
- Price, C., O. Pechony, and E. Greenberg, 2007: Schumann resonances in lightning research, *J. Lightning Res.*, 1, 1–15.
- Reeve, N., and R. Toumi, 1999: Lightning activity as an indicator of climate change, *Quart. J. Roy. Met. Soc.*, 125, 893–903.
- Rind, D., 1998: Just add water vapor, *Science*, 281, 1152.
- Ryu, J.H., and G.S. Jenkins, 2005: Lightning-tropospheric ozone connections: EOF analysis of TCO and lightning data, *Atmos. Environ.*, 39, 5799–5805.
- Sato, M., and H. Fukunishi, 2005: New evidence for a link between lightning activity and tropical upper cloud coverage, *Geophys. Res. Lett.*, 32, L12807, doi:10.1029/2005GL022865.

- Satori, G., and B. Ziegler, 1996: Spectral characteristics of Schumann resonances observed in central Europe, *J. Geophys. Res.*, 101, 29663–29669.
- Satori, G., and B. Ziegler, 1999: El Niño related meridional oscillations of global lightning activity, *Geophys. Res. Lett.*, 26, 1365–1368.
- Satori, G., E. Williams, and V. Mushtak, 2008: ELF Electromagnetic Signatures of Global Lightning Activity, this volume.
- Schumann, U., and H. Huntrieser, 2007: The global lightning-induced nitrogen oxides source, *Atmos. Chem. Phys.*, 7, 2623–2818.
- Sekiguchi, M., M. Hayakawa, A.P. Nickolaenko, and Y. Hobara, 2006: Evidence on a link between the intensity of Schumann resonance and global surface temperature, *Ann. Geophys.*, 24, 1809–1817.
- Sherwood, S., V.T.J. Phillips, and J.S. Wettlaufer, 2006: Small ice crystals and the climatology of lightning, *Geophys. Res. Lett.*, 33, L05804, doi:10.1029/2005GL025242.
- Shindell, D.T., G. Faluvegi, N. Unger, E. Aguilar, G.A. Schmidt, D.M. Koch, S.E. Bauer, and R.L. Miller, 2006: Simulations of preindustrial, present-day, and 2100 conditions in the NASA GISS composition and climate model G-PUCCINI, *Atmos. Chem. Phys.*, 6, 4427–4459.
- Toumi, R., and X. Qie, 2004: Seasonal variation of lightning on the Tibetan Plateau: A spring anomaly? *Geophys. Res. Lett.*, 31, L04115, doi:10.1029/2003GL018930.
- Wallace, J.M., and P.V. Hobbs, 2006: *Atmospheric Science: An Introductory Survey*, Academic Press, New York.
- Williams, E.R., 1992: The Schumann resonance: A global tropical thermometer, *Science*, 256, 1184–1187.
- Williams, E.R., 1994: Global circuit response to seasonal variations in global surface air temperature, *Mon. Wea. Rev.*, 122, 1917–1929.
- Williams, E.R., 2005: Lightning and climate: A review, *Atmos. Res.*, 76, 272–287.
- Williams, E.R., et al., 2002: Contrasting convective regimes over the Amazon: Implications for cloud electrification, *J. Geophys. Res.*, LBA Special Issue, 107, D20, 8082, doi:10.1029/2001JD000380.
- Williams, E., T. Chan, and D. Boccippio, 2004: Islands as miniature continents: Another look at the land-ocean lightning contrast, *J. Geophys. Res.*, 109, D16206, doi:10.1029/2003JD003833.
- Williams, E.R., V. Mushtak, D. Rosenfeld, S. Goodman, and D. Boccippio, 2005: Thermodynamic conditions favorable to superlative thunderstorm updraft, mixed phase microphysics and lightning flash rate, *Atmos. Res.*, 76, 288–306.
- Williams, E., and S. Stanfill, 2002: The physical origin of the land-ocean contrast in lightning activity, *C. R. Physique*, 3, 1277–1292.
- Williams, E.R., and G. Satori, 2004: Lightning, thermodynamic and hydrological comparisons of the two tropical continental chimneys, *J. Atmos. Sol. Terr. Phys.*, 66, 1213–1231.

Chapter 25

Impact of Lightning on Air Chemistry and Climate

Volker Grewe

Abstract The study shows that climate change does not necessarily lead to an increase in lightning as proposed by studies linking lightning to convective cloud top heights, but may reduce lightning. The impact of lightning on air chemistry and on climate is studied using simulation results obtained with a coupled ensemble climate-chemistry model from 1960 to 2020. The model simulates lightning and lightning induced nitrogen oxides (NO_x) using a parameterisation based on the convective mass flux (updraft velocity). The computed flash frequency distribution over the globe is broadly in agreement with satellite observations, except for some oceanic regions. The results show, different from general expectations, a decrease in lightning activity in a warming climate. The decrease occurs because of less frequent though stronger convective events. Hence lightning decreases in total flash frequency, although individual events produce more lightning. The computed decrease in lightning NO_x emissions is overlaid with an increase in sensitivity of ozone production to NO_x amounts, which first leads to an increase in lightning ozone until the 1970s and then to a decrease. The sensitivity of climate in terms of radiative forcing to ozone changes is generally decreasing during the simulation.

Keywords Atmospheric chemistry · Climate · Lightning · Modelling · Observations

25.1 Introduction

Lightning discharges produce nitrogen oxides (NO_x), leading to global emissions in the range of $5 \pm 3 \text{ Tg(N)}$ per year, which represents roughly 10% of all nitrogen oxide emissions (Schumann and Huntrieser, 2007). Since in contrast to surface sources of NO_x , lightning is always connected to deep convective transport into the

V. Grewe (✉)

Deutsches Zentrum für Luft- und Raumfahrt (DLR), Institut für Physik der Atmosphäre, Oberpfaffenhofen, 82234 Wessling, Germany
e-mail: volker.grewe@dlr.de

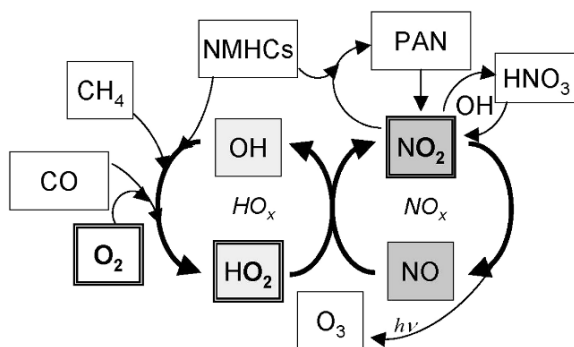
upper troposphere, its impact on ozone (O_3) is much larger than for surface sources (e.g. Wu et al., 2007). Furthermore lightning often occurs in regions which are less affected by other sources, e.g. over tropical oceans, or continental remote areas. This leads to a contribution of lightning NO_x to ozone of around 40% in the tropical free troposphere (Grewe, 2007).

Tropospheric ozone is produced by reactions, which include hydrocarbons, producing HO₂ and nitrogen oxides (NO),



forming NO_2 , which can be photolysed in the troposphere producing atomic oxygen and recombined with oxygen to form ozone (Fig. 25.1). Hence, the efficiency of an emitted NO molecule to produce ozone depends on the availability of HO_x radicals and the lifetime of NO_x . A limiting factor for the lifetime in the free troposphere is the conversion of NO_2 into HNO_3 , which is soluble and can be washed out by precipitating clouds.

Ozone is an important greenhouse gas, which contributes by approximately 5% to the background greenhouse effect. Tropospheric ozone changes contribute with a radiative forcing of 0.35 W/m^2 to the total anthropogenic radiative forcing of 1.6 W/m^2 , i.e., contribute by 20% to the recent anthropogenic warming (IPCC, 2007). (Radiative forcing, RF, is defined as the change in radiation flux at the tropopause due to a perturbation). Therefore ozone formed by lightning NO_x emissions plays an important role in the climate system, since it largely contributes to the atmospheric ozone concentration and since it affects ozone in the upper troposphere (Toumi et al., 1996), where its impact on radiative forcing is larger than at lower levels (Lacis et al., 1990; Hansen et al., 2005). Radiative forcing is a good indicator for climate change, i.e. near-surface temperature change, in the case of perturbations to well-mixed greenhouse gases. For other climate agents, especially ozone, it has a limited applicability, since the inhomogeneity of the perturbation affects its climate impact. For example, European and Asian NO_x emissions lead to very different ozone change pattern and hence different changes in radiative forcing. The



calculated near-surface temperature change per unit radiative forcing (= climate sensitivity) differs in the order of 20% (Berntsen et al., 2005).

Lightning NO_x emissions also reduce the concentration of the greenhouse gas methane, since they change the HO_x partitioning, i.e. the OH to HO₂ ratio, towards OH via reaction (25.1), enhancing the reaction of OH with methane (Fig. 25.1) (Isaksen and Hov, 1987). The importance of the ozone increase and methane decrease on radiative forcing depends on altitude and latitude, where the emissions occur. In the tropical upper troposphere, where most of the lightning NO_x emissions occur, the ozone impact is calculated to be approximately 6 times larger than the methane impact (Grewe and Stenke, 2008).

Climate change may also impact lightning activity and the effectiveness of an emitted NO molecule to produce ozone. A possible link between global surface warming and the global atmospheric electrical circuit was pointed out (Williams, 1992; 1994; Price, 1993; Markson and Price, 1999; Harrison, 2004). Positive correlations between surface temperatures and lightning activity were found (see Schumann and Huntrieser, 2007 for a summary). IPCC (Trenberth and Jones, 2007) clearly stated that precipitation observations over oceans are not reliable enough to derive trends. On the other hand, most pronounced changes in convection and precipitation are expected to occur over oceans with an increase in precipitation at equatorial latitudes and a decrease at mid-latitudes (Meehl and Stocker, 2007). Brinkop (2002) analysed a climate change simulation and showed that although precipitation increases in a future climate, convective precipitation and the number of convective events decreased. Another climate change study by Del Genio et al. (2007) found similar results, indicating a decrease in the number, but increase in the strength of lightning producing storms. The implications of these studies on future changes in lightning are unclear, because the mechanism driving lightning changes is not well established. This implies that depending on whether the number of convective events, the strength of convective events (updraft velocities), convective precipitation, or convective cloud top heights are best correlated with lightning changes, lightning frequencies may either increase or decrease in a future climate.

Schumann and Huntrieser (2007) gave an overview on modelling studies, which investigated the impact of future climate change on lightning. Increases in lightning of 10–15% per 1 K of warming were found in multi-decadal modelling studies with a range of 0–60% per K. However all of these studies applied lightning parameterisations, which differ in the formulation over ocean and land to account for observed differences and all of them coupled lightning frequencies to simulated convective cloud top heights.

Here I present chemistry-climate simulations, which are broadly in agreement with the findings of the IPCC (2007) and include a lightning parameterisation, which depends on the convective mass flux. Hence, the parameterisation differs substantially from earlier modelling studies on the development of future lightning frequencies. The results show, as indicated above, a decrease in lightning activity.

25.2 Global Modelling of Lightning and Its NO_x Production

25.2.1 Simulation and Observation of Lightning

In general, the parameterisation of lightning frequencies in general circulation models is coupled to another parameterisation, the convection scheme. This implies that the driving parameters are not resolved by the model, since the relevant processes are occurring on the sub-grid scale. All parameterisations of lightning NO_x production consist of three parts: (1) an estimate of total lightning frequencies, (2) a separation between intra-cloud and cloud to ground lightning, and (3) a vertical effective emission profile. Main differences among the various approaches, besides a total global scaling, occur for the first part, the estimate of the lightning frequency. In most models a correlation between convective cloud top heights and lightning frequencies (Price and Rind, 1992) is applied, which is based on observational data. However, two different formulas are applied for oceanic and continental lightning to account for observational evidence that oceanic and continental lightning do not differ significantly in convective cloud top height, but in lightning frequencies. Other approaches include additionally latent heat release (Flatøy and Hov, 1997), convective precipitation rate (Meijer et al., 2001; Allen and Pickering, 2002), convective available potential energy (Choi et al., 2005) or convective vertical mass fluxes as indicator for updraft velocities (Allen et al., 2000; Grewe et al., 2001). None of those approaches is proven to be superior. However, some are more physically based, like the mass flux schemes, since lightning occurs from the breakdown of charge separation, which is built up by strong updrafts including hydrometeors (Takahashi, 1984).

Cloud-to-ground flashes (CG) are expected to be more energetic and hence produce more NO, which however is still under debate (Dye et al., 2000; Fehr et al., 2004). Price and Rind (1993) found a correlation between the CG fraction and the thickness of the cold cloud layer (0°C to cloud top). The NO produced by lightning discharges has an initial emission profile. However, convection rapidly redistributes the lightning emitted nitrogen oxides, on time scales, which are not resolved by climate models. Therefore, effective vertical profiles from cloud resolving models (Pickering et al., 1998) are often applied.

Comparisons to satellite data have shown that none of these parameterisations reflect all characteristics of the observed lightning pattern (Tost et al., 2007). However, the parameterisations chosen here, which is based on convective mass fluxes (see below) is among those which simulates best the spatial correlation, standard deviation and root mean square error in the spatial pattern compared to LIS/OTD data (Tost et al., 2007).

In the following, model results are presented based on a state-of-the-art stratosphere-troposphere climate-chemistry model (E39/C) (Hein et al., 2001; Dameris et al., 2005; Grewe, 2007), which includes a convective mass flux based parameterisation of lightning (Grewe et al., 2001), CG-IC separation (Price and Rind, 1993), and effective vertical emission profiles (Pickering et al., 1998). The results are based on an ensemble simulation from 1960 to 2020 (Dameris et al., 2006; Grewe, 2007), which employs realistic external forcings, like increase in greenhouse

gases (CO_2 , CH_4 , CFCs, N_2O), ozone depleting substances (CFCs), major volcanic eruptions, quasi-biennial-oscillation, and sea surface temperatures.

Figure 25.2 (first row) shows observed and simulated annual mean flash frequencies. Its distribution over land is well reproduced, in shape and absolute numbers. Over the oceans, especially in the tropics, lightning frequencies are generally overestimated with the exception of some oceanic regions, e.g. the South China Sea, Gulf of Mexico, and regions east to the continents. Figure 25.2 (middle row) shows the amplitude of the seasonal cycle. In the extra-tropics it is dominated by the summer-time lightning and hence follows in pattern the annual mean lightning distribution.

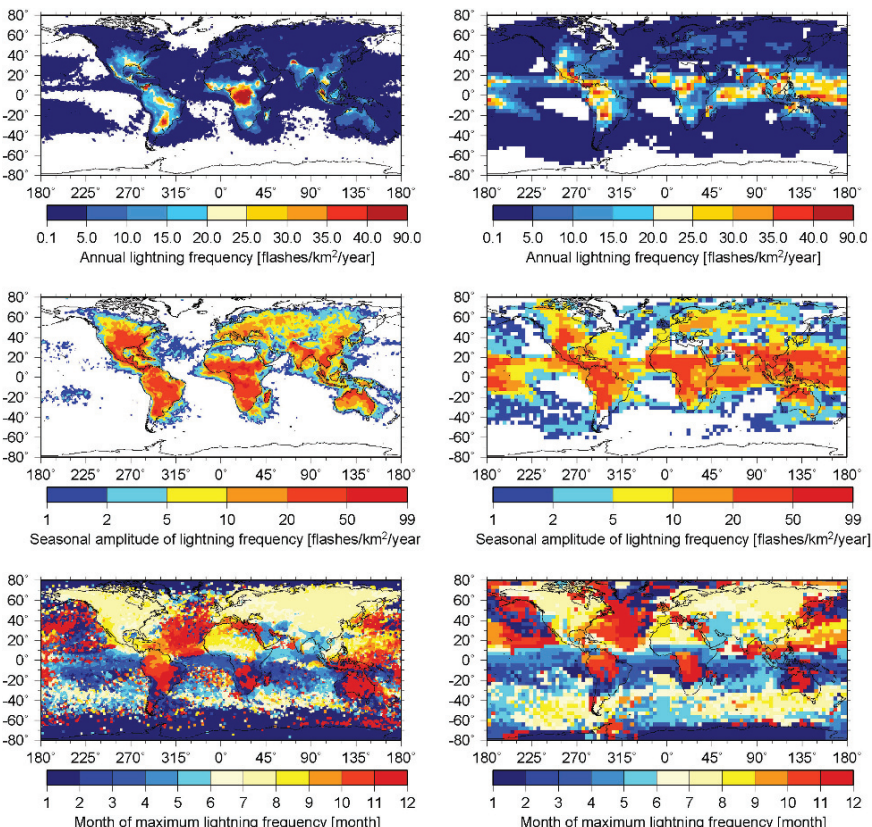


Fig. 25.2 Inter-comparison of observed (left) and simulated (right) lightning properties. Observational data comprise a merged data set from two space-born optical sensors (OTD and LIS) (Christian et al., 2003). *First row:* annual mean lightning frequencies (flashes/ km^2/year). *Second row:* lightning amplitude (flashes/ km^2/year), i.e. difference between minimum and maximum climatologically monthly mean values. Simulated lightning occurrences are scaled to derive the observed annual mean lightning frequencies of 46.6 flashes/s. *Last row:* month of maximum climatological monthly mean lightning values. Climatologies are based on the years 1995–2005 for observational data and 1990–1999 for the simulated data (See also Plate 45 in the Color Plate Section on page 626)

At tropical latitudes, e.g. in Africa, peak values are obtained at around 10° of both hemispheres with lower values at the equator due to the semi-annual cycle. The month of the maximum lightning occurrence is shown in the last row of Fig. 25.2. It clearly shows that the summertime maximum of northern hemisphere mid-latitude continental lightning (yellow) and the wintertime oceanic maximum (winter storms) are well reproduced.

25.2.2 Climate Change and Lightning

Figure 25.3 shows the global mean simulated lightning frequencies (ensemble mean in black and the ensemble range in red). A significant decrease is found of around 2 flashes per second ($\sim 0.3\%$ per decade) over the whole simulation period. A large fraction of the inter-annual variability arises from the natural variability due to El Niño dashed with an increase in flash frequencies during El Niño periods, though the number of convective events decreases (not shown), which is in agreement with satellite data (Hamid et al., 2001). Intra-cloud and cloud-to-ground lightning are both contributing equally to the simulated trend (not shown). Two effects are important for the simulated decrease: A decrease in the number of convective events and an increase in the strength of individual events. Both are counteracting processes with respect to the simulated flash frequencies. However, the increase of flashes frequencies per convective event are not compensating the decrease in flashes frequencies due to the decrease in the number of convective events.

Figure 25.4 shows the horizontal pattern of the changes in number of convective events (a) and estimate of the mean updraft (b), derived from the mean convective vertical mass flux divided by the density. Decreases in the number of events and increases in the estimated updrafts occur in the Mexican Gulf and the Caribbean Sea, the Northern equatorial Pacific and at the coasts of East Africa and India. Hence

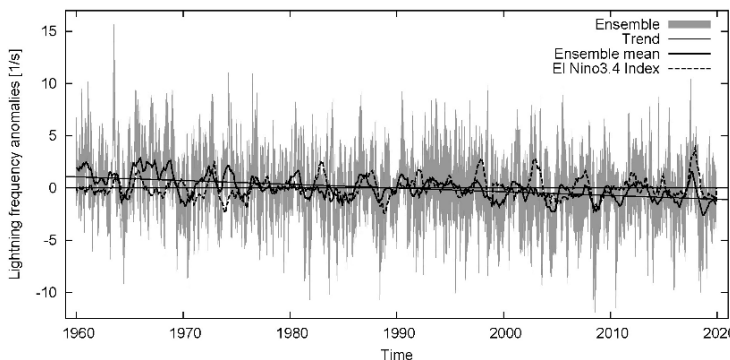


Fig. 25.3 De-seasonalized globally and monthly mean flash frequency anomalies for a climate-chemistry ensemble simulation (flashes/s). The envelope marks the range of the model simulation. A 1-year running mean is added in *thick black*, the El Niño index in *dashed* and a trend line in *thin black*. The statistically significant trend is 2.15 ± 0.11 flashes per 60 years

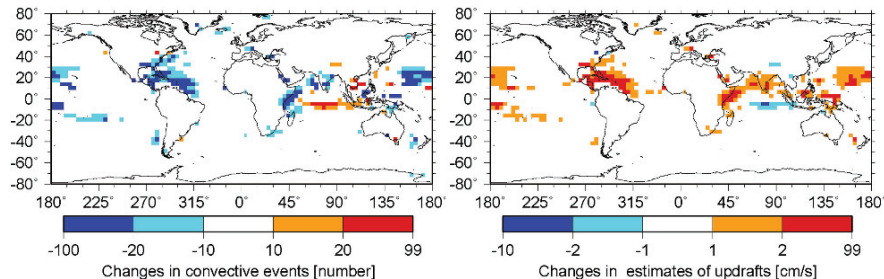


Fig. 25.4 Left: changes in the simulated number of convective events in the ensemble climate-chemistry simulation between the years 2010–2019 and 1960–1969. Only changes, which are statistically significant with an assumed error of 1% are shown. Right: as left, but for estimates of mean updrafts (density weighted upward mass flux) per convective event (cm/s) (See also Plate 46 in the Color Plate Section on page 627)

mainly oceanic regions are affected by the climate change induced lightning changes in this simulation.

The observational basis for the detection of lightning trends is weak, since satellite data have only been available for a decade and the interannual variability is large. However, Price and Asfur (2006) detected a decrease in inferred African lightning from 1960 to 2000, based on 300 hPa water vapour re-analysis data, which they showed to be correlated to lightning activity at least for a shorter time period, in which water vapour and lightning data were both available.

25.2.3 NO_x Production by Lightning

Figure 25.5 shows the simulated source of lightning NO_x . Maximum lightning emissions occur in the upper troposphere, approximately 3–4 km below the tropopause, reflecting the main convective outflow. During the winter season mid-latitude oceanic storms have a minor contribution. On the northern summer hemisphere a clear maximum is simulated in mid-latitudes, which is not apparent on the Southern hemisphere in DJF. Note, that the only other in-situ local sources of NO_x are aircraft emissions, which are clearly separated from the lightning source. However, transport mixes NO_x emitted by lightning and aircraft.

25.3 Impact of Lightning on Atmospheric Composition and Climate

25.3.1 Ozone Changes from Lightning

In the troposphere, nitrogen oxide emissions enhance ozone concentrations. Various anthropogenic and natural NO_x sources contribute to the tropospheric ozone budget

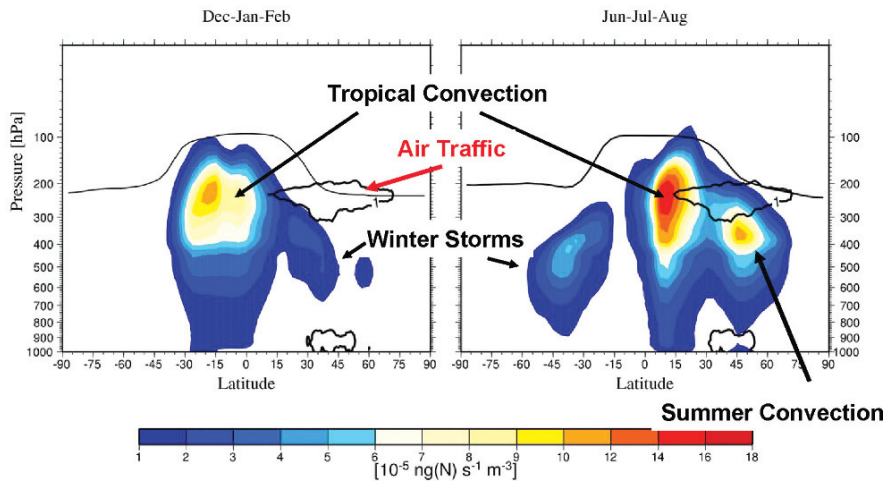


Fig. 25.5 Simulated zonal mean distribution of lightning NO_x emissions ($10^{-17} \text{ kg(N/m}^3\text{/s)}$) for DJF (left) and JJA (right). The black line indicates the location of the tropopause, black isolines the location of air traffic NO_x emissions (See also Plate 47 in the Color Plate Section on page 627)

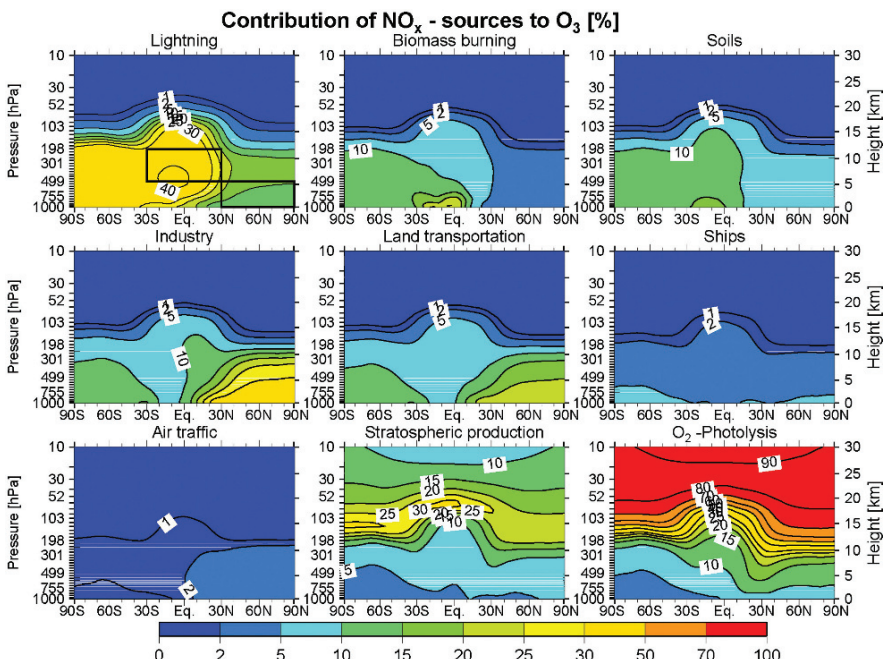


Fig. 25.6 Contribution (%) of the zonal and decadal (1990–1999) mean simulated ozone according to their sources: lightning, biomass burning, soils, industry, surface traffic, ships, air traffic, stratospheric production of nitrogen. Ozone from production caused by oxygen photolysis is added (See also Plate 48 in the Color Plate Section on page 628)

(Fig. 25.6). Lightning clearly contributes most to ozone in the tropical mid and upper troposphere (~40%). Lightning has also a pronounced impact on the extra-tropical southern hemisphere, which results from extra-tropical lightning, but also from export of tropical ozone, produced by tropical lightning NO_x emissions (Grewe, 2006). In the northern hemisphere, anthropogenic emissions are much larger than in the southern hemisphere and hence the lightning impact is less, but still in the order of 10–15% in the upper troposphere, more intense in summer. Since the lightning NO_x emissions occur in the upper troposphere the longer lifetimes increase the impact on ozone. The ozone production efficiency is larger for upper tropospheric emissions than for surface sources (Table 25.1). As a mean value for the period 1990–1999 a NO_x molecule emitted from lightning results in a production of around 90 molecules of ozone, whereas surface sources have only an efficiency of 20 molecules. NO_x emissions from air traffic have efficiency in ozone production of around 50 molecules ozone per emitted NO_x, which is less than for lightning, although they have similar vertical emission profiles. However, aircraft emissions are located at higher latitudes than lightning and occur partly in the stratosphere; hence in regions which differ remarkably with respect to NO_x and ozone lifetimes. Therefore also the impact on ozone differs significantly.

Figure 25.7 shows changes in lightning induced ozone (2) relative to a mean over the whole simulation period. First, an increase and then a decrease in ozone are simulated. The decrease in lightning ozone is less than the decrease in the lightning

Table 25.1 Ozone production efficiency for emitted NO_x molecules. ‘Surface’ indicates the mean for all surface NO_x sources

NO _x source	Lightning	Surface	Aircraft
Ozone production efficiency (molecules ozone per emitted NO _x molecule)	~90	~20	~50

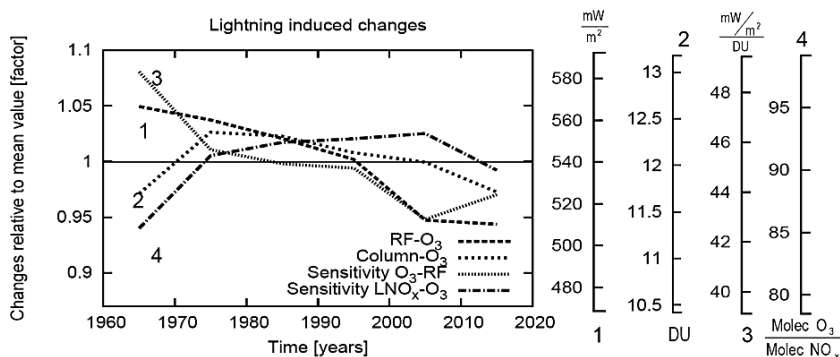


Fig. 25.7 Changes of lightning induced ozone (2), its radiative forcing (1), the efficiency of an lightning NO_x molecule to produce ozone (4) and the efficiency of an lightning induced ozone molecule on its radiative forcing (3). The changes are expressed relative to the ensemble mean value of all 6 decades from 1960 to 2019. Additionally the absolute values are indicated on the right with the same colour code and order

NO_x emissions. Hence, the change in the chemical composition leads to an increase in the ozone production efficiency (4) by around 10% from the 1960 to the 2000, with an indication of a reversion of this trend at the end of the simulation.

25.3.2 Climate Impact of Lightning

The impact of ozone on climate is calculated in terms of radiative forcing. From climate simulations it is well known that RF scales linearly with changes in global mean near-surface temperatures at least in the case of well-mixed green house gases. For short-lived species, as ozone, the perturbation has a spatial pattern which affects this linearity (e.g. Shine et al., 2005). However, RF can be used as a first indicator for impact on climate change; especially in this case, since the spatial pattern of the lightning ozone changes are less pronounced than the total ozone changes.

A mean value of around 540 mW/m^2 is calculated for the lightning induced ozone, which compares well with the finding by Toumi et al. (1996) (100 mW/m^2 for 1 Tg of nitrogen per year) but is 5 times larger than the estimate by Hopkins (2003). Figure 25.7 shows the evolution of the RF changes due to ozone from lightning (curve 1). Due to the increasing background ozone concentration the effectiveness of an ozone molecule to perturb radiation is decreasing and hence the ratio between the lightning-ozone-RF and lightning-ozone is decreasing by 10–15% over the simulation period.

25.4 Summary

The simulation of lightning occurrences in a climate-chemistry model is a challenge. Flash frequencies have to be parameterised in connection with a cloud scheme. Currently, a number of parameterisations are applied, which calculate the flash frequencies as a function of the convective cloud top height, precipitation, droplet size, or mass fluxes (estimate for updraft velocities). The latter is applied in this study in a simulation with a coupled ensemble climate-chemistry model from 1960 to 2020. Comparisons to satellite data have shown that none of these parameterisations reflect all characteristics of the observed lightning pattern. The approach in this study clearly showed that the month of the peak lightning occurrence is well simulated as well as annual mean lightning pattern, including the amplitude of the seasonal cycle, except for oceanic region, which are not close to the coast. There lightning is overestimated, which might result from the lightning or the convection parameterisation.

Climate change has the largest impact on convection over the oceans. Model simulations suggest less frequent but stronger convective events, which is also a result in this study. The implication on lightning is a decrease in total flash frequency, although individual events produce more lightning. The contribution of lightning on ozone is simulated to be around 40% in the tropical free troposphere. In the

ensemble simulation, a general increase in NO_x occurs due to increase in anthropogenic emissions, which leads to an increase in the ozone production efficiency until it is reversed during the last decade (2010–2020). The net ozone production is still positive, but increase in ozone production per emitted NO molecule slows down after 2010, due to competing ozone production and destruction reactions.

The decrease in lightning NO_x emissions hence is overlaid with the increase in ozone production efficiency, which first leads to an increase in lightning ozone until the 1970s and then to a decrease. This means that the changes in lightning-ozone are first dominated by the increased ozone production efficiency and later by the decrease in lightning frequencies.

The radiative forcing per unit ozone, i.e. the sensitivity of radiative forcing on ozone changes, is decreasing during the simulation, except for the last decade. Hence the decrease in lightning-ozone induced radiative forcing changes is a consequence of decreasing lightning frequencies resulting from less but stronger convective events and a decreased efficiency of tropospheric ozone to alter radiative forcing. Increased ozone production efficiency is counteracting but dominates only in the first part of the simulation, i.e. the 60 s.

A weakness of the simulation is the overestimate of lightning frequencies over oceanic regions, i.e. the regions where most of the trends in convection occur. However, some parts of the trends occur in the Caribbean Sea and Indonesia, where the simulated lightning frequencies are reasonable. Anyway, the study shows that climate change does not necessarily lead to an increase in lightning as proposed by studies linking lightning to convective cloud top heights, but may reduce lightning.

Acknowledgments The v2.2 gridded satellite lightning data were produced by NASA LIS/OTD Science Team (Principle Investigator, Dr. Hugh J. Christian, NASA / Marshall Space Flight Center) and are available from the Global Hydrology Resource Center (<http://ghrc.msfc.nasa.gov>). Many thanks to my colleagues Katrin Obermaier, who calculated the radiative forcing values, Hella Garny, Hartmut Höller and Ulrich Schumann for discussions and internal review and Arthur Schady for helping in processing the LIS/OTD data.

References

- Allen, D., Pickering, K., Stenchikov, G., Thompson, A., and Kondo, Y.: A three-dimensional total odd nitrogen (NO_y) simulation during SONEX using a stretched-grid chemical transport model, *J. Geophys. Res.*, 105, 3851–3876, doi:10.1029/1999JD901029, 2000.
- Allen, D. J. and Pickering, K. E.: Evaluation of lightning flash rate parameterizations for use in a global chemical transport model, *J. Geophys. Res.*, 107, 4711, doi:10.1029/2002JD002066, 2002.
- Berntsen, T. K., Fuglestvedt, J. S., Joshi, M. M., Shine, K. P., Stuber, N., Ponater, M., Sausen, R., Hauglustaine, D. A., Li, L.: Response of climate to regional emissions of ozone precursors: sensitivities and warming potentials, *Tellus B*, 57, 283–304, doi:10.1111/j.1600-0889.2005.00152.x, 2005.
- Brinkop, S.: Aspects of convective activity and extreme events in a transient climate change simulation, *Meteorol. Z.*, 11, 323–333, 2002.

- Choi, Y., Wang, Y., Zeng, T., Martin, R. V., Kurosu, T. P., and Chance, K.: Evidence of lightning NO_x and convective transport of pollutants in satellite observations over North America, *Geophys. Res. Lett.*, 32, L02805, doi:10.1029/2004GL021436, 2005.
- Christian H. J., et al.: Global frequency and distribution of lightning as observed from space by the Optical Transient Detector, *J. Geophys. Res.*, 108(D1), 4005, doi:10.1029/2002JD002347, 2003.
- Dameris, M., Grewe, V., Ponater, M., et al.: Long-term changes and variability in a transient simulation with a chemistry-climate model employing realistic forcing, *Atmos. Chem. Phys.*, 5, 2121–2145, 2005.
- Dameris, M., Matthes, S., Deckert, R., Grewe, V., and Ponater, M.: Solar cycle effect delays onset of ozone recovery, *Geophys. Res. Lett.* 33, L03806, doi:10.1029/2005GL024741, 2006.
- Del Genio, A. D., Yao, M.-S., Jonas, J.: Will moist convection be stronger in a warmer climate?, *Geophys. Res. Lett.*, 34, L16703, doi:10.1029/2007GL030525, 2007.
- Dye, J. E., et al. An overview of the Stratospheric-Tropospheric Experiment: Radiation, Aerosols, and Ozone (STERAO)-Deep Convection experiment with results for the July 10, 1996 storm, *J. Geophys. Res.*, 105(D8), 10023–10045, 2000.
- Fehr, T., Höller, H., and Huntrieser, H.: Model study on production and transport of lightning-produced NO_x in a EULINOX supercell storm, *J. Geophys. Res.*, 109, D09102, doi:10.1029/2003JD003935, 2004.
- Flatøy, F. and Hov, Ø.: NO_x from lightning and the calculated chemical composition of the free troposphere, *J. Geophys. Res.*, 102, 21373–21381, 1997.
- Grewe, V., Brunner, D., Dameris, M., Grenfell, J. L., Hein, R., Shindell, D., and Staehelin, J.: Origin and variability of upper tropospheric nitrogen oxides and ozone at northern mid-latitudes, *Atmos. Environ.*, 35, 3421–3433, 2001.
- Grewe, V.: The origin of ozone, *Atmos. Chem. Phys.*, 6, 1495–1511, 2006.
- Grewe, V.: Impact of climate variability on tropospheric ozone, *Sci. Total Environ.*, 374, 167–181, doi:10.1016/j.scitotenv.2007.01.032, 2007.
- Grewe, V. and Stenke, A.: AirClim: an efficient tool for climate evaluation of aircraft technology, *Atoms. Chem. Phys.*, 8, 4621–4639, 2008.
- Hamid, E., Kawasaki, Z.-I., and Mardiana, R.: Impact of the 1997–98 El Niño event on lightning activity over Indonesia, *Geophys. Res. Lett.*, 28, 147–150, 2001.
- Hansen, J., Sato, M., Ruedy, R., et al.: Efficacy of climate forcings, *J. Geophys. Res.*, 110, D18104, doi:10.1029/2005JD005776, 2005.
- Harrison, R. G.: The global atmospheric electrical circuit and climate, *Surv. Geophys.*, 25, 441–484, 2004.
- Hein, R., Dameris, M., Schnadt, C., et al.: Results of an interactively coupled atmospheric chemistry-general circulation model: comparison with observations, *Ann. Geophys.*, 19, 435–457, 2001.
- Hopkins, A. E.: Lightning NO_x and tropospheric ozone formation in the NASA GISS global carbon model, GSSP (Graduate Student Summer Program of the NASA Goddard Space Flight Center's Earth-Sun Exploration Division, in collaboration with the Goddard Earth Sciences and Technology Center of the University of Maryland Baltimore County), <http://gest.umbc.edu/studentopp/2003gsspreports.html>, 2003.
- IPCC, 2007: Climate Change 2007: The Physical Science Basis. Contribution of Working Group I to the Fourth Assessment Report of the Intergovernmental Panel on Climate Change [Solomon, S., D. Qin, M. Manning, Z. Chen, M. Marquis, K. B. Averyt, M. Tignor and H. L. Miller (eds.)]. Cambridge University Press, Cambridge, United Kingdom and New York, NY, USA, 996 pp.
- Isaksen, I. S. A. and Hov, Ø.: Calculation of trends in the tropospheric concentration of O₃, OH, CO, CH₄, and NO_x, *Tellus*, 39B, 271–285, 1987.
- Lacis, A. A., Wuebbles, D. J., and Logan, J. A.: Radiative forcing of climate by changes in the vertical distribution of ozone, *J. Geophys. Res.*, 95, 9971–9981, 1990.
- Markson, R. and Price, C.: Ionospheric potential as a proxy index for global temperature, *Atmos. Res.*, 51, 309–314, 1999.
- Meehl, G. A. and Stocker, T. F.: Global Climate Projections, in IPCC, 2007: Climate Change 2007: The Physical Science Basis. Contribution of Working Group I to the Fourth Assessment

- Report of the Intergovernmental Panel on Climate Change [Solomon, S., D. Qin, M. Manning, Z. Chen, M. Marquis, K. B. Averyt, M. Tignor and H. L. Miller (eds.)]. Cambridge University Press, Cambridge, United Kingdom and New York, NY, USA, 996 pp.
- Meijer, E. W., van Velthoven, P. F. J., Brunner, D. W., Huntrieser, H., and Kelder, H.: Improvement and evaluation of the parameterisation of nitrogen oxide production by lightning, *Phys. Chem. Earth*, 26, 577–583, 2001.
- Pickering, K. E., Wang, Y., Tao, W. K., Price, C., and Müller, J. F.: Vertical distributions of lightning NO_x for use in regional and global chemical transport models, *J. Geophys. Res.*, 103, 31203–31216, doi:10.1029/98JD02651, 1998.
- Price, C. and Rind, D.: A simple lightning parameterization for calculating global lightning distributions, *J. Geophys. Res.*, 97, 9919–9933, doi:10.1029/92JD00719, 1992.
- Price, C.: Global surface temperatures and the atmospheric electrical circuit, *Geophys. Res. Lett.*, 20, 1363–1366, 1993.
- Price, C. and Rind, D.: What determines the cloud-to-ground lightning fraction in thunderstorms?, *Geophys. Res. Lett.*, 20, 463–466, doi:10.1029/93GL00226, 1993.
- Price, C., and Asfur, M., Inferred long term trends in lightning activity over Africa, *Earth Planets Space* 58, 1197–1201, 2006.
- Schumann, U. and Huntrieser, H.: The global lightning-induced nitrogen oxides source, *Atmos. Chem. Phys.*, 7, 3823–3907, 2007.
- Shine, K., Berntsen, T., Fuglestvedt, J., and Sausen, R.: Scientific issues in the design of metrics for inclusion of oxides of nitrogen in global climate agreements, *PNAS*, 44, 15768–15773, 2005.
- Takahashi, T.: Thunderstorm electrification – A numerical study, *J. Atmos. Sci.*, 41, 2541–2557, 1984.
- Tost, H., Jöckel, P., and Lelieveld, J.: Lightning and convection parameterisations – uncertainties in global modelling, *Atmos. Chem. Phys.*, 7, 4553–4568, 2007.
- Toumi, R., Haigh, J. D., and Law, K. S.: A tropospheric ozone-lightning climate feedback, *Geophys. Res. Lett.*, 23, 1037–1040, doi:10.1029/96GL00944, 1996.
- Trenberth, K. E. and Jones, D. E.: Observations: Surface and Atmospheric Climate Change, in: IPCC, 2007: Climate Change 2007: The Physical Science Basis. Contribution of Working Group I to the Fourth Assessment Report of the Intergovernmental Panel on Climate Change [Solomon, S., D. Qin, M. Manning, Z. Chen, M. Marquis, K. B. Averyt, M. Tignor and H. L. Miller (eds.)]. Cambridge University Press, Cambridge, United Kingdom and New York, NY, USA, 996 pp.
- Williams, E. R.: The Schumann resonance: A global tropical thermometer, *Science*, 256, 1184–1187, 1992.
- Williams, E. R.: Global circuit response to seasonal variations in global surface air temperature, *Mon. Wea. Rev.*, 122, 1917–1929, 1994.
- Wu, S., Mickley, L. J., Jacob, D. J., Logan, J. A., Yantosca, R. M., and Rind, D.: Why are there large differences between models in global budgets of tropospheric ozone?, *J. Geophys. Res.*, 112, D05302, doi:10.1029/2006JD007801, 2007.

Chapter 26

Lightning and NO_x Production in Global Models

Kenneth Pickering, Heidi Huntrieser and Ulrich Schumann

Abstract In the upper troposphere lightning is the major contributor to the production of nitric oxide, which is a critical precursor gas for ozone production. It is therefore important that this source is simulated with a high accuracy in global chemical transport models and global chemistry/climate models. This chapter reviews development of the parameterization of lightning-produced nitric oxide in such models and the various components required such as flash rate distribution, NO production per flash and its vertical distribution. The results from simulations with different global models, the uncertainties and the impact on ozone are discussed.

Keywords Lightning · Nitrogen oxides · Aircraft observations · Chemical transport modelling · Cloud-resolved modelling · Tropospheric ozone

26.1 Introduction

Nitric oxide (NO) is produced in very hot lightning channels through the Zel'dovich mechanism (Zel'dovich and Raizer 1967) due to oxygen (O₂) and nitrogen (N₂) dissociation. As the channels cool to 3000–4000 K, NO is formed in the resulting plasma and is "frozen in" during the subsequent cooling to ambient temperature. Within seconds NO is converted to NO₂ by reaction with ambient ozone (O₃) and – during daytime – photolysed back to NO. An equilibrium is reached after about 100 s known as the photostationary state. The sum of NO and NO₂ is referred to as NO_x.

The magnitude of the NO_x production per lightning flash and the total global production are still a matter of debate. Schumann and Huntrieser (2007) have provided a comprehensive summary of the current knowledge of lightning-NO_x (LNO_x) production and suggest that the total global production, is 2–8 Tg/a with a most likely value of 5 Tg/a. (Here and below, the production rate is given in terms of

K. Pickering (✉)

NASA Goddard Space Flight Center, Laboratory for Atmospheres, Greenbelt, MD, USA
e-mail: Kenneth.E.Pickering@nasa.gov

equivalent nitrogen mass per year.) They state that this amount represents approximately 10% of the total NO production from all sources, but a far larger share of the amount emitted into the upper troposphere. NO is the most critical precursor gas for photochemical ozone production in the troposphere. Therefore, accurate knowledge of NO from the lightning source is essential in estimating ozone production rates.

Tropospheric ozone is the third most important greenhouse gas (IPCC 2007) with an estimated global annual average radiative forcing of 0.35 W/m^2 with $0.25\text{--}0.65 \text{ W/m}^2$ uncertainty. Radiative forcing associated with ozone is most sensitive to changes in ozone in the upper troposphere and lower stratosphere. LNO_X production occurs primarily in the middle and upper troposphere, and some of that produced lower in the atmosphere is convectively transported upward. It is known that the O₃ production efficiency per NO_X molecule typically increases with height, due to the longer lifetime of NO_X in the upper troposphere compared to the boundary layer. The lifetime increases as the chemical destruction rate decreases which is the case in the upper troposphere due to the colder and drier environment. Therefore, LNO_X has the greatest potential to influence ozone production in the middle and upper troposphere, and especially in tropical regions where the flash rate and insolation are highest (see Fig. 18 in Schumann and Huntrieser (2007) from Grewe (2007)). Aside from the aircraft source with 0.7 Tg/a (Schumann and Huntrieser 2007), lightning is the only other source of NO_X emitted directly into the upper troposphere. Therefore, it is important that we improve our knowledge of the magnitude and location of LNO_X production.

An accurate representation of the LNO_X source strength and temporal and spatial distribution is needed in global chemical transport models (CTM) and global chemistry/climate models (GCM or CCM). Offline chemical transport models are typically driven by meteorological fields produced by global data assimilation systems (e.g., National Center for Environmental Prediction (NCEP), European Centre for Medium Range Forecasts (ECMWF), and Global Modeling and Assimilation Office (GMAO)). Fields of winds, temperatures, convective fluxes, and cloud cover from these assimilation systems are used in the calculation of advection and chemical transformations. In such models there is no interaction between the resulting chemical distributions and the meteorology. Some global climate models run with online chemistry allowing radiative feedback due to changes in concentrations of atmospheric trace gases or aerosols. This radiative forcing can affect the atmospheric dynamics in the model leading to perturbed circulation patterns.

This chapter will review efforts in representing the LNO_X source in such offline and online models. Specifically, it will review the research that has led to the development of the various components of LNO_X parameterizations required for such global models. These components include a method to specify the geographic and temporal distribution of flashes (Section 26.2), an amount of NO production per flash (Section 26.3), and a method of specifying the effective vertical distribution of LNO_X emissions, including the effects of convective transport (Section 26.4). Our final section describes the information concerning LNO_X gained from such global models, the uncertainties and its impact on O₃ (Section 26.5).

26.2 Flash Rate Distributions

Lightning has been monitored from ground-based networks in a number of countries and detected routinely from space by satellites since 1988 and 1995, respectively. Both types of systems have generated a wealth of data concerning lightning flash rates. However, these data cannot be used directly in global or regional models for several reasons. Injecting NO from lightning at the times and locations of observed flashes will not necessarily match in space and time with the convective transport of ozone precursors in the model. The resulting ozone photochemistry will not be accurate. Ground-based network data also cannot be used because the systems with most geographic coverage record mainly CG flashes and only a few of the IC flashes. The satellite data, which does record both CG and IC flashes, cannot be used because of the very small amount of coverage on a daily basis. Gridded climatologies of the Optical Transient Detector (OTD) and Lightning Imaging Sensor (LIS) data have been constructed (<http://thunder.nsstc.nasa.gov/data>). However, these data suffer from the same problem (mismatch with model convection) as any observational data set if they are used directly in a model. Therefore, parameterizations for estimating flash rates in the model must be employed. These typically use various meteorological variables from the driving meteorological assimilation or from the climate model as predictors of flash rate. This approach makes the assumption that the meteorological fields used to drive the model adequately represent the deep convection which leads to the occurrence of lightning.

A number of global CTMs have used the cloud-top height from the driving meteorological model for estimating lightning flash rates. Theoretical and observational formulation of a relationship between flash rate and the fifth power of the cloud height stems from early work by Vonnegut (1963) and Williams et al. (1985). Formal power laws for predicting flash rates for total lightning from cloud-top height were derived by Price and Rind (1992). Separate equations for continental and marine lightning were presented as follows:

$$\begin{aligned} F_c &= 3.44 \times 10^{-5} H^{4.9} && \text{continental} \\ F_m &= 6.40 \times 10^{-4} H^{1.73} && \text{marine} \end{aligned}$$

where F is the total flash rate in flashes per minute and H is the cloud-top height in kilometers. These power laws were originally meant to apply for maximum flash rates and cloud-top height. However, they have been applied in many CTMs on an instantaneous basis. Limitations of this approach have been discussed by e.g. Ushio et al. (2001), Allen and Pickering (2002), and Boccippio (2002). Ushio et al. (2001) analyzed Tropical Rainfall Measuring Mission (TRMM) precipitation radar and LIS flash data to show that instantaneous cloud-top height and flash rates can be related. However, resulting best fit power law relationships varied considerably with location and season. Through comparison of model estimated flash rates (predicted using cloud-top height from the GEOS-STRAT meteorological assimilation) with OTD/LIS data Allen and Pickering (2002) noted that the Price and Rind scheme

underestimated flashes over the oceans by a factor of seven, overestimated the flash rates over tropical South America, and underestimated tropical African flashes. Boccippio (2002) observed that the Price and Rind marine parameterization is inconsistent with Vonnegut's original theoretical framework, and suggested a revised scaling relation.

Observational work by Petersen and Rutledge (1998) has suggested regime-dependent relationships between flash rate and convective precipitation. Meijer et al. (2001) and Allen and Pickering (2002) derived relationships for predicting CG flash rate (flashes per minute) using convective precipitation (CP in mm day⁻¹) from the meteorological models driving chemical transport. Allen and Pickering reported that separate continental and marine formulas were needed as shown below. These formulas are applicable for 2° × 2.5° grid cells using the GEOS-STRAT data. The CG fraction of the total flash rate was derived from the relationship to cold-cloud thickness of Price and Rind (1993).

$$F_{CG\text{ocean}} = 0.0523 - 0.048CP + 0.00545CP^2 + 0.0000368CP^3 - 0.000000371CP^4$$

$$F_{CG\text{land}} = 0.0375 - 0.0476CP + 0.00541CP^2 + 0.000321CP^3 - 0.00000293CP^4$$

Stronger updrafts within a thunderstorm lead to greater charge separation within the cloud, which may lead to greater flash rates. Price and Rind (1992) discuss relationships between updraft velocity and flash rate, which were applied by Pickering et al. (1998). Allen et al. (2000) were the first to utilize the upward cloud mass flux (M in kg m⁻² min⁻¹) from a convective parameterization in a global model as a predictor of flash rate. Through tests over the eastern USA and western North Atlantic, they found that separate marine and continental formulas were not needed when this predictor variable is used. Allen and Pickering (2002) formalized the relationship between flash rate and upward cloud mass flux (a fourth-order polynomial) and applied it globally. The flash rates (flashes per minute for a 2° × 2.5° grid cell) predicted by this formula must be adjusted for grid cell size and scaled upward to account for IC flashes. In general, flashes over the oceans were better predicted than with the cloud-top height approach, but flashes were overpredicted over the western Pacific. Over the US the mass flux approach also performed better than the convective precipitation scheme (see Fig. 26.1).

$$F_{CG} = -0.234 + 0.308M - 0.719M^2 + 0.523M^3 - 0.0371M^4$$

Grawe et al. (2001) introduced a combination of updraft velocity w (m s⁻¹) and cloud thickness D (m) in a prediction formula for the total flash rate F (flashes per minute).

$$F = 1.54 \times 10^{-5}(wD^{0.5})^{4.9}$$

The grid cell average updraft velocity had to be derived from the parameterized upward mass flux as follows:

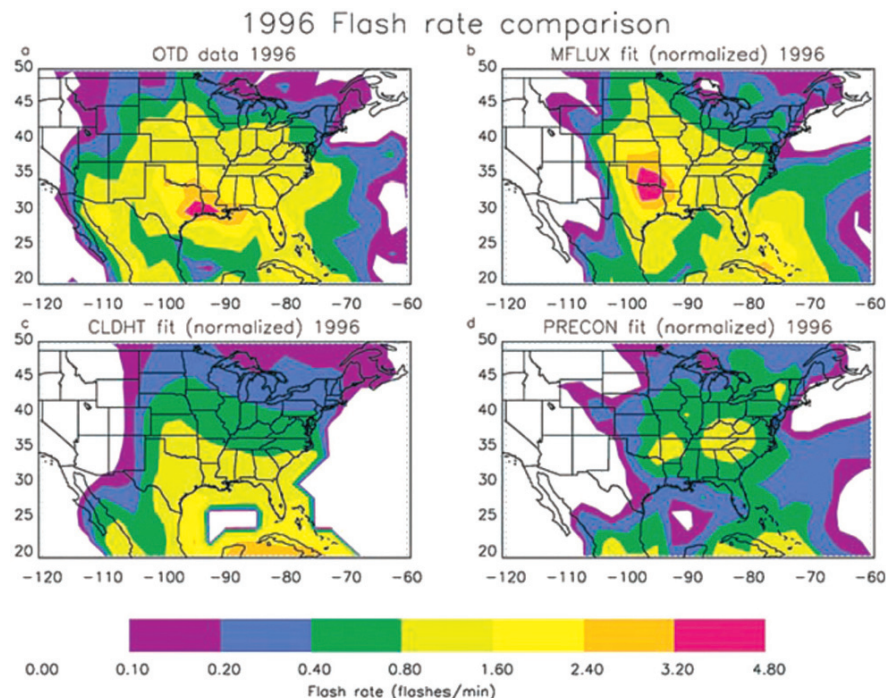


Fig. 26.1 Observed and predicted flash rates from three schemes over the US and Western Atlantic (from Allen and Pickering 2002) (See also Plate 49 in the Color Plate Section on page 629)

$$w = \sum (mf_i / \rho_i)(h_i / D)$$

where mf_i is the upward convective mass flux in $\text{kg m}^{-2} \text{ s}^{-1}$ in layer i , ρ_i is the mass density (kg m^{-3}), h_i is the thickness of the cloud layer i in meters, and D is the overall cloud thickness in meters.

Thermodynamic indicators of atmospheric instability such as convectively available potential energy (CAPE) may also be related to flash rate. Choi et al. (2005) developed such a relationship for use in a regional CTM.

Recently data from the TRMM satellite have been used to derive relationships between microphysical variables and lightning flash rates. Besides LIS, TRMM carries a precipitation radar. Data have been analyzed from these two instruments to derive two formulations which may be applicable in global models. Petersen et al. (2005) demonstrated a regime-independent relationship (see Fig. 26.2) between the column integrated precipitation ice mass, expressed as ice water path (kg/m^2), and the flash rate density (flashes/ $(\text{km}^2 \text{ d})$). This relationship was found to be invariant between land, ocean and coastal regimes (in contrast to rainfall) and therefore applicable to the global scale. Cecil et al. (2005) compared LIS flash rates and precipitation features defined as contiguous areas having at least 20-dBZ near-surface reflectivity or 85-GHz polarization corrected temperature (PCT) ≤ 250 K. They found that

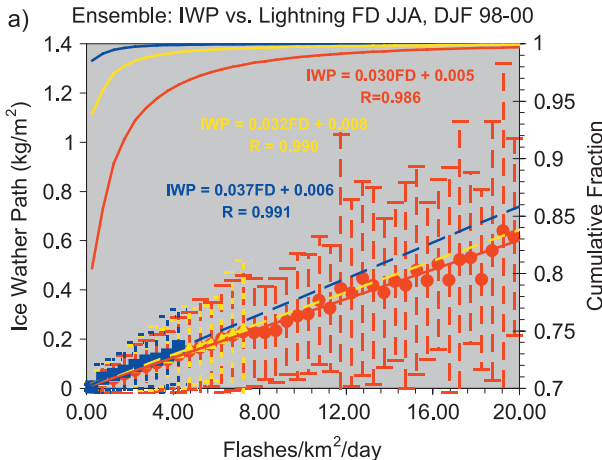


Fig. 26.2 Relationship of ice water path (IWP) vs. LIS flashes (from Petersen et al. 2005) (See also Plate 50 in the Color Plate Section on page 629)

for storms with the same brightness temperature, size and radar reflectivity aloft, the maritime storms are considerably less likely to produce lightning compared to continental storms. An explanation for these differences might be the lower cloud base of maritime clouds causing growth of large, precipitating raindrops below the freezing level, leaving less residual cloud water to become supercooled and form ice and graupel particles. Gauthier et al. (2006) and Sherwood et al. (2006) have further elucidated the roles of precipitation-size and cloud ice in determining lightning frequency. Recently, Futyan and DelGenio (2007) derived a relationship between flash rate (in flashes per minute per unit convective rain area of 300 km^{-2}) and the height (H in km) of the radar reflectivity top (defined as 17 dBZ). A slightly stronger relationship was found between flash rate and the depth (D_{cold} in km) of the layer between the freezing level and the radar reflectivity top (Fig. 26.3).

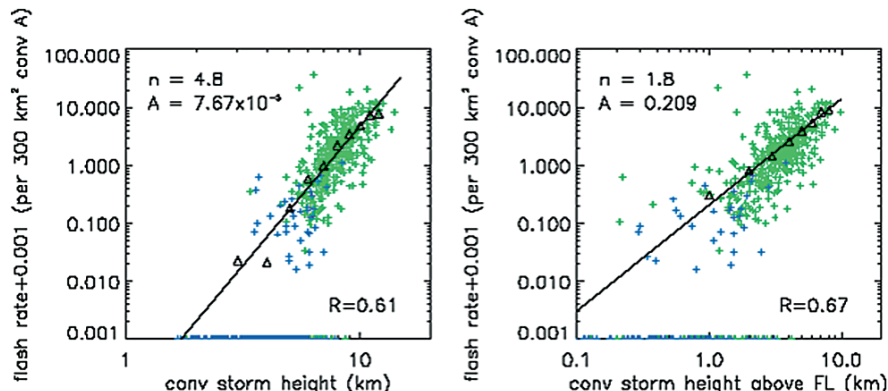


Fig. 26.3 Relationships of LIS flashes vs. radar top height (left) and vs. the depth between freezing level and radar top height (right) (from Futyan and DelGenio 2007) (See also Plate 51 in the Color Plate Section on page 630)

$$F = 7.67 \times 10^{-5} H^{4.8}$$

$$F = 0.209 D_{\text{cold}}^{1.8}$$

It was stated that this relationship captures both regional and continental-maritime contrasts in lightning occurrence and flash rate.

Treatment of cloud microphysics within atmospheric general circulation models has gradually become more sophisticated, and may soon reach the point where flash rate schemes using microphysical variables may be viable. Soon it may be possible to implement the parameterization suggested by Futyau and DelGenio (2007) in global models by using the predictions of the large particle top height. However, up to now the cloud microphysics included in the convection parameterization in the global models is too simplified to determine e.g. the ice water path, as discussed in Tost et al. (2007).

An additional microphysically-based scheme has been derived from ground-based radar and 3-D lightning mapping array data (Deierling et al. 2005, 2008). In this scheme, the flash rate is a function of the product of the upward flux of cloud ice crystals and of the downward flux of precipitation-size ice (graupel). It is unlikely that reliable estimates of such fluxes are going to be obtained from GCMs in the near future. However, this scheme has been employed in a cloud-resolving model by Barthe and Barth (2008). Dual-doppler radar and VHF total lightning observations have been examined by Deierling and Petersen (2008) to determine that the flash rate was well correlated with updraft volume above the -5°C level when the vertical velocities exceeded 5 m/s in the Southeast US and 10 m/s over the High Plains of the US.

Recently, a new technique has been developed to obtain better geographic and temporal distribution of flashes than can be provided by any of the above described methods. This method (Sauvage et al. 2007; Martin et al. 2007) involves adjusting the flash rates obtained from the prediction equations using the OTD/LIS climatology. The adjustments can be performed on a regional and monthly basis. This procedure is also being employed in NASA's Global Modeling Initiative CTM (Allen et al. 2008).

26.3 NO Production per Flash

Estimation of NO production per flash has been performed using a variety of methods. The earliest estimates came from theoretical considerations of energy dissipation per flash and NO production per unit of energy. More recently, production estimates have been provided from laboratory spark measurements, detailed analysis of aircraft NO measurements taken in storms, cloud-resolved modeling constrained by observed flash rates and aircraft NO measurements from storm anvils, satellite NO₂ observations in relation to observed flashes, and best-fit calculations between observations and global model NO production rates. Details of each of these estimation techniques are presented below and in Section 26.5.

Price et al. (1997) formulated a lightning NO production scenario of 1100 moles per CG flash and 110 moles per IC flash through an analysis of theoretical concepts and observational data (1 mole = 6.02×10^{23} molecules = 14 g of nitrogen). Their

analysis yielded 6.7 GJ per CG flash, and based on acoustical data an estimate of 10% of this value for IC flashes was made. An NO molecule production value of $10 \times 10^{16} \text{ J}^{-1}$ was assumed in estimating the moles per flash, which is in accordance with the average value of $8.5 \pm 4.7 \times 10^{16}$ estimated by Lawrence et al. (1995) from summarizing theoretical values found in the literature. However, the energy per CG flash value used by Price et al. is considerably greater than the 0.4 GJ per flash from the often cited Borucki and Chameides (1984) paper.

Laboratory spark experiments were conducted by Wang et al. (1998). They found that NO production increased nearly linearly with atmospheric pressure and quadratically with peak current of the flash. At surface pressure and typical values of peak current in the range 10–30 kA, the NO production was $15\text{--}40 \times 10^{16} \text{ J}^{-1}$. These values are larger than that assumed by Price et al. (1997). However, Wang et al. estimated that $\sim 50\text{--}150$ moles per flash was produced by typical strokes (36 kA), which is well within the range of the average value of $\sim 110\pm 170$ moles per flash estimated by Lawrence et al. (1995) from summarizing theoretical and laboratory values found in the literature and with the Price et al. (1997) value for IC flashes.

Aircraft measurements of NO in thunderstorm anvils conducted in field campaigns over the last 10–15 years (see Fig. 26.4) have yielded considerable information on NO production per flash, particularly when combined with observed lightning flash counts. Spikes in NO measured in the anvils of storms from the Stratosphere Troposphere Experiment: Radiation, Aerosol, Ozone (STERAO) field project in Colorado, USA in 1996 were analyzed by Stith et al. (1999) to yield a production rate in terms of NO molecules per unit flash length, which was extrapolated to flash lengths from 5 to 50 km. The resulting estimates ranges from 21

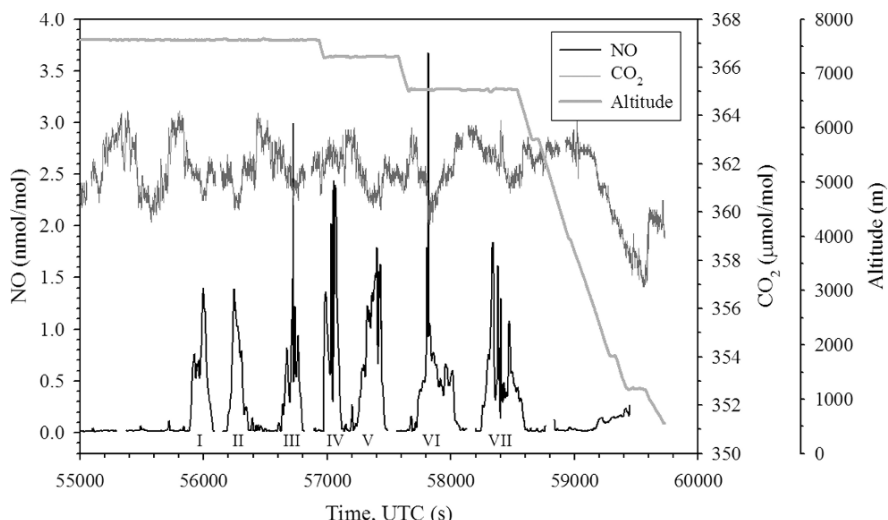


Fig. 26.4 Mixing ratio of NO (black line) and CO₂ (dark gray line), and altitude (light gray line) versus time from the EULINOX flight of 17 July 1998 over southern Germany. Seven penetrations of a squall line at different altitudes are labeled I–VII (from Huntrieser et al. 2002)

to 210 moles NO per flash, which is in accordance to the range found by Höller et al. (1999) and Huntrieser et al. (2002) during the airborne Lightning-produced NO_x (LINOX) and The European Lightning Nitrogen Oxides Project (EULINOX) experiments in 1996 and 1998 over Central Europe. Ridley et al. (2004) analyzed NO observations from the upper portion of anvils of Florida thunderstorms observed during the Cirrus Regional Study of Tropical Anvils and Cirrus Layers - Florida Area Cirrus Experiment (CRYSTAL-FACE) field project in 2002. These NO observations were related to observed flashes from the National Lightning Detection Network (NLDN) with a finding that the Florida storms analyzed had larger NO production rates per flash (55–382 moles) than storms from previous midlatitude field projects. Recently, Huntrieser et al. (2008) performed a detailed examination of the combination of anvil observations by aircraft and lightning strokes observed by the Lightning Location Network (LINET) system in São Paulo State in Brazil during the TROCCINOX experiments in 2004 and 2005. Results for tropical and subtropical thunderstorm events were contrasted in terms of NO production and stroke peak current, stroke release height and stroke component length. Simultaneous observations of LINET strokes and LIS flashes for one occasion were used to scale the estimated NO production rate per LINET stroke to the rate per LIS flash. The importance of scaling observed strokes or flashes from a local or regional system to global observations (OTD/LIS) was stressed, since observed production rates in single storms have been used to estimate the global LNO_x production rate. On average, tropical thunderstorms were found to produce less NO per LIS flash (86 moles) compared to subtropical thunderstorms (160 moles). The equivalent mean annual global LNO_x production rate was estimated to be 1.6 and 3.1 Tg/a, respectively. No distinct differences in the peak current frequency distribution were observed which could cause this difference in production rates. Also the difference in stroke release height was found to have only a minor influence. Instead the differences seem to be related to longer stroke component lengths in the subtropical thunderstorms compared to the tropical thunderstorms (factor of 2 difference). In fact, a larger mean flash length is supported by observations with a local flash detection systems (Huntrieser et al. 2008). The results suggest that the higher vertical wind shear observed in the subtropical compared to tropical thunderstorms during TROCCINOX may be responsible for the longer stroke component lengths. Up to now the flash length and the vertical wind shear has not been considered in any models simulating LNO_x.

Cloud-resolved chemical models have been used along with lightning flash rate and anvil NO observations to constrain estimates of NO production per flash. A series of cloud-resolved chemistry simulations described below has been conducted for individual storms observed in CRYSTAL-FACE (Ridley et al. 2004; Lopez et al. 2006), EULINOX (Huntrieser et al. 2002), and STERAO (Dye et al. 2000). All of these storms included research aircraft measuring chemical and meteorological properties at anvil levels. The time, location, and sometimes peak current of CG lightning occurrences were recorded by ground-based systems, and during STERAO and EULINOX, total lightning activity (IC + CG) was in addition mapped by a very high frequency (VHF) interferometer. Furthermore, all experiments included

extensive satellite and radar observations of storm development. The dynamical evolution of each storm was simulated using a cloud-resolving model and the temperature, wind, and hydrometeor fields were then used to drive an offline cloud-scale chemical transport model. For each storm, various LNO_x production per flash scenarios were simulated and model results were compared with in-cloud aircraft observations of NO_x through use of mean profiles, column NO_x mass, and probability distribution functions to determine which scenario was the most appropriate.

A detailed description of the cloud-scale CTM developed at the University of Maryland is found in DeCaria et al. (2005). In this version of the model, LNO_x production is parameterized using observed IC and CG flash rates and a specified scenario of P_{IC} and P_{CG} to calculate the mass of NO injected into the cloud per time step. The NO produced by CG flashes is distributed unimodally in the vertical according to a Gaussian distribution centered at the altitude of the -15°C isotherm, while the NO produced by IC flashes is distributed bimodally with peaks at -15°C and at a cloud-height dependent anvil altitude. These distributions are based on the vertical distributions of VHF sources of IC and CG flashes presented in MacGorman and Rust (1998). A pressure dependence for NO production is also included. At each model level, the LNO_x is distributed uniformly to all grid cells within the 20 dBZ contour computed from simulated hydrometeor fields. An example of the NO_x distribution within the July 29, 2002 CRYSTAL-FACE storm is shown in Fig. 26.5.

Table 26.1 shows the production scenarios (Ott et al., 2008) estimated for five midlatitude and subtropical storms from the STERAO, EULINOX, and

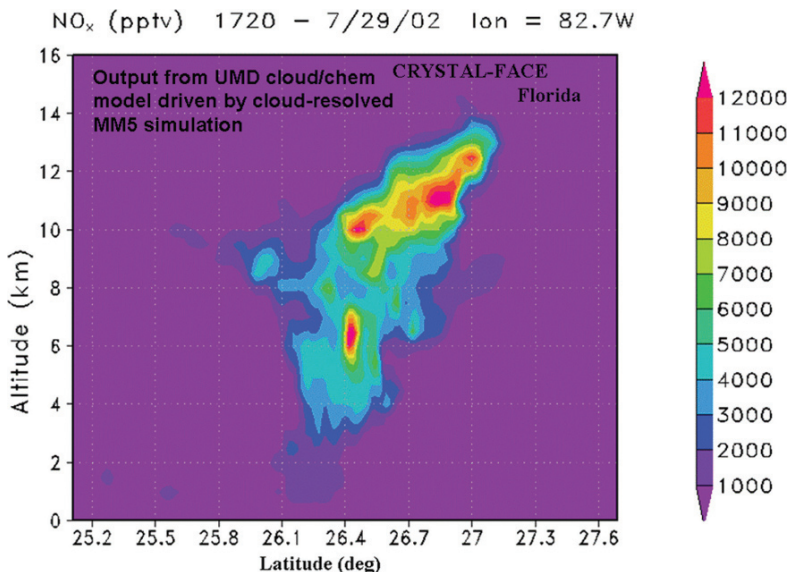


Fig. 26.5 Vertical cross section of NO_x (pmol mol⁻¹) through the July 29, 2002 CRYSTAL-FACE storm simulation using the University of Maryland cloud-scale CTM (See also Plate 52 in the Color Plate Section on page 630)

Table 26.1 LNO_x production in five midlatitude and subtropical storms simulated with the University of Maryland cloud-scale CTM and compared with theoretical estimates

Field project	Date	P _{CG} (moles/flash)	P _{IC} /P _{CG}
STERAO	July 10, 1996	460	0.75–1.0
STERAO	July 12, 1996	390	0.6
EULINOX	July 21, 1998	360	1.15
CRYSTAL-FACE	July 16, 2002	700	0.9
CRYSTAL-FACE	July 29, 2002	590	0.6–1.5
Mean		500	0.94
Price et al. (1997)		1100	0.1
Based on NALDN peak current (Orville et al. 2002)		508	NA

CRYSTAL-FACE campaigns using the University of Maryland cloud-scale CTM. Also listed is the production scenario from Price et al. (1997) which was used in calculating the vertical profiles of LNO_x mass presented in Pickering et al. (1998). In all cases, P_{CG} was estimated to be less than the 1100 moles per CG flash given in Price et al. (1997). In addition, the ratio of P_{IC} to P_{CG} was greater than the commonly assumed value of 0.1 presented by Price et al. (1997). Over the five storms simulated, the average estimated P_{CG} was 500 moles NO and the average P_{IC}/P_{CG} ratio was 0.94, corresponding to 470 moles NO for P_{IC}. For individual storms the P_{CG} values ranged from 360 to 700 moles per flash. The median peak current (16.5 kA for negative CG flashes and 19.8 kA for positive CG flashes which account for 10.9% of the total) of the North American Lightning Detection Network (NALDN) presented in Orville et al. (2002) would correspond to a P_{CG} value of 508 moles NO when using the Price et al. (1997) relationship between peak current and energy dissipated. This value agrees well with our estimate of 500 moles NO per CG flash. Therefore, the cases we have simulated appear to be representative. Assuming the average production scenario over the five simulated midlatitude and subtropical storms, an average IC to CG ratio of 3 (Boccippio et al. 2001), and a global flash rate of 44 s⁻¹ (Christian et al. 2003) yields a global LNO_x source of ~9 Tg/a. The value of 9 Tg/a falls within the range obtained by Price et al. (1997) using the cloud-top height flash distribution based on International Satellite Cloud Climatology Project (ISCCP) deep convective clouds and 1100 moles/flash and 110 moles/flash for CG and IC flashes, respectively. However, the global LNO_x production value of 9 Tg/a is distinctly higher than the values resulting from extrapolating production per flash findings from laboratory measurements (1–3 Tg/a) and airborne field campaigns described above (3 Tg/a based on Huntrieser et al. (2002) and 1.1–7.5 Tg/a based on Ridley et al. (2004)). If the hypothesis of Huntrieser et al. (2008) regarding tropical flashes being less productive of LNO_x than midlatitude and subtropical flashes holds true for tropical cloud simulations, the global estimate based on such simulations would certainly decrease.

Other cloud-resolved models with chemical tracers have also been used in estimating NO production per flash. For example, Skamarock et al. (2003) used a cloud resolving model (COMMAS) to estimate the flux of NO_x out of the

anvil of a STERAO thunderstorm and compared the computed flux with that from aircraft measurements to determine the production per flash (43 moles NO per flash averaged over total flashes). This analysis used the observed flash rate from a VHF interferometer which in addition detected a number of short duration flashes for which it is unknown if they produce NO molecules. Barthe and Barth (2008) simulated the same STERAO storm using the WRF-AqChem model of Barth et al. (2007). However, this simulation was performed with the flash rate parameterization of Deierling et al. (2008), which yielded 121 moles per flash (averaged over total flashes) and a conclusion from sensitivity studies that the short-duration flashes made very little NO. In this study the location of the LNO_x source was filamentary instead of volumetric, as in most previous studies, which yield a LNO_x production rate in the lower range compared to other studies.

Fehr et al. (2004) used a cloud-resolved version of MM5 with a lightning placement scheme in a simulation of the same EULINOX storm as simulated by Ott et al. (2007) with the cloud-scale CTM developed at the University of Maryland. Roughly similar values of P_{CG} (335 moles per flash from Fehr et al. and 360 moles per flash from Ott et al.) were obtained from the two models, but Fehr et al. obtained a larger value (1.4) of the per flash IC/CG production ratio than Ott et al. (1.15). A high value of this ratio is also needed to explain the high variability of NO data obtained from aircraft flying thought the thunderstorm anvil. It has been suggested that the NO concentration signatures would be smoother than observed if the NO originated largely from CG flashes (Höller et al. 2000). Ridley et al. (2005) have recommended that global models be run with the assumption of comparable production of NO by both types of lightning discharges.

Cloud-resolved models with explicit cloud electrification (Zhang et al. 2003; Barthe et al. 2005) have also been used in estimating LNO_x production. Such models simulate the processes of hydrometeor charging, charge separation, and the lightning discharge. Zhang et al. simulated a short-lived storm, generating 18 flashes over a 38-minute simulation, which yielded 2.03×10^{22} molecules NO per meter of flash channel, which is in the range of observations from other storms. The Barthe et al. model was applied to the 10 July STERAO storm, producing peaks of ~ 4 nmol mol⁻¹ in the anvil similar to the airborne observations. LNO_x production per flash values were not provided from these models.

Case studies and global distributions of enhancements of tropospheric column NO₂ observations from satellite have also been used in estimates of LNO_x production. Beirle et al. (2006) used GOME tropospheric column observations of the number of NO₂ molecules per unit area of up to 4×10^{15} cm⁻² over the Gulf of Mexico along with NLDN flash observations, and a climatological IC/CG ratio to estimate that these CG flashes produced 90 (32–240) moles of NO per flash and 1.7 (0.6–4.7) Tg/a globally. Boersma et al. (2005) used the global GOME NO₂ data along with a global chemical transport model to estimate a global LNO_x source strength of 1.6–6.4 Tg/a. Using the OTD/LIS climatological estimate of 44 s⁻¹ for the global mean flash rate, this source strength implies a production per flash of 82–328 moles NO per flash.

26.4 Vertical Distribution of LNO_x Emissions

Many early CTMs made the assumption that LNO_x emissions were equally distributed in the vertical. The common assumptions were a constant mass or a constant mixing ratio (pressure dependent) with altitude. However, as more aircraft observations of NO_x and O₃ become available in the 1990s, it was noted that the influence of deep convection on LNO_x was most dominant in the middle to upper troposphere (e.g. Ridley et al. 1996; Huntrieser et al. 1998). Pickering et al. (1998) performed 2-D cloud-resolved model simulations of observed thunderstorms from several environments (midlatitude continental, tropical marine, and tropical continental) which were constrained with measured flash rates or observed anvil-NO_x mixing ratios. These simulations were conducted with the Price et al. (1997) assumptions concerning LNO_x production per flash and with a flash placement scheme that was more crude than in more recent cloud-resolved modeling. The LNO_x mass in the model was integrated across the domain upon dissipation of the simulated storm and the percentage of this mass in each 1-km layer was computed. Profiles of the LNO_x mass derived in this way have been used in numerous global CTMs as the effective vertical distribution of LNO_x emissions (summarized in Schumann and Huntrieser 2007). The Pickering et al. (1998) profiles indicated that a majority of LNO_x is deposited above 8 km. A secondary maximum was found in the boundary layer as a result of downdrafts, yielding a C-shaped profile. Cloud-resolved simulations of a midlatitude supercell by Fehr et al. (2004) show even more pronounced maxima in the outflow region and boundary layer compared to Pickering et al. (1998). In an alternative scheme for simulations with a GCM, Kurz and Grewe (2002) used a simple quadratic parabola C-shape fit representing the LNO_x mass emissions.

However, more recent observations from STERAO, EULINOX and TROCCI-NOX have failed to find any significant LNO_x maxima in the boundary layer. More recent modeling studies (e.g., DeCaria et al. 2005; Ott et al. 2007), using more realistic flash placement schemes (e.g., the unimodal CG and bimodal IC flash channel distributions described above) and production per flash schemes, also do not show significant amounts of LNO_x in the boundary layer. Ott et al. (2008) summarized the results of 3-D cloud-resolved modeling of several midlatitude and subtropical storms (including those discussed by DeCaria et al. 2005; Ott et al. 2007) in terms of the vertical profile of LNO_x upon storm dissipation. Results show only small amounts (<7% in midlatitudes and <3% in subtropics) of LNO_x in the boundary layer, in accordance with observations. The other significant change from the Pickering et al. (1998) profiles is that the upper tropospheric maxima in percentage of LNO_x mass is now located at somewhat lower altitude in the new model output. In comparison to these prescribed vertical placements of LNO_x, a further approach has been developed by Mari et al. (2006) where a mass-flux formalism was implemented into a mesoscale model. No a-priori vertical placement of LNO_x is therefore necessary. The vertical distribution of LNO_x results from the redistribution of LNO_x emissions inside the convective scheme. Labrador et al. (2005) examined the effects of the vertical distribution of LNO_x emissions on atmospheric chemistry using a

global CTM and noted that the shape of such vertical profiles is not only important in determining the large-scale distributions of NO_x but also of OH.

26.5 Applications and Performance of Global Models for Estimating the LNO_x Source and Its Impact on Global NO_x and Ozone Distributions

Global CTMs have been used to estimate the global source strength for LNO_x. This goal is achieved by comparing model mixing ratios of NO_x or O₃ with observations from ozonesondes, research aircraft, or satellite, followed by adjustment of the LNO_x source strength to obtain the best match with these observations. Numerous studies of this type have been conducted with a variety of models. Results of such analyses have been summarized by Schumann and Huntrieser (2007) and they suggest that the total global production is 2–8 Tg/a with a most likely value of 5 Tg/a. Early work used nitrate deposition data to constrain the LNO_x source strength (e.g., Penner et al. 1991). In more recent years sufficient aircraft and satellite data have become available to use for this purpose. Large data sets of aircraft observations influenced by LNO_x outflow from deep convection are valuable in allowing estimates of the global lightning source to be made with relative confidence. For example, Staudt et al. (2002, 2003) used data from the PEM Tropics A and B experiments to constrain the GEOS-Chem model and obtained estimates of 6 and 5 Tg/a, respectively. Satellite observations of tropospheric column NO₂ provide global coverage, but the NO₂ signal from lightning in standard satellite retrievals is only marginally greater than the noise in the measurements. Boersma et al. (2005) analyzed GOME NO₂ data in conjunction with the TM3-CTM and found that the global LNO_x source strength was between 1.6 and 6.4 Tg/a. Martin et al. (2007) used SCIAMACHY tropospheric column NO₂, which has better spatial coverage and resolution than GOME, in conjunction with the GEOS-Chem model (see Fig. 26.6). The resulting best-fit LNO_x source strength was 6 Tg/a. Schumann and Huntrieser (2007) report that simulations from several global models, with their preferred LNO_x parameterizations, were compared to trace gas observations from TROCCINOX (e.g. NO_x, CO and O₃). The evaluation method used (developed by U. Schumann) allows one to determine also the uncertainty range of the best estimate (based on the root-mean-square deviation between model results and observations) and the model sensitivity to the global LNO_x source rate. The best result was achieved with the TM4-CTM and a convective precipitation based parameterization which yield 4.8 ± 2.5 Tg/a for the annual global LNO_x production rate.

Tost et al. (2007) performed a comprehensive study with a global GCM where several state-of-the-art convection parameterizations were combined with different lightning parameterizations based on cloud-top height, updraft velocity and mass flux, and convective precipitation. A large variability in the results was found and none of the combinations approximately reproduced the observed lightning distributions from OTD/LIS. The updraft scheme developed by Grewe et al. (2001) in

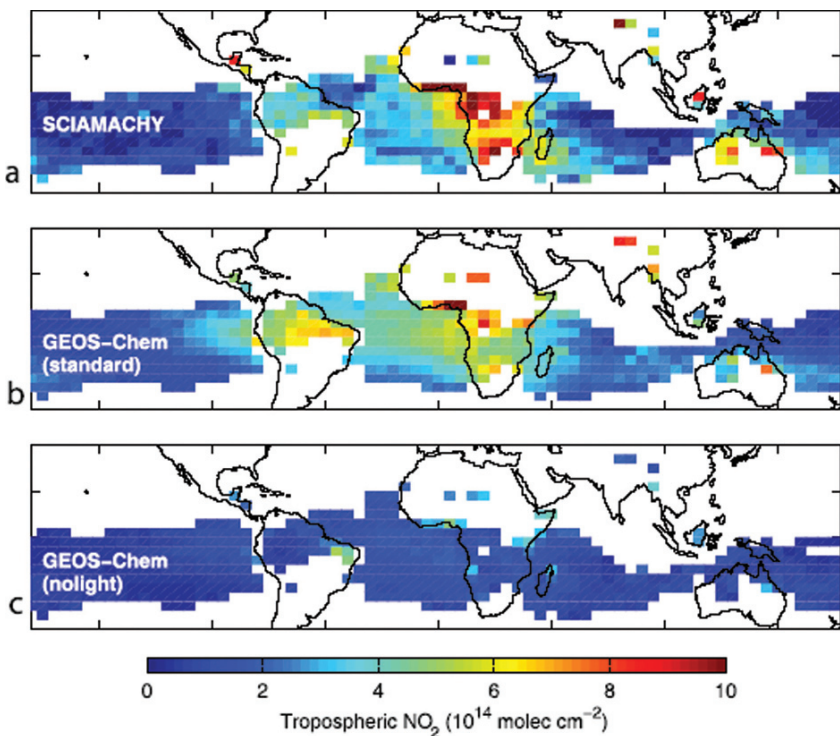


Fig. 26.6 SCIAMACHY tropospheric NO₂ column map compared with GEOS-Chem with 6 Tg/a from lightning and a GEOS-Chem run without lightning from Martin et al. (2007). Data are shown for regions where the model indicates the lightning contribution to be greater than 60% and the surface source contribution less than 25% (See also Plate 53 in the Color Plate Section on page 631)

combination with the Tiedtke (1989) scheme, which was especially developed for this GCM, scored better than most other combinations. However, the flash density over tropical oceans was overestimated and the maximum in flash density over Africa was underestimated. Even if the cloud-top height is not directly linked to cloud electrification, this approach was robust in combination with different convection parameterizations and with respect to both spatial and temporal variations of flash density. In contrast, Schumann and Huntrieser (2007) summarized that the LNO_x parameterizations based on the updraft and the convective precipitation schemes seem to simulate the variability of convection and lightning flash rates better than the parameterization based on cloud-top height.

Once a best-fit global LNO_x production is determined for a particular model, the model can be used to estimate the overall influence of LNO_x emissions on the large-scale distributions of NO_x and tropospheric ozone. Estimates of the fraction of NO_x due to LNO_x are generally obtained by running the model with and without the lightning source and subtracting the resulting NO_x fields. A general conclusion is that lightning is the dominant NO source for the upper troposphere over the entire year in the tropics and in the summer in the midlatitudes (e.g., Lamarque et al. 1996;

Berntsen and Isaksen 1999; Levy et al. 1999; Hauglustaine et al. 2001; Bond et al. 2002). Model simulations by Grewe (2007) show up to 70% of NOy (NOy includes all reactive odd nitrogen, also called fixed nitrogen) in the tropical upper troposphere is from lightning (see Fig. 17 in Schumann and Huntrieser (2007)). The impact of lightning on tropospheric reactive nitrogen NO_x and nitrogen reservoir species (HNO₃, peroxyacetyl nitrate (PAN), N₂O₅, and HNO₄) has been evaluated using a global chemical/transport model by Tie et al. (2001). Over 60% of the increase in total nitrogen species concentration when lightning was added to model was in the form of HNO₃. The increase in PAN accounts for approximately 20–30% of the nitrogen enhancement by lightning in the middle troposphere. Over 30% of tropospheric O₃ is formed by enhanced photochemistry due to LNO_x in the tropics

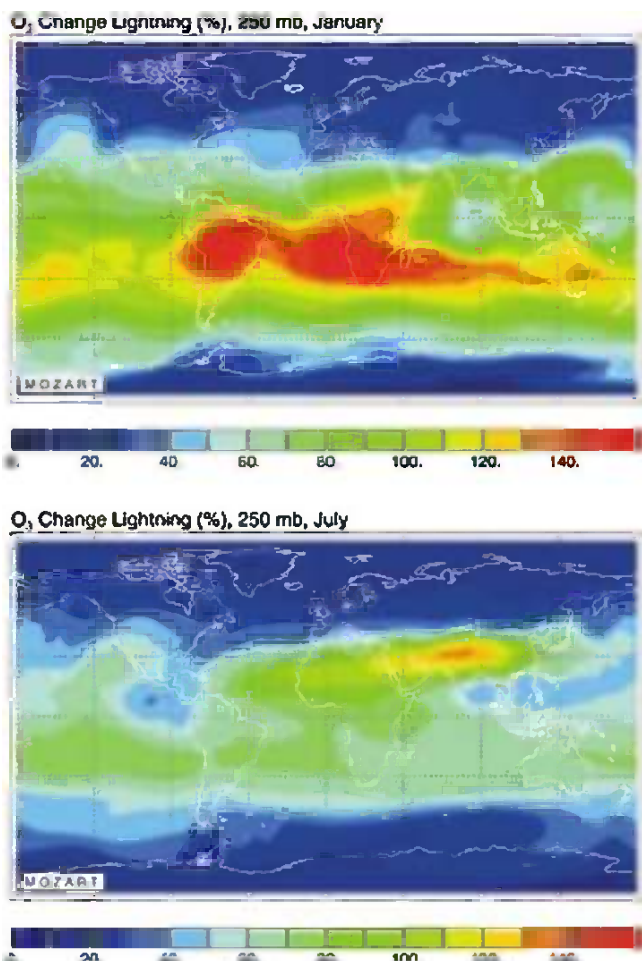


Fig. 26.7 Percentage increase in upper tropospheric (250 hPa) ozone due to lightning (from Hauglustaine et al. 2001) (See also Plate 54 in the Color Plate Section on page 632)

and over areas extending well into both hemispheres (Grewe 2007). Other models have yielded higher percentages. Hauglustaine et al. (2001) ran the MOZART CTM with and without LNO_x and found that ozone increases over the simulation without LNO_x were 150% over South America and Africa and >100% over the South Atlantic during the Southern Hemisphere summer. In Northern Hemisphere summer the ozone increases were 120% over South Asia and 20–50% over North America and Europe (see Fig. 26.7).

26.6 Conclusions

The range of values used for the global LNO_x production rate in more recent studies is still wide and range from 1 to 20 Tg/a, though more detailed recent studies support the smaller range of 2–8 Tg/a. However, for assessing the contribution to the NO_x and O₃ budgets especially in the tropics, the required LNO_x accuracy is about 1 Tg/a (Schumann and Huntrieser 2007). For most other tasks an accuracy of 5 Tg/a is enough, which is less than the range of best estimates suggested by Schumann and Huntrieser (2007). Considerably more research will be required to narrow the uncertainty to 1 Tg/a. Especially, more detailed field observations with 3-D lightning mapping arrays and airborne in-situ measurements of NO_x in the anvil outflow region of thunderstorms are required, which can help to improve the LNO_x parameterization in cloud-resolving models. These improvements can then be implemented to global models. Furthermore, detailed satellite measurements of lightning, precipitation and NO₂ with global cover are now available which are essential for evaluation of global models and can be used to adjust the models to the observations. The continuous increase in the resolution of satellite measurements and global models will also contribute to decrease the uncertainty range of LNO_x.

References

- Allen, D., Pickering, K., Stenchikov, G., Thompson, A., Kondo, Y.: A three-dimensional total odd nitrogen (NO_y) simulation during SONEX using a stretched-grid chemical transport model. *J. Geophys. Res.* **105**, 3851–3876 (2000). doi:10.1029/1999JD901029
- Allen, D.J., Pickering, K.E.: Evaluation of lightning flash rate parameterizations for use in a global chemical transport model. *J. Geophys. Res.* **107**, 4711 (2002). doi:10.1029/2002JD002066
- Allen, D.J., Pickering, K.E., Rodriguez, J.M., Duncan, B., Strahan, S., Logan, J., Damon, M.: Impact of lightning NO production on upper tropospheric NO_x and O₃ in the GMI model. *J. Geophys. Res.* in preparation (2008)
- Barth, M.C., Kim, S.-W., Wang, C., et al.: Cloud-scale model intercomparison of chemical constituent transport in deep convection. *Atmos. Chem. Phys.* **7**, 4709–4731 (2007)
- Barthe, C., Molinié, G., Pinty, J.-P.: Description and first results of an explicit electrical scheme in a 3D cloud resolving model. *Atmos. Res.* **76**, 95–113 (2005)
- Barthe, C., Barth, M.C.: Evaluation of a new lightning-produced NO_x parameterization for cloud resolving models and its associated uncertainties. *Atmos. Chem. Phys. Discuss.* **8**, 6603–6651 (2008)

- Beirle, S., Spichtinger, N., Stohl, A., et al.: Estimating the NO_x produced by lightning from GOME and NLDN data: a case study in the Gulf of Mexico. *Atmos. Chem. Phys.* **6**, 1075–1089 (2006)
- Berntsen, T.K., Isaksen, I.S.A.: Effects of lightning and convection on changes in tropospheric ozone due to NO_x emissions from aircraft. *Tellus* **51B**, 766–788 (1999)
- Boccippio, D.J., Cummins, K.L., Christian, H.J., Goodman, S.J.: Combined satellite- and surface-based estimation of the intracloud-cloud-to-ground lightning ratio over the continental United States. *Mon. Wea. Rev.* **129**, 108–122 (2001)
- Boccippio, D.J.: Lightning scaling relations revisited. *J. Atmos. Sci.* **59**, 1086–1104 (2002)
- Boersma, K.F., Eskes, H.J., Meijer, E.W., Kelder, H.M.: Estimates of lightning NO_x production from GOME satellite observations. *Atmos. Chem. Phys.* **5**, 2311–2331 (2005)
- Bond, D.W., Steiger, S., Zhang, R., Tie, X., Orville, R.E.: The importance of NO_x production by lightning in the tropics. *Atmos. Environ.* **36**, 1509–1519 (2002)
- Borucki, W.J., Chameides, W.L.: Lightning: estimates of the rates of energy dissipation and nitrogen fixation. *Rev. Geophys. Space Phys.* **22**, 363–372 (1984)
- Cecil, D.J., Goodman, S.J., Boccippio, D.J., Zipser, E.J., Nesbitt, S.W.: Three years of TRMM precipitation features, Part I: radar, radiometric, and lightning characteristics. *Mon. Wea. Rev.* **133**, 543–566 (2005)
- Choi, Y., Wang, Y., Zeng, T., Martin, R.V., Kurosu, T.P., Chance, K.: Evidence of lightning NO_x and convective transport of pollutants in satellite observations over North America. *Geophys. Res. Lett.* **32**, L02805 (2005). doi:10.1029/2004GL021436
- Christian, H.J., Blakeslee, R.J., Boccippio, D.J., et al.: Global frequency and distribution of lightning as observed from space by the Optical Transient Detector. *J. Geophys. Res.* **108**, 4005 (2003). doi:10.1029/2002JD002347
- DeCaria, A.J., Pickering, K.E., Stenchikov, G.L., Ott, L.E.: Lightning-generated NO_x and its impact on tropospheric ozone production: a three-dimensional modeling study of a Stratosphere-Troposphere Experiment: Radiation, Aerosols and Ozone (STERAO-A) thunderstorm. *J. Geophys. Res.* **110**, 1–13 (2005). doi:10.1029/2004JD005556
- Deierling, W., Latham, J., Petersen, W.A., Ellis, S.M., Christian Jr., H.J.: On the relationship of thunderstorm ice hydrometeor characteristics and total lightning measurements. *Atmos. Res.* **76**, 114–126 (2005)
- Deierling, W., Petersen, W., Latham, J., Ellis, S., Christian Jr., H.J.: The relationship between lightning activity and ice fluxes in thunderstorms. *J. Geophys. Res.* **113**, D15210 (2008), doi: 10.1029/2007JD009700
- Deierling, W., Petersen, W.: Total lightning activity as an indicator of updraft characteristics. *J. Geophys.* **113**, D16210 (2008), doi: 10.1029/2007JD009598
- Dye, J.E., Ridley, B.A., Skamarock, W., et al.: An overview of the Stratospheric-Tropospheric Experiment: Radiation, Aerosols, and Ozone (STERAO)-Deep Convection experiment with results for the July 10, 1996 storm. *J. Geophys. Res.* **105**, 10023–10045 (2000)
- Fehr, T., Höller, H., Huntrieser, H.: Model study on production and transport of lightning-produced NO_x in a EULINOX supercell storm. *J. Geophys. Res.* **109**, 1–17 (2004). doi:10.1029/2003JD003935
- Futyan, J.M., Del Genio, A.D.: Relationships between lightning and properties of convective cloud clusters. *Geophys. Res. Lett.* **34**, L15705 (2007). doi:10.1029/2007GL030227
- Gauthier, M.L., Petersen, W.A., Carey, L.D., Christian Jr., H.J.: Relationship between cloud-to-ground lightning and precipitation ice mass: a radar study over Houston. *Geophys. Res. Lett.* **33**, L20803 (2006). doi:10.1029/2006GL027244
- Grewe, V., Brunner, D., Dameris, M., Grenfell, J.L., Hein, R., Shindell, D., Staehelin, J.: Origin and variability of upper tropospheric nitrogen oxides and ozone at northern mid-latitudes. *Atmos. Environ.* **35**, 3421–3433 (2001)
- Grewe, V.: Impact of climate variability on tropospheric ozone. *Sci. Total Environ.* **374**, 167–181 (2007). doi:10.1016/j.scitotenv.2007.01.032
- Hauglustaine, D., Emmons, L., Newchurch, M., Brasseur, G., Takao, T., Matsubara, K., Johnson, J., Ridley, B., Stith, J., Dye, J.: On the role of lightning NO_x in the formation of tropospheric ozone plumes: a global model perspective. *J. Atmos. Chem.* **38**, 277–294 (2001)

- Höller, H., Finke, U., Huntrieser, H., Hagen, M., Feigl, C.: Lightning-produced NO_x (LINOX): experimental design and case study results. *J. Geophys. Res.* **104**, 13911–13922 (1999). doi:10.1029/1999JD900019
- Höller, H., Fehr, T., Thery, C., Seltmann, J., Huntrieser, H.: Radar, lightning, airborne observations and modelling of a supercell storm during EULINOX. *Phys. Chem. Earth B*, **25**, 1281–1284 (2000)
- Huntrieser, H., Schlager, H., Feigl, C., Höller, H.: Transport and production of NO_x in electrified thunderstorms: survey of previous studies and new observations at midlatitudes. *J. Geophys. Res.* **103**, 28247–28264 (1998). doi:10.1029/98JD02353
- Huntrieser, H., Feigl, C., Schlager, H., et al.: Airborne measurements of NO_x, tracer species, and small particles during the European lightning nitrogen oxides experiment. *J. Geophys. Res.* **107**, 4113 (2002). doi:10.1029/2000JD000209
- Huntrieser, H., Schumann, U., Schlager, H., Höller, H., Giez, A., Betz, H.-D., Brunner, D., Forster, C., Pinto Jr., O., Calheiros, R.: Lightning activity in Brazilian thunderstorms during TROCCINOX: implications for NO_x production. *Atmos. Chem. Phys.* **8**, 921–953 (2008)
- Intergovernmental Panel on Climate Change: *Climate Change 2007 – The Physical Science Basis, Contribution of Working group 1 to the Fourth Assessment Report*, 996 pp. Cambridge University Press, Cambridge (2007)
- Kurz, C., Grewe, V.: Lightning and thunderstorms, Part I: Observational data and model results. *Meteorol. Z.* **11**, 379–393 (2002)
- Labrador, L.J., von Kuhlmann, R., Lawrence, M.G.: The effects of lightning-produced NO_x and its vertical distribution on atmospheric chemistry: sensitivity simulations with MATCH-MPIC. *Atmos. Chem. Phys.* **5**, 1815–1834 (2005)
- Lamarque, J.F., Brasseur, G.P., Hess, P.G., Mueller, J.F.: Three-dimensional study of the relative contributions of the different nitrogen sources in the troposphere. *J. Geophys. Res.* **101**, 22955–22968 (1996)
- Lawrence, M.G., Chameides, W.L., Kasibhatla, P.S., Levy II, H., Moxim, W.: Lightning and atmospheric chemistry: The rate of atmospheric NO production, in: Volland, H. (ed.) *Handbook of Atmospheric Electrodynamics*, pp. 189–202. CRC Press, Boca Raton, Florida (1995)
- Levy II, H., Moxim, W.J., Klonecki, A.A., Kasibhatla, P.S.: Simulated tropospheric NO_x: its evaluation, global distribution and individual source contributions. *J. Geophys. Res.* **104**, 26279–26306 (1999)
- Lopez, J.P., Fridlind, A.M., Jost, H.-J., et al.: CO signatures in subtropical convective clouds and anvils during CRYSTAL-FACE: an analysis of convective transport and entrainment using observations and a cloud-resolving model. *J. Geophys. Res.* **111**, D09305 (2006). doi:10.1029/2005JD006104
- MacGorman, D.R., Rust, W.D.: *The Electrical Nature of Storms*. 422 pp. Oxford University Press, Oxford (1998)
- Mari, C., Mari, C., Chaboureau, J.P., Pinty, J.P., et al.: Regional lightning NO_x sources during the TROCCINOX experiment. *Atmos. Chem. Phys.* **6**, 5559–5572 (2006)
- Martin, R.V., Sauvage, B., Folkins, I., Sioris, C.E., Boone, C., Bernath, P., Ziemke, J.: Space-based constraints on the production of nitric oxide by lightning. *J. Geophys. Res.* **112**, D09309 (2007). doi:10.1029/2006JD007831
- Meijer, E.W., van Velthoven, P.F.J., Brunner, D.W., Huntrieser, H., Kelder, H.: Improvement and evaluation of the parameterisation of nitrogen oxide production by lightning. *Phys. Chem. Earth*, **26**, 577–583 (2001)
- Orville, R.E., Huffines, G.R., Burrows, W.R., Holle, R.L., Cummins, K.L.: The North American lightning detection network (NALDN) – First results: 1998–2000. *Mon. Wea. Rev.* **130**, 2098–2109 (2002)
- Ott, L.E., Pickering, K.E., Stenchikov, G.L., Huntrieser, H., Schumann, U.: Effects of lightning NO_x production during the 21 July European lightning nitrogen oxides project storm studied with a three-dimensional cloud-scale chemical transport model. *J. Geophys. Res.* **112**, D05307 (2007). doi:10.1029/2006JD007365

- Ott, L., Pickering, K.E., DeCaria, A., Stenchikov, G., Lin, R.-F., Wang, D., Lang, S., Tao, W.-K.: Production of lightning NO_x and its vertical distribution calculated from 3-D cloud-scale chemical transport model simulations. *J. Geophys. Res.* in preparation (2008)
- Penner, J.E., Atherton, C.S., Dignon, J., Ghan, S.J., Walton, J.J., Hameed, S.: Tropospheric nitrogen: a three-dimensional study of sources, distributions, and deposition. *J. Geophys. Res.* **96**, 959–990 (1991). doi:10.1029/90JD02228
- Petersen, W.A., Rutledge, S.A.: On the relationship between cloud-to-ground lightning and convective rainfall. *J. Geophys. Res.* **103**, 14025–14040 (1998). doi:10.1029/97JD02064
- Petersen, W.A., Christian, H.J., Rutledge, S.A.: TRMM observations of the global relationship between ice water content and lightning. *Geophys. Res. Lett.* **32**, 1–4 (2005). doi:10.1029/2005GL023236
- Pickering, K.E., Wang, Y., Tao, W.K., Price, C., Müller, J.F.: Vertical distributions of lightning NO_x for use in regional and global chemical transport models. *J. Geophys. Res.* **103**, 31203–31216 (1998). doi:10.1029/98JD02651
- Price, C., Rind, D.: A simple lightning parameterization for calculating global lightning distributions. *J. Geophys. Res.* **97**, 9919–9933 (1992). doi:10.1029/92JD00719
- Price, C., Rind, D.: What determines the cloud-to-ground lightning fraction in thunderstorms?. *Geophys. Res. Lett.* **20**, 463–466 (1993). doi:10.1029/93GL00226
- Price, C., Penner, J., Prather, M.: NO_x from lightning, I. Global distribution based on lightning physics. *J. Geophys. Res.* **102**, 5929–5941 (1997). doi:10.1029/96JD03504
- Ridley, B.A., Dye, J.E., Walega, J.G., Zheng, J., Grahek, F.E., Rison, W.: On the production of active nitrogen by thunderstorms over New Mexico. *J. Geophys. Res.* **101**, 20985–21005 (1996)
- Ridley, B., Ott, L., Pickering, K., et al.: Florida thunderstorms: a faucet of reactive nitrogen to the upper troposphere. *J. Geophys. Res.* **109**, 1–19 (2004). doi:10.1029/2004JD004769
- Ridley, B.A., Pickering, K.E., Dye, J.E.: Comments on the parameterization of lightning-produced NO in global chemistry-transport models. *Atmos. Environ.*, **39**, 6184–6187 (2005)
- Sauvage, B., Martin, R.V., van Donkelaar, A., Liu, X., Chance, K., Jaeglé, L., Palmer, P.I., Wu, S., Fu, T.-M.: Remote sensed and in situ constraints on processes affecting tropical tropospheric ozone. *Atmos. Chem. Phys.* **7**, 815–838 (2007)
- Schumann, U., Huntrieser, H.: The global lightning-induced nitrogen oxides source. *Atmos. Chem. Phys.* **7**, 3823–3907 (2007)
- Sherwood, S.C., Phillips, V.T.J., Wetzlaufer, J.S.: Small ice crystals and the climatology of lightning. *Geophys. Res. Lett.* **33**, L05804 (2006). doi:10.1029/2005GL025242
- Skamarock, W.C., Dye, J.E., Defer, E., Barth, M.C., Stith, J.L., Ridley, B.A., Baumann, K.: Observational and modeling-based budget of lightning-produced NO_x in a continental thunderstorm. *J. Geophys. Res.* **108**, 4305 (2003). doi:10.1029/2002JD002163
- Staudt, A.C., Jacob, D.J., Logan, J.A., Bachiochi, D., Krishnamurti, T.N., Poisson, N.: Global chemical model analysis of biomass burning and lightning influences over the South Pacific in austral spring. *J. Geophys. Res.* **107**, 4200 (2002). doi:10.1029/2000JD000296
- Staudt, A.C., Jacob, D.J., Ravetta, F., Logan, J.A., Bachiochi, D., Krishnamurti, T.N., Sandholm, S., Ridley, B., Singh, H.B., Talbot, B.: Sources and chemistry of nitrogen oxides over the tropical Pacific. *J. Geophys. Res.* **108**, 8239 (2003). doi:10.1029/2002JD002139
- Stith, J., Dye, J., Ridley, B., Laroche, P., Defer, E., Baumann, K., Huebler, G., Zerr, R., Venticinque, M.: NO signatures from lightning flashes. *J. Geophys. Res.* **104**, 16081–16089 (1999)
- Tie, X., Zhang, R., Brasseur, G., Emmons, L., Lei, W.: Effects of lightning on reactive nitrogen and nitrogen reservoir species in the troposphere. *J. Geophys. Res.* **106**, 3167–3178 (2001). doi:10.1029/2000JD900565
- Tiedtke, M.: A comprehensive mass flux scheme for cumulus parameterization in large-scale models. *Mon. Wea. Rev.* **117**, 1779–1800 (1989)
- Tost, H., Jöckel, P., Lelieveld, J.: Lightning and convection parameterisations – uncertainties in global modeling. *Atmos. Chem. Phys.* **7**, 4553–4568 (2007)
- Ushio, T., Heckman, S.J., Boccippio, D.J., Christian, H.J., Kawasaki, Z.-I.: A survey of thunderstorm flash rates compared to cloud top height using TRMM satellite data. *J. Geophys. Res.* **106**, 24089–24095 (2001)

- Vonnegut, B.: Some facts and speculations concerning the origin and role of thunderstorm electricity, in: Atlas, D., Booker, D.R., Byers, H., et al. (eds.) *Severe Local Storms*, Meteorol. Monogr., vol. 5, no. 27., pp. 224–241. Am. Meteor. Soc., Boston (1963)
- Wang, Y., DeSilva, A.W., Goldenbaum, G.C., Dickerson, R.R.: Nitric oxide production by simulated lightning: Dependence on current, energy, and pressure. *J. Geophys. Res.* **103**, 19149–19159 (1998)
- Williams, E.: Large-scale charge separation in thunderclouds. *J. Geophys. Res.* **90**, 6013–6025 (1985)
- Zel'dovich, Y.B., Raizer, Y.P.: *Physics of Shock Waves and High Temperature Hydrodynamic Phenomena*. 566–571 pp. Academic, San Diego, CA (1967)
- Zhang, X., Helsdon Jr., J.H., Farley, R.D.: Numerical modelling of lightning-produced NO_x using an explicit lightning scheme: 2. Three-dimensional simulation and expanded chemistry. *J. Geophys. Res.* **108**, 4580 (2003). doi:10.1029/2002JD003225

Chapter 27

Lightning Protection of Structures

Marek Łoboda

Abstract The paper deals with actual methodology of lightning protection of structures based on IEC 62305 series of standards, which have been introduced as European (CENELEC) norms EN under the same number. Lightning affecting a structure can cause damage to the structure itself, to its occupants and contents, including failure of internal electrical and electronic systems. The damages and failures may also extend to the surroundings of the structure and even involve the local environment. The scale of this extension depends on the characteristics of the structure and on the characteristics of the lightning flash. When there is a desire to eliminate any avoidable risk, the decision to provide adequate lightning protection shall be based on a risk assessment, strictly following the recommendations resulting from such an assessment. Protection measures are directed to reduce the risk according to the type of damage and shall be considered effective only if they conform to the requirements of relevant standards:

- for protection against injury to living beings and physical damage in a structure (IEC 62305-3);
- for protection against failure of internal systems (IEC 62305-4);
- for protection of services (IEC 62305-5).

The selection of the most suitable protection measures shall be made by the designer according to the share of each risk component in the total risk R and according to the technical and economic aspects of the different protection measures.

Keywords Lightning protection · Overvoltage protection · Lightning hazard · Lightning protection measures

M. Łoboda (✉)

Warsaw University of Technology; Department of High Voltage Engineering and Electrical Apparatus, ul. Koszykowa 75, 00-665 Warsaw, Poland
e-mail: marek.loboda@ien.pw.edu.pl

27.1 Introduction

There are no devices or methods capable of modifying the natural weather phenomena to the extent that they can prevent lightning discharges. Lightning flashes to, or near, structures (or services connected to the structures) are hazardous to people, to the structures themselves, to their contents and installations, as well as to services. The destructive power of lightning arises from high energy generated by lightning cloud to, ground discharge channels and the lightning stroke current. This is why the application of lightning protection measures is essential.

As with most engineering problems, the achievement of satisfactory lightning protection requires a statement of the problem, consideration of the techniques available for its solution and then marriage of the solution to the problem.

The need for protection, the economic benefits of installing and the selection of adequate protection measures should be determined in terms of risk management, which is currently the subject of international or national standards related to lightning protection of structures and objects on the ground.

27.2 Lightning Risk Analysis

The lightning cloud-to-ground discharges are random natural phenomena, which may cause damage related to the direct strike and to the indirect (nearby) strikes to a structure. The source of damage is lightning current, hazardous not only to people but also to structures and installations with connections inside a structure, on a structure or around them. This hazard can result in damage to the entire structure as well as failure or malfunction of electrical and electronic equipment. Consequential effects of damages and failure can be extended to the proximity of the structure and may involve its environment.

To reduce the damage due to lightning it is necessary to take protection measures, which may significantly reduce the risk, defined as the probable annual loss in a structure (Flisowski and Mazzetti 1984).

For lightning risk analysis, the following set of data is required:

- Lightning ground flash or stroke density in the region where the structure and incoming services are located,
- Characteristics of the structure, its type and content,
- Characteristics of services entering the structure (mains, telecommunication and data lines),
- Characteristics of immunity to overvoltages of internal installation and equipment,
- Protection measures provided against direct strike, the propagation of a fire, explosion and other mechanical and thermal lightning effects,
- Measures to limit the consequences of damage (e.g. redundancy of electrical system, alternative power supply line, etc.),
- Amount of consequential losses and costs depending on the extent of the damage.

Special attention is actually paid to the lightning hazard caused by indirect flashes, which, as well as direct flashes to the structure or to the incoming lines, may cause failure of electrical and electronic equipment due to overvoltages resulting from resistive and inductive coupling of this equipment with the lightning current.

According to (IEC 62305-1, 2006) the annual risk of lightning damage can be described by the following relation:

$$R = (1 - e^{-NP}) \cdot L \quad (27.1)$$

where: N – annual number of lightning flashes influencing the structure and its equipment, P – probability of damage or malfunction due to individual lightning flash causing specified damage to the structure or its equipment, L – coefficient taking into account the mean amount of a peculiar type of damage, its extent and consequential effects, which may occur as the result of a lightning strike.

Assuming that $NP \ll 1$, the relation (27.1) may be expressed in a simplified form:

$$R = N \cdot P \cdot L \quad (27.2)$$

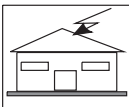
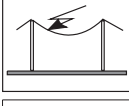
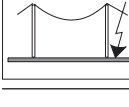
which is very useful for practical applications and fundamental for risk analysis according to recent IEC publication (IEC 62305-2, 2006).

As a result of direct or indirect strikes (sources of damage) and types of damage, alone or combined with others, different consequential losses in a structure may appear, depending on the characteristics of the structure and its equipment. So that was very convenient for practical application to create a set of risk components, related to the type of damage and type of loss.

The following classification (shown in Table 27.1) was applied (IEC 62305-2, 2006):

- Source of damage
 - Direct flash to the structure (S_1)
 - Lightning flash to ground near the structure (S_2)
 - Direct flash to incoming services (S_3)
 - Lightning flash to ground near incoming services (S_4)
- Type of damage
 - Injury to people due to touch and step voltages (D_1)
 - Fire, explosion, mechanical destruction, etc. due to physical effects of lightning (D_2)
 - Failure of electrical and electronic systems due to overvoltages (D_3)
- Type of loss
 - Loss of human life (L_1)
 - Loss of services to the public (L_2)
 - Loss of cultural heritage (L_3)
 - Loss of economic values (L_4)

Table 27.1 Damage and losses depending on different points of strike

Point of strike	Source of damage	Structure		Service	
		Type of damage	Type of loss	Type of damage	Type of loss
	S ₁	D ₁	L ₁ , L ₄	D ₁	L ₁ , L ₄ L ₁ ,
		D ₂	L ₁ , L ₂ L ₃	D ₂	L ₂
		D ₃	L ₁ , L ₂ L ₄		
	S ₂	D ₃	L ₁ , L ₂ , L ₄		
	S ₃	D ₁	L ₁ , L ₄	D ₁	L ₁ , L ₄
		D ₂	L ₁ , L ₂ L ₃ ,	D ₂	L ₁ , L ₂
		D ₃	L ₄ L ₁ , L ₂ ,		
	S ₄	D ₃	L ₁ , L ₂ , L ₄	D ₃	L ₂ , L ₄

As a result of this classification the total value of risk R may be subdivided: with reference to the type of lightning flash:

$$R = R_D + R_I, \quad (27.3)$$

where: R_D – risk due to direct flashes striking the structure, R_I – risk due to indirect (nearby) flashes,

– with reference to the type of damage:

$$R = R_S + R_F + R_O, \quad (27.4)$$

where: $R_S = R_A + R_U$ – risk due to shock to human beings, $R_F = R_B + R_V$ – risk due to physical damage, $R_O = R_M + R_C + R_W + R_Z$ – risk due to failure of electrical and electronic system caused by overvoltages.

The layout of lightning risk components is shown in Fig. 27.1.

The value of each risk component can be calculated according to formula (27.2) taking into account the following parameters:

$$N = N_g A C_d \quad (27.5)$$

$$P = \sum_1^n \left(P_x \prod_1^m k_j \right) \quad (27.6)$$

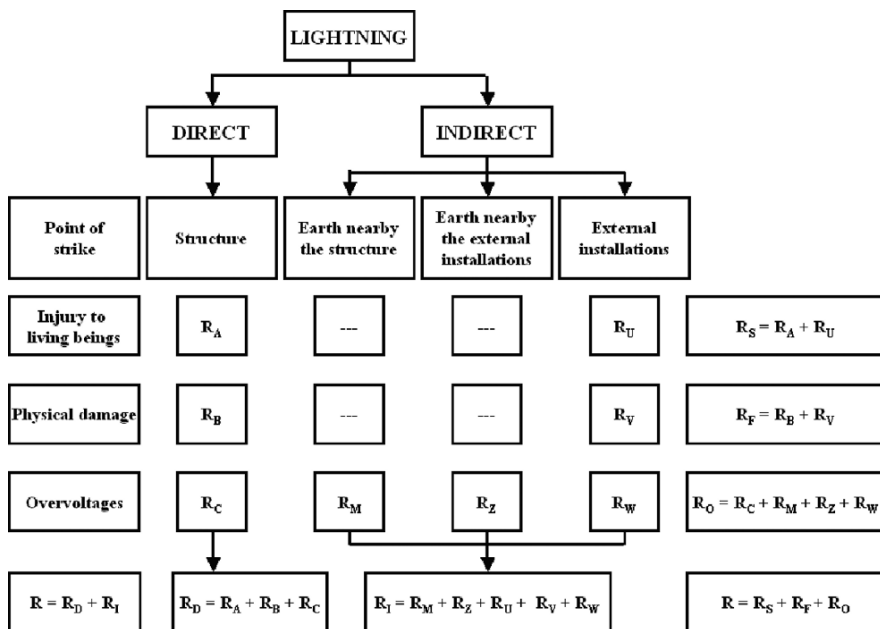


Fig. 27.1 Lightning risk components according to IEC (EN) 62305-2

where: N_g – lightning ground flash density, in the number of lightning flashes per km^2 and per year; A – the collection area of cloud-to-ground flashes of the structure and incoming lines (km^2) influencing the equipment; C_d – environmental factor related to location of the structure (see Table 27.3); P_x – partial probability related to the unprotected structure; k_j – reduction coefficient taking into account the effectiveness of applied protection measures.

For evaluation of the need for lightning protection it is necessary to:

- identify components R_x which make up the risk and calculate their values,
- calculate the total risk value R ,
- identify maximal tolerable risk value R_a ,
- compare the total risk value with tolerable value. for each type of damage:

If $R \leq R_a$ – lightning protection is not necessary, if $R > R_a$ protection measures are adopted in order to reduce to $R < R_a$. Representative values of tolerable risk R_a given in (IEC 62305-2:2006), where lightning flashes involve loss of human life or loss of social or cultural values, are reported in Table 27.2.

To make easier calculations of required lightning risk analysis the IEC Risk Assessment Calculator (RAC) has been developed by members of WG 9 within TC 81 IEC (IEC 62305-3:2006). It fits on a single screen computer (see Fig. 27.2) and enables the user to conduct risk calculations for typical structures without requiring

Table 27.2 Typical values of tolerable risk

Type of losses	Tolerable risk R_a
Loss of human life	10^{-5}
Loss of service to the public	10^{-3}
Loss of cultural heritage	10^{-3}

The screenshot displays the IEC Risk Assessment Calculator interface. It includes sections for Structure's Dimensions, Conductive Electric Service Lines, Types of Loss, Structure's Attributes, Other Underground Services, Protection Measures, and Calculated Risks. A note at the bottom right provides information about the IEC lightning risk assessment calculator.

	Tolerable Risk [R _a]	Direct Strike Risk [R _d]	Indirect Strike Risk [R _i]	Calculated Risk [R]
Loss of Human Life:	1.00E-05	=> 7.78E-05	+ 1.38E+04	= 2.18E+04
Loss of Public Services:	1.00E-03	=> 0.00E+00	+ 0.00E+00	= 0.00E+00
Loss of Cultural Heritage:	1.00E-03	=> 0.00E+00	+ 0.00E+00	= 0.00E+00
Economic Loss:	1.00E-03	=> 2.33E-04	+ 7.27E-04	= 9.60E-04

Fig. 27.2 Layout of lightning risk assessment calculator screen

deep knowledge of details and methodology covered by the IEC (IEC 62305-2:2006, Surtees et al. 2005).

The RAC was intended as a simplified tool and does not implement full functionality of the written standard and provides the risk components for relatively uncomplicated structures. Some parameters found in written standard are in the RAC software defaulted to fixed values, and the user is only permitted to make selections from a limited subset of choices. Parallel to the development of the IEC 62305 standard, the adequate software has been developed in different countries. One of available proposals is Alternative Lightning Risk Calculation Software (ALRISK), which is intended to be available both online via Internet and/or as an individual copy for a single PC (Loboda, 2006).

27.3 Basic Features of Lightning Protection of Structures

Lightning as it occurs in nature has an infinite variety of current and electromagnetic impulse wave shapes. However, it must be described in the form that can be

Table 27.3 Maximum lightning current parameters corresponding to lightning protection levels

Current parameters	Symbol	Unit	Lightning Protection Level		
			I	II	III
First short duration stroke					
Peak current	I	kA	200	150	100
Short stroke charge	Q_{short}	C	100	75	50
Specific energy	W/R	MJ/ Ω	10	5,6	2,5
Time parameters	T_1/T_2	$\mu\text{s}/\mu\text{s}$			10 / 350
Subsequent short duration stroke					
Peak current	I	kA	50	37,5	25
Average steepness	di/dt	kA/ μs	200	150	100
Time parameters	T_1/T_2	$\mu\text{s}/\mu\text{s}$			0,25 / 100
Long duration stroke					
Long stroke charge	Q_{long}	C	200	150	100
Time parameters	T_{long}	s			0,5
Flash					
Flash charge	Q_{flash}	C	300	225	150

used to select and specify protection systems. According to the actual new series of International (IEC) and European standards (EN) (IEC 62305-1:2006, IEC 62305-2:2006, IEC 62305-3:2006, IEC 62305-4:2006) related to lightning protection of structures, the maximum lightning current parameters (see Table 27.3) have been defined according to lightning protection levels (LPL).

The protection level LPL is used to define lightning as the source of damage. For each protection level a set of maximum (sizing criteria) and minimum (interception criteria) lightning current parameters values are fixed. The maximum values of lightning current parameters influence the sizing selection of protection measures. The minimum values of lightning current parameters have an influence on the positioning of the air termination system of an LPS in order to intercept the lightning flashes direct to the structure.

Four protection levels I, II, III, IV are defined in IEC (EN) standard (IEC 62305-1:2006). Maximum values of lightning current parameters are reported in Table 27.3. For protection level I the fixed maximum values should not be exceeded by a probability of 99%. According to the polarity ratio (10% positive and 90% negative flashes), values taken from positive flashes must have probabilities below 10%, and those from negative flashes below 1%. The maximum values of protection level I are reduced to 75% for level II and to 50% for level III and IV (IEC 62305-1:2006).

27.3.1 Lightning Protection System

The Lightning Protection System (LPS) will protect buildings and structures from fire or mechanical destruction, and persons in the buildings from injury and even

death (IEC 62305-3:2006). LPS comprises an external and internal protection. External LPS is intended to:

- intercept a direct lightning strike to the structure (with an air termination system);
- Safely conduct the lightning current towards earth (using a down-conductor system);
- disperse the lightning current into the earth (using an earth termination system).

The function of the internal LPS is:

- to prevent dangerous sparking within the structure.

This is achieved using either equipotential bonding or a separation distance (and hence electrical insulation) between the external LPS components and other electrically conducting elements internal to the structure using direct metallic bonding connections or installing Surge Protective Devices (SPD's).

Examples of external and internal LPS are shown in Fig. 27.3.

27.3.1.1 Air Termination System

The function of the air termination system of the LPS is to prevent direct lightning strikes from damaging the volume to be protected. By correct dimensioning of the air-termination system, the effects of a lightning strike to the structure can be reduced in a controlled way. Air-termination components installed on a structure will be located in corners, exposed points and edges (especially on the upper level of any facades). To determine the arrangement and placement of air-termination, the following methods can be used (IEC 62305-3:2006):

- rolling sphere method,
- protection angle method,
- mesh method,

The rolling sphere method is suitable in all cases. It is based on the electrogeometric model, which defines the point of strike of the lightning flash developed from cloud to earth by a stepped leader. When the leader has got within a few hundred meters from earth (it can only approach the earth from a certain distance), this is called the final striking distance d , whose length is proportional to the peak value of the lightning current I and corresponds to the radius of the rolling sphere (see Fig. 27.4).

The protection angle method is derived from the electrogeometric model too (the angle is determined by the radius of the rolling sphere). This method is suitable for simple-shaped buildings, but it is subject to the limits of the air-termination height.

The mesh method is suitable where planes surfaces are to be protected. The meshed air termination system can be used universally regardless of the height of a structure and shape of its roof.

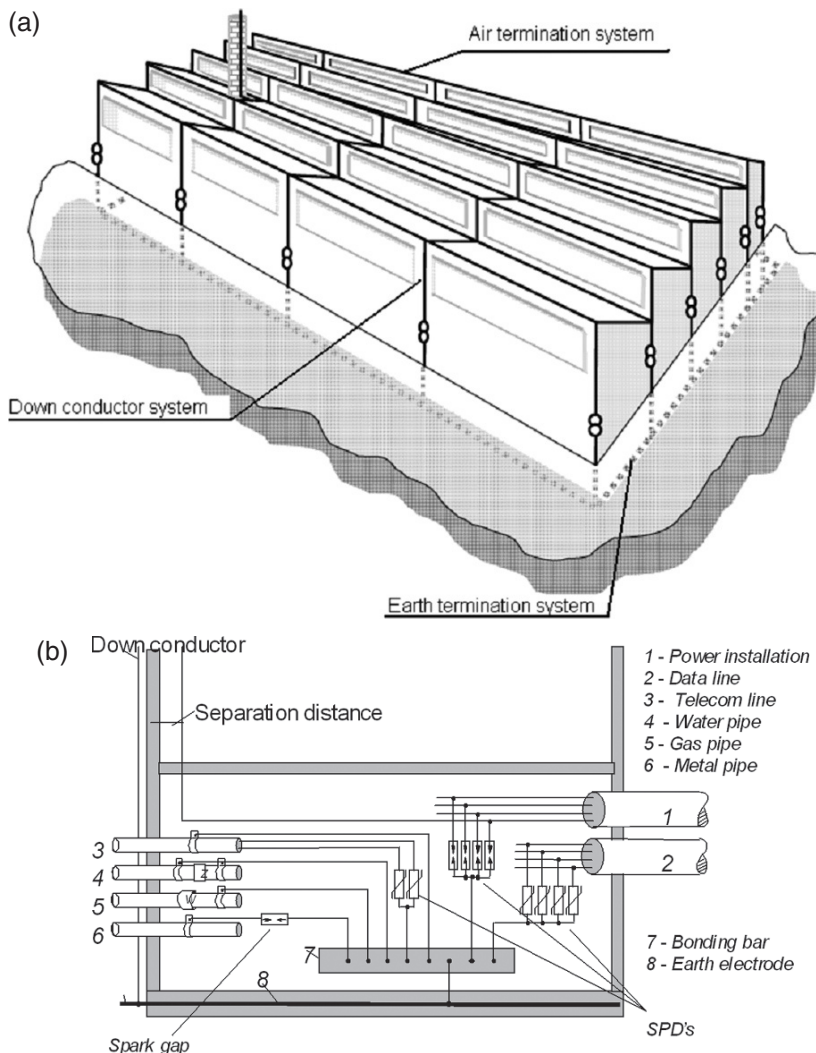


Fig. 27.3 Lightning protection system (LPS): (a) external, (b) internal

The values for the protection angle, rolling sphere radius and mesh size for each class of LPS are given in Table 27.4 (IEC 62305-3:2006).

27.3.1.2 Down Conductor System

The down conductor system is an electrically conductive connection between the air termination system and earth termination system, whose function is to conduct an intercepted lightning current to earth without damage to the structure. In order

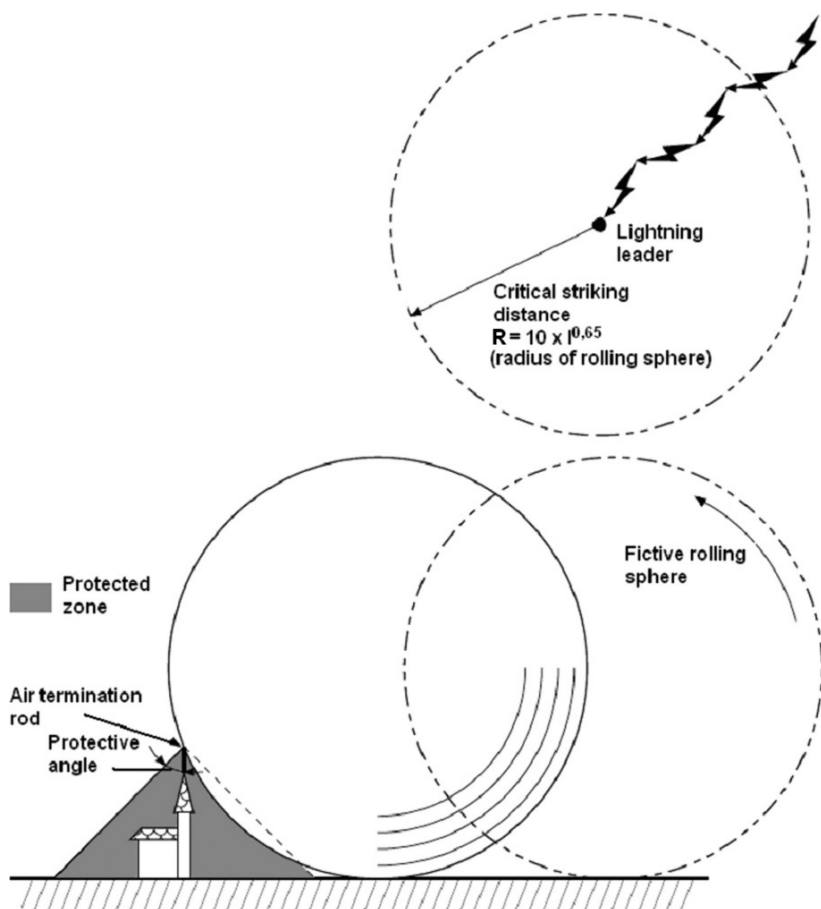


Fig. 27.4 Defining the point of strike based on the electrogeometric model

Table 27.4 The rolling sphere radius, mesh size and protection angle of air termination system corresponding to LPL

Protection method			
Class of LPS(LPL)	Rolling sphere radius R (m)	Mesh size M (m)	Protection angle (α°)
I	20	5×5	
II	30	10×10	
III	45	15×15	
IV	60	20×20	

The graph plots Protection angle (α°) against height (h m). Four curves are shown for LPL I, II, III, and IV. As height increases, the protection angle decreases. Higher LPL levels correspond to larger protection angles at a given height.

LPL	Height h (m)	Protection angle α ($^\circ$)
I	0	70
I	10	60
I	20	50
I	30	40
II	0	65
II	10	55
II	20	45
II	30	35
III	0	60
III	10	50
III	20	40
III	30	30
IV	0	55
IV	10	45
IV	20	35
IV	30	25

Method for design of the termination system is shown in Fig. 27.5.

LPL - lightning protection level, h - height of structure

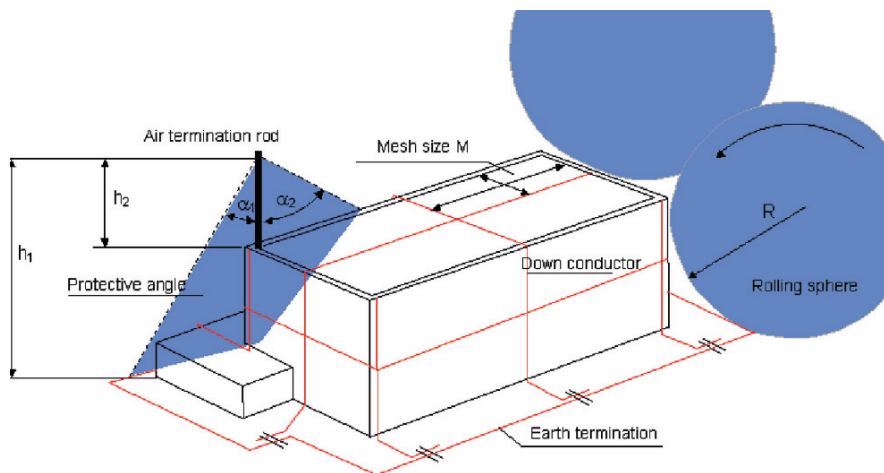


Fig. 27.5 Method for designing of air termination for buildings (IEC 62305-3:2006)

to reduce the probability of damage due to lightning current flowing in the LPS, the down-conductors should be arranged in such a way that from the point of strike to earth:

- several parallel current paths exist;
- the length of the current paths is kept to a minimum (straight, vertical, no loops);
- the equipotential bonding to conducting parts of the structure is performed whenever required.

For high structures lateral connection of down-conductors at ground level and every 10 m to 20 m of height is considered to be good practice. The installation of as many down-conductors as possible, at equal spacing around the perimeter and interconnected by ring conductors, reduces the probability of dangerous sparking and facilitates the protection of internal installations (i.e. this condition is fulfilled in metal framework structures and in reinforced concrete structures in which the interconnected steel is continuously electric).

The example geometry of the down-conductors and of the ring conductors affects the separation distance and required distances between down conductors, according to (IEC 62305-3:2006), are shown in Fig. 27.6.

27.3.1.3 Earth Termination System

Earth termination system is the continuation of air-termination and down-conductor systems to discharge the lightning current into the earth. It also will create equipotential bonding between down conductors and a potential control in the vicinity of walls of the structure.

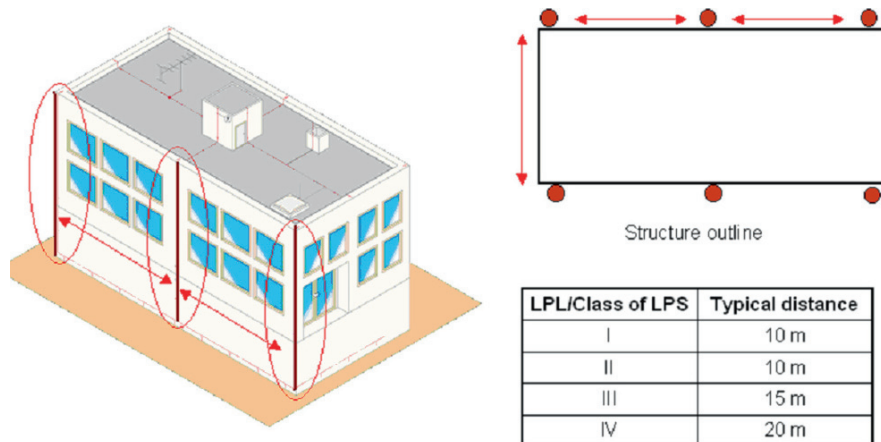


Fig. 27.6 Down conductor system (IEC 62305-3:2006)

When dealing with the dispersion of the lightning current into the ground, whilst minimizing any potentially dangerous overvoltages, the shape and dimensions of the earth termination system are the important criteria. In general, a low earthing resistance (lower than 10Ω when measured at a low frequency) is recommended. From the viewpoint of lightning protection, a single integrated structure earth-termination system is preferable and is suitable for all purposes (i.e. lightning protection, power system and telecommunication system).

In the IEC standard (IEC 62305-3:2006) there are classified earth electrode arrangements into Type A and Type B. For both types of electrode arrangement, the minimum electrode length l_1 is the function of the LPL (class of lightning protection) and resistivity of soil (Fig. 27.7).

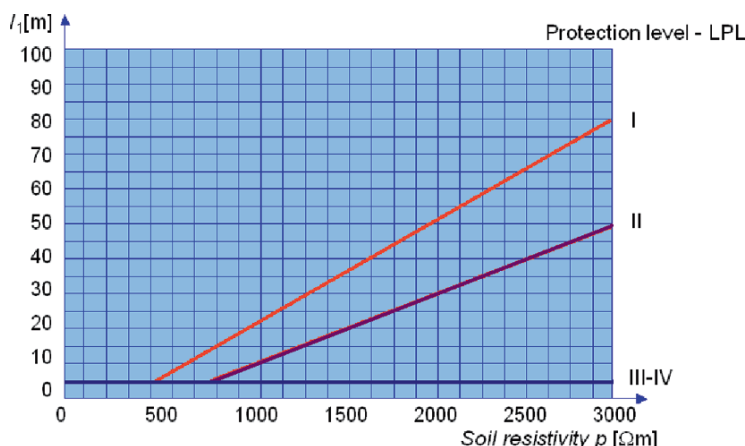


Fig. 27.7 Minimum lengths of earth electrodes (IEC 62305-3:2006)

The type A arrangement comprises horizontal or vertical earth electrodes connected to each down-conductor. The total number of earth electrodes should not be less than two. The minimum length of each earth electrode at the base of the down conductor is l_1 for horizontal electrodes; or $0,5 l_1$ for vertical (or inclined) electrodes. For combinations of vertical and/or horizontal earth electrodes, the total equivalent length will be considered. The minimum length for the electrode may be disregarded if an earth electrode earthing resistance at low frequency is less than 10Ω .

The type A electrode does not fulfil the equipotentialisation bonding requirements between down conductors and the potential control, so that will be interconnected to split the partial lightning current equally. This interconnection can be made underground or on the surface.

The type B arrangement of earth electrodes comprises a ring conductor external to the structure, in contact with the soil for at least 80% of its total length, or a foundation earth. This kind of earth electrode may also be meshed. For the ring earth electrode (or foundation earth electrode), the mean radius r of the area enclosed by the ring earth electrode (or foundation earth electrode) should not be less than the value l_1 in Fig. 27.7. When the required value of l_1 is larger than the convenient value of r , additional horizontal or vertical (or inclined) electrodes should be added whose individual lengths l_r (horizontal) and l_v (vertical) are given by:

$$l_r = l_1 - r \quad (27.7)$$

and

$$l_v = (l_1 - r)/2 \quad (27.8)$$

The number of additional electrodes should not be less than the number of down-conductors, with a minimum of two. The supplementary electrodes should be connected to the ring earth electrode at points where the down-conductors are connected and, as much as possible, equidistantly. If they are connected to the foundation earth electrode (Fig. 27.8) care should be taken with materials of the electrode and the connection to the foundation earth electrode.

27.4 Internal Lightning Protection

The internal LPS is required for all installed electrical power consumer's installation to avoid the occurrence of dangerous voltages within the structure, i.e. hazardous touch voltages between the protective conductor of the low voltage installation and metal, water, gas and heating pipe (see Fig. 27.3b).

Equipotentialisation can be achieved by interconnecting the LPS with:

- structural metal parts;
- metal installations;



Fig. 27.8 Foundation earth electrode in construction

- external conductive parts;
- electrical and electronic installation within the structure to be protected.

Lightning equipotential bonding between LPS and such systems is only recommended if the required separation distance cannot be reached. Interconnecting means:

- bonding conductors, where the electrical continuity is not provided by natural bonding;
- installing surge protective devices (SPD), where direct connections with bonding conductors is not feasible.

The manner in which lightning equipotential bonding is achieved is important and will be discussed with the electric power operator, the telecommunication network operator and other operators or authorities concerned, as there may be conflicting requirements.

27.5 Protection Against Lightning Electromagnetic Impulse (LEMP)

Protection against Lightning Electromagnetic Impulse (LEMP) is based on the principle of Lightning Protection Zones (LPZ) (IEC 62305-4:2006). According to this principle the structure containing systems to be protected will be divided into LPZ

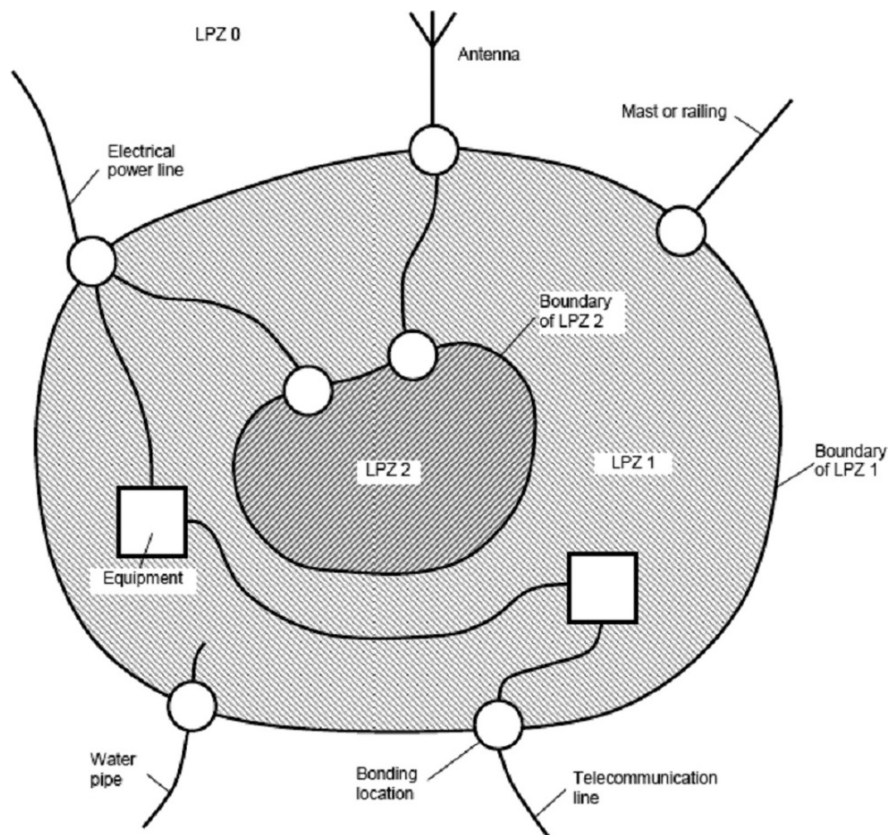


Fig. 27.9 Principle for the division into different LPZs: (a) general, (b) example for a structure with an application of SPD for power supply

according to the treatment generated by LEMP. Suitable LPZs can be defined by assigned volumes of space where the LEMP severity is compatible with the withstand level of the internal systems enclosed. Successive zones are characterized by significant changes in the severity of the LEMP. The boundary of an LPZ is defined by the protection measures employed (see Fig. 27.9a).

27.5.1 Concept of Lightning Protection Zones (LPZ)

With respect to lightning treatment, the following LPZs are defined (IEC 62305-4:2006):

27.5.1.1 Outer Zones

LPZ 0 – Zone where the risk is due to the whole (un-attenuated) lightning electromagnetic field and where the internal systems may be subjected to a full or partial lightning surge current. LPZ 0 is subdivided into:

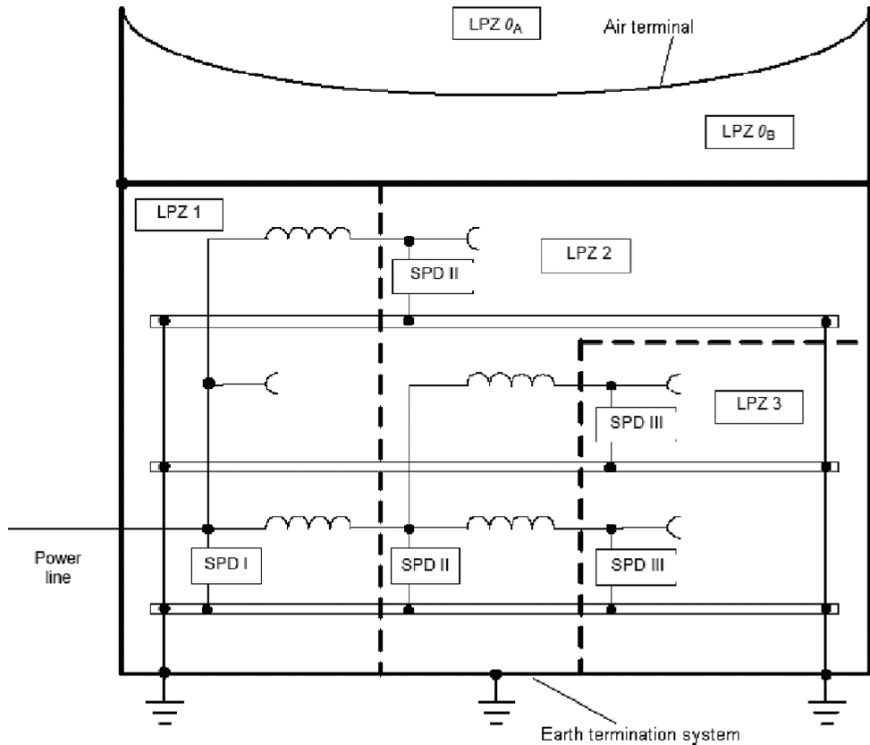


Fig. 27.9 (continued)

- LPZ 0_A – Zone where the risk is due to the direct lightning flash and full lightning electromagnetic field. The internal systems may be subjected to a full lightning surge current;
- LPZ 0_B – Zone protected against direct lightning flashes, but where the risk is the full lightning electromagnetic field. The internal systems may be subjected to partial lightning surge currents.

Inner zones: (protected against direct lightning flashes)

- LPZ 1 – Zone where the surge current is limited by current sharing and by SPDs at the boundary. Spatial shielding may attenuate the lightning electromagnetic field.
- LPZ 2 ... n – Zone where the surge current may be further limited by current sharing and by additional SPDs at the boundary. Additional spatial shielding may be used to further attenuate the lightning electromagnetic field.

For new buildings and effective structures, protection of electronic systems can be achieved, with a minimum of costs, if they are designed together with the building

and before its construction. In this case components of the structure such as metal reinforcement, girders or buttresses can be integrated into the LEMP.

For existing structures the cost of LEMP installation is usually higher as it should be appropriately chosen LPZs and upgraded existing installations

The LPZs are implemented by the installation of lightning protection measures, which include installation of a coordinated SPDs system and/or magnetic shielding. Depending on the number, type and withstand level of the equipment to be protected, a suitable LPZ can be defined. These may include small local zones (e.g. equipment enclosures) or large integral zones (e.g. the volume of the whole structure) (see Fig. 27.9b).

27.5.2 Basic Protection Measures

Basic protection measures against LEMP include (IEC 62305-4:2006):

27.5.2.1 Earthing and Bonding

The earthing system conducts and disperses the lightning current into the earth while the bonding network minimizes potential differences and may reduce the magnetic field to prevent hazardous potential drops between all devices in the inner LPZs. Earthing and bonding should always be ensured, in particular, bonding of every conductive service directly or via an equipotential bonding SPD, at the point of entry to the structure.

The low inductance equipotential bonding network may be achieved by means of interconnections between all metal components aided by bonding conductors inside the LPZ of a building or structure (Fig. 27.10).

27.5.2.2 Magnetic Shielding and Line Routing

Spatial shielding attenuates the magnetic field inside the LPZ, arising from lightning strikes direct to or near the structure, and reduces internal surges. Shielding of internal lines, using shielded cables or cable ducts, minimizes internal induced surges. Spatial shielding, shielding and routing of internal lines can be combined or used separately (Fig. 27.11).

Shielding of external lines entering the structure reduces surges from being conducted onto the internal systems.

Routing of internal lines will minimize induction loops and reduce internally induced surges.

27.5.2.3 Installation of Coordinated SPD System

Protection of internal systems against surges requires coordinated SPD installation, which limits the effects of external and internal surges. Energy coordination is needed to avoid overstress to the SPDs within a system. The individual stresses of

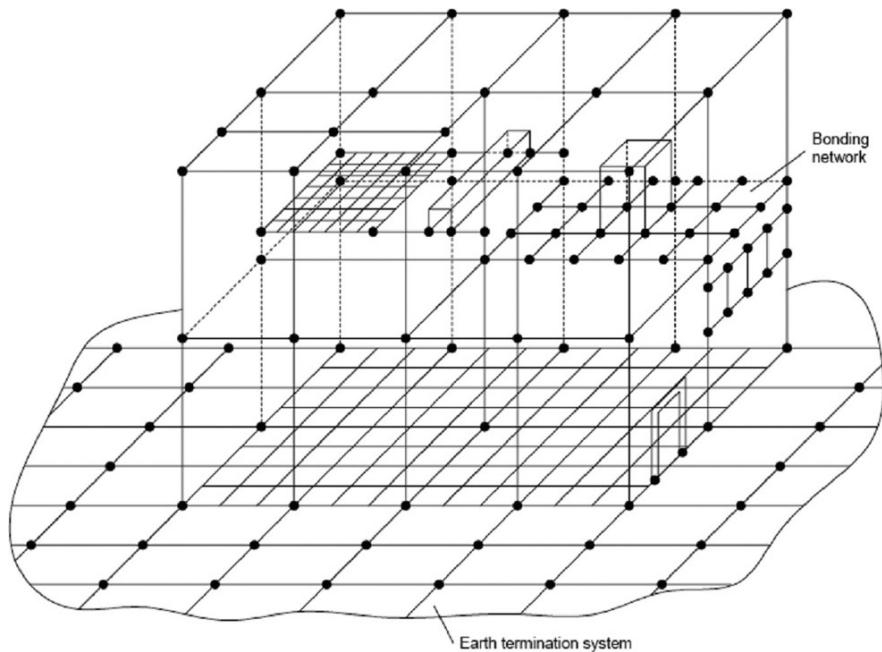


Fig. 27.10 Example of a three-dimensional earthing system consisting of the bonding network interconnected with the earth termination system (IEC 62305-4:2006)

SPDs, depending on their location and characteristics, must therefore be determined. As soon as two or more SPDs are installed in the cascade, a study of the coordination of the SPDs and the equipment being protected is needed.

Energy coordination is achieved if the portion of energy which each SPD is subjected to is lower than, or equal, to its withstand energy. The withstand energy should be obtained from:

- electrical testing according to IEC 61643-1 (IEC 61643-1:2005);
- technical information provided by the SPD manufacturer (Lightning Protection Guide 2007).

The basic model of the energy coordination for SPDs is shown in Fig. 27.12. This model is only valid when the impedance of the bonding network and the mutual inductance between the bonding network and the installation formed by the connection of SPD 1 and SPD 2, is negligible.

27.6 Conclusion

With the development of electrical and electronic systems, whose susceptibility to lightning and other transients has increased significantly, a number of current

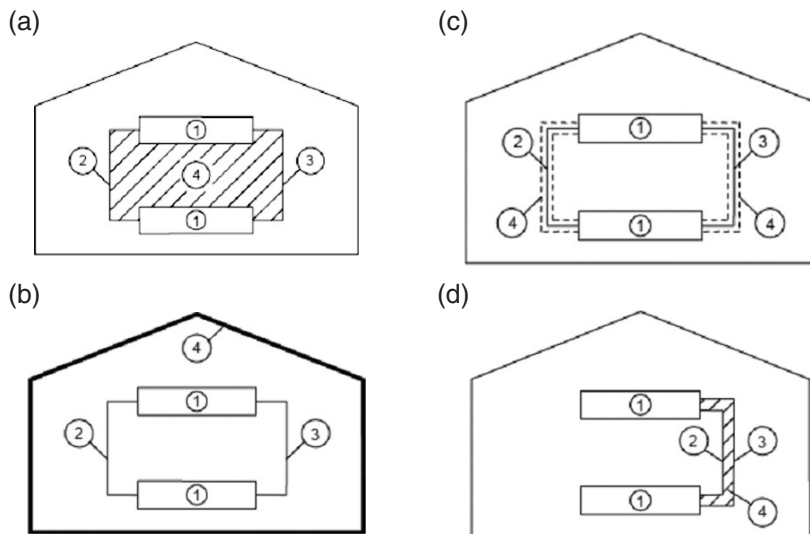


Fig. 27.11 Reducing induction effects by line routing and shielding measures according to IEC 62305-3:2006: (a) unprotected system, (b) reducing magnetic field inside an inner LPZ by its spatial shield, (c) reducing the influence of the field on lines by line shielding, (d) reducing the induction loop area by line routing; 1-equipment, 2-line a (for example electric), 3-line b (for example electronic), 4-induction loop

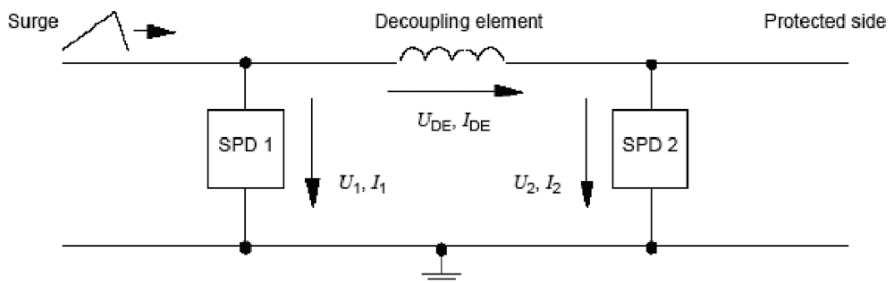


Fig. 27.12 Basic model for energy coordination of SPD

research efforts have been undertaken to face this problem. Following worldwide scientific and technical work, a new series of IEC standards on lightning protection of structures has been developed.

They are based on scientifically proven theories and experimentation taking into account the matter and lay down requirements for design and installation of external and internal Lightning Protection Systems for structures and buildings, protection against services entering the buildings and the protection of electrical and electronic systems.

Based on the lightning risk analysis, a better understanding of the criteria needed for design, installation and maintenance of lightning protection measures has been

achieved. A better understanding of the design and the use of air termination systems, and earthing and bonding systems as well, has meant significant progress has been made in the description of protection measures to reduce the failure of electrical and electronic systems inside buildings and structures.

References

- Flisowski Z. Mazzetti C.: "A new approach to the complex assessment of the lightning impending over buildings", *Bulletin of Polish Academy of Sciences*, no.9/10, 1984.
- IEC 61643-1:2005. Low-voltage surge protective devices – Part 1: Surge protective devices connected to low-voltage power distribution systems – Requirements and tests.
- IEC 62305-1:2006. Protection against lightning – Part 1: General principles
- IEC 62305-2:2006 Protection against lightning – Part 2: Risk management: Assessment of risk for structures.
- IEC 62305-3:2006 Protection against lightning – Part 3: Physical damage to structures and life hazard.
- IEC 62305-4:2006 Protection against lightning – Part 4: Electrical and electronic systems within structures.
- Surtees A.J., Gillespie A., Kern A., Rousseau A.: "The risk assessment calculator as simple tool for the application of the standard IEC 62305-2", *Proc. VIII International Symposium on Lightning Protection (VIII SIPDA)*, 21st–25th November 2005, Sa Paulo, Brazil.
- Łoboda M., Szewczyk M., Flisowski Z.: "Comparison of lightning risk calculation results using different software based on new standard IEC62305-2", *Proc. 28th International Conference on Lightning Protection (ICLP 2006)*, September 18–22, 2006, Kanazawa, Japan.
- Lightning Protection Guide. Dehn und Söhne. 2nd update edition, September 2007.

Color Plate Section

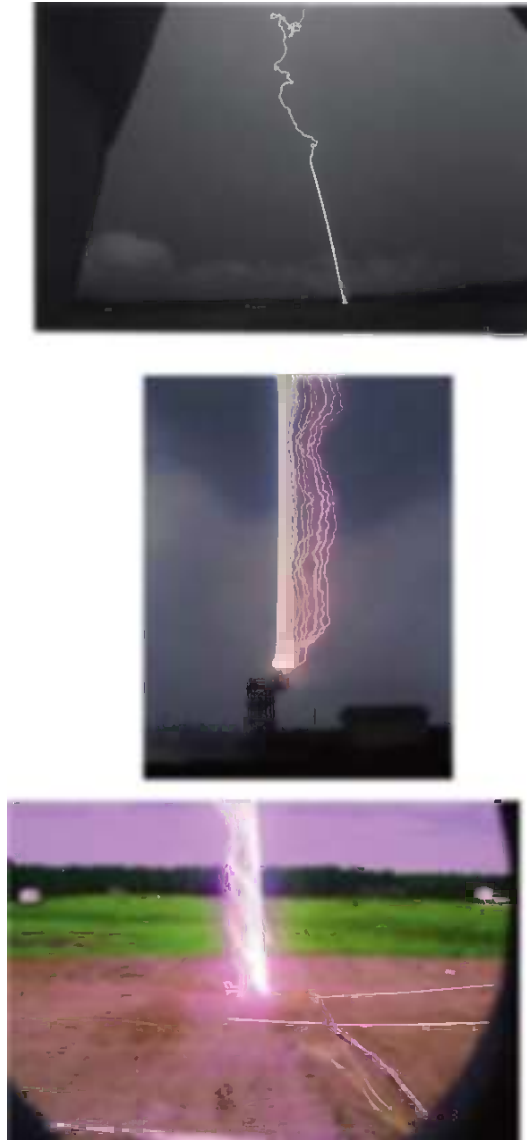


Plate 1 Photographs of lightning flashes triggered at Camp Blanding, Florida. Top – a distant view of a strike to the test runway; middle, a strike to the test power system initiated from the tower launcher; bottom – a strike initiated from the underground launcher at the center of a $70 \times 70 \text{ m}^2$ buried metallic grid (See also Figure 2.2 on page 27)



Plate 2 Photograph of ground surface arcing associated with the second stroke (current peak of 30 kA) of flash 9312 triggered at Fort McClellan, Alabama. Lightning channel is outside of field of view. One of the surface arcs approached the right edge of the photograph, a distance of 10 m from the rocket launcher. Adapted from Fisher et al. (1994) (See also Figure 2.12 on page 45)

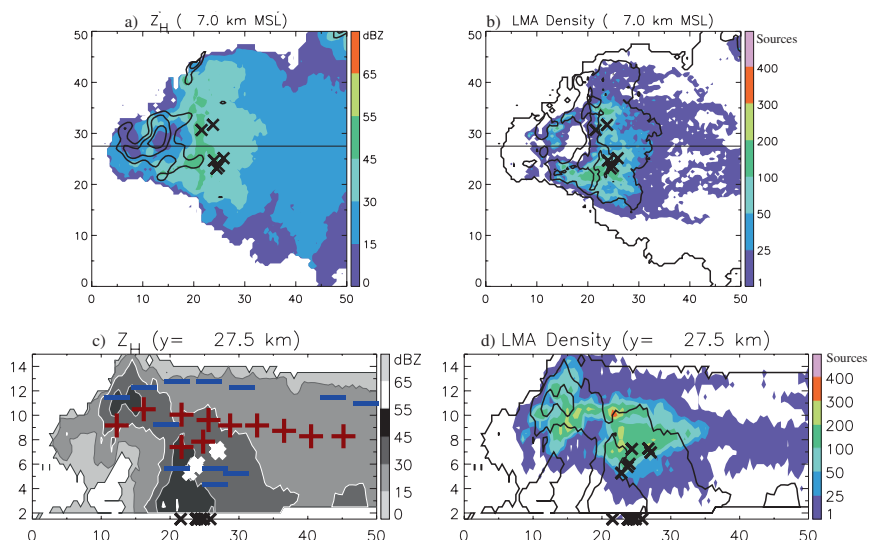


Plate 3 Representative cross sections of the 29 June 2000 supercell at 2325 UTC. Horizontal cross sections of (a) radar reflectivity (ZH) and (b) LMA source density at 7 km altitude. East-west vertical cross sections of the same quantities along the lines indicated in (a) and (b). LMA source density plots show the number of sources within 2.5 (5.0) km of each horizontal (vertical) cross section. Updraft contours every 10 m s^{-1} are overlaid as thin black lines in (a). ZH contours are overlaid for reference in (b) and (d), with intervals of 0, 30, and 45 dBZ. The \times symbols overlaid on (a) and (b) and along the bottom of (c) and (d) indicate the NLDN strike locations of positive CG flashes. The \times symbols at higher altitudes on (c; white) and (d; black) indicate the LMA-inferred origin locations of positive CG flashes. Only those CG flashes that struck within 5 km of the cross-section plane are shown on the vertical cross sections in (c) and (d). LMA-inferred charge structure is overlaid in (c) as a composite schematic with red plus (*blue minus*) symbols for positive (negative) charge. (Adapted from Wiens et al. 2005) (See also Figure 4.7 on page 102)

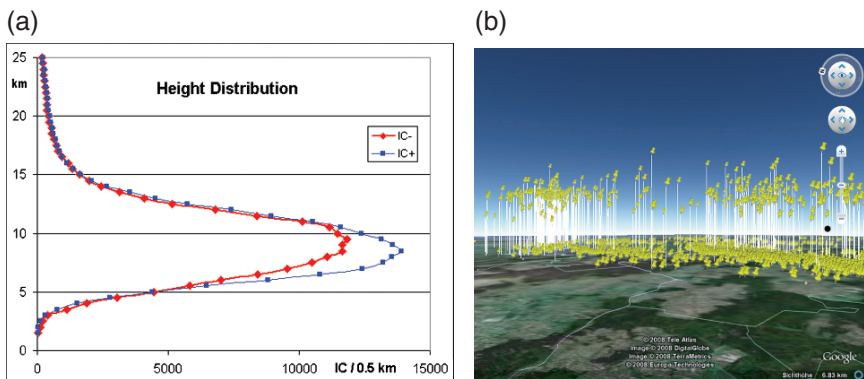


Plate 4 (a) Emission height distribution of IC-strokes (from Betz et al., 2007). (b) Three-dimensional view of a thunderstorm, enabled by the total-lightning capability of LINET: CG-strokes are placed at ground and IC-strokes are shown at their individual VLF/LF emission heights (see Fig. 5.12a); the vertical lines serve to guide the eye to their 2D-locations (See also Figure 5.12 on page 130)

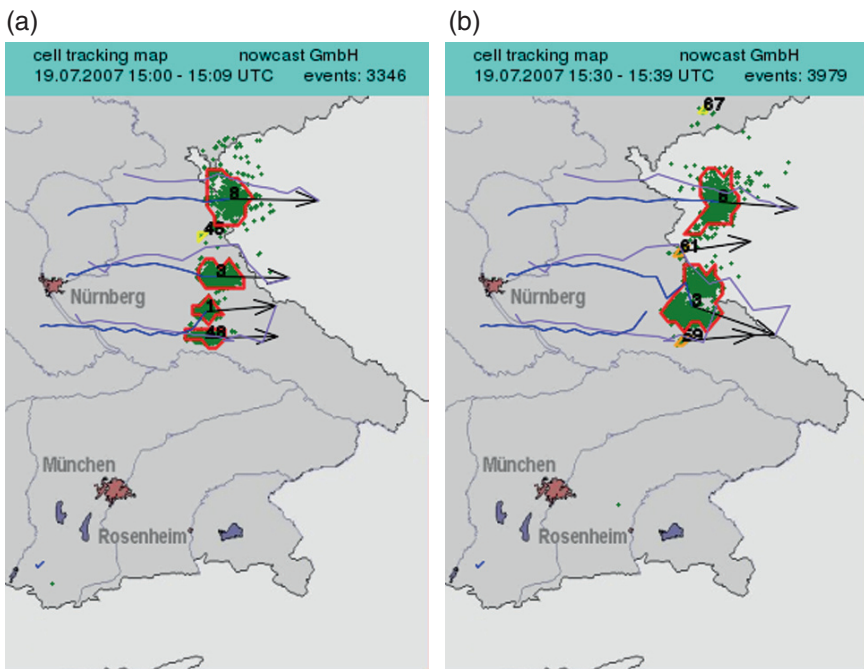


Plate 5 Cell-tracking of a storm on 19 July 2007 in Southern Germany: identified cells and propagation of the actual cell center (blue trace), and the center positions predicted one hour in advance (purple trace), for the time intervals 15:00-15:10 (*left*) and 15:30-15:40 (*right*) (See also Figure 5.17 on page 135)

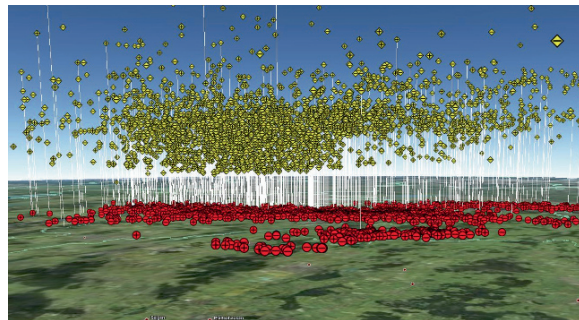


Plate 6 Storm on 07 July 2007 approaching Munich from south-west, displayed with the LINET 3D-visualization from 17-18 UTC; the number of IC's has sharply increased and surpasses the CG stroke-number by a factor of 4, indicating severe weather conditions. CG: red, near ground; IC: yellow, located in the determined emission height (the vertical lines serve to estimate the 2D positions) (See also Figure 5.19 on page 137)

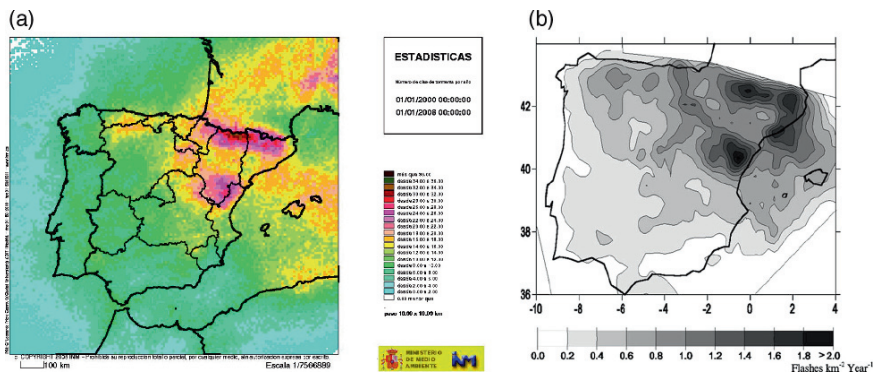


Plate 7 (a) Annual average of the number of thunderstorms days per year in the Iberian Peninsula (2000–2007), from (Pérez and Zancajo, 2008) with permission from AEMET; and (b) Annual average of the CG flash density (1992–2001), from Rivas Soriano et al. (2005) with permission from Elsevier (See also Figure 7.8 on page 169)

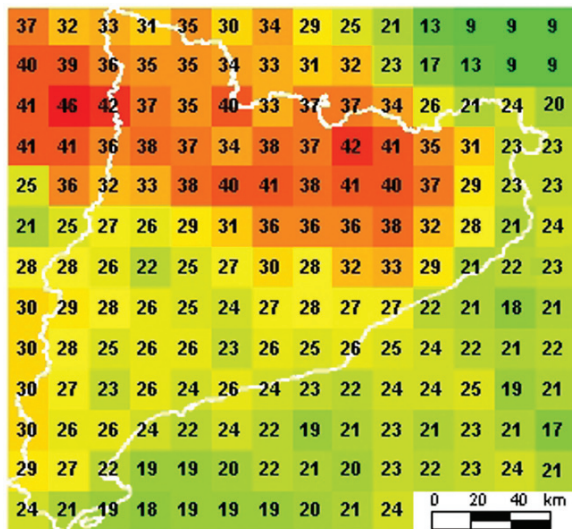


Plate 8 Annual average (2003–2007) of the number of thunderstorm days in Catalonia, calculated in a 20×20 km mesh basis (See also Figure 7.12 on page 173)

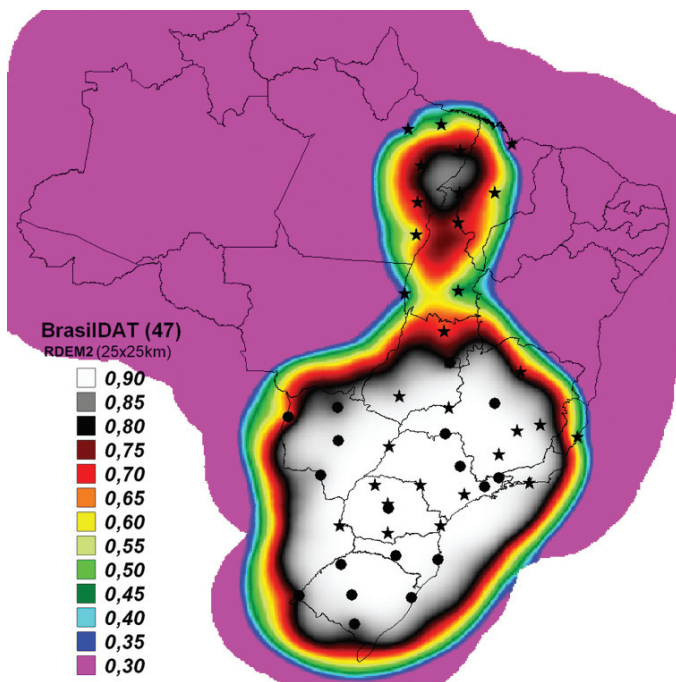


Plate 9 The BrasilDAT network detection efficiency computed by the RDEM2 model, for a spatial resolution of 25×25 km (See also Figure 9.2 on page 213)

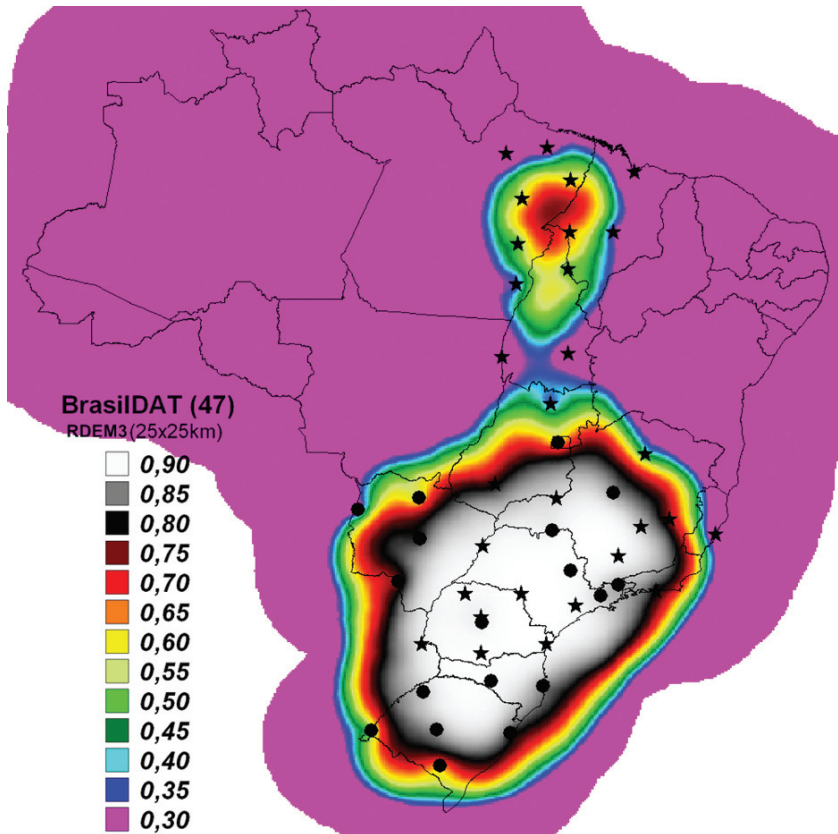


Plate 10 The BrasilDAT network detection efficiency computed by the RDEM3 model, for a spatial resolution of 25×25 km (See also Figure 9.3 on page 214)

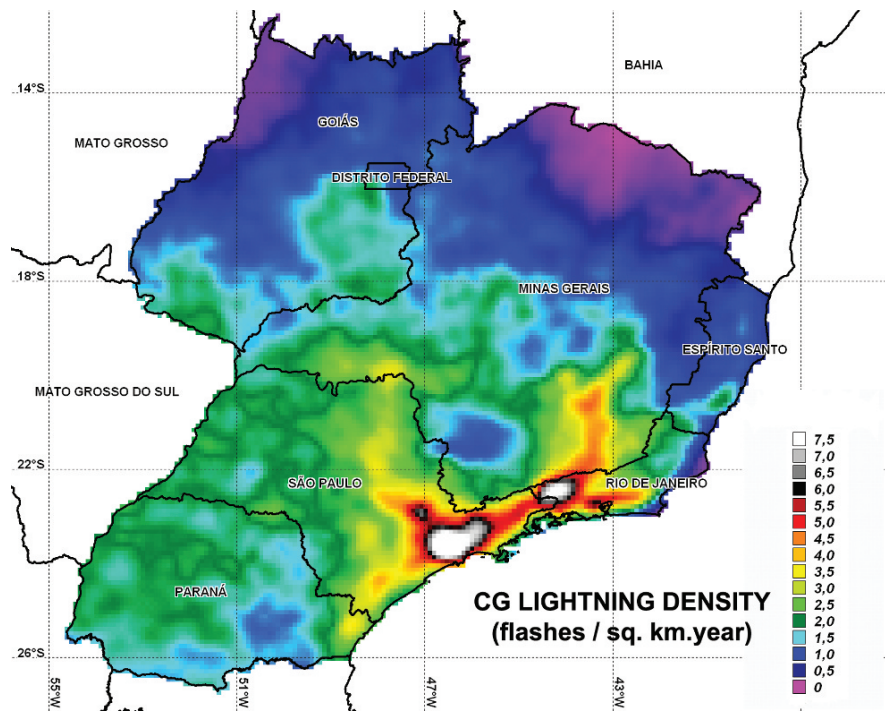


Plate 11 Annual average CG lightning flash density in the Southeast region of Brazil from 1999 to 2004 for a spatial resolution of 10×10 km. Regions in white correspond to densities larger than $7.5 \text{ flashes } \text{km}^{-2} \text{ year}^{-1}$. No correction for the DE was applied (See also Figure 9.4 on page 215)

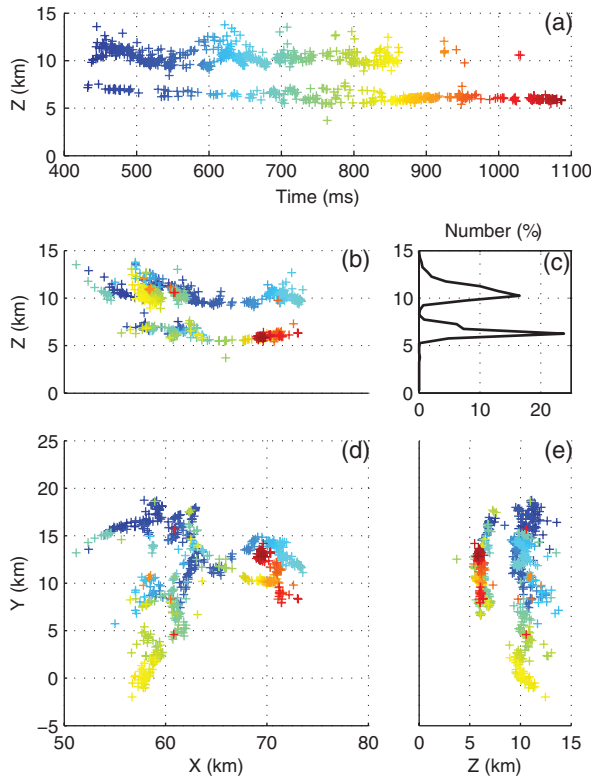


Plate 12 Case of an intracloud flash (23 August 1993, 1804:32 UT) with (a) time series of LDAR source altitude; (b) XZ projection of the LDAR sources; (c) vertical distribution of the LDAR sources per 500-m vertical increment; (d) ground projection of the LDAR sources; (e) YZ projection of the LDAR sources (See also Figure 10.3 on page 239)

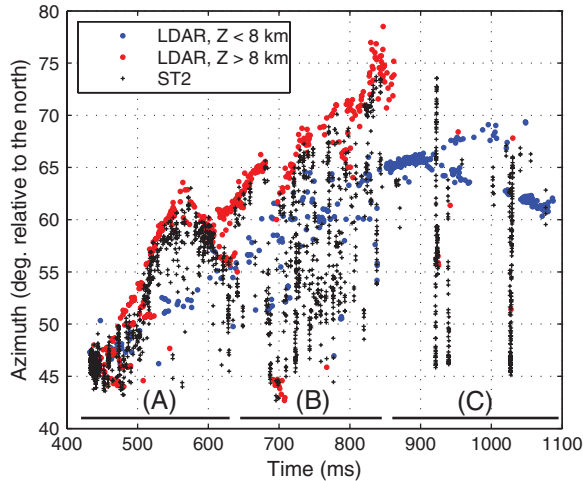


Plate 13 Time evolutions of LDAR and ST2 sources plotted in azimuth ST2 axis. Red and blue dots correspond to high-altitude and low-altitude LDAR sources respectively while interferometric ST2 measurements are plotted with pluses (See also Figure 10.5 on page 240)

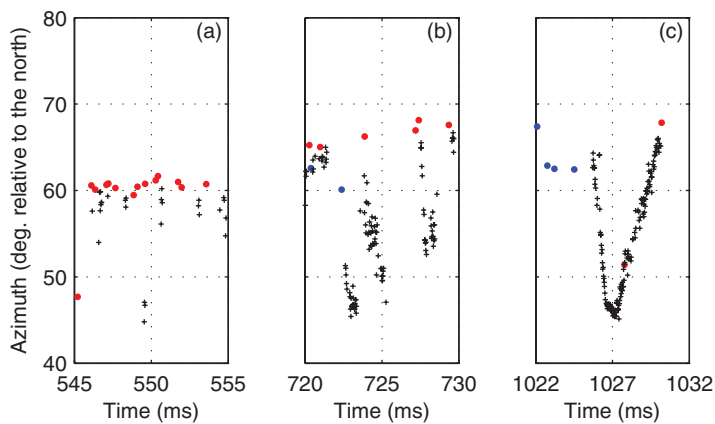


Plate 14 Same as in Fig. 10.4 but for three different 10-ms periods during the studied flash (See also Figure 10.6 on page 241)

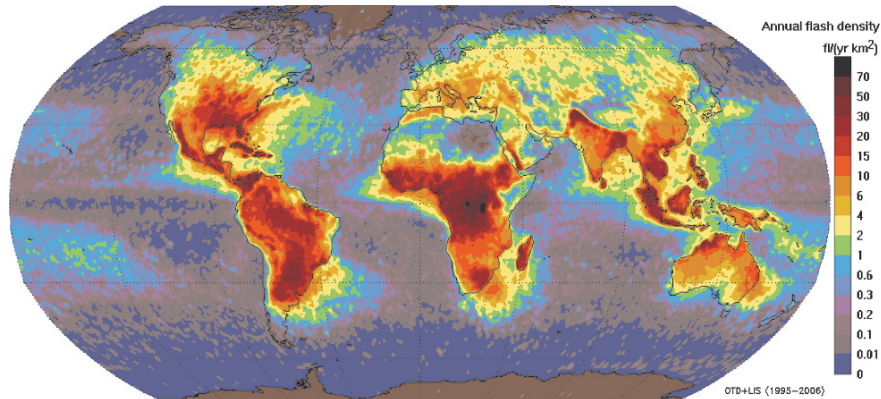


Plate 15 Global distribution of annual lightning flash density (in fl/km² yr) from 11 years of combined OTD and LIS observation (1995–2005). Note the maximum in Central Africa and the land-ocean difference. (From the NASA LIS/OTD gridded data) (See also Figure 12.5 on page 282)

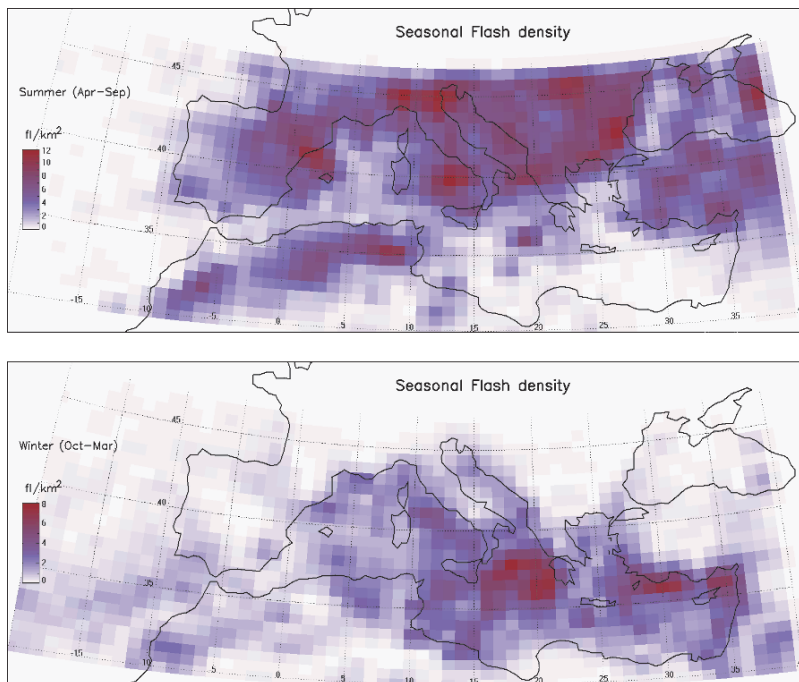


Plate 16 Seasonal lightning flash density in the Mediterranean region derived from 5 year OTD data for the summer (top) and winter months (bottom). Due to the sparse sampling the interannual variance is high, single storms dominate the picture. Note the different color scaling (See also Figure 12.7 on page 283)

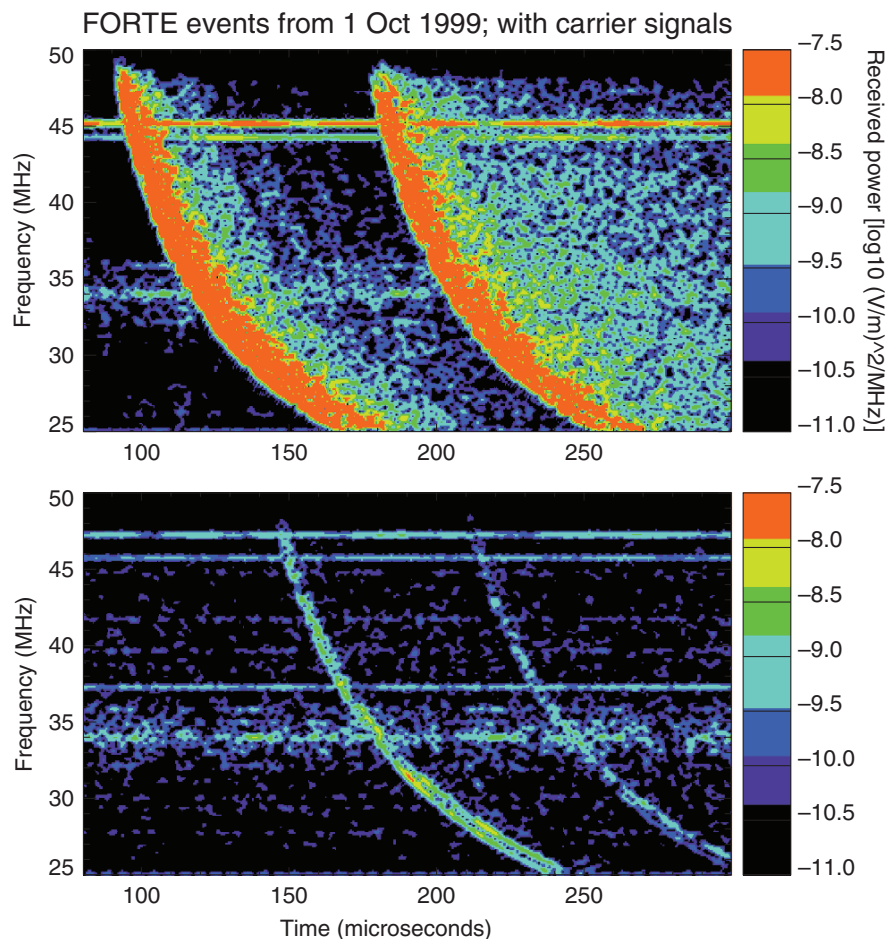


Plate 17 Spectrograms of a (top) strong intracloud pulse typically associated with a VLF NBE and (bottom) a weaker polarized/coherent intracloud pulse. Note the difference in pulse width and strength between the two events, as described in Jacobson and Light (2003). The ionospherically-induced, frequency-dependent dispersion is evident in the graphics, as well as the geomagnetic splitting (most visible in the lower panel at the lower frequencies of the primary signature). In addition to the lightning signals, one can discern interference from anthropogenic radio transmissions, apparent as narrow, horizontal bands. In each spectrogram, the ground-reflection accounts for the echo which occurs approximately 50–75 μ s after the primary pulse (See also Figure 13.2 on page 295)

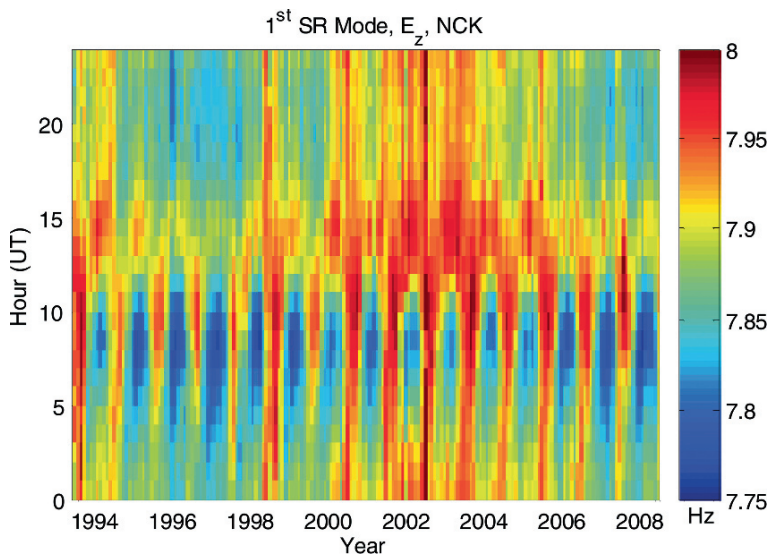


Plate 18 Diurnal-annual frequency distribution of the 1st SR mode for the E_z field component recorded at NCK, Hungary (See also Figure 16.7 on page 355)

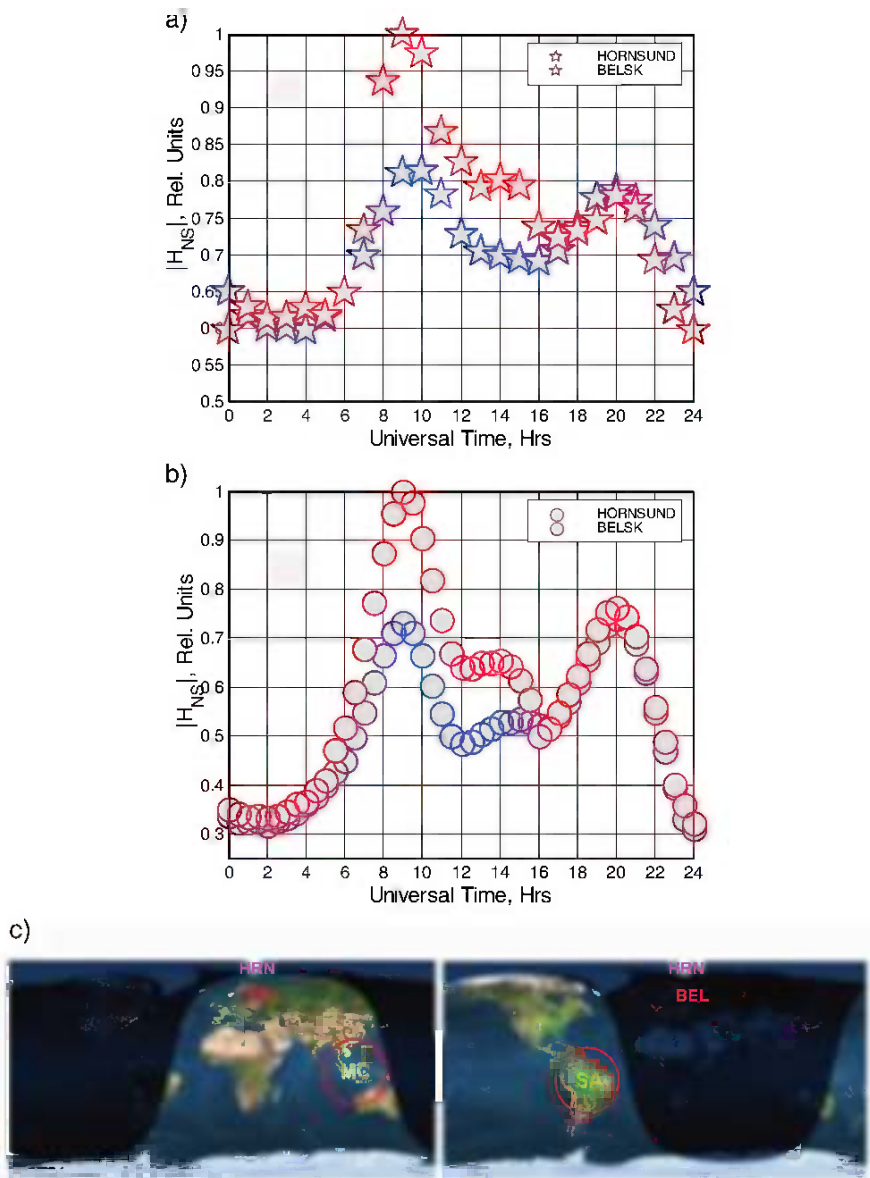


Plate 19 (a) The normalized diurnal variations of the north-south magnetic background field observed at the Belsk (Poland) and Hornsund (Spitsbergen) ELF stations in February, 2005. (b) The TDTE-simulated diurnal variations of the north-south magnetic background field for the Belsk and Hornsund ELF stations in February. (c) The positions of the Belsk and Hornsund ELF stations relative to the day/night boundary during the respective periods of the maximum activities in the Asian (left) and American (right) “chimneys” (See also Figure 16.15 on page 368)

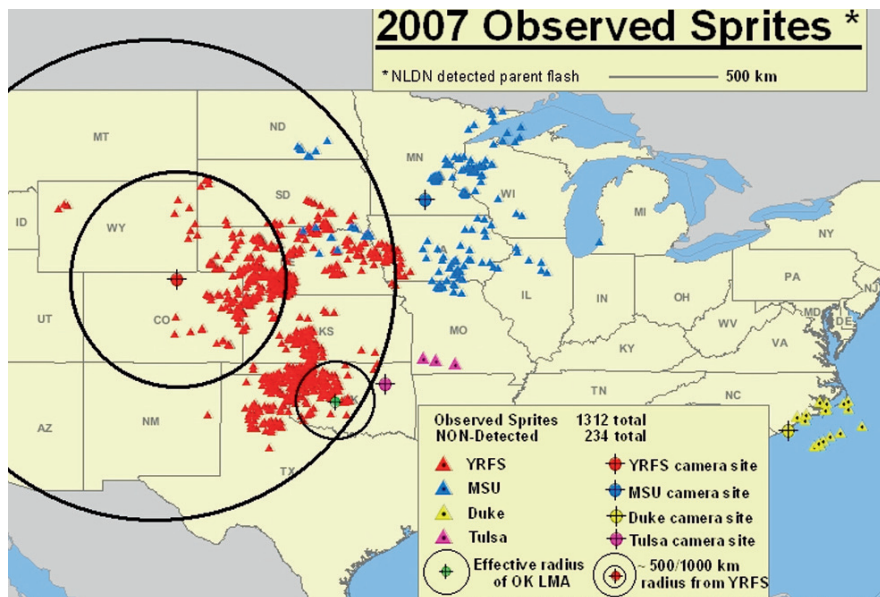


Plate 20 The optically confirmed TLEs (almost all sprites) during 2007 having NLDN-detected parent CGs (See also Figure 17.3 on page 394)

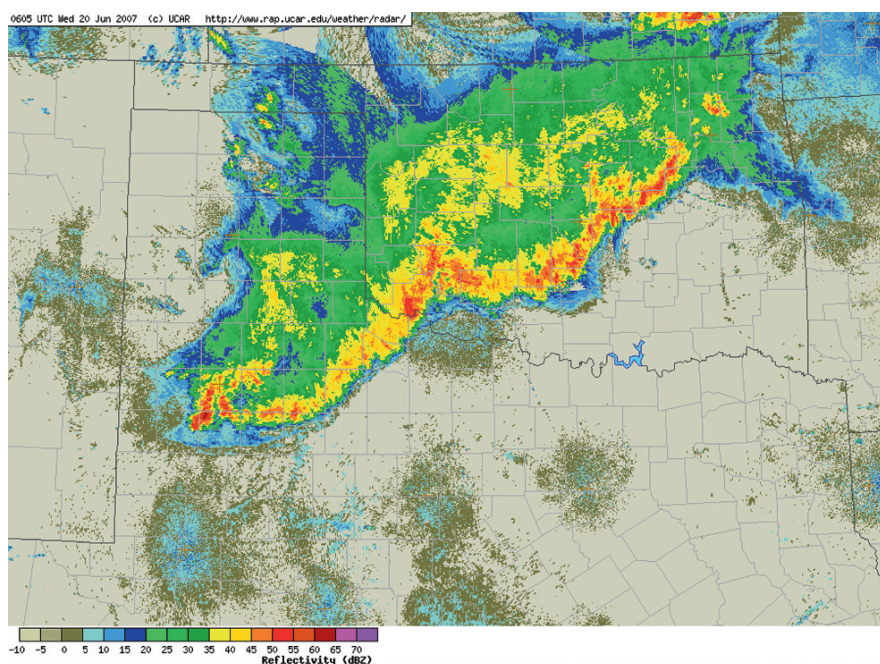


Plate 21 NEXRAD reflectivity mosaic at 0605 UTC 20 June 2007 showing the classic leading edge/trailing stratiform structure of the MCC (See also Figure 17.5 on page 396)

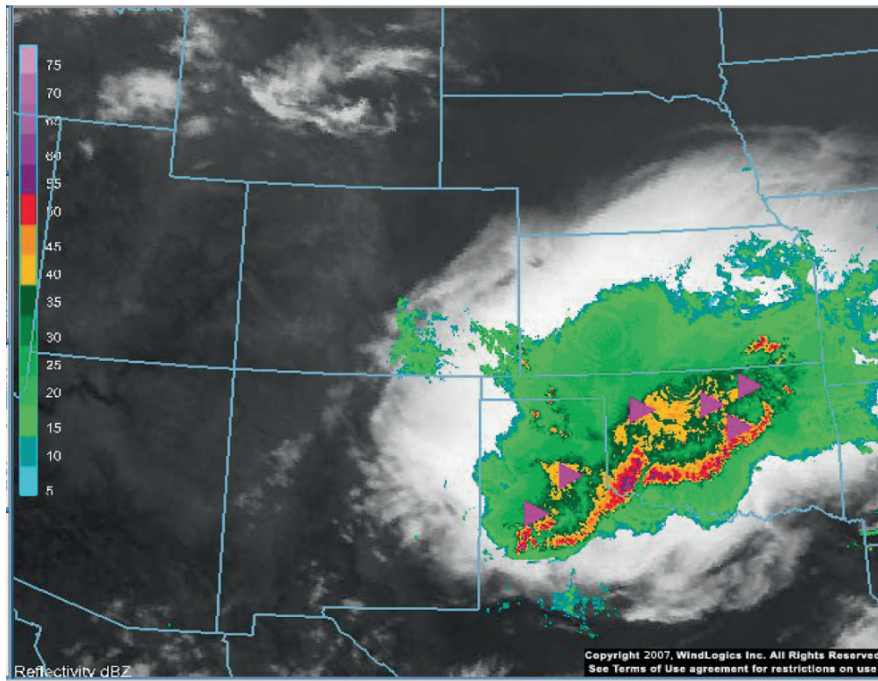


Plate 22 Display at 0600 UTC 20 June 2007 showing large peak current +CGs >75 kA for the preceding 5 minutes superimposed over the NEXRAD mosaic of composite reflectivity (See also Figure 17.7 on page 398)

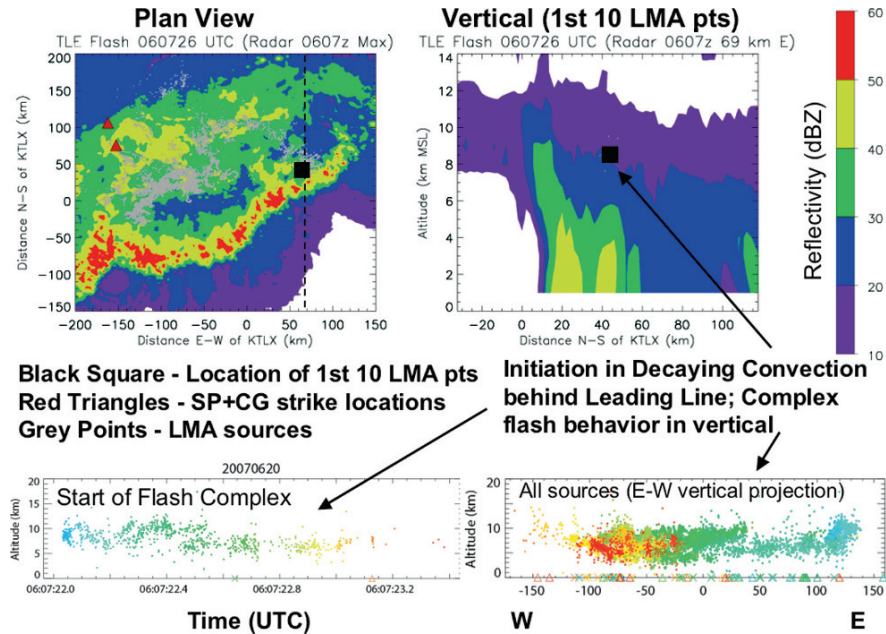


Plate 23 The gray dots plot the path of a discharge approaching 300 km in total length. It initiated around 8 km AGL (white dot) above a convective element behind the leading edge and then propagated rearward and downward. The red triangles show the two +CG sprite parents (See also Figure 17.14 on page 403)

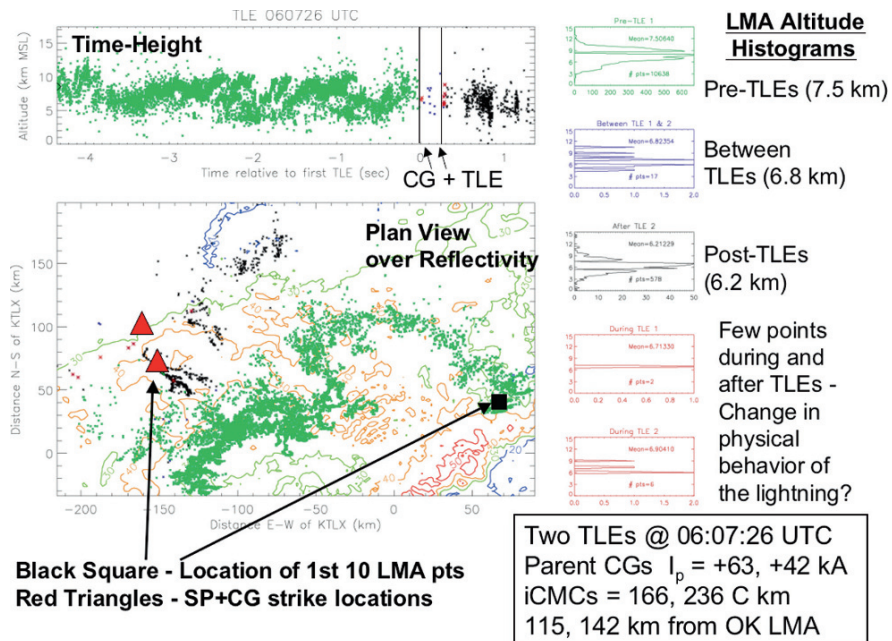


Plate 24 A close up view of the 290 km long, 5.6 seconds discharge that produced two sprites from the +CGs (red triangles) at 0607 UTC 20 June 2007 (See also Figure 17.15 on page 404)

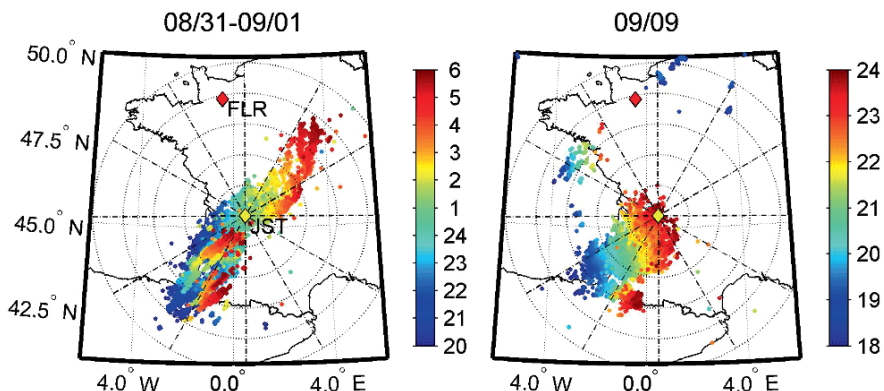


Plate 25 (Left): Lightning activity recorded by Météorage in August 31st 2005 at 20 UTC to September 1st at 6 UTC; colour of the flash location is time related. Diamonds indicate location of infrasound stations: St Just (JST) in yellow and Flers (FLR) in red. Concentric circles indicate distance from JST station with a 100-km distance between each. (Right): same as left but for September 9th from 18 to 24 UTC (See also Figure 18.1 on page 419)

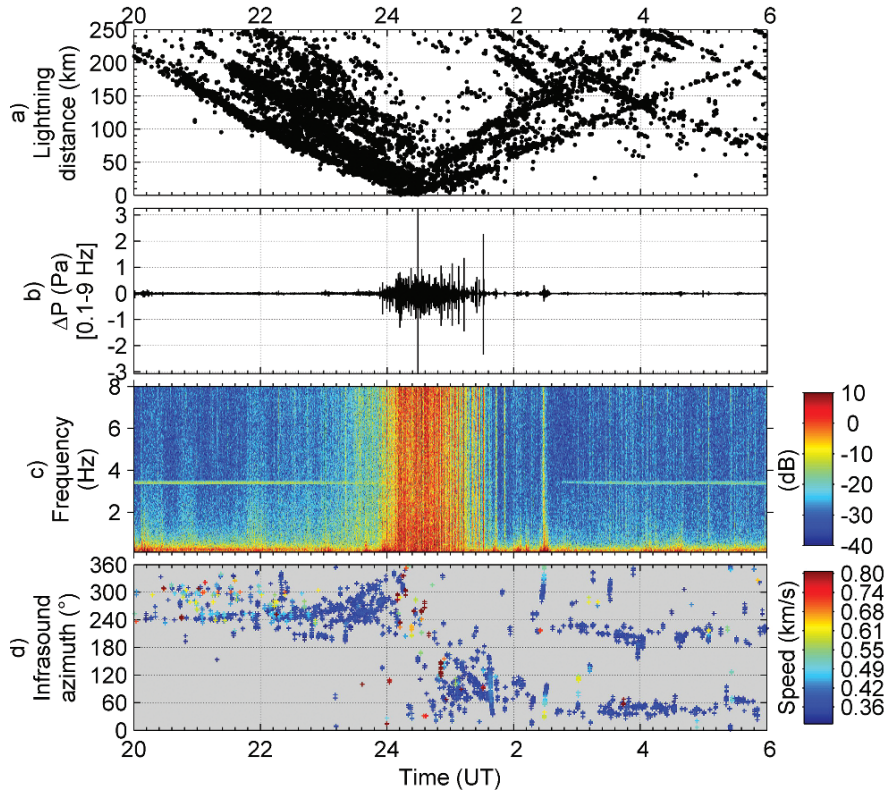


Plate 26 Data recorded from August 31st at 20 UTC to September 1st at 6 UTC. (a): Lightning distance vs. time taking account propagation time of acoustic wave. (b): Pressure recorded by the central sensor in JST station and filtered from 0.1 to 9 Hz. (c): Spectrogram of the pressure signal. (d): Infrasound azimuth of arrival where colour indicates the apparent speed (See also Figure 18.2 on page 421)

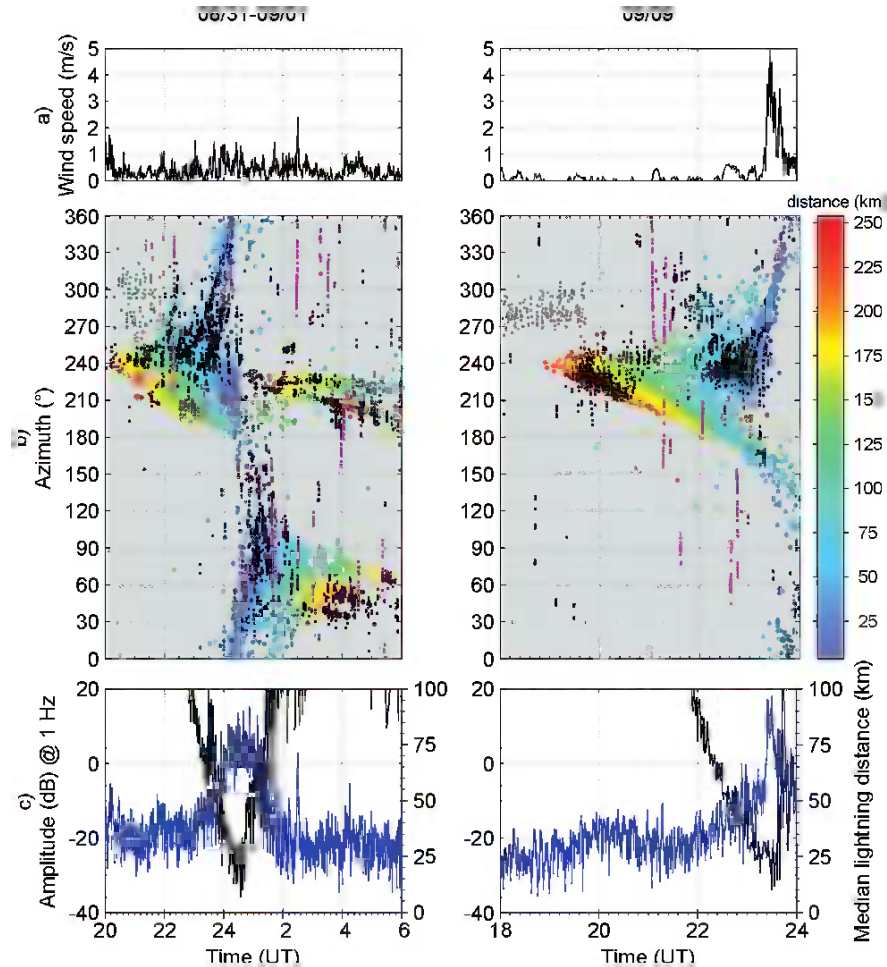


Plate 27 (a) Wind speed from August 31st at 20:00 UTC to September 1st at 6:00 UTC (*left*) and on September 9th from 18:00 UTC to 24:00 UTC (*right*). Wind measurements have been realised at ground level at the central station location. (b) Comparison of lightning azimuths (*coloured circles* – colour indicating lightning distance as shown on legend at right) and infrasound azimuths (*coloured dots*; *black* for lightning, *purple* for long lasting events, and *grey* for microbarom). (c) Comparison of the signal amplitude (in dB) at 1.00 ± 0.02 Hz (*blue*) and the median distance of lightning (*black*) (See also Figure 18.3 on page 422)

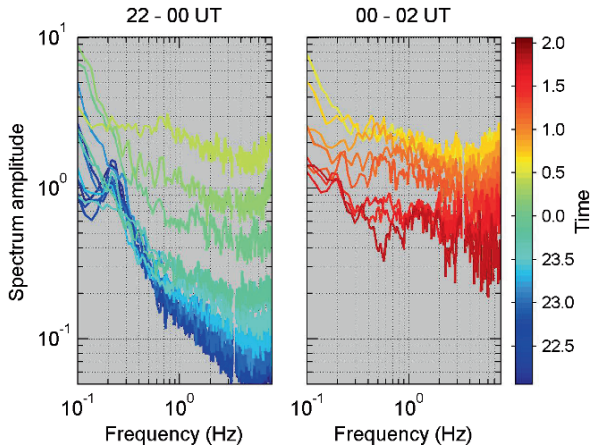


Plate 28 Mean infrasound spectra, per 10-minutes interval, for data recorded from August 31st at 22:00 UTC to September 1st at 02:00 UTC. From 22:00 to 23:00 UTC, the peak at 0.2–0.3 Hz reveals microbarom (See also Figure 18.6 on page 426)

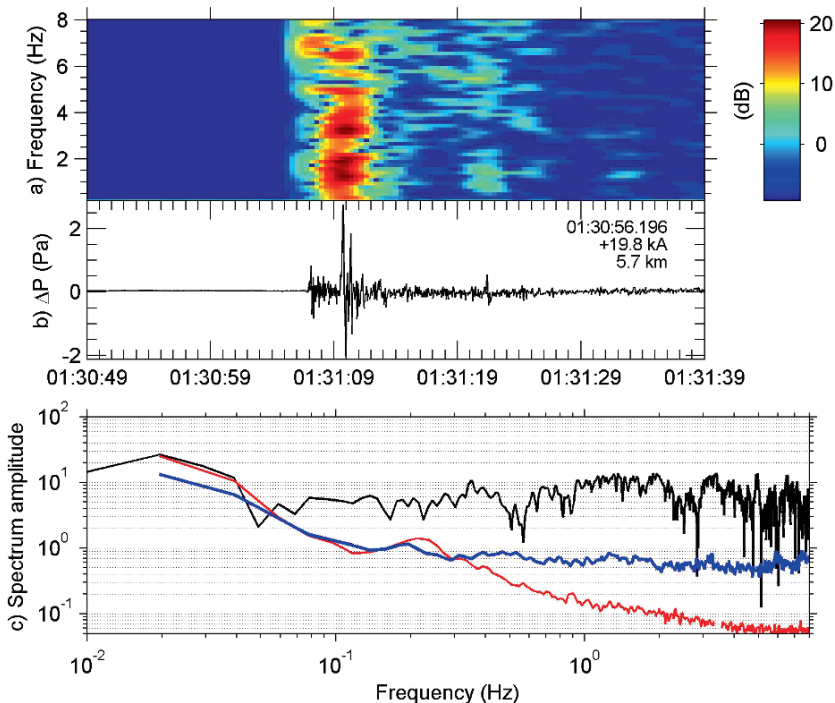


Plate 29 (a) Spectrogram of the infrasound signal recorded on September 1st at 01:31:08 UTC plotted on panel. (b) Characteristics of the related CG are written in the right upper corner of panel (b). (c) Spectrum of the signal (*black*) compared to mean spectra calculated around this time (*blue*) and at 22:00 UTC on August 31st (*red*) (See also Figure 18.7 on page 427)

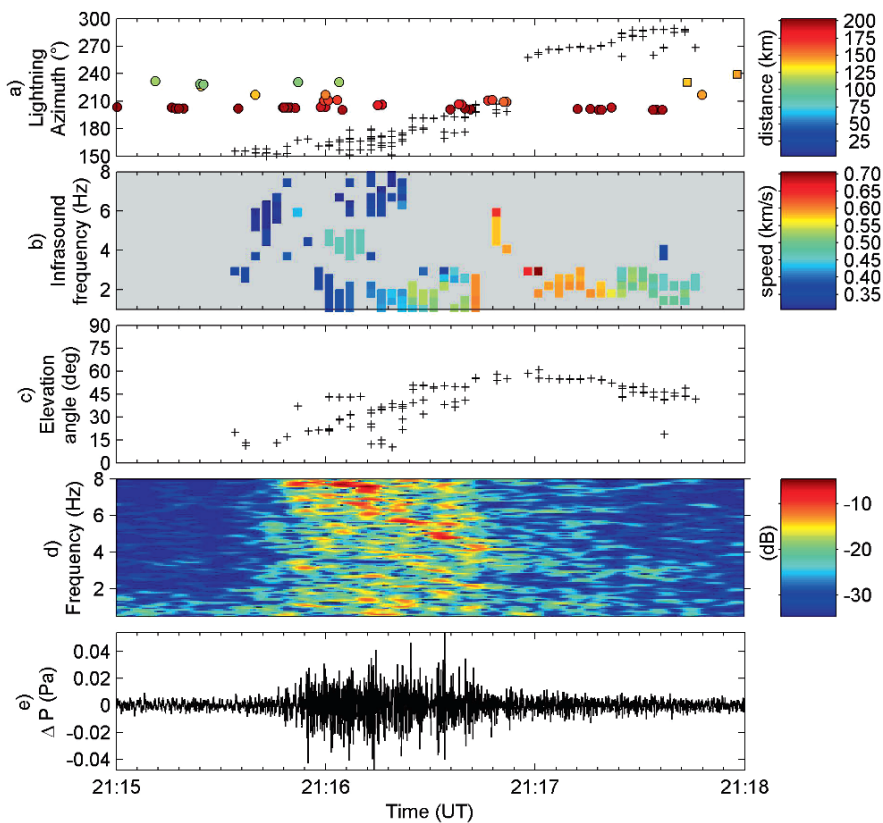


Plate 30 Long duration infrasound recorded on September 9th 2005 from 21:15 to 21:18 UTC. (a) Comparison of lightning azimuth (colored circles and squares – color indicates lightning distance, circle for -CG discharge and square for +CG) and infrasound azimuth (+). (b) Infrasound apparent speed vs. time and infrasound frequency. (c) Elevation angle deduced from infrasound apparent speed. (d) Spectrogram of infrasound signal. (e) Pressure amplitude in the 0.5–9 Hz band (See also Figure 18.8 on page 430)

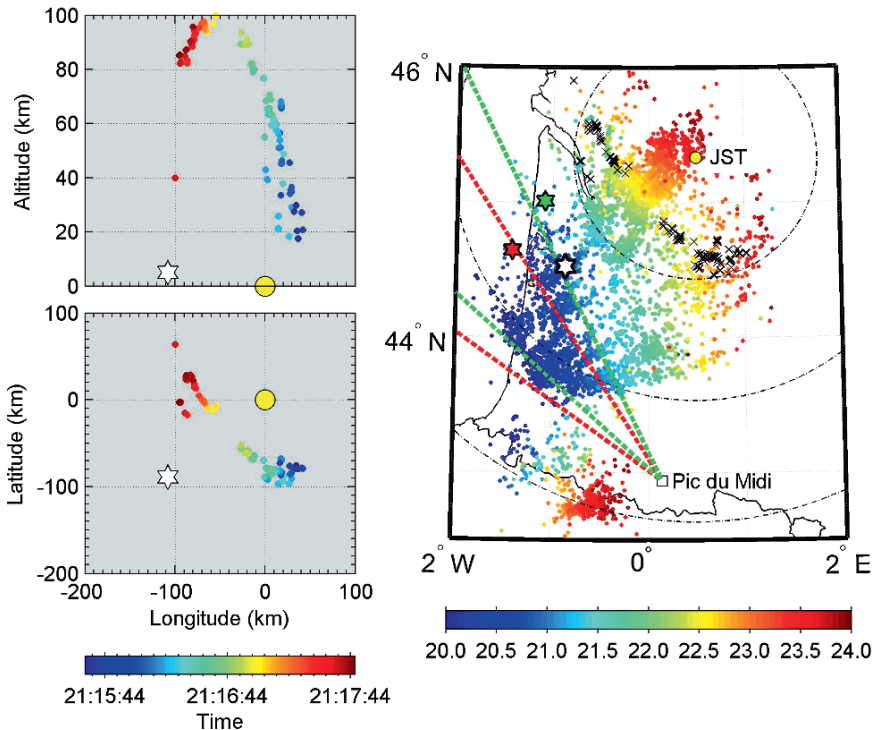


Plate 31 (Left): Infrasound source locations in horizontal (bottom) and vertical (top) plane deduced from long duration event (Fig. 18.8) wave parameters and plotted with colored dots (colors indicating time). Location of parent lightning is shown with black and white star and JST station with yellow circle. **(Right):** Lightning activity on September 9th 2005 from 20 to 24 UTC (colored dots). Field of view of Pic du midi camera is delimited with red dashed lines at the time when first sprite is observed during that night (20:35:42; +CG location with red star). It turns clockwise, to follow thunderstorm motion, and is plotted in green dashed lines when the second sprite was observed at 21:18:39 UTC (+CG location with green star just outside the field of view). Meanwhile, infrasound from sprite is measured following +CG lightning occurring at 21:10:40 UTC (black and white star). Infrasound source locations are plotted with black crosses in horizontal plane (reported from bottom left panel) (See also Figure 18.9 on page 431)

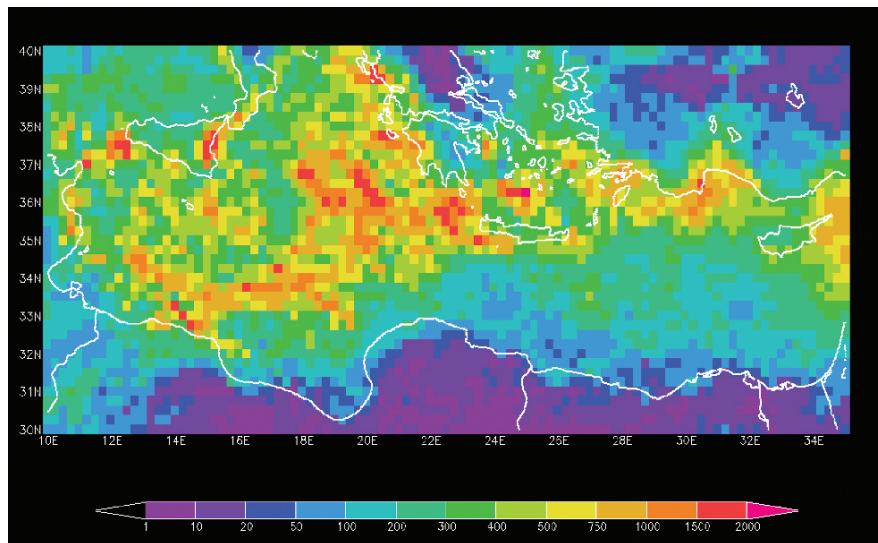


Plate 32 Cloud to ground lightning in 0.25×0.25 degrees grid boxes recorded by ATD system in the region of the Central and Eastern Mediterranean during the period October 2003—March 2004 (See also Figure 19.1 on page 434)

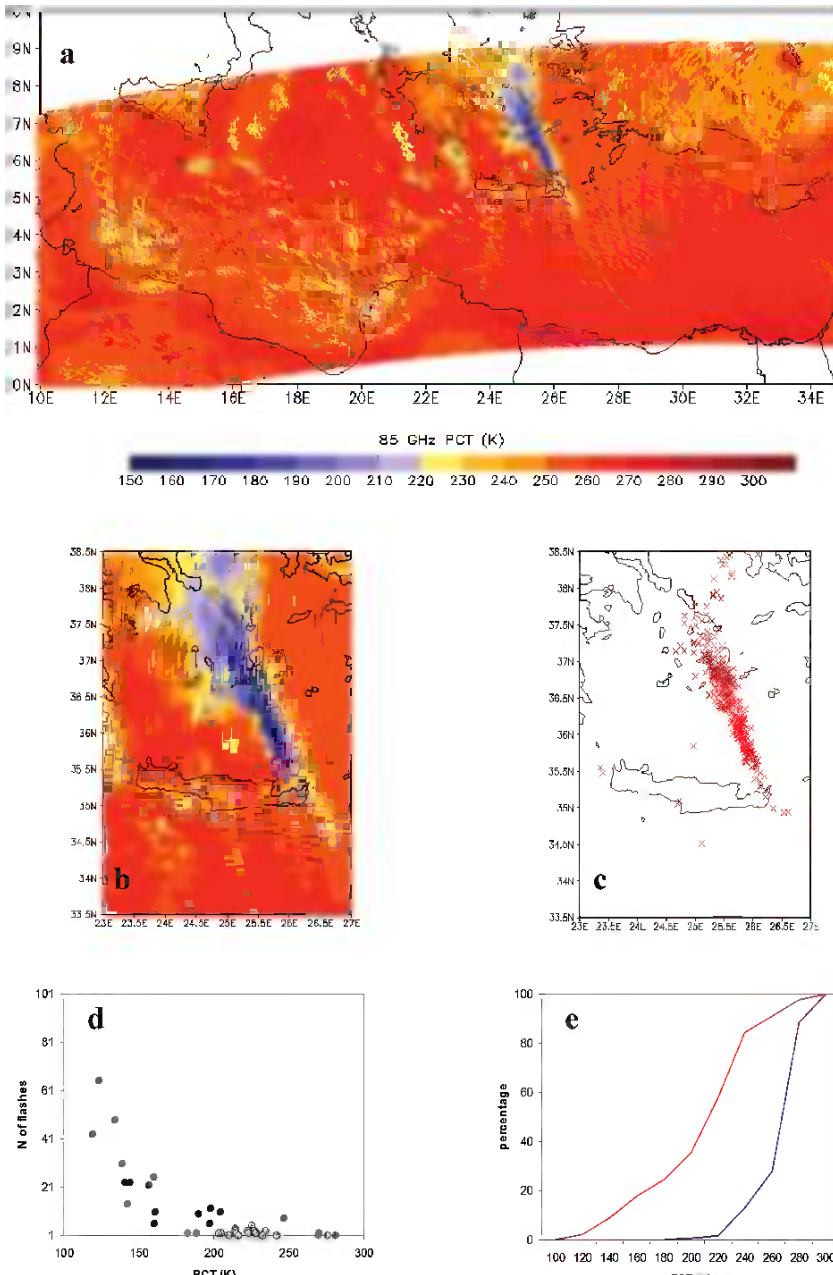


Plate 33 TRMM overpass at 1500 UTC 24 December 2003: (a) PCT at 85 GHz in K, (b) zoom in (a), (c) cloud to ground lightning sensed by ATD ± 10 min around the overpass, (d) distribution of PCT values versus the number of lightning flashes, (e) cumulative frequency of number of pixels with (red line) and without (blue line) recorded lightning (See also Figure 19.2 on page 438)

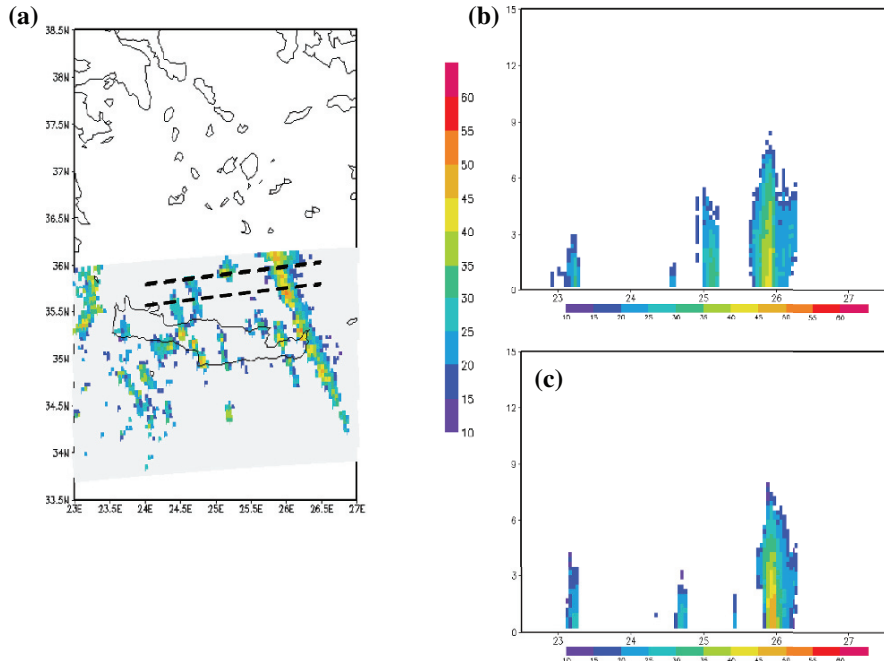


Plate 34 TRMM/PR overpass at 1500 UTC 24 December 2003: (a) PR at 2 km height (b), (c) cross sections of reselectivity along the 2 dashed lines shown in (a) (See also Figure 19.3 on page 439)

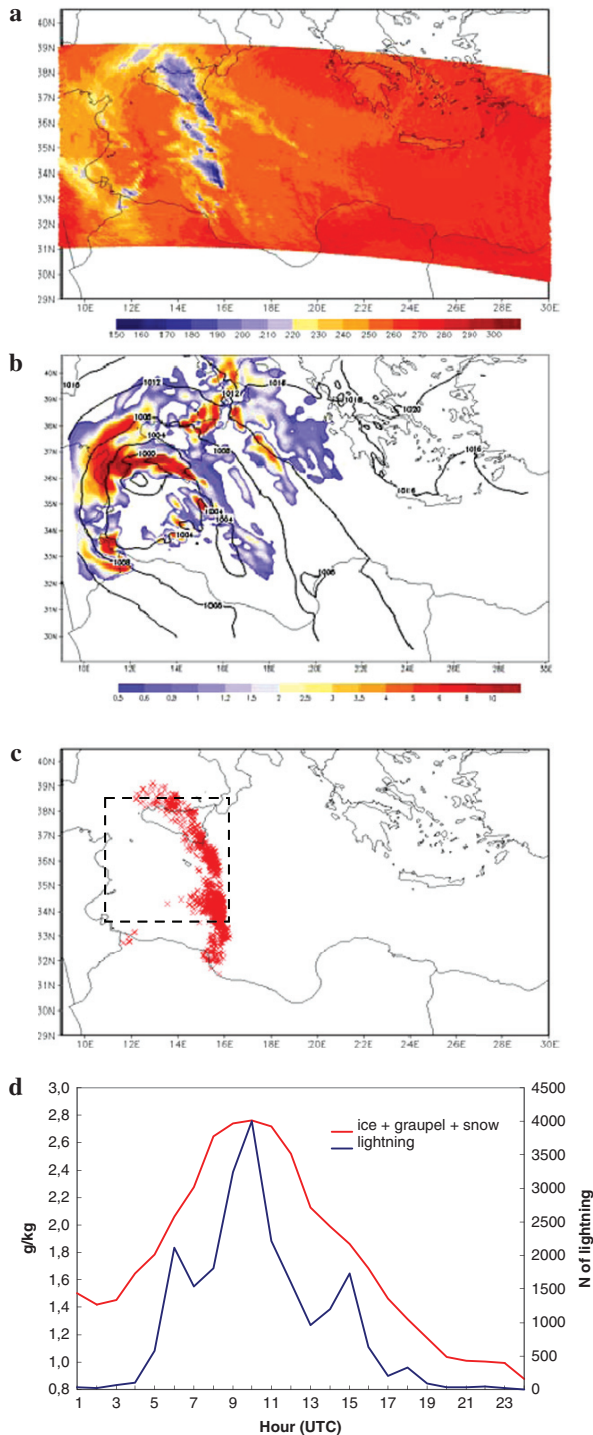


Plate 35 (continued)

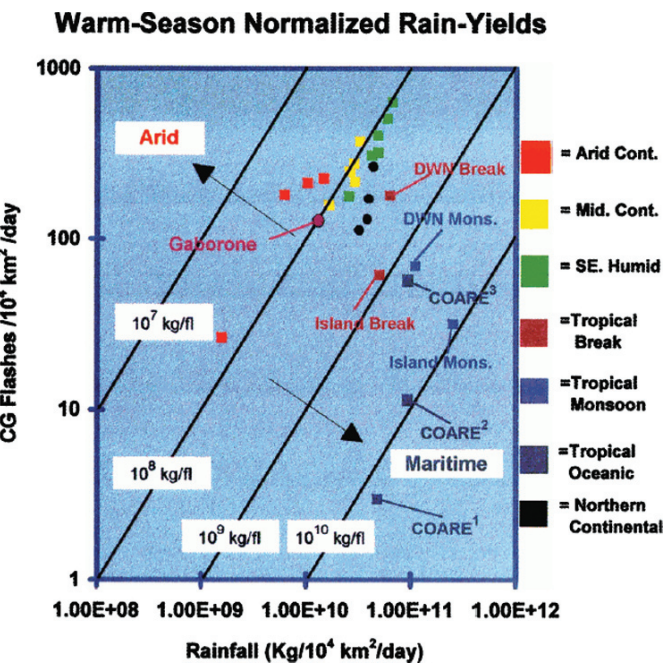


Plate 36 Summer or warm-season normalized CG flash density (flashes/ $10^4 \text{ km}^2/\text{day}$, on the ordinate) versus rainfall ($\text{kg}/10^4 \text{ km}^2/\text{day}$, on the abscissa). Sloping solid *black lines* are contours of constant rain yield (kg/fl). Each data point is coloured and labelled (as indicated in the figure) according to each specific rainfall regime discussed in the text. The *large bold arrows* indicate directions for which more “arid” or “tropical oceanic” rainfall regimes are encountered. (From Petersen and Rutledge, 1998) (See also Figure 20.2 on page 454)

Plate 35 (a) PCT at 85 GHz in K derived by TRMM overpass at 1130 UTC 13 December 2005, **(b)** MMS column integrated mixing ratio of ice+snow+graupel in g/kg and sea level pressure in hPa (*black line*) valid at 12 UTC, **(c)** 1 h lightning activity recorded by ZEUS from 1130 to 1230 UTC, **(d)** time evolution of lightning (*blue line*) and average of column integrated mixing ratio of ice+snow+graupel within the area denoted with the *dotted rectangle* in (c) (See also Figure 19.5 on page 442)

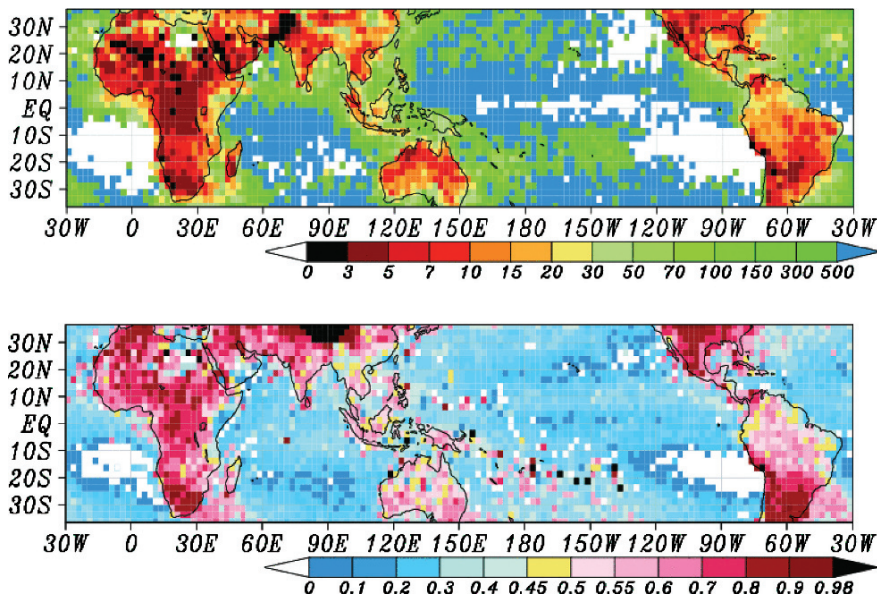


Plate 37 Global distributions of 3-year (March 1998–February 2001) TRMM observations: (a) mean RPF and (b) Tall Convective Rain Contribution to surface rain with a threshold of -20°C . Units for the colour scales are 10^7 kg fl^{-1} (a) and fraction contribution (0–1) (b). RPF averages are obtained by dividing the total precipitation amount by the total flash number for the averaging period. (From Takayabu, 2006) (See also Figure 20.5 on page 458)

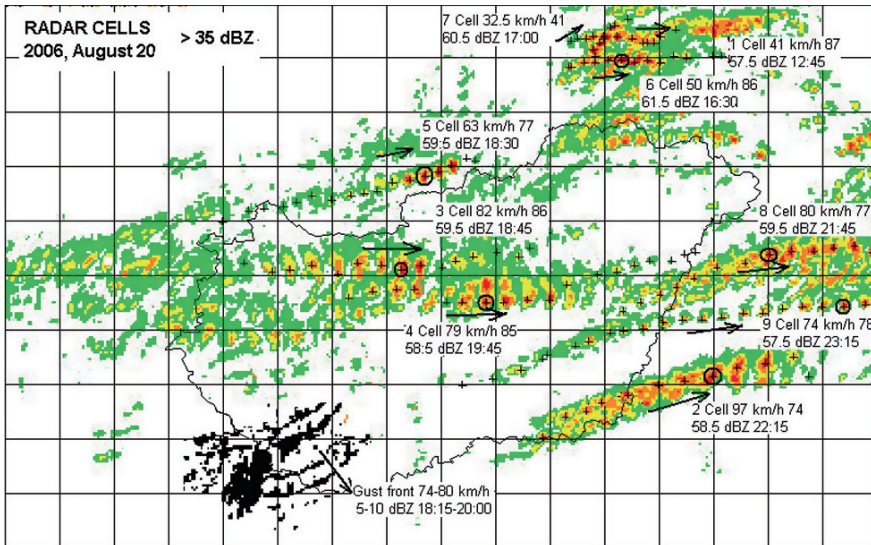


Plate 38 Tracked radar cells in 15 min patterns with a 35 dBZ threshold on 20 August 2006. The main parameters are shown in boxes: cell ID, mean velocities and directions, maximum reflectivity, and time of occurrence. The radar cell with ID 3 hit Budapest. The grid size is 50 km (See also Figure 21.1 on page 470)

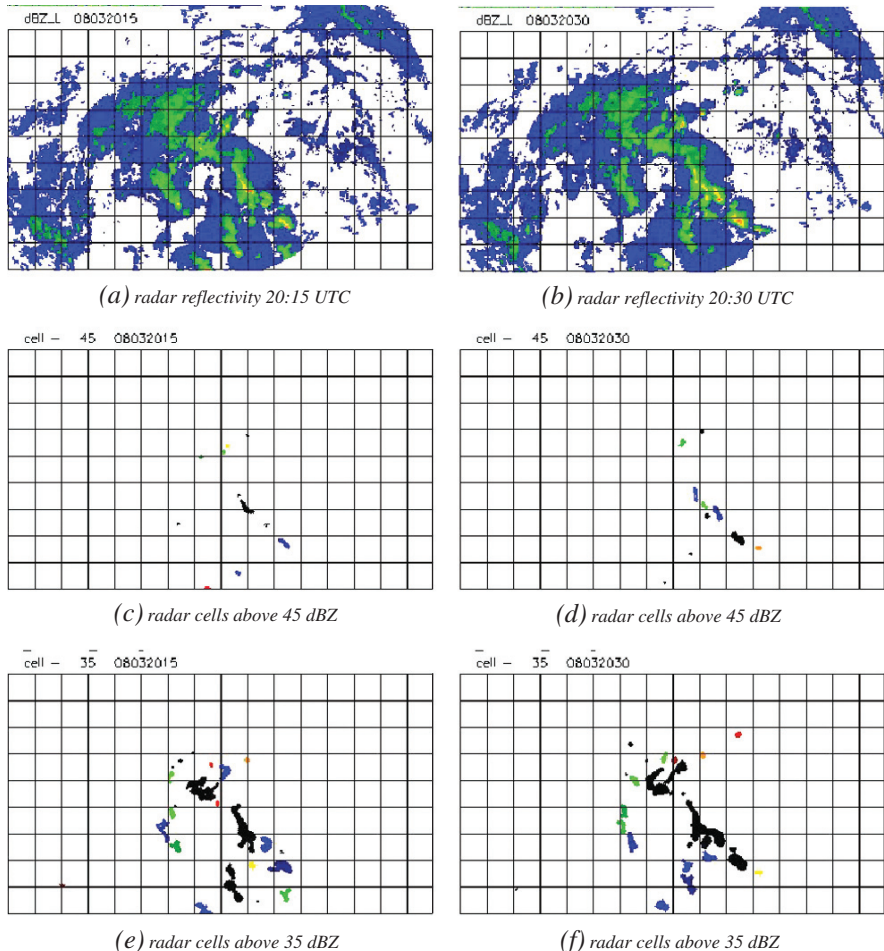


Plate 39 Radar cell products of the automatic cell identification applied for SAFIR HMS data on 3 August 2005 for two subsequent time steps 20:15 UTC (*left panels*) and 20:30 UTC (*right panels*). Remark: The colors represent the cell ID valid for a given time step and thresholds only (See also Figure 21.6 on page 477)

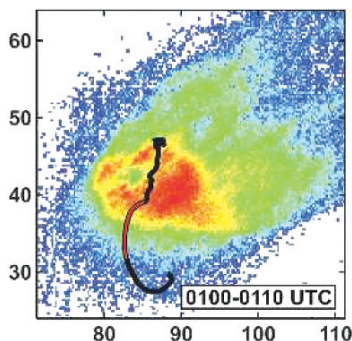


Plate 40 A lightning hole is visible in the 10-min total lightning flash density of a STEPS supercell on 6 July 2000. Axis labels denote kilometres east and north of the observation network centre, while the coloured line gives the ascent track of a measuring balloon (adapted from MacGorman et al., 2005) (See also Figure 22.4 on page 498)

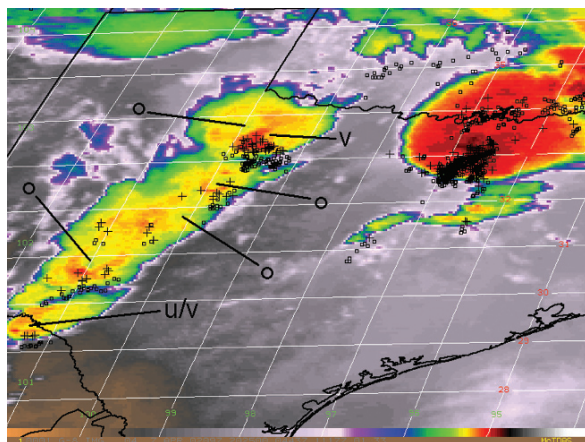


Plate 41 GOES 8 channel 4 enhanced images of the early stage of a leading-line, trailing stratiform MCS over Texas on 7 April 2002, 2025 UTC. NLDN flash overlay ($+$ = CG+, φ = CG-) 10 min before to 5 min after image time (cf. Dotzek et al., 2005a). Cold-ring signatures are marked by o-symbols, and cold-U, cold-V are indicated as well (See also Figure 22.5 on page 499)

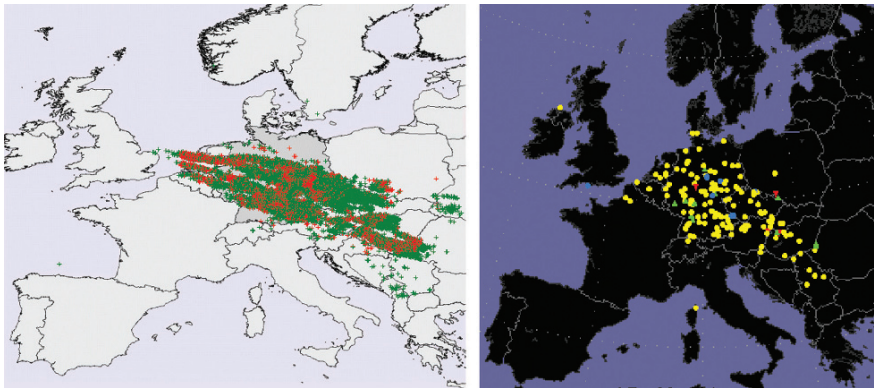


Plate 42 Traces of embedded severe thunderstorms in the cold front of extra-tropical cyclone “Emma” on 1 March 2008, 000-2400 UTC. *Left:* 67811 LINET strokes (red: IC, green: CG). *Right:* 162 ESWD severe weather reports (yellow: damaging wind, red: tornado, green: large hail, blue: heavy precipitation) (See also Figure 22.8 on page 502)

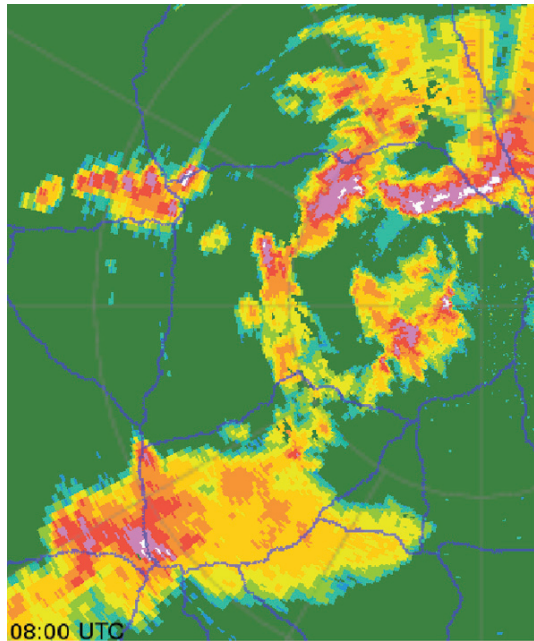


Plate 43 Weather-radar CAPPI image at 08 UTC, near the time of highest activity in Fig. 23.1. Small white areas represent radar echo exceeding 47 dBZ. The radar is near the right boundary, south of the NE peak echo, and the distance to the central peak echo, at lower left, is about 100 km (See also Figure 23.2 on page 513)

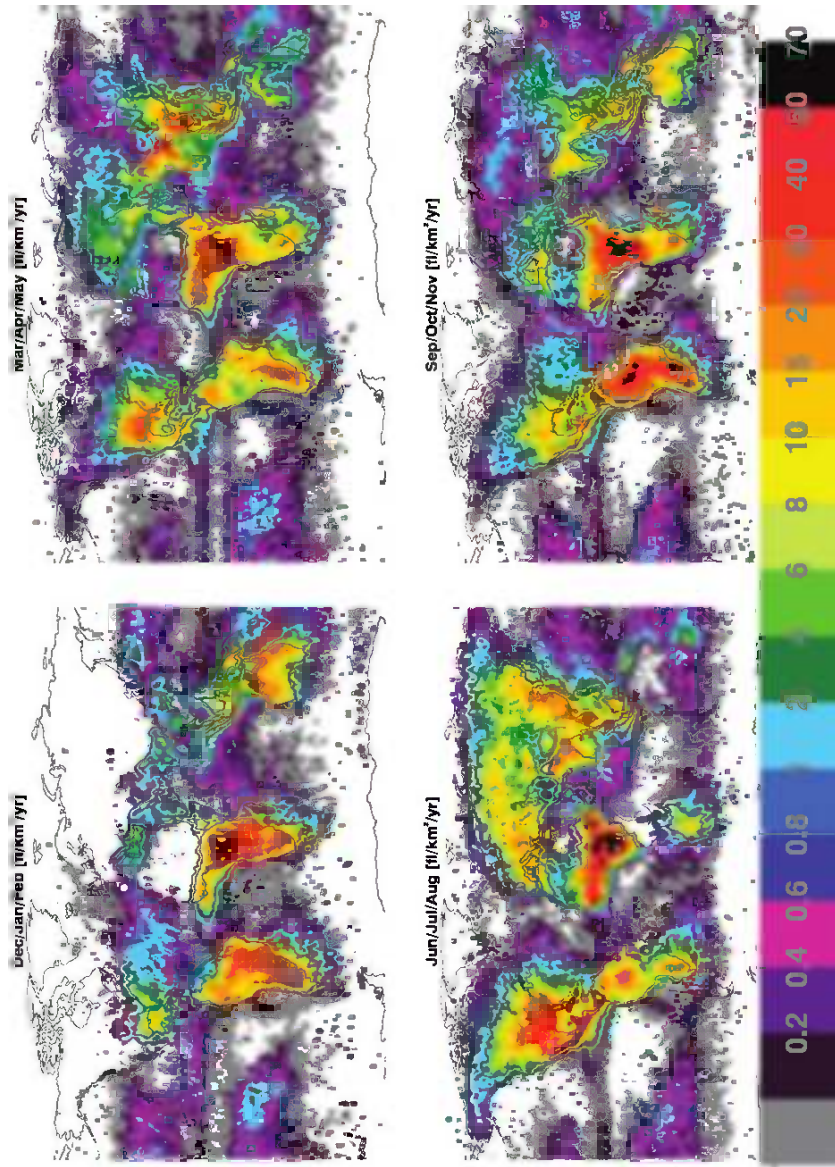


Plate 44 Seasonal maps of the OTD/LIS satellite-observed lightning derived from 5 years of data collected from May 1995 to March 2000 (Christian et al., 2003) (<http://thunder.mastf.nasa.gov>) (See also Figure 24.1 on page 523)

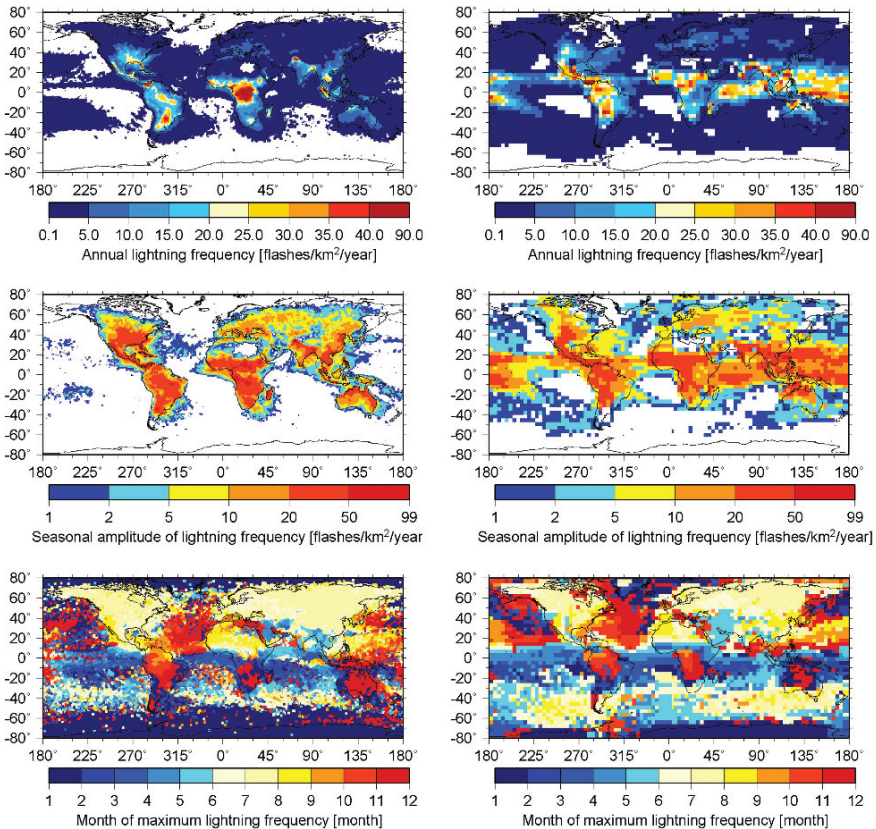


Plate 45 Inter-comparison of observed (*left*) and simulated (*right*) lightning properties. Observational data comprise a merged data set from two space-born optical sensors (OTD and LIS) (Christian et al., 2003). *First row*: annual mean lightning frequencies (flashes/km²/year). *Second row*: lightning amplitude (flashes/km²/year), i.e. difference between minimum and maximum climatologically monthly mean values. Simulated lightning occurrences are scaled to derive the observed annual mean lightning frequencies of 46.6 flashes/s. *Last row*: month of maximum climatological monthly mean lightning values. Climatologies are based on the years 1995–2005 for observational data and 1990–1999 for the simulated data (See also Figure 25.2 on page 541)

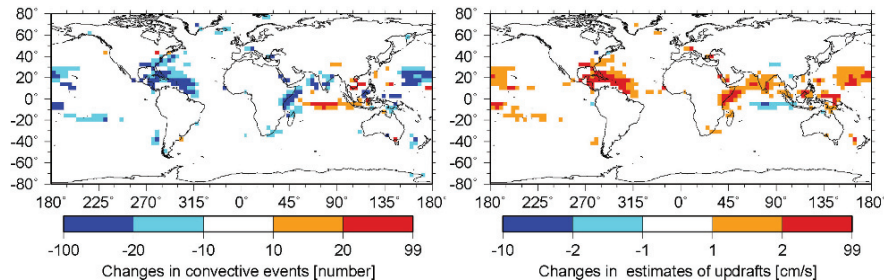


Plate 46 Left: changes in the simulated number of convective events in the ensemble climate-chemistry simulation between the years 2010–2019 and 1960–1969. Only changes, which are statistically significant with an assumed error of 1% are shown. Right: as left, but for estimates of mean updrafts (density weighted upward mass flux) per convective event (cm/s) (See also Figure 25.4 on page 543)

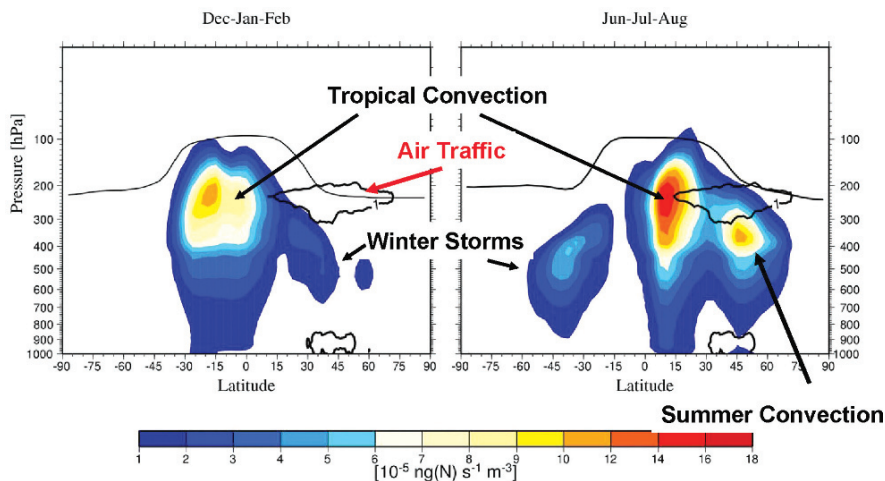


Plate 47 Simulated zonal mean distribution of lightning NO_x emissions ($10^{-17} \text{ kg(N)/m}^3/\text{s}$) for DJF (left) and JJA (right). The black line indicates the location of the tropopause, black isolines the location of air traffic NO_x emissions (See also Figure 25.5 on page 544)

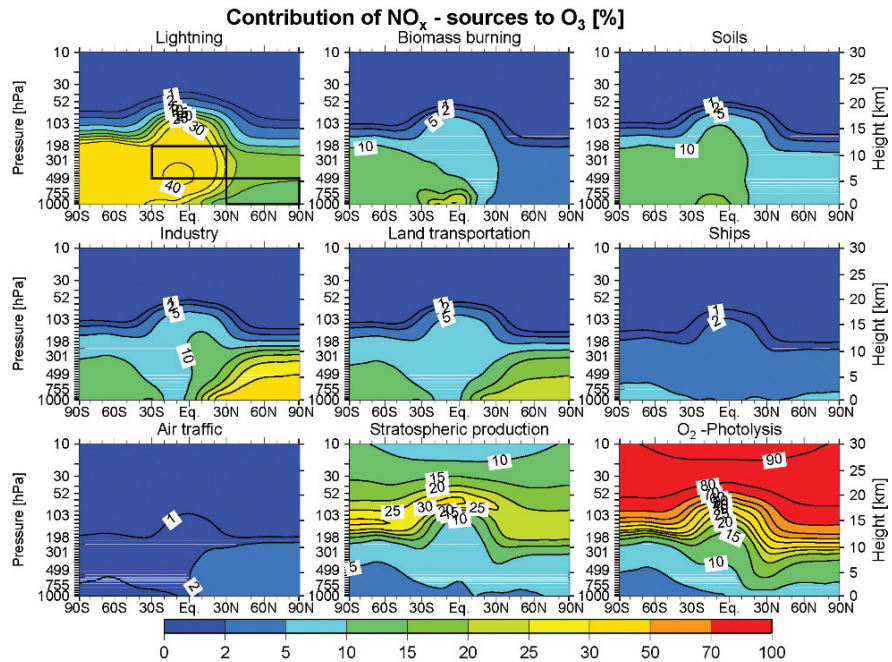


Plate 48 Contribution (%) of the zonal and decadal (1990–1999) mean simulated ozone according to their sources: lightning, biomass burning, soils, industry, surface traffic, ships, air traffic, stratospheric production of nitrogen. Ozone from production caused by oxygen photolysis is added (See also Figure 25.6 on page 544)

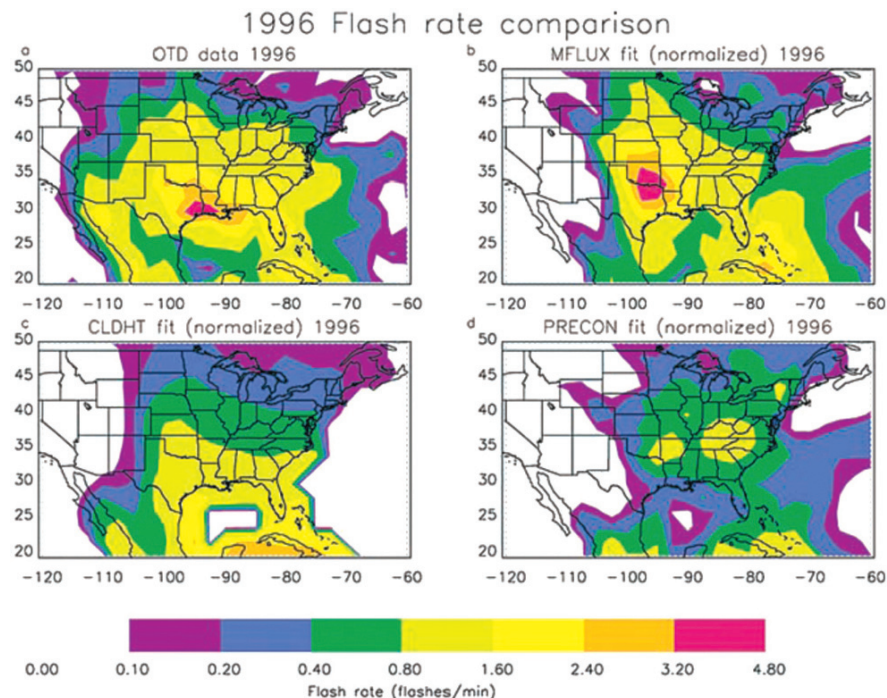


Plate 49 Observed and predicted flash rates from three schemes over the US and Western Atlantic (from Allen and Pickering 2002) (See also Figure 26.1 on page 555)

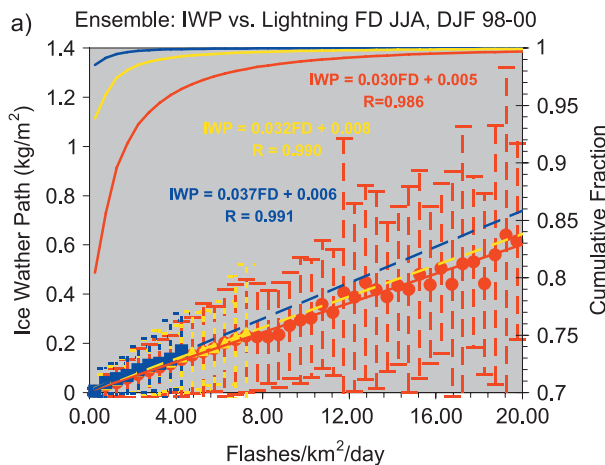


Plate 50 Relationship of ice water path (IWP) vs. LIS flashes (from Petersen et al. 2005) (See also Figure 26.2 on page 556)

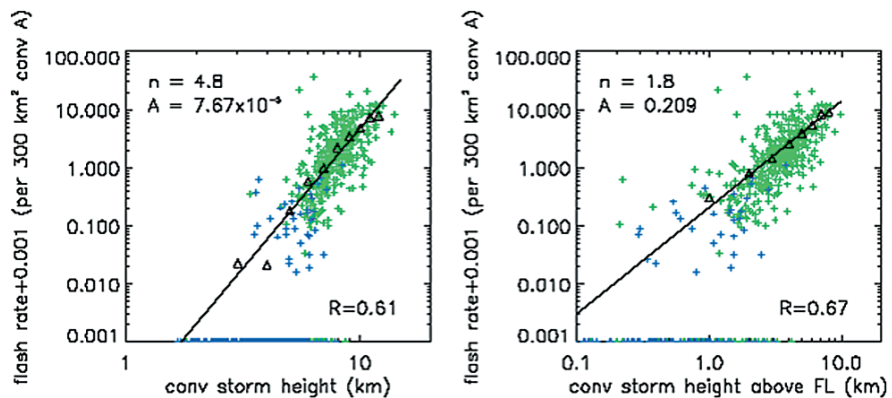


Plate 51 Relationships of LIS flashes vs. radar top height (*left*) and vs. the depth between freezing level and radar top height (*right*) (from Futyana and DelGenio 2007) (See also Figure 26.3 on page 556)

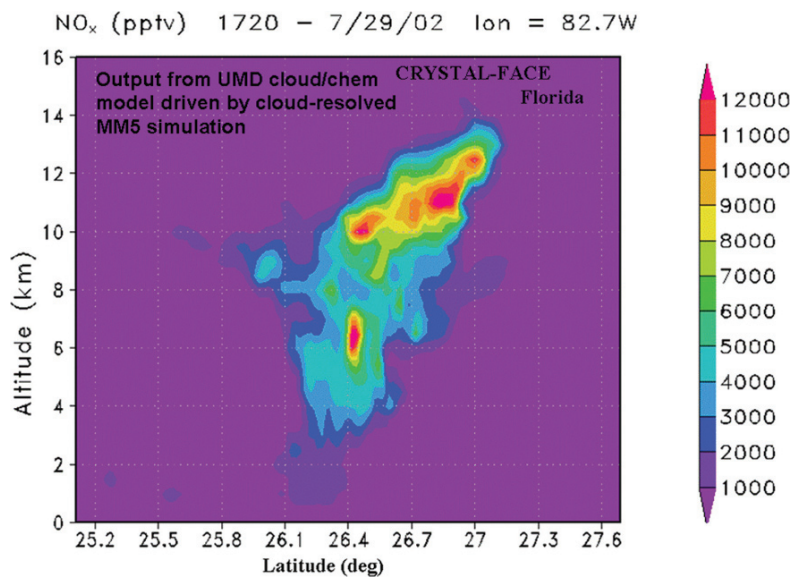


Plate 52 Vertical cross section of NO_x (pmol mol⁻¹) through the July 29, 2002 CRYSTAL-FACE storm simulation using the University of Maryland cloud-scale CTM (See also Figure 26.5 on page 560)

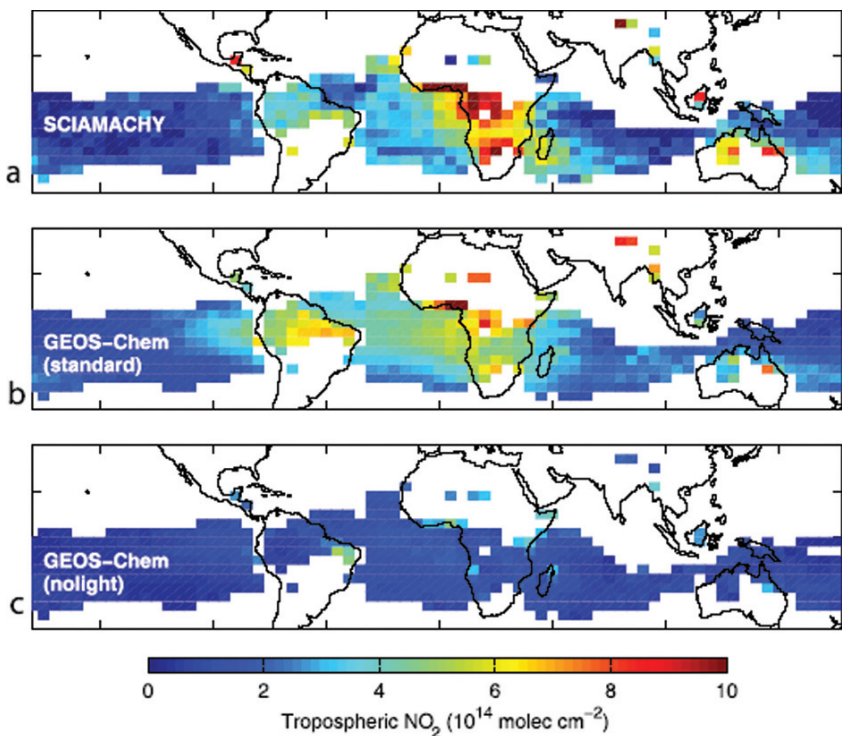


Plate 53 SCIAMACHY trop. NO_2 column map compared with GEOS-Chem with 6 Tg/a from lightning and a GEOS-Chem run without lightning from Martin et al. (2007). Data are shown for regions where the model indicates the lightning contribution to be greater than 60% and the surface source contribution less than 25% (See also Figure 26.6 on page 565)

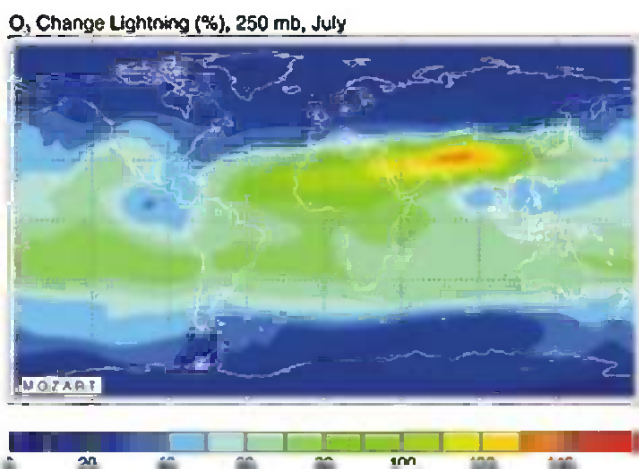
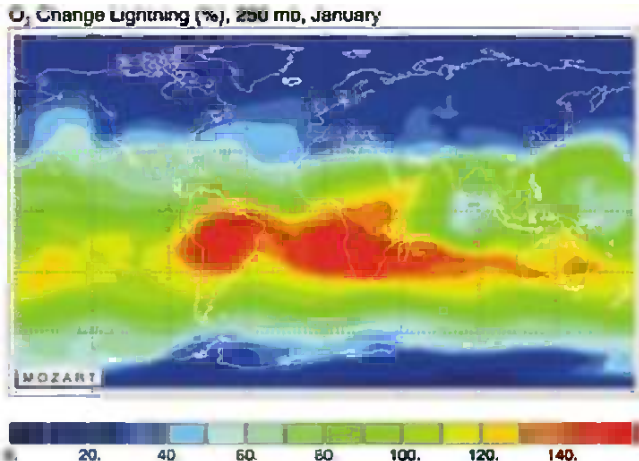


Plate 54 Percentage increase in upper tropospheric (250 hPa) ozone due to lightning (from Hauglustaine et al. 2001) (See also Figure 26.7 on page 566)

Index

A

AC global circuit, 378
Action integral, 7, 8, 37
Active phase, 241
Aeronomical data, 361
Aerosol hypothesis, 459, 525
Aerosol particle, 459
Africa, 350, 353, 374, 376, 377
African easterly waves, 377
Aircraft emission, 545
Aircraft and lightning interaction, 142–145
Air-earth current, 379
Airmass thunderstorm, 526
Air termination system, 580, 581, 582
ALEXIS satellite, 287, 288
Altitude triggering, 25, 29, 35
Ambiguities, 263
Amplitude distribution, 126
 of IC-strokes, 131
Annual solar march, 375
Annual variation, 373–374
Antarctica, 355, 373, 376
Anthropogenic climate change, 488
Anthropogenic warming, 538
Anti-cyclonic, 526
Anvil, 94, 106
Anvil clouds, 63
Areal variation, 347, 378
Around-the-globe waves, 348, 357, 362
Asymmetrical waveguide, 363
Attachment process, 3, 4, 26, 29, 30, 32, 35
Attenuation, 348, 366, 367
 rate, 358
Audio magnetotellurics, 370
Australia, 187, 188, 189, 190, 191, 192, 193,
 200, 201
Azimuthal magnetic field, 11, 16, 18

B

Background signal, 349, 350, 354, 363, 366
Ball antenna, 370
Balloon E soundings, 58
Baroclinic instability, 526
Belsk, 367, 368
Bi-directional leader, 62, 71, 73
Bi-directional propagation, 234, 241
Blackbeard experiment, 287, 288, 294,
 296, 301
Boundary layer, 521
Bounded weak echo region (BWER), 86, 87,
 102, 103, 500
Brazil, 209
Breakdown, 232
Bremsstrahlung, 332
Brightness temperature, 435

C

Calibration bench, 263
Camp Blanding, 24, 27, 31, 38, 39, 40, 42, 44
CAPE (convective available potential energy),
 379
Catalan Lightning Detection Network, 161,
 164, 165, 173
Cavity, 354
Cell
 development, 469, 472, 475
 identification, 468, 469, 474, 475, 477, 482
 segmentation, 473, 483, 484
 tracking, 135, 468, 469, 472, 474, 484, 485
Center of electrical activity, 433
CG (cloud-to-ground)
 discharges, 494
 flashes, 232, 540
 flash initiation, 61, 68
 -IC discrimination, 117, 128
 lightning, 88, 104, 106
CGR3 lightning flash counter (LFC), 192

- CGR4 lightning flash counter (LFC), 199, 200
 Channel base current, 2, 8, 9, 14, 16, 19
 Characteristic layers, 349
 Charge, 1, 2, 3, 4, 5, 7, 8, 13, 14, 16, 19
 deposition, 76, 77, 100
 moment, 349
 reversal, 87
 separation, 488, 493
 structure, 97, 100, 104, 105, 108, 109
 Charged cloud particles, 233
 Charge moment change, 388, 391, 396,
 405, 411
 network, 390, 395
 Chemical transport model (CTM), 552
 Chimney, 530
 regions, 350, 351
 CIGRE-500 lightning flash counter (LFC),
 190, 191, 194
 Circulation weather types, 169, 170
 Classical triggering, 25, 28, 30
 “Classic” Lorentzian concept, 371
 Clausius Clapeyron relation, 379
 Climate
 change, 521, 529
 -chemistry model, 546
 and lightning, 546
 sensitivity, 539
 Close lightning electromagnetic
 environment, 47
 Cloud
 base, 556
 discharge, 253, 254, 268
 flash, 130
 mass flux, 554
 -resolved chemical model, 559
 top, 489, 491
 conduction current, 378
 height, 553
 Cloud condensation nuclei (CCN), 525
 Cloud-to-ground (CG)
 flash, 448
 lightning, 291, 299, 300, 301, 303
 stroke, 115
 Cloudiness, 377
 Cloud lightning (IC), 115, 116, 127
 Cold front, 511
 Cold-ring, 487
 Cold runaway electron mechanism, 333
 Collisional charging, conductive,
 non-conductive, 87, 97, 101
 Complex characteristic altitudes, 359, 360
 Complex demodulation technique, 370–371
 Complex eigenvalue, 371
 Conditional instability, 375, 376, 377
 Conductivity, 354, 370
 Continental convection, 524
 Continuing current, 5, 8
 wave shape, 221
 Convection, 373, 376, 379, 521
 over ocean, 539
 Convective
 cell, 511
 cloud, 509
 core, 509
 precipitation, 554
 rainfall, 448
 rate, 149
 region, 455
 updraft, 60
 Convective available potential energy (CAPE),
 196, 204, 379, 394, 488, 540, 555
 Conventional breakdown, 333
 Corona discharge, 233
 Cosmic-ray flux, 341
 Coupling corrections, 263
 Critical electric field, 332 fig 15.1
 CRYSTAL-FACE project, 559
 Cumulonimbus, 509–510
 Current
 half-peak width, 39, 40, 41
 moment, 357, 360
 peak, 38, 41, 42, 558
 Cyclone, 501
 Cyclonic rotation, 526
- D**
 Damping, 370, 371
 Dart leader(s), 26, 235, 335, 343, 344
 Day-night asymmetry, 347, 369
 Day-night boundary, 363
 5-day wave, 377–378
 6, 5-day wave, 377–378
 DC global circuit, 379
 DC magnetic field, 370
 Deep convection, 376
 Deep moist convection, 489
 Defense Meteorological Satellite Program
 (DMSP), 313
 Derecho, 499
 Detection efficiency, 119, 122, 123, 124, 165,
 166, 211, 279
 Detection efficiency model (DEM), 211
 Detectors, x-ray, 334
 DFP (daily frequency pattern), 354, 375
 Dipole moment, 87
 Direction finding (DF), 120, 352–353

- Diurnal cycle, 282, 522
Diurnal variation, 350, 351, 354–355, 365, 367, 368, 373
Double-CO₂ climate, 532
Downburst, 95, 489, 491
Down conductor system, 581, 583, 584
Downward negative lightning discharge, 1, 2, 19
DS-type model, 15
3D time-of-arrival, 115
DU, 13, 14, 15, 16, 19
3D-visualization of lightning, 137
3D-visualization of strokes, 130
Dynamic range, 370
- E**
- Earth-ionosphere
cavity, 347, 353, 354, 364, 369, 370, 371, 378
resonator, 353, 354
Earth Observing System (EOS), 309
Earth termination system (earthing system), 583, 589, 590
Easterly waves, 377
Effective frictional force, 332 fig 15.1
Eigenfrequency, 356, 371
Eigenvalue, 357, 358, 371
Electrical discharges, 380, 488, 489
Electric field (E), 58, 350, 351, 365, 370, 379
maximum, 343
Electrification, 69, 71, 86, 99, 435, 448, 459
process, 232
Electrodes, 370
Electrogeometric model, 580, 582
Electromagnetic field, 5, 11
Electron detachment, 233
Electronic detachment, 233
Electrons, runaway, 331–333, 340–344
Electrostatic potential (V), 58
ELF (extremely low frequency), 347, 348, 349, 351, 357, 358, 359, 360, 361, 363, 364, 365, 367, 368, 370, 371, 377
El Niño, 532
Elves, 352, 388, 390, 393
Emission height distribution, 130
Emma, 501
Energetic radiation, 331–334
Energy dissipation, 557
Energy spectrum, TGF, 338 fig 15.4
Engineering model, 11, 12, 14, 19
ENSO (El Niño Southern Oscillation), 379–380, 530
E profile, 61, 77
- Equinox, 374
Equipotential bonding (bonding system), 585, 586, 589
Equivalent potential temperature, 96
EULINOX experiment, 559, 563
European Severe Weather Database (ESWD), 501
Eurosprite, 418, 427
Exclusion zone, 220
External lightning protection, 579–580, 581, 591
Extra-tropical cyclones, 492–493, 502
Extremely low frequency (ELF), 522
Extreme weather, 487
- F**
- False alarm rate (FAR), 280
Fast Fourier analysis (FFT), 117
Fast On-orbit Recording of Transient Events (FORTE) satellite, 290, 291, 292, 294, 296, 297, 300, 301, 302, 303, 304
FDTD (finite-difference-time-domain modeling), 369
Flash, 469, 470, 471, 474, 476, 477, 479, 480, 482, 485
activity, 466, 473, 474, 475, 476, 477, 482, 485
cell, 466, 468, 469, 475, 476, 478, 483, 485
components, 231, 234
correlation, 513–514
counters, 222
density, 512–513
detection efficiency, 124
duration, 8
flood, 85
flooding, 450
length, 559
rate, 87, 89, 93, 94, 95, 100, 518
and increasing rain flux, 320
Flash cell, 515
analysis, 516–519
definition, 515
development, 518
lifetime, 510, 517
size, 516
Flash extent density (FED), 265
Forced wave, 377
FORTE satellite, 277
Forward flank downdraft, 86
Free wave, 377
Freezing level, 458
Frequency, 348

Frequency variations, 354, 356

Frontal thunderstorms, 526, 527

Front duration, 7, 8

Fujita scale, 491

Fulgurites, 44, 46, 47

G

Gamma-ray flashes, 336–338

Gamma-ray and x-ray observations, 334–340

General circulation of the atmosphere, 524

Geographical distribution of lightning, 282

Geomagnetic activity, 377

GEOS Chem model, 564

Geostationary Lightning Mapper (GLM), 310, 311, 326

Geostationary Operational Environmental Satellite (GOES), 311

Geostationary satellite, 280, 284

Global change, 348, 378

Global circuit, 378, 379

Global climate change, 347, 380

Global climate model, 552

Global lightning, 348, 350, 351, 353, 354, 356, 361, 364, 366, 371, 373, 374, 375, 376, 378, 380

Global lightning climatology, 281–283

Global modeling of lightning, 540

Global NO_x model, 564–567

Global observation, 280

Global surface air temperature, 380

Global temperature, 374

Global tropical temperature, 380

Global warming, 378

Global wave, 377

GOES image, 499

Graupel, 86, 87, 92, 97, 101

Graupel-ice collisions, 494

Greenhouse gas, 539

Ground-based observations, 522

Grounding conditions, 43, 51

Ground surface arcing, 44, 45, 48

Grouping algorithm, 264

H

Hadley circulation, 526

Hail, 86, 91, 92, 93, 94, 95, 96, 101, 102

Hail-bearing thunderstorm, 179–182

Hail probability, 181

Hail storm, 495–496

Halos, 390, 391, 393, 401, 408, 411

Hanning-window, 371

Heat capacity, 373, 375

Heavy precipitation, 490

Helicity, 490

Helio-geo-latitude, 361, 362

Helio-geo-trajectories, 362

Hierachical agglomerative clustering, 174

High cloud coverage, 529

High pressure cell, 526

High-speed digital video camera, 217

Hook echo, 84

Hornsund, 367, 368

Hovmoller diagram, 377

Hurricane, 287, 304, 489, 492

Katrina, 501

season, 376

Hydrometeors, 489

I

IC (intracloud)

:CG ratio, 93, 94, 96, 136, 100, 180

discharges, 494

flash, 232, 240

initiation, 68, 71

recognition with VLF/LF strokes, 129

-stroke, 130, 131

Ice

crystal size, 529

particles, 435

water content, 529

water path, 555, 556

Impulse charge, 8

Impulse charge moment change, 391–392, 406, 407

Impulsive emissions, 257

Indian Ocean, 376

Induction coil, 367, 371

Infrared TB's, 313

Infrasound, 419

Infrasound from lightning, 417–431

amplitude, 420, 424

detection, 421, 423, 425

mechanism, 420, 426

spectrum, 420, 425–427

Infrasound from sprite, 427–432

amplitude, 428

location, 429, 431

mechanism, 428

Initial breakdown, 134

Initial continuous current (ICC), 26, 29, 30, 33, 34, 35

Initial current variation, 33

Initial discharge stage, (IS), 26, 33, 34

In-situ calibration, 263

Instability, 376, 377, 379, 521

Instrumented tower, 223

Integration, 258, 262, 263

- Interferometry, 254, 259, 260, 264, 265, 266
Internal lightning protection, 585–586, 591
International Center for Lightning Research and Testing (ICLRT), Camp Blanding, 334–335
Inter-tropical convergence zone (ITCZ), 526, 530
Intertropical Front (ITF), 375
Intracloud (IC) flash, 448
Intracloud lightning (IC), 161, 182, 190, 192, 235, 237, 238, 241, 243, 281, 287, 291, 293, 299, 326, 420, 540, 542
Intraseasonal variations, 376–377
Invariants, 354, 372
Inverted dipole, 104, 106, 495
Inverted-polarity charge structure, 163, 181, 182
Inverted tripole, 105, 106
Ionizing radiation, 354
Ionosphere, 349, 357, 367, 369, 371
Ionospheric disturbance, 360
Ionospheric potential, 379
ITCZ, 375
- J**
Junction stage, 241
- K**
K-change, 247
Kennedy Space Center, 28, 38, 39, 40, 43, 379
Keraunic level, 169
Keraunograph, 161, 163, 164
Kew Observatory, 379
K-processes, 134
- L**
Laboratory discharges, 233
Laboratory sparks, x-rays from, 338–340 fig 15.5, 558
Lag time, 452
LAMPINET (lightning location network), 143, 148, 149
Land/Ocean contrast, 456–459
Lapse rate, 531
Large peak current CGs, 399
Latitudinal migration, 375
LDAR, 236–237
Leader velocity, 243
Legendre function, 357
LF cloud, 268
Lightning, 187, 194, 195, 465, 466, 467, 470, 473, 484
activity, 347, 348, 349, 350
antenna, 351
channel, 11, 13, 14, 15, 16, 17, 18, 19
discharge, 1–2, 19
distribution, 192
flash density, 189, 192, 193
ground flash density, 190, 192, 193
hazard, 573, 575
hole, 100, 101, 498
-initiated wildfires, 201
initiation, 64–66, 333
input energy, 32
jump, 91
mapping, 68, 73
mediated telephone injuries, 201
and microwave temperatures, 323
monitoring, 510
path, 72
polarity, 93, 96, 97, 493
and precipitation, 320
protection, 573, 574, 577, 578, 579, 583, 585–590
measures, 573, 591
and radar, 319, 320
registration, 190, 194
risk components, 576, 577
risk of lightning damage, 574, 576–578
rocket-triggered, 331, 334, 337
source, 347, 348, 349, 351, 356, 357, 360, 366, 375
statistics, 151
types, 494
x-rays from natural cloud-to-ground lightning, 335–336
- Lightning detection and ranging (LDAR), 88
Lightning flash counter (LFC), 188, 196, 199
Lightning Imaging Sensor (LIS), 236, 246, 276, 279, 309, 311, 373, 522
Lightning Location Systems (LLS), 210
Lightning Mapping Array (LMA), 88, 105, 242, 246, 248, 390, 557
Lightning protection level (LPL), 579, 582, 584
Lightning Protection System (LPS), 579, 581, 585
Lightning Protection Zones (LPZ), 586, 587, 588, 589
Line routing, 589, 591
LINET (lightning location network), 115–138, 150, 236, 249, 440, 501, 502
LINET sensor map, 118
Liquid water, 488
Liquid water content (LWC), 86, 96, 99, 232
LIS (Lightning Imaging Sensor), 126, 436

- Location
 accuracy, 119, 162, 165, 280, 440
 techniques, 264
- Long-term variations, 378–380
- Lorentzian, 354, 363, 371, 372
- Los Alamos National Laboratory (LANL),
 287–288, 293, 298, 303–304
- Los Alamos Sferic Array (LASA), 288,
 291–292, 294, 302, 304, 306
- Lower characteristic altitude, 361, 365, 367
- Low-light television, 391
- LS-type model, 15
- Luminosity, 2, 5, 8, 9
- M**
- Madden-Julian Oscillation (MJO), 376
- Magnetic-direction finding, 164
- Magnetic field, 350, 351, 353, 370
- Mapping, 264–265, 266, 267, 268
- Maritime Continent (MC), 350, 351, 366, 374
- Maximum dI/dt, 8
- Maximum E magnitude, 64, 65
- M-component, 32, 34, 51, 412
- MCS, 254, 267
- MDF (magnetic direction finding), 146
- MDUD, 15, 16, 17, 18, 19
- Mediterranean database, 314–316
- Meridional circulation, 525
- Meridional lightning distribution, 374, 375
- Mesocyclone, 84, 85, 93, 95
- Mesocyclonic storm, 490
- Mesoscale convective complex (MCC), 394,
 488, 491, 526
- Mesoscale convective system (MCS), 59,
 62–63, 100, 353, 388, 391, 394,
 455, 488, 491–492, 510, 526
- Mesoscale lightning, 353, 377
- Mesoscale stratiform charge structure, 62
- Mesoscale stratiform cloud, 62, 63
- Mesosphere, 348, 352, 380
- Meteosat Third Generation (MTG)
 satellite, 311
- Microbarometer, 418
- Microphysical properties, 435–440
- Microwave, 458
- Microwave TB's, 313
- Midlatitude synoptic storm systems, 526
- Migration of lightning, 375–376
- Ming Dynasty, 377
- Mixed phase region, 449, 459
- Mixing ratio ice+snow+graupel, 443
- MM5 model, 440–441
- Modeling lightning leader x-ray emission,
 341–342
- Modes, 354, 355, 356, 367, 369
- Moisture, 376
- Monsoon, 525
- Monte Carlo simulations, 337, 340, 342
- MTLD, 12, 13, 19
- MTLE, 12, 13, 14, 19
- MTLL, 12, 13, 19
- Multicell, 83
 storm, 490
- N**
- Nagycenk, 352, 356, 369, 370, 371, 375, 379,
 380
- Narrow Bipolar Event (NBE), 255, 287, 288,
 291–293, 294, 295, 296, 298, 299,
 300, 301, 304
- National Lightning Detection Network
 (NLDN), 236, 237, 296, 301, 302,
 390, 392, 393, 399, 410
- Negative discharge, 235
- Negative stepped leader, 234, 244
- Network design, 117–119
- Nitrogen oxides (NOx), 529
- NLDN,*see* National Lightning Detection
 Network (NLDN)
- Noise, 261–263
- Noise Figure, 262
- Non-inductive, 448
 charging mechanism, 493
- Non-uniform model, 359–361
- North America, 350
- Nowcasting, 254, 266–268, 488
 of storms, 284
 of thunderstorms, 116, 253–268
- NOx, 559, 560, 563, 564
 from lightning, 248–249, 539, 540–
 543, 546
 production, 32, 51
- Nuclear weapons, 379
- O**
- Oceanic convection, 522
- ONERA mapper, 238
- Optical detectors, 522
- Optical lightning signatures, 287–304
- Optical power, 273
- Optical pulse, 273, 274–275, 278
- Optical radiation, 236, 272
- Optical spectrum of lightning, 272
- Optical Transient Detector (OTD), 236, 237,
 244, 278, 279, 312, 375, 524
- Orographic effect, 316
- Orographic forcing, 527
- Outside updraft, 60

- Ozone, 529
 budget, 543–544
 production, 552
- P**
- Peak
 current, 6, 7, 8, 9
 frequency, 354, 356, 371
- Permalloy core, 370
- PERUN (lightning location network), 132
- Phase, 358, 362, 365, 371, 374, 377
 velocity, 358, 365
- Photostationary state, 551
- Polar front, 526
- Polarity reversal, 94, 95
- Polarization corrected brightness temperatures (PCTs), 323, 324
- Polarization corrected temperature, 435
- Positive CG flash, 454
- Positive discharge, 233, 495
- Positive flash, 353
- Positive leader, 235
- Positron and x-ray feedback, 342–343 fig 15.6
- Potential gradient, 351, 379
- Potential well, 74, 75, 76, 78
- Precipitation, 84, 85, 95, 511
 charge, 61
 features, 315
 ice mass, 555
 over ocean, 539
 unshielding hypothesis, 103
- Precipitation Radar (PR), 313, 316, 436
- Preliminary breakdown, 74, 75, 244, 256
- PROFEO (lightning detection network), 248
- Prony algorithm, 372
- Propagation, 263
 law, 123
 parameters, 357, 358, 359, 360, 361, 367
 speed, 4, 5, 8, 9, 12
- Protection against Lightning Electromagnetic Impulse (LEMP), 586–590
- Q**
- Q-burst, 347, 352, 353, 377
- R**
- Radar, 348, 361, 450, 458, 465, 466, 467, 468, 469–472, 474–483, 484, 485, 510
 cell, 465, 466, 469, 470, 472, 475, 476, 477, 479, 485
 cores (U-shaped, V-shaped), 491
 reflectivity, 102, 436, 439
- Radiation burst, 235
- Radiative forcing, 538
- Rainfall, 374, 375, 377–378
 measurement technique, 455
 regime, 454
- Rainfall Lightning Ratio (RLR), 177–179
- Rain-to-Thunder days Ratio (RTD), 451, 456
- Rain-yield Per Flash (RPF), 449, 450, 451
- Real Time Event Processor (RTEP), 310
- Rear flank downdraft (RFD), 84
- Recoil streamer, 235, 256, 268
- Relative detection efficiency (RDE), 212
- Relativistic feedback mechanism, 333
- Relativistic Runaway Electron Avalanche (RREA) mechanism, 333
- Residual location error, 121, 122
- Resonance mode, 348, 353
- Resonator, 353, 354, 356
- Return stroke, 26, 29, 30, 48, 234, 244
 current, 4, 5, 7, 11
 model, 1, 11–16, 17
 speed, 9, 30
- RF emission, 254
- Rhode Island, 351, 352, 358, 359, 361, 362, 363, 364, 365, 371, 372, 373, 377, 379
- Riming rate, 87
- RINDAT (lightning location network), 124
- Ring of fire, 526
- Risetime, 9, 11, 12, 14, 16, 36, 41
- Rocket-triggered lightning, 332, 334, 337
- Rocket-and-wire technique, 23
- Rossby wave, 377
- Rotating updraft, 490
- RPF variability, 451
- Runaway breakdown, 333, 340
- Runaway electron(s), 233, 332–333, 341
 avalanches, 340–341
 simulations, 340
 theory and modeling, 340–343
- S**
- SAFIR, 165, 466, 467, 468, 475, 477
- Satellite based lightning detection, 275
- Satellite observations, 456, 522
- Scattering of light in clouds, 273–274
- Schumann resonances, 347–380, 522, 527
- Seasonal analysis, 315–316
- Seasonal changes, 282
- Seasonal migration, 375–376
- Seasonal variations, 194, 372, 373
- Seawater attachment, 302
- Semiannual variation, 374
- Severe storm, 88, 91, 454
- Severe weather, 137, 162, 179, 180, 181, 491

- Sferic/atmospheric, 291, 292, 293, 294, 296, 297, 302
 Shielding, 589, 591
 Shortwave radiation, 374
 Simulation of lightning, 546
 Single-cell storm, 489
 Single-station method, 350
 Skin currents, 370
 SNR, 261
 Solar cycle (11-year), 354
 Solar heating, 376
 Solar insolation, 521
 Solar march, 375
 Solar maximum, 356
 Solar minimum, 356
 Solar rotation period, 376
 Solar wind, 377
 Solar x-ray, 354
 Source intensity, 369
 Source-observer geometry, 354
 South America, 350, 351, 365, 374, 376
 Southern Mediterranean Region, 311
 Space charge region, 232
 Spanish Lightning Detection Network, 161, 164
 Special SensorMicrowave/Imager (SSM/I), 313
 Spectral methods, 347, 370–373
 Spherical coordinates, 360, 362
 Spider lightning, 267
 Sprite(s), 352, 361, 362, 363, 388, 390, 391, 392–394, 403, 404–410
 Squall lines, 452
 SR intensity, 347, 351, 352, 369, 380
 Static instability, 526
 Stepped leader, 29, 30, 255, 256, 335, 343
 STEPS, 388, 389, 391
 STERAO experiment, 558, 563
 Storm severity, 488
 Stratiform region, 455
 Stray flashes, 511
 Streamer, 233
 Stroke
 detection efficiency, 127
 discrimination, 165, 166, 167
 duration, 8
 locations, comparison, 150
 Sub-tropics, 525
 Supercell, 59, 60, 62, 83, 84–87, 91, 93, 94, 100, 107, 394, 411
 airflow, 85
 thunderstorm, 490–491
 Supercooled liquid water, 86
 Surface
 pressure, 376, 377
 temperature, 373, 375
 Surge protective device (SPD), 586, 587, 588, 589, 590, 591
 Symmetrical waveguide, 363
- T**
- TCS, 12, 13, 14, 15, 19
 TDTE (two-dimensional telegraph equation), 347, 360
 simulation, 361, 362, 363, 365
 solution
 analytical, 361
 numerical, 367
 technique, 360
 Temperature, 373, 374, 375, 376, 379, 380
 Terminator, 365, 366, 369
 Terrestrial gamma ray flashes (TGFs), 337
 Theory and modeling, runaway electron theory, 340–343
 Thermal capacity, 524
 Thermal equator, 524
 Thermal hypothesis, 459, 525
 Thermal inertia (of ocean), 375
 Thermalized channels, 233
 Thermodynamic properties, 375
 Thundercloud, 510
 Thunderdays, 188, 189, 190, 194, 195, 198, 374
 Thunderstorm, 265, 348, 350, 354, 356, 378, 466, 471, 472–484
 cells, 465–485
 charge distribution, 59
 day, 171, 173, 174, 222
 electrification, 524
 hazards, 200
 Thunderstorm Energetic Radiation Array (TERA), 344
 Tilted dipole, 102, 103, 106
 Time-of-arrival (TOA), 120, 142, 161, 164, 236, 254, 257, 259, 263, 264, 265–266
 Time interval between strokes, 8
 TLE (transient luminous event), 348
 TL model, 13, 15
 Tornado, 84, 85, 91, 92, 93, 95
 non-mesocyclonic, 489
 Total lightning, 115, 116, 128, 132–134, 253, 265, 267, 279
 event rates, 133
 Tower-induced lightning, 119
 Trade winds, 525

- Trailing stratiform precipitation, 403
TRMM Microwave Imager (TMI), 313, 436
Transient luminous events (TLE), 94, 387, 390, 401, 404, 410
Transient (Schumann resonance), 347, 352, 354, 359, 361, 372, 377
Transitionospheric Pulse Pair (TIPP), 287, 295, 296, 301
Transmission line model, 11, 12
Traveling current source, 12
Triggered lightning, 23–50, 224
Tripole structure, 97, 98, 103–104, 106
TRMM, 436, 443
TROCCINOX campaign, 124, 125
TROCCINOX experiment, 559, 563, 564
Tropical atmosphere, 376, 377, 379
Tropical convection, 531
Tropical cyclone, 492–493, 501
Tropical precipitation, 530
Tropical Rainfall Measuring Mission (TRMM), 276, 284, 309, 314–315
Tropical region, 216–217
Tropical storms, 284
Tropics, 350, 374
Tropospheric chemical mechanism, 538
Tropospheric chemistry, 529
Tropospheric ozone, 538
Twenty megahertz And Twelve bit Receiver (TATR), 289
See also, Fast On-orbit Recording of Transient Events (FORTE) satellite
- U**
ULF (ultra low frequency), 348
Uniform cavity, 369
Uniform model, 354, 357, 359–361
Updraft(s), 379, 542–543
 intensity, 524–525
 velocities, 540
 volume, 557
Upper characteristic altitude, 361
Upward connecting leader, 3, 4, 30, 32, 35, 51
Upward discharge, 66
Upward positive leader (UPL), 26, 30, 33
- V**
Variation with latitude, 197
Vertical charge moment, 349, 352
Vertical electric field, 10, 11, 15, 16, 17, 18
Vertical NO_x distribution, 563
Vertical precipitation profile, 313
Vertical velocity, 448, 457, 459
Very high frequency (VHF) lightning signatures, 254–257, 263–264, 265–266, 268, 290, 291, 293, 294, 296, 297, 300, 301, 302, 303, 304
- VHF interferometric technique, 236
VHF,*see* Very high frequency (VHF) lightning signatures
VHF Sources, 163, 165, 181
VLF/LF
 cloud strokes, 129
 lightning signatures, 288, 291, 293, 294, 295, 298, 304
 network, 115–138, 236
VLF (very low frequency), 377
Vortical hot towers, 304
V profile, 61
- W**
Warmer climates, 379
Warmer world, 379
Warm front, 526
Warning, 267, 268
Water production, 466, 471, 472–474, 475, 482, 483, 485
Water vapor, 374, 376, 379, 528
Waveform discrimination, 116
Waveguide, 353, 357, 359, 360, 361, 363, 365, 366, 370
Wavelength, 260
Wavenumber-1, 376, 377
Western Pacific Ocean, 376
Westward propagation, 377
Wind gust damage, 202–204
Wind shear, 489, 559
WWLLN, 408, 410
- X**
X-ray(s), 32
 burst, 354
 detectors, 335
 emission from lightning, open questions on, 343–344
 feedback mechanism, 343
 and gamma-ray observations, 334–340
 from laboratory sparks, 338–340 fig 15.5
 from natural cloud-to-ground lightning, 335–336 fig 15.3
 and positron feedback, 343
 from triggered lightning, 334–335 fig 15.2
- Y**
Yucca Ridge Field Station (YRFS), 391
- Z**
Zel'dovich mechanism, 551
ZEUS (lightning detection network), 440, 443